Proceedings

32nd ASPE Annual Meeting

October 29 - November 3, 2017

The Westin Charlotte
Chartlotte, North Carolina, USA

American Society for
Precision Engineering

P.O. Box 10826, Raleigh, NC 27605-0826
(919) 839-8444 | Fax (919) 839-8039

Proceedings of

The Thirty-Second Annual Meeting of the

American Society for Precision Engineering

October 29 – November 3, 2017
The Westin Charlotte
Charlotte, North Carolina, USA

The American Society for Precision Engineering (ASPE) is a multidisciplinary professional and technical society concerned with research and development, design, manufacture and measurement of high accuracy components and systems. ASPE activities encompass relevant aspects of mechanical, electronic, optical and production engineering, physics, chemistry, and computer and materials science. Membership is open to anyone interested in any aspect of precision engineering.

Founded in 1986, ASPE provides a focus for a diverse but important community. Other professional organizations have covered aspects of precision engineering, always as a sideline to their principal goals. ASPE is based on the core of generic concepts necessary to achieve precision in any application; independent of discipline, ASPE intends to be the focus for precision technology -- and to represent all facets from research to application.

The Annual Meeting has evolved into an international forum for the exchange of ideas and presentation of research results relating to precision engineering, metrology, controls, and system integration. Precision engineers and scientists from private industry, government laboratories, and universities meet to learn about the latest developments and to exchange ideas about the future directions of these technologies.

ASPE -- The American Society for Precision Engineering
301 Glenwood Avenue, Suite 205, Raleigh, NC 27603
P.O. Box 10826, Raleigh, NC 27605
Telephone: 919- 839-8444
www.aspe.net

Preface

This book comprises the proceedings of the 32nd ASPE Annual Meeting. The contributions reflect the authors' opinions and are published as presented to ASPE, without change. Their inclusion in this publication does not necessarily constitute endorsement by the ASPE, or its editorial staff.

Individual readers of this book and nonprofit libraries acting for them are permitted to make fair use of the material contained in this book to be used in teaching or research; provided they copy said paper in total, as written by the author. Permission is granted to quote excerpts from the scientific or technical works in this book with proper acknowledgment of the source to include: The author's name, the book name, and the ASPE tag line. Reproduction of figures and tables is likewise permitted from the contents of this book, provided that the same acknowledgment of the same source and content is permitted.

Any other type reproduction, systematic copying or multiple reproduction of any material in this book is expressly prohibited except with the written permission of the ASPE editorial staff, addressed to the Society's headquarters

ISBN 978-1-887706-74-2

2017

American Society for Precision Engineering
301 Glenwood Avenue, Suite 205
Raleigh, NC 27603

Printed in the United States of America

Organizing & Technical Program Committee

Annual Meeting Chairperson

Vivek G. Badami
Zygo Corporation

Technical Leadership Committee Chairpersons

Dannis M. Brouwer, University of Twente

Controls and Mechatronics

Brandon M. Lane, National Institute of Standards & Technology
Characterization

Jimmie A. Miller, University of North Carolina-Charlotte

Metrology Systems

Robert M. Panas, Lawrence Livermore National Laboratory

Micro and Nano Technologies

Deepak Ravindra, Micro-LAM

Precision Manufacturing

Mark A. Stocker, Cranfield Precision, Division of Fives Landis Ltd.

Precision Design

Committee Members

Gorka Aguirre, IK4-IDEKO
Luis A. Aguirre, 3M Company
David A. Arneson, Professional Instruments Company
Rick Baade, Eindhoven University of Technology
Andrew Bagley,
Cranfield Precision, Div. of Fives Landis Ltd.
Barkin Bakir, Western Michigan University
Martin F. Bamberger, DWFritz Automation
Michael L. Barkman, Zygo Corporation
Marcin B. Bauza, Carl Zeiss Industrial Metrology
Alex Bean, Corning Tropel Corporation
Eric Belski, Aerotech, Inc.
Michael Binnard, Nikon Research Corp of America
Niels Bosmans, KU Leuven
Christopher A. Brown, Worcester Polytechnic Institute
Eric S. Buice, Lawrence Berkeley National Laboratory
Andrew Cao, Lawrence Livermore National Laboratory
Nelson Cardenas, Oculus
Shih-Chi Chen, The Chinese University of Hong Kong
Chi-Fai Cheung, The Hong Kong Polytechnic Univ.
Andre A. Claudet, Sandia National Laboratories
Michael A. Cullinan, The University of Texas at Austin
Timothy M. Dalrymple, Magic Leap, Inc.
Andrew J. Devitt, New Way Air Bearings
John W. Dorsey-Palmateer,
Boeing Research & Tech., Retired
Thomas A. Dow, North Carolina State University
Andrew Duenner, Magic Leap, Inc.
Ahment Alper Dumanli, Oregon State University
Nicholas J. Duncan, Aerotech, Inc.
Martin R. Dury, National Physical Laboratory
Kevin E. Elliott, Corning, Inc.
Jonathan D. Ellis, University of Rochester
Kaan Erkorkmaz, University of Waterloo
Christopher J. Evans,
University of North Carolina-Charlotte
Massimiliano Ferrucci, National Physical Laboratory
Pete J. Fitsos, Lawrence Livermore Nat'l Laboratory
Craig R. Forest, Georgia Institute of Technology
Sean Garner, Corning Incorporated
Anthony W. Gatica, M3 Design, Inc.
Steven R. Gillmer, MIT Lincoln Laboratory
Axel Grabowski, Physik Instrumente GmbH & Co. KG
Robert D. Grejda, Corning Tropel Corporation
Thomas Haase, Physik Instrumente GmbH & Co. KG
Gregory L. Holst, Georgia Institute of Technology
Jonathan B. Hopkins, Univ. of California – Los Angeles
Bradley H. Jared, Sandia National Laboratories
Michael R. Johnson, Magic Leap, Inc.
Sajad Kafashi, University of North Carolina-Charlotte
Byron R. Knapp, Professional Instruments Company
Mark T. Kosmowski, Electro Scientific Industries, Inc.
William S. Land II, Aerotech, Inc.
Richard K. Leach, University of Nottingham
ChaBum Lee, Tennessee Technological University
Don A. Lucca, Oklahoma State University
Stephen J. Ludwick, Aerotech, Inc.
Dan E. Luttrell, Kriterion, LLC
Eric R. Marsh, The Pennsylvania State University
Fabrice Matichard, LIGO Caltech/MIT
Kate M. Medicus, Optimax Systems, Inc.

Glenn J. Miller,
Cranfield Precision, Div. of Fives Landis Ltd.
Hossein Mohammadi, Western Michigan University
Joshua D. Montaño, Los Alamos National Laboratory
Darcy Montgomery, Cedarflat Precision Inc.
Bala Muralikrishnan,
Nat'l Institute of Standards & Technology
Minkyun Noh, Massachusetts Institute of Technology
Bartosz Nowakowski, Hysitron, Inc.
Brian P. O'Connor, Aerotech, Inc.
Chinedum E. Okwudire, University of Michigan
Joseph D. Owen,
University of North Carolina-Charlotte
Ozkan Ozturk, Canon Nanotechnologies, Inc.
Paul R. Parise, Convergent Technologies
Steven R. Patterson,
University of North Carolina-Charlotte
Mark E. Peeples, Electro Scientific Industries, Inc.
Antonius T. Peijnenburg, VDL ETG
Michael G. Pierse,
Cranfield Precision, Div. of Fives Landis Ltd.
Jon R. Pratt, Nat'l Institute of Standards & Technology
Suresh Kumar Ramasamy, Apple Inc.
Sourabh K. Saha,
Lawrence Livermore National Laboratory
Burak Sencer, Oregon State University
Richard M. Seugling,
Lawrence Livermore National Laboratory
Hongliang Shi, Goldey-Beacom College
Deming Shu, Argonne National Laboratory
Alexander H. Slocum,
Massachusetts Institute of Technology
Stuart T. Smith, University of North Carolina-Charlotte
Robert A. Smythe, Äpre Instruments, LLC
Rongrong Sun, Washington State University
Shingo Tajima, Oregon State University
John S. Taylor, University of North Carolina-Charlotte
Joshua Tarbutton,
University of North Carolina-Charlotte
Hy D. Tran, Sandia National Laboratories
David L. Trumper,
Massachusetts Institute of Technology
Mario O. Valdez, Los Alamos National Laboratory
Lucas M. Valdez, Los Alamos National Laboratory
Jan van Eijk, MICE bv
Herminso Villarraga-Gómez, Nikon Metrology, Inc.
Curtis S. Wilson, Omron Delta Tau
Xiangzhi Yu, University of Rochester
Rayne Zheng, Virginia Polytechnic Institute
Lei Zhou, Massachusetts Institute of Technology
John C. Ziegert, University of North Carolina-Charlotte

ASPE gratefully acknowledges the time and the effort given by the Organizing and Technical Program Committee to bring the precision engineering community this program.

Contents

Preface ii

Organizing Committee . . . . . iii-iv

Table of Contents v

ASPE Lifetime Achievement Award vi

ASPE Distinguished Service Award vii

2017 Scholarship Recipients and Sponsors viii

Sustaining Corporate Sponsors . . . . . ix-x

Corporate Sponsors xi

Technical Paper Index 1-12

Technical Papers 15-666

Author Index 667

ASPE Lifetime Achievement Award

Professor Ekkard Brinksmeier

University of Bremen

The Lifetime Achievement Award was conceived to honor particularly noteworthy contributions to the advancement of the discipline and/or Society over a career of service in precision engineering, and this year, ASPE is pleased to present this very special award to **Professor Ekkard Brinksmeier** for leadership in developing manufacturing technology and associated metrology over a broad range of fabrication processes for nearly 4 decades.

Professor Brinksmeier's early seminal contributions in evaluation of surface integrity has been followed with continuing contributions over the intervening 35 years or so in the understanding of the effect of processes including grinding, hard turning and single point diamond turning on the near surface structure and properties of a variety of materials. At one extreme of the size scale of single point diamond machining, his group pioneered what we now know as the "slow slide servo" approach to manufacturing large off-axis aspherics by on-axis machining. At the other end of the spectrum, Brinksmeier's group developed "micro-chiseling" to produce molds for replication of arrays of retroreflectors.

For many, the high temperatures generated in fine grinding of hard steels was a limitation. For Brinksmeier's group it was an opportunity. With appropriate control, this localized heat source could provide a combination of material removal and heat treatment – the birth of the concept of "grind-hardening." Chemistry is established as one limitation on the materials that can be "diamond turned." Some focused on the fundamental chemistry. Brinksmeier and his colleagues asked a different question; can we modify the surface chemistry to limit the chemical wear? The answer is "yes."

Prof. Dr.-Ing. habil. Prof. h.c. Dr.-Ing. E.h. Ekkard Brinksmeier graduated from the University of Hannover, Germany. He received his Dr.-Ing. Degree in mechanical engineering in 1982 and worked as Chief Engineer from 1982-1992 at the Institute for Production Engineering and Machine Tools, IFW, Hannover University, Germany.

After finishing his habilitation (extra scientific thesis) in 1992 he became a Full Professor at the University of Bremen, Director of the IWT, Institute for Materials Science, and Director of the LFM, Laboratory for Precision Machining. His scientific interests and research areas lie in the field of advanced manufacturing processes with special focus in the areas of ultraprecision machining processes down to nanometer tolerances, process integration, the development of sensor integrated tools, research and development of advanced coolants in metal cutting, and the generation of functional surfaces by machining. He has been the coordinator of the Transregional DFG Collaborative Research Center SFB/TR4, "Process Chains for the Replication of Complex Optics" from 2001-2012. In 2014 he became the coordinator of a new established Collaborative Research Center SFB/TRR 136 "Process Signatures" which focuses on surface integrity and which involves participation of the universities of Bremen, Aachen, and Stillwater, Oklahoma, USA. He has published and co-authored more than 600 scientific papers and employs 30 scientific staff (Ph.D. candidates), most of them funded by third party projects.

Prof. Brinksmeier has received several awards, most notably the CIRP F. W. Taylor Medal, and the DFG Gottfried Wilhelm Leibniz Award being the most prestigious German research award. He was also awarded an Advanced Investigator Grant of the European Research Council, ERC, and has received the SME Frederick W. Taylor Research Medal from SME. Since the year 2012 he holds an Honorary Dr.-Ing. Degree from the Technical University Aachen, Germany, has received the Lifetime Achievement Award from eu**spen** in 2014, and was awarded an Honorary Professorship of Tianjin University, China, in 2017.

Prof. Brinksmeier is Fellow and Past President of CIRP, Fellow and Past President of the European Society for Precision Engineering and Nanotechnology, eu**spen**, Fellow of SME, and Fellow of ISNM, and held leadership positions of several associations and institutions including DFG, AiF and others.

ASPE Distinguished Service Award

Dr. Byron R. Knapp

Professional Instruments Company

The Distinguished Service Award was conceived to honor noteworthy contributions and service to the Society, and this year, ASPE is pleased to present this award to **Dr. Byron R. Knapp**. Dr. Knapp has been a member of ASPE for the last twenty years. He has served on the ASPE Board of Directors for multiple years as Vice President, President, Immediate Past President and as Nominating Committee Chair, Nominating Committee Chair-Elect and Nominating Committee Immediate Past Chair. Dr. Knapp served as the co-chairperson for the 2008 Summer Topical Meeting and as Chairperson for the 2013 Annual Meeting, and he has served on numerous Annual Meeting committees. He assisted Jim Bryan and continues helping Eric Marsh with the ASPE tutorial on Precision Spindle Metrology. Recently Dr. Knapp has served as Exhibits Chairperson and as fundraiser for the Annual Meeting and the Student Challenge.

Dr. Knapp's career in precision engineering began helping out as an undergraduate in the lab of new Penn State faculty member Eric Marsh. For the next seven years, Dr. Knapp was fortunate to learn from Professor Marsh during the school year and at ANSYS, NIST, Weldon Machine Tool, Professional Instruments, Tropel, and Moore Tool during the summers. He went on to receive his BS, MS, and PhD degrees in Mechanical Engineering. Dr. Knapp joined Professional Instruments Company in 2008 as Senior Engineer responsible for design analysis, finite element analysis, modal and dynamic testing, and forays into oil hydrostatic spindles. As a student and a professional, he has published at ASPE meetings including both oral and poster presentations on topics from Hubble instrument alignment to Blu-ray mastering.

2017 Scholarship Recipients

National Science Foundation Grants

Students who are studying at United States Institutions are supported by the National Science Foundation under Grant No 1644838 to attend the 32nd Annual Meeting of the American Society for Precision Engineering. Support is in the form of the conference registration fee.

ASPE is grateful to the National Science Foundation for its support of students to attend the 32nd Annual Meeting of the American Society for Precision Engineering. This support provides student participants with opportunities to exchange ideas with leading reserachers and engineers from worldwide industrial and governmental facilities, as well as with students and faculty from both domestic and international universities. Student participants will learn the latest research areas and results in precision engineering fields of interest. These opoortunities will not only improve the students' knowledge in the field, but also develop scientists and engineers who are ideally suited to create the next generation of designs in optics, metrology and VSLI manufacturing that will push manufacturing and measurement capabilities.

Carl Zeiss Student Scholarship

The winner of the 2017 Carl Zeiss Student Scholarship is **Ian S. Ladner**, The University of Texas at Austin (Michael A. Cullinan, Advisor). This award includes the ASPE Annual Meeting registration fee, 4 tutorial fees, lodging and travel expenses to the Annual Meeting. In addition, the scholarship provides for travel and lodging to Maple Grove, Minnesota to visit Carl Zeiss Industrial Metrology. Mr. Ladner is the fifth recipient of the Carl Zeiss Student Scholarship awarded through ASPE.

ASPE Student Scholarships

ASPE is proud to award 2 student scholarships for the 32nd ASPE Annual Meeting in Charlotte, North Carolina. This year's scholarship recipients are **Abolfazl Zolfaghari**, Tennessee Technological University (ChaBum Lee, Advisor) and **Navid Farahi**, University of North Carolina-Charlotte (Faramarz Farahi, Advisor). The ASPE Student Scholarships include a waiver of the Annual Meeting registration fee and 4 tutorial fees. It also includes an honorarium to cover travel and lodging expenses to the 32nd ASPE Annual Meeting in Charlotte. The ASPE Student Scholarships were made possible by Corning Incorporated, Lion Precision, Moore Nanotechnology and many contributing members.

ASPE 2017 Sustaining Corporate Sponsors

3M Company
St. Paul, MN 55144
Phone: 888-364-3577
www.mmm.com

Aerotech, Inc.
101 Zeta Drive
Pittsburgh, PA 15238-2897
Phone: 412-963-7470
www.aerotech.com

Ametek Precitech, Inc.
44 Blackbrook Road
Keene, NH 03431
603-357-2511
www.precitech.com

Carl Zeiss Industrial Metrology LLC
6250 Sycamore Lane North
Maple Grove, MN, 55369
Phone: 763-744-2400
www.zeiss.com/metrology

Chardon Tool
115 Parker Court
Chardon, OH 44024
440-286-6440
www.ChardonTool.com

Cranfield Precision
Division of Fives Landis Ltd.
Woburn House
3 Adams Close
Kempston, Bedford, MK42 7 JE
United Kingdom
Phone: +44 (0)1234 312820
www.cranfieldprecision.com

Lion Precision
563 Shoreview Park Road
St. Paul, MN 55126-7014
Phone: 651-484-6544
www.lionprecision.com

Mahr Inc.
1144 Eddy Street
Providence, RI 02905
401-782-3168
www.mahr.com

ASPE 2017 Sustaining Corporate Sponsors

Makino
7680 Innovation Way
Mason, OH 45040
Phone: 513-573-7200
www.makino.com

Moore Nanotechnology Systems LLC
230 Old Homestead Highway
Swanzey, NH 03446
Phone: 603-352-3030
www.nanotechsys.com

New Way Air Bearings
50 McDonald Boulevard
Aston, PA 19014
610-494-6700
www.newwayairbearings.com

Physik Instrumente
16 Albert Street
Auburn, MA 01501
508-832-3456
www.pi-usa.us

Specialty Components
14 Village Lane
Wallingford, CT 06492
203-284-9112
www.specialtycomponents.com

VDL Enabling Technologies Group USA
3758 Spinnaker Court
Fremont, CA 94538-1706
510-996-4662
www.vdletg.com

ASPE 2017 Corporate Sponsors

ADCOLE Corporation
669 Forest Street
Marlborough, MA 01752
Phone: 508-485-9100
www.adcole.com

Alicona
1261 Humbracht Circle
Suite G
Bartlett, IL 60103 USA
Phone: 630-372-9900
www.alicona.com

Center for Precision Metrology
University of North Carolina at Charlotte
9201 University Blvd.
Charlotte, NC 28223
Phone: 704-687-8499
cpm.uncc.edu/

Contour Fine Tooling, Inc.
143 Jaffrey Road
Marlborough, NH 03455
Phone: 603-876-4908
www.contour-diamonds.com

Corning Inc.
Corning, NY 14831
Phone: 607-974-3842
www.corning.com

K & Y Diamond
2645 Diab
Laurent, Quebec H4S 1E7
Canada
514-333-5606
www.kydiamond.ca

Philips Innovation Services
High Tech Campus 7
5656 AE Eindhoven
The Netherlands
31-40-27-48060
www.innovationservices.philips.com

Prior Scientific, Inc.
80 Reservoir Park Drive
Rockland, MA 02370
781-878-8442
www.prior-us.com

Professional Instruments Company
7800 Powell Road
Hopkins, MN 55343
952-933-3315
www.airbearings.com

Zygo Corporation
Laurel Brook Road
Middlefield, CT 06455-0448
Phone: 860-347-8506
Toll-free: 800-ZYGO-NOW
www.zygo.com

Technical and Poster Sessions

Welcome Remarks & Session 1

Precision Engineering Potpourri

Tuesday, October 31, 2017, 8:00 AM - 10:00 AM

Session Chairs: Robert D. Grejda (Corning Tropel Corporation) and Brian P. O'Connor (Aerotech, Inc.)

1. **Diamond Tool Wear/Built-up Edge Machining Ferrous Materials**
   Dow, T. A.; Garrard, K. P. (North Carolina State University); Suit, B. M. (Lockheed Martin) 15
2. **Optical Form and Relational Metrology of Aspheric Micro Optics**
   Colonna de Lega, X.; Dresel, T.; Liesener, J.; Fay, M. F.; Gilfoy, N.; Delldonna, K.; de Groot, P. J. (Zygo Corporation) 20
3. **Optimal Three-Point Mounts for Square and Rectangular Plates**
   Verdirame, J. M.; Nayfeh, S. A. (Physical Precision, LLC) 24
4. **The Problem of 'Weak' Equivalence in Measurement Comparisons: X-ray CT Metrology Case**
   Villarraga-Gómez, H. (Nikon Metrology, Inc.); Smith, S. T. (University of North Carolina-Charlotte) 30
5. **Additive Manufacturing of Reflective Optical Components**
   Jared, B. H.; Chavez, T.; Choi, J.; Cook, A. W.; Dianotnio, C. B.; Reinholtz, W.; Saavedra, M. P.; Saiz, D. J.; Winrow, E. G. (Sandia National Laboratories) 36
6. **Contactless Shape Manipulation of Thin Substrates Using Air Bearing Table**
   Spaan-Burke, T. M.; van Dam, T.; Overschie, P. M.; Spaan, H. A. M. (IBS Precision Engineering) 40

Session 2

Controls & Mechatronics

Tuesday, October 31, 2017, 10:30 AM - 12:00 PM

Session Chairs: Dannis M. Brouwer (University of Twente) and Stephen J. Ludwick (Aerotech, Inc.)

1. **Trends in Control Techniques for Precision Mechatronic Systems**
   Brouwer, D. M. (University of Twente); Ludwick, S. J. (Aerotech, Inc.); Okwudire, C. E. (University of Michigan); Peijnenburg, A. T. (VDL Enabling Technologies Group) 46
2. **Detailed Experimental Evaluation of the Compliant Joint Method for Feedforward Compensation of Pre-Motion Friction**
   Dong, X.; Okwudire, C. E. (University of Michigan) 52
3. **Multi-Axis Trajectory Generation with Optimal Frequency Spectrum for Vibration Avoidance**
   Dumanli, A. A.; Sencer, B. (Oregon State University) 57

4. **Strong and Quiet Linear Iron-core Synchronous Motor**
Yoon, J. Y.; Trumper, D. L. (Massachusetts Institute of Technology) 63

5. **Hybrid Design Approach for Constrained Layer Dampers to Balance Dynamic Performance in Combination with Geometrical Contraints**
Verbaan, K.; Duiven, M.; Henselmans R.; Nuij, P. W. J. M.; Rijlaarsdam, D. J. (NTS-Group). 68

Session 3

Characterization

Wednesday, November 1, 2017, 8:30 AM - 10:00 AM

Session Chairs: Brandon M. Lane (National Institute of Standards & Technology) and Christopher J. Evans (University of North Carolina-Charlotte)

1. ***Characterization: Extracting Key Signatures from Complex Data**
Lane, B. M. (National Institute of Standards & Technology)

2. **Observations on Stitching Interferometry on Parts with Radically Different Surface Topographies**
Hovis, C. D.; Reese, Z.; Shahinian, H.; Evans, C. J. (University of North Carolina-Charlotte) 72

3. **Quantification of Part Profile Scanning Error**
Javidpour, F.; Morse, E. P. (University of North Carolina-Charlotte) 78

4. **Experimental Verification of One Side Constrained Minimum Total Least Square Algorithm for Planar Datum Establishment and Associated Uncertainty Analysis**
Kang, W.; Morse, E. P. (University of North Carolina-Charlotte) 84

5. **An Evaluation of Non-contact Laser Scanner Performance Using Calibrated Artifacts**
Gomez, M.; Vaccaro, C.; Maness, C.; Lawrence, C.; Murray, C.; Vargas, L.; Caskey, G. W.; Evans, C. J.; Schmitz, T. L. (University of North Carolina-Charlotte) 90

Session 4

Precision Micro-Nano Developments

Wednesday, November 1, 2017, 10:30 AM - 12:00 PM

Session Chairs: Robert M. Panas (Lawrence Livermore National Laboratory) and Michael A. Cullinan (The University of Texas at Austin)

1. ***Overview of Research in Precision Micro- and Nano-technology**
Panas R. M. (Lawrence Livermore National Laboratory)

2. **Integration of Wafer-Level Solar Cells and Micro-Optic Concentrators for Micro-Scale Concentrating Photovoltaics**
Jared, B. H.; Hains, C.; Keeler, G. A..; Miller, B. K.; Paap, S. M.; Saavedra, M. P.; Sweatt, W. C.; Tauke-Pedretti, A.; Wood, M. (Sandia National Laboratories); Li, L.; Li, D.; Gu, T.; Hu, J. (Massachusetts Institute of Technology) 95

3. **DMD-Based Random-Access Scanner for Fast 3D Imaging and Fabrication**
Geng, Q.; Wang, D.; Chen, S-C (The Chinese University of Hong Kong). 99

***No Abstract Available**

4. **Design of High Resolution and High Force MEMS Tensile Testers for Direct Metrology of Submicron Polymer Features**
Ladner, I. S.; Cullinan, M. A. (The University of Texas at Austin); Saha, S. K.; Cao, A. (Lawrence Livermore National Laboratory). 103

5. **Automated Assembly with Optical Tweezers**
Shaw, L.; Chizari, S.; Porter, M.; Austin, S.; Hopkins J. B. (University of California - Los Angeles) 109

6. **Multi-Beam Interference Lithography Based on Evanescent Wave for Functional Nano-Complex Surface**
Masui, S.; Suzuki, Y.; Matsumoto, Y.; Michihata, M.; Takamasu, K.; Takahashi, S. (The University of Tokyo) 113

Session 5

Metrology Systems

Wednesday, November 1, 2017, 1:30 PM - 3:00 PM

Session Chairs: Jimmie A. Miller (University of North Carolina-Charlotte) and Kate M. Medicus (Optimax Systems, Inc.)

1. ***The Role of Precision Engineering for the Revision of the International System of Units**
Schlamminger, S. (National Institute of Standards & Technology)

2. **Computer Generated Holograms as 3-Dimensional Calibration Artifacts**
Parks, R. E. (Optical Perspectives Group, LLC); Ziegert, J. C.; Groover, J. (University of North Carolina-Charlotte) 117

3. **Colored Light Interferometry**
Abolbashari, M. (Optoniks, Inc.); Azari, M.; Habibi, N.; Farahi, F. (University of North Carolina-Charlotte). 121

4. **Dense Error Evaluation for Laser Trackers**
Morse, E. P.; Heysiattalab, S. (University of North Carolina-Charlotte); Wang, J. (Southwest Jiaotong University) 127

Session 6

Applications of Precision Design and Manufacturing to Telescopes and Synchrotron Optics

Thursday, November 2, 2017, 8:30 AM - 10:00 AM

Session Chairs: Jonathan D. Ellis (University of Rochester) and Senajith B. Rekawa (Lawrence Berkeley National Laboratory)

1. **Optomechanical Design and Fabrication of a Snap Together Freeform TMA Telescope**
Horvath, N.; Barron, I.; Owen, J. D.; Dutterer, B. S.; Davies, M. A. (University of North Carolina-Charlotte); Schiesser, E.; Bauer, A. M.; Rolland, J. P. (University of Rochester) 133

2. **Fabrication of Lightweight Monocrystalline Silicon Mirror Segments to Enable High Resolution X-ray Telescopes**
Biskach, M.; Riveros, R. E.; Zhang, W. W. (NASA Goddard Space Flight Center); Allgood, K.; Kearney, J.; Mazzarella, J.; Solly, P. (Stinger Ghaffarian Technologies, Inc.) 139

***No Abstract Available**

3. **Fabrication of X-ray Imaging Mirrors for an Achromatic and High-Resolution Full-Field X-ray Microscope**
Yamada, J.; Matsuyama, S.; Yasuda, S.; Sano, Y.; Yamauchi, K. (Osaka University) 143

4. **Design of Positioning System for X-ray Split and Delay**
Shi, H.; Zhu, D.; Schafer, D.; Barada, A. H.; James, J. H.; Lee, L.; Johnson, T.; Sun, Y.; Gumerlock, K. L.; Zhang, L.; Osier, T. O.; Whitney, R. A.; Smith, B. E. (SLAC National Accelerator Laboratory) 147

Session 7

Precision Design

Thursday, November 2, 2017, 10:30 AM - 12:00 PM

Session Chairs: Mark A. Stocker (Cranfield Precision, Division of Fives Landis Ltd.) and Mark T. Kosmowski (Electro Scientific Industries, Inc.)

1. ***Precision Machine Design Review**
Stocker, M. A. (Cranfield Precision, Division of Fives Landis Ltd.)

2. **Paradigm Change in Gear Inspection Based on a Holistic Description, Measurement and Evaluation of Gear Flanks**
Goch, F. G.; Ni, K.; Peng, Y. (University of North Carolina-Charlotte); Guenther, A. (Reishauer AG) 151

3. **Error Budgeting Analysis for Determining Axis Configuration of Ultra Precision Jig Grinding Machines**
Badrawy, S. J. (Moore Nanotechnology Systems, LLC) 158

4. **Additively Manufactured Lattice Structures for Precision Engineering Applications**
Elmadih, W.; Syam, W. P.; Maskery, I.; Leach, R. K. (University of Nottingham) 164

5. **Design of a Long-Travel, Flexure-Based Nanopositioner with Reduced Higher Order Resonant Modes**
Roy, N. K.; Cullinan, M. A. (The University of Texas at Austin) 170

Session 8

Precision Manufacturing Technology

Thursday, November 2, 2017, 1:30 PM - 3:00 PM

Session Chairs: Deepak Ravindra (Micro-LAM Technologies, LLC) and Lucas M. Valdez (Los Alamos National Laboratory)

1. ***Precision Machining Review**
Ravindra, D. (Micro-LAM Technologies, LLC)

2. **Recent Advances in Ultra-precision Milling with Multiple-cutting Edges**
Schönemann L.; Riemer, O.; Brinksmeier, E. (University of Bremen) 175

3. **Grinding of Silicon Carbide for Freeform Optics**
Shanmugam, P.; Sizemore, N. E.; Owen, J. D.; Davies, M. A. (University of North Carolina-Charlotte); Fess, E.; Hamel, J.; Ross, J. (Optipro Systems, LLC); Lambropoulos, J. C. (University of Rochester) 180

***No Abstract Available**

4. **An Investigation of Multi-Jet Polishing of Precision Surfaces**
Cheung C-F.; Wang, C. J.; Ho, L.-T.;
Lee, W. B. (The Hong Kong Polytechnic University) 186

5. **High-pressure Aerostatic Bearing Technology - Combining Robustness with Speed, Thermal Stability and Low Errors in Motion**
Dupont, R. (Levicron GmbH) 192

Poster Session 1

Tuesday, October 31, 2017, 4:30 PM - 6:00 PM

Session Chairs: Brian P. O'Connor (Aerotech, Inc.) and Michael L. Barkman (Zygo Corporation)

Additive Manufacturing

1. **Current Use and Potential of Additive Manufacturing for Optical Applications**
Brunelle, M.; Ferralli, I.; Whitsitt, R.; Medicus, Kate M. (Optimax Systems, Inc.) 198

Characterization, Data Reduction and Applications of Measurement Science

2. **Statistical Analysis of Surface Measurements and Images**
Azimi, F.; Young, B.; Mullany, B. A. (University of North Carolina-Charlotte) 204

3. **Metrology Techniques for Evaluating and Aligning DESI Focal Plate Structure**
Duan, Y.; Ahlen, S. P. (Boston University); Buice, E. S.;
Claybaugh, T. M. (Lawrence Berkeley National Laboratory) 208

4. **Experimental Fused Illumination Mechanism Design with Discriminant Function for Steel Plate**
Kim, G-B; -Bum; Doek, C-E (Korea National University of Transportation) 214

5. **Any-Degree-of-Freedom Registration of Three-Dimensional Surfaces with Unbalanced Deviations**
Liu, S.; Cheung C-F; Wang, C. J. (The Hong Kong Polytechnic University) 219

6. **Methods to Determine the Center of Contrast Targets from Terrestrial Laser Scanner Data**
Rachakonda, P. K.; Muralikrishnan, B.; Sawyer, D. S.
(National Institute of Standards & Technology); Wang, L. (China Jiliang University). 223

7. **Compensation of Measured Frequency Response Functions Using Accelerometer Models and Inverse RCSA**
Satyanarayana, H.; Schmitz, T. L. (University of North Carolina-Charlotte 230

8. **Task-Specific Measurement Uncertainty of a Hemispherical Artifact**
Valdez, L. M.; Valdez, M. O.; Montaño, J. D. (Los Alamos National Laboratory) 236

9. **Characterizing Spatial Resolution of a Fringe Projection System for Measuring Additively Manufactured Surfaces**
Zhang, B.; Davies, A. D.; Ziegert, J. C.; Evans, C. J.
(University of North Carolina-Charlotte). 241

Historical and/or Education Perspective on Precision Engineering

10. **Managing Risks when Single-Point Diamond Machining a 24-Day-Cut Germanium Blazed Diffraction Grating**
Montesanti, R. C.; Kuzmenko, P. J.; Little, S.; Bixler, J. V.; Jackson, J. L.; Mirkarimi, P.; Priest, R. E.; Thelin, P. A.; Watkins, J. A.; Yoxall, B. E. (Lawrence Livermore National Laboratory) 246

Metrology Systems and Techniques

11. **Stress Induced Frequency Modulation of a Microchip Green Laser**
Arumugam, K.; Smith, S. T.; Her, T.-H. (University of North Carolina-Charlotte) 253

12. **Simultaneous Measurement of Backlash and Geometric Errors of Linear Axes with a Laser Tracer**
Cong, H.; Chen, Y.; Zhang, C.; Han, L.; (Xi'an Jiaotong University) 257

13. **Multi-Scale Contextual Characterization via High Throughput Multi-beam Electron Microscopy**
Crosby, K. (Carl Zeiss Microscopy, LLC); Bauza, M. B. (Carl Zeiss Industrial Metrology); Garbowski, T.; Eberle, A. L. (Carl Zeiss Microscopy GMBH) 261

14. **Error Budgeting Analysis for X-ray Systems Using a 0D Uncertainty Model**
Cuadra, J. A.; Divin, C. J.; Panas R. M. (Lawrence Livermore National Laboratory) 267

15. **An Optical Method for In-situ Measurement of Form and Surface Profile of Axisymmetric Objects**
Farahi, N.; Babaie, J.; Ziegert, J. C.; Farahi, F. (University of North Carolina-Charlotte); Abolbashari, M. (Optoniks, Inc.) 272

16. **Attrition/Abrasive Wear Monitoring of Cutting Tools Based on Knife-Edge Interferometry**
Lee, C-B.; Zhao, R.; Jeon, S.; Zolfaghari, A. (Tennessee Technological University) 276

17. **Challenges in Measuring Spherical Geometry Using Terrestrial Laser Scanners**
Muralikrishnan, B.; Rachakonda, P. K.; Shilling, K. M.; Lee, V.; Sawyer, D. S.; Cheok, G. (National Institute of Standards & Technology); Cournoyer, L. (National Research Council of Canada) 281

18. **Optical Sensor for Use in the R-test**
Parks, R. E. (Optical Perspectives Group, LLC); Ziegert, J. C.; Groover, J. (University of North Carolina-Charlotte) 286

19. **Surface Area Measurement Using Curved Screen Deflectometry for Increased Dynamic Range and Sensitivity**
Pouyafard, A.; Davies, A. D. (University of North Carolina - Charlotte) 290

20. **Replication Assessment of Surface Texture at Sub-micrometre Scale**
Quagliotti, D.; Tosello, G.; Hansen, H. N. (Technical University of Denmark) 293

21. Alignment and Period Measurement of Critical-Angle Transmission Gratings Using a Scanning Laser Reflection Tool
Song, J.; Heilmann, R. K.; Schattenburg, M. L. (Massachusetts Institute of Technology); Bruccoleri, A. R. (Izentis, LLC); Hertz, E. (Harvard-Smithsonian Center for Astrophysics) 299

22. Fabrication of Probe Tips for Nanoscale 3D Metrology
Uchiyama, K.; Murakami, H. (The University of Kitakyushu); Katsuki, A.; Sajima, T. (Kyushu University); Yamamoto, T.; Nagata, R. (Inatsuki Science Co., Ltd); Fujiyoshi, K. (Fukuoka Industrial Technology Center) 305

23. Statistical Reduction Technique for Zero Position Error Between Sensors in Improved Sequential Three-Point Method
Uda, Y.; Natsume, Y.; Tamagawa, T.; Shimada, S. (Osaka Electro-Communication University); Imura, R. (Nagase Integrex Co., Ltd.) 311

24. Minimizing Task-Specific Uncertainty in CMM-Based Freeform Optics Metrology
Uwakwe, M.; Evans, C. J. (University of North Carolina-Charlotte) 315

25. Uncertainty Analysis for Part Density Determination via Hydrostatic Weighing
Valdez, M. O.; Montaño, J. D.; Valdez, L. M. (Los Alamos National Laboratory) 321

26. The Next Generation Heterodyne Interferometric Grating Encoder System for Multi-Displacement Measurement of a Wafer Stage
Wang, L. J.; Zhang, M.; Zhu, Y.; Ye, W. N..; (Tsinghua University); Ding, S. Q.; Jia, Z.; (Beijing Uprecision Tech Co., Ltd); Xia, Y. (University of Electronic Science and Technology) 326

27. Geometric Error Measurement and Compensation of a Rotary Table Using a Circular Ball Plate Artifact
Wang, Q.; Goch, F. G. (University of North Carolina-Charlotte) 332

28. Reference Metrology System for Compensation of Level Control in Precision State System
Woo, S.; Park, S-H. (Samsung Electronics Co., Ltd.) 337

29. Large Area Inspection Using a Multi-point, Tip-Based Nanometrology System
Yao, T-F.; Cullinan, M. A. (The University of Texas at Austin) 341

30. Development of an Innovative Sensor for Measuring Two-degree-of-Freedom Motions of Single-Axis Linear Nanopositioning Stage
Zolfaghari, A.; Jeon, S.; Lee, C-B. (Tennessee Technological University); Kim, G. (TRI-N Co. Ltd.) 346

Precision Design of Instruments and Machines

31. Axial and Radial Static Stiffness Testing for Ultra-Precision Air Bearing Spindle
Arneson, S.; Arneson, D. A.; Knapp, B. R.; Oss, D. D. (Professional Instruments Company) 352

32. **In-Line, Tip Based Nanometrology for Roll-to-Roll Manufactured Materials and Electronic Devices**
Connolly, L. G.; Cullinan, M. A. (The University of Texas at Austin) 355

33. **Design of a Precision, Active, High-Strain Composite (HSC) Hinge**
Echter, M. A.; Silver, M. J. (MIT Lincoln Laboratory); Peterson, M. E. (Air Force Research Laboratory) 360

34. **An Instrument to Measure Temporal Stability of Spring Compression Force**
Jaycox, A. W. (Lawrence Livermore National Laboratory); Lawton, K. M.; Patterson, S. R. (University of North Carolina-Charlotte) 366

35. **Error Analysis for a High-Precision Five Degree of Freedom Hybrid Mechanism for High-Power High-Repetition Rate Laser Operations**
Karim, S.; Piano, A.; Leach, R. K. (University of Nottingham); Tolley, M. (Science and Technology Facilites Council (STFC). 372

36. **Design and Testing of an Air Bearing Spindle at Low Speed for Nanometer-Level Asynchronous Error**
Knapp, B. R.; Arneson, D. A.; Oss, D. D. (Professional Instruments Company). 378

37. **Long-term Creep Measurements of 302 Stainless Steel and Elgiloy**
Lawton, K. M.; Patterson, S. R. (University of North Carolina-Charlotte) 382

38. **Development of Novel Two-DOF Nano-Positioning Stage with High Thermal Stiffness**
Lee, J-C.; Lee, H-H; Yang, S-H (Kyungpook National University) 387

39. **A Flexure-Based Multi-Layer Roll-to-Roll Printing Systems**
Li, C.; Chen, S-C. (The Chinese University of Hong Kong) 393

40. **Large Stroke High Support Stiffness Flexure Based Universal Joint**
Naves, M.; Aarts, R. G. K. M.; Brouwer, D. M. (University of Twente) 398

41. **Precision Mechanical Design and Test of Miniature Dynamic Mirror Benders with Laminar Flexure Bending Mechanism for X-ray Microfocusing**
Shu, D.; Kearney, S.; Anton, J.; (Argonne National Laboratory); Li, A.; Mao, C.; Yan, S.; Liang, D.; Pan, Y. (Shanghai Institute of Applied Physics) 403

42. **Design, Development and Testing of Large-caliber Precision CNC Double-sided Polishing Machine**
Sun, X.; Zhang, Z.; Zha, J.; Chen, Y. (Xi'an Jiaotong University); Chen, J. (Jiangsu Yichuang Institute of Intelligent Equipment Co.Ltd.) 407

43. **Design of a High-Speed Oscillating Blade Microtome**
Wang, J.; Li, C.; Chen, S-C. (The Chinese University of Hong Kong) 412

44. **Design Strategy for Cryogenic Optical Housing Using Stewart Truss with Dissimilar Materials**
Yoxall, B. E.; Montesanti, R. C.; Bixler, J. V.; Hunt, W. E.; Kuzmenko, P. J.; Priest, R. E. (Lawrence Livermore National Laboratory) 417

45. Gantry-Type Machine Tool Accuracy Enhancement Through Geometric Error Real-Time Compensation Based on Open-Architecture PA CNC
Zhang, C.; Cong, H.; Chen, Y. (Xi'an Jiaotong University) 422

46. Analysis of Error Motions of Hydrostatic Rotary Table
Zhang, P.; Chen, Y.; Cong, H. (Xi'an Jiaotong University) 427

Poster Session 2

Wednesday, November 1, 2017, 3:30 PM - 5:00 PM

Session Chairs: Brian P. O'Connor (Aerotech, Inc.) and Michael L. Barkman (Zygo Corporation)

Controls and Mechatronics

47. Vacuum Compatible Contactless Active Magnetic Linear Bearings for High Cleanliness Robotic Applications
Baade, R.; Steinbuch, M.; (Eindhoven University of Technology);
Peijnenburg, A. T. (VDL Enabling Technologies Group) 433

48. A High Performance Feedforward Tuning Approach for Ultra-precision Motion Control
Dai, L-Y.; Li, X.; Zhu, Y.; Zhang, M. (Tsinghua University) 439

49. Multi-Axis Trajectory Generation with Optimal Frequency Spectrum for Vibration Avoidance
Dumanli, A. A.; Sencer, B. (Oregon State University) 445

50. A Linear Positioning Stage Using a Thermal Actuator
Fan, C.; Smith, S. T.; Tarbutton, J. (University of North Carolina - Charlotte) 451

51. Basic Characteristics of Novel Hybrid Actuator Integrating a Thermal Bias Element and an Electromagnetic Driving Element
Hama, T.; Sato, K. (Toyohashi University of Technology) 456

52. Identification of Friction Energy Dissipation Using Free Vibration Velocity: Measurement and Modeling
Kossack, C.; Schmitz, T. L.; Ziegert, J. C.
(University of North Carolina-Charlotte). 462

53. The Velociprobe: Pushing the Limits with Fast and Robust Control
Mashrafi, S. T.; Salapaka, S. (University of Illinois at Urbana-Champaign);
Preissner, C. (Argonne National Laboratory). 468

54. Development of Dynamic Model to Estimate the Frequency Response of Four-Axis Machine Tools
Song, C-K.; Lee, C-H. (Korea Institute of Machinery & Materials (KIMM));
Dinh, P. V. (Korea University of Science and Technology). 474

55. Software-Based Compensation of Vibration-Induced Errors of a Commercial Desktop 3D Printer
Yoon, D.; Duan, M.; Okwudire, C. E. (University of Michigan). 478

56. Decouplable Coarse-Fine Stage for Improved Precision and Efficiency in Point-to-Point Positioning
Yoon, D.; Zeng, B.; Okwudire, C. E. (University of Michigan) 483

Micro and Nano Technologies

57. Microassembly Development for an Advanced Micromirror Array
Enstrom, K. G.; Uphaus, T. M.; Panas R. M.; Harvey, C.
(Lawrence Livermore National Laboratory) 489

58. Fabrication of Polycrystalline Diamond Molds by Micro EDM
Kasai, S.; Yan, J. (Keio University); Sodetai, T. (Seiko Instruments, Inc.) 494

59. Numerical and Experimental Investigations into Production of Hierarchical Textures
Patel, D. S.; Thalkar, M.; Jain, V. K.; Ramkumar, J.
(Indian Institute of Technology Kanpur) 498

60. Wafer Scale Exfoliation of Monocrystalline Micro-Scale Silicon Films
Ward, M.; Cullinan, M. A. (The University of Texas at Austin) 504

61. Development of Micro Ball Forming to Process Micro Structure on Curved Surface
Yamaguchi, K.; Nakano, T.; Kakutani, S.; Ota, M.; Egashira, K.
(Kyoto Institute of Technology) 508

62. Design and Modelling of a Bidirectional MEMS Thermal Actuator
Zhao, C.; Ladner, I. S.; Cullinan, M. A. (The University of Texas at Austin);
Song, A.; Hopkins J. B. (University of California - Los Angeles) 514

Precision Manufacturing Machines and Technologies

63. Investigation in Micro-EDM Techniques for Laser Target Application
Andre, J.; Barnay, N.; Gregoire, A.; Chicanne, C.; Theobald, M. (CEA) 520

64. Mechanical Machining Processes for Laser Target Manufacturing
Andre, J.; Schunck, J.; Gregoire, A.; DeDemo, G.; Chicanne, C.;
Theobald, M. (CEA) 524

65. Precision Hard Turning on a Lathe Retrofitted with an Oil Hydrostatic Spindle
Arneson, D. A.; Knapp, B. R. (Professional Instruments Company) 528

66. Thermal Errors of a Large 5-Axis Machine Tool Due to Cutting Fluid Influences - Evaluation with Thermal Test Piece
Blaser, P.; Wiessner, M.; Wegener, K. (Institute of Machine Tools and
Manufacturing ETH Zürich); Hernandez-Becerro, P.; Mayr, J. (inspire AG) 531

67. Stability in Modulated Tool Path Turning
Copenhaver, R.; Ziegert, J. C.; Schmitz, T. L. (University of North Carolina-Charlotte) 537

68. Fundamental Experiments of Additive Manufacturing Method by Selective Solidification Using Electrical Discharge
Furutani, K.; Tsuchiya, T.; Yamagishi, H. (Toyota Technological Institute) 543

69. Effect of the Additive Manufacturing Process on Cutting Forces in Hybrid Manufacturing
Gomez, M.; Honeycutt, A.; Schmitz, T. L. (University of North Carolina-Charlotte);
Heigel, J. (National Institute of Standards & Technology) 547

70. Precision Manufacturing of Internal Involute Gears Using 5-Axis Milling Center
Groover, J.; Goch, F. G. (University of North Carolina-Charlotte) 553

71. Force Measurement in Diamond Micro-Chiseling
Gurganus, D. K.; Sizemore, N. E.; Owen, J. D.; Davies, M. A. (University of North Carolina-Charlotte). 558

72. An Examination of Surface Location Error and Surface Roughness for Period-2 Instability in Milling
Honeycutt, A.; Schmitz, T. L. (University of North Carolina-Charlotte). 562

73. Fixed-Free Beam Dynamics Prediction for Thin Rib Machining by RCSA
Honeycutt, A.; Schmitz, T. L. (University of North Carolina-Charlotte). 568

74. The Challenges and Consequences of Material Uncertainties in Metal Laser Powder Bed Fusion
Jared, B. H.; Boyce, B.; Madison, J. D.; Ostien, J.; Rodelas, J.; Salzbrenner, B.; Swiler, L. P.; Underwood, O. D.; Saiz, D. J. (Sandia National Laboratories) 574

75. Analysis of Hydrophobicity of Micro-Channel and Micro-Pillar Patterns of Polymer for Orthodontic Retainer Fabricated by Mechanical Machining Process
Je, T-J.; Jeong, J-Y.; Lee, J-R; Jeon, E-C; Choi, D-S. (Korea Institute of Machinery & Materials (KIMM) 578

76. Multi-probe Error Separation
Keller, E. E.; Marsh, E. R.; Arneson, H. D. (The Pennsylvania State University); Knapp, B. R.; Arneson, D. A. (Professional Instruments Company) 583

77. Measurement of Dynamic Characteristics of Hydrostatic Spindle Against Radially Applied External Forces
Kirigaya, R.; Nakao, Y. (Kanagawa University); Hayashi, A. (Kanazawa Institute of Technology) Fedorynenko, D. (Chernihiv National University of Technology). 585

78. Laser Augmented Diamond Drilling Operation Using A Rotating Tool Design
Mohammadi, H.; Patten, J. A. (Western Michigan University) 589

79. UPC 300 Ultra Precise Diamond Turning Machine Optimized for Freeform Production
Niehaus, F.; Huttenhuis, S. (Schneider GmbH & Co. KG); Gauch, D. (Schneider Optical Machines, Inc.) 593

80. Dry Planarization Method Using a Transpport of Reactive Species
Ryokume, R.; Miyazaki, T.; Matsuyama, S.; Sano, Y.; Yamauchi, K. (Osaka University) 597

81. Manufacture and Assembly of Precision Planar Samples for Experiments at the National Ignition Facility
Savage, L; Castro, C.; Vargas, R. J.; Seugling, R. M.; Nikroo, A. (Lawrence Livermore National Laboratory); Lament, M. (Schafer Livermore Laboratory) 602

82. M-Uber: Uber-Type Assignment for Distributed Operator Machining Operations
Schmitz, T. L.; Ziegert, J. C. (University of North Carolina-Charlotte); Greis, N (University of North Carolina-Chapel Hill) 606

83. Milling of High-Alloyed Steel Molds for Precision Injection Molding of Microfluidical Parts
Schmuetz, J. (Beuth University of Applied Sciences) 609

84. Fiber Based Tools for Precision Polishing Applications
Shahinian, H.; Hassan, N.; Cherukuri, H. P.; Mullany, B. A. (University of North Carolina-Charlotte). 615

85. On Gyroscope Mechanism for Mobile Machining Machine
Shim, J.; Heo, S.; Hwang, J.; Ro, S-K. (Korea Institute of Machinery & Materials (KIMM) 620

86. Material Behavior in Ultra-Precision Flycutting of Germanium
Sizemore, N. E.; Shanmugam, P.; Owen, J. D.; Davies, M. A. (University of North Carolina-Charlotte); Meyer, D. (Foundation Institute of Materials Science) 624

87. How to Realize the Self-Protective Tool During Cutting of Difficult-Cut Material?
Song, X.; Takahashi, Y.; Ihara, T. (Chuo University) 630

88. Precision Polishing Technology of Ferroelectric PMN-PT Single Crystals for Smoother Surfaces
Takahashi, H.; Suzuki, H. Y.; Namba, Y. Y. (Chubu University) 636

89. Temperature Measurement of Burnishing Process by Electro-Conductive Tool
Tanaka, H.; Tanaka, H.; Sakamoto, H. (Sophia University) 642

90. Inverted Diamond Cutting of Right Triangular Retroreflectors: Surface Quality and Cutting Forces
Tauhiduzzaman, M.; Bordatchev, E. V. (National Research Council of Canada); Milliken, N.; Tutunea- Fatan, R. R. (Western University) 647

91. Fundamental Study on Thermal Stability of Micro Milling Spindle Supported by Water Hydrostatic Bearings Under Spindle Rotation
Yaguchi, T.; Nakao, Y. (Kanagawa University); Hayashi, A. (Kanazawa Institute of Technology). 651

92. Laser Cutting Out Process for Semiconductor Substrates Applying Laser Slicing Method
Yamada, Y.; Saitama T.; Ikeno, J.-I. (Saitama University) 657

93. Improving Surface Quality of Thin-Walled Double Side Aspheric Component by Machining Process and Measurement Optimization
Zha, J.; Chu, J.; Chen, Y.; Li, Y. (Xi'an Jiaotong University) 663

Technical Papers

DIAMOND TOOL WEAR/BUILT-UP EDGE MACHINING FERROUS MATERIALS

Thomas Dow, Kenneth Garrard, PEC, NC State University
Brandon Suit, Lockheed Martin, Orlando, FL

The objective of this paper [1] is to discuss the mechanisms that prevent diamond tools from creating the excellent surface finish achievable on non-ferrous metals to ferrous metals (steel and stainless steel). This is important because hard ferrous metals are extensively used to make injection-molding dies. As a result, significant post-polishing is needed to produce acceptable mold figure error and surface finish. Polishing also limits the features that can be included on the dies. Contributing factors such as tool wear, pick up of the workpiece material on the tool edge (BUE), tool temperature and machining forces have been investigated. The results of these machining experiments along with finite element models will lead to improved understanding of the process and potentially a way to improve the surface finish.

Tool Wear Diamond tool wear occurs at a much higher rate machining ferrous material than it does with non-ferrous materials and the detailed geometry of that wear is different. The wear affects the cutting process by changing the geometry of the cutting edge of the tool.

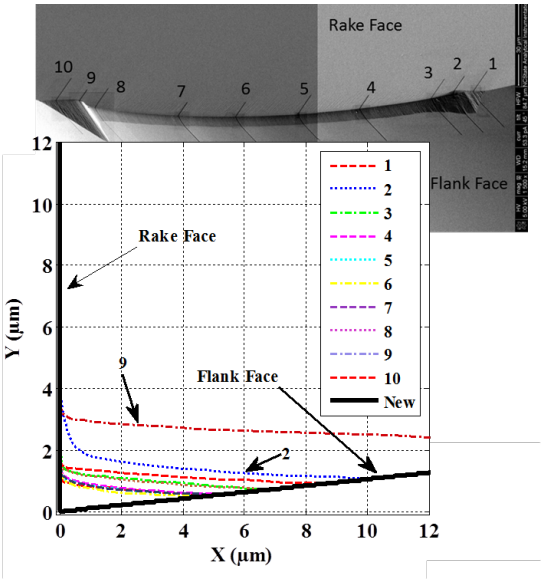

Figure 1. Tool wear at 10 locations across a round nosed diamond tool machining a flat 1215 steel workpiece at 8 m/s for 20 m.

Figure 1 shows the tool wear after cutting 1215 steel for 20 m at 8 m/s using a diamond tool with a 0.5 mm nose radius. After the experiment, the tool was cleaned with Keller's solution and measured in the SEM using the EBID technique[1] to write lines normal to the edge shown in Figure 1. Each line shows a cross section shape of the edge at that point on the tool face. It is clear that the depth of the wear is inversely proportional to the depth of cut and the largest wear occurs at the edges where the depth of cut goes to zero and the BUE is opposite.

However, this totally neglects the effect of the BUE on the machining process - like not acknowledging the elephant in the room. Figure 2 shows a tool edge before and after being cleaned with the Keller's for a 1215 experiment at 4 m/s.

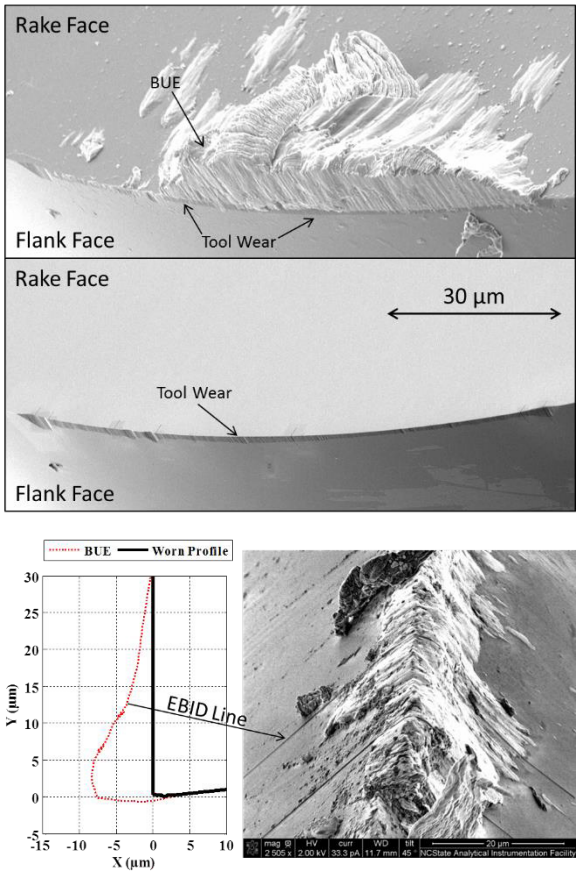

Figure 2. SEM/EBID images of BUE after cutting 1215 steel. The cross-section at left shows the

[1] Electron Beam Induced Deposition–EBID developed at the PEC by Drescher & Russell in 1991

tool wear in cross section is only 2% of the BUE area.

Tool Wear/BUE for Aluminum The geometry of the BUE when machining aluminum is very different than for steel. Figure 3 shows the same information as in Figure 2 but for a 6061-T651 aluminum workpiece. Figure 3 is similar to Figure 2 but the BUE does not interfere with the chip flow.

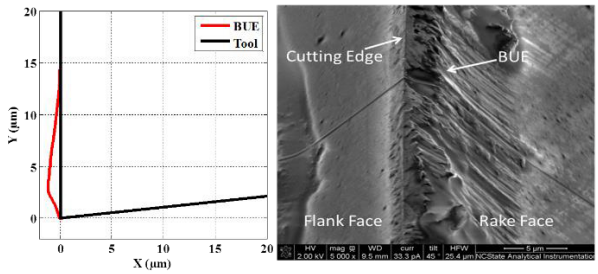

Figure 3. EBID measurement of a diamond tool used for non-overlapping aluminum machining. Pickup is shown but it is above the cutting edge and had little effect on the surface finish.

Tool Temperature Previous work on diamond tool wear while machining steel postulated the higher wear was due to higher tool temperatures and therefore increased chemical wear based on the Arrhenius model. The initial goal of this project was to measure the peak temperature and use this temperature to predict tool wear and compare with the EBID images of the worn tool. However, the BUE will influence the tool temperature as well as shield the tool from contact with the chip.

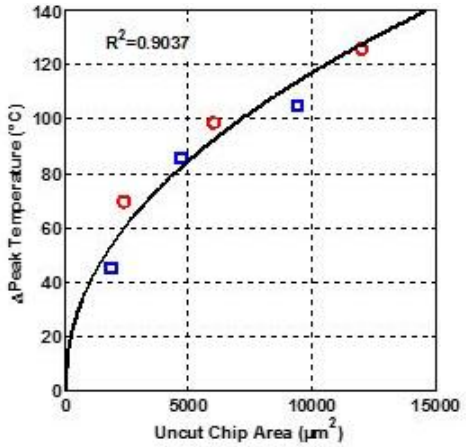

Figure4. Extrapolated peak tool temperature

The peak temperature in a machining process typically occurs along the primary shear zone in the chip and along the edge of the tool. The heat generated depends on the workpiece material, chip geometry, cutting speed and any BUE on the tool. The diamond tool is an excellent thermal conductor and will efficiently transfer the heat generated at the shearing interface to the bulk of the tool. Surface-temperature measurements were made using thin film platinum Resistance Temperature Detectors (RTDs) mounted to the tool. The RTDs offer high repeatability and nearly constant sensitivity but their size keeps them well away from the cutting edge on the scale of the chip size. Predicting the peak temperature requires extrapolation in an FEA model of the tool leading to peak temperature as a function of chip area shown in Figure 4.

Finite Element Modeling AdvantEdge is a Finite Element model of a machining process that can provide insight into the details of the forces and temperature at the tool edge. Operating conditions used for the experiments were modeled and the results compared to understand the effect of machining parameters on forces, heat generation, chip formation, tool temperature and tool wear. An analysis of the heat partitioning between the workpiece, chip and tool was also investigated to examine the effects of machining parameters. Two dimensional modeling (Figure 5) was used with straight edge diamond experiments and 3D models were explored to study the round nose tool experiments. In addition, finding the effect of heating on the material properties can be used to estimate the location of the zero velocity element and identify the location and shape of the BUE as in Figure 6.

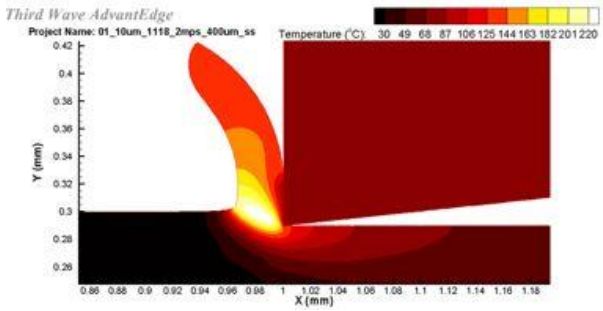

Figure 5. FEM model of the machining process

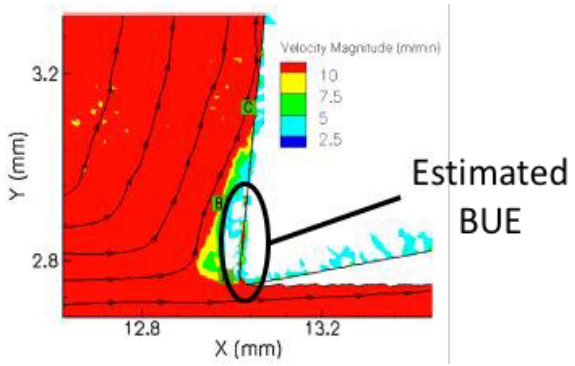

Figure 6. Location of BUE from FE model of cutting process based on zero velocity of element [2]

Surface Finish The goal of machining with a diamond tool is to utilize its hardness, high-quality geometry and edge sharpness to create a surface with low roughness and minimum form error. As applied to non-ferrous metals and plastics, DT can produce mirror finishes and form error less than 100 nm. However, extrapolating this performance to steel work-pieces has proven difficult. The goal of this project is to study the dynamics of BUE/tool wear to see if there are cutting conditions that optimize the surface finish.

In any machining operation, a pair of dynamic processes are taking place: 1) wear of the tool edge and 2) pickup of workpiece material on that edge. These two processes are difficult to separate because they take place at a small region near the tool edge and are hidden from view. The PEC developed an SEM technique in 1991 called EBID that can provide quantitative and qualitative measurements of the tool edge with or without a built-up edge. Twenty-two non-overlapping groove experiments were performed with a 0.5 mm round nose diamond tool at a 10 μm depth of cut and cutting speeds from 0.25 m/s to 8 m/s. These non-overlapping experiments, at a fixed depth of cut, capture the change in the groove geometry due to tool pickup as an increase in depth and tool wear as a depth of cut. The facing cuts were made on steel and aluminum workpieces and the grooves (Figure 7) were measured with a contacting surface profilometer and a non-contacting optical probe.

Aluminum Groove Experiments Facing operations with a 0.5 mm radius round nose tool on Aluminum 6061 were performed as shown in Figure 7. The goal was to develop a baseline for a material that can produce an excellent DT finish. A 10 μm depth of cut was used and the cutting speed ranged from 0.25, 1, 4 and 8 m/s. Cutting oil was used during the 10 m of cutting for each experiment. Force and RTD measurements were made during the experiments that showed the effect of changes in the material removal volume and the resulting grooves were measured with a surface profilometer.

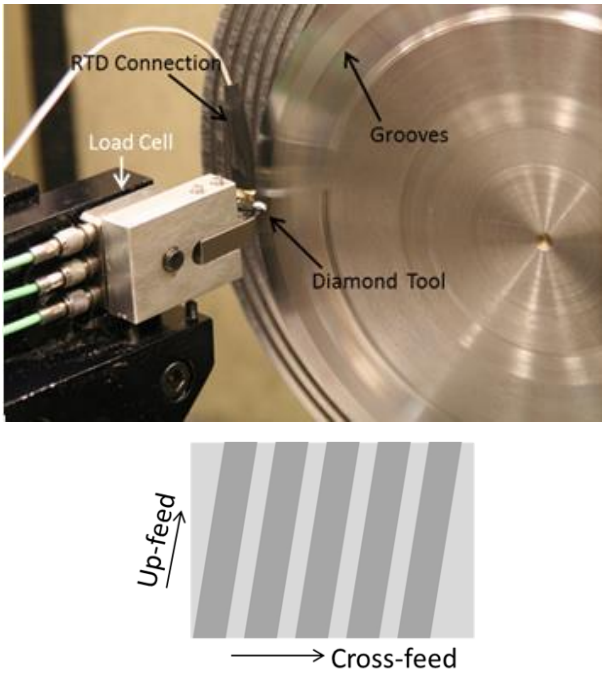

Figure 7. *Setup for cross feed of non-overlapping feed rate*

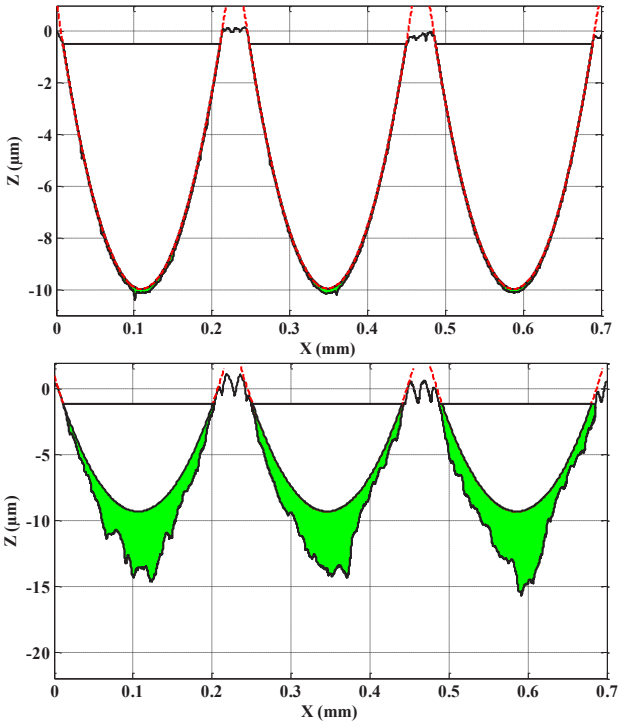

Figure 8. Non-overlapping cuts for aluminum (top) and 1215 steel (bottom) showing the difference between the tool shape and the groove

Steel Groove Experiments 1045 and 1215 steel were machined with a 0.5 mm radius round nose tool and lubrication. The non-overlapping groove geometry retains information on the location of the original surface. The depth of cut was 10μm with the cutting speeds of .25 to 8 m/s for cutting distances from 10 m and 20 m. A total of 21 experiments were performed. Before each experiment, the workpiece was prepared with a carbide tool to create a surface flat to 1 μm and surface roughness near 1 μm rms. Force and RTD measurements were taken during the experiments, while the grooves and tool wear were measured on the Talysurf.

Analysis of Tool Grooves After each experiment, tool grooves were measured using a TalySurf and an optical probe. Examples of the groove shapes for 6061T6 aluminum and 1215 steel are shown in Figure 8. Measurements were analyzed with a Matlab program to determine the cross sectional area of the groove. The effect of BUE can be determined by the size differential of the theoretical and actual groove. The effect of machining parameters on BUE were determined by comparing different experiments.

Tool Wear Measurements Tool wear measurements were made after each experiment using the EBID technique for tool wear shape.Straight edge diamond required only one measurement due to the uniform wear across the entire contact length. For round nose tool experiments, measurements were taken every 30 μm along the wear length of the cutting edge because the wear changed due to the changing chip thickness.

Built Up Edge (BUE) BUE occurs when the workpiece material sticks to the rake and/or flank regions of the tool. This occurs in ferrous materials that work harden materials, such as steel, but it also happens when machining aluminum alloys that also work harden and some that do not. This process is considered to occur dynamically and potentially at a cyclical rate. BUE affects surface finish by effectively changing the geometry of the cutting edge and thus, the cutting process. Experiments are done to examine the effect of BUE on the workpiece as well as measuring tools with BUE using an SEM.

Figure 9 shows the differential areas of the 1 m/s experiments as a function of cutting distance. Three experiments were conducted on 1215 steel for repeatability comparison while only one experiment was conducted on 1045 steel. The average area differential for the 1045 steel experiment varied by 700 μm^2 and indicates a rapid change in the extension of the tool. All three 1215 steel experiments started at very similar differential areas. At the 3.5 m mark, two continued the same trend, while one experiment had a dramatic increase in differential area. At the 8 m mark, the differential area dropped which implies that a section of BUE was removed. The grooves from this experiment then stayed at a consistent size and were comparative to the other two experiments.

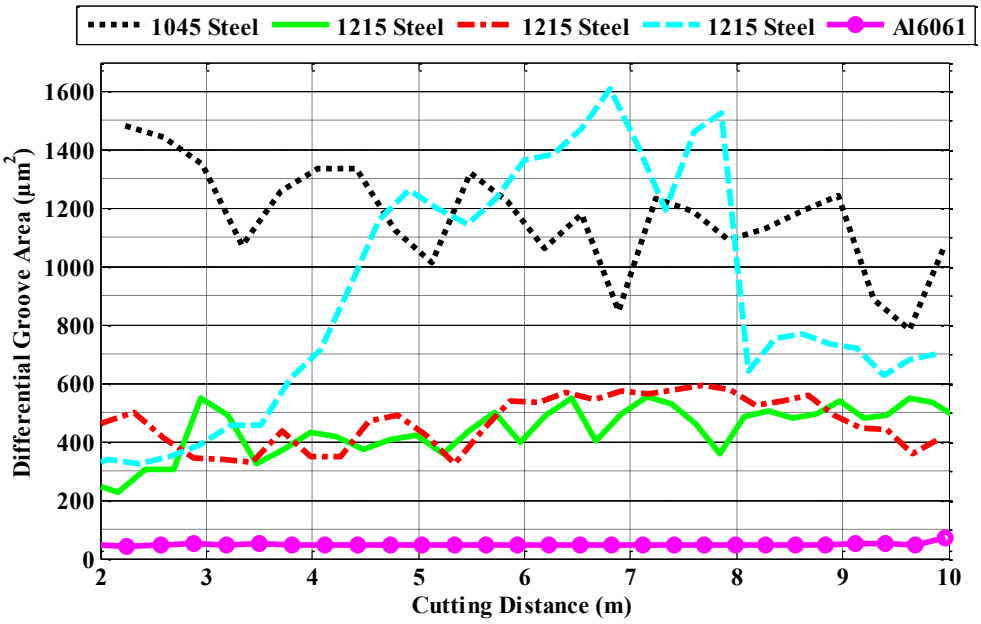

Figure 9. Difference in tool face area and groove area for 3 steels at 1 m/s

References:

1. Suit, Brandon, Analysis of Accelerated Tool Wear and Built Up Edge when Diamond Turing Ferrous Materials, MS Thesis, 2016. Available as pdf file in NC State Library https://repository.lib.ncsu.edu/bitstream/handle/1840.16/11182/etd.pdf?sequence=2&isAllowed=y

2. T. Childs, "Towards simulating built-up-edge formation in the machining of steel," CIRP Journal of Manufacturing Science and Technology, vol. 4, pp. 57-70, 2011.

OPTICAL FORM AND RELATIONAL METROLOGY OF ASPHERIC MICRO OPTICS

Xavier Colonna de Lega, Thomas Dresel, Jan Liesener, Martin Fay, Nathan Gilfoy, Kyle Delldonna, and Peter de Groot

Zygo Corporation, Middlefield, CT

INTRODUCTION

The last decade has witnessed the rapid growth of a new optics manufacturing industry dedicated to consumer electronics and compact automotive and medical imaging devices. Miniature cameras common to portable devices have evolved into sophisticated optical assemblies of advanced, injection-molded micro optics (FIGURE 1). More than a billion mobile phones shipped in 2016, which required the manufacturing of >15 billion individual lenses, or 40 million lenses a day.

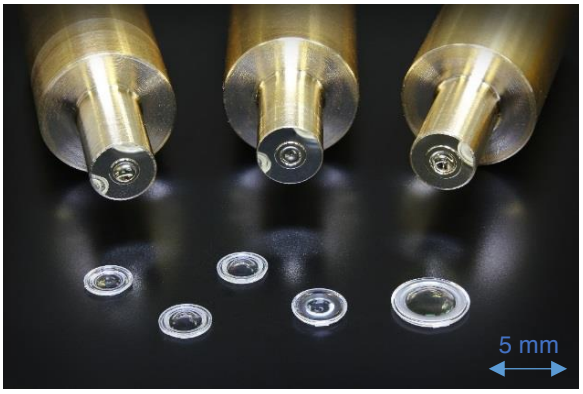

FIGURE 1. Microlenses and molds. The lenses are a few mm in diameter.

With these prodigious production rates it is obviously critical to rapidly identify yield problems, which are often associated with errors in the individual lenses and their relative alignment. Such issues are not readily isolated by merely assessing the final imaging quality of completed lens assemblies.

To address manufacturing quality concerns, surface form measurements on individual sample lenses and molds can reveal deviations from design as well as manufacturing defects in the molding process. Performance can be further improved through detailed measurement of molded features for mechanically locating centers of curvature, lens spacing and orientation of the elements when combined into the final lens assembly [1].

A common metrology strategy for microlenses relies on contact stylus metrology [2], often limited to just two orthogonal cross-sectional profile measurements, sometimes supplemented by optical measurements of some of the alignment features on the lenses.

Manufacturing yield improvements and tighter performance requirements for the aspheric surface form of camera microlenses are driving the industry to ever greater precision and metrology data density. The goal of the present work is to provide full-area metrology for surface form, waviness and texture, as well as metrology of the relative position of lens features with respect to mechanical location features (so-called “relational metrology”) – all in a single instrument, using high data density, non-contact optical metrology [3].

THE INSTRUMENT

FIGURE 2. Interference microscope with multi-axis staging for imaging microlenses.

We use coherence scanning interferometry (CSI) [4] in combination with five-axis staging for positioning micro-optics (FIGURE 2). The system

includes specialized objectives for form and relational measurements on the same platform. The instrument is integrated in a vibration, air and sound isolation enclosure, and is equipped with software specifically designed for this application.

SURFACE FORM MEASUREMENTS

The strategy for measuring aspheric form is to combine a sequence of areal topography maps at high lateral resolution into a full surface reconstruction. This “stitching” concept has been examined in prior work on larger-scale optics, for example, by Thunen and Kwon [5], Fan [6] and in the instrument developments at QED Technologies [7]. Tang [8] and Shimuzu et al. [9] have also considered using stitching methods with a microscope for smaller optics.

A challenge with any image stitching technique is the overall metrology frame, which in most cases requires precise knowledge of stage motions, in turn requiring encoding devices or additional metrology. We have found that stage precision requirements can be significantly loosened by using the correlation of surface microstructure between adjacent topography maps, which is detectable even on super-polished surfaces when using interference microscopy [10].

The measurement sequence consists of individual CSI imaging scans performed over an array of pre-programmed imaging areas, each of which is presented to the instrument with minimal tip and tilt. Once the data are acquired, software adjusts the position and orientation of each map with respect to the others, consistent with the concept of surface form and texture continuity, including the roughness present in each map at micron-scale spatial periods. The result is a full surface topography map with millions of individual data points. Data rates vary according to lens size and shape, but are on the order of several minutes per lens. The software also supports the mapping and discovery of unknown rotationally symmetric surfaces.

FORM MEASUREMENT RESULTS

FIGURE 3 illustrates the synthesized 3D Form Map for a microlens approximately 1.5 mm in diameter with an overall sag of 290 µm. The most common data processing entails subtracting the design prescription to show the deviation from the intended surface topography, as in FIGURE 4. A common alternative is to fit and subtract a rotationally symmetric asphere with adjustable parameters to characterize the lens shape.

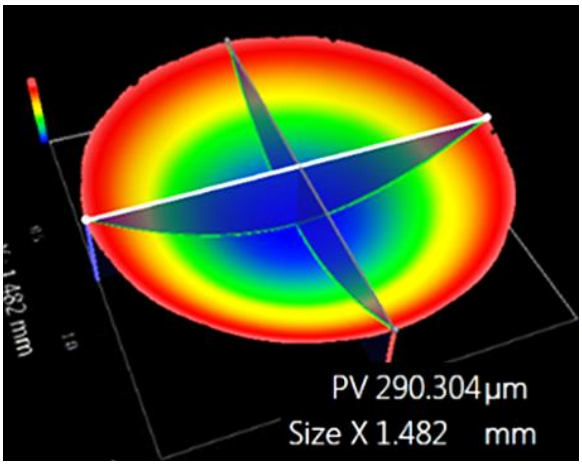

FIGURE 3. Areal surface topography of a smart phone microlens generated from a mosaic of interference microscopy maps.

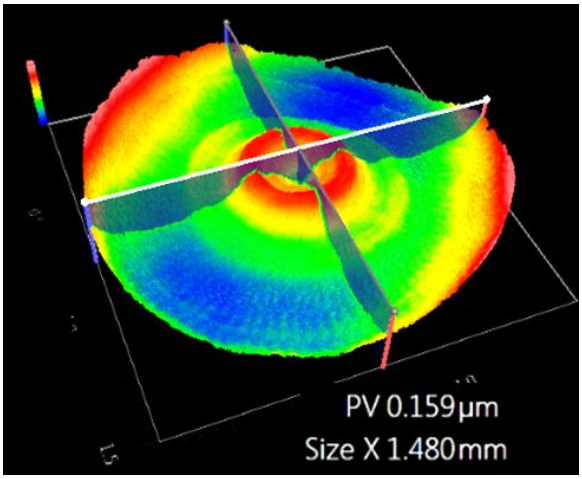

FIGURE 4. Same data as in FIGURE 3, after removal of the design aspheric form.

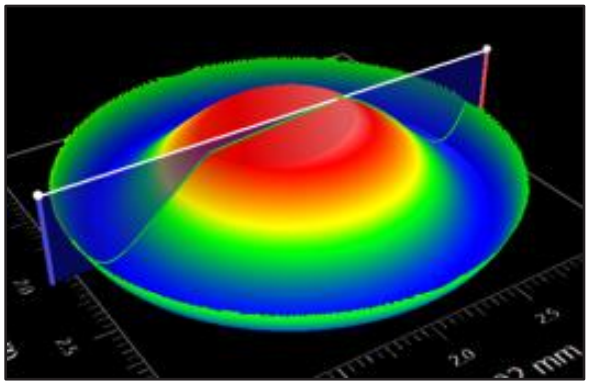

FIGURE 5. Form deviation map showing a manufacturing error (flat area around the apex). The lens diameter is 2.4 mm and the height scale in this image is 1.5 μm.

Often it is of interest to parameterize the deviation map as a series of 36 or more Zernike coefficients for export to optical design packages for analysis. Subtracting the surface form enables further analysis of the surface texture, including residual diamond turning marks, roughness and surface defects.

The new instrument has proven to be an effective means of discovering issues that can affect image quality [1]. FIGURE 5 illustrates a manufacturing problem with the flow and distribution of material during injection molding. In addition to the deviation from the design aspheric form, the material has failed to completely fill the mold, producing the truncated and flattened area near the lens apex.

FIGURE 6 illustrates the benefits of full-field, high-resolution measurements of surface texture. The image shows defects related to the diamond turning process of the lens molds as well as damage from previous measurements using a contact stylus-type form profiler.

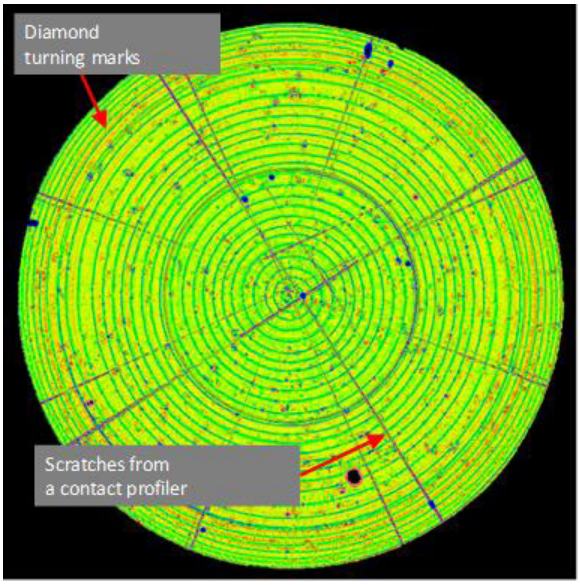

FIGURE 6. High-resolution, non-contact optical measurement of surface texture.

METROLOGY OF ALIGNMENT FEATURES

In addition to full-surface lens topography, a microscope-based system is an ideal platform for the evaluation of key lens features that control the spacing, centration and orientation of the lenses in the final assembly, as shown in FIGURE 7. These relational measurements employ a low-magnification objective, which is mounted on a turret along with the higher-magnification objective used for form measurements. The part fixtures shown in FIGURE 8 include reference datum planes to establish a local geometrical metrology frame. The topographical imaging results shown in FIGURE 9 enable quantitative evaluation of critical alignment parameters [11, 12], including the position of the functional optical surfaces with respect to interlocks and the relative position of the two sides of a lens.

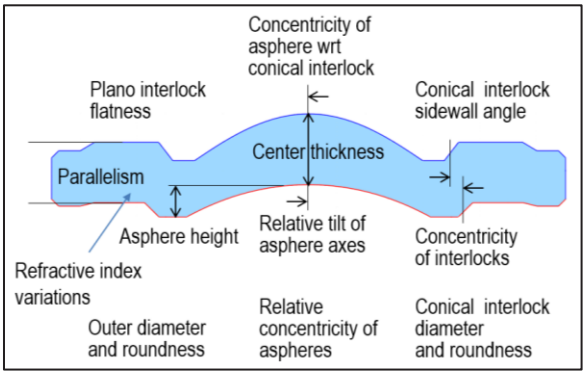

FIGURE 7. Relational metrology features critical to lens function and alignment.

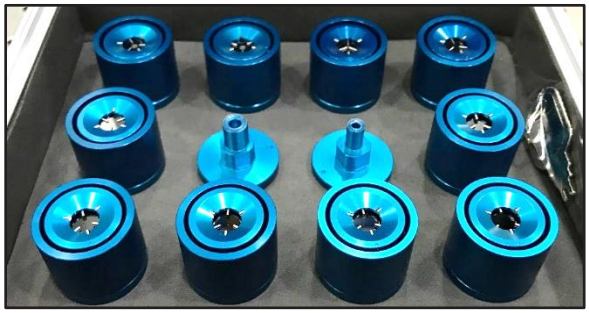

FIGURE 8. Custom part fixtures incorporating reference datum features.

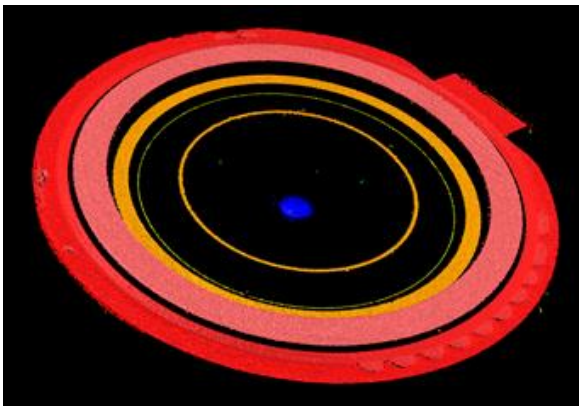

FIGURE 9. Imaging result for relational metrology, showing data collected at the apex of the functional optical surface (in blue) and data collected on outer plano surfaces, including a ring used for controlling lens tilt in the final assembly.

As with the surface measurements, the detailed 3D imaging reveals errors in the molding of mechanical locating features or interlocks that would otherwise go unnoticed until final assembly. FIGURE 10, for example, shows errors in the shape of a mechanical tilt control ring. Such molding errors could be repeated across a batch of many hundreds of lenses for a typical injection molding process. However, CSI-based metrology offers sufficient resolution, accuracy and throughput to identify and correct such mistakes before they significantly affect manufacturing yield.

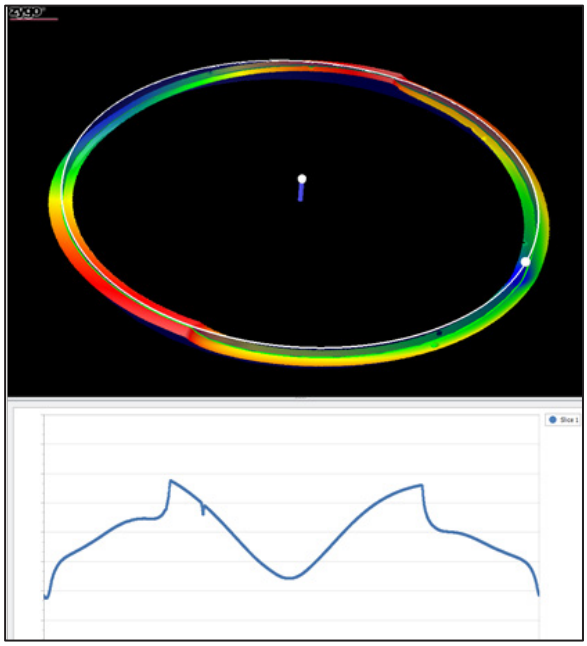

FIGURE 10. Measured shape and circumferential profile of the tilt control feature of an injection-molded lens. The vertical scale is approximately a micrometer.

SUMMARY

We have developed a new optical metrology system for micro optics based on the integration of interference microscopy, advanced staging, full-surface topography reconstruction and relational metrology techniques. Key benefits of this approach include full-surface imaging at high lateral resolution, and the ability to measure the shape and location of relational features critical to the alignment of completed lens assemblies, as well as the position of the functional optical surfaces with respect to such interlocks.

REFERENCES

[1] Colonna de Lega, X., Dresel, T., Liesener, J. *et al.*, Lessons learned from the optical metrology of molded aspheres for cell phone cameras. in *8th High Level Expert Meeting - Asphere Metrology*, Physikalisch-Technische Bundesanstalt. 2017;

[2] Scott, P. Recent Developments in the Measurement of Aspheric Surfaces by Contact Stylus Instrumentation. 2002; 4927: 199-207.

[3] de Groot, P. J., Challenges and solutions in the optical measurement of aspheres. in *Ultra Precision Manufacturing of Aspheres and Freeforms*, OptoNet Workshop. 2016;

[4] de Groot, P. Principles of interference microscopy for the measurement of surface topography. Advances in Optics and Photonics. 2015; 7: 1-65.

[5] Thunen, J. G., and Kwon, O. Y., Full aperture testing with subaperture test optics. in Proc. SPIE. 1983; 0351: 19-27.

[6] Fan, Y. J. Stitching interferometer for curved surfaces. Technische Universiteit Eindhoven, 1998.

[7] Tricard, M., Forbes, G., and Murphy, P. Subaperture metrology technologies extend capabilities in optics manufacturing. 2005; 5965: 59650B-59650B-11.

[8] Tang, S., Stitching: high-spatial-resolution microsurface measurements over large areas. in. 1998; 3479: 43-49.

[9] Shimizu, K., Yamada, H., and Ueyanagi, K. Method of and apparatus for measuring shape. US patent number 5,960,379. 1999.

[10] Dresel, T., Liesener, J., and de Groot , P. Measuring topography of aspheric and other non-flat surfaces. US patent number Application 20150192769. 2015.

[11] Fay, M. F., Colonna de Lega, X., and de Groot, P. J. Optical Evaluation of Feature Locations on Lenses. US patent number 9,599,534. 2017.

[12] Colonna de Lega, X. M., Fay, M. F., and de Groot, P. Optical evaluation of lenses and lens molds. US patent number Application 20160047712. 2016.

OPTIMAL THREE-POINT MOUNTS FOR SQUARE AND RECTANGULAR PLATES

Justin M. Verdirame and Samir A. Nayfeh
Physical Precision LLC, Laguna Beach, CA

INTRODUCTION

Exact-constraint or kinematic design principles are central to precision machine design. One of the simplest and most common kinematic methods for supporting plate-like objects is a three-point mount. With plates one cannot, in general, maximize the first natural frequency simply by placing three-points at the nodal locations as one can with a beam. In this paper we find the optimal three-point mount positions for square and rectangular plates which maximize the first natural frequency. For square and nearly square plates, the optimal support locations are not symmetric. For high-aspect-ratio rectangular plates, the optimal support locations correspond to the nodal locations of the first beam bending mode.

Based on the theory of the Rayleigh quotient, the upper bound first natural frequency of a plate with three constraints is its first free flexible mode (see for example [5]). However for a square plate without edge restraints as shown by Won and Park [11, 12], three point-supports are not sufficient to achieve the theoretical maximum. Nayfeh and Verdirame developed a set of constraints for square and circular plates [5] and rectangular plates [8], which according to Courant's minimax principle must exist, but these constraints are not as simple as the three-point mount. The three-point mount is widely used for its simplicity, but the optimal support locations are not readily available in the literature for square and rectangular plates. For circular plates, the optimal support positions are obtained from a number of references such as Yoder [14].

Numerous studies have looked at methods to optimize design of beams, plates, and plate-like structures (see Grandhi [3] for a review paper). Grubb developed a whiffletree for telescope mirrors to minimize their deflection due to self-weight in the 1800's [10], and formulas for their design are given by Hindle [4]. Yoder [14] provides a figure comparing the optimal support radius for circular plates due to gravity with a number of supports. Nomura and Wang [6] optimize the placement of supports under a free rectangular plate

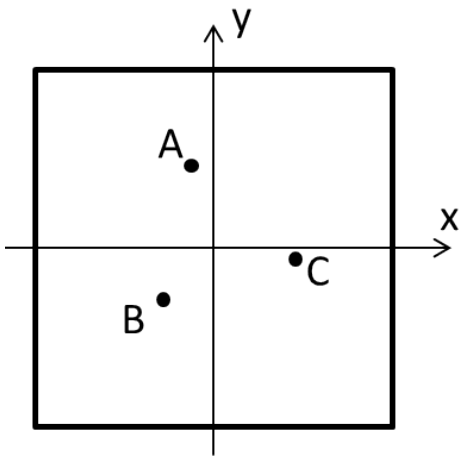

FIGURE 1. Square plate with three point-supports A, B, and C

using a Galerkin method. Wang et al [9] develop closed form sensitivities and a heuristic method to optimize support locations for maximum natural frequency. Son and Kwak [7] use eigenvalue sensitivities to optimize the boundary conditions and maximize the natural frequency of structures. Friswell [2] uses finite elements which contain the support conditions within each element to opitmize support placement and maximize natural frequency. Won and Park [13] develop the concept of upper bound eigenvalue and use optimal support loci to maximize the natural frequency. Akesson and Olhoff [1] use Courant's minimax principle to place spring supports of a beam in their optimal location to maximize its natural frequencies.

In this paper, we use the eigenvalue sensitivity and method of steepest descent as developed by Won and Park [13] to find the optimal three-point mount for square and rectangular plates without edge restraints. The previous works described above focus on systems with large numbers of springs or fixed boundary conditions, neither of which are commonly encountered in precision systems. In precision systems, free boundary conditions and three supports are frequently encountered. Additionally as shown below, the optimal solution for square or nearly square plates

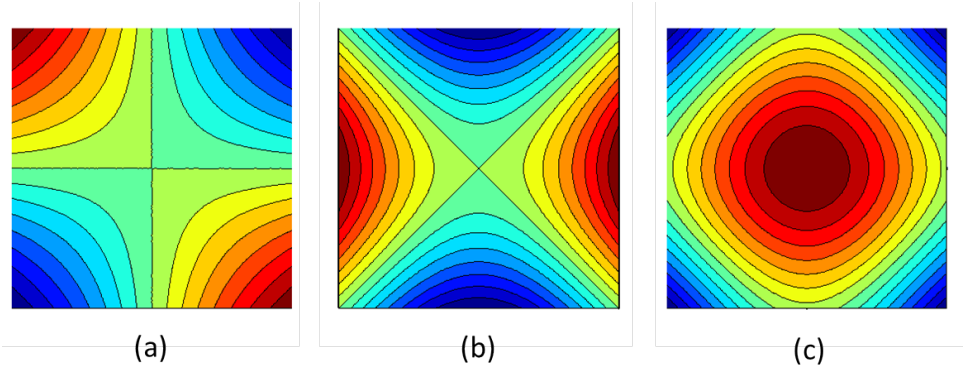

FIGURE 2. First three free-free flexible modes of a square plate (1 mm thick steel, 100 mm × 100 mm): (a) 326 Hz, (b) 476 Hz, (c) 600 Hz

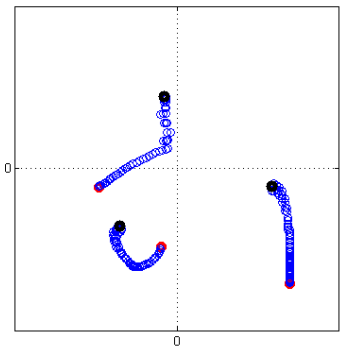

FIGURE 3. Location of support point iterations from initial guess (red) to optimal location (black)

is not trivial as the optimal support locations are neither symmetrically located around the center of the plate nor aligned with the axes of the plate.

THEORY

The eigenvalue sensitivity for a vibrating plate or beam as derived by Won and Park [13] is

$$\delta\lambda = -2\sum_{i=1}^{m} f_i \nabla u(\mathbf{p_i})^T v_i \delta z_i \qquad (1)$$

where f_i is the force in each support, $\nabla u(\mathbf{p_i})$ is the slope of the plate at each support, and $v_i \delta z_i$ is the incremental change in location of each support point. This equation shows that the eigenvalue sensitivity is proportional to the force in each support and local slope of the plate at each support. This is a general result. In cases where the node locations are the optimal support points, the forces are zero and thus the sensitivity is zero. In cases where the optimal support points do not lie on nodal lines, the sensitivity is still used for iteration, but the optimality condition is that two modes have equal frequency and moving the supports further would raise one frequency at the cost of lowering the other.

EXAMPLE – SQUARE PLATE

Consider a square plate with free edges and supported on three points whose locations are to be determined as shown in Figure 1. The first three flexible modes without supports are shown in Figure 2. An initial guess far from the optimal solution is chosen and shown in red in Figure 3. Using a finite element representation of the plate with 200 ×200 elements, the eigenvalue sensitivity, and method of gradient descent as described above, the iterative procedure is used to increase the natural frequency as shown in Figure 5 by adjusting the support locations (see Figure 3) until the first natural frequency is maximized. In this case, the maximum is approximately 10% below the theoretical upper bound. As seen with all of the cases where the three-point mount is unable to achieve the limit eigenvalue, the optimal support positions result in repeated eigenvalues. The coordinates for this optimal mount are given in Table 1, and one can see that the optimal support points do not fall on the axes of plate nor are they symmetrically arranged. If one uses a symmetric three-point mount configuration as sketched in Figure 6, then the maximum value is 267 Hz, or 18% below the limit eigenvalue.

RECTANGULAR PLATES

As the aspect ratio of a plate is increased and becomes more beam-like, the locations of the optimal three-point mount shift from the non-symmetric locations shown for the square plate to align with the nodal locations of the first bending mode. The critical aspect ratio is approximately

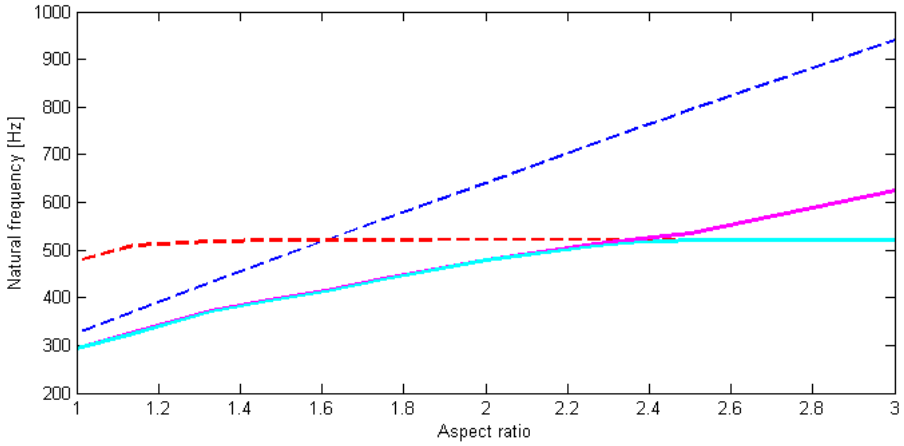

FIGURE 7. First two natural frequencies of free-free rectangular plates unconstrained and supported on optimal three-point mounts: torsion mode unconstrained (blue dashed), first beam bending mode unconstrained (red dashed), first mode on optimal three-point mount (cyan solid), second mode on optimal three-point mount (magenta solid)

TABLE 1. Optimal support locations for a square plate (origin is at the center of the plate)

Point	X/L	Y/L
A	-0.07	0.24
B	-0.13	-0.2
C	0.26	-0.02

2.4 as shown in Figure 7. Also plotted in the same figure are the first two natural frequencies of the unconstrained plate, which are the upper bound values for the constrained plate. For aspect ratios below 2.4, the three-point mount is unable to achieve the upper bound. For the aspect ratios below this critical value, the optimal three-point mount results in a repeated eigenvalue. For plates with aspect ratios greater than this critical value, the eigenvalues become distinct and the locations of the support positions which maximize the first mode are not unique. A second optimization can be performed over that set of points to optimize the second natural frequency as well.

In Tables 2 and 3 and Figures 8–10 we provide examples for rectangular plates. A rectangular plate with 4:3 aspect ratio has mode shapes given in Figure 8. From the figure as well as Table 2, one can see that the support points are still not aligned with the axis of the plate. However the mode shapes are beginning to resemble the twist and beam bending mode shapes. For a rectangular plate with 2:1 aspect ratio, the optimal support points are aligned with the axis of the plate as shown in Figure 9 and Table 3. In this case, the mode shapes clearly are clearly torsion and beam bending, but the eigenvalues are still repeated. The beam bending mode is not identical to the unconstrained mode shape, as can be seen by its asymmetry. Figure 10 shows the results of the optimization of the first natural frequency for a 3:1 rectangular plate. The first natural frequency achieves its limit eigenvalue and the two eigenvalues are distinct. As a results the support locations must align with the nodal lines of the unconstrained mode shape.

TABLE 2. Optimal support locations for a 4:3 rectangular plate (origin is at the center of the plate)

Point	X/L	Y/L
A	0.005	0.20
B	-0.19	-0.14
C	-0.22	-0.12

TABLE 3. Optimal support locations for a 2:1 rectangular plate (origin is at the center of the plate)

Point	X/L	Y/L
A	0	0.24
B	-0.16	-0.21
C	0.16	0.21

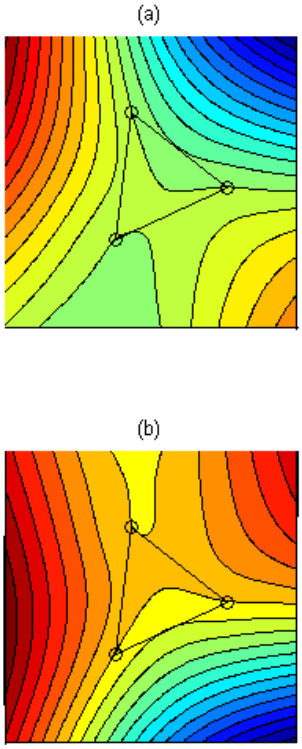

FIGURE 4. First two mode shapes with the optimal three-point mount locations; both natural frequencies are 293 Hz

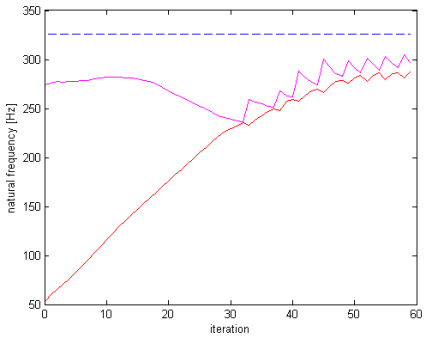

FIGURE 5. First two natural frequencies for the square plate on three point mount (red and magenta solid lines, respectively) from initial guess to convergence compared with the first free-free natural frequency (blue dashed).

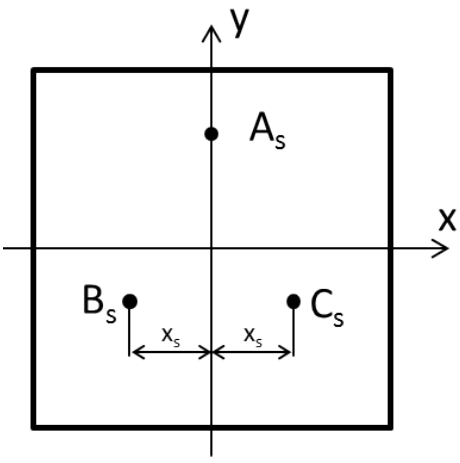

FIGURE 6. Square plate with three point supports A_s, B_s, and C_s where A_s lies on the axis of the plate and B_s and C_s are located symmetrically about the y *axis*

CONCLUSIONS

Square and rectangular plates and three point mounts are frequently encountered in precision engineering yet the optimal support locations are neither obvious in general nor readily available in the literature. We apply eigenvalue sensitivities with the finite element method to find the optimal three point mounts of square and rectangular plates. For the square plate, the optimal support locations are neither aligned with the axes of the plate nor located symmetrically. The maximum natural frequency is approximately 10% less than the limit eigenvalue but 10% greater than the maximum frequency that can be attained with a symmetric three-point mount. As the aspect ratio of the plate increases and becomes more beam-like, the support locations shift towards alignment with the axis of the plate and the nodal locations of the first bending mode. For aspect ratios greater than approximately 2.4, the optimal three-point mount locations correspond to the nodal locations of the first bending mode and the first limit eigenvalue is achieved.

REFERENCES

[1] B. Akesson and N. Olhoff. Minimum stiffness of optimally located supports for maximum value of beam eigenfrequencies. *Journal of Sound and Vibration*, 120(3):457–463, 1988.

[2] M. I. Friswell. Efficient placement of rigid supports using finite element models. *Communications in Numerical Methods in Engineering*, 22(3):205–213, 2006.

[3] R. Grandhi. Structural optimization with frequency constraints-a review. *AIAA journal*, 31(12):2296–2303, 1993.

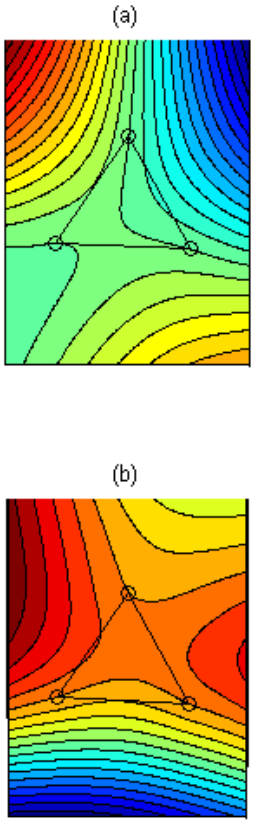

FIGURE 8. First two mode shapes for a 4:3 rectangular plate on its optimal three point mount.

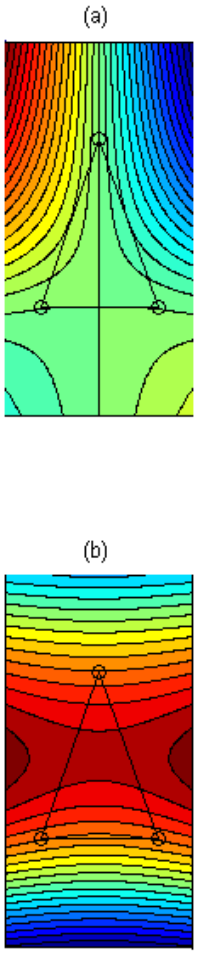

FIGURE 9. First two mode shapes for a 2:1 rectangular plate on its optimal three point mount.

[4] J. H. Hindle. Mechanical flotation of mirrors. *Advanced Telescope Making*, 1945.

[5] S. A. Nayfeh and J. M. Verdirame. Design of constraint systems based on the rayleigh quotient and minimax properties of eigenvalues. In *Proceedings of the 30th Annual Meeting*, pages 105–109, November 2015.

[6] S. Nomura and B. Wang. Free vibration of plate by integral method. *Computers & structures*, 32(1):245–247, 1989.

[7] J. H. Son and B. M. Kwak. Optimization of boundary conditions for maximum fundamental frequency of vibrating structures. *AIAA journal*, 31(12):2351–2357, 1993.

[8] J. M. Verdirame and S. A. Nayfeh. Design of constraint systems for rectangular plates based on the rayleigh quotient and minimax properties of eigenvalues. In *Proceedings of the Fifth Topical Meeting on Precision Mechatronic System Design and Control*, pages 62–67, April 2016.

[9] D. Wang, J. Jiang, and W. Zhang. Optimization of support positions to maximize the fundamental frequency of structures. *International journal for numerical methods in engineering*, 61(10):1584–1602, 2004.

[10] R. N. Wilson. *Reflecting Telescope Optics II: Manufacture, Testing, Alignment, Modern Techniques*. 2013.

[11] K.-M. Won. Eigenvalue sensitivity analysis of structures using lagrange multiplier method and its applications, 1997.

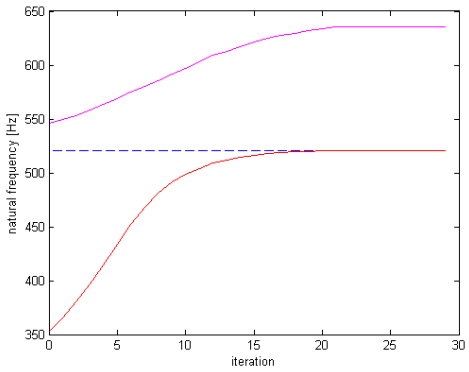

FIGURE 10. Optimization sequence for a 3:1 rectangular plate. The first natural frequency (red solid) achieves the limit natural frequencey (blue dashed) and it distinct from the second natural frequency (magenta solid).

[12] K.-M. Won and Y.-S. Park. The eigenvalue sensitivity of constrained structures using lagrange multiplier method and its applications. In *15th International Modal Analysis Conference*, pages 545–550, 1997.

[13] K.-M. Won and Y.-S. Park. Optimal support positions for a structure to maximize its fundamental natural frequency. *Journal of Sound and Vibration*, 213(5):801–812, 1998.

[14] P. R. Yoder Jr. *Opto-mechanical systems design*. CRC press, 2005.

THE PROBLEM OF 'WEAK' EQUIVALENCE IN MEASUREMENT COMPARISONS: X-RAY CT METROLOGY CASE

Herminso Villarraga-Gómez[1, 2], and Stuart T. Smith[1]
[1]Center for Precision Metrology, University of North Carolina at Charlotte, NC, USA
[2]Nikon Metrology, Inc., Brighton, MI, USA

In the world of experimentation and the science of measurement it is not possible to establish an equality relation ("=") between two distinct events or measurement results. This is so because, typically, there are uncertainties associated with measurement results. Nevertheless, establishing agreement (or equivalence relations) between measurement results that are supposed to represent the same measurand is of crucial importance, especially for the adequate assessment of interlaboratory comparisons. This paper addresses this problem by re-examining several concepts currently under development in the field of metrology (e.g., compatibility and traceability), and proposes complementary and alternative ideas for establishing equivalence of measurements in comparison schemas. Special attention is paid to the current state of measurements comparisons in the field of dimensional X-ray computed tomography (CT), by presenting a comprehensive study of statistical consistency (null-hypothesis testing) applied to the measurement results of two recent interlaboratory comparisons: the "CIA-CT Inter-laboratory Comparison" [1] and the "CT Audit" [2]. In general, in the field of metrology, the equivalence between measurement results is usually established by the so-called "metrological compatibility"—see Appendix B for definition—but this is a non-transitive concept, and it can be incompatible with the 'metrological traceability' definition given by the International Vocabulary of Metrology (VIM) [3] because "an unbroken chain of comparisons is a necessary but not sufficient condition for traceability" [4]. The artificial example, case (b), presented in Table 1 and in the comparisons depicted in Figure 1 (see Appendix A), expose this problem if Lab2 is considered the reference or calibrated measurement (pertaining to a higher echelon or standard) in the set of three measurements being compared. The mathematical constraint demanded by Eq. (*B.1*) gets broken when comparing the measurement results from Lab1 and Lab3 ($\zeta_{13} > 2$); this happens despite Lab1 being compatible with (and hypothetically traceable to) Lab2, and Lab3 being compatible with (and hypothetically traceable to) Lab2 as well. The set of results in the case (b) of Table 1, is not metrologically compatible despite having overlapping uncertainty intervals. By contrast, the measurements presented in case (a), see Figure 1, are compatible with each other and hold the transitivity property. The problem of 'weak' equivalence in measurement results (non-transitivity in general), and the paradoxes generated by concepts of 'compatibility' that are based on the VIM [3], are mainly rooted in the 'strict' mathematical formulation that does not fully recognize the differences between empirical data (or the world of empirical phenomena that happens in the laboratory [5]) and the world of symbolic expressions from the realm of mathematics (and logic) that is based in a language, "far too precise for expressing experimental knowledge" [4]. In recent developments of the theory of measurement, it has been suggested that the conditions of 'compatibility' need to be relaxed by fuzzy logics and 'mutual recognition arrangement', and that a 'weak transitivity' property could be defined to extend the 'metrological compatibility' concept to a full set of measurement results $\{q_1, q_2, \ldots, q_N\}$, so if each element q_i and q_j from the set is recognized as 'compatible' with and traceable to a reference measurement q_r, the compatibility between q_i and q_j can be drawn [4]. This definition relies heavily on the concept of 'metrological traceability', which intrinsically implies comparison of the elements in the set against a reference measurement of higher accuracy (and precision), and ultimately, relating the measurement results (from a working instrument) to the International System of Units (SI) through a documented unbroken chain of calibrations or comparisons [3, 6], each contributing to the measurement uncertainty as shown in Figure 2. Furthermore, the 'metrological compatibility' of the group should be anchored by a 'weak transitivity' property, see Appendix B. But this, at the same time, would imply that the 'compatibility' would be tainted by the 'weakness' adjective and the 'weak equivalence' in measurement results. This paper further explores these newly developed ideas, and proposes to complement them with the (also recently developed) concept of 'all-pair-difference' (APD) chi-square statistic χ^2_{APD} [7, 8, 9, 10] for

hypothesis testing in measurement science. The advantages of this new approach are illustrated by a comprehensive analysis of data obtained from interlaboratory comparisons of dimensional X-ray computed tomography (CT) measurements, specifically the results from the "CIA-CT Inter-laboratory Comparison" [1] and the "CT Audit" [2], which are the first interlaboratory comparisons performed in the field of X-ray CT metrology and are still two of only a few interlaboratory studies of international CT research collaboration referenced in the literature since 2012/2013. The null-hypothesis test of statistical consistency is performed with both the traditional chi-square statistic χ_c^2 (mediated by a reference value) and the unmediated χ_{APD}^2, and three different metrics: the E-scores (E_n), the robust Z-scores (Z'_{rob}), and the Z -scores without outliers ($Z'_{w/o}$)—see Appendix B for definitions—are used with each statistic for comparison. The election of the χ_{APD}^2 statistic in this study for performing measures of statistical consistency is justified by its potential in addressing the problem of 'weak equivalence'. The χ_{APD}^2 statistic directly uses peer-to-peer comparisons, unmediated by a reference value, and as such, it can distinguish pair-difference discrepancies that are hidden by traditional chi-square tests [10]. Thus, APD aggregates can be used across different chains of comparisons to verify the average agreement of the measurement-to-measurement 'compatibility' and consolidate pairwise traceability. It is worth mentioning, this research uses Monte Carlo simulation for a rigorous testing of the null-hypothesis and for evaluation of probabilities related to the chi-square statistics, χ_c^2 and χ_{APD}^2. Although χ_{APD}^2 does not require the comparison of X-ray CT measurements against reference values, the χ_c^2 statistic still needs them. Therefore, four different indicators of central tendency are studied here as possible representation of reference ('operative true values') data: the simple mean (SM), the inverse-variance weighted mean (WM), the median (MED), and external measurements obtained by coordinate measuring machines (CMM). From this list, special attention is paid to CMMs which are customarily used as a reference base for X-ray CT measurement comparisons, and additional considerations are presented for dealing with traceability issues so measurements can be properly traced through a hierarchy connected to national or international standards and the SI-units.

CONCLUSIONS

Since the 'metrological traceability' concept—as defined in the VIM—is closely tied to the 'metrological compatibility' idea (see text above), mathematical restrictions of rigorous definitions that are usually applied to define the concepts of compatibility and transitivity in measurement results can negatively impact the traceability of measurement results when compared to reference measurements of higher standards (with less uncertainty). This is illustrated by the artificial example analyzed above, case (b)—see Table 1 and Figure 1. Recently, the χ_{APD}^2 statistic has emerged as an alternative to address the statistical consistency of a set of measurement results by relying directly on peer-to-peer comparisons without using a reference value for the comparison. Combined with the mathematical rigor of traditional null-hypothesis testing, this idea can be used, to partially address the problem of 'weak equivalence' in measurement results, verify average agreement of measurement-to-measurement compatibility, and consolidate pairwise traceability across different chains of comparisons. The work presented here demonstrates this by analyzing the measurement results from two recent interlaboratory studies in the field of dimensional X-ray CT metrology. The analysis is performed with three different metrics (E_n, Z'_{rob}, $Z'_{w/o}$; see Appendix B) and concludes that the use of the χ_{APD}^2 statistic with the Z'_{rob} metric is the most discriminant for current assessment of X-ray CT metrology comparisons (see Figure 3 in Appendix A). This is because, on the one hand, the Z'_{rob} metric is more effectively shielded against outliers than the $Z'_{w/o}$ metric, and on the other hand, although the E_n metric is more frequently used in the literature, it leads to inconsistencies when uncertainties are not estimated in a uniform and consistent way [11]—the current situation of CT measurement comparisons. As a further matter, the χ_c^2 statistic mediated by either the simple mean or the inverse-variance weighted mean (based in pure X-ray CT data), produce results that, in the absence of a significant bias, coincide with those of the χ_c^2 statistic when CMM data is used as reference (if CMM uncertainties are smaller than what is expected from CT measurement). Effectively, CMM reference values serve as a first link in the traceability chain that connects dimensional X-ray CT data (from calibrated equipment) with the SI-unit of length.

APPENDIX A – TABLES AND FIGURES

TABLE 1. Example of 'compatibility' evaluation.

	Lab1	Lab2	Lab3	ζ_{12}	ζ_{32}	ζ_{13}
(a)	4 ± 0.6	3 ± 0.1	4 ± 0.6	1.56	1.56	0.00
(b)	2 ± 0.6	3 ± 0.1	4 ± 0.6	1.65	1.65	2.36

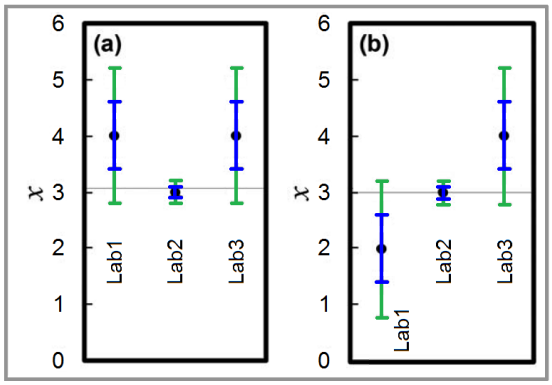

FIGURE 1. Graphical representation of the two different comparisons from Table 1.

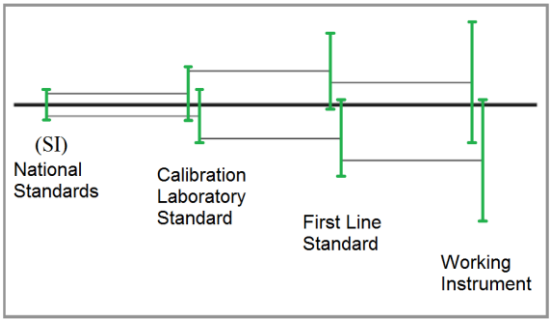

FIGURE 2. Scheme of 'metrological traceability'.

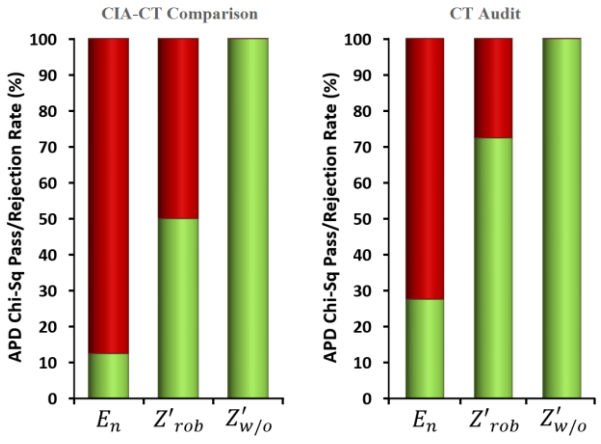

FIGURE 3. Rate of aceptance (green color) and rejection (red color) of the null-hypothesis of statistical consistency H_0 with the χ^2_{APD} statistic.

APPENDIX B – DEFINITIONS

Metrological Compatibility

Two comparable measurement results $q_i \equiv \{x_i, u_i(x_i)\}$ and $q_j \equiv \{x_j, u_j(x_j)\}$ for the same measurand, with u_i and u_j as the respective standard uncertainties for the measured values x_i and x_j, are said to have 'metrological compatibility' if [12, 13],

$$\zeta_{ij} = \frac{|x_i - x_j|}{u(x_i - x_j)} \leq \tau, \qquad (B.1)$$

with τ as the threshold factor (typically chosen to be equal to 2) for the standard uncertainty of the measurements' difference,

$$u(x_i - x_j) = \sqrt{{u_i}^2 + {u_j}^2 - 2\gamma u_i u_j}\,, \qquad (B.2)$$

where $\gamma = \gamma(x_i, x_j)$ is the correlation factor between the measurements in terms of their variances and covariances as defined in the Guide to the Expression of Uncertainty in Measurement (GUM) [14]. The concept of 'metrological compatibility' can be extended to a set of results $\{q_1, q_2, \ldots, q_N\}$ if all the possible combinations of pairs of results hold metrological compatibility [12, 13].

Equivalence Relation

Equivalence expresses sameness or similarity. In mathematics (e.g., see [15]), a relation R on a set A is called an 'equivalence relation' if and only if R is reflexive, symmetric, and transitive. Equality ("$=$") of real numbers is an example of an equivalence relation, so it is said that the real numbers x and y are equivalent if we simply have the following properties: $x = x$ (reflexivity); if $x = y$, then $y = x$ (symmetry); and if $x = y$ and $y = z$, then $x = z$ (transitivity).

Weak Transitivity

Let "$\approx$" be the relation of compatibility (indistinguishability and mutual substitutability [4]). If $q_i \approx q_j$ and $q_j \approx q_k$, with $q_k \equiv \{x_k, u_k(x_k)\}$ being another measurement result for the same measurand, not necessarily yields $q_i \approx q_k$, not

even for an 'unbroken chain' of compatibility comparisons $q_1 \approx q_2 \approx \cdots q_i \approx q_j \approx q_k \approx \cdots q_N$. But if each measurement (q_i and q_k) is recognized compatible with and traceable to a reference measurement q_r (presumably having smaller uncertainty than q_i and q_k), the compatibility between q_i and q_k could be drawn [4], i.e., $(q_i \approx q_r) \wedge (q_k \approx q_r) \longrightarrow (q_i \approx q_k)$.

Null-hypothesis Testing

The null-hypothesis of statistical consistency H_0 is typically contrasted against an alternative hypothesis of 'inconsistency' H_1, with definitions as follow

H_0: the observed dispersion in the measurement results of an intercomparison is consistent with the variances described by the interlaboratory uncertainties; i.e., the variances of the measured values $\{x_1, x_2, \ldots, x_N\}$ are less than or equal to their stated values $u_i^2(x_i)$, or more generally, less than or equal to the normalization factors ρ_{ir}^2 (see definitions below).

H_1: agreement among the participants from the intercomparison can be statistically rejected since the scatter in the measured values $\{x_1, x_2, \ldots, x_N\}$ exceeds what would be expected from the claimed uncertainties $u_i(x_i)$, or more generally, what would be expected from the variances described by the dispersion factors ρ_{ir}.

In this paper, the null-hypothesis is tested by evaluating the chi-square statistic χ_c^2, or alternatively one of the 'chi-square-like' statistics defined below (e.g., χ_{APD}^2).

Chi-square Statistic

The classical reduced chi-square statistic ${\chi_c}^2$ for a set of measurements $\{q_1, q_2, \ldots, q_N\}$ with ν degrees of freedom is defined as,

$$ {\chi_c}^2 = \langle \xi_{ir}^2 \rangle = \frac{1}{\nu} \sum_{i=1}^{N} \xi_{ir}^2 = \frac{1}{\nu} \sum_{i=1}^{N} \frac{(x_i - x_r)^2}{\rho_{ir}^2} \qquad (B.3) $$

with "ξ_{ir}" the proficiency testing metric of choice and ρ_{ir} its respective normalization factor extended for correlated measurements (i.e., including covariances between x_i and x_r). The ξ_{ir}-values represent the vector components of the L^2 space with the RMS-norm $\langle \xi_{ir}^2 \rangle^{1/2}$. For example, if "$\xi_{ir}$" represents the E_n-metric then the ξ_{ir}-values have the normalization factor defined as $\rho_{ir} \equiv \sqrt{{u_i}^2 + {u_r}^2 - 2\gamma_{ir} u_i u_r}$. If the ${Z'}_{rob}$-metric is used instead, the ξ_{ir}-values are defined as

$$ \xi_{ir} = {Z'}_{rob} \equiv \frac{(x_i - x_r)}{\sqrt{{\sigma_{rob}}^2 + {u_r}^2 - 2\gamma_{ir}\sigma_{rob} u_r}} \qquad (B.4) $$

with σ_{rob} the 'robust' standard deviation calculated by an iterative algorithm as presented in the ISO 13528 [16]. Similarly, if the ${Z'}_{w/o}$ -metric is selected, then the ξ_{ir}-values are equivalent to the ${Z'}_{w/o}$-scores defined as

$$ \xi_{ir} = {Z'}_{w/o} \equiv \frac{(x_i - x_r)}{\sqrt{{\sigma_{w/o}}^2 + {u_r}^2 - 2\gamma_{ir}\sigma_{w/o} u_r}} \qquad (B.5) $$

with $\sigma_{w/o}$ as a standard deviation calculated from the data set without outliers (i.e., taking outliers out).

Statistical Consistency

The set of measurements $\{q_1, q_2, \ldots, q_N\}$ with ν degrees of freedom, is said to be "statistically consistent" if

$$ \chi_c^2 \leq \chi_c^2(\alpha, \nu) \qquad (B.6) $$

for a factor $y_c \equiv \chi_c^2(\alpha, \nu)$ defined by the probability

$$ \alpha = P[\chi_c^2 > y_c] = \int_{\chi_c^2(\alpha,\nu)}^{\infty} f(\chi_c^2) d\chi_c^2 \qquad (B.7) $$

Here, $P[\chi_c^2 > y_c]$ is the probability of y_c being exceeded by the 'chi-square' quantity χ_c^2 resampled from N hypothetical Gaussian distributions with expected values equal to the reference value $\mu_i = x_r$ and having variances adequately described by the squared standard uncertainties $u^2(x_i - x_r)$ or by the normalization factors ρ_{ir}^2 defined above (in the extended cases of correlated measurements). A typical level of significance chosen for interlaboratory evaluations is $\alpha = 0.05$, i.e., $P[\chi_c^2 > y_c]$ should be larger than or equal to 5% for the statistical test to pass. This

means that deviations from expectations that are likely due to chance are within a 95% level of confidence, or in other words that the threshold for acceptance of randomness claim is 5% so a probability (or level of significance) $P[\chi_c^2 > y_c]$ lower than 5% will fail the test and reject the null-hypothesis H_0.

Pair-difference Chi-square Statistic

To provide a measure of agreement (or laboratory 'equivalence') for a particular measurement q_j compared with the other $(N-1)$ measurements, unmediated neither by an estimator of central tendency nor by a reference measurement q_r, a variant of the chi-square-like statistic χ_c^2 can be defined as follow [7, 8, 9, 10],

$$\chi_{PDj}^2 = \langle \xi_{ji}^2 \rangle = \frac{1}{N-1} \sum_{i=1, i\neq j}^{N} \xi_{ji}^2 = \frac{1}{N-1} \sum_{i=1, i\neq j}^{N} \frac{(x_j - x_i)^2}{\rho_{ji}^2} \qquad (B.8)$$

This is an average over all possible bilateral 'pair-differences' (PD) involving laboratory j , and compares the observed variances (of x_j from each x_i) respect to the dispersion expected by the claimed variances (and covariances) from ρ_{ji} . These PD aggregates basically characterize the average agreement of any measurement q_j with any other, averaged over all the measurements used for the comparison. Although the quantity χ_{PDj}^2 does not necessarily correspond to an exact reduced chi-square distribution [8, 10], it still provides a method for testing the null-hypothesis of statistical consistency H_0 but with $y_c = \chi_{PDj}^2(\alpha, \nu)$ and the variances ρ_{ir} exchanged for ρ_{ij}. In this case, the test of consistency addresses the { j —participant}-to-participants' equivalence by pairwise combination. The threshold for acceptance of the randomness claim is again 5% probability (or 0.05 level of significance), i.e., $P\left[\chi_{PDj}^2 > y_c\right] \geq 5\%$ would accept the null-hypothesis H_0 and pass the statistical test of consistency for 'pairwise equivalence' of the measurement q_j with all the other ($N-1$) measurements.

All-pair-difference Chi-square

One more variant of a 'chi-square-like' statistic can be extended to all the comparable pair-differences of a set of N measurement results, defining the 'all-pair-difference' (APD) statistical quantity [7, 8, 9, 10],

$$\chi_{APD}^2 = \langle \chi_{PDj}^2 \rangle = \langle \langle \xi_{ji}^2 \rangle \rangle = \frac{1}{N(N-1)} \sum_{j=1}^{N} \sum_{i=1, i\neq j}^{N} \frac{(x_j - x_i)^2}{\rho_{ji}^2} \qquad (B.9)$$

This is an average over all the distinct pair-differences χ_{PDj}^2 from the whole set of measurements $\{q_1, q_2, \ldots, q_N\}$. It is the aggregate average over all the non-degenerate pairs comparisons contrasting the experimental pair-differences against the scatter expected by the claimed variances (and covariances) from ρ_{ji}. The APD statistic is nearly an exact chi-square, and in the case of probability density distributions drawn from identical Gaussian distributions, it can be shown by Monte Carlo simulation that χ_{APD}^2 is distributed as an exact classical reduced chi-square χ_c^2 with $(N-1)$ degrees of freedom [8, 10]. The main difference χ_{APD}^2 has respect to the traditional χ_c^2 is that it is an unmediated aggregate (it does not depend of the selection of a particular reference value), and as such, they provide a measure of measurement-to-measurement agreement between all pairs of measurements. Accordingly, the null-hypothesis test of statistical consistency (with variances ρ_{ir} exchanged for ρ_{ij}) can be applied with $y_c = \chi_{APD}^2(\alpha, \nu)$ and $\nu = N-1$ for the conventional 5% 'cutoff' criterion. In this case, $P[\chi_{APD}^2 > y_c] \geq 5\%$ would be the necessary condition for accepting the null-hypothesis H_0 and pass the test of statistical consistency within a 95% level of confidence, indicating whether the dispersion of the results is suitable with the dispersions that would be expected from the claimed variances (and covariances) included in ρ_{ji}.

ACKNOWLEDGMENTS

The authors would like to express their appreciation to Alan G. Steele from the Institute for National Measurement Standards, National Research Council of Canada (Ottawa, Canada), for his cooperation in providing the toolkit software used for Monte Carlo simulation.

REFERENCES

[1] J. Angel and L. De Chiffre, "Inter laboratory comparison on Industrial Computed Tomography: CIA-CT comparison - Final report," Final Report, DTU Mechanical Engineering, Denmark, 2013.

[2] S. Carmignato, A. Pierobon and E. Savio, "Interlaboratory Comparison of Computed Tomography Systems for Dimensional Metrology: CT Audit," Final Report, University of Padova - Lab. MGI, Italy, 2012.

[3] BIPM/JCGM, "International Vocabulary of Metrology – Basic and general concepts and associated terms," 2012. [Online]. Available: http://www.bipm.org/utils/common/documents/jcgm/JCGM_200_2012.pdf.

[4] L. Mari and S. Sartori, "A relational theory of measurement: Traceability as a solution to the non-transitivity of measurement results," *Measurement,* vol. 40, p. 233–242, 2007.

[5] P. Bridgman, "How much rigor is possible in physics?," in *Henkin L, Suppes P, and Tarski A (Eds), The Axiomatic Method*, New York, NY (USA), North-Holland, 1959, pp. 225-237.

[6] G. Barbato, A. Germak and G. Genta, Measurements for Decision Making, Measurements and Basic Statistics, Bologna (Italy): Società Editrice Esculapio, 2013.

[7] A. J. Steele and R. J. Douglas, "Extending En for measuring science," *Metrologia,* vol. 43, pp. S235-S243, 2006.

[8] A. G. Steele and R. J. Douglas, "Extending chi-squared statistics for key comparisons in metrology," *Journal of Computational and Applied Mathematics,* vol. 192, pp. 51-58, 2006.

[9] A. Steele and D. R. J, "Establishing confidence from measurement comparisons," *Meas. Sci. Technol.,* vol. 19, pp. 1-13, 2008.

[10] R. J. Douglas and A. G. Steele, "Pair-difference chi-squared statistics for Key Comparisons," vol. 43, pp. 89-97, 2006.

[11] H. Villarraga-Gómez, R. J. Hocken, E. P. Morse and S. T. Smith, "Proficiency testing for interlaboratory comparisons on industrial computed tomography," in *ASPE Spring Topical Meeting - Volume 57*, Berkeley, CA (USA), pp 92-97, 2014.

[12] R. Kessel, R. N. Kacker and K. D. Sommer, "Combining results from multiple evaluations of the same measurand," *J. Res. Natl. stand. Technol.,* vol. 116, no. 6, pp. 809-820, 2011.

[13] R. N. Kacker, R. Kessel and K. D. Sommer, "Assessing differences between results determined according to the Guide to the Expression of Uncertainty in Measurement," *J. Res. Natl. stand. technol.,* vol. 115, no. 6, pp. 453-459, 2010.

[14] ISO/IEC Guide 98-3, Uncertainty of measurement - Part 3: Guide to the expression of uncertainty in measurement (GUM:1995), ISO copyright office, 2008.

[15] C. C. Pinter, A Book of Abstract Algebra, 2nd Ed, New York, NY (USA): McGraw-Hill, 1990.

[16] ISO 13528, Statistical methods for use in proficiency testing by interlaboratory comparisons, ISO copyright office, 2005, pp. 1-32.

ADDITIVE MANUFACTURING OF REFLECTIVE OPTICAL COMPONENTS

Bradley H. Jared, Tom Chavez, Junoh Choi, Adam W. Cook, Christopher B. Diantonio, William Reinholtz, Michael P. Saavedra, David J. Saiz, Edward G. Winrow
Sandia National Laboratories
Albuquerque, NM

High performance optical systems are commonly placed in extreme environments which produce strict constraints relative to size, weight, and power. Precision processes are also necessary for optical component fabrication due to surface form and finish requirements. As a result, design solutions are commonly sub-optimal, overly complex, expensive and difficult to fabricate and assemble. Additive manufacturing (AM) has recently garnered significant interest across a host of applications and industries intent on increasing design freedom and reducing the cost and lead-time for small quantity, high value fabrication lots. AM's use in optical systems, however, has been relatively restrictive due to inadequate part accuracies, rough surface finishes and material limits. Nevertheless, opportunities exist to leverage AM for optical systems, especially aggressively light-weighted reflective optics.

The feasibility of using AM to produce optical components has been demonstrated in the literature [1], and was initially explored at Sandia by designing and prototyping a simple 101.6mm flat mirror. The mirror was light-weighted using standard opto-mechanical design practices, Figure 1, and checked for gravity loads using finite element analysis, Figure 2. The geometrical freedom afforded by AM was leveraged by integrating flexural alignment features into the sub-frame to produce a monolithic structure impossible to generate by traditional manufacturing processes, Figure 3. The design was printed in Ti6Al4V using laser powder bed fusion after which a 0.5mm thick electroless Ni plating was applied to the front and rear mirror faces. Diamond turning of the front face was performed to generate the desired mirror surface. Nickel plating issues resulted in poor mirror surface form and finish. Lead time for the mirror assembly, however, was

FIGURE 1. Mirror structure design.

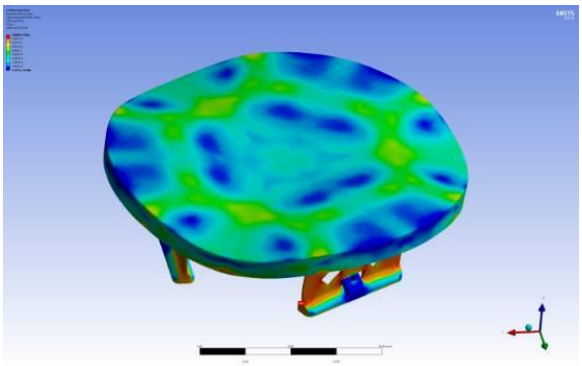

FIGURE 2. Mirror sag under axial gravity from a finite element analysis.

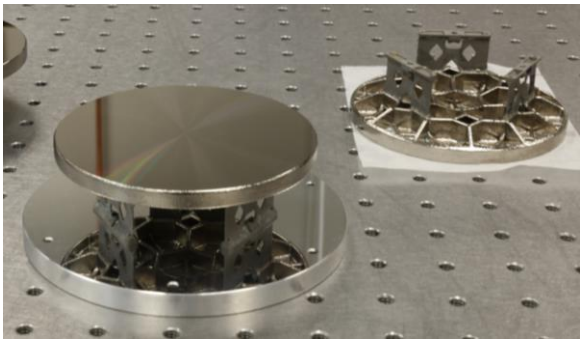

FIGURE 3. Additively manufactured Ti6Al4V mirror with integrated flexural alignment features. The printed Ti6Al4V has an electroless Ni coating which has been diamond turned.

reduced almost an order of magnitude compared to traditional fabrication and procurement routes. Such rapid fabrication highlights AM's potential to meet rapid response criteria necessary for optical components serving critical mission applications.

The initial mirror prototype prompted a new effort to develop and fabricate an AM based optical system that will be tested under relevant thermal and vibration environments. Issues identified with plating, form error and surface finish in the mirror prototype are being addressed. Further benefits of AM for reflective optical components, however, are also being considered. The larger available design space is being explored by using topology optimization to optimize mirror stiffness and weight, Figure 4. Integration of additional mirror features (ex. mounts, sunshades, tubes) into the monolithic structure is also being considered to eliminate mirror deformations associated with assembly.

The use of novel, ceramic materials for a monolithic optical structure is being developed due to their higher modulus of elasticity and lower coefficient of thermal expansion than traditional metals. Sandia has extensive experience developing processes and materials for additive manufacturing of ceramics using direct write printing [2]. This experience is being leveraged in current efforts to explore the design, process and material options available for optical components. Initial work to print, post-machine and sinter alumina parts is promising and has initiated work to explore processing to achieve optical surfaces. Figure 5 shows the

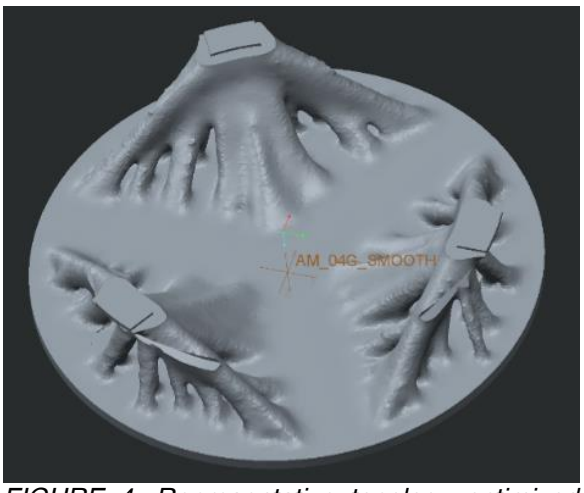

FIGURE 4. Representative topology optimized mirror structure design.

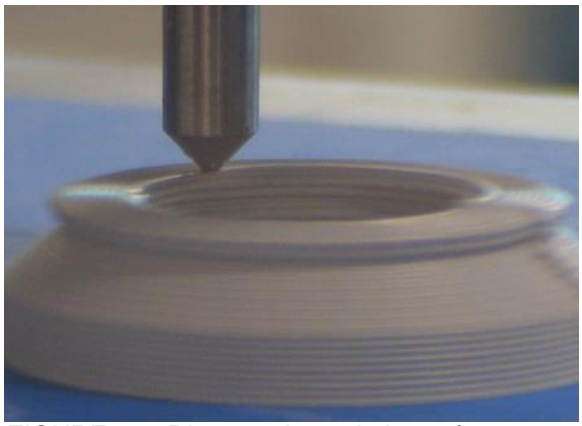

FIGURE 5. Direct write printing of a green ceramic part.

FIGURE 6. Direct write printing of a green ceramic part.

direct write process used to deposit an alumina ceramic material to print a representative ceramic structure. While printing green state alumina is simple conceptually, feedstock composition and rheometry must be carefully characterized, controlled and coupled with subsequently appropriate process conditions (ex. pressure and print tip velocity) to insure proper part filling, geometrical accuracy and green state stability. Figure 6 demonstrates a relatively simple puck sample used in development to explore necessary process steps such as printing, green-state machining, de-binding, sintering, and post-sinter grinding and polishing.

Additive processes for advanced ceramic materials do introduce access to geometries not typically achievable through traditional pressing and forming techniques. The complexity observed in metal and polymer materials is not

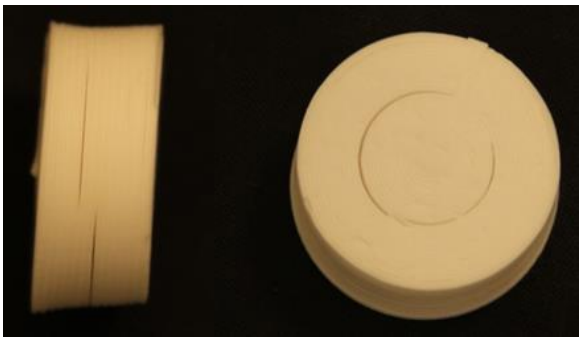

FIGURE 7. Part fractures and delamination produced by thermal stresses generated during burn-out and sintering.

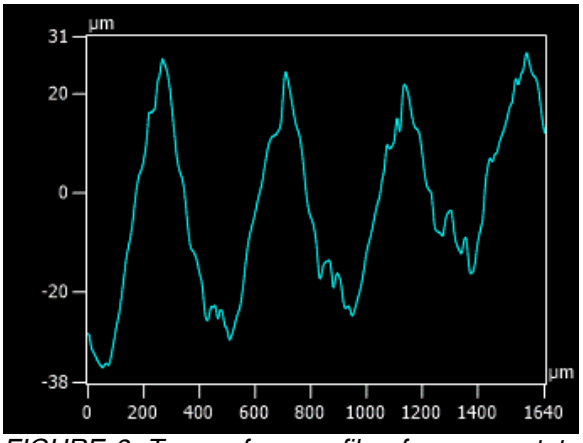

FIGURE 8. Top surface profile of a green state printed part.

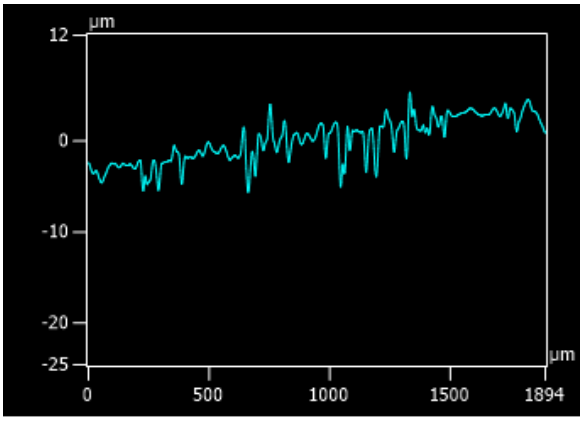

FIGURE 9. Top surface profile of a green state printed part that has been dry lapped.

necessarily accessible for fully dense ceramic materials, however, since green state materials must maintain their geometry despite limited strength. Thus, large overhangs are generally impractical. A primary challenge in ceramics, namely de-binding and sintering, remain as complicating processing factors. As with a

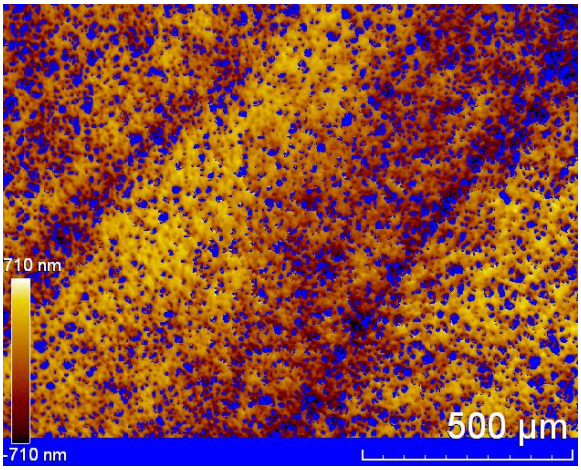

FIGURE 10. Initial polish on a sintered part.

traditional process, thermal processing is crucial to the final part and material as a low temperature de-binding cycle is coupled with a high temperature sintering step to transform the green state printed material to a near theoretical density ceramic form and material. Sintering introduces constraints on part geometries as a components surface area and volume impact organic binder burn-out paths. As a result, improper thermal processing of an AM fabricated ceramic part yields fractures and delamination at print layer interfaces, Figure 7.

Direct write printing of green state ceramic material is quite course. Visual inspection of the top surface of Figure 6 readily reveals the scan pattern from the printing process as well as a center tip similar to the zero velocity condition in face machining. Figure 8 reveals that the magnitude of this surface pattern is on the order of almost 70μm peak to valley, clearly unacceptable for optical components. Dry lapping the green state part quickly reduces the printed surface, Figure 9, but a limit around 4μm S_a was observed during processing that correlates closely with the size of the alumina particles in the feedstock material. Preliminary work, Figure 10, has shown as expected that lapping and polishing the sintered alumina provides a much smoother surface with S_a around 190nm. Significant improvements are expected, however, as on-going work is refining grinding and polishing sintered materials to achieve the form and finish necessary for optical components.

ACKNOWLEDGMENTS

Sandia National Laboratories is a multimission laboratory managed and operated by National

Technology and Engineering Solutions of Sandia LLC, a wholly owned subsidiary of Honeywell International Inc. for the U.S. Department of Energy's National Nuclear Security Administration under contract DE-NA0003525. This document has been reviewed and approved for unclassified, unlimited release, SAND2017-9772A.

REFERENCES

[1] Sweeney M, Acreman M, Vettese T, Myatt R, Thompson M. Application and testing of additive manufacturing for mirrors and precision structures. Proceedings SPIE 9574, Material Technologies and Applications to Optics, Structures, Components, and Sub-Systems II, September 2015.

[2] Cesarano J, Calvert P. Robocasting: direct fabrication of ceramics and composites, Ceramic Transactions, 83, p.241, 1997.

Contactless Shape Manipulation of Thin Substrates Using Air Bearing Table

Theresa M. Spaan-Burke[1], Teunis van Dam[1], Peter Overschie[1], Henny A.M. Spaan[1]
[1]IBS Precision Engineering,
Eindhoven, Netherlands

INTRODUCTION

Externally pressurized aerostatic bearings (from now on referred to as air bearings) are commonly used for conveying large area, thin substrates such as glass sheets [2], [3]. Pressurized air is provided through either orifices or a porous restrictor, establishing an air cushion on which the substrate floats. Regions of sub-atmospheric pressure ('vacuum holes or grooves') can be added to reduce the levitation height and improve the out-of-plane stiffness [3]. In addition, systems have been developed in which the substrate is not only levitated but also actuated in three planar directions, using viscous shear forces controlled by air jets or pressure differentials in the air gap [4]-[6]. A recent survey on this type of mechanisms is found in [7].

It is known that the pressure differentials below the substrate carried by an air bearing table influence the out-of-plane deformation. In theory, individual control of the pressure levels in separate regions of such an air table would allow a degree of control over this deformation. In this paper the feasibility of this concept is investigated. An air table is proposed with a number of separate air bearing regions and sub-atmospheric pressure regions. The pressure in the sub-atmospheric regions is controlled to bend the substrate into pre-defined shapes.

APPROACH

To prove the feasibility of the proposed technology, off-the-shelf Precision Air Bars (New Way Air Bearings®) were selected. Commercially available air bars were chosen over a custom design in order to reduce cost and lead time and because the stable behavior of these products is proven in Flat Panel Display applications. The air bars consist of a 2x8 array of rectangular porous air bearing sections, each containing a single 'vacuum hole' in its center. Here the term 'vacuum' is used to indicate a pressure that is sub-atmospheric. Normally the vacuum holes lead to a single chamber connected to an exhaust pump. For this situation the air bars were modified to allow individual control of the vacuum pressures.

A ø 150 mm circular reflective substrate was chosen as a sample substrate. The substrate deformation was captured using a Fizeau interferometer with ø 150 mm field of view. The geometry of the air bars and circular substrate is shown schematically in Figure 1. Two air bars are placed next to each other and the substrate is placed onto the resulting air table such that it overlaps with twelve of the vacuum holes. The remaining vacuum holes (20 in total) are not used. Only the twelve porous air bearing segments corresponding with the numbered holes are used; the remaining air bearing surface being sealed including those covered partly by the substrate. In this way, the air flowing out of these segments was prevented from forcing the edge of the substrate upwards without compensation of a vacuum hole. Figure 2 shows a schematic cross-section view of a single bearing segment and vacuum hole.

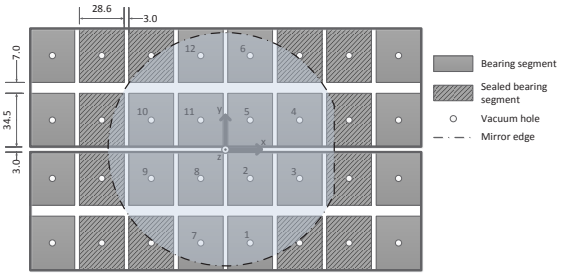

Figure 1. Layout of circular substrate on air table (top view) with definition of hole numbering and (x,y,z) coordinate system. Dimensions in mm.

A Finite Element simulation model was built with which the deformation of the substrate is predicted as a function of applied pressure levels. The ability to deform the substrate into shapes of different form and complexity is demonstrated by selecting a set of target forms, described by Zernike polynomials. The pressure differential patterns such that the resulting

substrate shapes approach these targets as close as possible were defined through this model.

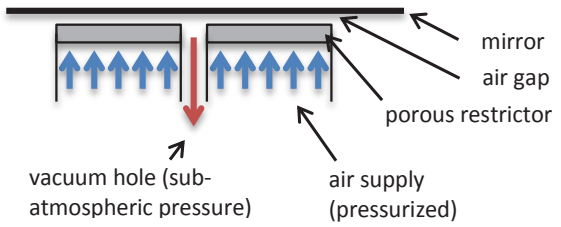

Figure 2 Schematic cross-section of single bearing segment and substrate (side view). The pressure differential between the porous air bearing region and the vacuum hole causes the thin substrate to deform.

An experimental setup was constructed to validate the outcome of the simulations. Vacuum pressure levels were manually manipulated using needle valves and a high-accuracy pressure meter. The resulting shape of the substrate was measured with a Fizeau interferometer. In comparing the measured and simulated substrate shape at identical pressure differential levels, the simulation model is validated.

In the simulation model, the initial deformation of the substrate could not be taken into account. To allow comparison between simulation and experimental results, only 'differential' deformed shapes are therefore compared. Both in the simulations and in the experiments a starting point is found where the pressure levels are optimized for a flat substrate, called the 'flat substrate reference'. In all the experiments where the substrate is forced into a certain shape by defined pressure differentials, the flat wafer reference shape is subtracted from the actual shape.

SIMULATION MODEL AND RESULTS

Nomenclature

h	local air film thickness (m)
H	thickness of porous restrictor (m)
L	characteristic bearing length (m)
p	pressure in air film (Pa)
p_{amb}	ambient pressure (Pa)
p_{in}	supply pressure (Pa)
R_s	specific gas constant of air (J/kgK)
T	temperature (K)
κ	permeability of porous restrictor material (m^2)
Λ	dimensionless bearing number = $12\kappa L^2/h^3H$
μ	dynamic viscosity of air (Pa·s)

To predict the behavior of the substrate floating on the air table a Finite Element model was created in COMSOL Multiphysics®. The model consists of a structural domain, solving for the displacement and deformation of the substrate, and a fluid domain, solving for the pressure in the air film below the substrate. The physical domains are coupled in two directions: the pressure from the fluid domain acts as a distributed load on the structure, while the deformation of the structure defines the height of the air gap in the fluid domain.

Calculation methods to solve the pressure in the air film for porous air bearings consist of a combination of the compressible Reynold's equation with a source flow term as described in literature [7],[8]. In [8], several methods are compared with each other and with experimental data for simple rectangular and circular bearing geometries. A 'no slip' condition in Reynold's equation is compared with various slip models and experimental data over a range of prescribed gap heights. Based on the results of this study and the (partly estimated) dimensions and conditions in this case, using the assumptions of no slip and 1D source flow is justified and will likely not cause more than 1% difference on the outcome of the calculations. The resulting equation describing the pressure in the air film is then given by:

$$\nabla\left(\frac{h^3}{12\mu R_s T}p\nabla p\right) = \frac{\kappa}{2H\mu R_s T}\left(p_{in}^2 - p^2\right) \qquad (1)$$

The combined model is solved for the geometry as presented in Figure 1 using the following conditions: H = 4.5 mm, p_{in} = 5.1 bar absolute, R_s = 287 J/kgK, T = 20°C, μ = 1.81e-5 Pa·s. The value for the permeability κ was determined empirically by measuring the mass flow through an air bar at a fixed pressure differential. In the grooves between the air bearing segments, ambient pressure is assumed: p_{amb} = 1 atm (1.013 bar).

For the substrate, it is assumed that the material properties and thickness are uniform and the substrate is initially flat and free of initial stresses. For the air bearing, it is assumed that the bearing surface is flat and the effective permeability and supply pressure are uniform over the entire surface of all twelve segments.

The calculation time to obtain the substrate shape for a single condition is approximately ten seconds.

Definition of Target Shapes

A set of Zernike polynomials is chosen as target shapes for controlled deformation of the substrate. The use of Zernike polynomials has the following advantages:

- The clear mathematical description of the shapes is convenient for comparison with the simulation outcome and experimental results
- The Zernike shapes are similar to the mechanical mode shapes of a free circular plate
- The Zernike shapes are orthogonal, which is useful for combining different shapes

Number	*Image*	*Description*
1		Piston
2,3		Tilt
4		Defocus
5,6		Astigmatism
7,8		Coma
7',8'		Coma, tilt corrected
9		2nd order spherical aberration
10,11	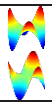	Trefoil

Table 1. Definition of Zernike 1-11. Zernike 4-8 and 10 are used as target shapes. On Zernike 7 and 8, a tilt correction is applied.

The first eleven Zernike shapes, according to the numbering used in [9], are listed in Table 1. Zernike 4-8 and 10 are chosen as target shapes. Zernike 1-3 are not taken into account since they are only rigid body motions and not deformations of the surface, and Zernike 9 and 12 and higher are cannot be realized with the limited number of control points in the chosen bearing configuration. Zernike 7 and 8 are corrected for tilt as shown in the table.

The pressure patterns optimized for each of the target shapes are shown in Table 2. The differential pressure patterns are always chosen such that the average is zero, keeping the average applied pressure at 100 mbar below ambient.

hole #	1	2	3	4	5	6	7	8	9	10	11	12	avg
Z4	25	-49	24	24	-49	25	25	-49	24	24	-49	25	0
Z5	-71	15	56	56	15	-71	-72	15	56	56	15	-72	0
Z6	-31	-14	-44	38	23	28	28	23	38	-44	-14	-31	0
Z7	2	-56	-20	-20	-55	2	5	44	24	24	44	5	0
Z8	14	45	13	-7	-55	-10	14	45	13	-7	-55	-10	0
Z10	-45	-5	26	26	-5	-45	42	13	-30	-30	13	42	0

Table 2. Differential pressure patterns for each Zernike setpoints (mbar).

The resulting calculated differential substrate shapes are shown in Figure 3 and the average fly height and P-V amplitude of these shapes are listed in Table 3.

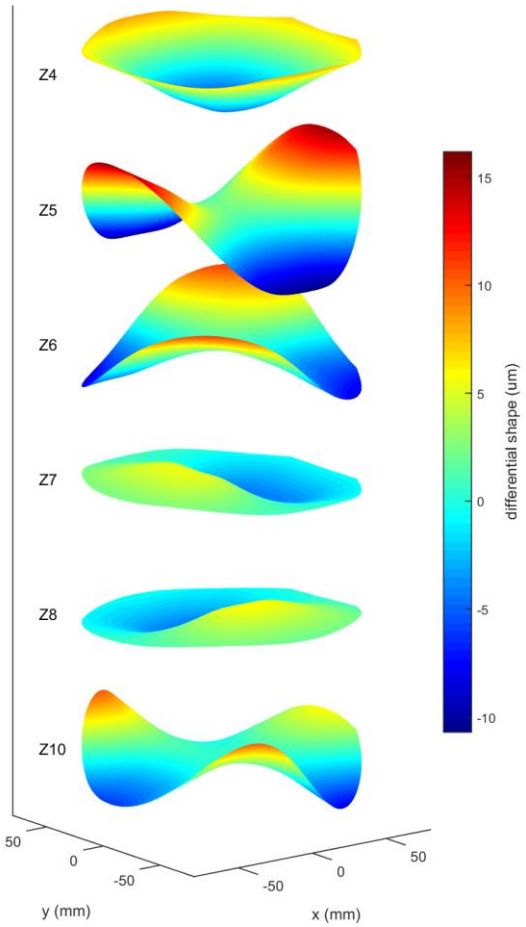

Figure 3. Calculated differential substrate shapes in µm using pressure patterns optimized for target Zernike shapes Z4-Z8 and Z10 (Table 2). All shapes scaled with the same ratio in z-direction

Shape	Average fly height (µm)	Amplitude of differential shape (µm P-V)	RMS deviation from Zernike (µm)
Z4	43.0	13.8	0.79
Z5	43.7	26.8	0.72
Z6	42.0	19.5	0.62
Z7	41.8	9.6	0.74
Z8	41.7	10.6	0.76
Z10	41.6	18.2	0.99

Table 3. Average fly height, P-V amplitude of differential shape and RMS deviation from Zernike for each of the calculated substrate shapes.

For each of the results, the best-fit corresponding Zernike shape is subtracted to get the 'shape deviation'. The RMS values of the shape deviation are also listed in Table 3.

Combining and Scaling Target Shapes

Simulations were conducted to demonstrate the possibility of combining and scaling the realized shapes. Although the equations are not linear, it might still be possible to achieve linear combinations of the individual target shapes using linear combinations of the corresponding pressure patterns. Therefore combined target shape '(Z4+Z6)/2' and a reduced target shape 'Z6/2' are defined. For the '(Z4+Z6)/2' target, the differential pressure level is given by the average of that for Z4 and Z6. For the 'Z6/2' target, the differential pressure level for Z6 is scaled down with a factor two.

The calculated differential substrate shape for (Z4+Z6)/2 and Z6/2 are compared with the 'expected' shapes – the corresponding combination and scaling of the previously calculated shapes for the individual Z4 and Z6 conditions. The results for (*Z4+Z6)/2* are shown in Figure 4. The P-V amplitude of the expected and calculated shapes, and the RMS deviation between the expected and calculated shapes are given in Table 4.

Although the equations describing the relation between pressure and substrate deformation are non-linear, the system behaves approximately linearly in this region: when combining and scaling the pressure patterns of two selected target shapes, the resulting substrate shapes match fairly well with the shapes that would be expected when combining or scaling the original shapes.

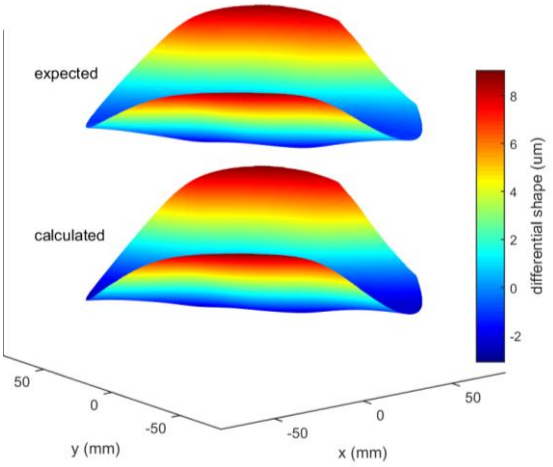

Figure 4. Expected and calculated differential substrate shape for combination of Z4 and Z6 '(Z4+Z6)/2'.

Shape	Amplitude expected diff. shape (µm P-V)	Amplitude calculated diff. shape (µm P-V)	RMS deviation (µm)
Z6/2	9.9	9.6	0.14
(Z4+Z6)/2	11.7	12.2	0.33

Table 4. Amplitude of expected and calculated shape and RMS deviation for combined and scaled target shapes.

EXPERIMENTAL SETUP AND PROCEDURE

The experimental setup is shown in Figure 5. The air bars are fixed to the bottom side of an interface plate. The specified flatness for each air bar is < 2 µm over the entire bearing surface (16 segments) and the air bars are aligned with respect to each other such that the flatness of the combined surface is < 3 µm. The hole in the interface plate indicates the location where the substrate (not shown) is placed onto the air table. The in-plane position and orientation of the substrate are fixed by four end-stops leaving a clearance of 0.1-0.2 mm to all sides. The center of the substrate is aligned with the center of the air table within ±1.5 mm in x and y direction. The orientation of the substrate relative to the air table is within ±1.0° of the orientation shown in Figure 1.

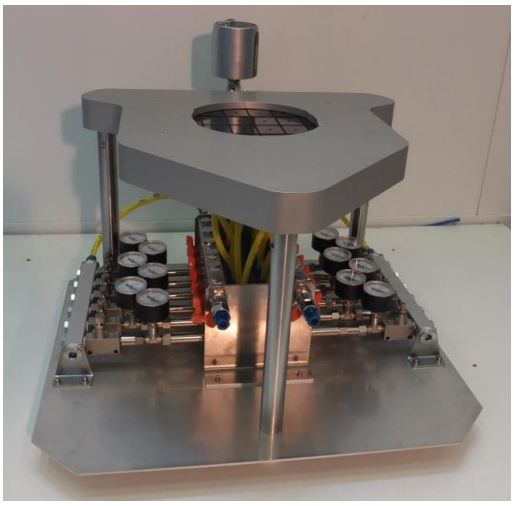

Figure 5. Experimental setup.

All porous bearing segments are connected to a single air supply line. The twelve vacuum holes are connected to twelve separate vacuum channels each with a needle valve for manipulating the pressure levels and a pressure gauge for rough pressure indication (see Figure 5). A set of manifolds connects the vacuum channels to a absolute pressure meter with a range of 0-1000 Torr (0-1.333 bar absolute) and an absolute accuracy of ± 2.5 mbar. Each vacuum channel can be connected to the pressure meter by means of a pneumatic valve.

The twelve vacuum pressure levels are manually set to the desired values by switching the vacuum channels one by one onto the pressure meter and manipulating the corresponding needle valve until the indicated value corresponds to the desired value within 1 mbar. Once all pressures are set, the interferometer image is taken. The image is converted into a height plot by µShape™ software.

EXPERIMENTAL RESULTS

The differential pressure patterns as used in the simulations for realizing the target shapes (Table 2) are applied. The shape of the substrate is measured for each of the conditions. The results are presented in Figure 6.

In Figure 7 cross sections are shown of the shapes, along with the shapes as predicted with the simulation model. The amplitude of the measured differential shapes and RMS deviation from the simulation results are shown in Table 5.

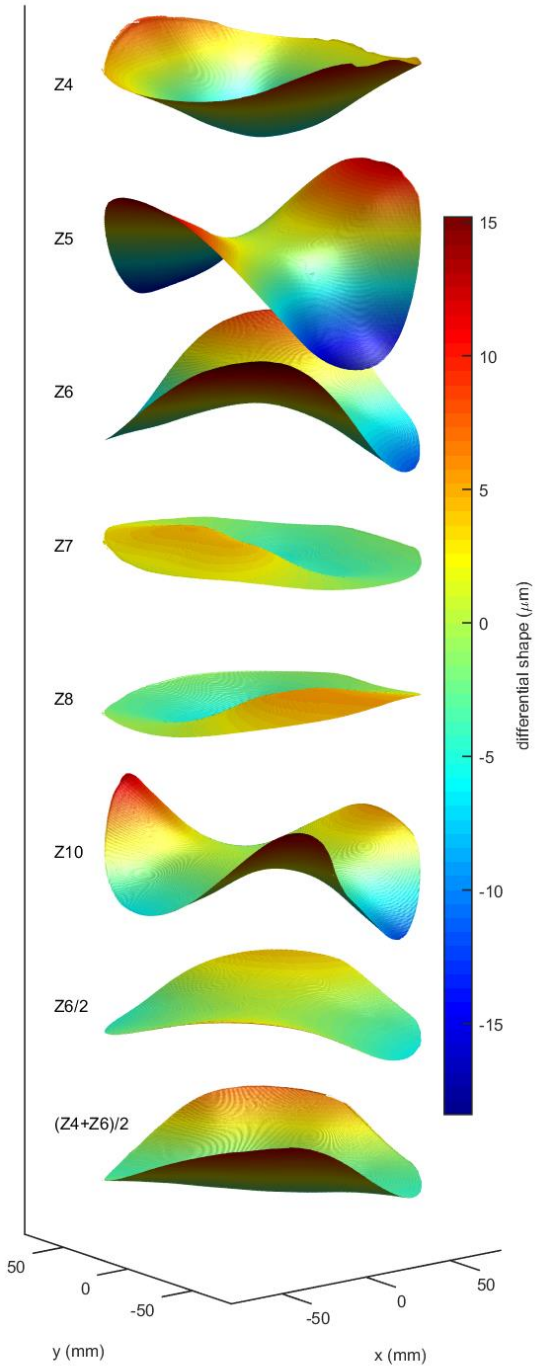

Figure 6. Measured differential substrate shapes for each of the Zernike target shape pressure patterns.

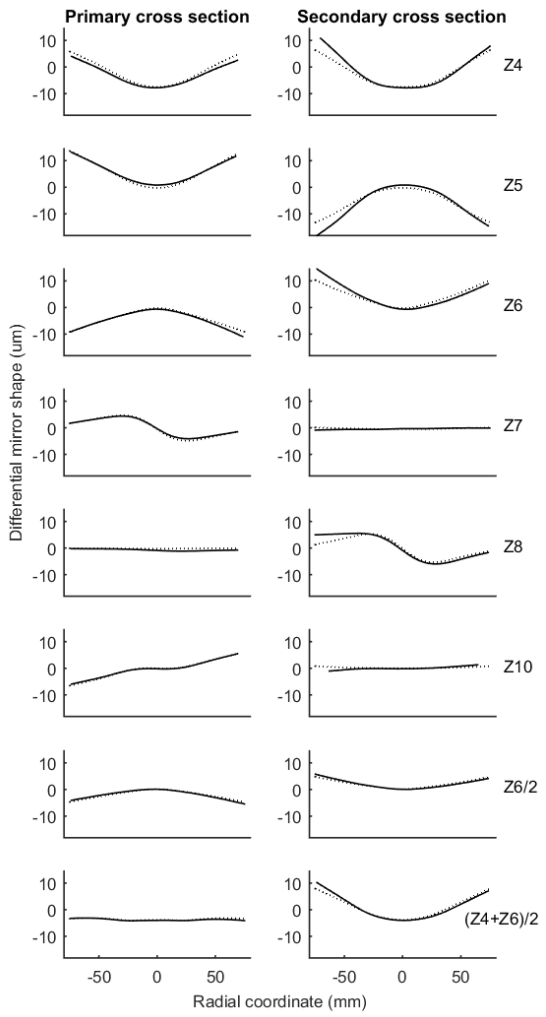

Figure 7. Cross sections of the differential substrate shape: experiments (solid line); simulations (dotted line). Primary –X axis; secondary-Y axis.

Shape	RMS deviation (µm)	Shape	RMS deviation (µm)
Z4	1.6	Z8	1.0
Z5	1.1	Z10	1.0
Z6	1.4	Z6/2	0.5
Z7	0.5	(Z4+Z6)/2	0.8

Table 5. Numerical results for the experiments.

DISCUSSION

Figure 7 and Table 5 show overall an excellent correlation between the simulated Zernike shapes and those measured. In the cross sections in Figure 7, it can be seen that a deviation between the calculated and measured shape occurs locally in most of the shapes, each time located in the south (negative y) or southwest (negative x, negative y) corner of the substrate as shown in Figure 6. Here the deviation is significantly larger than over the rest of the area. In the Z7 and Z10 shapes this effect is less clearly visible. For the Z7 and Z8 shape – where the peaks of the deformed shape are not on the edge of the substrate – the P-V value matches much better with the simulations than for the other shapes, where the peaks are on the edge. Based on these observations, the conclusion can be drawn that the differences between the measured and simulated shapes are dominated by effects at the edge of the substrate and especially the specific local effect at the south/southwest corner of the substrate. This latter effect may be caused by an artefact (local weakness) in the substrate; as in all cases it bends more extremely than predicted in this corner, regardless whether it bends upwards or downwards. This could be confirmed by 90° rotation of the substrate on the air table. Limited access to the interferometer precluded such a test, which will be part of future testing.

REFERENCES

[1] Saathof R, Schutten GJM, Spronck JW, Munnig Schmidt RH, Design and characterization of an active substrate for EUV-lithography, Precision Engineering 41 (2015) 102-110

[2] Hoetzle M, Dunifon T, and Rozevink L, Glass transportation system. U.S. Patent 6,505,483, 2003.

[3] Devitt AJ, Non-contact porous air bearing and glass flattening device. U.S. Patent 7,908,885, 2011.

[4] van Rij J *et al*. Planar wafer transport and positioning on an air film using a viscous traction principle. Tribology International, 42:1542–1549, 2009.

[5] Wesselingh J, Contactless Positioning using an Active Air Fil, PhD Thesis, ISBN978-90-9026437-0.

[6] Delettre A, Guillaume JL and Le Fort-Piat. "A new contactless conveyor system for handling clean and delicate products using induced air flows. IROS2010 RSJ International Conference IEEE, 2010.

[7] Laurent, GJ and Moon H, "A survey of non-prehensile pneumatic manipulation surfaces: principles, models and control." Intelligent Service Robotics 8.3 (2015): 151-163.

[8] Witelski T, Schwendeman D, and Evans. "Analysis of Pressurized Porous Air Bearings." (2005).

[9] Luong, TS *et al* "Numerical and experimental analysis of aerostatic thrust bearings with porous restrictors." Tribology International 37, no. 10 (2004): 825-832.

[10] Goodwin, EP, and Wyant JC, "Field Guide to Interferometric Optical Testing." SPIE, 2006: https://spie.org/publications/fg10_p24-25_zernike-polynomials.

TRENDS IN CONTROL TECHNIQUES FOR PRECISION MECHATRONIC SYSTEMS

Dannis M. Brouwer[1], Stephen J. Ludwick[2], Chinedum E. Okwudire[3], Ton T.A. Peijenburg[4]
[1]University of Twente, Enschede, The Netherlands
[2]Aerotech, Inc., Pittsburgh, PA USA
[3]University of Michigan, Ann Arbor, MI USA
[4]VDL ETG, Eindhoven, the Netherlands

INTRODUCTION

The objective of this paper is to present trends in mechatronics and control systems that are of interest to the precision engineering community. We have surveyed the presented papers of this year's EUSPEN's annual meeting, this year's ASPE annual meeting and recent issues of *Mechatronics*, *Control Engineering Practice*, *Precision Engineering*, *Journal of Dynamic Systems, Measurement and Control*, *Journal of Manufacturing Science and Engineering*, *CIRP Annals of Manufacturing Technology*, and the *IEEE/ASME Transactions on Mechatronics*. As evidenced by the quality of publications, the study of precision mechatronics remains a robust research area.

We identified four main trends in the recent publications. Feedforward control is becoming increasing sophisticated and effective via the use of higher-order dynamic models, multi-scale friction models, and iterative learning control techniques. Frequency-domain system identification techniques have seen complementary advancements, as an accurate dynamic model is critical to effective feedforward control. Mechanical design techniques for adding damping to structural resonances over broad frequency ranges improve the robustness of feedback controllers, and newly-developed magnetic actuation devices improve force density and reduce the nonlinearities of existing devices. Each of these trends will be discussed in the following sections.

ADVANCED FEEDFORWARD CONTROL

One aspect of feedforward control that is trending up is so-called beyond-rigid-body (BRB) feedforward control [1]. Traditional feedforward controllers consider the stage as a rigid body. Therefore, the feedforward controller considers only mass-times-acceleration inertial effects. BRB feedforward control considers the compliances in the stage. Okwudire et al. [2] propose a trajectory optimization approach for improved tracking of motion commands using CNC machines that experience unwanted vibration. In a similar vein, Sencer and Tajima [3] present a frequency-domain based approach for feed motion planning in CNC machine tools to avoid vibration. This trend towards BRB feedforward control is captured in this year's ASPE meeting through presentations by Dumanli and Sencer [4] on multi-axis trajectory generation for vibration avoidance, and by Yoon et al. [5] who apply BRB feedforward control to the compensation of vibration induced errors of a 3D printer.

We have also seen advances in iterative learning control (ILC), which is a feedforward control technique that uses errors from past iterations of a task to correct errors in future iterations. A major problem with traditional ILC is that it assumes that the trajectory being followed, as well as the plant dynamics and disturbances, remain invariant from iteration to iteration. This assumption does not hold in many practical situations so there is an effort to find ways of relaxing this assumption. Altin et al. [6] develop a framework for analyzing iteration-varying systems. Mandra et al. [7] propose an approach to improve the robustness of ILC by combining it with other feedforward methods and a disturbance observer. Boeren et al. [8] propose an ILC approach that can accommodate varying tasks, and apply it to a semiconductor bonding machine. There has also been advances in other aspects of ILC. For instance, Zsiga et al. [9], propose a new approach for design and analysis of ILC algorithms in the time-domain; their method allows the convergence rate of ILC to be specified in the design process, instead of being tuned by trial and error - as is the prevalent practice. Liu et al. [10], develop a Fast Fourier Transform algorithm that is real-time implementable on general microprocessors (e.g. Intel's x86 microprocessors); their new algorithm is motivated by, and applied to ILC. Lim et al. [11]

develop a multi-objective spatial ILC method applied to an additive manufacturing process with layer-to-layer repetitions. Note that spatial ILC is an emerging form of ILC which performs iterations in the spatial domain as opposed to the temporal domain.

Another aspect of feedforward control that has continued to see interest is feedforward friction compensation, where a model of friction is used to pre-emptively cancel out on-machine friction. Keck et al. [12] present a feedforward-like approach for identifying and compensating friction using an elastoplastic friction model. They address a major concern of robustness associated with feedforward friction compensation by enabling their method to adapt to short-term and long-term variations of friction. Feldman et al. [13] propose a friction identification approach that is capable of capturing the characteristics of nonlinear tangential elastic and friction forces arising in submicron motions. Ruderman [14] studies the break-away forces in actuated motion systems with nonlinear friction. Dong et al. [15] introduce a new method for compensating pre-motion friction in feedforward with the help of a compliant joint. Their compliant joint method allows very accurate and robust compensation of pre-motion friction using simple models of friction. This trend towards better understanding, modeling and compensation of friction is featured in this year's ASPE meeting through presentations by Dong et al. [16] on detailed experimental evaluation of the compliant joint approach, and by Kossack et al. [17] on a mechanism and technique for identification of friction using energy dissipation in free vibrations.

FREQUENCY-DOMAIN IDENTIFICATION

There appears to be increasing interest in frequency-domain system identification techniques, and many of the techniques reference the work of Pintelon and Schoukens [18]. Most notable have been advances in establishing the best linear approximation of a system with nonlinearities [19] and in categorizing and comparing methodologies for applying frequency domain identification methods to systems with nonlinearities [20]. These techniques have sound mathematical bases, but ultimately the experiments and data processing can be developed and scripted to the point where they generate meaningful frequency response plots with quantified uncertainty bounds and nonlinearity levels while requiring little manual intervention. Van der Maas et al [21] demonstrated the use of these techniques in measuring the frequency responses of the motion stages of a medical X-ray system.

Measured frequency responses form a non-parametric model of a real-world system that includes manufacturing errors, component imperfections, and response nonlinearities that are often neglected in a typical linearized lumped parameter model. The most widely-used and economical controllers employ a fixed structure (e.g. PID gains with a limited number of notch or low-pass filters), and van Solingen et al. have developed techniques for optimal selection of these fixed-structure gains given measured frequency response data [22]. Characterizing a multi-axis motion system with coupling between the axes requires a full grid of frequency responses which can be untenably time-consuming. Bruijnen et al. have addressed this problem with techniques for reducing the calculation time required for generating closed-loop responses for fixed-structure controllers designed around non-parametric models [23]. Taken together, these show further evidence of a trend towards automated system identification and controller tuning of even high-precision motion systems.

ACTIVE AND PASSIVE DAMPING

The performance of a feedback control system is largely determined by the plant behavior. Motion stages move principally as a rigid body at low frequencies, whereas at higher frequencies multiple vibration mode frequencies occur which limit the servo control bandwidth. The servo control bandwidth is limited by: 1) the frequencies of these modes, 2) the actuator and sensor locations which determine which modes appear in the measurement and how they present themselves (phase behavior), and 3) the modal damping of the resonances. Precision motion stages typically contain low modal damping values. This results in large motion amplification at the resonance frequencies and also transient responses that hardly damp out, which, subsequently, limit the amount of controller gain that can be applied. This in general limits the positioning accuracy of the stage in case of disturbances. Suppression of these modes by using notch filters in the feedback controller improve the bandwidth, but this can endanger the robustness of the closed-loop system for damping and/or frequency variations. As mechanical stage designs are pushed to the limits of stiffness, the option of damping to increase servo

bandwidth is gaining interest. Several methods are presented in literature:

1. The use of materials with high structural damping values is a first option. Often metals and ceramics are used predominantly because of their high specific stiffness, and in the case of ceramics, possibilities to apply low thermal expansion coefficients. However, these materials usually lack damping. Various approaches are available to increase the modal damping of those structures.

2. Constrained layers can be designed for vibration and sound control for specific frequency regions, in both passive and active variants. Typically a viscoelastic or other damping material is sandwiched between two sheets of stiff materials that lack sufficient damping by themselves. The ending result is that any vibration made on either side of the constraining materials (the two stiffer materials on the sides) is dissipated in the viscoelastic or middle layer. Verbaan [24] presents a hybrid design approach of constrained layer dampers for discontinuous surfaces.

3. Squeeze film dampers can result in very high damping values. In a squeeze film damper typically a viscous fluid or gas film is sandwiched between two sheets of stiff materials that lack sufficient damping by themselves. Motion perpendicular to the film direction and also in-plane of the film are damped due to the viscous forces.

4. Tuned Mass Dampers (TMD) typically comprise a mass, spring and damper tuned to a certain frequency (usually a disturbing resonance). The resonance excites the TMD much, due to the matched frequency, but the amplitude is damped in the TMD, extracting energy from the system. Therefore a TMD typically damps a single vibration mode. Multiple TMDs at different resonance frequencies can be added to obtain a more broadbanded damping behavior. Van Pinxteren [25] applies Tuned Mass Dampers (TMD) to the C-arm of an Interventional X-ray System and compares this method to an approach with local stiffness enhancement of the C-arm and the X-ray source interface, at similar mass and inertia.

5. To improve the modal damping over a broad frequency range, Robust Mass Dampers (RMDs) are proposed by Marano [26] and Verbaan [27]. It was shown that the bandwidth of a motion system can be increased by adding dampers to a motion stage. For good results with a minimum number of dampers added, the dampers have to have a broad-banded damping effect which is created by relatively high modal damping values. This is the main difference with tuned mass dampers, which contain relatively low modal damping values (10–25%). Robust mass dampers typically show modal damping values larger than 50%. Verbaan [27] showed broad-banded damping for a square plate stage model together with corresponding bandwidth improvements. An active damper was shown by Kondo [28]. The transient vibrations of a spindle head on the column of a milling machine caused by the deceleration of the column on the bed were shown to be damped by a hybrid dynamic absorber that uses an electromagnetic force.

6. High speed direct drives initiate jerk, which excites vibrations of the stage/tool and affects the achievable accuracy. Therefore, the jerk is usually limited by numeric control. One method to avoid excitation of frame vibrations and to increase the dynamics is by the use of Passive Jerk-Decoupling (JDC) by the means of a mechanical low-pass filter. Basically a spring and damper between the stator and the frame. Passive JDC come at the price of additional resonances due to the added mass-spring-damper system. At EUSPEN Denkena [29] presented a hybrid concept for active JDC. The extension of the passive JDC offers the potential to damp both the machine structure vibration and the additional JDC-resonance. Also at EUSPEN Ma [30] showed an integrated approach to design the optimal JDC for both the tracking error and the jerk induced to the machine frame.

ADVANCED MAGNETIC ACTUATION

Required force density and/or the reluctance (sic) to turn to rare-earth permanent magnets for reasons of availability or cost, may drive the application of reluctance motor topologies. One core limitation is the inherent non-linearity of such actuators, limiting the applicability in high-accuracy motion applications. By combining advanced linearization- and control schemes, Katalenic et al. [31] demonstrate that small force errors of $50\,\mathrm{mN}$ on a $200\,\mathrm{N}$ nominal force can be achieved, combined with a small remaining stiffness of $500\,\mathrm{N/m}$ at force levels of $100\,\mathrm{N}$. These numbers put reluctance actuator performance on par with Lorentz type actuators, but other factors such as clearance and useful (mechanical) stroke have to be considered in the comparison.

Iron core electromagnetic motors are typically good at achieving high force densities, but usually at the cost of vibrations due to cogging. Yoon et al. [32] propose a novel geometry for a rotary motor using fine teeth that suppress cogging and resulting vibration while maintaining a high shear force and resulting torque. In a similar purpose of reducing vibrations for a gearless elevator drive, a new method for selecting the number of pole slots has been developed by Doo-Young Kim et al. [33].

Magnetic levitation is familiar in the fields of transportation but also precision motion systems. In the latter category, it brings advantages in terms of eliminating stacked or H-shape geometries of linear guideways while providing vibration suppression and adjustability. A magnetically levitated rotary table, suitable for use in vacuum and without wire connections to the table is developed by Dyck et al. [34]. It builds on earlier ideas and realizes in nm-level positioning performance. The utilization of superconducting materials for levitation purposes is gaining traction. Kun Liu has conducted experiments with REBCO (rare-earth) superconducting tape, investigating the transient behavior of a superconducting stack-based maglev system [35]. Constant stiffness and low, but variable damping, are reported. With the advancements in equipment for operating superconducting systems, such as cryogenic coolers, the adaptation of these systems will undoubtedly increase in the years to come, addressing advantages in power dissipation and energy usage.

Permanent magnet configurations, more specifically Halbach arrays, have been proposed for different purposes. Firstly, Boisclair et al. [36] propose a novel approach using cylindrical Halbach arrays for static balancing of revolute joints in robotics. Secondly, Jiao et al. [37] have developed a compound Halbach magnet array for improving the force/weight ratio of an oscillating linear axis, e.g. for a fast tool servo.

In a paper by Dominguez et al. [38], a novel concept for a Magneto Rheological Cylinder damper geometry was proposed and studied. MR devices may still provide solutions for precise regulation of stiffness and damping.

To replace tethered catheters for navigating human blood vessels, a magnetic crawling robot is proposed that is powered by an external field that is both rotating and oscillating in the axial direction. The robot uses magnetic navigation (Jang et al. [39]). Positioning performance in a pulsating flow is better than traditional spiral robots. Magnetic navigation for micro-robots is also proposed by Zhang et al. [40], adding force control based on the magnetic measurements.

CONCLUSION

As was demonstrated by this review of recent publications, the techniques available to designers of precision mechatronic systems continue to advance. We look forward to additional growth with further development likely to be accelerated by the adoption of more real-time and ubiquitous collection of operating data from which better models and understanding can be developed.

REFERENCES

[1] J. Lunenburg, O. Bosgra, and T. Oomen, “Inversion-based feedforward design for beyond rigid body systems: A literature survey,” DCT Report: Eindhoven University of Technology, Tech. Rep., 2009 (accessed September 1, 2017). [Online]. Available: http://www.mate.tue.nl/mate/pdfs/11255.pdf

[2] C. Okwudire, K. Ramani, and M. Duan, “A trajectory optimization method for improved tracking of motion commands using cnc machines that experience unwanted vibration,” *CIRP Annals - Manufacturing Technology*, vol. 65, no. 1, pp. 373–376, 2016.

[3] B. Sencer and S. Tajima, “Frequency optimal feed motion planning in computer numerical controlled machine tools for vibration avoidance,” *Journal of Manufacturing Science and Engineering*, vol. 139, no. 1, p. 011006, 2017.

[4] A. Dumanli and B. Sencer, “Multi-axis trajectory generation with optimal frequency spectrum for vibration avoidance,” in *Proceedings of the 32nd annual meeting of the American Society for Precision Engineering*, 2017.

[5] M. D. Deokkyun Yoon and C. Okwudire, “Software-based compensation of vibration-induced errors of a commercial desktop 3D printer,” in *Proceedings of the 32nd annual meeting of the American Society for Precision Engineering*, Charlotte, NC, 2017.

[6] B. Altın, J. Willems, T. Oomen, and K. Barton, “Iterative learning control of iteration-varying systems via robust update laws with

experimental implementation," *Control Engineering Practice*, vol. 62, pp. 36 – 45, 2017.

[7] S. Mandra, K. Galkowski, and H. Aschemann, "Robust guaranteed cost ilc with dynamic feedforward and disturbance compensation for accurate pmsm position control," *Control Engineering Practice*, vol. 65, pp. 36 – 47, 2017.

[8] F. Boeren, A. Bareja, T. Kok, , and T. Oomen, "Frequency-domain ILC approach for repeating and varying tasks: With application to semiconductor bonding equipment," *IEEE/ASME Transactions on Mechatronics*, vol. 212, no. 6, pp. 2716 – 2727, 2016.

[9] N. Zsiga, S. van Dooren, P. Elbert, and C. H. Onder, "A new method for analysis and design of iterative learning control algorithms in the time-domain," *Control Engineering Practice*, vol. 57, pp. 39 – 49, 2016.

[10] J. Liu, B. Yan, and Q. Zou, "Optimal time-distributed fast fourier transform: Application to online iterative learning control—experimental high-speed nanopositioning example," *Mechatronics*, vol. 41, pp. 114 – 124, 2017.

[11] I. Lim, D. J. Hoelzle, and K. L. Barton, "A multi-objective iterative learning control approach for additive manufacturing applications," *Control Engineering Practice*, vol. 64, pp. 74 – 87, 2017.

[12] A. Keck, J. Zimmermann, and O. Sawodny, "Friction parameter identification and compensation using the ElastoPlastic friction model," *Mechatronics*, 2017.

[13] M. Feldman, Y. Zimmerman, M. Gissin, and I. Bucher, "Identification and modeling of contact dynamics of precise direct drive stages," *Journal of Dynamic Systems, Measurement, and Control*, vol. 138, no. 7, p. 071001, 2016.

[14] M. Ruderman, "On break-away forces in actuated motion systems with nonlinear friction," *Mechatronics*, vol. 44, pp. 1–5, 2017.

[15] X. Dong, X. Liu, D. Yoon, and C. E. Okwudire, "Simple and robust feedforward compensation of quadrant glitches using a compliant joint," *CIRP Annals - Manufacturing Technology*, vol. 66, no. 1, pp. 353 – 356, 2017.

[16] X. Dong and C. Okwudire, "Mitigating undesirable effects of pre-motion friction in mechanical-bearing-guided motion stages using a compliant joint," in *Proceedings of the 32nd annual meeting of the American Society for Precision Engineering*, 2017.

[17] C. Kossack, J. Ziegert, and T. Schmitz, "Identification of friction energy dissipation using free vibration velocity: Measurement and modeling," in *Proceedings of the 32nd annual meeting of the American Society for Precision Engineering*, 2017.

[18] R. Pintelon and J. Schoukens, *System Identification: A Frequency Domain Approach*. John Wiley & Sons, Inc., 2012.

[19] J. Schoukens, M. Vaes, and R. Pintelon, "Linear system identification in a nonlinear setting: Nonparametric analysis of the nonlinear distortions and their impact on the best linear approximation," *IEEE Control Systems Magazine*, vol. 36, no. 3, pp. 38–69, Jun 2016.

[20] D. Rijlaarsdam, P. Nuij, J. Schoukens, and M. Steinbuch, "A comparative overview of frequency domain methods for nonlinear systems," *Mechatronics*, vol. 42, pp. 11–24, 2017.

[21] R. van der Maas, A. van der Maas, J. Dries, and B. de Jager, "Efficient nonparametric identification for high-precision motion systems: A practical comparison based on a medical x-ray system," *Control Engineering Practice*, vol. 56, pp. 75–85, Nov 2016.

[22] E. van Solingen, J. Wingerden, and T. Oomen, "Frequency-domain optimization of fixed-structure controllers," *International Journal of Robust and Nonlinear Control*, 2016.

[23] D. Bruijnen and S. van der Meulen, "Faster computation of closed loop transfers with frequency response data for multivariable loopshaping," *IFAC-PapersOnLine*, vol. 49, no. 13, pp. 87–92, 2016.

[24] K. Verbaan, M. Duiven, R. Henselmans, P. Nuij, and D. Rijlaarsdam, "Hybrid design approach of constrained layer dampers for discontinuous surfaces," in *Proceedings of the 32nd annual meeting of the American Society for Precision Engineering*, 2017.

[25] J. van Pinxteren, J. Vermeulen, R. van Loon, and G. van Schothorst, “Addressing source-induced structural vibrations in an interventional x-ray system,” in *Proceedings of the 17th annual meeting of the European Society for Precision Engineering and Nanotechnology*, Hannover, DE, 2017, pp. 464–465.

[26] G. C. Marano, S. Sgobba, R. Greco, and M. Mezzina, “Robust optimum design of tuned mass dampers devices in random vibrations mitigation,” *Journal of Sound and Vibration*, vol. 313, no. 3, pp. 472 – 492, 2008.

[27] C. Verbaan, P. Rosielle, and M. Steinbuch, “Broadband damping of non-rigid-body resonances of planar positioning stages by tuned mass dampers,” *Mechatronics*, vol. 24, no. 6, pp. 712 – 723, 2014, control of High-Precision Motion Systems.

[28] E. Kondo, T. Nishimura, and D. Tabuchi, “Damping of transient vibrations of head on top of flexible column of milling machine using electromagnetic hybrid dynamic vibration absorber,” in *Proceedings of the 17th annual meeting of the European Society for Precision Engineering and Nanotechnology*, Hannover, DE, 2017, pp. 456–457.

[29] B. Denkena and F. Böhse, “Concept and control strategy for active jerk-decoupling of feed-drives,” in *Proceedings of the 17th annual meeting of the European Society for Precision Engineering and Nanotechnology*, Hannover, DE, 2017, pp. 422–423.

[30] J. Ma, S.-L. Chen, C. S. Teo, C. J. Kong, A. Tay, W. Lin, and A. A. Mamun, “Integrated design of controller and JDC by a constrained H_2 optimization algorithm,” in *Proceedings of the 17th annual meeting of the European Society for Precision Engineering and Nanotechnology*, Hannover, DE, 2017, pp. 434–435.

[31] A. Katalenic, H. Butler, and P. P. J. van den Bosch, “High-precision force control of short-stroke reluctance actuators with an air gap observer,” *IEEE/ASME Transactions on Mechatronics*, vol. 21, no. 5, pp. 2431–2439, 2016.

[32] J. Y. Yoon and D. L. Trumper, “Strong and quiet linear iron-core synchronous motor,” in *Proceedings of the 32nd annual meeting of the American Society for Precision Engineering*, Charlotte, NC, 2017.

[33] D.-Y. Kim, M.-R. Park, J.-H. Sim, and J.-P. Hong, “Advanced method of selecting number of poles and slots for low-frequency vibration reduction of traction motor for elevator,” *IEEE/ASME transactions on mechatronics*, vol. 22, no. 4, pp. 1554–1562, 2017.

[34] M. Dyck, X. Lu, and Y. Altintas, “Magnetically levitated rotary table with six degrees of freedom,” *IEEE/ASME transactions on mechatronics*, vol. 22, no. 1, pp. 530–540, 2017.

[35] K. Liu, G. Ma, C. Ye, W. J. Yang, G. Li, Z. Luo, and Y. Cai, “Experimental studies on the dynamic responses of coated superconductor stack levitated above a permanent magnet guideway,” in *Proceedings, 25th International Conference on Magnet Technology (MT-25) : Amsterdam, Netherlands, August 27-31 , 2017*.

[36] J. Boisclair, P.-L. Richard, T. Laliberte, and C. Gosselin, “Gravity compensation of robotic manipulators using cylindrical halbach arrays,” *IEEE/ASME Transactions on Mechatronics*, vol. 22, no. 1, pp. 457–464, 2017.

[37] Z. Jiao, T. Wang, and L. Yan, “Design of a tubular linear oscillating motor with a novel compound halbach magnet array,” *IEEE/ASME transactions on mechatronics*, vol. 22, no. 1, pp. 457–464, 2017.

[38] G. A. Dominguez, M. Kamezaki, and S. Sugano, “Proposal and preliminary feasibility study of a novel toroidal magnetorheological piston,” *IEEE/ASME transactions on mechatronics*, vol. 22, no. 2, pp. 657–668, 2017.

[39] B. Jang, J. Nam, W. Lee, and G. Jang, “A crawling magnetic robot actuated and steered via oscillatory rotating external magnetic fields in tubular environments,” *IEEE/ASME transactions on mechatronics*, vol. 22, no. 3, pp. 1465–1472, 2017.

[40] X. Zhang and M. B. Khamesee, “Adaptive force tracking control of a magnetically navigated microrobot in uncertain environment,” *IEEE/ASME transactions on mechatronics*, vol. 22, no. 4, pp. 1644–1651, 2017.

DETAILED EXPERIMENTAL EVALUATION OF THE COMPLIANT JOINT METHOD FOR FEEDFORWARD COMPENSATION OF PRE-MOTION FRICTION

Xin Dong[1], Chinedum E. Okwudire[1]
[1]Mechatronics and Sustainability Research Lab
Department of Mechanical Engineering, University of Michigan
Ann Arbor, MI, USA

OVERVIEW

The presence of pre-motion friction severely affects the accuracy of rolling-bearing-guided motion stages, leading to large position errors at velocity reversals. Compensating these errors accurately through feedforward control is challenging due to the need for complex friction models, and the variability of on-machine friction dynamics. Recent work done by the authors has shown that pre-motion friction can be accurately and robustly compensated with simple friction models by attaching the bearing to the moving table using a joint that is very compliant in the motion direction – i.e., the compliant joint method. However, only limited experimental results were reported, due to space constraints. This paper provides a more thorough evaluation of the compliant joint method through circle tests with various radii and velocities; large reductions of motion error are demonstrated in experiments.

BACKGROUND

Rolling bearings are widely used in (ultra) precision motion stages because of their low cost, large motion range, high off-axis stiffness and ruggedness [1]. They are also finding increasing use in ultra-precision stages due to their excellent in-position stability. When lubricated with small amounts of grease, rolling bearings can be used as vacuum-compatible substitutes for air bearings [2, 3]. However, rolling-bearing-guided motion stages experience pre-motion (i.e., pre-rolling/pre-sliding) friction, which behaves as a nonlinear spring due to elastoplastic deformation and micro-slip of their inherent rolling elements, end seals and wipers [2, 4]. As the stage tries to overcome pre-motion friction in tracking applications like triangular scanning or circular motion tracking, large positioning errors often occur at motion reversals; this is also known as quadrant glitches [3, 5].

Feedforward (FF) compensation is most often used to suppress the positioning errors due to pre-motion friction, beyond what is achievable using feedback control [3, 5–8]. In FF friction compensation, the friction force experienced by a stage is predicted and canceled out preemptively using a model of pre-motion friction, combined with the knowledge of the motion commands. Tracking performance can be significantly improved if the friction model is sufficiently accurate; however, this often leads to complex models that require relatively tedious identification process. Moreover, FF compensation using any pre-motion friction model is not robust to changes in on-machine friction dynamics that frequently occur as a function of time and/or stage position [6, 9]. Thus, they need frequent re-calibration or adaptation of parameters to maintain their effectiveness, which hampers their practicality [9].

Recent work [3] done by the present authors has shown that accurate and robust FF compensation of pre-motion friction can be achieved with a simple friction model by attaching the rolling bearing to the moving table of the stage using a compliant joint (i.e., compliant joint method). Experiments conducted on an ultra-precision stage equipped with a compliant joint prototype has demonstrated large reductions of motion errors and remarkable robustness during circle tests (with 20 mm radius). This paper extends the authors' prior work by experimentally evaluating the effects of the compliant joint method on FF compensation of pre-motion friction using circle tests with various radii and velocities.

COMPLIANT JOINT METHOD [3]

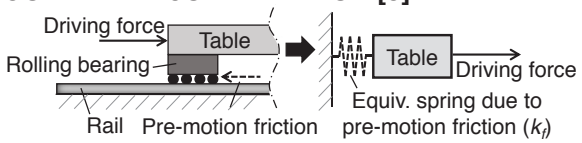

FIGURE 1. Schematic and spring model of a typical rolling-bearing-guided motion stage.

In a typical rolling-bearing-guided motion stage (see FIGURE 1), the bearing is rigidly attached to the moving table. Before gross motion (full sliding/rolling) begins, the stage experiences pre-motion friction due to its bearings' rolling elements and end seals/wipers [2–4]. Pre-motion friction can be modeled as an equivalent

nonlinear spring of stiffness k_f connecting the table to ground [3, 6]. When the motion stage starts from rest, k_f is initially very large; but as more driving force is applied to counteract pre-motion friction, k_f rapidly reduces and eventually becomes zero, allowing gross motion of the stage. Large positioning errors are developed as the servo controller tries to overcome the large value of k_f at beginning of the motion or at motion reversals.

The errors due to pre-motion friction can only be partially suppressed by feedback control, because a feedback controller must wait for errors to develop before it takes corrective actions. Therefore, FF compensation methods are often used with a model of pre-motion friction. To ensure satisfactory performance of FF compensation, accurate models of pre-motion friction are needed; but such models are often complex, with lots of parameters that must be identified. Moreover, pre-motion friction changes with time and/or stage position; so even with complex friction models, errors are introduced into k_f as the actual frictional stiffness varies.

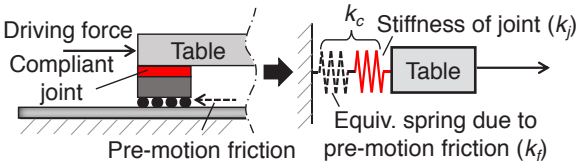

FIGURE 2. Schematic and spring model of a compliant-joint-augmented motion stage.

FIGURE 2 shows the compliant joint method (proposed by authors in [3]) for addressing the errors in k_f when using FF compensation. Rather than being rigidly attached to the moving table of the stage, the bearing is attached using a joint of stiffness k_j in the motion direction. Accordingly, the stage with the compliant joint can be modeled as a series combination of k_f and k_j, with combined stiffness $k_c = k_f k_j/(k_f + k_j)$.The sensitivity of k_c to errors in k_f is given by,

$$\frac{\partial k_c}{\partial k_f} = \left(\frac{\eta}{1+\eta}\right)^2 ; \text{ where } \eta = \frac{k_j}{k_f} \qquad (1)$$

Notice that if $k_j << k_f$, and k_j is precisely known, sensitivity of k_c to errors in k_f becomes very small. In other words, a very small k_j dominates the combined stiffness felt by the stage at the very beginning of motion (reversals). This indicates that if FF compensation is done using k_c instead of k_f, errors in k_f due to using a simple friction model or variations of friction will not affect the result much. Therefore, pre-motion friction can be accurately compensated (using k_c) even when a significant amount of error exists in k_f.

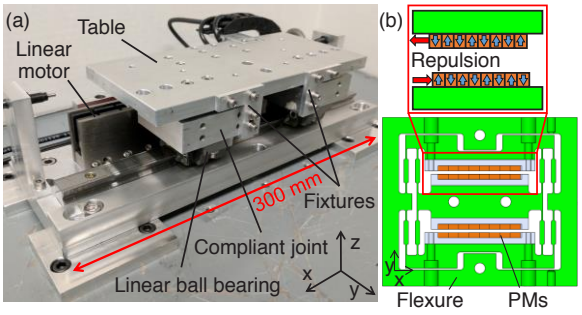

FIGURE 3. (a) Single-axis ultra-precision stage equipped with the compliant joint, and (b) CAD schematic of the compliant joint. (Note: fixtures are used to deactivate the compliant joints).

FIGURE 3 shows a single-axis rolling-bearing-guided ultra-precision stage [3] in which the designed compliant joint prototype is used to attach each bearing to the table. To achieve $k_j << k_f$, the compliant joint must have orders of magnitude less stiffness (in x direction) than the initial stiffness of pre-motion friction experienced by the bearing. Moreover. it must also maintain the same order of magnitude of off-axis stiffness as the rolling bearing so as not to unduly compromise the rigidity in the non-motion (i.e., y and z) directions. A flexure hinge is adopted in the design due to its non-contact and friction-free nature. To reduce the stiffness in the motion direction, the positive-stiffness flexure is combined in parallel with a negative-stiffness mechanism using repelling permanent magnets (PMs) to keep the net stiffness positive but smaller than that of the flexure alone (see FIGURE 3(b)). Details of the compliant joint design can be found in [3].

FEEDFORWARD COMPENSATION OF PRE-MOTION FRICTION (EXPERIMENTS)

Feedforward compensation of pre-motion friction is carried out on the stage shown in FIGURE 3(a). The compliant joints can be deactivated by installing the fixtures to lock the table rigidly to the bearings. FIGURE 4 shows the block diagram of the control scheme implemented on the stage using a real-time controller. A conventional PID controller is used for feedback control of the stage; it is tuned to 180 Hz closed loop bandwidth based on the rigid stage (i.e., stage with compliant joints deactivated) and the same PID gains are used with the compliant joints activated. Two popular pre-motion friction models are

implemented in the FF friction compensator, namely the Dahl model and generalized Maxwell-slip (GMS) model. Details about the friction models and identification of their parameters can be found in [3]. Note that the GMS model (identified with 20 parameters) is significantly more complex compared to the Dahl model (identified with 2 parameters).

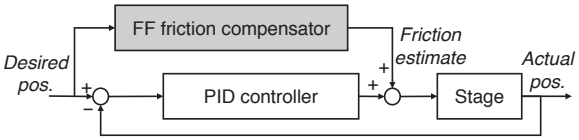

FIGURE 4. Block diagram of control scheme used in experiments, with PID feedback controller and feedforward friction compensator.

The performance of the compliant joint method is experimentally evaluated using several circle tests, with radii ranging from 5 μm to 5 mm, and tangential velocities ranging from 2 μm/s to 60 mm/s. Since the ultra-precision stage is a single-axis stage, without loss of generality, only the *x*-axis reference trajectories for the circular motions are utilized. The following cases are tested:

- Baseline: rigid stage without FF compensation;
- Rigid + Dahl FF: rigid stage with FF compensation using Dahl model (with 2 parameters);
- Rigid + GMS FF: rigid stage with FF compensation using GMS model (with 20 parameters);
- Compliant + Dahl FF (proposed): compliant stage with FF compensation using Dahl model; combined stiffness k_c (of compliant joint and pre-motion friction) is used;

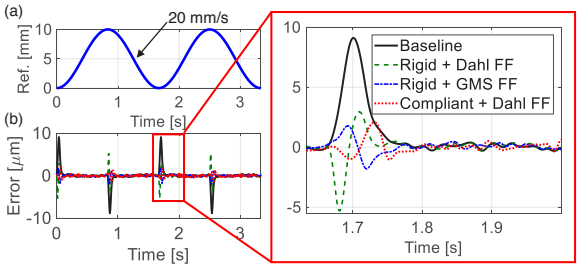

FIGURE 5. (a) x-axis reference position trajectory, and (b) tracking errors of the stage during circle test with 5 mm radius and 20 mm/s velocity.

FIGUREs 5 and 6 show the typical tracking performance obtained from the 5 mm and 5 μm radius circle tests. For the 5 mm radius circle, the baseline case suffers from large position error (with 8.99 μm peak error) at motion reversals due to the presence of pre-motion friction. Therefore, the average peak error after each velocity reversal is used to evaluate the performance of FF friction compensation. With Rigid + Dahl FF, the peak error is reduced to 5.29 μm. Due to the inaccuracy of the Dahl model, over-compensation is observed after each motion reversal, as highlighted by a large error spike toward the opposite direction of stage motion. When the GMS model is used in the FF compensator, the peak error is further reduced to 1.89 μm, resulting 79% reduction compared to the baseline case. This is due to the improved accuracy afforded by the GMS model compared to the Dahl model. However, Compliant + Dahl FF (with 1.74 μm peak error) achieves very similar performance as Rigid + GMS FF.

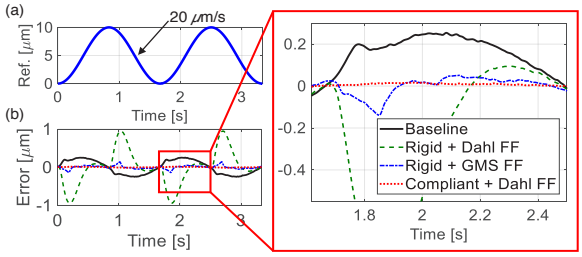

FIGURE 6. (a) x-axis reference position trajectory, and (b) tracking errors of the stage during circle test with 5 μm radius and 20 μm/s velocity.

For the 5 μm radius circle (see FIGURE 6), the baseline case has peak error of 0.25 μm. With Rigid + Dahl FF, the peak error is increased to 0.95 μm due to severe over-compensation after motion reversals. When the more complex GMS model is used instead, the peak error is reduced by 44% (to 0.14 μm), compared to the baseline case. However, Compliant + Dahl FF achieves significantly better tracking performance (with 0.02 μm peak error) than other methods. Because of the small radius (i.e., motion range) of the circle, the pre-motion frictional stiffness remains very large during the entire test; thus, the compliant joint with low stiffness becomes dominant constantly. Since the stiffness of the compliant joint is precisely known, almost perfect tracking is achieved with FF compensation.

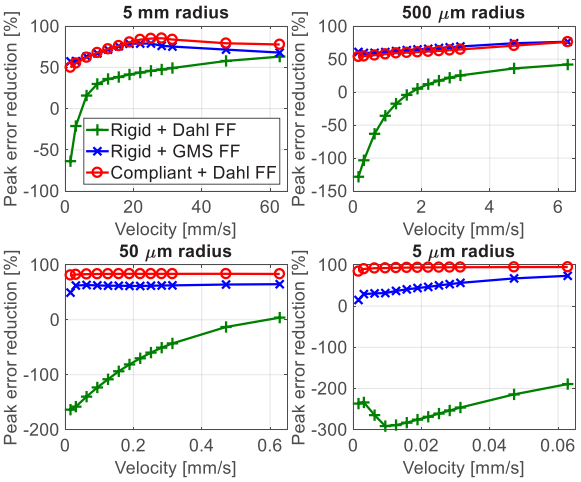

FIGURE 7. Comparison of tracking performance during circle tests.

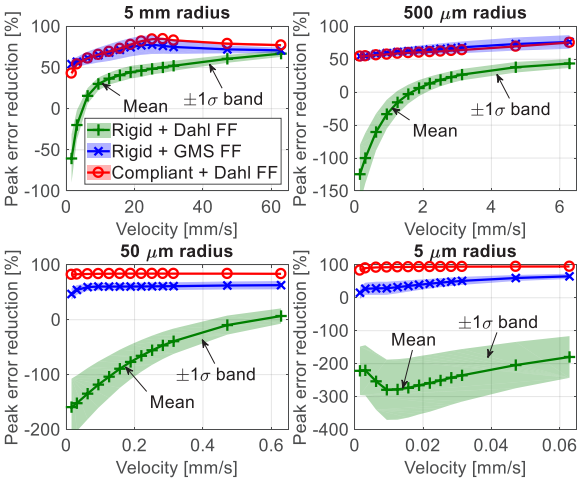

FIGURE 8. Comparison of tracking performance during circle tests with estimation errors introduced into the identified frictional stiffness. Note that the standard deviations of Compliant + Dahl FF are so small such that the shaded bands are hardly visible.

FIGURE 7 summarizes the percentage reductions in peak error achieved by different methods (relative to the baseline case) for the circle tests with various radii and velocities. It is observed that Rigid + Dahl FF performs even worse than the baseline case for circle tests with small radii and velocities. This relatively poor performance is mainly due to the large frictional stiffness estimation errors near motion reversals, even though the friction parameters were carefully identified. On the other hand, Rigid + GMS FF exhibits consistently better tracking performance than the baseline case due to its more-accurate estimation of pre-motion frictional stiffness. This indicates that complex models are required for accurate FF compensation of pre-motion friction for the rigid stage. However, the proposed Compliant + Dahl FF achieves similar level of performance during large range (5 mm and 500 μm radius) circle tests and significantly better performance during small range (50 μm and 5 μm radius) circle tests, compared to Rigid + GMS FF. When the motion range reduces, the pre-motion frictional stiffness during the circle tests becomes larger and the low-stiffness compliant joint becomes more dominant. This leads to more accurate compensation of the combined stiffness k_c (since $k_f << k_j$ for almost entire circle tests) and therefore, better tracking performance.

The robustness of FF compensation in the presence of model parameter errors (due to inaccurate modeling or variation of friction) is also tested. Deviations of 0, ±10%, ±20% and ±50% are introduced into the identified frictional stiffness of the rigid stage. For each deviation case, the equivalent stiffness parameter of the compliant stage (i.e., Compliant + Dahl FF) is re-calculated using the inaccurate frictional stiffness (see [3] for more details). The variations are compared in FIGURE 8 by plotting the mean percentage reductions of peak error (relative to the baseline case) together with the corresponding ±1σ (standard deviation) bands based on all deviation cases for each method. As seen from the figure, Rigid + Dahl FF and Rigid + GMS FF both suffer from large performance variations due to the modeling errors in their identified pre-motion frictional parameters. This indicates that frequent re-calibration is needed to ensure robust FF compensation for the rigid stage. On the other hand, Compliant + Dahl FF provides very robust tracking performance, due to the reduced sensitivity of combined stiffness k_c to errors in pre-motion frictional stiffness k_f. With the proposed compliant joint method, accurate and robust FF compensation of pre-motion friction is achieved in the presence of up to 50% errors in the identified frictional stiffness.

CONCLUSIONS

This paper extends authors' prior work by extensively evaluating the effects of the compliant

joint method on feedforward compensation of pre-motion friction in experiments. Large reductions of peak positioning errors are achieved during circle tests with various radii and velocities using feedforward compensation based on a simple friction model. Moreover, the FF compensation scheme shows remarkable robustness in the presence of up to 50% modeling errors in the identified frictional stiffness. Future work will analyze the impacts of the compliant joint method on the overall dynamics of the stage. It will also study the effects of the compliant joint on other undesirable phenomena caused by pre-motion friction of rolling bearings, such as slow settling in point-to-point positioning.

ACKNOWLEDGEMENT
The authors are grateful to Aerotech Inc. for donating some key components used in building the prototype stage. This work is funded by the National Science Foundation (NSF) Award #1562297.

REFERENCES
[1] Altintas Y, Verl A, Brecher C, Uriarte L, Pritschow G. Machine Tool Feed Drives. Annals of the CIRP 2011; 60(2):779–96.
[2] Dong X, Yoon D, Okwudire CE. A novel approach for mitigating the effects of pre-rolling/pre-sliding friction on the settling time of rolling bearing nanopositioning stages using high frequency vibration. Precision Engineering 2017; 47:375-88.
[3] Dong X, Liu X, Yoon D, Okwudire CE. Simple and robust feedforward compensation of quadrant glitches using a compliant joint. Annals of the CIRP 2017; 66(1):353-6.
[4] Al-Bender F, Symens W. Characterization of frictional hysteresis in ball-bearing guideways. Wear 2005; 258:1630–42.
[5] Jamaludin Z, Van Brussel H, Pipeleers G, Swevers J. Accurate Motion Control of XY High-speed Linear Drives Using Friction Model Feedforward and Cutting Forces Estimation. Annals of the CIRP 2008; 57(1):403–6.
[6] Yoon JY, Trumper DL. Friction Modeling, Identification, and Compensation Based on Friction Hysteresis and Dahl Resonance. Mechatronics 2014; 24(6):734–41.
[7] Juhász L, Maas J. Control of Hybrid Nanopositioning Systems for Trajectory-tracking Applications. Mechatronics 2013; 23(6):617–29.
[8] Itagaki H, Tsutsumi M. Control System Design of a Linear Motor Feed Drive System Using Virtual Friction. Precision Engineering 2014; 38(2):237–48.
[9] Reuss M, Dadalau A, Verl A. Friction Variances of Linear Machine Tool Axes. Procedia CIRP 2012; 4:115–9.

MULTI-AXIS TRAJECTORY GENERATION WITH OPTIMAL FREQUENCY SPECTRUM FOR VIBRATION AVOIDANCE

Alper Dumanli, Burak Sencer
School of Mechanical, Industrial and Manufacturing Engineering
Oregon State University
Corvallis, Oregon, USA

INTRODUCTION

This paper presents a novel spline trajectory generation technique for precision machine tools and industrial manipulators. A major source of vibrations in production equipment is inertial vibrations that are induced due to the frequency content of reference motion commands, i.e. reference trajectory. Modern motion planners generate smooth reference commands based on jerk or snap limited acceleration profiles [1]. The time derivative of acceleration, e.g. jerk, is considered to be the key parameter that controls smoothness of acceleration profile and thereby influences level of excitation. Industrial robotic systems rely on minimum jerk [2] trajectories for vibration mitigation. In precision manufacturing, structural resonances of equipment are known, and hence the objective is to attenuate frequency content of motion commands at around resonances. This can be achieved through filtering in the form of input shaping [3]. However, post-filtering introduces phase delay and distorts reference trajectory, which in return causes large contouring errors in multi-axis contouring. This paper introduces a "direct spline trajectory generation" technique with a frequency optimized acceleration profile [4] to avoid exciting residual vibrations along 2D spline trajectories. Reference acceleration profile is generated by solving an optimization problem that minimizes motion command's frequency spectrum in a desired band. Effectiveness of the proposed trajectory generation scheme is evaluated by experimental comparison against minimum jerk trajectories.

FREQUENCY OPTIMAL 2D CONTOURING

Trajectories used in precision manufacturing applications consist of a sequence of reference points that are generated by linear, circular or parametric spine interpolation [1]. Fig. 1 shows a typical 2D toolpath generated by quintic spline interpolation [5] passing through *M+1* waypoints/knots. The displacement profiles of *x* and *y* axes for n^{th} segment are defined as 5^{th} order polynomials of s_n:

$$\left.\begin{aligned} x_n(s_n) &= x(s_n) = \sum_{i=0}^{5} \alpha_i s_n^i \\ y_n(s_n) &= y(s_n) = \sum_{i=0}^{5} \beta_i s_n^i \end{aligned}\right\} \quad (1)$$

where $s_n=s_n(kT_s)$ is the sampled displacement, i.e. arc length. Here the displacement profile is defined as 11^{th} order polynomial function of time $t=kT_s$:

$$s(kTs) = a_{11}s(kT_s)^{11} + a_{10}s(kT_s)^{10} + \cdots + a_0 \quad (2)$$

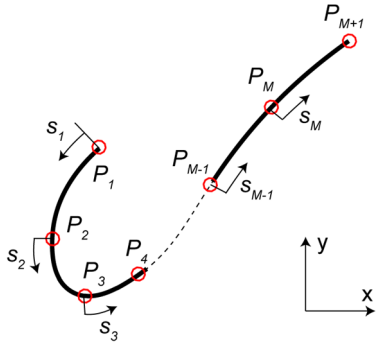

FIGURE 1. A Typical Spline Toolpath.

The axis acceleration profiles, i.e. d^2x/dt^2 and d^2y/dt^2, determine excitation forces delivered to the motion system and can derived through chain rule from equations (1) and (2) as:

$$\left.\begin{aligned} \ddot{x} &= \frac{d^2x}{dt^2} = \frac{d^2x}{ds^2}\left(\frac{ds}{dt}\right)^2 + \frac{dx}{ds}\frac{d^2s}{dt^2} = x''\dot{s}^2 + x'\ddot{s} \\ \ddot{y} &= \frac{d^2y}{dt^2} = \frac{d^2y}{ds^2}\left(\frac{ds}{dt}\right)^2 + \frac{dy}{ds}\frac{d^2s}{dt^2} = y''\dot{s}^2 + y'\ddot{s} \end{aligned}\right\} \quad (3)$$

The objective is to control the frequency spectrum of axis acceleration profiles by modulating the displacement and velocity profiles along the spline geometry. This can be achieved by finding parameters of the optimal displacement profile $\theta=[a_0, a_1, \ldots a_{11}]^T$, which minimizes the Discrete Fourier Transform (DFT) of axis accelerations within a predetermined $\omega\in[\omega_1,\omega_2]$ frequency band. The cost function for this problem can be postulated by taking DFT of axis acceleration profiles from Eq. (3) as follows:

$$J=\sum_{n=0}^{N}\left\{\left|\sum_{k=0}^{K}\ddot{x}(kT_s)e^{-j(\omega_1+n\Delta\omega)kT_s}\right|^2+\left|\sum_{k=0}^{K}\ddot{y}(kT_s)e^{-j(\omega_1+n\Delta\omega)kT_s}\right|^2\right\} \quad (4)$$

where $\omega_2=\omega_1+N\Delta\omega$, N determines the frequency discretization resolution and K is the number of total time samples in the trajectory.

LINEARIZATION OF THE OPTIMIZATION PROBLEM

Notice that the cost function given in Eq. (4) is non-linear due to the fact that x and y axis acceleration profiles are non-linear functions of tangential motion profile $\dot{s}$, $\ddot{s}$ and the geometric derivatives of the path x', x'', y' and y'' (see Eq. (3)). Although this problem can be solved using computationally expensive non-linear optimization techniques, the following presents an effective technique to determine the tangential motion profile.

We assume that an original tangential motion trajectory is already planned for this path. For instance, a minimum jerk path planning technique widely used in robotics literature, e.g. [6] and [7], may be used to plan a smooth trajectory for this path. This path is then used as a template to implement the following linearization techniques and hence final reference axis acceleration commands exhibit desired frequency characteristics.

Firstly, we start with the linearization of $\dot{s}^2$ which controls axis accelerations from Eq. (3). Using a simple 1st order Taylor series expansion around a point $\dot{s}(t=kT_s)=\dot{s}_T(kT_s)$,where $\dot{s}_T$ denotes the template feed profile, $\dot{s}^2$ can be expressed as

$$\dot{s}^2\cong(\dot{s}_T)^2+2(\dot{s}_T)(\dot{s}-(\dot{s}_T)) \quad (5)$$

Next, the geometric derivatives need to be evaluated at each time sample. Similarly, those geometric derivatives are also borrowed from template trajectory as:

$$\left.\begin{aligned}x'(kT_s)&\cong x_T'(kT_s)=x'(s_T(kT_s))\\x''(kT_s)&\cong x_T''(kT_s)=x''(s_T(kT_s))\\y'(kT_s)&\cong y_T'(kT_s)=y'(s_T(kT_s))\\y''(kT_s)&\cong y_T''(kT_s)=y''(s_T(kT_s))\end{aligned}\right\} \quad (6)$$

where x'_T, x_T'', y'_T and y_T'' denote geometric derivatives evaluated from the template trajectory. Illustration of the described approximation approach is given in Fig. 2.

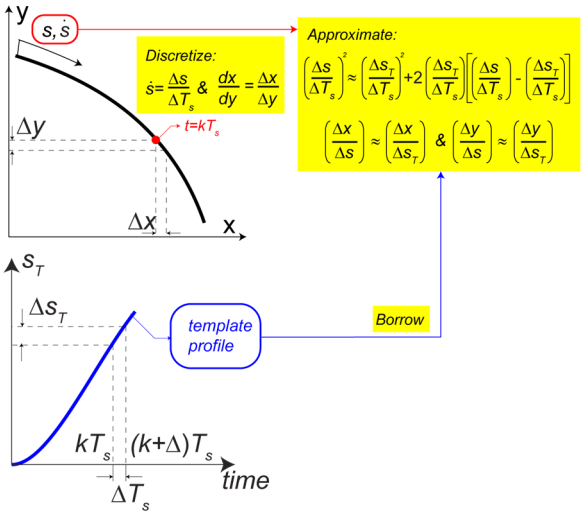

FIGURE 2: Approximation of nonlinear terms.

Substituting Eqs. (5) and (6) into Eq. (3), axis accelerations at k^{th} sample can be approximated;

$$\left.\begin{aligned}\ddot{x}(t=kT_s)&\cong x_J''\left(\dot{s}_J^2+2\dot{s}_J(\dot{s}-\dot{s}_J)\right)+x_J'\ddot{s}\big|_{t=kT_s}\\\ddot{y}(t=kT_s)&\cong y_J''\left(\dot{s}_J^2+2\dot{s}_J(\dot{s}-\dot{s}_J)\right)+y_J'\ddot{s}\big|_{t=kT_s}\end{aligned}\right\} \quad (7)$$

Finally, considering the entire trajectory consisting of M samples, Eq. (7) can be put in a vector form for mathematical convenience;

$$\left.\begin{aligned}\begin{bmatrix}\ddot{x}(0T_s)\\\ddot{x}(T_s)\\\vdots\\\ddot{x}(KT_s)\end{bmatrix}&=\left(2\boldsymbol{J_{X1}M_1}+\boldsymbol{J_{X2}M_2}\right)\underbrace{\begin{bmatrix}a_0\\a_1\\\vdots\\a_{11}\end{bmatrix}}_{\theta}-\boldsymbol{J_{X3}}\\\begin{bmatrix}\ddot{y}(0T_s)\\\ddot{y}(T_s)\\\vdots\\\ddot{y}(KT_s)\end{bmatrix}&=\left(2\boldsymbol{J_{Y1}M_1}+\boldsymbol{J_{Y2}M_2}\right)\underbrace{\begin{bmatrix}a_0\\a_1\\\vdots\\a_{11}\end{bmatrix}}_{\theta}-\boldsymbol{J_{Y3}}\end{aligned}\right\} \quad (8)$$

where

$$\boldsymbol{M_1}=\begin{bmatrix}0&1&2(0T_s)&\cdots&11(0T_s)^{10}\\0&1&2(T_s)&\cdots&11(T_s)^{10}\\\vdots&\vdots&\vdots&\ddots&\vdots\\0&1&2(KT_s)&\cdots&11(KT_s)^{10}\end{bmatrix}$$

$$\boldsymbol{M_2}=\begin{bmatrix}0&0&2&\cdots&110(0T_s)^{9}\\0&0&2&\cdots&110(T_s)^{9}\\\vdots&\vdots&\vdots&\ddots&\vdots\\0&0&2&\cdots&110(KT_s)^{9}\end{bmatrix}$$

$$\boldsymbol{J_{X1}}=diag\left\{x_T''(0T_s)\dot{s}_T(0T_s),\ldots,x_T''(KT_s)\dot{s}_T(KT_s)\right\}$$

$$\boldsymbol{J_{X2}}=diag\left\{x_T'(0T_s),\ldots,x_T'(KT_s)\right\}$$

$$\boldsymbol{J_{X3}}=diag\left\{x_T''(0T_s)\dot{s}_T^2(0T_s),\ldots,x_T''(KT_s)\dot{s}_T^2(KT_s)\right\}$$

$$\boldsymbol{J_{Y1}} = diag\left\{ y_T^{''}(0T_s)\dot{s}_T(0T_s), \ldots, y_T^{''}(KT_s)\dot{s}_T(KT_s) \right\}$$

$$\boldsymbol{J_{Y2}} = diag\left\{ y_T^{'}(0T_s), \ldots, y_T^{'}(KT_s) \right\}$$

$$\boldsymbol{J_{Y3}} = diag\left\{ y_T^{''}(0T_s)\dot{s}_T^2(0T_s), \ldots, y_T^{''}(KT_s)\dot{s}_T^2(KT_s) \right\}$$

are constant matrices. Using above linearized expressions for sampled accelerations $x(kT_s)$ and $y(kT_s)$, cost function J can be put in the following quadratic form

$$J = \underbrace{\left\| \begin{bmatrix} \boldsymbol{F}\left(2\boldsymbol{J_{X1}}\boldsymbol{M_1} + \boldsymbol{J_{X2}}\boldsymbol{M_2}\right) \\ \boldsymbol{F}\left(2\boldsymbol{J_{Y1}}\boldsymbol{M_1} + \boldsymbol{J_{Y2}}\boldsymbol{M_2}\right) \end{bmatrix}\theta - \begin{bmatrix} \boldsymbol{F}\boldsymbol{J_{X3}} \\ \boldsymbol{F}\boldsymbol{J_{Y3}} \end{bmatrix} \right\|^2}_{|\boldsymbol{A}\theta - \boldsymbol{b}|^2} \quad (9)$$

where

$$\boldsymbol{F} = \begin{bmatrix} e^{-j(\omega_1)0T_s} & e^{-j(\omega_1)T_s} & \cdots & e^{-j(\omega_1)KT_s} \\ e^{-j(\omega_1+\Delta\omega)0T_s} & e^{-j(\omega_1+\Delta\omega)T_s} & \cdots & e^{-j(\omega_1+\Delta\omega)KT_s} \\ \vdots & \vdots & \ddots & \vdots \\ e^{-j(\omega_1+N\Delta\omega)0T_s} & e^{-j(\omega_1+N\Delta\omega)T_s} & \cdots & e^{-j(\omega_1+N\Delta\omega)KT_s} \end{bmatrix}$$

Eq. (9) can be minimized in the sense of linear least squares to obtain the optimal trajectory parameters $\theta=[a_0, a_1, \ldots a_{11}]^T$.

Furthermore, kinematic boundary conditions such as initial and final position, velocity and acceleration constraints can also be imposed to further control the trajectory. They can be written in linear matrix form as:

$$\underbrace{\begin{bmatrix} 1 & (0T_s) & (0T_s)^2 & \cdots & (0T_s)^{11} \\ 0 & 1 & 2(0T_s) & \cdots & 11(0T_s)^{10} \\ 0 & 0 & 2 & \cdots & 110(0T_s)^9 \\ 1 & (KT_s) & (KT_s)^2 & \cdots & (KT_s)^{11} \\ 0 & 1 & 2(KT_s) & \cdots & 11(KT_s)^{10} \\ 0 & 0 & 2 & \cdots & 110(KT_s)^9 \end{bmatrix}}_{\boldsymbol{L}} \underbrace{\begin{bmatrix} a_0 \\ a_1 \\ \vdots \\ a_{11} \end{bmatrix}}_{\theta} = \underbrace{\begin{bmatrix} s_{init} \\ \dot{s}_{init} \\ \ddot{s}_{init} \\ s_{final} \\ \dot{s}_{final} \\ \ddot{s}_{final} \end{bmatrix}}_{\zeta} \quad (10)$$

and the final formal optimization problem is postulated as

$$\min_{\theta} J = \left|\boldsymbol{A}\theta - \boldsymbol{b}\right|^2, \; s.t.: \boldsymbol{L}\theta = \zeta \quad (11)$$

Converting (11) into an unconstrained optimization problem with the help of Lagrange Multipliers yields

$$\min_{\theta,\Lambda} J' = \left(\boldsymbol{A}\theta - \boldsymbol{b}\right)^{\dagger}\left(\boldsymbol{A}\theta - \boldsymbol{b}\right) + \Lambda\left(\boldsymbol{L}\theta - \zeta\right) \quad (12)$$

where Λ denotes the vector of Lagrange Multipliers and $(\boldsymbol{A}\theta-\boldsymbol{b})^{\dagger}$ indicates Hermitian Transpose of $(\boldsymbol{A}\theta-\boldsymbol{b})$. Analytical solution to the quadratic programming (QP) problem given in (12) is obtained as

$$\begin{bmatrix} \theta \\ \Lambda \end{bmatrix} = \begin{bmatrix} re\left(\boldsymbol{A}^{\dagger}\boldsymbol{A}\right) & \boldsymbol{L}^T \\ \boldsymbol{L} & \boldsymbol{0} \end{bmatrix}^{-1} \begin{bmatrix} \boldsymbol{A}^{\dagger}\boldsymbol{b} + \boldsymbol{A}^T\boldsymbol{b}^* \\ \zeta \end{bmatrix} \quad (13)$$

where $\boldsymbol{b}^*$ denotes the complex conjugate of $\boldsymbol{b}$.
Notice that the definition of the optimization problem so far has been for a single geometric spline segment. Since 2D toolpaths contain multiple spline segments, frequency spectrum of the total trajectory needs to be optimized through finding polynomial coefficients $[\theta_1, \theta_2, \ldots, \theta_M]$ of each displacement profile $[s_1, s_2, \ldots, s_M]$. In order to optimize the full/total trajectory, optimization problem depicted in (11) is expanded as

$$\min_{\theta} J_{full} = \left|\boldsymbol{A}_{full}\theta_{full} - \boldsymbol{b}_{full}\right|^2, \; s.t.: \boldsymbol{L}_{full}\theta_{full} = \zeta_{full} \quad (14)$$

where

$$\boldsymbol{A}_{full} = \begin{bmatrix} \boldsymbol{A}_1 & & & \boldsymbol{0} \\ & \boldsymbol{A}_2 & \ddots & \\ & & & \\ \boldsymbol{0} & & & \boldsymbol{A}_M \end{bmatrix}, \theta_{full} = \begin{bmatrix} \theta_1 \\ \theta_2 \\ \vdots \\ \theta_M \end{bmatrix}, \boldsymbol{b}_{full} = \begin{bmatrix} \boldsymbol{b}_1 \\ \boldsymbol{b}_2 \\ \vdots \\ \boldsymbol{b}_M \end{bmatrix}$$

$$\boldsymbol{L}_{full} = \begin{bmatrix} \boldsymbol{L}_{pos} \\ \boldsymbol{L}_{vel} \\ \boldsymbol{L}_{acc} \end{bmatrix}, \zeta_{full} = \begin{bmatrix} \begin{bmatrix} 0 & s_{1,final} & \cdots & 0 & \left(s_{M,final} - s_{M-1,final}\right) \end{bmatrix}^T \\ \begin{bmatrix} 0 & \cdots & 0 \end{bmatrix}^T \\ \begin{bmatrix} 0 & \cdots & 0 \end{bmatrix}^T \end{bmatrix}$$

and where $\boldsymbol{L}_{pos}$, $\boldsymbol{L}_{vel}$ and $\boldsymbol{L}_{acc}$ denote position, velocity and acceleration continuity constraint matrices respectively as

$$\boldsymbol{L}_{pos} = \begin{bmatrix} \begin{bmatrix} (0T_s)^0 & (K_1T_s)^0 \\ \vdots & \vdots \\ (0T_s)^{11} & (K_1T_s)^{11} \end{bmatrix} & & \boldsymbol{0} \\ & \ddots & \\ \boldsymbol{0} & & \begin{bmatrix} (0T_s)^0 & (K_MT_s)^0 \\ \vdots & \vdots \\ (0T_s)^{11} & (K_MT_s)^{11} \end{bmatrix} \end{bmatrix}$$

$$\boldsymbol{L}_{vel} = \begin{bmatrix} \begin{bmatrix} 0 & \cdots & 11(0T_s)^{10} \end{bmatrix}^T & & \boldsymbol{0} \\ & \boldsymbol{L}_{vel,cont} & \\ \boldsymbol{0} & & \begin{bmatrix} 0 & \cdots & 11(K_MT_s)^{10} \end{bmatrix}^T \end{bmatrix}$$

$$\boldsymbol{L}_{vel,cont} = \begin{bmatrix} \begin{bmatrix} \begin{bmatrix} 0 & \cdots & 11(K_1T_s)^{10} \end{bmatrix}^T \\ -\begin{bmatrix} 0 & \cdots & 11(0T_s)^{10} \end{bmatrix}^T \end{bmatrix}^T & & \boldsymbol{0} \\ & \ddots & \\ \boldsymbol{0} & & \begin{bmatrix} \begin{bmatrix} 0 & \cdots & 11(K_{M-1}T_s)^{10} \end{bmatrix}^T \\ -\begin{bmatrix} 0 & \cdots & 11(0T_s)^{10} \end{bmatrix}^T \end{bmatrix}^T \end{bmatrix}$$

$$\boldsymbol{L}_{acc} = \begin{bmatrix} \begin{bmatrix} 0 & \cdots & 110(0T_s)^9 \end{bmatrix}^T & & \boldsymbol{0} \\ & \boldsymbol{L}_{acc,cont} & \\ \boldsymbol{0} & & \begin{bmatrix} 0 & \cdots & 110(K_MT_s)^9 \end{bmatrix}^T \end{bmatrix}$$

$$\boldsymbol{L}_{acc,cont} = \begin{bmatrix} \begin{bmatrix} \begin{bmatrix} 0 & \cdots & 110(K_1T_s)^9 \end{bmatrix}^T \\ -\begin{bmatrix} 0 & \cdots & 110(0T_s)^9 \end{bmatrix}^T \end{bmatrix}^T & & \boldsymbol{0} \\ & \ddots & \\ \boldsymbol{0} & & \begin{bmatrix} \begin{bmatrix} 0 & \cdots & 110(K_{M-1}T_s)^9 \end{bmatrix}^T \\ -\begin{bmatrix} 0 & \cdots & 110(0T_s)^9 \end{bmatrix}^T \end{bmatrix}^T \end{bmatrix}$$

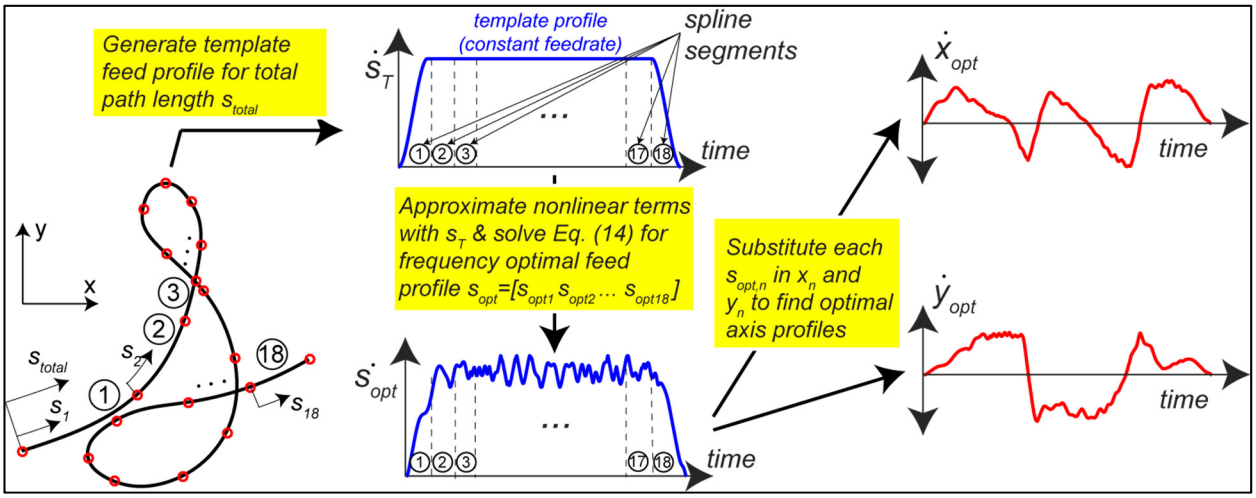

FIGURE 3: Trajectory Generation Strategy

Notice that the time required to travel along each spline segment is different where n^{th} spline segment has a duration of K_nT_s. Similar to the formulation given in (13), optimal displacement profile parameters for the full trajectory θ_{full} can be found analytically as

$$\begin{bmatrix}\theta_{full}\\ \Lambda_{full}\end{bmatrix}=\begin{bmatrix}re\left(\boldsymbol{A}_{full}^{H}\boldsymbol{A}_{full}\right) & \boldsymbol{L}_{full}^{T}\\ \boldsymbol{L}_{full} & \boldsymbol{0}\end{bmatrix}^{-1}\begin{bmatrix}\boldsymbol{A}_{full}^{H}\boldsymbol{b}_{full}+\boldsymbol{A}_{full}^{T}\boldsymbol{b}_{full}^{*}\\ \zeta_{full}\end{bmatrix} \quad (15)$$

Note that, acceleration and jerk limits along long moves can be incorporated as inequality constraints, which requires sequential quadratic programming (SQP) to be applied.

EXPERIMENTAL SETUP AND RESULTS

Proposed scheme allows direct generation of reference motion trajectories with frequency optimal acceleration profiles eliminating the need for post filtering. Solution procedure benefits from well-structured analytical expressions, which makes it suitable for real-time implementation on modern NC systems.

Fig. 3 presents the overall strategy to implement the proposed frequency optimal interpolation scheme on 2D spline tool-paths. In this experiment, the spline geometry shown in Fig. 4 is interpolated at constant speed and also based on the proposed technique. The path speed (feedrate) is set to 120 [mm/sec], and tangential acceleration is limited to 750 [mm/sec^2].

In order to demonstrate the effectiveness of the proposed technique, the planar motion platform shown in Fig. 5 is equipped with flexible beams with resonances in X and Y directions at *~8.4* and *~8* [Hz] respectively. In order to avoid exciting those resonances the attenuation band of the trajectory is set to $\omega\in$*[7.5,8.5]* [Hz].

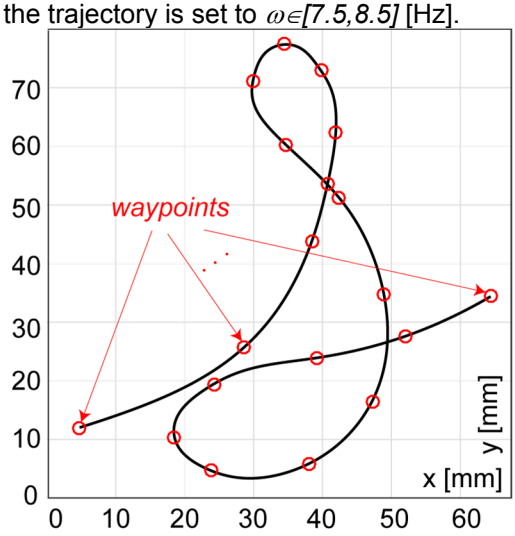

FIGURE 4: Geometric Path.

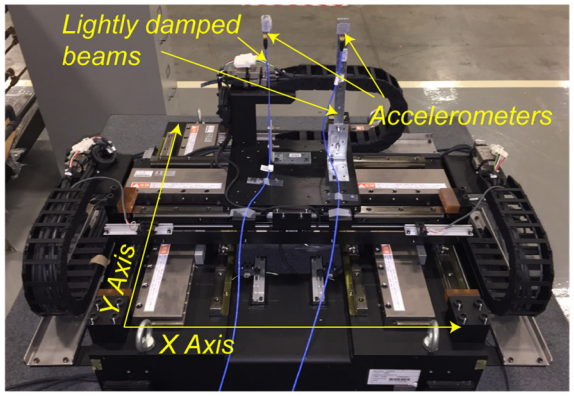

FIGURE 5: Experimental Setup.

Fig. 6 shows the original tangential motion profile and x and y axis motion commands. In comparison, Fig. 7 shows the trajectory

kinematics based on the proposed technique. As shown, the kinematic profiles fluctuate to attenuate the frequency spectrum in the desired band.

The frequency content of generated acceleration profiles is examined by taking DFTs of each acceleration profile shown in Fig. 8. As shown, proposed interpolation scheme can command reference motion with significantly attenuated frequency energy in a set band to effectively mitigate residual vibrations along 2D tool-paths. This eliminates the need for any post-filtering such as notch-ing or input shaping. The beams attached to the planar motion platform are equipped with PCB 3711B1130G accelerometers with a sensitivity of 6.8 [mV/(m/sec^2)]. Figures 9 and 10 show beam accelerations and their DFTs respectively for each axis. As seen, natural frequencies of the beams, which fall into attenuated frequency band, are significantly suppressed by the proposed trajectory generation method.

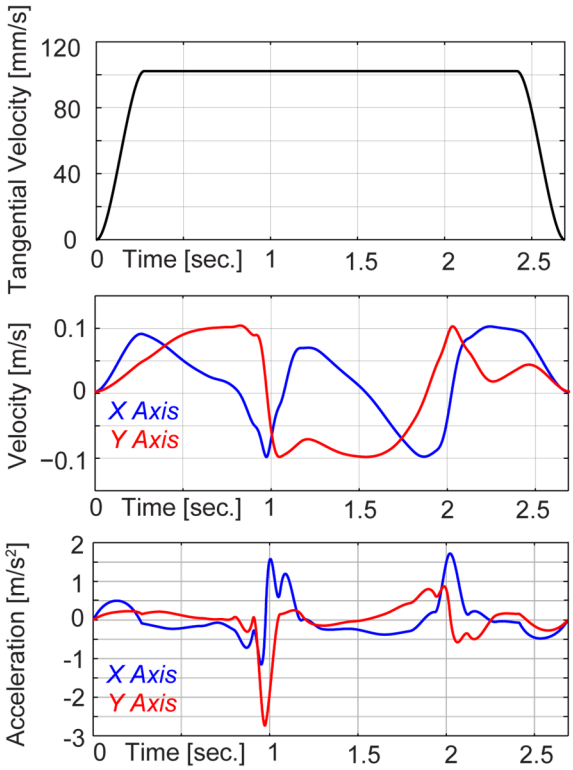

FIGURE 6: Kinematics of Template Trajectory.

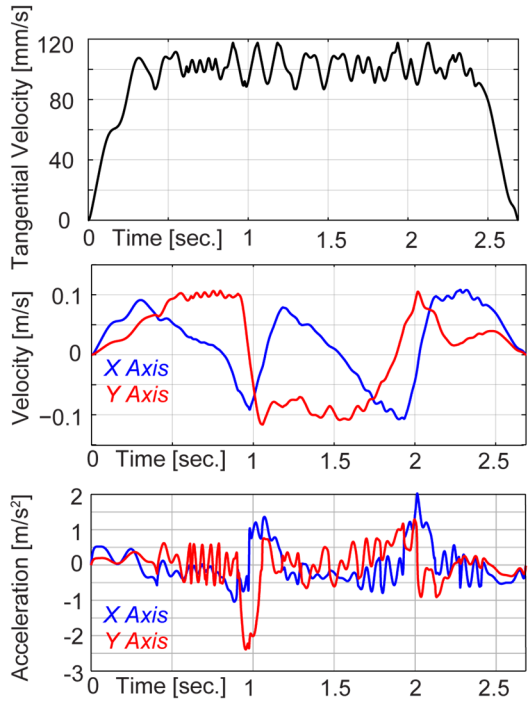

FIGURE 7: Kinematics of Proposed Trajectory.

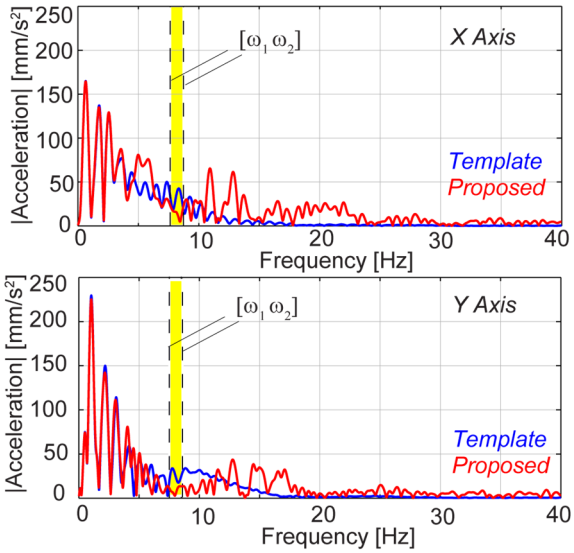

FIGURE 8: Frequency Spectrum of Acceleration Profiles.

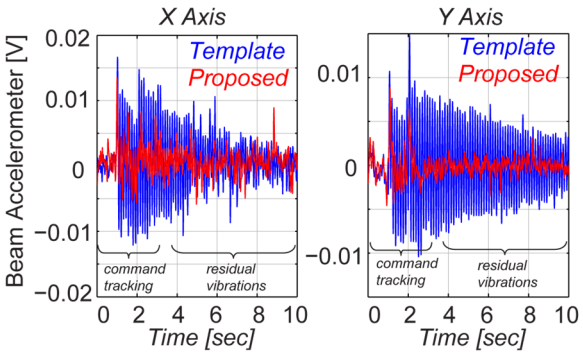

FIGURE 9: Beam Accelerations during Tracking Experiments.

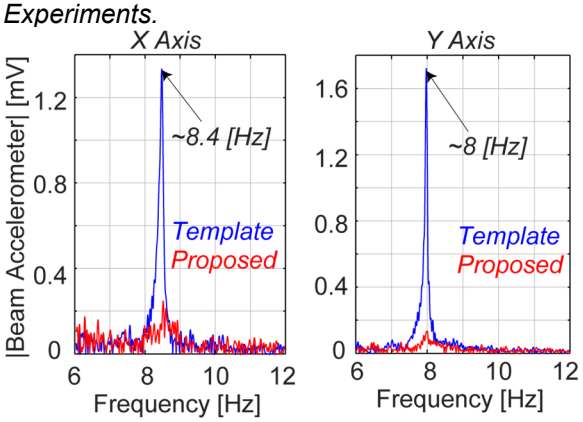

FIGURE 10: Frequency Spectrum of Beam Accelerations.

CONCLUSIONS

This paper presented a trajectory generation method for 2D to generate frequency optimal feed profiles along spline toolpaths. Proposed method generates a feed profile by solving an optimization problem where the frequency content of the resultant acceleration profiles of *x* and *y* axes is minimized. Experiments are carried out where the method is used to suppress natural frequencies of lightly damped beams attached to a planar motion platform and significant improvement compared to constant feedrate trajectories is observed.

REFERENCES

[1] Erkorkmaz, K. and Altintas, Y. High speed CNC system design. Part I: jerk limited trajectory generation and quintic spline interpolation. IMTM. 2001; 41(9): 1323-1345.

[2] Flash, T. and Hogan, N. The coordination of arm movements: an experimentally confirmed mathematical model. Journal of neuroscience. 1985; 5(7): 1688-1703.

[3] Singhose, W. and Singer, N.,. Initial investigations into the effects of input shaping on trajectory following. *ACC.* 1994; 3: 2526-2532.

[4] Sencer, B. and Tajima, S. Frequency Optimal Feed Motion Planning in Computer Numerical Controlled Machine Tools for Vibration Avoidance. Journal of Manufacturing Science and Engineering. 2017; 139(1): 011006.

[5] Wang F.-C., Wright P.K., Barsky B.A., Yang D.C.H. Approximately Arc-Length Parametrized C^3 Quintic Interpolatory Splines. Journal of Mechanical Design, Transactions of the ASME. 1999; 121(3): 430-439.

[6] Altintas Y., Erkorkmaz K.,. Feedrate optimization for spline interpolation in high speed machine tools. CIRP Annals-Manufacturing Technology. 2003; 52(1): 297-302.

[7] Chang B.-H., Hori Yoichi,. Trajectory Design Considering Derivative of Jerk for Head-Positioning of Disk Drive System With Mechanical Vibration. IEEE/ASME Transactions on Mechatronics. 2006 11(3): 273-279.

STRONG AND QUIET LINEAR IRON-CORE SYNCHRONOUS MOTOR

Jun Young Yoon, David L. Trumper
Department of Mechanical Engineering
Massachusetts Institute of Technology
Cambridge, MA, USA

INTRODUCTION

In the semiconductor industry, the pursuit of smaller chip size and higher throughput requires the next-generation lithography machines to have higher acceleration with tight accuracy in a sub-nanometer level. There have been efforts to increase the reticle stage acceleration by replacing iron-less Lorentz motors [1] with iron-core permanent magnet motors. However, it is observed that conventional iron-core motors emit a significant amount of noise, which is transmitted in both structural- and air-borne pathways. Such vibrations can disturb the lens and metrology-frame, thereby deteriorating the lithography system accuracy performance.

The industrial needs of both higher acceleration and lower noise motivate the design and testing of a new linear iron-core permanent magnet motor to simultaneously achieve high force and low noise. In this paper, we present a new five-phase iron-core permanent magnet motor, called a fine-tooth motor, that can fulfill both requirements. With our new fine-tooth motor, shown on the right in Figure 1, we have experimentally demonstrated the potential to significantly reduce the vibro-acoustic noise of iron-core motors while substantially enhancing the shear stress density, compared to a conventional 3-4 combination iron-core linear motor, which uses the configuration shown on the left in Figure 1.

NEW MOTOR DESIGN APPROACH

When an iron-core permanent magnet motor is operated, it experiences two major forces: one is the coil-driven force and the other is a force on the iron core such as cogging. Depending on the magnetic design of a motor, these forces can have high-frequency harmonics. Such high force harmonics can vibrate the moving stage, which is especially troublesome when the stage dynamics are excited. Such stage vibration can be transmitted through the system structure, and also can radiate as acoustic noise.

A conventional iron-core permanent magnet motor shown on the left side of Figure 1, often

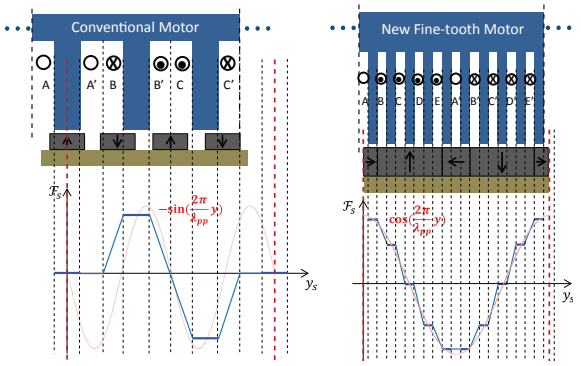

FIGURE 1. Stator MMF ($\mathcal{F}_s$) waveforms of the conventional linear iron-core motor (left) and our new fine-tooth motor (right).

called a 3-4 combination motor since 3 stator phases overlap with 4 permanent magnets, has a magnetic design that inherently generates high-frequency force harmonics. This can be seen from the coarse magneto-motive force (MMF) [2], which is illustrated at the bottom on the left in Figure 1. Due to the coarse iron-core teeth (only 3 in a unit period of two-pole pairs), we have a coarse stator MMF waveform (blue), which is different from the ideal fundamental waveform (red). Note that the realistic MMF curve can be considered as a sampled version of the ideal waveform with the iron-core tooth locations as the sampling points.

In order to reduce the high-frequency force harmonics, we take a new design approach of having fine teeth closely packed together as can be seen on the right side of Figure 1. The realistic stator MMF (blue curve) of our new motor agrees with the ideal waveform (red curve) much closely with less high harmonics, thereby generating less high-frequency force harmonics and therefore less vibro-acoustic noise. Our new motor has the magnetic design features of five phases, fine teeth [3, 4], narrow slots with high aspect ratio, and Halbach magnet array. Note that the Halbach pattern [5, 6, 7] is chosen to 1) increase the magnetic flux density in the working air gap and 2) have a smoother rotor MMF to help reduce high force harmonics.

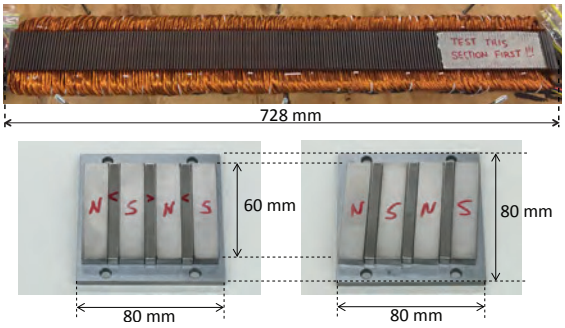

FIGURE 2. Pictures of our fine-tooth motor. Stator armature (upper), non-skewed (lower left), and skewed (lower right) magnet tracks.

EXPERIMENTAL TESTBED

Figure 2 shows pictures of our new fine-tooth motor armature (upper) and magnet tracks (lower). The armature is the motor stator with five-phase double-layer concentrated full-pitch coil windings while the short magnet track is the moving part with Halbach pattern. The key design parameters of our new motor and their values are given in Table 1. Note that the skew angle is chosen to be $4.4^\circ = \mathrm{atan}(4\,\mathrm{mm}/52\,\mathrm{mm})$ in order to cover a full tooth pitch of 4 mm within the motor width of 52 mm and therefore to minimize the cogging.

Figure 3 shows a picture of the experimental linear stage setup with our new fine-tooth motor. A permanent magnet track is mounted on the bottom of the moving air-bearing stage. Note that we replaced the motor, both stator armature and magnet track, with a conventional 3-4 combination motor when investigating the noise issue of such motors. Our experimental linear stage 1) runs on air bearings to avoid possible mechanical noise source caused by mechanical contacts of rolling-element bearings, 2) has shock absorbers at both travel ends for the purpose of safety in case of stage cycle failure modes, 3) has the real-time position feedback with the resolution of 0.1 μm, and 4) is position-controlled with a -3dB-bandwidth of 200 Hz by a real-time control loop running at a 10 kHz sample rate. We measure the vibrational and acoustic noises using accelerometers (356A26 and 353B15 by PCB Piezotronics) and microphones (130E20 by PCB Piezotronics), whose outputs are sampled at 50 kHz.

TABLE 1. Fine-tooth motor design values

Design Parameter	Value
Number of slots per pole (# of phase)	5
Tooth and slot width	2 mm
Slot depth	30 mm
Number of winding turns per slot	126
Wire gauge for winding	AWG 23
Vertical magnet width	14 mm
Horizontal magnet width	6 mm
Magnet thickness	7 mm
Magnet skew angle	4.4°
Motor width	52 mm

EXPERIMENTAL RESULTS

In order to validate the noise reduction of our new fine-tooth motor, the acoustic noise of both the conventional and the fine-tooth motors are measured with calibrated microphones while cycling the stage at $A_{max} = 25\,\mathrm{m/s^2}$ and $V_{max} = 1\,\mathrm{m/s}$. The measured acoustic noise cumulative amplitude spectra (CAS) [8, 9] comparisons during both an acceleration period and a constant-velocity region are shown in Figure 4. The overall noise level of the conventional motor is dominated by the flexible resonant stage dynamics for both acceleration and constant-velocity regions, mostly at 360 Hz and 630 Hz. The mode

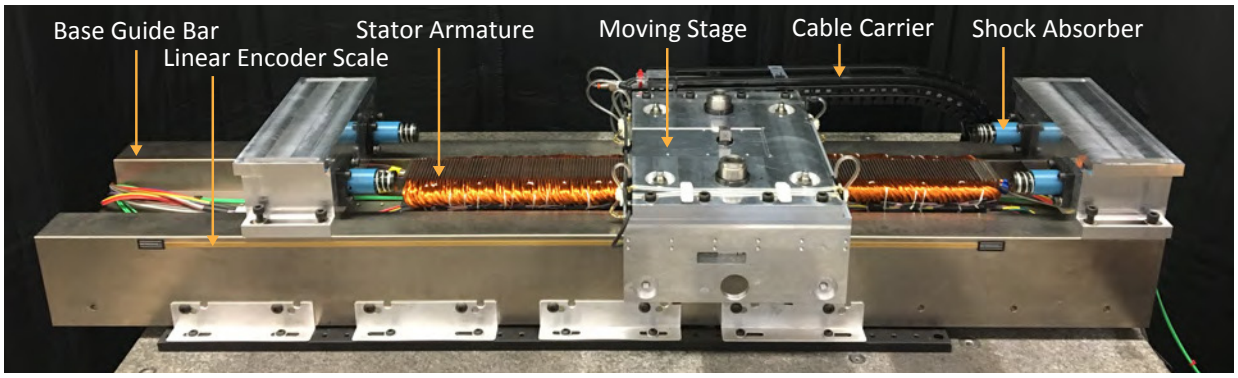

FIGURE 3. The experimental linear stage testbed with our new fine-tooth motor installed.

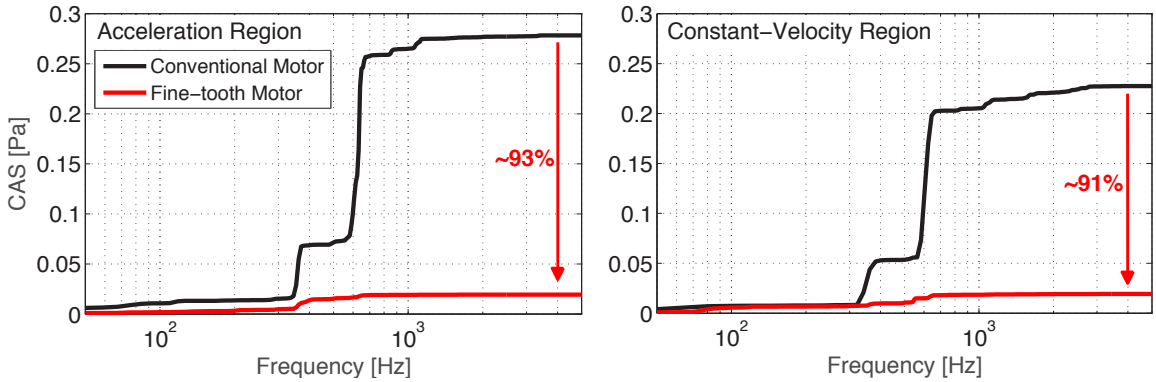

FIGURE 4. Acoustic noise cumulative amplitude spectrum (CAS) comparison between the conventional motor and our new fine-tooth motor during acceleration region (left) and constant-velocity region (right). Non-skewed magnets are used. Note that the final value is the noise standard deviation.

at 360 Hz is a rigid-body mode of the stage in the normal direction against the air bearing stiffness while the 630 Hz mode is a bending eigen-mode of our U-shape stage [10].

Such dynamics-oriented noise is significantly reduced when our fine-tooth motor is used as can be seen from the red CAS plots with much smaller jumps at those frequencies. Specifically, the overall noise within a bandwidth of 5 kHz is reduced by 93 % (from 0.28 Pa to 0.02 Pa) and 91 % (from 0.23 Pa to 0.02 Pa) for the acceleration region and the constant-velocity region, respectively. Note that this significant noise reduction in Pascals corresponds to about 20 dB reduction in the sound pressure level (SPL) from about 80 dB to 60 dB. Qualitatively, this is the noise difference between a big truck passing by and a quiet office. This substantial noise reduction is due to the magnetic design characteristic of fine teeth, reducing the high-frequency force harmonics as discussed in the previous section.

The cogging-oriented noise, mostly observed during the constant velocity region, is also significantly reduced by our new fine-tooth motor design. Figure 5 shows the spectrograms of acoustic noise measured while cycling the stage with our new fine-tooth motor with either non-skewed (left) or skewed (right) magnets. We command a velocity profile with increasing velocities from 1.6 m/s to 2.2 m/s at the maximum acceleration of 45 m/s^2 as indicated with the white curves in the plots. Note that the brighter blue portions in the plots indicate velocity-constant regions while the darker portions are for acceleration/deceleration

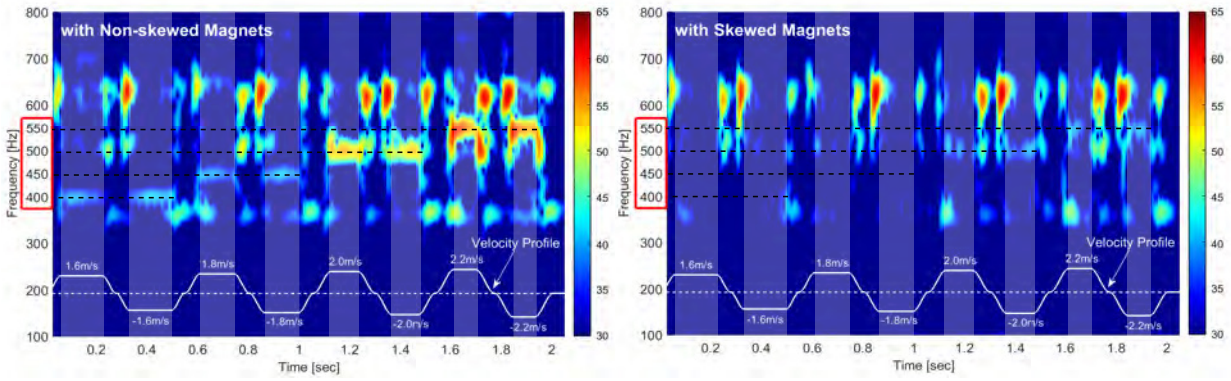

FIGURE 5. Spectrogram comparison of acoustic noise of new fine-tooth motor with non-skewed magnets (left) and skewed magnets (right). Velocity profile commanded to the stage is indicated in white. Spectrogram shows harmonic content in a moving window of data as a function of time. Note changes in harmonic content in constant-velocity regions vs. acceleration regimes.

regions. In the acceleration regions, we observe stage dynamic-oriented noises mostly at 360 Hz and 630 Hz as shown in the CAS plots. In the constant-velocity regions, on the other hand, the cogging-driven noises are dominant. Such noise is velocity dependent with the relationship of

$$\text{cogging noise frequency} = \frac{\text{stage velocity}}{\text{cogging period}}, \quad (1)$$

where the cogging period is equal to the tooth pitch of 4 mm for our new motor. As shown in the noise spectrogram with non-skewed magnets, these cogging-oriented noises are observed at 400, 450, 500, and 550 Hz for the stage velocity of 1.6, 1.8, 2.0, and 2.2 m/s, respectively. These noises are significantly reduced simply by using skewed magnets with a skew angle of only 4.4°. As an example, the cogging noise at 550 Hz is reduced approximately by 20 dB from 60 dB to 40 dB with skewed magnets. This significant cogging noise reduction is due to our fine-tooth design, allowing a small enough tooth pitch to be covered by skewed magnets without significantly compromising the thrust.

Beside the noise reduction, our new fine-tooth motor also shows potential for significant shear stress increase. Figure 6 shows a shear stress comparison between the conventional motor and our fine-tooth motor both in simulation (solid lines) and in experiment (dotted lines). Note that the experimental data points of the conventional motor are limited to relatively low power because this motor emitted too much vibro-acoustic noise even at a relatively low power level. For our new motor, the coil heating was the limiting factor for experiments at higher power levels. Note also that we used skewed magnets for both motors in both simulations and experiments. We use power dissipation per length in the abscissa to take the motor length difference into account for a fair comparison between two different motors. We can see that our new fine-tooth motor behaves closely to the simulation results, showing higher shear stress performance than the conventional motor at every power level. Specifically, at the power level of 20 W/mm, our fine-tooth motor shows about 19 % higher shear stress density than the conventional iron-core synchronous motor, and about 58 % higher shear stress density at a high power level of 500 W/mm. Such high power dissipation will require water cooling for steady-state operation, although this has not been included in our present design. Experimental data shown in Figure 6 was acquired in a short period of time, after which the motor was allowed to cool via air convection.

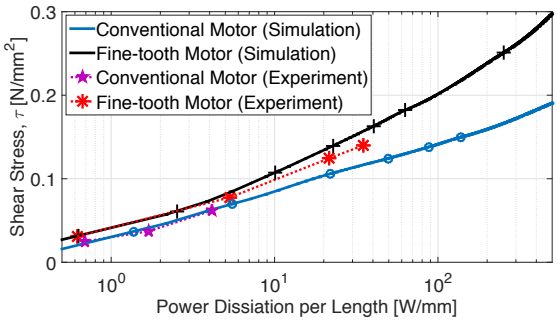

FIGURE 6. Motor shear stress performance comparison between conventional iron-core motor and our new fine-tooth motor.

CONCLUSION

We present in this paper a new fine-tooth motor with the design characteristics of fine-pitch iron-core teeth, narrow and deep slots, five-phase full-pitch concentrated windings, and a moving Halbach magnet array so as to simultaneously achieve low vibro-acoustic noise and high shear stress density at the same time. Experimentally observed stage dynamics-oriented noise is reduced by more than 90 % compared to a conventional 3-4 combination motor for both acceleration/deceleration and constant-velocity regions. The cogging-driven and velocity-dependent noise dominant during constant-velocity regions is further significantly reduced in our new motor design by minimizing the cogging force using skewed magnets together with a small tooth pitch design.

Our new fine-tooth motor also shows great potential for higher shear stress density than the conventional motors. Both the simulated and experimental results show higher shear stress density than the conventional 3-4 combination iron-core synchronous motor at every power level with even more potential at higher power levels. Our fine-tooth motor can be potentially utilized for industrial applications that require high acceleration and low noise at the same time, such as photolithography scanners.

ACKNOWLEDGMENT

This work was conducted with support from the ASML Company, Wilton, CT. We particularly appreciate fruitful discussions with Mark Schuster, Steve Roux, and Minkyu Kim at ASML. We would also like to thank Samsung Scholarship for their

financial support. We thank Fred Sommerhalter for his expertise and excellent work on the fabrication of challenging motor components.

REFERENCES

[1] Butler H. Position control in lithographic equipment. IEEE Control Systems Magazine. 2011;31(5):28–47.

[2] Fitzgerald AE, Kingsley C, Umans SD, James B, editors. Electric machinery. vol. 5. McGraw-Hill New York; 2003.

[3] Angle MG. Modeling, design, and optimization of permanent magnet synchronous machines [PhD Dissertation]. Massachusetts Institute of Technology. Department of Electrical Engineering and Computer Science; 2016.

[4] Banerjee A, Lang JH, Kirtley JL. Fine grain commutation: Integrated design of permanent-magnet synchronous machine drives with highest torque density. In: Electrical Machines (ICEM), 2012 XXth International Conference on. IEEE; 2012. p. 671–677.

[5] Halbach K. Design of permanent multipole magnets with oriented rare earth cobalt material. Nuclear instruments and methods. 1980;169(1):1–10.

[6] Ofori-Tenkorang J. Permanent-magnet synchronous motors and associated power electronics for direct-drive vehicle propulsion [PhD Dissertation]. Massachusetts Institute of Technology. Department of Electrical Engineering and Computer Science; 1997.

[7] Trumper DL, Williams ME, Nguyen TH. Magnet arrays for synchronous machines. In: Industry Applications Society Annual Meeting, 1993., Conference Record of the 1993 IEEE. IEEE; 1993. p. 9–18.

[8] Monkhorst W. Dynamic error budgeting: A design approach. TU Delft, Delft University of Technology; 2004.

[9] Jabben L. Mechatronic design of a magnetically suspended rotating platform. TU Delft, Delft University of Technology; 2007.

[10] Yoon JY. Linear iron-core permanent magnet motor with high force and low acoustic noise [PhD Dissertation]. Massachusetts Institute of Technology. Department of Mechanical Engineering; 2017.

Hybrid Design Approach for Constrained Layer Dampers to Balance Dynamic Performance in Combination with Geometrical Constraints

Kees Verbaan[1], Martijn Duiven[1], Rens Henselmans[1], Pieter Nuij[1] and David Rijlaarsdam[1]
[1]Systems Development Department
NTS-Group
Eindhoven, The Netherlands

INTRODUCTION

In modern positioning systems, and in fast and accurate processing and inspection steps specifically, move and settle times have to be small to enable high throughput. In addition, jitter values during standstill have to be low to achieve good positioning performance and process quality. The derived system requirements set the boundaries for the module requirements in terms of bandwidths of the control loops and, related to this, for the natural frequencies of the mechanical (sub)assemblies and the vibration isolation system as well as the mechanical damping of the structural parts. Nowadays, due to the fact that mechanical designs have to be made on the cutting edge of technological possibilities, mechanical damping gains attention in order to improve the performance further.

For lightly damped structures, the natural frequencies are determined by the geometry and the specific stiffness of the material applied. For motion stages, the minimal span is determined by the object size of the object to be processed. Given a certain material, this leads to the stages' height being the key stiffness parameter and, therefore, being the key parameter for its natural frequencies with corresponding mode shapes. These characteristics usually result in open-back or closed-back stage designs with a typical span-thickness-ratio smaller than 10, which indicates that a certain relative stage height is desired to guarantee dynamic performance.

Challenges in performance arise at the point that this ratio becomes substantially larger than 10 due to other functional or volume constraints. The implication of a thin stage will be that it has a low static stiffness in normal direction and, therefore, will show low natural frequencies. These properties, respectively, lead to 1) a relatively high transmissibility over the whole frequency range and, 2) combined with low modal damping will lead to large displacement amplification factors (Q-factor) at the resonance frequencies. In addition, a drawback arises from the fact that if a stages' natural frequencies decrease, that they shift to a frequency region in which the vibration isolation system is less effective: A larger part of the floor vibrational content will be transmitted into vertical displacement of the motion stage.

Different approaches exist to improve the dynamic performance of such a thin stage, such as applying materials with an larger specific stiffness, application of anisotropic fiber materials and design of geometrically complex mechanical structures to maximize the stiffness and minimize the effective mass. These solutions typically result from the classical design approach which aims for distributing mass and stiffness in the most efficient way. To improve the dynamic behavior further, a more integral design approach includes the design of passive damping. This leads to an integral approach in which all three mechanical system properties are designed; mass, damping and stiffness.

The design of passive damping in motion controlled systems is an active research area for high tech companies and proved to be very effective, especially in combination with taking the control loop in consideration[1]. One of the advantages of a large span-thickness-ratio wafer stage is that this specific geometry suits the application of a Constrained Layer Damper (CLD) very well: A CLD layer can be applied without changing a classical stage design drastically in contrast to well-known tuned mass dampers or robust mass dampers, which easily fit into a relatively high stage, but are more difficult to integrate in a thin stage.

DISCONTINUOUS CLD DESIGN

This paper describes a specific design approach for application of a CLD on a discontinuous surface. As an example, a motion stage with a span-thickness-ratio of 23 is used, which implies a relative thin geometry. A constrained layer

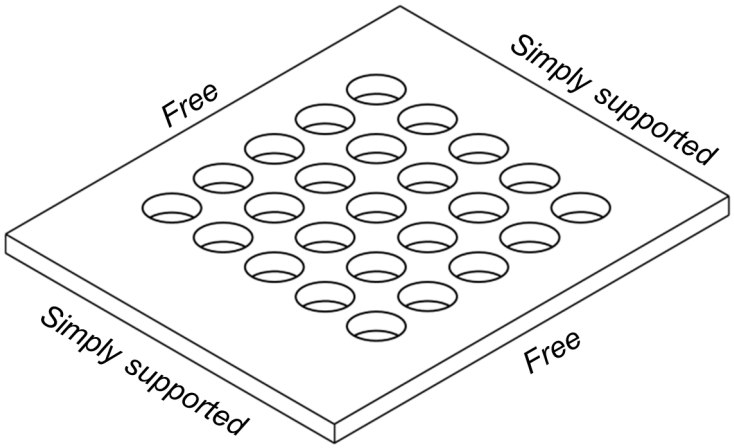

Figure 1, Drawing of the stage with the boundary conditions indicated in the figure.

damper (CLD) with limited thickness has been designed to improve the dynamic performance at the first dominant resonance frequency. The main displacement contribution of the corresponding m ode shape acts in vertical direction. As starting point in the design process, a rubber type is selected which shows good damping properties in the frequency range of the specific mechanical resonance. These types of materials can, for small strain values, be classified as Linear Viscoelastic (LVE) materials[4] of which the behavior can be expressed as a complex stiffness value as function of frequency. This complex stiffness can be divided into a storage modulus and loss modulus, which represent the ability of the material to store energy and dissipate energy per vibration cycle, respectively.

The geometrical design part of the stage with CLD starts with computing the undamped characteristics of the stage design by means of performing a modal analysis with the Finite Element Method (FEM). This type of analysis provides a high quality answer for the natural frequencies and mode shapes of complex geometries, including stress and strain distributions. The second step is approximation of these modal results by analytical equations[2] in order to be able to estimate variations in modal damping outside the FEM environment and enable optimization algorithms to be applied. Figure 1 shows the discontinuous shape and the

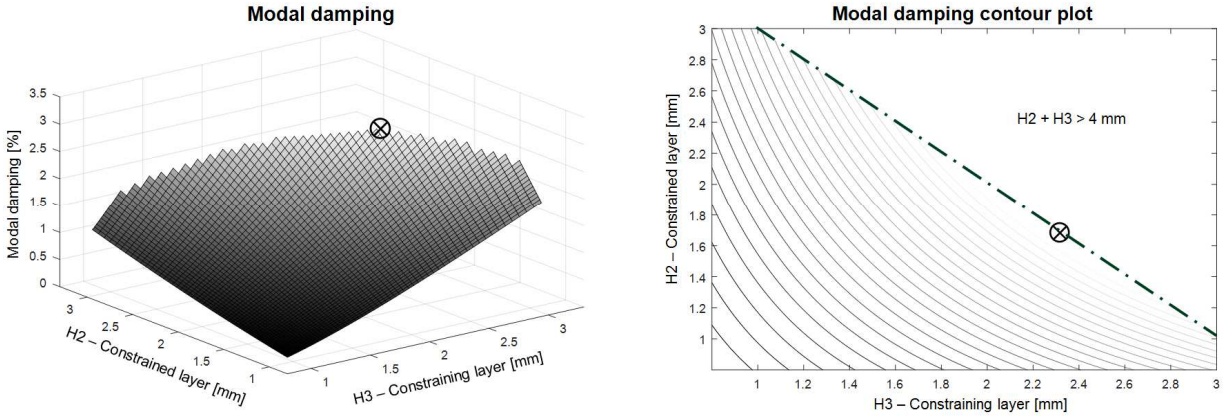
Modal damping
Modal damping [%]
H2 – Constrained layer [mm]
H3 – Constraining layer [mm]
Modal damping contour plot
H2 + H3 > 4 mm
H2 – Constrained layer [mm]
H3 – Constraining layer [mm]

Figure 2; the left figure shows the modal damping of the stage with continuous CLD layer as function of the constrained layer thickness (H2) and the constraining layer thickness (H3). The maximal CLD thickness (4 mm) with respect to overall stage thickness limits the achievable modal damping in this case. The right figure shows a contour plot of the same curve. The optimum damping value is indicated in both figures and amounts 3.2 %.

boundary conditions applicable for this case. Equations based on theory for continuous CLD layers, known as the RKU equations[3], are applied providing estimates for the modal damping of the stage with CLD layer added. In this equation, the materials' Young's moduli and loss factors, which are another representation of the storage and loss moduli, have to be filled into calculate the modal damping factor of the complex structure at the resonance frequency.

DAMPING OPTIMIZATION

The RKU equations allow for calculation of the modal damping value of a continuous plate with CLD layer applied. Parameters in the equation are the material mechanical properties and the dimensions of the 3 plates; the base plate (stage), the constrained layer (damping layer) and the constraining layer. An optimization algorithm is applied to find the maximal modal damping given boundary conditions with respect to the overall thickness. This is visualized in Figure 2. A minimal modal damping value is set as constraint to reduce the parameter space and improve convergence is the optimization process. The resulting value is an approximation for the modal damping of a continuous plate equipped with a CLD and amounts 3.2 %. This value has to be compensated for the discontinuities in the CLD layer.

This compensation factor is called Shear Efficiency Factor (SEF) which expresses the damping effectiveness of the discontinuous CLD layer w.r.t. the full-size continuous layer. The basis for this estimate lies in the relative shear displacement in the constrained layer which is introduced by the constraining layer with respect to the base layer. This strain deformation can be calculated as function of the mode shape and as function of the spatial coordinates of the base layer. The SEF is defined as the ratio of the integrated shear displacements over the discontinuous CLD surface with respect to the integrated shear displacement over the continuous layer. This factor expresses the effectiveness by taking the relative shear displacements into account as well as the effective CLD area. The SEF ranges from 0 if the discontinuous CLD area equals zero, to 1 for a full size and continuous CLD. For this specific stage the SEF value amounts 0.384. The overall modal damping value can be calculated by multiplying the SEF with the modal value obtained from the optimization. Assumptions in this approach are; 1) the mode shape has a sinusoidal shape[2] and 2) the neutral line during bending remains at the same height for the stage without and with CLD. Figure 3 visualizes the calculation of the SEF value by deriving the relative shear displacement in the constrained

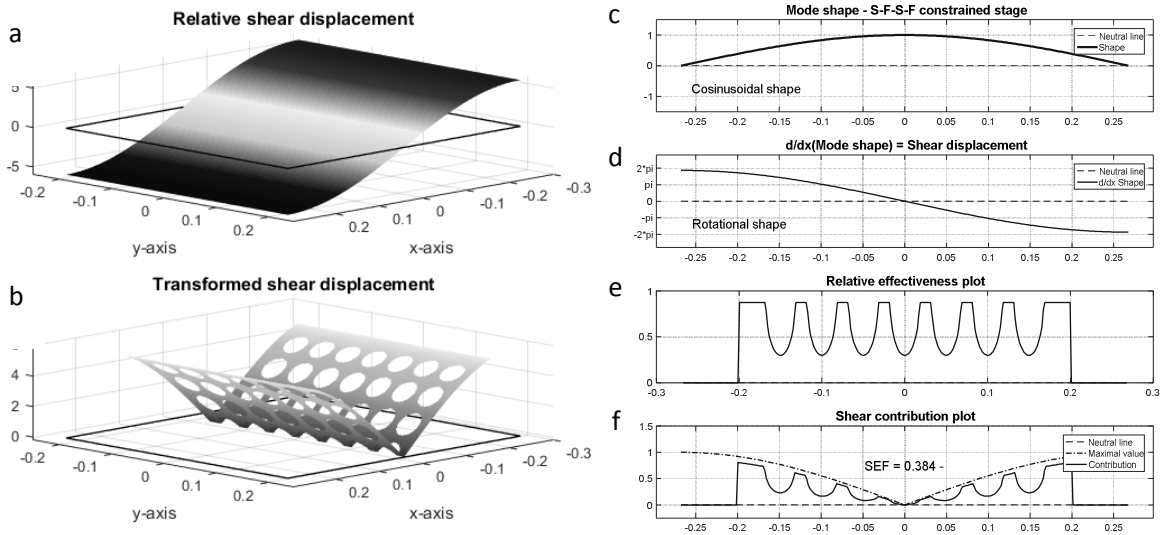

Figure 3, The left figures show the shear displacements for the continuous layer (a) and the absolute shear of the discontinuous layer (b). The right figures visualize the calculation of the SEF for discontinuous surfaces by integrating the shear components (d) over the complete CLD surface and compensate for the geometry (e). The result is the SEF (f).

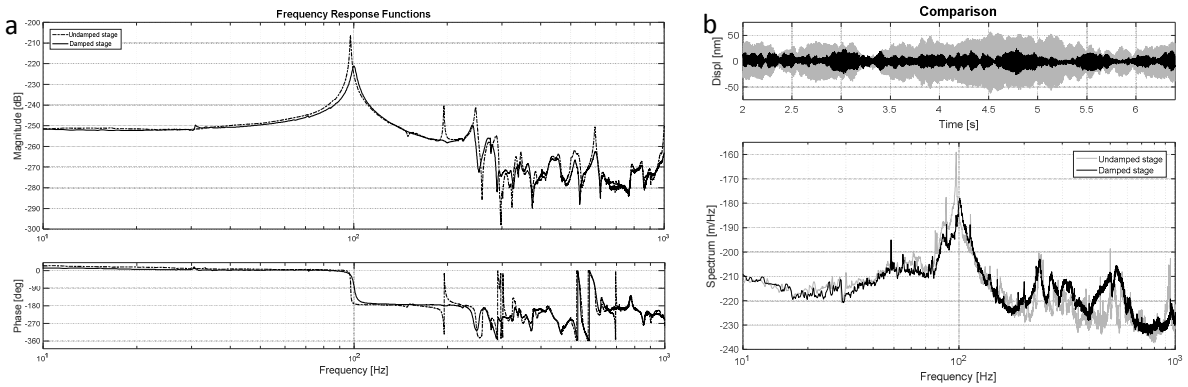

Figure 4, the left part shows different frequency response functions, resulting from the experimental analysis with stages with and without CLD implementation. The right figure shows the vibration spectra of the stage in vertical direction.

layer (a-d) from the mode shape (c) and subsequently multiplying by the effective surface (e), resulting in the effective average shear contribution (f). This contribution is shown as function of the area in (b).The application of this approach on the motion stage with holes as described in this paper results in a theoretical modal damping value of 1.22 % at the first resonance frequency around 100 Hz.

EXPERIMENTAL VALIDATION

Experimental validation has been performed by applying experimental modal analysis (EMA) on the motion stage, to measure the modal damping of the first flexible modes. The stage has been excited by an impulse hammer and stage displacement has been measured by a capacitive probe, connected to a data acquisition system, resulting in transfer function from force to displacement, see Figure 4a. The modal damping has been estimated at the resonance frequency and has been compensated for the numerical damping introduced by the exponential weighting function which is applied on the output displacement signal of the capacitive probe. This approach results in accurate modal damping values for the first flexible modes of the stage, being 1.19 % at a frequency of 97.7 Hz. This shows a damping increase factor of approximately 9 times, compared to the modal damping value of 0.127 % of the undamped stage. The vibration spectra of the motion stage with CLD have been measured with the capacitive probe and comparison has been made to the vibrational content of the motion stage without CLD. The time traces of both cases are presented in Figure 4b. These measurements show that the RMS amplitude has been reduced by a factor of 3.

DISCUSSION

It appears that the hybrid design approach as described, with a combination of undamped modal analysis by means of FEM and analytical estimates for the added damping, provides a realistic value for the overall modal damping value for a plate-like mechanical setup with a discontinuous constrained layer damper applied. The damping accuracy is within 10% for the example showed. This approach in analysis, combining results from FEM analysis with analytical estimates enables for optimization, which is a very powerful tool in an early design phase. If critical for the final performance, the performance can be validated with a fully harmonic calculation in FEM.

REFERENCES

1. Stan van der Meulen, *Enabling overlay/focus improvement via passive damping in ASML motion stages*, ASML Research Mechatronics & Control, St. Michielsgestel, The Netherlands, DSPE Conference 2016, October 5th 2017.
2. Blevins, R. D. (1979). *Formulas for natural frequency and mode shape*, Krieger Publishing company
3. Jones, D. I. (2001). *Handbook of viscoelastic vibration damping*, John Wiley & Sons.
4. Macosko, C. W., & Larson, R. G. (1994). Rheology: principles, measurements, and applications, John Wiley & Sons.

OBSERVATIONS ON STITCHING INTERFEROMETRY ON PARTS WITH RADICALLY DIFFERENT SURFACE TOPOGRAPHIES

Clark D. Hovis, Zachary C. Reese, Hossein Shahinian, Chris J. Evans
DEPARTMENT OF MECHANICAL ENGINEERING AND ENGINEERING SCIENCE
UNIVERSITY OF NORTH CAROLINA AT CHARLOTTE
CHARLOTTE, NORTH CAROLINA, USA

INTRODUCTION

Surfaces with widely different topographies have been measured by stitching on a coherence scanning interferometer [1] (CSI) and those results compared with data from full aperture measurements. Stitching interferometry has been widely used in the optics metrology industry for the past decade, but the technology has been in use for a much longer period. Early interferometric stitching was used mainly as a method to expand the measured area of a surface. While this expanded the data maps, these early stitching methods were only able to measure low order form deviations as adjacent sites overlapped minimally (if at all) and were stitched together using a polynomial fit [2,3]. Years later the development of pixel based stitching greatly pushed this technology forward. Overlapping larger portions of adjacent sites allowed for, not only greater lateral stitching capabilities, but also increased ability to measure surfaces with large departures [4]. This method is mainly used for the measurement of freeform and aspherical optics, where measuring such optics with conventional interferometer setups are very limited. The high magnification of CSI objectives enhances the lateral and slope of the measurements significantly. This specifically has potential in two rapidly growing fields: (1) the emergent freeform optics that pose both great manufacturing and metrology challenges, and (2) the use of additive manufactured (AM) metallic parts.

In both cases, measurements are required over relatively large lateral scales where there may be high slopes. Non-contact measurement of high slopes can be achieved using a high NA (or high magnification) interferometric objective, requiring stitching. CSI, may be a viable solution [5-7].

The stitching literature shows two artifacts in the data. Depending on the algorithm chosen, there can be differences in the data from the two raw data sets, which may –or may not – be related to the noise in each measurement. In addition, uncertainty in matching tip, tilt, slope and curvature in the overlap region may lead to bias in the estimation of the low order form.

In this paper we compare the results of a variety of stitching algorithms applied to some archetypal examples of the surface type identified above. In each case, a reference measurement was acquired using a full aperture tool. The sample surfaces were then measured in multiple overlapping sites and stitched together using Mx® (version 7.0.0.9). Four different stitching algorithms and three overlap merges were used. In all of the cases the differences in the results from the different algorithms are presented.

EXPERIMENTAL SETUP

Optical Flat

The first sample was an optically polished Ø40 mm BK7 flat mounted into a polycarbonate carrier. The sample was measured on the Fizeau interferometer using a transmission flat to obtain the reference measurement [8]. Next the sample was stitched over the entire aperture with the Nexview CSI. A 2.75x objective was used with a 1x tube lens. The sites were then stitched using three different overlap percentages: 10%, 20%, and 30%. Each of the stitches were run through all of the algorithm and merge choices in Mx. The algorithm choices include Adaptive Adjust, Cartesian (matches and aligns in 5 axes), Overlay (aligns based on stage coordinates), and Adjust XY (aligns and matches in 2 axes). The merge overlap choices are Average (averages the overlap region), Blend (interpolates overlap region), and No Merge (does not merge overlaps) [9].

Optical Freeform

This sample was fabricated in UNC Charlotte using a magnetorheological finishing machine (MRF) machine [10]. The freeform surface was machined into a base planar surface Ø40 mm BK7 glass. The surface departure had a clear

aperture of Ø35 mm with comatic component and astigmatic components with Fringe Zernike coefficients of approximately 3000nm [11]. The reference measurement was taken with the Fizeau interferometer using a transmission flat. The sample was then stitched over the entire aperture using the Nexview CSI. For this measurement a 2.75x objective was used with a 0.5x tube lens. The overlap percentage used was 20%. The data were processed using all algorithm and merge overlap choices.

Optical Convex

The convex part used for this experiment is a commercial grade plano-convex lens with a Ø12 mm that has a focal length of 84 mm. As with the previous samples, it was mounted into a polycarbonate carrier. It was measured on the Fizeau interferometer, using a transmission sphere was used that had an f# of 1.5 and a focal length of 154mm. It was stitched across the entire aperture on the Nexview CSI. For this measurement a 10x objective with a 1x tube lens was used, with an overlap of 20%. Like the previous experiments the stitch was ran through all the algorithms and merge overlap choices.

Metal Additive Manufactured Sample

The AM part utilized in this section of the paper was part of a large build conducted at The National Institute of Standards and Technology (NIST) in an EOS M270 DMLS machine. This 25cm X 25cm X 10cm cuboid was printed in Inconel (IN) 625 with a laser power and speed of 195 W and 800 mm/s respectively (Figure 1). Hatch pattern alternated between each layer in the X and Y directions for the entirety of the build. Fiducial marks extend 3 mm into the part from the bottom and left edges at a depth of 1 mm to ensure measurements from various instruments are taken over nominally the same area. Aside from these fiducial markings, all surfaces of the part have been left in their “as printed” state (i.e. subjected to no further finishing processes).

Using both a Zygo Nexview CSI and a MahrSurf LD 260 tactile profilometer, measurements were taken over a 1.4 mm square area at the corner of this fiducial marking. Optical height data of this area was captured over 16 sites using a 20X Mirau objective with a 418 μm FOV, and stitched together with the overlap region set to 20% of the FOV. Overlapped regions were matched to neighboring sites using the Cartesian and Blend settings. For the tactile data, 560 traces spanning 1.4 mm were taken across the lay of the scan lines with 2.5 μm between each trace. A 2.5 μm nominal diamond stylus was used and data point acquired at 0.2 μm spacing over the 1.4 mm trace. Data from both the tactile traces and the areal CSI measurement analyzed in Matlab.

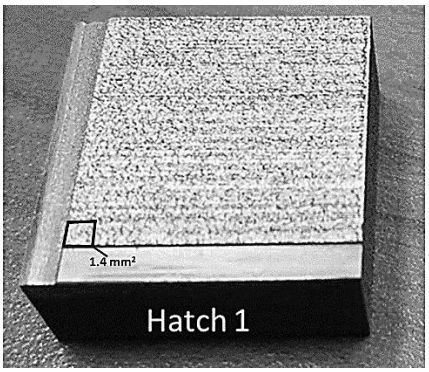

Figure 1. AM part used for study (measurement area highlighted)

DATA PROCESSING

Specular Surfaces

The data processing for flat, freeform, and convex were all identical except where it is stated.

The data was cropped and masked to the desired diameter. For the flat, freeform, and convex part: Ø38.45 mm, Ø35 mm, Ø11.6 mm were used respectively. The piston and tip/tilt were removed, and for the convex part power was also removed. The nans that occurred within the part diameter were then filled using linear interpolation. This was done to prevent the nans from affecting the filtering process. The next step was filtering the data using a FFT filter. The high pass cutoff was 0.2 mm.

Once the data was filtered the stitched CSI matrix was interpolated to the size of the Fizeau data matrix. Then the Sq (area RMS) was calculated in accordance with ISO 25178-2 [12]. Each of the different algorithms and merges were then subtracted from the Fizeau measurement. The Sq of these subtractions was also calculated. The data were also fit to Zernike Fringe Zernike polynomials to evaluate the consistency between the forms measurements. The Zernike terms were calculated through the sixth order, for both rotationally invariant and rotationally varying terms. Lastly, the average 1-D power spectral density (PSD) of the optics was calculated to examine the frequency content of the

measurements. This was done by extracting 360 profiles, one for every degree azimuth. For each profile the PSD was calculated, and then they were averaged together to get the average PSD of the surface.

Additive Surface

Profiles for both the optical and tactile data were processed identically. Each vertical profile spans the 1.4 mm area perpendicular to the lay of the scan lines had form up to an 8th order polynomial removed, and was fitted with a Gaussian convolution filter (2-800 μm) to isolate the surface roughness and the waviness in the surface [13]. Roughness profile parameters were averaged for comparison between the tactile and optical measurements. Average PSD was also calculated for the detrended profiles in to determine whether stitching artifacts are discernable in these rough AM surfaces. Values for these ISO parameters as well as the PSDs are then plotted below for direct comparison.

RESULTS AND ANALYSIS

Specular Surfaces

The reference measurements of specular samples, taken on the Fizeau interferometer, are shown in figure 2.

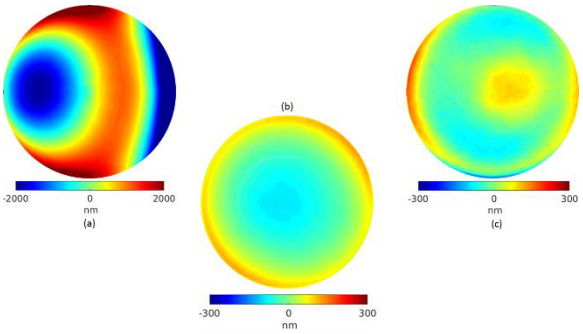

Figure 2. Reference measurements from the Fizeau. (a) Freeform. (b) Flat. (c) Convex with power removed.

The RMS of the residual values of the subtractions (referred to Sq∆ hereafter), are given in figure 3 and figure 4 for the flat and convex sample respectively.

As can be seen in Figure 3, for the flat, a 20% overlap produces the lowest Sq∆. The results for the 30% overlap stitch are higher than both the 10% and 20% overlap stitches. This is counter intuitive; a higher overlap might expected to give lower uncertainy arising from the stitching, but lead to a longer measurement time. The overlay algorithm, regardless of overlap merge, had a higher Sq∆. The other algorithms when using the same overlap percentage agree within 2nm of each other.

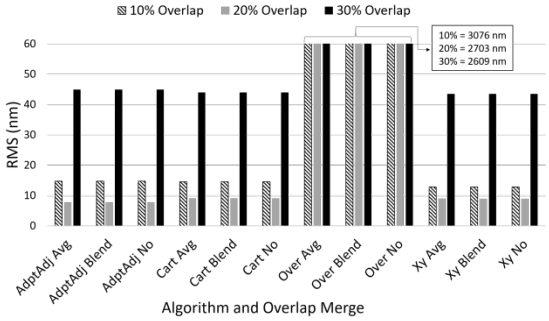

Figure 3. RMS values for the subtractions of the different algorithms and merge overlap from the Fizeau, for the flat

The results for the freeform were somewhat similar to the results of the flat. The overlay algorithm has a much higher Sq∆, and the other algorithms were within 8nm of each other. A major difference from the results of the freeform and the flat were that the Sq∆ was noticeably higher for the freeform, by a little over 300 nm. The adaptive adjust, cartesian, and adjust xy were 329nm, 321nm, and 323nm respectively. This difference is larger than would be expected from retrace errors in the Fizeau and uncorrected bias in the TF figure.

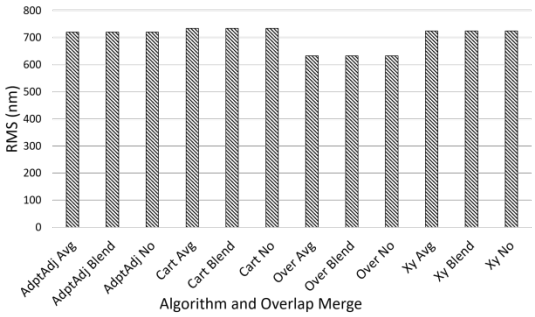

Figure 4. RMS values for the subtractions of the different algorithms and merge overlap from the Fizeau, for the convex.

The results for the convex part in Figure 4 show that, similar to previous results, the Sq∆ were within 15nm for all algorithms except for overlay. The Sq∆ was also higher than the results for either the flat or freeform, except with the overlay

algorithm, which was lower than both the other results. The overlay algorithm also had the lowest SqΔ for the convex part.

Figures 5-8 show the average PSD for the different algorithms and the reference. Only the average overlap merge is plotted because the PSDs for the same algorithm with different overlap merge are indistinguishable in the plots.

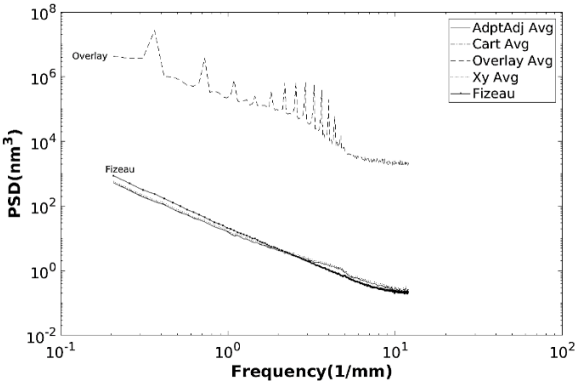

Figure 5. Average PSD graph for the flat with 10% overlap (only average merge overlap) and the Fizeau.

As with the SqΔ the PSD for the overlay algorithm is different than the other PSDs. The spikes in the overlay PSD appeared to have been caused by stitching artifacts in the measurement. These stitching artifacts occur where the profile taken crosses the stitched panels. Profile taken for each degree of rotation; spatial frequency for the spikes correlate with the different distances between crossings at site overlap regions. The other algorithms were much closer to the reference, however, still had minor deviations.

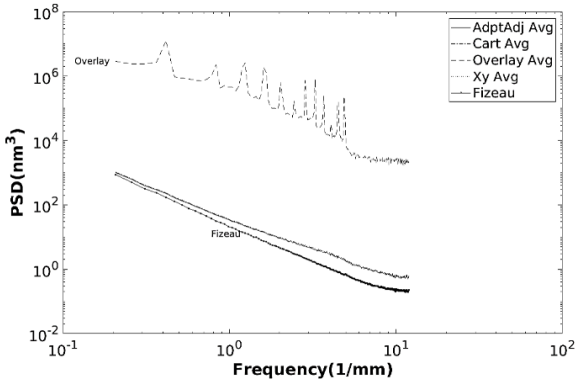

Figure 6. Average PSD graph for the flat with 20% overlap (only average merge overlap) and the Fizeau.

The results in Figure 6 for the flat with 20% overlap were similar to the results of the 10% overlap. The difference was that the 20% algorithms, outside of overlay, follow the reference very closely in the lower frequencies but deviate in the higher frequencies.

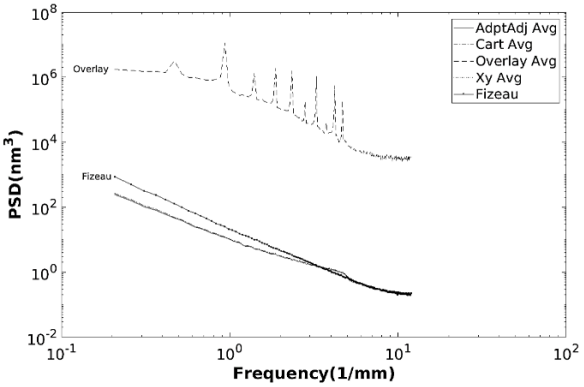

Figure 7. Average PSD graph for the flat with 30% overlap (only average merge overlap) and the Fizeau.

The PSDs in Figure 7 are similar for the overlay algorithm. The results for the other algorithms show a much higher deviation than has been seen and that deviation was in the lower frequencies. This higher deviation was also seen in RMS results, because the SqΔ for the 30% overlap were the highest of the three overlap percentages.

PSD results for the freeform were similar to the results for the flat with 20% overlap. The overlay algorithm still had the highest deviation from the reference, however, it was closer than any of the flat measurements. The stitching artifacts were still in the overlay algorithm, similar to the flat measurements. The other algorithms followed the reference closely in the lower frequencies, however, deviated greatly in the higher frequencies.

The results in Figure 8 show that unlike previous results the overlay algorithm was in line with the other algorithms. The overlay PSD still shows the stitching artifacts, however, it did not have as many as were found in the flat PSDs. It can also be seen that outside of where the stitching artifacts were, it was the closest to the reference for the convex part.

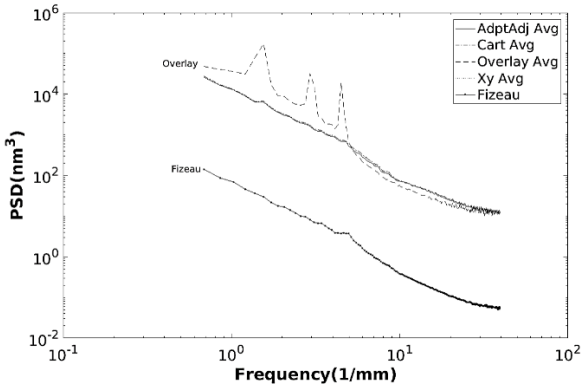

Figure 8. Average PSD graph for the convex (only average merge overlap) and the Fizeau.

The Zernike coefficients give what would be expected based off of the results of the subtractions. Results from the flat measurements, outside of overlay, were within 13nm of the Fizeau result, Zernikes from the freeform measurement showed that all the algorithms deviated from the Fizeau by 51-82nm, but were close to each other (within 31nm). Convex measurement results showed that overlay was closest to the Fizeau, differing by 107 nm. The other algorithms had greater deviations (246-270nm). Discrepancies between the zernikes and subtractions was due to the way the subtractions are calculated and the fact that the zernikes were only calculated to the 6th order.

Additive Surface

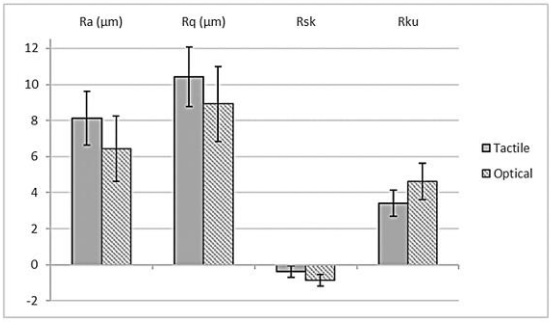

Figure 9. Comparison of ISO roughness parameters between optical and tactile measurements of an AM surface

Figure 9 shows the comparison of tactile and optical measurement methods based on the ISO parameters. Ra and Rq values for both the tactile and optical data agree to one standard deviation. This suggests that any stitching artifacts may be so small that, on a surface this rough, they do not affect the computed roughness parameters significantly.

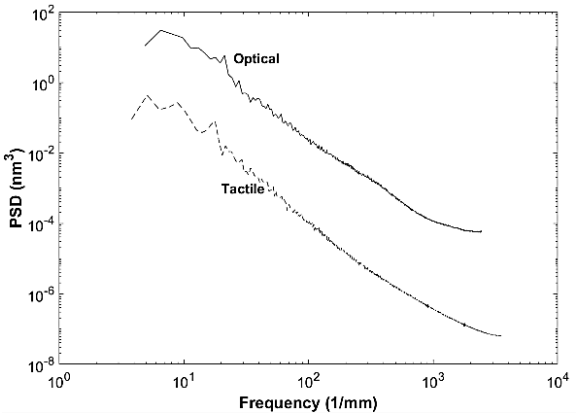

Figure 10. Average PSD comparison of optical and tactile measurements on AM surface

The PSD data (Figure 10) shows that the optical data appears higher (by 2 orders of magnitude or more) than that of the tactile over the full frequency spectrum. Further work is required to estimate the effects of different noise, morpohology, filtering from the stylus radius and slope limitations from the stylus included angle. Difference in the data density for the measurements must also be considered.

Although there is a clear offset in amplitude, the spikes of the PSD appear at similar spatial frequencies. This also suggests that the stitching artifacts in the surface are too small to influence results when measuring a surface of this roughness scale.

CONCLUSION

Stitching using a modern CSI provides expanded measurement bandwidth both in terms surface spatial frequencies and slopes. At lower spatial frequencies on the optical surfaces, deviations between reference and stitched results are observed. These depend on the surface characteristics and the stitching method chosen.

From an overlap percentage standpoint, the results of this paper largely coincide with the recommendations from the Mx Reference Guide. 15-25% overlap between sites is recommended and the 20% case from this paper yields the closest results to the reference measurement. The freeform and convex part yielded much higher RMS values for the subtractions than those seen in the flat. Future work is needed in

order to understand why these values vary from their respective references so greatly, as well as associated uncertainty values for these measurement comparisons.

From the measurements of the additive surface, it is impossible to discern stitching artifacts in the surface when comparing to reference profilometry data. To one standard deviation, the ISO parameters calculated for each are nominally the same. Preliminary PSD calculation of this surface backs this result as the peaks that appear in the optical data match those of the tactile data.

ACKNOWLEDGEMENTS

The authors would like to acknowledge Todd Noste, Greg Caskey, UNC Charlotte, Zygo Corp., the AM group at NIST, This work is supported by in part by the National Science Foundation I/UCRC Center for Freeform Optics (IIP-1338877 and IIP-1338898) and by the Center for Precision Metrology Affiliates.

REFERENCES

[1] Zygo Corporation. (2013). *Nexview Specifications SS-0098* . Retrieved from https://www.zygo.com/?sup=resource/manuals.cgi

[2] J. Thunen and O. Kwon, “Full aperture testing with subaperture test optics,” Wavefront sensing; Proceedings of the Conference, San Diego, CA, August 1982, N. Bareket, and C.L. Koliopoulos, Eds., 351, 19-27, SPIE - The International Society for Optical Engineering, Bellingham, WA, 1983.

[3] Murphy, Paul, et al. "Stitching interferometry: a flexible solution for surface metrology." *Optics and Photonics News* 14.5 (2003): 38-43.

[4] W. Chow and G. Lawrence, “Method for subaperture testing interferogram reduction”, Optics Letters, 8, 468-470, 1983.

[5] Gomez, Carlos, et al. "Optimization of surface measurement for metal additive manufacturing using coherence scanning interferometry." *Optical Engineering* 56.11 (2017): 111714.

[6] Jiang, Xiang. "Precision surface measurement." *Phil. Trans. R. Soc. A*370.1973 (2012): 4089-4114.

[7] Dutterer, Brian S., et al. "Diamond milling of an Alvarez lens in germanium." *Precision Engineering* 38.2 (2014): 398-408.

[8] Zygo Corperation. (2017). *Verifire Specifications SS-0115.* Retrieved from https://www.zygo.com/?/met/interferometers/verifire/

[9] Zygo Corporation. (2015). *Mx: Reference Guide OMP-0550.* Retrieved from https://www.zygo.com/?sup=resource/manuals.cgi

[10] QED Technologies (2012). *Q-22XE Reference Guide MAN1234-D.*

[11] Michael U. Uwakwe and Christopher J. Evans. "Minimizing Task-Specific Uncertainty in CMM-Based Freeform Optics Metrology". (2017)

[12] ISO/FDIS *25178-2 2010 Areal - Terms, definitions and surface texture parameters*

[13] ISO, EN. "4287: 2009." *Geometrical Product Specifications (GPS)-Surface texture: Profile method–Terms, definitions and surface texture parameters (ISO 4287: 1997+ Cor 1: 1998+ Cor 2: 2005+ Amd 1: 2009)(includes Corrigendum AC: 2008 and Amendment A1: 2009)*.

QUANTIFICATION OF PART PROFILE SCANNING ERROR

F. Javidpour, E.P. Morse
Center for Precision Metrology
Mechanical Engineering – UNC Charlotte
Charlotte, NC, United States

ABSTRACT
The recent advances in coordinate metrology and the availability of different profile scanning devices equipped with a variety of sensors has created challenges for quality control advisors and technicians trying to select the most suitable device for their measurement. In order to provide either a measure for the quality of profile scanning, or to evaluate the quality of parts in a batch, it is required to quantify the error of a scanned profile. In this work, sets of scanned data points are fitted to their nominal profiles (having irregular shapes) by the Least Squares method applied using a built-in Matlab optimization function. The residual errors of the fit are expressed as normal distances between the points and the nominal profile. This normal distance can be used later for graphical representation of deviations. Applying a convolution averaging filter to the error data enables the procedure to calculate the mean local deviation in each profile segment: this is a potential metric for the measured profile error. This quantity can be used for specification of instrument repeatability and reproducibility, and also in profile scanning uncertainty assessment.
Keywords
Profile scanning, point fitting, convolution averaging filter, profile error, coordinate metrology.

INTRODUCTION
Dimensional metrology, used for product conformance evaluation in the quality control process, is performed after manufacturing to ensure that the form, size, position and orientation of features satisfy the part specifications. Form and size are measured individually but position and orientation are specified with respect to reference features. Coordinate Measuring Machines (CMMs) are widely used to check the conformance of manufactured parts to design specifications. These machines – currently available in many different models and structures with versatile types of sensors, measure the coordinates of sampled points and associate these points with part features. Depending on the sensor type, the measured points can be on actual part surface or have an offset from that surface which is typically equal to probe radius in tactile methods. Optical sensors often have the ability to measure many points quickly, and return a "cloud" of points to the evaluation software.
After data collection, the data verification step processes the surface point data and compares it to the appropriate nominal part surface to establish compliance or non-compliance with the tolerance requirements.

Literature Review
There have been many researches done in the last two decades about this topic. Generally speaking, they can be categorized in two groups. The first group of papers such as [2,3,6] discuss methods to find a way for error evaluation and suggesting criteria for different purposes or shapes and papers in second group like [1,4,5,6] are about algorithm generation to fit the acquired point data to nominal profile which is mostly an optimization case.
Least Squares Method (LSM) and Minimum Zone are two commonly used error evaluation methods with some pros and cons for each one. A complete literature review of these methods is available at [2], in which an iterative Weighted Least Squares (WLS) method was used for point fitting and final error evaluation.
Qian et al [7] used an admissible transformation volume (ATV) to quantitatively characterize the quality of sample parts with respect to design tolerance specification. They also provided a noticeable review about the GD&T theories as well as methods to construct tolerance zones in their paper. Jiang et al [3] and Sun [4] worked on circular shapes. They respectively could reduce fitting uncertainty and apply Particle Swarm Optimization (PSO) on measured data to propose a new roundness evaluation algorithm.
In an almost new branch of work, Aidibe et al [8] proposed new mathematical models based on the order statistical theorem for identification and calculation of profile tolerance considering the

process capability and geometric complexity of a part.

LiMin [1], and more recently Kale [9] and He [6], worked on free-form surfaces. LiMin proposes a new fitting approach by localization and defining a constrained nonlinear least-squares optimization problem. Kale used a novel Medial Axis Transform (MAT) technique to create a point to point correspondence between a free-form machined surface and its nominal CAD model. In paper of He, the mathematical model used was based on point to surface distance function using second-order terms. The model solution was obtained by combining the Differential Evolution (DE) and Nelder-Mead (NM) algorithms, and was validated against the Least Squares method in a case study.

In spite of this work on part profile error evaluation and point fitting, there has been little work on characterizing the error in measurement or profile scanning. Every measurement has a level of uncertainty which is affected by various sources of error, so it is valuable if the effect of different contributors is understood in taking measurements with different instruments.

The first step in figuring out the measurement uncertainty is quantification of profile scanning error. If the error of measurement is quantified then the performance of instruments can be analyzed individually at different ambient conditions. Furthermore, it would be possible to compare distinct instruments and make the best choice considering characteristics of workpiece and atmosphere at which the instrument will be used.

PRESENT WORK

According to ASME Y14.5-2009 [10], profile tolerances are used to define a tolerance zone to control form or combinations of size, form, orientation and location of feature(s) relative to a true profile. A profile tolerance may be applied to an entire part, multiple features, individual surfaces, or to individual profiles taken at various cross sections through a part. There are two types of profile tolerance: profile of a surface and profile of a line [10]. The focus of this work is on the second type which is two-dimensional and the tolerance zone is normal to the nominal (true) profile at each line segment.

The workpiece may be constrained with one or two datums and the tolerance zone may be applied to one section of the nominal profile or "all-around" the profile. In this work the profile will be controlled with respect to a single datum which is for the bottom surface of workpiece, and the tolerance zone considered is an all-around profile tolerance. (Figure 1).

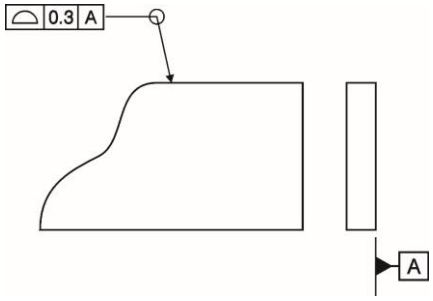

FIGURE 1. Example of profile specification-unconstrained orientation, all-around profile perimeter.

To have less complicated calculations of length and deviation of measured points, the desired profiles are composed of only lines and circular arcs with various dimensions. Two steel plate sample parts with non-regular shapes shown in figures 2 and 3 are selected and their profiles are scanned with different instruments.

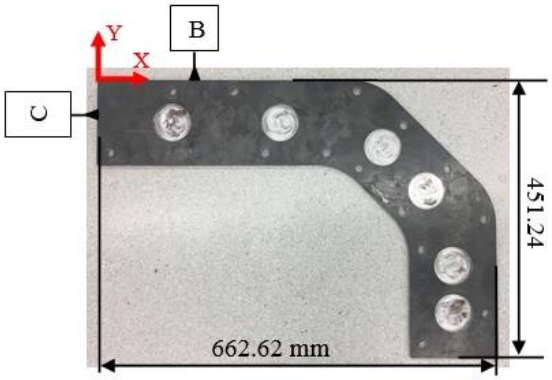

FIGURE 2. Part 1 and dimensions of outer profile

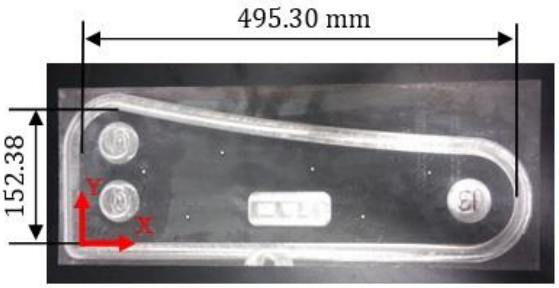

FIGURE 3. Part 2 and dimensions of slot profile

The parts are made of cold rolled steel and they have been manufactured with CNC machining process.

The measurand on part 1 (outer profile) is evaluated based on the position (X and Y

coordinates) of points on the outer surface around the part. The Cartesian coordinate system is defined by the top surface and two perpendicular edges (datums B and C). For part 2 the measurand (slot profile) uses the coordinates of points on the inner surface of slot projected onto the XY plane (datum A). The X and Y axes are defined by two perpendicular edges on part profile, but in this case are for reference only, as the profile control does not constrain the profile's location and orientation in the XY plane.

DATA PROCESSING PROCEDURE

Point Offsetting

After completion of scanning each part profile, the X and Y coordinates of points with respect to the origin of coordinate system (shown in figures 2 and 3) are available. For 2D evaluation, all of the points are projected to the XY plane, so the Z values for all points is zero.

In tactile measurements the device always monitors the position of the center point of probe or SMR (Spherically Mounted Retroreflector) and it is necessary to offset these center coordinates inward to find the coordinates of real contact points. For this purpose, first a similar feature (line or circular curve) is fitted to the measured points and then an offset normal to this feature equal to the radius of probe is made on the points (figure 4). It is assumed that the radius of probe is constant in different directions and no elastic deformation happens on contact point.

Since in optical methods the part profile points are measured directly, there is no need to offset them and this step is skipped.

Point Fitting and Calculation of Deviations

Because of errors happening during the machining process the part profiles are not exactly similar to the desired theoretical ones. In order to find out the error of each part profile, measured profiles need to be fitted to the true (nominal) profile and the unique minimum error based on the point deviations has to be calculated.

To fit the measured profile points to the nominal profile, Matlab code using the “fminsearch” function is generated to calculate the coordinates of projection of points and also the normal distance of points to the nominal profile. Then by using three degrees of freedom (translation along X and Y axes and rotation around Z) and least square algorithm the optimum fitting condition with minimum sum square of deviations is achieved. This condition can be considered unique for every measured data set and its variation with regard to the initial condition is negligible (table 1).

TABLE 1. Example of optimum output with different initial inputs for an instant data set of part 2.

Initial input			Optimum output		
Θ_i (deg)	X_i (mm)	Y_i (mm)	Θ_o (deg)	X_o (mm)	Y_o (mm)
0	0	0	0.0653	-0.0275	0.0095
0.5	0.1	0	0.0653	-0.0275	0.0095
1	-0.2	0.1	0.0653	-0.0275	0.0096
-0.33	0.22	-0.42	0.0653	-0.0275	0.0096
0.05	-0.02	0.035	0.0653	-0.0275	0.0095

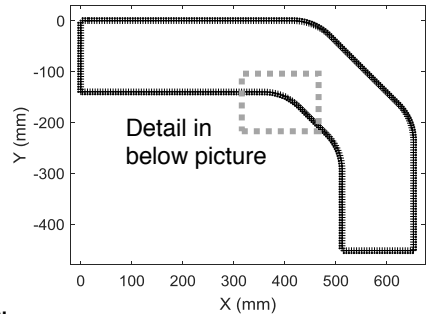

A.

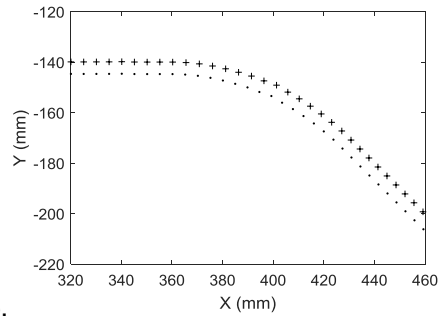

B.

FIGURE 4. Offsetting of tactile data points: A. General profile shape, B. Detail of picture A (dots- measured points, crosses- calculated contact points).

It is necessary to mention that this algorithm provides a local optimization and if the initial inputs are very different from the solution some of the measured points will be removed from the data source by the point distribution procedure. In other words, the correspondence between measured points on a particular segment of the profile and the matching nominal profile segment can be lost, resulting in a non-optimal fit.

To distribute the measured points between features (the profile segments), the coordinates of start and end point of every feature are considered, and if the measured points are located between them and their deviation is not too large then they belong to considered feature. Since on the joining areas points may be very close to the start or end point, removing of some points at these areas is inevitable. That's why closeness of the measured points to the nominal profile is a prerequisite for this procedure.
The location, or "length," of every individual point on the overall profile is defined as the distance of its projection onto the segment from the segment start point plus the length of previous segments from the part origin. The length is used to describe the point locations when the profile is unwrapped, as seen in Figures 5B and 6A. After execution of fitting, if the point is inside the closed path of profile its deviation would be negative and vice versa. Color coding can be used to distinguish different sets of deviations for every feature (figure 5).

Outlier removing and data filtering

As it is visible in figure 4, due to existing noise and vibration in measurement atmosphere there may be some sudden changes (spikes or drops) in the deviation of measured points. Furthermore, in optical measurement methods there may be some discrete clusters of points appearing around the profile whose deviation is much larger than the expected values in reality. The second group of outliers can be removed from data points by setting a threshold value on deviations, but the first type of undesired non-removable points always affect the output of analysis. To compensate the influence of these points a convolution rectangular averaging filter is applied on the deviation data.
Filtering also can provide a criterion to compare the deviation of measured points at different lengths in a specific profile segment. For this intention, a window with a fixed length (e.g. 30 mm) is assumed which is moving at fixed steps (eg.10 mm) around the profile and average of deviations inside the window is calculated and considered as the deviation of that segment.

MEAN LOCAL DEVIATION

The mean of point deviations inside every window represents the local deviation of the corresponding profile segment. The big advantage of using this parameter is that it specifies which segments of part profile have higher deviations, so the manufacturing process can be corrected to make the final part profile closer to the desired nominal profile.

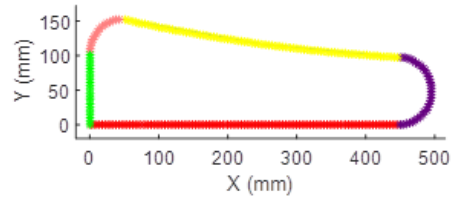

A.

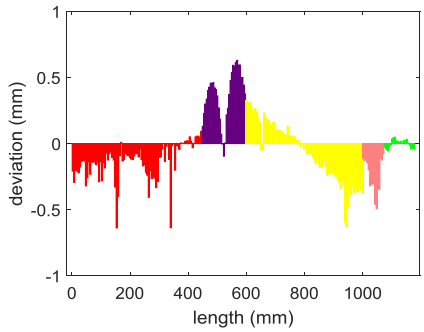

B.

FIGURE 5. A. Fitted points to the nominal profile B. graph of point deviations vs. point lengths

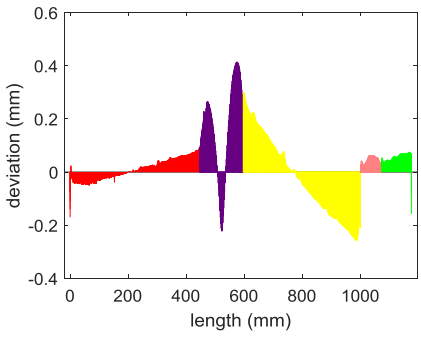

A.

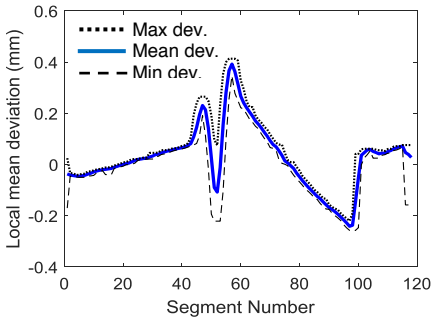

B.

FIGURE 6. A. Graph of point deviations of measured slot profile- after fitting B. Graph of local deviations after applying the convolution filter

Figure 6 represents the graphs of point deviations and mean local deviations. The horizontal axis in the local deviation graph shows the number of profile segment which starts from 1 and goes up as the filter window

moves by constant step increment around the part profile.

The window length of the applied filter in figure 6 is 30 mm and the step length is 10 mm. As it is visible in figure 6, sudden jumps and drops of point deviation are filtered out in the second graph and the mean deviation plot is more smooth, similar to the real part profile.

FILTER PARAMETERS AND LOCAL DATA RANGE

Figures 7 and 8 show respectively different local deviation and range graphs of the same data in figure 6, but with various filter parameters (Window Length (WL) and Step Length (SL)). It is comprehensible that with higher window length and shorter step length the mean local deviation graph would be smoother, but the range of local data (after shifting the mean deviation to zero) would be bigger in this condition. So it seems to be important to make a balance between a smooth continuous local deviation and low variation in local data. It is necessary that filter parameters are defined by considering amount of point deviations and their locations (lengths) on profile and required accuracy (neglected range).

MEASUREMENT EVALUATION

Selecting proper window and step length, in the next step enables us to calculate the described local mean deviation of each segment and use it as a criterion for profile measurement error quantification.

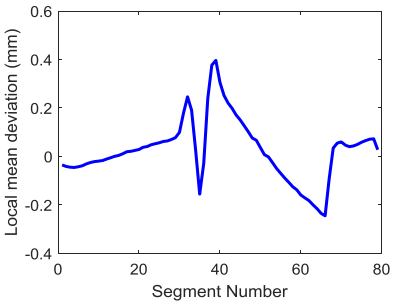

C.

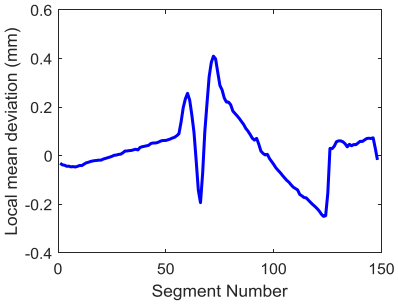

D.

*FIGURE 7. Influence of filter parameters on local mean deviation (A. WL=80 SL=5, B. WL=80 SL=60, C. WL=20 SL=15, D. WL=10 SL=8) *All variables are in mm*

By repeating one profile scan at different conditions with multiple instruments and comparing the resulted mean local deviations, there will be this opportunity to compare the performance of different profile scanning devices with each other and also verify or specify the instrument repeatability or reproducibility as well. Another noticeable usage of this error quantification method can be in profile scanning uncertainty assessment for 2D profiles.

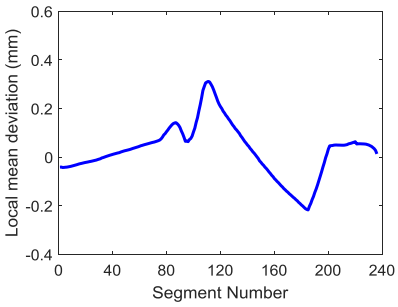

A.

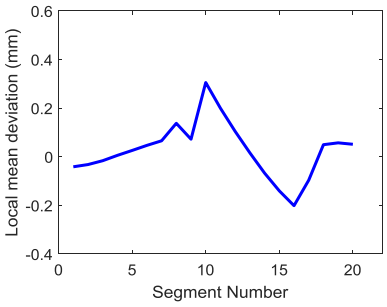

B.

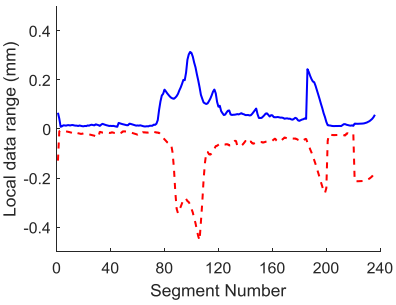

A.

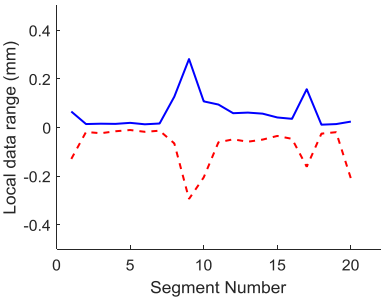

B.

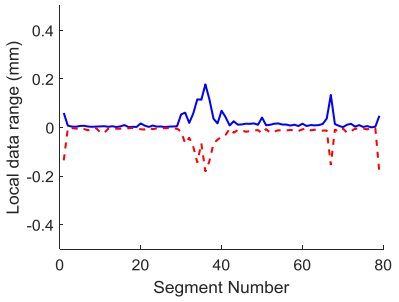

C.

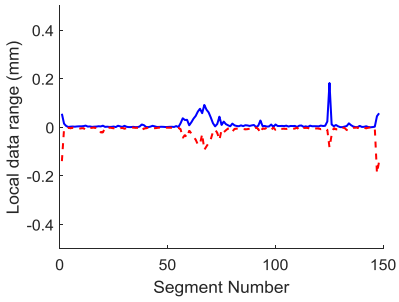

D.

*FIGURE 8. Influence of filter parameters on local deviation range (A. WL=80 SL=5, B. WL=80 SL=60, C. WL=20 SL=15, D. WL=10 SL=8) *All variables are in mm*

CONCLUSION

Profile fitting was accomplished by applying the *fminsearch* function of Matlab on the squared deviations of scanned 2D part profiles. It was shown through repeated tests that the optimum condition is unique if the measured profile has a slight dislocation in comparison with the nominal one. Point deviation graphs that use a different color for each profile segment makes it easier to observe which segments of profile have higher deviations that need to be corrected.

A convolution averaging filter applied to the measured data is able to provide a criterion for measurement error quantification, data comparison and instrument performance evaluation. This paper shows the influence of this filtering for a single instrument's measurement of the workpiece, but the same metric could be used to compare repeated measurements with the same instrument, or measurements with different instruments. This evaluation will be performed in future work.

REFERENCES

[1] LiMin, Z., ZhenHuan, X., Han, D., YouLun, X., & Kurfess, T. R. (August 01, 2004). A Distance Function Based Approach for Localization and Profile Error Evaluation of Complex Surface. *Journal of Manufacturing Science & Engineering, 126,* 3.).

[2] Xiangyang, Z., Han, D., Wang, M. Y., & Raman, S. (August 01, 2004). Form Error Evaluation: An Iterative Reweighted Least Squares Algorithm*. *Journal of Manufacturing Science & Engineering, 126,* 3.).

[3] Jiang, Q., Feng, H.-Y., OuYang, D., & Desta, M. T. (January 01, 2007). A roundness evaluation algorithm with reduced fitting uncertainty of CMM measurement data. *Journal of Manufacturing Systems, 25,* 3, 184.

[4] Sun, T.-H. (January 01, 2009). Applying particle swarm optimization algorithm to roundness measurement. *Expert Systems with Applications: Part 2, 36,* 2, 3428-3438.

[5] Kale, K. B., & Gurumoorthy, B. (January 01, 2013). Profile Tolerance Verification for Free-form Surfaces Using Medial Axis Transform. *Procedia Cirp, 10,* 5, 133-141.

[6] He, G., Zhang, M., & Song, Z. (August 01, 2015). Error evaluation of free-form surface based on distance function of measured point to surface. *Computer-aided Design, 65,* 2, 11-17.

[7] Qian, X., Robinson, D. M., & Ross, J. (January 01, 2005). Admissible transformation volume for part dimensional quality gauging. *Computer-aided Design, 37,* 13, 1335-1352.

[8] Aidibe, A., Tahan, A. S., & Abenhaim, G. N. (January 01, 2012). Distinguishing profile deviations from a part's deformation using the maximum normed residual test. *Wseas Transactions on Applied and Theoretical Mechanics, 7,* 1, 18-28.

[9] Kale, K. B., & Gurumoorthy, B. (January 01, 2013). Profile Tolerance Verification for Free-form Surfaces Using Medial Axis Transform. *Procedia Cirp, 10,* 5, 133-141.

[10] ASME Y14.5-2009, Section 8, Tolerances of profile.

EXPERIMENTAL VERIFICATION OF ONE SIDE CONSTRAINED MINIMUM TOTAL LEAST SQUARE ALGORITHM FOR PLANAR DATUM ESTABLISHMENT AND ASSOCIATED UNCERTAINTY ANALYSIS

Wenjun Kang[1], Edward P. Morse[1]

[1]Center for Precision Metrology, UNC Charlotte, Charlotte, NC 28223 USA

ABSTRACT

In the industrial world, from initial design to final product, data exchange is critical to product quality. Metrology is important to manufacturing processes, not only as a final conformance test but also in providing in-process measurements to monitor variability and functionality[1][2]. In terms of verifying whether or not a manufactured part conforms to the design specifications, critical dimensions are measured and compared to the part tolerance. Tolerances of profile, orientation, location, and runout are all directly related to datum references. An irregular (i.e., not perfectly flat) planar datum feature, when brought into contact with its corresponding datum feature simulator, could potentially generate various 'sitting' conditions[3], or as ASME Y14.5 states[4], "the part is unstable." In other words, there will be many candidate planar datums associated with one individual planar datum feature. For a datum reference frame(DRF), if the primary planar datum has this 'rocking' issue, then there will be a set of candidate DRFs generated, each of which has a different primary candidate datum.

Scholars and researchers have long attempted to address the rocking datum issue to find a solution that is both computable and matches engineering common sense. Different fitting methods based on sampled coordinate data have been proposed, and those which are successful enter both the tolerancing standards and applications. In the practical coordinate metrology world, the total least squares (Gaussian) fit and the mini-max (Chebyshev) fit, along with some others, are widely used and integrated in commercial Coordinate Measuring Machine (CMM) software for calculation and evaluation[5]. Recently, Shakarji and Srinivasan etc. propose a new method – the one-sided constrained minimum total least square algorithm (L2C) – for planar datum establishment and possible further extension to other geometries[6-11]. This algorithm uses a combination of convex hull calculation and total least square minimization (L2), providing a method to address the 'rocking datum' problem.

This paper reviews the L2C methodology and evaluate it with respect to the unconstrained least squares by analyzing actual measurement data collected using a CMM. The workpiece used for analysis has a sphere mounted on a rectangular block. The center location of sphere is determined in a DRF determined by planar surfaces of the block. The fitting results are compared between L2[12] and L2C. In doing this, we find that L2C is (as expected) more sensitive than L2 in the planar datum establishment. Furthermore, L2C for all three datum features are investigated. In addition, an uncertainty analysis that reflects the entire measurement process will be discussed. Although the sensitivity of the new method of datum establishment may be greater than other methods, it has more physical meaning behind it, and may be more intuitive for engineering interpretation and application. For example, it will have a full mechanical contact with the datum feature simulators (where possible) and may have a better applicable usage when applied to assembly engineering. Also – in terms of different sensor inspection processes – unevenly spaced measured data must be considered, and the new method has what amounts to a built-in weighting function; hence it may give a more reasonable evaluation result.

L2 DRF COMMERCIAL & RESEARCH ALGORITHM

Traditional coordinate metrology software often calculates and minimizes a p-norm function:

$$\min\left[\sum_{1}^{N}|di|^{p}\right]^{1/p}$$

Common p-values correspond to well-known methods, such as minimum total distance (L1),

minimum total least square (L2), and Chebyshev (L∞). Recently, Shakarji and Srinivasan proposed and published several papers on a one-sided constrained fitting algorithm based on combination of traditional methods and convex hull calculation. Both L1- and L2-norm based algorithms have been developed, each constrained to be "outside" the part material.

Before evaluating the L2C method, a reference measurement experiment is conducted to validate DRF construction. The measurement setup is shown in Figure 1, and measurement sampling strategies are shown in Figure 2 and Figure 3. A commercial industrial software L2 algorithm ("Package 1") output is compared with a least-squares MATLAB code to ensure consistency between the two methods.

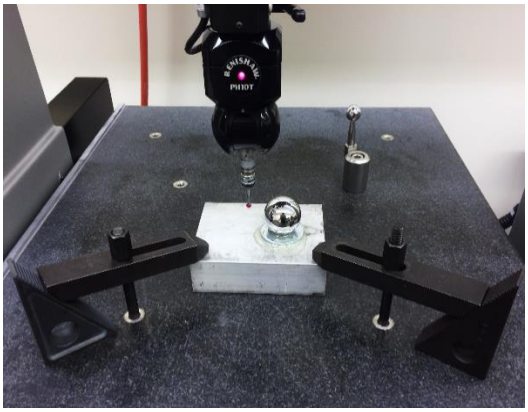

FIGURE 1. Measurement Setup.

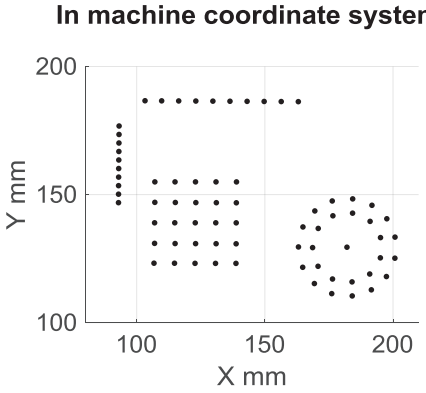

FIGURE 2. Sampling Strategy 5-By-5 Top View.

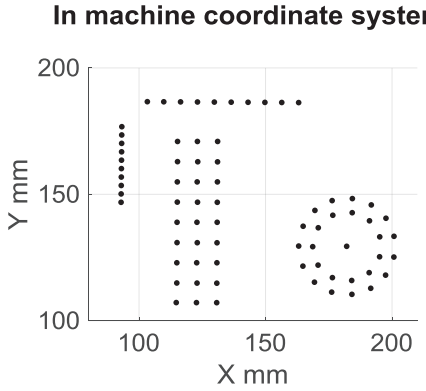

FIGURE 3. Sampling Strategy 3-By-9 Top View.

The CMM was used to measure the part, using the "Package 1" integrated L2-algorithm to output the sphere center location in a coordinate system built from the planar datum features. All the measured points were exported from the software, and used as input to the L2 MATLAB code, where the sphere center position is calculated again. Six repetitions of each sampling strategy were performed, and the algorithms from the commercial software and the MATLAB code provided nearly identical results.

The results of the least-squares comparison tests are shown in Table 1. The average values match very well, and the range of the data (maximum value - minimum value) are presented in Figure 4 and Figure 5. These results show a similar sensitivity in each axis in terms of fitting the DRF, also the additional reference parameter – the sphere diameter – shows close result with a variation within 1 μm. The differences seen are primarily due to the output data from Package 1. Because Package 1 only outputs the individual point data to the nearest micrometer, the data already contain a truncation error, which propagates a small error into the final result.

TABLE 1. Average values of commercial "Package 1" and MATLAB code.

	x(mm)	y(mm)	z(mm)	r(mm)
3x9 Package1	89.3357	-56.6757	22.6743	38.1020
3X9 MATLAB	89.3358	-56.6757	22.6745	38.1020
5X5 Package1	89.3352	-56.6812	22.6833	38.1008
5X5 MATLAB	89.3353	-56.6810	22.6835	38.1010

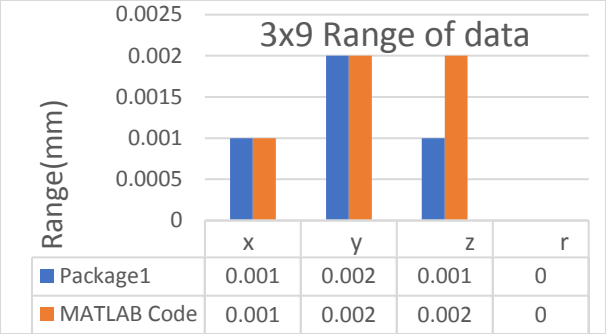

FIGURE 4. Range of 3x9 data.

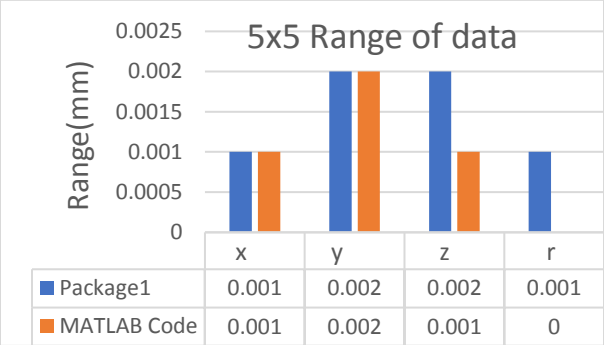

FIGURE 5. Range of 5x5 data.

An interesting side effect of using commercial software is that several methods generating the origin of DRF during its construction were revealed. To better illustrate this case, a 2D example is used. In commercial metrology software package 1, after L2 fitting of the primary datum, the secondary datum is constructed perpendicular to the primary, and through the centroid of the points taken from the secondary datum feature, as shown in Figure 6.

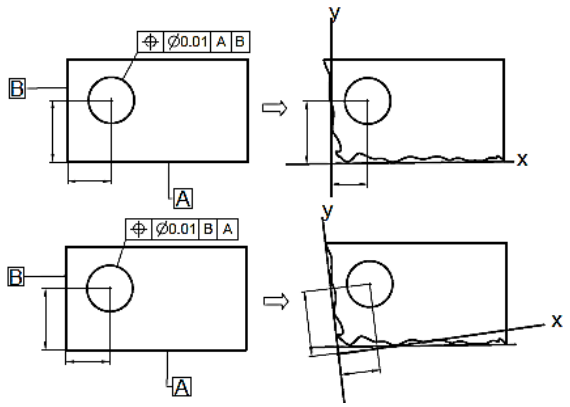

FIGURE 6. Package 1 method.

ISO 5459[13] requires the origin of the DRF lies on intersection of two perpendicular geometry, and the primary datum is still fitted using L2. But, the secondary datum is created tangent to the secondary datum feature, with the restriction that it is perpendicular to the primary datum. This is demonstrated in Figure 7.

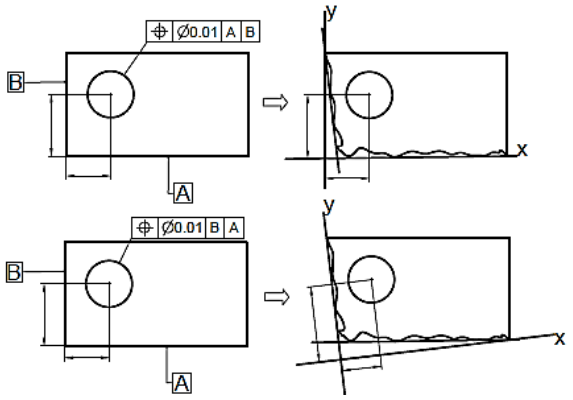

FIGURE 7. ISO 5459.

Package 2 appears to use another method for DRF construction. L2 fit of the measured points to the ideal geometries for both the primary and secondary datums will be used. The origin of the DRF that is created lies on the intersection of the two fitted geometries. The primary datum is based on its corresponding fitted geometry. However, the secondary datum is determined to be perpendicular to the primary datum, passing through the intersection (origin) of the two fitted features. This is illustrated in Figure 8.

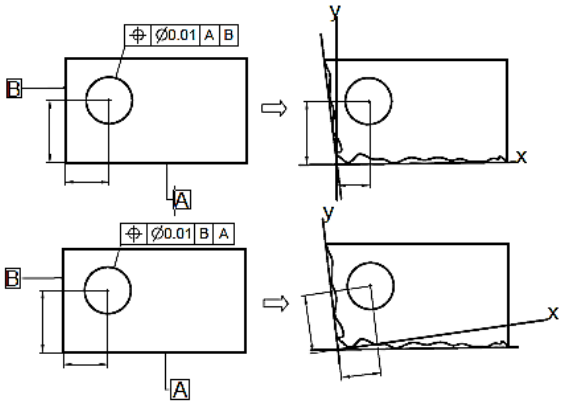

FIGURE 8. Package 2 method.

These different methods of DRF construction will produce different DRFs, and hence different locations for features referenced to the DRF. This effect is magnified if the datum features are significantly out of square. As can be seen, there still issues to be resolved in coordinate metrology, even in the basics such as DRF construction.

L2C- DRF ALGORITHM

After establishing a baseline by testing the L2 DRF construction, the one-sided constrained (L2C) algorithm is evaluated.

Based on the algorithm described in Shakarji's paper[8], experiment tests were performed using the data collected in the DRF experiments. Some additional work was performed in identifying the non-material direction (**a***) of the features. Instead of using a pre-determined **a***, a plane was fit to the measured points of primary geometry feature, then normal vector of the plane which directing to non-material side is defined as the direction of **a***. This vector is further used to guide the convex hull algorithm with respect to the non-material side. The procedure followed in datum construction per the L2C algorithm was:

1. According to drawing and measuring setup, compute the non-material direction of the measured data points(**a***).
2. Find convex hull of the measured data points.
3. Based on **a***, we further compute the non-material side of the convex hull.
4. Evaluate the weighted centroid of the non-material side of convex hull. (In 3D weight refers to the area of convex hull facet. In 2D, weight refers to the length of convex hull edge.)
5. Then find the plane (line) that lies on the non-material side of the convex hull and minimize the integral of squared distance from the surface $\int_s d^2 ds$ (L2C).

Constructing the rest of DRF is done as described by Shakarji in [8]. To test the L2C algorithm, the same measured points as before are used. To maintain a uniform comparison between methods, the ISO 5459 construction is used. The L2C method is expected to correspond to more variation in the results. The results that follow in Figure 9 and Figure 10 report the variation ranges of both sphere center coordinates and its diameter in the DRF constructed using L2 and L2C.

The L2C method is more sensitive than L2 method, with greater variation in x and y axes. In terms of primary datum (z axis), the variation is relatively small, probably due to the geometric relationship between the measured points and the sphere center.

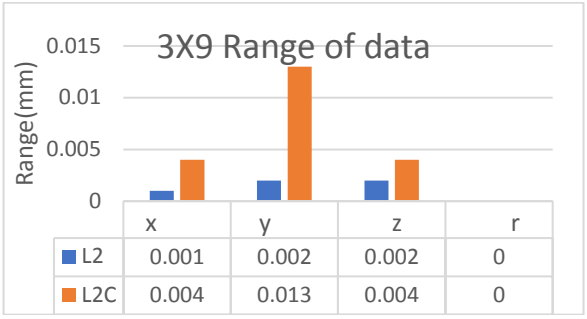

FIGURE 9. Range of 3x9 data.

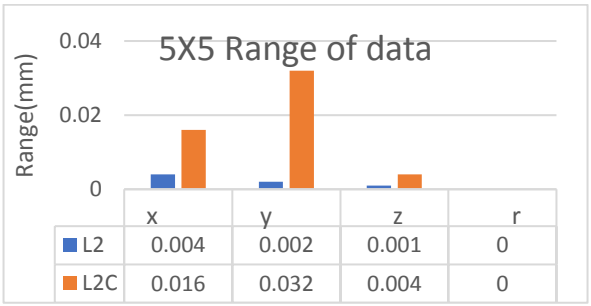

FIGURE 10. Range of 5x5 data.

MEASURING PROCESS INVOLVED ALGORITHM UNCERTAINTY ANALYSIS BY MONTE CARLO SIMULATION

Researchers used the Virtual CMM, simulation by constraints, the expert CMM, and traditional Monte Carlo approaches to estimate the measurement uncertainty for CMM measurement results[14]. Here, in order to estimate the measurement uncertainty, it is separated into two parts; one is propagated by measured sphere feature points, another part is propagated by measured DRF points.

Based on the CMM specification, considering maximum permissible error in each axis and combined three axes,

U1X 4.0+4.0L/1000 ≤ 5.5μm
U1Y 4.0+4.0L/1000 ≤ 5.6μm
U1Z 4.0+4.0L/1000 ≤ 5.3μm
U3 4.0+5.0L/1000 ≤ 7.2μm

the maximum MPE=7.2um was used to simulate single point variability. The basic simulation procedure is:

Step 1. Generate uniform distributed solid spherical MPE noise

Step 2. Add spherical MPE noise to each of the sphere's measured points.

Step 3. Fit a least squares sphere to the points in the previous step. (Repeat step 2-3 10000 times)

Step4. Find the minimum circumscribed sphere of all 10000 fitted sphere centers
Step 5. Use the center of sphere and radius to better estimate sphere feature L2 fitting induced uncertainty.

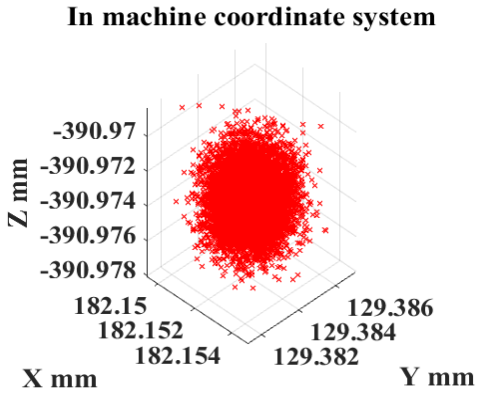

FIGURE 11. Cloud of sphere centers.

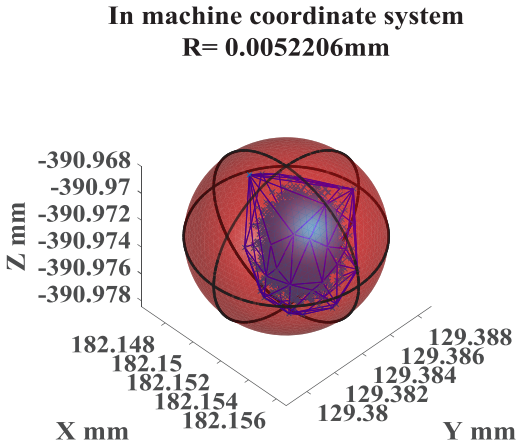

FIGURE 12. Minimum circumscribed sphere around the fitted centers.

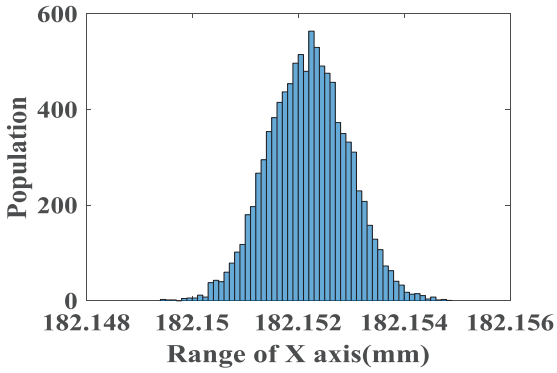

FIGURE 13. X axis distribution of the fitted sphere centers.

The results of this Monte Carlo simulation are shown in Figure 11 and Figure 12. The center location and radius of minimum circumscribed sphere can estimate the average location and the combined uncertainty of the measurement result. A histogram of the X coordinate of the sphere centers is shown in Figure 13. It reflects normal distribution, which is what is expected to be when combining many distributions together.

The second part uncertainty is propagated by DRF measured points. Following the primary-secondary-tertiary order, all the measured datum feature points are fitted by L2 and L2C. Figure 14 is an exaggerated illustration to show the variability of the DRF. This variability, in turn, influences the reported location of the sphere feature center. The combination of datum feature fitting and position evaluation is too difficult to analyze analytically, hence the reliance on the Monte Carlo method.

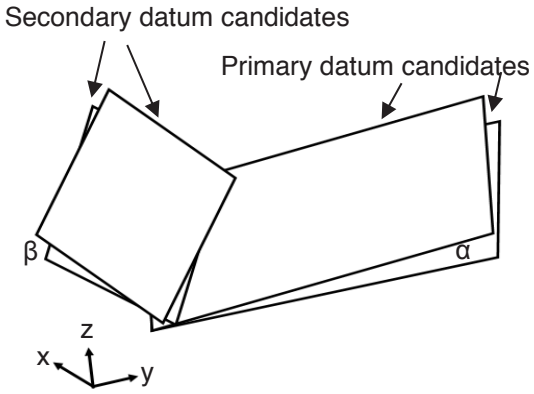

FIGURE 14. Variability of primary and secondary datum.

TABLE2. Monte Carlo Simulation result of L2 and L2C.

	Primary z(mm)	Secondary x(mm)	Tertiary y(mm)
3x9 L2	0.0001	0.0013	0.1070
3x9 L2C	2.0993	2.2581	0.1012
5x5 L2	0.0001	0.0016	0.1042
5x5 L2C	1.2122	1.6642	0.0803

To fully cover all the potential result, same average data method used. As we know, the differences are the worst scenario cases, which could be rarely happening. Considering measured sphere center location reference to its DRF,

the rotation variation becomes a translation in (x, y, z). The Monte Carlo simulation results are shown in Table 2.

As mentioned in previous section, the one-sided constraint on L2C makes it very sensitive to extreme points, so a larger variation is expected compared to L2, which has an averaging effect. In the L2C case, primary and secondary variation is much larger than tertiary one.

OTHER UNCERTAINTY SOURCES

The stated value of the CMM's MPE was the primary source of uncertainty used in estimating measurement uncertainty. This is not to suggest that other factors will not introduce uncertainty. There are many additional factors that could possibly contribute to the final uncertainty estimation. According to Wilhelm et al in their 2001 keynote CIRP paper[14], coordinate metrology uncertainty contributors are mainly divided into five main categories: hardware, workpiece, sampling strategy, fitting and evaluation algorithm and extrinsic factors. The measurements reported here could have, for instance, thermal factors involved in the result. Since the CMM used does not compensate thermal error automatically, and the operating environment AC controller has a limited resolution ±0.5 Fahrenheit, it could introduce a systematical bias of the final result. Also, unknown thermal gradient inside the machine and specimen will also introduce large uncertainty.

SUMMARY

This paper shows the one-sided least-squares algorithm L2C, initially proposed by Shakarji, is a computable solution for datum fitting, and can be quite close to the L2 result. It is certainly worth for pursuing additional investigation of this method, such as comparing it to the shifted L2 algorithms. Also, the evaluation of sphere center location has shown the uncertainty introduced by DRF fitting. For future commercial coordinate metrology software, integration of fitting algorithm uncertainty is a good direction to fully document the entire measurement result.

ACKNOWLEDGMENTS

The authors acknowledge the support and resources of the Center for Precision Metrology at UNC Charlotte. Some of this work was carried out under award #70NANB14H254 from NIST.

REFERENCES

[1] E.P. Morse, S. Heysiattalab, A.B. Feeney, T. Hedberg. Interoperability: linking design and tolerancing with metrology, Procedia CIRP Vol. 43, 2016

[2] D.J. Whitehouse, Handbook of surface metrology, CRC Press, 1994.

[3] W. Tandler, Establish Datum Reference Frames, Quality Digest, 2008.

[4] ANSI/ASME Y14.5M-2009 Dimensioning and Tolerancing

[5] R.J. Hocken,P.H. Pereira,Coordinate Measuring Machines and Systems,CRC Press, 2011.

[6] C.M. Shakarji, A. Clement, Reference Algorithms for Chebyshev and One-Sided Data Fitting for Coordinate Metrology, CIRP Annals, Vol.53, Issue 1, 2004.

[7] C.M. Shakarji, V. Srinivasan, Theory and Algorithms for Weighted Total Least-Squares Fitting of Lines, Planes, and Parallel Planes to Support Tolerancing Standards, Journal of Computing and Information Science in Engineering, 2013.

[8] C.M. Shakarji, V. Srinivasan, An Improved L_1 Based Algorithm for Standardized Planar Datum Establishment,Proceedings of the ASME, International Design Engineering Technical Conferences & Computers and Information in Engineering Conference, Buffalo, NY, 2014.

[9] C.M. Shakarji, Srinivasan, Vijay,Datum Planes Based on a Constrained L_1 Norm, Journal of Computing and Information Science in Engineering, Vol.15, 2015

[10] C.M. Shakarji, V. Srinivasan, Theory and Algorithm for planar datum establishment using constrained total least-squares, Procedia CIRP Vol. 43, 2016.

[11] C.M. Shakarji, V. Srinivasan, Computational Investigation for A New, Constrained Least-Squares Datum Definition for Circles, Cylinders, and Spheres, Proceedings of the ASME, International Mechanical Engineering Congress & Exposition, Phoenix, AZ, 2016.

[12] M.S. Shunmugam, On Assessment of Geometric Errors, Int. J. Prod. Res. v24, n2, 1986.

[13] ISO 5459:2011. Geometrical product specifications(GPS) - geometrical tolerancing - datums and datum systems.

[14] R.G. Wilhelm, R.J. Hocken, H. Schwenke, Task Specific Uncertainty in Coordinate Measurement, CIRP Annals, Vol. 50, Issue, 2001

AN EVALUATION OF NON-CONTACT LASER SCANNER PERFORMANCE USING CALIBRATED ARTIFACTS

Michael Gomez, Colleen Vaccaro, Chase Maness, Connor Lawrence, Carson Murray, Luis Vargas, Greg Caskey, Chris Evans, and Tony Schmitz
Mechanical Engineering and Engineering Science
University of North Carolina at Charlotte, Charlotte, NC

INTRODUCTION

Compared to traditional measuring techniques, non-contact laser scanning has the potential to offer industry a cost-effective method for quality assurance inspection, reverse engineering, and in-process metrology. However, establishing non-contact laser scanning measurement uncertainty is challenging due to multiple factors which affect scan results, including optical properties of the scanned surface, orientation of the surface within the work volume, and lighting conditions [1]. In this paper, evaluation of the resolution and repeatability is presented for selected non-contact scanning systems. This evaluation was completed through a statistical evaluation of multiple measurements and comparison of the mean values for feature dimensions to calibrated measurement artifacts. The selected non-contact laser scanning systems include the ROMER Absolute Arm 7525SI with integrated scanner (ROMER) and ATOS Core 300 (ATOS). This effort is the outcome of a two-semester senior design project sponsored by the UNC Charlotte Center for Precision Metrology Affiliates and, therefore, represents a combination of research and education efforts at the university.

Two artifacts were designed and manufactured by the senior design team to test the non-contact laser scanner resolution and repeatability. The point cloud data sets obtained from the laser scanners were processed using two different software packages: Geomagic Studio and GOM Inspect, to examine potential differences in reported results. The feature dimensions extracted from the software analyses were then compared to the measurements obtained using a Zeiss Prismo 7 Navigator coordinate measuring machine (CMM).

VERIFICATION ARTIFACTS

Artifacts were designed and test procedures defined to obtain both qualitative and quantitative data regarding the performance of the laser scanning systems. Factors which are identified in the results include the instrument resolution, measurement volume, and time-to-scan [1]. Furthermore, artifact properties, such as orientation within the work volume, thermal expansion, surface features, and material were considered [2].

Two artifacts were designed and constructed. The step cube artifact displayed in Fig. 1 was designed for both qualitative and quantitative assessments. The face with the smaller holes (left view) was designed to determine the smallest feature (hole) that could be identified in a scan in order to establish the resolution of the laser scanning system. The larger holes (right view) and the step heights (top surface in both views) were used to quantify step heights, hole diameters, and center-to-center distances of the holes.

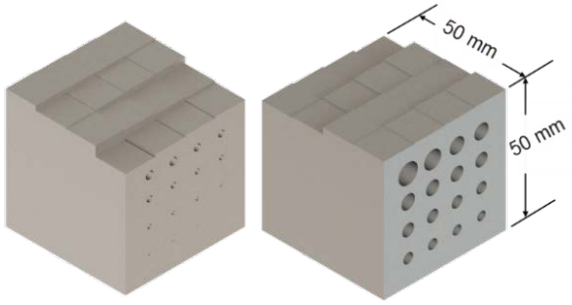

Figure 1. Step cube artifact.

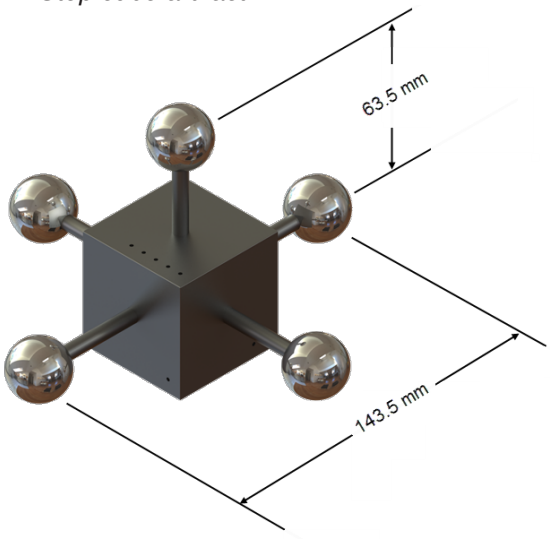

Figure 2. Ball cube artifact with 440 stainless steel spheres. The spheres are labeled 1-5 using holes on the corresponding surface for inspection purposes.

The ball cube artifact is shown in Fig. 2. This artifact includes spheres so that diameters and

center-to-center distances can be measured. The lines that define the center-to-center distances between the spheres of the ball-cube form a measurement pyramid which enables a geometric assessment of accuracy within the measurement volume [1]. See Fig. 3.

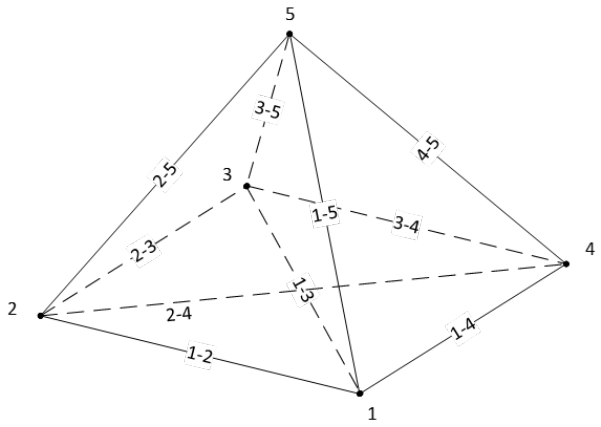

Figure 3. Measurement pyramid.

The step cube and ball cube artifact material was 316 stainless steel. Due to the measurement limitations imposed by the high reflectivity, an *i*-PrOH-TiO_2 [3] solution was sprayed on the artifacts prior to scanning. Therefore, dimensional changes were incurred due to the variation in particle distribution across the artifact surface. To potentially investigate this effect, the ball cube artifact was designed to enable the stainless steel spheres to be replaced by aluminum oxide spheres.

Scans were performed and the measurement point clouds were analyzed to compare artifact dimensions, including sphere/hole diameters, sphere/hole center-to-center distances, and step heights, to CMM measurement results.

STEP CUBE ARTIFACT

Analysis of the step cube artifact included a qualitative inspection of the face of the artifact with the smallest hole array; see Fig. 4. An array of 16 holes with nominal diameters ranging from 3.2 mm to 0.2 mm were used to determine the ability of the laser scanning system to detect small features. This experiment was completed in order to observe difference in resolution between the two scanning systems. Note that GOM Inspect was used to process point cloud geometries due to factors which are discussed later in this paper.

As shown in Fig. 4, five scans were completed using the ROMER scanning system. The scanner was able to identify the 0.4 mm hole two out of five times, while it was unable to identify the 0.2 mm hole in its point cloud in any scan. All other holes were observed in all five scans.

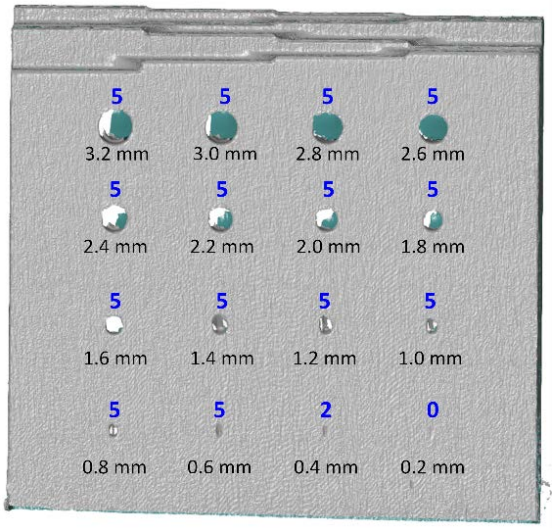

Figure 4. A representation of a ROMER point cloud generated for qualitative inspection of the step cube. A series of five scans were completed and a visual inspection was performed on the corresponding point clouds.

The qualitative analysis of the small hole array for the ATOS is presented in Fig. 5. Of the five scans, the 0.4 mm hole was visible 1 out of 5 times. As before, the scanning system was unable to identify the smallest hole at 0.2 mm.

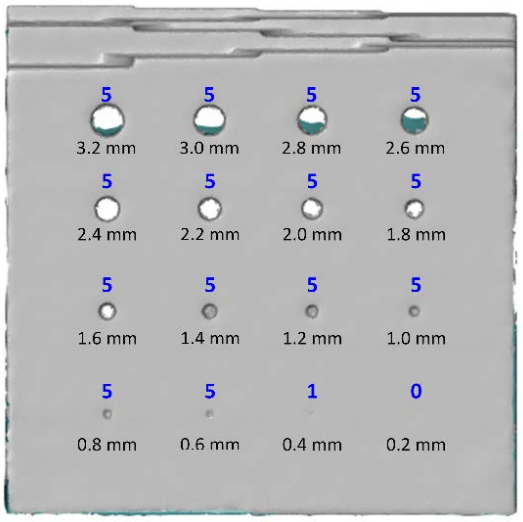

Figure 5. A representation of an ATOS point cloud generated for qualitative inspection of the step cube.

Figure 6 displays a comparison of deviations in hole diameter from the CMM values for the two scanning systems. The diameter was realized by cylindrical fitting elements for the holes. The hole diameter numbering system is shown in Fig. 7 with hole 16 being the smallest hole relative to the reference hole 1. The ATOS error bars, which represent the 95% confidence intervals from repeated measurements, are smaller between the two scanning systems.

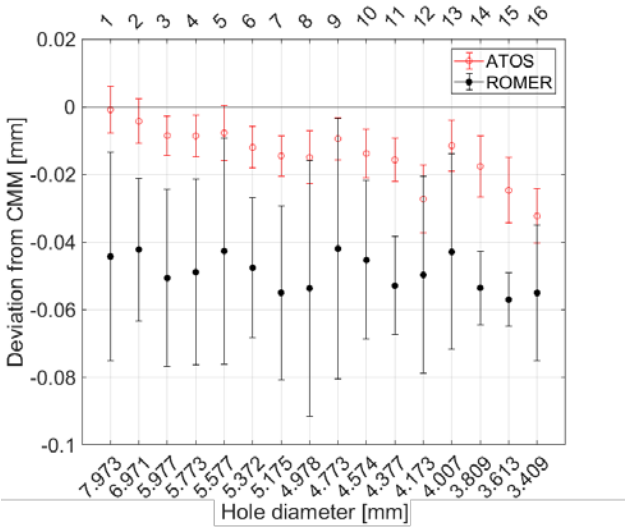

Figure 6. Mean values and 95% confidence intervals for step cube hole diameters. There were five sets of tests for the ATOS scanner and four sets for the ROMER scanner.

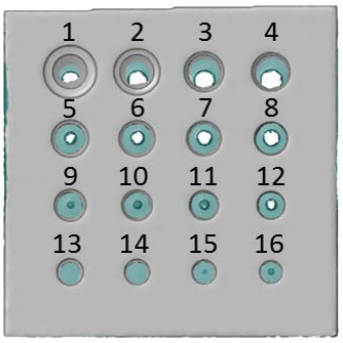

Figure 7. Hole diameter identification for the step cube artifact.

The cylindrical fitting elements were used to determine center-to-center distances between holes as well; see Fig. 8. The ATOS system again exhibited higher repeatability.

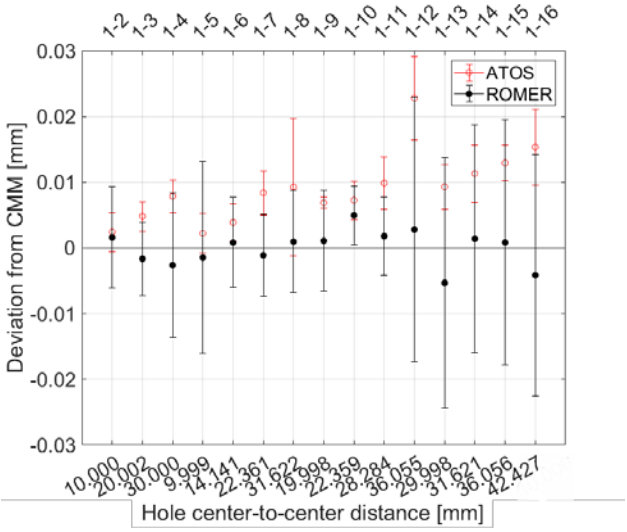

Figure 8. Mean values and 95% confidence intervals for hole center-to-center distance of the step cube artifact.

Figure 9 displays the deviations in step heights from the CMM values for the step cube. Planes were fit to each of the (nominally) flat steps and differences in step heights were measured with respect to a reference plane. The step height numbering system is displayed in Fig. 10 with step height 16 being the lowest step relative to the reference plane 1.

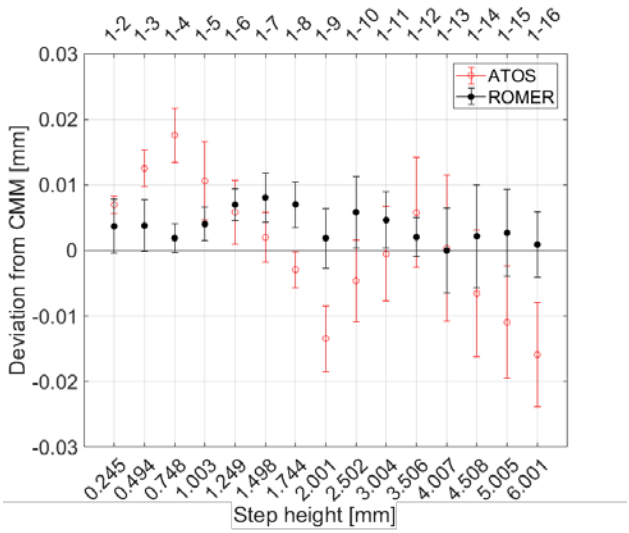

Figure 9. Mean values and 95% confidence intervals for the differences in step heights of the step cube artifact. There were five sets of tests for the ATOS scanner and five sets for the ROMER scanner.

Figure 10. Step height identification for the step cube artifact.

BALL CUBE ARTIFACT

Figure 11 displays the deviation in sphere diameters from the CMM measurements for the two scanning systems. Preliminary results demonstrate a bias for both systems relative to the CMM. The ATOS yielded sphere diameters which were 24 µm to 30 µm smaller than the CMM results. Conversely, the ROMER gave sphere diameters which were 31 µm to 40 µm larger.

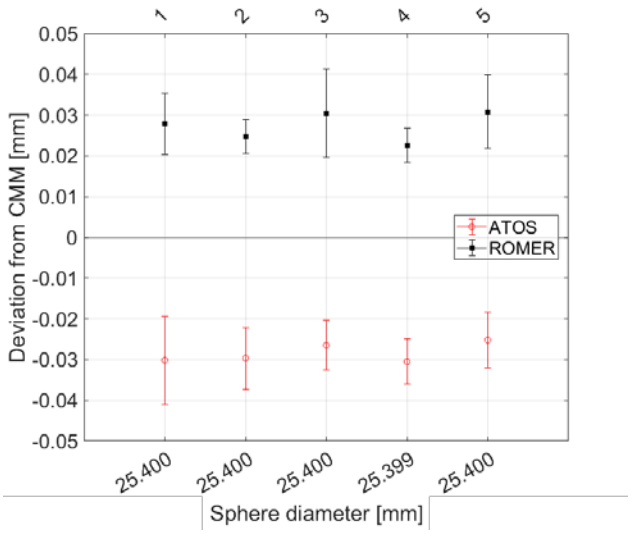

Figure 11. Mean sphere diameters for the stainless steel ball cube artifact. Values were obtained by averaging the results obtained from five point clouds for the ROMER and ATOS scanners.

Figure 12 displays deviations in center-to-center distances between the ball cube spheres. The measured distances from the ATOS and ROMER systems follow similar trends.

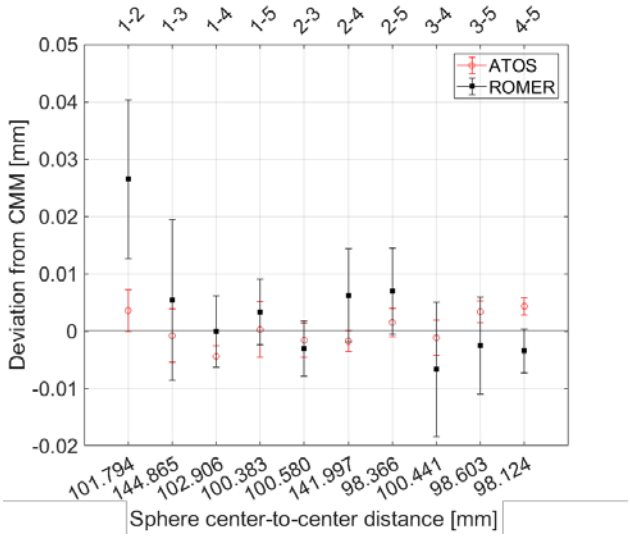

Figure 12. Mean values and 95% confidence intervals for center-to-center distances between spheres for the ball cube artifact.

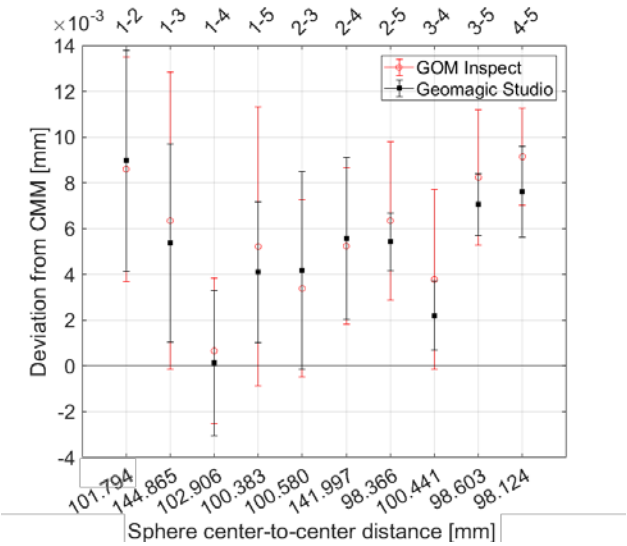

Figure 13. A comparison was performed using a single point cloud from the ball cube. The point cloud was analyzed five times using both Geomagic Studio and GOM Inspect by the same operator.

ADDITIONAL TESTS

The repeatability for dimensional analyses completed using the Geomagic Studio and GOM Inspect software packages is demonstrated in Fig. 13. For this study, a single point cloud data file (obtained using the ATOS system) was analyzed five times by a single operator using both software platforms. It was observed that there was a significant difference in the time needed to complete the analyses. To fully analyze one point cloud in Geomagic Studio, it required, on average, 10 minutes. The time was approximately 4 minutes for the same operator to analyze the scan in GOM Inspect.

The stainless steel gage spheres were replaced with aluminum oxide spheres in an attempt to eliminate the application of the *i*-PrOH-TiO_2 [3] solution. Initial tests were performed on the two scanning systems resulting in an incomplete point cloud. The aluminum oxide spheres, therefore, did not improve the restrictions imposed by high reflectivity.

CONCLUSIONS

The purpose of this project was to assess the measurement resolution and repeatability for two non-contact laser scanning systems using calibrated artifacts. Two systems were considered: the ATOS Core 300 and ROMER Absolute Arm 7525SI. The laser scanning systems measured three-dimensional point clouds from the artifact surfaces. Measurement challenges included artifact orientation within the work volume and surface reflectivity. The artifacts were designed to enable measurement of various geometrical features, including hole diameter, sphere diameter, and distance between feature centers.

The dimensions obtained from point cloud data depend on the fitting techniques used in the geometric modeling analysis software. GOM Inspect and Geomagic Studio were evaluated in this study. While point cloud software can be traceable to standards organizations, the geometric modeling process can result in measurement variation between operators.

ACKNOWLEDGEMENTS

The authors gratefully acknowledge partial financial support from the UNC Charlotte Center for Precision Metrology Affiliates, machining support from B. Dutterer and J. Dalton, and equipment support from J. Raquet, E. Morse, F. Javidpour, and GOM Americas Inc.

REFERENCES

[1] M.R. Dury, S.B. Brown, M.B. McCarthy, and S.D. Woodward, 2015, 3D Optical Scanner Dimensional Verification Facility at the NPL's "National FreeForm Centre", Laser Metrology and Machine Performance XI (LAMDAMAP 2015), Huddersfield, UK.

[2] Y. Liu, 1997, Comparison of Tactile Probe CMM and Laser Scanning Techniques for Reverse Engineering, M.S. Thesis, University of Windsor, Ontario, Canada.

[3] T. Brajlih, T. Tasic, I. Drstvensek, B. Valentan, M. Hadzistevic, V. Pogaca, J. Balic, and B. Acko, 2011, Possibilities of Using Three-Dimensional Optical Scanning in Complex Geometrical Inspection, Journal of Mechanical Engineering, 57/11: 826-833.

INTEGRATION OF WAFER-LEVEL SOLAR CELLS AND MICRO-OPTIC CONCENTRATORS FOR MICRO-SCALE CONCENTRATING PHOTOVOLTAICS

Bradley H. Jared, Christopher Hains, Gordon Keeler, Bill K. Miller, Scott M. Paap, Michael P. Saavedra, William C. Sweatt, Anna Tauke-Pedretti and Michael Wood
Sandia National Laboratories
Albuquerque, NM
Lan Li, Duanhui Li, Tian Gu and Juejun Hu
Massachusetts Institute for Technology
Cambridge, MA

A novel micro-scale concentrating photovoltaic (CPV) concept is in development to integrate wafer-level solar cells with micro-optical concentrators. This hybrid micro-CPV approach combines the performance of CPV with the form factor and low system costs of flat panel PV to enhance system conversion efficiency and reduce material and fabrication costs. Previous work at Sandia demonstrated the concept and viability of micro-CPV, as a series of microsystems-enabled photovoltaics (MEPV) prototypes were generated using multi-junction, microscale solar cells with micro-optic concentrators [1-2]. Cell efficiencies and optical transmissions approaching 30% and 90% respectively were achieved, while concentrations of 100X and 200X were demonstrated in different prototypes [3].

Current work will provide performance gains over initial efforts by adding optical functionality to the photovoltaic behavior of crystalline silicon solar cells. Such duality is achieved by etching four-sided pyramidal cones with 35.3° side angles through 280 μm thick Si cells, Figure 1. When processed properly, the sub-30 nm RMS surfaces act as reflective mirrors and further concentrate the visible light. High performance multi-junction III-V cells are bonded to the bottom of the Si cell, at the opening of the reflective cavity, Figure 2. A PDMS lens array is cast above the Si cell, similar to prior work [4]. In this construct, solar energy is captured in two different forms. Highly scattered, diffuse light is collected by the low efficiency silicon, just as in flat plate PV. Direct, incident sunlight, however, is focused by the PDMS concentrating lens and the reflector cavity onto the higher efficiency III-

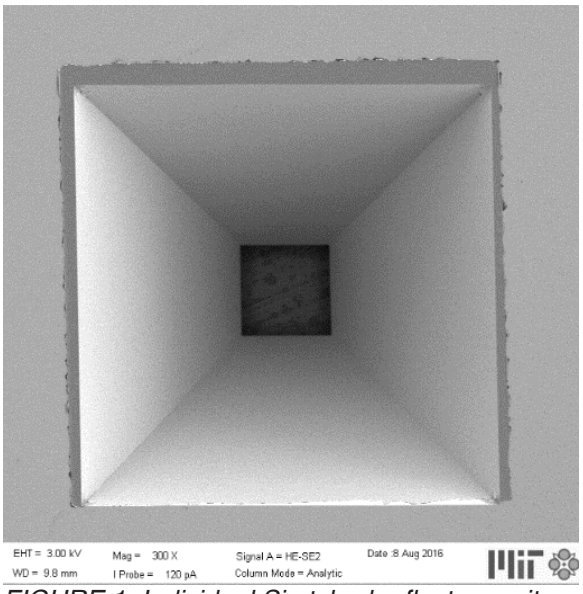

FIGURE 1. Individual Si etched reflector cavity.

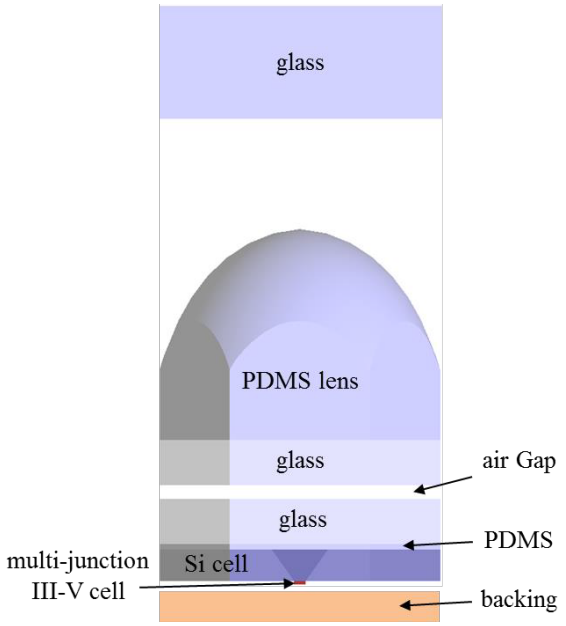

FIGURE 2. Schematic of the micro-CPV prototype unit.

V cells. Combining refractive and reflective optical elements enables higher concentration of incident light while maintaining system collection angles [5]. Predictions have shown that collecting both diffuse and incident light could provide 40-55% more energy than conventional flat plate PV, and 15-40% more energy than traditional CPV. Cell and optic modules have been processed separately and will be assembled and performance tested for the presentation.

The prototype package consists of a 9x11 array of elements in a 25mm square footprint with a total thickness on the order of 5mm. PDMS optics will provide >90% optical efficiency with 400X concentration and a roughly ±2° acceptance angle using eighth order aspheric curves. The optics are cast in PDMS onto 300μm thick Schott AF32 glass using an aluminum mold. Optical surfaces in the mold, Figure 3, are micro-machined and then diamond milled, as in prior work [3]. After casting lenses onto the AF32 glass, Figure 4, the lens array is mounting into the bottom of a machined Macor frame to insure module rigidity. A piece of 3mm thick Schott BK-7 glass is then mounted to the top of the frame to seal the entire optic assembly from environmental contamination, Figure 5. A pin-hole scanning technique was used to characterize individual lens elements in the array. A 635nm laser source is expanded to uniformly illuminate a 5μm pin-hole aperture located in front of the optic. Transmitted light through the aperture and optic is collected onto a silicon photodiode, Figure 6. Measurements

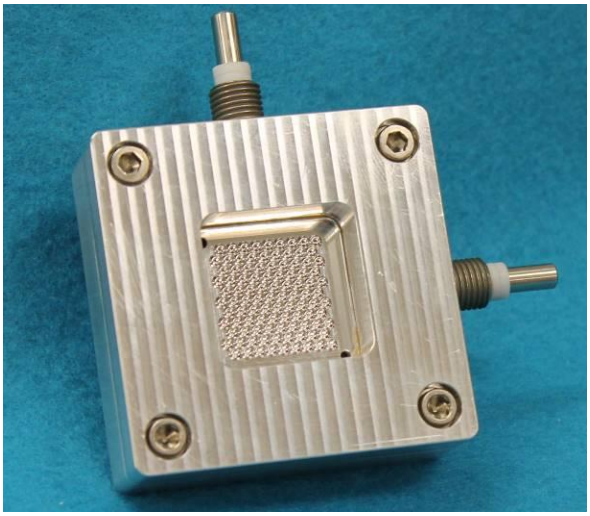

FIGURE 3. Optic surface side of the aluminum mold utilized to cast the 9x11 optic array.

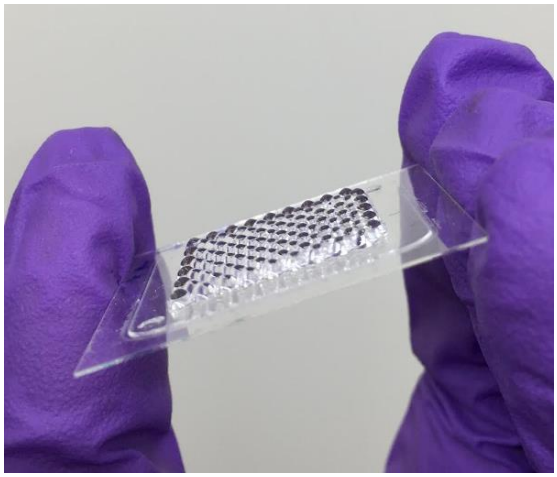

FIGURE 4. Molded 9x11 optics array.

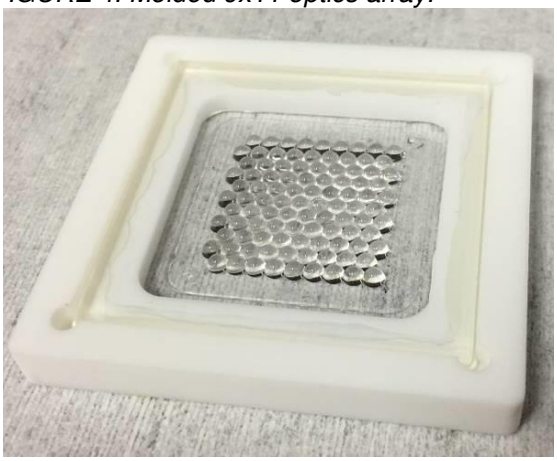

FIGURE 5. Optic array mounted in a Macor frame.

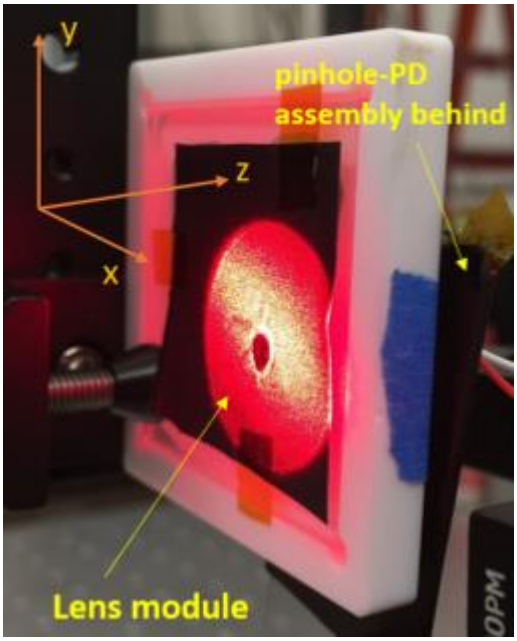

FIGURE 6. Pin-hole and silicon photodiode arrangement for lens characterization.

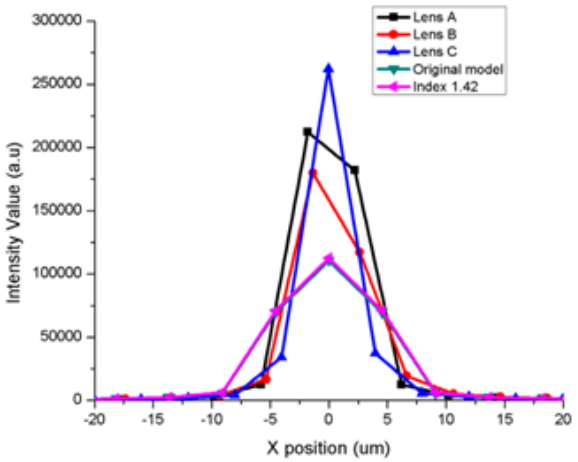

FIGURE 7. Intensity profile along the X-axis at the optical focal plane.

are taken every 4μm in X and Y and every 10μm in Z. Illumination intensity is directly proportional to photodiode current. Figure 7 compares the intensity profiles of three different lenses in the array across their horizontal axis with simulation results from Lighttools. Full width half max (FWHM) spot sizes are roughly 6μm, well within the 100μm opening of the Si cell arrays. FWHM for the model is 11μm, suggesting greater curvature in the lens profiles and/or a higher than expected refractive index for the PDMS material.

Cell development has demonstrated the bonding of multi-junction III-V InGaP/GaAs solar cell arrays to the bottom of an inactive 20x20mm silicon cell. The active area of the III-V cells are 100μm square and are aligned to the refective

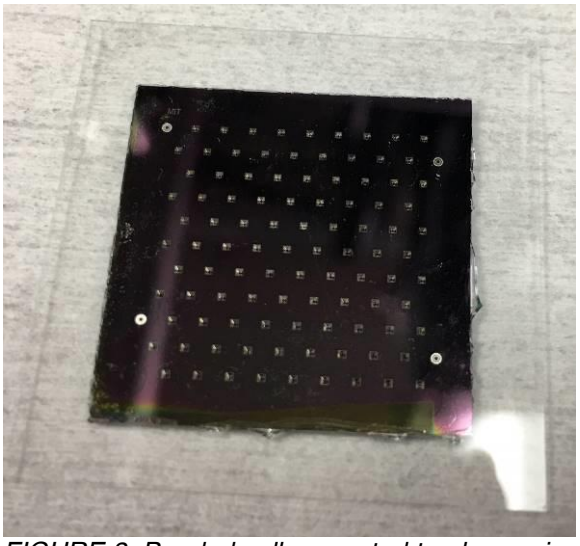

FIGURE 8. Bonded cells mounted to glass using PDMS.

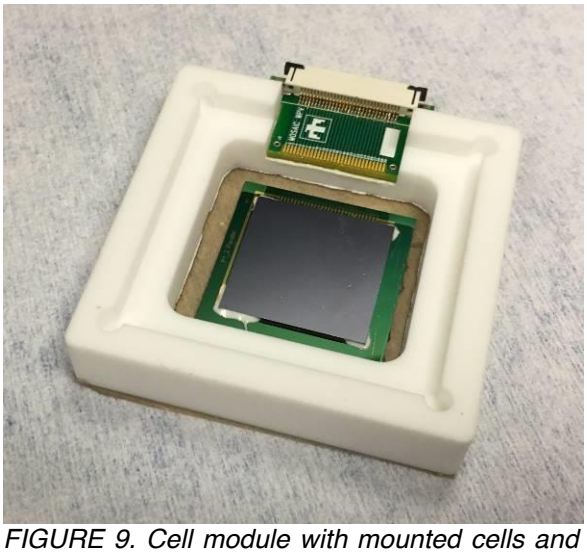

FIGURE 9. Cell module with mounted cells and PCB breakout board with ribbon cable connector.

mirror cavities in the silicon during bump bonding. The Si/InGaP/GaAs stack is mounted to 300μm thick AF32 glass using PDMS, Figure 8. This cell stack is then mounted into a Macor frame along with a PCB breakout board, Figure 9. The interconnect pads from the Si are wire bonded to the PCB pads to allow electrical interfacing with the outside world.

Since cell and optic modules are now completed, the final step is to align them optically and test. For this prototype, the two modules will not be physically connected, but mounted onto stages to allow characterization of module performance as a function of linear and rotational offsets and/or errors. This work remains on-going and will be provided during the presentation.

ACKNOWLEDGMENTS

Sandia National Laboratories is a multimission laboratory managed and operated by National Technology and Engineering Solutions of Sandia LLC, a wholly owned subsidiary of Honeywell International Inc. for the U.S. Department of Energy's National Nuclear Security Administration under contract DE-NA0003525. This document has been reviewed and approved for unclassified, unlimited release, SAND2017-9875A.

REFERENCES

[1] Gupta V, Cruz-Campa, J, Okandan M, Nielson G. Microsystems-Enabled Photovoltaics: A Path to the Widespread

Harnessing of Solar Energy. Future Photovoltaics. May 2010.
[2] Nielson, G., et al. Microfabrication of microsystem-enabled photovoltaic (MEPV) cells. SPIE Proc. Advanced Fabrication Technologies for Micro/Nano Optics and Photonics, 2011. Vol. 7927, no. 4.
[3] Jared B, et al. Efficient micro-concentrator for microsystems-enabled photovoltaics. Proceedings of ASPE. Boston, MA, 2014.
[4] Jared B, et al. Micro-concentrators for a microsystems-enabled photovoltaic system. Optics Express. Vol. 22, Issue S2. A521-A527.
[5] Gu, T., et al. "Wafer-level Integrated Micro-Concentrating Photovoltaics." Optical Nanostructures and Advanced Materials for Photovoltaics, PTh3A. 1. Optical Society of America, 2016.

DMD-BASED RANDOM-ACCESS SCANNER FOR FAST 3D IMAGING AND FABRICATION

Qiang Geng, Dien Wang, and Shih-Chi Chen*
Department of Mechanical and Automation Engineering
The Chinese University of Hong Kong
Shatin, N.T., Hong Kong SAR, China
*Email: scchen@mae.cuhk.edu.hk

We present a revolutionary way to manipulate and steer ultrafast lasers based on a digital micromirror device (DMD). The DMD scanner performs 3D or random-access scanning, achieving a scanning speed of 22.7 kHz, scanning range of ~103 × 206 × 524 μm^3, and scanning resolution (i.e., minimum step size) of 270 nm and 130 nm in the axial and lateral directions respectively when paired with a 40X objective lens. To demonstrate the performance, the DMD scanner is used to perform 3D two-photon excitation (TPE) imaging on pollen samples as well as two-photon polymerization (TPP) to fabricate 3D structures.

INTRODUCTION

Precise and fast laser beam steering and scanning methods are the foundation of laser scanning microscopes and 3D nano-fabrication systems. Although a variety of high-speed beam scanning methods are available, e.g., resonant galvanometric scanner, polygonal mirrors, and electrically tunable lenses etc., they can only perform fast linear scanning and lack the capability to perform fast scanning among randomly selected points in space, which is critical for both bio-imaging and nano-fabrication. For example, if a scanner can access all points in its work space at equal speed, complex / hollow structures can be fabricated at a much higher build rate compared to the current raster-scanning process used in 3D additive manufacturing systems. To realize 3D random-access scanning using a DMD, we apply the principle of binary holography [1], where each calculated hologram corresponds to a specific point in space. Here, the DMD is used as a programmable binary mask, consisting of several million micromirrors. Each micromirror is an independent pixel with two stable angular positions, i.e., ±12°. For axial scanning, one can program holograms of spherical wavefronts of increasing or decreasing radii to the DMD [2]. For lateral scanning, one can vary the titled phase term with increasing or decreasing periods of fringes [3]. The superposition of the axial and lateral scanning holograms enable 3D random-access scanning [3].

SYSTEM CONFIGURATION

Figure 1 presents the optical configuration of the DMD-based TPP fabrication system as well as TPE imaging system.

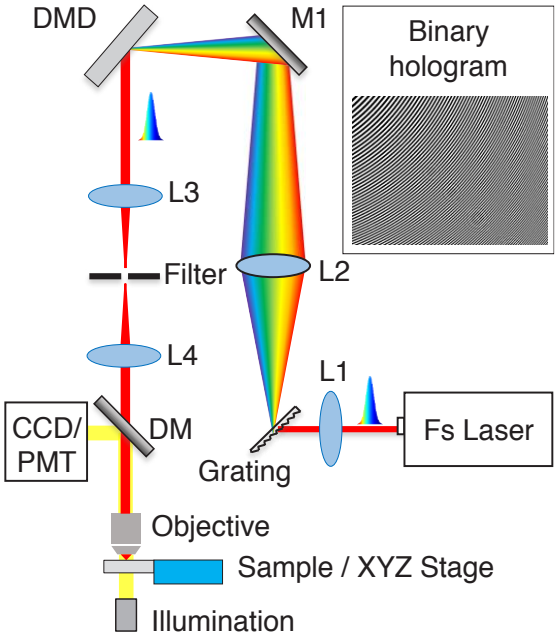

FIGURE 1. Optical configuration of the TPP fabrication system and TPE imaging system, enabled by DMD random-access scanner; M1, M2: high-reflectivity mirrors; DM: dichroic mirror; L1, L2, L3, and L4: lenses

The laser source is a Ti:sapphire femtosecond laser (Chameleon Ultra II, Coherent) with a repetition rate of 80 MHz and an average power of 3.3 W. First, the input laser beam is appropriately expanded to ensure the DMD aperture (DLP 4100 0.7" XGA, 1024 × 768 pixels, Texas Instrument) is fully filled. As the DMD functions both as a programmable binary hologram and a blazed grating, it introduces

negative angular dispersion to the laser beam. To remove the angular dispersion, a blazed transmission grating and a mirror (M1) are included in the light path to generate positive angular dispersion [4]. After the DMD, the dispersion-free laser beam is guided to an infinity-corrected objective lens (Nikon CFI S Fluor 40X Oil, NA = 1.3, WD = 0.22 mm) via a 1:1 telescope, consisting of an achromatic lens L3 and a tube lens L4. An iris diaphragm is placed at the back focal plane of L3 to spatially select the -1st order diffraction of the hologram. To observe the fabrication process, a microscopic imaging system is built in conjunction with the fabrication system. As shown in Figure 1, the microscope shares the objective lens with the fabrication setup. A transillumination light source illuminates the translucent sample. The image or video of the sample is then acquired by a CCD camera after the dichroic mirror (DM). The photoresist (IP-Dip, Nanoscribe) is mounted on a motorized precision xyz stage for positioning.

The optical configuration of the TPE microscope is the largely identical to the TPP system. The only difference is that the CCD camera is replaced by a photomultiplier tube (PMT, R10699 and C7950, Hamamatsu), which is synchronized to the DMD trigger signals. A data acquisition card (NI USB-6363, National Instruments) collects and processes the PMT signals to form 3D images. These operations are fully automated by a custom-developed LabVIEW program.

AXIAL & LATERAL SCANNING

Axial scanning along the optical axis (i.e., z-axis) is realized by applying binary holograms of spherical wavefronts of increasing or decreasing focal lengths [2]:

$$\varphi(x,y) = \frac{\pi(x^2+y^2)}{\lambda f} \quad \textbf{(1)}$$

where λ is the wavelength and f is the focal length of the spherical wavefront. Binary holograms of the spherical wavefronts in Eq. (1) is generated based on Lee holography [1]; and can be calculated as

$$h(i,j) = \begin{cases} 1, & -\frac{q}{2} \le \frac{R(x,y)}{T} + \frac{\varphi(x,y)}{2\pi} + k \le \frac{q}{2} \\ 0, & otherwise \end{cases} \quad \textbf{(2)}$$

where $h(i, j) \in \{0, 1\}$, $(1 \le i \le m; 1 \le j \le n; i, j \in \mathrm{N})$ represents the pixels on the DMD; 1 and 0 refer to the "on" and "off" states respectively; m and n refer to the number of rows and columns respectively; T is the grating period of the hologram; k is an integer; and q $(0 \le q \le 1/2)$ is a constant that determines the widths of the fringes.

Lateral scanning can be realized by changing the tilted phase term [3], i.e., $R(x,y)/T$ in Eq. (2), as $R(x,y)$ determines the bias and tilted angle of the fringe patterns and T determines the period of the fringes. In other words, T may be used to control the separation of diffracted beams from the 0th diffraction order. Figure 2 illustrates the working principle of lateral scanning: To scan the focal point from left (red point) to right (green point), assuming T is constant, one only needs to reduce the value of $R(x,y)$. By appropriately selecting the values of $R(x,y)$ and T, lateral scanning in both x- and y- axes can be achieved. In combination with the axial scanning, three-axis random-access scanning can be realized by using a single DMD. When selecting design parameters, it is worthwhile to note that a large T value may cause the diffracted beams to overlap in space, while a small T value may cause the tilted phase term to exceed the range of the inequality in Eq. (2), and thus no modulation will be performed.

As the DMD scanner is capable of scanning arbitrary paths in space, all conventional scanning strategies, e.g., raster, spiral, or Lissajous scanning trajectories, can be easily implemented on the DMD platform. In addition, the dwell time at each point on the scanning path can also be arbitrarily controlled, realizing selective optical stimulation.

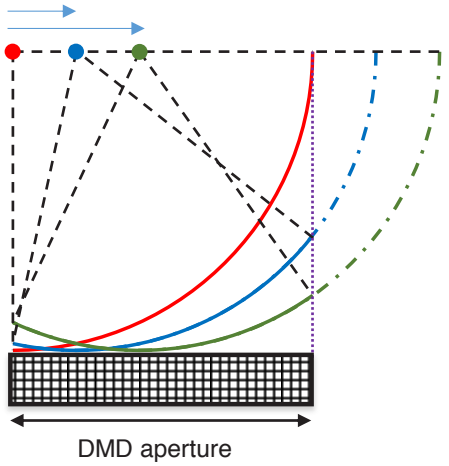

FIGURE 2. Working principle of lateral scanning based on binary holography: The focal point can be scanned from left (red) to right (green) by reducing the value of the tilted phase term, i.e., R(x,y)/T, in Eq. (2), i.e, reducing the value of R(x,y) when T (grating period) is constant.

SCANNING RANGE AND RESOLUTION

The relationship between the scanning performance and the DMD parameters, i.e., pixel size and aperture size, have been studied and reported in [3]. From the parametric model, we can conclude that (1) the lateral scan range is inversely proportional to the DMD pixel size (d) and the magnification of the objective lens(M_{obj}); the axial scan range is inversely proportional to d^2 and M_{obj}^2; and (2) the minimum step size in the lateral direction is inversely proportional to the aperture size (D); the minimum step size in the axial direction is inversely proportional to D^2. Based on the system presented in Fig. 1, the scan range is calculated to be 103 × 206 × 524 μm^3. If a DMD of higher resolution is used, e.g., DLP6500 (d = 7.68 μm), the work volume can be increased by more than a factor of 10. If a low magnification objective lens is used, the work volume can be further increasesed.

Considering the minimum step size, i.e., the smallest variation of binary patterns that will result in a consistent step, assuming the DMD aperture is fully filled by the laser beam, based on the system's DMD model, the lateral/axial minimum step size is calculated to be 0.12/0.27 μm respectively, which is better than typical lateral/axial scanning resolution of TPP fabrication systems, i.e., 0.4/1.4 μm. In other words, our new DMD scanning method, although being entirely discrete and digital, can fabricate continuous structrues with better resolution, and follow arbitrary trajectories in space. Note that the minimum step size can be further reduced by using DMDs of more pixels.

TPP FABRICATION EXPERIMENTS

In conventional TPP systems, the fabrication is performed by a pair of galvanometric scanners that raster-scan the x-y plane. To build 3D structures, a linear stage moves the build plane axially after a layer is completed. This layer-by-layer sequential fabrication process limits the printing speed of complex / hollow structures. Comparing with the conventional method, the total fabrication time of the DMD-based TPP system is only proportional to the total solid volume regardless of the level of complexity. This is because the DMD can randomly access any point in space with equal speed, i.e., 22.7 kHz or 5mm/s, presenting great advantages for fabricating complex structures. In addition, precision laser dose control (i.e., gray scale control) can be achieved by extending the dwell time of the laser focus at any point within the DMD work volume, which cannot be achieved by galvo scanners due to the inertia of mirrors.

To demonstrate the capability of scanning along arbitrary paths, a spiral path with elevating height is designed and illustrated in Fig. 3. Next, holograms of all scan points along the path are generated and loaded to the DMD memory. Note that each point along the path corresponds to a different hologram.

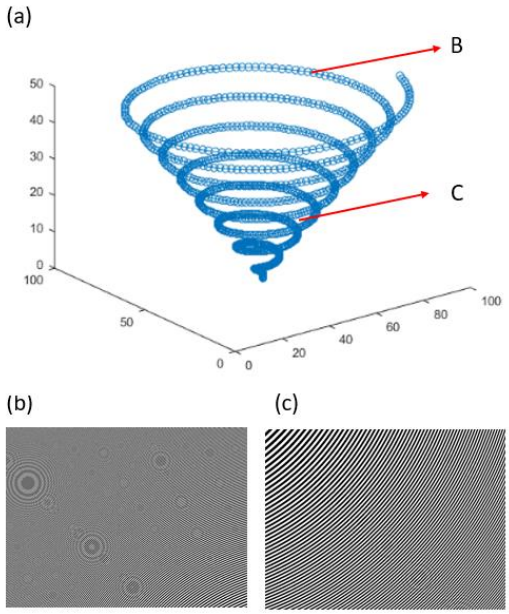

FIGURE 3. Illustration of an arbitrarily generated scanning path for TPP; the holograms of two different points on the scan path (B and C) are shown in Fig. 3B and 3C, respectively.

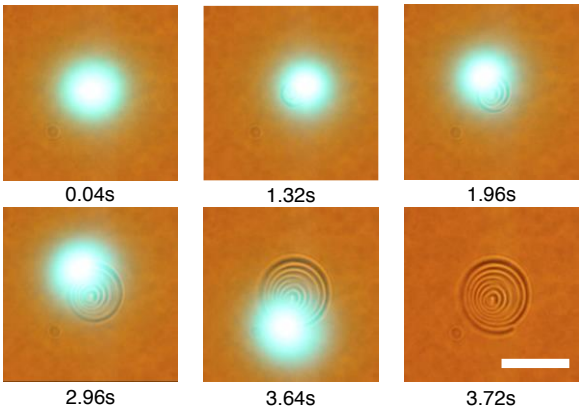

FIGURE 4. Time sequence of the spiral scanning and fabrication process performed by the DMD holography scanner. Scale bar is 25 µm.

Figure 4 presents a time sequence of the fabrication process recorded by a CCD camera,

where the focal point precisely scans the planned path, shown in Fig. 3A, and the green emissions confirm the two-photon process. In the experiments, a total of 9,300 holograms are generated to perform the spiral scan; the laser power is set at 10 mW; and the dwell time for each pixel is 400 μs. (Total scanning time is 3,720 ms). Note that the dwell time is purposely set slow for the CCD camera to capture the structure writing process.

Next, we experimentally validate that 3D structures written by the DMD scanner have comparable resolution with conventional raster scanning systems. Figure 5 presents the SEM image of a DMD-scanner fabricated planer grating structure at the DMD's highest pattern rate, i.e., 22.7 kHz. In the experiment, the DMD first fabricates a cubic substrate (20 × 20 μm^2), followed by a grating structure with a target pitch of 1200 nm. In the experiment, 16,000 holograms are generated and used to scan and fabricate the structure. The entire fabrication process is completed within 700 ms, i.e., the pixel dwell time is 44 μs; or the DMD scans at 22.7 kHz. Figure 5B presents a zoom-in view of the grating structure after development, where the linewidth is measured to be 382 nm.

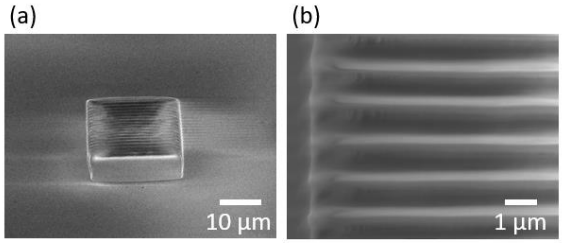

FIGURE 5. DMD Illustration of fabricated structures via TPP: (a) SEM image of printed straight lines with 0.4/1.2 µm linewidth/pitch on a 20 µm X 20 µm cube substrate. (b) Zoomed SEM image of printed straight lines.

TPE IMAGING EXPERIMENTS

By replacing the CCD camera with a PMT, shown in Fig. 1, the TPP fabrication system can be used as a TPE microscope with the unique random-scanning capability. To demonstrate the capability of scanning along arbitrarily defined paths or surfaces in space, the DMD is programmed to scan along spherical and sinusoidal surfaces on pollen samples at 22.7 kHz. Figure 6 presents the imaging results, which show comparable resolution with conventional raster-scanning TPE microscope. In Fig. 6, each optical cross-sectional image contains 100 × 100 pixels, i.e., 10,000 holograms are loaded to the DMD controller for performing this task.

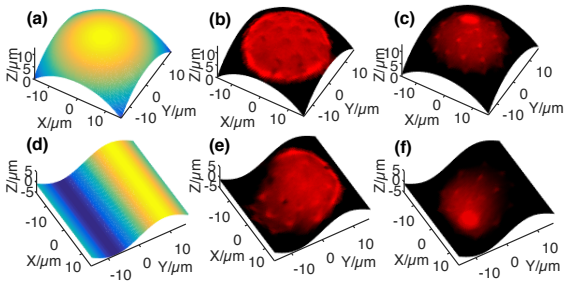

FIGURE 6. Cross-sectional images of two selected pollen grains on arbitrarily programmed spherical and sinusoidal surfaces

CONCLUSION

We present the design of a DMD 3D random-access scanner for applications in TPE imaging and TPP fabrication. In the experiments, we demonstrate the DMD scanner can scan along arbitrarily defined lines and surfaces at the DMD pattern rate, i.e., 22.7 kHz. The new scanning method presents unique advantages in writing complex / hollow structures or imaging scattered points in space, e.g., in vivo neuronal imaging in brains, at high-speed without compromising the fabrication and imaging resolution, which outperforms conventional raster scanning systems. The new method may generate significant impact to the nano-fabrication and biomedical imaging fields.

ACKNOWLEDGMENT

This work is supported by the HKSAR Research Grants Council (RGC), General Research Fund (GRF), (CUHK 439813 & 14202815).

REFERENCES

[1] Lee W. Binary Synthetic Holograms. Applied Optics. 1974, 13(7): 1677-1682.

[2] Cheng J, Gu C, Zhang D, Wang D, and Chen S. Ultrafast Axial Scanning for Two-photon Microscopy via a Digital Micromirror Device and Binary Holography. Optics Letters. 2016, 41(7): 1451-1454.

[3] Geng, Q, Gu C, Cheng J and Chen S. Digital Micromirror Device-based Two-photon Microscopy for Three-dimensional and Random-access Imaging. Optica. 2017, 4(6): 674-677.

[4] Cheng J, Gu C, Zhang D and Chen S. High-speed Femtosecond Laser Beam Shaping Based on Binary Holography Using a Digital Micromirror Device. Optics Letters. 2015, 40(21): 4875-78.

DESIGN OF HIGH RESOLUTION AND HIGH FORCE MEMS TENSILE TESTERS FOR DIRECT METROLOGY OF ADDITIVELY MANUFACTURED SUBMICRON FEATURES

Ian S. Ladner[1,2], Sourabh K. Saha[2], Andrew Cao[2], and Michael A Cullinan[1]
[1]Department of Mechanical Engineering
The University of Texas at Austin
Austin, Texas, USA
[2]Lawrence Livermore National Laboratory
Livermore, CA, USA

ABSTRACT

This paper presents the design of a microelectromechanical system (MEMS) for metrology of additively manufactured (AM) sub-micron polymer parts and nanomaterials such as graphene. The nanomaterial specimen is suspended across two platforms, each lying on a set of capacitive sensors. A thermal actuator pulls the first displacement capacitive sensor whereas the second force capacitive sensor is connected to the actuator through the suspended feature being tested. For precise and accurate characterization of a variety of materials, two different tensile testers have been designed, one with a high displacement resolution of 0.25 nm, Design 1, and the other with a high load capacity of 25 mN, Design 2. Thus, these tensile testers can be used to generate the force-displacement curves for the suspended features, thereby enabling the characterization of the mechanical properties of nanomaterials with unprecedented precision.

INTRODUCTION

Graphene, polymers, and other nanomaterials are emerging candidate materials for transistors, MEMS, and microfluidic devices. However, one of the critical factors limiting their widespread use is limited knowledge of scale dependent material properties, such as elastic modulus and elongation at break, which emerge in the submicron region [1]. A key challenge in characterizing submicron scale features is handling of the sample during the integration between the tested part and metrology system. To address this challenge, previous studies have focused on solving a subset of this problem by adopting in-situ metrology techniques. For example, previous studies have presented in-situ mechanical characterization of multi-walled carbon nanotubes [2] and MEMS sensors to characterize strain tunability of graphene resonators [3]. Here, we extend this concept of in-situ metrology and present the design of MEMS tensile testers that can generate force-displacement responses for a variety of nanomaterials.

A schematic of this tensile tester design and the initial prototype of the fabricated device are shown in Fig. 1. These first-version devices were reused from previous work on tunable graphene resonators and demonstrate the feasibility of integrating an AM part onto the MEMS sensor device. The AM part was fabricated on the commercial *Nanoscribe GT* system via two-photon lithography [4]. Here, we present the design of an improved second

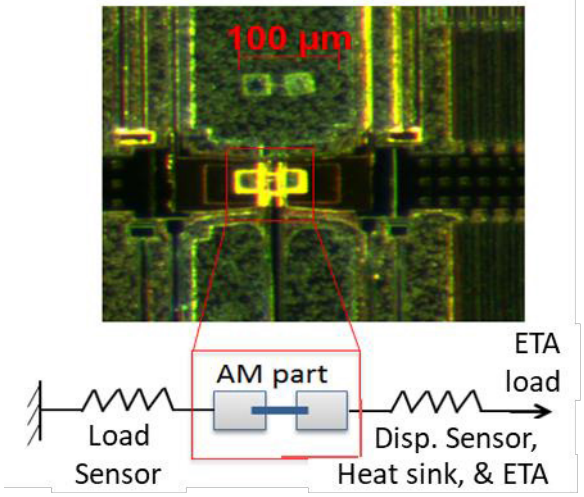

Figure 1: Schematic and first-version fabricated device of the MEMS sensor

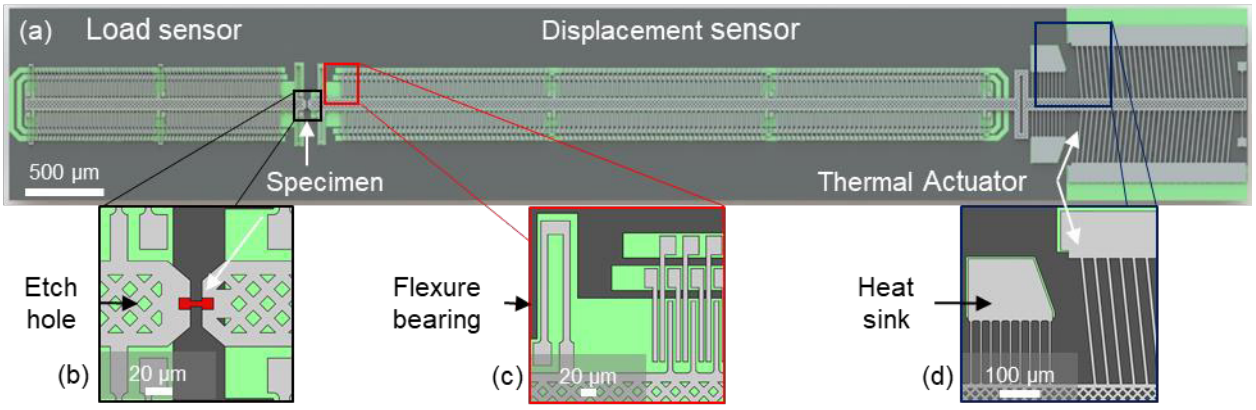

Figure 2: Solid model of the Design 1 tensile tester is shown in (a). (b), (c), and (d) are zoomed in on the specimen across the clamps, the displacement sensor flexure bearing and differential capacitor fingers, and the thermal actuator respectively. In (c) each green trace connects to a different set of fingers to form the electrical contacts for the differential capacitor.

prototype of the MEMS sensors that specifically address (i) the force and displacement resolution and range requirements for AM parts and (ii) resolve fabrication challenges. Specifically, the system is redesigned with stiction control features to resolve fabrication errors and allow wet transfer of parts.

MEMS TENSILE TESTER SYSTEM DESIGN

A model of the high displacement resolution tensile tester is shown in Fig. 2. A chevron style electrothermal actuator (ETA) generates load on the specimen from the displacement stage. Integrated heat sink beams limit the impact of operating temperature on the specimen. Double parallelogram folded-beam pairs suspend and guide the moving shuttle of the displacement sensor. The load stage is composed of only the differential capacitor sensor and folded-beam pairs. Tips at the end of both the displacement and load stage are placed to locate the specimen platforms. Design methods that follow are based off of previous work by Guoao Sun [3], with the notable addition of stiction control.

Thermal Actuator Design

The chevron style ETA is a set of inclined beams in a fixed-guided boundary condition which generates an axial force upon Joule heating. This actuation method is displacement controlled and applies constant strain to the test specimen. Force generated by the actuator can found with Equation 1.

$$F_{ETA} = 2N_{ETA}EA_{ETA}\alpha\Delta T \sin\theta \qquad \text{Eq. 1}$$

Here N_{ETA} is the number of beam seats, E the elastic modulus, A_{ETA} the cross sectional area, α the coefficient of thermal expansion, ΔT the average beam temperature, and θ the incline beam angle as shown in Fig. 3.

Stiffness of the ETA, K_{ETA}, combines all of the displacement sensor components: displacement sensor double parallelogram style flexure bearings K_{disp}, heat sink beams K_{HS}, and ETA beams. Double parallelogram style flexures are used to reduce out-of-plane motion of the central shuttle. The stiffnesses are defined by Equations 2, 3, and 4.

$$K_{disp} = 2N_{disp}\frac{Eb_{disp}^3 h}{L_{disp}^3} \qquad \text{Eq. 2}$$

$$K_{HS} = 2N_{HS}\frac{Eb_{HS}^3 h}{L_{HS}^3} \qquad \text{Eq. 3}$$

$$K_{ETA} = 2N_{ETA}\left(\sin^2\theta\frac{Eb_{ETA}h}{L_{ETA}} + \cos^2\theta\frac{Eb_{ETA}^3 h}{L_{ETA}^3}\right) + K_{HS} + K_{disp}$$

Eq. 4

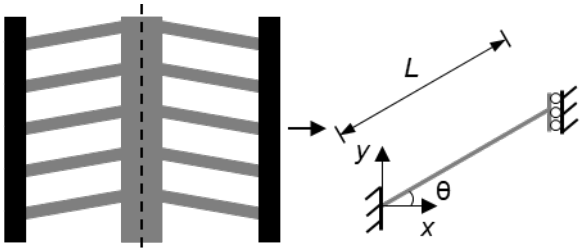

Figure 3: Schematic of a chevron style thermal actuator and a single beam with fixed-guided boundary conditions.

Here, L and b are the beam length and width respectively, h is the beam thickness which is same across all components to simplify fabrication.

Sensor Design

The differential capacitance sensor designed for this work is composed of individual capacitive units shown in Fig. 4. Each unit consists of one moving finger attached to the central shuttle, M, and two stationary fingers, S_1 and S_2. Initially, the gaps between the moving finger and the stationary fingers are equal, d_0. The individual capacitance values are shown in Equations 5 through 7.

$$C_1 = n\varepsilon\left(\frac{A_1}{d_0+\Delta d}+\frac{A_2}{g}+0.65\frac{A_1}{h}\right) \quad \text{Eq. 5}$$

$$C_2 = n\varepsilon\left(\frac{A_1}{d_0-\Delta d}+\frac{A_2}{g}+0.65\frac{A_1}{h}\right) \quad \text{Eq. 6}$$

$$C_3 = n\varepsilon\left(\frac{A_1}{d_3}+0.65\frac{A_1}{h}\right) \quad \text{Eq. 7}$$

where n is number of units, ε is relative permittivity of air, A_1 is the initial overlap area shown in the blue cross hatch pattern in Fig. 4,

Δd is the displacement of M, A_2 is initial overlap of finger and substrate below, g is the gap between finger and substrate, and d_3 is the spacing being S_1 and S_2. Displacement by Δd generates a change in capacitance, ΔC, which is

$$\Delta C \approx \frac{2n\varepsilon A_1}{d_0^2}\Delta d \quad \text{E. 8.}$$

ΔC is set to 0.1 fF for the displacement resolutions of each sensor on Design 1 and 2. This value is twice the previously reported value of 0.5 fF by Espinosa [2] to account for additional noise generated from the wired connection between the MEMS device and MS3110 capacitive readout IC on a separate PCBs.

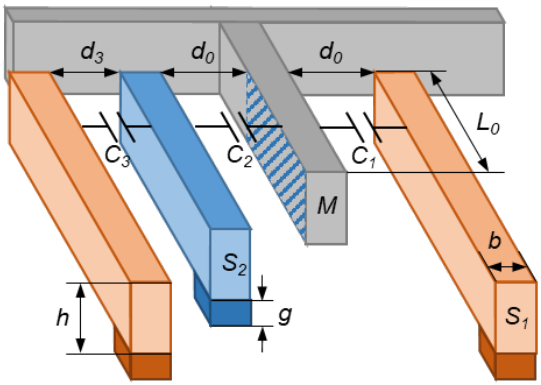

Figure 4: Schematic of differential capacitor with labels. The blue gradient pattern on the M beam represents the initial overlap area, A_1.

Mechanical Model

A lumped mechanical model, Fig. 5, is used to tune the geometry of the ETA, heat sinks, and displacement and load sensor flexure bearings. The resulting system of equations is

$$x_{load} + x_s = x_{ETA} \quad \text{Eq. 9}$$

$$K_{load}x_{load} = K_s x_s \quad \text{Eq. 10}$$

$$K_s x_s + K_{ETA}x_{ETA} = F_{ETA} \quad \text{Eq. 11}$$

where x is the displacement and K is the stiffness of the load sensor, *load*, and specimen, *s*, respectively. Approximate values for Design 1 and 2 specimen stiffness, K_s, are 140 N/m and 8 N/m respectively. K_{ETA} is set to be much greater than K_s and K_{load} to maintain displacement control. The range of the load sensors are defined by K_{load}.

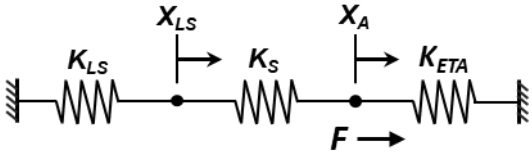

Figure 5: Lumped mechanical model.

Stiction Control

Stiction is a failure mode that is common in MEMS devices where drying after the wet release etch produces capillary forces large enough to permanently adhere the newly suspended structures to the substrate, Fig. 6. Traditionally MEMS devices will only encounter this failure mode during the release etch, however a robust stiction analysis would allow the tensile tester to utilize wet transfer methods for specimens.

Capillary and surface-to-surface adhesion are the main sources of stiction this design will encounter during wet transfer. Mastrangelo and Hsu [5] introduced characteristic equations for both the elastocapillary and peel number respectively. The elastocapillary number, N_{EC}, determines if the elastic energy in a suspended geometry is greater than the applied capillary forces. Peel number, N_P, determines if the suspended geometry will release when brought in contact with another surface. Traditionally, the

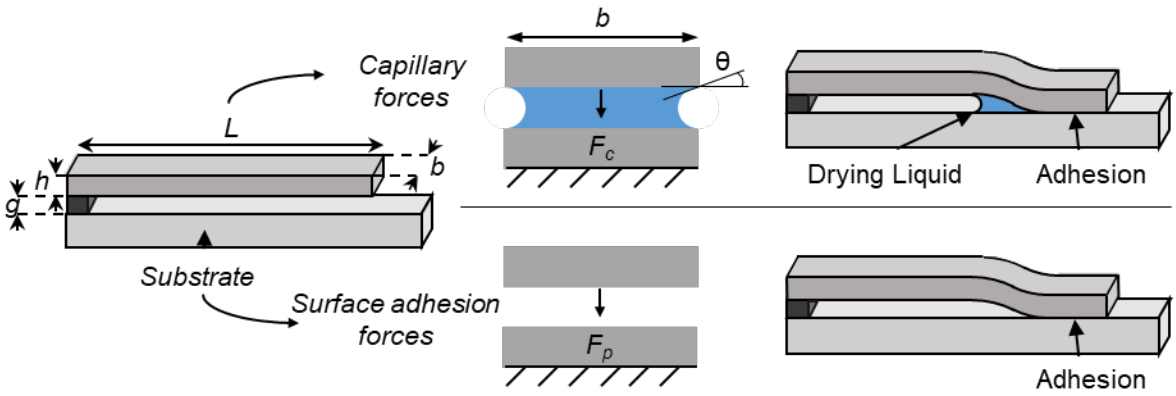

Figure 6: Top portion illustrate capillary force, F_c, induced stiction modeled by the elastocapillary number, and surface adhesion, F_p, results in stiction modeled by the peel number.

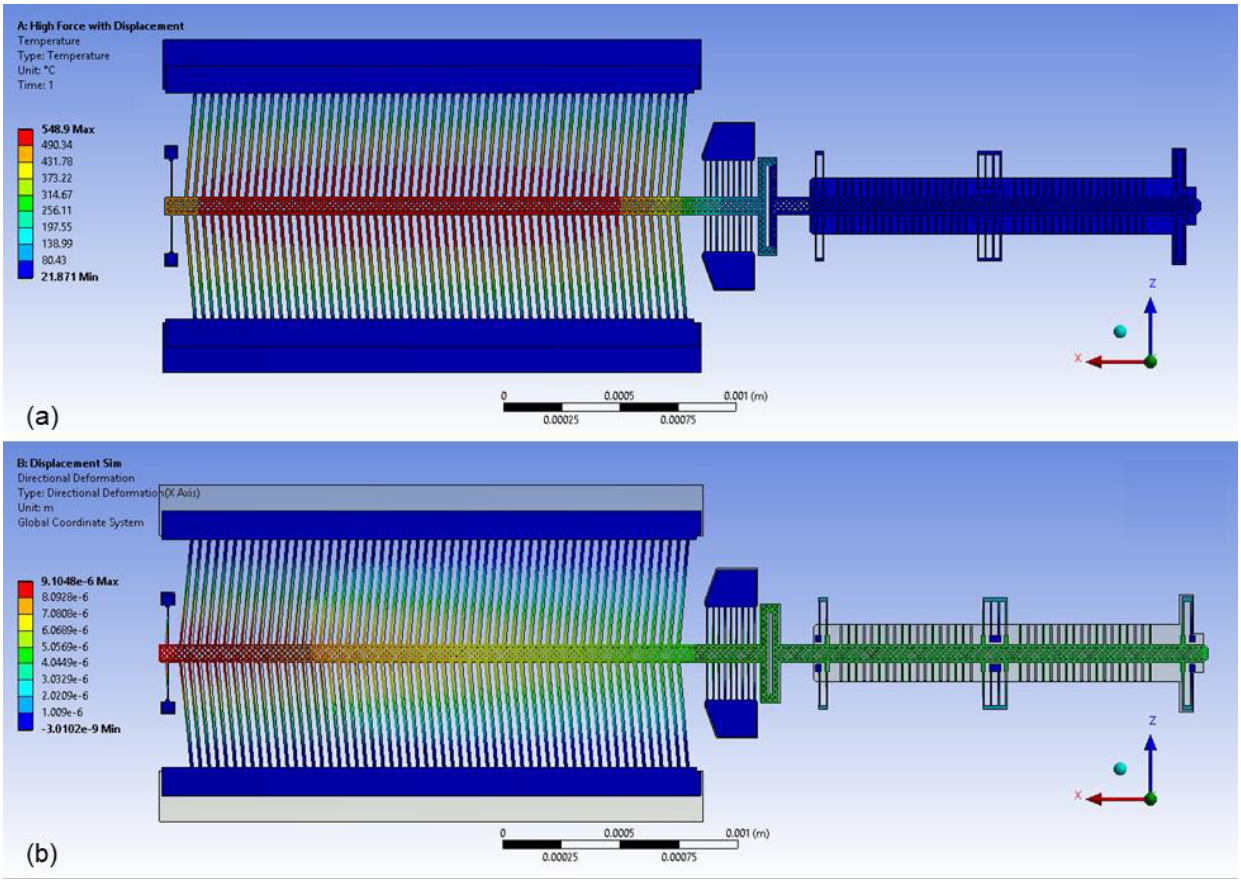

Figure 7: (a) Electrothermal simulation with a maximum temperature of approximately 550°C. A probe was placed on the tip to determine the specimen temperature of 31°C. (b) Mechanical simulation results with the temperature profile as the input load. Displacement at the tip is 4.13 μm X, 10 nm Y, and 5 nm Z.

numbers are set to one and solved for the critical length [5]

$$L_{EC} = \left[\frac{2Eg^2h^3}{9\gamma_l \cos\theta_c(1+h/b)}\right]^{0.25} \quad \text{Eq. 12}$$

$$L_P = \left(\frac{2Eg^2h^3}{9\gamma_s}\right)^{0.25} \quad \text{Eq. 13}$$

where γ_l is liquid surface tension, θ_c is liquid contact angle, and γ_s is solid surface tension.

Vertical and horizontal stiction analysis was conducted on all suspended elements in the design with safety factors of 1.5 for capacitor

fingers and a minimum of 2 for flexure bearings and thermal actuator beams. For our configuration, in Eq. 12 and 13 during horizontal analysis, g is either d_0 or d_3, h is b, and b is h.

In order to achieve the range for the displacement sensor of Design 1 and load sensor of Design 2, the length of the shuttle is in millimeter range, which necessitates additional methods to reduce stiction. This is accomplished by adding hemispherical dimples to the base to reduce the contact area [6]. Spacing between the dimples is set to 60 μm in order to achieve a minimum safety factor of 2 and maximum of 6 of peel number and elastocapillary number.

Design 1 and 2 Results

The device layer is 8 μm of heavily doped polysilicon with $E = 170$ GPa and $\alpha = 2.5\times10^{-6}$ [7]. The performance of Design 1 and 2 is given in Table 1 with a $\Delta T = 550°C$.

Table 1: MEMS tensile tester designed performance.

	Design 1	Design 2
K_s	140 N/m	8 kN/m
Max F	265 uN	25.1 mN
F Resolution	30 nN	3 uN
Max Δd	1.5 um	3.1 um
Δd Resolution	0.25 nm	2 nm

Electrothermomechanical finite element analysis (FEA) of Design 2 in Fig. 7(a) shows the temperature increase and displacement at the specimen. The tip temperature only increases to 31°C which limits the impact of the ETA on the specimen temperature and thus validity of tensile testing data. Displacement at the tip is 4.13 μm which is a good match for displacement without a specimen. Additionally, the out-of-plane displacement is less than 10 nm. This ensures high accuracy and precision during specimen loading.

CONCLUSION

The design of two MEMS tensile testers for the characterization of nanomaterials has been presented. These MEMS sensors provide high precision, in-situ metrology for determining mechanical properties of nanomaterials. In addition, elastocapillary and peel numbers are considered during the design of all suspended structures to allow wet transfer of nanomaterials post fabrication.

ACKNOWLEDGEMENTS

This work was performed under the auspices of the U.S. Department of Energy by Lawrence Livermore National Laboratory under Contract DE-AC52-07NA27344 and by the University of Texas at Austin under Subcontracts B617787 and B621043. Funding available from LDRD-16-ERD-047. Release #LLNL-ABS-728286.

REFERENCES

[1] H. Gao, B. Ji, I. L. Jager, E. Arzt, and P. Fratzl, “Materials become insensitive to flaws at nanoscale: Lessons from nature,” *Proc. Natl. Acad. Sci.*, vol. 100, no. 10, pp. 5597–5600, 2003.

[2] H. D. Espinosa, Y. Zhu, and N. Moldovan, “Design and operation of a MEMS-based material testing system for in-situ electron microscopy testing of nanostructures,” *J. Microelectromech. S.*, vol. 16, no. 5, p. 1231, 2007.

[3] G. Sun, J. H. Cho, and M. Cullinan, “A Method to Manufacture Repeatible Graphene-Based NEMS Devices at the Wafer-Scale,” *Proc. ASME 2016 Int. Manuf. Sci. Eng. Conf.*, pp. MSEC2016–8567, 2016.

[4] S. K. Saha, “Process and Equipment of Two-Photon Polymerization Based Submicron Additive Manufacturing,” in *31st Annual Meeting of the American Society of Precision Engineering*, 2016.

[5] C. H. Mastrangelo and C. H. Hsu, “A simple experimental technique for the measurement of the work of adhesion of microstructures,” *Technical Digest IEEE Solid-State Sensor and Actuator Workshop*. pp. 208–212, 1992.

[6] N. Tas, T. Sonnenberg, H. Jansen, R. Legtenberg, and M. Elwenspoek, “Stiction in surface micromachining,” *J. Micromechanics Microengineering*, vol. 6, no. 4, pp. 385–397, 1996.

[7] Y. Zhu, A. Corigliano, and H. D. Espinosa, “A thermal actuator for nanoscale *in situ* microscopy testing: design and characterization,” *J. Micromechanics Microengineering*, vol. 16, no. 2, pp. 242–253, 2006.

Automated Assembly with Optical Tweezers

Lucas A. Shaw, Samira Chizari, Sydney Austin, Jonathan B. Hopkins
Mechanical and Aerospace Engineering
University of California, Los Angeles
Los Angeles, CA, USA

ABSTRACT
The aim of this work is to demonstrate two advances towards automated manufacturing with holographic optical tweezers (HOTs): (1) a video-feedback-enabled closed-loop automation strategy for positioning large groups of microparticles simultaneously, and (2) a two-photon polymerization chemistry and automated process control algorithm suitable for adhering adjacent particles together. Optical tweezer systems hold the potential to delicately handle and assemble micro- and nano-scale components, but are traditionally low-throughput machines that require a skilled operator. Our system automates many common optical tweezing functions, further improving optical tweezers' prospects as a viable method for micromanufacturing in colloidal media.

INTRODUCTION
Optical tweezers (OTs) [1] provide a powerful tool for micromanipulation and microassembly [2]. In the past two decades, holographic optical tweezers (HOTs) have parallelized OT systems by using a computer-controlled spatial light modulator (SLM) to divide a single input beam into multiple continuously-powered optical traps that can be individually positioned in three dimensions [3]. Unlike other methods for microfabrication such as microstereolithography [4] or electrophoretic deposition [5], the HOT approach allows for an unmatched level of precision in handling and placing microscale objects [6]. The versatility and dexterity of this approach offers the first promising path towards fabricating practical volumes of custom engineered microgranular crystals [7], which offer unique nonlinear dynamic properties that can efficiently route stress waves [8].

In this work, we present two advances towards automated and scalable assembly of colloidal microspheres with the HOT approach: (1) a video-feedback-enabled closed-loop automation strategy for positioning dozens of microparticles simultaneously, and (2) a localized two-photon polymerization chemistry and automated process monitoring algorithm suitable for adhering adjacent particles. The combination of the presented techniques advances the HOT approach towards automated fabrication of microarchitectured metamaterials.

EXPERIMENTAL SETUP
The experimental HOT setup (Fig. 1) consists of a single continuous-wave (CW) laser at 532nm (Laser Quantum Opus 3W), a liquid crystal polarization rotator (LCPR; Meadowlark Optics LPR-100-0532) for rapid power modulation, a 256-by-256 pixel phase-only SLM (Boulder Nonlinear Systems HSP0532-256), and a 100x oil immersion microscope objective (Olympus Plan Apo Lambda, NA 1.45). A Fresnel block is placed at the Fourier plane of the SLM to remove its zero-order undiffracted spot [9].

The ultrafast laser system used for initiating two-photon polymerization reactions includes a Spectra Physics MaiTai eHP DS laser (fs laser). The beam is rapidly switched on and off with an acousto-optic modulator (AOM; IntraAction ATM-802DA2 and ME-802-6) and scanned with a 2D galvanometer mirror system (galvo; Thorlabs GVS012 and National Instruments NI 9263).

Two cameras (Thorlabs DCC1545M) provide simultaneous imaging at 20x and 100x magnifications. The system can rapidly switch between two imaging techniques: (1) darkfield illumination, in which particles have well-defined edges that allow for very robust tracking, and (2) brightfield illumination, in which photopolymer solidified by the femtosecond joining laser is more visible. All system hardware is controlled via MATLAB on a mid-range Dell Precision T3600 computer with a 3.0 GHz quad-core processor and 12 GB of RAM.

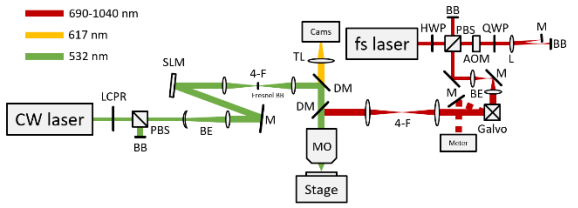

FIGURE 1. Block diagram of the experimental HOT setup (shown in green) and imaging column (shown in yellow).The two-photon joining system (shown in red) will be discussed in the next section. BB: beam block, PBS: polarizing beamsplitter, M: mirror, HWP/QWP: half- or quarter-wave plate, BE: beam expander, 4-F: 4-F telescope lens system, DM: dichroic mirror, TL: tube lens.

CLOSED-LOOP CONTROL FOR AUTOMATED AND PARALLELIZED POSITIONIG

We now present an automation strategy that allows for parallelized and scalable manipulation of large groups of microparticles. Previously, many HOT systems required skilled operators for the complex task of precisely coordinating many microparticles [10,11], but our HOT system utilizes a new closed-loop positioning algorithm that relies on video feedback to rapidly adjust to new obstacles or changing environmental conditions. Previously-published approaches used *a priori* calculations in static environments [12] or were too computationally intensive to scale to dozens of particles [13]. In contrast, the proposed algorithm has the advantage of low computational overhead, enabling real-time operation and the ability to react to new visual information, such as ambient flow or immobilized particles. Furthermore, the algorithm reassigns available particles to desired destinations at each iteration, ensuring that the projected total travel time is minimized.

The process begins with a user-specified set of destination coordinates representing the desired final shape. The general algorithm proceeds as follows:

1. An image is captured by a widefield camera with a field of view of 150μm by 125μm.
2. Particle centroids are determined from the captured image by performing a background subtraction (i.e. a low-passed image is subtracted from the original), adaptive image thresholding, and a connected-component analysis (MATLAB's *regionprops* command). Detected noncircular objects are considered to be obstacles.
3. Particles that are separated by one diameter are typically agglomerated. The distance from each particle centroid to every other particle centroid is used to identify freely-floating, non-agglomerated particles.
4. The linear bottleneck assignment problem (LBAP) is solved [14] to optimally assign detected, non-agglomerated particles to destination locations while minimizing the maximum single path length.
5. A movement action vector is calculated for each assigned particle. The vectors point from the assigned particles' locations to their respective destinations in a straight line. The vector lengths are limited to the optimal step size as determined by *a priori* step-size-versus-step-rate test data.
6. A repulsion vector is calculated to prevent particles from colliding. Particles that are close together are programmed to repel each other with a $1/R^2$ magnitude.
7. Movement action and repulsion vectors are summed and used to calculate an updated set of optical trap locations. The standard Gerchberg-Saxton algorithm [15] with three iterations is used to calculate a new phase pattern for the SLM. If the total number of traps changes due to the appearance or disappearance of particles, the laser power is modulated via the LCPR to maintain a constant amount of power per trap.
8. The remaining cost (i.e. the distances remaining for all particles) is calculated. If all distances are within an acceptable threshold (e.g. 500nm), the control loop ends; if not, the loop iterates from step 1.

The closed-loop controller and aforementioned optical system was used to manipulate between 30-56 polystyrene microparticles of 6.0μm diameter (Figs. 2 and 3). In these examples, the control loop ran at 5 Hz and utilized 6 μm steps.

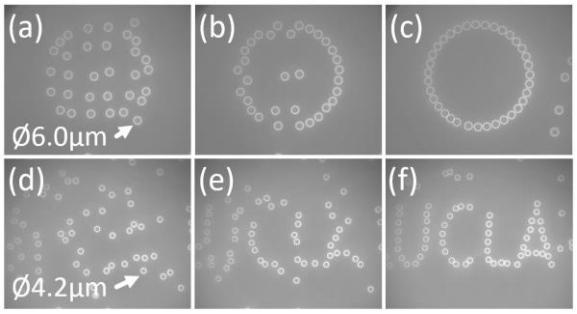

FIGURE 2. Particles are reconfigured into a 35-particle circular pattern (a-c) in six seconds. A "UCLA" pattern is created from 56 particles in eight seconds. Images were acquired through a 20x using darkfield illumination.

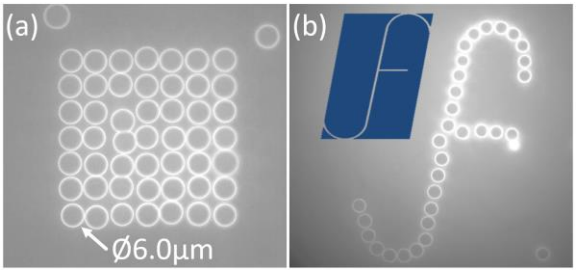

FIGURE 3. Two additional assemblies created with the proposed automation approach. A 7-by-7 array forms a 2D microgranular lattice (a). Arbitrary shapes, such as the Flexible Research Group "f"-logo, require only a set of input coordinates (b). Images were acquired through a 20x camera using darkfield illumination.

PARTICLE JOINING

We now present two advances in particle joining: (1) a new aqueous chemistry that allows for simultaneous and decoupled optical trapping at visible wavelengths and two-photon polymerization at near-infrared wavelengths, and (2) an automated process control used to ensure particle-to-substrate adhesion. The ability to robustly join colloidal particles will enable a variety of microdevices, from granular metamaterials [7] to microfluidic devices [16].

Our unique low-viscosity, water-based medium supports rapid particle positioning and its water-soluble component chemicals are easy to mix. The medium consists of DI water, 1.1M acrylamide monomer, 58mM bis-acrylamide cross-linker, and 9.5mM Irgacure TPO-L. We favor Irgacure TPO-L because of its water solubility, high two-photon polymerization efficiency over a large spectral range in the infrared (610-680nm), and low one-photon polymerization efficiency at the wavelength of our HOT laser (532nm) [17], which allows for simultaneous and decoupled trapping and joining. We employ a similar strategy for joining to those presented in [16,18] but utilize HOT for parallel and scalable manipulation.

When the particles reach their destinations, adjacent particles are automatically joined via a directed femtosecond pulsed beams at 760nm (Fig. 4). The automated joining sequence occurs as follows:

1. A trapped particle reaches its destination and its coordinates are converted to the necessary galvo voltages required to steer the femtosecond pulsed laser to its location.
2. The camera field-of-view is reduced to an area-of-interest (AOI) around the particle for hardware-level, high-framerate monitoring.
3. The galvo mirror positions are updated, the femtosecond laser shutter is opened, and the AOM is switched on, allowing femtosecond pulses to reach the particle.
4. The AOI is monitored at 40 Hz for one of two end conditions: (1) the standard deviation of the location of the particle's centroid drops below a set threshold, signaling a reduction in Brownian motion indicative of adherence to the substrate [19], or (2) the overall brightness of the image increases in response to accumulation of photopolymer.
5. When the end condition is met, the AOM is switched off and the femtosecond laser shutter is closed.

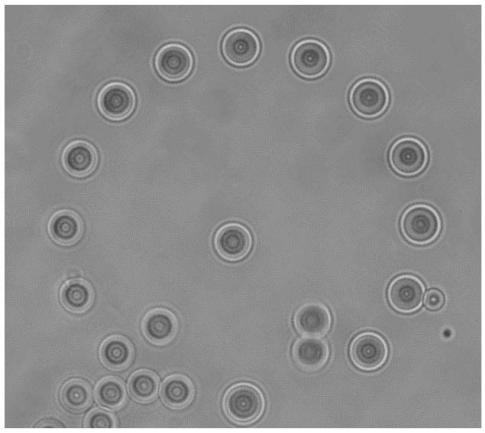

FIGURE 4. A series of 6µm-diameter particles were adhered to the substrate. Images were acquired through a 20x camera using brightfield illumination.

CONCLUSION

In this work we demonstrated two advances towards automated assembly of colloidal microspheres: (1) a closed-loop algorithm for simultaneous positioning of multiple particles, and (2) a chemical medium that supports decoupled handling and joining.

This work was primarily supported by the Air Force Office of Science Research under award number FA9550-15-1-0321. Byung “Les” Lee is gratefully acknowledged.

REFERENCES

[1] Ashkin A. Acceleration and Trapping of Particles by Radiation Pressure. Phys Rev Lett 1970;24:156–9. doi:10.1103/PhysRevLett.24.156.

[2] Ostendorf A, Ghadiri R, Ksouri SI. Optical tweezers in microassembly. Proc SPIE 2013;8607:86070U–86070U–11. doi:10.1117/12.2006127.

[3] Grier DG. A revolution in optical manipulation. Nature 2003;424:810–6. doi:10.1038/nature01935.

[4] Melchels FPW, Feijen J, Grijpma DW. A review on stereolithography and its applications in biomedical engineering. Biomaterials 2010;31:6121–30. doi:10.1016/j.biomaterials.2010.04.050.

[5] Pascall AJ, Qian F, Wang G, Worsley MA, Li Y, Kuntz JD. Light-directed electrophoretic deposition: A new additive manufacturing technique for arbitrarily patterned 3D composites. Adv Mater 2014;26:2252–6. doi:10.1002/adma.201304953.

[6] Köhler J, Ksouri SI, Esen C, Ostendorf A. Optical screw-wrench for microassembly. Microsystems Nanoeng 2017;3:16083. doi:10.1038/micronano.2016.83.

[7] Boechler N, Eliason JK, Kumar A, Maznev AA, Nelson KA, Fang N. Interaction of a Contact Resonance of Microspheres with Surface Acoustic Waves. Phys Rev Lett 2013;111:36103. doi:10.1103/PhysRevLett.111.036103.

[8] Nesterenko VF. Propagation of Nonlinear Compression Pulses in Granular Media. J Appl Mech Tech Phys 1983;24:733–43.

[9] Zhang H, Xie J, Liu J, Wang Y. Elimination of a zero-order beam induced by a pixelated spatial light modulator for holographic projection. Appl Opt 2009;48:5834–41. doi:10.1364/AO.48.005834.

[10] Leach J, Wulff K, Sinclair G, Jordan P, Courtial J, Thomson L, et al. Interactive approach to optical tweezers control. Appl Opt 2006;45:897–903. doi:10.1364/AO.45.000897.

[11] Park I-Y, Sung S-Y, Lee J-H, Lee Y-G. Manufacturing micro-scale structures by an optical tweezers system controlled by five finger tips. J Micromechanics Microengineering 2007;17:N82–9. doi:10.1088/0960-1317/17/10/N03.

[12] Chapin SC, Germain V, Dufresne ER. Automated trapping, assembly, and sorting with holographic optical tweezers. Opt Express 2006;14:13095–100. doi:10.1364/OE.14.013095.

[13] Banerjee AG, Chowdhury S, Losert W, Gupta SK. Real-time path planning for coordinated transport of multiple particles using optical tweezers. IEEE Trans Autom Sci Eng 2012;9:669–78. doi:10.1109/TASE.2012.2200102.

[14] Pundir PS, Porwal SK, Singh BP. A New Algorithm for Solving Linear Bottleneck Assignment Problem. J Inst Sci Technol 2015;20:101–2.

[15] Gerchberg RW, Saxton WO. A practical algorithm for the determination of phase from image and diffraction plane pictures. Optik (Stuttg) 1972;35:237–46. doi:10.1070/QE2009v039n06ABEH013642.

[16] Terray a., Oakey J, Marr DWM. Fabrication of linear colloidal structures for microfluidic applications. Appl Phys Lett 2002;81:1555. doi:10.1063/1.1503176.

[17] Mendonca CR, Correa DS, Baldacchini T, Tayalia P, Mazur E. Two-photon absorption spectrum of the photoinitiator Lucirin TPO-L. Appl Phys A Mater Sci Process 2008;90:633–6. doi:10.1007/s00339-007-4367-0.

[18] Dawood F, Qin S, Li L, Lin EY, Fourkas JT. Simultaneous microscale optical manipulation, fabrication and immobilisation in aqueous media. Chem Sci 2012;3:2449. doi:10.1039/c2sc20351k.

[19] Shaw L, Chizari S, Panas RM, Shusteff M, Spadaccini C, Hopkins JB. Planar Microparticle Assembly and Photopolymerized Joining with Holographic Optical Tweezers. Opt Lett 2016;41. doi:0146-9592/16/153571-04.

Multi-Beam Interference Lithography Based on Evanescent Wave for Functional Nano-Complex Surface

Shuzo Masui[1], Yuki Suzuki[1], Yuki Matsumoto[1], Masaki Michihata[2], Kiyoshi Takamasu[1], and Satoru Takahashi[2]
[1]Department of Precision Engineering,
The University of Tokyo, Bunkyo-Ku, Tokyo, Japan
[2]Research Center for Advanced Science and Technology,
The University of Tokyo, Meguro-Ku, Tokyo, Japan

INTRODUCTION

In recent years, the functional surface structure of living organisms attracts attention and has been studied in the field of biomimetics [1,2]. For example, anti-reflection function of moth eyes, structural color of morpho butterfly etc. Many nano-processing studies have been done to fabricate these functional structures. However, with processing methods such as mask lithography and laser scanning, it is difficult to make a complex surface structure as shown in Fig. 1 with a large area. Because it has complicated dynamics not only in the plane but also in the vertical direction.

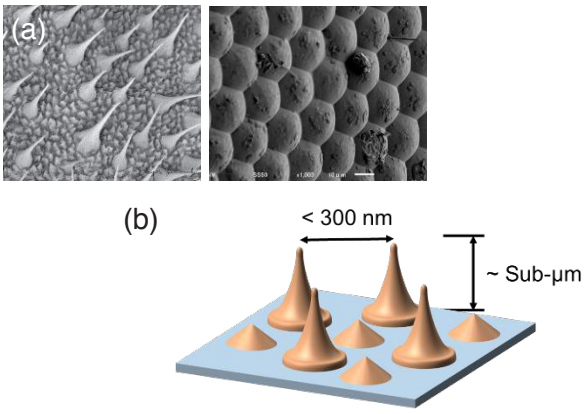

FIGURE 1. Typical nano-complex surface (a) SEM image [3] (b) Schematic

Therefore, we have been developed multi-beam interference lithography using evanescent wave. The evanescent wave is the localized energy at the interface not propagation light. Though some studies utilizing evanescent wave have been reported [4,5], most of them were limited to simple line and space or dot patterns. Therefore, by constructing curing simulation and experimental devices that enables arbitrary interference of up to six beams. It is clarified that the nano-complex surface can be fabricated by a multi-beam interference lithography using evanescent wave.

MULTIBEAM INTERFERENCE LITHOGRAPHY

Evanescent wave

The evanescent light is localized electromagnetic wave which does not propagate from interface. In the coordinate system shown in Fig. 2, the evanescent light is generally expressed as follows:

$$E = A\exp(-z/\beta)\exp(i\omega t - ik_1 x\sin\theta) \left(\beta = \frac{1}{k_2}\sqrt{\left(\frac{n_1}{n_2}\right)\sin^2\theta - 1}\right). \quad (1)$$

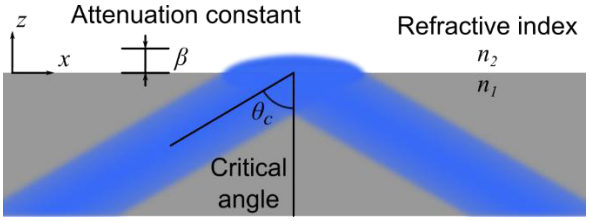

FIGURE 2. Schematic of evanescent wave

Here A, ω and t, respectively, represents the amplitude, the angular frequency, and time. The wave number in higher refractive index media is k_1 and lower one is k_2. The attenuation constant indicating the exudation length of the evanescent light is β. This equation shows the feature that the evanescent wave propagates in the x direction but decays exponentially in the z direction and localized.

Multi-beam interference

Next, the multi-beam interference of evanescent light and propagating light will be described. The polarization of each beams is expressed by using the Jones vector J and amplitude A is calculated by Fresnel's equation. As a result, the electric field of each light is as follows:

$$E(\boldsymbol{r}) = \boldsymbol{J}\cdot A\exp(i\omega t - i\boldsymbol{k_1}\cdot\boldsymbol{r}). \quad (2)$$

Then, the intensity I of the whole interference by m beams ($E_1, E_2, \ldots, E_m$) can be described by

$$I = |\boldsymbol{E}|^2 = (\boldsymbol{E}_1 + \cdots \boldsymbol{E}_m) \cdot (\boldsymbol{E}_1^* + \cdots \boldsymbol{E}_m^*) = \sum_{i=1}^{m} |\boldsymbol{E}_i|^2 + \sum_{p>q}^{m} \boldsymbol{E}_p \cdot \boldsymbol{E}_q^*. \quad (3)$$

This equation shows that the interference pattern can be calculated as the sum of the intensity of each beam itself and combinations of each two-beam interference. Finally, in negative type lithography, photosensitive resin cures when the time-averaged intensity $\langle I \rangle$ exceeds the curing threshold.

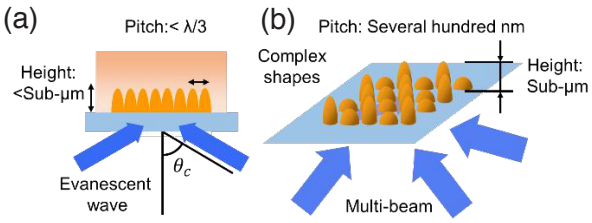

FIGURE 3 Evanescent interference lithography (a) Basic two beams (b) Multi-beam

CURING SIMULASION

We simulated the intensity distribution and cured shapes of proposed method. The coordinate system is designed as shown in Fig.4. For the m_{th} beam, the incident angle θ_m is defined as the angle from z axis and azimuth angle ϕ_m is from positive direction of x axis. A_m and j_m represents amplitude and polarization. These parameters are summarized for each beam is the matrix form in Fig.4.

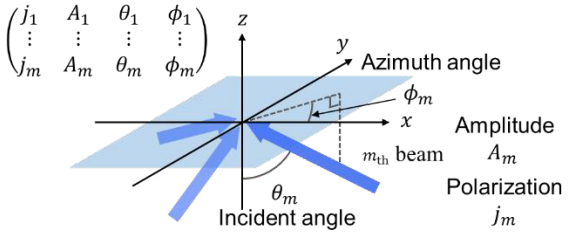

FIGURE 4. Definition of coordinate system

At first, we limited to the one-dimensional interference of several beams to consider intensity distribution of multi-beam interference. The conditions are wavelength λ =488 nm, refractive index in the substrate, resin n_1, n_2 =1.78, 1.5. Under this condition, critical angle is 58°.

Counter propagating two evanescent wave interference was calculated as shown in Fig. 5.

Each beam has equal amplitude and incident angles are θ_1, θ_2=60°. Intensity profile distributed at equal intervals d =158 nm in the x direction and attenuated in the z direction was obtained. The period of interference fringes d is determined by following equation:

$$d = \frac{\lambda}{2n_1 \sin\theta_{1,2} \sin\left(\frac{\phi_1 - \phi_2}{2}\right)} \quad (4)$$

Therefore, various spatial frequencies can be obtained by multi-beam interference at various angles. The point that differs from the interference between the propagation lights is that the interval d changes depending on the wavelength in the substrate and the incident angle. As a result, it is possible to obtain finer structures than using interference lithography without evanescent wave.

Next, three beams interference combining evanescent and propagating light is shown in Fig.6. It turned out that the combination of the evanescent wave and another propagation beam can make complex structure similar to Fig.1(a). If the intensity of the propagating light exceeds curing threshold, the interference fringe of evanescent wave gets buried. However, it was found that complex structures difficult to fabricate by the conventional methods can be processed by the proposed method.

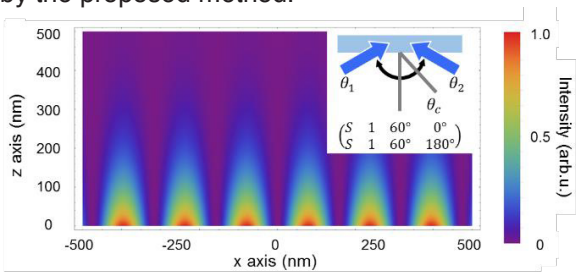

FIGURE 5. Interference of Counter propagating two evanescent wave

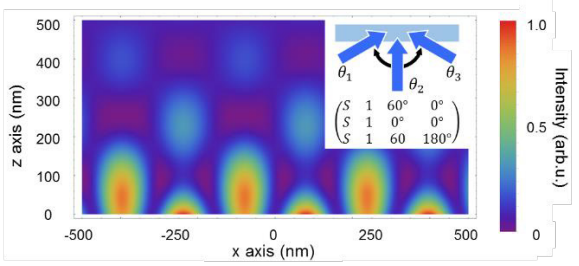

FIGURE 6. Interference of counter propagating evanescent wave and propagation light

Next, the three-dimensional cured shapes were analyzed based on simulated intensity

distribution. The simulated conditions and results are shown in Fig.7. To fabricate complex two-dimensional structures two beams with narrow angle are incident from three directions. We considered that one-dimensional interference fringes from three directions make hexagonal shapes (Fig.7 translucent line). Furthermore, by optimizing the incident condition, it is thought that shapes like a moth eye structure. In theoretical analysis, this method has great potential to fabricate complex surface structure.

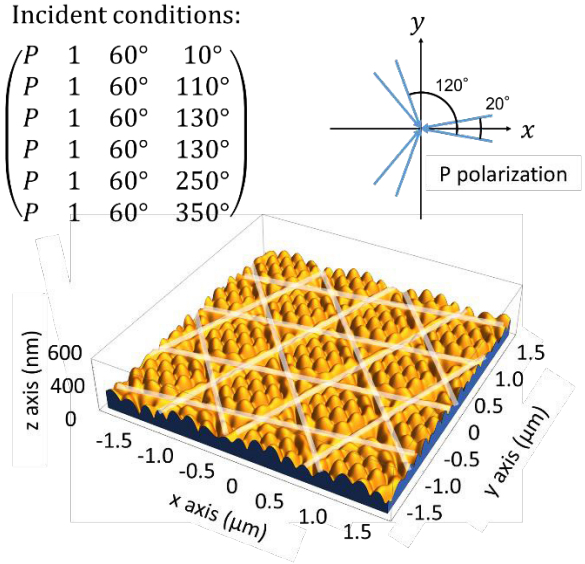

FIGURE 7. Two beams from three directions interference; two-dimensional complex pattern

FUNDAMENTAL EXPERIMENT

Experimental setup

We conducted basic experiments to confirm processing characteristics of proposed method. Schematic diagram of experimental setup is shown in Fig.8. The light source is a semiconductor laser (λ=488 nm) and it was split into six beams by a fiber splitter. In addition, each beam was expanded to a beam diameter of 6.4 mm, a polarization was adjusted by polarizers. A glass substrate (n = 1.78) was placed on a hexagonal sapphire prism (n = 1.78). Immersion oil (n = 1.78) filled between the prism and the substrate to match each refractive index. For the photocurable resin, urethane acrylate resin (UA 510H) was used with an initiator reacting at λ=488 nm (Irgacure 784) at a concentration of 1.0 %wt. Experimentally, the intensity of each beam and the exposure time were adjusted so that the exposure energy becomes 50 mJ/cm^2.In addition, because radical polymerization type resins cause curing inhibition due to dissolved oxygen, exposure was carried out after nitrogen gas blowing for 1.5 hours. Experimentally, it was confirmed that the dissolved oxygen concentration in the resin decreased to about 0.1% by nitrogen blowing for 1.5 hours.

For demonstration of concept of proposed method, basic experiments were conducted under two kinds of exposure conditions. First, the two evanescent waves interference with narrow azimuth angle to obtain micro-order interference fringes. The second condition is two beams from three directions to fabricate two-dimensional complex structures like Fig.7.

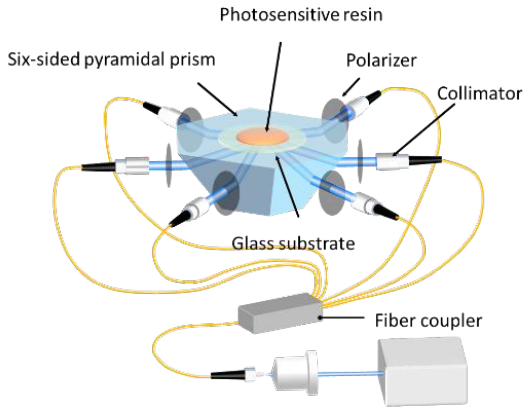

FIGURE 8. Schematic of experimental setup

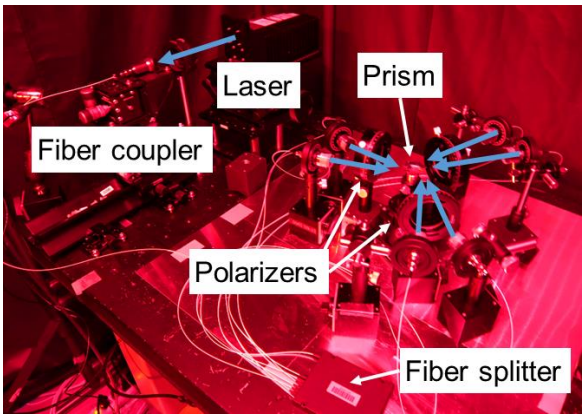

FIGURE 9. Picture of experimental devices

Experimental results

First, to verify basic processing characteristics line and space structure is fabricated by two evanescent wave exposures. The incident angles are 60°, the azimuth angles difference $\phi_1 - \phi_2$ are 16° and both beams are P polarization. The experimental condition is shown in Fig.10 and the observation images of the fabricated structure by the optical and atomic force microscope are shown in Fig. 10, 11. The pitch of interference fringe is 1.2 μm, the height is 260 nm on average.

It was confirmed that the pitch and the profile agree well with the analysis result shown in Fig. 11(a). The structure was observed in the range of 5 mm × 10 mm, and fabrication with a large area can be performed.

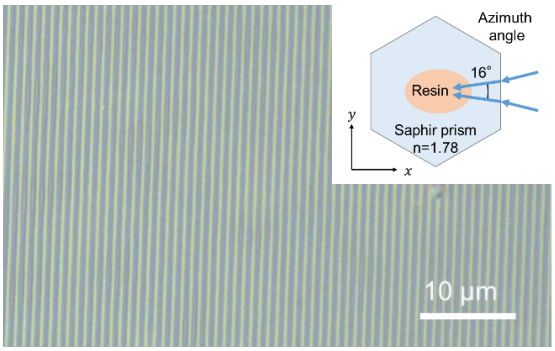

FIGURE 10. Image of optical microscope

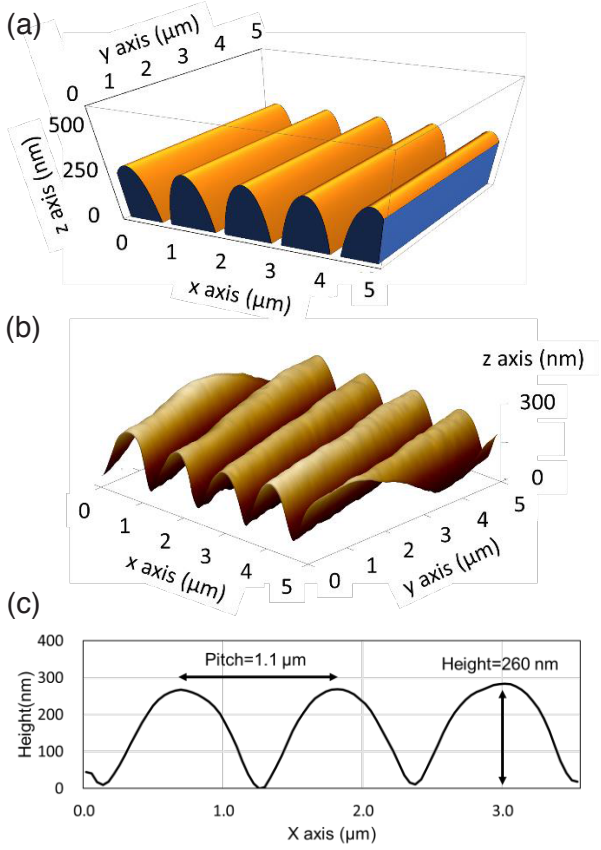

FIGURE 11. (a) Cured shape in simulation (b)Image of AFM (c)Cross-sectional plot (AFM)

Next, the observed image of two beams from three directions are shown in Fig 12. Hexagonal structures can be observed and each peak is spaced at 1600 nm, which agrees well with the theoretical value of 1690 nm. From Equation 3, it could be seen that the 1.6 μm hexagonal structure is formed by overlapping interference of each two beams. As a result, it was confirmed that not only a one-dimensional periodic structure due to basic two beams interference but also a complicated two-dimensional periodic structure can be fabricated.

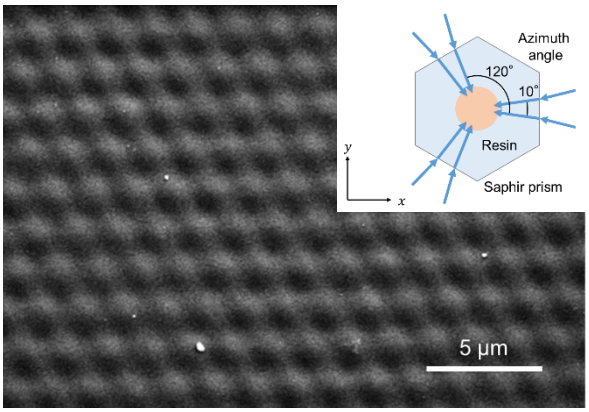

FIGURE 12. SEM image of hexagonal pattern by six beams interference

CONCLUSION

We proposed the application of multi-beam evanescent interference lithography to fabricate functional nano-complex surface. It turned out that intensity distribution of multi-beam interference has unique nanostructures. Furthermore, in the basic experiments, we could fabricate the complex shapes that were in good agreement with the analysis as one- and two-dimensional periodic structures. Therefore, it was confirmed that our fabrication method has potential applicability to wide range of surface structures. As a future work, we will fabricate finer structures and evaluate optical functionality (e.g., antireflection, form birefringence).

REFERENCES

[1] P. B. Clapham, M. C. Hutley, “Reduction of Lens Reflexion by the “Moth Eye” Principle”, *Nature*, vol. 244, pp.281-282, 1973

[2] A. R. Parker, "515 million years of structural colour." *Journal of Optics A: Pure and Applied Optics* 2.6 (2000): R15.

[3] “CATERPILLARBLOG” https://caterpillarblog.com/

[4] J. C. Martnez-Anton, “Surface relief subwavelength gratings by means of total internal reflection evanescent wave interference lithography,” J. *Opt. A Pure Appl. Opt.*, vol. 8, pp. S213–S218, 2006.

[5] Sainov, Simeon, et al. "High spatial frequency evanescent wave holographic recording in photopolymers." *Journal of Optics A: Pure and Applied Optics* 5.2 (2003): 142.

Computer Generated Holograms as 3-Dimensional Calibration Artifacts

Robert E. Parks[1], John C. Ziegert[2], and Jesse Groover[2]
[1]Optical Perspectives Group, LLC
Tucson, AZ, USA
[2]Department of Mechanical Engineering and Engineering Science
University of North Carolina at Charlotte
Charlotte, NC, USA

ABSTRACT
The positioning accuracy of multi-axis machine tools and coordinate measuring machines are often checked using ball bars or ball plates where the spatial locations of the balls are externally calibrated to provide a traceable artifact[1,2]. In use, the individual ball surfaces are probed in at least 4 places with a tactile sensor and the points of contact fit to the equation of a sphere to determine the center of the ball. The method is tedious, indirect and semi-static. Furthermore, it is difficult or impossible to create artifacts that truly span the three-dimensional work volume of machines because some features become occluded by others and cannot be accessed.

CGHs AS CALIBRATION ARTIFACTS
This paper explores the use of computer generated holograms (CGH) as virtual 3D calibration artifacts for multi-axis machine tools. A CGH can be fabricated on a fused silica photomask substrate using a microlithographic process to create very high accuracy artifacts that emulate a wide variety of 3-D shapes, including arrays of balls, cylinders, cones, etc. The virtual features on the CGH are interrogated with a point source of light such as produced by an autostigmatic microscope (ASM)[3,4]. The location of the ball centers in two directions parallel to the plane of the CGH can be read by the ASM with resolution of less than one micrometer, and to a few μm in the third dimension.

Two CGH artifacts are demonstrated here. Figure 1a shows a CGH that has a hexagonal close-packed array of Fresnel zone patterns on 28 mm centers in the CGH plane. Within each pattern are concentric Fresnel zones simulating different ball centers, or heights above the CGH, at heights of 5, 15, 45 and 135 mm. The small zones between the larger array have virtual radii of 6.35 and 12.7 mm to match the radii of common ball sizes. Figure 1b shows an axicon[5] that simulates a cone whose central axis is perpendicular to the plane of the CGH.
In use, the CGH is probed at each plane of virtual balls, or along each virtual line, providing

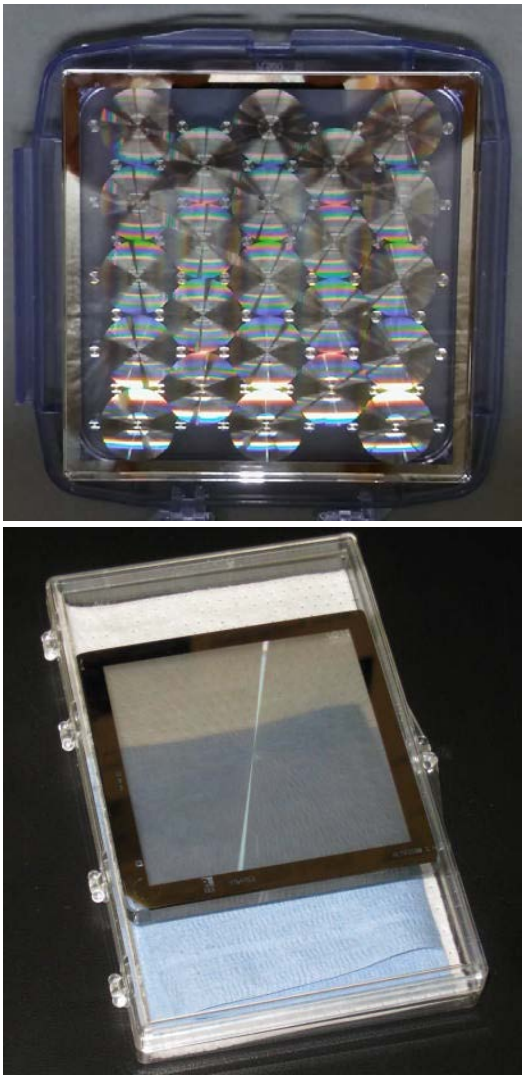

FIGURE 1: a) virtual 3-D ball array CGH; b) virtual axicon CGH

a check of the positioning accuracy of the machine in three dimensions. In principle, scale errors in all three directions can be measured, along with straightness and squareness of the axes. By comparing positioning errors along parallel lines in the workspace, roll, pitch and yaw error motions of each axis can also be determined.

In this research, a Point Source Microscope is used as the ASM and a Mori Seiki NMV5000 CNC 5-axis milling machine as the test bed. Figure 2 shows the PSM mounted on the spindle of the machine, and the virtual ball array CGH mounted on the table. Note that the PSM allows the ball center positions to be determined in three dimensions with a single measurement, and with sub-micron accuracy in X and Y, and a few microns in Z.

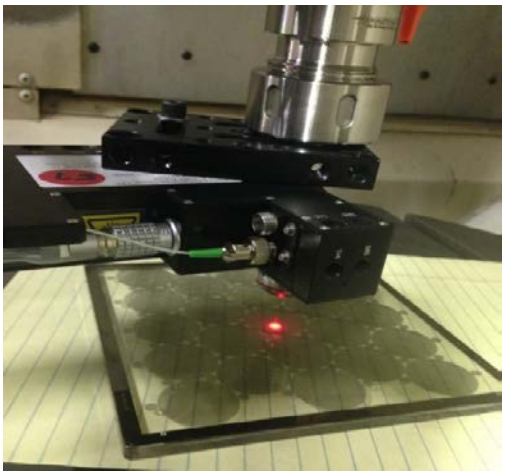

FIGURE 2. CGH on table and PSM mounted in the spindle of the Mori Seiki NMV5000.

PSM SCALE FACTOR DETERMINATION

The PSM "measures" in the X-Y plane by determining the location of the centroid of the reflected spot on a CCD pixel array. Pixel locations are converted into metered coordinates by moving the PSM over known displacements while recording the pixel location of the centroid. Figure 3 shows typical calibration data, resulting in scale factors in the X direction of 1.287 µm/pixel and in the Y direction of 1.285 µm/pixel. The PSM can also estimate position in the Z-direction by evaluating the focus quality of the reflected spot with uncertainties estimated to be in the range of a few microns. Because of the higher uncertainties, the Z measurements of the PSM were not used in this research.

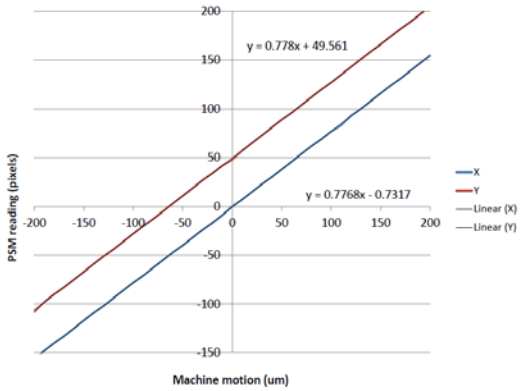

FIGURE 3: PSM Scale factor data in X and Y directions. Curves offset vertically for clarity.

PSM MEASUREMENT REPEATABILITY

The repeatability of the PSM was evaluated by mounting it on a Moore UMM located in a well-controlled environment. This machine is highly stable with vibrational disturbances and axis positioning repeatability on the nanometer level.

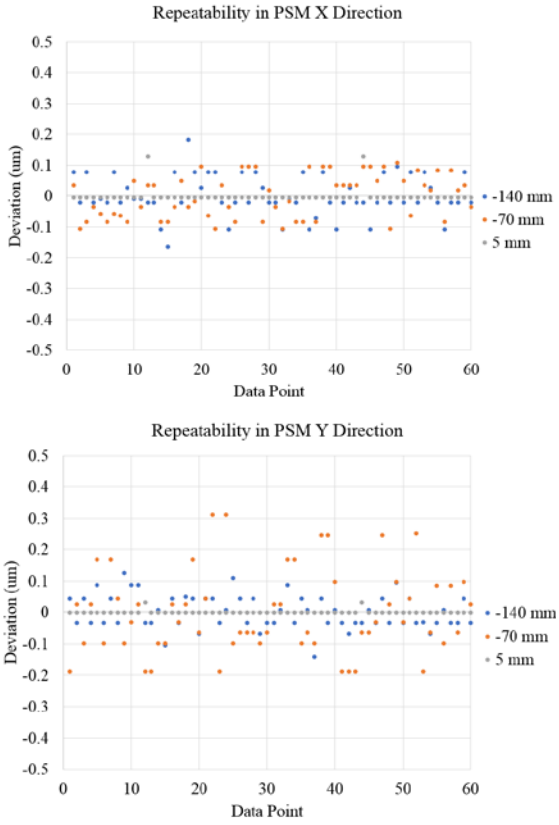

FIGURE 4. PSM measurement repeatability in the X and Y directions.

The PSM was focused on the axicon CGH at distances of 5, 70 and 140 mm from the surface, and readings were taken at 10 second intervals over a period of 10 minutes. Figure 4 shows the results of these measurements in the X and Y directions.

It can be seen that the PSM measurements are repeatable to within a few tenths of a micron. Measurements were also taken by jogging the machine away from the initial position and back multiple times. The results are virtually identical to Figure 4, and consistent with the nanometer-level positioning repeatability of the Moore UMM. The better repeatability at 5mm is largely due to the very short optical path in air.

MORI SEIKI Z-AXIS STRAIGHTNESS MEASUREMENT USING THE AXICON CGH

The axicon CGH was mounted on the table of the Mori Seiki milling machine, and the axes moved to center the PSM over the virtual vertical axis of the CGH. The Z-axis of the machine was then exercised bi-directionally over 300 mm of vertical motion in 5 mm increments. The C-axis of the machine was then rotated 180 degrees and the process repeated; enabling a reversal calculation to separate the straightness errors of the machine Z-axis from the straightness errors of the CGH virtual axis. The best-fit straight line, representing the misalignment between the CGH and machine axes, was removed from each data set. Figures 5 and 6 show the results of these measurements.

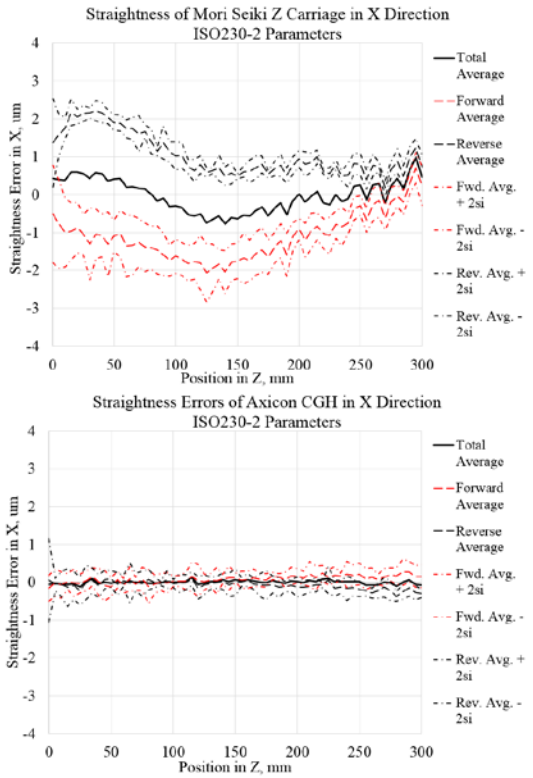

FIGURE 5. a.) Straightness of the Mori Seiki Z axis in the X direction, b.) Straightness of the axicon CGH virtual axis in the X direction.

The results show that the straightness of the axicon CGH virtual axis is on the same order of magnitude as the measurement repeatability of the PSM, reflecting the expected accuracy of the semiconductor lithographic processes used to create it.

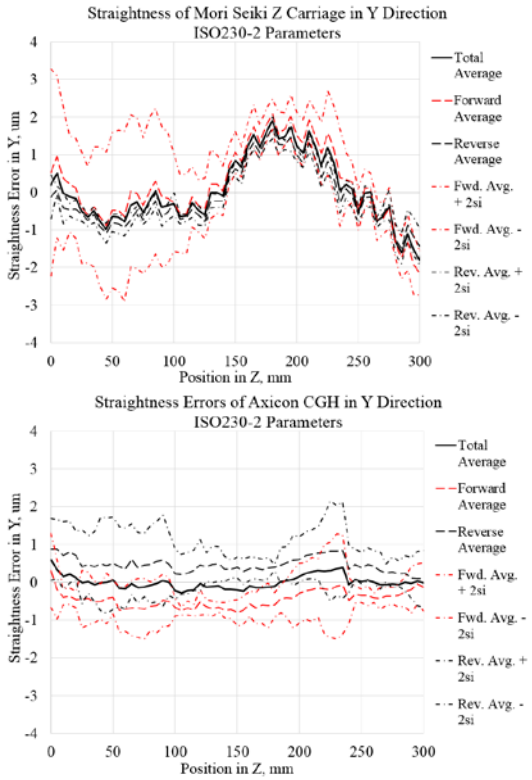

FIGURE 6. a.) Straightness of the Mori Seiki Z axis in the Y direction, b.) Straightness of the axicon CGH virtual axis in the Y direction.

MORI SEIKI VOLUMETRIC POSITIONING ACCURACY USING THE VIRTUAL 3-D BALL ARRAY CGH

The virtual 3-D ball array CGH was mounted on the Mori Seiki table, as shown in Figure 2. The CGH was aligned with the machine by jogging the machine until the center virtual ball at the lowest level was centered on the PSM display, and rotating the machine C axis until the furthest

virtual ball along the X direction had no errors in the Y direction. The machine was then programmed to move to the location of every virtual ball center, and then record the location of the center point relative to the PSM. Each point was approached by moves in the positive X and Y directions, so no axis reversal errors are included in the data. It is assumed in this data that the CGH and PSM measurement tool

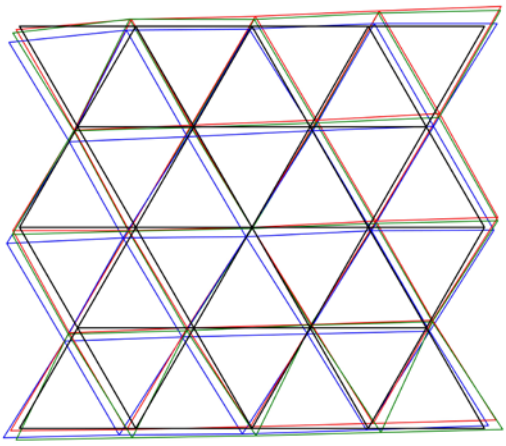

FIGURE 7. Mori Seiki positioning errors using virtual ball array CGH. Black is nominal point location, red at 5 mm above CGH, green at 15 mm and blue at 45 mm. (Note: Errors magnified 4000X for visibility)

were perfect and all errors are in the machine. Figure 7 shows the results.

Several features are immediately obvious in Fig. 7; there is an overall counterclockwise skewness at all 3 heights. At the lower 2 heights the maps are fairly well aligned, but as the spindle was raised another 30 mm the 45 mm height pattern shifts as a whole toward the minus x and y directions.

In addition, since there are data at 3 heights it is possible to connect corresponding points vertically to determine pitch and roll, while the rotation at the apexes of the triangles gives local yaw. It is apparent there is more data in this map than first appears.

CONCLUSIONS AND FUTURE WORK

Clearly these experiments have barely begun to make use of the potential data here. Also, the CGH used in the experiments was designed to see if it would behave as expected, rather than as an artifact for machine tool calibration. A next version of the CGH would have virtual points evenly spaced in the vertical direction and at larger distances from the CGH to better fill the work volume of a machine tool.

There is also the question of reversal and how to separate errors in the metrology from errors in the machine with the virtual ball artifact. One possibility for reversal is to flip the CGH upside down and view the virtual points through the back of the CGH.

ACKNOWLEDGEMENTS

One of us (R. P.) would like to acknowledge the help and hospitality of John Ziegert, and his student, Jesse Groover, for the use of the Mori Seiki machine in John's Lab and the taking and analysis of the data for this paper by Jesse.
Also, we acknowledge Chunyu Zhao of Arizona Optical Metrology for designing and supplying the CGHs used in this work.

REFERENCES

1. Xiaogeng Jiang, Robert J. Cripps,"A method of testing position independent geometric errors in rotary axes of a five-axis machine tool using a double ball bar", International Journal of Machine Tools & Manufacture 89 (2015) 151–158

2) Liebrich, T., et. al. "Static and dynamic testing of machine tools" (2010), www.inspire.ethz.ch/iwf/specials/mttrf/research/static_dynamic_2010.pdf

3) Drysdale, C.V., "On a simple direct method of determining the curvatures of small lenses", Trans. Opt. Soc. London, **2**, 1-12, (1900).

4) Steel, W.H., "The Autostigmatic Microscope", Optics and Lasers in Eng., **4**, 217-27 (1983).

5) McLeod, J. H., "The Axicon: A new type of optical element", JOSA, 44, 592-7 (195

6) Point Source Microscope, a commercially available ASM, www.optiper.com.

COLORED LIGHT INTERFEROMETRY

Mehrdad Abolbashari,[1,*] Mohammad Azari,[2,3] Nasim Habibi,[2,3] Faramarz Farahi,[2,3]

[1]OPTONIKS CORP, PORTAL Building, 9319 Robert D. Snyder Road, Charlotte, NC 28223, USA
[2]Center for Optoelectronics and Optical Communications
[3]Center for Precision Metrology
University of North Carolina at Charlotte
Charlotte, NC, 28223, USA
Corresponding author: m.abolbashari@optoniks.com

1.INTRODUCTION

White light interferometry is a well-known interferometric technique for profilometry [1]–[3]. A broadband source (white light) with short coherence length is used as the light source; when the interferometer is balanced, the visibility of the signal is maximum and decreases rapidly by unbalancing the interferometer due to the short coherence length of the light source. Knowing the exact length of one arm of the interferometer and locating where the interferometer is balanced, the length of the other arm of the interferometer can be obtained. There are different methods to locate maximum visibility of interferometer fringes [4]–[7]; one of these methods is finding the peak of the envelope of the output signal of the interferometer [4], [7]. This is where all the interferograms corresponding to different wavelengths of the light source overlap to form sharp clear fringes. Figure 1 shows a typical output of the white light interferometer where the light source has a broadband Gaussian spectral profile.

There are two issues that are associated with the white light interferometry; one is the measurement resolution and the other is the need for a mechanical scan to obtain the interferograms.

One way to increase the resolution of the system is to increase the bandwidth of the light source, which results in a narrower envelope. There are several techniques to make a broadband light source or increase the resolution. Gerges et al. [8] have proposed the use of a multimode laser diode as a broadband light source, Chinn and Swanson [9] used a frequency-tunable light source to make a broadband light source, Zhang and Sato [10] proposed implementing a broadband light source by optimal synthesis of LEDs to improve the resolution in Optical Coherence Tomography (OCT), Tripathi et al. [11] combined the spectra of two superluminescent diodes to generate a spectrum with significant modulation to improve the OCT images.

Akcay and Rolland [12] used a light source and a programmable spectral processor to shape the spectrum in order to increase resolution by improving the point spread function in OCT, Hsu et al. [13] used dispersive materials to shape the spectrum of a non-Gaussian light source to increase resolution of OCT images, Choi et al. [14] employed a fiber-based spectral filtering using long period fiber grating and erbium doped fiber absorber to produce a Gaussian shape spectrum to increase the resolution in OCT, and Gong et al. [15] optimized the point spread function of the light source by a spectral shaping technique to increase the resolution in an OCT system.

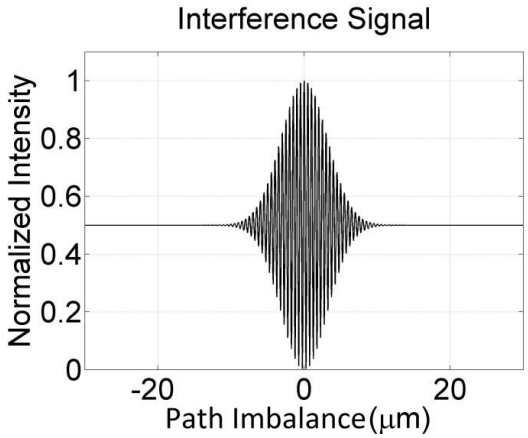

Figure 1: The output signal of a white light interferometer with a light source with Gaussian shape spectrum in the range of 450nm-550nm.

In all previously reported works, the focus has been on the first issue, that is the measurement resolution in white light interferometers, and the issue of meachanical scan has not been addressed. The solutions that have been proposed for resolution enhancement are either based on broadening the light spectrum or improving the shape of the peak for an interference signal with only one peak.

In this paper we introduce a new technique, Colored Light Interferometry (CLI), that offers a better resolution than a conventional white light interferometer, and minimizes or eliminates the need for mechanical scanning, which in turn increases the measurement

speed and eliminates a mechanical source of error. CLI improves the measurement resolution by generating an interference signal with multiple peaks and using the correlation between the peaks. As it will be shown, this can be accomplished by designing the interference signal and calculating the corresponding light source spectrum. Methods to conduct the white light interferometry measurements by manipulating the light source spectrum will be described. Two specific examples, measurement of a step artifact and the measurement of a sloped surface will be given to show how the measurement can be facilitated and improved by CLI. We will discuss how this technique can be used for measurement of free form profiles with minimum or no need to mechanical scan. Additionally, by using this technique, a white light interferometer will be capable of measuring thickness of multilayer films with no vertical scan.

In the next section the theoretical aspect of CLI will be described and an example is presented. Next, the techniques for step measurement with no or minimum mechanical scan are explained. Finally, measuring the slope with minimum or no meachanical scan will be explored.

2.COLORED LIGHT INTERFEROMETRY PRINCIPLE

Mathematically speaking, for a source with the spectrum of $s(f)$, the interferogram of an interferometer can be expressed as

$$S(\tau) = \int_0^\infty s(f)\big(1 + cos(2\pi f\tau)\big)df = \int_0^\infty s(f)df + \int_0^\infty s(f)cos(2\pi f\tau)df \quad (1)$$

where τ represent the delay time between two arms of the interferometer, and the transmittance of the interferometer and the detector response are assumed to be flat and equal to one.

The second term on the right hand side of the equation (1) is the interference term and can be stated as

$$F(\tau) = \int_0^\infty s(f)cos(2\pi f\tau)df = \int_0^\infty \big(s_e(f) + s_o(f)\big)cos(2\pi f\tau)df = 2\int_{-\infty}^{+\infty} s_e(f)cos(2\pi f\tau)df \quad (2)$$

where $s_e(f)$ and $s_o(f)$ are even and odd parts of the source spectrum.

Since $s(f)$ is a real function, then the interference can be written as

$$F(\tau) = 2\int_{-\infty}^{+\infty} s_e(f)cos(2\pi f\tau)df = 2Re\left\{\int_{-\infty}^{+\infty} s_e(f)e^{+i2\pi f\tau}df\right\} = 2Re\{\mathfrak{F}^{-1}(s_e(f))\} \quad (3)$$

where $\mathfrak{F}^{-1}(.)$ is the inverse Fourier transform and $Re\{.\}$ is the real part.

Conversely, if $F(\tau)$ is the interference pattern, since $F(\tau)$ is a real and even function, then the light source spectrum can be calculated as

$$s(f) = 2s_e(f) = \mathfrak{F}\{F(\tau)\} \quad for\ f \geq 0 \quad (4)$$

where $\mathfrak{F}\{.\}$ is the Fourier transform.

Equation (3) is used in the Fourier spectroscopy to calculate the spectrum of the light source and equation (1) defines the envelope of the interference pattern that is used in white light interferometry.

As it is seen in equations (3) and (4), the interference pattern and the light source spectrum are the Fourier transform pair and therefore a light source with a broader bandwidth results in an envelope with narrower peak, hence better measurement resolution.

In CLI, a combination of sources or a source with an engineered spectrum will be used to shape the output signal of the interferometer. As an example, Figure 2 shows interference signal for three Gaussian sources with spectra in the ranges of 400nm-500nm, 500nm-600nm, and 600nm-700nm. As it is shown, the shape of the signal is different from Figure 1 and other than a main peak at zero path imbalance, there are two other peaks at about 4μm distance from the main peak. These peaks are correlated and as it will be shown below, their correlation information can be used to identify the main peak more precisely (resolution improvement), which is indicator of the balanced position.

In the above example, assume that the sampling rate is $1/T_s = 50$ samples/μm and we select the sample with maximum value to represent a peak position (zero path imbalance). Since the sampling positions are not always in synchronous with the balanced position, for a conventional white light interferometer the resolution will be half of the sampling period i.e. the actual balanced position will be within ±0.01μm of the detected peak position where the intensity is maximum. Now we define jitter as the distance between actual balanced point and where the measured value of interferemeter signal is maximum. As it is shown in Figure 3.a when the jitter is whithin the error range ($\pm T_s/2$), the detected peak position shows the zero path imbalance. For CLI, in the above example, other than the main peak we have two side peaks. We define the geometrical mean position of those peaks as a detected peak position. Figure 3.b shows the detected peak position when the jitter is again

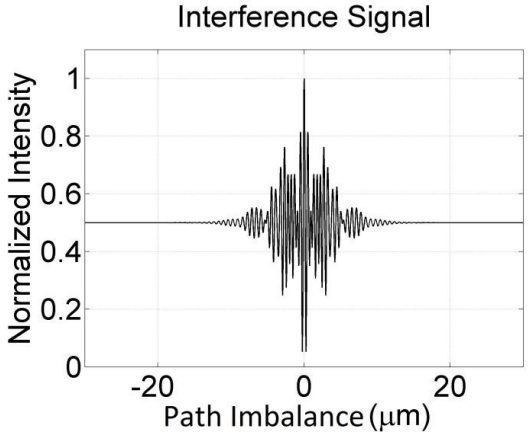

Figure 2: The output signal of a white light interferometer with a combination of three light sources with Gaussian shape and the bandwidths of 400nm-500nm, 500-600nm and 600nm-700nm.

within $\pm T_s/2$. As it is seen the CLI can detect the nonzero path imbalance even when the jitter is within the error range of conventional white light interferometer; namely, when the jitter is greater than about $T_s/4$ the CLI detects the jitter, e.g. unlike conventional white light interferometer, CLI can distinguish between the jitter of $+T_s/3$, 0, and $-T_s/3$. Therefore, in this example, CLI enhances the performance of a conventional white light interferometer by a factor of two.

In the next section we demonstrate how the CLI is capable of measuring the steps of an artifact with minimum or no mechanical scan.

3.STEP MEASUREMENT

The main aspect of CLI is the interference signal design. The interference signal is designed in order to obtain better resolution, simpler peak detection and faster measurement speed, reduce the need for mechanical scanning, and/or less computational cost.

To demonstrate the performance gain using CLI we describe a few practical scenarios. The first scenario is the measurement of a step artifact. We design an output

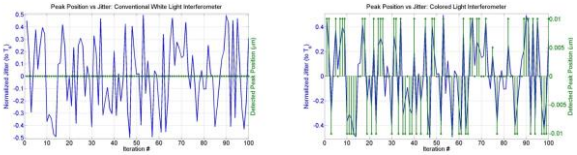

(a) (b)

Figure 3: The detected peak position (green line) for jitter (distance between the actual balanced position and the detected peak position) whithin $\pm T_s/2$ (blue line) where $T_s = 0.02\mu m$. (a): The white light interferometer cannot detect the jitter when the jitter is within half of the sampling period. (b): The CLI detects the jitter by exploiting the extra information from side peaks and therefore can improve the resolution of the measurement system.

interference signal that has two distinct peaks away from the main peak at τ_0 distance from the main peak, which corresponds to the step size $d = c\tau_0$ where c is the speed of light in the medium. Equation (4) is used to calculate the light source spectrum based on the output signal design. The output signal can be represented as:

$$F_m(\tau) = F(\tau) + {}^1\!/_2\{F(\tau-\tau_0) + F(\tau+\tau_0)\} \quad (5)$$

where $F(\tau)$ is the interference signal for light source with simple flat or Gaussian spectrum in visible range.

Using equation (4), the spectrum of the light source (for positive frequencies) is calculated as:

$$\begin{aligned} S_m(f) = \Im\Big\{ & F(\tau) + {}^1\!/_2\{F(\tau-\tau_0) \\ & + F(\tau+\tau_0)\}\Big\} \\ & = s(f) \\ & + {}^1\!/_2\, s(f)\{e^{i2\pi f\tau_0} \\ & + e^{-i2\pi f\tau_0}\} \\ & = s(f)[1+cos(2\pi f\tau_0)] \\ & = 2s(f)cos^2(\pi f\tau_0) \quad for\ f \\ & \geq 0 \end{aligned} \quad (6)$$

where $s(f)$ is the spectrum of light source with a simple flat or a Gaussian shape in the visible range. As equation (6) indicates, the amplitude of spectrum $s(f)$ is modulated. To implement such a light source, the light source should be frequency modulated. One way to realize this frequency modulation is to use a series of notch filters in front of a broadband light source $s(f)$. Using a spatial light modulator (SLM) along with a diffractive grating or a prism are two practical ways for spectral shaping [12]. Two examples of SLMs are the DMD (Digital Micromirror Device) and LCoS (liquid Crystal on Silicon) modulators with resolution up to 1920x1080 that can sample the visible spectrum (400nm-700nm) with resolution of 300/1920 = 0.156nm. Therefore a high resolution spectrum can be shaped to achieve the designed interference signal.

Figure 4 shows the interference signals and the light spectrum when $s(f)$ is a flat spectrum in the visible range (400nm-700nm) (Figure 4.a,b), and when $s(f)$ is a Gaussian spectrum in the visible range (Figure 4.c,d) with $\tau_0 = 50 \times 10^{-15} sec$, which corresponds to the $15\mu m$ step height. Therefore, when a camera is used to acquire interference images of a step function with $15\mu m$ step height, the visibility should never be zero along the whole image that covers both the lower and the upper levels of the step artifact.

One interesting scenario is when the approximate step height is known in advance. In this situation the interference signal can be designed to have two peaks with the separation equivalent to the typical step height and the exact step height is measured by minimally scanning around the typical height value. For example, if

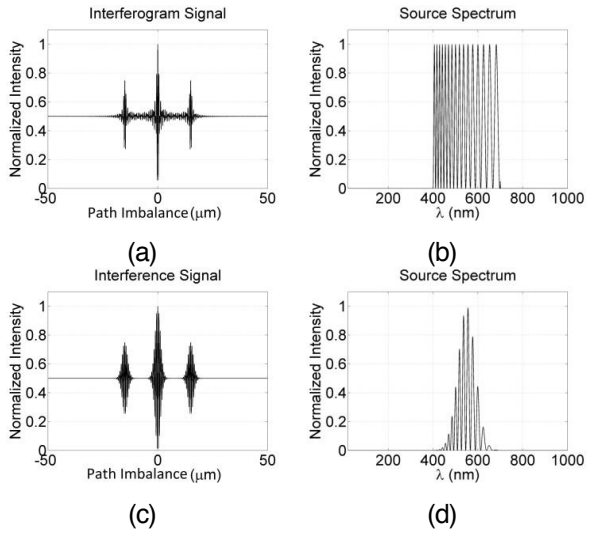

Figure 4: The output signals and corresponding light source spectrums for CLI. (a): The interference signal of CLI with a main peak and two side peaks and (b): its corresponding spectrum derived from a flat spectrum in visible range modulated by a cosine function. (c): The interference signal of CLI with a main peak and two side peaks and (d): its corresponding spectrum derived from a Gaussian spectrum in visible range modulated by a cosine function.

the step height is 100 μm, then an interference signal with peak separation equivalent to 100 μm is designed and by moving about ±5 μm around this typical value the exact height can be measured in the range of 95 μm - 105μm. Note that in this scenario, the mechanical scanning to measure the step height is reduced by about tenfold, which is a significant improvement. Figure 5 shows the interference signal for pixels at lower level (Figure 5.a) and upper level of a step profile where the step height is 100 μm (Figure 5.b, solid line), 99 μm (Figure 5.c, dashed line), and 101 μm (Figure 5.d, dotted line). The top signal is the signal from the lower level of the step profile that shows the main peak of the interference signal. The designed interference signal also has two side peaks at 100 μm distance from the main peak. Therefore for a 100 μm step profile, the side peak is present without further mechanical scan (Figure 5.b). For a 99 μm step profile, the side peak appear when the moving arm of interferometer is moved one micrometer (Figure 5.c). The side peak for a 101 μm step profile appears after one micrometer mechanical scanning at the other direction (Figure 5.d), Therefore, as it is shown, by typical vertical scanning equivalent to 10% of what is needed in conventional white light interferometers, the exact step height can be measured for the height values between 95 μm and 105 μm.

When the step height is unknown, the following steps should be taken; first, the interference signal with one peak is made and one level of step is identified. Then the

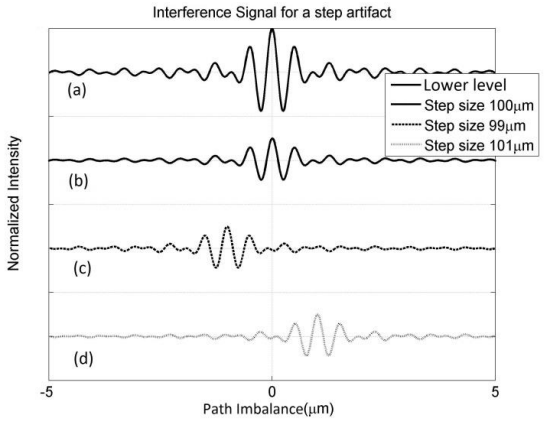

Figure 5: The interference signal for different points of step artifacts where the light source spectrum is shaped in order to have an interference signal with two peaks with 100μm separation. The top signal is the interference signal from lower level of step artifact. The next signal is the interference signal of the upper level point of the step artifact when the step size is 100 μm and the other two signals correspond to upper level points of the step artifacts with the step heights of 99μm and 101μm, respectively.

spectrum of the light is electronically adjusted to produce two peaks in the interference signal, and the separationbetween peaks is changed electronically until the visibility of each point at the other level of step reaches maximum. This occurs when the separation between the peaks is equivalent to the step height. Therefore the height can be measured electronically without any mechanical movement. Figure 6 shows the interference signal in terms of modulation index (τ_0 in equation (6)) for step size 50μm, 100μm, 150μm, and 200μm. Since the relation between the modulation index and the path imbalance is known ($d = c\tau_0$), the step height can be measured when the peak of interference signal in Figure 6 is determined. This method, by its nature, is very fast since it does not rely on any mechanical movements.

Comparing the two mentioned scenarios reveals that the first one can be implemented with less complexity (shorter range of modulation index) or higher resolution (better spectral resolution) in the expense of more mechanical scanning, while the second offers a faster measurement technique. We should note that both methods require less mechanical scanning compared to the conventional white light interferometry.

Now we discuss how the measurement of CLI can be determined. Since we need to synthesize a modulated spectrum we have to consider both the sampling period for spectrum synthesis and the number of samples required to synthesize a sinusoidal signal (to represent the modulation). Considering the resolution of 0.156nm for the spectrum shaping and assuming that one period

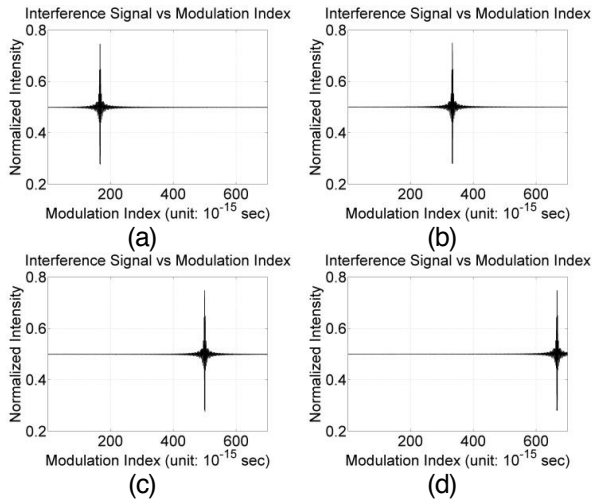

Figure 6: The interference signal versus the modulation index for the step height of (a): 50μm, (b): 100μm, (c): 150μm, and (d): 200μm. The position of the peak of the interference signal ($\tau_{0,peak}$) is related to the step height (d_{ss}) with the equation $d_{ss} = c\tau_{0,peak}$ where c is the speed of light in the medium.

of sinusoidal signal can be represented with four samples, the maximum range for measuring a step artifact without mechanical movement is about 250μm using the current SLMs (e.g DMD or LCoS) with 1920x1080 pixels. The basic spectrum for this calculation is the flat spectrum in the range of 400nm-700nm. The range is calculated based on equation (6) and using the period of sinusoidal spectrum that has the shortest length in the wavelength domain.

$$\text{range of measurement} = \frac{\lambda_{min}^2}{\Delta\lambda} = \frac{0.4^2}{.625 \times 10^{-3}} = 256\mu m \qquad (7)$$

where $\Delta\lambda$ is the length of the shortest period of sinusoidal spectrum in the wavelength domain.

If a line DMD array (similar to line cameras) is developed with a size of 8000 pixels, the range of measurement can be expanded to about 1mm and with a line DMD array of 16K pixels the range can be

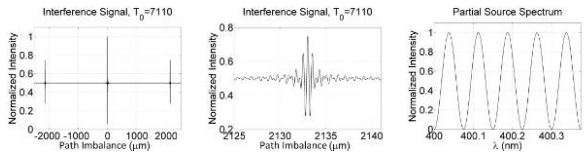

Figure 7: Interference signal and partial spectrum of the corresponding light source to generate two peaks with 2000μm separation. (a): interference signal, (b): second peak of interference signal at 2133 μm separation from the main peak, and (c): part of the light source spectrum in the range of 400nm-400.4nm.

increased to 2mm; i.e. a step artifact with the step height of up to 2mm can be measured without mechanical movement. **Error! Reference source not found.** shows the interference signal and the part of the corresponding light source spectrum.

Since DMDs have frame rates of up to 24K fps, the bottleneck in measurement time would be the camera frame rate and not how fast the spectrum of light source can be reshaped.

4.SLOPE MEASUREMENT

The slope measurement is another application of CLI where the slope profile is measured with minimum or no mechanical scanning; the spectrum of light source is shaped statically or dynamically to measure the slope profile electronically other than mechanically.

The slope measurement can be achieved by obtaining interference envelops at specified distances from each other. Knowing those separations, which correspond to the different heights, and also lateral locations of interference envelops' peaks, which can be calculated from the pixel pitch of the camera and system magnification, the slope can be calculated. The interference signal for this task can be specified as in equation (5), in simplest form, and the number of peaks can be increased to enhance the accuracy of measurement. For example, to have three peaks (five peaks total, since the interference signal is symmetric), the interference signal and corresponding light source spectrum can be expressed as

$$\begin{aligned} F_m(\tau) = F(\tau) &+ \frac{a_1}{2(a_1+a_2)}\{F(\tau-\tau_1) \\ &+ F(\tau+\tau_1)\} \\ &+ \frac{a_2}{2(a_1+a_2)}\{F(\tau-\tau_2) \\ &+ F(\tau+\tau_2)\} \end{aligned} \qquad (8)$$

$$\begin{aligned} &S_m(\tau) \\ &= \Im\Bigg\{F(\tau) \\ &+ \frac{a_1}{2(a_1+a_2)}\{F(\tau-\tau_1)+F(\tau+\tau_1)\} \\ &+ \frac{a_2}{2(a_1+a_2)}\{F(\tau-\tau_2)+F(\tau+\tau_2)\}\Bigg\} \\ &= 2s(f)\left[\frac{a_1}{(a_1+a_2)}cos^2(\pi f\tau_1)\right. \\ &\left.+ \frac{a_2}{(a_1+a_2)}cos^2(\pi f\tau_2)\right] \quad f \geq 0 \end{aligned} \qquad (9)$$

Figure 8 shows the interference signal and the corresponding spectrum where $s(f)$ is a flat spectrum in the visible range (400nm-700nm), $a_1 = a_2 = 1$, and $\tau_2 = 2\tau_1 = 100 \times 10^{-15} sec$, which correspond to the

path difference $15\mu m$ and $30\mu m$, respectively. As it is shown in the Figure 8.a, other than the main peak, there

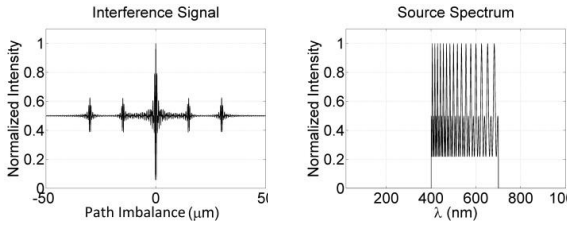

(a) (b)

Figure 8: The output signals and corresponding light source spectrums for CLI. (a): The interference signal of CLI with a main peak and four side peaks and (b): its corresponding spectrum derived from a flat spectrum in visible range modulated by two cosine functions.

are two peaks at $15\mu m$ and $30\mu m$ distance from the main peak that can be used for slope measurement.

The number of peaks and the relative positions of the peaks can be designed to enable the measurement of the slope with higher precision and reliability.

Similar to what mentioned in step profile measurement, there are two general approaches for slope measurement. The first approach assumes that the approximate slope profile is known, therefore an interference signal with the typical slope is designed and then the mechanical scan is used to accurately determine the slope profile. In this approach we look at two fixed pixels of the camera while mechanically scanning. If multiple pixels (areas) be monitored for finding the slope profile, the need for mechanical scanning further decreases. The second approach uses the electronic scanning to change the relative distance between the peaks in interference signal to calculate the slope profile of the object. The former approach requires a less complicated electronics while the latter approach is mechanically less complicated. Note that both approaches have less mechanical scanning compared to the conventional white light interferometers. As before the position of the peaks can be changed electronically,

As stated above, both variable steps and slope profiles can be measured using CLI technique. Therefore a freeform object can be measured with minimum or no mechanical scan using CLI.

Measuring thickness of a multilayer film is another capability of CLI technique with minimized vertical scan, since the thickness measurement using white light interferometry has the same principle as step height measurement.

5.CONCLUSION

The colored light interferometry introduces a tool to design a custom interference signal to facilitate simpler measurement and increase the overall performance of the white light interferometer. We have shown that the the interference signal can be designed by shaping the light source spectrum to measure a step profile and slope profile with minimum or no mechanical scanning. The scanning is done electronically by dynamically shaping the light source spectrum, which results in interference signals with multiple peaks with dynamic distance from each other. Hence, the CLI can measure the profile of a freeform artifact with minimum or no mechanical scanning. Furthermore, the CLI is a faster, more precise, more reliable, and more flexible than conventional white light intereferometers, therefore improves the overall performance of the measurement system.

REFERENCES

[1] P. de Groot and L. Deck, "Surface Profiling by Analysis of White-light Interferograms in the Spatial Frequency Domain," *J. Mod. Opt.*, vol. 42, no. 2, pp. 389–401, Feb. 1995.

[2] S.-W. Kim and G.-H. Kim, "Thickness-Profile Measurement of Transparent Thin-Film Layers by White-Light Scanning Interferometry," *Appl. Opt.*, vol. 38, no. 28, p. 5968, Oct. 1999.

[3] P. Pavliček and O. Hýbl, "White-light interferometry on rough surfaces--measurement uncertainty caused by noise.," *Appl. Opt.*, vol. 51, no. 4, pp. 465–73, Feb. 2012.

[4] K. G. Larkin, "Efficient nonlinear algorithm for envelope detection in white light interferometry," *J. Opt. Soc. Am. A*, vol. 13, no. 4, p. 832, Apr. 1996.

[5] J. C. Wyant, "White Light Interferometry," in *Proc. SPIE 4737, Holography: A Tribute to Yuri Denisyuk and Emmett Leith*, 2002, pp. 98–107.

[6] S. Ma, C. Quan, R. Zhu, C. J. Tay, L. Chen, and Z. Gao, "Application of least-square estimation in white-light scanning interferometry," *Opt. Lasers Eng.*, vol. 49, no. 7, pp. 1012–1018, Jul. 2011.

[7] P. Pavliček and V. Michálek, "White-light interferometry—Envelope detection by Hilbert transform and influence of noise," *Opt. Lasers Eng.*, vol. 50, no. 8, pp. 1063–1068, Aug. 2012.

[8] A. S. Gerges, T. P. Newson, and D. A. Jackson, "Coherence tuned fiber optic sensing system, with self-initialization, based on a multimode laser diode.," *Appl. Opt.*, vol. 29, no. 30, pp. 4473–80, Oct. 1990.

[9] S. R. Chinn, E. A. Swanson, and J. G. Fujimoto, "Optical coherence tomography using a frequency-tunable optical source," *Opt. Lett.*, vol. 22, no. 5, p. 340, Mar. 1997.

[10] Y. Zhang, M. Sato, and N. Tanno, "Resolution improvement in optical coherence tomography by optimal synthesis of light-emitting diodes," *Opt. Lett.*, vol. 26, no. 4, p. 205, Feb. 2001.

[11] R. Tripathi, N. Nassif, J. S. Nelson, B. H. Park, and J. F. de Boer, "Spectral shaping for non-Gaussian source spectra in optical coherence tomography," *Opt. Lett.*, vol. 27, no. 6, p. 406, Mar. 2002.

[12] A. C. Akcay, J. P. Rolland, and J. M. Eichenholz, "Spectral shaping to improve the point spread function in optical coherence tomography," *Opt. Lett.*, vol. 28, no. 20, p. 1921, Oct. 2003.

[13] I.-J. Hsu, C.-W. Sun, C.-W. Lu, C. C. Yang, C.-P. Chiang, and C.-W. Lin, "Resolution Improvement with Dispersion Manipulation and a Retrieval Algorithm in Optical Coherence Tomography," *Appl. Opt.*, vol. 42, no. 2, p. 227, 2003.

[14] E.-S. Choi, J.-H. Na, and B.-H. Lee, "Spatial Resolution Enhancement with Fiber - based Spectral Filtering for Optical Coherence Tomography," *J. Opt. Soc. Korea*, vol. 7, no. 4, pp. 216–223, 2003.

[15] J. Gong, B. Liu, Y. L. Kim, Y. Liu, X. Li, and V. Backman, "Optimal spectral reshaping for resolution improvement in optical coherence tomography," *Opt. Express*, vol. 14, no. 13, p. 5909, 2006.

DENSE ERROR EVALUATION FOR LASER TRACKERS

Edward Morse[1], Jindong Wang[2], Saeed Heysiattalab[1]
[1] Center for Precision Metrology
University of North Carolina at Charlotte, USA
[2]School of Mechanical Engineering
Southwest Jiaotong University, CHINA

ABSTRACT
The performance evaluation of laser trackers is based on the determination of errors in the measurement of calibrated reference lengths [1-3]. For large-scale systems, the lengths used in performance evaluation typically vary between 1 m and 40 m. Although these tests reveal instrument errors over a large portion of the measuring volume, there is little revealed about systematic effects in smaller measuring volumes that may, in turn, have a strong influence on workpiece evaluation. This paper describes an experimental method for obtaining error values for laser trackers in smaller measuring volumes, but at a higher resolution than available from standardized tests.

INTRODUCTION
Laser trackers allow for the measurement of large workpieces, assemblies, and products with individual point accuracies of better than 100 µm, even at ranges of dozens of meters [4]. Higher accuracies can be attained in smaller workzones, and laser trackers are often used to measure smaller (dimensions ≈ 1 m) workpieces, due to the portable nature of the instruments. However, the specifications of laser tracker performance by the manufacturers are usually based on the entire possible work volume. The work described in this paper investigates the structure of a laser tracker's measurement errors can be revealed by comparing the movement of a large, high-accuracy coordinate measuring machine (CMM) to the measurements of this movement taken with the laser tracker. We note that this is the converse of work that has been done in the past, where laser trackers or other tracking interferometers are used – either in direct measurement mode, or in multi-lateration – to determine the geometric errors of a CMM or machine tool [5-8].
Three laser trackers are used in these experiments, so that any specific pattern of errors revealed with an instrument could be evaluated relative to the other laser trackers. Although the different instruments performed differently, there were no definitive cases where one laser tracker exhibited surprisingly different behavior from its counterparts.

PERFORMANCE VERIFICATION METHODS
The performance of laser trackers is quantified by various national standards and guides [1,2], as well as the recently published international standard ISO 10360-10 [3]. None of these documents require that the instrument manufacturer meet a specific level of performance, but instead give well-defined tests and the associated parameterization of the test results. In this way, when a manufacturer states a Maximum Permissible Error (MPE) for some performance parameter, the meaning of this value is clear. Additionally, values for the same performance parameter can be compared between the specifications of different manufacturers. Because ISO 10360-10 has only recently become available, the literature of various laser tracker manufacturers still contains a wide variety of accuracy descriptions, as shown in Table 1.

TABLE 1. Examples from current laser tracker specifications

Specification	Value
Horizontal Scale Bar measurement	31 µm at 2 m
UXYZ – Full Range	15 µm + 6 µm/m
Static Accuracy (IFM)	±10 µm *or* 5 ppm (2 sigma) *Whichever is greater*

The testing of laser trackers follows the principles of testing other coordinate measuring instruments, in that point-to-point measurement capability is tested throughout the measuring volume, and local variability and repeatability are tested in a small region (usually measuring a precision sphere). In addition, the alignment of the tracker's rotary axes is evaluated through two-face (also called plunge-and-reverse) tests.

In order to determine if an instrument is suitable for a measuring task, the quantity that we might most wish to know is the "accuracy of determining a single point in space." Naturally, this is not an easily quantifiable value, as the location of a single point requires the determination of a reference coordinate system, which in turn requires other measurements. The most similar measurand to a single point, and one that is used throughout instrument testing, is the distance between two points. Not only is this a very simply-described measurand, but there are many artefacts available that provide a traceable realization of the measurand (gauge blocks, step gauges, scale bars, etc.). Where testing of an instrument is carried out through the measurement of two-point lengths, the location and orientation of these lengths must be carefully considered so that the geometric errors of the instrument are revealed. Muralikrishnan et al [9] have identified the sensitivity of the measurement error of different artefact locations to the individual errors of laser trackers, and this work has been utilized in the creation of ISO 10360-10.

One difficulty in the testing of laser trackers is that very long (from 2.3 m to over 10 m) reference lengths are needed to perform testing according to the standards, and traceable artefacts that realize these reference lengths can be very expensive. Some reference lengths can be calibrated in situ at the time of testing using a reference laser interferometer, but this can be time consuming. Alternatively, the stability of a network of fixed points can be exploited by measuring these points from a series of different locations [10]. During the development of ISO 10360-10 it was discussed in the working group (ISO TC213/WG10) that it would useful to have a "calibrated hemisphere, or cap" that could be placed over the tracker to determine the extent of the angular errors of the instrument, since every laser tracker will be subject to the same errors over longer distances due to the beam passing through the environment. Although a clever idea, this concept was determined to be impractical, as an artefact of sufficient size would not be very portable and it would be difficult to maintain its calibration status. A similar idea is to use the accuracy of a machine tool or CMM to serve as a reference for laser tracker measurements. Work has been done by Ouyang et al [11,12] to investigate the angular errors of a laser tracker using a CMM, and Muralikrishnan et al [13] have used a rotating device holding a retroreflector to check the ranging errors of a laser tracker as a function of azimuth angle. Each of these experiments utilizes custom-made apparatus, and performs checks only in the horizontal plane of measurement (corresponding to a laser tracker elevation angle of zero). Acero et al [14] have used an indexing platform for a laser tracker to provide virtual reference distances from fixed points. In addition, dynamic tests of laser tracker performance have been reported using an air-bearing spindle to generate a circular reference geometry [15].

INSTRUMENT EVALUATIONS

This section of the paper describes the reference CMM used in the experiments, the method used to obtain the compensated location of the target held by the CMM, the collection of different arrays of points using the laser trackers, and the comparison of these data to the CMM reference locations.

a) b)

FIGURE 1) a) Detail of the retroreflector connection to the CMM and b) example of the retroreflector being measured within the CMM volume.

Reference CMM

The CMM used for these tests is a Leitz PMMF with a measuring volume of 3.0 m x 2.0 m x 1.6 m. The specification of the MPE for length measurement is 2.3 + L/400 µm, where L is the length of the reference length in mm. This would give an upper error bound of about 4 µm for locations in a 500 mm cube, and up to 8.3 µm for locations on a spherical surface 2.4 m in diameter. For the purposes of the experiments described here, the coordinate locations provided by the CMM will be treated as "conventional true values" having an uncertainty appropriate for a given purpose [16].

In order to benefit from the stated performance specification of the CMM, reference positions must have the volumetric compensation of the CMM's error map applied. To accomplish this, a pin nest for a half inch (12.7 mm) diameter spherically mounted retroreflector (SMR) was used. The pin was turned down and threaded with an M5 thread so that it could be mounted in the normal probe extensions, as shown in Figure 1a). The length of the extension was chosen so that the offset from the CMM probehead to the center of the SMR was similar to the offset used for the system's reference probe. The measuring software was then used as if the reference probe was in place, and the CMM controller was queried for the current stylus location with the volumetric compensation of the CMM's error map applied. To verify that the compensation was, in fact, applied, a stylus assembly with two significant opposing horizontal offsets was made active and the locations queried at different heights in the machine volume. The reported relative position of the offset tips changed with z-height, indicating that the compensation for z-roll of the CMM was being applied.

The arrangement for the simultaneous measurements using the CMM and the laser trackers is shown in Figure 1b). A local coordinate system origin was chosen within the CMM volume, and the pattern of points to be collected was initiated from that point. A delay of 4 s was taken between each CMM movement to allow any dynamic motion of the CMM to settle and then for each instrument to record the location. The laser tracker software was programmed to wait for a "stable point" at which time it measured the current location of the retroreflector center. The data for both the CMM and laser tracker were stored for later comparison.

Cartesian grid tests

The first series of tests performed had the CMM move in a simple 3-dimensional grid pattern which filled a cube. The center of this cubic region varied between 2.0 m and 2.5 m from the laser tracker. The region was 500 mm on each side, and a point spacing of 50 mm resulted in a point set of 1331 points per test. To evaluate the instruments through a variety of angles, the base of the laser tracker was rotated, resulting in different grid locations in the laser tracker coordinates, as shown in Figure 2.

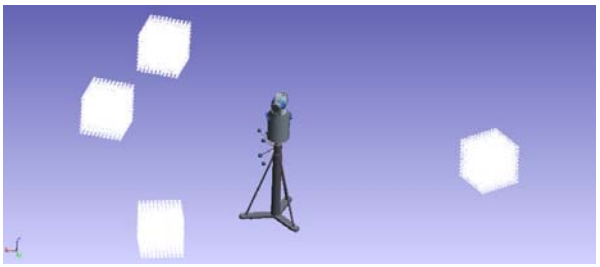

FIGURE 2) Software representation of several grid locations measured by adjusting the orientation of the laser tracker base.

The measured positions from the laser tracker were matched to the reference data from the CMM (the compensated locations reported using the CMM software) using a least-squares fit. The residuals from the fit were presented using a spatial vector plot. Examples of these plots are shown in Figure 3 (oblique view) and Figure 4 (yz-plane projection). The visualization of these errors is challenging, as the errors change throughout the volume and any two-dimensional projection obscures the evolution of these errors.

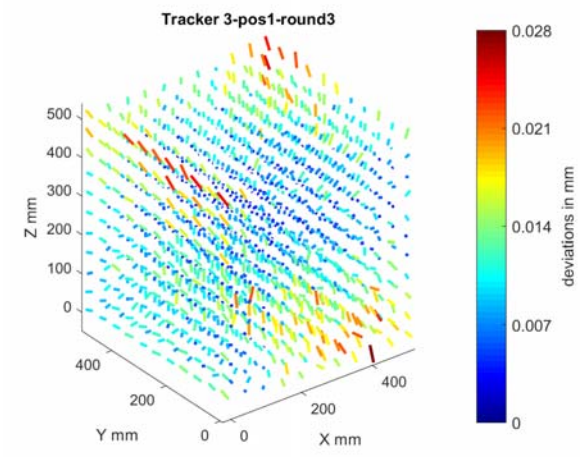

FIGURE 3) Oblique view of errors after fitting measured to reference

It is clear from the yz-projection in Figure 4 that the errors are significantly smaller in the y-direction, which corresponds, in this case, to the ranging direction of the laser tracker.

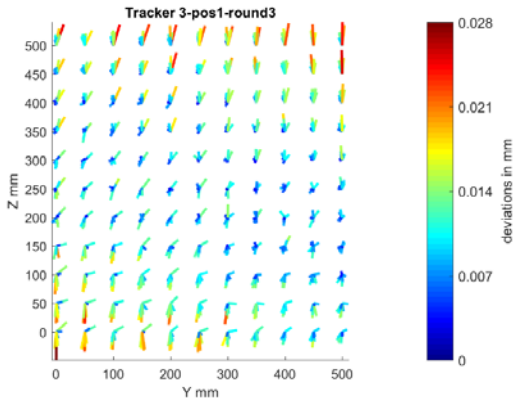

FIGURE 4) Planar view of residual errors

As the data can be reported in 'native' laser tracker coordinates, the direction of the coordinates (range, azimuth, and elevation) can be extracted, and the residual errors broken down into these components. For a point (x, y, z) in tracker coordinates, the unit vectors describing the range (R), azimuth (A), and elevation (E) directions are calculated as

$$\hat{e}_R = \frac{(x,y,z)}{\|(x,y,z)\|}, \quad \hat{e}_Z = (0,0,1),$$

$$\hat{e}_A = \hat{e}_Z \times \hat{e}_R, \text{ and } \hat{e}_E = \hat{e}_A \times \hat{e}_R.$$

The residuals (Δ) from fitting to the CMM reference positions – expressed in Cartesian laser tracker coordinates – are then separated into the spherical coordinate contributions by taking the inner (dot) product of the residual with each of the unit vectors,

$$\delta_A = \Delta \cdot \hat{e}_A, \quad \delta_E = \Delta \cdot \hat{e}_E, \text{ and } \quad \delta_R = \Delta \cdot \hat{e}_R.$$

An example of this decomposition applied to a population of residuals is shown in Figure 5. New basis vectors are calculated for each point in the measured set, as the range, azimuth, and elevation directions are unique to the point. The smaller variation in the range direction is expected, and the larger deviation in the elevation direction seems reasonable as well.

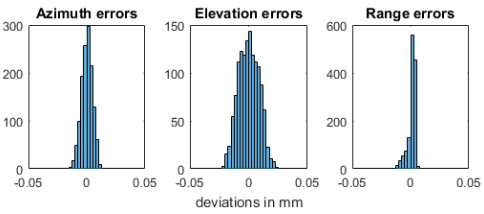

Figure 5. histograms of errors shown in laser tracker 'native' coordinates

Linear tests

Following the first sets of grid tests, the agreement between the laser tracker in "pure ranging" mode (i.e. with minimal deviation in azimuth and elevation) and the CMM moving in one axis was investigated. These data represent measuring lines along which the instruments should each have the best performance. Over nearly two meters in the CMM y-direction, the deviations of the laser tracker measurements were no more than 5 µm and deviations from a linear slope fit, shown in Figure 6, were less than 0.6 µm.

The source of the slope observed in the data is, we believe, due to the temperature recorded by the CMM part sensor. Although both the CMM and the laser tracker are in the same environment, the CMM is designed to report the size of objects having a "normal CTE" of approximately 12 × 〚10〛^(-6)/ K. Therefore, the data obtained by the CMM would be "scaled" by about 5 parts in 106 for a part temperature of 20.4 °C, resulting in the slope of the fit shown in Figure 6. The temperature in the laboratory is specified to be 20 °C ± 0.5 °C, and additional testing is required to verify how the thermal compensation parameters are being applied in the CMM software.

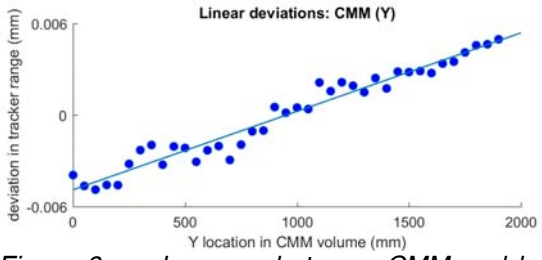

Figure 6. scale errors between CMM and laser tracker

Spherical shell tests

The final series of tests involves measurement points in a spherical shell about the tracker. Because the minimum recommended measuring distance of the laser tracker used in this test is greater than 1 m, the measuring volume of the CMM constrained the reference points to a grid that covered 180 degrees of azimuth and 45 degrees of elevation at a distance of 1.2 m from the tracker, as shown in Figure 7 and Figure 9.

A benefit of this test is that a large range of angles is measured, which can reveal linearity and eccentricity errors of the rotary encoders. In addition, since the measurement points

"surround" the tracker, errors in the zero-setting of the ranging sensor (sometimes referred to as the R0 parameter) and scaling errors will also be revealed.

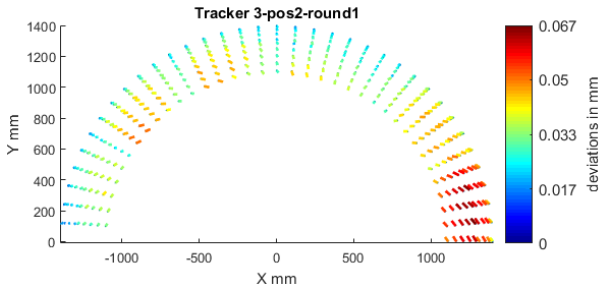

FIGURE 7. Errors in measurement of a spherical shell dataset

A representative set of data is presented. In Figure 7, the largest errors occur in regions that are approximately 150 degrees apart in the azimuth direction (10 o'clock and 3 o'clock in the figure). The errors are also dependent on the elevation angle, and would not necessarily be revealed by testing only at an elevation of zero degrees.

In Figure 8, the residual errors are decomposed into the laser tracker coordinate directions, and while the variation in range errors is again the smallest, there is a bias in the range errors which is not captured in the Cartesian grid measurements.

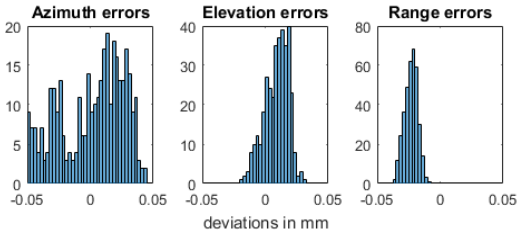

FIGURE 8. Histograms of errors shown in laser tracker 'native' coordinates

One difficulty encountered in the performance of this test is that the SMR must be frequently re-oriented so that it is always pointing – within its acceptance angle – at the laser tracker. The quality of the pin nest minimizes the errors introduced during re-orientation, and no systematic shift between orientations was observed in the data collected during these experiments.

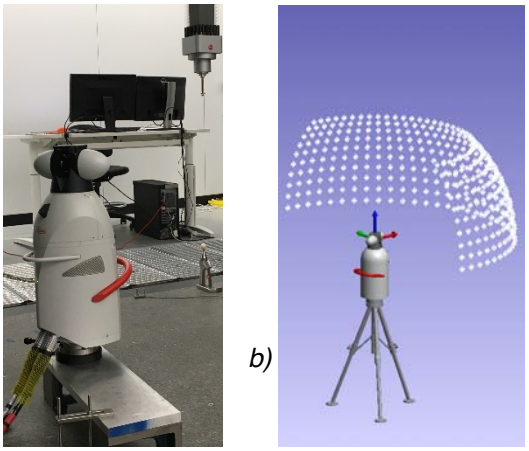

FIGURE 9. a) tracker setup for spherical shell measurement and b) scaled representation of data collected.

SUMMARY AND CONCLUSIONS

This paper has described a series of experiments to capture dense error maps of laser tracker measurements using a large, high-accuracy CMM. The error maps reveal the variability and interaction of errors in the azimuth and elevation directions of the laser trackers, and also the performance of the instruments within a regular cubic measuring volume. A potential use of these data in the future is to provide verification of laser tracker performance, or to update the compensation of the tracker errors as part of a calibration. While sparse point-to-point measurements can reveal gross errors in the angular encoders and the geometric alignment of the laser tracker, these dense data have the opportunity to provide more information about the axes, as well as correlation between the axes. The method also benefits from being relatively quick, with the data acquisition phase of most tests taking less than two hours.

Future work will focus on linking pairs of the spherical shell measurements to give a more complete picture of laser tracker errors around the full azimuthal range. To facilitate the ease of spherical measurements, the use of an active retroreflector is being considered, so that manual re-orientation of the SMR is not needed and a full set of spherical measurements can be completed without interruption. The influence of an active reflector on the ability to obtain compensated spatial data from the CMM must also, of course, be considered. An alternative to using the active reflector would be the use of an n = 2 cat's-eye reflector [17], if one of suitable geometry could be obtained.

ACKNOWLEDGEMENTS

The authors acknowledge the support of the resources made available by the Center for Precision Metrology (CPM) and the Energy Production and Infrastructure Center (EPIC), both at UNC Charlotte.

REFERENCES

[1] ASME B89.4.19-2006 Standard—Performance Evaluation of Laser-Based Spherical Coordinate Measurement Systems, www.asme.org. 2006

[2] VDI/VDE part 10, Accuracy of Coordinate Measuring Machines: Characteristics and their Checking: Acceptance and Reverification Tests of Laser Trackers, Düsseldorf: Verein Deutscher Ingenieure 2011

[3] ISO 10360-10, Geometrical Product Specifications (GPS) – Acceptance and reverification tests for coordinate measuring systems (CMS) – part 10: Laser trackers for measuring point-to-point distances, ISO Geneva 2016

[4] Schmitt, R. H., et al. "Advances in Large-Scale Metrology–Review and future trends." CIRP Annals-Manufacturing Technology 65.2 (2016): 643-665.

[5] Schwenke, H., et al. "Error mapping of CMMs and machine tools by a single tracking interferometer." CIRP Annals-Manufacturing Technology 54.1 (2005): 475-478.

[6] Umetsu, Kenta, et al. "Geometric calibration of a coordinate measuring machine using a laser tracking system." Measurement science and technology 16.12 (2005): 2466.

[7] Schwenke, H., et al. "On-the-fly calibration of linear and rotary axes of machine tools and CMMs using a tracking interferometer." CIRP Annals-Manufacturing Technology 58.1 (2009): 477-480.

[8] Aguado, Sergio, et al. "Identification strategy of error parameter in volumetric error compensation of machine tool based on laser tracker measurements." International Journal of Machine Tools and Manufacture 53.1 (2012): 160-169.

[9] Muralikrishnan, B., Sawyer, D., Blackburn, C., Phillips, S., Borchardt, B., & Estler, W. T., ASME B89.4.19 performance evaluation tests and geometric misalignments in laser trackers. Journal of Research of the National Institute of Standards and Technology, 114, 1, 21-35.

[10] Hughes, Ben, et al. "Laser tracker error determination using a network measurement." Measurement science and Technology 22.4 (2011): 045103.

[11] Ouyang, J. F., et al. "Laser tracker calibration using coordinate measuring machine." Proc. ASPE 2005 Annual Meeting in Norfolk, VA. 2005.

[12] Ouyang, J. F., et al. "Angular error calibration of laser tracker system." Proc. Advanced Laser Technologies 2005. International Society for Optics and Photonics, 2006.

[13] Muralikrishnan, B., et al. "Measuring scale errors in a laser tracker's horizontal angle encoder through simple length measurement and two-face system tests." Journal of research of the National Institute of Standards and Technology 115.5 (2010): 291.

[14] Acero, R., et al. "Application of virtual distances methodology to laser tracker verification with an indexed metrology platform." Measurement Science and Technology 26.11 (2015): 115010.

[15] Morse, E., and Welty, V.. "Dynamic testing of laser trackers." CIRP Annals-Manufacturing Technology 64.1 (2015): 475-478.

[16] JCGM100:2008, Guide to the Expression of Uncertainty in Measurement (GUM), www.bipm.org

[17] Takatsuji, Toshiyuki, et al. "Whole-viewing-angle cat's-eye retroreflector as a target of laser trackers." Measurement Science and Technology 10.7 (1999): N87.

OPTOMECHANICAL DESIGN AND FABRICATION OF A SNAP TOGETHER FREEFORM TMA TELESCOPE

Nicholas W. Horvath[1], Isaac W. Barron[1], Joseph D. Owen[1], Brian S. Dutterer[1], Eric Schiesser[2], Aaron Bauer[2], Jannick P. Rolland[2], Matthew A. Davies[1]
[1]Mechanical Engineering
University of North Carolina at Charlotte
Charlotte, North Carolina, USA
[2]Institute of Optics
University of Rochester
Rochester, New York, USA

INTRODUCTION

Freeform optics can allow for more compact imager designs that do not sacrifice image quality as compared to traditional designs using spherical and aspherical optics[1,2,3,4,6]. In this work, a three mirror anastigmat (TMA) off-axis in-plane optical design, as shown in Figure 1, is the baseline for a diffraction-limited, 250 mm aperture, wide-field-of-view telescope using three freeform mirrors.

The work reported here focuses on the opto-mechanical design and tolerance quantification and qualitative performance testing for this novel system design[1]. The first objective of this work was optomechanical design and the construction of the system targeting the mirror placement tolerances necessary to maintain diffraction limited performance. The second objective of this work was to connect measurements of the attained assembly uncertainty to image quality. The end goal is to systematically connect measured assembly uncertainties with image performance and to provide feedback to optical designers on the methods for and the costs of maintaining these tolerances. Although the study here targeted a 1/3rd scale system with an 83 mm aperture, the methods are applicable to larger scale systems as well. Methods of precision manufacturing[5], precision assembly using kinematic mounts[7,8], and precision metrology are combined to achieve this goal.

DESIGN OVERVIEW

To meet the objectives, the initial optical design was first reduced by a factor of three. This reduction in size allowed the entire assembly to be measured in a Leitz PMM-F 30-20-16 coordinate measuring machine (CMM) with a volumetric length measuring error of no more than 3 μm over the size of the optical system. Although the full-scale system will be

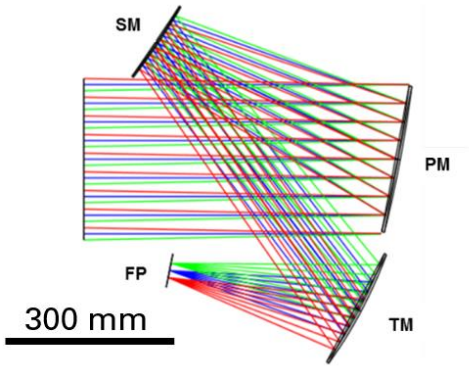

FIGURE 1. Three-mirror off-axis design.

implemented in silicon carbide, the scaled down system was constructed with an aluminum 7075-T6 housing and C464 Naval brass mirrors. This allowed the mirrors to be prototyped by coordinated axis turning and the housing to be manufactured monolithically by high-speed machining. The optics were designed with fiducials to establish the coordinate systems of the freeform surfaces for independent measurement in a Mahr LD260 profilometer.

The TMA is an in-plane optical design, because of this, it facilitated manufacture with a monolithic housing and a removable top-shell allowing for metrology of the assembly. Mirrors are constrained on the perimeter of a monolithic frame using kinematic mounts, making it a so-called snap-together system. The frame design takes advantage of both high-speed machining of the monolithic aluminum frame and ultra-precision coordinated-axis diamond turning and milling of the optical surfaces, locating features, and metrology fiducials on the mirrors. More than 90% of the initial material on the optical blanks and the housing was removed by high-speed machining with a Makino A55 milling machine. Each optic was completed on a Moore 350 FG

FIGURE 2. Overall optomechanical CAD design

diamond machining center with a single manufacturing setup. Wherever possible, finish machining of the optics and the housing was completed with a minimum number of repositioning steps. Thus, the accuracy of the machining centers was transferred into the housing and the optics.

The optics were designed with metrology fiducials around the clear aperture of the prescription, while mounting spheres (recessed for clearance) for a kinematic coupling were machined on a flange extending beyond the optical surfaces and fiducials. This allowed the optical surface, metrology fiducials, and kinematic spheres to be manufactured in one machine setup without repositioning.

The kinematic mounts on the optics were preloaded by an array of flexures[9], which provide a controlled approximate point-load over each kinematic sphere/V-groove coupling[7,8]. The flexure array is mounted to the frame. A raised area that pushes against the back of the kinematic sphere. Therefore, the optics are secured only by the force applied by the flexure, which seats the sphere into the V-grooves on the frame. This reduces the distortion of the frame and the optical surface and targets precise, repeatable, and predictable placement of the optics. Such a system is classified as a snap-together component.

Lastly, a removable top shell, with built-in stray light baffling and entrance pupil baffles were designed. The nylon top shell was manufactured on a Fortus 400 MC 3D printer. Flexible clips were positioned around the perimeter to constrain the shell while producing little strain in the frame.

A computer model of the opto-mechanical system without the top shell is shown in Figure 2. Figure 3 shows the shell with internal baffling.

FIGURE 3. Top shell with stray light baffling

DESIGN METHODS

Housing Design and Fabrication

To develop a snap-together system with no mechanical adjustment of the optics, the uncertainties in the system were minimized. Based on computer modeling a set of target uncertainties were developed. A Monte Carlo simulation was completed in Code V optical simulation software to confirm the system would only require defocus adjustment to remain diffraction limited. The target uncertainties for each optic are given in Table 1. The table also includes the expected uncertainties for the first prototype as the manufacturing methods were developed.

TABLE 1. Target uncertainties for mechanical design and manufacture

Specification per Optic Location	Expected Uncertainty	Target Uncertainty
Positioning (X-Y) (μm)	14	5
Positioning (Z) (μm)	9	3
Clocking (μrad)	141	28
Tilt (μrad)	86	17

A monolithic housing was manufactured by high-speed machining. This approach was used to transfer machine accuracies into the housing and minimize stack-up errors inherent in multi-piece assembled systems. The single-piece housing was machined from a solid piece of 7075-T6 aluminum. Over 95% of the original material was removed with high-speed machining on a Makino A55 machining center. All mounting features for the optics were placed around the perimeter of the housing.

Three V-grooves, spaced equally 120° apart, were machined into the three optic locations,

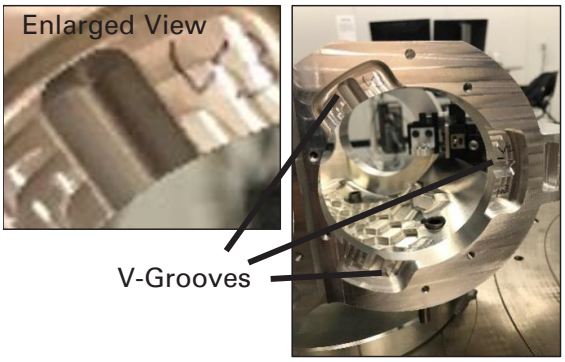

FIGURE 4. V-grooves for kinematic mounts

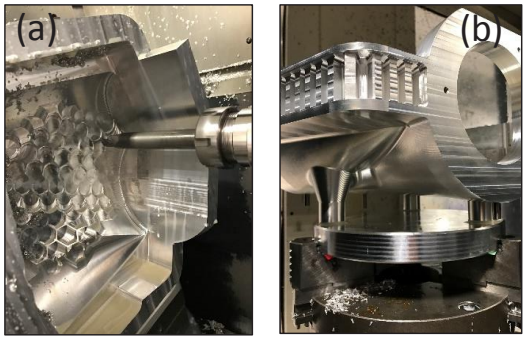

FIGURE 5. (a) Machining of strengthening ribs on flor of housing and (b) side view

completing one mating half of the kinematic coupling as shown in Figure 4.

The housing was designed to have adequate stiffness while minimizing the overall weight. The lower shell was designed to conform to the light path, which minimized the overall volume. The thickness of the lower portion of the housing was 2 mm. A 4 mm tall, 0.5 mm thick hexagonal system of stiffening ribs was machined throughout to improve the strength-to-weight ratio. The side rails also contain stiffening ribs. FEA simulation shows that housing deflections due to mass loading are less than 10 nm for each of the optical planes. Figure 5 shows the housing features during the manufacturing process.

The focal plane array (FPA) for the system was mounted inside the housing and had one degree-of-freedom (defocus). This monolithic design allowed for all the critical mounting features to be machined in a single machining setup with the same tool.

Optic Mechanical Design and Fabrication

The optics were also monolithic with the mounting features, optical surfaces, and metrology fiducials

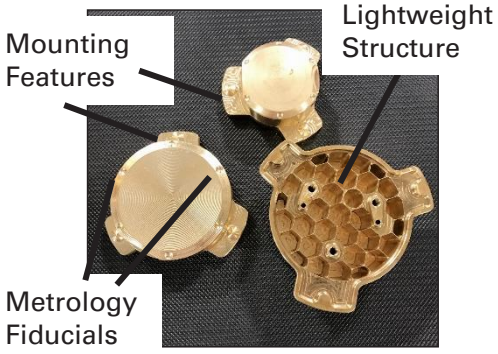

FIGURE 6. Rough machined optics

all made in one machine setup. The optics were made from C464 Naval brass, and were light-weighted with similar methods for the housing. The face sheet thickness was 1.5 mm thick, and the web thickness of the hexagon lightweight structure was 0.4 mm. These parameters were chosen to reduce any print through on the optical surface. Validation by FEA shows deflection of the face sheet due to tool forces were less than 5 nm. The rough machined mirrors are shown in Figure 6.

Also shown in Figure 6, are the metrology fiducials, reference datums, and the kinematic alignment spheres in their rough-machined shape. The kinematic spheres are the other mating half to the V-grooves found on the housing. The tabs on the optics have a unique size to ensure proper optical orientation during installation.

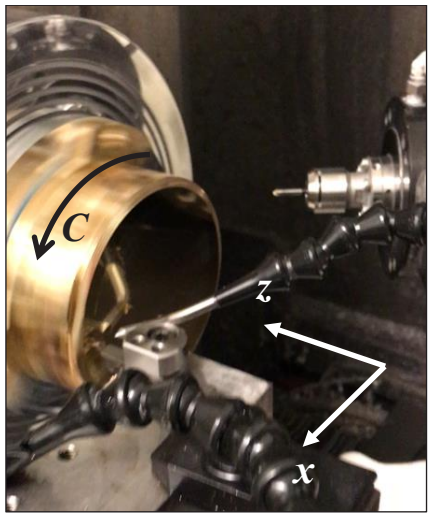

FIGURE 7. Slow-tool-servo diamond turning (x-z-C) and milling of the mounting features

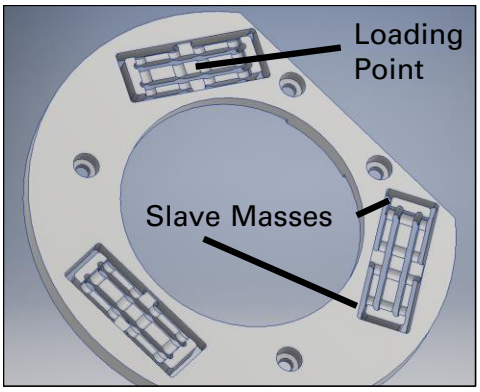

FIGURE 8. CAD model of loading flexures

The freeform optical prescriptions were diamond turned with slow-tool-servo, while the metrology and mounting features were diamond milled in the same machining setup. Figure 7 shows the in-process diamond turning of the optics with the milling spindle in place.

Mechanical Fastening and Optical Alignment

The optics are constrained kinematically by a 3-sphere/3-V-groove kinematic coupling. The forces that hold the couplings together are approximate point loads at each sphere applied by a flexure array.

Each flexure contains 6 elements, with 2 slave mass ends to avoid over constraint. Each array contains three flexures to provide the point load at each kinematic sphere location. The flexure array model is shown in Figure 8. Once the array is bolted to the housing, each flexure presses with a raised boss over the back of the sphere, in turn raising the element, displacing the flexure and providing a calculated force.

To constrain the optics, 7.5 N of force is applied to each sphere. Once the applied force was determined, the flexure elements were designed and the stiffness was tuned to produce approximately 125 µm of elastic displacement. The positions of the optical surfaces were adjusted by this amount relative the kinematic balls to compensate. The flexure array behavior was simulated with FEA and mechanically verified. The results were within the estimated uncertainty of the flexure behavior due to manufacturing. The FEA results along with a cross section description are shown in Figure 9.

Once the mathematical model, FEA simulation, and the mechanical test all matched within the expected uncertainty, stresses on the elements and mounting interfaces were calculated.

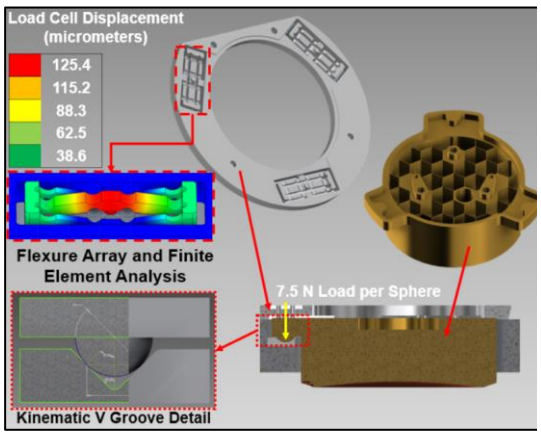

FIGURE 9. Optic mounting system detail

The stress of the flexure elements remained 5 times less than the yield of the aluminum 6061-T6 used for manufacture. The Hertzian stresses for the kinematic coupling had a minimum safety factor of 1.9. The displacement of the coupling due to the load from the flexures was also calculated, and showed only a 1 µm displacement of the optical face.

One main goal of the work was to identify sources of assembly errors in the final system. Combining the kinematic coupling, with a flexure constraint system provided a deterministic and repeatable component with no adjustment of the optics after assembly required.

FINAL ASSEMBLY

The final system was assembled in less than 10 minutes and will produce images with only defocus adjustment. Figure 10 below shows the final assembled system without the top-shell (Figure 10 (a)) and with the top-shell and stray light baffling (Figure 10 (b)).

VERIFICATION PLAN

The assembly errors will be measured in a Leitz PMM-F 30-20-16 coordinate measuring machine (CMM). Functional testing will be performed at the Air Force Research Laboratory (AFRL).

First, a random ball test using a red Zygo Fizeau interferometer will be performed. This test will involve placing a 10 mm precision ground silicon nitride sphere at the focal point of the telescope. To place the sphere, a kinematic mount and stage assembly was added to the telescope, as shown in Figure 11.

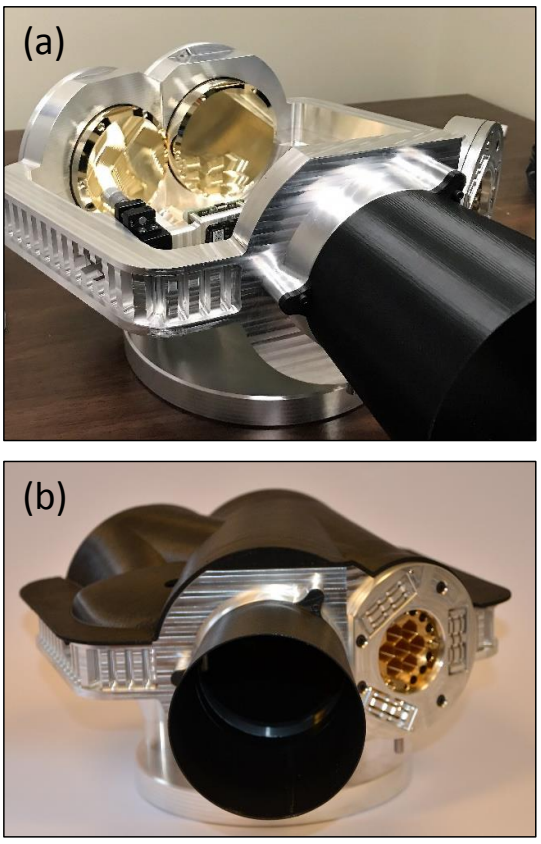

FIGURE 10. (a) Open system revealing primary and tertiary optics and (b) closed system with shell and stray light baffling

The three-stage assembly will allow for adjustment of the sphere's position in relation to the focal point of the system. The random ball test will involve measuring random patches of the sphere and averaging the optical path difference (OPD) of each patch to obtain an estimate of the reference[10].

Next, a Foucault knife-edge modulation transfer function (MTF) test will be conducted. A collimated light source will illuminate the entrance pupil and a knife edge will be "scanned", sliding in one dimension, across the focal plane of the system, with the MTF derived from the gathered data[11]. The final functional test performed will be capturing images from a tower of engineering targets at a distance up to 3 km away.

Once functional testing is completed, a Leitz PMM-F 30-20-16 will be used to measure both the fully assembled system as well as the individual components. The spherical fiducials placed around the clear aperture of each mirror will be utilized for the measurement of the mirror placement and orientation of the system. This data will then be placed into an optical model of the telescope and the error results will be compared to the results obtained from functional tests. This will allow the functional tests to be directly related to mirror placement errors with the ability to induce additional errors into the system and observe the effects on to the functional performance. Analysis of these effects will enable verification of mirror placement tolerances.

Additional advanced testing of the telescope can be undertaken for wave-front image quality across the field of view, measured in RMS and P-V errors using full-field-display interferometry as exemplified in Fuerschbach[11]. The aforementioned tests will quantify the system and determine if it is diffraction limited as designed.

Initial Functional Test Results

While quantitative data will be taken throughout the verification plan, initial photographs were taken with an Edmunds EO-5012M CMOS Monochromatic camera module. The camera module was affixed to a single translational stage to allow for defocus adjustment. This adjustment is the sole source of adjustment in the system.

Theoretically, the system was designed to be diffraction limited near 1000 meters or greater. The image shown below in Figure 12 is at 850 m with no filtering or contrast adjustments.

DISCUSSION AND CONCLUSIONS

Often optical imaging systems such as telescopes are manufactured and assembled with enough degrees-of-freedom to allow for in-situ adjustments until a desired imaging performance is achieved. While successful in most instances, this technique typically does not identify the major sources of uncertainty in the

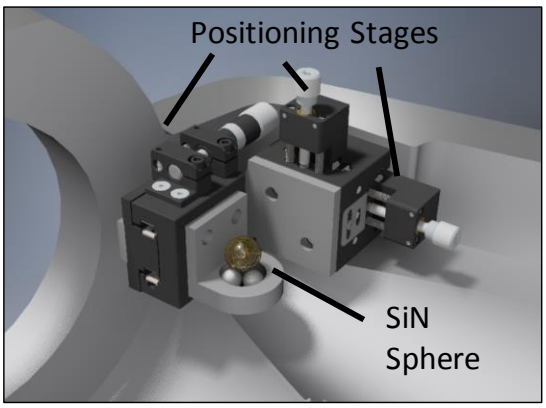

FIGURE 11. Random ball test setup

FIGURE 12. Building image at 850 m.

system and their effects on imaging performance. Freeform optical designs can be more compact, planar, and potentially less sensitive to assembly tolerances. Because they are planar and compact, these designs are small enough to be placed in a precision CMM to identify the major assembly uncertainty sources and to quantify overall assembly uncertainties. Through optical simulations, these assembly uncertainties, in addition to the measured errors on the optical surfaces themselves can be connected to imaging performance/functional testing. Results of assembly uncertainty measurements, errors in the machined freeform optical surfaces, and image quality measurements will be reported in future work.

ACKNOWLEDGEMENTS
This research was supported by the NSF I/UCRC Center for Freeform Optics (IIP-1338877 and IIP-1338898). The authors thank Dr. Chris Evans (UNCC) and Dr. Tom Nelson and Dr. Peter Marasco (AFRL) for valuable help and input.

REFERENCES

[1] Bauer AM, Schiesser EM, Rolland JP. Analyzing the Aberration Fields of a Three-mirror Telescope and Correcting them Using Freeform Zernike Surfaces. Optical Design and Fabrication 2017, OSA Technical Digest (online) (Optical Society of America, 2017), paper JW3C.4.

[2] Bret-Dibat, Thierry, Vincent Albouys, Jacques Berthon, N. Bouzou, Pierre Etcheto, David Laubier, and K. Mercier. Tests of a High-resolution Three-mirror Anastigmat Telescope. Sensors, Systems, and Next-Generation Satellites III, 1999.

[3] Fuerschbach, Kyle, Gregg E. Davis, Kevin P. Thompson, and Jannick P. Rolland. Assembly of a Freeform Off-axis Optical System Employing Three φ-polynomial Zernike Mirrors. Optics Letters Opt. Lett. 39, no. 10 (2014): 2896.

[4] Fuerschbach, Kyle, Jannick P. Rolland, and Kevin P. Thompson. Theory of Aberration Fields for General Optical Systems with Freeform Surfaces. Opt. Express Optics Express 22, no. 22 (2014): 26585.

[5] M. Davies, J. Owen, J. R. Troutman, D. L. Barnhardt, and T. J. Suleski, Ultra-Precision Diamond Machining of Freeform Optics for the IR, in Imaging and Applied Optics 2015, OSA Technical Digest, Optical Society of America, 2015 paper FM1B.1.

[6] Risse, S., A. Gebhardt, C. Damm, T. Peschel, W. Stöckl, T. Feigl, S. Kirschstein, R. Eberhardt, N. Kaiser, and A. Tünnermann. Novel TMA Telescope Based on Ultra Precise Metal Mirrors. Space Telescopes and Instrumentation 2008: Optical, Infrared, and Millimeter, 2008.

[7] Slocum, Alexander H. Precision Machine Design. Prentice-Hall: Englewood Cliffs, NJ, 1992.

[8] Slocum, Alexander H. Design of Three-groove Kinematic Couplings. Precision Engineering 14, no. 2 (1992): 67-76.

[9] Smith, S. T. Flexures: elements of elastic mechanisms. London: Taylor & Francis, 2003.

[10] Parks RE, Evans C, Shao L. Calibration of Interferometer Transmission Spheres. OSA, OF&T, Hawaii 1999.

[11] Rodríguez G, Villa J, Ivanov R, González E, Martínez G. Foucault test: a quantitative evaluation method. J. Opt. Soc. Am. A 33, 1604-1611, 2016.

[12] Reimers J, Bauer A, Thompson KP, Rolland JP. Freeform spectrometer enabling increased compactness. Light: Science and Applications, 2017.

FABRICATION OF LIGHTWEIGHT MONOCRYSTALLINE SILICON MIRROR SEGMENTS TO ENABLE HIGH RESOLUTION X-RAY TELESCOPES

Michael P. Biskach[1], Kim D. Allgood[1], John D. Kearney[1], James R. Mazzarella[1], Raul E. Riveros[2], Peter M. Solly[1] and William W. Zhang[3]
[1]Stinger Ghaffarian Technologies, Inc.
Greenbelt, MD, USA
[2]Center for Research and Exploration in Space Science and Technology
University of Maryland Baltimore County
Baltimore, MD, USA
[3]Astrophysics Science Division
NASA Goddard Space Flight Center
Greenbelt, MD, USA

INTRODUCTION

Previously constructed X-ray telescopes were designed with some degree of tradeoff between cost, collecting area and resolution for mirror assemblies. By leveraging several desirable characteristics of monocrystalline silicon, the Next Generation X-ray Optics (NGXO) team at NASA Goddard Space Flight Center is developing new approaches to generate accurate, lightweight mirror segments to enable future high resolution, high collecting area, and affordable X-ray telescopes. Monocrystalline silicon when compared to previously used mirror segment materials has low thermal expansion, high thermal conductivity, high stiffness, and is readily available for purchase. Most importantly, the stress-free nature of monocrystalline silicon due to the defect-free crystal structure enables surface figure recovery after a lightweighting process is completed. The NGXO team has developed and tested a number of unique processes to lap, slice and polish thin yet accurate mirror segments out of commercially available monocrystalline silicon blocks. The use of chemical etching and surface polishing to remove damaged regions of the atomic lattice to maintain zero internal stress is used to recover surface figure of lightweight mirror segments. Each segment is polished to a Wolter-I shape with a <1 arc-second RMS axial slope error at <1 mm in thickness. The segment production process is parallelized and requires <20 hours of labor per segment. The mirror fabrication process is flexible enough to manufacture segments for a range of X-ray telescopes and science goals including wide field-of-view survey telescopes (such as NASA's STAR-X), spectroscopy, and calorimetry. High resolution, lightweight monocrystalline silicon mirror segment production continues to mature with affordable, diffraction limited X-ray telescopes as the long term goal.

FABRICATION REQUIREMENTS

There exist a number of budgetary and engineering requirements that constrain X-ray mirror fabrication research efforts.

Telescope Requirements

For new X-ray telescope concepts to be considered for funding, the proposed mission science goals and objectives require higher collecting area and higher angular resolution from the focusing optics that can be manufactured within a set budget and schedule. Existing X-ray telescopes provide either high angular resolution (Chandra X-ray telescope at 0.5 arc-seconds over 400 cm^2 collecting area [1]) or high collecting area XMM-Newton (15 arc-seconds over 1475 cm^2 collecting area [2]). To enable gathering of new astrophysical data, future X-ray telescope concepts feature high angular resolution over a large collecting area which can be achieved with a high number of accurate yet thin focusing shells or segments. See Table 1 for an example set of segment requirements for a medium sized X-ray telescope concept.

TABLE 1. An example set of mirror segment requirements for a medium sized X-ray telescope concept.

Mirror Segment Properties	Value	
Total Number	6k-7k	
Unique Prescriptions	300	
Thickness	<1.0	mm
Height	100	mm
Width	80 – 100	mm
Radius	150 – 750	mm
Cost	<$3k	
Axial Surface Slope Error RMS	<1.0	arc-sec
Microroughness	<5	Å
Focusing Resolution (Half-Power Diameter, HPD)	<5.0	arc-sec

Material Properties

Monocrystalline Silicon has a number of advantageous material properties for use, see Table 2. The most important characteristic of monocrystalline Silicon is the internally stress-free structure that allows segment lightweighting without distortion of the polished figure unlike other materials such as amorphous glass or metal alloys. Blocks of monocrystalline Silicon are commercially available.

TABLE 2. Material properties of Monocrystalline Silicon.

Material Property	Value	
Cost	~$250	per kg
Density	2.35	g/cm
Young's Modulus	130-169	GPa
Thermal Conductivity	148	W/m-K
Thermal Expansion	2.6×10^{-6}	$°K^{-1}$

SEGMENT FABRICATION PROCESS

Fabrication techniques must be amenable to parallelization to meet a 2-3 year production schedule, must not raise per segment cost above mission requirements, and achieve and maintain the polished figure requirements.

The segment production process described in the following section implements a traditional lapping and polishing approach adapted to the segment geometry and developed using affordable machines that can be built or purchased quickly, and requires <20 hrs of labor [3]. The segment fabrication process that is employed allows for many segments to be fabricated from a single block to reduce material waste.

Slicing

The rough form of the reflecting surface is sliced out of a block of monocrystalline Silicon with the desired radius, see Figure 1a-1b.

Lapping

The sliced block surface is then lapped with decreasing sized abrasive particles and sets the lowest spatial orders of the reflecting surface shape. The layer of dislocations and damage to the crystal structure along the reflecting surface is minimized and will be polished away in a later step, see Figure 1b.

Lightweighting

The lapped block surface is then sliced again to the desired segment thickness exposing a new block surface for future lapping. The ~0.5 – 1.0 mm thick segment with the lapped reflecting surface can now undergo additional fabrication steps to remove the damaged crystal structure, see Figure 1c.

Acid Etching

Deep reactive ion etching is used to remove the damaged crystal structure from the back surface and edges of each segment.

Polishing

The lapped reflecting surface of each segment is then polished to further improve the mid-high spatial frequency errors and remove the damage layer created by lapping, see Figure 1d.

Trimming

To accurately set the segment height and width, the central region of each segment is trimmed

and the segment edges are discarded. Trimmed edges are also polished thereby eliminating the last portion of damaged crystal structure in the entire segment, see Figure 1e.

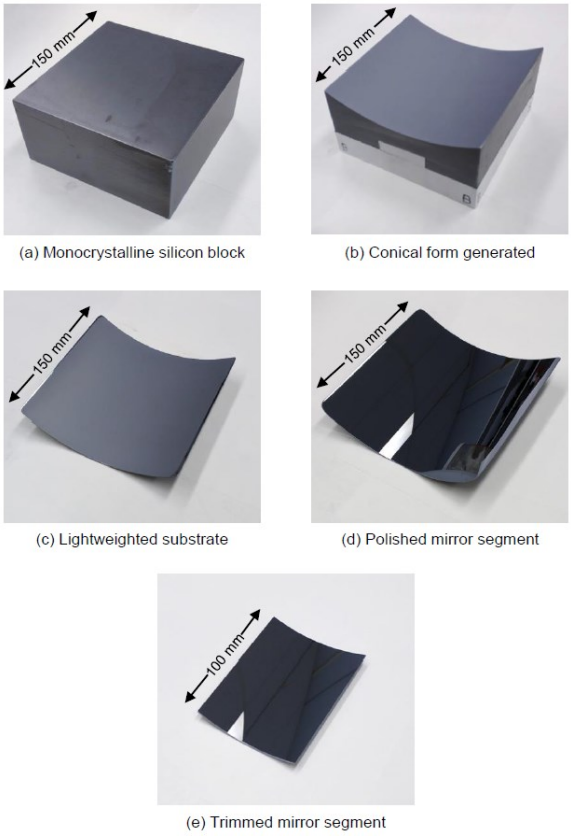

FIGURE 1. Fabrication steps for lightweight Silicon X-ray mirror segments [4].

Figure Correction

Under investigation is the potential addition of a post segment polish figure correction using surface metrology data to correct low order figure errors. One such process that has been successfully demonstrated on polished segments is Ion Beam Figuring (IBF). Charged ions erode surface atoms from the Silicon mirror segment with a calibrated removal function such that high spots are reduced to correct low order surface figure errors (features > ~5 mm in size can be improved). Using two iterations of IBF to correct one polished mirror segment resulted in a theoretical resolution of 0.44 arc-seconds HPD at 1 keV based on surface metrology data, see Figure 2.

While the IBF process requires specialized machinery and processing time (1-3 hours per segment), the additional per segment cost is acceptable for proposed high resolution X-ray telescope concepts.

X-ray Test Verification

At the 600-m X-ray beamline located at the Goddard Geophysical and Astrophysics Observatory, a pair of mirror segments that underwent the fabrication process described in this paper (including IBF figure correction) were aligned and measured to have an angular resolution of 3.5 arc-seconds HPD at 4.5 keV [5].

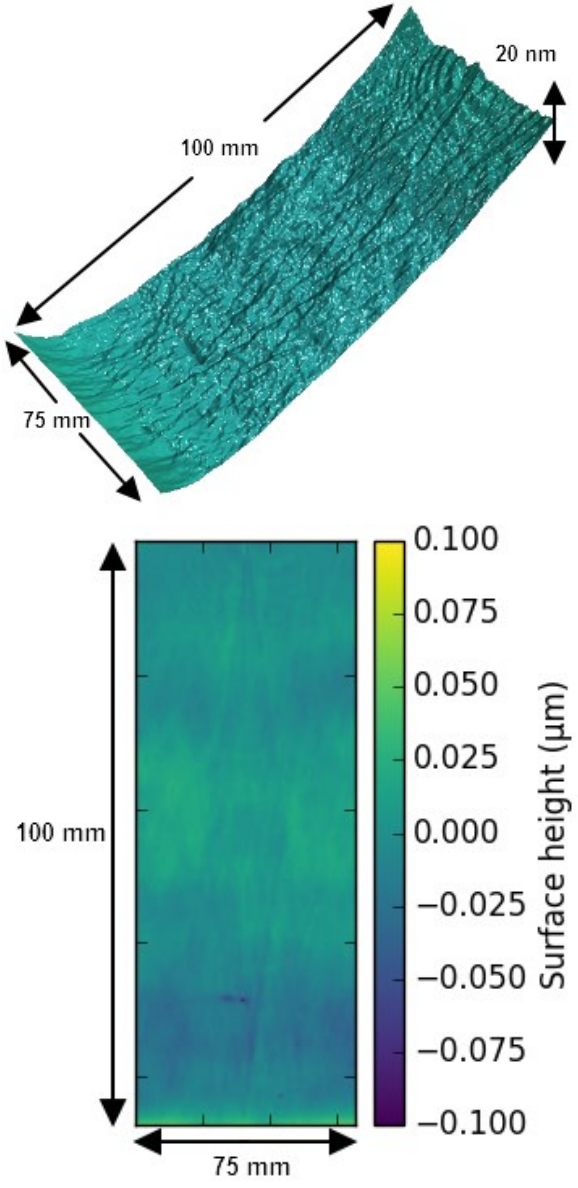

FIGURE 2. Surface metrology data for a Silicon X-ray mirror segment after polishing and Ion Beam Figuring processes. The lowest orders

have been removed (up to 2nd order) to show detail.

CONCLUSIONS

The fabrication process is currently flexible enough to support a wide range of X-ray telescope configurations and instruments (wide-field survey, spectroscopy and calorimetry missions). Interferometric measurements of the reflecting surface and X-ray performance verification tests confirm the high angular resolution that can be achieved with thin monocrystalline Silicon mirror segments. The segment fabrication steps are parallelizable and employs a traditional lapping and polishing approach for a material with properties conducive for use on a space telescope and has abundant published fabrication research in the semiconductor industry. As we continue to develop the fabrication process for lightweight, high resolution monocrystalline Silicon X-ray mirror segments we will continue to improve the resolution towards the diffraction limit while at the same time improve the fabrication process and machinery to reduce segment fabrication costs to support the next generation of X-ray telescopes.

REFERENCES

[1] VanSpeybroeck L, et al. Performance expectation versus reality. SPIE Proceedings. 1997; 3113: 89.

[2] Gondoin P, et al. X-ray multi-mirror (XMM) telescope. SPIE Proceedings. 1994; 2279: 86-100.

[3] Zhang W, et al. Monocrystalline silicon and the meta-shell approach to building X-ray astronomical optics. SPIE Optical Engineering & Applications, Optics for EUV, X-Ray, and Gamma-Ray Astronomy VIII. 2017.

[4] Riveros R, et al. Progress on the fabrication of lightweight single crystal silicon X-ray mirrors. SPIE Optical Engineering & Applications, Optics for EUV, X-Ray, and Gamma-Ray Astronomy VIII. 2017.

[5] Chan K, et al. Kinematic alignment and bonding of mirrors for high-resolution x-ray optics. SPIE Optical Engineering & Applications, Optics for EUV, X-Ray, and Gamma-Ray Astronomy VIII. 2017.

Fabrication of X-ray imaging mirrors for an achromatic and high-resolution full-field X-ray microscope

Jumpei Yamada, Satoshi Matsuyama, Shuhei Yasuda, Yasuhisa Sano, and Kazuto Yamauchi
Department of Precision Science and Technology, Graduate School of Engineering, Osaka University, Osaka, Japan

INTRODUCTION

In the X-ray region, many types of focusing and image-forming optics are developed and applied to X-ray microscopy and microanalysis. X-ray focusing mirrors, which utilize a total-reflection effect and geometrical property of an ellipse or parabola, are regarded as one of the best methods for generating X-ray nanofocused beams owing to their large acceptable aperture, high reflectivity, and achromaticity. However, X-ray focusing mirrors must be precisely fabricated because X-ray wavelengths are so short. To realize diffraction-limited focusing, the mirrors require a shape accuracy of a few nanometer peak-to-valley (PV). In addition, the surface roughness should be equivalent to that of a high-quality silicon wafer, in order not to degrade the reflectivity. To realize such high-quality X-ray focusing mirrors, we have developed ultraprecise surface figuring techniques such as elastic emission machining [1] and ion beam figuring (IBF) [2]. Additionally, optical metrology such as microstitching interferometer (MSI) [3] and relative angle stitching interferometer (RADSI) [4] have been developed to measure aspherical shapes. Utilizing the surface figuring and measurement methods, tow-dimensional 30 nm X-ray focusing could be done [5] with a crossed-mirror configuration (Kirkpatrick-Baez (KB) mirror [6]) (Fig. 1 (a)).

In contrast to the case of the focusing, the KB mirror is not suitable for the image-forming (imaging) because it suffers from narrow field-of-view that stems from the coma aberration. To overcome the problem, we have developed the advanced KB mirror [7, 8] based on concave and convex mirrors, which consists of two pairs of elliptical concave and hyperbolic convex mirrors that are aligned perpendicularly to each other (see Fig.1 (b)). In the one-dimensional imaging mirror pair, a mathematical focal point of the hyperbola coincides with that of the ellipse (Fig. 1 (c)). Thus, it satisfies the Fermat's principal and Abbe's condition; the spherical aberration and coma aberration are eliminated. Furthermore, the

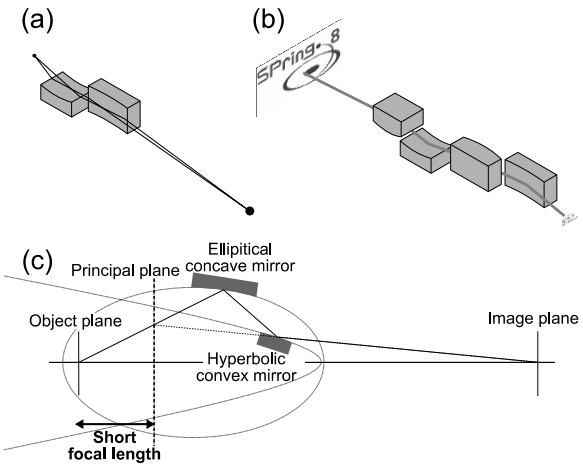

Figure 1. Schematic diagrams of (a) the KB mirror, (b) the advanced KB mirror based on concave and convex mirrors, and (c) cross section of (b).

combination of concave and convex mirrors enable the focal length to be short which leads to high magnification imaging. The short focal length is highly advantageous to practical application of X-ray analysis and laboratory size X-ray sources.

Although this optical system has the potential to realize achromatic and high-resolution X-ray imaging, the mirrors used in the advanced KB system require twice as high shape accuracy, because of double reflection. In this study, we fabricated the one-dimensional imaging mirror pair. Then, demagnification imaging test was performed at synchrotron radiation facility of SPring-8.

OPTICAL DESIGN OF MIRRORS

We designed a one-dimensional imaging mirror pair for hard-X-ray imaging with sub-50-nm resolution under total-reflection conditions. The length of the entire imaging system was set to be approximately 2 m so that it is compatible for practical application in synchrotron radiation facility and laboratory-size X-ray sources. The

glancing incident angles were less than 6 mrad. The lengths of the mirrors were approximately 8 mm, which is remarkably short compared to those of conventional X-ray mirrors. The focal length of the optical system was 6.51 mm, resulting in a magnification factor of 321 even with such a compact setup. The numerical aperture of the system was 1.6×10^{-3}, which would realize a resolution of 40 nm at an X-ray energy of 10 keV. Wave-optical calculations based on Fresnel–Kirchhoff's diffraction integral, which we previously developed [9, 10], revealed that both mirrors should be fabricated with a peak-to-valley (PV) shape accuracy of 2 nm [8].

FABRICATION RESULTS OF MIRRORS

We fabricated the elliptical concave and hyperbolic convex mirrors using the IBF system for surface figuring, and MSI and RADSI for measurement. The mirrors were fabricated on the Si-Cz (001) ingot substrates with effective areas of 8.2 x 3.0 mm^2 (ellipse) and 8.7 x 3.0 mm^2 (hyperbola). We processed the mirrors with the deterministically controlled dwell time of the ion beam. The distribution of the dwell time was calculated from the distribution of removal amounts by the deconvolution method. The total processing time was 45.7 hours. Figure 2 shows the fabrication results of hyperbolic convex and elliptical concave mirrors. The residual shape errors were approximately 2 nm PV, which were sufficient values comparing with the required shape accuracy.

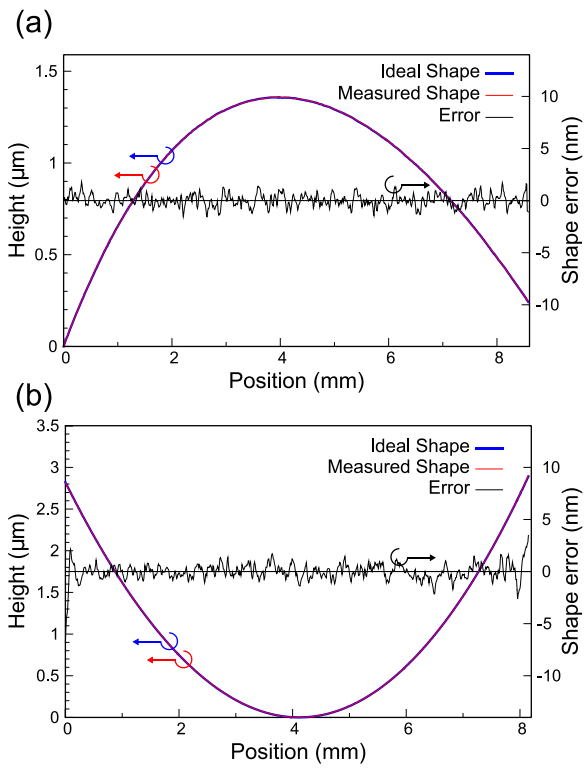

Figure 2. Fabrication results of (a) hyperbolic convex mirror and (b) elliptical concave mirror.

The residual shape errors predominantly existed in a range of spatial wavelength of 0.1-0.3 mm. The spatial resolution of the shape correction by the IBF processing was limited by the diameter of the ion beam, which was 0.5 mm. Thus, it was suggested that the high-frequency shape errors originated from the primary surface of the substrate that was finished by conventional polishing. Figure 3 shows the results of power spectral density (PSD) analysis of the shape errors of elliptical and hyperbolic mirrors before and after processing. PSDs with a spatial frequency ranging from 0.02 mm to 0.3 mm were obviously dependent on the primary shape errors. A highly accurate pre-polishing method for the substrate will be needed to decrease shape errors.

After the mirror fabrication, the surfaces of the mirrors were coated with molybdenum (Mo) to obtain high reflectivity of X-ray. Surface roughness characterization using a white-light interference microscope (Zygo, NewView 5030), as shown in Figure 4, revealed that Mo-coated surfaces have root-mean-square (RMS) roughness values of approximately 0.35 nm over areas of 64 × 48 μm^2, which were almost same values as those of unprocessed surfaces. These smooth surfaces would not degrade the reflectivity for X-rays.

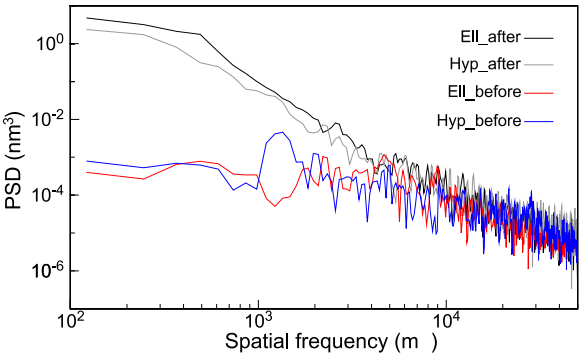

Figure 3. Comparison of power spectral density function of the before and after shape errors of elliptical and hyperbolic mirrors, shown in log scale.

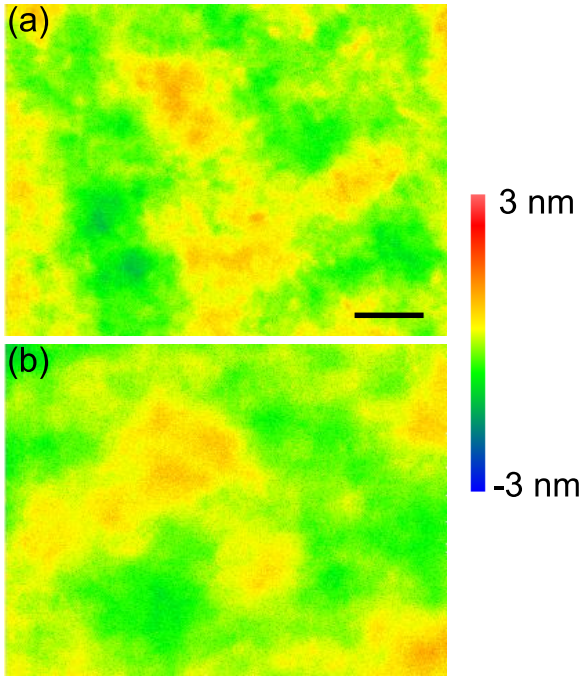

Figure 4. Surface profiles (64 × 48 μm²) of the (a) elliptical and (b) hyperbolic mirrors, the RMS roughness values of which were 0.357 and 0.348 nm, respectively, measured by a white-light interference microscope after the coating. The scale bar is 10 μm.

DEMONSTRATION EXPERIMENTS

A one-dimensional demagnification imaging (focusing) test was performed at BL29XUL of SPring-8. Fig. 5 schematically describes the experimental set up installed at BL29XUL (experimental hutch 2) of SPring-8. The demagnification imaging allows us to precisely evaluate the experimental line spread functions (LSFs), which directly determine the performance of the imaging system. A cross slit was placed at approximately 2 m upstream from the mirrors for generating a practical point source. A demagnified image of a slit with 10 μm width was formed at 6.5 mm downstream from the principal plane of the mirrors. A wire scanning method with a 200-μm-diameter gold wire, ion chanmber and a PIN photodiode was used to evaluate the intensity profile of the demagnified image.

Fig. 6 shows the measured LSF with full width at half-maximum (FWHM) of approximately 40 nm at an X-ray energy of 10 keV. When the conventional mirror optics was used, the FWHM of 40 nm could never be achieved because of the limitation of magnification. The results indicated that our system would enable a high-spatial-resolution imaging with compact, e.g., ~2 m setup thanks to combination of concave and convex surfaces and precisely fabricated mirrors.

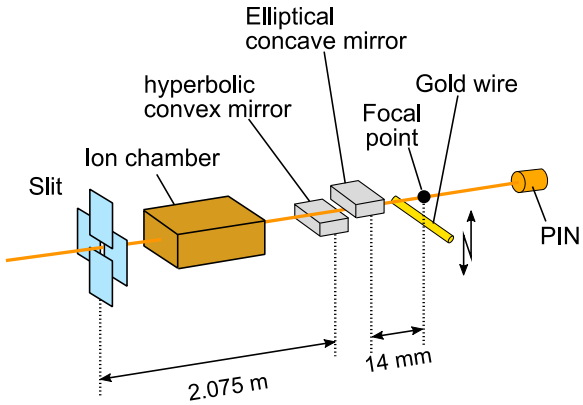

Figure 5. Schematic of experimental setup installed at BL29XUL of SPring-8.

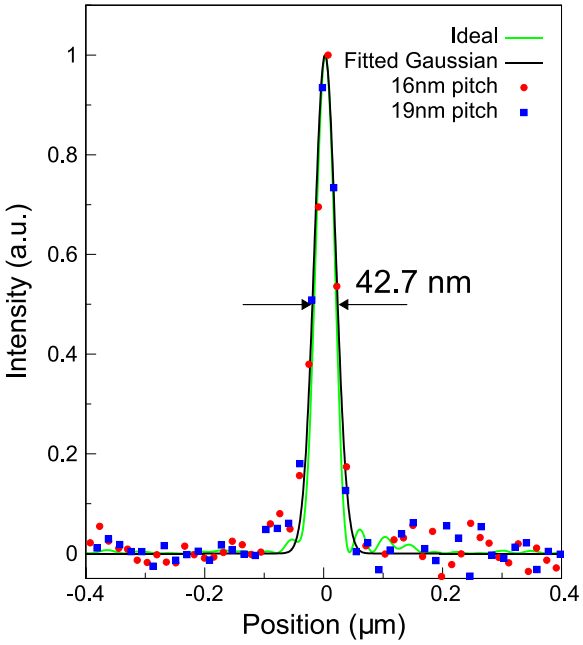

Figure 6. Measured LSF at an X-ray energy of 10 keV.

ACKNOWLEDGEMENTS

The authors wish to thank Drs. Tetsuya Ishikawa, Makina Yabashi and Yoshiki Kohmura of SPring-8/RIKEN for helpful discussions and support. This research was supported by JSPS KAKENHI (Grant No. JP26286077). It was partially supported by JSPS KAKENHI (Grant No. JP16H06358), JSPS Fellows (Grant No. JP16J009530) and JSPS Core-to-Core Program on International Alliance for Material Science in Extreme States with High Power Laser and XFEL.

REFERENCES

[1] Yamauchi K., Mimura H., Inagaki K., and Mori Y. “Figuring with sub-nanometer-level accuracy by numerically controlled elastic emission machining.” Rev. Sci. Instrum. **73** 4028 – 4033 (2002).

[2] Yamada J., Matsuyama S., Sano Y., and Yamauchi K. #Development of ion beam figuring system with electrostatic deflection for ultraprecise X-ray reflective optics.” Rev. Sci. Instrum. **86** 093103 (2015).

[3] Yamauchi K., Yamamura K., Mimura H., Sano Y., Saito A., Ueno K., Endo K., Souvorov A., Yabashi M., Tamasaku K., Ishikawa T., and Mori Y. “Microstitching interferometry for X-ray reflective optics.” Rev. Sci. Instrum. **74** 2894 (2003).

[4] Mimura H., Yumoto H., Matsuyama S., Yamamura K., Sano Y., Ueno K., Endo K., Mori Y., Yabashi M., Tamasaku K., Nishino Y., Ishikawa T., and Yamauchi K. “Relative angle determinable stitching interferometry for hard X-ray reflective optics.” Rev. Sci. Instrum. **76** 045102 (2005).

[5] Matsuyama S., Mimura H., Yumoto H., Sano Y., Yamamura K., Yabashi M., Nishino Y., Tamasaku K., Ishikawa T., and Yamauchi K. “Development of scanning x-ray fluorescence microscope with spatial resolution of 30 nm using Kirkpatrick-Baez mirror optics.” Rev. Sci. Instrum. **77** 103102 (2006).

[6] Kirkpatrick P. and Baez A. V. “Formation of optical images by X-rays.” J. Opt. Soc. Am. **38**(9) 766-774 (1948).

[7] Kodama R., Ikeda N., Kato Y., Katori Y., Iwai T. and Takeshi K. “Development of an advanced Kirkpatrick-Baez microscope.” Opt. Lett. **21**(17) 1321-1323 (1996).

[8] Yamada J., Matsuyama S., Sano Y., and Yamauchi K. “Simulation of concave–convex imaging mirror system for development of a compact and achromatic full-field x-ray microscope.” Appl. Opt. **56**(4) 967-974 (2017).

[9] Yamauchi K., Yamamura K., Mimura H., Sano Y., Saito A., Endo K., Souvorov A., Yabashi M., Tamasaku K., Ishikawa T. and Mori Y. “Wave-optical evaluation of interference fringes and wavefront phase in a hard-X-ray beam totally reflected by mirror optics.” Appl. Opt. **44** 6927 (2005).

[10] Matsuyama S., Mimura H., Yumoto H., Yamamura K., Sano Y., Endo K., Mori Y., Nishino Y., Tamasaku K., Ishikawa T., Yabashi M. and Yamauchi K. “Diffraction-limited two-dimensional hard-X-ray focusing at the 100 nm level using a Kirkpatrick-Baez mirror arrangement.” Rev. Sci. Instrum. **76** 083114 (2005).

DESIGN OF POSITIONING SYSTEM FOR X-RAY SPLIT AND DELAY

Hongliang Shi*, Diling Zhu, Donald W. Schafer, Andrew H. Barada, Justin H. James, Lance Lee, Tyler Johnson, Yanwen Sun, Karl L. Gumerlock, Lin Zhang, Ted O. Osier, Randy A. Whitney, Brian E. Smith, Josep Nicholas, Onaopemipo P.O.Alagbe, Aymeric Robert
SLAC National Accelerator Laboratory
Stanford University
Menlo Park, CA 94025

INTRODUCTION

The ability to split femtosecond free electron laser pulses and recombine them with an adjustable delay has numerous scientific applications such as X-ray photon correlation spectroscopy and X-ray pump X-ray probe measurements. Osaka et al. [1] developed a split-delay X-ray optics using Si(220) crystals. Pardini et al. [2] designed a a mirror-based delay line for X-rays at the Lawrence Livermore National Laboratory. Currently, a wavefront-splitting based hard X-ray split-delay system is under development at Linac Coherent Light Source (LCLS) at SLAC National Accelerator Laboratory [3].

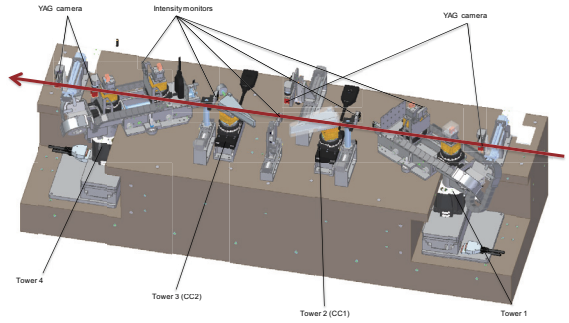

FIGURE 1. Split and delay system overview.

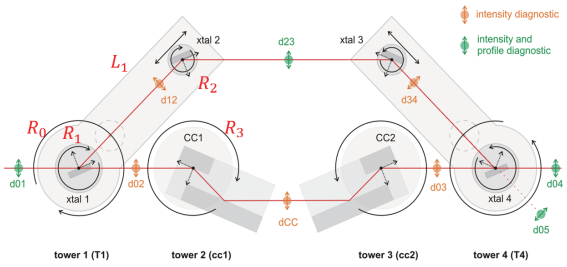

FIGURE 2. Beam propagation with motion system.

*address all correspondence to this author, Email: hshi2@slac.stanford.edu.

After conceptual design process, we present in this paper an updated design of a motion system, which is placed symmetrically on a granite table for SLAC hard X-ray optical split and delay system, shown in Fig. 1. The design configuration incorporates a horizontal scattering geometry using a series of Si(220) crystal reflections. These crystals are placed on two delayed arms and two fix-delay arms of the motion system. By means of positioning the delay and constant arms, the split and delay system covers the energy range between 7 keV and 12 keV, and a delay range from -10 picoseconds (ps) up to 500 ps.

One of the primary technical challenges in the realization of such split-delay system is how to maintain the spatial overlap of two micron-scale focal spots in the sample plane during the time delay adjustments. Our design features a new design of a planar air bearing based delay line to minimize the parasitic angular motion as well as to increase the overall stability of the crystal manipulation motion stacks. A lot of work has been done regarding air bearing stage [4]. Ro et al. [5] presented a linear ultra-precision air bearing stage with active magnetic preloads. Erkorkmaz et al. [6] designed a 2DOF translational stage by adopting air bearing arrangement. However, when those air bearing stages are connected to other stages in a serial chain to achieve a multi-DOF motion, the translational motion error of the air bearing stage is coupled with the motion errors of other stages connected due to the serial chain effect. In this paper, we proposed a design of air bearing based linear stage, which is capable of decoupling the parasitic motion errors by setting the granite table as a reference plane and adopting a 2DOF flexure mechanism to decouple the motion created from the driving lead screw.

MOTION SPECIFICATION

As shown in Fig. 2, the two delayed arms are named as tower 1 and tower 4, which mainly in-

cludes three rotational displacement R_0, R_1, R_2 and a translational displacement L_1. The two constant arms are named as tower 2 and 3, which has a main rotational displacement R_3.

The control of energy is achieved by the rotational angles of R_0, R_1, R_2 and R_3. In the operation, a target energy between 7 keV and 12 keV is selected and Bragg angle [7] is calculated correspondingly. R_0 rotates to $2\theta_\beta$. R_1 and R_2 rotate to -θ_β. R_3 of tower 2 and 3 rotates to the position of -$2\theta_\beta$. 2 crystal channel cuts are mounted on the top of tower 2 and 3. A free electron X-ray laser is split into two beams when it hits the first crystal on tower 4. The delay of the beam is controlled by L_1. The beam reflected from the channel cut is noted as the fixed beam. On the contrary, the other beam is denoted as the delayed beam which reflected by the crystals mounted on tower 1 and 4. Setting the fixed beam as the reference beam, the delay of the up beam can be achieved by controlling the motion of the tower 1 and 4.

The bottom R_0 is rotated to a certain $2\theta_\beta$, the energy of the X-ray can be selected to 7 keV. R_1, R_2 and R_3 rotate correspondingly. By moving the air bearing based translational stage, the delay of the X-ray is achieved at 7 keV. In order to control the energy to selected 12 keV, tower 1 and 4 rotates to a new target position. Again, the delay at 12 keV can be achieved by the translational displacement of the translational stage. In order to align, calibrate and test the system, tower 1 and 4 can also reach the position vertical or parallel to the beam propagation direction.

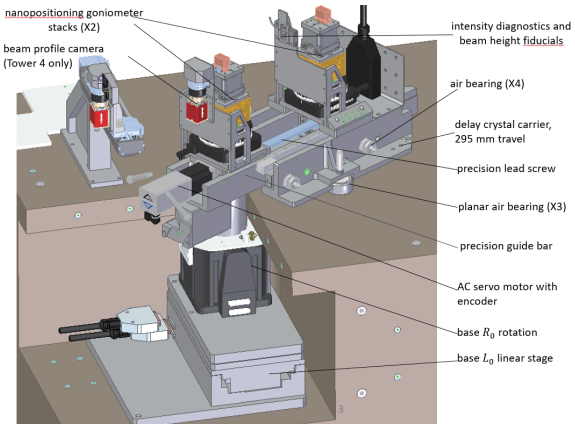
nanopositioning goniometer stacks (X2)
beam profile camera (Tower 4 only)
intensity diagnostics and beam height fiducials
air bearing (X4)
delay crystal carrier, 295 mm travel
precision lead screw
planar air bearing (X3)
precision guide bar
AC servo motor with encoder
base R_0 rotation
base L_0 linear stage

FIGURE 3. Design of tower 1 and 4.

The detail design of tower 1 and 4 are shown in Fig. 3. A translational stage, L_0, is mounted to the base of the granite table, which is only used to move tower 1 and 4 to a none operation mode in which the beam bypasses the split and delay system. During operation, the translational stage is moved and fixed at the position shown in Fig. 3. On the top of the translational stage, there is a rotational stage R_0. This stage is used to achieve the base $2\theta_\beta$ rotation. On the top of R_0, we designed an air bearing based stage to achieve ultra-precision translational motion. This translational motion controls the delay of the beam. The design in detail is shown in next section. On the top of the translational stage, there are two identical sets of stages to align and mount single crystal silicon A and B. It includes X-Y position stage, goniometer, and Z position stage from bottom to up. Beam profile camera, intensity diagnostics and beam height fiducials are mounted for the beam testing and calibration.

The motion specification and the choice of the positioning stage are shown in Fig. 4 in detail. The main stages, L_1, $R_0 - R_3$ are the Aerotech stages[8] [1]. The auxiliary stages includes: 1. the bypass mode stages L_0 and L_2. 2. the Attocube piezo stages [9] and the Newport manual stages [10] used to align the top crystal to the beam propagation. The motion and the function of the auxiliary stages in alignment are not illustrated in detail here.

DESIGN OF AN AIR BEARING BASED LINEAR STAGE

As illustrated in the previous section, when tower 1 and 4 rotate to a target Bragg angle position, L_1 is used to control the beam delay by changing the relative distance between crystal A and crystal B. Thus, the design of the translational stage is critical. There are 3 specifications in evaluating the performance of the translational stage in this split and delay system. 1. The parasitic rotational angle. During the motion of the stage, the parasitic rotational angle of the stage should be less than 4 μrad. For example, the vertical parasitic motion caused by the granite table surface directly affects the overlap of the two beams. 2. Stability. Crystal B on the carrier block needs to be in a stable status so that the fixed and delayed

[1] Certain commercial equipment, instruments, or materials are identified in this paper in order to specify the design. Such identification is not intended to imply recommendation or endorsement by the SLAC National Accelerator Laboratory, nor is it intended to imply that the materials or equipment identified are necessarily the best available for the purpose.

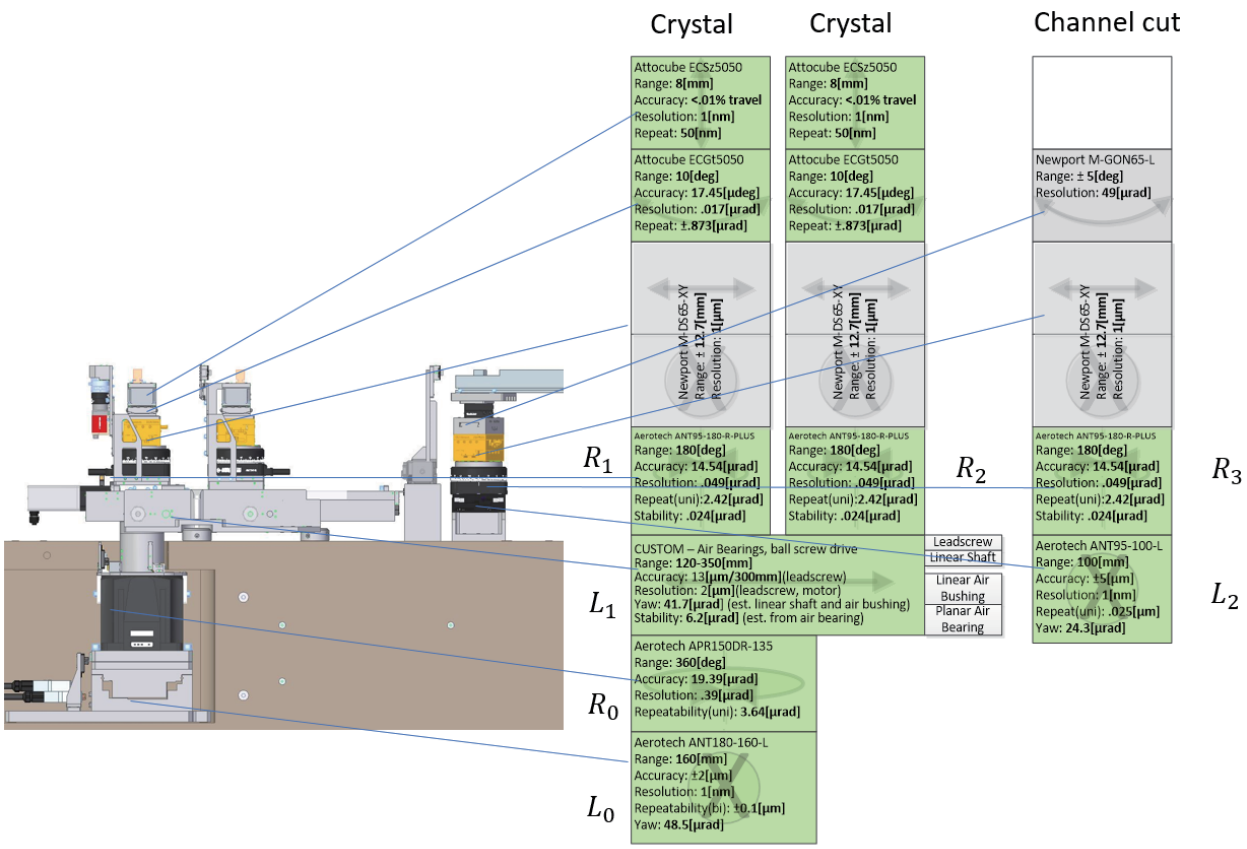

FIGURE 4. Motion specification.

beams are able to overlapped. 3. Accuracy. The accuracy of the translational stage is 3 μm.

In this manuscript, we propose an air bearing based linear stage to meet the three specifications for controlling the delay of the beams. As shown in Fig.3, the air bearing stage is composed of a well machined guide bar and a moving carriage block. Inside of the guide bar, a lead screw drive is installed. An AC servo motor with encoder is mounted to the lead screw. The nut of the lead screw system is mounted to a center flexure of the carriage block. The carriage block slides on the guide bar through four horizontal air bearings, which are mounted inside of the carriage block. Three vertical air bearings are mounted symmetrically to the carriage block with the working surface facing to the granite table. By relying on the three vertical air bearings, the carriage block floats on the granite table. The center flexure has 2DOF translational compliance and it decouples the parasitic translational motion of the lead screw.

As a conclusion, the stage is designed by adopting ultra-low friction based air bearing, flexure mechanism for decoupling parasitic motion, and a precise lead screw system. The out-of-plane parasitic rotational angle is determined by the vertical displacement of the three air pads and further determined by the flatness of the granite table. The stability of the stage is directly determined by the stability of the granite table through three air pads because the motion of the carriage block is decoupled from the guide bar through the flexure. The accuracy of the stage is determined by linear encoder. Compared to directly mounting a traditional motion stage to R_0 in serial, this air bearing stage features achieving the serial translational motion, while diminishing the parasitic motion error from the assembly angle, wobble angle, eccentric angle. Most importantly, traditional linear stage is mounted as a cantilever beam and thus the vertical vibration caused by R_0 could be amplified with the motion of the carriage.In contrast, the vertical vibration of this air bearing stage is directly related to the granite table through three air

pads without the amplification factor of cantilever beam.

CONCLUSIONS

In conclusion, we present an updated design of a multi-DOF positioning system for split and delay of hard X-ray of Linac Coherent Light Source at SLAC National Accelerator Laboratory. By means of positioning the delay and constant arms, the split and delay system covers the energy range between 7 and 12 keV, and a delay range from -10 ps up to 500 ps. This system features an novel ultra-precision air bearing based linear stage, which is capable of decoupling the parasitic motion errors by setting the the granite table as a reference plane and adopting flexure mechanism to decouple the motion from lead screw.

ACKNOWLEDGMENT

This manuscript has been authored by Stanford University SLAC National Accelerator Laboratory under Contract No. DOE Contract DE-AC02-76SF00515 with the U.S. Department of Energy. The United States Government retains and the publisher, by accepting the article for publication, acknowledges that the United States Government retains a non-exclusive, paid-up, irrevocable, world-wide license to publish or reproduce the published form of this manuscript, or allow others to do so, for United States Government purposes.

REFERENCES

[1] Osaka T, Hirano T, Yabashi M, Sano Y, Tono K, Inubushi Y, et al. Development of split-delay x-ray optics using Si(220) crystals at SACLA. Proc SPIE. 2014;9210:921009–921009–10.

[2] Pardinia T, Hill R, Decker T, Alameda J, Soui R, Aquila A, et al. The MEL-X project at the Lawrence Livermore National Laboratory: a mirror-based delay line for x-rays. Proc SPIE. 2015;9589.

[3] Zhu D, Sun Y, Schafer DW, Shi H, James JH, Gumerlock KL, et al.. Development of a hard x-ray split-delay system at the Linac Coherent Light Source; 2017.

[4] Gao W, Arai Y, Shibuya A, Kiyono S, Park CH. Measurement of multi-degree-of-freedom error motions of a precision linear air-bearing stage. Precision Engineering. 2006;30(1):96 – 103.

[5] Ro SK, Kim S, Kwak Y, Park CH. A linear air bearing stage with active magnetic preloads for ultraprecise straight motion. Precision Engineering. 2010;34(1):186 – 194. CIRP-CAT 2007.

[6] Erkorkmaz K, Gorniak JM, Gordon DJ. Precision machine tool XY stage utilizing a planar air bearing arrangement. CIRP Annals - Manufacturing Technology. 2010;59(1):425 – 428.

[7] Als-Nielsen J, McMorrow D. Elements of Modern X-ray Physics. John Wiley and Sons, Inc.; 2011.

[8] Aerotech stage. https://www.aerotech.com/;.

[9] Attocube stage. http://www.attocube.com/;.

[10] Newport stage. https://www.newport.com/;.

PARADIGM CHANGE IN GEAR INSPECTION BASED ON A HOLISTIC DESCRIPTION, MEASUREMENT AND EVALUATION OF GEAR FLANKS

Gert Goch[1], Kang Ni[1], Yue Peng[1] and Anke Guenther[2]
[1]Center for Precision Metrology, UNC Charlotte, Charlotte, NC, USA
[2]Reishauer AG, Wallisellen, Switzerland

INTRODUCTION

Gears have a decisive importance for the functionality of automotive, aerospace and machinery transmission systems [1]. The demanding geometric accuracy requirements for gears are indispensable to reduce the noise emission and increase the power density. Various manufacturing technologies from roughing [2] to finishing [3] have been significantly improved in the past decades to produce high quality gears with complex flank modifications. Gear inspection on a high level of accuracy and speed is indispensable for a modern gear production from both quality control and process improvement perspectives. CNC-controlled tactile Gear Measuring Instruments (GMIs) and Coordinate Measuring Machines (CMMs) have been dominating over the past decades. Line oriented measurement and evaluation of gear geometric features such as profile, helix and pitch deviations are well established in current gear tolerancing and evaluation standards [6], enabling a standardized inspection procedure for an automobile-size gear, in which several deficiencies have been identified [8].

Today, complex surface structures on gear flanks modifying “purely involute” gear flank geometry are well established at gear manufacturers that aim at improving the functional performance [6]. It is necessary to obtain topographical information on entire gear flanks to diagnose manufacturing process variations, to assess the gear quality, and even to predict the gear meshing conditions [4,5]. Therefore, a paradigm change from a line oriented gear inspection representing the state-of-the-art to an area oriented, holistic gear measurement and evaluation is needed requiring:

- A complete 3D geometric description of gear flanks;
- A non-contact measuring system that enables a reliable data acquisition of all flanks in reasonable time;
- An effective evaluation method for calculating all gear deviation parameters from areal measurement data.

This paper offers a systematic approach for key technical aspects of future inspection technologies for the cylindrical gear.

CONVENTIONAL LINE ORIENTED GEAR INSPECTION

FIGURE 1 shows a typical CMM based measurement with multiple-styli configuration, highlighting the location of profile, helix (red lines) and pitch point (yellow dots) on a gear sample. Correspondingly, the evaluation charts and parameters for a measured profile, including total profile deviation (F_α), profile form deviation ($f_{f\alpha}$), and profile slope deviation ($f_{H\alpha}$) are illustrated in FIGURE 2, according to the latest ISO standard [6]. The marked L_α is the profile evaluation length and g_α is the length of path of contact in profile direction.

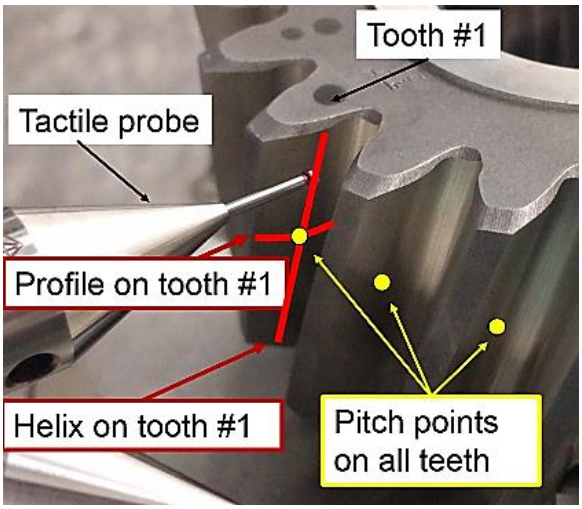

FIGURE 1. Characteristic lines and points on gear flanks in conventional gear inspection.

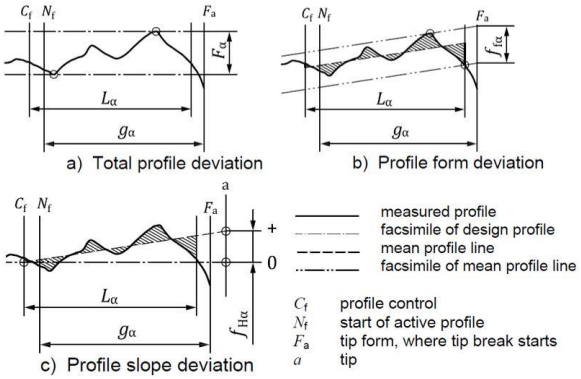

FIGURE 2. Conventional gear evaluation charts for line oriented flank measurement [6].

HOLISTIC DESCRIPTION OF GEAR FLANKS WITH 3-D MODIFICATIONS

For the 3-D flank of a helical gear (i.e. $\beta_b \neq 0$), the flank equation can be generated by "threading" the origin of the involute profile (yellow dot in FIGURE 3) along the base helix line (black line). This is mathematically realized by describing the initial angle Λ of the 2-D involute Equation (1) as a function of the third dimension z :

$$\begin{cases} x = r_b \cdot [\cos(\xi + \Lambda(z)) + \xi \cdot \sin(\xi + \Lambda(z))] \\ y = r_b \cdot [\sin(\xi + \Lambda(z)) - \xi \cdot \cos(\xi + \Lambda(z))] \\ z = z \end{cases}, \quad (1)$$

Here, $\Lambda(z) = \eta_b + z \cdot \tan\beta_b / r_b$ is a function of the helix angle on the base circle β_b, the z coordinate and the base space half angle η_b. In Equation (1), the size of each tooth is determined by the range of the rolling angle ξ and the position of each tooth is governed by a Λ angle, whose η_b angle is determined by the number of teeth of the gear [9].

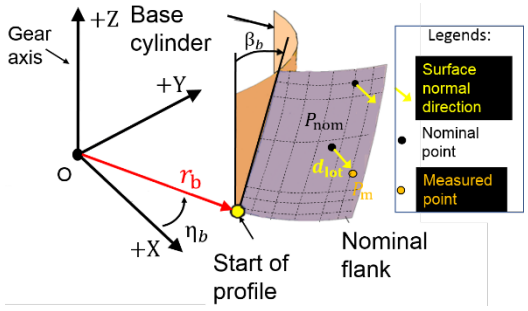

FIGURE 3. One 3D helical flank surface generated by basic geometry parameters.

Applying the aforementioned "threading" model, a unique distance called "plumb line distance" is obtained for any measured point (subscripted with "m") given in cylindrical or Cartesian coordinates (x_m, y_m, z_m) = (ρ_m, φ_m, z_m) [9]. The plumb line distance is the shortest distance from the measured point to the 3D helical gear flank analytically expressed as:

$$|\vec{d}_{lot}| = \frac{r_b}{\sqrt{1+\tan^2\beta_b}}\left\{\sqrt{\frac{\rho_m^2}{r_b^2} - 1} - \arctan\left(\sqrt{\frac{\rho_m^2}{r_b^2} - 1}\right) - \varphi_m + \eta_b + z_m\frac{\tan\beta_b}{r_b}\right\} \quad (2)$$

$|\vec{d}_{lot}|$ is the plump line distance. The aggregated individual plumb line distances form a vector representation of the entire distance map, denoted by $\boldsymbol{d}_{lot}$. Setting $\boldsymbol{d}_{lot}$ to 0 is equivalent to a surface function $F(\rho_{nom}, \varphi_{nom}, z_{nom}; r_b, \alpha_t, \beta, z) = 0$ for the nominal gear geometry. This means that a function $\boldsymbol{d}_{lot} = F(\rho_m, \varphi_m, z_m) = a$ denotes an equidistant surface with a constant deviation of a to the nominal helical gear flank. This interpretation of the d_{lot}-formula offers another major advantage for gear metrology. As for other geometries inspected with CMM technology, where the nominal surface can be described by a function $F(x, y, z) = 0$ (like cylinders, spheres, circles, etc.), neither nominal point coordinates nor surface normal directions are required to evaluate the deviations between actual and nominal gear geometry.

To be consistent with the generation principle and the representation of deviations in conventional evaluation methods, a UVD coordinate system is constructed as shown in FIGURE 4.

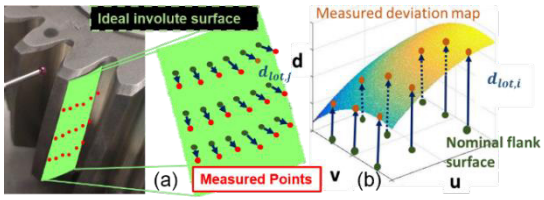

FIGURE 4. Generation of areal deviation and distance map (a), illustration of measured points and ideal involute surface; (b) representation of areal distance map in (u,v,d) coordinate system.

Coordinate u is the generation along the profile direction (roll length, which is the same for the conventional profile evaluation); coordinate v is the generation along the helix direction (z coordinate of the corresponding nominal point, which is the same for the conventional helix evaluation); coordinate d is the value of plumb line distance. As shown in FIGURE 4 (b), the calculated plumb line distances collectively form a distance map of the measured flank in the UVD coordinate system. This map contains only the distances between the actual and nominal gear

flank, so a “pure involute” surface in XYZ coordinate system is equivalent to a plane with d = 0 everywhere. Therefore, for an unmodified gear, whose reference geometry is a “ pure involute” surface, the distance map contains undesired deviations only, which is analyzed for the deviation parameters.

AREAL MEASUREMENT OF CYLINDRICAL GEAR FLANKS

Two instruments were used to capture areal point clouds of a ground gear sample. As shown in FIGURE 5 (a), the gear was measured by a Leitz PMMF302016 CMM equipped with a “star” probe configuration of eight styli. Each flank was scanned in profile direction with 51 distinct lines along transverse planes from the bottom to the top of the gear. The collected point clouds of all flanks represent an areal dataset as shown in FIGURE 5 (b), obtained in about 2.5 hours. An optical CMM (Nikon HN3030) was also used to collect a second area oriented dataset from the same gear sample, in significantly shorter time (several minutes). as shown in FIGURE 6 (a) and (b). The optical instrument captured about 480,000 raw points per flank including sections of the bottom and top lands. A quarter of those points lie within the evaluation range and were used in areal evaluation.

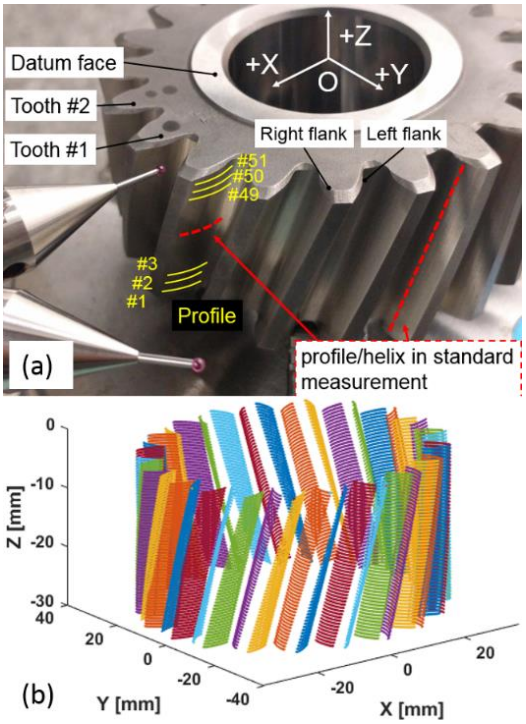

FIGURE 5. Areal flank measurement using a tactile instrument (CMM without rotary table): (a), location of multiple profiles measured on a left flank; (b) raw point clouds of measured flanks.

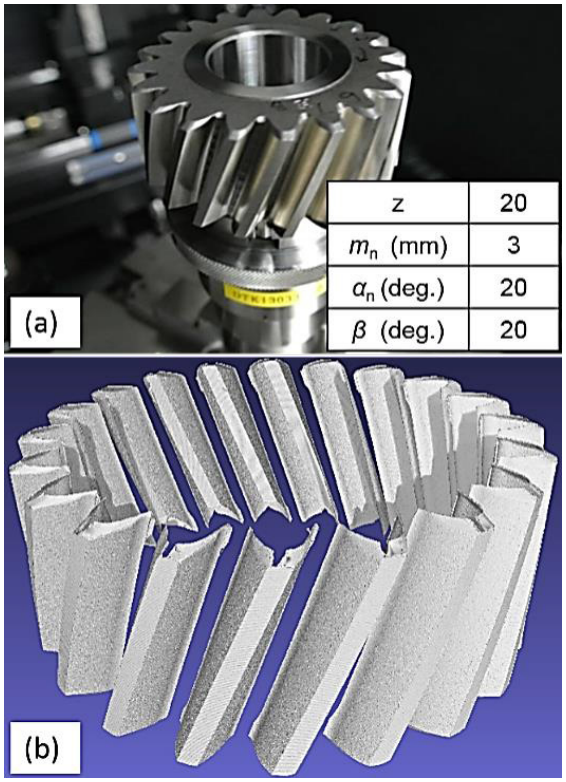

FIGURE 6. Areal flank measurement of the same gear sample as in FIGURE 5, using an optical instrument: (a), setup during optical scanning; (b), raw point clouds of measured flanks.

AREAL EVALUATION OF GEAR FLANKS

DEFINITIONS OF AREAL CHARACTERISTIC PARAMETERS

To characterize the captured areal point clouds covering an entire flank, a set of areal parameters is preferred. According to [12], the areal parameters could be obtained by approximation algorithms based on least-squares method over the evaluation zone, which is bounded by the profile and helix evaluation ranges. Alternatively, a new set of areal parameters (denoted with a superscript “A”) is proposed, as an extension of the standardized line oriented parameters [11].

TABLE 1. Definition and symbolic of a selected list of line oriented [6] vs. areal gear parameters. (“dev.” abbreviated for deviation)

Definition	Line	Areal
Profile slope modification	$C_{H\alpha}$	$C_{H\alpha}^{A}$
Profile slope dev.	$f_{H\alpha}$	$f_{H\alpha}^{A}$
Profile crowning modification	C_{α}	C_{α}^{A}
Profile crowning dev.	N.A.	$f_{C\alpha}^{A}$
Profile form dev.	$f_{f\alpha}$	f_{f}^{A} form dev.
Helix form dev.	$f_{f\beta}$	
Total profile dev.	F_{α}	F_{f}^{A} total form dev.
Total helix dev.	F_{β}	
Single pitch dev.	f_{pi}	f_{pi}^{A}
Cumulative pitch dev.	F_{pi}	F_{pi}^{A}

The 3D illustration of the areal profile slope deviation ($f_{H\alpha}^{A}$) is shown in FIGURE 7.

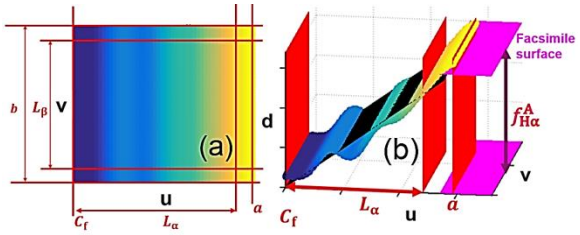

FIGURE 7. Illustration of the areal gear parameters $f_{H\alpha}^{A}$ obtained in a deviation map: (a), top view of the evaluation zone; (b) side view of the areal deviation map.

CALCULATION OF AREAL PARAMETERS BY 2D CHEBYSHEV METHOD

As explained in [10], the information of areal deviations and modifications are intrinsically contained in the areal distance map such as the one in FIGURE 7 (b). Since they are linearly and independently superimposed in the surface normal direction, a decomposition approach was applied to separate the various components into a set of orthogonal base functions, composed of low order 2D Chebyshev polynomials. They are graphically illustrated in FIGURE 8.

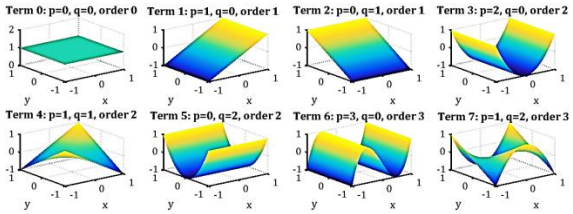
Term 0: p=0, q=0, order 0
Term 1: p=1, q=0, order 1
Term 2: p=0, q=1, order 1
Term 3: p=2, q=0, order 2
Term 4: p=1, q=1, order 2
Term 5: p=0, q=2, order 2
Term 6: p=3, q=0, order 3
Term 7: p=1, q=2, order 3

FIGURE 8. Graphical illustration of the first eight terms (i =0,1, 2,…,7) of 2D Chebyshev polynomials C_i.

Based on their geometric similarity, each term of the low order 2D Chebyshev polynomial can be assigned to one areal component (deviation and/or modification). In addition, due to the orthogonality property of 2D Chebyshev polynomials, the amount of each areal component (characterized by the corresponding areal parameters) can be uniquely determined by the value of the corresponding coefficients for the polynomial base. Equation (3) gives the areal distance map, $D(x,y)$, which is approximated by a linear combination of 2D Chebyshev polynomials.

$$D(x,y) \approx D'(x,y) = \sum_i^N A_i C_i(x,y), \quad (3)$$

where, N is the number of 2D Chebyshev terms used for reconstructing $D'(x,y)$ as an approximation of $D(x,y)$. The 2D Chebyshev coefficients A_i are given by the double integral:

$$A_i = \frac{1}{K}\int_{-1}^{1}\int_{-1}^{1}\frac{D(x,y)C_i(x,y)dxdy}{\sqrt{1-x^2}\sqrt{1-y^2}}, \quad (4)$$

where, K is the normalization factor for 2D Chebyshev polynomials.

VERIFICATION ON GEAR ARTIFACT

Besides the proven effectiveness of the 2D Chebyshev method via numerical simulation [10], it is necessary to verify the method with experimental data. A modification artifact (FRENCO® Gear Artifact M, see FIGURE 9) was measured with the Leitz CMM.

This artifact was specially manufactured to provide different types and amounts of gear modifications on its 36 left flanks. Four of the flanks with their corresponding modifications (profile slope, helix slope, profile crowning and helix crowning of left flanks indicated by “#10”, “#19”, “#20” and “#30”, respectively) were used to test the 2D Chebyshev algorithm as shown in the bottom left corner of FIGURE 9. For areal

evaluation, a total of 99 profile lines were scanned on all flanks without using a rotary table.

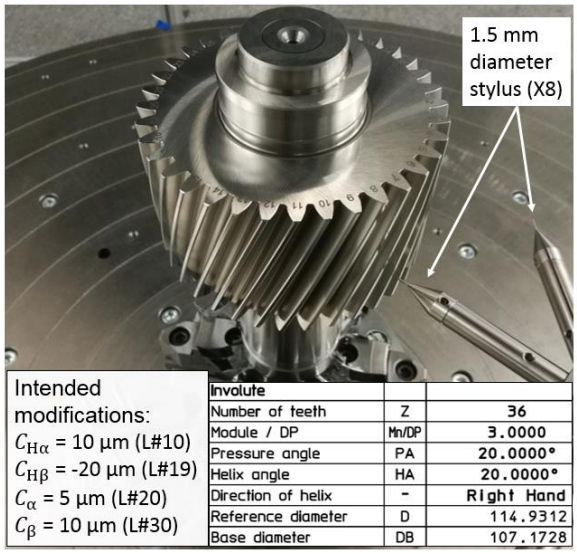
1.5 mm diameter stylus (X8)
Intended modifications:
$C_{H\alpha}$ = 10 µm (L#10)
$C_{H\beta}$ = -20 µm (L#19)
C_{α} = 5 µm (L#20)
C_{β} = 10 µm (L#30)
Involute
Number of teeth Z 36
Module / DP Mn/DP 3.0000
Pressure angle PA 20.0000°
Helix angle HA 20.0000°
Direction of helix - Right Hand
Reference diameter D 114.9312
Base diameter DB 107.1728

FIGURE 9. Basic geometry of the artifact and the intended types of flank modifications on four left flanks at selected teeth.

The measurement results of those four flanks are summarized in TABLE 2. All of the line oriented parameters are adopted from the calibration certificate by standard single line measurement, which have a claimed ± 3 µm extended measurement uncertainty. The areal parameters are evaluated by 2D Chebyshev method. The closeness between the certified line oriented measurement and the areal results shows the effectiveness of the 2D Chebyshev method. However, a detailed investigation of measurement and evaluation uncertainty of the areal parameters (i.e. measurands) is needed in future.

TABLE 2. Comparison between standard line oriented evaluation and the areal evaluation results for four types of flank modifications.

Type of flank modification	Intended [µm]	Line [µm]	Areal [µm]
Profile slope	10	10.2	9.5
Helix slope	-20	-17.6	-16.5
Profile crowning	5	5.7	4.5
Helix crowning	10	9.5	9.6

HOLISTIC EVALUATION OF AREAL DATA OF AND GLOBAL PARAMETERS FOR A WHOLE GEAR

Deviations on gear flanks can result from a diversity of error sources in gear manufacturing processes. In general, two types of deviations could be categorized, each having specific origins in manufacturing processes. The first type is a repeated pattern of deviation, recognized on all teeth, that is caused by errors imposing the same influence on every tooth during manufacturing. For example, an error in a hobbing tool's pressure angle introduces the same profile slope deviation on each tooth, since this tool cuts every tooth during machining. Repeated positioning errors during tooling or systematic kinematic errors in the tool motion control system leave the same deviations on each tooth during a cyclic cutting operation. The other type of deviation is observed on individual flanks, which might be caused by varying machining conditions in manufacturing such as, temperature gradients within the machine tool, tool wear, vibrations, or inhomogeneous material properties of gears etc. Therefore, a holistic evaluation procedure and corresponding sets of parameters are suggested to identify and quantify both repeated patterns observed on all teeth and the individual patterns varying from tooth to tooth. Both types of deviation parameters are necessary for a comprehensive assessment of to fully assess the variation of manufacturing processes and its impact on gear quality. The areal measurement data of the gear sample shown in FIGURE 5 and FIGURE 6 are used as example in the following discussion. This gear was finished by continuous generation grinding. All 20 right flanks were evaluated by 2D Chebyshev method, in which the first 6 2D Chebyshev coefficients were used to reconstruct the areal distance maps.

The areal reconstruction results (tactile CMM) of the first 7 right flanks are shown FIGURE 10. The color-coded plots represent the reconstructed individual areal maps, among which a repeated pattern (slope and crowning) is obvious on every flank in the profile direction.

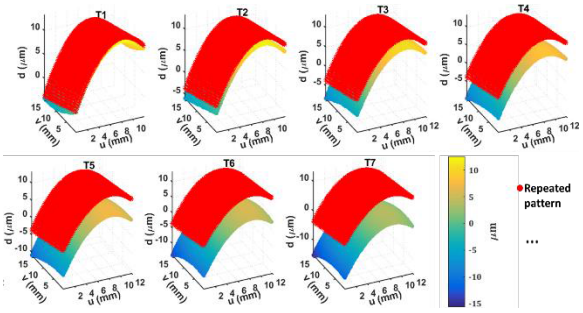

FIGURE 10. Areal distance maps of first 7 reconstructed individual flanks and the repeated pattern for all 20 teeth (measured by tactile CMM, areal evaluation).

The same procedure is used for displaying the optical measurement results, as shown in FIGURE 11.

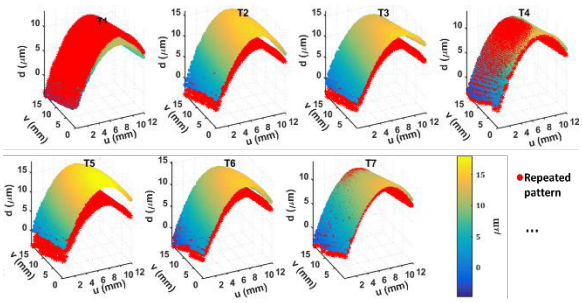

FIGURE 11. Areal distance maps of first 7 reconstructed individual flanks and the repeated pattern for all 20 teeth (measured by optical CMM, areal evaluation).

In FIGURE 10 and FIGURE 11, the repeated pattern (in red) is constructed by its corresponding areal global parameters listed in TABLE 3. The reconstructed individual areal maps show a variety of vertical shifts with respect to the repeated pattern, which is the individual cumulative pitch deviation. The discrepancy of the cumulative pitch deviation between tactile and optical measurement is caused by a different clamping, resulting in a different eccentricity that influences the cumulative pitch deviation. The latter is manifested in FIGURE 10 and FIGURE 11.

In the conventional evaluation, only 16 lines on four teeth are measured in total. However, there is no publication found about an overall evaluation of all flanks in order to extract common shares of flank deviations. Also, the current gear evaluation standards do not distinguish between global gear parameters and individual tooth parameters. To address this issue, five global parameters are investigated for the gear sample measured by tactile and optical instruments. The global parameters are denoted with "g" subscriptions as listed in TABLE 3 for either line oriented or areal evaluation results. The three results coded by the columns A, B and C are obtained from different measurement strategies and evaluation methods. One is the result of a conventional line-oriented inspection procedure (using averaged parameters collected on four teeth only). The other two are based on areal measurements and evaluations, one of them based on tactilely probed data and the other on optically measured data.

TABLE 3. Line oriented vs. area evaluation results of the ground gear sample.

Parameter [µm]	Symbol	A	B	C
Profile slope dev.	$f_{\mathrm{H\alpha g}}^{\mathrm{A}}, f_{\mathrm{H\alpha g}}$	9.7	10.9	8.9
Helix slope dev.	$f_{\mathrm{H\beta g}}^{\mathrm{A}}, f_{\mathrm{H\beta g}}$	-4.1	-3.6	-3.4
Profile crowning	$C_{\mathrm{\alpha g}}^{\mathrm{A}}, C_{\mathrm{\alpha g}}$	9.0	7.1	8.6
Helix crowning	$C_{\mathrm{\beta g}}^{\mathrm{A}}, C_{\mathrm{\beta g}}$	-0.5	0.0	0.0
Flank twist	$S_{\mathrm{g}}^{\mathrm{A}}, S_{\mathrm{g}}$	2.0	-0.5	-1.2

The automobile gear sample used in this comparison is ***not*** a calibrated artefact, therefore, the evaluation results presented in TABLE 3 do ***not*** aim to access the performance of certain measuring instruments or sensor principles. Instead, they aim at a comparison of the proposed evaluation methods alone. This result shows the capability of the 2D Chebyshev method, which offers evaluation results comparable to conventional line oriented methods. The discrepancy can be explained by the fact that the measured data were captured with different instruments (two tactile and one optical), that the evaluations were carried out based on different surface areas of the measuring object (entire flank versus two lines), and that the measuring conditions might have been different.

CONCLUSIONS AND FUTURE WORK

In this paper, a paradigm shift from line oriented measurements and evaluations to a holistic area oriented gear inspection is proposed, comprising areal gear measuring method and areal evaluation strategies. New areal gear parameters are introduced as extensions of the conventional line oriented gear parameters describing both modifications and deviations. The effectiveness of using an orthogonal decomposition algorithm based on 2D Chebyshev polynomials to calculated areal gear parameters meets the increasing demand for an improved holistic evaluation of whole gear flanks. This especially applies when a large amount of point clouds become available by means of optical gear measuring technologies.

Future work includes two areas, firstly to investigate the measurement uncertainty of the presented areal parameters (measurands); secondly, to apply the developed areal gear

evaluation method to the correlation between the areal parameters, the manufacturing process variations and the functional performance of cylindrical gears.

ACKNOWLEDGEMENT

This work is funded by the Affiliates Program of the Center for Precision Metrology (CPM) at UNC Charlotte. The authors gratefully acknowledge the support from Hexagon-Leitz at Wetzlar-Germany, Siemens Energy at Charlotte-USA, Reishauer at Wallisellen-Switzerland, Nikon at Yokohama-Japan and Boston Gear at Charlotte-USA.

REFERENCES

[1] Goch G. Gear metrology. CIRP Annals-Manufacturing Technology 2003; 52, Vol. 2: 659-695.

[2] Bauzakis K.-D., Lili E., Michailidis N., Friderkos., Manufacturing of cylindrical gears by generating cutting processes: A critical synthesis of analysis methods. CIRP Annals – Manufacturing Technology 2008; 57, Vol. 2: 676-696.

[3] Karpuschewski B. Knoche H.-J., Hipke M., Gear finishing by abrasive processes. CIRP Annals – Manufacturing Technology 2008; 57, Vol. 2: 621-640

[4] Lotze, W., Härtig, F. 2001, “3D Gear measurement by CMM,” Fifth International Conference of Laser Metrology and Machine Performance (LAMDAMAP), WIT Press, pp.333-344.

[5] Pfeifer T. Kurokawa S., Meyer S.,Derivation of parameters of global form deviations for 3-dimensional surfaces in actual manufacturing processes. Measurement 2001; 29: 179-200.

[6] ISO, 2013, “Cylindrical gears - ISO system of flank tolerance classification - Part 1: Definitions and allowable values of deviations relevant to flanks of gear teeth,”, ISO 1328-1.

[7] ISO, “Gears - Cylindrical involute gears and gear pairs - Concepts and geometry,” ISO 21771 (2007).

[8] Goch G., Ni K., Peng Y., Guenther A. Future gear metrology based on areal measurements and improved holistic evaluations. CIRP Annals – Manufacturing Technology 2017; 66, Vol. 1: 469-474.

[9] Guenther A., 1996, Flächenhafte Beschreibung und Ausrichtung von Zylinderrädern mit Evolventenprofil, Diploma Thesis, University of Ulm, Germany.

[10] Ni K., Peng Y., Characterization and evaluation of involute gear flank data using an areal model. Proceedings of the 31st ASPE Annual Meeting 2016; 184-189.

[11] Peng Y. Ni K. Goch G. Areal evaluation of involute gear flanks with three-dimensional surface data, Proceedings of the 2017 AGMA Fall Technical Meeting.

[12] Stoebener D., von Freyberg A., Fuhrmann M., Goch G., Areal parameters for the characterization of gear distortions. Mat.-wiss.u.Werkstofftech. 2012; 43: 120 – 124.

Error Budgeting Analysis for Determining Axis Configuration of Ultra Precision Jig Grinding Machines

Sinan Badrawy
Moore Nanotechnology Systems, LLC
Swanzey, New Hampshire, USA

INTRODUCTION

The ever-increasing demand for consumer goods, which is driven by technological advancement and higher consumer expectations in performance and functionality, sets the stage for a shorter product life cycle with higher accuracy requirements. This is particularly true for the consumer electronics mold industry. During the past decade, accuracy requirements of dimension, form, and finish of injection mold tooling has increased. In particular, these demands require improved accuracy, reliability, and productivity from jig-grinding machines. These types of grinding machines are predominantly used to generate precision features such as holes and contours with surface finishes at a sub-micron level. The demand for higher productivity and accuracy leads to investigating alternative machine configurations that would not only support the finish operation through jig-grinding, but that also allows the pre-finish operation of hard milling.

In order to satisfy these demands, investigation and development of a next generation machine concept based upon the well-established jig-grinding machine with alternative kinematic configurations, must be furthered. However, prior to machine design and layout, an error budgeting analysis was conducted on three possible kinematic machine configurations to determine the most suitable design for ultra precision jig-grinding applications with respect to accuracy, repeatability and productivity.

KINEMATIC AXIS CONFIGURATIONS

Prior to determining the possible kinematic axis configuration, it is essential to define the required relative motion between the tool and the workpiece. In general, jig-grinding can be defined as the coordinated motion between a grinding wheel and a workpeice generating prismatic features through either reciprocal, planetary or NC-Path motion, or the combination thereof [1]. Based on this definition any proposed/investigated kinematic configuration has to support these defined motions (Figure 1).

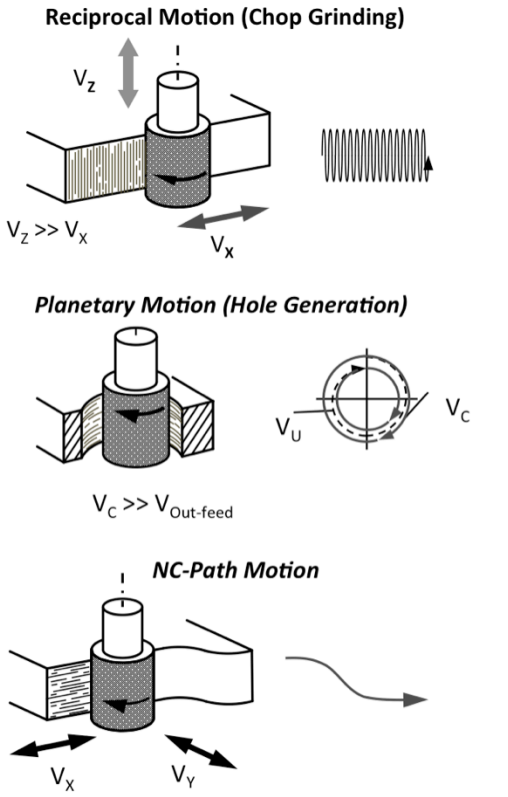

Figure 1. Classification of jig-grinding operations by the relative motion between grinding wheel and workpiece

While mathematically a large possible kinematic configuration could satisfy the required motions, it is important to consider technological and economic constraints in selecting suitable kinematic configuration. For example; the planetary motion can be mathematically generated through 12 different axis configurations between the tool and the workpiece, yet most of these configurations are difficult or irrational to realize. Therefore, only three kinematic configurations that would enable the planetary motion to satisfy the economic and technological constraints were selected for this analysis (Figure 2).

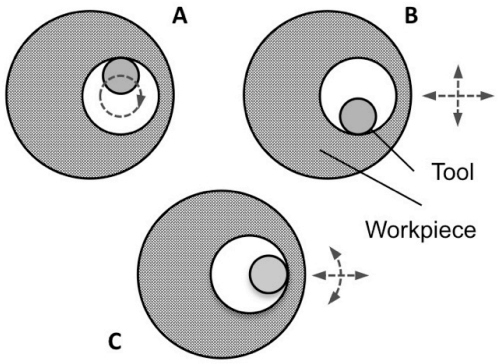

Figure 2, Possible kinematic configurations for generating a circular motion between the tool and the workpiece. A) Moving a single rotary axis. B) Moving two linear axes. C) Moving a rotary and a linear axis.

Configuration "A" represents the classic jig-grinding kinematic configuration, feeding the center of the grinding tool to a desired diameter and rotating around the C-Axis. Configuration "B" generates the planetary/circular motion through interpolation between two linear axes. Configuration "C" generates this motion through a coordinated oscillation of a rotational (C-Axis) and a linear axis (X or Y-Axis).

STRUCTURAL LOOP

Based on the previously defined axis kinematics, the simplified embodiment of machine concepts can now be established for each configuration. These embodiments represent the structural layouts of a machine concept and are essential for visualizing the major mechanical elements that are required for supporting the previously defined axes configurations. During the process of establishing the structural layout, it is important to incorporate precision design principals (i.e. shortening the structural loop length to minimize displacement, reducing Abbe offset, symmetrical arrangement of components, etc.), ergonomic aspects, minimization of manufacturing and assembly efforts, as well as allocation of real-estate for peripheral-processes supporting equipment such as dresser, tool changer, pallet changers, etc. (Figure 3).

The structural loop for each layout can be established by tracking the forces generated between the tool and the workpiece. This loop defines the structural element and their joints that are required for maintaining the position between the tool and the workpiece. Every structural component as well as every simplified axes assembly representation that is in the path of the structural loop is assigned a coordinate system $E_{in,m}$ (Figure 4) [2, 3]. As can be seen, two kinematic chains, tool chain ${}^{R}E_{Tool}$ and workpiece chain ${}^{R}E_{Work}$, are established as an open kinematic structure loop with a common reference frame R. Both chains, ${}^{R}E_{Tool}$ and ${}^{R}E_{Work}$, represent the resulting translation and orientation errors of tool and the workpiece chain relative to the reference coordinate R; E_X, E_Y, E_Z, E_U, E_W and E_C represent the *Motion* errors in translation and orientation to the X, Y Z, U, W and C-Axis, respectively. The orientation and offset errors between two adjacent axes assemblies or any elements between any adjacent axes, *Fixed* errors, are represented with by the coordinates $E_{Jin,m}$. Through applying the Homogeneous Transformation Matrix (HTM) method, the errors caused by each chain link can be transformed into the reference frame R

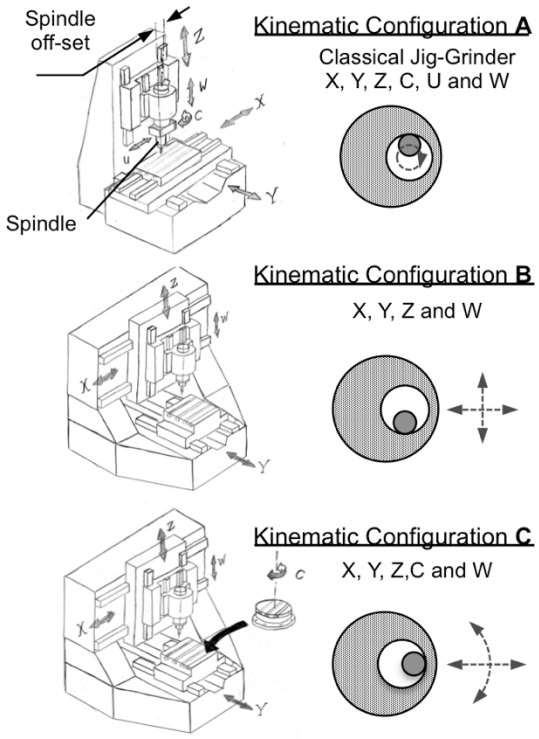

Figure 3, Schematic embodiment of machines that would support the kinematic configuration for generating a circular motion.

$$ {}^{R}E_{Tool} = \prod_{m=1}^{M} E_{im} \cdot E_{Jim} \quad (1) $$

$$ {}^{R}E_{Work} = \prod_{n=1}^{N} E_{in} \cdot E_{Jin} \quad (2) $$

From this the resulting positional error between the tool and the workpiece can be calculated (according to Slocum A.H. 1992) through:

$$E_{Pos} = {}^{R}E_{Work}{}^{-1} \cdot {}^{R}E_{Tool} \quad (3)$$

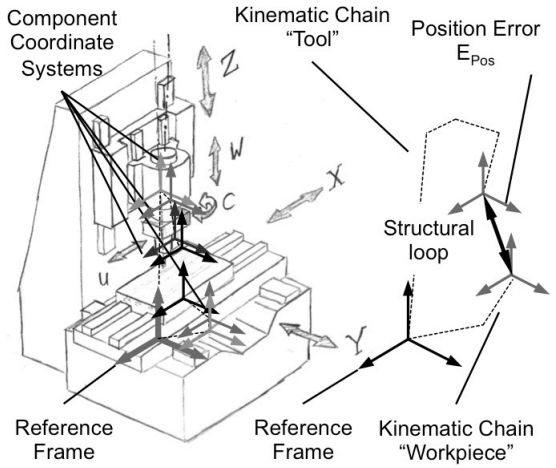

Figure 4, Structural loop with component coordinate systems for configuration A.

PRELIMINARY ERROR BUDGET ANALYSIS

Once the structural loops for the different layouts are established, each structural component as well as each simplified axis assembly is assigned a coordinate system. Figure 5 reflects, as an example, the complexity of the kinematic chains for machine configurations A (X, Y, Z, C, U and W).

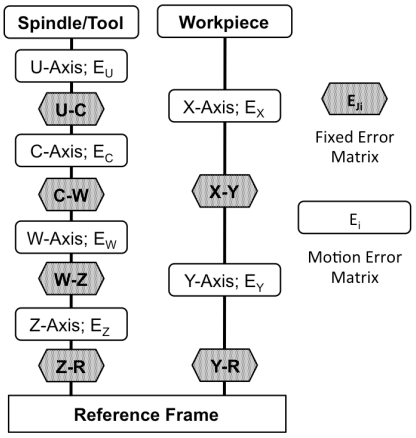

Figure 5, Kinematic model for the investigated kinematic machine configuration A.

The analysis/investigation used to determine the most suitable jig-grinding machine configuration that would meet the set requirement for accuracy was based on four major error sources in machine tools; kinematic and geometry, induced structural load, thermal displacement and process loads. However, since the magnitudes of process load in jig-grinding are only a fraction of induced structural loads their influence on the resulting positional error between the tool and the workpiece were neglected.

Kinematic and Geometry Errors

The first step of an error budget analysis is to do a preliminary investigation of the influence of the kinematic and geometric error on the positional error between the tool and the workpiece. For each of previously defined kinematic chains links, an estimated error is budgeted based on experiences of achievable manufacturing and assembly accuracies. In conjunction with estimated structural dimensions, it was predicted, early on, that for all three kinematic machine configurations the required machine accuracy (<0.5 micron) cannot be achieved. Further, this preliminary analysis showed that about 40% of the error between the tool and the workpiece is a result of the orientation errors between adjacent axes assemblies. If the joints between the axes assemblies and the machine structure could be eliminated, not only could the overall positional accuracy between the tool and workpiece could be increased, but the overall static stiffness of the machine structure would also be elevated. This preliminary analysis motivated the investigation for conceptualizing alternative design solution that would eliminate critical joint surfaces between components and/or sub assemblies.

Traditionally, in the precision machine tool industry, to achieve a good contact between two components and/or assemblies, joint surfaces are often specified with tight tolerances. Typical surface flatness requirements are in the order of 1 to 2 microns over an area of 800 x 500 mm. The manufacturing sequences for such surfaces are rough machining, and grinding followed by either hand lapping or scrapping. This ensures that the flatness error between two adjacent components will minimize its influence on the accuracies of the joint component, and in particular, the motion accuracy of the of slide assemblies. Nevertheless, a flatness error will always remain and will ultimately affect the motion accuracies of a slide assembly.

To exclude these deformations (fixed errors) from the kinematic chains a bonding technique was developed that ensures a proper joining

between the components, eliminating form imprints causing motion errors on adjacent slides assemblies and minimizing any the orientation error between two axes. The illustration of this technique is highlighted in Figure 6. Through controlled deformation of an axis assembly by pushing/pulling on strategically designed location the motion accuracy as well its orientation to the other axes can be adjusted to very small to very small values. After the adjustment and verification of its accuracy, a specially designed bonding agent with minimal heat generation and curing volume change is injected between the two assemblies. It is important to re-measure the motion accuracy of the axis assembly and to readjust the push/pull point if necessary during the curing process.

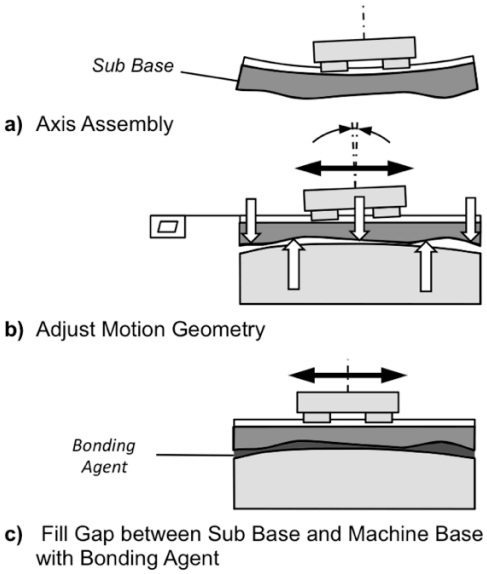
Sub Base
a) Axis Assembly
b) Adjust Motion Geometry
Bonding Agent
c) Fill Gap between Sub Base and Machine Base with Bonding Agent

Figure 6, Adjustment of Axis Motion Accuracy through Bonding.

Through applying this bonding technique all the fix error components of the kinematic chain links can now be eliminated and only the axes motion errors remain. This enables the possibility of achieving the set required accuracy of <0.5 micron for all three kinematic configurations.

Induced Structural Loads

Induced structural loads are caused by the mass of moving machine components, which generate translation and angular displacements between the tool and the workpiece due to the compliance of the kinematic chain structure. Typically, sources of these loads are gravitation, centrifugal, inertial and preload forces. Therefore, analyzing the stiffness of the kinematic chains is an imperative task for understanding and evaluating the kinematic machine configurations with respect their accuracies.

Under the consideration of the volumetric transformation of an axis, the corresponding HTM can be expressed as

$$E_{in,m} = \begin{bmatrix} 1 & -\varepsilon_{zi} & \varepsilon_{yi} & P_{Xi}+\delta_{xi} \\ \varepsilon_{zi} & 1 & -\varepsilon_{xi} & P_{Yi}+\delta_{yi} \\ -\varepsilon_{yi} & \varepsilon_{xi} & 1 & P_{Zi}+\delta_{zi} \\ 0 & 0 & 0 & 1 \end{bmatrix} \quad (4)$$

While P_{Xi}, P_{Yi} and P_{Zi} are the offset between to adjacent coordinate frames or axes, δ represents the translational in x, y and z, and ε the rotational displacement around x, y and z of each chain link respectively. With a generalized load vector $\overline{F}$, containing the spatial forces and the moments, and the stiffness matrix $\overline{K}_i$ of a component, the resulting displacement matrix $\overline{\delta_\iota}$ can be determined for each kinematic chain link.

$$\overline{\delta_\iota} = \overline{F} \Big/ \overline{K_\iota} \quad (5)$$

As highlighted earlier, one of the important grinding operations in jig-grinding is the reciprocal motion of the grinding wheel (Figure 1). This operation is accomplished through oscillating the linear W-axis. Typical oscillation frequencies could reach up to 210 strokes/min (3.5 Hz) with stroke length of 25 mm. Depending on the spindle mass and the masses of the oscillated components, the generated acceleration forces would cause displacements that are exceeding the required machine accuracy. In order to minimize these acceleration forces the design solution is to co-align the gravitational center of spindle, W- and Z-axis. During reciprocal motion, the Z-axis will simultaneously accelerate in the opposing motion direction of the W-axis. However, since the mass of the Z-axis is much greater than the spindle and W-axis combined, the overall required acceleration would be proportionally smaller, and with that, its motional amplitude (Figure 7). Therefore, the actual stroke or reciprocal resulting distance s_R is the difference of the W- (s_w) and Z-axis (s_z) stroke.

$$s_R = s_w - s_z \quad (6)$$

As indicated above, this design concept can only be applied if the gravitational center of all

moving masses co-aligns. Hence, this solution is only applicable for the machine configurations B and C and not A. Since the kinematic principle of configuration A is based on a lateral out feed, the spindle axis relative to the rotating C-axis, the gravitational center of the spindle can not be aligned to the Z and W-axis. Therefore, depending on the out-feed amount and the spindle mass, an inertia moment is generated. To limit these loads the mass of spindle has to be kept to a minimum.

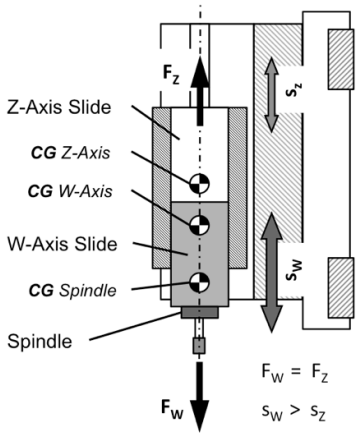

Figure 7, Design concept for minimizing inertia forces during reciprocal motion.

By incorporating the design solutions that address the geometrical errors as well as the induced structural loads into the error budget analysis, a comparison of the resulting error between the tool and the workpiece is predicted (Figure 8). It should be noticed that the highlighted results represent the predicted error based on a combined planetary and reciprocal motion at 80% of maximum velocity and acceleration of the machine axis. These motions are typically applied during grinding of holes. Therefore, the errors of interest are the positional error E_{PosXY} in the XY plane and the resulting angular tool orientation error $\Delta\varphi_{ToolXY}$.

Machine Configuration A shows the highest predicted positional and angular errors between the tool and the workpiece. Induced loads contribute to the largest amount of error by the induced loads (63%) due to the decentered location of the spindle. This arrangement not only causes inertia loads during a reciprocal motion but also induces gravitational forces on the structure during planetary motion. In contrast, Configuration C shows the lowest error and is the least influenced machine structure by the induced loads (34%). This is mainly a result of the co-axial arrangement of the gravitational center of moving masses and the kinematic arrangement for generating planetary motion. Through this configuration, the inertial forces of the stacked axes Y, Z and W, which are generated during a planetary motion, are eliminated.

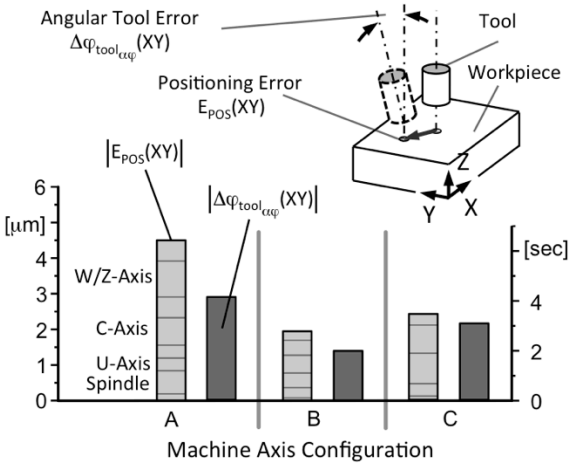

Figure 8, Effect of the kinematic/geometry error and induced structural load errors on positioning displacement between tool and workpiece

Thermal Displacement

As suggested by Bryan [4], the effects of thermal sources in a machining environment, can be: room/environment, heat added or removed by the coolant system, people, heat generated by the machine, and heat generated by the cutting process. Due to the complexity of a machine system and the difficulty of defining proper thermal boundaries for each link of the kinematic chains, it is important to analyze the thermal displacement of the entire system through FEA modeling. To simplify this analysis, only the internal heat sources that are generated by the machine and coolant systems were considered. The results of the thermal FEA are the displacement sum of all links in the kinematic chain relative to the reference frame. These results are then reflected into thermal displacement matrixes for the tool and the workpiece chain and added to previously determined positional displacement error caused by the kinematic/geometry and induced load.

Nonetheless, prior investigation of the thermal displacement between tool and workpiece basic precision principles should be integrated, whenever applicable, into the conceptual design of the three investigated machine configurations.

These design principles are: thermal neutral arrangement of heat sources, minimizing thermal affected dimensions, integrating thermal barriers or heat sink, integration of material with low CTE, and minimizing the overall thermal gradient through integration of high efficiency components (work lights, motors etc.).

The resulting predicted error between the tool and the workpeice caused by the kinematic/ geometry errors, the induced load, as well as the determined thermal displacement for the three investigated machine configurations, is shown in Figure 9. This thermal analysis was based on a predicted temperature rise of 3 °C. This temperature increase has a much greater impact on the thermal displacement for machine Configuration A then Configuration B or C. A majority of the higher displacement is a result of stacking the W- on to the Z-axis. Unlike machine configuration B and C, the center of the spindle, W and Z-Axis, are co-aligned to each other (thermal neutral arrangement).

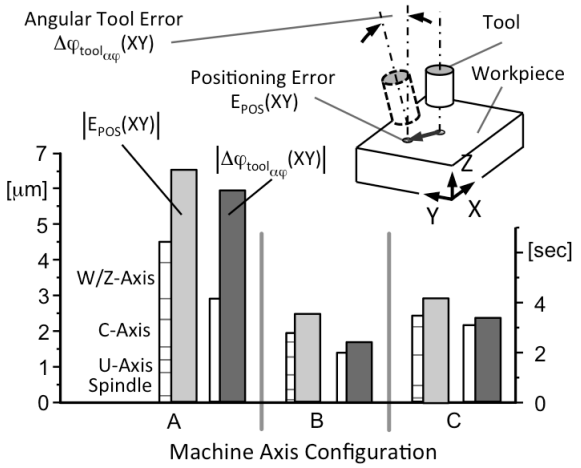

Figure 9, *Thermal error displacement between the tool and the workpiece*

Based on these analyses, the kinematic machine configuration C would promise the least amount of error between the tool and the workpiece. However, besides the technical advantages of this configuration, other aspects, such as organizational infrastructure, marketing and predicted costs, have to be taken into consideration for selecting a valid configuration. The advantage of configuration C in comparison to B is mostly due to the added rotational C-Axis. Yet this added technical advantage is only marginal and will add a much higher unjustified cost to the final product. Based on this, the machine configuration B was selected as a platform from a next generation jig-grinding machines.

CONCLUSION

The advancement of consumer electronics evoked the market demand for manufacturing equipment with higher productivity and accuracy. This led to the need for developing a new ultra precision jig-grinding machine. Prior machine design and an error budgeting analysis was conducted on three possible kinematic machine configurations to determine the most suitable configuration with respect to accuracy, repeatability and productivity.

The analysis/investigation was based on the major machine error sources, kinematic and geometric, induced load, and thermal displacement. To evaluate the influence of the kinematic machine configuration to the final positional and angular error between the workpiece and the tool, a homogeneous matrix transformation model was developed to link all the coordinate systems of the kinematic chains to each other.

In conjunction with static and thermal FEA's, as well as applying budgetary tolerance for required manufacturing and assembly components, a final machine kinematic configuration that could meet the required machining accuracy, repeatability, and productivity, was selected.

Additionally, this analysis shows that through incorporating the error budgeting methodology prior to design not only helps to determine the best suitable kinematic configuration, but also forces the development of new precision design and assembly principles to increase the accuracy of major sub-components and their fitments.

REFERENCES

[1] DIN 8589– Part 11, "Grinding with rotational tool; Classification, subdivision, terms and definitions", 2003-09.

[2] Dang Chi Cong, Bui Ba Chinh and Hwang Jooho, "Volumetric Error Model for Multi-Axis Machine Tools", 43rd Proceedings of North American Manufacturing Research Institution of SME, 2015.

[3] Alexander H. Slocum, "Fundamentals of Design, Error Budgets", November 2012.

[4] J. B. Bryan, "International Status of Thermal Error Research", UCRL-50285, 17th General Assembly CIRP, September 1967

ADDITIVELY MANUFACTURED LATTICE STRUCTURES FOR PRECISION ENGINEERING APPLICATIONS

Waiel A. Elmadih[1], Wahyudin P. Syam[1], Ian Maskery[2] and Richard Leach[1]
[1]Manufacturing Metrology Team
[2]Centre for Additive Manufacturing
University of Nottingham
Nottingham, NG7 2RD, UK

INTRODUCTION

Additive manufacturing (AM) is limited by fewer design constraints than conventional manufacturing [1]. Therefore, AM provides higher design flexibility and allows fabrication of highly complex geometries, for example, lattice structures. Compared to solid structures, lattice structures allow designs that incorporate highly-tailored mechanical properties so that the requirements of applications are met with efficient use of resources [2].

Representative stress-strain curves for solid and lattice structures are shown in FIGURE 1. In FIGURE 1, the area under the curve up to the densification strain is the energy absorbed per unit volume of material. The energy absorption is small for a solid, compared to lattice structures that benefit from long plastic plateau regions in their stress-strain curves.

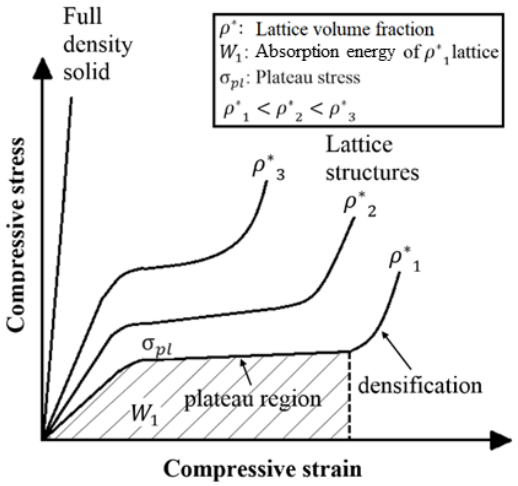

FIGURE 1. Representative stress-strain curves of a full density solid and lattice structures of different density fraction, adapted from [1].

The length of this plateau region, and the stress at which it occurs, depends on the lattice material, volume fraction, unit cell configuration, and the number of lattice cells in a structure [1]. As such, with the same total volume, different lattice configurations can have different mechanical properties. There has been considerable research focus on the manufacturability and strength-to-weight ratio of some lattice structures [3]–[5]. However, there is little published work investigating lattice structures for vibration isolation and thermal expansion control; both of which are significant for precision engineering applications. Many applications need structures that can be isolated from external vibration, for example, the tool in a CNC machine and the probe of an optical metrology system. High stiffness structures are often used, which increase the natural frequency, achieving vibration damping [6]. Taking an alternative and complementary approach, this paper discusses applications of lattice structures for vibration isolation.

FIGURE 2 shows the vibration response of a structure, with natural frequency f_n to an external vibration source with frequency f . When $f_n = f$, a resonance occurs, leading to a large displacement amplitude. [6]. To have higher vibration isolation efficiency, a structure should have a low f_n, which can be achieved by lowering the stiffness of the structure. But, there is a practical limit: if the stiffness is too low, the structure will be unable to sustain the mass load of the body of interest (work tool/probe). Lattice structures possess high strength-to-weight ratio for their mass, providing low stiffness at relatively high strength [1].

In this study, various configurations of strut-based lattice structure are investigated with a combination of finite element analysis (FEA) and experimental assessment. Information gained in this study shows that lattice structures can be used to tune the design of a structure to have a desired f_n for a specific vibration isolation application, effectively setting up a mechanical band-gap. In practice, external vibration sources commonly have multiple dominant frequencies,

so f_n should be optimised for a specific range of frequencies. A case study in which a metrology frame for an optical system is to be designed, will be used to demonstrate how f_n for the lattice structures can be optimised for a specific frequency range.

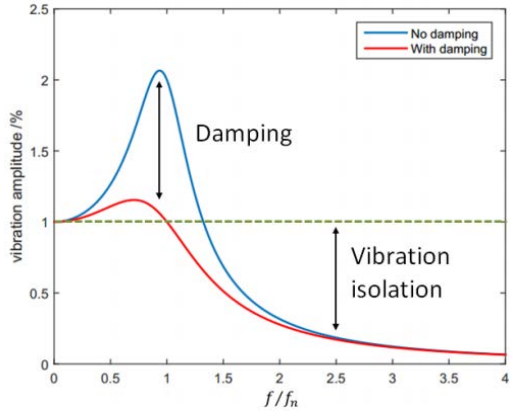

FIGURE 2. Vibration damping and isolation.

LATTICE DESIGN AND FABRICATION

Strut-based lattices are used in this study as they are periodic open-cell cellular structures that possess bending characteristics that give longer plateau regions than closed cell cellular structures, and thus can absorb more energy than periodic closed-cell cellular structures [1],[7].

CAD design

The design of lattice structures for AM poses a significant challenge. We have developed a simple design tool, in the form of equation (1). This allows us to construct a range of lattice unit cells with predefined volume fraction, *V*. Lattice strut diameters were calculated using equation (1), thus

$$d^3\left(\pi\left(\frac{a_2}{16}+\frac{a_3}{16}+\frac{b\sqrt{2}}{8}+\frac{c\sqrt{3}}{4}+e\right)\right) + d^2\left(S_l\pi\left(\frac{a_1}{16}+\frac{a_2}{16}+\frac{a_3}{16}+\frac{b\sqrt{2}}{8}+\frac{c\sqrt{3}}{4}\right)\right) - V = 0 \quad (1)$$

where the length of a unit cell is fixed at 30 mm; d is the strut diameter; S_l is the cell length; a_1 is the number of horizontal struts of length S_l as they appear in top and bottom views of a single lattice cell; a_2 is the total number of vertical struts of length C_l as they appear in top and bottom views of a single lattice cell; a_3 is the total number of vertical struts of length C_l as they appear in front, back and side views; b is the total number of diagonal struts on all faces; c is the number of diagonal members across the centre of the lattice cell; V is the filled volume of the lattice cell; and e is the constant of intersection volume equal to 0 when c = 0, 0.181021 when c = 2, and 0.636638 when c = 4 [8].

CAD was used for the design of single unit cells which were then tessellated to create lattice structures (as illustrated in *FIGURE 3*).

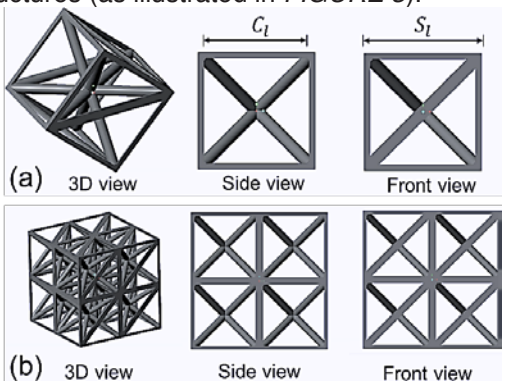

FIGURE 3. (a) Example of single lattice cell as designed with Creo Parametric CAD software, and (b) example of 2×2×2 periodic lattice cells as tessellated with Autodesk Inventor CAD software.

Samples with lattice behaviour

There is a minimum required number of lattice unit cells that a structure should have in order for it to exhibit lattice behaviour, hence, the designed lattices should be tested to determine whether they exhibit lattice behaviour [9]. Experimental compression tests were carried out on samples of similar overall size, volume fraction and, cell configuration, but of variable number of tessellations: 2×2×2, 3x3×3 and 4×4×4. The samples are shown in FIGURE 4. The purpose of these experimental compression tests is to determine the minimum number of cells that represent a lattice structure, which will later be used in the study.

Three replicas of each sample were compressed at a constant compression speed of 1 mm·min^{-1}. The results of the compression tests with the three samples are shown in the form of load-displacement curves in FIGURE 5. All samples took the curves up to the densification area, which essentially means all tested samples exhibited lattice behaviour. This

means that 2×2×2 lattices represent the minimum number of lattices that can be used in this study.

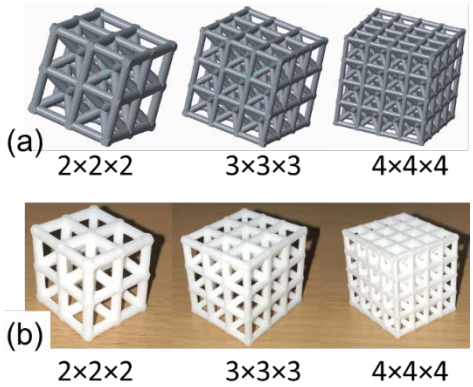

FIGURE 4. (a) Design of compression test samples, and (b) compression test samples as manufactured from Nylon 12 powder on an EOS P100 selective laser sintering machine with a building powder layer height of 100 µm.

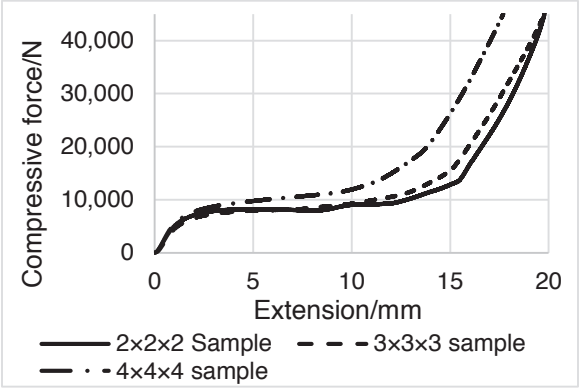

FIGURE 5. Compression test curves of lattice samples of different unit cells.

Lattice structure identification

The lattice structures used in this study are of different volume fraction, different number of nodes and different cell configurations. For the purpose of individual characterisation, every lattice cell was assigned a unique code in the form of ($x_1x_2x_3x_4$-x_5), where $x_1$is the number of nodes in a 2D view of the single cell, $x_2x_3x_4$ denotes the volume fraction taking, for example, a value of '010' for a 10 % lattice cell, and x_5 is an identification number of the struts configuration. A total of twenty-three lattice cell configurations were developed based on a fixed number of nodes. Each configuration formed the basis for three different volume fraction cells: 10 %, 20 % and 30 %. FIGURE 6 shows the lattice cells of 10 % volume fraction in a 2×2×2 tessellation.

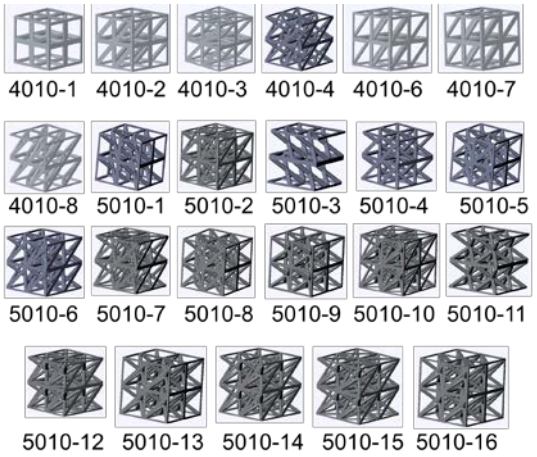

FIGURE 6. CAD models of the lattices used in this study, all in 2×2×2 tessellation and of 10 % volume fraction.

MODELLING ISOLATION PROPERTIES

The CAD models shown in FIGURE 6, along with their corresponding versions of 20 % and 30 % volume fraction, were analysed using ANSYS Workbench FEA. To ensure the calculations had converged with respect to the element size, we determined the first f_n of the structures using a range of element sizes from 25 mm to 0.25 mm. At an element size of 1 mm, the difference between subsequent results had fallen below 1 % for Nylon-12 samples of (60×60×60) mm size. Therefore, we used elements of 1 mm for all subsequent calculations. The base surfaces of the models were constrained in all degrees of freedom. The harmonic response to a vertical load of 0.1 N, vibrating at a frequency in the range 0.1 Hz to 1000 Hz (with 10 Hz frequency intervals) acting on the upper surface was simulated. The displacements due to the generated harmonic vibration in the vertical direction were calculated. The simulated spectra of the 4010-x and 5010-x lattice models are shown in FIGURE 7, where the peaks represent f_n of each model. The 5010-x lattice types have peaks at higher frequencies than the corresponding 4010-x lattices with the same number of unit cells, except for the 5010-3 lattice, which has the lowest natural frequencies among all the tested samples. This makes the 5010-3 cell a good candidate for vibration isolation. However, the 5010-3 cell has more resonance frequencies within the testing range than the 4010-8 cell. Consequently, the 5010-3 cell can complicate the control of vibration isolation

because the 5010-3 cell has high number of resonance peaks that need to be controlled for providing vibration isolation, and thus, the 4010-8 cell is more appropriate for vibration isolation control.

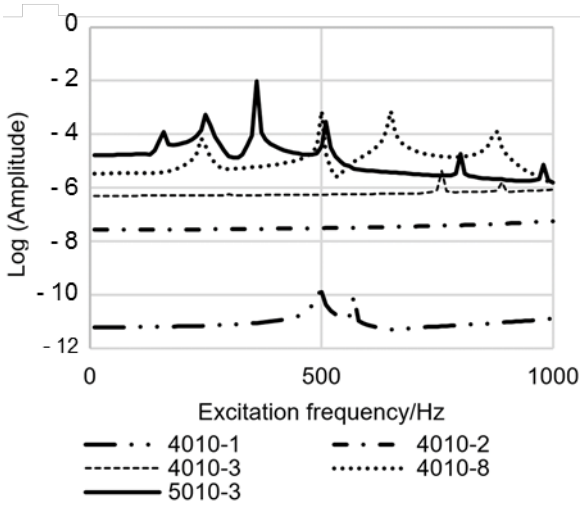

FIGURE 7. Results from harmonic response simulations of the 4010-x and 5010-x lattice types in 2×2×2 tessellations.

The models with lower volume fraction showed lower natural frequencies than models of higher volume fraction. This is most likely due to the lower stiffness of the lower volume fraction models.

For experimental verification of these results, three samples each of the 4010-8 and 4030-1 lattices were manufactured and the harmonic responses in the vertical direction were tested. Each sample was fixed to a shaker (shown in FIGURE 8) which vibrated in the range of 0.1 Hz to 1000 Hz for the 4010-8 samples, and a range of 0.1 Hz to 3000 Hz for the 4030-1 samples (all with < 1 Hz frequency intervals) and the reaction of the bottom surface of the sample was measured using a force sensor attached to the shaker. The frequency range for the experimental testing of each sample was chosen based on the range at which f_n was obtained using FEA for each sample. The positions of the natural frequency peaks are in 90.6 % average agreement with the frequencies at which they appeared in the simulation results. Comparison between average experimental results and simulation results are shown in FIGURE 9.

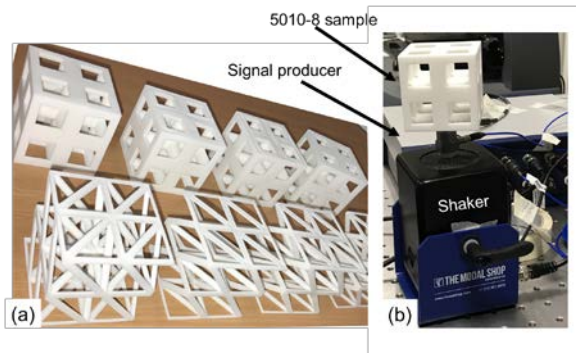

FIGURE 8. (a) Selective laser sintering manufactured samples for experimental verification, (b) vibration experiment setup.

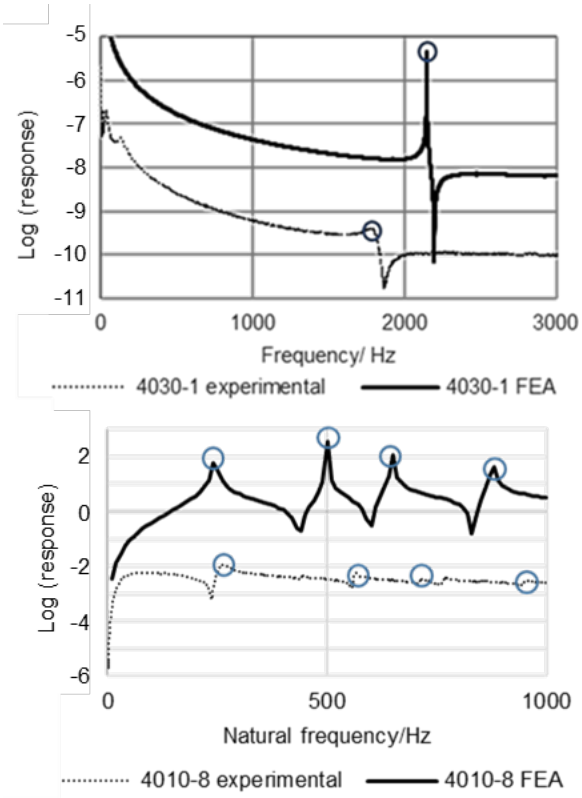

FIGURE 9. Experimental verification of the natural frequencies for vertical excitation of the 4030-1 (top) and 4010-8 (bottom) lattice structures.

The effect of the size of the lattice cells on the natural frequencies was simulated. The following sizes were chosen: 30 mm, 22.5 mm and 16.875 mm, while keeping the number of tessellations constant at 2×2×2. From the FEA results, it can be concluded that decreasing the cell size results in higher natural frequencies. This is likely due to the excitation of shorter wavelength vibration modes than are permitted in

larger structures of the same volume fraction, as shown in FIGURE 10.

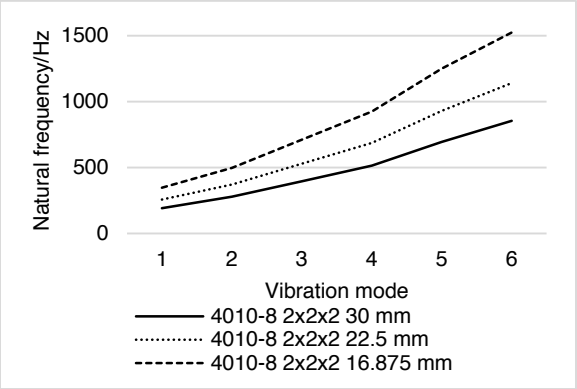

FIGURE 10. The effect of lattice cell size on f_n.

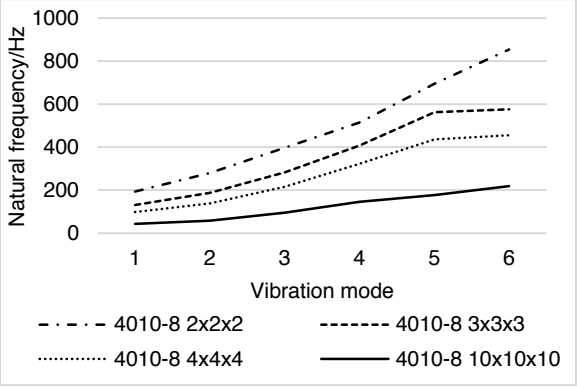

FIGURE 11. The effect of the number of tessellations of lattice cells on f_n.

In addition, increasing the number of tessellations, for a constant cell size and volume fraction, reduces f_n of the structure, which is thought to be related to increased strut bending in structures with a higher number of tessellations. This was confirmed by testing samples of tessellations of 2, 4, 5 and 10, in three-dimensions, as shown in FIGURE 11.

CASE STUDY

The structural frame of a new all-optical coordinate measuring system was manufactured with selective laser sintering from Nylon-12 using lattice structures to hold the mass of a 1 kg probe and isolate mechanical vibrations in the z-direction arising from the movement of the stage which drives the probe, which vibrates in the range from 40 Hz to 80 Hz.

Determining the lattice cell size

There are two options for the selection of the cell size and number of cell tessellations that can fill a volume in space with low f_n: (a) large size cells with low number of tessellations, or (b) smaller cells with a higher number of tessellations. The results, so far, do not suggest which route is more appropriate. As a result, a study was conducted with the aim of suggesting the most appropriate route to obtain lower f_n. The study comprised the design of (30×30×30) mm lattice structure samples using 4010-8 cells of different sizes: 15 mm, 7.5 mm, and 3.75 mm. By default, cells of less size need a higher number of tessellations to fill the (30×30×30) mm space. FEA (results are summarised in TABLE 1) showed that larger size cells had lower first mode f_n than smaller ones with a higher number of tessellations.

TABLE 1.The coupled effect of cell size and number of tessellations at constant volume fraction on the first f_n of the lattice structures.

Cell size/ mm	Sample size/mm	Number of cells	1st mode f_n/ Hz
15	30	8	409.97
7.5	30	64	421.51
3.75	30	512	467.88

As a result, the most suitable cell size for the structural frame must have two tessellations in the direction of the shortest dimension (two is the lowest number of tessellations that can represent a lattice as discussed previously). Subsequently, 30 mm cells were used to construct the body of the structural frame because the shortest dimension was the thickness of the structural frame (60 mm). The structure used the 4010-8 cell, for the reasons discussed above, and then varied the volume fraction, and the number of tessellations to get the isolation to the desired range.

Verification with in-situ harmonic test

The design of the structural frame comprises three identical sub-frames each kinematically coupled to the stage of the optics through balls in v-grooves located on top of each sub-frame. The sub-frame, shown in FIGURE 12, is stiffened at the back through the use of a solid swept stiffener, and in both sides through the use of perforated swept surfaces to further damp the vibration in x- and y- directions. The harmonic response to the compressive working load of 10 N, with excitations ranging from 0.1 Hz to 1500 Hz, was modelled with frequency intervals of 1 Hz. A safety factor of two was used for the maximum working load which was applied to the top of the frame.

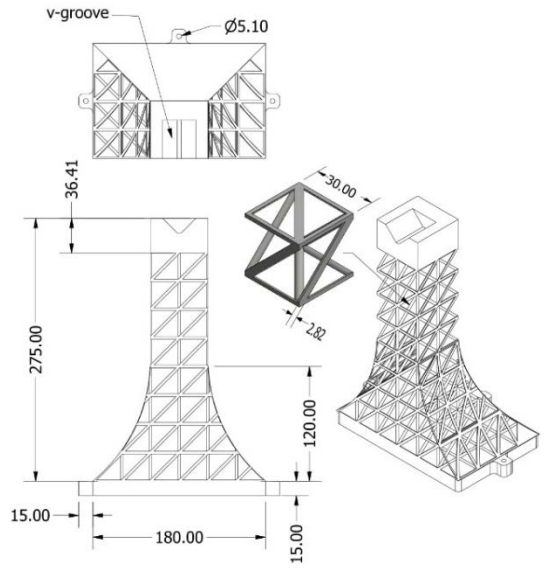

FIGURE 12: Design of the structural sub-frame for isolating vertical excitations arising from the movement of the stage of the optics using lattice structure, dimensions in millimetres.

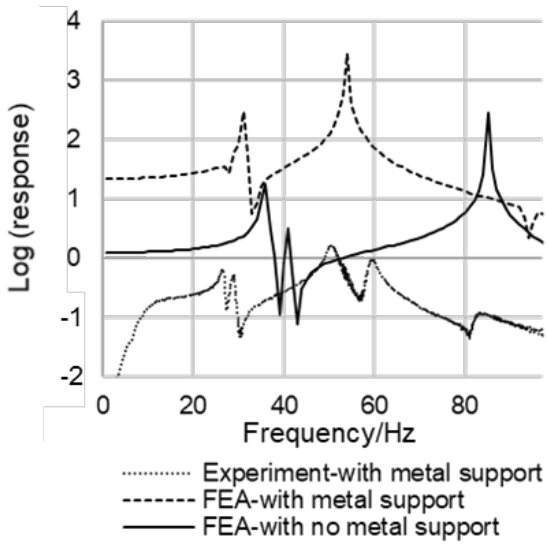

FIGURE 13: Harmonic response of one sub-frame.

The structure succeeds in isolating excitations in the range of 38 Hz and 83 Hz, with maximum displacement of 2 % of the length of the frame, see FIGURE 13. Additional metal support was used to mount the sub-frame on the shaker which affected the harmonic results obtained from experiment. The positions of f_n peaks from FEA of similar conditions to the conditions of the experiment are in 89.8 % average agreement with the frequencies at which they appeared in the experiment results.

CONCLUSION

Before lattice structures can be used for vibration isolation of a system, the dynamic behaviour of the system has to be understood. Then, the lattice characteristics can be tailored to isolate the resonance peaks of the system. The control of the natural frequency is the major step towards tailoring the lattice structure. The study reveals that the natural frequency of a lattice structure can be reduced by increasing cell size, reducing volume fraction, and/or increasing the number of tessellations of a singular lattice cell, and vise versa. The work was funded by the EPRSC project EP/M008983/1.

REFERENCES

[1] L. J. Gibson and M. F. Ashby. Cellular Solids: Structure and Properties. Cambridge University Press, Cambridge: 1999.

[2] O. Rehme and C. Emmelmann. Rapid Manufacturing of Lattice Structures with Selective Laser Melting, Proc. SPIE 2006; 6107:192-203.

[3] C. Yan, L. Hao, A. Hussein, P. Young, and D. Raymont. Advanced Lightweight 316L Stainless Steel Cellular Lattice Structures Fabricated via Selective Laser Melting, Mater. Des. 2014; 55: 533-541.

[4] C. Yan, L. Hao, A. Hussein, and D. Raymont. Evaluations of Cellular Lattice Structures Manufactured Using Selective Laser Melting, Int. J. Mach. Tools Manuf. 2012; 62: 32-38.

[5] M. Santorinaios, W. Brooks, C. J. Sutcliffe, and R. A. W. Mines. Crush Behaviour of Open Cellular Lattice Structures Manufactured Using Selective Laser Melting, WIT Trans. Built Environ. 2006; 85: 481-490.

[6] T. L. Schmitz and K. S. Smith. Mechanical Vibrations: Modeling and Measurement. Springer, New York: 2011.

[7] O. Rehme. Cellular Design for Laser Freeform Fabrication. Gottingen: 2010.

[8] M. Moore. Symmetrical Intersections of Right Circular Cylinders, Math. Gaz. 1974; 58: 181-185.

[9] W. P. Syam, J. Wu, B. Zhao, I. Maskery, W. Elmadih, and R. K. Leach. Design and Analysis of Strut-based Lattice Structures for Vibration Isolation. Precision Engineering. 2017; In press.

DESIGN OF A LONG-TRAVEL, FLEXURE-BASED NANOPOSITIONER WITH REDUCED HIGHER ORDER RESONANT MODES

Nilabh K Roy and Michael A Cullinan
Department of Mechanical Engineering,
The University of Texas at Austin
Austin, Texas, USA

ABSTRACT

This paper presents the design of an XY nanopositioning flexure stage with 2" travel with underconstraint eliminator (UE) for the micro-scale selective laser sintering system (μ-SLS). The modified double parallelogram flexure (DPF) stage design pushes out the low in-plane uncontrollable resonance frequencies present in a DPF stage. A comparison of the dynamic performance between the XY stage with underconstraint eliminator (UE) and the XY stage without UE has been presented.

INTRODUCTION

For building parts with feature sizes on the order of 1μm using μ-SLS system described in [1], it is required to have an overlay accuracy on the order of 100nm. Since the optical setup can sinter a maximum area of 2 mm^2 at once and the size of wafers to be sintered is 2" X 2", it is desired to have a positioning stage with sub-micron accuracy and repeatability and have a travel range of 2".

To achieve a long motion range with sub-micron step resolution and high accuracy, flexure bearings are commonly chosen because they have almost zero backlash and minimal hysteresis due to their lack of friction. Therefore, flexures have been the favored alternative to other linear motion systems including piezoelectric motor stages [2] and ball screw/ lead screw [3,4] based systems. Many 2D flexure based parallel-kinematic positioning stages have been proposed by researchers. In previous works, DPF design has been used to achieve strokes as long as a centimeter [5,6]. In our previous work [7], a stacked structure using DPF bearings was designed to achieve the desired motion range. However, a double parallelogram suffers from a drawback in the sense that it enables both the intermediate stages and final stages to have same degree of freedom. This leads to unwanted degrees of freedom on the intermediate stages which may interfere with the controller performance if the corresponding modes (associated with resonances of intermediate stages) fall within the operating frequency range [8]. Many studies have proposed solutions to mitigate this problem [9,10]. More recently, a nested linkage design based upon the external linkage design for eliminating the underconstraint has been presented in [11]. A new XY nanopositioning stage design using the UE was introduced in [7] to achieve the desired 2" travel range. Prototypes for both the DPF stage design and the modified DPF design with UE [7] have been developed for experimental testing. A comparison of their static and dynamic performances has been presented based on the experimental results. Additionally, these have also been compared with the FEA predictions. A linear model estimate for the frequency response of the modified DPF stage has been included as well.

Figure 1a) shows the static FEA results of the DPF stage with an input force of 1N. Stiffness along primary axis of motion was estimated to be 844 N/m.

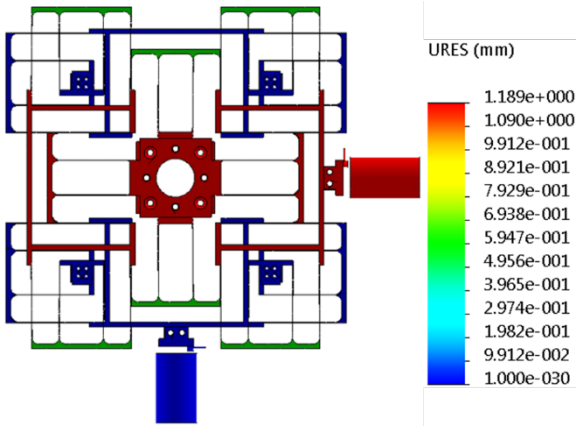

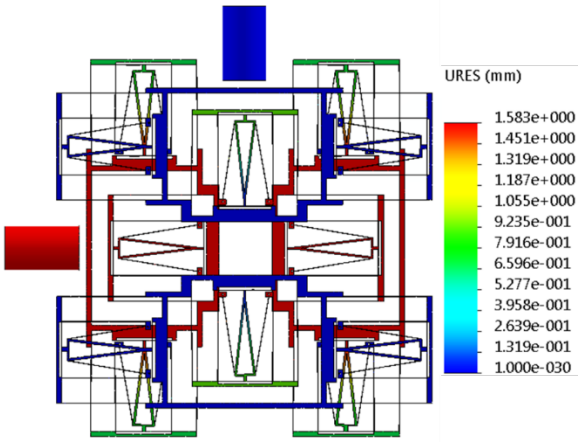

FIGURE 1. Static FEA simulation of deformation induced by an input force of 1N for a) DPF b) modified DPF stage

Dynamic FEA analysis of the stage showed uncontrollable modes at 21.4 and 21.7 Hz which falls in the working range of 50Hz for the stage. Thus, a modified DPF stage (see Fig 1b) with similar desired stiffness- 611 N/m, was designed based on the UE mechanism proposed in [11]. This design enables the uncontrolled resonance modes to be moved out to much higher frequencies making the nanopositioner much easier to control.

EXPERIMENTAL SETUP

The experimental setup of the developed precision positioning system is shown in Figure. 2. The stage is driven by two voice coil actuators (VCAs) capable of delivering a maximum stoke of 42.5 mm in either direction with maximum driving force of 117 N. The displacement of the stage is measured using a capacitive sensor. For actuation and sensor measurement, a National Instruments (NI) cRIO-9033 real-time controller equipped with NI-9263 analog output module and NI-9239 analog input module is employed to produce excitation signals and acquire sensor readings, respectively.

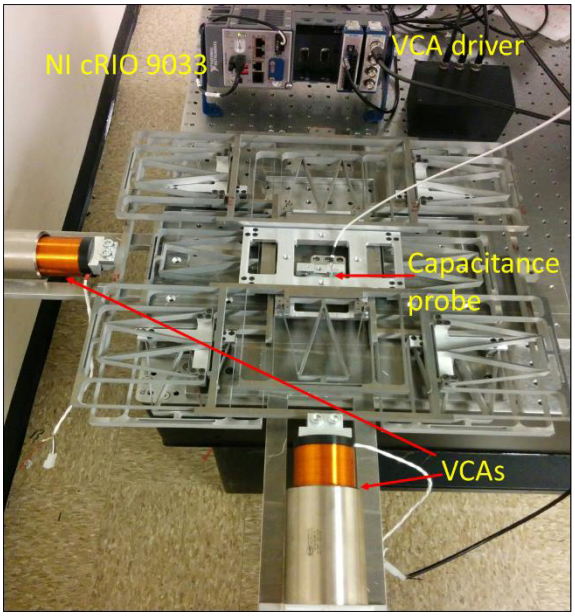

FIGURE 2. Experimental setup for modified DPF stage

A similar experimental setup is used for the DPF stage to obtain the experimental parameters for the stage.

COMPARISON OF STATIC PERFORMANCE

For stiffness measurement of the two stages, input voltage steps of constant magnitudes were applied every two seconds to the stages and the displacement of the stages were measured using the capacitive sensor. The stiffnesses of the stages can be calculated from the slopes of their respective displacement of the stage vs input voltage graphs. Figure 3 shows the highly linear relationship between the displacement of the stage vs input voltage for the DPF stage.

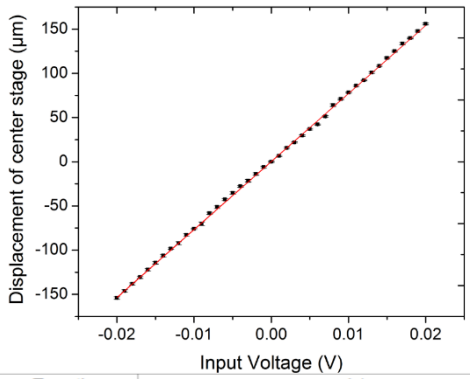

Equation		y = a + b*x	
Adj. R-Square		1.0	
		Value	Standard Error
Displacement of center stage	Intercept	0.0	--
	Slope	7701.3	26.2

FIGURE 3. Displacement vs. Input voltage graph for DPF stage

The force constant (K_f) of the VCA is 14.6 N/A and the current amplifier's gain (K_a) is 1.00 ± 0.14 A/V. So, the stiffness of the stage can be obtained by

$$K_{measured} = K_f * \frac{K_a}{Slope * 10^{-6}} \quad (1)$$

This gives a measured stiffness value of 1896 ± 265 N/m which is more than two times the stiffness value predicted by FEA. Similarly, the stiffness of the modified DPF stage was calculated from the slope of the displacement of the stage vs input voltage graph and was found to be 1157±162 N/m.

The differences in the simulated FEA stiffnesses and experimental stiffnesses can be attributed to the manufacturing errors and limits of waterjet cutting of these flexure units. The accuracy of waterjet cutting depends on the thickness of the material. As the plate thickness increases, the feature sizes at the top and bottom of the plate can be substantially different. And, a change in thickness of the beams from top to bottom changes the overall stiffness of the flexure. On inspection, the flexure beams did not have the expected rectangular cross section. Instead, the cross section resembled more like a trapezoid changing the inertia of the beam and thus the stiffness estimate needed to be corrected accordingly. A correction factor based on the ratio of inertia of trapezoidal cross section and a rectangular cross section can be used to correct the FEA predicted estimate. Thus, the FEA predictions can be made more accurate by getting the estimates from FEA (using rectangular beam cross section) and then multiplying the estimate by the correction factor (which can be simply obtained by taking measurements of the thickness of the beams at the top and bottom) or by modifying the CAD model to consider the trapezoidal geometry of flexures to accommodate the thickness variation due to the manufacturing process.

Measurements were taken for the thickness of the beams for both DPF and modified DPF stages. Thickness at the top of the beam for DPF stage was found to be 0.56 ± 0.10 mm and at the bottom of the stage was found to be 0.73 ± 0.08 mm. The correction factor, from the ratio of inertia of a trapezoidal and a rectangular cross-section, was found to be 2.204 ± 0.637. For the modified DPF stage, the correction factor was obtained to be 2.41 ± 0.72.

Table 1 lists the FEA predicted stiffnesses, corrected FEA estimates and experimental results. The corrected estimates are much closer to the experimental estimates validating the hypothesis that the change in inertias of the flexure beams due to the manufacturing errors were significant.

TABLE 1. Comparison of the stiffness (FEA and corrected estimates) with experimental estimates for both DPF and modified DPF stages

	FEA prediction	Corrected estimate	Experimental
DPF stage	841	1854 ± 535	1896 ± 265
Modified DPF stage	611	1475 ± 441	1158 ± 162

The noise levels for both the stages were found by collecting the displacement data for the stages at zero actuation voltages. The magnitude of the noise in DPF stage was found to be 0.393 ± 0.006 µm. Noise in the modified DPF stage was found to be 0.106 ± 0.008 µm. These noise levels limit the resolution of the stages. Modified stage thus provided an improved resolution. However, the resolutions can further be improved by

implementing closed loop control algorithms for running these stages.

COMPARISON OF DYNAMIC PERFORMANCE

Finite element modal analysis (see Table 2) of the DPF stage showed that the first uncontrollable mode which was encountered at 21 Hz with DPF stage, has been moved out to 84 Hz with modified DPF stage. To compare the response of the two stages experimentally, a Gaussian noise signal of appropriate strength was used as the input signal and the response data was collected at a sampling rate of 1000 Hz. This fast data collection rate ensures that all the dynamics of the stage are captured completely as the first 6 modes of both the stages are found under 100 Hz. Fourier transform of input and output data were used to determine the frequency response of the stages. Figure 4 shows the magnitude plot of the two stage designs. From the magnitude response plot, it can be observed that the uncontrollable resonances have been moved out from 25Hz to 86Hz with a slight change in primary resonant frequency. The next resonance of the main stage occurs at around 118 Hz which is again the same for both stages.

TABLE 2. Comparison of the modal frequencies of DPF and modified DPF stages obtained through FEA

	Frequency (Hz)	
Mode no.	DPFS	Modified DPFS
1	4.98 (+)	5.8 (+)
2	4.98 (+)	5.8 (+)
3	21.45 (-)	72.97 (X)
4	21.7 (-)	84.03 (X)
5	21.73 (-)	84.07 (X)
6	22.7 (-)	84.18 (-)

\+ In plane & controllable X Out of plane

\- In plane and uncontrollable

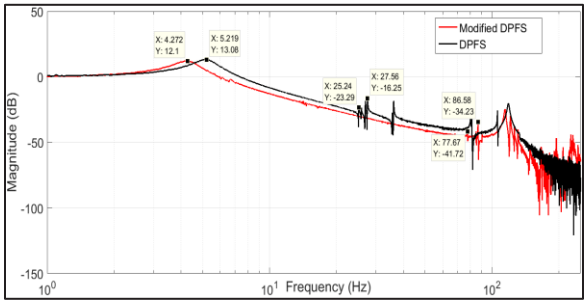

FIGURE 4. Magnitude response plots for the two stages

The experimental results also show a very good agreement with the FEA predicted results. A low resonant frequency limits the operating speed for the stage and to achieve fast tracking using these nanopositioning stages, a suitable control algorithm design is required. System identification of the modified DPF stage was carried out to derive a model which can be used to develop a model based control for the stage.

SYSTEM IDENTIFICATION

A 3rd order linear model estimate between the desired displacement and actual displacement of the stage was fitted to the experimental frequency response of the stage. Figure 5 shows the fitting between the model response and experimental frequency response.

$$G(s) = \frac{-1.724s^2 + 722.3s + 106.2}{s^3 + 6.677s^2 + 730s + 4.792e - 08} \quad (2)$$

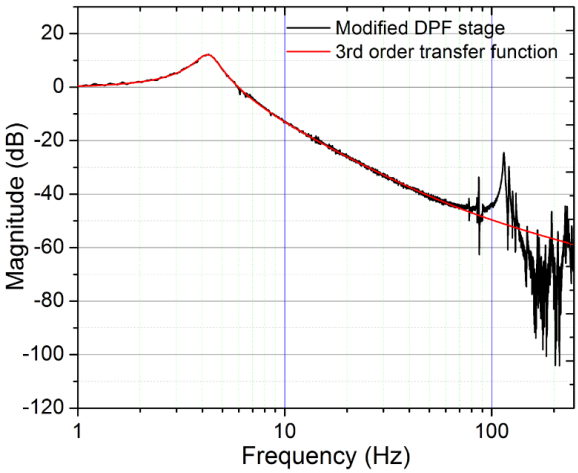

FIGURE 5. Comparison of the fitted transfer function with experimental frequency response of the stage

Open loop plant response

Figure 6 shows the response of the plant to a reference input signal. The input signal contains two different step frequencies (2 Hz and 5 Hz) to illustrate the tracking performance of the stage in open loop. From the response plot, the tracking performance is not good for either of the step frequencies. For the slower steps, the stage oscillates around the reference. However, the overshoots are large and the stage doesn't appear to be settling down indicating poor damping. For the faster steps (5Hz), due to the low resonant frequency, the stage does not have enough time to even finish one oscillation and

there is hardly any tracking of the reference signal. Thus, the need to design and develop a closed loop control for the stage to achieve better tracking performance.

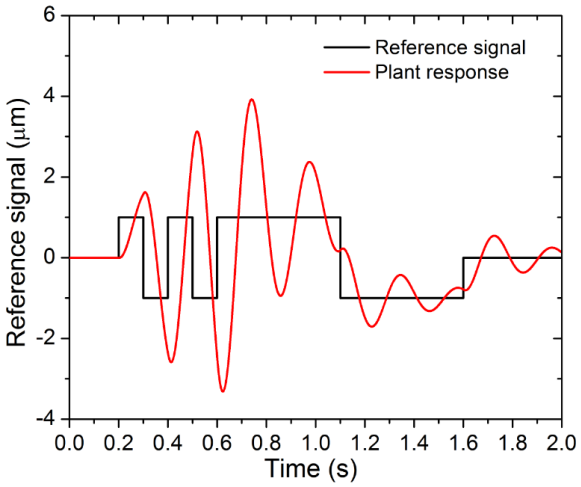

FIGURE 6. Open loop tracking performance of the stage

CONCLUSION AND FUTURE WORK

The dynamic experimental results are in good agreement with FEA simulations and both predict the uncontrollable modes to move out to 84 Hz (FEA) and 86 Hz (experimental) for modified DPF stage from 21 Hz (FEA) and 25 Hz (experimental) for DPF stage. The stiffnesses of the two stages are also found to be close to the corrected FEA estimates. A linear model for the modified DPF stage has been identified. The response of the model in open loop is found to be inadequate for tracking applications due to a low resonant frequency and low damping. Further steps include developing a closed loop control for faster and better tracking performance.

REFERENCES

[1] Roy, N. K., Foong, C. S., and Cullinan, M. A., 2016, "Design of a Micro-scale Selective Laser Sintering System," 2016 Annual International Solid Freeform Fabrication Symposium.

[2] Fleming, A. J., and Leang, K. K., 2014, Design, modeling and control of nanopositioning systems, Springer.

[3] Slocum, A. H., 1992, Precision machine design, Society of Manufacturing Engineers.

[4] Smith, S. T., 2000, Flexures: elements of elastic mechanisms, CRC Press.

[5] Xu, Q., 2013, "Design and Development of a Compact Flexure-Based XY Precision Positioning System with Centimeter Range," (c), pp. 1–11.

[6] Awtar, S., and Parmar, G., 2013, "Design of a large range XY nanopositioning system," J. Mech. Robot., **5**(2), p. 21008.

[7] Roy, N. K., and Cullinan, M. A., 2016, "Design of a flexure based xy precision nanopositioner with a two inch travel range for micro-scale selective laser sintering," Proceedings - ASPE 2016 Annual Meeting, American Society for Precision Engineering, ASPE, pp. 395–400.

[8] Awtar, S., 2003, "Synthesis and analysis of parallel kinematic XY flexure mechanisms," Massachusetts Institute of Technology.

[9] Trutna, T. T., and Awtar, S., 2010, "An enhanced stability model for electrostatic comb-drive actuator design," ASME 2010 International Design Engineering Technical Conferences and Computers and Information in Engineering Conference, pp. 597–605.

[10] Brouwer, D. M., Otten, A., Engelen, J. B. C., Krijnen, B., and Soemers, H., 2010, "Long-range elastic guidance mechanisms for electrostatic comb-drive actuators."

[11] Panas, R. M., and Hopkins, J. B., 2015, "Eliminating Underconstraint in Double Parallelogram Flexure Mechanisms," J. Mech. Des., **137**(9), p. 92301.

RECENT ADVANCES IN ULTRA-PRECISION MILLING WITH MULTIPLE-CUTTING EDGES

Lars Schönemann[1,2], Oltmann Riemer[1], and Ekkard Brinksmeier[1,2]
[1]LFM Laboratory for Precision Machining and
[2]MAPEX Center for Materials and Processes
University of Bremen
Germany

INTRODUCTION

The manufacture of complex optical parts, such as lenses and molds with freeform or microstructured surface, is heavily reliant on diamond milling as a machining process [1]. While the complexity of the machined parts was steadily increased in the past decades [2], most milling processes still require extensive amounts of machining time [3]. Due to the high precision and tight tolerances of optical surfaces, the air bearing spindles applied are typically operated at low speeds ($n \approx 1000\,\mathrm{min}^{-1}$ to $3000\,\mathrm{min}^{-1}$), in order to keep dynamic disturbances as low as possible [4]. Moreover, typically only one single cutting edge is involved in these processes ("fly-cutting") [5]. Even a small difference in cutting radius would in the best case lead to an increase in surface roughness, whereas deviations larger than the maximum undeformed chip thickness (normally only a few micrometers) cause subsequent cutting edges not to be engaged in the cutting procedure at all. Consequently, a high precision tool alignment mechanism is mandatory for the application of multiple cutting edges in diamond milling processes.

THERMAL TOOL ALIGNMENT

To increase the economic efficiency of ultra-precision milling processes, a novel tool alignment mechanism based on thermal expansion has been developed (Figure 1a). Initial findings on the actuator concept and its behavior in a static test stand (Figure 1b) have been presented at the 2015 ASPE Annual Meeting [6]. It was shown that using a commercially available infrared light emitting diode (IR-LED) with $P_{LED} = 0.43\,\mathrm{W}$, an elongation of several hundred nanometers could be achieved. Subsequent developments were shown at the 2016 CIRP HPC conference [7]. Here, a closed loop control of the thermal expansion was introduced, which allows for setting the acutator to an arbitrary position with a precision of $\Delta l < 10\,\mathrm{nm}$ across a $l > 1\,\mathrm{mm}$ stroke.

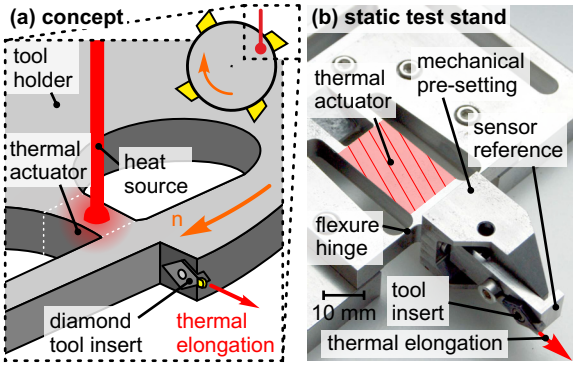

FIGURE 1. Concept and static test stand for thermal tool alignment

TRANSFER OF ACTUATOR CONCEPT TO A SPINDLE SETUP

For evaluating the thermal actuator mechanism in a spindle setup, the mechanism has to be integrated into a tool holder for fly-cutting. The current design is based on a $\varnothing 130\,\mathrm{mm}$ and $12\,\mathrm{mm}$ thick steel disc made of 1.2083 type steel. Compared to the static test setup, based on 1.7225 type steel, this alloy features a lower thermal conductivity ($\kappa = 22.6\,\mathrm{W\,m^{-1}\,K^{-1}}$ vs. $42.6\,\mathrm{W\,m^{-1}\,K^{-1}}$) and the same coefficient of thermal expansion ($\alpha = 11.1\,\mu\mathrm{m\,m^{-1}\,K^{-1}}$). Thus, it should achieved a similar stroke at a longer time constant, which has been investigated in preliminary finite element (FE) simulations. For this, a STEP model of the actuator design was imported into a commercially available FE-software and meshed accordingly. As boundary condition, a natural convection of all faces to room temperature ($20\,^{\circ}\mathrm{C}$) was added and a load resembling two LED light sources was introduced at the same position on the top and bottom face of the actuator. Then, the transient heat transfer was calculated according to the material properties of the selected steel types. In a second step these results were used as load for the calculation of the thermally induced static stresses. Figure 2 shows the resulting temperature of a single point on the

top face and the shift of the tool tip as a result of the thermal expansion for both steel types.

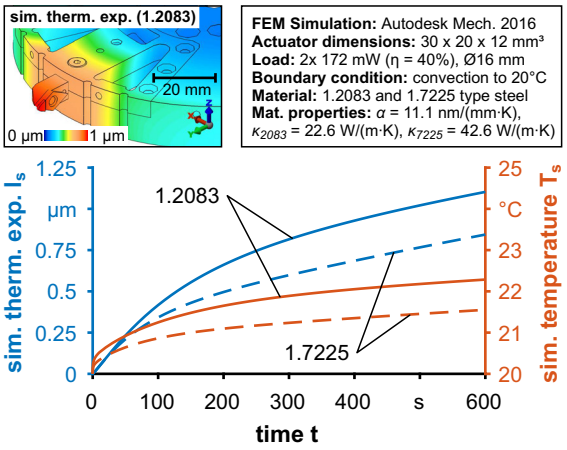

FIGURE 2. FE-simulation of the thermal expansion for 1.2083 and 1.7225 type steel

It can be seen that after $t = 600\,\mathrm{s}$ of constant heat input, the 1.2083 type steel is able to reach a significantly higher temperature of $T_{\mathrm{max},2083} = 22.29\,^{\circ}\mathrm{C}$ than the 1.7225 alloy ($T_{\mathrm{max},7225} = 21.55\,^{\circ}\mathrm{C}$). This results in a larger thermal expansion of the stainless steel actuator ($l_{\mathrm{max},2083} = 1102.77\,\mathrm{nm}$) than of the 1.7725 ($l_{\mathrm{max},2083} = 844.16\,\mathrm{nm}$). Thus the 1.2083 type steel is favorable for the novel tool holder design, as it offers a better performance and additionally improved corrosion resistance.

The size of the steel disc allows for up to four thermal actuators to be integrated. However, the current design only features two at $180\,^{\circ}$ spacing for reasons of symmetry and simplicity (Figure 3). The acutator itself has a size of $30 \times 20 \times 12\,\mathrm{mm}^3$. It is divided into two parts of equal thickness: a base part directly cut out of the steel substrate and a lid mounted onto the base. At the rear face, both parts are connected to the tool holder via two $2.5\,\mathrm{mm}$ wide struts, while the front is supported by specifically designed flexure hinges at both sides to improve the actuators' tangential stiffness.

In contrast to previous designs, the pre-alignment mechanism has been changed from an add-on component at the circumference of the tool holder to an integrated design within the thermal actuator. Now a $36 \times 6.35 \times 6.35\,\mathrm{mm}^3$ tool shank, which can hold standard tool inserts, is clamped inside the actuator. The tool shank can be moved radially by shifting a $5\,^{\circ}$ wedge mechanism within the actuator, in order to realize a pre-alignment of the diamond

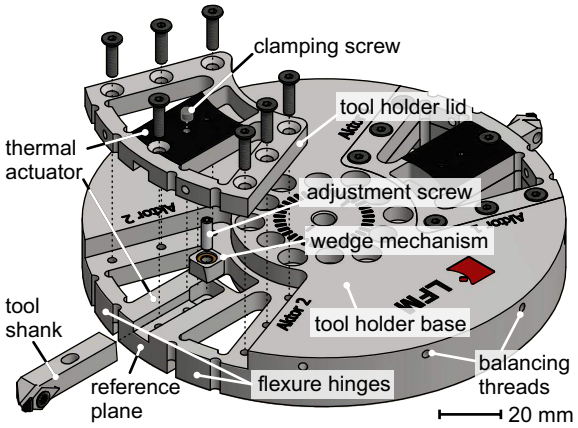

FIGURE 3. Actuator design for spindle setup

cutting edge. This allows for a radial alignment of the cutting edge within a range of approx. $200\,\mu\mathrm{m}$ with a precision of $<1\,\mu\mathrm{m}$.

As the radial position of the cutting edge cannot be measured directly, a reference ring was added at the circumference of the tool holder. Being connected to the thermal actuator, it is expected to yield a similar thermal expansion.

EXPERIMENTAL RESULTS

In the following sections, the performance of the mechanical pre-alignment mechanism and the thermal actuator will be presented and discussed. For all tests, the actuator was mounted either on the main spindle of a Kugler BEP-200 balancing experimental platform or on a motorized Professional Instruments Model 4R BlockHead® spindle, both of which feature air bearings. The setup on the Kugler BEP-200 is shown in Figure 4.

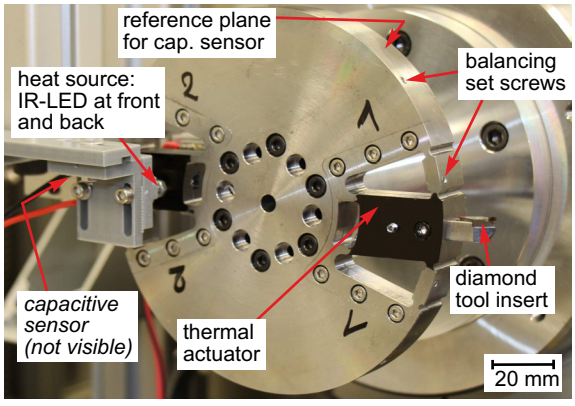

FIGURE 4. Test setup on Kugler BEP-200

The required heat input is generated by an Osram SFH-4783 infrared LED with a centroid wavelength of $\lambda_c = 850\,\text{nm}$, a half angle of $\varphi = \pm 12°$ and a radiant intensity of $I_e = 2.3\,\text{W}\,\text{sr}^{-1}$. The thermal expansion is measured at the reference ring via a capacitive sensor (CPL-490 with 2G-C8-0.5 probe from IBS Precision Engineering) which offers a resolution of 1 nm at a bandwidth of 50 kHz, across 50 µm measuring range. The performance of the pre-alignment mechanism is assessed via a dial gauge.

Pre-alignment mechanism

The results for the pre-alignment mechanism are depicted in Figure 5. The two point clouds show the measured shift l of the tool shank in outwards and inwards direction, i.e. for increasing and decreasing the fly-cut radius, against the revolution of the fine threaded adjustment screw in 90° increments. In addition, a linear fit of both measurements is given.

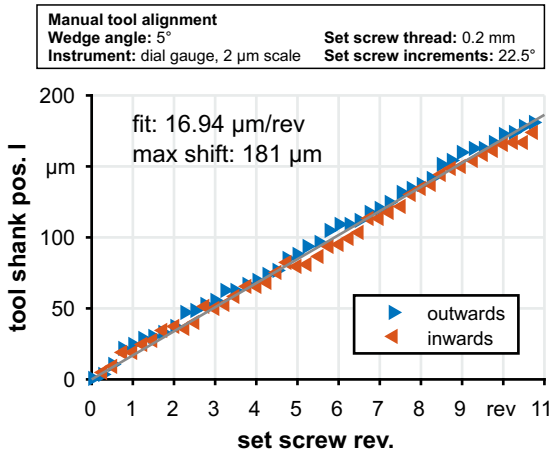

FIGURE 5. Radial shift of toolshank via wedge mechanism

The maximum measured shift is $l_{\text{max}} = 181\,\mu\text{m}$, which is close to the theoretical maximum of $l_{th} 11\,\text{rev} \cdot 0.2\,\text{mm/rev} \cdot \tan 5° = 192.48\,\mu\text{m}$. The shift per revolution of the set screw was determined via the fit to be $\Delta l_{\text{rev}} = 16.94\,\mu\text{m}$ which also is near the theoretical value of $\Delta l_{\text{rev,th}} = 17.5\,\mu\text{m}$. The remaining deviations are attributed to machining tolerances of the tool holder. This means that a $1/17$ revolution (21.18°) of the set screw has to be performed in order to achieve the desired accuracy of $\Delta l_{\text{des}} < 1\,\mu\text{m}$. Previous experiments have already shown that smaller increments might be set by hand.

Thermal expansion (clamped spindle)

The thermal expansion of the novel actuator was first evaluated with a clamped spindle, in order to compare its performance with the static setup and the FE-simulations. For these experiments, the LED heat source was continuously operated at full power and the position of the reference plane was measured using the capacitive probe, until a saturation could be observed. Each measurement was repeated three times in order to analyze the repeatability. Figure 6 shows the mean (solid) and standard deviation (shaded) of the measured thermal expansion for two test cases, with and without forced convection, of the 1.7225 based tool holder on the Kugler BEP-200.

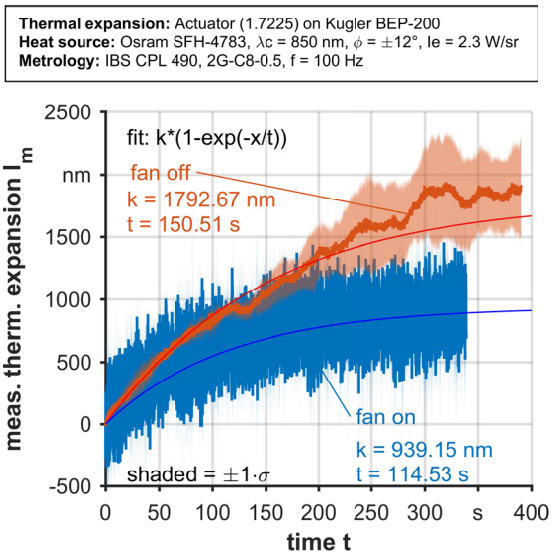

FIGURE 6. Measured thermal expansion of the 1.7225 based actuator with and without forced convection on the Kugler BEP-200

The red curve shows the results for a test case without external influences. The actuator reaches a steady state after about 400 s at around 2000 nm expansion. All three measurements are in good accordance during the first 150 s to 200 s, as indicated by the low standard deviation. After that, the spread of the three measurements increases.

The blue curve shows the second test case, in which a forced convection was induced by a fan directed at the actuator to simulate the rotation of the spindle (cf. [6]). Due to turbulence and vibration of the fan, the noise of the measurement signal is considerably increased. However, all three measurements are in good accordance, as can be deduced from the small standard deviations.

Despite the additional cooling, the actuator is able to expand to about 1000 nm.

The measured values were fitted to an exponential function $f(x) = k \cdot \left(1 - e^{-x/t_h}\right)$ for determining the actuator gain k and its time constant t_h. For the test case without forced convection the gain was calculated to $k = 1793\,\text{nm}$ and the time constant to $t_h = 150\,\text{s}$. Compared to the initial FE-simulations, this is about $112\,\%$ more expansion than expected. This large deviation is likely to be caused by a difference between the modeled and the actual values of the model parameters, especially the convection rate (library value from the FE-software) and the coefficient of absorption (textbook value). As expected from the measurement results, the gain of the actuator is significantly reduced ($k_{\text{fan}} = 939\,\text{nm}$) when applying a forced convection to the setup. Additionally, the maximum expansion is reached in less time ($t_{h,\text{fan}} = 115\,\text{s}$). This, however, is still within the desired range of $k_{\text{des}} \geq 1\,\mu\text{m}$.

In subsequent experiments the novel tool holder, based on 1.2083 type steel was investigated on the PI Model 4R spindle as shown in Figure 7.

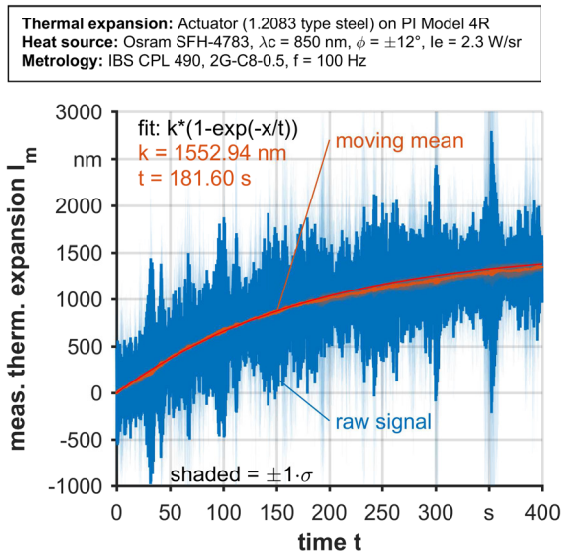
Thermal expansion: Actuator (1.2083 type steel) on PI Model 4R
Heat source: Osram SFH-4783, λc = 850 nm, ϕ = ±12°, Ie = 2.3 W/sr
Metrology: IBS CPL 490, 2G-C8-0.5, f = 100 Hz
fit: k*(1-exp(-x/t))
k = 1552.94 nm
t = 181.60 s
moving mean
raw signal
shaded = ±1·σ
meas. therm. expansion l_m
nm
time t
s

FIGURE 7. Measured thermal expansion of the 1.2083 based actuator on the PI Model 4R spindle

The measurement shows a large noise in the raw signal (blue), the origin of which is yet unclear. After applying a moving mean function across 100 values, however, a stable signal was obtained (red). The calculated gain of $k = 1553\,\text{nm}$ is slightly lower than for the 1.7225 type steel actuator, but still exceeds the desired 1000 nm. The time constant is increased to $t_t h = 181.6\,\text{s}$, as could be expected from the lower thermal conductivity of this substrate.

Measurements with rotating spindle

The performance of the actuator ultimately has to be evaluated on a spindle setup. This requires a triggering of the heat source to only illuminate the desired proportion of the tool holder, i.e. only one of the actuators or each actuator with a dedicated heat input. For a first assessment, the measurement of the reference plane and the heat output of the LED were done continuously. The results are shown in Figure 8 depicting several consecutive revolutions of the spindle at $n = 300\,\text{min}^{-1}$.

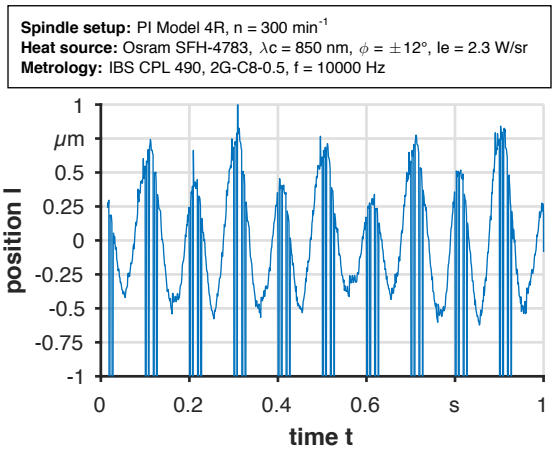
Spindle setup: PI Model 4R, n = 300 min-1
Heat source: Osram SFH-4783, λc = 850 nm, ϕ = ±12°, Ie = 2.3 W/sr
Metrology: IBS CPL 490, 2G-C8-0.5, f = 10000 Hz
position l
µm
time t
s

FIGURE 8. Measurement of the reference plane with rotating spindle

The signal shows additional disturbances during rotation, comprising the runout of the reference plane as well as the unbalance of the tool holder and other spindle dynamics. Nevertheless, a repeating pattern can be observed. The measured signal gets out of range on several occasions during one revolution, which is due to the cutouts of the flexure hinges. A future possibility for triggering would be to evaluate this drop of the signal value and utilize it for the control of the heat source.

After processing the signal and segmenting it according to the signal dropouts, a single revolution could be isolated, as shown in Figure 9. Here, it becomes evident that although the bandwidth of the measurement was at a very high rate of $f = 10\,000\,\text{Hz}$, only very few data points are obtainable for the position of the actuator. For a good assessment of the thermal expansion, either the measurement rate has to be increased further or

the signal has to be averaged over several revolutions. In the current state, a thermal expansion cannot be observed properly.

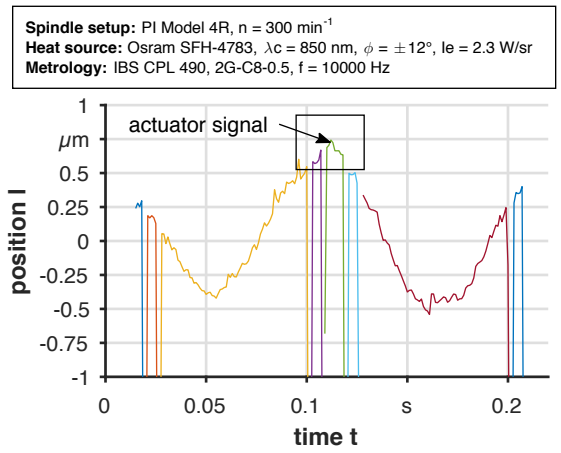

FIGURE 9. Zoom into the measurement signal for one revolution of the spindle

SUMMARY AND OUTLOOK

Tool alignment with nanometer precision is mandatory for diamond milling with multiple cutting edges. In previous publications, the authors have shown, that an actuator based on thermal expansion is able to achieve this goal. Whereas previous studies focused on the demonstration of the functional principle in a static test stand, this paper describes how the concept is transferred to a spindle setup. The design of the complete tool holder was shown as well as experimental data on the manual tool pre-alignment and the measured thermal expansion on the spindle setup.

The next steps will include reducing the measurement noise of the spindle setup and synchronizing the control of the heat source with the rotating spindle. This requires a triggering of both the measurement signal of the capacitive probe and the thermal output of the LED. Furthermore, new ways for increasing the heat input to the actuator have to be found, because a single LED is not capable of generating enough heat during rotation as it is only capable of illuminating the target face of the acutator for a short period.

ACKNOWLEDGMENTS

The authors would like to thank the German Research Foundation (DFG) for funding this work as part of the sub project “Ultra-precise milling with multiple diamond tools” within the research unit FOR1845 “Ultra-precision High Performance Cutting”.

REFERENCES

[1] Dornfeld D, Min S, Takeuchi Y. Recent Advances in Mechanical Micromachining. CIRP Annals - Manufacturing Technology. 2006;55(2):745–768.

[2] Thompson KP, Rolland JP. Freeform Optical Surfaces: A Revolution in Imaging Optical Design. Optics and Photonics News. 2012;23(6):30.

[3] Brinksmeier E, Preuss W. Micro-machining. Philosophical Transactions of the Royal Society A. 2012;370:3973–3992.

[4] Zhang SJ, To S. The effects of spindle vibration on surface generation in ultra-precision raster milling. International Journal of Machine Tools and Manufacture. 2013;71:52–56.

[5] Zhang SJ, To S, Zhu ZW, Zhang GQ. A review of fly cutting applied to surface generation in ultra-precision machining. International Journal of Machine Tools and Manufacture. 2016;103:13–27.

[6] Schönemann L, Riemer O, Brinksmeier E. Using controlled thermal expansion for tool alignment in ultra-precision milling. In: 30th ASPE Annual Meeting; 2015. p. 91–94.

[7] Schönemann L, Riemer O, Brinksmeier E. Control of a Thermal Actuator for UP-milling with Multiple Cutting Edges. In: Wertheim R, Ihlefeldt S, Hochmuth C, Putz M, editors. Procedia CIRP. vol. 46; 2016. p. 424–427.

GRINDING OF SILICON CARBIDE FOR FREEFORM OPTICS

Prithiviraj Shanmugam[1], Nicholas E. Sizemore[1], Joseph D. Owen[1], Edward Fess[2], Joshua Hamel[2], James Ross[2], John Lambropoulos[3], Matthew A. Davies[1]
[1]Mechanical Engineering and Engineering Science
University of North Carolina at Charlotte, Charlotte, NC, USA
[2]Optipro Systems, LLC, Ontario, NY, USA
[3]Department of Mechanical Engineering
University of Rochester, Rochester, NY, USA

INTRODUCTION

Silicon Carbide (SiC) has gained significant interest among researchers and industry for optical applications due to its mechanical strength, thermal shock resistance and chemical inertness. Freefrom optics enable compact, economical and unobscured designs that can be less sensitive to positioning uncertainties when compared to traditional designs: examples include three-mirror anastigmats (TMAs) for telescopes and imaging spectrometers. SiC freeforms are of particular interest for TMA telescope designs operating in extreme environments. However, mechanical properties such as high brittleness and low fracture toughness makes SiC a challenging material to machine, and freeform surfaces add significant complexity. Numerous studies have been conducted to understand the process mechanics in machining SiC [1]. However, extensive research that outlines the surface response of different grades machined under identical process parameters is limited. SiC has many grades that vary in mechanical properties depending on manufacturing methods [2]. Machining of brittle materials like SiC involve ductile deformation and brittle fracture depending on the process parameters [1,3,4]. Currently, grinding and polishing remain the most productive processes for manufacture of SiC freeform optics [5].

Initially this work focused on analyzing the effect of grinding parameters on different grades of SiC in raster grinding [6]. The current study investigates the effect of grinding parameters on surface roughness in different grades using different grinding configurations and synthesizes the earlier results with new results to characterize surface mechanics of the process. From a fracture standpoint, significant subsurface damage (SSD) is induced into the part during grinding [6]. Shafrir et. al. [5] performed experiments on CVD grade SiC to assess subsurface damage using magneto-rheological finishing (MRF) spotting technique. This technique studies the evolution of RMS roughness (Rq) at the base of an MRF spot/dimple as a function of material removed to assess the subsurface damage. The MRF spotting technique was adopted into phase 1 to assess SSD in different grades. In this study, the MRF spotting technique is used to assess SSD of CVD grade ground using different configurations.

EXPERIMENTAL PROCEDURE

Previously in [6], the focus was on studying the effect of raster grinding parameters on CVD, CVC, direct sintered and silicon infiltrated grades on a Makino A55. The current study analyses the surface integrity in CVD and reaction bonded grades of SiC ground on an Optisonic 1250X using different configurations and wheel diameters. Also, as a preliminary step towards studying freeform surfaces, test spheres were ground in different grades using cup grinding wheels on a SXL 500.

Grinding Experiments

Two different configurations (Figure 1), raster and spiral grinding with disk grinding wheels 50.8 mm and 25.4 mm in diameter, were tested. The process parameters and wheel specifications are given in Tables. 1, 2 and 3. The wheel speed was maintained at 6800 rpm.

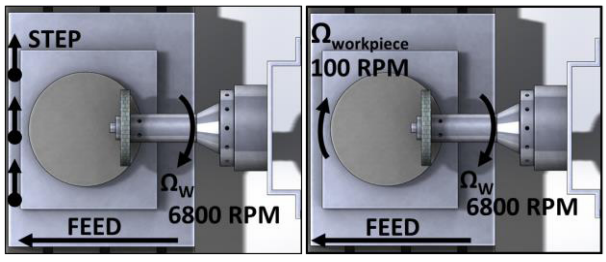

(a) (b)

Figure 1: Configurations: (a) raster (b) spiral

TABLE 1. Grinding Wheel Specifications

Mode of grinding	Arbor Size (mm)	Grit Size (μm)	Bond type
Roughing	12.7	40	Metal
Medium		10-20	Metal
Fine		2-4	Copper Resin

TABLE 2. Raster Grinding Parameters

Grinding Mode	Grit Size (μm)	Feed (mm/min)	Step (mm/pass)	Depth (mm)
Rough	40	1000	0.5	0.1
Medium	10-20	1000	0.2	0.02
Finish	2-4	100	0.05	0.02

TABLE 3. Spiral Grinding Parameters

Grinding Mode	Grit Size (μm)	Feed (mm/min)	Workpiece speed (rpm)	Depth (mm)
Rough	40	1	100	0.1
Medium	10-20	1	100	0.02
Finish	2-4	1	100	0.02

For the test spheres, cup grinding wheels having 500 μm grit size with a copper-resin bond and 10-20 μm grit size with metal bond were used for rough and finish grinding respectively. The wheel and workpiece speeds were 5000 rpm and 92 rpm respectively. The process parameters and grades used for these tests are as shown in Table 4.

TABLE 4. Cup Grinding Parameters

Grade	Depth (μm)	Feed rate (Rough) (mm/min)	Feed rate (Finish) (mm/min)
Silicon infiltrated	30	0.25	0.03
Reaction bonded	30	0.05	0.01
Direct Sintered	30	0.15	0.03

MRF spotting experiment

MRF spotting experiments were performed on a QED Q22 – XE CNC machine. The MRF fluid is a diamond based slurry (QED D10). The details of the spotting experiments are described in [6]. The spotting experiments in CVD grade samples that were finish ground in [6] revealed that dimples with spotting intervals less than 1-minute were required to quantify the subsurface damage with more certainty. This was taken into consideration when spotting CVD samples in the current study using 20-second spot intervals

MEASUREMENT PROCEDURE

The sample surfaces and spots were measured using a Zygo Nexview scanning white light interferometer (SWLI) with a 20x Mirau objective and a JEOL JSM 6480 scanning electron microscope (SEM)

Measurement of ground surface roughness

SWLI enables quantification of surface integrity in terms of average roughness (Sa), RMS roughness (Sq) and peak to valley roughness (Sz), and the data were processed in MATLAB®. Measurements were made using a 20x objective across the sample area of different grades that were ground using different grinding parameters. Waviness was removed by an 80 μm high pass Gaussian filter.

Measurement of subsurface damage using MRF spots

Each MRF spot surface was measured at 3 locations at the deepest region of the spots with a SWLI using 20x objective. The evolution of Sa, Sq and Sz were analyzed as a function of spotting interval/depth. The roughness parameters show a monotonic decrease with increased spotting time until leveling off after a spotting time dependent on the sample. Beyond this point, the roughness parameters might begin to increase again or remain steady depending on process-material interactions. Figure 2 shows a typical example of change in roughness parameters with spotting time in a CVC grade sample [6].

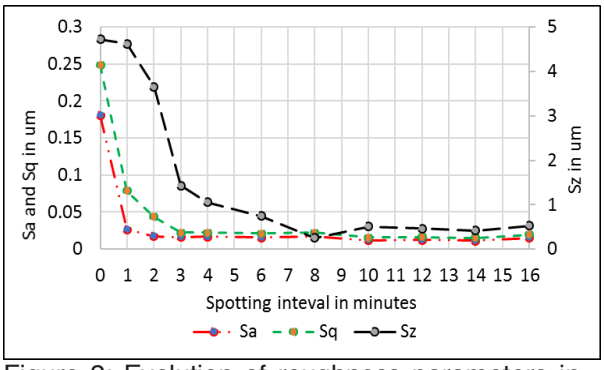

Figure 2: Evolution of roughness parameters in rough ground CVC grade

RESULTS AND DISCUSSION

Summary of Previous Results

Initial experiments on a Makino A55 showed best surface finish in CVC and CVD grade SiC when ground under identical parametric conditions [6]. SSD measurements also concluded that CVC and CVD had the least subsurface damage. However, the minimum spotting time used for these tests appears to have penetrated through the subsurface damage layer, and hence, the damage couldn't be quantified. The spotting time was therefore modified in the current study. Further details of previous work is available in [6].

Surface Measurements

In the current test, each surface, ground with different parameter sets, was measured at 15 different locations. Surface parameters, Sa, Sq and Sz were calculated as per ISO 4287-1997 [7], and corresponding average estimates were calculated as per 4288-1996 [8]. All data were processed in MATLAB®. Waviness was filtered with an 80 μm high pass filter.

CVD grade SiC

Surface measurements of the raster ground CVD grade with medium grinding parameters (Table 2) gave average roughness estimates of Sa and Sq of 74.7 nm and 100 nm respectively. Under finish parameters, the average estimates of Sa and Sq for the same configuration were 2 nm and 2.5 nm respectively. In the spiral configuration, the medium parameter set yielded a better surface finish of average Sa 61.5 nm and average Sq 84.3 nm. However, the finish ground surface yielded an average Sa of 8.5 nm and average Sq of 10.3 nm. Figures 3 and 4 shows SWLI images of surfaces ground under finish parameters.

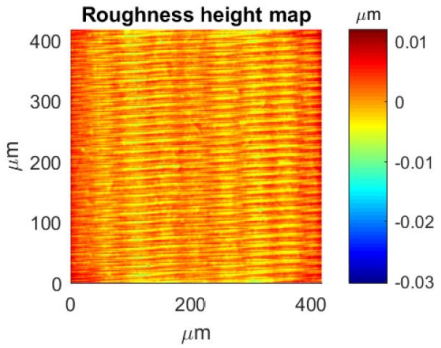

Figure 3: SWLI measurement of raster ground CVD SiC. Sa = 2.1 nm, Sq = 2.7 nm and Sz = 42.4 nm.

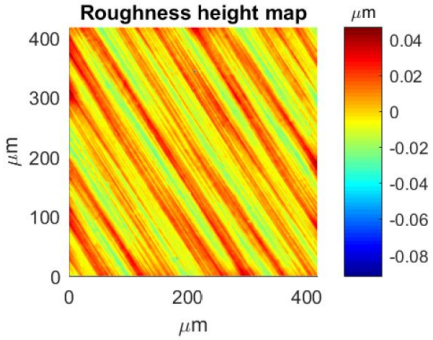

Figure 4: SWLI measurement spiral ground CVD. Sa = 9.6 nm, Sq = 11.6 nm and Sz = 138.8 nm.

These surfaces were also imaged under a scanning electron microscope to elucidate the nature of material removal during grinding process. Figure 5 shows SEM images of CVD sample ground using medium and finish parameters.

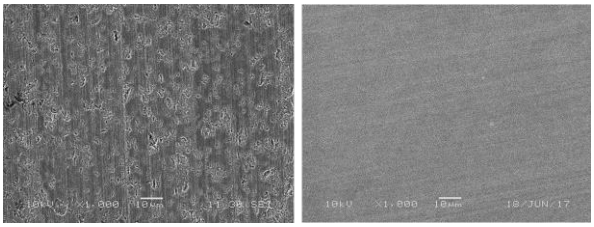

(a) (b)

Figure 5: CVD (a) medium ground (b) finish ground (1000x magnification).

In both configurations, the surface ground with medium parameters indicated dominance of brittle fracture while the finish surface was dominated by ductile deformation.

Reaction bonded grade SiC

Two reaction bonded samples were raster ground using parameters in Table 2. The variable was the wheel diameter: 25.4-mm and 50.8-mm. Surface measurements were performed, and the data were processed as per aforementioned procedure. Figure 6 summarizes the Sa and Sq results.

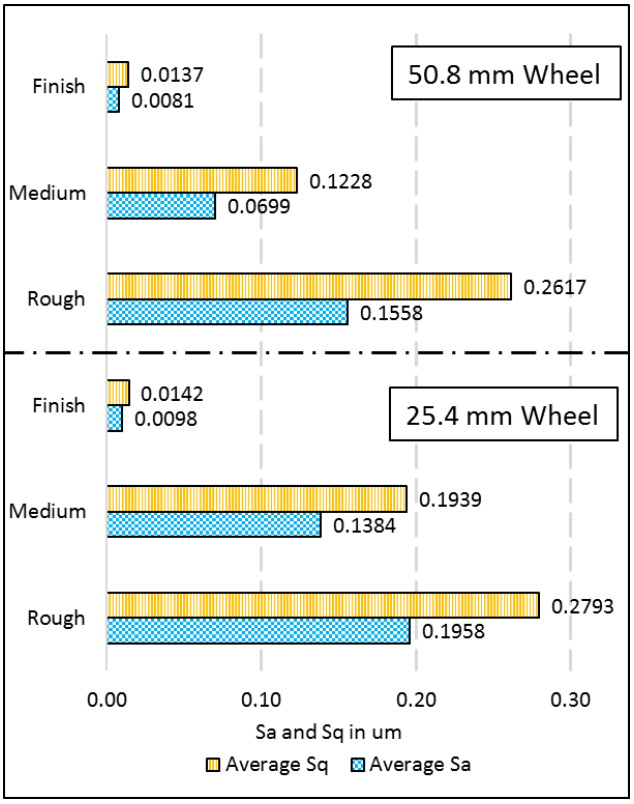

Figure 6: Surface roughness measurements in reaction bonded samples.

Figure 6 indicated that, under identical grinding conditions, the larger diameter wheels produced slightly better surface finish than the smaller diameter wheel. Figure 7 shows SEM images acquired using secondary electron imaging and back scatter electron imaging. Back scattering electron imaging is comprised of three modes. The composition mode contrasts the difference in composition of the surface while the topography mode contrasts the topographical features of the surface. Shadow mode enables further interpretation of the surface features by combining compositional and topographical modes.

Figure 7 utilized composition mode to show the presence of two different materials on the surface, silicon and silicon carbide. By comparing the composition mode image with the shadow and topography mode images, it can be observed that the mode of material removal changed continuously across the surface. Silicon, being the softer material among the two, experienced ductile deformation while SiC underwent partial brittle fracture. The SEM images of the same grade ground using finish parameters are shown in Figure 8.

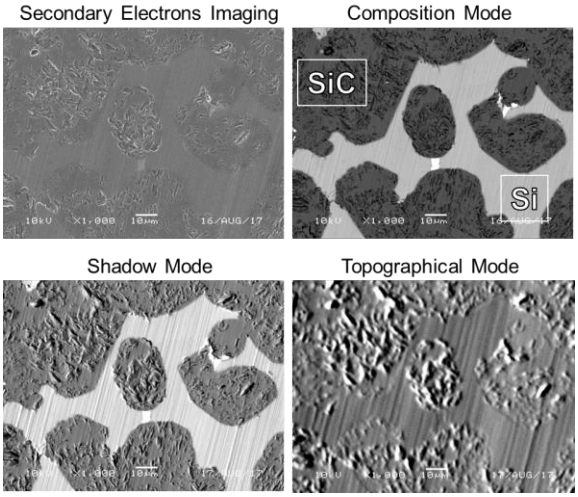

Figure 7: SEM images of reaction bonded sample surface ground with 2-inch wheels (1000x Magnification).

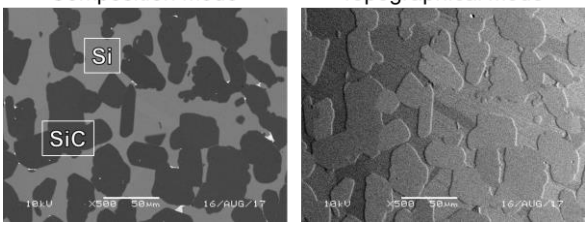

Figure 8: Backscatter Electron Images of finish ground reaction bonded sample
(500x Magnification)

In Figure 8, the composition mode shows the grain boundaries of silicon and SiC. Topographical mode shows that the silicon grains are ground at a much faster rate than SiC, thus creating a step like feature between grains of different material.

Subsurface Damage measurements

CVD grades ground using raster and spiral configurations were analyzed using the MRF spotting technique.

CVD – Spiral Ground

MRF spots with short spotting time intervals of 20 seconds were used to measure smaller depths of SSD. Figure 9 and 10 depicts roughness at the base of spots as a function of spotting interval for medium and finish ground surfaces respectively.

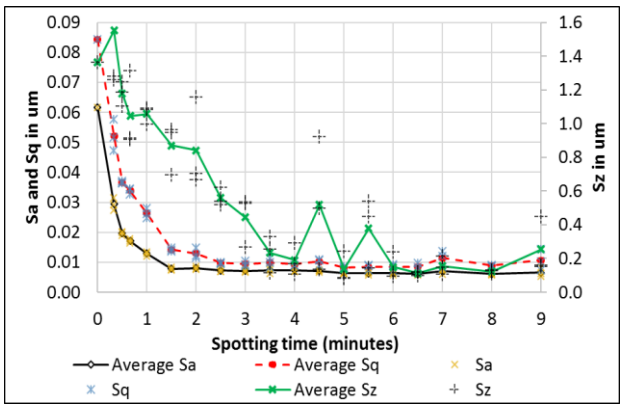

Figure 9: Subsurface damage estimation in medium spiral ground CVD.

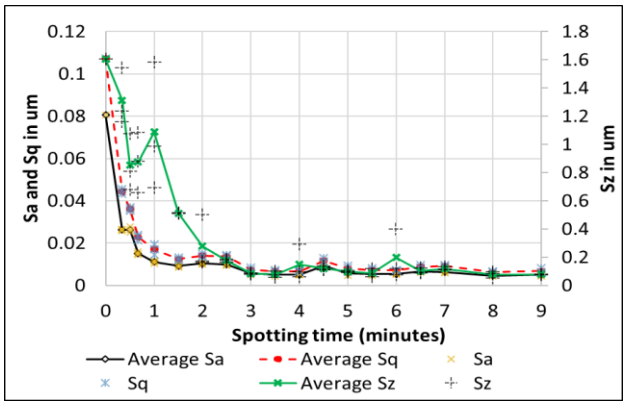

Figure 11: SSD analysis of Medium raster ground CVD sample.

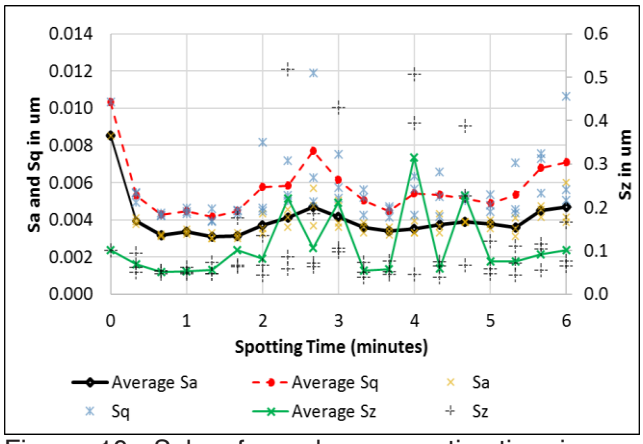

Figure 10: Subsurface damage estimation in finish spiral ground CVD.

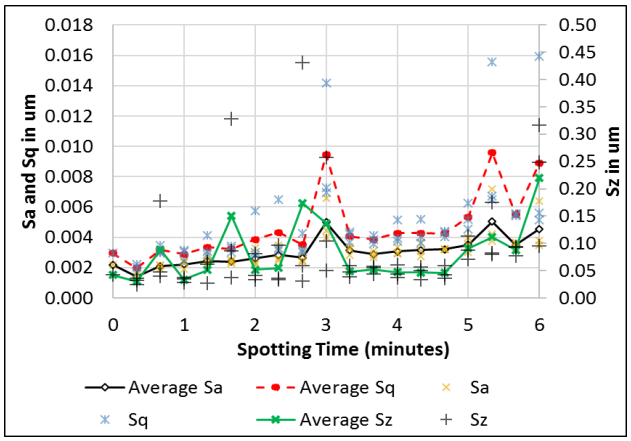

Figure 12: SSD analysis of finish raster ground CVD sample.

This study is conducted by analyzing the change in average estimates of roughness values, Sa, Sq and Sz as spotting time increases. Figure 9 suggests that the roughness values converge to a stable value after 6 minutes. The corresponding spot depth gives an estimate for the subsurface damage and was found to be 3 μm. For the finish ground surface, Figure 10 shows leveling of roughness values in approximately 40 seconds. The corresponding estimate of subsurface damage was approximately 0.3 μm.

CVD – Raster Ground

Similar tests were completed on the CVD grade sample that was ground in raster configuration. Figures 11 and 12 show the subsurface damage analysis for medium and finished ground surfaces, respectively.

MRF spot analysis of medium ground sample show that the roughness values converge at 2.5 minutes. The subsurface damage was estimated to be approximately 1.7 μm. The finish ground surface in Figure 12 show that the roughness values do not show an initial decrease even at spotting times less than 1 minute. As a result, it can be hypothesized that the subsurface damage is less than the depth of the first spot i.e. 20-second spot. Hence the subsurface damage was estimated to be less than 0.2 μm. Further experiments are required to estimate the subsurface damage with more certainty.

TRANSITION TOWARDS FREEFORM: TEST SPHERES

As a preliminary step towards understanding the surface mechanics and surface response to process parameters for more complex geometries, test spheres were manufactured in 3 different grades of SiC. Initial measurements using a Fizeau interferometer (as shown in figure 13) and scanning white light

interferometer were done. These show less than 2 µm of form error dominated by astigmatism.

Surface measurements in SWLI showed that among the three grades, the direct sintered grade had the best surface finish with Sa 10 nm, Sq 26 nm and Sz 968 nm. The surface finish of reaction bonded sample was Sa 27 nm, Sq 52 nm and Sz 1376 nm. The surface finish of silicon infiltrated grade was Sa 58 nm, Sq 283 and Sz 9776 nm. Higher values of Sz can be attributed to pits present on the surface. Further study with different grinding configurations under identical parameters are still required to make any conclusions on the surface/subsurface response in test spheres.

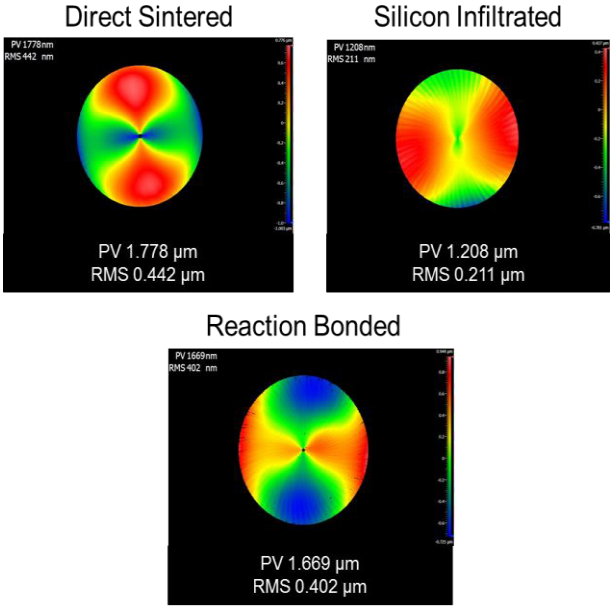

Figure 13: Fizeau measurements of test sphere. (Piston, tilt and power removed)

CONCLUSION

The surface and subsurface response of SiC samples ground using different configurations have been analyzed here. SEM enabled better understanding of the material removal mechanics in ground samples. Backscatter electron imaging revealed the nature of surface mechanics during grinding in non-homogenous material such as reaction bonded grade. Surface study using SWLI measurements in the CVD samples ground in different configurations showed that spiral finish grinding imparts more surface and subsurface damage than in raster configurations. However, it was also shown that better surface finish can be obtained with medium grinding in a spiral configuration. Further study is required to understand the mechanics of material removal in different configurations. Future studies would also include grinding samples using a combination of configurations and identifying the best set that would yield better surface integrity for freeform optics.

ACKNOWLEDGEMENTS

Experiments using Optisonic 1250X and SXL 500 were performed at Optipro Systems, LLC. This research is supported by the NSF I/UCRC Center for Freeform Optics (IIP-1338877 and IIP-1338898).

REFERENCES

[1] Saurav Goel, “The current understanding on the diamond machining of silicon carbide”, J. Phys. D: Appl. Phys Vol. 47 (2009) 243001.

[2] AH Rashed, “Properties and Characteristics of Silicon Carbide”, POCO graphite, Inc.

[3] Jiwang Yan, Zhiyu Zhang, Tsunemoto Kuriyagawa, “Mechanism for material removal in diamond turning of reaction bonded silicon carbide”, International Journal of Machine Tools and Manufacture 49 (2009) 366-374.

[4] Shogo Takesue, Kazutoshi Katahira, Jun Komotori, “A study on PCD tool surface reconditioning technique for SiC micromachining”, Procedia CIRP 14 (2014) 355-359.

[5] SN Shafrir, JC Lambropoulos, SD Jacobs, “Subsurface damage and microstructure development in precision micro-ground hard ceramics using magnetorheological finishing spots”, Applied Optics, Vol. 46 No. 22 (2007) 5500 – 5515.

[6] Prithiviraj Shanmugam, Joseph Owen, Sivan Salzman, John Troutman, John Lambropoulos, Matthew A Davies, “Fundamentals of material removal in silicon carbide for freeform optics”, Conference: Proc. ASPEN/ASPE Spring Topical (2017) pg. 35 - 38

[7] ISO 4287-1997, International Standard, “Geometrical Product Specification (GPS) – Surface Texture: Profile Method – Terms, definitions and surface texture parameters”

[8] ISO 4288-1996, International Standard, “Geometrical Product Specification (GPS) – Surface Texture: Profile Method – Rules and procedures for the assessment of surface texture”

AN INVESTIGATION OF MULTI-JET POLISHING OF PRECISION SURFACES

C.F. Cheung *, C.J. Wang, L.T. Ho, and W.B. Lee
Partner State Key Laboratory of Ultra-precision Machining Technology
Department of Industrial and Systems Engineering
The Hong Kong Polytechnic University, Hung Hom, Kowloon, Hong Kong

INTRODUCTIONS

Fluid jet polishing (FJP) [1,2] is one of the promising polishing methods as compared to other polishing methods. This is particularly true for its unique advantages, such as high machining accuracy, suitable for polishing various complex surfaces (especially for steep, concave aspheric surfaces), no tool wear, no temperature increase of the workpiece during polishing, and can be used on many kinds of materials including optical glass, ceramics, semiconductor materials, crystal materials, hard alloys, etc. [3-6]. However, there still exist limitations of FJP. Low polishing efficiency is one of the main limitations, which affects its application in polishing medium-large size components. Besides, it also takes a relatively long time to polish a small size component as compared to other polishing methods.

According to the reported literatures [7,8], the material removal rate can be increased by increasing the fluid pressure and slurry concentration. However, high fluid pressure would lead to bad surface finish, while high slurry concentration would not only make it difficult to control its stability, but also lead to the congestion of the slurry supply system. Moreover, the enhancement is limited by only a single jet. Beyond that, researchers also attempted to add the pressured gas into the fluid jet to enhance the polishing efficiency [9]. Although it can increase the material removal rate, the polished surface has deeper surface defects and poorer surface finish than the traditional FJP. Recently, Beaucamp et al. [10] proposed a novel ultrasonic cavitation assisted fluid jet polishing to enhance the polishing efficiency. However, the enhancement of the efficiency is less than 4 times of the normal fluid jet polishing according to the reported results. Hence, an effective way to largely enhance the polishing efficiency (i.e. tens or hundreds of times) of FJP is still much needed. With this in view, multi-jet polishing (MJP) process was developed to address this problem [11]. In the MJP process, many orifices are designed and fabricated in a larger size nozzle. In MJP, the input fluid with relatively high energy can be distributed to each individual fluid jet which owns the energy similar to the single jet polishing (SJP) process. Hence, the polishing efficiency is largely increased depending on the number of the orifices. In this paper, an investigation and discussions of MJP were carried out.

MULTI-JET POLISHING PROCESS

In MJP process, pressurized polishing fluid mixed with water and abrasive particles is delivered by a pump to a purposely designed converging nozzle. The jet impinges the workpiece and thus generating material removal. The configuration of the orifices on the MJP nozzle can be customized with linear, circular, or square array topologies as shown in Fig. 1. It can be used to polish various kinds of surfaces, including flat and freeform surfaces. Specifically, the linear distributed MJP nozzle can be used to undertake the polishing work on circular or cylindrical surfaces as shown in Fig. 1(e) and Fig. 1(f).

MATERIAL REMOVAL CHARACTERISTICS

Material removal rate

Comparison experiments for studying material removal rate were firstly conducted, and the experiments were undertaken on ZEEKO IRP200 seven axes computer controlled ultraprecision polishing machining system as shown in Fig. 2. Several types of MJP nozzles were purposely designed for conducting the experiments as shown in Fig. 3(a). The diameter of each orifice is 300□m.

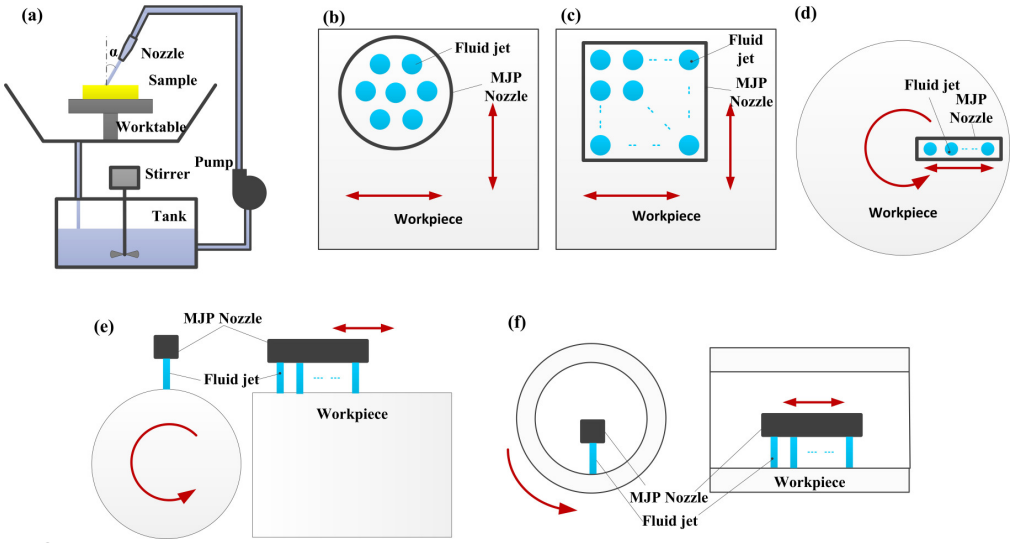

FIGURE 1. Schematic diagram of Multi-Jet Polishing (MJP) process and several typical polishing situations: (a) MJP process system, (b) polishing using a circular distributed MJP nozzle, (c) polishing using a square array type distributed MJP nozzle, (d) linear distributed MJP nozzle polishing circular samples, (e) linear distributed MJP nozzle polishing cylindrical surface and (f) linear distributed MJP nozzle polishing internal surface.

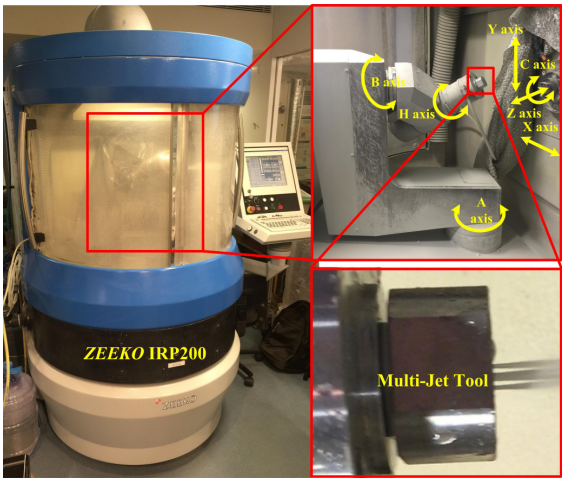

FIGURE 2. Photographs of experimental setup.

Experiments for studying the tool influence function generation were conducted on nickel copper (NiCu) alloy and BK7 optical glass under the same polishing conditions as summarized in TABLE 1. The polishing slurry for polishing NiCu is wt.10% 4000# silicon carbide, whose average particle size is about 3.2 μm. The polishing slurry for BK7 is 10 wt. % Cerox SUPER 1663 CeO_2, with the average size of 1.5 μm. Fig. 3(b) demonstrates the generated TIF contour of these three nozzles on NiCu.

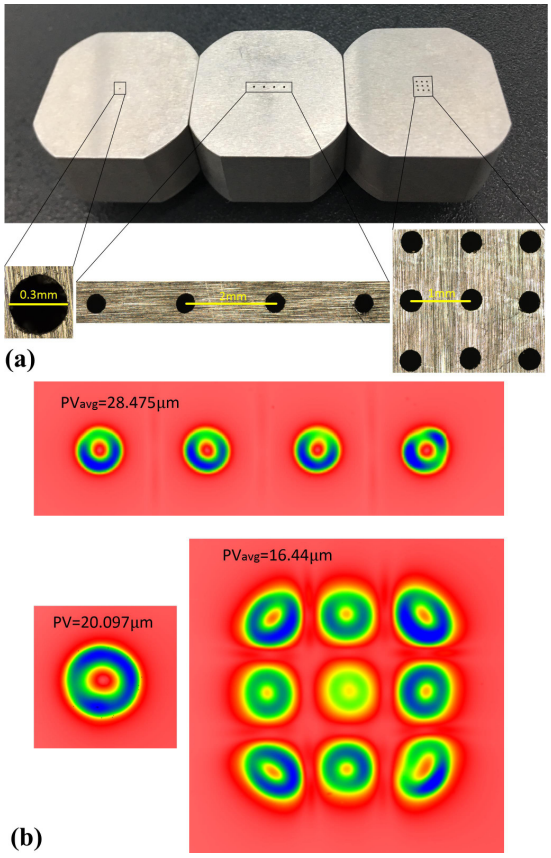

FIGURE 3. Photographs of the purposely designed SJP and MJP nozzles for the experiments and corresponding TIFs on Nickel copper alloy surfaces: (a) nozzles, (b) TIFs.

TABLE 1. Polishing conditions for the TIF generation experiments

Fluid pressure	6 bars
Stand-off distance	3 mm
Impinging angle	90 degree
Dwell time	3 minutes

Figure 4 shows the comparison results of material removal rate adopting different nozzles both on NiCu and BK7. The results indicate that the material removal rate of MJP is much higher than that for SJP, and the enhancement of the removal rate is almost proportional to the number of orifices integrated in the MJP nozzle.

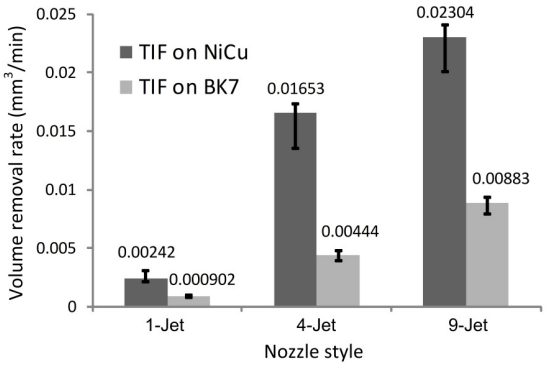

FIGURE 4. Comparison of the material volume removal rate of these three kinds of nozzles on nickel copper alloy and BK7 optical glass.

Effects of polishing parameters to the surface roughness

The effect of two main polishing factors to the surface roughness was investigated, which are fluid pressure and stand-off distance. As shown in Fig. 3(a), a 9-jet MJP nozzle was used in this experiment. Moreover, a total of 8 groups of experiments were conducted on BK7 optical glass and single crystal silicon (100) as shown in Table 2. Those surfaces werepre-polished to mirror surface to reduce the effect of the original surface.

Figure 5 shows the analysis results of the effects of these two factors to the polished surface roughness, which is the average arithmetic roughness (Ra) value of three measured results. The results indicate that the fluid pressure has great influence on the surface roughness, and a larger fluid pressure leads to an increase of surface roughness. The effect of the stand-off distance is insignificant to the surface roughness, and no obvious relationship was observed between the stand-off distance and the surface roughness. Moreover, it is interesting to note that when the fluid pressure is 3 bars and the stand-off distance is 4 mm, the surface roughness is the smallest among them.

TABLE 2. Experimental design of the effect of polishing factors

No.	Fluid pressure (bars)	Stand-off distance (mm)	Slurry	Sample material
A1	3	2, 4, 6	10 wt.% CeO_2 ,	BK7 optical glass
A2	4	2, 4, 6		
A3	5	2, 4, 6		
A4	6	2, 4, 6		
B1	3	2, 4, 6	5 wt.% SiC	Single crystal silicon
B2	4	2, 4, 6		
B3	5	2, 4, 6		
B4	6	2, 4, 6		

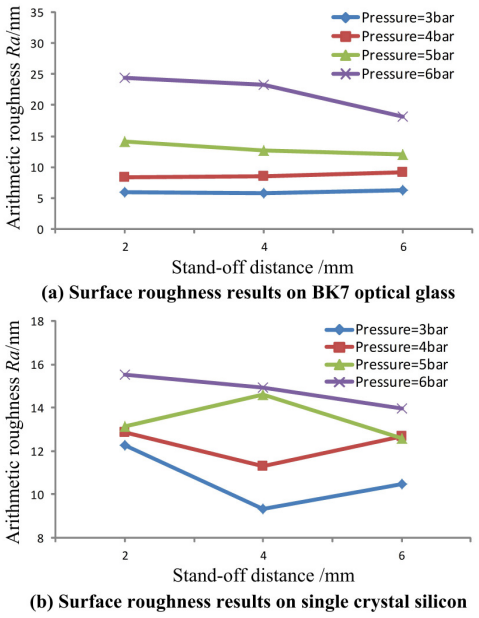

FIGURE 5. Analysis of effects of fluid pressure and stand-off distance to the surface arithmetic roughness on BK7 optical glass and single crystal silicon surface (The roughness value is the average arithmetic roughness value of 3 measured surface roughness value)

Surface texture after polishing on different materials

To compare the surface texture after polishing by MJP on different materials, polishing experiments were conducted on BK7, single

crystal silicon (110) and stainless steel under the same polishing conditions as tabulated in Table 3. The surface of these samples before polishing are rough surfaces as shown in the first row of Fig. 6, which was measured by Zygo Newview 3D profilometer. And the polished surface textures of them have also been shown in the second row of Fig. 6. The arithmetic roughness (Ra) of the polished surface of BK7, single crystal silicon and stainless steel are 22 nm, 31 nm, and 42 nm, respectively. It suggests that the surface roughness on the hard-brittle materials such as BK7 glass and single crystal silicon is lower than that on ductile metal surface such as stainless steel under the same polishing conditions. It is also observed from the results on BK7 and NiCu as we reported in Ref. [11]. It can be explained that the indentation depth for the ductile surface is deeper than that for the hard-brittle surface under the same particle impact energy. And these surface results were polished after only one cycle under the polishing conditions as shown in Table 3. Their surface roughness can be further improved through subsequently polishing process. Figure 7 shows the photo of several regions on single crystal silicon surface before and after polishing in this experiment. Mirror-like surface can be achieved on single crystal surface after MJP.

TABLE 3. Polishing conditions comparison of surface textures

Fluid pressure	3 bars
Stand-off distance	4 mm
Impinging angle	90 degree
Polishing path	Raster path
Path pitch	0.1 mm
Path region	2 mm ×2 mm
Feed rate	6 mm per minute
Polishing time	~7 min

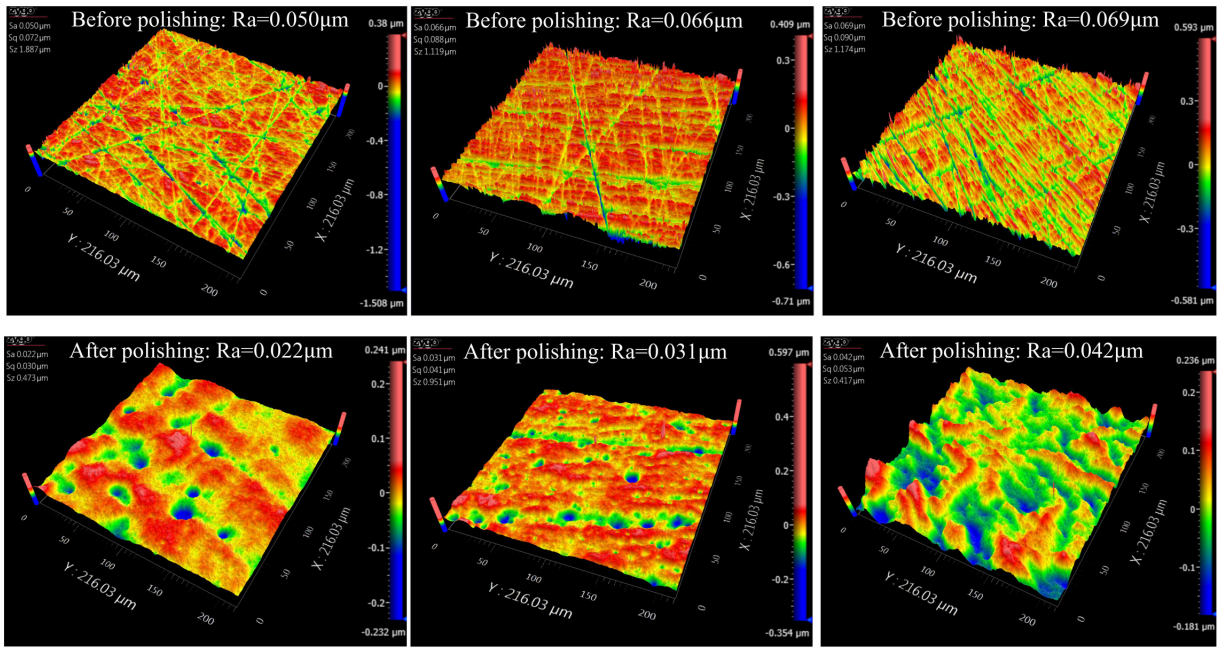

(a) BK7 (b) Single crystal silicon (c) Stainless steel

FIGURE 6. Comparison of surface topography of different materials polished by MJP

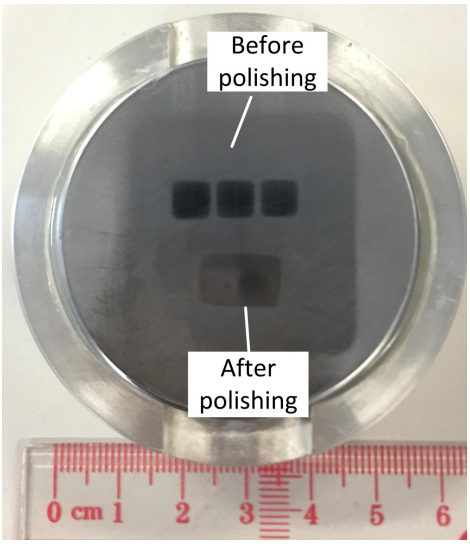

FIGURE 7. Snapshots of single crystal silicon surfaces before and after polishing

DISCCUSIONS

Material removal rate comparison

Limited by the maximum fluid pressure of our experimental device, only a few orifices were integrated in one nozzle in the present study. However, the results have proven the feasibility of MJP. Through increasing the size and number of the orifice in the designed nozzle with a higher fluid pressure, it can be used to polish medium-large surfaces. The volume removal rate (VRR) of single jet polishing on BK7 using 0.3mm diameter nozzle is only 9 x 10 mm^3/min. Normally, VRR of single fluid jet polishing varies from 1 x 10^{-4} mm^3/min to 0.01 mm^3/min when the nozzle diameter is ~1 mm, and the peak removal rate (PRR) varies from 0.1 μm/min to 10 μm/min. The removal rate could be influenced by many factors, such as slurry concentration, fluid pressure, stand-off distance, particle type, workpiece material, etc. Assuming that 100 Ø1mm orifices are integrated in one MJP nozzle, then the VRR could be up to ~1mm^3/min. This material removal rate is comparable or even larger to the VRR of magnetorhelogical finishing (MRF) on BK7 as reported in literature [12], which is smaller than 0.9mm^3/min. Moreover, the number of the orifice could be much more than 100 in the MJP nozzle, which would further enhance its VRR.

Applications

Classical single jet polishing can only be used to polish small size surfaces and edge of large surfaces. With the successful development of the MJP process, the application of fluid jet polishing technology can be further extended to the polishing of medium-large size freeform surfaces, such as mirrors used in high-power laser system, large scale functional surfaces, etc. Moreover, the MJP nozzle can be purposely designed for polishing of various kinds of surfaces, such as cylindrical surfaces, internal surface, etc., as shown in Fig. 1.

Beaucamp et al. [6] successfully combined the single fluid jet polishing and bonnet polishing process for the fabrication of hard X-ray molding dies. Identically, MJP could also be combined with bonnet polishing for the optimization of process chain for high efficiency manufacturing of industrial products. This will be studied in the future work.

CONCLUSIONS

A novel Multi-Jet Polishing (MJP) process is presented in this paper. The experimental results show that it not only possesses a much higher polishing efficiency than that of single jet polishing (SJP), but also reaches the surface accuracy at the equivalent level to the single jet polishing. The experimental investigations of MJP also indicate that the fluid pressure has great influence on the surface roughness, and the larger fluid pressure leads to larger surface roughness. The effect of the stand-off distance is very small to the surface roughness, and no obvious relationship was observed between the stand-off distance and the surface roughness. In addition, the polishing results on different materials also infer that the surface roughness after MJP for ductile metal materials is larger than that for hard-brittle materials. The development of the MJP polishing process will help to extend the application of fluid jet polishing to medium-large size surfaces.

ACKNOWLEDGEMENTS

The work described in this paper was mainly supported by the funding support to the Partner State Key Laboratories in Hong Kong from the Innovation and Technology Commission (ITC) of the Government of the Hong Kong Special Administrative Region (HKSAR), China. The

authors would also like to express their sincerely thanks to the financial support from the Research Office (Project code: BBX7).

REFERENCES

[1] Faehnle OW, Brug HV, Frankena HJ. Fluid jet polishing of optical surfaces. Appl. Opt. 1998; 37:6771–6773.

[2] Booij SM. Fluid Jet Polishing-possibilities and Limitations of a New Fabrication Technique (Ph.D. thesis), Delft University, 2003.

[3] Fang H, Guo PJ,Yu JC, Surface roughness and material removal in fluid jet polishing. Appl. Opt.2006; 45: 4012-4019.

[4] Tsai FC., Yan BH, Kuan CY, Huang FY. A Taguchi and experimental investigation into the optimal processing conditions for the abrasive jet polishing of SKD61 mold steel. Int. J. Mach. Tools Manuf. 2008; 48: 932-945.

[5] Beaucamp A, Namba Y, Freeman R. Dynamic multiphase modeling and optimization of fluid jet polishing process. CIRP Ann. – Manuf. Technol. 2012; 61: 315–318.

[6] Beaucamp A, Namba Y. Super-smooth finishing of diamond turned hard X-ray molding dies by combined fluid jet and bonnet polishing. CIRP Ann.-Manuf. Technol. 2013; 62: 315-318.

[7] Chen FJ, Miao XL, Tang Y, Yin SH. A review on recent advances in machining methods based on abrasive jet polishing (AJP). Int. J. Adv. Manuf. Technol. 2017; 90: 785-799.

[8] Zhu HT, Huang CZ, Wang J, Li QL, Che CL. Experimental study on abrasive waterjet polishing for hard–brittle materials. Int. J. Mach. Tools Manuf. 2009;49: 569-578.

[9] Messelink WACM, Waeger R, Wons T, Meeder M, Heiniger KC, Faehnle OW. Prepolishing and finishing of optical surfaces using fluid jet polishing. Proc. SPIE 2005;5869:586908.

[10] Beaucamp A, Tomoya K, Zensaku K. A novel ultrasonic cavitation assisted fluid jet polishing system. CIRP Ann.-Manuf. Technol.2017.

[11] Wang CJ, Cheung CF, Ho LT, Liu MY, Lee WB. A novel multi-jet polishing process and tool for high-efficiency polishing. Int. J. Mach. Tools Manuf. 2017;115:60-73.

[12] Donald G, Jacobs SD, Kordonski WI, Dumas P. Precision optics fabrication using magnetorheological finishing. In Critical Review Collection, pp. 102890H-102890H. International Society for Optics and Photonics, 2017.

High-pressure aerostatic bearing technology - Combining robustness with speed, thermal stability and low errors in motion

Dr. Ralf Dupont
Levicron GmbH, Non-Contact-Precision-Motion
67661 Kaiserslautern, Germany

PEFACE

For ultra-precision machining under heavy load oil-hydrostatic spindles offer outstanding surface finish and robustness. Peripherals to run this kind of spindle and the required sealing technology on the other hand lead to very high upfront investments and operating costs. Also, excessive bearing losses at higher speeds prevent this spindle type from being used for ultra-precision milling and grinding. Under shaft rotation shear losses in fluid bearings depend on the fluid viscosity, but almost not on the fluid pressure. Consequently, increased air supply pressure to an aerostatic bearing gives nearly proportionally increased load capacity and stiffness at only slightly increased bearing losses.

Together with a new bearing orifice design the reader is presented a high-pressure aerostatic bearing system as part of a new motor spindle development that combines the load capacity of oil-hydrostatic bearings with the accuracy, speed, simplicity and energy consumption level of aerostatic bearing systems. Modifications on the aerostatic bearing system of an existing motor spindle will show the reader that also such spindles can be operated at higher pressures to gain load capacity and robustness while maintaining their error motion, high-speed and power consumption properties at the same time.

A simplistic sealing technology and of-the-shelf compressor solutions lead to significantly lower upfront investments than those that are required for oil-hydrostatic spindle solutions. Also running costs are lower due to remarkably reduced energy consumption.

The new motor spindle features a newly developed aerostatic shaft rotary feedthrough, a patented innovative spring-less automatic HSK-E40 tool interface and 4 Nm motor torque. With this development, the end user is given a true full-range CNC tool spindle with automatic HSK-E40 tool interface capable of rough cutting and ultra-precision machining at speeds of up to 60.000 rpm.

NOMENCLATURE

- a – bearing diameter
- d – orifice diameter
- h_0 – static bearing gap
- l – length: orifice to journal end
- n – number of orifices per row
- p_0 – supply pressure
- p_a – ambient pressure
- C_D – discharge coefficient
- D – journal diameter
- L – journal bearing length
- P – shear friction losses
- R – gas constant
- T – absolute temperature
- W_r – journal load capac.
- E – rela. shaft eccentricity
- μ – dynamic gas viscosity
- θ – angular coordinate

SPINDLES WITH OIL-HYDROSTATIC BEARINGS

Oil-hydrostatic bearings give excellent damping and relatively low errors in motion. The required sealing technology, the peripherals to run this spindle type and cost-intensive maintenance on the other hand lead to high upfront investment and operating costs. Shear losses in the bearing gaps of rotational fluid bearings depend on oil viscosity and shear speed and result in excessive bearing losses with speed even at large bearing gaps. This also drives poor thermal spindle and machine behavior. Pockets in the common design of oil-hydrostatic bearings, in addition, lead to partly turbulent flow and thus to increased errors in shaft motion.

HIGH-PRESSURE AEROSTATIC BEARINGS

Shear losses in fluid bearings predominantly depend on fluid viscosity, but almost not on pressure. Increasing the supply pressure to an aerostatic bearing thus leads to increased load capacity and stiffness, but at almost constant shear losses according to (1) for a journal bearing under concentric conditions.

(1) $P_j = \frac{\mu \pi D^3 L \omega^2}{4 h_0}$ where μ is the dynamic viscosity.

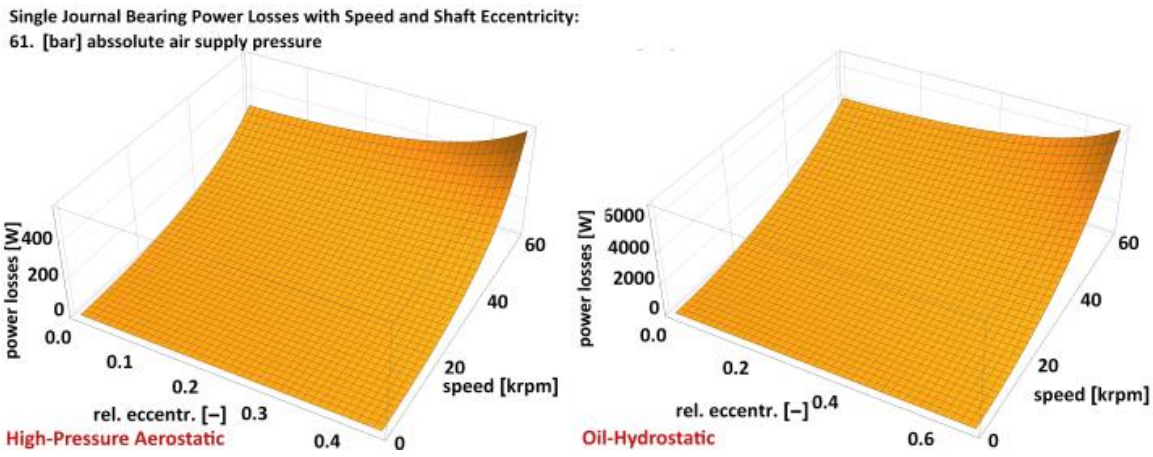

FIGURE 1: Journal bearing shear losses with speed and relative shaft eccentricity for a high-pressure aerostatic and oil-hydrostatic slot bearing system with same bearing dimensions (bearing gap not incl.)

Figure 1 illustrates the difference in shear losses of an oil-hydrostatic and aerostatic journal bearing under shaft rotation.

Thus, high-pressure aerostatic bearings combine a high load capacity, as known from oil-hydrostatic bearings, with low shear losses at high rotation speeds, a simplistic design and lowest errors in motion, as known from aerostatic bearings.

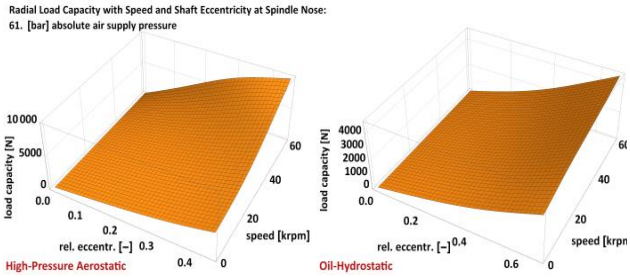

FIGURE 2: Radial load capacity at spindle nose with speed and relative shaft eccentricity for a high-pressure aerostatic and oil-hydrostatic slot journal bearing and for same bearing dimensions (bearing gap not incl.)

Furthermore, the simplistic sealing technology allows a cost-effective and service-friendly spindle design.

PATENTED BEARING ORIFICE DESIGN FOR LOW AIR CONSUMPTION [2]

With increased supply pressure, also air consumption of an aerostatic bearing becomes unacceptably high if designed with state of the art orifices. Even though bearing orifices with a small cross section area would result in lower bearing stiffness at concentric shaft conditions, they would lower the air consumption and lead to a higher bearing stiffness at larger shaft deflections, where under these conditions larger orifices would choke. To manufacture orifices of under 30 microns in diameter a patented laser drilling process has been developed.

FIGURE 3: Laser drilling process to create small diameter capillaries

Along with a 65% reduction in air consumption even the ultimate load capacity was improved compared to standard bearing orifices. The smaller orifices and the laser drilling process enable an economical bearing design with hundreds of single jets per bearing and lower the shaft errors in motion. An orifice design with no pockets (= capillary) not only lowered the shaft error in motion, surprisingly it even improved the ultimate load capacity compared to orifices with pockets and stiffness at large shaft eccentricities.

MODIFYING EXISTING AEROSTATIC SPINDLES TO RUN ON HIGHER PRESSURES

After verifying that all the parts and assemblies involved can handle the higher air pressure an increase in bearing supply pressure can indeed

lead to improved stiffness and load capacity values. However, the original orifice design is likely to be not optimal what again would require a redesign. Larger orifice diameters lead to increased stiffness values for journal bearings at concentric shaft conditions, but also would lead to choked conditions at higher shaft eccentricities in direction of the eccentricity. Smaller orifice diameters thus lead to an increased load capacity and stiffness for large shaft eccentricities at reduced air consumption. Especially with thrust bearings large orifice diameters are generally used that need to be reduced to lower the air consumption of the bearing. Figure 4 shows that the static bearing stiffness of an aerostatic journal bearing at higher supply pressure is remarkably higher at large shaft eccentricities ε if capillaries with a smaller diameter d are used.

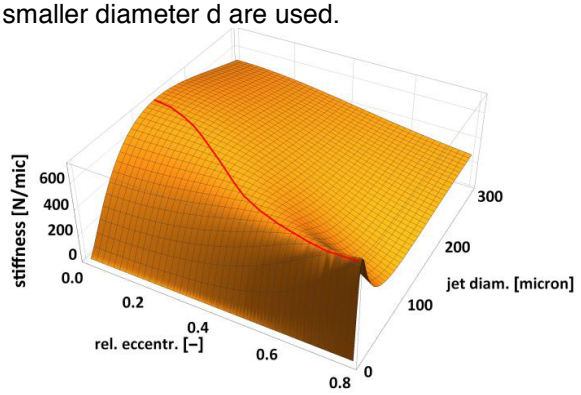

FIGURE 4: Journal bearing static stiffness with shaft eccentricity and orifice (jet) diameter

Equation (2) to (5) explain in a simplified approach the relationship between orifice diameter d and the restoring force W_r of a journal segment at no rotation. The angle of this segment (slot) is defined as $2\pi/n$ [Rad] where n is the number of orifices around the perimeter D and where two rows of orifices are used with a distance l from the bearing ends with an overall journal length of L [1]. The slot area of this single segment thus is defined as $(\pi/n)L$.

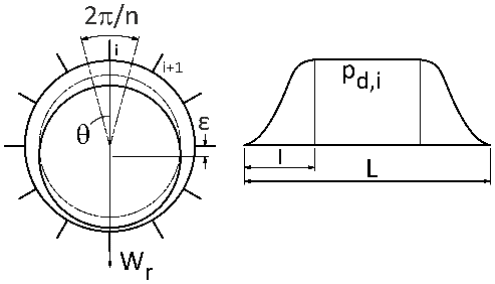

FIGURE 5: Journal bearing segmented load capacity approach

$$(2)\quad W_r = p_d\,(2L - 2l)\;D\;Sin\left(\frac{\pi}{n}\right) + 2\left(\frac{2}{3}(p_d - p_a)\;l\;D\;Sin\left(\frac{\pi}{n}\right)\right.$$

$$(3)\quad p_d = \frac{2\,(p_0 - p_a)}{1 + \left(1 + \frac{4}{G^2}\right)^{1/2}} - p_a$$

$$(4)\quad G = F_p \cdot F_g \cdot \frac{(l\;C_d\;\pi\;\boldsymbol{d})}{a\,(\;_0\,(1 - Cos\;\theta))^2}$$

$$(5)\quad F_p = \frac{\frac{p_a}{p_0}}{\left(1 + \frac{p_a}{p_0}\right)\left(1 - \frac{p_a}{p_0}\right)^{\frac{1}{2}}}$$

$$(6)\quad F_g = \frac{24\;\mu\;(2\;R\;T)^{\frac{1}{2}}}{p_a}$$

Not included in this simplified system of equations are non-axial flow and dispersion that both lower the static load capacity of a journal bearing as well as an aerodynamic drag under shaft rotation. But they show the non-linear influence of the orifice diameter on bearing load capacity and stiffness with shaft eccentricity for an aerostatic journal bearing.

UASD-H25 – Modified tool spindle operated at 20 bar

As a very successful pre-test an existing aerostatic tool spindle was modified and optimized to operate at 20 and 30 bar bearing air supply pressure.
An optimization of the orifice design for Levicron's aerostatic motor spindle ASD-H25/A lead to 300 % radial load capacity at 330 % air pressure and at only 190 % of air consumption.

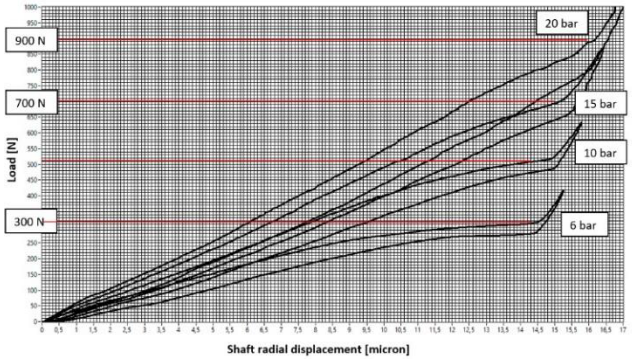

FIGURE 6: ASD-H25/A - optimized radial load capacity, taken 20 mm from spindle nose at different supply pressures

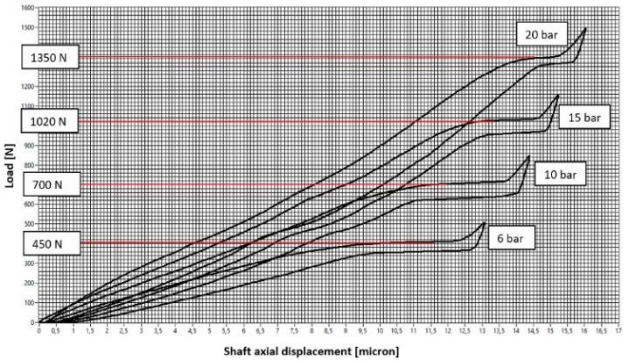

FIGURE 7: ASD-H25/A - optimized axial load capacity at different supply pressures

With 900 N ultimate radial load capacity, taken 20 mm from the spindle nose, and 20 bar supply pressure this aerostatic motor spindle not only outperforms roller bearing tool spindles with respect to speed, accuracy and thermal behaviour, but also offers a higher load capacity.
To confirm the load capacity, the accuracy and the shaft errors in motion a combined rough and finish machining test was carried out. A steel mold for an optical reflector was milled. The mold was made from ELMAX [4] at a hardness of 60 HRC. For roughing a standard 6 mm carbide cutter with a torus shaped tip was used, for finish machining a 3 mm CBN tool of the same shape.

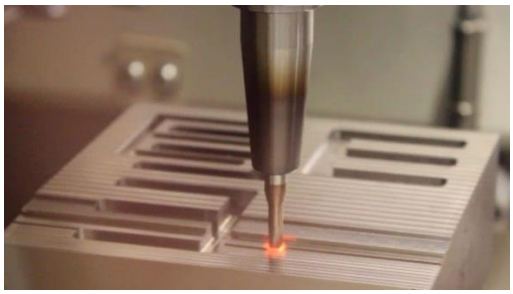

FIGURE 8: Stress test in ELMAX, HRC60, with a worn-out tool [5]

For rough machining cutting parameters were used that deliberately exceeded the tool limit to investigate the difference in cutting load between a new tool and a worn one.
The side load the tool created during rough machining was measured by the change in axis current. For this the axis current was measured during the machining with no workpiece and compared to the axis current when really cutting.
Where the fresh tool created a radial load of 200 N in direction of axis movement, a worn tool created more than 600 N as shown in Figure 8.

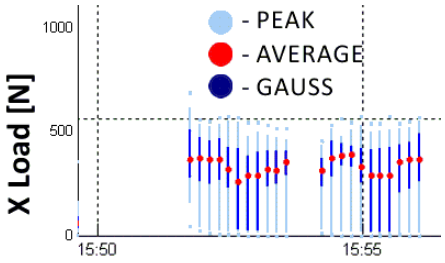

FIGURE 9: Tool side load during rough machining with a worn tool by recording and comparing the axis current [5]

The load limit of the spindle was measured to be approx. 650 N. Considering an overhang of 85 mm from the spindle nose to the tool tip the failure load matched the previous static measurements of 900 N. The form accuracy and surface finish after finish machining also matched the values taken with the standard spindle model.

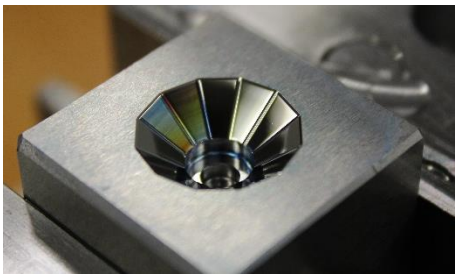

FIGURE 10: Finish machined reflector mold [5] to verify accuracy and error-motion
With increased

OFF-THE SHELF COMPRESSOR SOLUTIONS AND HIGH-PRESSURE REGULATIONS FOR MACHINE TOOLS

For aerostatic bearings, the behavior of the load capacity with bearing supply pressure is not linear and degressive. Also, the higher the supply pressure the more the spindle designer needs to take care of thermal effects caused by air expansion and condensation. The supply pressure thus needs to be as high as necessary, but as low as possible to reduce the air flow and thermal effects.
Government regulations in some Asian countries set the threshold between low and mid pressure for gases to 50 bar. Above this pressure particular measures for health and safety are mandatory.
Although an air pressure of 40-60 bar appears to be high, there are off-the shelf compressor solutions available that also match the air consumption of the spindle. For example, air compressors

for breathing air fill a main tank of 50-80 l with 350 bar and are used to fill scuba tanks.

FIGURE 11: Bauer I12 F02 Verticus 3 – Breathing air compressor [6]

Fully loaded it can supply an aerostatic spindle with 50 bar air pressure for about 30 minutes. After reaching a pressure threshold the compressor starts to re-load the main tank again.

IMPROVED CNC TOOL-SPINDLE STANDARDS [3]

Key features like an automated and monitored tool change, spindle liquid cooling, coolant through shaft and shaft vector control are industry standard for CNC tool spindles and are also features of the new development. To use the new spindle at speed of up to 60.000 rpm an HSK-E40 tool clamping system had to be developed to overcome issues of inconsistent balancing and shaft dynamics with state of the art HSK clamping systems.

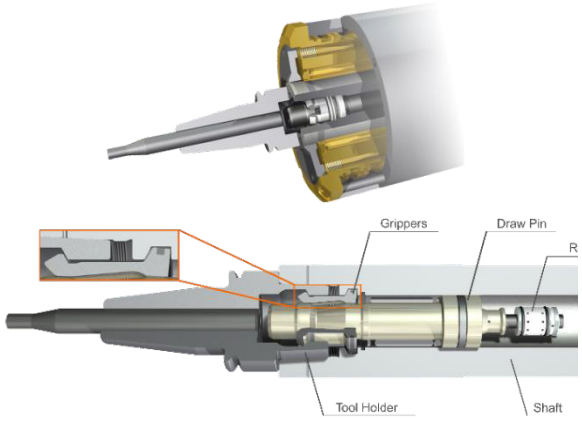

FIGURE 12: Patented spring-less HSK-E40 tool clamping system [3]

This new spring-less tool clamping system is self-locking, includes only 2 movable parts and thus allows 50% more spindle speed than any other HSK-E40 tool spindle. Its compact design and the drastically reduced numbers of parts also improves the shaft dynamics significantly and is furthermore maintenance-free. An aerostatic rotary feedthrough which allows flood cooling, spray mist, air or even vacuum to be guided to the tool tip was developed and integrated into the tool clamping system.

Furthermore, the patented bearing technology [2] allows the integration of a very efficient thin-film liquid cooling. Along with its huge cooling area, the high coolant velocity reduces the spindle soak time to under 5 minutes and the thermal shaft growth to values better 5 microns. Since this cooling surrounds any heat source within the spindle like a curtain the spindle remains thermally neutral against the machine it is installed in.

High chip load mostly occurs at rough machining with large tools. For finish machining often small tools at small cutting depths are used. For idling or finish machining with small tools the spindle can be operated at 10 bar air supply pressure to lower the air consumption even further.

SUMMARY

The new high-pressure aerostatic bearing system combines the load capacity of an oil-hydrostatic bearing system with the speed capability, accuracy and energy consumption of an aerostatic bearing system. A new developed process for the creation of very small bearing orifices not only reduced the air consumption by 65 %, but lead also to increased load capacity and stiffness values at large shaft eccentricity.

Pre-tests and cutting trials with a modified aerostatic tool spindle showed that existing spindle can be modified to give a significantly higher load capacity and thus robustness if a higher bearing supply pressure is used.

FIGURE 13: Levicron's UASD-H40 [3] - True full range CNC tool spindle featuring an HSK-E40 tool interface and high-pressure aerostatic bearing system

The new spindle development [3] features a high-pressure aerostatic bearing system as well as improved standards for CNC machining spindles and represents the first true full-range CNC tool

spindle with automated HSK-E40 tool clamping capable of rough machining steel as well as high-speed ultra-precision machining of optical components.

TABLE 1: Comparison of UASD-H40 spindle development with industry standard HSK-E40 roller bearing spindle

Feature / Units	Industry Standard	UASD060H40
Tool Interface [-/-]	HSK-E40	HSK-E40
Spindle Diameter [mm]	120	120
Max. Speed [rpm]	42.000	60.000
*) Radial Stiffness, concentric Shaft [N/µm]	100 - 200	120
*) Radial Stiffness, 80% shaft eccentric. [N/µm]	n.a.	400
*) Radial load capacity [N]	max. 4.000	max. 3.500
*) Axial load capacity [N]	max. 3.000	max. 5.000
Thermal Shaft Growth [µm]	20 – 50	< 5
Maintenance interval [h]	4.000 – 8.000	∞
Wear-free [-/-]	No	Yes
Max. speed cont. operation	No	Yes
Motor Torque [Nm]	3 – 5	4, continuous
Max. Shaft Power S1 [kW]	8 – 12	11
IKZ pressure, absol. [bar]	1 – 60	0 – 60
Air consumption [Nl/min]	100	250

REFERENCES

[1] J W Powell J W. The design of aerostatic bearings. The Machinery Publishing Co. Ltd. 1970

[2] United States Patent 2014 Gas Bearing and Method of Manufacturing the same US 8,882,353 B2

[3] Levicron GmbH, Germany. http://levicron.com/produkte?lang=en. 2017

[4] Uddeholms AB, Sweden. ELMAX Superclean

[5] Röders GmbH, Germany. Machining trials for Levicron GmbH. 2017

[6] BAUER COMP Holding GmbH, Germany. K Compressor products. 2016

CURRENT USE AND POTENTIAL OF ADDITIVE MANUFACTURING FOR OPTICAL APPLICATIONS

Matthew Brunelle, Ian Ferralli, Rebecca Whitsitt, Kate Medicus
Optimax Systems, Inc.
Ontario, NY, USA

INTRODUCTION

Additive manufacturing has gained popularity in many industries due to its ability to create complex shapes without adding significant cost. This can be leveraged for use in optical applications. Novel designs for part blocking, slurry containment, tooling housings, and fixturing for measurement can be easily realized through additive manufacturing. Examples of these types of components will be shown and discussed. The potential of, and challenges associated with, additively manufacturing optical components for reflecting applications is also discussed.

Background

Additive manufacturing (AM) is used and seen at Optimax in a variety of ways and in many forms. The most widely used process, both at Optimax and across industries, is fused filament fabrication (FFF) [1]. FFF uses a heated nozzle to deposit a stream of softened thermoplastic in a "2-dimensional" layer onto a platform, as seen in Figure 1. The platform is then lowered by the layer thickness, usually 50 μm to 1.75 mm, and the next layer is printed onto it. Printing continues in this layerwise fashion until a finished 3-dimensional part is produced. The concept of lowering, or raising, a platform and depositing a material layer is very common in AM technologies and is used by all the techniques included in this paper.

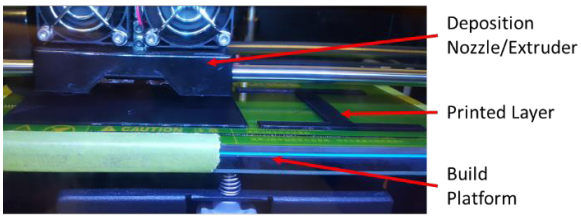

FIGURE 1. FFF printer depositing the second build layer of a part.

Stereolithography (SLA) is the other AM technique available at Optimax. SLA partially, or fully, submerges the build platform in a photoactive resin and uses UV light to selectively cure the layer. The layer thickness used in SLA is generally smaller than FFF, on the order of 5-100 μm, providing better vertical resolution. The source of the UV light varies from machine to machine and as the technology has developed, manufacturers have moved from UV projection to UV laser scanning, which provides higher resolution and reduces the time it takes to cure one layer of material. Different material options are available, but SLA parts are generally thermoset polymers.

Optimax has also seen several parts manufactured using powder bed fusion processes, such as selective laser sintering (SLS) and selective laser melting (SLM). These technologies use fine, on the order of 10-100 μm diameter, powders as feed stock. This powder is spread in thin, approximately 10-100 μm thick, layers using a blade or roller system and then fused together. SLS and SLM both use a focused laser to either fuse together (SLS) or fully melt (SLM) the powder in a layerwise fashion. SLM is used to create prototype and functional metal components and SLS can be used to produce parts of nearly any material; metal, plastic, ceramic, and glass components have been made using direct or indirect SLS [2].

All of the processes mentioned above require support structure to build complex geometries like undercuts and overhangs. An example of support structure are shown in Figure 2.

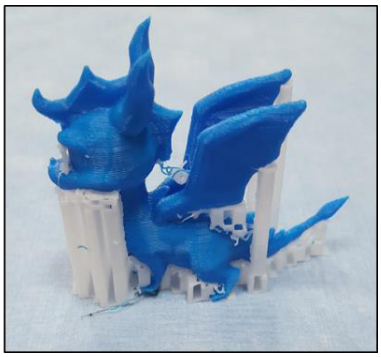

FIGURE 2. A finished FFF printed part (blue) with support structure (white) attached.

The material used to create support structure varies depending on the process. FFF is unique, in that it can build support structure from a material other than the material used for the desired geometry. This is done by adding a second extruder head onto the existing platform which deposits a second material. The secondary (or supporting) material is often designed so that it can be chemically removed from the desired part, simplifying the post-processing. SLA, SLS, and SLM cannot utilize more than one material at a time, necessitating mechanical removal of the support structure. Mechanically removing the support can be time consuming, complicated, and parts must be designed with support structure removal in mind or risk building a non-functional part. An example part with poorly planned support structure is shown in Figure 3.

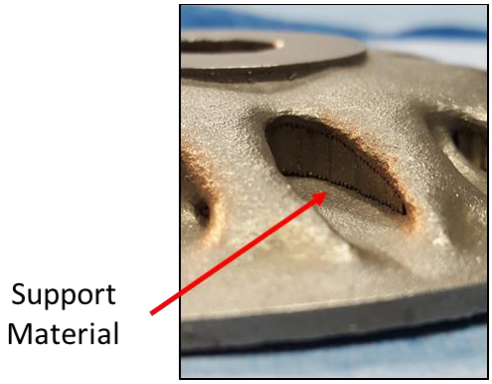

FIGURE 3. SLM printed component with irremovable support structure.

Several AM technologies can be used to create ceramic green bodies, which must be debinded and sintered to produce functional components. Both SLA and SLS are used for this purpose by heavily doping a polymer feedstock with ceramic particles. The polymer is cured or fused together depending on the process, trapping the ceramic particles in place and creating a green body. When SLS is used in this fashion it is known as “indirect SLS”. The part is then debinded to remove the polymer component and sintered to create a nearly-fully-dense high-purity ceramic component; densities reaching 99.6% of theoretical density have been reported [3]. It is important to note that green bodies shrink 25-50% during the debinding and sintering steps, this shrinkage must be accounted for in the design of the component.

POLYMER PRINTING AT OPTIMAX

FFF and SLA are the two AM technologies available in-house at Optimax. Both are capable of printing plastic components and they are utilized by almost every area at Optimax for a variety of purposes. One prime example for AM components is slurry containment.

FFF is capable of producing watertight vessels which are often used for custom polishing applications. SLA can also be used to create watertight vessels, but FFF is preferred due to the relatively low cost of producing parts. This enables more efficient use of expensive polishing slurry and prevents slurry contamination by allowing custom vessels to be sealed and stored for later use. These vessels can be printed in different colors as well, so they are easily organized by abrasive size, job number, or department. An example containment vessel is shown in Figure 4, this slurry dam is used to streamline the manufacturing process of the part by reducing the number of machines needed to finish certain features of the optic. The dam is removed during grinding and step features are ground into the optic blank using a bound abrasive tool. Once generated, the slurry dam is attached and filled with polishing slurry and a traditional optical lap is used to finish the step features using the slurry available in the container. Both operations are done in the same machine and the finished part and slurry are then removed without contaminating the machine.

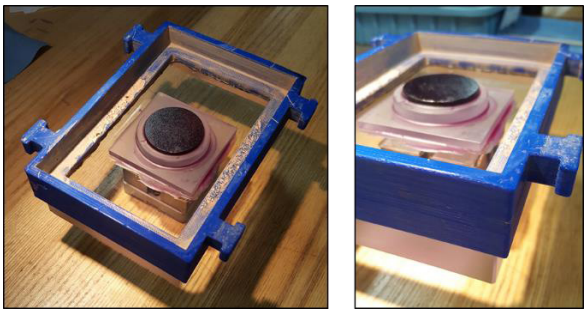

FIGURE 4. FFF printed slurry dam (blue) used for slurry containment during polishing.

Custom tooling housings are also made using FFF. These housings protect sensitive alignment and locating features from abrasive slurry which would otherwise corrode the interfacing surfaces. Figure 5 shows an example housing used to protect the mounting features which connect the polishing spindle to the end effector of a robotic polishing platform.

FIGURE 5. FFF printed tooling housing (white) covering interfacing surfaces.

The manufacturing flexibility of AM also allows complex secondary features to be added to the design without added manufacturing cost. The housing shown above includes mounting points that slurry lines nest into, ensuring slurry is delivered exactly where it is needed. These features would be non-trivial and expensive to manufacture using traditional methods, but can be included in the design of the AM part for the minimal cost of the extra material.

The dimensional accuracy of parts made using FFF is generally lower than that of SLA. For this reason, SLA is used when tighter tolerances are necessary. SLA also provides added flexibility in material choice; transparent, flexible, castable, and high temperature resistant resins are available for specialized applications [4]. High temperature resistant resins can be used to quickly manufacture custom blocking bodies for components that would otherwise be difficult to hold. An example blocking body is shown in Figure 6, which was printed using a high temperature resistant resin to allow the part to be blocked using stacking wax or pitch. The blocking body was designed to allow clearance for the backing structure on the metal part that can also be seen in the figure.

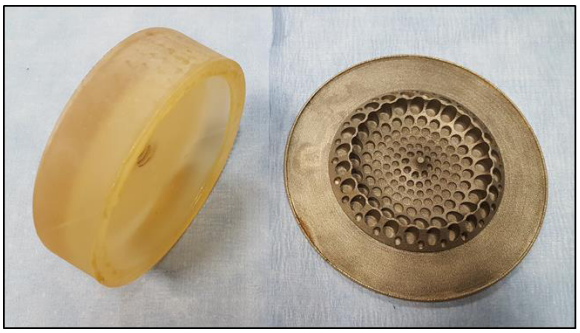

FIGURE 6. SLA printed blocking body (yellow) designed for an SLM printed mirror.

Traditional optical shapes like spheres, prisms, cylinders, and aspheres have well established blocking procedures and tooling which are not applicable to extreme freeform geometries. Freeform optics often prove challenging to hold securely during processing and measurement, several pieces of metrology equipment are also limited in the area or angle-from-horizontal that they can measure. AM is used for these parts to create custom metrology fixtures cost-effectively. SLA-produced fixtures are dimensionally accurate enough that they often do not require any post processing to securely interface with freeform surfaces. The polymer materials used are also soft enough that the potential for damage to the optical surface is minimal. The multi-surface monolithic freeform optic shown in Figure 7 rests on two polished optical surfaces so that a third surface can be measured on the ultra-accurate 3D profilometer. This piece of equipment requires that the surface under test is less than 45 degrees from horizontal and provides the most consistent data when the surface is nearly horizontal. The fixture shown in the figure was created at Optimax using SLA.

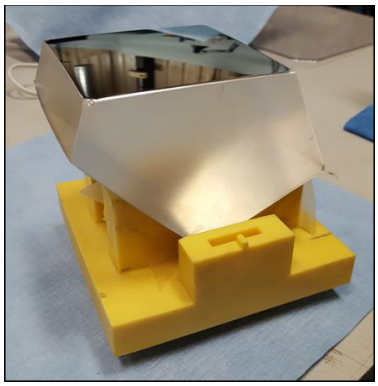

FIGURE 7. SLA printed metrology fixture (yellow) holding a freeform monolithic telescope optic.

SLA and FFF are often used to create physical models for complex components. The ability to hold a component during the quotation or design phase has proven invaluable, providing clarity to optical drawings which can often be confusing. The multi-surface monolithic freeform mentioned above was printed using FFF during the design phase with surface labels added into the print. This ensured that consistent terminology was used by all parties during manufacturing process planning meetings.

Physical models also streamline the metrology process by providing setup parts for the creation of coordinate measuring machine (CMM) programs. Previously, CMM programs were written when the first serial number was completed, slowing the manufacturing process by creating a bottleneck at the metrology step and putting the finished parts at risk. In many cases, SLA printed parts are dimensionally accurate enough to use as setup parts; allowing ample time to write and test CMM programs without risking damage to finished components. An example of an SLA printed part being used in this manner is shown in Figure 8.

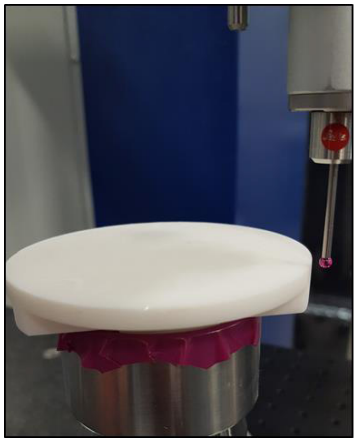

FIGURE 8. SLA printed model (white) being used to write and test CMM programs.

METAL OPTICS

Recently, Optimax has begun researching the feasibility of producing metal reflecting optics through SLM. These optics are typically produced through CNC machining and finished with diamond turning. This method of production is very conducive to the manufacture of extreme freeform geometries, but are mainly used in IR applications due to the mid-spatial frequencies and roughness induced into the optical surface by the diamond turning process. An additional smoothing step using magnetorheological finishing, traditional polishing, or sub-aperture polishing is necessary if turned mirrors are to be used for applications at wavelengths lower than the IR. Processing using diamond turning also limits the material options available due to unpaired d-shell electron interactions at the cutting interface [5]. Many materials that cannot be diamond turned can be manufactured using SLM, an optically relevant example is FeNi36, also known as “Invar-36”. FeNi36 is an iron-nickel alloy with a near-zero coefficient of thermal expansion, making it desirable for cryogenic and space applications. An example FeNi36 optic made using SLM is shown in Figure 9.

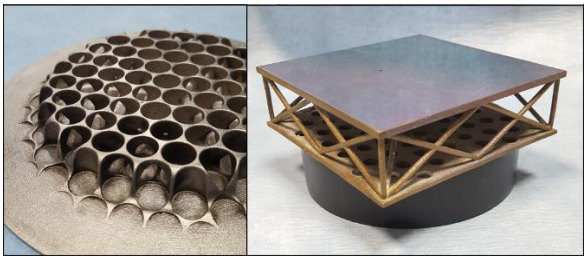

FIGURE 9. SLM printed mirrors with lightweight backing structures. (Left) FeNi36 spherical mirror. (Right) Steel plano mirror.

Due to the layerwise manufacturing method utilized by SLM, complex geometries like freeform surfaces and lightweight backing structures can be produced. Opening the design space for lightweight mirrors to include geometries that are impossible to manufacture using traditional methods. Examples of lightweight mirror structures produced using AM are shown in Figure 9. Internal features like cooling channels can also be printed for high energy applications where thermal distortion is a concern.

Another advantage of AM is the ability to produce monolithic optical structures, simplifying the optomechanical design. Features like kinematic mounts, baffles, and mounting features for actuators can be included in the design of the backing structure.

The primary drawback of using SLM manufactured mirrors is indicative of many AM processes, they cannot produce fully dense materials. Relative densities of nearly 100% are possible in materials with well-established SLM processes [6-9], but all components manufactured through AM and polished at Optimax have exhibited voids on the finished optical surface. Voids in SLM manufactured parts are caused by many factors including: material

impurities, uneven powder packing density, laser power fluctuations, and spatter and evaporation of the metal in the melt pool. These factors are very difficult or impossible to control. Examples of voids found in SLM printed parts are shown in Figure 10.

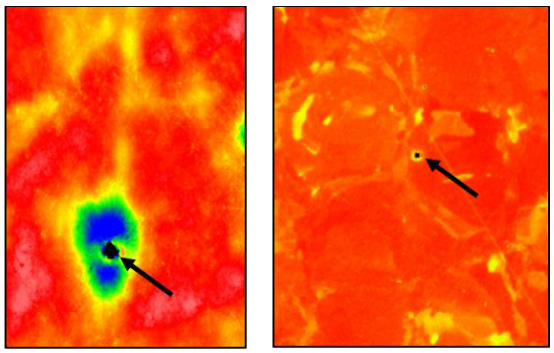

FIGURE 10. Micrographs of voids seen in SLM produced parts, measured with scanning white light interferometer.

Voids on an optical surface cause scatter, reducing the efficacy of the optical system and may be sources of stress in high energy applications. Surface defects can be mitigated by adding a cladding layer. One method of applying cladding is electroplating. Electroplated material is generally free of voids and can be polished to an acceptable surface roughness for imaging applications.

Several other concerns about the utilization of SLM manufactured metal optics should also be noted. Weight and areal density are generally higher with metal components than glass or ceramic, this fact discourages the use of metal mirrors in space or high altitude applications where weight is a major concern. Well-designed lightweight backing structures can help to mitigate these effects. Another concern is the temporal stability of the printed material; since the part is locally heated throughout the manufacturing process, finished parts often have internal stresses. These stresses can bring the long-term dimensional stability of the finished optics into question. Annealing processes can be used to reduce these stresses.

CERAMIC OPTICS

High performance optical ceramics like spinel, AlON, magnesium fluoride, calcium fluoride, zinc sulfide, and zinc selenide are used for optical applications which require non-standard material properties. Many of these materials are desirable due to their transmission band, abrasion resistance, and/or strength; making them especially applicable for manufacturing infrared domes and windows. There is a push to design and manufacture large extreme freeform components from these materials. Acquiring these materials in the sizes needed for large freeform shapes is very challenging and lead times would be significantly improved if processes were developed for additively manufacturing these materials to an optical quality.

Several technologies exist to additively manufacture ceramic components, including ceramic SLA and indirect SLS. These techniques involve post-print thermal processing to create a functional component. Fully dense, optically transparent materials have not been demonstrated using these techniques, so current applications are limited to optomechanical components and mirror substrates. Polished surfaces of ceramics produced through SLA or indirect SLS can also exhibit voids, similar to AM metal components, as shown in Figure 11. Further research is needed to determine the feasibility of using a cladding layer to fill the surface defects and reduce the potential of scattering.

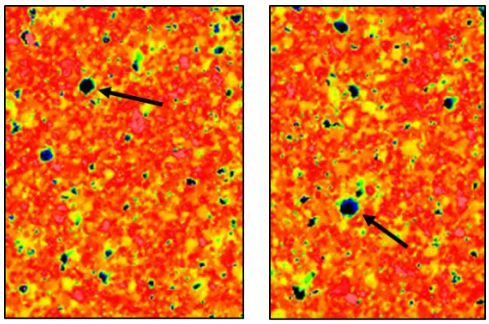

FIGURE 11. Micrographs of voids in ceramic SLA produced Al2O3 parts, measured with scanning white light interferometer.

Direct ink writing (DIW) is another AM technique capable of printing ceramic and glass materials. DIW uses an extrusion nozzle similar to FFF, but deposits a ceramic or glass particle filled paste which is then thermally processed into a fully dense component. This method of manufacture was recently used at Lawrence Livermore National Laboratory to produce optically transparent fused silica glass [10]. This technology is still in the development stage.

CONCLUSIONS

The flexibility and relatively lost cost of producing polymer parts with FFF and SLA has benefitted Optimax. Quickly creating measurement fixtures, blocking bodies, and slurry dams has allowed several manufacturing and metrology steps to be streamlined. Slurry containment vessels and tooling housings have been printed and used to protect sensitive and expensive kinematic systems from corrosion. Using labelled physical models for process planning has reduced confusion and the likelihood of errors. CMM programs can be written without a finished part, preventing damage to the optical components and reducing the time it takes to measure finished parts. AM of functional optical components is in its infancy, but has the potential to open the design space by providing near-net shaped extreme freeform geometries, lightweight and functional backing structures, and internal cooling channels. Further research is needed to realize the full potential of optics made through AM.

ACKNOWLEDGEMENTS

Some of the work shown was completed with SBIR/STTR grant funding from NASA under contract numbers NNX15CM29P and NNX15CG20P, and from The MDA under contract number HQ0147-16-C-7804.

REFERENCES

[1] Palermo E. Fused Deposition Modeling: Most Common 3D Printing Method. LiveScience [Internet]. 2013 Sept [cited 2017 Aug 8]. www.livescience.com/39810-fused-deposition-modeling.html

[2] Brandt M. Laser Additive Manufacturing: Materials, Design, Technologies, and Applications. Cambridge: Woodhead; 2016. p. 163-176.

[3] Lithoz GmbH. Additive Manufacturing Systems for Ceramics. Lithoz.com [Internet]. 2017 [cited 2017 Aug 8]. http://www.lithoz.com/en/products/am-systems/#1481464943778-a2177c02-aa4a.

[4] Formlabs Inc. Add Materials. Formlabs.com [Internet]. 2017 [cited 2017 Aug 8]. https://formlabs.com/store/us/form-2/buy-materials/.

[5] Paul E, Evans C, Mangamelli A, McGlauflin M, Polvani R. Chemical aspects of tool wear in single point diamond turning. Precision Engineering. 1996;18.1:4-19.

[6] EOS GmbH – Electro Optical Systems. Material data sheet: EOS StainlessSteel GP1 for EOSINT M 270. EOS.com [Internet]. 2009 [cited 2017 Aug 8]. https://www.eos.info/material-m

[7] EOS GmbH – Electro Optical Systems. Material data sheet: EOS NickelAlloy HX. EOS.com [Internet]. 2015 [cited 2017 Aug 8]. https://www.eos.info/material-m

[8] EOS GmbH – Electro Optical Systems. Material data sheet: EOS MaragingSteel MS1. EOS.com [Internet]. 2014 [cited 2017 Aug 8]. https://www.eos.info/material-m

[9] EOS GmbH – Electro Optical Systems. Material data sheet: EOS CobaltChrome MP1. EOS.com [Internet]. 2011 [cited 2017 Aug 8]. https://www.eos.info/material-m

[10] Nguyen D, Meyers C, Yee T, Dudukovic N, Destino J, Zhu C, et al. 3D-Printed Transparent Glass. Advanced Materials. 2017 Jul 12;29.26: 1701181

Statistical Analysis of Surface Measurements and Images

Farzad Azimi, Benjamin Young, Brigid Mullany
Department of Mechanical Engineering and Engineering Science
University of North Carolina at Charlotte
Charlotte, North Carolina, USA

INTRODUCTION

The functionality and importance of surfaces has long since been a topic of great interest in the engineering world. Among other things, the topography of a surface affects the nature of the mechanical interaction between two surfaces [1-5] the dispersion and reflection of incident electromagnetic rays [6], and the nature of fluid interactions with the surface [7]. It can also provide insights on surface and subsurface integrity [6, 8]; traits known to impact the performance and longevity of surfaces under fluctuating mechanical, thermal, or chemical conditions [9]. Understanding the impact of the manufacturing process on the final surface finish, and hence part functionality, should result in higher quality components with increased commercial value. This has led to much research on how to best measure and characterize surfaces, with a goal of identifying metrics capable of linking manufacturing process performance to final part functionality. Analysis of the surface measurement data has evolved over time from simple statistical based parameters to more complex wavelet and fractal analysis. Excellent review papers detailing the evolution of surface metrology are as follows [10-13]. International standards have also been developed to provide guidelines on how to measure, and describe surfaces. The ISO 25178-2 focusses on methods of characterizing areal surface measurements [14]. The wide range of metrics available to quantify surfaces have been likened, on more than one occasion, to a 'parameter rash' [15]. Despite all the available metrics, there are still challenges facing manufacturers in linking process performance to robust surface metrics, and in detecting desired (e.g. specified topographies) and undesired surface features (e.g. scratches, dirt and dig/pits). Taking these gaps into consideration, and while being mindful of contributing to the parameter rash, this work outlines an alternative analysis method that enables the detection and quantification surface anomalies and characteristics using only surface height data.

METHODOLOGY

This new approach takes areal surface information, i.e. a 2.5D surface map or even an optical image, and instead of treating it as N×M data points and calculating single statistical based parameter values such as the ubiquitous *Sa*, *Sq*, *Ssk*, or *Sku* values, the data set is considered as series of profiles, i.e. each column is treated as a separate profile, and the statistical parameter of choice is calculated for each profile, i.e. *Ra*, *Rq*, *Rsk*, or *Rku*. The standard deviation, skewness, or kurtosis of the resulting parameter distribution can then be calculated. For demonstrating the approach, the standard deviation of the calculated *Rq* values will be used, i.e. σ_{Rq}. The same N×M data set is then rotated some number of degrees about its center, giving a new set of line profiles. The *Rq* values are recalculated, as is the corresponding σ_{Rq}. Finally, all the calculated σ_{Rq} values are plotted in a polar plot formation, i.e. σ_{Rq} versus rotational angle, θ. Figure 1 gives a visual depiction of the steps involved, and raises a few procedural points 1) the process works if the statistical parameter is calculated for each row instead of column. 2) The data set is cropped to ensure that the rectangle superimposed on the rotated data set contains only surface data. The size of the cropped data set is $N/\sqrt{2}$ where N is the smaller of N×M terms. 3) In this work, the dataset will be rotated a full 360° degrees in 1° intervals. 4) The resulting polar plot is rotationally symmetric; in reality only a rotation of 180° is required to capture all information.

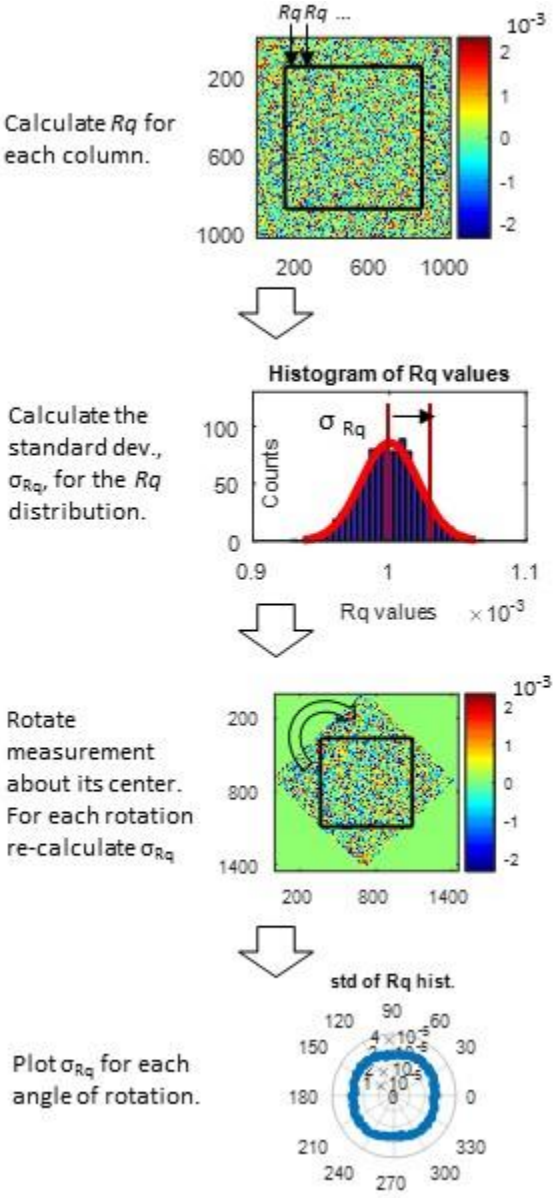
Rq Rq ...
Calculate Rq for each column.
Histogram of Rq values
Calculate the standard dev., σRq, for the Rq distribution.
Counts
σ Rq
Rq values
Rotate measurement about its center. For each rotation re-calculate σRq
std of Rq hist.
Plot σRq for each angle of rotation.

Figure 1. Ilustrate 4 different steps to achieve σ_{Rq} polar plot. Note: Arbitary scales depicted in the areal map. The generated image has a size of 1024×1024 pixels.

In figure 1 the surface measurement being processed is a theoretically perfect Gaussian surface map that was generated in MATLAB™ (mean, μ = 0, standard deviation, σ =0.001, skewness = 0 and kurtosis=3). As a result the standard deviation of the *Rq* histogram, σ_{Rq}, is independent of the rotational angle, giving a circular polar plot. Changing the standard deviation of the incoming surface, i.e. effectively the root mean square surface roughness value, *Sq*, will simply increase the diameter of the polar plot.

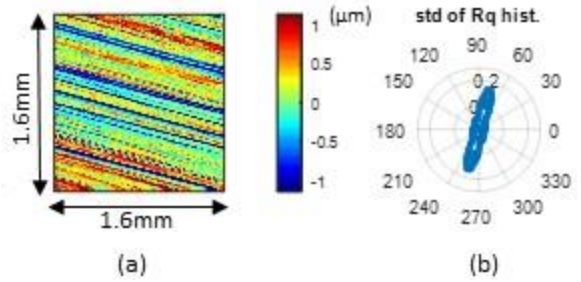

Figure 2. a) Ground surface as measured by a scanning white light interferometer (5×), b) σ_{Rq} polar plot.

Most machined surfaces tend not to be completely isotropic in nature whereby machine tool path marks are evident on the surface. While surface directionality can be detected using the ISO 25178-2 texture aspect ratio value, *Str*, [17], the proposed polar plots can capture both anisotropic surface characteristics and their orientation. Figure 2(a) depicts a ground surface, while figure 2(b) depicts the corresponding polar plot. Deviation from a circular polar plot, to one containing lobes indicates deviation from a perfectly Gaussian surface. Rotating the original measurement image in a clockwise direction by the same angle entrained between the apex of the lobe and 0° will result in the grinding marks being aligned in a vertical direction.

The polar plots can also capture surface features such as scratches and imperfections/digs that are not necessarily easy to isolate or characterize from conventionally used ISO 25178-2 height or hybrid parameters. Figure 3(a) depicts a theoretical Gaussian surface generated in MATLAB™ with a scratch on its surface. The scratch is nominally 200 pixels long and 5 pixels wide. The polar plot resulting from rotating this theoretical measurement through 360° is depicted in figure 3(b). The pointed lobe is generated by the presence of the scratch. The maximum standard deviation value obtained from of any of the 360 *Rq* histograms is recorded when the scratch aligns vertically, giving five columns, corresponding to the width of the scratch, with *Rq* values significantly larger than the columns not containing a scratch. This results in 5 bins in this *Rq* histogram that are far removed from the main distribution of the *Rq* values, increasing the standard deviation of this histogram, see figure 3(c) right. As the measurement is rotated so that the scratch is no longer vertical, the scratch spans more columns, thus the pixels associated

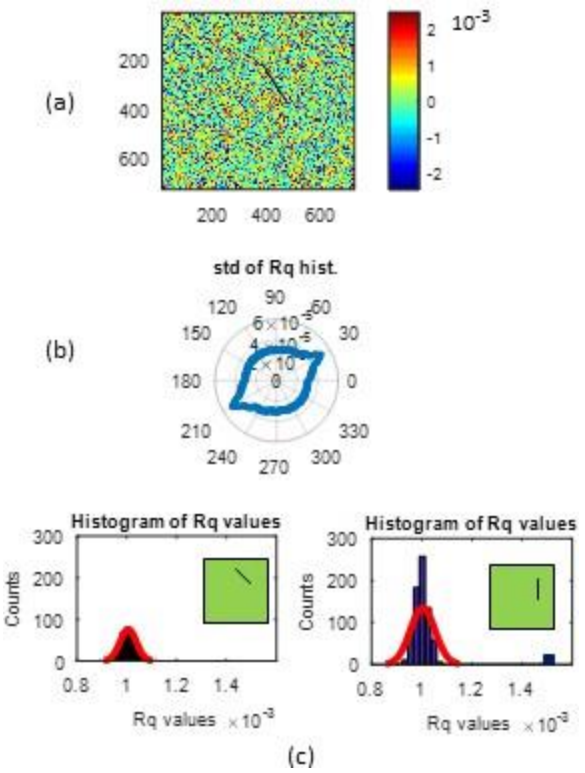

Figure 3. Theoretical Gaussian surface with a scratch, b) σ_{Rq} polar plot, c) left, histogram of Rq values at θ=0º; right, histogram of Rq values when scratch is vertical. Note: The generated image has a size of 1024×1024 pixels. The cropped version is illusrated here.

with it have less of an effect on the *Rq* values of these columns, thus reducing the spread to the *Rq* histogram, and hence its standard deviation, figure 3(c) left. Again, the angle entrained between the apex of the lobe and 0° gives an indication of the orientation of the scratch on the surface.

The polar plots do not provide insights on the location of the scratch. Multiple, non-parallel scratches will result in multiple spikes on the polar plot. The approach, as described here, is not capable of differentiating between multiple parallel scratches and one wide scratch. The ability of the method to detect scratches depends mostly on the length and depth of the scratch, and the number of columns in the measurement field of view. Deeper, longer scratches are obviously easier to detect. For detection of a shorter scratch, e.g. less than half the length of the field of view, the *Rq* of the column containing the scratch must be sufficiently large so that it lies outside the *Rq* distribution for a surface not containing a scratch. In the initial analysis, the *Rq*

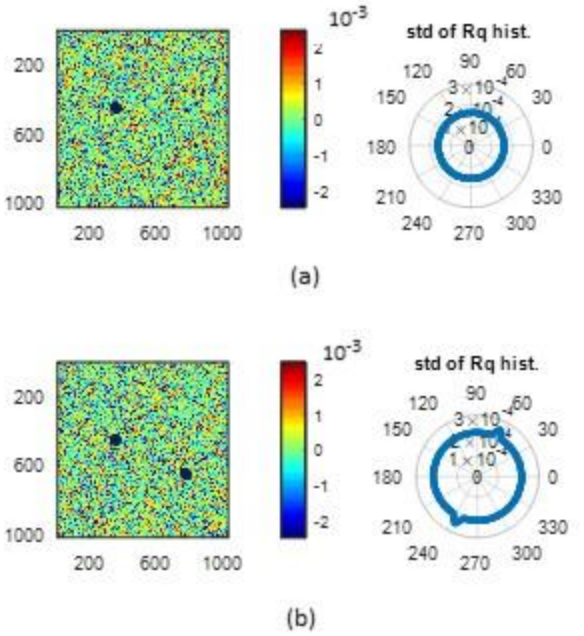

Figure 4. Gaussian surface with one circular defect, and its σ_{Rq} polar plot b) Gaussian surface with two circular defects and its σ_{Rq} polar plot. Note: The generated image has a size of 1024×1024 pixels.

of the column containing the scratch must be greater than $\mu_{R_q} + 3.2\sigma_{R_q}$ where μ_{Rq} is the average value of *Rq* distribution. The method has increased sensitivity if the 3rd and 4th moments of the *Rq* histogram are utilized i.e. the skewness and kurtosis, instead of the standard deviation.

Defects, such as a pit or dig on a surface, affect the polar plots in a different manner. A single, circular, imperfection on a Gaussian surface will simply increase the size of the radius of the σ_{Rq} polar plot. If there are two circular defects on the surface, the radius of the polar plot increases and a rounded lobe will appear at the angle of rotation where the two defects co-align and are contained within the same columns, see figure 4.

While all the data used to this point is either real or generated height map data, the technique can be applied to grayscale images too. Figure 5 depicts a polar plot generated from a grayscale, 5× optical microscope image of a lapped sample. The resulting polar plot detects the two lay directions of the lapped surface, i.e. at 26° and 137°.

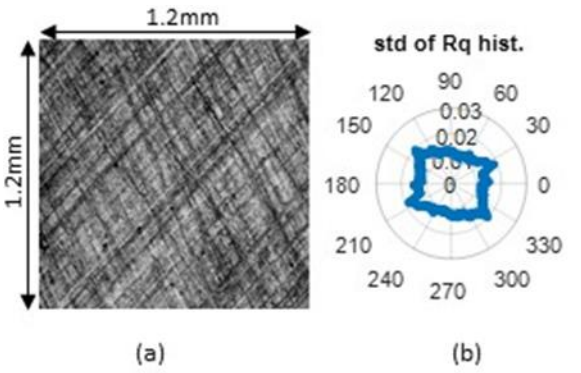

Figure 5. 5× optical microscope image of a lapped surface, b) Standard deviation of Rq histograms' polar plot.

CONCLUSION AND FUTURE WORK

This paper outlines the basic aspects of a new surface analysis method. By treating areal data as a series of profiles, spatial surface features, such as directionality and direction, can be quantified from simple height data or grayscale values. Both scratches and digs can be identified using this method. Work is ongoing to fully understand the sensitivity of the approach to scratch and dig sizes, and how to estimate the number and magnitude of the surface anomalies from the polar plots. The ability of the technique to quantify other spatial features, such as engineered, periodic, textured surfaces, is underway.

ACKNOWLEDGEMENTS

This research was supported by UNC Charlotte's Center for Precision Metrology and partially supported by NSF's IR/D program.

REFERENCES

[1] Archard, J. *Elastic deformation and the laws of friction*. in *Proceedings of the Royal Society of London A: Mathematical, Physical and Engineering Sciences*. 1957. The Royal Society.

[2] Archard, J., *Surface topography and tribology.* Tribology, 1974. **7**(5): p. 213-220.

[3] Greenwood, J. and J. Tripp, *The contact of two nominally flat rough surfaces.* Proceedings of the institution of mechanical engineers, 1970. **185**(1): p. 625-633.

[4] Onions, R. and J. Archard, *The contact of surfaces having a random structure.* Journal of Physics D: Applied Physics, 1973. **6**(3): p. 289.

[5] Whitehouse, D.J. and J. Archard. *The properties of random surfaces of significance in their contact*. in *Proceedings of the Royal Society of London A: Mathematical, Physical and Engineering Sciences*. 1970. The Royal Society.

[6] Bruzzone, A., et al., *Advances in engineered surfaces for functional performance.* CIRP Annals-Manufacturing Technology, 2008. **57**(2): p. 750-769.

[7] Bhushan, B., J.N. Israelachvili, and U. Landman, *Nanotribology: friction, wear and.* Nature, 1995. **374**: p. 13.

[8] Stout, K.J. and L. Blunt, *Three dimensional surface topography*. 2000: Elsevier.

[9] Nélias, D., et al., *Role of inclusions, surface roughness and operating conditions on rolling contact fatigue.* Journal of tribology, 1999. **121**(2): p. 240-251.

[10] Dong, W., P. Sullivan, and K. Stout, *Comprehensive study of parameters for characterizing three-dimensional surface topography I: Some inherent properties of parameter variation.* Wear, 1992. **159**(2): p. 161-171.

[11] Dong, W., P. Sullivan, and K. Stout, *Comprehensive study of parameters for characterizing three-dimensional surface topography II: Statistical properties of parameter variation.* Wear, 1993. **167**(1): p. 9-21.

[12] Dong, W., P. Sullivan, and K. Stout, *Comprehensive study of parameters for characterising three-dimensional surface topography: III: Parameters for characterising amplitude and some functional properties.* Wear, 1994. **178**(1-2): p. 29-43.

[13] Dong, W., P. Sullivan, and K. Stout, *Comprehensive study of parameters for characterizing 3-D surface topography IV: parameters for characterizing spatial and hybrid properties.* Wear, 1994. **178**.

[14] *ISO 25178-2:2012: Geometrical product specifications (GPS). Surface texture: Areal Part 2: Terms, definitions and surface texture parameters*. 2012: ISO.

[15] Whitehouse, D., *The parameter rash—is there a cure?* Wear, 1982. **83**(1): p. 75-78.

METROLOGY TECHNIQUES FOR EVALUATING AND ALIGNING DESI FOCAL PLATE STRUCTURE

Yutong Duan[1], Eric S. Buice[2], Todd M. Claybaugh[2], and Steven P. Ahlen[1]
[1]**Physics Department**
Boston University
Boston, MA, 02215 USA
[2]**Engineering Division**
Lawrence Berkeley National Laboratory
Berkeley, CA, 94720 USA

INTRODUCTION

The Dark Energy Spectroscopic Instrument (DESI) is the next-generation ground-based dark energy experiment to be installed on the 4-meter Mayall Telescope at the Kitt Peak National Observatory (KPNO) in Arizona. DESI will complement imaging surveys such as the Dark Energy Survey (DES) and the Large Synoptic Survey Telescope (LSST) in studying the evolution of dark energy and growth of large-scale structures in the expansion history of the universe. Arrays of robotic actuators and fibre-fed spectrographs are capable of collecting spectra from 5,000 targets simultaneously. Through the study of baryon acoustic oscillation (BAO) and redshift-space distortion (RSD), DESI will provide new constraints on models of dark energy, modified gravity, inflation, and the sum of neutrino mass. During a five-year survey, DESI will make a three-dimensional map of over 35 million galaxies, covering $14,000\,\mathrm{deg}^2$ of the sky and reaching to redshift $z \sim 3.5$.

A key component of DESI is the focal plate structure, mainly consisting of 10 petals, 10 guide/focus/alignment (GFA) cameras, 1 focal plate ring (FPR), 5,000 positioners, and 120 illuminated fiducials (Fig. 1). 5,000 robotically actuated positioners are arranged in a hexagonal pattern with a $10.4mm$ pitch, evenly distributed in ten pie-slice-shaped, identical petals. Each fibre can be positioned freely within the patrol disk of a positioner. Fiducials serve as fixed datums on the focal plate and help reduce optical distortion and improve accuracy of fibre positioning. Given the optical design of DESI[1], it is vital that the fibre tips point in the direction of the chief rays and that the patrol disks of the positioners maximally coincide with the aspherical focal surface, in order to ensure alignment of the optical fibres with galaxies and high photon throughput (the percentage of light along the chief ray captured by the fibre). These requirements mandate not only stringent tolerances on the focal plane parts, but also precise alignment in the integration of focal plate structure, posing great challenges for design, machining, and metrology.

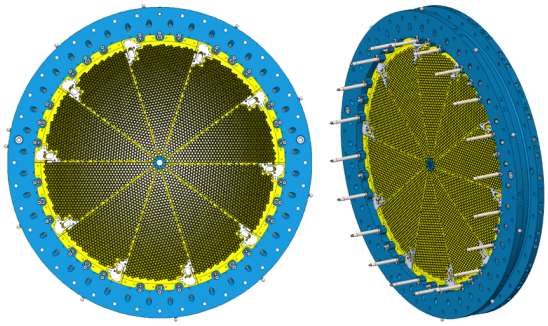

FIGURE 1. CAD model of DESI focal plate structure showing the appearance when ten petals and the focal plate ring (FPR) are integrated.

FIGURE 2. Close look at the petal hole details. The upper portion of each hole is a precision bore of height $h = 20.5\,\mathrm{mm}$; on top of each hole are threads and a precision spotface flat to $10\,\mu\mathrm{m}$.

In a petal, each of the 514 holes in which positioners and illuminated fiducials will be installed points in a unique chief ray direction, and constrains the orientation of the fibre positioner (Fig. 3 and 4). On the

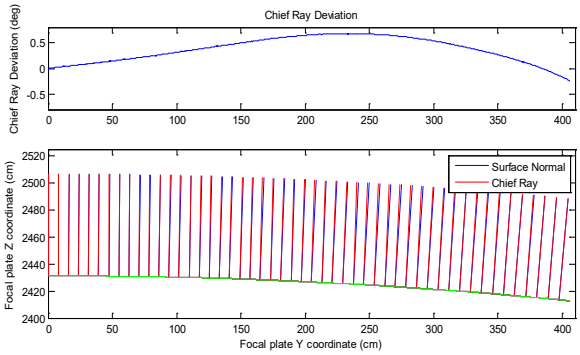

FIGURE 3. The chief ray directions, which the precision bores are slant drilled to match, are different from the surface normal of the petal.[1]

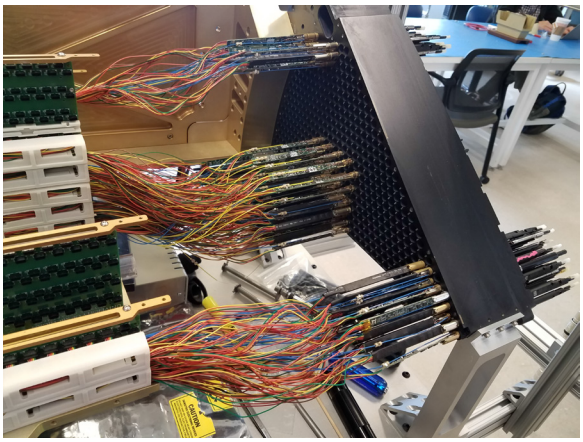

FIGURE 4. An engineering model petal. Direction of each positioner is constrained by the precision bore. Positioners extend out from the spotface by $86.5\mathrm{mm}$*, putting fibre tips at the aspherical focal surface.*

top of each hole is a critical spotface perpendicular to the cylinder axis on which the positioner bearing cartridge is situated, which rests the fibre tip (extends out by 86.5 mm from the spotface along the cylinder axis) into the depth of focus of corrector optics (Fig. 2). The quality of a petal is evaluated in terms of not only the specifications, but more importantly, its science performance.

As of August 2017, eight production petals have been machined and anodised, among which five have been test-fitted in the FPR. With petal production approaching completion at Boston University and integration and alignment efforts currently underway at Berkeley Lab, this paper outlines the metrology process, analysis of metrology data, usage of metrology data in the petal-ring integration and alignment, and preliminary results for the first five official DESI petals.

METHODS

All petals were machined at Scientific Instrument Facility at Boston University and coated by Plating For Electronics, Waltham, MA with organic black anodising to reduce reflection of stray photons from un-targeted galaxies. The spherical top surface of petals above the spotfaces was sandblasted to reduce reflection of light. BU contracted with Dial Machine in Rockford, IL to machine the FPR and coat it with inorganic black anodising. Petal metrology was performed at Zeiss Industrial Metrology in Marlborough, MA on a Contura CMM. The description of CMM programming below incorporates certain improvements which were found to be indispensable and implemented during the testing of the programme.

Petal Metrology

Each precision bore was measured by the probe scanning along two circular paths at the top and the bottom of the bore. Three iterations of three-sigma clipping filter were applied before the cylinder fit, as it was found that 0.3 mm ruby styli were very sensitive to any burr or anodising fragment inside bores. The cylinder fit yields average diameter of the bore and its axial direction. The CMM then looked for the critical spotface relative to the corresponding cylinder already found beneath it, and took a circular path on the flat surface which defines the plane. This guarantees the probe almost always completes a perfect circular path without running off the plane into the hole or touching the top sandblasted surface above the spotface. The spotface centre was the intersection between the cylinder axis and the spotface plane. A single run of the CMM programme takes less than 20 hours. Each cylinder axis is specified by nutation and precession angles (θ, φ), which are the ordinary spherical polar and azimuthal angles. Calypso expresses the direction of cylinder axis $\hat{n}$ as two projection angles onto $XZ-$ and $YZ-$plane,

$$A_1 = \tan^{-1} \frac{x}{z} \tag{1}$$

$$A_2 = \tan^{-1} \frac{y}{z} \tag{2}$$

where x, y, z are components of the axial unit vector $\hat{n}$, i.e. $x = \hat{n} \cdot \hat{i}, y = \hat{n} \cdot \hat{j}, z = \hat{n} \cdot \hat{k}$, and $\hat{n}$ is the measured, actual direction of axis. The actual nutation and precession angles (θ, φ) can then be calculated from (A_1, A_2) using their definitions,

$$\theta = \tan^{-1} \frac{\sqrt{x^2 + y^2}}{z} = \tan^{-1} \sqrt{\tan^2 A_1 + \tan^2 A_2} \tag{3}$$

$$\varphi = \tan^{-1} \frac{y}{x} = \tan^{-1} \frac{\tan A_2}{\tan A_1}. \tag{4}$$

Several hand checks were in place for the bore diameter in addition to CMM measurements. A Mitutoyo 3-point holtest (bore gauge) calibrated with a precision gauge ring was used to manually measure the bore diameters on four of the production petals. Pin gauges and bearing cartridges (a precision positioner part) were also used to verify the diameter and the fit. To double check nutation angles, a creative technique was developed using a Mitutoyo optical comparator and a pin gauge of appropriate size sticking out of the hole. Projection of the pin gauge on the screen was measured to find the nutation angle to an accuracy of 0.02°. Three datum tooling balls made of silicon nitride were glued to petal widely apart with epoxy for establishing a fixed reference frame. These data help verify the machining quality of the petals, determine if they meet their specifications, and align the petals in the integration phase.

Comparing Coordinate Systems

The basic way of establishing a coordinate system (CS), or alignment, on a CMM is by providing three datums ABC in the drawing. However, for a part as complicated as the petal where over five hundred holes are closely packed all carrying fine features, a naïve ABC alignment would result in all positional and directional features being out of tolerance due to imperfect datums. In particular, datum A of the petal is flat to 10 µm but datums B and C are only specified to 100 µm because they do not mate with any other surface when integrated and are therefore not critical. In order to find a reasonable CS in which the metrology data become informative, Calypso performed a geometric best-fit alignment by fitting the data to 514 cylinders and 514 spotfaces. The best-fit alignment was in a peculiar convention which was difficult to decode and apply, making a necessary check to recover the transformation parameters in a standard convention and confirm the results. It was also important to independently seek alignments using other customised criteria and compare the resulting throughput, as it was unknown if the best-fit alignment also maximised throughput.

Scripts to recover the best-fit alignment and produce other alignments were written in Python 3.6 using Scipy.optimize module and the Sequential Least SQuares Programming (SLSQP) algorithm[2]. The transformation formalism used in the scripts is

$$r' = Rr + T = R_z(\gamma)R_y(\beta)R_x(\alpha)\begin{bmatrix}x\\y\\z\end{bmatrix} + \begin{bmatrix}T_x\\T_y\\T_z\end{bmatrix} \quad (5)$$

where R_x, R_y, R_z are 3×3 rotation matrices in the usual convention[3].

Evaluating Science Performance of Petals

The acceptability of petals depends on if they meet the requirements for their science performance. Throughput helps evaluate how well the petals actually perform in observation. Features directly impacting throughput were the diameters and axial directions of precision bores, and the positions of spotface centres. Tilt (combined angular error), defocus (focus error), and projected throughput loss for each hole were calculated from metrology data assuming ideal alignment. First, to calculate tilt, nutation and precession angles were converted to Cartesian unit vectors,

$$\hat{n}(\theta,\varphi) = \sin\theta\cos\varphi\hat{i} + \sin\theta\sin\varphi\hat{j} + \cos\theta\hat{k}, \quad (6)$$

which defines the actual and nominal cylinder axis as unit vectors,

$$\hat{n} \equiv \hat{n}(\theta,\varphi) \quad (7)$$

$$\hat{n}_0 \equiv \hat{n}(\theta_0,\varphi_0). \quad (8)$$

The tilt is then simply

$$\delta = \cos^{-1}(\hat{n}\cdot\hat{n}_0). \quad (9)$$

From a recent DESI fibre focal ratio degradation (FRD) study by Jelinsky[4], we extracted the dependence of throughput on tilt as a simple quadratic polynomial,

$$T_1(\delta) = -0.0133\cdot\delta^2 - 0.0175\cdot\delta + 1 \quad (10)$$

where the tilt δ must be in degrees. $T_1(\delta)$ gives negative throughput for very large tilt, and is limited to 0 as a lower bound. Second, to calculate defocus, note that the fibre tip is positioned at a distance of 86.5 mm from the spotface centre in the axial direction, according to the fibre positioner design. Let $\vec{x}$ and $\vec{x}_0$ be the actual and nominal spotface centres. Then the actual and nominal fibre tip positions are

$$\vec{r} = \vec{x} + 86.5\cdot\hat{n} \quad (11)$$

$$\vec{r}_0 = \vec{x}_0 + 86.5\cdot\hat{n}_0 \quad (12)$$

Defocus is the absolute offset of fibre tip along the chief-ray direction,

$$\delta f = |\delta\vec{r}\cdot\hat{n}_0| = |(\vec{r}-\vec{r}_0)\cdot\hat{n}_0| \quad (13)$$

The impact of defocus on throughput was previously studied by Besuner and Sholl at Berkeley Lab[5]. The throughput as a normalised function of defocus can be modelled by a 5th-order polynomial,

$$T_2(\delta f) = -1.804\cdot10^{-14}\cdot\delta f^5 + 1.593\cdot10^{-11}\cdot\delta f^4 - 5.955\cdot10^{-10}\cdot\delta f^3 - 3.433\cdot10^{-6}\cdot\delta f^2 + 3.251\cdot10^{-7}\cdot\delta f + 1 \quad (14)$$

where δf must be in unit of microns. $T_2(\delta f)$ also gives negative throughput for very large defocus, and is limited to 0 as a lower bound. Finally, the total throughput is naturally the product

$$T(\delta, \delta f) = T_1(\delta) T_2(\delta f) \tag{15}$$

and it is easier to read and think of throughput loss, $1 - T(\delta, \delta f)$ which is the quantity plotted in our analysis.

Petal-Ring Integration and Alignment

The FPR was integrated with five production petals on a Zeiss Accura CMM with Calypso at Berkeley Lab. The FPR was measured without any petals installed to avoid distorting the ring, which served as the baseline for later measurements with petals installed. A new focal plane coordinate system, denoted CS5, was generated for each measurement performed. Ten mounting locations in the ring are numbered by integers from 0 to 9, and the first petal was installed at location 0. A study of torque effects was carried out with three petals, where M8 screws were torqued to 19 N m or 28.5 N m. Datasets were taken to check the reproducibility of alignment with the configuration held constant. After two other petals were added to locations 3 and 7, FPR deformation was further examined by quantifying flatness of FPR datum A, concentricity of FPR datum B, and shift of datum tooling balls around the ring. After five petals were mounted at locations $\{0, 2, 4, 6, 8\}$ with a centre ring cap that joins the tips of the petals (Fig. 5), we went through several configurations and measured the datum tooling balls, from which the actual position, orientation, and throughput of the petal were evaluated. Based on the petal-ring geometry, the Python script inferred possible outcomes with the one-degree-of-freedom rotation and recommended an optimal rotation which would maximise throughput. Adjustments were made accordingly to mounting hardware accessories. After three iterations of trial, adjustment, and verification, we arrived at a configuration that gave the best throughput to date and not far from the theoretically optimal alignments.

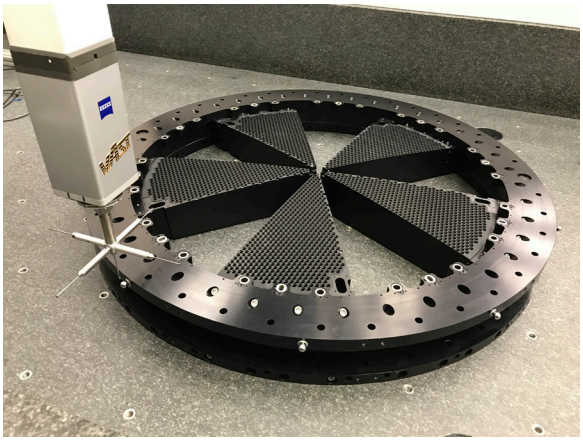

FIGURE 5. Integration of FPR and five petals. The CMM only need measure various datums to check alignments, without having to touch any petal hole.

PRELIMINARY RESULTS AND DISCUSSION

Table 1 summarises metrology results for the first six production petals, including the average throughput evaluated from tilt and defocus calculations. Fig. 6 shows plots for the most important two, spotface centre z and nutation angle, to which the throughput is most sensitive, in a heatmap and as a function of radius $r \equiv x^2 + y^2$. The z-deviation plot always concaves up, because clamping and drilling exerted great stress on soft aluminium, resulting in a curved petal when the stress is relieved. Nutation angle sees larger deviations near the centre (small r), most likely due to measurement errors, since $\theta \in [0.25°, 5.88°]$ across the petal and decreases toward the centre where chief-rays are almost parallel to the optical axis at $\theta = 90°$, and measurement errors start to dominate for θ close to zero. With few holes' nutation angles out of tolerance, the petals showed excellent

TABLE 1. Metrology statistics for the first six production petals in the best-fit alignment. Data columns are mean δ deviations from nominal diameter, spotface centre x, y, z, nutation, and precession, and throughput loss. Parentheses represent plus-minus tolerances or 1-sigma uncertainties (RMS errors).

PTL	$\delta D/\mu\mathrm{m}(^{+18}_{+08})$	$\delta x/\mu\mathrm{m}(15)$	$\delta y/\mu\mathrm{m}(15)$	$\delta z/\mu\mathrm{m}(15)$	$\delta\theta/°(0.03)$	$\delta\varphi/°(0.03)$	$(1-\eta)/\%(0.0^{+0.5}_{0.0})$
00	10.7(18)	0.4(116)	−3.8(72)	0.2(111)	−0.002(25)	−0.339(384)	0.08(11)
01	11.4(13)	−9.3(66)	−0.7(137)	0.3(83)	−0.033(13)	0.167(321)	0.09(18)
02	11.2(31)	−7.3(155)	−0.2(120)	0.7(117)	−0.028(35)	0.029(478)	0.12(24)
03	3.2(9)	−4.8(60)	−3.6(123)	0.4(88)	−0.021(12)	−0.161(236)	0.07(6)
04	6.2(24)	−11.0(100)	−1.9(181)	0.9(105)	−0.043(25)	0.056(714)	0.13(8)
05	6.7(7)	−2.7(119)	−4.0(85)	0.2(103)	−0.014(11)	−0.230(343)	0.07(7)

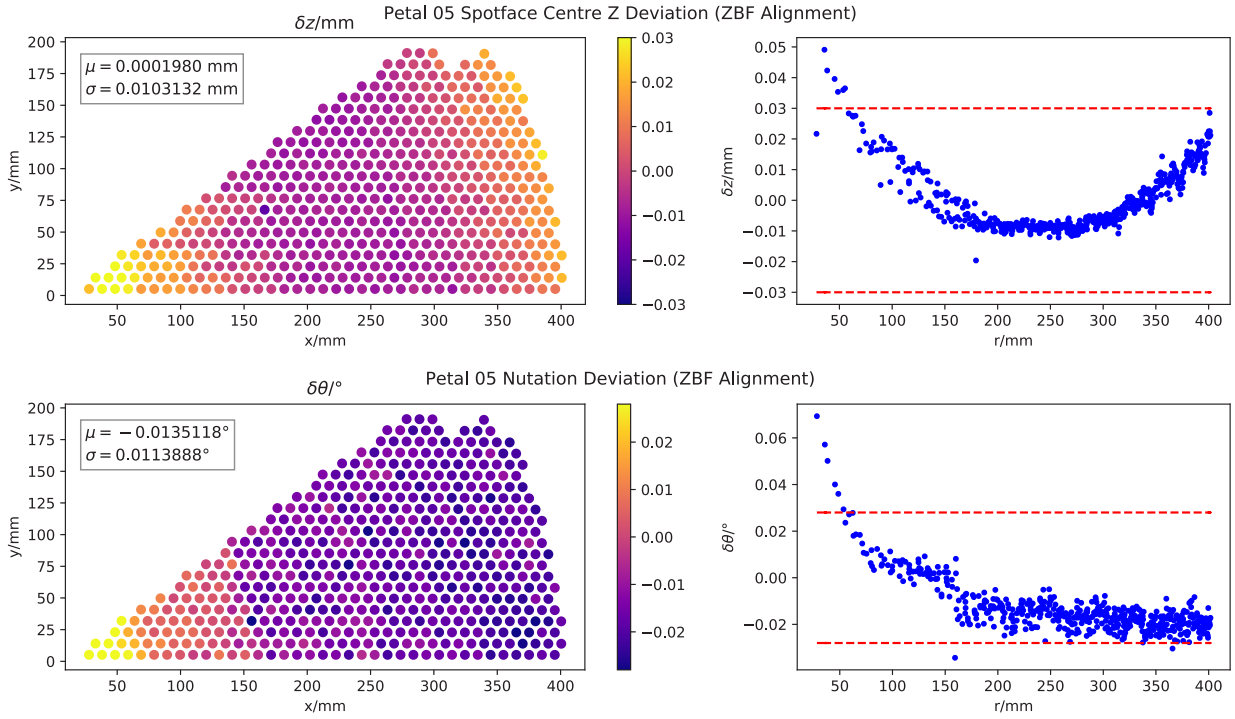

FIGURE 6. Two important metrology features for PTL05, the latest petal surveyed. Top panel shows spotface z deviation in mm and bottom panel nutation deviation from nominal in degrees. Dashed red lines represent the upper and lower tolerances. Mean deviations and RMS errors are shown as μ and σ in the text boxes.

quality for most features, with the exception being diameter and precession angle.

TABLE 2. Average diameter comparison between CMM and hand measurements with a Mitutoyo 3-point holtest. Hole population measured is 514 (all holes) on PTL01 and PTL02, 200 on PTL03, and 100 on PTL04. CMM values are systematically smaller than the actual diameter by around 5 µm.

PTL	$D_{\mathrm{CMM}}/\mathrm{mm}$	$D_{\mathrm{hand}}/\mathrm{mm}$	$\Delta D/\mathrm{mm}$
01	8.3114(13)	8.3156(13)	−0.0042
02	8.3112(31)	8.3142(42)	−0.0030
03	8.3035(12)	8.3088(20)	−0.0053
04	8.3074(29)	8.3139(30)	−0.0065

For diameter, a systematic difference was observed between CMM results and hand measurement results using a Mitutoyo holtest or pin gauges, shown in Table 2. The discrepancy can be attributed to the surface roughness of the anodising layer, as the CMM styli touch the surface very gently whereas any hand tool, just like the positioners to be installed into the holes, puts much larger pressure on the surface. The systematic difference well below 10 µm was regarded normal. By the holtest standard, the actual bore diameters meet the specifications, and lie on the tight side, which was exactly intended in order to reduce positioner free play inside the hole. Large errors in precession angle were entirely expected, as φ depends on the projection of cylinder axis onto the xy-plane, and for a precision bore of height $h = 20.5\,\mathrm{mm}$ at a nutation angle $\theta \in [0.25°, 5.88°]$, the length of the projected axis $l_{\mathrm{proj}} = h \sin\theta \in [0.09\,\mathrm{mm}, 2.1\,\mathrm{mm}]$, corresponding to an uncertainty of about 0.3°. In fact, given the excellent statistics for other features, we believe the precession angles are much closer to specification.

The petal's local best-fit coordinate system certainly renders the most number of features within specifications. Several other alignments were analysed, some shown in Table 3. The best-fit alignment (ZBF) provided excellent throughput while maintaining the best geometric fit. TPT alignment aimed at optimising throughput only, ignoring all geometric conditions, and yielded slightly better throughput. The difference between the two is below 0.15% and practically negligible. Integrating and properly aligning the petals in the FPR turned out difficult, and achieving either would be a success. Throughout the tests,

TABLE 3. Comparison of mean throughput loss in two theoretical alignments and the best actual alignment achieved on CMM. Columns are best-fit (ZBF), throughput-optimising (TPT), and actual (ACT). PTL05 had not been integrated. Numbers in parenthesis are standard deviations among all holes.

PTL	$(1-\eta)/\%(0.0^{+0.5}_{0.0})$		
	ZBF	TPT	ACT
00	0.084(115)	0.0078(1230)	0.80(38)
01	0.086(184)	0.083(185)	2.43(318)
02	0.121(241)	0.118(238)	0.53(88)
03	0.070(58)	0.069(70)	0.27(49)
04	0.125(83)	0.124(83)	0.86(70)
05	0.070(74)	0.065(90)	

petal mounting was highly reproducible in terms of alignment and throughput. Distortion of the ring was on the order or 100 µm. The best actual alignments found to date in Table 3, compared to the smallest possible throughput loss in theory, still have room for improvement. The actual losses are fairly close to the upper bound, although holes at the centre are subject to losses up to 14% because of the tilt. Actual alignment and predicted outcome with a recommended rotation are shown in Fig. 7.

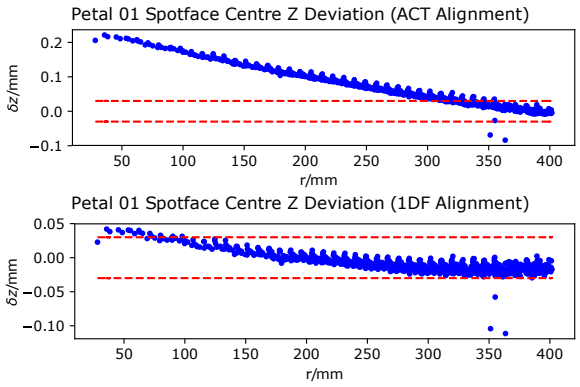

FIGURE 7. The programme recommends a one-degree-of-freedom rotation based on the actual alignment measured and the throughput optimiser. Top panel shows actual z-deviation for PTL01 where the nose of the petal is tilted up. Bottom panel predicts what z-deviation would appear if the rotation is applied. The three outlines far away from the cluster were confirmed to be due to CMM measurement errors. The x and y plots combined with z help visualise the tilt of petal and apply adjustments.

CONCLUSION

A precision high-energy physics experiment like DESI requires micron-level precision in the building of the instrument. CMM metrology makes it possible to verify the machining quality of extremely complicated precision parts, and can assist in integration and alignment of components. Utilising CAD-enabled, fully automated CMM metrology, we successfully measured all features of the DESI petals and FPR that are relevant to the science performance, an otherwise prohibitive task for conventional metrology methods or the manual CMM approach. Complete metrology data allowed for evaluation of the science performance of petals and guided the integration and alignment of DESI focal plate structure. The preliminary results with five petals are promising and have proven the validity of these techniques. As the other five petals arrive at Berkeley, we are confident in the integration and alignment procedures leading to mean throughput loss below 0.5% for all ten petals.

ACKNOWLEDGEMENTS

This research is supported by the Director, Office of Science, Office of High Energy Physics of the U.S. Department of Energy under Contract No. DE–AC02–05CH1123, and by the National Energy Research Scientific Computing Center; additional support for DESI is provided by the U.S. National Science Foundation, Division of Astronomical Sciences under Contract No. AST-0950945 to the National Optical Astronomy Observatory; the Science and Technologies Facilities Council of the United Kingdom; the Gordon and Betty Moore Foundation; the Heising-Simons Foundation; the National Council of Science and Technology of Mexico, and by the DESI Member Institutions.

REFERENCES

[1] Sholl M, Miller T, Jelinsky P. DESI-0329-v15: DESI Echo 22 Optical Design. DESI Project Document Database. 2015;.

[2] Jones E, Oliphant T, Peterson P, et al.. SciPy: Open source scientific tools for Python; 2001– . [Online; accessed <today>]. Available from: `http://www.scipy.org/`.

[3] Weisstein EW. Rotation Matrix From MathWorld–A Wolfram Web Resource;. [Online; accessed <today>]. Available from: `http://mathworld.wolfram.com/RotationMatrix.html`.

[4] Jelinsky P. DESI-2707-v1: DESI FRD Budget Flow Down Requirements. DESI Project Document Database. 2017;.

[5] Besuner R, Sholl M. DESI-0347-v3: DESI Systems Engineering Throughput Budget. DESI Project Document Database. 2014;.

EXPERIMENTAL FUSED ILLUMINATION MECHANISM DESIGN WITH DISCRIMINANT FUNCTION FOR STEEL PLATE

Gyung-Bum Kim[1], Cho-Eun Doek[2]
[1]Department of Aeronautical & Mechanical Design Engineering
Korea National University of Transportation
Chungju, Chungbuk, South Korea
[2]Department of Graduate School
Korea National University of Transportation
Chungju, Chungbuk, South Korea

1. INTRODUCTION

Steel plate is probably the most important of all metals in terms of its quantum and variety of use. The inspected surface in manual inspection is about 0.05% of the total steel surface produced. Due to high line speed, fatigue and other adverse factors, inspection process is hardly satisfactory. Thus the manual inspection process is not sufficient to guarantee defect-free surface of steel products with reasonable degree of confidence. Today, vision-based automated surface inspection systems are produced by many reputed companies. Technology of vision-based automatic inspection of steel products, even though not 100% accurate, has matured and developed so far. Real-time inspection of steel surfaces faces a number of challenges, which may be enumerated as hazardous site, operating speed, varieties of surface defects, large number of cameras. In addition, three characteristics including noise such as low-contrast, inhomogeneous and featureless, are included in steel surface image.[1-3]

In this paper, a fused illumination mechanism is experimentally designed to treat with three properties of steel plate and to effectively discriminate defect region from defect-free one. Its design is performed, based on application of discriminant measure to typical surface defect images of steel plates.

2. FUSED ILLUMINATION MECHANISM DESIGN

Typical surface defects[4] of steel plates are consist of scale, scab, crack, foreign object, Hole, etc. They are described in Fig. 1. For the direct reflection component of the light which is incident to steel plate surface with defect-free, this surface region is perceived to camera more brightly than defect one. A scale defect is described as irregular and wide shape, in contrast to other defects. A scab is represented, similar to scale. However, it appears depending on its inclusion surface characteristics. Star crack is in the shape of unevenness and has a small area, compared with other cracks. Foreign material defects are an uneven surface defect depending on foreign object shapes. Hole defects have a dark intensity resulting from light absorption.

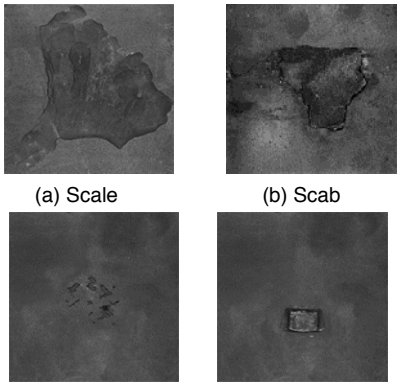

(a) Scale (b) Scab

(d) Star crack (f) Foreign object

Fig. 1 Steel plate defects

2.1 ILLUMINATION MECHANISMS and THEIR PARAMETERIZATION

Basic illumination mechanisms[5] for differentiated surface defect images include directional illumination(DI), bi-directional illumination(BI), co-axial illumination(CI) and dome illumination(DOI), etc. They are represented in Fig. 2. DI has diffuse reflection in case of uneven surface and results in smooth image. However, its image looks dark. BI is applied to make up for this disadvantage. CI has the same axis between camera and illumination. It can generate even and light image. DOI has the advantage of even image without a shadow, irrespective of any object shape.

The fused illumination mechanism is combined with these basic mechanisms above, and then it can make mutual supplementary of them. It generally results in even and distinguished images. BI & CI can make the reduction of shadow effect due to BI. DOI & CI can acquire even and bright image, regardless of irregular surface shapes. In this paper, this fused illumination is experimentally designed to maximize the contrast between defect region and defect-free one. Also, we've tried to be practically applied to surface inspection of steel plate.

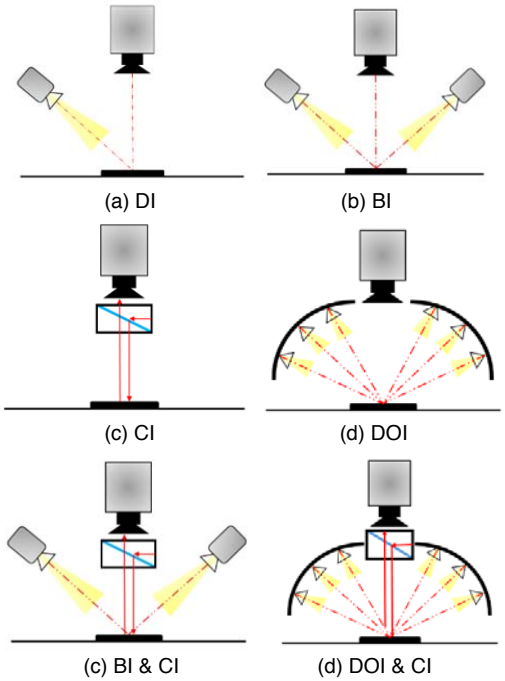

Fig. 2 Illumination mechanisms

The parameterization of illumination mechanisms is made according to the angle and height of illumination. The effect of illumination angle for DI and BI has been investigated. The angle is changed from 30° to 70° with interval 10°. Here, 5 images can be acquired in DI and BI. DOI has 3 channels(up, middle, low) according to illumination structure height, which can be controlled respectively. Then 7 images are obtained in the DOI. In the same manner of BI, BI & CI have 5 images according to angle change of illumination. Also, DOI & CI 7 images according to channel. We have experimented using 5 surface defect specimens of steel plate. We make use of totally 145 images, which include 25 images for DI / BI / BI&CI and 35 images for DOI / DOI & CI, respectively. Based on these images, the fused illumination mechanism and its parameter are identified with a discriminant measure.

2.2 DISCRIMINANT MEASURE

The fused illumination mechanism and its parameters are determined using the discriminant measure which represents the degree of separating defect-free region and defect one. In this paper, the fisher ratio[6] and tenengrad-euclidean[7] function have been used. The first one is based on mean and variance of defect and defect-free one, individually. The next one is modelled using defect boundary information.

The fisher ratio DF_{fr} in Eq. 1 is generally used for representing the separating degree between interested regions. It is computed large, as each region variance is low and mean difference is large.

$$DF_{fr} = \frac{(m_1 - m_2)^2}{v_1 + v_2} \quad (1)$$

Here, m, v is mean and variance for each interested regions, respectively

The tenegrad-euclidean DF_{te} in Eq. 2 is modelled using the difference of boundary information between defect-free region and defect one.

$$DF_{te} = \left(F_{te-d} - F_{te-df}\right) \quad (2)$$

$$F_{te} = \sum_x \sum_y I(x,y)^2, \qquad I(x,y)^2 > T$$

$$\mathrm{I(x,y)} = \sqrt{[I_x(x,y) + I_y(x,y)]^2}$$

Here, F_{te-d}, F_{te-df} means tenegrad-euclidean function in the defect and defect-free region. $\mathrm{I(x,y)}$ is boundary information and computed using the first sobel filter in the horizontal and vertical direction. T is an arbitrary threshold for limiting boundary information and then makes some noise be reduced a little. It is aware that the larger tenegrad-euclidean function DF_{te}, the larger the discriminant degree. In this paper, two discriminant measures mentioned above are applied to 145 images acquired on illumination

mechanisms, and then their performance is investigated based on image contrast quality.

3. EXPERIMENTION RESULTS

Fig. 3 shows that maximum fisher ratio for 5 surface defect specimens is represented according to each illumination mechanism. Here, DI has maximum fisher ratio for line crack, in comparison to other defects. In the same manner, BI, BI & CI, DOI, DOI & CI have maximum fisher ratio for scab, scale, foreign material and star crack, respectively.

Table 1 shows that a illumination mechanism are selected by fisher ratio for a defect and then representative illumination mechanism are determined as DOI(middle). This determination was predicted beforehand, because DOI in itself have even and smooth image quality. On the other hand, BI & CI has a low fisher ratio. The large fisher ratio does not surely mean maximum contrast between defect and defect-free region. Therefore, defect images resulting from maximum and minimum fisher ratio are investigated in Table 2. In case of intuitive look of result images, best images are nearly similar to worst ones in the part of no feature contrast.

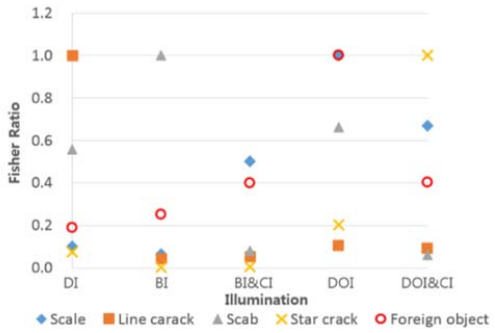

Fig. 3 Maximum fisher ratios of surface defects for illumination mechanisms

Table 1 Optimum illumination mechanism by fisher ratio

Surface defects	Illumination for a defect (Parameter)	Optimum illumination
Scale	DOI (Middle)	DOI (Middle)
Scab	BI(30˚)	
Line crack	DI(50˚)	
Star crack	DOI&CI (Low)	
Foreign object	DOI(Middle)	

Table 2 Image comparisons selected by fisher ratio

Defects	Best images by DOI	Worst images by BI & CI
Scale	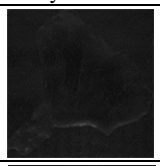	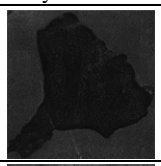
Scab	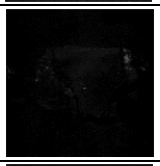	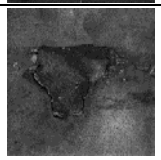
Line crack	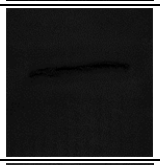	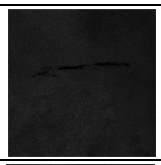
Star crack	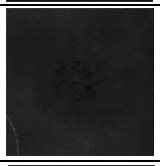	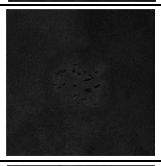
Foreign object	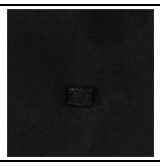	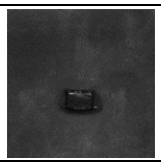

In addition, it is aware that the worst images for scale, scab and foreign material are clear and distinct than the best ones. Another problems are for a discriminant degree to be differently computed according to the selection of interested region. As shown in Table 3, there is very large difference of fisher ratio according to the area selection. Therefore, it is necessary to apply other discriminant function, which is tenengrad-euclidean function with boundary information.

Table 3 Fisher ratios for the change of defect area(DA) and defect-free area(DFA).

Line crack Image	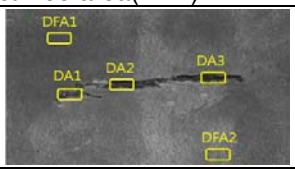	
	DFA 1	DFA 2
DA 1	0.2438	0.0174
DA 2	0.1993	0.0548
DA 3	0.0625	0.1495

The boundary information is generally more characteristic and consistent than intensity one, and is appropriate for even, featureless and low-contrast images.

Fig. 4 shows that maximum tenengrad-euclidean functions are represented according to each illumination mechanism. Here, BI & CI has maximum tenengrad-euclidean for all defects, exclusive of its parameter values. Then the optimum illumination mechanism is determined as BI & CI(70^{o}) in Table 4. This is very opposite to the mechanism selected by fisher ratio, which is very low in BI & CI. Accordingly, defect images resulting from maximum and minimum tenengrad-euclidean are investigated in Table 5. All best images are bright and distinct in comparision to the worst ones. This fused illumination mechanism makes discrimination between defect and defect-free region clearly and consistently.

4. CONCLUSIONS

In this paper, surface defects and typical illumination mechanisms for steel plates are analyzed, and the fused illumination mechanism is experimentally designed by the discriminant function.

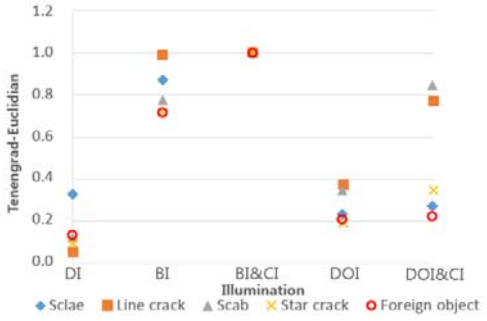

Fig. 4 Maximum tenegrad-euclideans of surface defects for illumination mechanisms

Table 4 Optimum illumination mechanism by tenegrad-euclidean function

Surface defects	Illumination for a defect (Parameter)	Optimum illumination
Scale	BI&CI(70˚)	BI&CI (70˚)
Scab	BI&CI(60˚)	
Line crack	BI&CI(70˚)	
Star crack	BI&CI(70˚)	
Foreign object	BI&CI(70˚)	

Table 5 Image comparisons by tenengrad-euclidean function

Defects	Best images by BI&CI	Worst images By DI
Scale	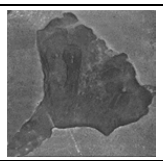	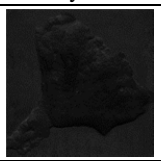
Scab	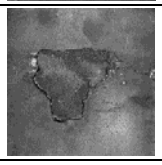	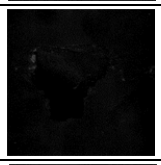
Line crack	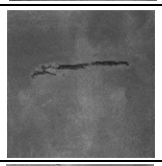	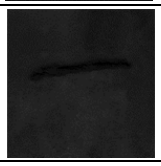
Star crack	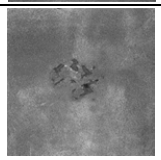	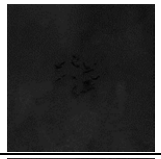
Foreign material	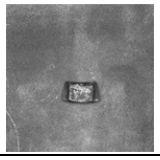	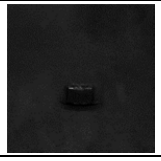

The discriminant function is applied for the evaluation of images acquired by illumination mechanisms. It is confirmed that the tenegrad-euclidean function gives consistent results for all defects, in comparison to fisher ratio. The fused illumination mechanism is determined as BI & CI and its parameter values are extracted, based on the discriminant function. Its performance is verified by intuitive image looks. It is judged that the proposed fused illumination mechanism could apply effectively to surface inspection system.

ACKNOWLEDGEMENT

This research was supported by Basic Science Research Program through NRF funded by the Ministry of Education (2015R1D1A1A01056691)

REFERENCES

[1] Bae, H. M., Park, C. H., Yun, J. P. and Choi,

S. H., 2014, “Optic Method for Surface Defect Inspection of Cold Strip”, *Journal of Institute of Control, Robotics and Systems*, pp. 61~64

[2] Nirbhar Neogi, Dusmanta K Mohanta, Pranab K Dutta, 2014, “Review of Vision-based Steel Surface Inspection Systems”, *EURASIP Journal on Image and Video Processing*, pp. 1~5.

[3] Kim, S. J., Cho, E. D., Kim, G. B., 2017, “Surface Defect Analysis of Steel Plate and Investigation of Illumination Parameters for Surface Inspection”, *Proceedings of IPIU 2017*

[4] Moon, C. I., Choi, S. H., Joo, W. J., Kim, K. B. and Kim, C. H., 2007, “Development of a Neural Network Classifier for the Classification of Surface Defects of Cold Rolled Strips”, *Journal of Korean Society of Precision Engineering*, Vol. 24, No.4, pp. 79.

[5] Kim, D. I., Lee, S. H., Kim, K. B., 2015, “Development of Plate Surface Defect Detection Technique using Image Processing”, *Journal of ICROS,* Vol30, pp.447~448

[6] Do, L. N., Yang, H. J., 2012, “Classification of Cognitive States from MRI data using Fisher Discriminant Ratio and Regions of Interest”, *International Journal of Contents*, Vol.8, No.4, pp. 3~4.

[7] Lee, S. H., Kim, J. H., Choi, B. T., Ko, S. J., 1998, “Autofocusing Algorithm for Video Camera using the Difference of Medians”, *Journal of KICS,* Vol.23, No.1, pp.41~51.

ANY-DEGREE-OF-FREEDOM REGISTRATION OF THREE-DIMENSIONAL SURFACES WITH UNBALANCED DEVIATIONS

M. Y. Liu*, C. F. Cheung, and C. J. Wang
Partner State Key Laboratory of Ultra-precision Machining Technology, Department of Industrial and Systems Engineering, The Hong Kong Polytechnic University, Kowloon, Hong Kong
*Corresponding author (Samuel.liu@connect.polyu.hk)

INTRODUCTION

Registration of 3D surfaces [1] is one of the most important and most widely used technologies for the characterization of the target 3D surfaces. Since the reference surface and the target surface are normally in different coordinates, coordinate transformation is done by registration to register the target surface to the reference surface for further data processing such as determination of the deviation from the target surface to the reference surface.

A lot of research has been devoted to study various methods for registration of 3D surfaces. The most famous one is iterative closed points (ICP) method [2] and its variations [3]. Other methods are also commonly seen in the literatures such as least square method [4] and intrinsic feature method [5]. Most of the methods are used for full degree of freedoms (DOFs), i.e. for 3D surfaces there are 6 DOFs including 3 DOFs for translations along x, y, z axes and 3 DOFs for rotations around x, y, z axes. For characterization of high precision 3D surfaces such as ultra-precision freeform surfaces, 6 DOF methods may be the most reasonable methods since these methods utilize all the available DOFs for the rigid-body transformation to minimize the deviation from the target surface to the reference surface, i.e. the cost function directly related to the difference between the target surface and the reference is minimized.

In many other cases such as characterization of the influence function of fluid jet polishing [6], bonnet polishing [7], where the target surfaces usually have large unbalanced deviations regarding to the reference surfaces, registration with full 6 DOFs may result in unwanted tilting or shifting, although the deviation from target surface to the reference is minimized. This is because the large unbalanced deviation affects in a specific DOF which is not reasonable according to the a priori knowledge.

In this paper, an any-degree-of-freedom (ANY-DOF) registration method is presented for registration of 3D surfaces with unbalanced deviations. With the a priori knowledge or pre-processing technology, the target surface and the reference surface are firstly aligned with some simple features such as plane and sphere and hence some specific DOFs are fixed. After that, the target surface and the reference surface are then registered with the remaining DOFs using the proposed ANY-DOF method. The K-dimensional-tree (Kd-tree) data modelling and Levenberg-Marquardt method are utilized for solving the ANY-DOF registration problem. With proposed method, the unwanted DOFs alignment can be avoid to have a better characterization result of the target surface.

ANY-DEGREE-OF-FREEDOM (ANY-DOF) REGISTRATION METHOD

The any-degree-of-freedom (ANY-DOF) method is shown in FIG. 1. The reference surface is firstly modelled with the Kd-tree modelling method [8]. The measured surface is then transform using the transformation matrix with the unknown variables according to the desired DOFs registration. The nearest neighbours from the transformed surface to the reference surface are determined and the distances are calculated with the help of the Kd-tree model. The cost function aims to minimize the distance and the nonlinear problem is solved by the Levenberg-Marquardt method. Hence, the unknown variables are determined and the final transformation matrix for the ANY-DOF registration is solved.

It is interesting to note that the number is variables can be from 1 to 6, which means it can be any of the combinations of the translation along x, y, z axes and rotation around x, y, z axes. The Kd-tree data modelling is employed to speed up the search of nearest neighbour points.

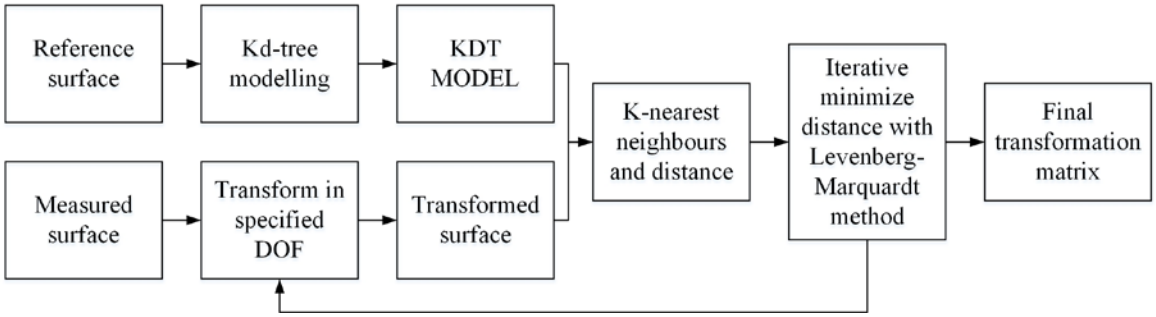

FIGURE 1. Diagram of the ANY-DOF registration method

In the Levenberg-Marquardt method, an initial value is given and usually setting the initial values to zeros is effective. The rigid-body transformation has 6 DOF, i.e. translation along x, y, z axes and rotation about x, y, z axes, representing the yaw, pitch, and roll angles. The translation matrix can be determined by

$$T_x(v_x)=\begin{bmatrix}1&0&0&v_x\\0&1&0&0\\0&0&1&0\\0&0&0&1\end{bmatrix} \quad (1)$$

$$T_y(v_y)=\begin{bmatrix}1&0&0&0\\0&1&0&v_y\\0&0&1&0\\0&0&0&1\end{bmatrix} \quad (2)$$

$$T_z(v_z)=\begin{bmatrix}1&0&0&0\\0&1&0&0\\0&0&1&v_z\\0&0&0&1\end{bmatrix} \quad (3)$$

where v_x, v_y, and v_z are the translation variables along x, y, z axes. The rotation matrix can be determined by

$$R_x(\alpha)=\begin{bmatrix}1&0&0&0\\0&\cos(\alpha)&-\sin(\alpha)&0\\0&\sin(\alpha)&\cos(\alpha)&0\\0&0&0&1\end{bmatrix} \quad (4)$$

$$R_y(\beta)=\begin{bmatrix}\cos(\beta)&0&\sin(\beta)&0\\0&1&0&0\\-\sin(\beta)&0&\cos(\beta)&0\\0&0&0&1\end{bmatrix} \quad (5)$$

$$R_z(\gamma)=\begin{bmatrix}\cos(\gamma)&-\sin(\gamma)&0&0\\\sin(\gamma)&\cos(\gamma)&0&0\\0&0&1&0\\0&0&0&1\end{bmatrix} \quad (6)$$

where α, β, and γ are the rotation variables about x, y, z axes.

The final transformation matrix with all 6 DOFs can be determined by

$$M=R_x(\alpha)R_y(\beta)R_z(\gamma)T_x(v_x)T_y(v_y)T_z(v_z) \quad (7)$$

For the ANY-DOF method, the final transformation matrix is the matrix multiplication of any of translation matrix or rotation matrix of the specific DOF. For the point set P of the target surface, the transformed point set P' can be determined by

$$P'=PM \quad (8)$$

Assume point set X represents the reference surface, the cost function is determined by

$$F=rms(D) \quad (9)$$

where D is the vector of the shortest distances from every point in X to P'. Solving the registration problem is minimizing the cost function which is a non-linear least squares problem, and this is done with the Levenberg-Marquardt algorithm. The variables to solve is the translation and rotation according to the DOF and the variables are initial to be zeros and iteratively solved with the Levenberg-Marquardt algorithm.

EXPERIMENTS AND DISCUSSIONS

In order to verify the effectiveness of the proposed method, two experiments were conducted with different DOFs for the registration and the results are compared to the traditional ICP method so as to demonstrate the advantage of the proposed method.

Registration with 3 translations + 1 rotation

The first experiment considers 3 translations along x, y, z axes and 1 rotation about z axis. The experiment is to register the measured surface to the simulation surface after fluid jet polishing [6]. Since the actual measured surface has large distortion in some area comparing to the simulation surface, this will introduction large

rotation error about x and y axes in the traditional 6 DOF registration process. In this experiment, the DOF for rotation about x and y axes are fixed and remains the 3 translation and rotation about z for registration.

The simulation surface is shown in FIG. 2 and the measured surface is shown in FIG. 3. The data shows that there is significant difference between the simulated surface and the measured surface.

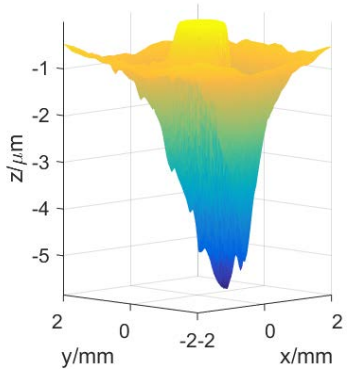

FIGURE 2. Simulated surface

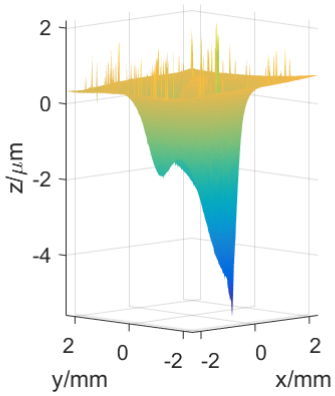

FIGURE 3. Measured surface

The registration result using the proposed method is shown in FIG. 4 while that for ICP method is shown in FIG. 5. The result using the proposed method shows good alignment of the two surfaces while that by using the ICP method shows a large rotation error. Without any constraints, the rotation error is caused by the large difference between the simulated surface and the reference surface. With the proposed method, since the rotation about x and y axes are fixed, the registration is only performed on the specific DOF.

Registration with 3 translations

Another experiment is done where only 3 translations are considered. The data is also obtained from fluid jet polishing. Since the data is supposed to be rotational symmetry, the rotation about z axis is not consider in the experiment. The measured surface was adjusted to be without tilting using the relatively flat area before the measurement. As a result, the rotations about x and y axes are also negligible. Hence, the registration is only performed for the translations along x, y, and z directions.

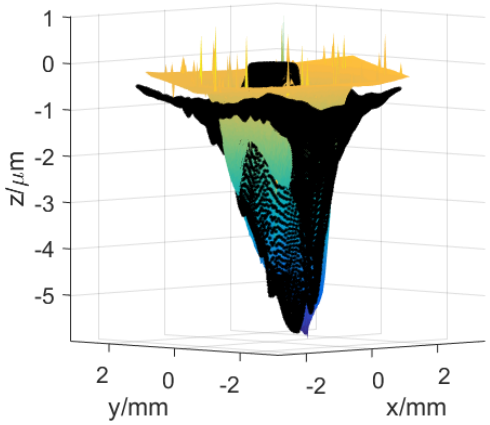

FIGURE 4. Registration result with the proposed method

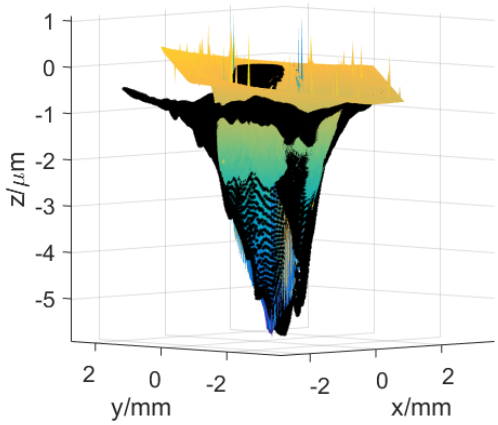

FIGURE 5. Registration result with the ICP method

The simulated surface and the measured surface are shown in FIG. 6 and FIG. 7. The registration result by using he proposed method and the ICP method are shown in FIG. 8 and FIG. 9. Similar to the result in the previous experiment, the proposed method shows a better result regarding the tilting registration using the ICP method. The large tilting result of the ICP method is due to the large unbalanced error in the measured surface, which is not expected in the ideal simulation case.

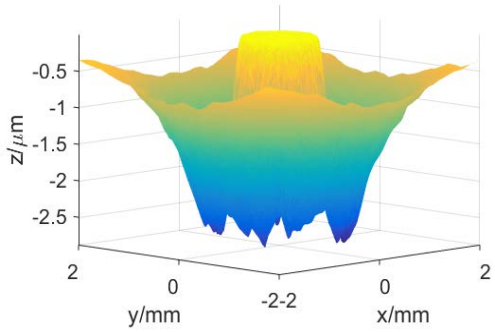

FIGURE 6. Simulated surface

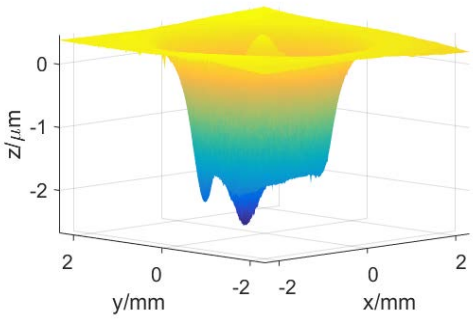

FIGURE 7. Measured surface

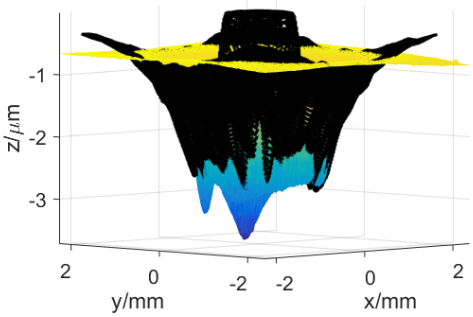

FIGURE 8. Registration result with the proposed method

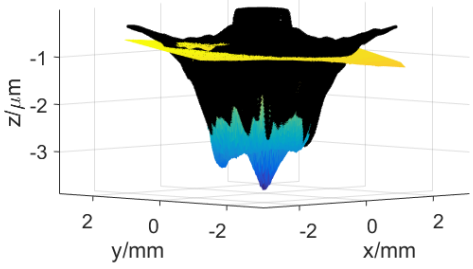

FIGURE 9. Registration result with the ICP method

CONCLUSION

An any-degree-of-freedom (ANY-DOF) method is developed for registration of 3D surfaces. Its advantage is that it can freely determine any of the DOF for registration of the target surface and the reference surface. The successful development of this method is useful for the characterization of 3D surfaces with a large unbalanced deviation to the reference surfaces.

ACKNOWLEDGMENT

The work was also supported by the National Natural Science Foundation of China (No. 51675456), China National Program and a PhD studentship (project account code: RTHC) from The Hong Kong Polytechnic University.

REFERENCES

[1] Zhang Z. Iterative point matching for registration of free-form curves and surfaces. International journal of computer vision. 1994;13:119-52.

[2] Besl PJ, McKay ND. A method for registration of 3-D shapes. IEEE Transactions on pattern analysis and machine intelligence. 1992;14:239-56.

[3] Rusinkiewicz S, Levoy M. Efficient variants of the ICP algorithm. 3-D Digital Imaging and Modeling, 2001 Proceedings Third International Conference on: IEEE, 2001. p. 145-52.

[4] Cheung CF, Li HF, Lee WB, To S, Kong LB. An integrated form characterization method for measuring ultra-precision freeform surfaces. International Journal of Machine Tools and Manufacture. 2007;47:81-91.

[5] Ren MJ, Cheung CF, Kong LB, Jiang XQ. Invariant-Feature-Pattern-Based Form Characterization for the Measurement of Ultraprecision Freeform Surfaces. IEEE T Instrum Meas. 2012;61:963-73.

[6] Wang CJ, Cheung CF, Ho LT, Liu MY, Lee WB. A novel multi-jet polishing process and tool for high-efficiency polishing. International Journal of Machine Tools and Manufacture. 2017;115:60-73.

[7] Cao Z-C, Cheung CF, Ho LT, Liu MY. Theoretical and experimental investigation of surface generation in swing precess bonnet polishing of complex three-dimensional structured surfaces. Precision Engineering. 2017;50:361-71.

[8] Bentley JL. Multidimensional binary search trees used for associative searching. Communications of the ACM. 1975;18:509-17

METHOD TO DETERMINE THE CENTER OF CONTRAST TARGETS FROM TERRESTRIAL LASER SCANNER DATA

Prem Rachakonda*, Bala Muralikrishnan*, Daniel Sawyer*, Ling Wang**

*Dimensional Metrology Group,
Engineering Physics Division
National Institute of Standards and Technology,
Gaithersburg, MD, USA

**Department of Automation, School of Mechanical and Electrical Engineering,
China Jiliang University, Hangzhou,
Zhejiang Province, 310018, P. R. China

1 INTRODUCTION

Terrestrial laser scanners (TLSs) are instruments that can measure 3D coordinates of objects at high speed using a laser, resulting in high density 3D point cloud data. Contrast targets are some of the most common targets used with TLSs to establish a scale or register multiple scan datasets. These targets are also known as checkerboard targets or signalized targets and their design provides a way to calculate their geometric center by using intensity data along with the dimensional data. Large contrast targets are needed when scanning at longer distances; however, unlike other geometric targets such as spheres, fabrication of large contrast targets is relatively inexpensive. Even though contrast targets are used with TLSs, the algorithms to calculate their centers are proprietary and/or work only with proprietary data formats.

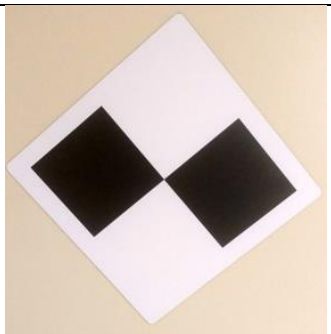

Figure 1: Picture of a contrast target

In this context, this paper provides a novel method that was developed at the National Institute of Standards and Technology (NIST) to calculate the derived point or the center of a contrast target (henceforth termed as CCT) and compares its performance with commercial software, in various scan conditions.

2 PROCEDURE TO OBTAIN THE CENTER OF THE CONTRAST TARGET

Calculating the center of a contrast target has not been studied extensively in open literature. This paper describes one method to obtain the center of a contrast target which involves multiple steps, where each successive step attempts to refine the center of the target obtained in the previous step. For the target depicted in Figure 1, the center is the location where the two black squares meet.

Most software that are provided by TLS manufacturers output intensity or color data along with dimensional data for their scans. For this procedure, the dimensional data was exported along with intensity data (XYZI format). Some TLSs provide dimensional data along with color intensity (XYZRGB). Here, X, Y, Z correspond to the dimensional data, I is the intensity data and R, G, B correspond to red, green, blue channel intensity data. If the data obtained is in the form of XYZRGB, the RGB data needs to be converted to intensity values using a weighted sum using the formula $I = 0.299 \times R + 0.587 \times G + 0.114 \times B$ [1]. Subsequently, the XYZI formatted data can be processed using the following steps to obtain the center of a contrast target.

1. Extract the data corresponding to the region of interest of the contrast target within the scene.
2. Calculate an approximate 3D location of the center of the target using 2D imaging methods.
3. Obtain a refined location of the center of the target using dimensional and intensity data.

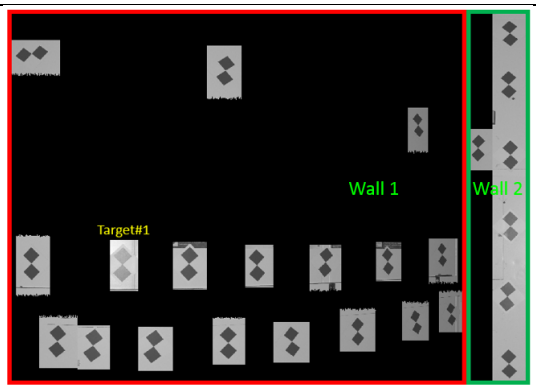

Figure 2: Intensity image from a TLS showing multiple targets mounted on two walls

2.1 Extract targets' regions of interest

The first step in this process was to extract the regions of interest from a scan. This step lowers the complexity and number of computations needed to find the 2D center of the target. Figure 2 is the extracted intensity image of a scan which shows multiple checkboard targets placed around a room in different orientations. Data corresponding to individual targets need to be cropped/separated. This process needs to be performed for both the dimensional and the intensity data.

This cropping of the data (XYZI) can be done either manually or automatically. The manual method may use any point cloud manipulating software for cropping, whereas the automatic methods may use a template matching method. For this work, all the regions of interest were cropped manually once for the first dataset and the same cropping regions were used to crop the remaining datasets. All subsequent processing described next was performed using automated methods.

2.2 Calculate the target's approximate 3D center using 2D imaging methods

To obtain the center of the target, the intensity information can be used to generate a 2D image of the target. Subsequently, this image is processed using edge detection methods along with the Hough transform [2]. These methods aid in detecting the intersecting lines in a checkerboard-like pattern [3]. The Hough transform is a mature algorithm and is built into software like MATLAB* which was used to process this data. As is usual with many image processing algorithms some level of adjustments is required when the nature of the image changes (low contrast, high noise etc.). The steps to extract an approximate target center (CCT) were as follows:

i. Each cropped XYZI dataset was processed and an image was generated to show a single contrast target as shown in *Figure 4*a.

ii. The image generated by the previous step was cropped further using a circular mask to display the central region where the two black squares touch each other. Care must be taken to avoid any other regions with intersecting lines/corners as shown in *Figure 4*b. The masking was done automatically using a predefined mask position and size. Using a square mask instead of a circular mask would lead to detection of

* Disclaimer: Commercial equipment and materials may be identified in order to adequately specify certain procedures. In no case does such identification imply recommendation or endorsement by the National Institute of Standards and Technology, nor does it imply that the materials or equipment identified are necessarily the best available for the purpose.

additional lines that are at the edges of the square mask.

iii. Lines/edges were emphasized in masked image using a "Canny edge" algorithm.

iv. A Hough transform was performed on the image from the previous step and the intersecting lines are obtained. It is possible that there may be more than two lines due to the nature of the image (unclean targets, uneven target plane, shadows etc.). Care must be taken to apply appropriate filters to obtain only two intersecting lines at the center of the target.

v. The two lines obtained in the previous step were intersected to obtain a 2D approximation of the center of the contrast target CCT_1 as shown in *Figure 4*c.

In the event of failure of the 2D method described above, a manual method may be used to pick the approximate 2D center from the image. It should be noted that CCT_1 was obtained from image data in units of pixels. Even though the pixels are integer numbers, CCT_1 may not have integer values.

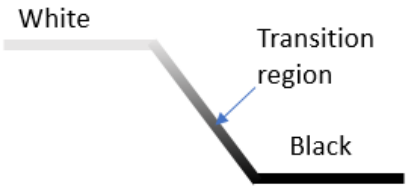

Figure 3: Illustration of the transition or fall-off regions of a contrast target

Each pixel in the 2D image has a corresponding 3D coordinate and an intensity value. To obtain an approximate 3D center, the pixel center coordinates CCT_1 are rounded and an integer pixel location CCT_2 closest to the CCT_1 was obtained. This modified pixel location has a corresponding 3D coordinate X_3, Y_3, Z_3 and intensity value I_3. The 3D coordinate corresponding to CCT_2 was then $CCT_3 = (X_3, Y_3, Z_3)$.

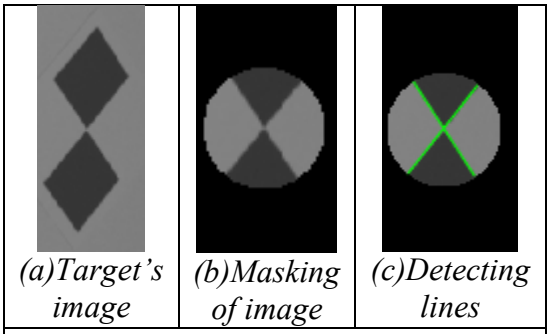

(a)Target's image | *(b)Masking of image* | *(c)Detecting lines*

Figure 4: Use of Hough transform to detect the intersecting lines of a contrast target.

2.3 Calculate a refined target center using dimensional and intensity data

One method to calculate the 3D center of the contrast target was described in the previous sub-section. When multiple scans of the same target were processed, the approximate 3D coordinates of the centers (CCT_3) were found to have poor repeatability ($1\sigma > 1$ mm), much larger than the expected repeatability of the system and the setup. To improve the calculation of target centers, a new method was conceived which uses intensity data along with dimensional data in non-radial directions. To perform this, first the 3D data in Cartesian coordinate system was converted to data in a spherical coordinate system of form (H, V, R), where H is the horizontal/azimuth angle, V is the vertical/elevation angle and R is the radial distance to each measured point.

A new dataset was created that was comprised of the angles H, V and the intensity data I. Henceforth, this will be referred as the HVI domain in this paper. The radial data (R) was ignored at this point. To improve the results, the following modifications were performed on the data:

1. The density of data in the HVI domain was increased to 300 times the original point density by interpolation using a cubic polynomial. This was found to lower the uncertainty in calculating the intersection point. Although cubic

polynomial interpolation has a possibility of wild swings in the interpolated points, the data was visually inspected after interpolation to ensure that such issues do not exist in the region of interest (fall-off region in Figure 3). Other interpolation techniques were also explored, however cubic interpolation was observed to perform adequately for most datasets.

2. In an ideal scan of a contrast target, the intensity data typically has a minimum value of 0 (black) and maximum value of 1 (white). However, most scans of contrast targets don't have such values for their black and white regions. For example, the intensity may range from 0.25 to 0.75. To lower the uncertainty of determining the CCT, intensity data was normalized/scaled from 0 to 1.

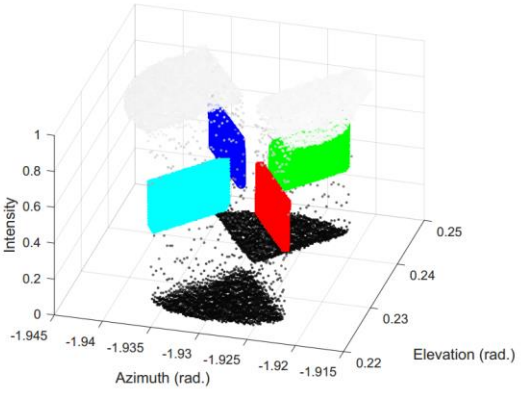

Figure 5: Transition regions of the target (colored) in the HVI domain that are in between the extreme intensity values.

In the HVI domain, the intensity values corresponding to the intersecting lines in a 2D image have a sharp fall-off as illustrated in Figure 3. In this fall-off region, the intensity drastically changes from $I \approx 1$ to $I \approx 0$. These regions in the HVI domain are shown in Figure 5 where the colored regions in the middle are the high density interpolated points corresponding to the fall-off region. The following steps are then performed to obtain the intersection point:

a. The fall-off region in the HVI domain was obtained by discarding the surfaces corresponding to extreme intensities (black and white in Figure 5) that are over 0.5 times the standard deviation (0.5 σ) from the mean intensity value. This value of 0.5 σ was empirically determined and it ensured that only data belonging to the intersecting fall-off regions were obtained.

b. This fall-off region was then split into four parts after truncating the central cylindrical region close to the approximate center. This is performed using an automated method and this truncation enables the intersecting regions to be separated into four parts (as shown by the colored regions in Figure 5).

c. The intensity data from four datasets in the HVI domain was then discarded, keeping only H and V. This process essentially collapses the data to a single plane in HV domain, yielding datasets corresponding to four lines on the target.

d. In this step, a 2D intersection point in the HV domain was obtained. This can be obtained in one of three ways:

   i. The four line datasets can be intersected using a least-squares method in the HV domain to yield the center of the target (H_c, V_c).

   ii. The four line datasets can be grouped together into two datasets corresponding to two lines. These datasets can be least-squares fit to two lines, which can then be intersected to obtain (H_c, V_c).

   iii. Alternatively, before step#c, the four surfaces in the HVI domain (colored regions in Figure 5) can be fit to planes. These four plane equations can be solved using a

least-squares method to perform a four-plane intersection. This method results in an intersection point (H_c,V_c,I_c) and thereby obtaining a center (H_c, V_c) in 2D.

Table 1: Comparison of the target center parameters

Target #	Method#1 (µm)				Method#2 (µm)				L (m)	M	D	θ°
	σH1	σV1	σR1	σD1	σH2	σV2	σR2	σD2				
1	48	76	40	53	75	96	34	63	4.4	1.2	1.2	2
2	37	68	29	51	35	76	26	53	4.5	1.0	1.0	11
3	48	71	33	53	47	65	28	47	4.5	0.9	0.9	6
4	54	69	30	53	50	70	27	52	4.5	0.9	1.0	6
5	57	80	27	59	50	80	24	57	4.7	0.9	1.0	15
6	48	72	36	47	46	69	30	46	4.7	0.9	1.0	16
7	35	67	28	37	35	64	27	41	4.7	1.0	1.1	19
8	42	85	36	62	41	82	34	62	4.8	1.0	1.0	22
9	16	86	28	55	12	81	25	53	4.9	0.9	1.0	15
10	8	64	24	34	14	63	23	34	5.0	1.2	1.0	18
11	60	87	32	72	57	86	28	69	5.0	0.9	1.0	26
12	39	111	21	72	46	118	25	76	5.1	1.1	1.1	5
13	55	123	29	87	55	121	24	84	5.1	0.9	1.0	6
14	38	94	33	67	40	94	30	65	5.2	1.0	1.0	31
15	18	108	22	70	23	107	21	71	5.2	1.1	1.0	5
16	64	124	29	87	66	120	28	85	5.2	1.0	1.0	5
17	13	120	22	75	19	119	19	75	5.4	1.1	1.0	5
18	56	102	34	75	56	100	29	74	5.4	0.9	1.0	34
19	34	129	17	78	20	123	19	76	5.6	0.9	1.0	4
20	24	108	39	71	23	115	30	70	5.7	0.9	1.0	23
21	48	109	34	75	47	107	36	76	5.7	1.0	1.0	39
22	66	115	30	82	61	109	29	80	6.2	1.0	1.0	44
23	25	111	30	69	23	116	26	73	6.3	1.0	1.1	44
24	51	122	31	81	50	119	24	81	6.4	0.9	1.0	47
25	65	120	30	88	63	118	34	85	6.6	1.0	1.0	47

In general, it was found that 2D line intersection of two lines was more repeatable than the other two methods to yield an intersection point (H_c, V_c). Both the plane and line fitting routines were performed iteratively after excluding data points whose corresponding residuals exceeded three times the standard deviation of the residuals. The iterations were terminated when there were no more points to exclude.

e. The radial value of the center (R_c) was the radial value of CCT_3 in spherical coordinate system. It should be noted that CCT_3 was calculated using 2D imaging methods described in section 2.2. This value of R_c is an approximate value and will be improved in the subsequent steps.

f. The center (H_c, V_c, R_c) was then converted to a Cartesian coordinate system to obtain $CCT_4 = (X_c, Y_c, Z_c)$.

g. As a final step, CCT_4 was projected onto the plane of the contrast target in the XYZ domain. This was performed by intersecting the line joining the origin and CCT_4 with the plane of the contrast target. This projected point $CCT_5 = (X_p, Y_p, Z_p)$ was the final center of the contrast target. This projection method was required to ensure that the final center CCT_5 lies on the plane of the contrast target.

3 TEST METHODOLOGY

To understand the currently available methods and to compare them with the method described in this paper, three commercial software packages were used and repeatability studies were conducted. Two contrast targets were scanned 10 times and their CCTs and the standard deviations (1σ) of those CCTs were calculated using each software. Lower 1σ values of all the 3D coordinates (σx, σy, σz) indicates a more robust algorithm. This metric however considers only the precision of the centers but not their accuracy. It should be noted that there may be other software which may perform better, but were inaccessible to the authors at the time of writing this paper. One commercial software (Method#1) yielded lowest 1σ values (lower by an order of magnitude) and this software was used to compare the method described in this paper (Method#2).

3.1 Test setup

The test setup involved placing 25 contrast targets on two walls as depicted in Figure 2. These targets were square in shape, ≈ 225 mm wide, fabricated out of a flexible plastic material and have a magnetic backing for the purposes of mounting. Seven targets were mounted on a wall (green wall) on the right distributed vertically and the rest are

mounted on a wall that was perpendicular (red wall), distributed horizontally. Even though these targets appear to be in the same plane in Figure 2 (planar view), they are in fact on two walls that are perpendicular. The TLS was placed at approximately 5 m from both the walls and the distance to each target (L) and the angles of incidence (θ) are listed in *Table 1*. The angle of incidence θ is the angle between the target's surface normal and the laser beam at the target's nominal center.

To perform an evaluation, these targets were scanned 10 times using a TLS. One such scan is depicted in Figure 1. Data acquired by this TLS was exported both to its own proprietary file format and to the XYZI format. Commercial software (Method#1) was used to process the data in this proprietary file format and the CCT of all the targets were obtained. This software did not have the capability to process the data in the XYZI format.

After processing the data, the standard deviation of the centers in spherical coordinates calculated by Method#1 was σ_1, and as calculated by Method#2 was σ_2. Here $\sigma_1 = (\sigma_{A1}, \sigma_{E1}, \sigma_{R1})$ and $\sigma_2 = (\sigma_{A2}, \sigma_{E2}, \sigma_{R2})$. To perform a comparison in the units of length, the standard deviations in azimuth and elevation were multiplied by the average radial distance value of the center. i.e., $\sigma_{H1} = R_1 \times \sigma_{A1}$, $\sigma_{V1} = R_1 \times \sigma_{E1}$, $\sigma_{H2} = R_2 \times \sigma_{A2}$, $\sigma_{V2} = R_2 \times \sigma_{E2}$. Here R_1 and R_2 were the average radial distances of the center as determined by Method#1 and Method#2 respectively. Two other parameters, σ_{D1} and σ_{D2} were calculated, which were the 1σ values of the distances of the centers about the mean value of the center calculated by Method#1 and Method#2 respectively. These are listed in *Table 1* along with a parameter $D = \sigma_{D2}/\sigma_{D1}$.

Ideally, the corresponding standard deviation values of both the methods (σ_1 and σ_2) should be equal, but they are not. To make the comparison simpler, a quality factor M given by equation 1 was introduced to compare the methods at each CCT and *Table 1* shows all the parameters calculated using both the methods using the 10 repeat measurements. This method of comparison is useful since Method#1 was found to be consistently producing centers with lower variation among the three commercial software packages that were evaluated.

$$M = \frac{M_{AZ} + M_{EL} + M_{RR}}{3} \qquad 1$$

where,

$M_{AZ} = \frac{\sigma_{A2}}{\sigma_{A1}}$, $M_{EL} = \frac{\sigma_{E2}}{\sigma E_1}$ and $M_{RR} = \frac{\sigma_{R2}}{\sigma_{R1}}$.

If the standard deviation values from both the methods are identical, M = 1. If Method#1 performs better than Method#2 then M > 1 and *vice versa* if M < 1. There may be cases where M = 1 if Method#1 outperforms in one component and underperforms in another. This metric M gives a good estimate of the overall method performance and M_{AZ}, M_{EL}, M_{RR} reveal the performance of the method in individual spherical coordinate components.

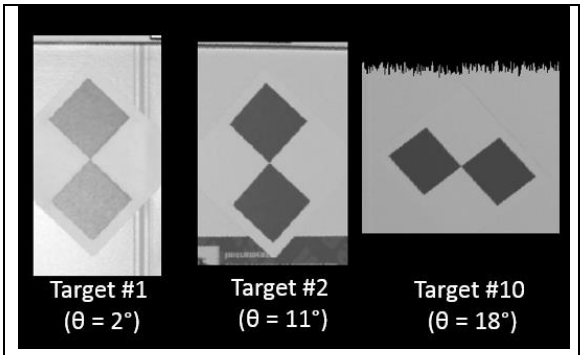

Figure 6: Intensity images of targets at various angles(θ) and orientations.

3.2 Summary and discussion of results

The centers of the contrast targets were calculated using a method involving multiple steps. The steps described in this paper are summarized below:

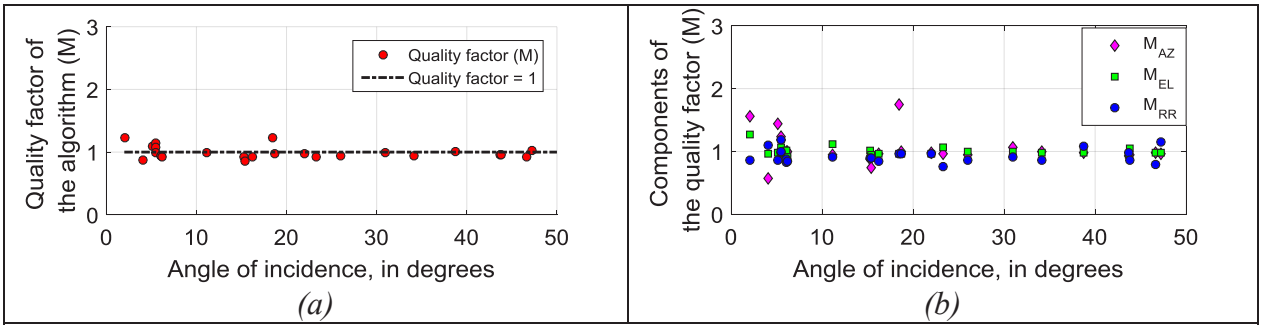

Figure 7: Performance of the NIST method at various angles

- CCT_1: 2D center (using image processing)
- CCT_2: 2D center (integer values of CCT_1)
- CCT_3: 3D center corresponding to CCT_2.
- CCT_4: 3D center (HVI domain method)
- CCT_5: CCT_4 projected on target's plane

Two notable trends affected the quality of Method#2. First, it was observed that the value of M was *not* significantly dependent on the angle of incidence (θ), but on the intensity variations in the black and the white regions of the target as shown in Figure 6. Targets that were placed at $\theta < 7°$ (shallow incidence angles) resulted in high intensity regions in the black part of the target. Second, target #10 also showed higher value of M as it was oriented differently compared to all the other 24 targets (see Figure 6). However, overall it can be observed from *Figure 7*b that Method#2 performs reasonably well in all the three components.

The distances between the centers obtained from Method#1 and Method#2 were calculated and the average distance between the centers at all the locations was ≈ 0.14 mm. There was no systematic bias that was observed in the azimuth or elevation coordinate differences of centers from both the methods, but there was a bias in the radial direction, an average of ≈ 0.12 mm. This bias could be a result of ensuring that the CCT is on the least-squares fitted plane of the target. It should be noted that the accuracy of either method cannot be ascertained using a single point measurement. Such a comparison would require test procedures involving calibrated lengths between two contrast targets in various orientations.

4 CONCLUSION

This paper presents a novel method developed at NIST to calculate the center of a contrast target and compares it with the results from other available software. It was observed that the NIST method performs reasonably well for most targets. More work is planned to ascertain the method's performance for various test cases (target orientations, data densities etc.). This is to ensure that the parameters used to deduce the target centers are more robust and applicable for scans with varying data quality.

5 REFERENCES

[1]ITU-R BT.601-71 - Studio encoding parameters of digital television for standard 4:3 and wide-screen 16:9 aspect ratios https://www.itu.int/dms_pubrec/itu-r/rec/bt/R-REC-BT.601-7-201103-I!!PDF-E.pdf (Accessed 8/2/2017)

[2]Duda, R., Hart, P., "Use of Hough Transformation to Detect Lines and Curves in Pictures", Communications of the ACM, January 1972, Vol.15, No. 1

[3]http://www.vision.caltech.edu/bouguetj/calib_doc/htmls/example.html (Accessed 6/21/2017)

COMPENSATION OF MEASURED FREQUENCY RESPONSE FUNCTIONS USING ACCELEROMETER MODELS AND INVERSE RCSA

Harsha Satyanarayana and Tony L. Schmitz
Mechanical Engineering and Engineering Science
University of North Carolina at Charlotte, Charlotte, NC

INTRODUCTION

Machining operations may be stable or unstable depending on the cutting parameters and machine-spindle-holder-tool assembly frequency response function (FRF). Stable cutting conditions can be predicted using analytical stability models [1-3]. These models require knowledge of the assembly FRF and the cutting force model. The FRF can be obtained by measurement or modelling. For the latter, Schmitz and Donaldson [4] first presented the Receptance Coupling Substructure Analysis (RCSA) method to predict the machine-spindle-holder-tool FRFs by coupling individual component FRFs (or receptances). This method reduces measurement time because assembly FRFs can be predicted rather than measured. Subsequent efforts by the authors have improved the technique [5-14].

In this paper, another novel application of RCSA is presented to improve FRF measurement accuracy. In modal testing the tool tip FRF is measured using an instrumented hammer to excite the structure and an accelerometer to record the corresponding response. However, the measured FRF is slightly different than the actual tool tip FRF due to the accelerometer mass and cable effects. Mass loading compensation has been previously studied in [15-17]. To build on these prior efforts and compensate for both mass loading and cable damping, the inverse RCSA approach is applied here. In this approach, a model of the accelerometer-cable is decoupled from the measured FRF to isolate the structure's FRF. Experimental results are presented for three setups: 1) 12.7 mm diameter cantilever rod; 2) 6.35 mm diameter cantilever rod; and 3) clamped-clamped-clamped-free boundary condition thin ribs.

RCSA BACKGROUND

RCSA is a powerful tool for predicting assembly receptances, or FRFs, using individual component receptances. The component receptances obtained from measurements or modelling (analytical or numerical) are coupled using appropriate connection parameters to predict the assembly receptance [1]. The coupling might be rigid, flexible, or flexible-damped based on the assembly configuration [18]; see Fig. 1.

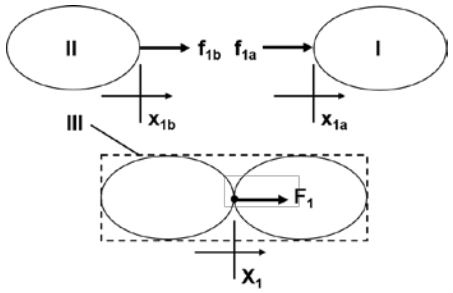

Figure 1. Two component RCSA model: I and II are individual components while III is assembly of I and II.

The components' direct receptances can be described as $h_{1a1a} = \frac{x_{1a}}{f_{1a}}$ and $h_{1b1b} = \frac{x_{1b}}{f_{1b}}$ for components I and II, respectively. The compatibility condition for rigid coupling is defined to be $x_{1b} - x_{1a} = 0$. The equilibrium condition, $f_{1a} + f_{1b} = F_1$, must also be described in order to equate the sum of internal (component) forces to the external (assembly) force. Finally, the assembly direct receptance at coordinate X_1 can be expressed as shown in Eq. 1.

$$H_{11} = \frac{X_1}{F_1} = h_{1a1a} - h_{1a1a}(h_{1a1a} + h_{1b1b})^{-1} h_{1a1a} \quad (1)$$

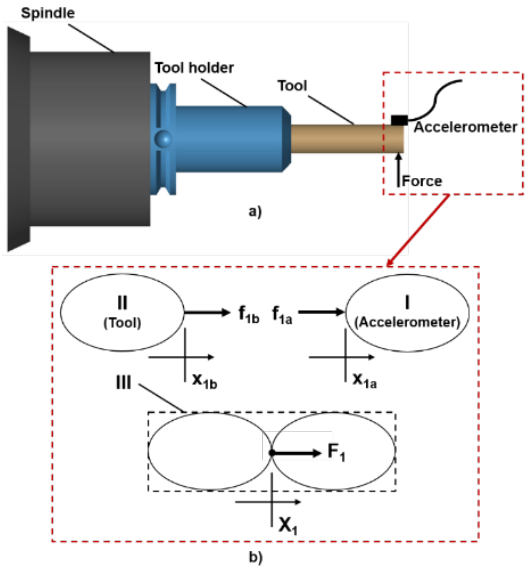

Figure 2. FRF measurement and the RCSA model.

INVERSE RCSA FOR MEASURED RECEPTANCE COMPENSATION

Tool tip receptances are often measured using an instrumented hammer to excite the structure and a low-mass accelerometer to measure the response to the applied force (Fig. 2a). However, the experimental receptance is different from the actual tool tip receptance due to the accelerometer mass and cable effects. The mass and cable effect can be compensated using inverse RCSA. Figure 2b shows the RCSA model for the accelerometer-tool assembly. In the model, it is assumed that the accelerometer is rigidly coupled to the tool tip.

The measured assembly receptance is $H_{11} = \frac{X_1}{F_1}$. The accelerometer and tool's direct receptances are described as $h_{1a1a} = \frac{x_{1a}}{f_{1a}}$ and $h_{1b1b} = \frac{x_{1b}}{f_{1b}}$, respectively. Using inverse RCSA, the actual tool tip receptance, h_{1b1b}, is:

$$h_{1b1b} = -h_{1a1a} + h_{1a1a}(h_{1a1a} - H_{11})^{-1}h_{1a1a} \qquad (2)$$

The accelerometer receptance is defined to be $h_{1a1a} = \frac{1}{-m\omega^2 + ic\omega}$, where *m* is the accelerometer mass and *c* is the viscous damping coefficient that quantifies the cable's energy dissipation. Note that *c* can be set to zero if damping compensation is not desired.

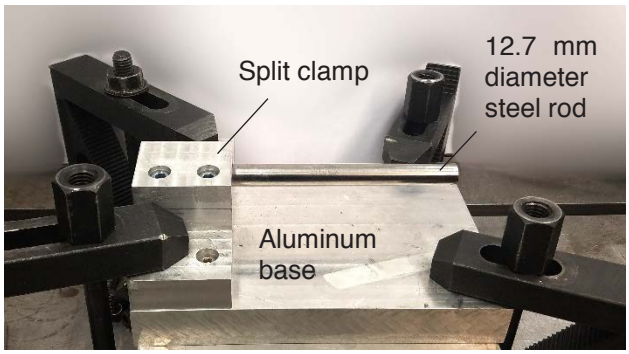

Figure 3. 12.7 mm diameter rod setup.

RESULTS

Experiments were performed on two setups: 12.7 mm diameter and 6.35 mm diameter steel rods with clamped-free boundary conditions. Figure 3 displays a photograph of the 12.7 mm diameter rod measurement platform. A split clamp was used to hold the rod at the desired cantilever length. The 6.35 mm diameter rod was clamped in an ER16 collet holder with a CAT-40 interface, which was then secured using a manual draw bolt in a spindle nose attached to a large steel block; see Fig. 4.

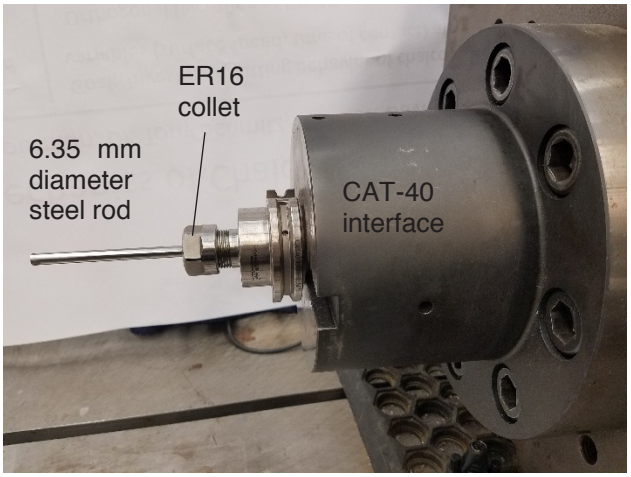

Figure 4. 6.35 mm diameter rod setup.

For both rod diameters, multiple stickout lengths were selected and measurements were performed with: a medium-size accelerometer (PCB 352A21), a small-size accelerometer (PCB 352C23), and a laser vibrometer (Polytec OFV-534). The latter provided a non-contact measurement reference with no mass loading. To obtain the accelerometer-cable masses, measurements were performed using an Ohaus AV264C Adventurer ProAnalytical Balance (0.1 mg resolution).

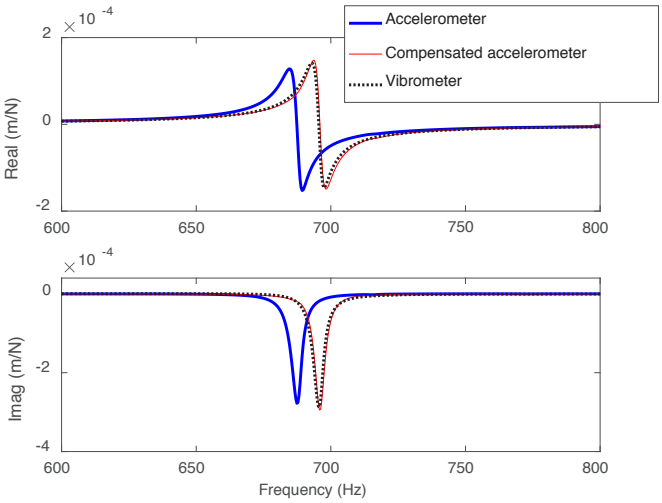

Figure 5. Results for 12.7 mm diameter rod with a stickout length of 102 mm using the medium accelerometer.

Figure 5 shows the measurement and compensation results for the 12.7 mm diameter rod with a stickout length of 102 mm using the medium accelerometer, where the accelerometer-cable mass was 706 mg. It is seen that the accelerometer FRF has a lower natural frequency than the vibrometer (non-contact)

FRF. Using Eq. 2 and the measured mass, the mass-loaded FRF was compensated to remove the mass loading effect. This result matches closely with the vibrometer result (the phase error in the vibrometer measurement due to a small time delay between the hammer and vibrometer amplifying electronics was compensated using the technique described in [19]).

A summary of the 12.7 mm diameter rod measurement results for both accelerometers at four different stickout lengths is provided in Table 1. The average percent error in the compensated result for all tests is 0.005%. Prior to compensation, the percent error in natural frequency for the medium accelerometer was 1.0% and 0.4% for the small accelerometer.

Table 1. 12.7 mm diameter rod mass compensation results.

Stick -out (mm)	Vibr. natl. freq. (Hz)	Accel. natl. freq. (Hz)	% error	Comp. natl. freq. (Hz)	% error
Medium accelerometer (706 mg)					
102	695.4	687.4	1.10	695.8	-0.05
111	597.8	592	0.97	598.5	-0.11
118	538.3	533.3	0.92	537.5	0.15
124	492.1	487.1	1.01	492.1	0
Small accelerometer (275 mg)					
102	698.1	695	0.44	698.1	0
111	613.8	611.5	0.37	614.2	-0.06
118	555.4	552.8	0.46	555	0.07
124	503	501.3	0.33	502.8	0.03

Measurement results for the 6.35 mm diameter rod are presented in Table 2. The average percent error in the compensated results for all tests is -0.09%. Prior to compensation, the percent error in natural frequency for the medium accelerometer was 5.8% and 2.4% for the small accelerometer.

Table 2. 6.35 mm diameter rod mass compensation results.

Stick -out (mm)	Vibr. natl. freq. (Hz)	Accel. natl. freq. (Hz)	% error	Comp. natl. freq. (Hz)	% error
Medium accelerometer (680 mg)					
79	688.2	646.0	6.1	688.9	-0.10
89	546.3	516.0	5.5	547.0	-0.13
Small accelerometer (275 mg)					
79	687.8	671.0	2.4	688.2	-0.06
89	545.5	532.2	2.4	545.9	-0.07

*Stickout lengths are approximate. Different setups were used between the small and medium accelerometers.

In addition to the 6.35 mm diameter rod measurements, experiments were also performed on two clamped-clamped-clamped-free boundary condition thin ribs. The 6.35 mm diameter rod and ribs represent examples of flexible structures that may have both their FRF natural frequency(s) and amplitudes affected by the contact measurement approach. For the ribs, one rib material was 6061-T6 aluminum and the other was 6Al-4V titanium. The titanium rib was approximately an order of magnitude stiffer than the aluminum rib at the center of the unsupported edge. The small accelerometer and laser vibrometer were used for the rib measurements. The setup is shown in Fig. 6, where the thin ribs were fixed to the table using cyanoacrylate and the measurement location was the center of the unsupported edge.

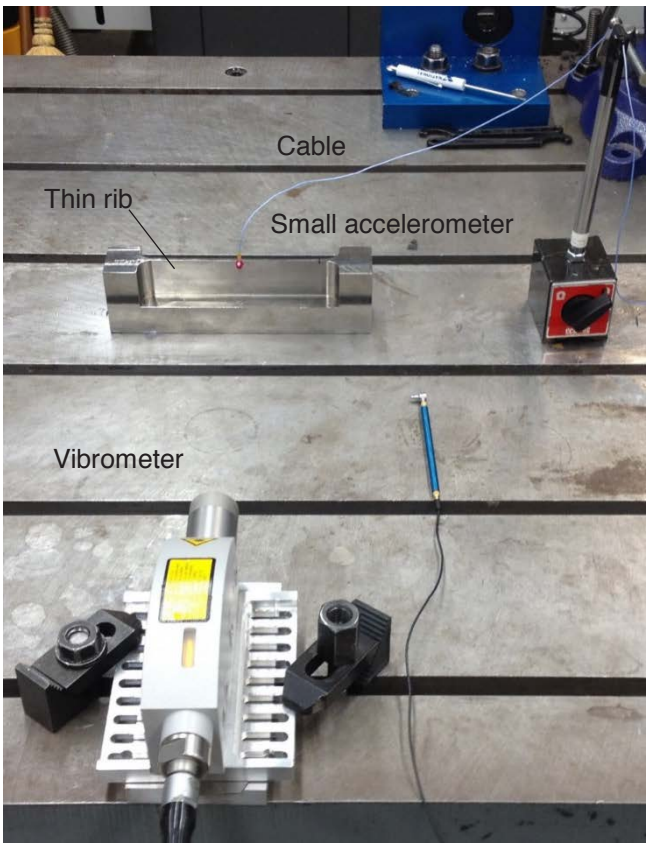

Figure 6. Thin rib setup.

Figures 7-9 display measurement and compensation results. In Fig. 7, FRFs for the 6.35 mm diameter rod with a stickout length of 89 mm are displayed. It is seen that the accelerometer-based FRF has a lower natural frequency (due to the mass loading) and a reduced amplitude (due to the cable damping). The measured accelerometer-cable mass was substituted in its modeled receptance and the damping

coefficient was adjusted to provide an amplitude match between the compensated FRF and vibrometer FRF. The aluminum and titanium rib results are shown in Figs. 8 and 9. The mass loading and damping compensation results for the 6.35 mm diameter rod and both ribs are summarized in Table 3.

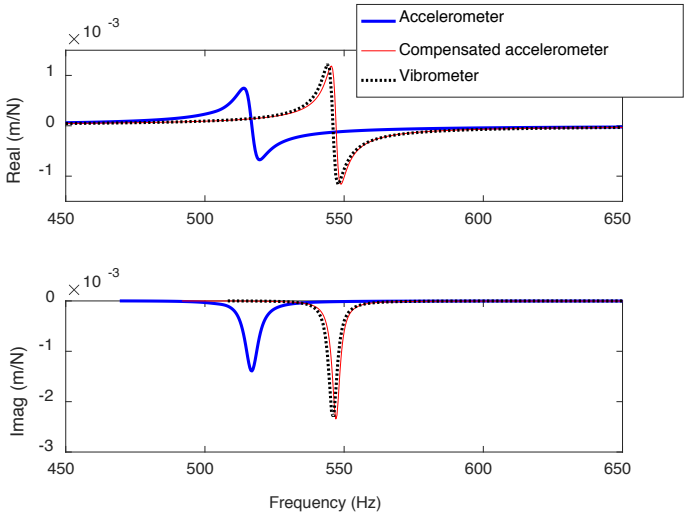

Figure 7. 6.35 mm diameter rod results for medium accelerometer with 89 mm stickout length.

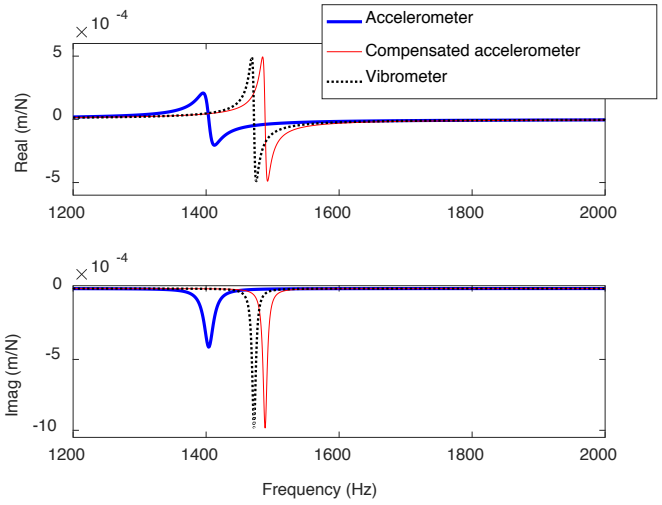

Figure 8. Aluminum rib results.

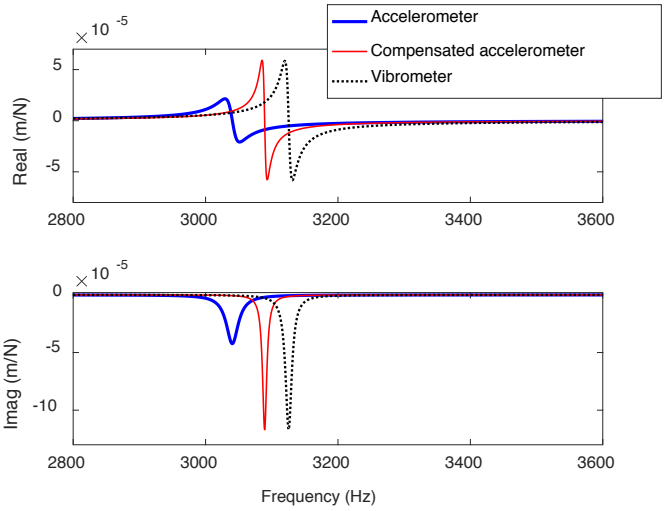

Figure 9. Titanium rib results.

Table 3. Mass loading and damping compensation results.

Struc-ture	Vibr. natl. freq. (Hz)	Accel. natl. freq. (Hz)	% error	Comp. natl. freq. (Hz)	% error	c (N-s/m)
6.35 mm rod	Medium accelerometer (680 mg)					
79 mm	688.2	646.0	6.1	688.9	-0.10	0.13
89 mm	546.3	516.9	5.4	547.0	-0.13	0.15
6.35 mm rod	Small accelerometer (275 mg)					
79 mm	687.8	671.0	2.4	688.2	-0.06	0.07
89 mm	545.5	532.2	2.4	545.9	-0.07	0.07
Rib	Small accelerometer (286.4 mg)					
Al 6061-T6	1472	1404	4.6	1488	-1.13	0.17
Ti 6Al-4V	3125	3040	2.7	3089	1.16	0.85

Although this does not represent a comprehensive study of cable damping effects, conclusions can be drawn from Table 3. First, for a single structure and a single accelerometer, the damping value was consistent. Specifically, 1) c = 0.07 N-s/m for both 6.35 mm diameter rod measurements using the small accelerometer; and 2) c = 0.13 N-s/m and 0.15 N-s/m for the 6.35 mm diameter rod measurements using

the medium accelerometer. Presumably, the change is c values is due to the difference in cables and/or cable configuration between the two accelerometers/setups.

Second, the *c* value may scale with the structure's stiffness. Of the three structures, the 6.35 mm diameter rod was the most flexible, followed by the aluminum rib, and, finally, the titanium rib. Considering the small accelerometer, the *c* values increase from 0.07 to 0.17 to 0.85, respectively, for these three setups. Future testing will focus on an improved understanding of the viscous damping coefficient required to compensate for cable-based energy dissipation.

CONCLUSIONS

This paper described the application of inverse Receptance Coupling Substructure Analysis (RCSA) to mass and damping compensation for accelerometer-based impact testing. The measurement (assembly) FRF was used together with a point mass-viscous damping model of the accelerometer-cable to determine the compensated tool point FRF using the analytical inverse RCSA approach. Experiments were completed for: 1) two rod diameters and multiple stickout lengths for clamped-free rod boundary conditions; and 2) thin ribs with clamped-clamped-clamped-free boundary conditions. The average percent error in compensated natural frequency over all 14 tests reported in this study was -0.02%.

A limitation to the compensation procedure is that a first-principles approach to predict the viscous damping coefficient based on cable properties is not presented. However, the absence of physics-based models is true, in general, for mechanical damping in structures. Consider finite element analysis, for example. The eigensolution (natural frequencies and mode shapes) can be predicted quite accurately if boundary conditions are properly described. However, if scaled FRFs are desired, the damping type and values must be entered based on the user's prior experience. The approach presented here provides a mechanism for incorporating damping, as well as mass, in FRF compensation and motivates future work to approximate, tabulate, and (potentially) model the cable behavior.

ACKNOWLEDGEMENTS

This material is based upon work supported by the National Science Foundation under Grant No. CMMI-1561221.

REFERENCES

[1] Tlusty, G., 2000, Manufacturing Processes and Equipment, Prentice Hall, Upper Saddle River, NJ.

[2] Altintas, Y., 2000, Manufacturing Automation: Metal Cutting Mechanics, Machine Tool Vibrations, and CNC Design, Cambridge University Press, Cambridge, UK.

[3] Schmitz, T.L. and Smith, K.S., 2009, Machining Dynamics: Frequency Response to Improved Productivity, Springer, New York, NY.

[4] Schmitz T.L. and Donaldson R.R., 2000. Predicting High-Speed Machining Dynamics by Substructure Analysis, CIRP Annals-Manufacturing Technology, 49/1: 303-308.

[5] Schmitz, T., Davies, M., Medicus, K., and Snyder, J., 2001, Improving High-Speed Machining Material Removal Rates by Rapid Dynamic Analysis, Annals of the CIRP, 50/1: 263-268.

[6] Schmitz, T., Davies, M., and Kennedy, M., 2001, Tool Point Frequency Response Prediction for High-Speed Machining by RCSA, Journal of Manufacturing Science and Engineering, 123: 700-707.

[7] Duncan, G.S., Tummond, M., and Schmitz, T., 2005, An Investigation of the Dynamic Absorber Effect in High-Speed Machining, International Journal of Machine Tools and Manufacture, 45: 497-507.

[8] Schmitz, T. and Duncan, G.S., 2005, Three-Component Receptance Coupling Substructure Analysis for Tool Point Dynamics Prediction, Journal of Manufacturing Science and Engineering, 127/4: 781-790.

[9] Schmitz, T. and Duncan, G.S., 2006, Receptance Coupling for Dynamics Prediction of Assemblies with Coincident Neutral Axes, Journal of Sound and Vibration, 289/4-5: 1045-1065.

[10] Schmitz, T., Powell, K., Won, D., Duncan, G.S., Sawyer, W.G., and Ziegert, J., 2007, Shrink Fit Tool Holder Connection Stiffness/Damping Modeling for Frequency Response Prediction in Milling, International Journal of Machine Tools and Manufacture, 47/9: 1368-1380.

[11] Cheng, C.-H., Duncan, G.S., and Schmitz, T., 2007, Rotating Tool Point Frequency Response Prediction using RCSA, Machining Science and Technology, 11/3: 433-446.

[12] Filiz, S., Cheng, C.-H, Powell, K., Schmitz, T., and Ozdoganlar, O., 2009, An Improved Tool-Holder Model for RCSA Tool-Point Frequency Response Prediction, Precision Engineering, 33: 26-36.

[13] Schmitz, T., 2010, Torsional and Axial Frequency Response Prediction by RCSA, Precision Engineering, 34: 345-356.

[14] Kumar, U. and Schmitz, T., 2012, Spindle Dynamics Identification for Receptance Coupling Substructure Analysis, Precision Engineering, 36/3: 435-443.

[15] Ewins, D.J., 2009, Modal Testing: Theory, Practice and Application, 2nd Ed., Wiley, New York, NY.
[16] Özşahin, O., Özgüven, H.N., and Budak, E., 2010, Analysis and Compensation of Mass Loading Effect of Accelerometers on Tool Point FRF Measurements for Chatter Stability Predictions, International Journal of Machine Tools and Manufacture, 50/6: 585-589.
[17] Olvera, D., Elías-Zúñiga, A., Martínez-Romero, O., de Lacalle, L.L., Martínez-Alfaro, H., Siller, H.R., and Pineda, M.W., 2016, Improved Predictions of the Stability Lobes for Milling Cutting Operations of Thin-wall Components by Considering Ultra-miniature Accelerometer Mass Effects, The International Journal of Advanced Manufacturing Technology, 86/5-8: 2139-2146.
[18] Schmitz, T.L. and Smith, K.S., 2012, Mechanical Vibrations: Modeling and Measurement. Springer, New York, NY.
[19] Ganguly V. and Schmitz T.L., 2014, Phase Correction for Frequency Response Function Measurements, Precision Engineering, 38: 409-413.

TASK-SPECFIC MEASUREMENT UNCERTAINTY OF A HEMISPHERICAL ARTIFACT

Lucas M. Valdez[1], Mario O. Valdez[2] and Joshua D. Montano[3]
[1] Manufacturing Science and Engineering
[2]Production Agency Quality
[3] Prototype Fabrication
Los Alamos National Laboratory (LANL)
Los Alamos, NM, USA

INTRODUCTION

Measurement uncertainty has long been utilized in all coordinate measurements as a way of validating the measurement result [1]. The *ISO Guide to the Expression of Uncertainty in Measurements* (GUM) has been the accepted standard used throughout government institutions, academia and industry for estimating measurement uncertainty. However, as more complex geometries require the derivation of complicated measurement models, where linearized approximations are no longer valid, specialized task-specific uncertainty analysis had been developed [2]. Task-specific uncertainty is defined as "*the measurement uncertainty associated with the measurement of a specific feature using a specific measurement plan*" [2].

There are multiple methods for determining task-specific uncertainty: sensitivity analysis, expert judgement, experimental methods with calibrated artifacts, computer simulations, hybrid methods and historical data using statistics [2], of which simulation is preferred. The most common simulation methods are the Virtual CMM, Simulation by Constraints (SBC), the Expert CMM (ECMM) and general Monte Carlo, with SBC the most commonly used [3] [4] [5] [6] [7] [8] and implemented on several form and size measurements. ISO has a standard which specifically details requirements for writing or developing task-specific measurement uncertainty using computer simulations [9].

This paper will focus on estimating the task-specific uncertainty of a calibrated hemispherical (hemi-sphere) shell Coordinate Measuring Machine (CMM) artifact, using offline uncertainty simulation software, where the measurands are inner and outer profiles. The artifact and measurement process will be described, followed by how the task-specific measurement uncertainty is determined.

MEASUREMENT ARTIFACT AND PROCESS

Hemispherical Shell

The CMM artifact is a thick-walled, hemisphere shell, made of AISI A2 tool steel. It has an 8 mm thick flange with datum A on the bottom of the flange, datum B is the central axis of the outer cylindrical-feature and datum C is a fiducial (flat surface) perpendicular to datum A. It has three, 120° equally-spaced, counter-bore holes for clamping down a holding fixture. The inner and outer contour profiles have tolerances of ±0.020mm. See FIGURE 1 for a description of datum reference system.

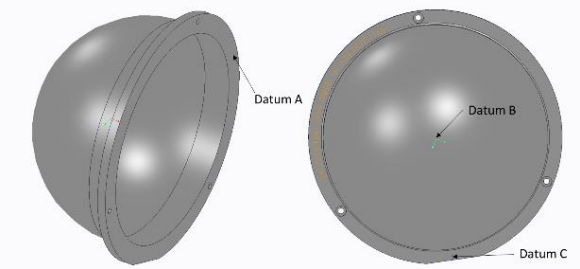

FIGURE 1. CAD Model of Hemispherical Artifact (Unclassified).

Measurement Program

Measurement data is collected every 2° from 0° to 88° including 0°, which results in 45 data points in the polar direction and measured every 1.5° from 0° to 355.5°, including 0° in the azimuth direction which will equate 238 polar bands of data, for each contour. A total of 10,710 data points is collected from a single contour and 21,420 points total. FIGURE 2 shows the measurement directions for both inner and outer contours of the hemispherical shell. All data collection is achieved using dynamic/continuous scanning.

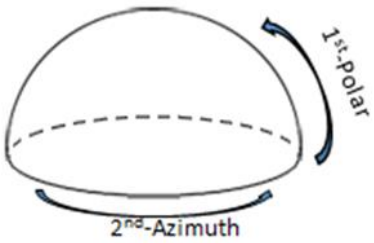

FIGURE 2. Measuring Direction of Hemispherical Shell (Unclassified)

Measurement Setup

The artifact is mounted on a custom fixture, which holds the artifact with three pegs. A mock measurement setup can be seen in FIGURE 3.

FIGURE 3. Measurement Setup (Unclassified)

FIGURE 4 shows the styli used to gather measurements of the inner and outer contours of the artifact.

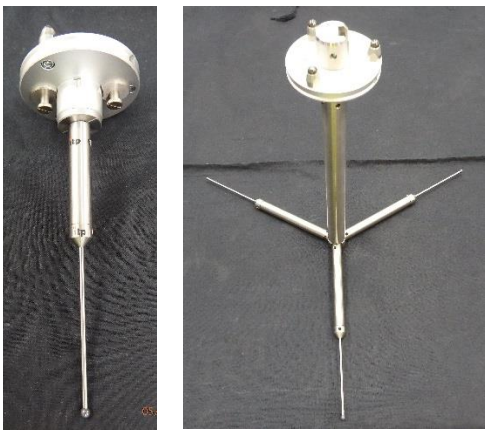

FIGURE 4. Inner Contour Measurement Stylus, Left; Outer Contour Measurement Styli, Right (Unclassified)

PROFILE UNCERTAINTY

Background

Since the measurands are the inner and outer profiles, classical uncertainty analysis becomes a formidable task which does not have a preferred approach. Uncertainty estimates for form and size measurements have been done previously [4], however, not much has been done on profile measurements. This may be the result of several factors, such that profile tolerances can cover form, orientation, size and location of the geometry [10] and only specific Geometric Dimensioning and Tolerancing (GD&T) may be sought. This research intends to investigate and estimate the uncertainty analysis of the inner and outer profiles of the calibrated artifact, where the profiles are of the most interest due to the relationship with the radial wall thickness calculation.

Uncertainty Analysis Method

The preferred approach taken in this research is to utilize the SBC principles. SBC is chosen on the premise that the authors feel more confident that it will help isolate the main sources of error more accurately and its ability to handle different error states.

SBC utilizes both Full Parametric States (FPS) and acceptance testing criteria (e.g. ISO or B89), which establishes performance evaluation parameters (i.e., linear accuracy, offset of volumetric performance, volumetric performance and repeatability). These parameter estimations however, do not fully constrain the CMM to rigid body errors. SBC can be used to:

1. Establish a set of hypothetical CMM error states that are consistent with either B89 or ISO standards.
2. Simulates the measuring process of the intended object using each CMM in the measurement bounding set.
3. Noting the range of the final measurement result obtained through the simulations.

The main error sources affecting the measurements will be the CMM, the environment, the probing system and the form error. Simulations will be conducted in different combinations of all error sources and then individual error sources. All simulations will be analyzed individually for both the inner and outer profiles. Each simulation results in the mean

error, standard deviation and the overall uncertainty, for a 95% confidence level.

RESULTS

Uncertainty Reporting

In reporting the uncertainty, it was determined that all four sources, as well as all combinations would be tested. The combination of the sources, would come out to a total of 15 runs, for each contour, totaling, 30 simulations. TABLE 1 shows the sources and the combinations.

TABLE 1. Uncertainty Source and Combinations

Error Sources
CMM, Environment, Probe, Form
Environment, Probe, Form
CMM, Probe, Form
Probe, Form
CMM, Environment, Form
Environment, Form
CMM, Form
Form
CMM, Environment, Probe
Environment, Probe
CMM, Probe
Probe
CMM, Environment
Environment
CMM

Uncertainty Calculations

The uncertainty analysis is done by SBC method, however, the way the software calculates the uncertainty from sources is by calculating the standard deviation and the mean error. Eq. 1 shows the uncertainty formula:

$$U = 2\sigma + \bar{\varepsilon} \quad (1)$$

Where σ, the standard deviation and $\bar{\varepsilon}$, is the mean error. The uncertainty is calculated the same way NIST determines uncertainty via SBC. Thus the results for the inner contour and outer contour are reported with the standard deviation, the mean error and the uncertainty.

Inner Contour

The inner contour points, 10,710, are used in the simulation software. The average time for the simulation was approximately two hours. TABLE 2 shows the results for the inner contour.

TABLE 2. Inner Contour Results

Interactions - Inner Contour (100 iterations)			
Error Source	Standard Deviation (µm)	Mean Error (µm)	Uncertainty (µm)
CMM, Environment, Probe, Form	2.67	5.61	10.95
Environment, Probe, Form	2.97	5.79	11.73
CMM, Probe, Form	0.73	2.74	4.20
Probe, Form	0.68	2.49	3.85
CMM, Environment, Form	2.52	3.74	8.77
Environment, Form	3.34	4.49	11.18
CMM, Form	0.56	1.43	2.54
Form	0.00	0.00	0.00
CMM, Environment, Probe	3.03	7.04	13.09
Environment, Probe	3.02	6.82	12.87
CMM, Probe	0.62	3.32	4.56
Probe	0.72	3.01	4.45
CMM, Environment	3.11	5.80	12.01
Environment	3.25	4.98	11.48
CMM	0.58	1.71	2.86

From TABLE 2, the results show that our largest uncertainty is coming from the environment. This seems viable, since the lab that the data was collected in, had several temperature excursions, from various sources. Our smallest source was from the form error, which is logically sound since this artifact is traceable to NIST and had very low form error upon calibration. Overall, the uncertainty for the inner contour was within specification.

Outer Contour

The outer contour points, 10,710, are used in the simulation software. The average time for the simulation was approximately two hours. TABLE 3 shows the results for the outer contour.

TABLE 3. Outer Contour Results

Interactions - Outer Contour (100 iterations)			
Error Source	**Standard Deviation (µm)**	**Mean Error (µm)**	**Uncertainty (µm)**
CMM, Environment, Probe, Form	6.32	6.77	19.41
Environment, Probe, Form	6.77	3.12	16.65
CMM, Probe, Form	5.51	3.59	14.61
Probe, Form	4.72	5.15	14.58
CMM, Environment, Form	3.50	5.22	12.21
Environment, Form	3.04	5.91	11.98
CMM, Form	3.28	5.18	11.74
Form	3.18	5.28	11.64
CMM, Environment, Probe	3.21	5.06	11.49
Environment, Probe	2.91	4.21	10.04
CMM, Probe	1.76	3.23	6.74
Probe	2.02	2.65	6.70
CMM, Environment	0.48	1.71	2.67
Environment	0.52	1.41	2.45
CMM	0.00	0.00	0.00

From TABLE 3, the results show that the probe contribution showed the largest uncertainty. This makes sense, since there were three probes used in measuring the outer contour. A single probe could not be used for measuring the outer contour, thus multiple probe configuration was needed. This in of itself had a tremendous effect on the uncertainty. The lowest uncertainty was from form error again. With the same rationalization as the inner, because it is traceable to NIST and had low form error, it is appropriate that form error was the lowest.

CONCLUSION

In conclusion the simulation by constraints technique has proved to be a valuable method for estimating the task specific measurement uncertainty. The research presented here also identified the largest error contributors and areas where future investments and efforts should be applied in achieving improved measurements.

FUTURE WORK

In future efforts, the same experiment will be run again, however, this time more than one run will be conducted for each error source. This way statistics can be run on the values and one would have a much better understanding of the sources of uncertainty and how they are affecting the measurements. Also, more than just these types of artifacts will be run, to get a better understanding of how the sampling, geometries and measuring processes will affect the uncertainty.

REFERENCES

[1] *JCGM 100:2008 - Evaluation of Measurement Data - Guide to the Expression of Uncertainty in Measurement,* BIPM, 2008.

[2] R. G. Wilhelm, R. Hocken and H. Schwenke, "Task Specific Uncertainty in Coordinate Measurement," *CIRP Annals - Manufacturing Technology,* vol. 50, no. 2, pp. 553-563, 2001.

[3] S. D. Phillips, D. Borchardt, D. Sawyer, W. T. Estler, D. Ward, K. Eberhardt, M. S. Levenson, M. McClain, B. Melvin, T. Hopp and Y. Shen, "The Calcualtions of CMM Measurement Uncertainty via the Method of Simulations by Constraints," in *American Society for Precision Engineering*, Norfolk, 1997.

[4] K. D. Summerhays, M. P. Henke, C. W. Brown, R. P. Henke and J. Baldwin, "A Tool for Determining Task-Specific Measurement Uncertainties in GD&T Parameters Obtained from Coordinate Measuring Machines," in *American Society for Precision Engineering*, 2002.

[5] S. D. Phillips, B. Borchardt, A. J. Abackerli, C. Shakarji, D. Sawyer, P. Murray, B. Rasnick, K. D. Summerhays, J. M. Baldwin, R. P. Henke and M. P. Henke, "The Validation of CMM Task Specific Measurement Uncertainty Software," in *American Society for Precision Engineering Summer Topical*, Charlotte, 2003.

[6] K. D. Summerhays, J. M. Baldwin, D. A. Campbell and R. P. Henke, "Application of Simulation Software to Coordinate Measurement Uncertainty Evaluation," in *American Society for Precision Engineering*, 2004.

[7] K. D. Summerhays, "Conformance, Tracebility and the Rising Role of Measurement Uncertainty," *Fabricating & Metalworking,* pp. 54-56, June/July 2005.

[8] J. Beaman and E. Morse, "Experimantal Evaluation of Software Estimates of Task Specific Measurement Uncertainties for CMMs," *Precision Engineering,* vol. 34, pp. 28-33, 2010.

[9] ISO, "Geometrical Product Specification - Coordinate Measuring Machines: Technique for determining the uncertainty in measurement - part 4: Evaluating task-specific uncertainty using simulation," 2008.

[10] *ASME Y14.5.1M Mathematical Definition of Dimensioning and Tolerancing Principles,* American National Standards, 2012.

[11] S. Phillips and K. Summerhays, *Measurement Sampling Strategies,* 2015.

Characterizing Spatial Resolution of a Fringe Projection System for Measuring Additively Manufactured Surfaces

Bin Zhang[1], Angela Davies[1], John Ziegert[2], and Christopher Evans[2]
[1]Department of Physics and Optical Science
The University of North Carolina at Charlotte,
Charlotte, NC, USA
[2]Department of Mechanical Engineering and Engineering Science
The University of North Carolina at Charlotte,
Charlotte, NC, USA

INTRODUCTION

One of the biggest challenges for metal additive manufacturing is the inability to control surface quality. An approach to solve this problem is to use in-situ metrology systems. Fast data acquisition and a relatively long working distance make fringe projection a viable solution for in-situ metrology of layered metal additive manufacturing process [1], [2]. Surfaces created by metal additive processes, particularly the laser powder bed fusion (LPBF) process, are rough, porous and textured. The roughness and texture are the results of laser scanning and are related to the process parameters such as laser power, scan velocity, and hatch distance (laser step over). The combination of the parameters creates a unique surface texture with rich spatial frequency content. Figure 1 shows such a texture with a fused square on a layer of Inconel-625 metal powder. The laser scan path is along the vertical axis with a step over of 90 µm. The laser power is 290 W, and the scan speed is 110 mm/s. The fused surface is measured in situ by a fringe projection system. The measured topography shows clear periodic structures near the bottom edge along the x-axis (Figure 1 (d)). Fourier analysis of the measured profile shows a strong peak at the spatial frequency corresponding to twice the hatch distance, suggesting a merge of two scans due to the closeness (time-wise) of the two scan paths.

The capability to resolve such detailed texture relies on the instrument's spatial resolution. One metric that characterizes the spatial resolution for a topography measuring instrument is the instrument transfer function (ITF) [3]. ITF delivers the factor by which the amplitude of a spatial frequency component drops with increasing spatial frequency.

In this paper, we study the applicability of ITF to a fringe projection system for measuring additively manufactured surfaces and provide a practical method to measure ITF using a stepped surface.

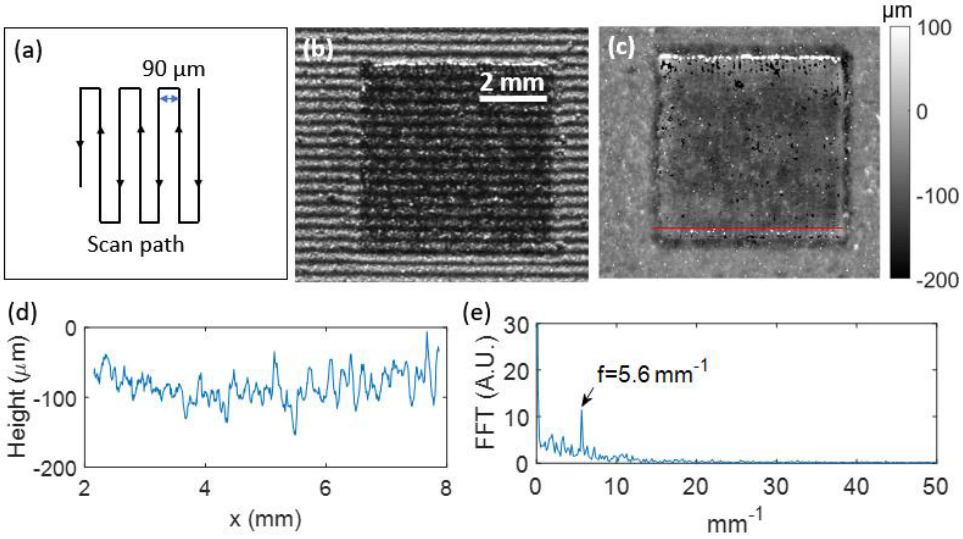

FIGURE 1. A fused square on a layer of Inconel-625 metal powder created by the LPBF process: (a) laser scan path, (b) sinusoidal fringe pattern on a fused layer of powder, (c) the height map of the fused powder layer, (d) a cross-section profile near the bottom edge of the fused region, and (d) the Fourier spectrum of the line trace.

FRINGE PROJECTION SYSTEM

The fringe projection system is developed for a LPBF machine created at the Edison Welding Institute (FIGURE). The fringe projection system consists of a commercial DLP projector (Vivitek Qumi Q5) and a machine vision camera (Point Grey Flea 3). The projector is mounted on top of the chamber, illuminating the powder bed through an AR coated glass window at a 35° angle. The camera is mounted inside the chamber, approximately 200 mm above the powder bed. To generate a high-density fringe pattern, the original projection lens is replaced with a 125-mm achromatic doublet lens and an adjustable lens tube. This lens can project an image of approximately 45 × 28 mm^2 at approximately 800 mm. The fringe pitch is 0.35 mm. The camera has a resolution of 4096 × 2160 pixels and a field of view of 28 × 15 mm, giving a pixel footprint (pixel pitch at object space) of 6.8 μm per pixel.

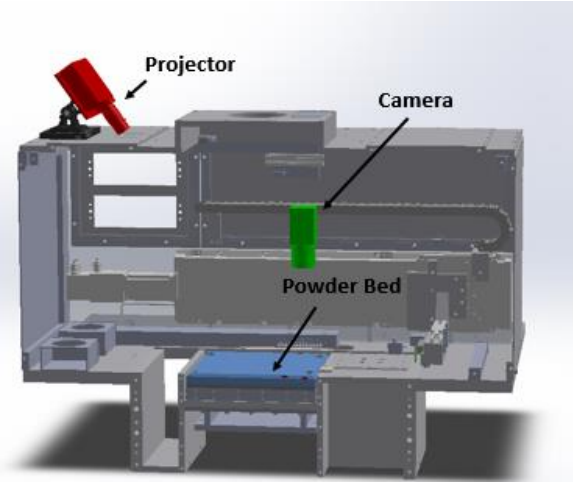

FIGURE 2. An in-situ fringe projection system for a LPBF machine (some parts are hidden for clear visualization).

The fringe projection system uses a phase shifting algorithm to measure the height variation of the object [4]. The fringe pattern is a sinusoidally-modulated gray scale image. The irradiance distribution is written as

$$I_i(x,y) = I_0\left[1+\cos\left(\frac{2\pi x}{p}+\delta_i\right)\right], \qquad (1)$$

where *i* indicates the i^{th} image, I_0 is the irradiance modulation, *p* is the fringe pitch, and δ is the phase-shifting step size which is given by

$$\delta_i = \frac{i-1}{N}2\pi, \qquad i = 1,\dots,N. \qquad (2)$$

where *N* is the total number of phase steps. A seven-step (*N*=7) phase shifting algorithm is chosen in this study as a balance between the number of required images and the lowest phase error. The seven captured fringe images give the wrapped phase of the surface, namely

$$\phi(x,y) = arctan\left(\frac{-\sum_{i=1}^{N}\sin(\delta_i)I_i(x,y)}{\sum_{i=1}^{N}\cos(\delta_i)I_i(x,y)}\right). \qquad (3)$$

After obtaining the wrapped phase map, a phase unwrapping algorithm is used to unfold the wrapped phase, which lies in the range from -π to π, to an extended range. Next, the carrier phase is removed from the unwrapped phase map by fitting it to Legendre polynomials. Finally, the remaining phase map is converted to the height map using a pre-calibrated system parameter called the effective wavelength. Details of these procedures can be found in our previous paper [5]. The relation between the height map and the remaining phase map is written as

$$z(x,y) = \lambda_{eff}(x,y)\cdot\phi(x,y), \qquad (4)$$

where *z(x,y)* is the height map of the measured surface, and $\lambda_{eff}(x,y)$ is the effective wavelength map.

INSTRUMENT TRANSFER FUNCTION

The foundation of an ITF analysis is the linear theory, i.e. for a linear system, the output *g(x)* can be expressed as the convolution of the input *f(x)* and the system impulse response *h(x)*, namely

$$g(x) = f(x)\otimes h(x). \qquad (5)$$

In the spatial frequency domain, it is written as

$$G(f) = F(f)\cdot H(f), \qquad (6)$$

where *G(f)*, *F(f)* and *H(f)* are the Fourier transform of *g(x)*, *f(x)* and *h(x)*, respectively. For an input being a height map, the function *H(f)* is called the ITF. Thus, ITF is the ratio of the Fourier transform of the measured surface to the Fourier transform of the true surface. namely

$$H(f) = \frac{G(f)}{F(f)}. \qquad (7)$$

To characterize an instrument with an ITF, the instrument must be justified as a linear system. A linear system can be determined by the superposition property in the linear theory, i.e. the output of the sum of several inputs equals to the sum of the output of each individual input. In other words, the system must be surface independent. We show the fringe projection

system satisfies this property when certain conditions are met [6]. Specifically, a fringe projection system can be approximated as a linear system when two conditions are met: 1) the amplitude of each spatial frequency component of the surface is much smaller than the effective wavelength, and 2) the width of the point spread function of the camera (25 μm) is much smaller than the effective wavelength (0.5 mm). The first condition states that the linearity is related to the amplitude of the surface. To draw a linearity boundary for a measured surface, we calculate the ITF from the simulations of fringe projection measurements of sinusoidal surfaces. The ITF does not change until the amplitude of the sinusoidal surface reaches to a limit, suggesting the linearity region is under a maximum amplitude at that spatial frequency. We define the linearity limit as the amplitude at which the ITF changes by 1%. Figure 3 shows this surface amplitude limit over a spatial frequency range between 1 to 100 cycles/mm.

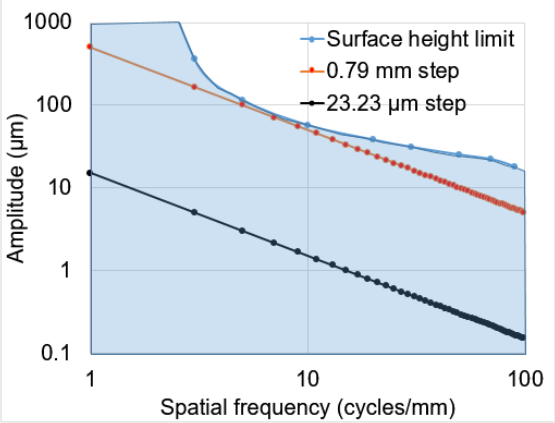

FIGURE 3. The surface height limit defines the maximum amplitude for each spatial frequency component of a measured surface for the system to behave approximately linear. A 23-μm stepped surface is below the linearity limit.

To measure the ITF experimentally, we need a test specimen which satisfy two needs: 1) it contains spatial frequency from 0 to an expected cut-off frequency, and 2) the amplitude of each spatial frequency component is smaller than the linearity limit. A stepped surface satisfies these criteria. A stepped surface contains infinite spatial frequency components; each component has an amplitude inversely proportional to its spatial frequency. The step height determines the amplitude of each spatial frequency component, which can be calculated through a Fourier analysis. A stepped surface with a step height below 0.79 mm is within the linear region (see Figure 3). A 23.23-μm step height standard is available in the lab, and is used to measure the ITF.

Conventionally, the ITF is calculated as the ratio of the Fourier transform of the measured step surface to a mathematically perfect step surface, or equivalently the ratio of the square roots of the power spectral density (PSD) functions of the measured and the mathematically perfect step surfaces [7]. In this method, a windowing process is usually used because the boundary of a step is not continuous. The windowing will cause loss of spatial frequency content. A better way to circumvent this problem is to duplicate and fold the step profile to create an artificial double-sided step profile, and to calculate the ITF with the double-sided step profiles.

Measurement of the ITF starts with measuring the stepped surface (VSLI 23.23 μm). The challenge of measuring this surface is the specular surface finish, meaning the scattered light is weak. This causes a low signal-to-noise ratio in the measured topography. Figure 4 shows a fringe pattern on the stepped surface and the height map of the stepped region outlined in red. Even with the highest illumination setting for the projector and a long exposure time (30 seconds) for the camera, the fringe visibility is still very low, leading to noise in the measured height map. The measurement noise can be reduced by averaging many line traces across the edge, but this requires alignment of the line traces with respect to the step edge. This process is similar to the slanted knife edge technique [8]. Figure 5 (a) shows the superimposed step profiles where each line trace is aligned at the step edge. The combined 1-D step profile has a much higher data density; thus, the measurement noise can be reduced by resampling the data. Since the Nyquist sampling rate (106 cycles/mm) is already higher than the camera cut-off frequency (95 cycles/mm), there is no need to oversample the step profile. Thus, we chose a sampling interval equal to the pixel pitch, namely 4.7 μm. The sampling interval is marked by the vertical lines in Figure 5 (a). The height and the x position values are averaged in each sampling interval, and the averaged step profile is shown in Figure 5 (b).

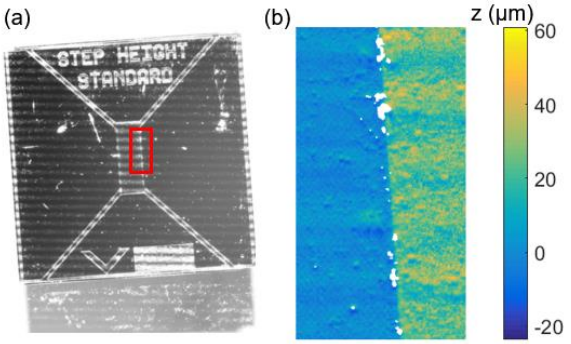

FIGURE 4. Measuring a 23-μm stepped surface with fringe projection: (a) the fringe pattern on the stepped surface, and (b) the measured height map of the outlined region.

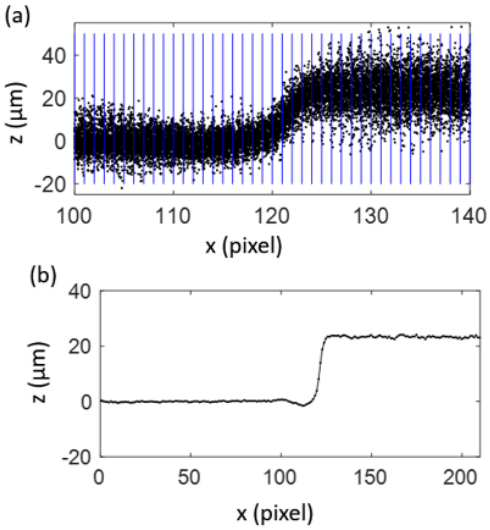

FIGURE 5. Resampling the slanted stepped surface: (a) superimposed step profiles where each profile is aligned along the step edge; the vertical lines show the sampling intervals. (b) The averaged step profile.

The noise on the upper and lower surfaces of the step has been greatly reduced after the resampling, but it is still not enough for a reasonable ITF. Even using the averaged line traces, the noise is not negligible. This causes large errors on the resultant ITF curve. Since ITF is only related to the transition between the lower and the upper surfaces of a step, the noise on the surfaces can be suppressed and this process shouldn't affect the ITF calculation. Thus, we can further reduce the noise by multiplying a noise suppression ratio of 0.1 to the two surface regions outlined in red in Figure 6 (a). Since the transition region is visually determined, it can introduce uncertainty to the ITF result. To evaluate this uncertainty, the window size is varied slightly from the visually determined windows, and the deviation in the ITF is added to the total uncertainty of the measured ITF. The boundary discontinuity issue is circumvented by duplicating and folding the step profile to form a double-sided step profile (Figure 6 (b)). The ITF is calculated by dividing the measured step profile by the mathematically perfect profile. To evaluate the measurement uncertainty, the stepped surface is measured 10 times, and ten ITFs are calculated. The average of the ten ITFs is shown in Figure 7.

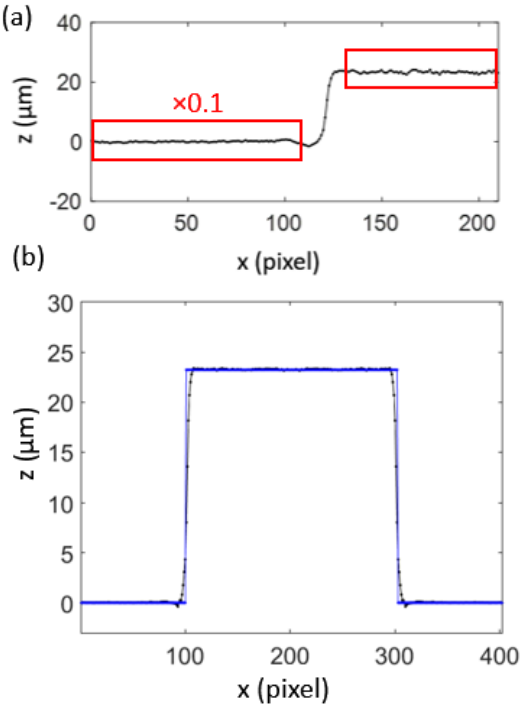

FIGURE 6. Further noise reduction on the averaged step profile: (a) The noise on the lower and upper surfaces are reduced by multiplying by a small coefficient. (b) The measured step profile (black) and the mathematically perfect step profile (blue) are duplicated and folded to form double-sided step profiles.

The total uncertainty of the measured ITF includes the repeatability, the uncertainty of choosing the step transition region, the uncertainty of choosing the noise suppression ratio and the uncertainty of finding the step angle (see Figure 7). To validate the measured ITF curve, a prediction of the ITF curve is generated through simulation using the measured MTF curve. A 2D PSF is created from the measured MTF by assuming the PSF is circularly symmetric, and the convolution of the irradiance map and the PSF is calculated. The uncertainty of the ITF prediction is also calculated, and it considers the inability of imaging the step at the best focal plane.

This uncertainty is the deviation of the predicted ITF curve caused by a PSF defocus of ±0.5 mm. This number equals to the range over which the paraxial blur spot is no bigger than the airy disk of the system. Comparison between the ITF measurement and the ITF prediction reveals that the ITF measurement is valid. The measured ITF curve falls on the lower bound of the ITF prediction band suggesting some defocus exists in the stepped surface measurements.

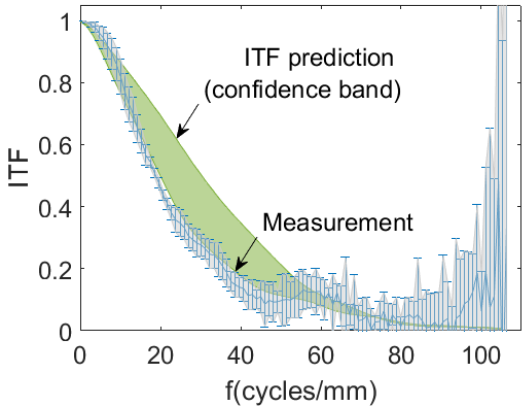

FIGURE 7. The measured ITF compared with a theoretical ITF prediction.

CONCLUSIONS

Measurements of rough and textured surfaces created by an addtive processe require the instrument to have adequate spatial resolution. The spatial resolution can be characterized by the ITF, but the instrument must be linear. We found a fringe projection system can be approximated as a linear system under two conditions: 1) the relative height of the surface is much smaller than the working distance of the camera, and 2) the amplitudes of sinusoidal components of the surface are under the linearity limit. We also measured the ITF of a fringe projection system with an appropriate stepped surface. The measurement results are compared with a predicted ITF (confidence band) calculated through simulations. The comparison shows that the measured ITF agrees with the ITF prediction.

ACKNOWLEDGEMENT

This work is partially supported by Edison Welding Institute, American Makes, National Institute of Standards and Technology, and North Carolina Research Opportunity Initiatives.

REFERENCES

[1] B. Zhang, J. Ziegert, F. Farahi, and A. Davies, “In situ surface topography of laser powder bed fusion using fringe projection,” *Addit. Manuf.*, vol. 12, pp. 100–107, 2016.

[2] B. Zhang, J. Ziegert, and A. Davies, “In Situ Surface Metrology of Laser Powder Bed Fusion Processes Using Fringe Projection 2 Department of Mechanical Engineering and Engineering Science,” in *Proceedings ASPE 2016 Summer Topical Meeting*, 2016, no. 1.

[3] P. de Groot, X. C. De Lega, and X. C. de Lega, “Interpreting interferometric height measurements using the instrument transfer function,” *Fringe 2005*, vol. 2005, pp. 30–37, 2006.

[4] S. S. Gorthi and P. Rastogi, “Fringe projection techniques: Whither we are?,” *Opt. Lasers Eng.*, vol. 48, no. 2, pp. 133–140, Feb. 2010.

[5] W. S. Land, B. Zhang, J. Ziegert, and A. Davies, “In-Situ Metrology System for Laser Powder Bed Fusion Additive Process,” *Procedia Manuf.*, vol. 1, pp. 393–403, 2015.

[6] B. Zhang, A. Davies, J. Ziegert, and C. Evans, “Application of instrument transfer function to a fringe projection system for measuring rough surfaces,” in *SPIE Proceedings Optics+Photonics*, 2017.

[7] C. R. Wolfe, J. D. Downie, and J. K. Lawson, “Measuring the spatial frequency transfer function of phase-measuring interferometers for laser optics,” in *Proceedings of SPIE*, 1996, vol. 2870, pp. 553–557.

[8] P. D. Burns, “Slanted-Edge MTF for Digital Camera and Scanner Analysis,” *Burns*, vol. 3, pp. 135–138, 2000.

MANAGING RISKS WHEN SINGLE-POINT DIAMOND MACHINING A 24-DAY-CUT GERMANIUM BLAZED DIFFRACTION GRATING

**Richard C. Montesanti, Paul J. Kuzmenko, Steve L. Little,
Jay V. Bixler, John L. Jackson, Paul B. Mirkarimi,
Robert E. Priest, Peter A. Thelin, Joel A. Watkins, Brian E. Yoxall
Lawrence Livermore National Laboratory
Livermore, CA, USA**

INTRODUCTION

An optical system designed to use a diffraction grating to disperse light can only meet its system performance goals if the grating meets or exceeds its specifications; and an optical system that must be delivered by a certain date and has a grating on its critical path in the project plan cannot be successful if the grating is late. For a germanium blazed immersion grating that pushes limits on what can be fabricated with confidence, detailed planning and active risk management is essential for mitigating known risks, dealing with new risks as they arise, and maintaining a balance between knowing when good enough is being achieved versus pushing further towards a perfect grating. This paper describes risk management for producing what will be referred to as the Ge24 grating, which is expected to enable demonstration of the optical system science goals, and shares a lesson learned on preparing the germanium substrate for cutting the grooves.

BACKGROUND

The Ge24 germanium immersion grating, shown if Figure 1, was flycut with a single-point diamond tool on the Precision Engineering Research Lathe (PERL) at the Lawrence Livermore National Laboratory (LLNL) in May – June 2017, and then coated in June – July 2017. The grating has an area of 30 mm x 30 mm (along-groove and cross-groove directions), line pitch of 319 line/mm, and blaze angle of 15 degree. Based on total groove length, the Ge24 grating is the second largest diffraction grating cut with the PERL, requiring twenty-four days of machining[1]. The Ge24 grating benefits from previous work at LLNL using the PERL in a flycutting configuration to produce blazed immersion gratings in infrared optical materials [1-8]. The reader is referred to [1] for an in-depth discussion on flycutting a grating and the attendant configuration of a two-axis diamond turning machine; cutting parameters details; and key risks, mitigations, and trade-offs when producing a grating by single-point diamond flycutting.

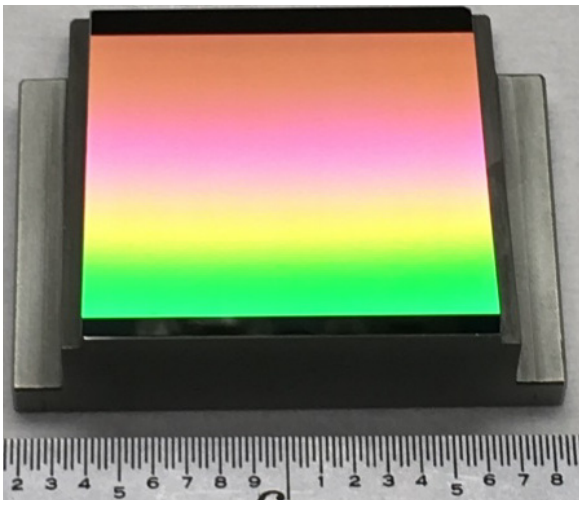

FIGURE 1. The Ge24 grating after cleaning germanium swarf and cutting fluid residue from the grating cut, and before adding the high reflectivity coating. (Scale numbering is 0.1 in.)

FMEA AND RISK ASSESSMENT

Producing the Ge24 grating presented significant challenges and risks, so it was treated as a project in of itself. Figure 2 shows the rolled-up schedule of the one-hundred tasks that were planned and managed, many of which defined the critical path for the higher level project the grating was being made for. At the beginning of the Ge24 grating project discussions among project team members identified risks associated with producing the grating and possible ways of dealing with them. By applying some rigor, that information was captured in the Failure Modes and Effects Analysis (FMEA) and risk assessment shown in Table 1.

LLNL-CONF-735830

[1] The largest is a germanium blazed immersion diffraction grating referred to as 002u, which required twenty-eight days of machining [1].

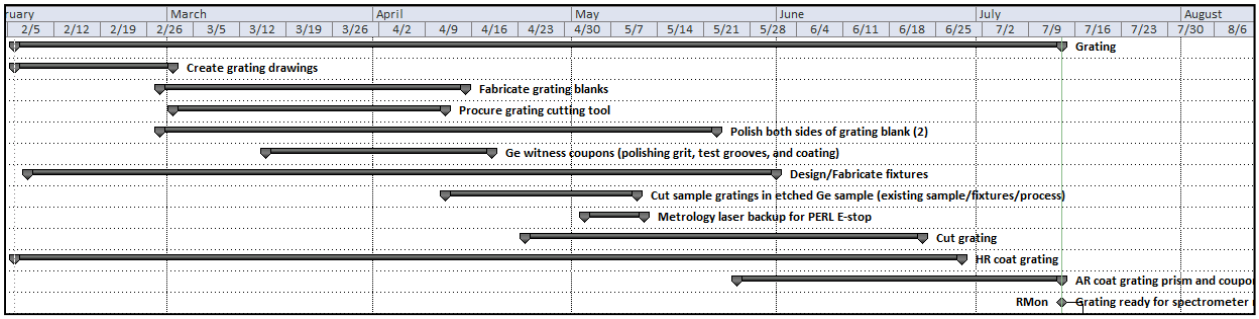

Figure 2 Major tasks for producing the Ge24 grating, represented as a roll-up of one-hundred tasks.

The risk assessment informs trade-offs and project decisions, so for projects with limited resources and aggressive timelines it is essential to perform this assessment at the outset of the project in order to identify possible show-stoppers and develop fallback plans, and to better ensure that attention and efforts are applied to the most critical items.

Creating an FMEA and performing a risk analysis is described here by stepping through the first risk item identified in Table 1: polishing grit on or embedded in the grating blank surface. (1) A Failure Mode (a bad thing that could happen) associated with the risk is identified: grating groove cutting tool gets damaged. (2) The Effects of that undesirable event are described: tool produces poor groove shape quality and increased groove face roughness. (3) The Analysis aspect of the FMEA involves:
(3a) Describing the consequences of the effects in terms of metrics that are meaningful to the project: broadening of diffracted lines, reduced line depth, and reduced signal-to-noise ratio.
(3b) Identifying the consequence type: Health and Safety, Environmental, Cost, Schedule, Technical, and Political and Public;
(3c) Determine the consequence severity; and
(3d) Determine the likelihood of occurrence.
(4) The Risk Analysis considers consequence severity and likelihood of occurrence when assigning a risk level. Consequence severity and likelihood of occurrence, and their mapping to a risk level, are subjective and based on guidance from the project's home institution and/or sponsor.
(5) A Mitigation of the risk is prescribed, and then the consequence type, severity, and likelihood of occurrence are reevaluated, as is the risk level. Mitigations can be used to change the risk type to a more acceptable one; referring to the fourth risk item in Table 1, an insoluble technical risk (from a practical standpoint) was turned into a manageable schedule risk.

The two most significant identified risk areas for the Ge24 grating were (1) the possibility of the grating cutting tool edge encountering residual abrasive particles on the grating substrate introduced during earlier substrate polishing, and (2) the reliability of the PERL machine and its utilities. Regarding residual polishing grit, reference [9] discusses precautions when single-point diamond machining a substrate that was polished; this risk is explored and discussed further in the next section. Ensuring that the PERL machine would run uninterrupted in a stable environment for the twenty-four days needed to cut the Ge24 grating posed technical and logistical challenges. PERL was designed and built more than thirty years ago [10], most of the subsystems are unique and/or outdated, full recovery from unexpected stoppages is not always possible, and ancillary systems such as temperature stability and pressurized air for the machine depends on a chain of systems outside of PERL that present multiple single-point failure scenarios.

As chance would have it, on day 20 of the 24-day Ge24 grating cut, the high pressure air system feeding the PERL spindle failed. Fortunately the PERL machine had just been placed in a safe configuration for this possibility – because a warning light on the high pressure air compressor prompted the extended Ge24 grating team to address an impending problem – and the machine and grating were not damaged. During the FMEA planning, events like the compressor failure were anticipated and motivated evaluating the consequences to the grating (see risks R2 and R3 in Table 1). Knowing beforehand that it would be acceptable to stop and start PERL during the grating cut, up to four times if necessary, provided clear guidance on how to handle certain events during the grating cut that might otherwise prompt an ad hoc declaration of the cut being a failure and irreversibly ending it.

Failure Modes and Effects Analysis (FMEA) and Risk Assessment Project: Ge24 Date: 28 Feb 2017 Lead author: Rick Montesanti

					Prior to mitigation					After mitigation				
Nmbr	Risk item	Failure Mode	Effects	Consequences	Consequence Type	Consequence Severity	Likelihood of Occurrence	Risk Level	Mitigation	Consequence Type	Consequence Severity	Likelihood of Occurrence	Risk Level	Comments
Grat R1	Polishing grit on or embedded in grating blank surface	Groove cutting diamond tool gets damaged	Poor groove shape quality; increased groove face roughness	- Line broadening - Reduced line depth - Reduced SNR	Technical	Moderate	Probable	1	Cut sample grating into a substrate polished with same process as grating substrate	Technical	Moderate	Remote	2	002u grating blank was etched to remove subsurface damage (and possible residual lapping grit), and then pre-machined flat with a diamond tool
Grat R2	PERL/facility interuptions during a long grating cut	Stopping/restarting PERL causes out-of-phase ruled sections	Out-of-phase sub-gratings	- Line broadening - Reduced line depth - Reduced SNR	Technical	Moderate	Probable	1	UPS on PERL control system and motor drivers, with backup laser interforemeter to capture groove placement if E-stop	Technical	Moderate	Remote	2	Analsyis indicates that up to 5 separate ruled sections would be acceptable
Grat R3	PERL utilities / environment loss	Fluctuations in buidling-supplied air and water temperature / pressure affect PERL	Groove spacing variations	- Line broadening - Reduced line depth - Reduced SNR	Technical	Moderate	Probable	1	Schedule multiple machine/building checks every day, and maintain consistent contact with key facility personnel	Technical	Moderate	Remote	2	Boiler failure on 22nd of 002u 28-day grating cut was caught before significant impact, building chiller failure on 24th day prompted pause in cutting
Grat R4	Severe weather swings	PERL laser interferomter is sensitive to air pressure changes	Groove spacing variations	- Line broadening - Reduced line depth - Reduced SNR	Technical	Moderate	Infrequent	2	Expect grating to be cut Apr-May 2017 (after winter storms); can choose to stop up to 4 times	Schedule	Moderate	Remote	2	002u gating was cut Nov-Dec 2015, and allowed to ride through rain storms (acceptable grating produced)
Grat R5	Extended PERL failure	Outdated/unique subsystems not readily replaced	Recovery from some stoppages require weeks	- Grating cut delayed for an extended period	Schedule	High	Infrequent	1	Short of major PERL upgrades, which are out of scope, already exercising practicable vigilance	Schedule	High	Infrequent	1	PC-based user interface became un-responsive during 002u grating cut; did not reboot it and kept going
Grat R6	Grating cleaning	Grating cutting oil (tacky paraffin-based) not completely removed before HR coating	Poor adhesion of HR coating	- Reduced SNR - Contamination inside spectometer	Technical	Moderate	Infrequent	2	Test clean sample gratings, with rigor on procedure, materials, and tests	Technical	Moderate	Remote	2	002u grating HR coating is bubbled/lifting in certain areas; inadequate cleaning of cutting oil not ruled out
Grat R7	Grating HR coating adhesion	LLNL aluminum coating on 002u Ge grating has poor adhesion	Reduced % of grating surface with HR coating	- Reduced SNR - Contamination inside spectrometer	Technical	Moderate	Infrequent	2	Test coatings on sample gratings, with rigor on procedure and materials; other coating materials?	Technical	Moderate	Remote	2	002u grating HR coating is bubbled/lifting in certain areas; occurred after coated grating was air shipped in Dec-Jan 2015-16

Table 1. Failure Modes and Effects Analysis (FMEA) and risk assessment performed at the beginning of the Ge24 grating project. This list is a subset of the risks identified and tracked for the higher level optical system project. After fabricating the grating an additional risk associated with grating cleaning (number R7) was discovered: removing fixturing adhesive residue from the prism entrance face.

SUBSTRATE PREPARATION

The original plan for cutting the Ge24 grating included chemically etching the as-ground substrate to remove the outer layer of subsurface damaged material and any residual abrasive particles, followed by pre-machining to reduce the volume of material to be removed by the grating cutting tool, as was done for the earlier 002u grating [1]. As described in [1-8], etching has been shown as an effective way of removing the layer of subsurface damaged material, which if not removed will cause material tear-out during grating groove cutting.[2] For gratings that take a long time to cut – like Ge24 (24 days) and 002u (28 days), the number of cutting days that a sharp diamond tool can be subjected to and still provide acceptable groove quality is not well established, so reducing the

[2] Readers who have shoveled snow or sand off a backyard patio paved with bricks that are not cemented down will be familiar with a similar mechanism; loose bricks get pulled out.

volume of material to be removed provides a hedge on tool life.[3]

Etching and then pre-machining the Ge24 substrate was expected to add two weeks to the higher level project critical path, which presented schedule risk so an alternative path for removing the subsurface damaged material and addressing possible residual abrasive particles was sought.

Fairly recent work at LLNL to produce the WINERED [2,5] and NIRISS [3] gratings reports some success when single-point diamond machining a grating into an as-polished ZnSe substrate. This suggested the possibility of being able to cut the Ge24 grating directly into an as-polished germanium surface; with careful polishing the substrate surface could be made flat and presumably damage-free in a few days instead of a few weeks – which was attractive.

Early work on the WINERED grating reports using 3 micron diameter diamond abrasive to prepare the substrate, and concluded that the subsequent poor groove quality was due to tear-out of damaged subsurface material caused by polishing [5]. Later work on the WINERED grating reports risks with cutting a grating into an as-polished ZnSe substrate, so the substrate was chemically etched after polishing to remove the subsurface damaged material [2]. Work on the NIRISS grating reports that the ZnSe substrate was prepared by polishing only (no chemical etching), and that the subsequent good groove quality indicated that the as-polished substrate was free of subsurface damage [3]. From [3], the diamond tool used to cut the NIRISS sample grating and then the two NIRISS gratings was subjected to at least 322 hours (13.4 days) of cutting as-polished ZnSe, and tool wear was not identified as an issue.

Taken together, the previous work cutting gratings into an as-polished ZnSe substrate [2,3,5] provides an unclear indication on whether a 24-day cut in an as-polished germanium substrate would be successful. Carefully polishing the germanium Ge24 grating substrate with a very fine abrasive – 0.04 micron diameter alumina was ultimately used – would likely produce a surface with acceptable subsurface damage, but the specter of tool wear during a long grating cut caused by possible residual polishing compound needed to be addressed.

The Ge24 grating team weighed technical and schedule risks associated with substrate preparation. At one end of the discussion was the conservative approach prescribed by [9], “treat it as if residual abrasive particles are embedded in the surface”. At the other end was an optimistic belief that the positive results from the ZnSe grating efforts [2,3,5] would translate to the Ge24 grating. The middle ground reached was to mitigate the risk by cutting a test grating in a germanium substrate prepared exactly the same way as the Ge24 grating substrate would be, in a parallel effort that was off the project critical path[4]. A shortcoming of the middle-ground is that it neglects the time needed to rule out the presence of abrasive particles. Assuming the same aerial density of particles in the test and Ge24 grating substrates, unless that density were high enough to make tool wear apparent during the few days spent cutting the test part, the test cut would need to last the same fraction of the 24-day cut as the fraction of grating area that needed to have acceptable grooves, nominally 1.0.

GRATING GE24 CUTTING RESULTS

Figure 3 provides insight to the question on whether a grating can be single-point diamond machined in a germanium substrate that was polished but not etched or pre-machined.

[3] The cutting edge of a diamond tool is fragile due to its extreme sharpness, so encountering even just a few abrasive particles can damage it. Tool edge damage can be in the form of fractures (that can be very apparent) or accelerated wear (which can be more insidious since its cumulative nature may take longer than anticipated to become apparent).

[4] Regarding examining an as-polished substrate for possible residual polishing compound before cutting a grating, conclusively ruling out abrasive grit on the surface or just below it requires a survey of the entire surface that can reveal the presence of even just a few 0.04 micron diameter particles. The number of particles of this size that a diamond tool cutting edge can survive striking is unknown to the authors, but common sense says to avoid it. For a 30 mm x 30 mm grating, the ratio of 0.04 micron particle cross-section area versus grating area is 1 in 7e11, so if there were 700,000 abrasive particles on the surface or embedded just below it, finding just one of them is a one-in-a-million undertaking outside the Ge24 project scope.

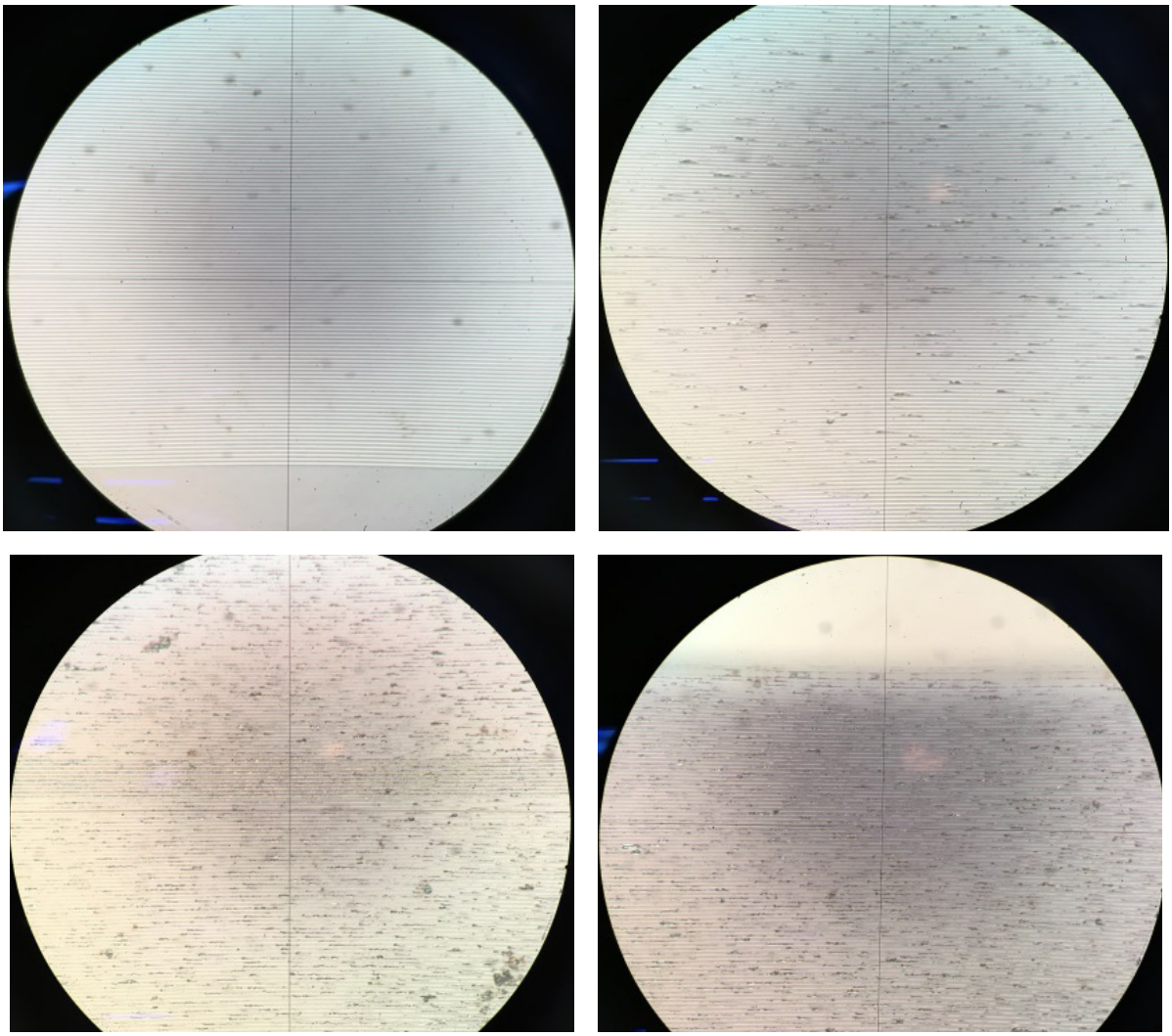

FIGURE 3. Optical microscope images of the Ge24 grating grooves at 500x magnification showing grooves formed near day 1 (upper left), day 12 (upper right), day 20 (lower left), and day 24 (lower right). The in-focus spots are predominantly groove peak chips, made to look worse by a doubling effect caused by straight down illumination and viewing of the ninety degree included-angle grooves. The region of ~10 overlapping grooves due to the PERL stop/restart on day 20 is just above the horizontal crosshair. The central dark regions in the images are an artifact of the camera used to record the images.

The Ge24 grating grooves formed near day 1 of the cut look great, indicating a good (sharp) diamond tool and negligible subsurface damage in the as-polished substrate. The aerial density of groove peak chipping increases slightly as the cut proceeded, and then more rapidly during the last half of the 24-day cut. This suggests initial slight wear of the diamond tool cutting edge followed by accelerated wear, which could be caused by residual polishing compound or a weak diamond tool. Note that if the Ge24 grating were a 30 mm wide by 15 mm grating (along-groove and cross-groove directions) the groove quality would be bracketed by the day 1 and day 12 images, and likely declared a very good grating. Considering Figure 3 and referring to the NIRISS grating discussion in the previous section, thirteen days of cutting an as-polished ZnSe substrate may not have been long enough to make tool wear apparent if fine abrasive particles were present.

Figure 4 brackets the groove quality for the 002u grating which took 28 days to cut [1], providing insight on how long a diamond tool can stay sharp while cutting a germanium grating. There is very little difference in groove quality across the 002u grating, suggesting negligible wear of a good diamond tool when cutting a germanium substrate that was etched and pre-machined after it had been earlier cut with an abrasive.

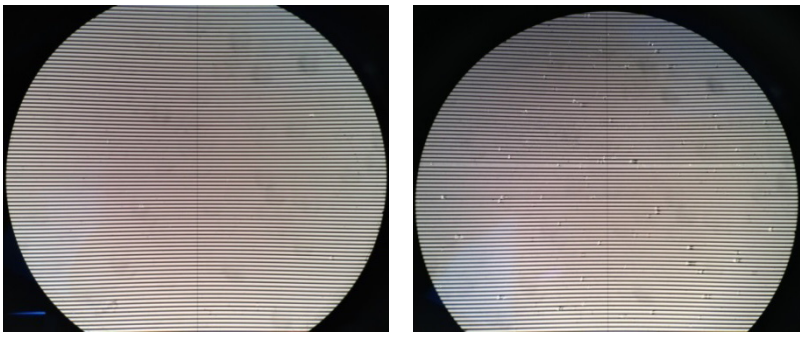

FIGURE 4. Optical microscope images of the 002u grating [1] grooves at 200x magnification showing grooves formed near the beginning (left) and near the end (right) of the 28-day cut. Slight (acceptable) chipping appear as small breaks in the lines. What appears to be a missing groove in the image on the right is actually a shallow groove associated with a PERL facility chiller failure on day 24. The apparent non-straightness of the grooves is an artifact of the camera used to record the images. Figure 4 is scaled to provide the same apparent groove density as shown in Figure 3.

GRATING GE24 EXPECTED TO ENABLE

The measured Ge24 grating diffracted beam wavefront quality is 0.55 wave peak-to-valley and 0.081 wave RMS as measured with a Fizeau interferometer externally illuminating the full ruled surface at 633 nm, which is acceptable.

Figures 5 and 6 show the coated grating. Since the grating is to be used in immersion, an anti-reflection coating was placed on the entrance face of the grating prism, and a high-reflectivity coating was placed on the grating surface. Both coatings look great and have good adhesion.

The groove peak chips in the Ge24 grating will cause increased wide-angle scatter and reduced collection efficiency for the intended diffracted wavelength order. Taken together, these effects will reduce the expected signal-to-noise ratio for the optical system the grating was designed for. Though not ideal, the grating will still enable the optical system to demonstrate the science goals it was designed for, albeit at a lower level than hoped for. The increased scatter and reduced efficiency due to the chips can be quantified, and the measured performance of the optical system can be scaled to a prediction of what a more perfect grating could achieve.

From the viewpoint of the larger project that the grating Ge24 project lies in, success is measured by whether or not the goals of the larger project can be tested while adhering to the aggressive timeline set for it, and whether those tests can provide meaningful results. From this viewpoint the Ge24 grating is a success.

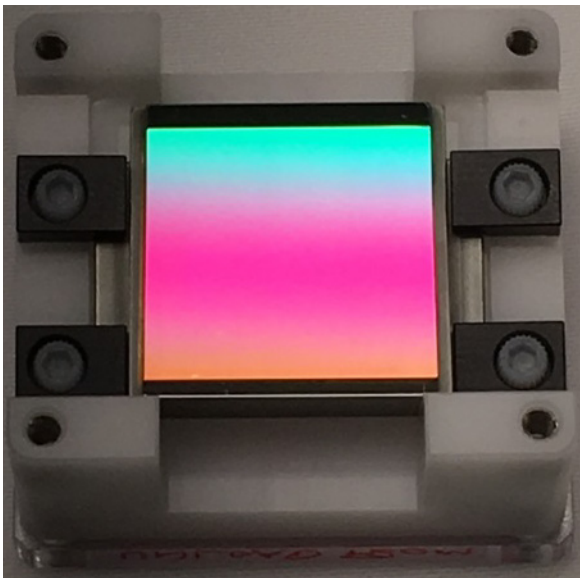

FIGURE 5. The Ge24 grating in its metrology-storage-shipping fixture (top cover removed), after coating with Au on Cr (binder) to provide high reflection for internal illumination.

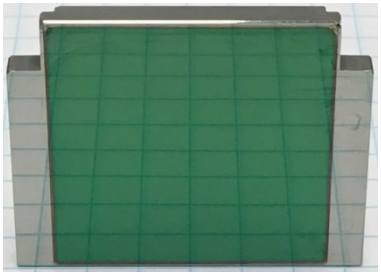

FIGURE 6. Entrance face of the Ge24 grating with a vendor-proprietary anti-reflection coating.

SUMMARY

An FMEA and risk assessment performed at the beginning of a project is an efficient and effective way of identifying risks and collecting ways to deal with them. The risk assessment informs trade-offs and project decisions, so for projects with limited resources and aggressive timelines helps identify possible show-stoppers, develop fallback plans, and better ensure that attention is applied to the most critical items.

A germanium grating substrate that was polished but not etched or pre-machined to remove possible residual polishing compound might retain enough abrasive particles to cause accelerated wear of a diamond tool used to cut grating grooves, so is contraindicated.

The Ge24 grating appears to be good enough to enable the optical system it was designed for to demonstrate its intended science goals.

ACKNOWLEDGEMENTS

This work was performed under the auspices of the U.S. Department of Energy by Lawrence Livermore National Laboratory under Contract DE-AC52-07NA27344.

An extended team was engaged during the fabrication and coating of the Ge24 grating. The authors thank John Benedict, Don Bennett, Rich Cobiseno, Steve Gemberling, Paul Geraghty, Dustin Moring, Jim Morton, Darron Nielsen, and Emanuel Rey of LLNL; Andreas Zickler of Photonics Sense; Joe Boyle of F1 Optics, Peter Kawalec of Chardon Tools; and Michael Middleton of Universal Thin Film Lab.

REFERENCES

[1] Montesanti, R.C., Little, S.L., Kuzmenko, P.J., Bixler, J.V., Jackson, J.L., Lown, J. G., Priest, R.E., Yoxall, B.E., “Strategies for Single-point Diamond Machining a Large Format Germanium Blazed Immersion Grating”, Proceedings SPIE, Advances in Optical and Mechanical Technologies for Telescopes and Instrumentation II, Volume 9912, (2016).

[2] Ikeda, N., Kobayashi, N., Kuzmenko, P. J., Little, Mirkarimi, P. B., Alameda, J. B., Kaji, S., Sarugaku, Y., Yasui, C., Kondo, S., Fukue, K., Kawakita, H., "ZnSe immersion grating in the short NIR region," Proc. SPIE 9151, Advances in Optical and Mechanical Technologies for Telescopes and Instrumentation, 915144, (2014).

[3] Kuzmenko, P. J., Little, S. L., Albert, L., Aldridge, D. A., Doyon, R., Maszkiewicz, M., Touahri, D., "Diamond machining of ZnSe grisms for the Near Infrared Imager and Slitless Spectrograph (NIRISS) onboard JWST," Proc. SPIE 9151, Advances in Optical and Mechanical Technologies for Telescopes and Instrumentation, 915159, (2014).

[4] Kuzmenko, P. J., Little, S. L., Little, L. M., Wilson, J. C., Skrutskie, M. F., Hinz, P. M., Leisenring, J. M., Durney, O., "Fabrication and testing of germanium grisms for LMIRcam," Proc. SPIE 8450, Modern Technologies in Space- and Ground-based Telescopes and Instrumentation II, 84503P, (2012).

[5] Kuzmenko, P. J., Little, S. L., Ikeda, N., Kobayashi, N., "Progress in the Fabrication of a Prototype ZnSe Immersion Grating for the WINERED Spectrograph," Proc. SPIE 7739, Modern Technologies in Space- and Ground-based Telescopes and Instrumentation, 77393U, (2010).

[6] Kuzmenko, P. J., Little, S. L., Ikeda, N., Kobayashi, N., "Fabrication and testing of diamond-machined gratings in ZnSe, GaP, and bismuth germinate for the near infrared and visible," Proc. SPIE 7018, Advanced Optical and Mechanical Technologies in Telescopes and Instrumentation, 70184Q, (2008).

[7] Kuzmenko, P. J., Davis, P. J., Little, S. L., Little, L. M., Bixler, J. V., "High efficiency germanium immersion gratings," Proc. SPIE 6273, Optomechanical Technologies for Astronomy, 62733T, (2006).

[8] Kuzmenko, P. J., Little, L. M., Davis, P. J., Little, S. L., "Modeling, fabrication, and testing of a diamond-machined germanium immersion grating," Proc. SPIE 4850, IR Space Telescopes and Instruments, (2003).

[9] Montesanti, R. C., Thompson, S. L., "A Procedure for Diamond Turning KDP Crystals," Lawrence Livermore National Laboratory Technical Report, UCRL-ID-121651, (1995).

[10] Donaldson, R. R., Thompson, D. C., "Design and performance of a small precision CNC turning machine," CIRP 36th General Assembly (August 16-22, 1986), Lawrence Livermore National Laboratory Technical Report, UCRL-94173, (1986).

STRESS INDUCED FREQUENCY MODULATION OF A MICROCHIP GREEN LASER

Kumar Arumugam[1], Stuart T Smith[1], and Tsing-Hua Her[1]
[1]University of North Carolina at Charlotte
Charlotte, North Carolina, USA

INTRODUCTION

Miniaturized and low-cost frequency-modulation laser is essential for wide-spread adoption of laser interferometers that employs frequency modulation or heterodyne techniques. One example is a fiber based Fabry-Perot Interferometry (FFPI), as shown schematically in *Figure 1*[1]. A frequency modulated laser traverses through a 2 × 2 fiber coupler. The probe end of the fiber is positioned against the mirror attached on a surface whose displacement we intend to measure. The light reflected by the mirror gets coupled to the fiber and reach the photodetector, which measures the intensity of the reflected light. To avoid the stray reflection from air entering back into the fiber, the adjacent end to the probe end is submerged in the refractive index matching liquid inside a container coated with black paint. An optical isolator prevents the light entering back in to the laser and destabilizing it.

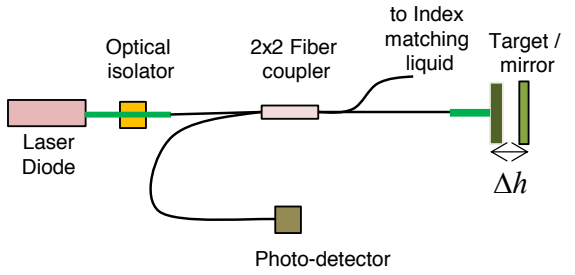

Figure 1: Practical FFPI setup

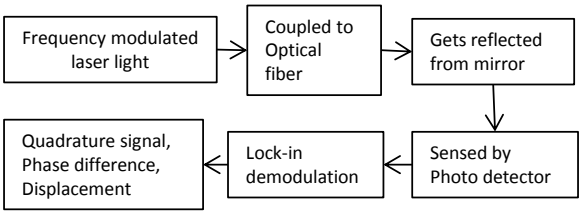

Figure 2: Flowchart of displacement measurement

The displacement (Δh) of the mirror is measured using the phase difference between the sub harmonics of the signal measured at the photodetector. To produce these harmonics, the frequency of the laser has to be modulated [1] after which the displacement can be calculated from

$$\Delta h = \frac{\lambda_0}{4\pi}\left[\tan^{-1}\left(\frac{I_{if}}{I_{jf}}\right)+2\pi n\right],$$

where I_{if} and I_{jf} are the intensities of the sub harmonics with indices i and j representing odd and even integer values, n is the number of rotations of the quadrature signal and λ_0 is the fundamental wavelength of the laser (532 nm).

FREQUENCY MODULATION

The laser source is a commercially available green microchip laser that is composed of a Neodymium doped yttrium orthovanadate (Nd: YVO_4) that is optically glued to a Potassium Titanyl Phosphate (KTP) crystal. The two end faces of the crystal pair are coated with high reflectors at 1064 nm, forming a miniaturized laser cavity. When pumped by a 808-nm laser diode, the laser emits both 1064 and 532 nm radiations. A piezo electric actuator is used to compress the Nd: YVO_4 and KTP crystal pair. The compressive stress, and corresponding strain, increases the length of the crystal pair due to Poisson's ratio effect. This, and optical property effects, changes the frequency (wavelength) of the resulting output beam (*Figure 3*) [2].

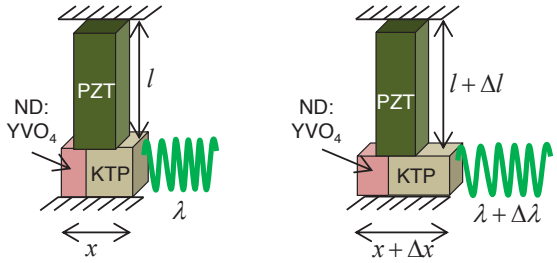

Figure 3: PZT compressing the crystal pair

To create the compressive stresses, the actuator and crystal pair are stacked together and clamped [Thorlabs CPO2, CPO2B] (*Figure 4*). The current and the temperature of the infra-red pump diode is stabilized using a temperature controlled mount [ThorlabsTCLDM9] connected to a current driver [Thorlabs LDC220C] and a temperature stabilizer [SDL-803] respectively (*Figure 4*). A capacitance gauge [Lion C1-C] is used to measure the deflection of the clamp, this deflection is proportional to the deformation of the assembly and used to validate that the crystal is being compressed, the value of this compressive force is not currently measured.

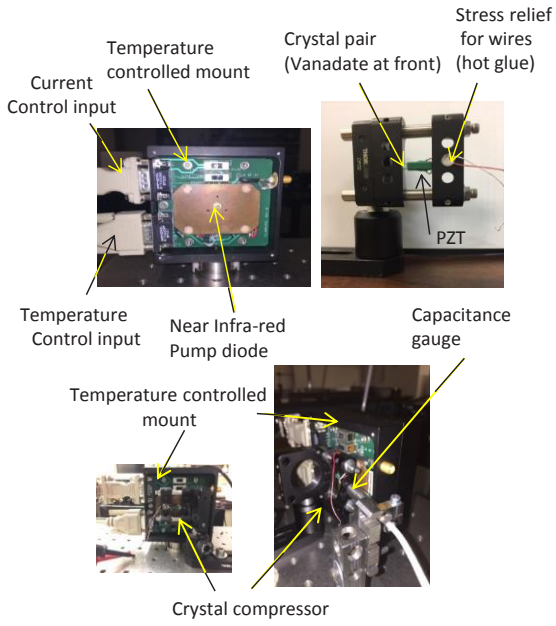

Figure 4: Crystal compressor – Assembly

EXPERIMENTAL SETUP

To evaluate frequency modulation, a Michelson interferometer is assembled (*Figure 5*). An IR filter is used to block any residual infra-red light from the pump diode and vanadate. The intensity of the output beam of the interferometer is measured using a photo detector [Thorlabs DET36A] and recorded using an oscilloscope [Agilent DSO6054A]. optical path length difference, $\Delta x = 0.28 - 0.15 = 0.13$ m (from *Figure 5*), which will be used to extract magnitude of frequency modulation during data analysis.

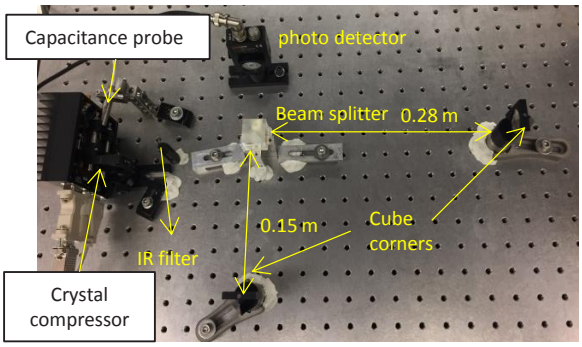

Figure 5: Michelson interferometer

PRELIMINARY EXPERIMENTAL RESULTS

Figure 7 shows the output (green line) from the Michelson interferometer with a sinusoidal voltage being applied to the piezoelectric actuator over approximately two and a half cycles of loading. Subsequent deformation of the support frame is also shown (black line in the plot). The intensity of the beam is reduced significantly at both the peak and valley of these load cycles. However, between these extremes approximately five complete fringes are visible.

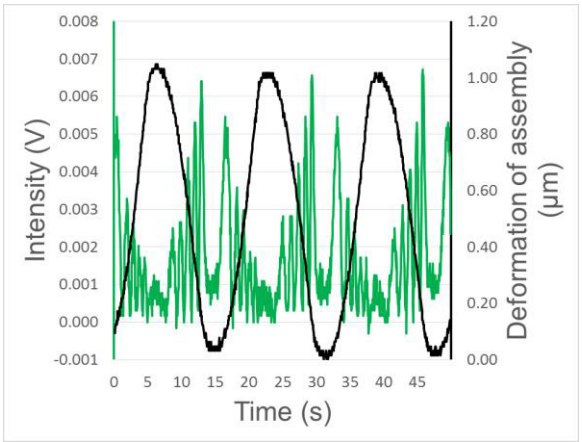

Figure 6: Fringes detected by the photodetector

In a single frequency Michelson interferometer, the phase difference for two recombining beams after traversing path lengths x_1 and x_2 is

$$\phi = \frac{4\pi\left(x_1 - x_2\right)}{\lambda} = \frac{4\pi\Delta x}{\lambda},$$

where, λ is the optical wavelength (532 nm). For two different wavelengths, the phase for each is

$$\phi_1 = \frac{4\pi\Delta x}{\lambda_1};\ \phi_2 = \frac{4\pi\Delta x}{\lambda_2},$$

and the expected phase shift with a constant cavity length interferometer changing from one frequency to another is

$$\phi_2 - \phi_1 = \Delta\phi = \frac{4\pi\Delta x\Delta\lambda}{\lambda_1\lambda_2} \simeq \frac{4\pi\cdot\Delta x\cdot\Delta\lambda}{\lambda^2}$$
$$= 5.77\times10^{12}\Delta\lambda.$$

Assuming that these fringes are a consequence of a frequency shift of the output from the laser, the above equations can be used to determine this value of this shift. For this experiment $\Delta\phi = 2\pi m$ with m being around five, corresponds to a wavelength shift of 5.45 pm or a frequency shift of 5.77 GHz.

INTENSITY VARIATION

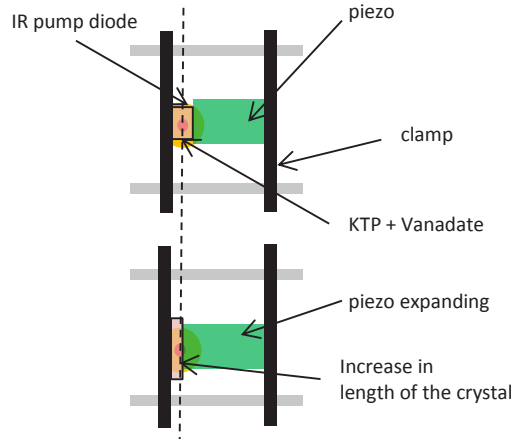

Figure 7: Offset of the crystal pair

Figure 6 also shows that the intensity of the output is reduced significantly at both the peak and valley of these load cycles. While the latter is unknown, we suspect the former may be due to the fact the crystal pair offsets from the focus of IR pump diode as the piezoelectric actuator

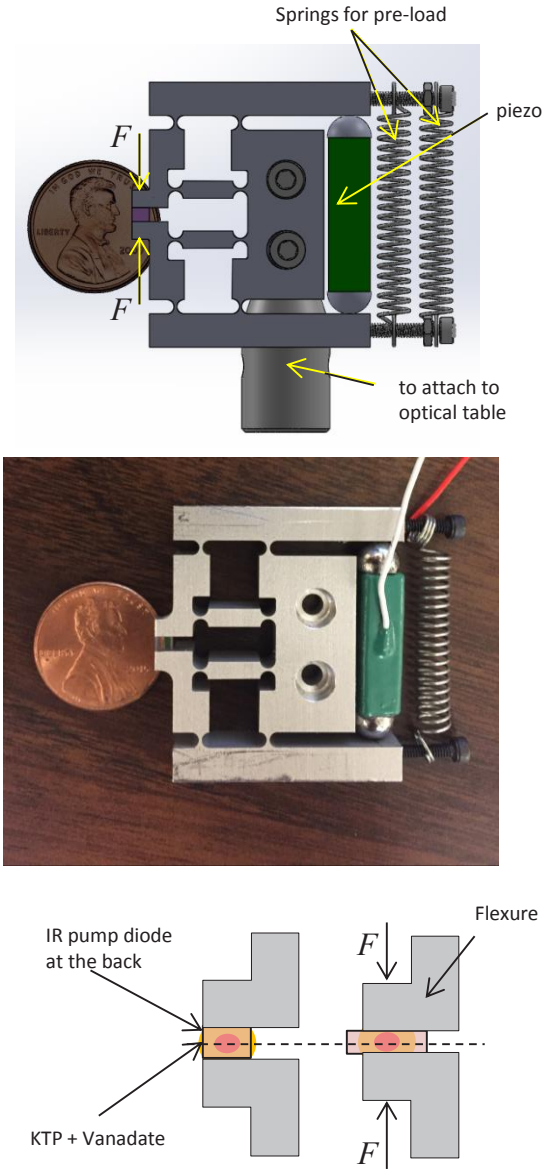

Figure 8: (a) solid model of the flexure assembly (b) fabricated flexure (c) schematic showing the maintenance of intensity coupled from pump diode to the crystal pair

compresses it from one side and increases its length. This causes the amount of light traversing through the crystal to reduce. *Figure 7* is an exaggerated schematic of this hypothesis. Additionally, it is found that coupling is also sensitive to alignment of the various elements of the microchip laser that would also be effected by motions during compression.

In an effort to reduce the intensity variation during compression, a new flexure assembly

has been designed and fabricated (*Figure 8*). For this new design, expansion of the piezoelectric actuator in the flexure provides an equal force (shown as F in the figure) on both the top and bottom of the crystal pair with a line of symmetry through the mechanism so that there is no net force on the crystal and actuator to change its position.

CONCLUSIONS

The paper presents an ongoing study to determine the feasibility of modulating a microchip laser by applying compressive forces on the crystal pair. Early experiments indicate a frequency shift in reasonable agreement with that presented in [2]. However, with the current experimental apparatus the large changes in intensity of the signal during loading make phase measurements impractical. It is speculated that this intensity variation is, in part, caused by the loading mechanism that is currently being redesigned to eliminate relative motions of the optical assembly during compression. Additional instrumentation is also needed to validate the deformations of the assembly during the experiments and also determine the value of the applied stresses to the frequency doubling crystal elements. By doing this, it is hoped to eliminate other mechanisms that might be responsible for the observed fringes (such as tilting of the output beam so that it follows a different path length around the interferometer) and obtain estimates of the compressive stress induced frequency shift with reasonable estimates of the uncertainty of this value for comparison to other studies.

ACKNOWLEDGEMENTS

We would like to thank Joseph Dalton and Brian Dutterer for machining the flexure.

REFERENCES

[1] Bartosz K. Nowakowski B.K., Smith D.T. and Smith S.T., Development of a - miniature, multichannel, extended range Fiber Fabry-Perot Fiber- Optic Laser Interferometric system for low frequency Si-traceable displacement measurement, Proc. EuSPEn, **15**, p.157 – 158.

[2] Mann G., Stefan Seidel and Horst Weber, Influence of mechanical stress on the conversion efficiency of KTP and LBO, SPIE Vol. 3823, 1999, p. 289 – 297.

SIMULTANEOUS MEASUREMENT OF BACKLASH AND GEOMETRIC ERRORS OF LINEAR AXES WITH A LASER TRACER

Hongdong Cong, Yaolong Chen, Chengyong Zhang, Lin Han
School of Mechanical Engineering
Xi'an Jiaotong University
Xi'an, 710049, PR China

INSTRUCTIONS

The objective of this work is to develop a new error mapping model considering backlash and geometric errors of 3-axis machine tools altogether with a laser tracer. With the new model, the error mapping accuracy could be improved further and plenty of downtime for calibration could be saved.

The laser tracer was developed for calibration, monitoring and accuracy enhancement of measuring machines and machine tools. For the measurement procedure, the tracer is positioned at several different locations, tracking the reflector mounted on the spindle and measuring the actual path of the machine in its entire working volume. The geometric error calibration of machine tools with a laser tracker or laser tracer has gained popularity for its high efficiency and large measurement range.

Most research work attributes the deviations between the nominal reflector position and the real reflector location to geometric errors. While in fact many other factors, like backlash and thermal errors may also contribute to the deviation [1]. Aguado et al. [2] adjust measurement strategy to minimize the influence of backlash, but it consumes more time compared with traditional method.

Taking into account the above, we propose a new error mapping model considering backlash and geometric errors altogether. With the new model, geometric errors and backlashes could be identified at the same time.

THE NEW ERROR MAPPING MODEL

We propose a new error mapping model considering backlash and geometric errors altogether. With the new model, the error mapping accuracy could be improved further and plenty of downtime for calibration could be saved. For error calibration, a set of laser displacements measured by a laser tracer from four different positions is sufficient for calculation. For each reflector position, a displacement equation could be acquired as follows.

$$\left\| P_i - Q_k \right\| = d_j + l_{ik} \tag{1}$$

P_i is the i-th measured point. Q_k is the j-th tracer position. l_{ik} are the relative distance between the i-th target point and the j-th tracer. d_k is the dead path length of j-th tracer.

As a consequence, the redundant equations about displacements are constituted, and the coordinates of target points are expressed as a function of 21 geometric errors and 3 backlashes of three linear axes. Then it is transformed into a least square problem about geometric errors and backlashes.

$$\min \sum_{i=1}^{m} \sum_{k=1}^{4} \left(L_{ik} - l_{ik} \right)^2 \tag{2}$$

L_{ij} is given by:

$$L_{ik} = \left\| C_{kinematic,i} P_i^* + A_{direction} C_{backlash,i} - Q_k \right\| - d_k \tag{3}$$

$C_{kinematic,i}$ is the machine kinematic model with rigid-body assumption. P_i^* represents the ideal position of P_i. $C_{backlash,i}$ stands for the backlash. $A_{direction}$ is a diagonal matrix and its values depend on the movement orientation.

Then it demands adjustment of measurement paths. To simplify the calculation afterwards and make it possible to measure backlash of measured points at end of axis stroke, overshoot measured points and points of change of direction are needed, as shown in figure 1.

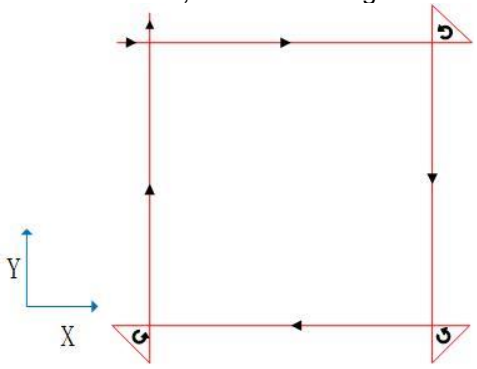

FIGURE 1. a measurement path sketch map.

At last, the linear iterative algorithm is used to obtain the approximation functions of geometric errors and backlash, reducing the volumetric error. Iterative initial values of tracer positions are calculated assuming that P_i equals to P_i^*. Other iterative initial values like geometric errors and backlashes could be got via linear square method.

Simulation is made to identify geometric errors of a 3-axis machine tool whose backlash errors are not well compensated. The random error of axes and the length measurement uncertainty of a tracer are introduced to make the simulation closer to the actual case. The repeatability of each axis is set to 1μm, and the length measurement uncertainty of laser tracer is set to 0.2μm+0.3μm/m(k=2). Other factors that may influence the calibration are ignored.

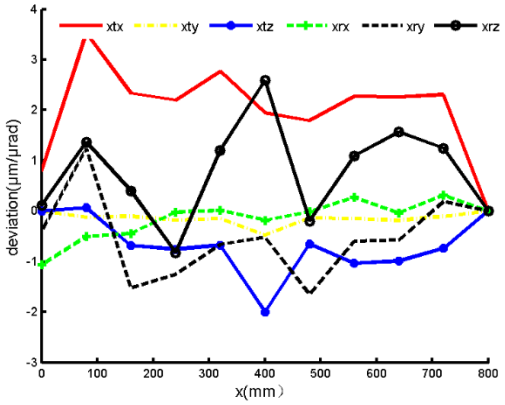

FIGURE 2. deviation between default geometric error values of X axis and calculated values with traditional method.

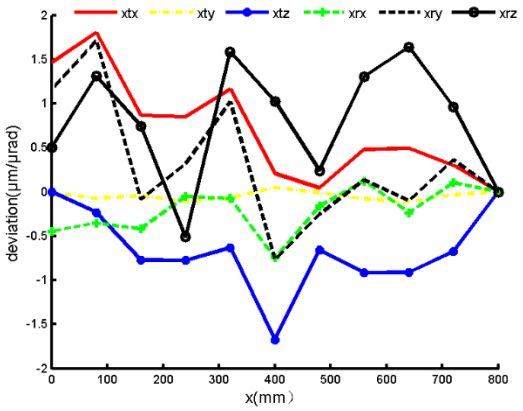

FIGURE 3. deviation between default geometric error values of X axis and calculated values with proposed method.

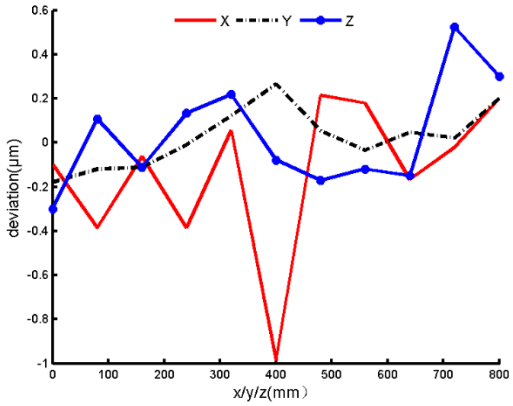

FIGURE 4. deviation between default backlash values of X/Y/Z axis and calculated values with proposed method.

As can be seen from figure 2-3, X axis geometric error values calculated with proposed method are closer to the preset values, and the identified values of X/Y/Z axis backlash correspond closely to default ones, with the largest deviation of 1 μm as shown in figure 4.

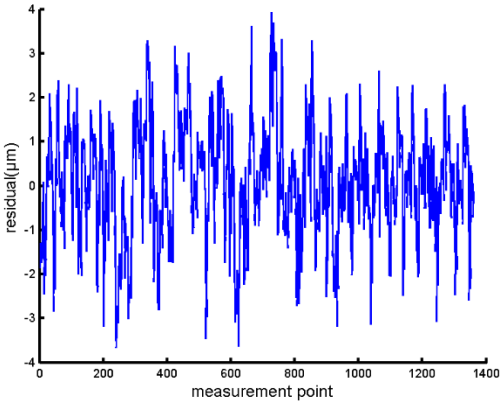

FIGURE 5. residuals between default length values and corrected values with traditional method.

Figure 5-6 indicate the residuals which are the differences of measured and corrected lengths. It shows that the new algorithm matches the real case better. The residuals got with the proposed method can be attributed to the repeatability of three axes and the length measurement uncertainty of the laser tracer. It can be concluded that the proposed method can improve the identification accuracy, and it also proves that backlash do affect the measurement uncertainty of geometric errors.

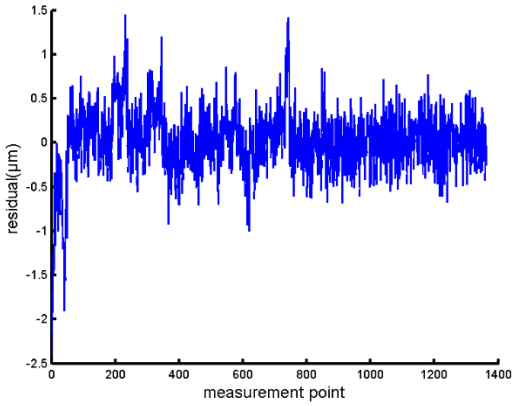

FIGURE 6. residuals between default length values and corrected values with proposed method.

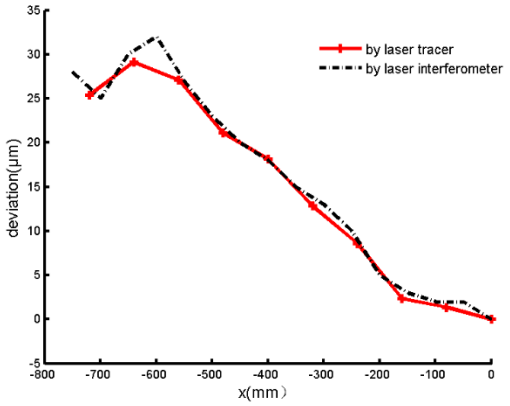

FIGURE 8. deviation between backlash values of Y axis measured by a laser tracer and the ones measured by a laser interferometer.

EXPERIMENT

To verify the simulations, experiments are carried out on one 3-axis gantry machine tools. During the process, environment temperature were kept 20±0.5 degrees centigrade. X/Y/Z axes all have a repeatability of about 5 μm. The first step is to measure X/Y/Z axis backlashes, which are conducted by a Renishaw XL-80 laser interferometer. Then backlashes are well compensated by CNC. In addition, Geometric error components calibration is carried out by an Etalon laser tracer from four different positions. At last, laser tracer traces the same trajectory from the same location again to gauge backlash and geometric errors, after cancelling backlash compensation.

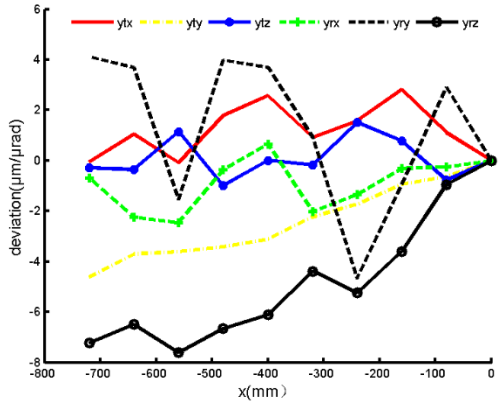

FIGURE 9. deviation between geometric error values of Y axis measured by a laser tracer with backlash compensation and without backlash compensation.

FIGURE 7. Experimental setup.

Take X axis for example, backlash values measured with the laser tracer are similar with the ones measured with the laser interferometer, with the largest deviation of 3.9 μm, as shown in figure 8. Geometric error values measured without backlash compensation also coincide with the ones measured with backlash compensation to some degree, as illustrated in figure 9. Deviations of positioning error and roll are comparatively large might be caused by thermal errors. Besides, figure 10-11 show that the new algorithm fits much better with measured laser lengths than the traditional method. As for the residuals, it is caused probably by the repeatability of machine tools and thermal errors.

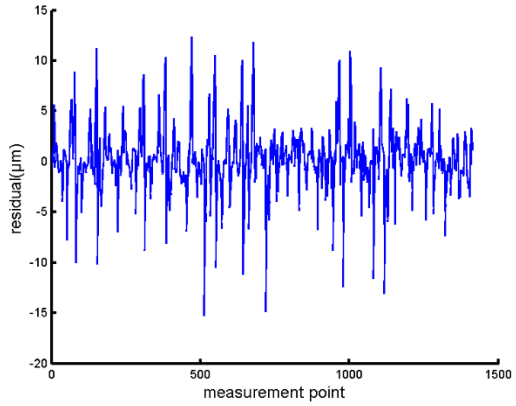

FIGURE 10. residuals between measured length values and corrected values with traditional method.

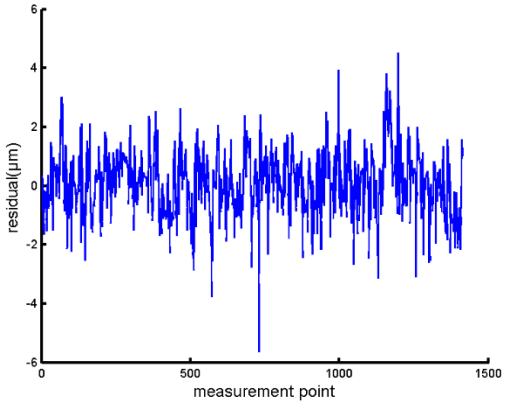

FIGURE 11. residuals between measured length values and corrected values with proposed method.

CONCLUSION

This paper proposes a new error mapping model considering backlash and geometric errors altogether. With the new model, geometric errors and backlashes could be identified by a laser tracer at the same time. Simulation and experiment were conducted to verify its effectiveness and practicality. With the new model, the error mapping accuracy could be improved further and plenty of downtime for calibration could be saved. Besides, it also shows that repeatability and thermal error influences the identification accuracy of proposed method.

ACKNOWLEDGEMENTS

This work was financially supported by National Science and Technology Major Project of the Ministry of Science and Technology of China (No. 2015ZX04001002 and No. 2017ZX04013001).

REFERENCES

[1] Linares, J. M., Chaves-Jacob, J., Schwenke, H., Longstaff, A., Fletcher, S., & Flore, J., et al. Impact of measurement procedure when error mapping and compensating a small cnc machine using a multilateration laser interferometer. Precision Engineering. 2014; 38(3): 578-588.

[2] Aguado, S., Santolaria, J., Samper, D., Aguilar, J. J., & Velázquez, J. Improving a real milling machine accuracy through an indirect measurement of its geometric errors. Journal of Manufacturing Systems. 2016; 40: 26-36.

MULTI-SCALE CONTEXTUAL CHARACTERIZATION VIA HIGH THROUGHPUT MULTI-BEAM ELECTRON MICROSCOPY

Kyle Crosby[1], Marcin B. Bauza[2], Tomasz Garbowski[3] and Anna L. Eberle[3]
[1]Carl Zeiss Microscopy, LLC
Thornwood, NY 10594, USA
[2]Carl Zeiss Industrial Metrology, LLC
Maple Grove MN 55369, USA
[3]Carl Zeiss Microscopy GmbH
Oberkochen BW 73447, Germany

INTRODUCTION

Characterization workflows have historically suffered from an inability to simultaneously detect both the macroscale and the nanoscale details of a component in a meaningful way. While traditional optical microscopy is well suited for surveying large regions of interest in rapid fashion and thus providing the device level perspective, it fails to provide insight on the nanoscale structure that ultimately determines material processing, properties, and applications of a component. Due to diffraction based boundary conditions, optical microscopy is constrained to performing tasks where features of interest are several hundred nanometers or larger [1]. On the flip side, traditional electron microscopy is well suited for very accurately probing minute structures of interest, however, this technology fails to provide the necessary throughput for appreciable large area analysis as required to determine bulk properties. Due to field of view and signal to noise based boundary conditions, electron microscopy in practice is constrained to performing tasks where the region of interest is a mere several hundred microns or smaller [2]. This dilemma ultimately manifests into a struggle between microscopic anomaly and bulk statistical relevance, with potentially different conclusions depending on which tools are employed for a given imaging task.

Details of the multi-beam scanning electron microscope will be described as it pertains to applications in Connectomics (brain mapping), semiconductor industry, shale rock analysis, particle inclusions on precision engineered surfaces, and reverse engineering of IC devices.

MOTIVATION

During the last decades, most electron microscopy developments aimed for better resolution or more sophisticated detection capabilities. However, acquisition speed remained basically the same. Contextual representation of material properties across multiple length scales has therefore been hindered due to throughput limitations of high resolution techniques or resolution limitations of high throughput imaging tools, until now. Conventional SEM is generally too slow for large area imaging because efficient detectors currently have a maximum acquisition speed of about 20 megapixels per second and because efforts to boost signal by increasing beam currents lead to increased Coulomb effects [3] and therefore a decrease in ultimate resolution. With the advent of a commercial multi-beam scanning electron microscope, shown in Figure 1 and described previously by Eberle et al [4], concurrent high throughput and high resolution imaging is opening new domains for multi-scale characterization based on parallel probing dynamics.

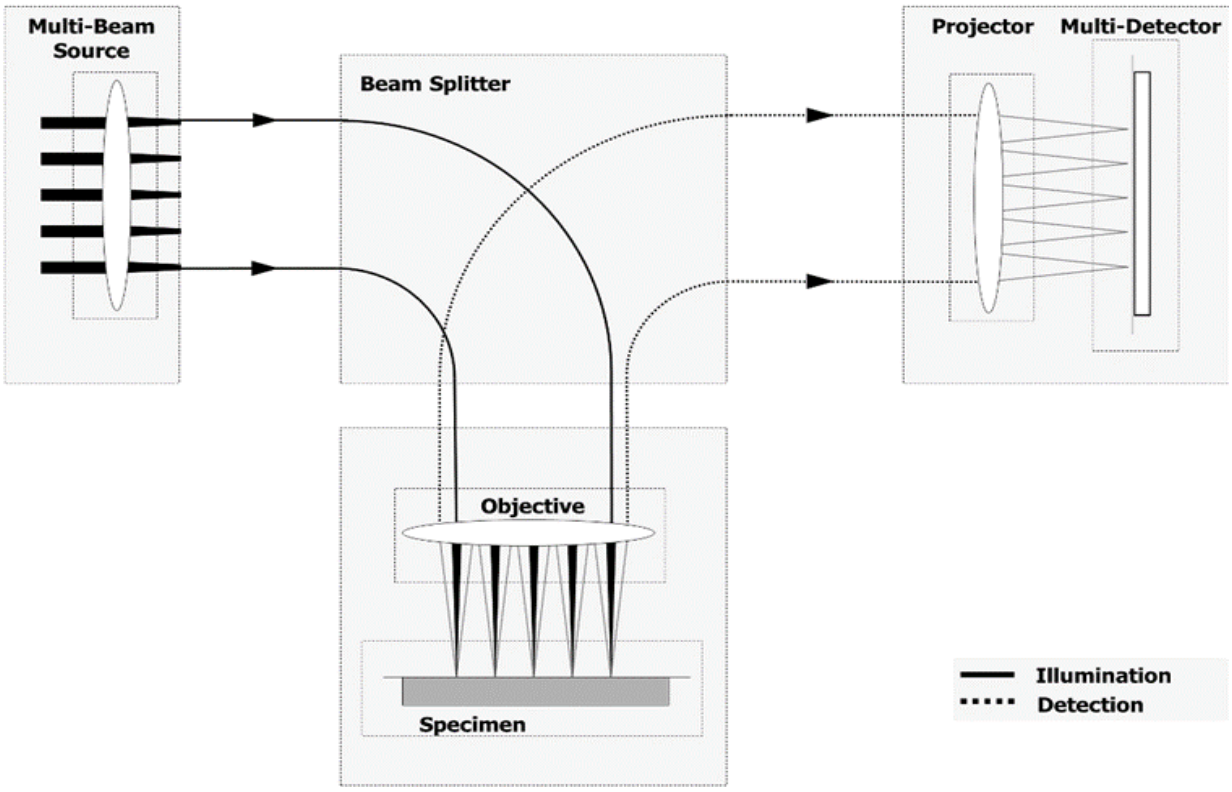

FIGURE 1. Schematic of the multi-beam SEM principle [4]. *Generated from a single field emission electrode, the illuminating beam is broadened and split into multiple beams by a multi-hole aperture (shown combined as multi-beam source). The primary beam array is focused onto the sample surface, emanating secondary electrons are collected through the objective lens and projected into the detection path. The multi-detector consists of a combination of scintillating material and photo diodes, which detect changes in signal intensity for each secondary electron beam, while the illuminating primary electron beams scan over the sample surface.*

REALIZATION

The basic principle of operation is the same as with any other single beam SEM, wherein the sample is illuminated with a single focused electron beam probe of about one nanometer size. The primary electron beam is scanned line by line over the sample, producing secondary electron yield which is recorded pixel by pixel, generating the final SEM image. In the case of ZEISS MultiSEM 505, a multi-beam source produces an array of 61 electron beams that are subsequently focused onto the sample. Secondary electrons emanate from each primary electron spot and are imaged onto a multi-detector with one detection channel for each electron beam. The 61 electron beams are scanned over the sample with one global scanner, and a secondary electron signal is acquired for each scan position of each beam. A complete image of the region underneath the primary beam array is thus obtained in the time it takes one beam to scan its small sub-area (see Figure 2). With this approach the data acquisition can be accelerated by a factor of 61, a detail which requires the data acquisition system to also be highly parallelized in order to accommodate the large data acquisition rates. A second variety of the system, the ZEISS MultiSEM 506, operates with 91 beams and therefore a 3.5 larger field of view (see Figure 3) and a fivefold higher beam current per individual beam [5]. With the ZEISS MultiSEM 506, we clearly demonstrate that our modular design of a multi-beam SEM enables easy scaling to higher currents per beam and higher beam numbers.

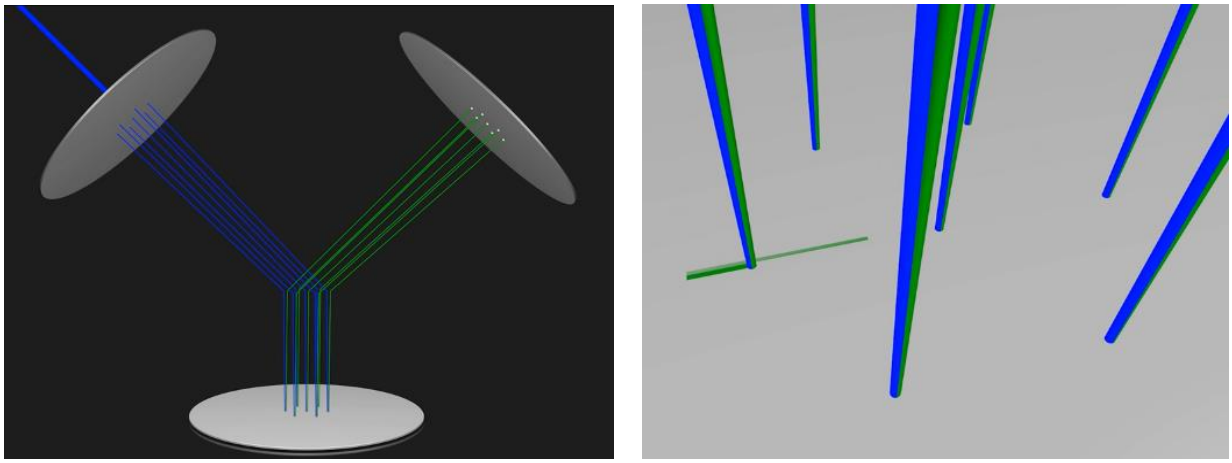

FIGURE 2. Visualization of the basic principle of operation. Multiple primary electron beams (blue) within a single column are scanned in parallel over a sample. One dedicated detector per secondary electron beam (green) enables parallel detection of the signals from all beams. For simplicity, only 7 beams are shown in this sketch. A video animation of the operation principle is available on the internet at https://www.zeiss.com/semiconductor-manufacturing-technology/products-solutions/process-control-solutions/multisem-505-506.html#video---images

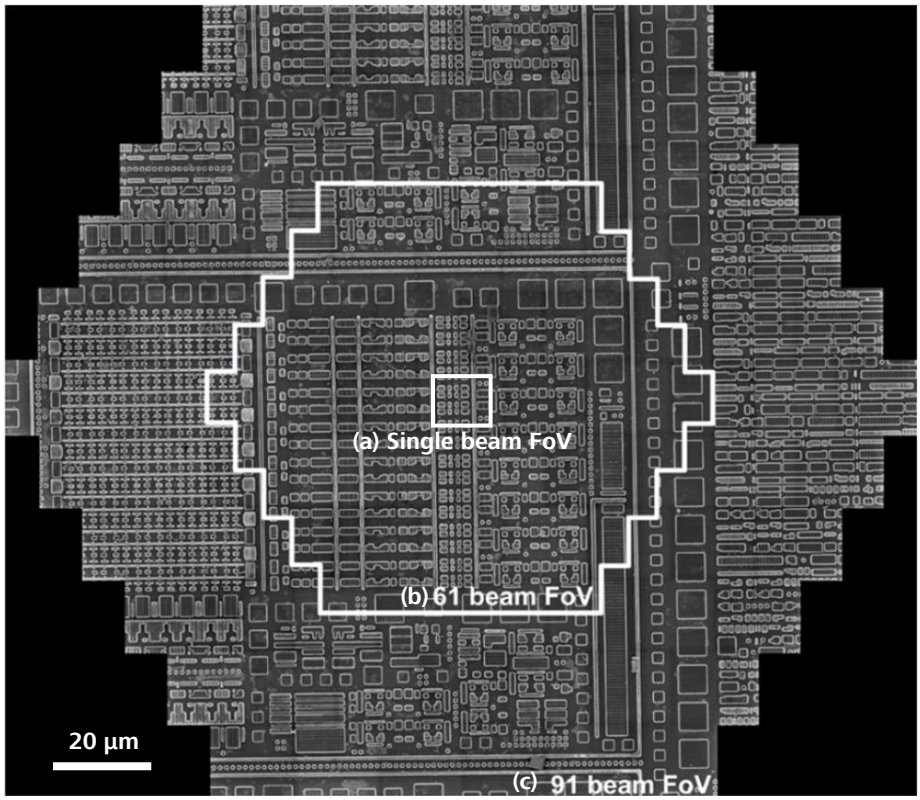

FIGURE 3. De-layered graphical processing chip showing a comparison between the field of view (FoV) captured per unit time (i.e. in a single image capture event) for (a) traditional single beam SEM, (b) 61 beam MultiSEM 505, and (c) 91 beam MultiSEM 506 configuration respectively.

APPLICATIONS

Out of the fields that will require high throughput imaging at nanometer resolution, two have already emerged, namely connectomics and reverse engineering of integrated circuits. However, we expect the application range of the multi-beam SEM to grow further, including geosciences, semiconductor industry as well .as precision engineering.

Connectomics

In neurobiological basic research, there is an increasing need to image large volumes of brain tissue at high resolution to gain insight into neural circuitry and the analysis of such extended cellular structures [6]. Future research directions already point toward reconstructing a whole brain with the aim of mapping its connectome, i.e. the brain's wiring diagram (see Figure 4). The long acquisition times of conventional SEM devices had prevented such projects in the past, since with traditional technology 3D mapping of only one cubic millimeter of brain tissue would have taken 6 years. However, with the ZEISS MultiSEM, this time is reduced to several months [7].

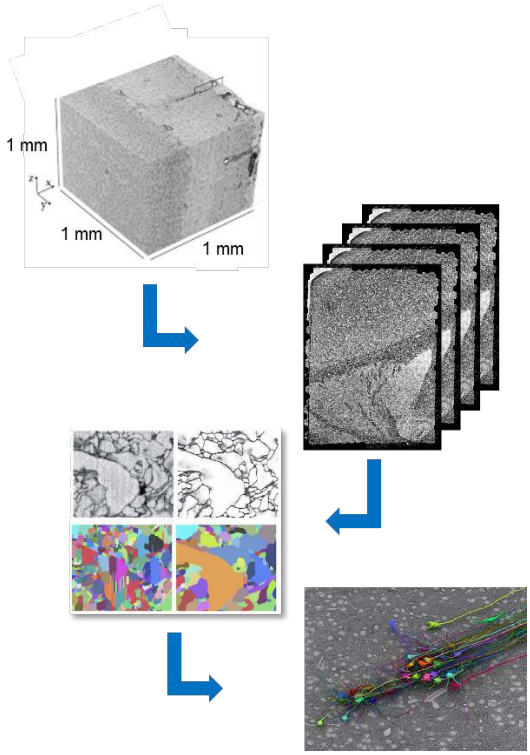

FIGURE 4. Schematics of the typical connectomics workflow aiming for the reconstruction of neural circuits. Sample with courtesy of J. Lichtman, Harvard.

Reverse Engineering

The 3D reconstruction and circuit extraction of modern microelectronics is a routinely used approach to qualify trusted suppliers and avoid threat through built in malware [8], or to search for violations of intellectual property. The capability to image the entire chip area of several circuit layers at nanometer resolution is a major benefit the MultiSEM can offer for the increasingly smaller feature sizes in latest and upcoming technology nodes. Figure 3 shows an example image taken from such a de-layered sample.

Shale Rock

The understanding of fluid flow within porous rock samples is important to researchers and industry alike, to evaluate the mechanisms, efforts and therefore profitability of extracting natural resources. Investigating larger areas of shale rock samples (see Figure 5) increases the statistical significance. When coupled with correlative mineralogy information, advanced image segmentation techniques are promising tools for elucidating the composition of the sample down to the nanometer scale [10].

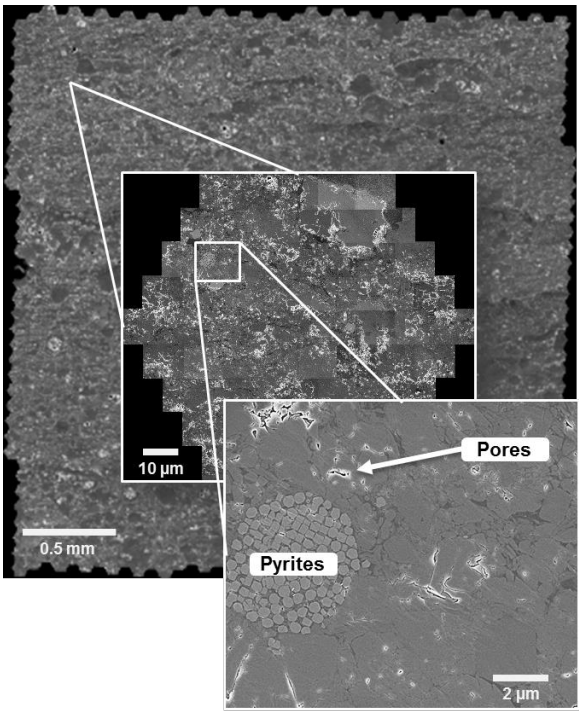

FIGURE 5. Example images acquired with MultiSEM 505 from a high maturity shale rock sample, with broad ion beam polished surface. Sample with courtesy of L. Hathon, Houston.

Semiconductor industry

As the structure size in semiconductor devices continues to decrease, there is a need for detection of particles or pattern defects that are only few nanometers in diameter. Comprehensively identifying these with an SEM requires that large areas be scanned for features at nanometer resolution. Increasing the assessable region of interest is of high importance in this field because these materials contain structures that are interconnected across many length scales [9].

Precision Engineered Surfaces

Manufacturing quality control efforts are also pushing further into the nano-realm as defects of interest become better understood on this length scale. As such, appropriate characterization tools must keep pace with industrial setting productivity while simultaneously providing suitably accurate probing. MultiSEM imaging of engineered surfaces allows for particle inclusion, porosity, and machining defects to be identified in rapid macroscale fashion at nanoscale exactitude, see Figure 6. Moreover, a unique "birds eye" view of larger areas of interest bringing new capability of defining macro effects of process changes, while still observing localized nano-effects. With current push with subtractive manufacturing methods this will allow better understanding of tool/surface interaction on a broader sample scale. Finally, growing application of additive manufacturing will require broader understanding of surface and part quality vs additive process, and MultiSEM opens new possibility for faster surface analysis.

CONCLUSIONS

Comprehensive characterization reveals a more thorough understanding of complex manufacturing processes by providing the details of property, processing, structure and function of interrelated phenomena across length scales. Traditional imaging characterization methods typically suffer from the throughput versus resolution duality which fails to provide appreciable statistical relevance along with highly meticulous detail. With the MultiSEM platform, simultaneous high throughput and high resolution studies are now possible due to the massively parallel electron beam imaging mechanism employed.

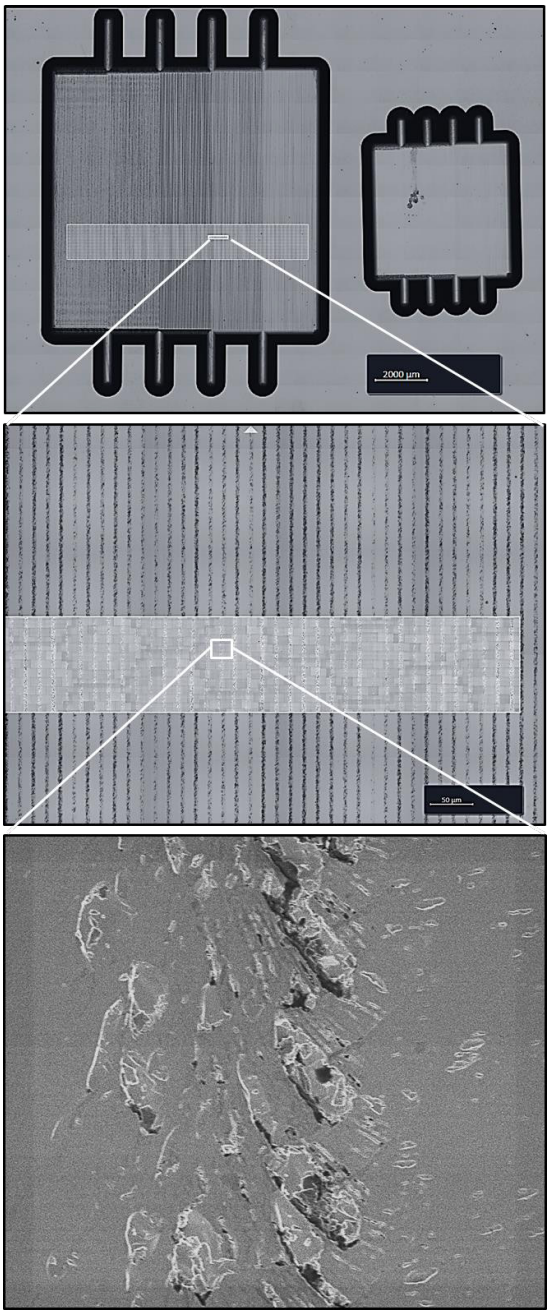

FIGURE 6. Example images acquired with MultiSEM 505 from Germanium sample with milled patch testing. Top and middle images are low-resolution overview images taken with a light microscope to facilitate navigation on the sample, middle image shows the superimposed MultiSEM dataset, and bottom image shows the image from one individual beam out of the hexagonal array. Sample with courtesy of Center for Precision Engineering at UNC Charlotte.

REFERENCES

[1] Slayter EM, Slayter HS. Light and electron microscopy. Reprint. New York: Cambridge Univ. Press; 1994.

[2] Orloff J. Handbook of charged particle optics. Boca Raton: CRC Press/Taylor & Francis; 2009.

[3] Goldstein JI, Newbury DE, Echlin P, Joy DC, Lyman CE, Lifshin E, et al. Scanning Electron Microscopy and X-ray Microanalysis: Third Edition. Boston, MA: Springer US : Imprint : Springer; 2003.

[4] Eberle AL, Mikula S, Schalek R, Lichtman JW, Knothe Tate ML, Zeidler D. High-resolution, high-throughput imaging with a multibeam scanning electron microscope. J Microsc 2015;259:114–20. doi:10.1111/jmi.12224.

[5] Kemen T, Malloy M, Thiel B, Mikula S, Denk W, Dellemann G, et al. Further advancing the throughput of a multi-beam SEM. In: Cain JP, Sanchez MI, editors. Proc SPIE, 2015, p. 94241U. doi:10.1117/12.2188560.

[6] Lichtman JW, Denk W. The big and the small: challenges of imaging the brain's circuits. Science 2011;334:618–23. doi:10.1126/science.1209168.

[7] Haehn D, Hoffer J, Matejek B, Suissa-Peleg A, Al-Awami A, Kamentsky L, et al. Scalable Interactive Visualization for Connectomics. Informatics 2017;4:29. doi:10.3390/informatics4030029.

[8] IARPA-BAA-15-12. RAVEN - Rapid Analysis of Various Emerging Nanoelectronics n.d. https://www.iarpa.gov/index.php/research-programs/raven/raven-baa.

[9] Malloy M, Thiel B, Bunday BD, Wurm S, Mukhtar M, Quoi K, et al. Massively parallel E-beam inspection: enabling next-generation patterned defect inspection for wafer and mask manufacturing. In: Resnick DJ, Bencher C, editors. Proc SPIE, vol. 9423, San Jose, California: 2015. doi:10.1117/12.2175535.

[10] Eberle A, Garbowski T, Bhattiprolu S, Crosby K, Zeidler D. High Throughput Shale Rock Imaging Using Multi-Beam Scanning Electron Microscopy. Microsc Microanal 2017;23:2114–5. doi:10.1017/S1431927617011230.

Error Budgeting Analysis for X-ray Systems Using a 0D Uncertainty Model

J. Cuadra[1], C. Divin[1], R. Panas[1]
Lawrence Livermore National Laboratory
Livermore, CA, USA

INTRODUCTION

Error budgeting for X-ray Computed Tomography (XCT) systems is yet to be implemented using all sources of error from each of the acquisition components which include mainly the source and detector. A quantification/estimate of the uncertainty via error budgeting is crucial for precision-type metrology applications using XCT since it is an effective nondestructive technique for medical imaging, characterization of materials, and dimensional as well as quality control assessments of manufactured parts [1–3]. Its increasing demand in dimensional metrology and quality assessment of complex manufactured part can be attributed to being able to nondestructively measure inaccessible internal features. Furthermore, XCT can characterize and measure multi-material components and assembled parts permitting both dimensional and material quality assessment in a single task [4,5]. XCT meets most basic requirements for medical and material characterization applications; however, dimensional CT metrology tends to require higher accuracy and spatial resolution [1,2,6]. Furthermore, the X-ray CT measurements are influenced by many different parameters resulting in additional error sources to those in traditional techniques such as coordinate measuring machines (CMMs) or optical methods. Such errors and uncertainties are intrinsic of the experimental setup and the tomographic reconstruction algorithms implemented for data post-processing. Some of these error sources are present in the environment, source, detector and other components include the temperature, humidity, mechanical vibrations, beam hardening effects, quantum efficiency, threshold determination, and others [1,6–8]. A 0D uncertainty model that attempts to characterize measured X-ray transmission and quantify the dominant sources of error in each data acquisition hardware component is presented and applied to a commercial XCT system herein.

METHODOLOGY

The 0D uncertainty model developed herein takes into account the signal variation as measured at a single pixel, including uncertainties and sensitivities from different data acquisition XCT system components and it implements a systems approach [9]. The 0D model is applied to a specific XCT system and it considers only errors which have no larger scale form, and thus does not require higher dimensional modelling. Inasmuch, the object is assumed to be a block of uniform thickness from the perspective of the studied pixel 'point' on the detector and quantify its corresponding uncertainty. Figure 1 displays the overall parameters included in the model for each XCT

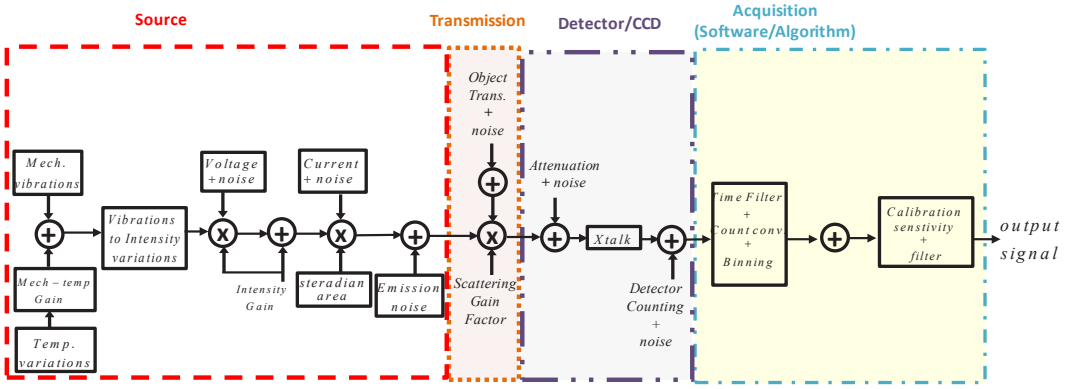

Figure 1: Graphical representation of the 0D model for a conventional XCT system including corresponding sources of error

system component in the form of a signal variation flow graph. For instance, the source includes mechanical vibrations at the source and with respect to the detector, ambient and component temperature effects, electrical current statistics noise and source emission variation which could affect the final emission of X-rays before they are recorded by the detector. Similarly, other sources of noises are acquired in the transmission and detector components since the object attenuation and scattering as well as the efficiency and count noise of the detector affect the final output signal. The signal variation flow graph also captures effects due to detector pixel cross talk, afterglow response, dark field offset (i.e. background noise of the detector) and a binning parameter in addition to a calibration term that normalizes the final response of the model output signal (Ψm).

$$\psi_m = ((((\sigma_{emission} + (G_{intensity} + (\sigma_{mech} + \sigma_{temp}\alpha_{mech/temp}) \cdot \alpha_{\Delta intensity/mech} + \sigma_{voltage} \cdot \alpha_{\Delta intensity/voltage})(\sigma_{current} + I)) \cdot \eta_o + \sigma_{\eta o}) G_{scattering}\eta_{eff} + \sigma_{\eta eff})G_{cross talk} + \sigma_{detector noise}) \cdot G_{binning} t_{exposure} \quad (1)$$

where σ, G, α, I, η_o, η_{eff} and t represent sources of error, gain factor, conversion coefficients, current, attenuation value, detector intrinsic efficiency and time. Furthermore, the signal variation flow graph depicts the use of low and high pass filtering to create a bandwidth of the uncertainty in terms of variance as a function of frequency. The variance is obtained by calculating the power spectral density function since the time measurements are treated as random processes and its statistical characteristics can only be described by the power of the noise instead of the amplitude (i.e. conventional Fourier Transform). The detailed variables used in XCT system source component of the model are depicted in Equation (2). This component of the model can be simplified to:

$$r_{ps} = \sigma_{ns} + (1 + \sigma_{\Omega})\Omega G_S \left\{ \begin{matrix} 1 + \alpha_{GS\theta x}\sigma_{G\theta x} + \alpha_{GS\theta y}\sigma_{G\theta y} + \\ \alpha_{GSVs}\sigma_V \end{matrix} \right\} \cdot (\sigma_I + I_s) \quad (2)$$

where Ω is the pixel solid angle as a function of the source coordinates, G_s is the X-ray intensity (flux) gain factor term, I_s is the current (for the case of electrically driven sources), σ_{ns}, σ_I, $\sigma_{G\theta x}$, $\sigma_{G\theta y}$, σ_Ω and σ_V are the noise parameters for the emission variation, current, angular variation in θx and θy, pixel solid angle variation and voltage, respectively. Equation (2) also includes $\alpha_{GS\theta x}$, $\alpha_{GS\theta y}$, and α_{GSV} which are the sensitivity coefficients for the angular variations in θx and θy in addition to the source voltage. This model for the XCT source also includes temperature variations and sensitivity coefficients which are comprised in the angular and pixel solid angle variations. The final output for Source model is r_{ps} which is the count rate (X-rays/second) produced by the XCT source. In the case of the model for the material/object transmission effects, the number of uncertainties includes a binomial noise

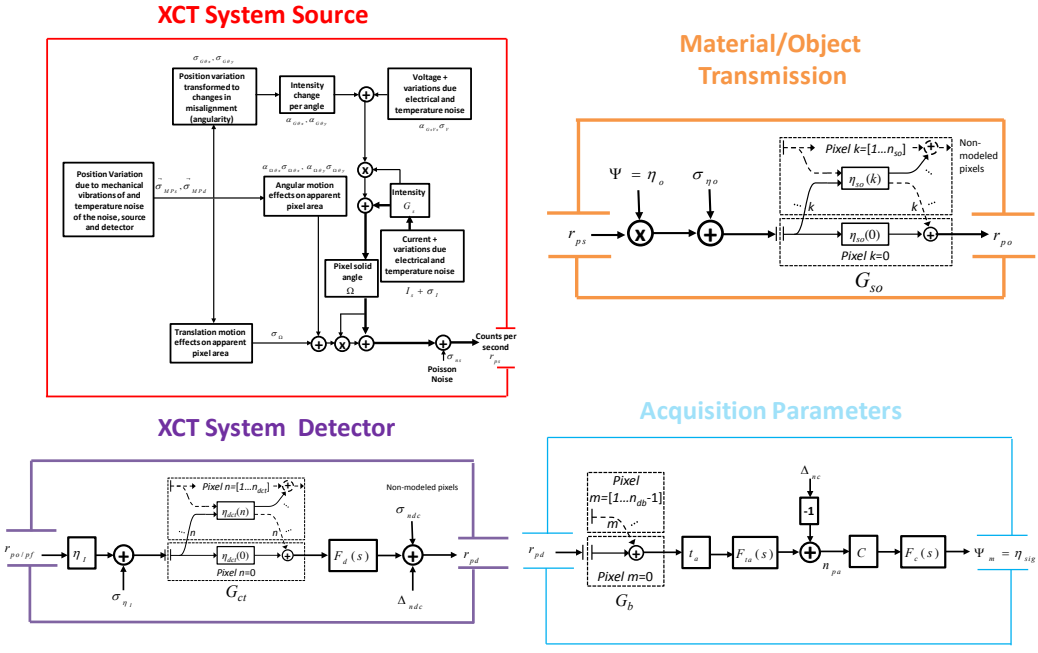
XCT System Source
Position variation transformed to changes in misalignment (angularity)
Intensity change per angle
Voltage + variations due electrical and temperature noise
Position Variation due to mechanical vibrations of and temperature noise of the noise, source and detector
Angular motion effects on apparent pixel area
Intensity
Current + variations due electrical and temperature noise
Pixel solid angle
Translation motion effects on apparent pixel area
Counts per second
Poisson Noise
Material/Object Transmission
Pixel k=[1...n_so]
Non-modeled pixels
Pixel k=0
XCT System Detector
Pixel n=[1...n_dc]
Non-modeled pixels
Pixel n=0
Acquisition Parameters
Pixel m=[1...n_db-1]
Pixel m=0

Figure 2: Signal variation flow graphs for all X-ray data acquisition components.

from attenuation term ($\sigma_{\eta o}$), a term for a specific object transmission (η_o) of the object and a gain factor associated to scattering (G_{so}). The output signal, r_{po}, in count rate units for the object transmission can be represented by:

$$r_{po} = \left(\sigma_{\eta o} + \eta_o r_{ps}\right) G_{so} \quad (3)$$

The output of the source or material/object transmission model, i.e. r_{ps} and r_{po} correspondingly, may be the input for an optical filter model with an output signal r_{pf}. This optical filter model is basically the material/object transmission model without any scattering term and it describes the count rate attenuation due to an optical filter. Moreover, any other type of filtering can be treated similarly by applying an additional transmission model. The model applied for the detector component describes the uncertainty measured by the noise due to the intrinsic efficiency ($\sigma_{\eta I}$) and counts (σ_{ndc}) of the system. In the model, the zero mean variations (unbiased) relative to a parameter are represented as σ while biases relative to the parameter value upon system calibration are denoted as Δ. The systemic error due to the offset from the counts (Δ_{ndc}), a cross talk factor (G_{ct}), a detector dynamics filter (F_d) and the count rate signal from either the object transmission (r_{po}) or the optical filter are included in the XCT detector model. The final signal yields (r_{pd}) in counts per second:

$$r_{pd} = \sigma_{ndc} + \Delta_{ndc} + G_{ct} F_d \left(\sigma_{\eta I} + \eta_I \cdot r_{po}\right) \quad (4)$$

Ultimately, the final output signal of the X-ray system is obtained by passing the signal from r_{pd} through a binning factor (G_b), converting it to counts by multiplying by the acquisition time (also referred as exposure time, t_a) as well as factoring a low pass filter (F_{ta}), applying a calibration offset (Δ_{nc}) and calibration factor (C) as well as implementing a high pass filter (F_C) adjusted by the time interval between system calibrations. The final equation (n_{sig}) gives formulation for the signal associated with the object transmission:

$$n_{sig} = F_C(s) C(-\Delta_{nc} + F_{ta}(s) t_a G_b r_{pd}) \quad (5)$$

The power spectral density function of each signal noise (sources of error), $S_n(f)$, is scaled by their respective frequency dependent sensitivities and geometrically summed to obtain the full system noise spectral density:

$$S_{\psi m}(f) = \sum_n \left|\frac{\partial \psi_m (2\pi i f)}{\partial \sigma_n}\right|^2 S_n(f) \quad (6)$$

An estimate of the noise variance is calculated by integrating the system spectral noise density over a frequency range. Then, the total uncertainty is expressed as

$$\sigma_{\psi m} = \sqrt{\int_{f_{min}}^{f_{max}} S_{\psi m}(f) \partial f} \quad (7)$$

The inputs for the model provided by the user include specific parameters from the XCT setup and spatial and time varying intensity and noise parameters as well as sensitivity coefficients. For instance, the setup parameters include exposure time, source-to-detector distance, current, and others. On the other hand, the intensity is measured on plane perpendicular to the X-ray path; and noise parameters are sources of error which are characteristic of the acquisition and thus need to be measured. These parameters consist of the mechanical vibrations, temperature variations and sensitivity coefficients, and others. Hence, the model requires in total 7 experimental measurements to apply the uncertainty model for a given XCT system. These measurements are essentially inputs for the time variations and sensitivities related to motion, temperature, intensity, and other types of noises. These experimental procedures include: (i) characterizing the X-ray source intensity, (ii) dark field counting noise, (iii) temperature fluctuations and thermal sensitivities, (iv) electrical potential and current fluctuations, (v) scattering measurements, (vi) pixel dynamics parameters (i.e. cross-talk and afterglow effects) and (vii) mechanical vibrations.

PRELIMINARY RESULTS AND DISCUSSION

The preliminary results consist of data acquired from 3 out of the 7 experimental measurements and uncertainty maps at each XCT component. The measurements for the model were obtained from a commercial system from *Zeiss Xradia*.

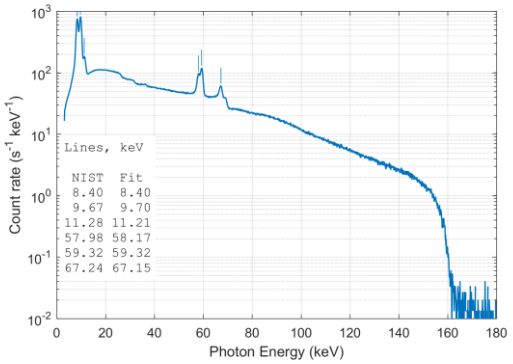

Figure 3: X-ray system spectrum for 160 k V at 0.3 W.

The first set of results was obtained from the X-ray flux intensity. These results involved using a X-123CdTe Amptek X-ray spectrometer (i.e. a single pixel detector) to measure both the spectral response and intensity for a 60 second

exposure time and a 160 kV at 0.3 W energy and power level. The flux was limited by the aperture of the single pixel detector. The 2048 channels in the detector were calibrated using the characteristic lines (shown in a table on the plot) of a tungsten anode. The bremsstrahlung X-ray source spectrum is shown in Figure 3 in units of count rate per keV. The intensity is the spatial average of the flux measured at positions on the plane perpendicular to the X-ray path. Figure 3 also depicts a decay as the energies get higher. Figure 4 shows a 15 x 7 mosaic-type measurement of the X-ray flux. Figure 4a and 4b show the spot size at 80 keV and 140 keV.

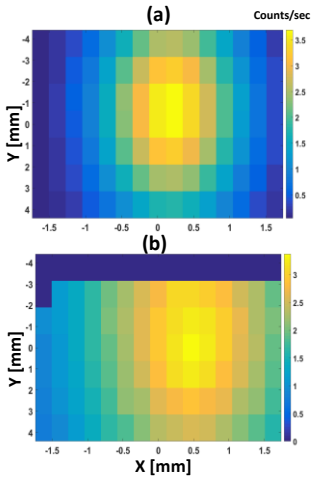

Figure 4: XCT system source intensity map integrated at two energy levels: (a) 80 keV and (b) 140 keV.

Another key measurement for the model is recording the thermal noise and sensitivity. All thermal effects relate to any motions or thermal expansion that could occur in the XCT components due temperature variations. Figure 5 displays the temperature spectral density functions at different hardware components when the XCT system is on and off. These measurements were taken in 10 second intervals for 48 hour period using thermocouples. The results show that the thermal response is comparable to low pass filter. Another experiment regarding the temperature measurements is the thermal sensitivity of the XCT system which is performed by varying temperature and recording the displacements.

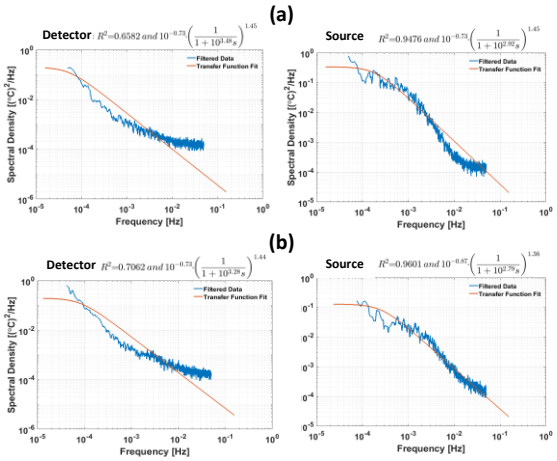

Figure 5: XCT system thermal spectral density response for the detector and source XCT system (a) on and (b) off.

The temperature variations are converted into motion which is then added to the mechanical vibrations of the components. This vibration analysis is recorded using tri-axial accelerometers. Figure 6 shows the spectral density functions for 3 translational components of the vibrations. The X- and Y- axes have a comparable behavior which shows flicker noise at low frequencies. On the hand, the Z-axis behaves as a low pass filter similar to the thermal response in Figure 5.

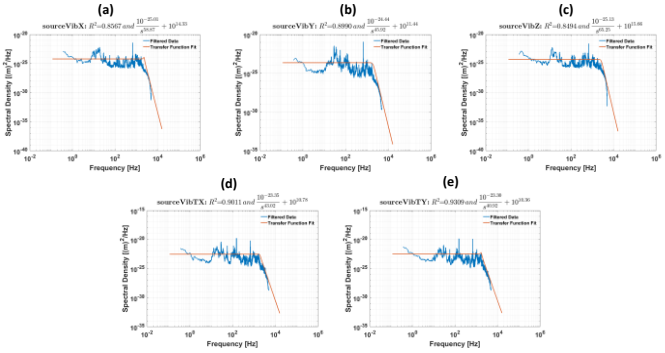

Figure 6: XCT system vibration spectral density response of the source in the (a) X-, (b) Y- and (c) Z-axes, (d) rotation about X, and (e) rotation about Y.

In the model, all motions are measured from vibrations and temperature variations and then based on a source-detector distance are used to calculate misalignment on the intensity G_S and any effects on the pixel solid angle Ω. Other crucial measurements need to be performed in order to implement the 0D uncertainty model.

CONCLUSION

The results from the model are an insight into the intensity and signal noise responses of an XCT system. When the model implemented, the results would include the total uncertainty on pixel coordinates at a given energy level and characteristic acquisition parameters. Both results are essential for precision metrology applications since they are informative data that can potentially identify dominant sources of error with the goal of improving the performance of the XCT system measurements. Furthermore, the uncertainty model will be extended from 0D (single pixel) to higher dimensional uncertainties with a target of mapping the full range of variation observed in XCT measurements.

ACKNOWLEDGEMENTS

This work was performed under the auspices of the U.S. Department of Energy by Lawrence Livermore National Laboratory under Contract DE-AC52-07NA27344. LLNL-CONF-738286.

REFERENCES

1. Carmignato, S. *et al.* Testing of x-ray microtomography systems using a traceable geometrical standard. *Meas. Sci. Technol.* **20,** 084021 (2009).
2. Kruth, J. P. *et al.* Computed tomography for dimensional metrology. *CIRP Ann. - Manuf. Technol.* **60,** 821–842 (2011).
3. Shah, P., Racasan, R. & Bills, P. Comparison of Different Additive Manufacturing Methods Using Optimized Computed Tomography. *6th Conf. Ind. Comput. Tomogr.* (2016).
4. Villarraga, H., Lee, C., Corbett, T., Tarbutton, J. A. & Smith, S. T. Assessing additive manufacturing processes with X-ray CT metrology. in *American Society for Precision Engineering, ASPE* (2015).
5. Villarraga, H., Lee, C., Charney, S. P., Tarbutton, J. A. & Smith, S. T. Dimensional metrology of complex inner geometries built by additive manufacturing. in *American Society for Precision Engineering, ASPE* (2015).
6. Carmignato, S., Pierobon, A., Rampazzo, P., Parisatto, M. & Savio, E. CT for Industrial Metrology – Accuracy and Structural Resolution of CT Dimensional Measurements. *Conf. Ind. Comput. Tomogr.* 161–172 (2012).
7. Carmignato, S. Computed tomography as a promising solution for industrial quality control and inspection of castings. *Metall. Sci. Technol.* **30,** 5–14 (2012).
8. Carmignato, S. Accuracy of industrial computed tomography measurements: Experimental results from an international comparison. *CIRP Ann. - Manuf. Technol.* **61,** 491–494 (2012).
9. Panas, R. M., Cullinan, M. A. & Culpepper, M. L. Design of piezoresistive-based MEMS sensor systems for precision microsystems. *Precis. Eng.* **36,** 44–54 (2012).

AN OPTICAL METHOD FOR IN-SITU MEASUREMENT OF FORM AND SURFACE PROFILE OF AXISYMMETRIC OBJECTS

Navid Farahi[1, 2, 3], Mehrdad Abolbashari[5], Jonathan Babaie[1, 2, 3], John Ziegert[1, 4], Faramarz Farahi[1, 2, 3]

[1]Center for Precision Metrology, University of North Carolina, Charlotte, NC 28223, USA

[2]Center for Optoelectronics and Optical Communications, University of North Carolina, Charlotte, NC 28223, USA

[3]Department of Physics and Optical Science, University of North Carolina, Charlotte, NC 28223, USA

[4]Department of Mechanical Engineering and Engineering Science, University of North Carolina, Charlotte, NC 28223, USA

[5]OPTONIKS CORP, PORTAL Building, 9319 Robert D. Snyder Road, Charlotte, NC 28223, USA

INTRODUCTION

Measurement of the form and profile of large axisymmetric parts with a large varying slope with micron-level resolution is a challenge in manufacturing. Currently, the part is dismounted off the machine for measurement, which is a time-consuming process. An in-situ technique enabling on-machine measurement of form and surface features eliminates this problem and eliminates the challenge of realigning the part on the machine if additional machining steps are needed.

A few methods, such as coordinate measuring machines (CMM) and laser scanners [1] are available for measuring the 3D profile of large objects. CMM offers high accuracy but needs the part to be taken off the machine for measurement. On the other hand, laser scanners can be used for on-machine measurement of the part, if just a single line scan is sufficient. However, they are not suitable for measurement of sharp slope [2,3]. Other methods include Structured Light Projection (SLP) techniques. SLP methods are fast but challenges include calibration for large objects as well as projecting high-frequency fringe patterns to achieve high resolution [4].

In this article, we discuss an adaptive fringe projection technique (AFPT) reported by Samara et.al. [5]. We will present challenges associated with adaptive fringe projection when applied to large objects and required modifications will be explored. We will introduce a new system where the adaptive fringe projection is combined with SLP. We project adaptive fringes, such that if the form of the object is perfectly matched with the initial design, the fringes will appear as straight and parallel lines, similar to those observed if the surface was flat. Any deviation from straight and parallel lines seen in the camera image is directly related to deviation from the ideal form and size. This method enhances the resolution of the system while maintaining a large dynamic range.

SYSTEM DESIGN

Figure 1a shows a schematic of the AFPT setup. Adaptive fringes are projected on the workpiece using a DMD projector and a camera captures the image of the fringes. The projector lens is select-

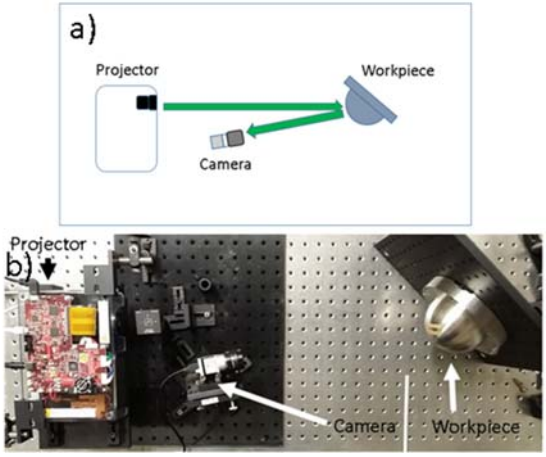

FIGURE 1. a) Schematic of an Adaptive Fringe Projection setup. b) Adaptive Fringe Projection setup.

ed to have a depth of focus appropriate with the large piece to be measured. In addition, in order

to have the maximum number of fringes for the measurement, the field of view of the lens has to be large enough to cover the area needed for measurement

METHOD

Adaptive fringes are projected onto the workpiece using a digital projector and a camera captures parallel fringes with minor distortion due to surface features. We use the CAD model of the part to create a fringe pattern such that when projected on the part, produce straight parallel lines from the camera perspective. This is achieved by relating CCD pixel coordinates to projector pixel coordinates, using the Inverse Coordinate Transformation Function.

To do this, we require all system parameters such as decenters and tilts of the lenses used in the system, distances and angles of cameras and projector in the object coordinate system. Finding system parameters and calibration of the system are done in two steps by using a known workpiece close to the CAD design, e.g. a *master part*. The two steps are as follows:

1- We simulate the system and use an optimization algorithm to find a set of system parameters. The simulated system includes DMD and CCD screens, camera and projector lenses and the workpiece. After finding the system parameters we are able to calculate the Inverse Coordinate Transformation Function from camera pixel coordinates to DMD pixel coordinates. This is necessary to make adaptive fringes. Figure 2a shows the workpiece. In order to find the Coordinate Transformation Functions, we project a set of point spots (Figure 2b) onto the workpiece and capture an image by the camera (Figure 2c). We use coordinates of these points on the DMD and CCD as inputs to our simulated system. We assume the system works in the geometrical optics regime and the lenses are pinholes. Figure 2d shows the object spherical coordinates from the camera point of view. Figure 2e shows a typical trace on the workpiece used for calibration.

2- We choose a spherical coordinate system based on the geometry of our workpiece and we desire to find a direct relation between the change in the radius of the part and the interferometric phase, so we start with the following equation to calibrate the system:

$$dr = C \times d\varphi \qquad eq.1$$

where dr is the difference between the measured radius and a predefined value based on the initial design for each point on the object, C is the calibration parameter and $d\varphi$ is the phase value for each point that is obtained by subtracting the simulated phase map of perfect design (form)

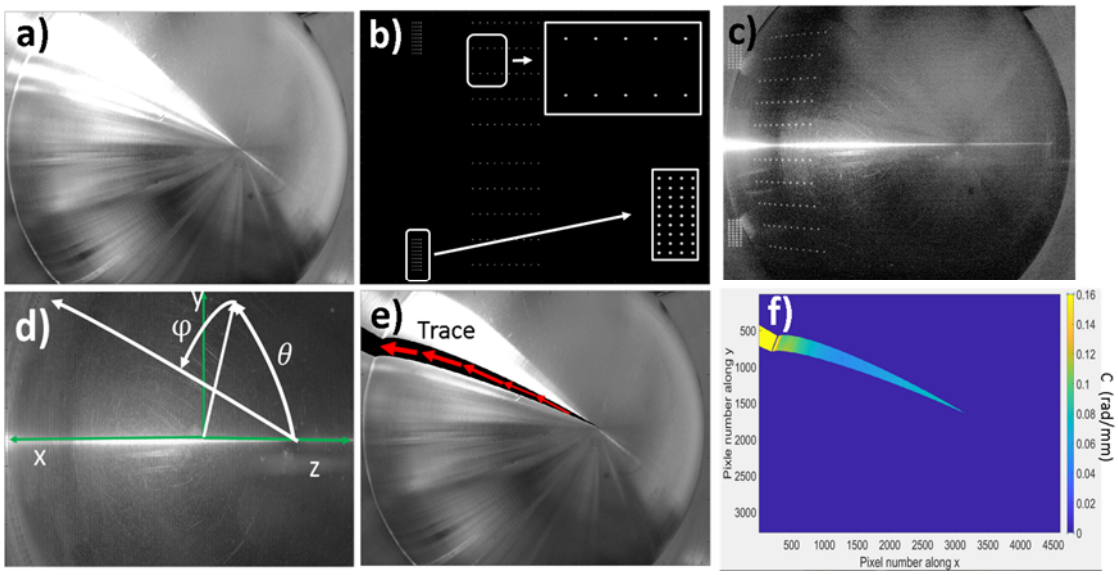

FIGURE 2. These figures show a) the hemispherical workpiece, b) a set of point pattern projected on the object, c) a captured image from the object, d) chosen spherical coordinate system on the object, e) a selected trace on the object, f) calibration parameter C for each pixel on the trace obtained through calibration process. Trace depicted in (e) is used for the measurement.

from the phase map acquired by the experiment. As we will see, in our experiment we use the initial values of the radii from the CMM measurement data.

We project adaptive fringes and obtain a phase map φ associated with deviation from the ideal form using a 7 bucket phase shifting algorithm, which is mathematically shown as [6]:

$$\varphi = tan^{-1}\left(\frac{7(I_3-I_5)-(I_1-I_7)}{8I_4-4(I_2+I_6)}\right). \qquad eq.2$$

We calculate $d\varphi$ by subtracting the carrier phase from the above phase map. Hence, we can obtain *dr* from *eq*.1 and use calibration parameter *C* (figure 2f) over the trace shown in figure 2e. Because of the axisymmetric form of our workpiece, it is sufficient to make the measurement over one arbitrary trace such as one shown in figure 2e.

EXPERIMENT AND RESULTS

The test object is a hemispherical workpiece with a nominal radius of 51.00 mm on a flat base as shown in Figure 2a. Figure 3 shows CMM data plotted over half of an arbitrary trace passing through the pole. The arrows show the starting point (A) of CMM data is just above the flat base and end point (B) is at the pole of the hemisphere. The profile is plotted in a spherical coordinate system (object coordinate system) and its origin is on the symmetry axis, on the flat base. The CMM data plot

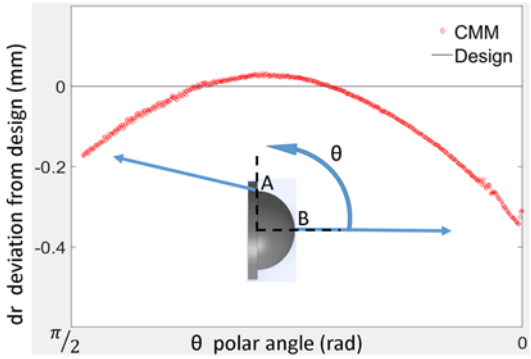

FIGURE 3. The plot of CMM data of the workpiece.

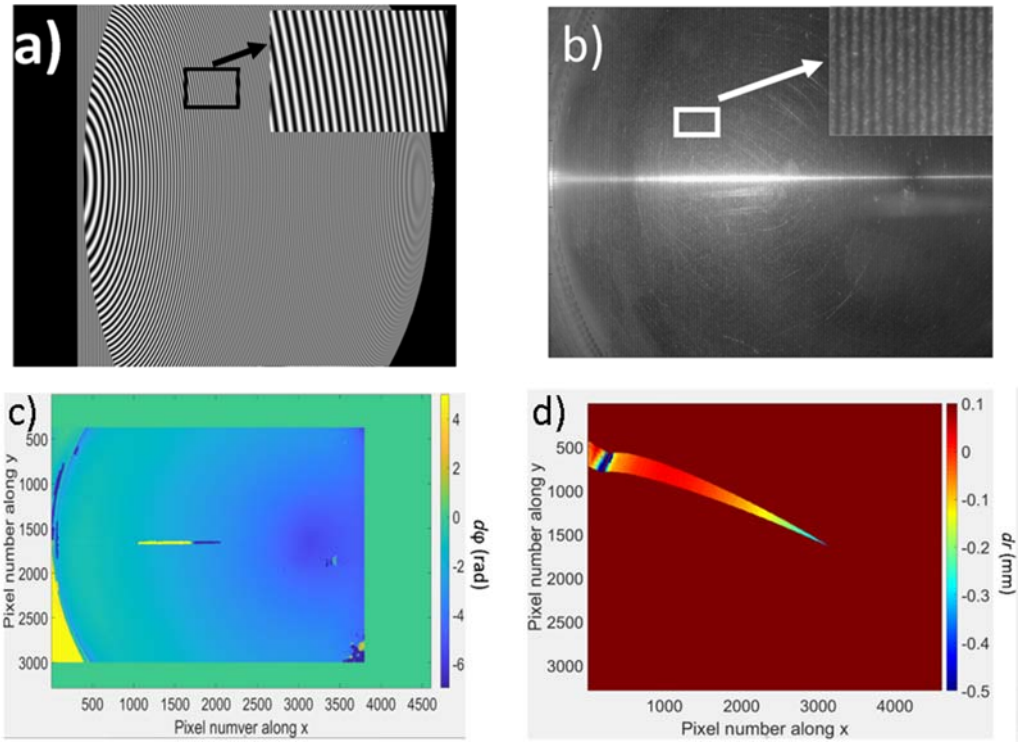

FIGURE 4. These figures show a) a sample high-frequency adaptive fringes on DMD projector, b) a camera image taken of those adaptive fringes projected onto the workpiece, c) the phase map of the adaptive fringes, d) dr measured for each pixel on the trace, e) the plot of all measurement in comparison with CMM data, f) a zoomed in plot for the framed region in (e).

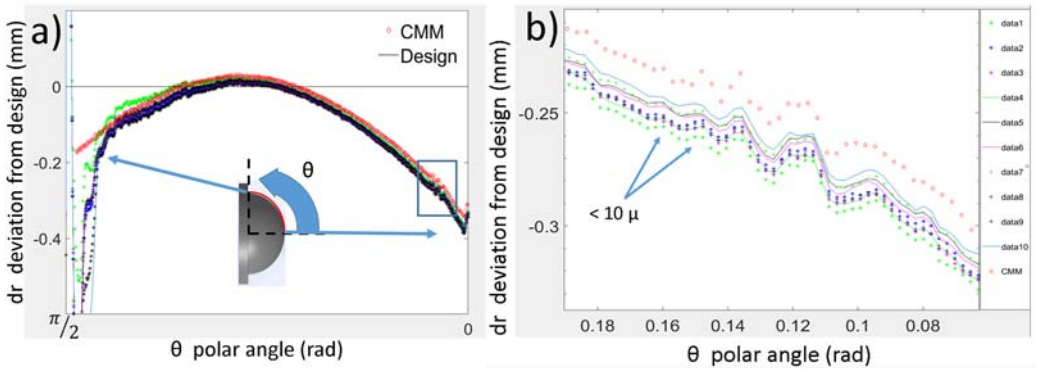

FIGURE 5. These figures show a) the plot of all optical and CMM measurement in comparison with the initial design, b) a zoomed in plot for the framed region in (a).

shows how the workpiece deviates from the initial ideally hemispherical design.

Figure 4a shows the projected adaptive fringes and Figure 4b shows an image captured by the camera. As it is clearly seen in the zoomed image in Figure 4b, the straight fringes on the camera have minor distortions that represent the deviations from the CAD model. Figure 4c shows the phase map corresponding to these deviations. We, therefore, calculate dr by substituting $d\varphi$ and C in *eq.*1 (Figure. 4d).

We take 10 successive measurements every 30 minutes for a repeatability and sensitivity test of the system. Figure 5a shows the plot of CMM data as well as the plots of these 10 measurements for comparison. The results are in a very good agreement with CMM data, except the region approaching θ equal $\frac{\pi}{2}$. As the slope of different regions on the part relative to the optical axis of the system varies, we face a situation where a few pixel on the camera cover a large area on the object; as a result, a phase discontinuity occurs and consequently calculated dr values are unreliable. Adding a second camera to our system will eliminate this problem. Figure 5b shows a 'zoomed in' plot of the framed region on the right side of Figure 5a. As it shows, our data are repeatable with the precision of less than 10 microns.

CONCLUSION

We have shown an adaptive fringe projection technique is capable of measuring the form of a large part in comparison with the design parameters and is able to measure small form deviations of large axisymmetric workpieces with a precision and repeatability better than 10 microns.

The system measures the deviation of radius from the design value in spherical coordinates, which is the type of information needed for the 3D profile of an object with spherical form. Our method effectively provides the absolute value of radius as a function of polar angle.

In this method, unlike CMM technique, the need to take the workpiece off the machine is eliminated. The developed system is fast and can be used for on-machine measurement.

We are in the process of adding a second camera in order to increase the field of view of our system.

REFERENCES

[1] Leach R, editor. Optical measurement of surface topography. Berlin: Springer; 2011. 27-33.

[2] Kusnoto B, Evans CA. Reliability of a 3D surface laser scanner for orthodontic applications. American Journal of Orthodontics and Dentofacial Orthopedics. 2002; 122(4):342-8.

[3] Kumar S, Tiwari PK, Chaudhury SB. An optical triangulation method for non-contact profile measurement. Industrial Technology, 2006. ICIT 2006. IEEE International Conference. 2006 Dec 15. 2878-2883.

[4] Gorthi SS, Rastogi P. Fringe projection techniques: whither we are?. Optics and lasers in engineering. 2010; 48:133-40.

[5] Samara A, Farahi F, Davies A. Dynamic range enhancing technique for form, waviness and roughness measurements using fringe projection. InProc. SPIE 2005 Jul 31. 5879: 150-161.

[6] Malacara D, editor. Optical shop testing. John Wiley & Sons; 2007: 595.

ATTRITION/ABRASIVE WEAR MONITORING OF CUTTING TOOLS BASED ON KNIFE-EDGE INTERFEROMETRY

ChaBum Lee[1], Rui Zhao[2], Seongkyul Jeon[1], Abolfazl Zolfaghari[1]
[1]Department of Mechanical Engineering
Tennessee Technological University
Cookeville, TN, USA
[2]Division of Mechanical Design
GE Appliances
Lafayette, GA, USA

INSTRUCTIONS

The accuracy of a precision machine tool greatly depends on the feed accuracy and stiffness of the bearings and linear guide. While conventional general-purpose machine tools used in most machine shops have an accuracy of several micrometers, precision machine tools provide enhanced positioning resolutions, typically 10 nm in linear (*XYZ*-axes) and 0.0001° in angular (*B*-axis) directions. The enhanced positioning accuracy ensures work piece accuracies to a few tens of nanometers with less than 5 nm of surface finish error. Therefore, micro-to-nanoscale cutting tool wear significantly influences the machined part quality in terms of precision machining. In general, the integrity of the cutting tool is ensured by inspection before and after machining.

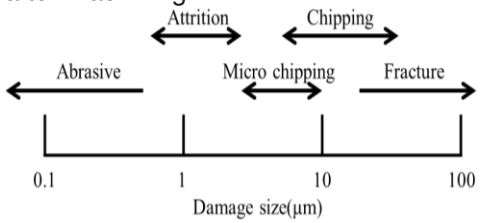

FIGURE 1. Classification of cutting tool wear.

Wear of cutting tools is caused by material stress and thermal change at the tool edge [1], which in turn depend on the cutting mode such as turning, milling, and drilling as well as the cutting conditions and cutting fluid [2-4]. Cutting tool wear can be classified as abrasion (nanoscale), attrition (microscale), chipping (mesoscale), and fracture according to the damage size as shown in Figure 1.

As the micro-nano scale wear progresses, the morphology and dimensional accuracy of the cutting tool is reduced and the worn cutting tool has to be replaced. In mass production systems, the tool is replaced on a schedule, while precision cutting tools, such as a diamond cutters, are replaced according to the condition of the tool due to high costs. Currently, the machining operator visually inspects the cutting tool conditions, but this method cannot be applied to micro-nanoscale cutting tool wear detection. For more accurate results, the scanning electron microscopes (SEM), atomic force microscopes (AFM), touch-triggered stylus probes (TSP), stereo microscopes with a digital camera attachment, computer vision systems, coordinate measuring machines (CMM), cutting force measurement, and acceleration measurement are used to measure cutting tool wear parameters [5,6]. In addition, more advanced measuring techniques using white light interferometry or confocal microscopy can be applied when a nanoscale analysis is necessary [7]. However, all these methods require a machine operator to remove the cutting tool from a tool fixture for inspection, and they are less efficient in providing the necessary cutting tool information, such as morphology, wear, and chipping conditions, quantitatively.

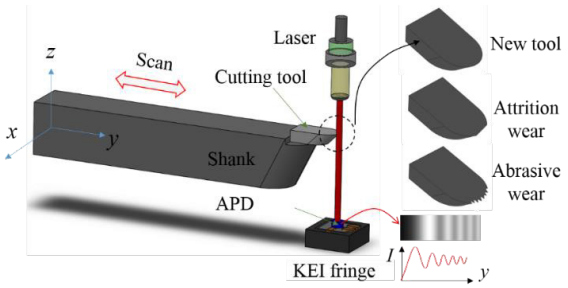

FIGURE 2. Knife-edge interferometry for cutting tool wear monitoring.

MEASUREMENT PRINCIPLE

Unlike the conventional cutting tool monitoring techniques mentioned above, there is a technical gap that prevents directly measuring or monitoring the cutting tool conditions easily, conveniently and affordably.

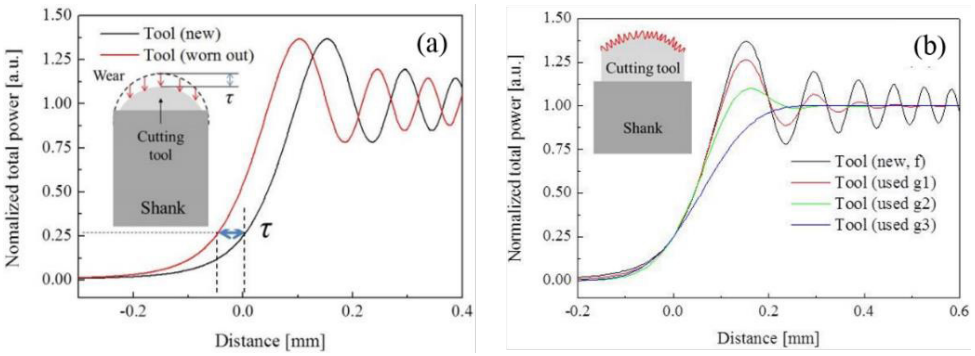

FIGURE 3. KEI effects on cutting tool wear: (a) attrition wear and (b) abrasive wear.

In this study, a novel method based on knife-edge interferometry (KEI) combined with cross-correlation for characterizing cutting tool wear is proposed. An incident wavefront of the light diffracts or bends when it strikes the sharp edge of an obstacle that transverses the propagation direction. Due to interference of two superimposing waves (geometrical wave from the primary source of light and the boundary diffraction wave from the secondary source), a diffraction pattern can be visible at the detector plane. The Huygens-Fresnel Principle explains this effect.

A novel KEI method illustrated in Figure 2 is proposed to provide cutting tool wear monitoring. Unlike an amplitude-splitting interferometer, such as the Michelson interferometer, the KEI utilizes constructive and destructive interference of the transmitted wave and the diffracted wave at the edge of a precision cutting tool under testing. The interference fringes produced by diffraction at the cutting tool edge are highly sensitive to cutting tool geometry as well as its morphology. A laser beam is incident on the cutting edge, and the photodetector (PD) scans a small area near the cutting tool edge to measure the edge diffraction intensity. To study the effects of precision cutting tool conditions (attrition wear and abrasive wear) on the interferometric pattern, a cross-correlation method (Eq. 1) that shows the relationship between KEI scan data of the new tool and used tool is used,

$$f(t) \otimes g(t) = \int f(\tau) g(t-\tau) d\tau \qquad (1)$$

where the two functions *f(t)* and *g(t)* represent the normalized light intensity for the new and worn cutting tools, and $\otimes$ denotes convolution.

The *cross-correlation* is a measure of similarity of two series as a function of the displacement of one relative to the other. For example, in Figure 3, as the tool edge roughness increases, the oscillation amplitude of the interferogram decreases and the phase shift of the interferogram increases due to tool edge attrition. Outputs of cross-correlation return the pattern shift, τ, and similarity of the two curves. As previously studied, a rougher and duller edge morphology correlates to a weaker interferogram (interference pattern) intensity because the reflection from a rough surface is diffusive, which weakens the interference pattern. If the edge morphology change does not shift the curves but reduces the amplitude of oscillation, the cross-correlation results return similarity of two curves with no lag.

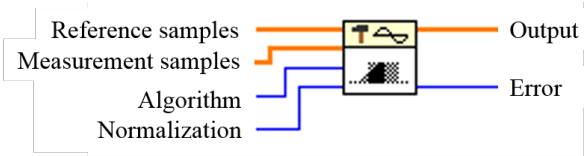

FIGURE 4. LabView diagram for correlation.

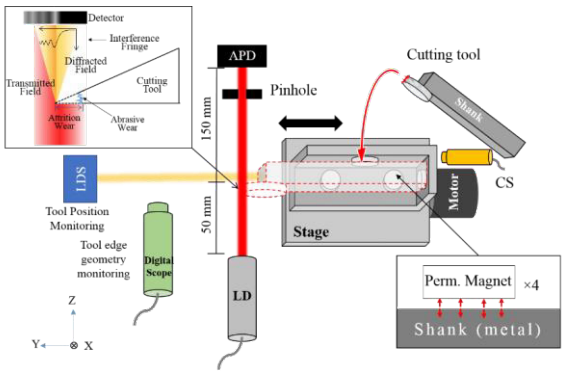

FIGURE 5. Experiment setup.

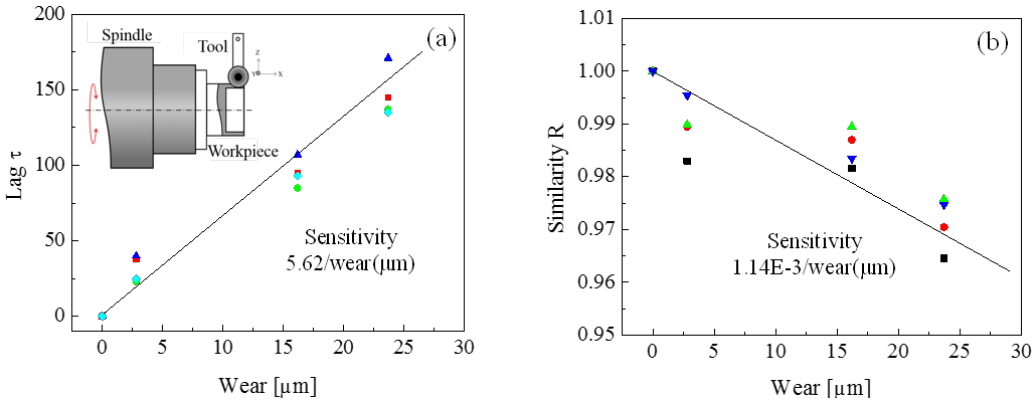

FIGURE 6. Cross-correlation results of knife-edge interferometric fringes with respect to wear conditions: (a) attrition and (b) abrasive.

For cross-correlation calculation, LabView hardware collects the signals and software calculates the correlations between reference samples and measurement samples as shown in Figure 4. An algorithm specifies the correlation method to use and computes the cross-correlations using the direct method of linear correlation. Normalization specifies the method for computing the cross-correlation between two inputs.

EXPERIMENTS

The following cutting tool was selected: radius of curvature 6 mm, thickness 2.5 mm with a carbide round cutter insert. As illustrated in Figure 5, the experiment setup consists of the cutting tool, a single-axis precision stepping motor-driven linear stage, a laser diode (LD, 5 mW, λ 633 nm), an avalanche photodiode (APD, size ϕ 0.23 mm), a capacitive sensor (CS, 10 nm resolution) and a laser displacement sensor (LDS, 1 μm resolution). A digital microscope is used to monitor cutting tool edge geometry, and CS and LDS are used to monitor initial cutting tool position and the trajectory of the stage, respectively. LD and APD are placed 50 mm and 150 mm apart from the cutting tool, respectively. To remove the cutting tool setting error, four permanent magnets are placed on the bracket to properly hold the tool. The Al rod (ϕ30 mm) was machined with the cutting tool in a lathe with no working fluid to accelerate the cutting tool wear. The cutting conditions were a spindle velocity of 1,120 rpm, a depth of cut of 50 μm, and a feed rate of 0.1 m/rev. The cutting tool conditions were monitored based on the cutting length: 0 m, 3 m, 6 m, and 9 m. Attrition wear was measured 10 times each by an optical microscope, and then was averaged at each cutting length. The KEI fringes of the cutting tool were obtained by scanning the cutting tool after machining a certain cutting length. Prior to scanning, the position of the cutting tool was measured by CS and LDS and placed at the same position whenever the cutting tool was scanned. As a reference, the KEI fringe of the new cutting tool was obtained, and the KEI fringe of the new tool was cross-correlated with the used tool's fringe. The fringes were collected with a National Instrument data acquisition device (NI6351) with 50 kHz sampling frequency, while collecting the CS and LDS outputs. The wear characteristics of the cutting tool with a radius of curvature of 6 mm were investigated by measuring the interferometric fringes of the tool while cutting an aluminum workpiece in a lathe. The fringes were measured four times each under the different cutting tool conditions, including the lag, similarity and damping ratio of fringes, and the variation of cross-correlation outputs was estimated. As a result (Figure 6), the attrition and abrasive wear of the cutting tool showed a linear relationship of 5.62 lag/wear (μm) and 1.14E-3/wear (μm), respectively.

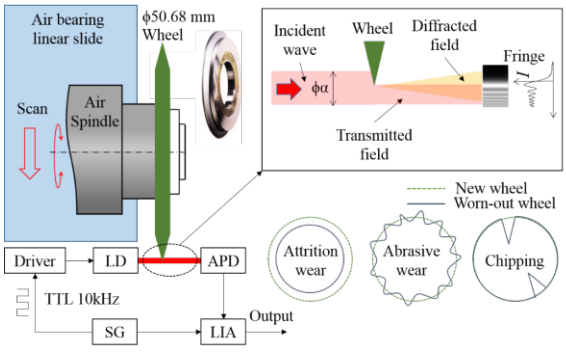

FIGURE 7. Dicing wheel wear monitoring.

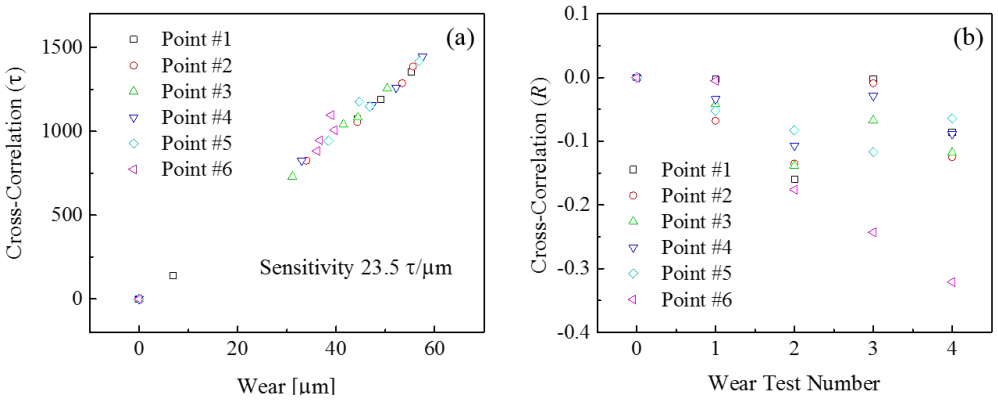

FIGURE 8. Results of cross-correlation of the fringes measured at six different measurement points.

Similarly, the KEI technique was applied to a non-contact, convenient, efficient dicing wheel cutting tool wear monitoring technique as shown in Figure 7. In Figure 8, the cross-correlation results show that the averaged sensitivity is 23.5 lag(τ)/wear(μm) and *R* tends to lower as the number of machining cycles increases. The *R* number was set to zero when it correlates with its own. Estimating the wheel edge equality quantitatively is limited to current surface measurement technology even though the validation work is necessary in this work. Here, the cross-correlation method was used to see the relative degradation of wheel edge quality. As a result, the attrition wear of the wheel became increasingly pronounced as the cutting length increased. However, the abrasive wear at the wheel edge was too difficult to identify because a new cutting tool edge was created by the attrition wear itself. Although the wheel wore down around the end of the wheel edge, the new wheel edge remained sharp. It is thought that the abrasive wear can be detected by the proposed method if there is significant wear such as chipping or if there only exists the abrasive wear in the machining processes. The chipping effect of the dicing wheel on the edge diffraction fringe was investigated. The reference fringe pattern was measured by scanning the edge of the new dicing wheel. After machining under a severe condition (Figure 9b), the fringe pattern shift was found to be 110 μm and *R* was -0.211. Also, its peak voltage was approximately 5% lower than that of reference fringe, and the rate of decay of the oscillation from the logarithmic decrement of the fringe patterns, (a) and (b), was 0.159 and 0.116, respectively. This ratio also can be used to estimate the wheel wear. The edge diffraction pattern of the chipped area was measured. Because the LD beam diameter (ϕ3 mm) is larger than the chipped depth of 1 mm, the fringe pattern can be observed due to the diffraction from the Al wheel base.

However, the pattern (c) was found to be slightly different from the typical patterns, (a) and (b). The weak fringe oscillation can be considered as the diffraction effect at the Al wheel base. As a result, the fringe patterns according to attrition, abrasive and chipping wear conditions are clearly different, and the wear condition is predictable through analyzing the fringe patterns.

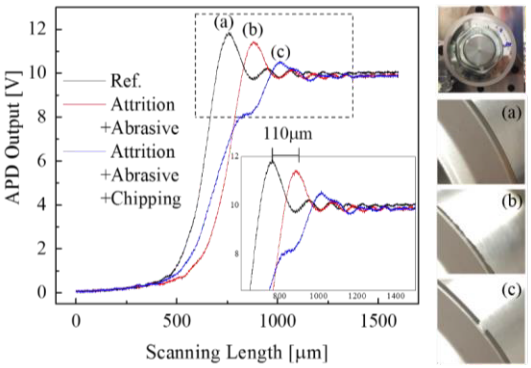

FIGURE 9. Fringe patterns according to attrition, abrasive and chipping wear conditions of the dicing wheel.

CONCLUSION

A simple, low-cost and convenient cutting tool wear monitoring technique by KEI was theoretically and experimentally discussed. The proposed measurement method can measure both attrition wear and abrasive wear using

cross-correlation of KEI fringes of two different cutting tool conditions. In the experiment, the cutting tool attrition and abrasive wear showed a linear relationship of 5.62 lag/wear(μm) and 1.14E-3/wear(μm) for the insert tool, 23.5 lag(τ)/wear(μm) for the wheel, respectively. However, the abrasive wear at the end of the cutting tool edge was too difficult to identify because a new cutting tool edge was created by the attrition wear. Although the cutting tool wore down at the end of the tool edge, the new cutting tool edge created by attrition remains sharp. Also, it was found that the effect of cutting fluid can be avoided by blowing the compressed air or cleaning it with alcohol. Furthermore, it was shown that the diamond cutting tool wear conditions can be monitored by the proposed method. This indicates that the proposed method can be directly used for cutting tool radius compensation in on-machine measurement applications and makes possible a high-resolution diagnosis of precision cutting tool wear.

ACKNOWLEDGEMENT

The research was supported by NSF (Award Number: CMMI 1463502) through Tennessee Technological University. Similarly, this work was supported by the Center for Manufacturing Research at Tennessee Technological University. Also, the author acknowledges the support of National Instruments in the form of an academic research travel grant, which enabled him to attend this conference.

REFERENCES

[1] Geoffrey Boothroyd and Winston A. Knight, Fundamentals of Machining and Machine Tools Third Edition, CRC Press, 2005.

[2] Yeon Hwang, Tsunemoto Kuriyagawa and Sun-Kyu Lee, Wheel curve generation error of aspheric microgrinding in parallel grinding method, International Journal of Machine Tools and Manufacturing, Vol. 46, pp. 1929-1933, 2006.

[3] Frederick Winslow Taylor, On the Art of Cutting Metals, American Society of Mechanical Engineers, 1907.

[4] Sun-Kyu Lee, Yuji Miyamoto, Tsunemoto Kuriyagawa and Katsuo Syoji, Effects of minimizing hydrodynamic pressure in ultra-precision mirror grinding, International Journal of Machine Tools and Manufacturing, Vol. 44, pp. 1031-1046, 2004.

[5] Wei Gao, Precision Nanometrology: Sensors and Measuring Systems for Nanomanufacturing, Springer, 2010.

[6] Fred Waters, Fundamentals of Manufacturing for Engineers, UCL Press, 2003.

[7] Arnaud Devillez, Samuel Lesko and Wayne Mozer, Cutting tool crator wear measurement with white light interferometry, Wear, Vol. 356, No. 1-2, pp. 56-65, 2004.

CHALLENGES IN MEASURING SPHERICAL GEOMETRY USING TERRESTRIAL LASER SCANNERS

Bala Muralikrishnan[1], Prem Rachakonda[1], Meghan Shilling[1], Vincent Lee[1], Daniel Sawyer[1], Geraldine Cheok[1], and Luc Cournoyer[2]

[1]National Institute of Standards and Technology, Gaithersburg, MD 20899
[2]National Research Council of Canada, Ontario, Canada K1A0R6

INTRODUCTION

Terrestrial laser scanners (TLSs) measure 3D coordinates in a scene by recording the range, the azimuth angle, and elevation angle of discrete points on target surfaces. They are increasingly used in a variety of applications, including manufacturing and civil infrastructure systems. However, the error sources of these instruments are not yet adequately characterized. There is a lack of standardized test procedures [1] and detailed uncertainty budgets for TLS measurements are seldom available. As Lichti et al. [2] described, measuring curved surfaces using TLS has always proved problematic. In this context, we describe here the challenges involved in measuring a spherical geometry using TLS.

Spherical geometry is commonly found in manufacturing environments. In addition, sphere targets are sometimes introduced into a scene to register scans from multiple positions of a TLS. Target spheres are also used to construct calibrated reference lengths to evaluate the performance of a TLS [3, 4]. A spherical geometry is preferred for registration and performance evaluation experiments because its geometry appears the same from all view points, and it is reasonably straightforward to reduce the point cloud data to a single point, its center.

However, from experiments performed at the laboratories of the Dimensional Metrology Group at NIST, we know that some TLS systems are incapable of obtaining a reliable point cloud from the surface of a spherical target. The changing surface curvature, averaging of the laser spot on the surface, multiple reflections from nearby surfaces and many other factors contribute to the scanned data of the sphere appearing either smaller (squished) or larger (flared) than the actual sphere. This not only means that the radius of the sphere is incorrectly determined but there is also an error in locating the center of the sphere, whose error direction depends on the scanner position. Center location error is of consequence in multiple applications including scan registration and scanner performance evaluation experiments conducted using scale bars with sphere targets on ends.

In this paper, we explore the problem of sphere measurements through experiments and simulations, highlighting the challenges in measuring as simple a geometry as a sphere using TLS.

SPHERE SQUISHING/FLARING AND UNCONSTRAINED RADIUS

Several factors affect the sphere point cloud data as mentioned earlier. We discuss experiments conducted to estimate the effect of mounting and point density on sphere radius in this section.

Effect of mounting

In order to examine the effect of mounting conditions on the observed sphere radius, we mounted a 50 mm nominal radius media-blasted aluminum semi-sphere in three different ways as shown in Fig. 1. In case (a), the sphere is mounted centrally on a 45.72 cm x 45.72 cm (18 in x 18 in) aluminum plate with a clearance of 1.27 cm (0.5 in) around the sphere. In case (b), laser absorbing black flock paper is glued around the sphere (forming a 3.81 cm (1.5 in) annulus) to absorb some of the secondary reflections. In case (c), the sphere is mounted on a much smaller aluminum plate that also has black flock paper glued on it.

The form error of the sphere was measured to be 10 μm on a coordinate measuring machine (CMM). The flatness of the plate (Fig. 1(a) and (b)) was measured on a CMM to be 55 μm over its entire surface but only 20 μm over a central circular region of radius 200 mm.

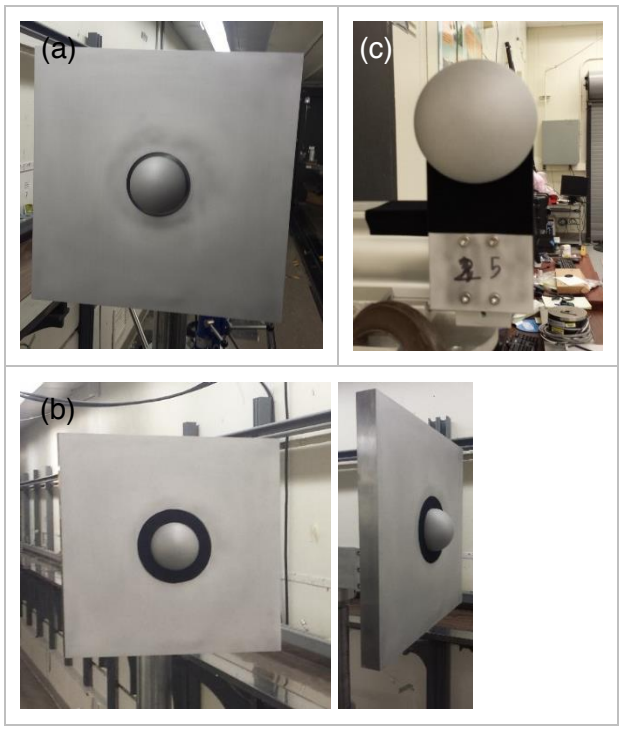

FIGURE 1. (a) a 50 mm radius sphere mounted centrally on a 45.72 cm x 45.72 cm (18 in x 18 in) plate, (b) 3.81 cm (1.5 in) ring of flock paper glued around the sphere to absorb secondary reflections, (c) sphere mounted on a smaller plate with flock paper glued on it

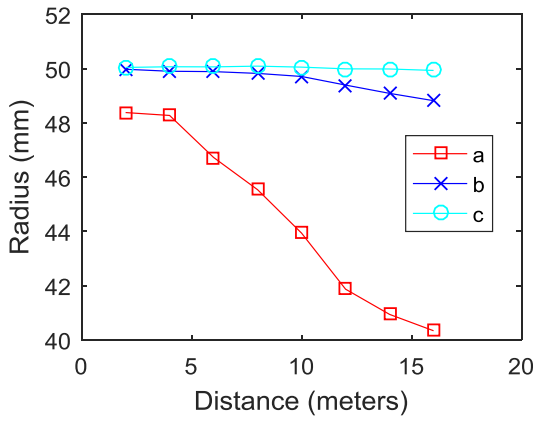

FIGURE 2. Unconstrained least-squares best-fit radius as a function of distance for three different cases of mounting, case (a) corresponds to Fig. 1(a), case (b) corresponds to Fig. 1(b), and case (c) corresponds to Fig. 1(c).

The sphere was scanned four times each at distances of 2 m through 16 m in steps of 2 m and an unconstrained least-squares best-fit sphere was fit to the data. The scans were performed at point density of 90 points per degree along the azimuth and elevation angle directions. Fig. 2 shows the unconstrained least-squares best-fit radius (average from the four scans) for each of the three cases, which illustrates that the mounting of the sphere has a significant influence on the unconstrained radius.

When mounted on a plate with no laser absorbing flock paper, secondary reflections from the plate have a significant impact on the data quality causing the sphere to appear increasingly squished at far distances. The radius drops from 48 mm at 2 m down to as low as 40 mm at 16 m. In case (c) where a much smaller plate with laser absorbing flock paper is used, secondary reflections are significantly reduced resulting in the radius holding steady at 50 mm even at 16 m scan distance. It should be noted that points in the outer periphery of the sphere are not considered in the determination of the center; only the region of the sphere that lies within a central cone angle of 120° are used in the calculation.

Effect of point density

To examine the effect of point density on the observed radius, a white plastic sphere of nominal radius 75 mm is scanned at different point densities from six through 57 points per degree (equal sampling intervals along both the azimuth and elevation angle directions). The sphere was placed at a distance of about 5 m from the instrument. The data are fit using an unconstrained radius least-squares best-fit sphere algorithm and the resulting radius is shown in Fig. 3.

Changing point density affects the mirror rotation speed (for the instrument used in this study), likely resulting in changing the extent of spatial averaging over the curved sphere surface, thereby affecting sphere radius. Fig. 3 shows that the radius changes by at least 3 mm from point density of 6 to 57 points per degree.

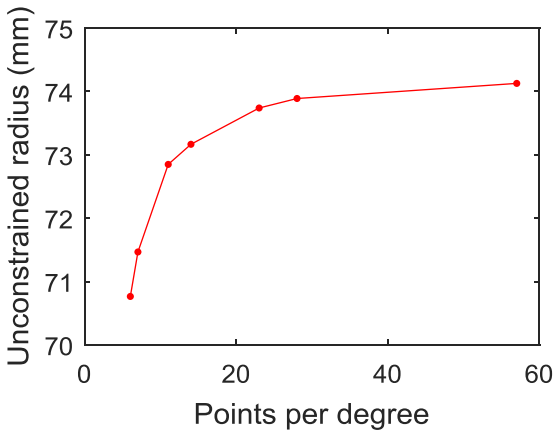

FIGURE 3. Unconstrained radius as a function of point density

SPHERE SQUISHING/FLARING AND CENTER ERROR

While the error in the radius can be determined by comparing the radius obtained by the TLS against that obtained using a reference instrument such as a coordinate measuring machine (CMM), the error in the center is not as easily estimated because the location of the true center of the sphere is an unknown quantity. As the amount of squishing and flaring increases, it proportionally changes the location of the center as determined by the TLS.

The error in the center location arises because the squishing/flaring effect is more pronounced on the outer periphery of the sphere, i.e., region where the angle of incidence is larger. It is assumed that the TLS records the correct range when the laser beam is normally incident on the surface, i.e., the region of the sphere that is closest to the TLS (see Fig. 4). A least-square fit, constrained to the calibrated radius of the sphere, does not eliminate the center error as described in the simulations in the next sub-section.

To estimate the magnitude of the error in the center location of the sphere, we consider the artifact shown in Fig. 1 (b). We refer to this as the plate-sphere artifact. The distance from the center of the sphere to the plate is calibrated using a CMM. The plate serves as the reference for the TLS measurements; an error in locating the center of the sphere will appear as an error in the sphere-center to plate distance. The idea, therefore, is to infer the sphere center location error from the error in the sphere-center to plate distance.

In the next sub-section, we describe a simulation to estimate the error in the center based on the extent of squishing/flaring, i.e., the unconstrained radius obtained from the measured point cloud. Subsequently, we describe experimental data in support of this simulation.

Simulations

The schematic in Fig. 4 illustrates profiles of a real sphere surface (solid gray line) and the point cloud (solid black line) of that sphere as measured by a TLS. The measured surface in this illustration appears more ellipsoidal than spherical, with the long axis oriented along the ranging direction, i.e., the sphere appears squished. The data are segmented so that data within a cone opening angle of 120° is retained. As can be seen in the figure, a constrained fit based on the calibrated radius of the sphere produces a center O_1 that is farther away from the TLS than the true center O. An unconstrained fit produces a center O_2 that is closer to the TLS than the true center O.

To evaluate the effect of sphere

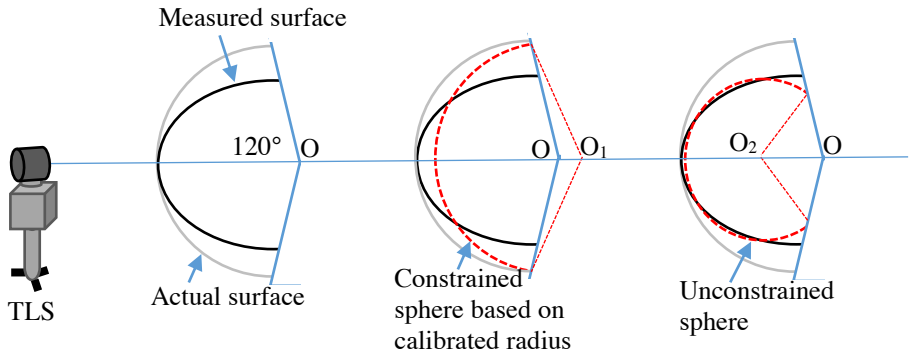

FIGURE 4. Error in the center coordinate because of apparent squishing of sphere

squishing/flaring, the quantity of interest is the error in the center O_1O. It is difficult to quantify the center error O_1O because the true center O is an unknown quantity. However, the measured data does provide another potentially useful quantity, the unconstrained least-squares best-fit radius, from which we can estimate the error in the center O_1O through a simple simulation.

For this purpose, we first perform an unconstrained orthogonal least-squares fit on the measured data to determine the unconstrained radius r_{uc}. This provides an estimate of the extent of squishing or flaring of the sphere for this TLS/target combination under these measurement conditions. We then numerically generate a sphere data set with a radius r_{uc}, centered at a distance $r-r_{uc}$ from the origin where r is the calibrated radius of the sphere, and truncated over a cone opening angle of 120°. The data is generated at the same sampling interval as that of the measured data. We then perform a constrained orthogonal least-squares fit with a radius equal to the calibrated radius of the sphere target. The distance of the constrained center from the origin of the coordinate system is an estimate of the center error O_1O. In Fig. 5, we plot the center error as a function of the unconstrained radius for a sphere of nominal radius 50 mm. The plot shows that the error in locating the center increases by 0.24 mm for every 1 mm change in the observed unconstrained radius.

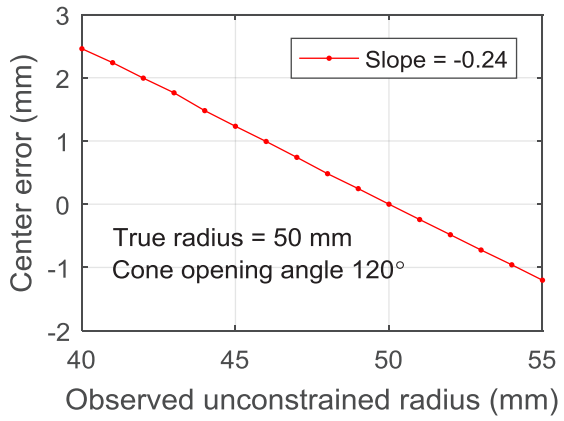

FIGURE 5. Center error along the TLS ranging direction as a function of unconstrained radius

The plot in Fig. 5 may be assumed to be linear for all practical purposes, although in reality it is not. The slope of the graph is -0.24 for a cone opening angle of 120°. The slope factor can be calculated for other cone opening angles in the same manner as described above. While Fig. 5 is based on a sphere of nominal radius 50 mm placed 10 m away and sampled at 92 points per degree, simulations indicate that the results are not strongly influenced by the distance to the target, the point density, or the radius of the sphere.

Verifying the simulation through an experiment

In order to experimentally validate the above simulation, we mounted a sphere of nominal radius 50 mm on an aluminum plate as shown in Fig. 1(b). The front surface of the plate is media-blasted to a matte finish. The sphere-center to plate distance was calibrated on a contact probe CMM and determined to be 0.02 mm.

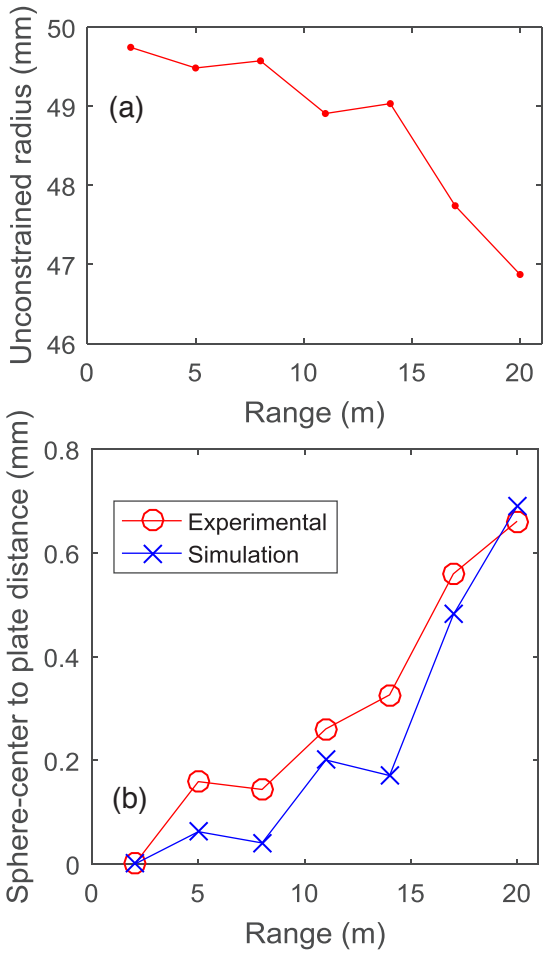

FIGURE 6. (a) Unconstrained radius as a function of distance (b) Sphere-center to plate distance

The artifact is scanned four times each at distances of 2 m through 20 m in increments of 3 m. The sphere data from the scan is fit to an unconstrained radius least-squares best-fit sphere and the resulting average radius from the four scans as a function of range is shown in Fig. 6 (a). It is clear that there is considerable squishing at the 20 m distance compared to the 2 m distance, with an unconstrained radius of 46.9 mm at 20 m and 49.7 mm at 2 m. From the simulations in the previous section, we anticipate the center to have moved by -0.24*(46.9-49.7) = 0.672 mm. The experimentally determined change of the sphere-center to plate distance is 0.66 mm, which is in excellent agreement with the simulations. Fig. 6(b) shows the change in the sphere-center to plate distance with respect to that at the reference position (2 m distance) obtained experimentally at the different ranges along with the simulation predictions based on unconstrained radius. This experiment validates the simulation and clearly confirms the movement of the constrained fit center because of sphere squishing/flaring.

CONCLUSIONS

TLSs are increasingly used in applications requiring accuracies on the order of few tenths of a millimeter or more. However, the error sources in these systems are not carefully documented and detailed uncertainty budgets are not available. In this context, we describe the challenges associated with measuring a spherical geometry using a TLS. We have found that the sphere point cloud obtained from a TLS is impacted by the material in close vicinity to the sphere and this sometimes results in the sphere appearing squished or flared. Other factors such as averaging of the returns over a laser spot, the shape of the spot, etc., also affect squishing/flaring. While the error in the observed radius due to squishing/flaring can be easily quantified, the error in the center location is more challenging to estimate. For this purpose, we built the plate-sphere artifact, where the distance from the center of the sphere to the plate is calibrated. We infer the error in the sphere center location from the calculated distance between the sphere center and the plate. The experiments and simulations described in this paper indicate that care must be taken when processing TLS data because of the potential for error sources that are not yet understood.

Many applications require stitching of point clouds which in turn require registration. Based on the results in this study, obtaining sub-millimeter accuracy during registration using sphere targets will be a challenge. Also, this study clearly indicates that if relative range measurements are performed (i.e., measurements along the radial direction of a scanner) using sphere targets, the observed error may not only be due to the intrinsic error in the range measurement technology, but also due to the geometry of the sphere target and the properties of the surfaces that surround it.

REFERENCES

[1] Beraldin J.-A, Mackinnon D, and Cournoyer L, Metrological characterization of 3D imaging systems: progress report on standards developments, 17th International Congress of Metrology, 2015

[2] Lichti D D, Gordon S J, Stewart M P, Franke J, and Tsakiri M, Comparison of digital photogrammetry and laser scanning, Proceedings of International Workshop on Scanning for Cultural Heritage Recording - Complementing or Replacing Photogrammetry, Corfu, Greece, September 1-2 ,2002.

[3] Rachakonda P, Muralikrishnan B, Lee V, Sawyer D, Phillips S and Palmateer J. A method of determining sphere center to center distance using laser trackers for evaluating laser scanners, Proceedings of the Annual Meeting of the ASPE, Boston, 2014.

[4] Bala Muralikrishnan, Meghan Shilling, Prem Rachakonda, Wei Ren, Vincent Lee, Daniel Sawyer, Toward the development of a documentary standard for derived-point to derived-point distance performance evaluation of spherical coordinate 3D imaging systems, Journal of Manufacturing Systems, 37, 2015, p. 550-557

Optical Sensor for use in the R-test

Robert E. Parks[1], John C. Ziegert[2], and Jesse Groover[2]
[1]Optical Perspectives Group, LLC
Tucson, AZ, USA
[2]Department of Mechanical Engineering and Engineering Science
University of North Carolina at Charlotte
Charlotte, NC, USA

ABSTRACT
We present a description of an attachment for an autostigmatic microscope that uses two objectives set at right angles to unambiguously locate the center of a ball in all 3 translational degrees of freedom, and that can be used to perform the "R" test, or to scan a ball plate, to determine machine tool precision dynamically.

INTRODUCTION
Now that five axis machining centers are in wide use, it is advantageous to have a means of verifying their precision over the volume of their workspace that is precise, rapid to perform and is dynamic to show the machine performance in the mode that is used for production. Two methods are commonly used for this performance verification, a ball plate of fixed balls placed at several elevations within the work volume[1] and the "R" test[2] where a multi-axis sensor is attached to the work spindle and is commanded to track the motions of a ball fixed to the work table as the rotary axes are exercised. Of the two methods the "R" test allows sweeping the work volume fairly rapidly in a continuous motion and yields an assessment of machine performance faster than the ball plate.

Typical sensors for performing the "R" test consist of a measurement head containing a set of 3 or more contact or non-contact displacement sensors arranged in orthogonal directions and that engage the surface of the target ball and record deviations from the nominal, or centered, position. The sensor head used for the "R" test can also be used to scan a ball plate, but because each is surrounded in all 3 axes the measurements cannot be performed dynamically.

We present an optical sensor that is unobstructed in one axis so that it may be used as an "R" test sensor but may also be used to scan a ball plate, or an array of fine ground cylinders

BALL CENTER FINDER ATTACHMENT
The ball center finder (BCF) is an attachment for an autostigmatic microscope[3,4] (ASM), an optical instrument analogous to an autocollimator but with a finite focus. The BCF replaces the single objective found on ASMs with a beamsplitter to divide the collimated beam exiting the ASM into two beams that are then turned at 90 degrees by fold mirrors and directed into a pair of objectives set at right angles to each other as shown in Fig. 1.

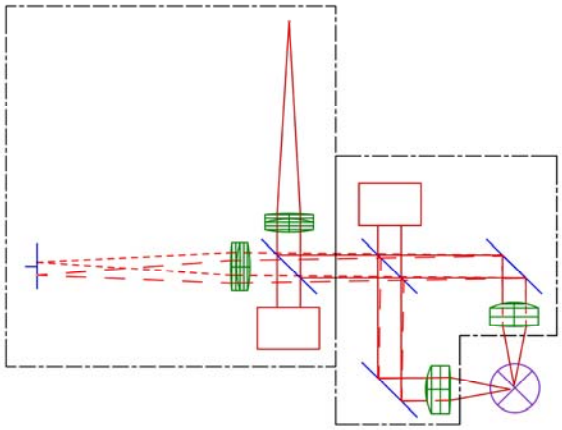

FIGURE 1 Schematic diagram of an ASM with the BCF (right) attached focused at the cneter of a ball.

The ASM is the roughly square outline in the upper left of the Fig. 1A and the BCF is the square outline with a cutout in the lower right. Inside the cutout is a ball and the light from the two objectives is focused at the center of the ball. The ball acts like a convex mirror and reflects the light back into the BCF and ASM over paths nearly identical to the paths directed at the ball. The beam-splitter in the ASM directs the light through a tube lens to focus on the detector. If the ball were perfectly aligned to the objectives, and if the BCF were perfectly aligned, the beams of light from the two objectives would focus in precisely the same spot on the detector.

Any misalignment of the ball relative to the objectives will produce two spots on the detector, one from each objective, and the relative positions of the spots determine the amount of misalignment of the ball in all three axes.

BEHAVIOR OF THE BCF

In use on a 5-axis machine tool the cutout of the BCF is pointed downward from the spindle so the two objectives each point downward at 45 degrees to the machine Z axis as shown in Figure 2. In this position, the spindle may be rotated to allow unobstructed motion of the measurement head along either the X or Y axis of the machine. In the data presented here, the unobstructed path of the BCF was oriented along the machine X axis.

As the ball is moved from its centered location in any coordinate direction, the spots on the detector move according to the optical layout of the system, making it possible to unambiguously detect sub-micrometer motions in all three coordinate directions.

RESULTS

The BCF was attached to the spindle of a 5 axis Mori Seiki NMV5000 CNC milling machine as shown in Fig. 2 in order to determine the response of the BCF to motions in each of the 3 machine axes, and to calibrate the pixel motion on the detector of the PSM[5] with the machine motion.

The data in Fig 3 shows the response of the two spots to machine motion in each of the 3 axes individually over the linear range of the sensors. The data show the response was as predicted. There is almost no motion of the spots where there should be none and linear response where there should be. The slopes of the lines give the sensitivity in pixels per micron of machine motion.

work table (above). BCF and PSM mounted on the spindle of a Mori Seiki NMV5000 showing orientation of BCF to machine X axis (lower).

From the slope data in Fig. 3 the sensitivities are 0.543 µm/pixel in X and 0.750 µm/pixel in Y and Z, with the ratio of the sensitivities in X to that in Y and Z being very close to sin 45°, as expected from the orientation of the sensors.

These values are very close to the sensitivities of 0.530 µm/pixel in X and 0.749 µm/pixel in Y and Z predicted for the nominal design. Note that the design of the BCF provides two independent measurements of motions of the ball center in the X direction, one from each objective.

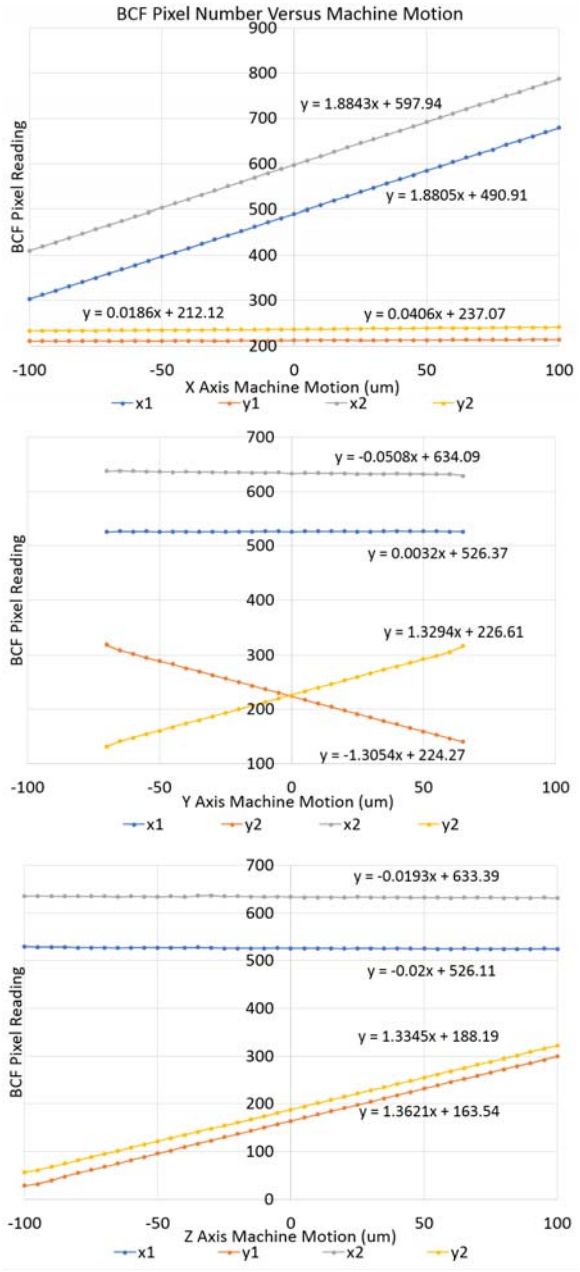
BCF Pixel Number Versus Machine Motion
BCF Pixel Reading
y = 1.8843x + 597.94
y = 1.8805x + 490.91
y = 0.0186x + 212.12
y = 0.0406x + 237.07
X Axis Machine Motion (um)
x1
y1
x2
y2
y = -0.0508x + 634.09
y = 0.0032x + 526.37
y = 1.3294x + 226.61
y = -1.3054x + 224.27
Y Axis Machine Motion (um)
y = -0.0193x + 633.39
y = -0.02x + 526.11
y = 1.3345x + 188.19
y = 1.3621x + 163.54
Z Axis Machine Motion (um)

FIGURE 3. Response of the BCF for machine motions in each of the 3 axes, X, Y and Z, top, middle and bottom, respectively. x1 and y1 are the spot location for one spot and x2, y2 the other in units of pixels on the PSM detector. The scale of all 3 graphs are the same in both axes.

Figure 4 shows the residuals from best fit straight lines to the data in Figure 3, where the X data are averages of the two independent X measurements. Without additional calibration of the machine motions, it is not known if the residual errors are due to the machine positioning accuracy or the BCF. However, looking at the detrended data for the 3 motions gives a feeling for the ultimate sensitivity of the BCF.

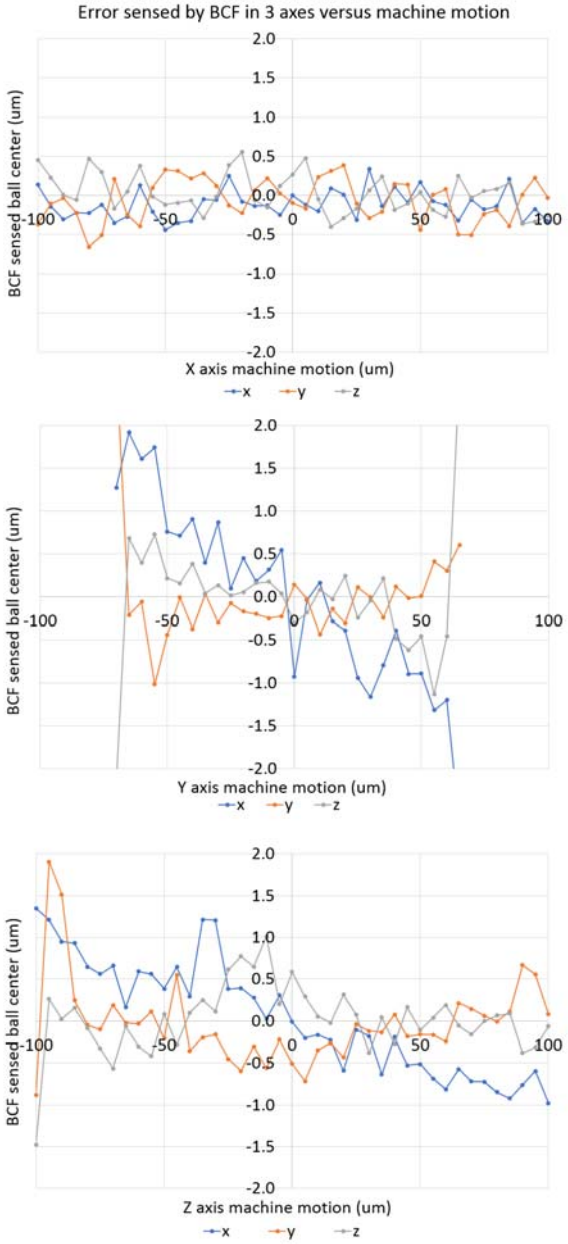
Error sensed by BCF in 3 axes versus machine motion
BCF sensed ball center (um)
X axis machine motion (um)
x
y
z
Y axis machine motion (um)
Z axis machine motion (um)

FIGURE 4. Detrended data for the BCF in the 3 axes of machine motion, X to Z, top to bottom. Blue is the BCF X axis response, orange Y, and gray Z. All graphs are the same scale in both axes for easy comparison.

These data show that the range over which the BCF is linear is limited to around ±50 μm and that there is probably some small misalignment that accounts for the slope in the X axis data when only the Y and Z are moving.

TABLE ROTATION TEST

Once the sensitivity factor of the BCF was known it was possible to do a test where the C axis of the machine was rotated 360° in 10° increments while the spindle followed. The ball was mounted toward the edge of the table as seen in Fig. 3 so that it swept out a radius of about 308 mm. The BCF data for this test is shown in Fig. 5.

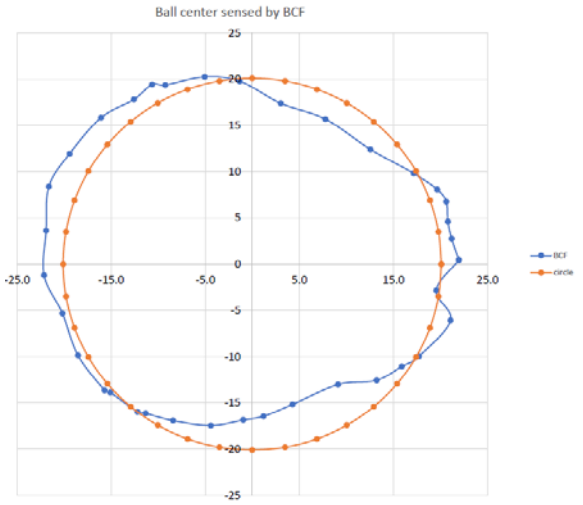

FIGURE 5. BCF sensed errors in the X and Y axes as the C axis was rotated 360° in 10° increments. The units are μm so the worst difference between a perfect circle (orange) and the BCF readings (blue) was about 5 μm.

There is no reason this test could not have been done dynamically as the machine moved but caution was used on these initial experiments. The maximum indicated in-plane error during this test was about 5 μm, which is composed of errors in the machine controller's knowledge of the as-built position of the table axis of rotation, positioning and reversal errors of the machine X and Y axes, and any residual errors in the BCF measurements.

Further, the BCF also provided information on the apparent error in the Z motion as the table rotated. This data is shown in Fig. 6 where the peak-to valley excursion is about 12 μm but not in a smooth sine curve as one would expect if the error were due solely to an axis misalignment.

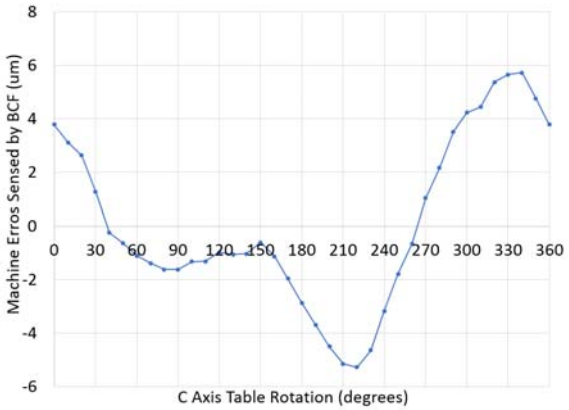

FIGURE 6. Z axis reading sensed by the BCF as the work table rotated 360°

FUTURE WORK AND CONCLUSIONS

It has been shown that the BCF performs essentially as it was designed to do, to be an optical R-test sensor capable of tracking a ball and having the capability to scan along a row of balls in one direction. It remains to do further testing where the full 5 axis motion of the machine is scanned dynamically. Also, tests of repeatability and some sort of absolute calibration such as reversal needs to be done to verify the performance of the BCF alone rather than as a part of the overall machine performance.

ACKNOWLEDGEMENTS

One of us (R. P.) would like to acknowledge the help and hospitality of John Ziegert, and his student, Jesse Groover, for the use of the Mori Seiki machine in John's Lab and the taking and analysis of the data for this paper by Jesse.

REFERENCES

1) Liebrich, T., et. al. "Static and dynamic testing of machine tools" (2010), www.inspire.ethz.ch/iwf/specials/mttrf/research/static_dynamic_2010.pdf

2) Florussen, G.H.J. and Spaan, H.A.M., "Dynamic R-test for rotary tables on 5-axis machine tools", Procedia CIRP **1**, 536-9 (2012).

3) Drysdale, C.V., "On a simple direct method of determining the curvatures of small lenses", Trans. Opt. Soc. London, **2**, 1-12, (1900).

4) Steel, W.H., "The Autostigmatic Microscope", Optics and Lasers in Eng., **4**, 217-27 (1983).

5) Point Source Microscope, a commercially available ASM, www.optiper.com.

SURFACE AREA MEASUREMENT USING CURVED SCREEN DEFLECTOMETRY FOR INCREASED DYNAMIC RANGE AND SENSITIVITY

Ali Pouyafard[1,2], Angela Davies[1,2]
[1]Center for Precision Metrology,
University of North Carolina at Charlotte,
Charlotte, NC 28223, USA
[2]Department of Physics and Optical Science,
University of North Carolina at Charlotte,
Charlotte, NC 28223, USA

INTRODUCTION

Phase measuring deflectometry has been introduced as a promising solution to providing fast full-field non-contact surface area measurements of specular freeform surfaces [1]. The system measurement is based on the volumetric geometry of the screen, test part, and camera system; and, calibration of the system is usually done assuming certain standard models for the components along with triangulation-based photogrammetric techniques for position estimation. Many works have aimed at reducing errors that are introduced in the geometric calibration which is the main factor limiting the accuracy of the measurement. Calibration and positioning of the deflectometry screen is based on a perfect flat plane model with evenly spaced pixels. However, the shape of the commercially available LCD screens can have considerable deviations from a flat screen due to fabrication errors, mechanical mounts, etc.

In this work, we have enabled the calibration of screen through a new calibration method that allows for geometrical imperfections and general departures from a flat plane. We have shown the capability of our method in capturing the true form of the LCD screen in a deflectometry system. We have also shown the capability of this approach to characterize a spherical screen. This is done by simulating this calibration process and a deflectometry measurement in FRED Optical Engineering Software (Photon Engineering LLC). Measuring convex surfaces with deflectometry, requires increased screen size and/or decreased distance of the screen to the test surface, which reduces the sensitivity of the measurement. Spherical screens can be particularly of interest in measuring surfaces with large dynamic slope range without sacrificing sensitivity. This work can add quantitative capabilities to deflectometry systems that have so far been limited to surface inspection [2].

PHASE MEASURING DEFLECTOMETRY

The basic setup of a deflectometry system is shown in Figure 1. The reflected images of a series of known screen patterns from the object surface are captured with one or more cameras. The shape of the surface modulates the incoming screen pattern, thus the captured reflections by the camera contain geometric information about the surface of the object.

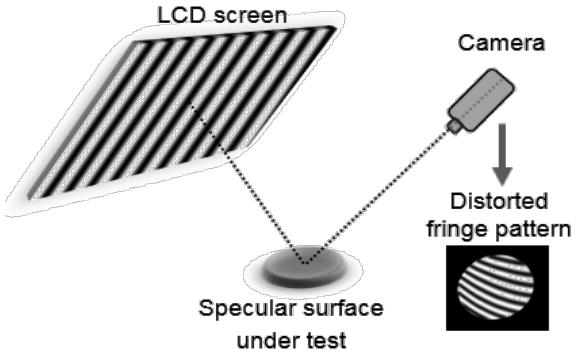

Figure 1. The setup of a phase measuring deflectometry system.

SENSITIVITY OF THE MEASUREMENT TO ANGULAR AND LATERAL RESOLUTION

The schematic of a deflectometry system is shown in Figure 2. The displacement of the position of the incoming ray from the screen with respect to a change in the slope of the surface for a certain point, such as point P in Figure 2, can be approximated with this proportionality:

$$\Delta\varphi \propto d \cdot \tan(2\alpha) \quad (1)$$

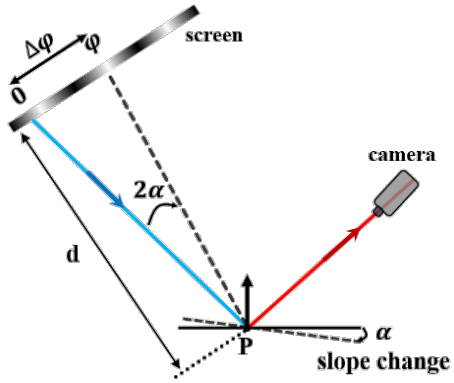

Figure 2. Sensitivity of deflectometry to slope changes can be controlled by the screen size and distance to the surface.

By moving the screen away from the surface and increasing d, any angular resolution is achievable. However, in so doing, we are decreasing the range of measurable slopes given a certain screen size. Screens, or more generally pattern generators with a spherical geometry, can be used to maintain a large range of determinable slopes without the need for increasing the screen-to-surface distance.

CURVED SCREEN DEFLECTOMETRY

In conventional deflectometry, the geometrical calibration of the screen is commonly performed using photogrammetry. In this work, the geometrical calibration of the screen position, orientation, and shape is performed solving a calibration function that captures the relationship between the phase measurements and other parameters in the system as described in Equation 2.

$$\Delta\varphi = f(\vec{r}, \alpha, \dots). \quad (2)$$

The $\Delta\varphi$ is the difference between the measured phase of the surface at point $\vec{r}$ with slope α with the phase of a flat surface at the same position in the measurement volume as indicated in Figure 2. By measuring a known surface (known $\vec{r}, \alpha$), we can use the above function to determine the screen geometrical shape, position, and orientation.

SIMULATION AND RESULTS

To verify this calibration method, a deflectometry setup is simulated in FRED with a pinhole camera model and a spherical LCD screen with a radius of 0.5 m. By using reverse ray tracing, we can launch rays from the image plane of the camera and get the position of their intersection with the LCD.

By simulating the measurement of a known convex surface, we can solve Equation 2 to get the screen position, orientation, and shape. Before introducing any error in the measurement, the modeled spherical screen can be perfectly characterized by using an initial estimate offset by 10mm in radius and position, and a few degrees in orientation.

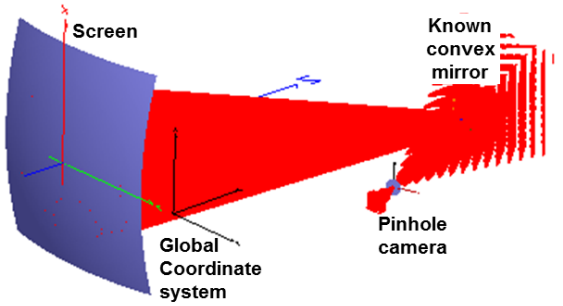

Figure 3. Deflectometry system simulated in FRED. By measuring a known surface, the screen is geometrically calibrated.

After geometrical calibration of the screen, a full deflectometry measurement is simulated for a freeform surface. The test mirror has a cubic surface with a circular aperture similar to an Alvarez lens with 2.93mm sag over a 50mm diameter given by Equation 3.

$$z(x, y) = A\left(\frac{1}{3}x^3 + xy^2\right). \quad (3)$$

Parameter A controls the surface sag over a given area and is set equal to 2e-3 mm^{-2}.

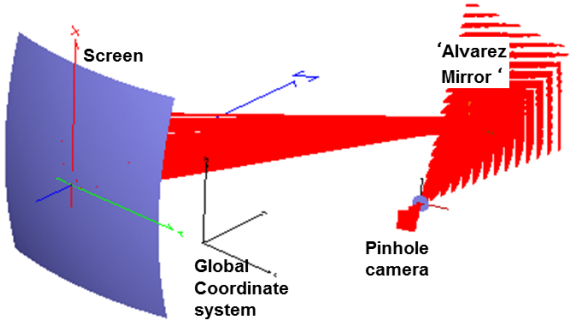

Figure 4. A full deflectometry simulation is carried out for a freeform surface.

The simulated Alvarez surface is shown in Figure 5. The fringe patterns for the test surface are simulated using FRED and are shown in Figure 6.

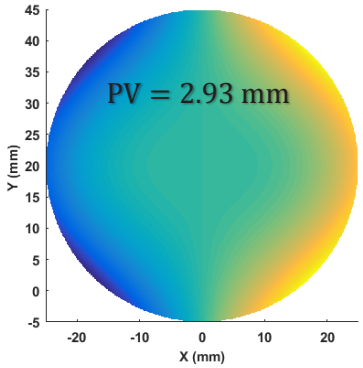

Figure 5. Simulated freeform Alvarez surface with PV=2.93mm and D=50mm.

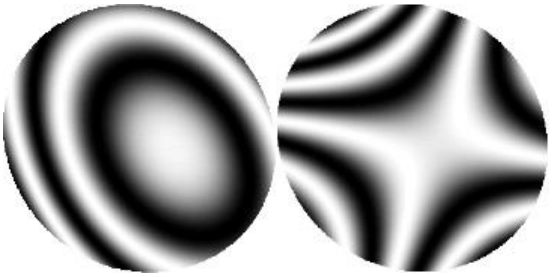

Figure 6. Simulated fringe patterns in two directions for the Alvarez surface (D=50mm).

To get the surface profile, the surface slope values are calculated and integrated on an analysis plane. The analysis plane is chosen to be the best fit plane of the simulated Alvarez surface that can be obtained by a few point measurements on the surface as it is common in a mono-deflectometry measurement. Using a modal integration method [3], the surface height profile can be reconstructed (Figure 7). The residuals of the reconstructed surface are shown in Figure 8, which shows 75nm peak to valley deviation from the simulated Alvarez surface with D=50mm, and is due to the choice of the integration plane and integration method.

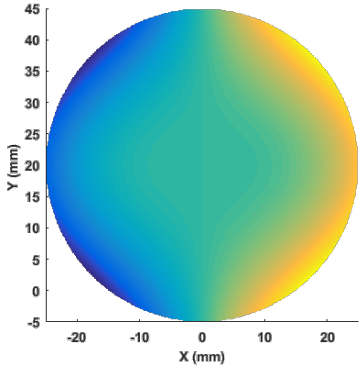

Figure 7. Reconstructed surface.

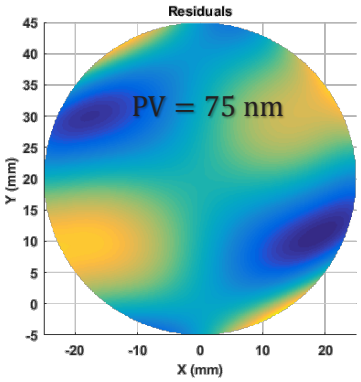

Figure 8. Surface residuals with PV = 75nm, after integration of the calculated surface slopes on the best-fit plane of the Alvarez surface.

CONCLUSION

Geometrical errors in calibration of deflectometry system is the main factor limiting the measurement accuracy. Modeling of the LCD screen has been almost exclusively based on a perfect plane with evenly spaced pixels without considering its shape deformations. We have shown that we can geometrically model and calibrate an LCD screen of any shape in a deflectometry system. Calibration of spherical screens can enable quantitative measurements for deflectometry systems that have been limited to surface visual inspection [2].

REFERENCES

[1] Knauer M, Kaminski J, Häusler G. Phase Measuring Deflectometry: A new approach to measure specular free-form surfaces. Proc. of SPIE. 2004; 5457: 366-376.

[2] Cilip C, Pratt D, Bauza M. Visual Inspection of Cosmetic and Functional Defects in a Manufacturing Environment. ASPE. 2013.

[3] Zhao C, Burge J. Orthonormal vector polynomials in a unit circle, Part I: basis set derived from gradients of Zernike polynomials. Optics Express. 2007; 15.26: 18014-18024.

REPLICATION ASSESSMENT OF SURFACE TEXTURE AT SUB-MICROMETRE SCALE

Danilo Quagliotti[1], Guido Tosello[1], and Hans N. Hansen[1]
[1]Department of Mechanical Engineering
Technical University of Denmark
Kgs. Lyngby, Hovedstaden, Denmark

INTRODUCTION

Precision molding and micro injection molding (μIM) have been the main replication technologies allowing for a rapid reduction of the dimensions of the products and, consequently, for the realization of new advanced micro and nano systems. Such miniaturization in the manufacture of polymer micro-parts and parts with micro and nano surfaces is still in progress and requires new specially developed solutions in all the steps of injection molding processes [1]. The achievement of a full surface replication of the tool insert component, when molding the polymer melt, is essential in advanced μIM technology [2]. A replication process requires reproducing a master geometry by conveying it to a substrate material. It is typically induced by means of different energy sources (usually heat and force) and a direct physical contact between the master and the substrate. Furthermore, concepts of advanced products may be founded on combined processes and process chains, including large variety of materials (mainly polymers, glass or metals) and different dimensional scales. Hence, it is particularly critical when dealing with increasingly small dimensions in micro and nanostructured surfaces. In addition, because of the replication nature of molding processes, the required specifications for the manufacture of micro molded components must be ensured by means of a metrological approach to surface replication and dimensional control of both master geometry and replicated substrate [3]-[4]. Therefore, a detailed knowledge is necessary of not only absolute dimensions and geometrical quantities, but also of the measurement uncertainty, which is a decisive parameter to deal with the quality assurance of micro and nano manufactured components [5].

In this context, the quality of the achieved surface texture replication was assessed by the replication fidelity, i.e., comparing the produced parts with the tool used to replicate the geometry. Furthermore, the uncertainty of the replication fidelity was achieved by propagating the uncertainties evaluated for both masters and replicas. Finally, despite the specimens investigated were made of thermoplastic polymers, the techniques employed are general and can be used to describe any kind of material of the replicated substrate.

SUB-MICRO POLISHED SURFACES

The master surfaces used to carry out the study were four steel specimens, which belong to a set for mold finish comparison, with different polished flat surfaces in the sub-micrometer range (diamond buff polishing, grit paper polishing, stone polishing, dry blast polishing).

Examples of a master and corresponding replicated substrate are in *FIGURE 1*, whilst nominal characteristics provided by the manufacturer [6] are in *TABLE 1*.

Metrology task and uncertainty evaluation

The four steel masters and four corresponding replicated polymer surfaces were measured in the center, using a laser scanning confocal microscope, performing areal acquisitions by both 50× and 100× objective lenses.

Measurements in the same areas were ensured checking geometrical similarity of analogous profiles of both steel masters and polymer replicas. In addition, the acquisitions of 50× lens (258 μm×258 μm) were cut at the same field of view of 100× lens (129 μm×129 μm) and resampled to the same number of pixels (4096×4096).

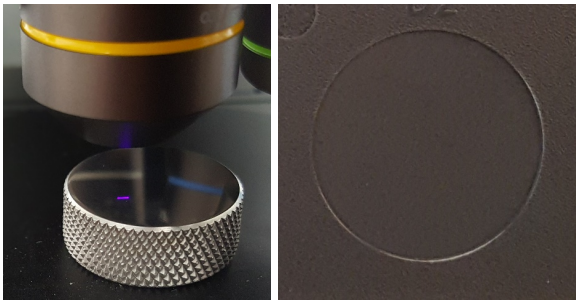

FIGURE 1. Example of a master surface (left) and corresponding replicated substrate (right).

TABLE 1. Specifications of the steel masters under investigation and nominal Ra roughness intervals provided by the manufacturer [6]. The measured Sa values of the masters are also in the table for comparison.

Specimen	Surface finish	Nominal interval, *Ra* /nm	Measured values, *Sa* /nm
T1	Diamond buff (grade 15)	51–76	35±4
T2	320 Grit paper	102–127	75±3
T3	400 Stone	635–711	291±19
T4	400 Dry blast (glass bead 11)	660–813	879±18

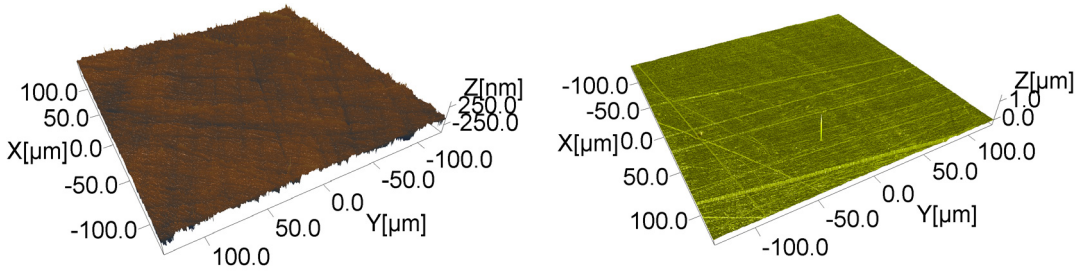

FIGURE 2. Diamond buff polishing: master surface (left) and corresponding replicated substrate (right).

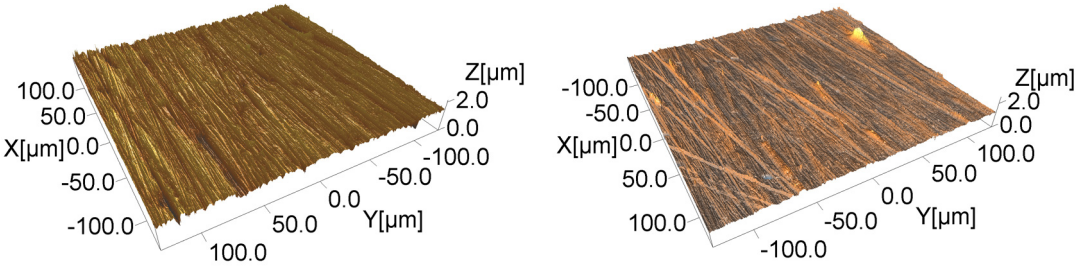

FIGURE 3. Grit paper polishing: master surface (left) and corresponding replicated substrate (right).

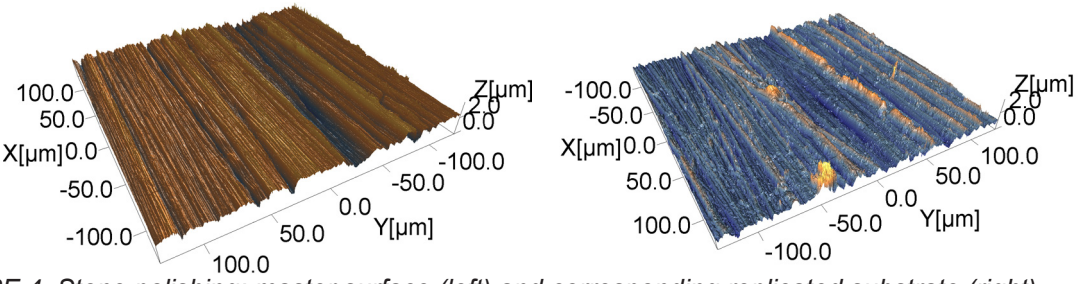

FIGURE 4. Stone polishing: master surface (left) and corresponding replicated substrate (right).

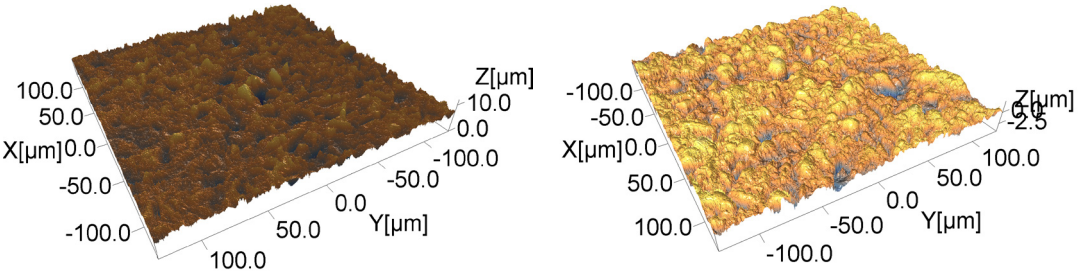

FIGURE 5. Dry blast polishing: master surface (left) and corresponding replicated substrate (right).

Examples of measurement for both master and replicated surfaces of each type of polishing are in *FIGURE 2* to *FIGURE 5*.
The replication fidelity was considered the complement to 100 % of the relative deviation replica-master, evaluated according to the following formula

$$f_R = \frac{Sx_{polymer}}{Sx_{master}} \quad (1)$$

and investigated by areal roughness parameters about the amplitude (*Sx* ≡ *Sq*) and the slope (*Sx* ≡ *Sdq*).
The uncertainty was evaluated by means of calibrated artefacts for the environmental noise and the repeatability of the instrument. Additionally, the uncertainty model considered the calibration uncertainty of the artefacts used, possible effects of temperature and the contributors related to the reproducibility of masters and replicas. The expanded uncertainty was then calculated as a confidence interval of approximately 95 % (coverage factor $k = 2$).
The standard uncertainty of the replication fidelity was evaluated propagating the combined uncertainties of masters and replicas accounting Equation (1) and considering uncorrelated quantities, i.e., according to

$$\mathrm{u}_{\mathrm{f_R}} = \left(\sum_j \frac{\partial f_R^2}{\partial Sx_j} u_{Sx_j}^2 \right)^{1/2} \quad (2)$$

Once more, the expanded uncertainty was obtained with a coverage factor $k = 2$

$$\mathrm{U}_{\mathrm{f_R}} = 2\mathrm{u}_{\mathrm{f_R}} \quad (3)$$

RESULTS
Results of the measurements and associated uncertainty budgets are in *TABLE 2* for the masters and in *TABLE 3* for the replicated surfaces. Average values of the replication fidelity for the four types of polished surfaces investigated are in *TABLE 4*. The evaluated uncertainties for replication fidelity are in *TABLE* 4 (relative propagated combined uncertainties) and *TABLE 5* (propagated expanded uncertainties). These results are also summarized in *FIGURE 6*.
By the examination of tables and figures, it comes out that a good amplitude replication was achieved for stone polished surfaces with a replication fidelity of 95 %. The dry blast ones were evaluated with an amplitude replication fidelity of 70 %. The worst amplitude replication was achieved for both diamond buff and grit paper polished surfaces with a replication fidelity of, respectively, 47 % and 56 %.
The tendency is almost the same for slope replication but the replication fidelity values are lower: 67 % for stone polished surfaces. 50 % for dry blast polished surfaces. 51 % for grit paper polished surfaces. 33 % for diamond buff polished surfaces.

DISCUSSION
At a first analysis of the results, it glances off that uneven topographies are worse replicated with respect to the regular ones.
Uniformities or dominant directions of the texture can be inspected in the angular spectra given in *FIGURE 7*, for both masters and replicas of all types of surfaces investigated.
The polished surfaces are pseudo-random topographies, where uniformity in the masters is introduced by the polishing itself in the form of partial order of the texture direction. In such cases, the replication fidelity slightly increased.

TABLE 2. Results related to the measurements of the steel masters and corresponding uncertainty budget.

Masters		Diamond buff		Grit paper		Stone		Dry blast	
		Sq /nm	*Sdq* /1	*Sq* /nm	*Sdq* /1	*Sq* /nm	*Sdq* /1	*Sq* /nm	*Sdq* /1
Average		48	0.16	108	0.21	379	0.46	1201	1.77
Background noise	u_n	1	0.01	1	0.01	1	0.01	1	0.01
Calibration certificate	u_c	0.7	0.001	0.7	0.001	4.7	0.002	4.7	0.002
Instrument repeatability	u_p	0.2	10^{-4}	0.2	10^{-4}	7	0.003	7	0.003
Effect of temperature on artefact	u_b	2×10^{-6}	9×10^{-10}	2×10^{-6}	9×10^{-10}	10^{-5}	9×10^{-9}	10^{-5}	9×10^{-9}
Reproducibility on master	u_{mp}	3	0.02	2	0.02	10	0.05	5	0.02
Effect of temperature on master	u_{mt}	6×10^{-5}	2×10^{-7}	6×10^{-5}	2×10^{-7}	10^{-3}	10^{-6}	10^{-3}	10^{-6}
Expanded uncertainty	U	6	0.04	4	0.05	25	0.11	20	0.03

TABLE 3. Results related to the measurements of the polymer replicas and corresponding uncertainty budget.

Replicas		Diamond buff		Grit paper		Stone		Dry blast	
		Sq /nm	*Sdq* /1	*Sq* /nm	*Sdq* /1	*Sq* /nm	*Sdq* /1	*Sq* /nm	*Sdq* /1
Average		23	0.05	60	0.11	360	0.31	843	0.89
Background noise	u_n	1	0.01	1	0.01	1	0.01	1	0.01
Calibration certificate	u_c	0.7	0.001	0.7	0.001	4.7	0.002	4.7	0.002
Instrument repeatability	u_p	0.2	10^{-4}	0.2	10^{-4}	7	0.003	7	0.003
Effect of temperature on artefact	u_b	2×10^{-6}	9×10^{-10}	2×10^{-6}	9×10^{-10}	10^{-5}	9×10^{-9}	10^{-5}	9×10^{-9}
Reproducibility on replica	u_{rp}	2	0.01	3	0.01	15	0.03	13	0.06
Effect of temperature on replica	u_{rt}	6×10^{-5}	2×10^{-7}	6×10^{-5}	2×10^{-7}	10^{-3}	10^{-6}	10^{-3}	10^{-6}
Expanded uncertainty	U	5	0.02	7	0.03	35	0.07	31	0.12

TABLE 4. Results of the replication fidelities, deviations of the replicas from the masters (shortage—complement to 100 % of the replication fidelity), sensitivity coefficients (derivatives of Equation (2)) and relative propagated uncertainties.

Replication fidelity		Diamond buff		Grit paper		Stone		Dry blast	
		Sq	*Sdq*	*Sq*	*Sdq*	*Sq*	*Sdq*	*Sq*	*Sdq*
Replication fidelity	f_R /%	47	33	56	51	95	67	70	50
Shortage	R_D /%	53	67	44	49	5	33	30	50
Sensitivity coefficients (master)	$\lvert c_{S,m}\rvert$ /1	-1.0	-182.2	-0.5	-227.1	-0.3	-136.9	-0.1	-28.2
Sensitivity coefficients (replica)	$\lvert c_{S,r}\rvert$ /1	2.1	610.7	0.9	481.6	0.3	215.7	0.1	56.6
Propagated uncertainty	u_{fR} /%	6	8	4	9	6	10	1	3

TABLE 5. Propagated expanded uncertainties of the replication fidelity.

Uncertainty of replication U_{fR}[(a)]	Diamond buff		Grit paper		Stone		Dry blast	
	$U_{fR,Sq}$ /nm	$U_{fR,Sdq}$ /1	$U_{fR,Sq}$ /nm	$U_{fR,Sdq}$ /1	$U_{fR,Sq}$ /nm	$U_{fR,Sdq}$ /1	$U_{fR,Sq}$ /nm	$U_{fR,Sdq}$ /1
Propagated (Equation (6.3-1))	6	0.03	8	0.04	42	0.10	34	0.12

[(a)]Note: conversely to *TABLE* 4 (combined uncertainties), the values reported here are expanded uncertainties.

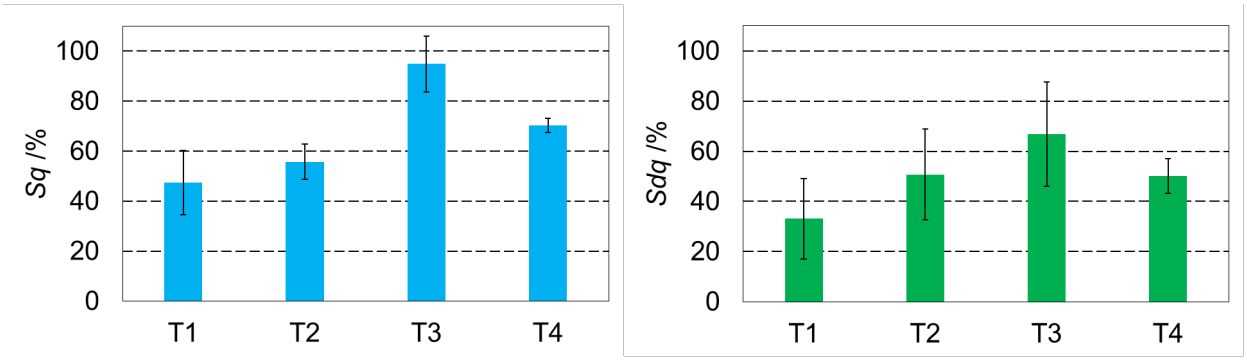

FIGURE 6. Replication fidelity of the amplitude (Sq—left) and slope (Sdq—right). The error bars indicate the propagated expanded uncertainties.

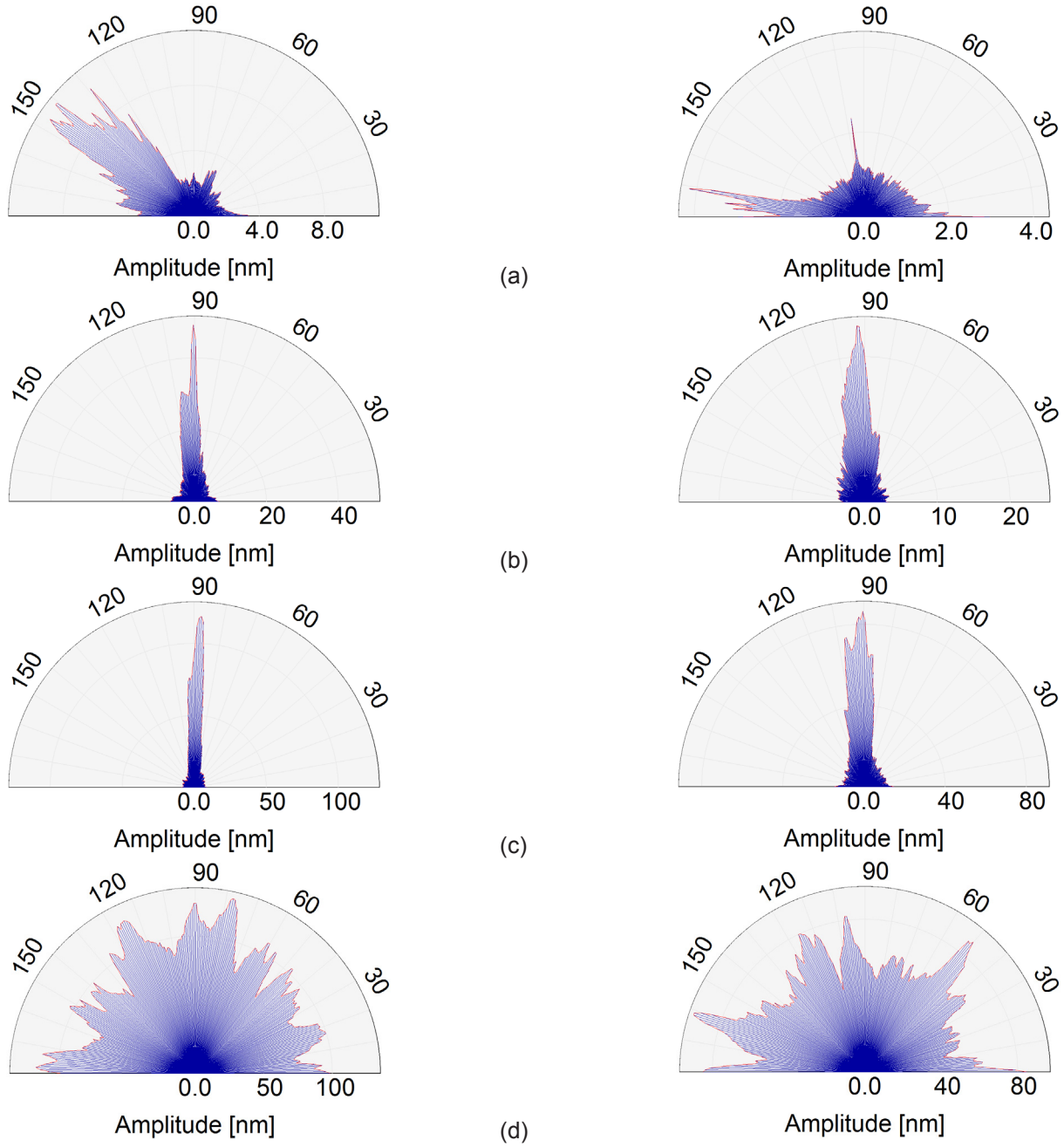

FIGURE 7. Angular spectrum of the masters (left side) and of the replicated substrates (right side). (a): Diamond buff polishing. (b): Grit paper polishing. (c): Stone polishing. (d): Dry blast polishing.

Nevertheless, a deeper analysis cannot ignore that height and slope replications are obtained as overall average considering, respectively, *Sq* and *Sdq* roughness parameters. This means that the assessment of the replication fidelity by means of roughness parameters is not univocally determined when the unevenness is substantial. For instance, a small deficit in the achieved replication of a certain replica might produce large differences in the local slopes (*Sdq* calculated values) with respect to the master surface. Correspondingly, even though *Sq* (or, equivalently, *Sa*) is less sensitive to variations because the amplitude is

unambiguously defined in the vertical direction, a similar trend may be experienced for the height replication assessment of irregular random substrates, where local changes among portions of replicated uneven surfaces produce large variations in the average values. In other words, if sub-domains of somehow uniform portions can be identified in an uneven surface, they can be differently replicated so that the overall replication assessment would flatten the calculation to a certain value included in a larger variability interval.

In the specific case, such effect can be noticed for *Sdq*: comparing the graphs in *FIGURE 6* (left and right sides of the figure), the slope replication has a trend that follows the one of the amplitude but with smaller values of replication fidelity and larger uncertainty intervals.

Conversely, considering *Sq* of the stone polishing replicas, a pretty good replication is calculated inside a quite large evaluated uncertainty, which was, indeed, due to a poor performance of the instrument (see *TABLE 2* and *TABLE 3*).

More complete information is provided by the angular spectra, as already shown in *FIGURE 7*, because evaluated considering all the directions on a surface under investigation, which can be compared between each couple of master and replica. Nonetheless, they are more complicated to deal with when quantitative data are to be extracted.

CONCLUSION

The investigation of four couples of masters and replica-molded specimens allowed introducing metrological techniques for analyzing the replication fidelity of a μIM process. In particular, it was established the amplitude and slope replication of the features on a replicated surface using *Sq* and *Sdq* roughness parameters. The uncertainty of the replication fidelity was assessed by propagation of the variances, considering the expression of the replication fidelity as model equation for the propagation. The proper evaluation of the uncertainty, in fact, is of central importance to extract useful information from the process. If the uncertainty associated with the instrument becomes dominant, it would hide the sought variability of the manufacturing process and, hence, the replication would be altered by the poor measurement results. Furthermore, the use of the angular spectrum was shown as a qualitative visual comparison of master and replicated surfaces.

Eventually, the investigation also highlighted a certain inadequacy of the areal roughness parameters when unevenness are present on the topographies under analysis. The roughness parameters, in fact, operate an averaging of local geometries so that uneven ‘distributed’ features are ‘lumped’ in one single value. The outcome is an apparent flattening of the replication of local geometries, above all when the slope is considered. This last point is already matter of a new investigation.

FUTURE WORK

Surfaces are areal entities in nature and, nowadays, modern instruments provide areal topography measurements with complete 3D areal datasets mapping a surface. In other words, the measurand is a 3D map of the height of the surface under measurement with respect to its least-squares fit plane (pixels).

The direct calculation of height and slope deviations between masters and replicas from the 3D areal dataset, included the corresponding uncertainty, will be a new tool for the assessment of the molding replication.

REFERENCES

[1] Heckele M. Schomburg W K. Review on micro molding of thermoplastic polymers. J. Micromechanics Microengineering. 2004; 14: R1–14.

[2] Hansen H N, Hocken R J, Tosello G. Replication of micro and nano surface geometries. CIRP Annals, Manuf. Technol. 2011; 60: 695–714.

[3] Tosello G, Hansen H N, Marinello F, Gasparin S. Replication and dimensional quality control of industrial nanoscale surfaces using calibrated AFM measurements and SEM image processing. 2010; CIRP Annals, Manufacturing Technology. 59-1: 563-8.

[4] Tosello G, Marinello F, Hansen H N. Characterisation and analysis of microchannels and submicrometre surface roughness of injection moulded microfluidic systems using optical metrology. Plastics, Rubber and Composites, Macromolecular Engineering. 2012; 41-1: 29-39.

[5] Hansen H N, Carneiro K, Haitjema H, De Chiffre L. Dimensional Micro and Nano Metrology. CIRP Annals, Manufacturing Technology. 2006; 55-2 721-743.

[6] DME Mold Finish Comparison Kit. DME Company, www.dme.net.

Alignment and period measurement of critical-angle transmission gratings using a scanning laser reflection tool

Jungki Song[1], Ralf K. Heilmann[1], Alexander R. Bruccoleri[2], Edward Hertz[3], and Mark L. Schattenburg[1]
[1]Space Nanotechnology Laboratory, MIT Kavli Institute for Astrophysics and Space Research, Massachusetts Institute of Technology, Cambridge, Massachusetts 02139, USA
[2]Izentis LLC, PO Box 397002, Cambridge, MA 02139, USA
[3]Harvard-Smithsonian Center for Astrophysics, Cambridge, MA, USA

INTRODUCTION

This paper reports progress toward developing a scanning laser reflection (LR) tool for alignment and period measurement of critical-angle transmission (CAT) gratings. Arrays of CAT gratings that cover apertures of space-based x-ray telescopes can produce scientifically important high-resolution x-ray spectra of astrophysical sources. CAT gratings were developed by combining advantages of blazed reflection gratings and conventional transmission gratings. It requires a relatively small number of gratings to cover large telescope apertures, the gratings have relaxed alignment tolerances and low mass, and show high diffraction efficiency [1]. The fabrication process for CAT gratings is described elsewhere [2-6]. Period variations are a potential limiting factor for very high resolving power. Intrinsic period variations due to interference of spherical wavefronts, mounting (or bonding) of gratings, and change of temperature could cause period variations. Angular misalignment between grating facets can degrade the resolving power as well by directing photons to erroneous positions on the detector.

According to an error budget for the NASA *Arcus* MIDEX mission proposed in 2016 [7], period variations over entire grating facets have to be less than ~0.03 nm. Alignment requirements can be found in Ref. [8]. A precision metrology tool that can characterize period variations in multiple grating facets in air is critical for quality control when producing a large number of CAT gratings. Likewise, methodology for the alignment of multiple CAT grating facets needs to be developed to achieve large effective area.

We looked back on a scanning LR tool developed in 1994 for measurements of period variations in the High-Energy Transmission Grating Spectrometer (HETGS) for the *Chandra X-ray Observatory* [9]. A specularly reflected beam and a first-order diffracted beam were used to record local period variations, surface slope variations, and grating line orientations. We rebuilt the tool with the addition of a normal-incidence beam. The normal-incidence beam is not sensitive to surface height changes (i.e., either due to surface topography or tilt error of grating surface relative to raster-scan plane), and led to more precise measurements of slope variations, surface height change, period variations, and grating line orientations. The addition of a normal-incidence beam enabled the tool to be used for measurements of both period variations and angular misalignments.

In this work, we demonstrate measurement capability of a scanning LR tool for in-grating period variations of a test reflection grating (RG) sample that shows mostly intrinsic period variations from the interference lithography process. Roll alignment of two CAT gratings was demonstrated using the tool and a custom-designed grating alignment assembly (GAA) testbed. All three angles were aligned to satisfy requirements for *Arcus* mission [8]. The final measurement of roll misalignment agrees with roll measurements performed at the PANTER x-ray test facility.

EQUIPMENT SETUP

The scanning LR tool is comprised of a 325 nm HeCd laser, a high-precision XY stage, a 3-axis rotation stage, a grating mount, and three position-sensitive detectors (PSD). The beam from the UV laser is split into two beams, which are reflected by mirrors (or beam splitters) to be incident upon the same spot on the grating with different incidence angles (60º and 0º for the angled-incidence and normal-incidence beams, respectively). The angled beam was partially masked so that the projected beam forms a

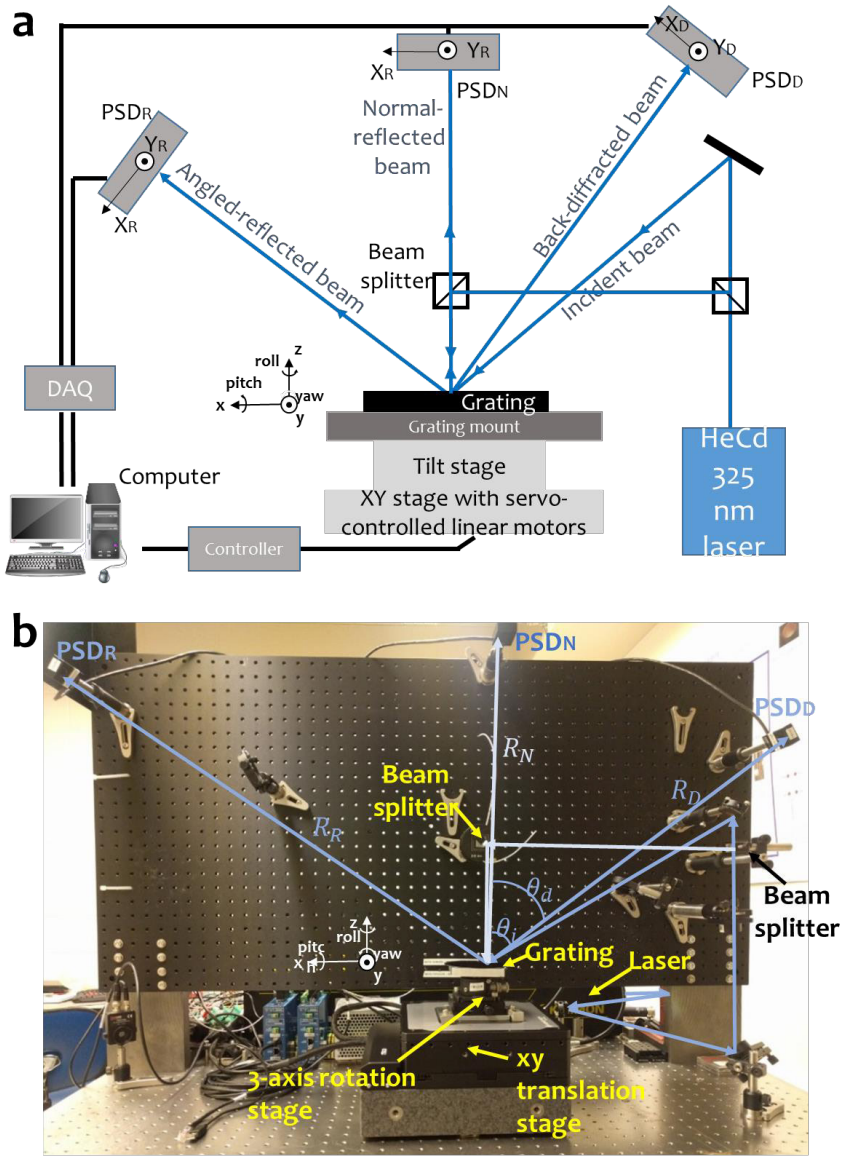

Figure 1. Laser reflection (LR) tool for measurement of angular misalignments and period variations. (a) Schematic of the LR tool. Coordinate systems for detectors and grating are shown. (b) LR Tool for angular alignment and period mapping. Angles and beam path lengths are also shown.

similar (approximately circular) shape as the normal-incidence beam on the grating. The diameter of the incident beams can be adjusted to be 0.25-1 mm in diameter using pairs of focusing lenses. Figure 2 shows a schematic and photograph of the tool. Coordinate systems for detectors and grating (Figure 1a), incidence/back-diffracted angles (θ_i, θ_d) and path lengths for angled-reflected, normal-reflected, and back-diffracted beams (R_R, R_N, R_D) (Figure 1b) are shown. PSDs find the centroid of beams with a sampling frequency of 1000 Hz averaged for 2 seconds. A 3-axis rotation stage is used to reduce grating tilt error (yaw, pitch) about the axes of the raster scan and characterize the correction factor for yaw for period mapping.

SYSTEM CALIBRATION FOR PERIOD MEASUREMENTS

Test RGs that have the same nominal pitch (200 nm) and intrinsic period variations from spherical wave interference as the tested CAT gratings were used to evaluate the measurement capability of small period variations of the scanning LR tool. Details on fabrication and

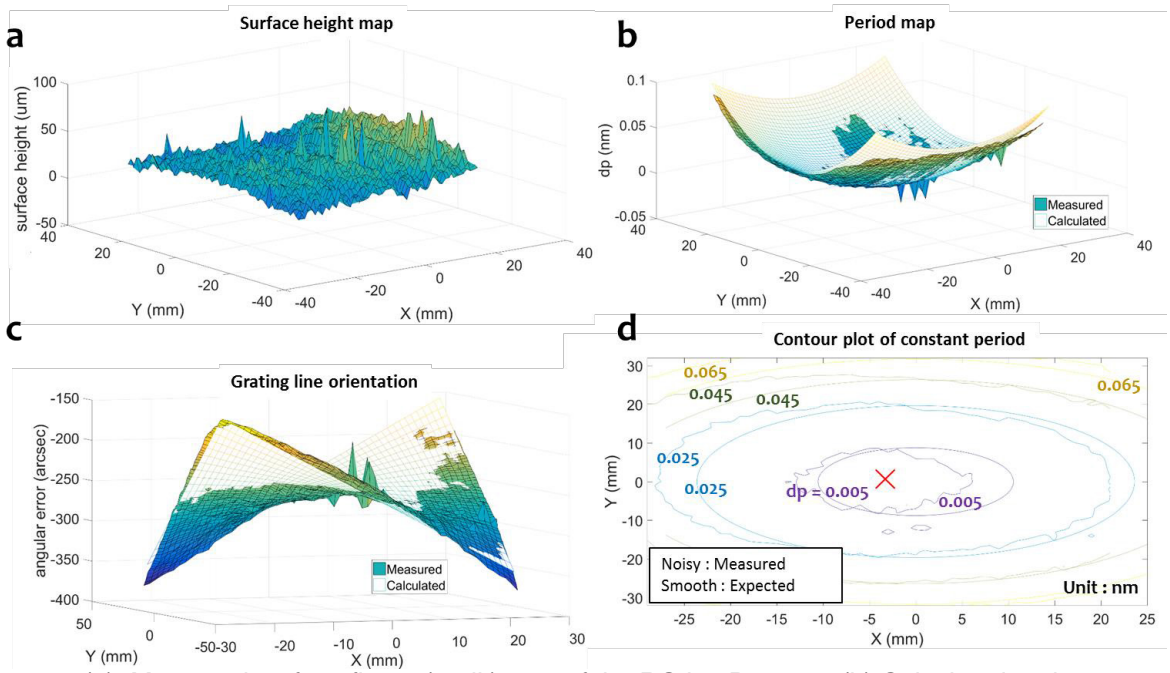

Figure 2 (a). Measured surface figure (or tilt) map of the RG in 3D space. (b) Calculated and measured period variations of the RG. The two plots were centered at (0,0) for comparison. (c) Calculated and measured variations of grating line orientation of the RG. The two plots were centered at (0,0) for comparison. (d) Measured (noisy) and theoretical (smooth) contour maps of constant period for the RG. Unlike Figure 4b, measured data were not centered. The offset between the center of the theoretical and measured data indicates that the interference pattern during resist exposure was not precisely centered in the middle of the wafer. Red 'X' located at (-4,0) on wafer substrate indicates the center of measured contour map. Spikes in 3D graphs are due to scratches on the surface of the RG.

measurement procedures for test RGs can be found in J. Song et al. [10].

Results for an example RG for surface topography (Figure 2a), measured and theoretical period variations and grating line orientations (Figure 2b, c), and displacement of an interference pattern on the wafer substrate (Figure 2d) when the grating lines were patterned with a Mach Zehnder Interferometer are shown. Figure 2a indicates the grating surface was well-leveled with the raster-scan plane. Figure 2b, c show good agreement between theoretical and measured period variations, and grating line orientations, respectively. Figure 2d characterized the center of interference to be ~4 mm displaced from wafer center. Theoretically expected values of period variations were calculated based on the spherical wave interference model [11, 12]. Since rate of change of period accelerates away from the center of interference pattern, it has to be well-aligned on the wafer substrate to minimize degradation of resolving power (a rectangular area at the wafer center is used to fabricate gratings).

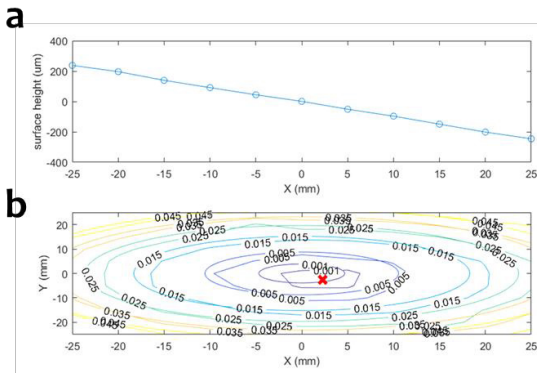

Figure 3. (a) Inclination of grating surface along the line at y=0. (b) Center of interference is measured to be at x = 3 mm when tilt error is -30 arc min, which is different from x = -4 mm when tilt error was controlled to be ~2 arc min.

It was found that tilt error between the grating surface and raster-scan plane significantly affects the measured position of a center of interference.

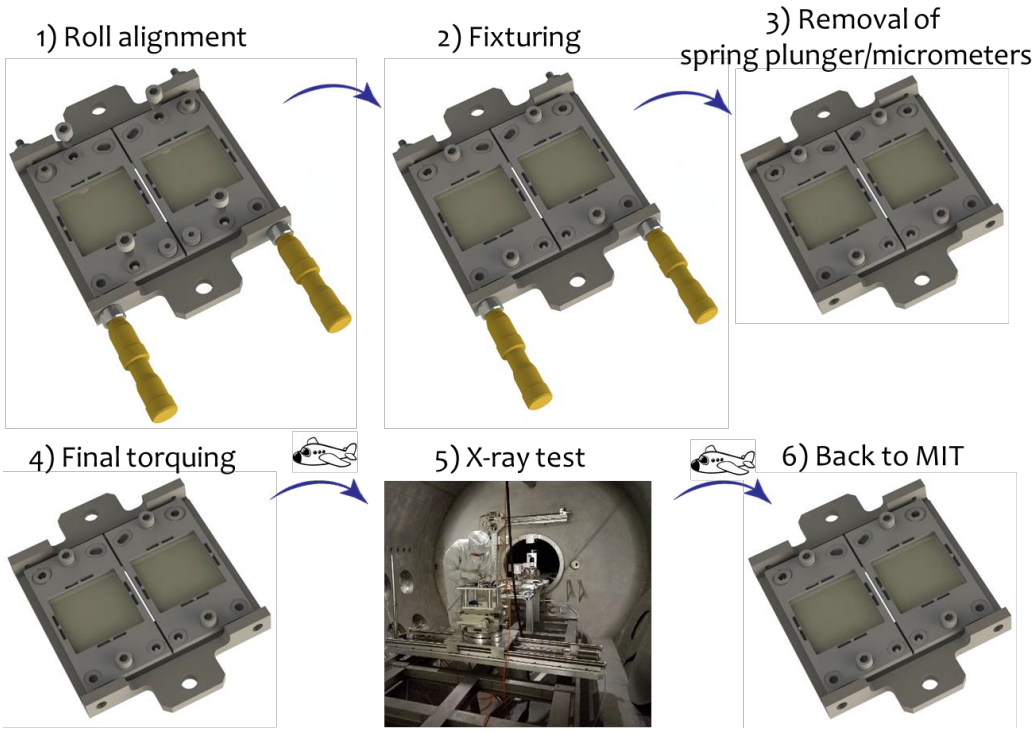

Figure 4. Sequence of roll measurements. Angular misalignments were measured after each step.

Inclination of grating surface induces a period error as follows:

$$dp_{error,tilt} = p\frac{cos\theta_d}{sin\theta_d + sin\theta_i}\frac{\mathrm{x}\sin\gamma}{R_d\cos\theta_i}\sin(\theta_i - \theta_\mathrm{d})$$

where θ_i, θ_d, are incident and diffracted angles, R_d is the path length for the diffracted beam, *p* is the nominal grating period, *x* is position along the x direction, and γ is tilt angle. This error term is expected to shift the minimum point of the period, inducing measurement error on the center of the interference pattern. For example, when the grating sample is purposely inclined by -30 arc min (Figure 3a), the measured center of interference shifts by 7 mm (from -4 mm to 3 mm) (Figure 3b). It can be addressed by either leveling the grating surface to the raster-scan plane with high accuracy, or by correcting for surface height change for period measurements using the normal-reflected and angled-reflected beams (Details can be found in J. Song et al. [10]).

CAT GRATING ALIGNMENT

Alignment of CAT gratings was demonstrated for the first time using a custom-designed GAA testbed and the LR tool. Details on design of GAA and measurement procedures for angular misalignments are shown in J. Song *et al.* [10].

Alignment steps were sub-divided into 1) alignment, 2) fixturing, 3) removal of spring plungers/micrometers, and 4) final torqueing. Measurements were taken after each step, and before and after trips between the PANTER X-ray Test Facility in Germany and MIT to understand

Table 1. Summary of measurement results after each step.

	Roll alignment	Fixturing	Removal of spring plungers/micrometers	Final torquing	X-ray test	Back to MIT	Arcus requirements [8]
dYaw [arcmin]	-0.9	+2.0	+2.0	+2.5	-	+2.2	± 15 arcmin
dPitch [arcmin]	+8.8	+14.1	+14.0	+10.6	-	+18.5	± 5 deg
dRoll [arcmin]	+3.8	+4.8	+3.4	+0.08	+3.6	+3.3	± 15 arcmin

Table 2. Error analysis on measurement of roll misalignment

Error source	Uncertainty	Roll error	Note
Θ_i Θ_d	±0.5 deg	±8.6 arcsec ±9.2 arcsec	$\Theta_i = 61\ deg,\ \Theta_d = 49\ deg$
R_d and R_N	± 10 mm	±65 arcsec	$R_d = 200\ mm,\ R_N = 230\ mm$
Detector error	± 5 um	±1 arcsec	Non-linearity error
Data processing error	± 0.1 mm	±18 arcsec	Error induced when averaging the data
Total error	-	±1.14 arcmin	-

the mechanical drifts of CAT gratings for each process and to verify alignment with x rays. Figure 4 summarizes the alignment (or travel) log at each step.

First, roll angles between gratings were adjusted and angular misalignments were measured several times to achieve Arcus alignment requirements [8]. Preloads were kept small and micrometers were retracted several times during alignment to reduce distortion of the frames. Next, the frames were locked in position with fixture screws and all other fasteners were removed. Measurement results after fixturing step indicate all three angles had drifted. Third, spring plungers and micrometers were removed to relax the forces applied to the frames. Fourth, the fixture screws were torqued again (3-5 in-lbs) to make sure the frames did not drift during the travels. Fifth, a roll angle and a resolving power of gratings were characterized with X-rays at PANTER [13]. Sixth, misalignments were recorded again after traveling back to MIT. The GAA testbed was carefully packed inside double Ziplock bags in a clean room environment before each travel to prevent contamination.

Table 1 summarizes the measured angular misalignments after each step. Values indicate line-averaged misalignments of X14 relative to X10. Definition for angular orientation can be found in J. Song et al. [10]. It is clear that all three angles drifted in each step, except only the roll drifted after removing spring plungers and micrometers. However, drifts of angles were small enough to meet Arcus requirements [8].

Error analysis on roll measurement is summarized in Table 2. Error sources include measurement errors of path length (R_D, R_N) and angles (θ_i , θ_d), detector errors, and data-processing errors. Values shown in the 'uncertainty' column assumes a worst-case scenario. Measurement errors of path lengths dominate the measured roll error. Total error is estimated to be ~±1.14 arc min (since the total error was calculated based on a worst-case scenario, the actual measurement error is expected be smaller).

CONCLUSION

The scanning LR tool was newly built and used for characterization of both period variations and angular misalignments of gratings. Addition of the normal-incidence beam enabled more accurate measurements of slope variations, and characterizations of tilt errors and the center of the interference pattern on the wafer substrate. Its capability for measurement of small period variations was demonstrated by measuring in-grating period variations for the test RG. The tool was also used to align two adjacently located CAT gratings to satisfy Arcus mission requirements. Measurement accuracy of angular misalignments between CAT gratings was analyzed to be ~±1.14 arc min.

FUTURE WORK

The scanning LR tool requires further improvements to measure period variations of CAT gratings and the actual flight hardware. Beam size has to be reduced (~ 200 μm), and motion planning algorithms need to be developed to scan inside the single grating membrane (for structural design of CAT gratings, please refer to Ref. [1]). Another issue has to do with "dimpling" of CAT grating membranes. While most of the area does not show dimples, some of the grating membranes are deformed and cause the beams to form non-Gaussian profiles after being reflected or diffracted from the membrane. Since PSDs measure the "center of mass" of illuminated beams, this can lead to bias in position measurements. Large-area UV-sensitive image sensors are an option being considered to tackle this problem. The GAA testbed needs further improvements; mechanical drifts should be reduced throughout the alignment processes and travel.

REFERENCES

[1] R. K. Heilmann, A. R. Bruccoleri, and M.L. Schattenburg, *High-efficiency blazed transmission gratings for high-resolution soft x-ray spectroscopy*. Proc. SPIE 9603, 960314-1, 2015.

[2] R. K. Heilmann et al., *Fabrication update on critical-angle transmission gratings for soft x-ray grating spectrometers*. Proc. SPIE 8147, 81471L-1, 2011.

[3] P. Mukherjee et al., *Plasma etch fabrication of 60:1 aspect ratio silicon nanogratings with 200 nm pitch*. J. Vac. Sci. Technol. B 28, C6P70, 2010.

[4] A. Bruccoleri et al., *Fabrication of nanoscale, high throughput, high aspect ratio freestanding gratings*. J. Vac. Sci. Technol. B 30, 06FF03, 2012.

[5] A. Bruccoleri et al., *Nanofabrication Advances for High Efficiency Critical-Angle Transmission Gratings*. Proc. SPIE 8861, 886119, 2013.

[6] A. Bruccoleri, R. K. Heilmann, and M. L. Schattenburg, *Fabrication process for 200 nm-pitch polished freestanding ultrahigh aspect ratio gratings*. J. Vac. Sci. Technol. B 34, 06KD02, 2016.

[7] R. K. Smith et al., *Arcus: the x-ray grating spectrometer explorer*. Proc. SPIE 10397 (paper 41), to be published, 2017.

[8] H. M. Günther et al., *Performance of a double tilted-Rowland-spectrometer on ARCUS*. Proc. SPIE 10397 (paper 26), to be published, 2017.

[9] D. Dewey, D. N. Humphries, G. Y. McLean, D. A. Moschella, *Laboratory Calibration of X-Ray Transmission Diffraction Gratings*. Proc. SPIE 2280, 257-271, 1994.

[10] J. Song et al. *Scanning laser reflection tool for alignment and period measurement of critical-angle transmission gratings*. Proc. SPIE 10399 (paper 40), to be published, 2017.

[11] J. Ferrera, M. L. Schattenburg, H. I. Smith, *Analysis of distortion in interference lithography*. J. Vac. Sci. Technol. B 14, 4009, 1996.

[12] M. E. Walsh, Ph.D. Thesis, *On the design of lithographic interferometers and their application*. 2004.

[13] R. K. Heilmann, et al., *Critical-angle transmission grating technology development for high resolving power soft x-ray spectrometers on Arcus and Lynx*. Proc. SPIE 10399 (paper 39), to be published, 2017.

Fabrication of Probe Tips for Nanoscale 3D Metrology

Uchiyama K[1], Murakami H[1], Katsuki A[2], Sajima T[2], Yamamoto T[3], Nagata R[3], and Fujiyoshi K[4]
[1] The University of Kitakyushu
[2] Kyushu University
[3] Inatsuki Science Co., Ltd
[4] Fukuoka Industrial Technology Center

INTRODUCTION

In recent years, the importance of measuring microstructures of mechanical microparts, microelectromechanical systems, micromolds, optical devices, microholes, *etc*. has been increasing owing to the advances in microfabrication technology. Particularly, to improve the functionality of a device, microscopic shape measurement methods have been proposed so far.

In this research, we propose a measurement principle using an optical fiber that can be easily realized with a small diameter and high-aspect ratio stylus. In this report, we will describe the miniaturization of a stylus shaft by etching using a temperature controller and the improvement of the stylus tip processing device using a CO_2 laser.

MEASUREMENT PRINCIPLE

Figures 1 (a) and 1 (b) show a photograph of the measurement system and a schematic of the laser-irradiated portion of the stylus. Figure 2 shows a cross-sectional view of Fig. 1 (b) in the XY plane as well as the measurement principle of the optical fiber probe. The measurement principle uses an optical fiber with a sphere made by melting the tip as a stylus. The stylus shaft is fixed to a tubular piezo drive element for posture adjustment. In addition, two laser diodes, each with a wavelength of 405 nm, are installed at a position tilted by approximately 60° with respect to the stylus, and a focused laser light is irradiated from the XY direction toward the stylus shaft. The laser light passing through the prism is reflected upward, and is irradiated to the stylus shaft. The laser irradiation as shown in Fig. 1 (b) makes it possible to install the system above the measured surface by using the prism, and interference with the measurement object can be avoided. The laser transmitted through the stylus shaft is received by two pairs of dual-element photodiodes installed on opposite sides with the stylus in between.

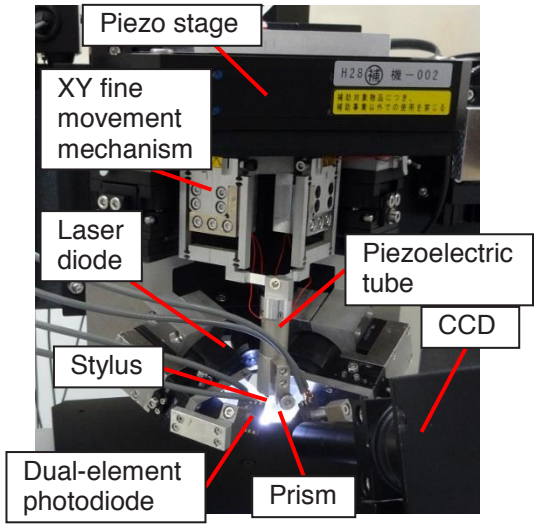

(a) Photograph of the measurement system

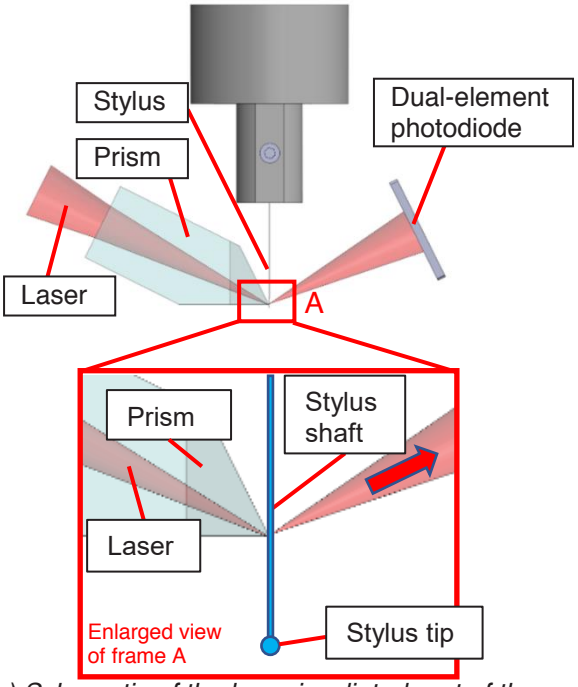

(b) Schematic of the laser-irradiated part of the stylus

FIGURE 1. Overview of the optical fiber probe

The light intensity values detected by each photodiode are converted into voltages, which are represented as I_{PX1}, I_{PX2}, I_{PY1}, and I_{PY2} (V). Before the stylus tip contacts the measured surface, the light intensities measured using each element of the dual-element photodiode are equal ($I_{PX1} = I_{PX2}$, $I_{PY1} = I_{PY2}$), as shown in Fig. 2(a). When the stylus tip contacts the measured surface in the X direction, the stylus shaft is displaced, and the light intensities of each element of the dual-element photodiode becomes unequal ($I_{PX1} = I_{PX2}$, $I_{PY1} > I_{PY2}$), as shown in Fig. 2(b). When the stylus shaft is displaced in the +X direction, the angle of refraction of the laser beam passing through the stylus shaft in the Y direction changes because of a shift in the irradiated part of the stylus shaft. Additionally, when the stylus tip contacts the measured surface in the Y direction, the light intensities of each element of the dual-element photodiode are no longer equal to each other ($I_{PX1} < I_{PX2}$, $I_{PY1} = I_{PY2}$). Hence, the contact direction and magnitude of the displacement of the output signals I_X and I_Y. When the stylus tip contacts the measured plane in the Z direction, the stylus shaft buckles and deflects. This deflection is also measured using the aforementioned method.

The displacement of the fiber stylus is magnified by the stylus shaft, which works as a rod lens. The surface of the microstructure is measured by recording the displacement of the stylus shaft and the coordinates at which the stylus makes contact with the surface being measured. The output signal I_X in the X direction using I_{PY1} and I_{PY2} and the output signal I_Y in the Y direction using I_{PX1} and I_{PX2} are defined by Equations (1) and (2), respectively.

$$I_X = I_{PY1} - I_{PY2} \quad (1)$$

$$I_Y = I_{PX1} - I_{PX2} \quad (2)$$

In general, the stylus shaft must be rigid to transmit the measuring force acting on the stylus tip to the force-detection mechanism installed at the root of the stylus shaft. However, because the deflection amplitude of the stylus shaft is measured using the proposed probe with the help of a laser-based non-contact method, the stylus shaft need not be rigid; this principle also applies to styluses with much smaller diameters and longer lengths. The deflection of the stylus shaft is determined using this measurement system. However, the displacement of the stylus tip cannot be directly measured using this method. The noises present in I_X and I_Y are removed via a synchronous-detection method using a lock-in amplifier.

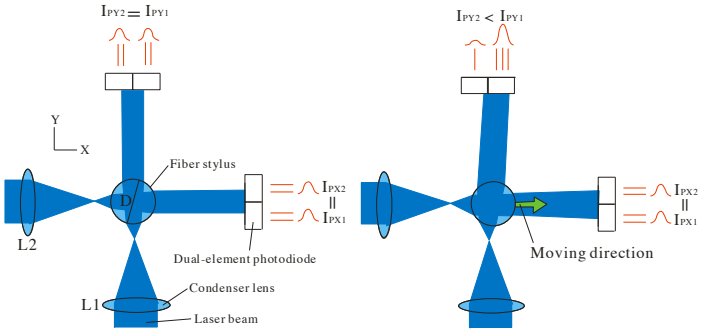

(a) Initial stage *(b) Displacement X*

FIGURE 2. Measurement principle

FABRICATION OF THE STYLUS

Previously, stylus shafts were manufactured by reducing the diameter of optical fibers by wet etching using hydrofluoric acid. However, the difficulty in handling owing to the toxicity of hydrofluoric acid and its high-reactivity as a solvent, controlling the etching rate is problematic. Therefore, the etching was achieved using QE-CL3N of Frostec Inc. as a new etching solvent. Furthermore, in the past, a CO_2 laser was irradiated from the lateral direction with respect to the stylus tip to melt it, and the tip was processed into a spherical shape by the surface tension to produce a stylus tip. However, because of the influence of the temperature gradient, the stylus tip bends in the laser irradiation direction with respect to the shaft in some cases. Therefore, we investigated whether the bending can be suppressed by irradiating the CO_2 laser from a vertically downward direction to the stylus.

Temperature control of etchant

The stylus shaft was fabricated using an acid-etch technique. First, the step index multi-mode optical fibers (core diameter: 105 μm, clad diameter: 125 μm) were stripped of their plastic layers, and subsequently, cleaned with acetone. The fiber-end face was then cleaved with a fiber

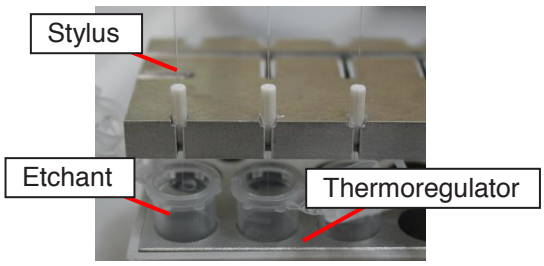

FIGURE 3. Temperature-controlled etching apparatus

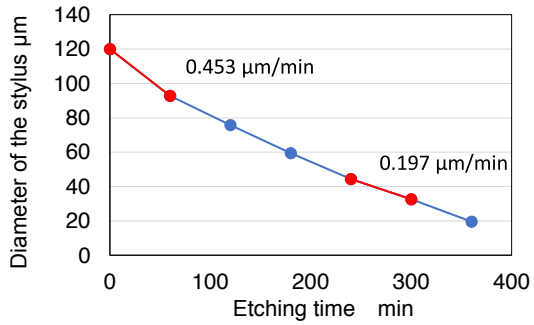

FIGURE 4. Relationship between the etching time and diameter of the stylus shaft (12% hydrofluoric acid solution)

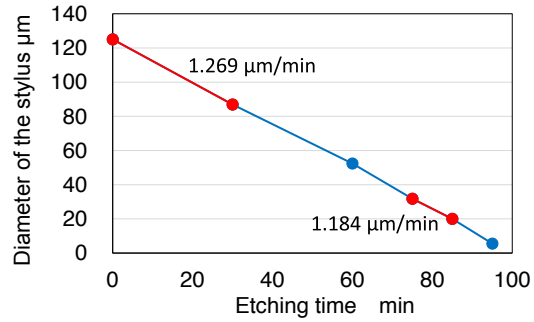

FIGURE 5. Relationship between the etching time and diameter of the stylus shaft (QE-CL3N)

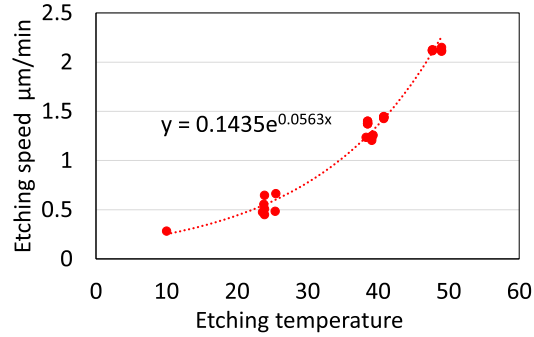

FIGURE 6. *Relationship between the etching rate and etching temperature (QE-CL3N)*

cleaver to be flat and vertical along the longitudinal direction because the shape of the fiber-end face after etching was affected by the shape before etching. We examined the reduction in the diameter of the optical fiber using QE-CL3N. As shown in Fig. 3, an etchant is placed in the temperature controller, and the tip of the optical fiber is immersed for etching. The results of an etching experiment using 12% hydrofluoric acid that was conducted in a previous study, are shown in Fig. 4 for reference. The average etching rate from the start to 60 min is 0.453 µm/min, but the average etching rate from 240 min to 300 min decreases to 0.197 µm/min. The reason for the etching rate decrease is that hydrofluoric acid tends to volatilize at room temperature, and its concentration varies with time. Figure 5 shows the experimental results of etching with QE-CL3N at a constant temperature of 40 °C. The average etching rate from the start to 30 min is approximately 1.269 µm/min, but the average etching rate from 75 min to 85 min is 1.184 µm/min. This shows that QE-CL3N is a stable liquid with a minimal change in the concentration with time.

Figure 6 displays the relationship between the etching temperature and etching rate of QE-CL3N. The temperature of the etching solution and average etching rate can be approximated by the exponential function shown in Fig. 6. Thus, the reaction rate increases exponentially with temperature in good agreement with the Arrhenius equation. Therefore, by using QE-CL3N it is possible to control the etching rate by varying the etching temperature.

Figure 7 shows the stylus produced in this work. As a result of the etching experiment to produce a target stylus diameter below 1 μm using the etching rate calculated from Fig. 6, a stylus with a diameter of approximately 0.58 μm was fabricated.

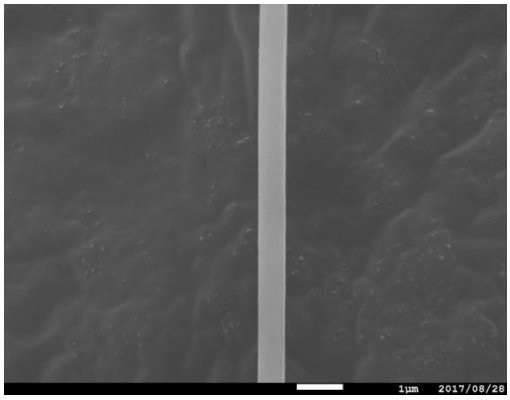

FIGURE 7. Result of the etching experiment to produce a target stylus diameter below 1 µm

Influence of cleaning liquid and number of uses of etchant

Next, we examined the variation in the surface texture of the stylus with the number of times the etching solution was used and the cleaning method after etching. Table 1 presents the various conditions of the etching experiments performed in this study. The experiments were conducted under practically the same conditions, except for those mentioned in Table 1. Figure 8 shows the results of the observations of the etched stylus via Scanning Electron Microscope.

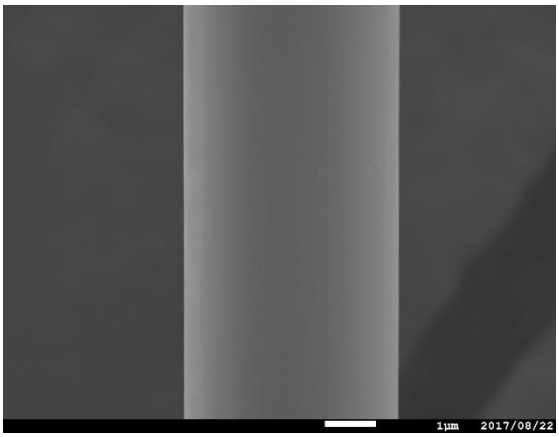

(a) First use etchants + Water washing

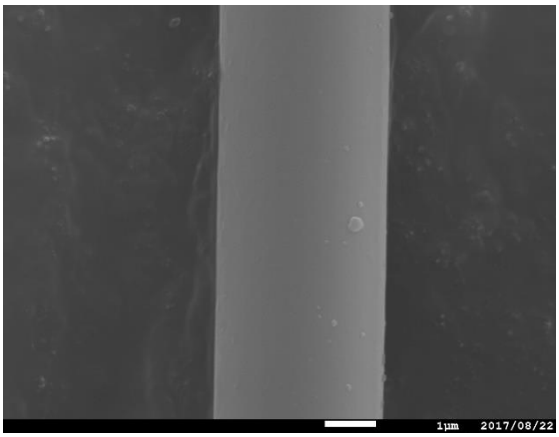

(d) First use etchants + Washing with aqueous sodium bicarbonate and water

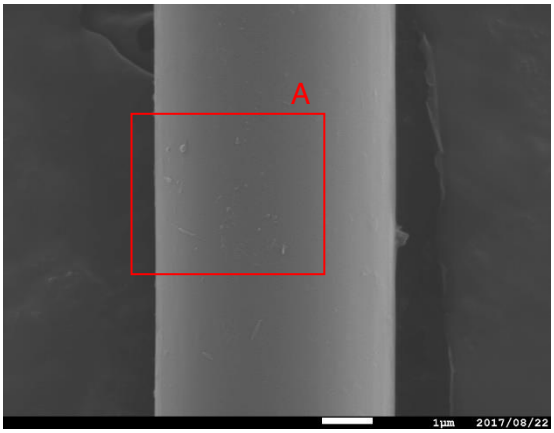

(b) Second use etchants + Water washing

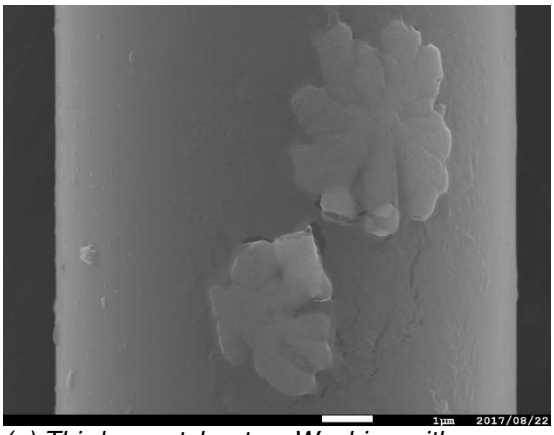

(e) Third use etchants + Washing with aqueous sodium bicarbonate and water

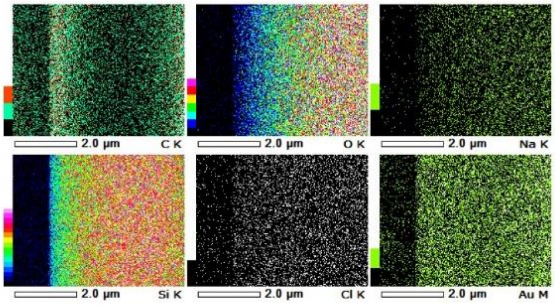

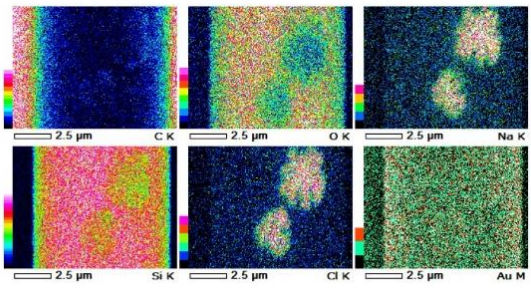

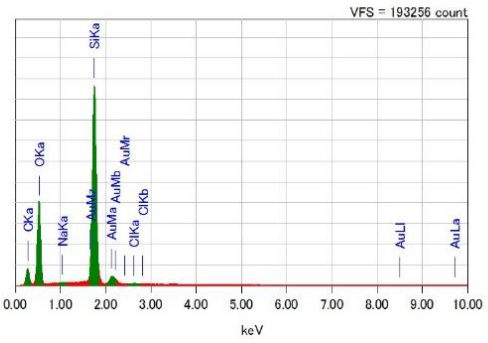

(c) Result of the elemental analysis of frame A in (b)

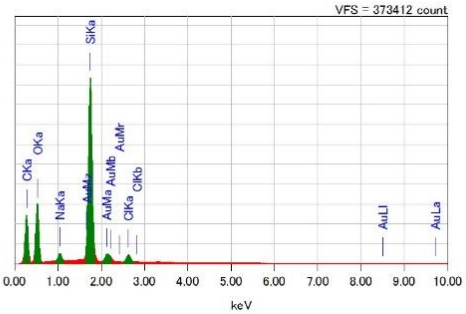

(f) Result of elemental analysis of (e)

FIGURE 8. Differences in the surface properties owing to the etching conditions

First, as shown in Fig. 8 (a), it is found that when the stylus is etched with an unused etchant and washed with water, excellent surface properties are obtained. Subsequently, as shown in Figure 8 (b), when the stylus is etched by applying an etching solution used once already and washing with water, traces of deposits are observed on the surface. Figure 8 (c) displays the results of the component analysis of such deposits in frame A in Fig. 8 (b) via Energy dispersive X-ray spectrometry (EDS). As can be seen from Figure 8 (c), except for Si and O, the main component of the stylus could not be detected on the stylus surface. From this it can be inferred that the stylus was etched and the dissolved stylus component was reattached. Next, after washing with an aqueous solution of sodium bicarbonate, known as a neutralizing agent for an acid solution, washing was again performed with water. An aqueous solution of sodium bicarbonate was employed so that the etchant remaining on the surface of the stylus could be neutralized and the etching reaction could be completely stopped to suppress the change in the surface properties after etching. Figure 8 (d) shows a stylus washed with an unused etchant and aqueous sodium bicarbonate solution. It can be seen that a small amount of deposit is generated on the surface by using aqueous sodium bicarbonate solution as the washing liquid. Figure 8 (e) depicts the stylus etched using an etchant used twice and then washed with aqueous sodium bicarbonate. Here, a high deposit is seen with respect to the stylus diameter. Figure 8 (f) presents the result of the component analysis via EDS. It is understood from the figure that the substance adhering to the stylus surface is a compound of Na and Cl, i.e., NaCl. The above observations as shown in Figs. 8 (d) and (e) reveal that when a bicarbonate compound is used as a cleaning liquid, the deposits on the surface increase. In addition, no improvement in the surface texture is observed by neutralizing the etching solution. Therefore, it is considered that it is appropriate to employ unused etchants for etching and water for cleaning under existing conditions.

Because the slight amount of etchant of 1.5 ml is used for fabricating the stylus shaft in this experiment, the etchant cannot be agitated. Therefore, a small amount of deposits are generated on the surface by using a used etchant. However, it can be inferred that it is possible to fabricate the stylus shaft without deposits by agitating the etchant, even when the stylus is etched with a used etchant.

Table 1. Various etching conditions

	Usage frequency of etchant	Cleaning solution after etching
(a)	First use	Water
(b)	Second use	Water
(c)	First use	Aqueous sodium bicarbonate (2%)+ water
(d)	Third use	Aqueous sodium bicarbonate (2%)+ water

Production of probe sphere by CO_2 laser

Next, a method for manufacturing the stylus tip using a CO_2 laser (C-55, COHERENT) was examined. Figure 9 shows a schematic of the stylus tip manufacturing apparatus using a CO_2 laser. The tip of the stylus is irradiated with the CO_2 laser focused by an objective lens and melted, and a tip is formed based on the surface tension. The laser wavelength is 10.6 μm, output power is 8 W, and focal length of the objective lens is 50 mm. Figure 10 illustrates the stylus tip formation state. As shown in Fig. 10, when the laser is applied to the stylus from the horizontal direction, a temperature gradient is generated inside the stylus and the stylus tip is displaced

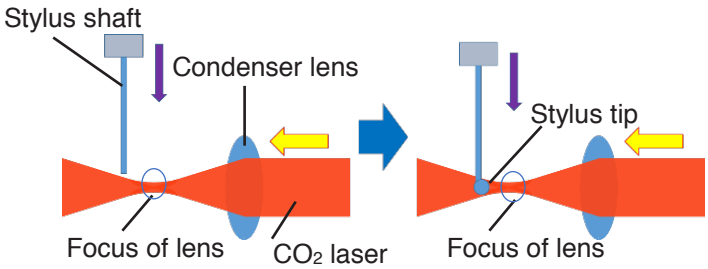

(a) Initial state *(b) Stylus tip production*

FIGURE 9. Fabrication method for stylus tip by a CO_2 laser

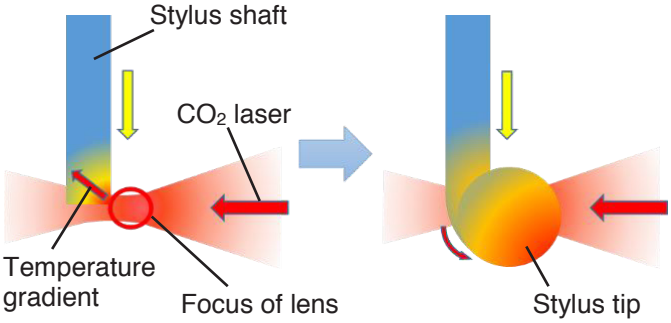

(a) Temperature gradient occur *(b) Stylus tip production*

FIGURE 10. Fabrication status of stylus tip

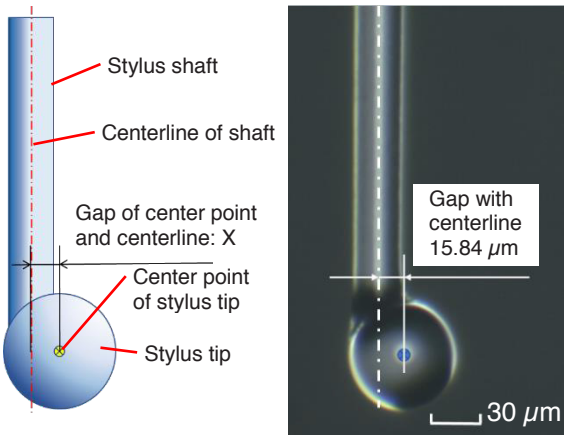

(a) Model of displacement of stylus tip from axis center

(b) Stylus tip after processing

FIGURE 11. Model of processing from the horizontal direction and photograph captured after the processing

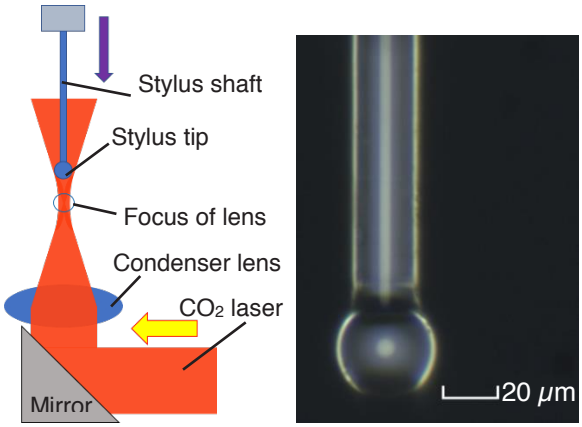

(a) Improved optical system

(b) Stylus tip after processing

FIGURE 12. Schematic of the improved optical system and a photograph captured after the processing

toward the higher temperature side [1]. Figure 11 (a) presents a schematic of the case in which the stylus tip is displaced from the centerline of the shaft. Figure 11 (b) shows a photograph of the processed tip of the stylus, and it confirms that the stylus tip is deviated from the center of the 15.84-μm axis. Next, a method to form stylus tip by irradiating the CO_2 laser to the stylus from a vertically downward direction was studied. Figures 12 (a) and (b) show a schematic of an improved optical system in which the laser can be irradiated to the stylus from a vertically downward direction using a mirror and a photograph of the stylus tip after the processing, respectively. Although it is difficult to measure accurately the extent of the deviation, the figures confirm that the deviation of the stylus tip from the axial center is drastically reduced. This demonstrates that machining from the vertically downward direction of the stylus reduces the deviation of the stylus tip after processing.

CONCLUSION

In this study, we confirmed that the etching rate can be controlled by varying the etching temperature by using QE-CL3N, and showed the possibility of easily realizing the target stylus diameter by temperature control. In addition, it was established that the surface texture of the stylus changed owing to the usage frequency of the etchant and the influence of the cleaning solution. Optimum etching conditions were found to be the application of unused etchant and water as the cleaning liquid under existing conditions. Subsequently, it was demonstrated that by irradiating the CO_2 laser from the vertical downward direction of the stylus, the deviation from the center axis of the stylus tip after processing was reduced.

Acknowledgments

This study was partly supported by METI Supporting Industry Program, JSPS KAKENHI Grant Number 26420392, NSK Foundation's Research Grant for the Advancement of Mechatronics and JST matching planner program.

REFERENCES

[1] T UEDA, K YAMADA, S OIKAWA, A HOSOKAWA. Basic Study on Laser Forming, Journal of the Japan Society of Precision Engineering, Vol. 67, No. 2, 2001, 300.

STATISTICAL REDUCTION TECHNIQUE FOR ZERO POSITION ERROR BETWEEN SENSORS IN IMPROVED SEQUENTIAL THREE-POINT METHOD

Yutaka Uda[1], Yudai Natsume[1], Tomoyuki Tamagawa[1], Shoichi Shimada[1] and Ryosuke Imura[2]
[1]Department of Mechanical Engineering
Osaka Electro-Communication University
Neyagawa, Osaka, Japan
[2] Nagase Integrex Co., Ltd.
Seki, Gifu, Japan

BACKGROUND

Demands are increasing for highly-precise surface shape measurement of large curved surface such as lens and reflecting mirror for telescope. However, there is no useful method for the purpose because of inevitable difficulties in preparing large tangible datum and to avoid the influence of error motions in measuring operation. On the other hand, the sequential three-point method, which does not require the tangible datum, is well known as a useful technique for on-machine straightness measurement of large parts [1]. However, if a zero position error between sensors exists, a large quadratic error component is superimposed on measured shape profile.

In previous papers [2] [3], the design concept of an improved sequential three-point method was proposed. In that method, the zero position error is compensated by measuring the inclination angle of sensor head.

In this paper, a statistical reduction technique for the zero positon error is proposed. To confirm the validity of the technique, numerical estimation of error fluctuation and measuring experiments are carried out.

SHAPE MEASURMENT OF CURVED SURFACE BY IMPROVED SEQUENTIAL THREE-POINT METHOD [2], [3]

Figure 1 shows the principle of sequential three-point method. The rigid sensor head, on which three displacement sensors F (front), C (center) and R (rear) are fixed at equal spaces of d, is scanned along a straight line (x-axis) on the specimen surface to be measured. The surface shape profile of the specimen is numerically calculated using the discontinuous displacement date obtained at every space of d as described in the following. The surface shape profile of the specimen and the output signals of the front, center and rear sensors are expressed by g(x) and $S_{3F}(x)$, $S_{3C}(x)$, and $S_{3R}(x)$ respectively. Supposing that the translational and rotational error motions of the sensor head are e_y and e_θ, respectively, the output signals of the sensors are expressed by Eqs. (1) to (3).

$$S_{3c}(x_i) = \mathrm{g}(x_i) + e_y(x_i) \quad (1)$$

$$S_{3F}(x_i) = \mathrm{g}(x_{i+1}) + e_y(x_i) + de_\theta(x_i) \quad (2)$$

$$S_{3R}(x_i) = \mathrm{g}(x_{i-1}) + e_y(x_i) - de_\theta(x_i) \quad (3)$$

To eliminate the error motions $e_y(x_i)$ and $e_\theta(x_i)$, the second differential output signals is calculated as expressed by Eq. (4), where $\Delta S_{3F}(x_i)$ and $\Delta S_{3R}(x_i)$ are the differences between output signals of the front and center sensors and between the center and rear sensors, respectively. Eq. (4) can be rewritten as the recurrence formula Eq. (5).

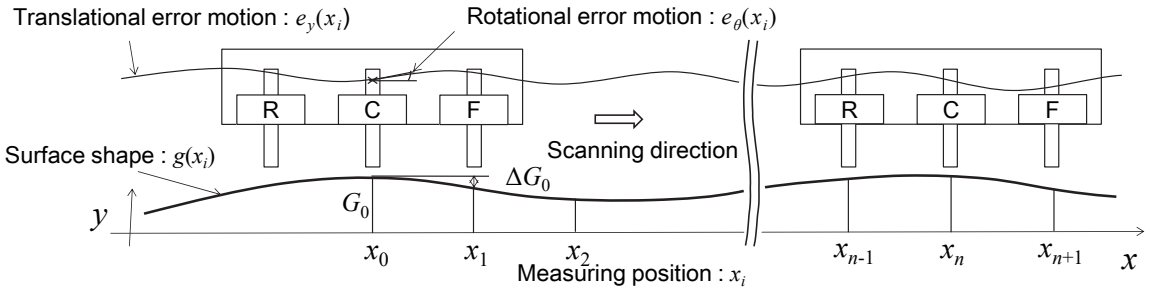

Figure.1 Principle of sequential three-point method

The formula means that the shape profile at x_{i+1} is sequentially obtained using the profile data obtained at x_i and x_{i-1}.

$$\Delta S_{3F}(x_i) - \Delta S_{3R}(x_i) = \{g(x_{i+1}) - g(x_i)\} - \{g(x_i) - g(x_{i-1})\} \quad (4)$$

$$g(x_{i+1}) = 2g(x_i) - g(x_{i-1}) + \Delta S_{3F}(x_i) - \Delta S_{3R}(x_i) \quad (5)$$

By replacing $g(x_0)$ and $g(x_1) - g(x_0)$ with G_0 and ΔG_0, respectively, surface shape profile $g(x_n)$ without any error motions is expressed by Eq. (6). Where G_0 is the height of specimen surface at starting point x_0 of measurement and ΔG_0 is the difference in height between x_0 and x_1.

$$g(x_n) = G_0 + n\Delta G_0 + \sum_{i=1}^{n}(n-i)\{\Delta S_{3F}(x_i) - \Delta S_{3R}(x_i)\} \quad (6)$$

When the three sensors have different zero positions as shown in Figure 2, the zero position error α cannot be eliminated. A large quadratic error component $n(n-1)\alpha/2$ is superimposed on shape profile as shown in Eq. (7).

$$g(x_n) = G_0 + n\Delta G_0 + \sum_{i=1}^{n}(n-i)\{\Delta S_{3F}(x_i) - \Delta S_{3R}(x_i)\} + \frac{n(n-1)}{2}\alpha \quad (7)$$

Furthermore, the specimen surface has large unevenness, the distance between surface and sensor exceeds the working range of the sensor during measuring operation. Therefore, the distance between measuring surface and tip of the center sensor h_a and rotational angle φ of the sensor head is adjusted so that the measuring surface always comes within the working range of every displacement sensors as shown in Figures 3 and 4. Both of h_a and φ to adjust the location and attitude of sensor head can be eliminated by the numerical calculations characteristic in sequential three-point method.

In sequential three-point method, the rotational error motion, that is inclination angle of sensor head $e_{\theta calc}(x_i)$ (same as $e_\theta(x_i)$ in Eq.), can also be sequentially calculated from the output signals of three displacement sensors using Eqs. (1) to (3) and (5). The zero position error α can be obtained by Eq. (8). As nd is equal to x_n-x_0, Eq. (8) can be rewritten as Eq. (9). Where, $\Delta e_{\theta calc}(x_{n,0})$ is the calculated value of difference in inclination angles of the sensor head between at starting point x_0 and finishing point x_n of measuring operation and $\Delta e_{\theta meas}(x_{n,0})$ is the directly measured value by an inclination sensor

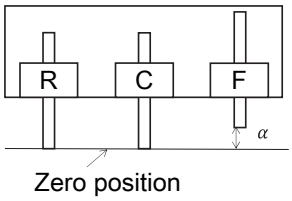

Figure.2 Zero position error between sensors

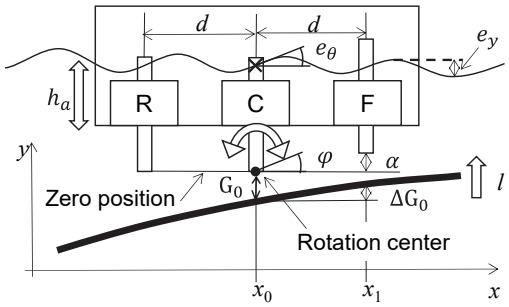

Figure 3 Principle of shape measurement of curved surface using improved three-point method

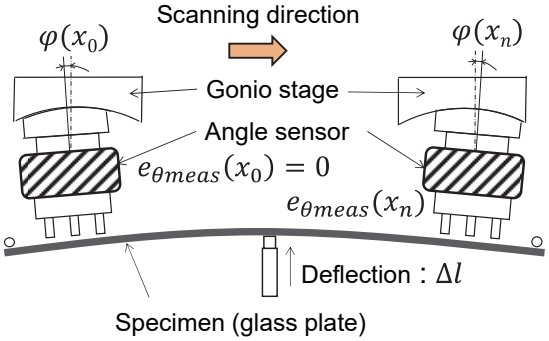

Figure 4 Experimental measuring equipment

mounted on the sensor head. Then, the accuracy of calculated zero position error is eventually governed by the measuring accuracies of the inclination sensor. The output signals of the sensor unavoidably include some random measuring error.

$$\alpha = \frac{d\{\Delta e_{\theta calc}(x_{n,0}) - \Delta e_{\theta meas}(x_{n,0})\}}{n} \quad (8)$$

$$\alpha = \frac{d^2\{\Delta e_{\theta calc}(x_{n,0}) - \Delta e_{\theta meas}(x_{n,0})\}}{x_n - x_0} \quad (9)$$

If the zero position error can be estimated with high reliability, the large quadratic error component can be significantly reduced. Therefore, submicrometer measuring accuracy can be expected on measuring the curved surface of 0.7 meter length.[2],[3]

STATIATICAL REDUCTION TECHNIQUE FOR ZERO POSITION ERROR BETWEEN SENSORS

Eq. (9) suggests that the zero position error between the sensors α can be calculated from the difference in inclination angles of the sensor head measured at two different measuring points. The two measuring points can be chosen in an arbitrary manner as expressed in Eq. (10), where $x_0 \leq x_p < x_q \leq x_n$.

$$\alpha_{qp} = \frac{d^2\{\Delta e_{\theta calc}(x_{q,p}) - \Delta e_{\theta meas}(x_{q,p})\}}{x_q - x_p} \qquad (10)$$

Statistics suggests that, in general, by increasing the number of measured data, the random measuring error can be reduced by an averaging effect. To increase the number of measured data, a shifting technique of the sensor head is proposed in this work as shown in Figure 5. Supposing that the length of specimen is L=nd, the differences in inclination angles of sensor head are sequentially measured between at x_p and x_q by shifting the two measuring points with a space of d keeping the equal distance of L-md between two measuring point, where 0≤m≤n. By the procedure, m+1 data of zero position error α_{qp} are obtained. The number of data collected from the inclination sensor within one scanning of the sensor head increases by decreasing the distance L-md between x_q and x_p or by increasing m. The larger the number of measured data, the smaller the fluctuation of the average value of zero position error.

On the other hand, the influence of measuring error is in inverse proportion to the distance L-md=x_q-x_p as shown in Eq. (10). Therefore, the zero position error is normalized using the distance between two measuring points as expressed in Eq.(11).

$$\beta_{qp} = \alpha_{qp} \times \frac{x_n - x_0}{x_q - xp_i} \qquad (11)$$

The numerical analyses suggest that the optimum value for the distance L-md to obtain the most effective averaging effect is exists depending on the number of n.

NUMERICAL ESTIMATION OF ERROR REDUCTION AND MEASURING EXPERIMENT

To ascertain the statistical reduction technique for zero position error described above, the change

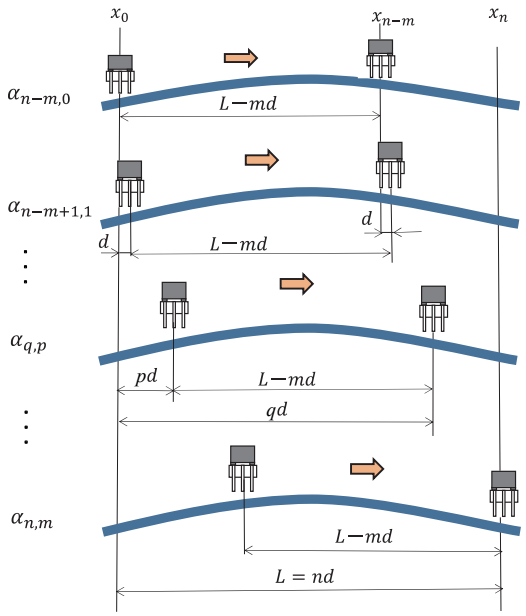

Figure 5 Statistical reduction technique for zero position error between sensors

of standard deviation of the measured inclination angle with the change of m is investigated. Supposing that a digital inclination sensor is used for the measuring of inclination angle and that the one scale unit of which is Δs, possible measuring error are three cases as -Δs, 0 and +Δs. The every error occurs with same probability. The possible measuring errors arising in measuring the difference in inclination angle between at arbitrary two different points x_p and x_q are -2Δs, -Δs, -Δs, 0, 0, 0, +Δs, +Δs and +2Δs. The number of possible errors is 3^2=9 and the every error also occurs with same probability. In this case the standard deviation of the measuring error is 1.225Δs. If the data of inclination difference increases to m sets, the number of possible errors exponentially increases to 9^{m+1} and the standard deviation decreases. The solid line in Figure 6 shows the change in standard deviation with the change of m.

The measuring experiment was carried out using the equipment as shown in Figure 4. A glass plate with smooth surface was used as a test piece to be measured. The length, width and thickness of the plate were 1200mm, 25mm and 5mm, respectively. The plate was supported at both ends with a distance of 1150mm. To produce curved surfaces, a deflection Δl of about 1mm is given at the center between the supporting points of the scale by a micrometer. The distance between sensors d was 30mm and the number of total measuring points was 35.

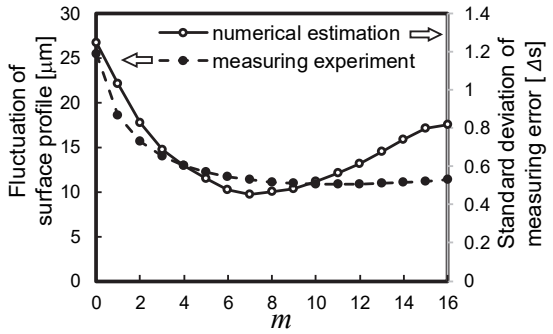

Figure 6 Numerical estimation of change in standard deviation of defference in inclination angles

Figure 7 shows the fluctuation of shape profiles from the average profile of four trials without any compensation for quadratic error component due to zero position error between the displacement sensors. The large quadratic components the amplitudes of which are a few tens of micrometers are observed. By the compensation of zero position error using the inclination angle of sensor head measured at the starting and finishing points (in case that m in Figure 5 is equal 0), the fluctuation is decreased to smaller than 15μm as shown in Figure 8. Figure 9 shows the fluctuation of shape profiles with compensation of zero position error by the technique proposed in this work. In this case, m is supposed to be 8. The results show that the fluctuation in zero position error is 60% reduced by the statistical reduction technique proposed. The change in fluctuation of shape profiles measured is shown by dotted line in Figure 6. When the number of measuring points is 35, the optimum number of m is estimated to be 8.

SUMMERY

The fluctuation of zero position error in improved sequential three-point method is 60% reduced by applying the statistical reduction technique proposed comparing that measured from the difference in inclination angles at the both end of specimen .

REFERENCES

[1] Obi, M., Furukawa, S. : A study of the measuring for straightness using a sequential point method", 1991, Trans. JSME, C-57, 542, 3197-3201.

[2] Tamagawa, T., Uda, Y., Shimada, S., Imura, R. : Development of surface shape measuring machine of large optics by sequential three-point method, 2014, Proc. Japan Society for Precision Engineering 2014 Autumn Meeting, 823-824. (in Japanese)

[3] Natsume Y., Tamagawa, T., Uda, Y., Shimada, S., Imura, R. : Surface Shape Measurment of Large Curved Surface Applying Improved Sequential Three-Point Method, 2016 Proc.31-ASPE Autumn Meeting, 351-354

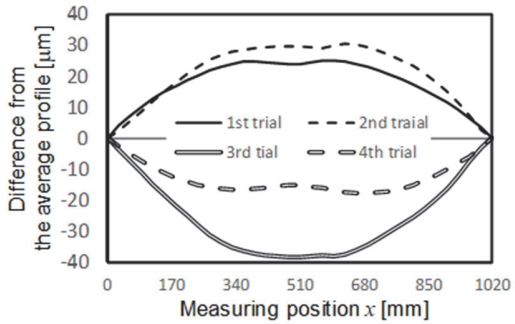

Figure 7 Fluctuation of shape profile without compensation of quadratic error component

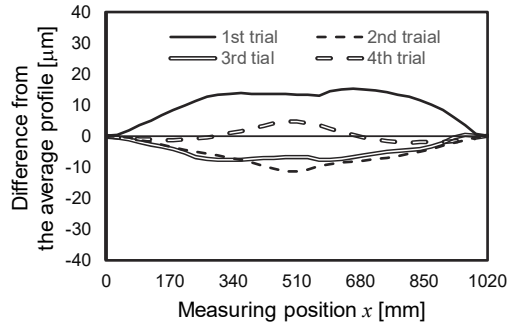

Figure 8 Fluctuation of shape profile with compensation of quadratic error component (m=0)

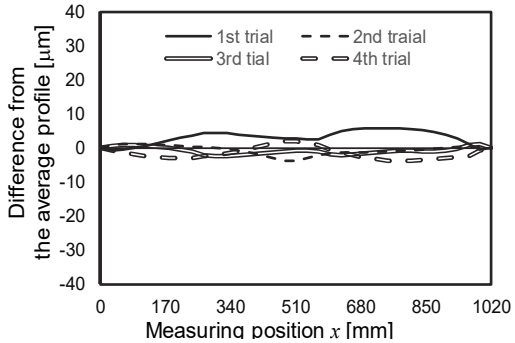

Figure 9 Fluctuation of shape profile with compensation of quadratic error component (m=8)

MINIMIZING TASK-SPECIFIC UNCERTAINTY IN CMM-BASED FREEFORM OPTICS METROLOGY

Michael U. Uwakwe, and Christopher J. Evans
Center for Precision Metrology
University of North Carolina at Charlotte
NC 28223, USA

INTRODUCTION

All measurements of surface form involve a comparison between the form of the part under test, and a reference. In coordinate measuring machine (CMM) measurements, this reference is the machine geometry. The measurement results typically show a height map representation of the part but these contain error contributions from the machine. This paper demonstrates and applies an in-situ self-calibration technique, Shift-Rotation, to CMM-based freeform optics metrology. This error-separation technique minimizes task-specific uncertainty in freeform measurements by separating machine errors from part surface measurements. Shift-Rotation has been in use in interferometry for testing optical surfaces [1, 2, 3, 4], and the idea is here, extended to measurements from CMMs.

Simulations were used to demonstrate how the Shift-Rotation technique separates freeform measurements into components of the test part and components from machine error contributions. Simulations were also used to carry out task-specific uncertainty analyses. Using Monte Carlo simulations [5], the uncertainty contributions from some potential uncertainty sources associated with this error separation technique were estimated. These uncertainties were expressed as maps, the same size and data density as the measurand, and show the spatial distribution of the uncertainty within the aperture.

This error-separation technique was then implemented on freeform measurements on a Zeiss F-25 micro-CMM and a Mahr LD 260 surface profiler. Error separation of these results led to best estimates of the freeform surface; these were then compared to optical measurements of the same freeform surface, measured on a Zygo Verifire (Fizeau) interferometer and a Zygo NexView (SWLI) interferometer.

SIMULATIONS OF THE SHIFT-ROTATION TECHNIQUE

The Shift-Rotation error separation technique decomposes freeform measurement results into four components: two from the part and two from machine error contributions. These components are classified as being either rotationally varying (RV) or rotationally invariant (RI), and the sum of the two separated components of the freeform part represent a best estimate of the freeform without machine error contributions.

In these simulations, combinations of Zernike polynomials were used to represent the part and machine error components. These simulations were deliberately performed with large form deviations and the amplitudes of the simulated machine errors are also deliberately large. The following example shows a Shift-Rotation error separation of a simulated freeform measurement.

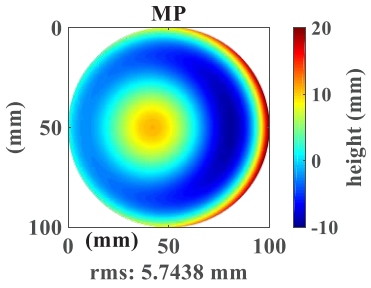

FIGURE 1. A simulated measurement of a freeform surface.

This simulation depicts the freeform surface and includes errors from the measuring machine. To separate the components in the above height map, the “Rotation” portion of the Shift-Rotation technique was used to solve for the RV components of the part and machine, while the “Shift” portion solved for the RI components.

Results from these decompositions are summarized in Figure 2. The sum of the two separated components of the freeform part,

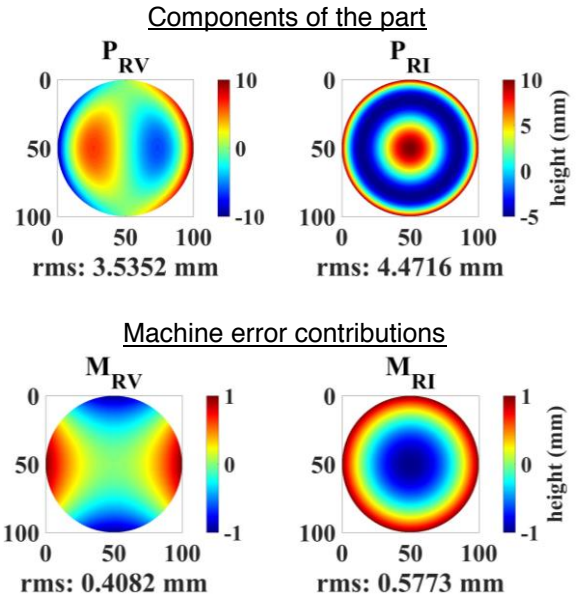

FIGURE 2. Shift-Rotation decomposition of the simulated freeform surface.

represented a best estimate of the freeform without machine error contributions. Using Monte Carlo, standard uncertainties were obtained to accompany the best estimate of the freeform. In the N-rotation technique, simulated measurements of the part were made after the part was rotated to four positions separated by 90°. Since these angles are sources of uncertainty, a standard uncertainty was evaluated after each nominal rotation angle randomly varied within a uniform distribution with upper and lower limits of ± 0.05°.

The rotation axis, about which the part rotates, was considered as another source of uncertainty. A standard uncertainty was obtained after the rotation axis of every simulated part-rotation randomly translated within a 300-μm square center. Uncertainty arising from uncertainty in the translation distance (in the Shift technique) was also evaluated. A 2-mm nominal translation distance was input to the Monte Carlo, within a uniform distribution with upper and lower limits of ± 200 μm. Finally, a standard uncertainty from electronic noise and vibrations was evaluated. This was obtained after a uniform distribution of random noise, with a peak-to-valley of 30 nm, was added to every simulated part measurement.

Under the assumption that the above standard uncertainties were uncorrelated, a combined standard uncertainty was obtained from their root-sum-square [6]. This combined standard uncertainty is shown alongside the best estimate of the measurand in Figure 3.

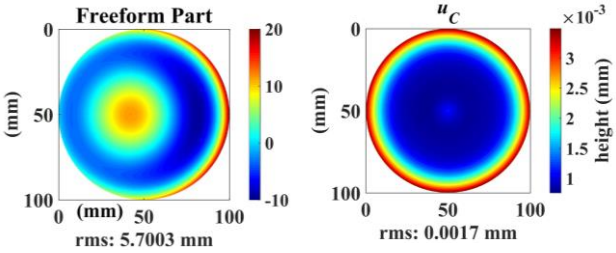

FIGURE 3. The best estimate of the simulated freeform surface (left) and its combined standard uncertainty (right).

The Shift-rotation was then implemented on freeform measurement results from the Zeiss CMM and Mahr profilometer. The next section introduces the freeform surface that was measured.

FREEFORM SURFACE TO BE MEASURED

The freeform surface measured in this project is shown in Figure 4. It was fabricated from a BK7 optical flat, on a magnetorheological finishing (MRF) machine and is housed in a polycarbonate mount with four silicon carbide balls and a reference mark that transfer coordinates from MRF to metrology. The freeform part has an outer diameter of 40-mm and a 35-mm clear aperture.

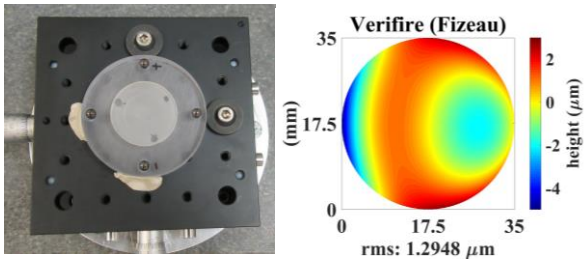

	Zernike coefficients (nm)				
	Z (2, 0)	Z (2, -2)	Z (2, 2)	Z (3, -1)	Z (3, 1)
Verifire (Fizeau)	-22	-129	-2390	125	2392

FIGURE 4. The freeform surface to be measured on a Zeiss F-25 CMM, a Mahr LD 260 surface profiler, a Zygo Verifire (Fizeau) and a Zygo NexView (SWLI) interferometer.

A Fizeau measurement (used as a reference during comparisons) of this sample, and some of its low-order Zernike coefficients, are also shown in Figure 4.

FREEFORM MEASUREMENTS ON THE ZEISS F-25 CMM

A Cartesian measurement model was used to measure the freeform surface on the Zeiss F-25 CMM. Thirty-seven parallel profiles with 1-mm spacing in-between were scanned across the freeform surface. These profiles had data densities with point-coordinates measured every 1 μm along the x-axis, and are shown in Figure 5.

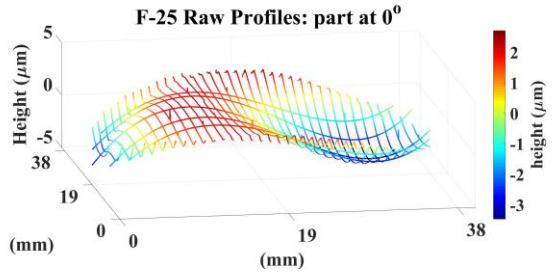

FIGURE 5. Pre-processed profiles from the Zeiss F-25 freeform measurements.

Between the first and thirty-seventh profile measurements, stage drifts and tilt changes could occur. To correct for these, additional profiles were measured. These were five parallel tie-profiles, measured perpendicular to the thirty-seven profiles and shown overlayed in Figure 5.

Roughness of these profiles was removed by applying a 0.8-mm λc low-pass Gaussian filter, in the spatial domain, to all the profiles. The profiles were then cropped from a 38-mm diameter to the 35-mm clear-aperture, and slope-corrected using the tie-profiles. Twelve Zernike polynomials were fit to these processed profiles and a surface was generated from the Zernike coefficients. These processed profiles and generated surface are shown in Figure 6.

The map in Figure 6 represents the first measurement of the freeform surface. Additional measurements were made because the Shift-Rotation error separation technique requires multiple measurements of the freeform surface at predefined angular orientations and translations of the part; these subsequent measurements followed the same measurement strategy and data-processing described above.

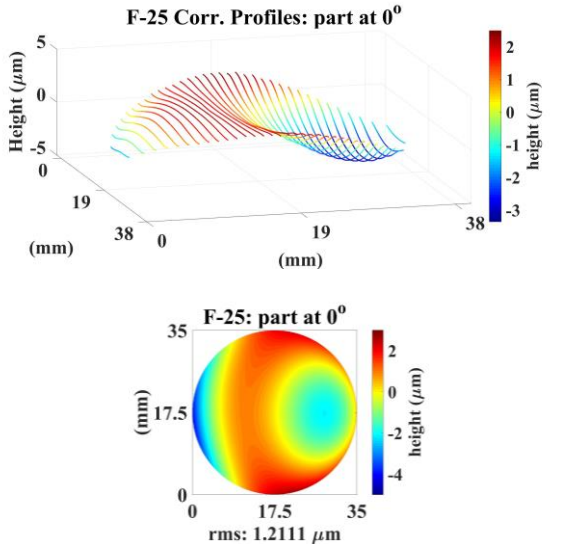

FIGURE 6. Zeiss F-25 CMM freeform measurement of the part in the initial position.

Separation of the rotationally varying components

To solve for the rotationally varying (RV) components of the freeform part, the freeform part was measured at five angular orientations separated by 72°. The number of angular orientations was chosen to be five because there was prior knowledge of the angular orders expected to be of significant amplitude on the freeform. The surfaces generated from the additional rotated-part measurements are shown in Figure 7.

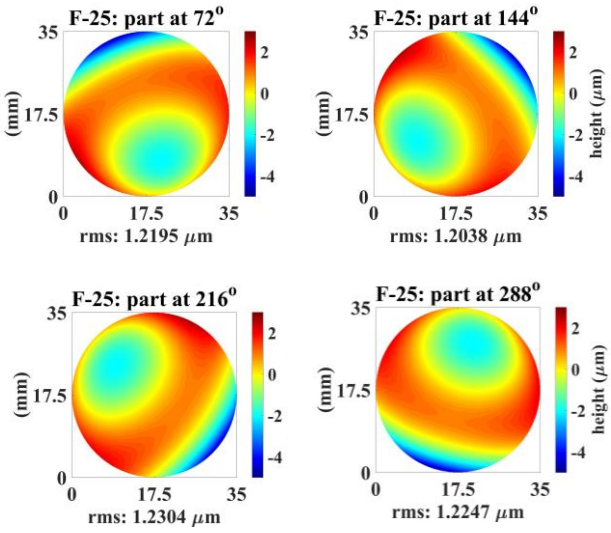

FIGURE 7. Zeiss F-25 CMM freeform measurements of the part at angular orientations separated by 72°.

The average of the five rotated-part measurements dropped out the RV component of the freeform surface [7]. After this separation, the residual RV components were attributed to the machine errors. These separated RV components of the freeform part and machine error contributions are shown in Figure 8.

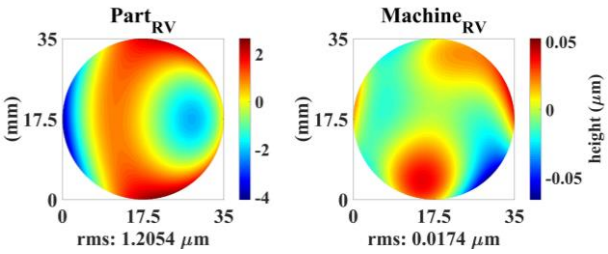

FIGURE 8. Rotationally varying component of the freeform surface (left). Rotationally varying component of the machine (F-25 CMM) errors (right).

Separation of the Rotationally Invariant Components

The Shift-technique was used to separate the rotationally invariant (RI) components of the freeform surface and machine error contributions. This separation required an additional measurement of the freeform surface, after a lateral translation with respect to an initial position. With respect to the initial position of the part, an additional measurement was made after shifting the part by a 1-mm distance, Δ. Initial and sheared measurement results are shown in Figure 9 (the shear direction was upwards).

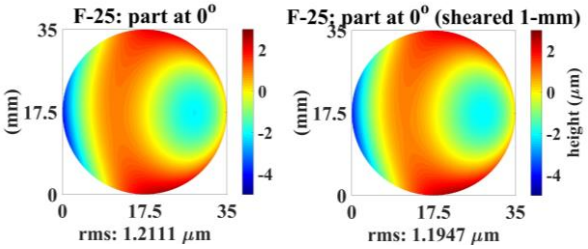

FIGURE 9. Initial and shifted measurements of the freeform surface.

Since the RV components of the part and machine have already been obtained from the previous section, these can be subtracted (in their respective orientations) from the maps in Figure 9. Alternatively, the N-rotation averaging can be applied to these maps to remove their RV components.

Under the assumption that the machine errors remained constant between the initial and shifted measurements, a difference between the residual maps gives the approximate slope of the part as shown in Figure 10.

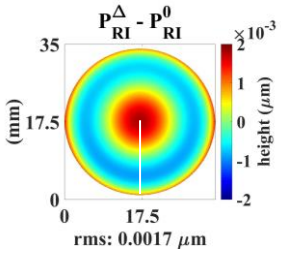

FIGURE 10. Approximate slope of the freeform part.

The goal of the following steps was to obtain the RI component of the part from this slope. A profile, **g**, was extracted from the part center to the edge in the – Δ direction (indicated by the white line in Figure 11). Each point in **g** is a height difference between two points (a distance Δ apart) in the desired radial profile, **f**. This profile **f** represents a radius from the RI surface of the part. The relationship between **f** and **g** was expressed as a system of linear equations: **g** = **H***f**, where **g** and **f** are column vectors and **H** is a design matrix that was built [8]. The design matrix was singular but its pseudo-inverse enabled a solution of the radial profile, **f**, shown in Figure 11.

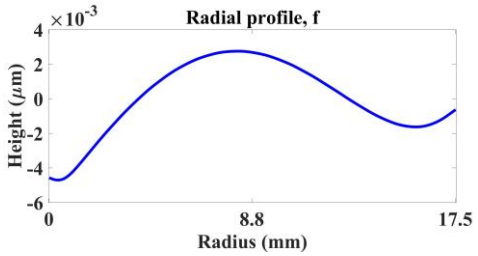

FIGURE 11. Radial profile of the RI freeform part.

The RI component of the freeform surface was then obtained by generating a surface from this solved radial profile. The final separated component, the RI component of the machine errors, was obtained by subtracting the separated RV components of the part and machine, and the RI part-component from the measurement of the part in its initial 0° orientation. These separated RI components are shown in Figure 12.

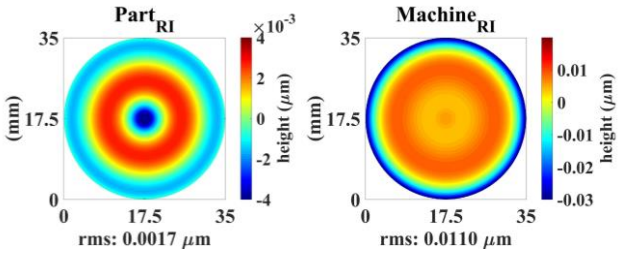

FIGURE 12. The RI components of the freeform surface and machine (F-25 CMM) error contributions.

The Best Estimate of the Freeform Surface, Separated from the Zeiss F-25 CMM Measurements

The maps in Figure 8 are the separated RV components of the freeform surface and machine errors while the maps in Figure 12 are the separated RI components. The sum of the two separated components of the freeform surface ($Part_{RV}$ and $Part_{RI}$) represented a best estimate of the freeform without machine error contributions, and this is shown in Figure 13.

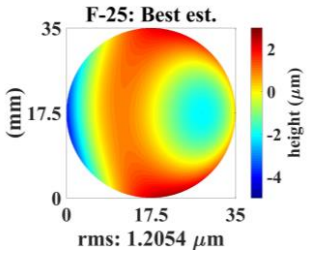

FIGURE 13. The best estimate of the freeform surface, without the RV and RI machine errors.

FREEFORM MEASUREMENTS ON OTHER MEASURING MACHINES

So far, the error separations have been performed on freeform measurements made on the Zeiss F-25 CMM. The freeform surface was also measured on three other machines: the Mahr surface profiler, Zygo Verifire (Fizeau) interferometer and Zygo NexView (SWLI) interferometer shown in Figure 14.

The measurement strategy used for the F-25 freeform measurements was also used to measure the freeform on the Mahr profiler. The same data processing, low-pass Gaussian filter and error separations applied to the F-25 measurement results, were also applied to the

Zeiss F-25 CMM

MarSurf LD 260

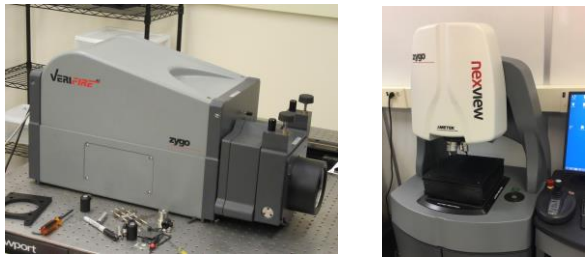

Zygo Verifire (Fizeau)

Zygo NexView (SWLI)

FIGURE 14. Four measuring machines used to measure the freeform surface.

Mahr measurements. The Mahr freeform surface measurements were made at the same angular orientations and translations of the part like those used during the F-25 measurements. From these measurement results, the Shift-Rotation error separation was used to obtain the best estimate of the freeform surface. This best estimate from the Mahr profilometer is compared to that from the F-25 CMM in Figure 15.

Figure 15 also includes results from optical measurements of the freeform surface measured on a Zygo Fizeau and a Zygo NexView interferometer. The NexView measurement result was obtained after stitching multiple acquisitions with an x-y blend stitching algorithm and a 20% overlap region between individual acquisitions. These comparisons were further expressed as the amplitudes (root-sum-square of the sine and cosine Zernike terms, where applicable) of the Zernike coefficients in Table 1. The table shows the dominant terms present on the freeform surface are astigmatism and coma. The comparison shows the best estimates from the Zeiss CMM and the Mahr profiler agree to within 35 nm.

TABLE 1. Zernike coefficient comparisons between the freeform measurements.

	Amplitudes of the Zernike coefficients (nm)						
	defocus	astig.	coma	trefoil	spherical	sec. astig	tetrafoil
F-25: best est.	30	2264	2171	145	49	225	140
Mahr: best est.	101	2280	2206	140	79	154	185
Verifire (Fizeau)	22	2393	2395	186	27	86	16
NexView (SWLI)	486	2572	2504	198	21	83	15

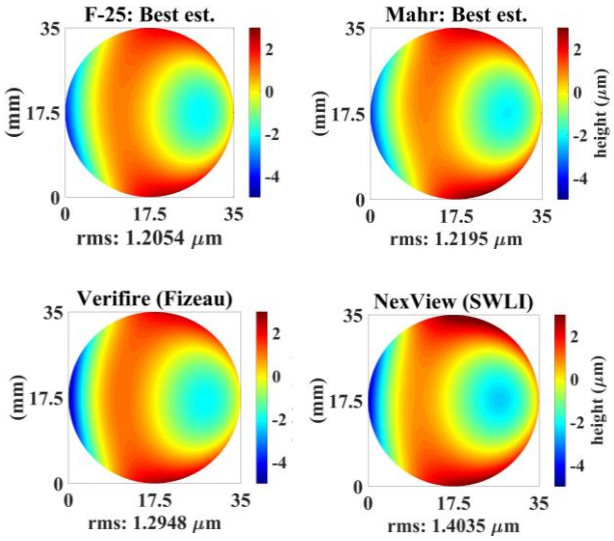

FIGURE 15. Freeform measurement results from the four measuring machines.

ACKNOWLEDGEMENTS

Immense gratitude goes to Dr. William Kuhn and Greg Caskey for their support, to the faculty and students of the Center for Precision Metrology at UNC Charlotte and the Center for Freeform Optics (CeFO). The author is very thankful for the National Science Foundation's sponsorship of this project, under NSF Award No. 1432990.

REFERENCES

[1] Ichikawa H, Yamamoto T, inventors; U.S. Patent No. 5,982,490. Apparatus and method for wavefront absolute calibration and method of synthesizing wavefronts 1999.

[2] Song W, Wu F, Hou X, Wu G, Liu B, Wan Y. Absolute calibration of a spherical reference surface for a Fizeau interferometer with the shift-rotation method of iterative algorithm. OPTICE. 2013; 52(3):033601-.

[3] Soons J A, Griesmann U. Absolute interferometric tests of spherical surfaces based on rotational and translational shears. SPIE Optical Engineering+ Applications; 2012: International Society for Optics and Photonics.

[4] Evans C J, Kuhn W P, inventors; U.S. Patent No. 7,446,883. Method and apparatus for tilt corrected lateral shear in a lateral shear plus rotational shear absolute flat test 2008.

[5] IUPAP B. Evaluation of Measurement Data—Supplement 2 to the 'Guide to the Expression of Uncertainty in Measurement'—Extension to any number of output quantities. 2011.

[6] Bell S. Measurement Good Practice Guide No. 11 (Issue 2). A Beginner's Guide to Uncertainty of Measurement National Physical Laboratory Teddington, Middlesex, United Kingdom. 2001.

[7] Evans C J, Kestner R N. Test optics error removal. Applied Optics. 1996; 35(7):1015-21.

[8] Kuhn W P, inventor; U.S. Patent No. 7,158,914. Precision surface measurement 2007.

UNCERTAINTY ANALYSIS FOR PART DENSITY DETERMINATION VIA HYDROSTATIC WEIGHING

Mario O. Valdez[1], Joshua D. Montaño[2] and Lucas M. Valdez[3]
[1]Production Agency Quality, [2]Prototype Fabrication, [3]Manufacturing Science and Engineering
Los Alamos National Laboratory
Los Alamos, NM, USA

INTRODUCTION

Accurate and precise density measurements via hydrostatic weighing requires the use of an analytical balance, configured with a suspension system, to both measure the weight of a part in water and in air (see *FIGURE 1*). Additionally, the densities of these liquid media (water and air) must be precisely known for the part density determination. To validate the accuracy and precision of these measurements, uncertainty statements are required. The work in this paper is a revision of an original, internal report written more than a decade ago [1], which complies with the principles and guidelines suggested by the *Guide to the Expression of Uncertainty in Measurement* (GUM) [2]. Furthermore, the updated uncertainty models are applied to an original example taken from the original report to estimate a new measurement uncertainty value and for a comparison as to what was originally determined.

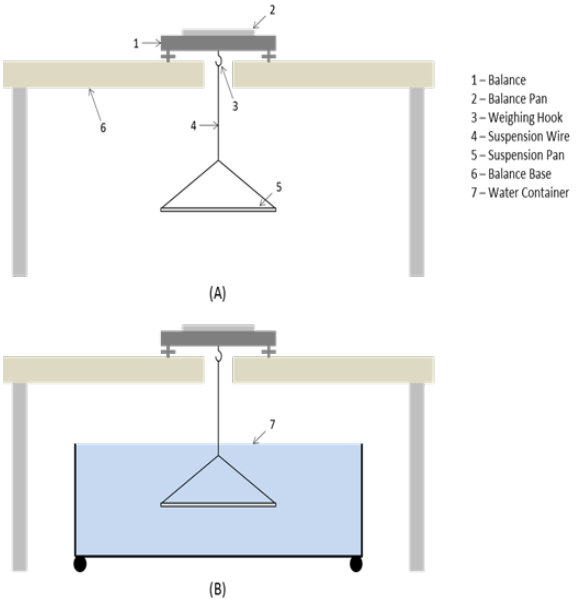

FIGURE 1. Measurement apparatus: (A) air; and (B) water.

BACKGROUND

Classical part density is determined using the relationship between the part's *true mass* and *true volume*. Unfortunately, it is not possible to exactly know these values, as there are random and systematic errors which contribute to the uncertainty of each quantity. Therefore, the most accurate method is measurements performed via hydrostatic weighing for density determination, where measurement models are determined [3] [4] [5], thus providing a very reliable method.

The theory goes as follows: a part's *conventional weight*, $\bar{W}$, is measured in media with different densities, where the conventional weight is defined as the difference between the weight from the gravitational load exerted by one medium (air) and the weight from the buoyant force exerted by the other medium (water). Therefore, the conventional weights of the part in medium one (air) and medium two (water) can then be determined by Eq. 1

$$\begin{aligned} \bar{W}_A &= g(M_x - \rho_A V_x) \qquad (in\ air) \\ \bar{W}_W &= g(M_x - \rho_W V_x) \qquad (in\ water) \end{aligned} \tag{1}.$$

A simultaneous solution of Eq. 1 provides values of M_x and V_x for which densities can be calculated. However, experimentation requires a linear force in the balance, thus making the force units arbitrary in which case the units of $M_x$and V_x will be unrecognizable. However their ratio (M_x/V_x) is in units of density like ρ_W and ρ_A, the true standards in the density measurement process.

Determination of the conventional values for $\bar{W}_A$ and $\bar{W}_W$ is done via the averaging of a series of measurements. From these average measurements, as well as the values for ρ_A

(density of air) and ρ_W (density of water), the part density can be determined by simultaneously solving Eq. 1. As a result, the measurement model of the part's density is shown in Eq. 2 below

$$\rho_O = \frac{W_A\rho_W - W_W\rho_A}{W_A - W_W} \quad (2).$$

To preserve consistency, the average weight measurements are represented with W instead of $\bar{W}$.

MODELING

Uncertainty of Part Density

With the determination of the part density modeled by Eq. 2, an uncertainty model is estimated via the principles of the GUM. Therefore, the uncertainty model is determined to be

$$u_{\rho_O} = \left[\left(c_{W_A}\cdot u_{W_A}\right)^2 + \left(c_{\rho_W}\cdot u_{\rho_W}\right)^2 + \left(c_{W_W}\cdot u_{W_W}\right)^2 + \left(c_{\rho_A}\cdot u_{\rho_A}\right)^2\right]^{1/2} \quad (3)$$

where the sensitivity coefficients for each of the influence quantities are determined as $c_i = \partial\rho_O/\partial x_i$. The sensitivity coefficients are determined to be

$$c_{W_A} = \frac{\partial\rho_O}{\partial W_A} = \frac{W_W(\rho_A - \rho_W)}{(W_A - W_W)^2}$$

$$c_{\rho_W} = \frac{\partial\rho_O}{\partial\rho_W} = \frac{W_A}{W_A - W_W}$$

$$c_{W_W} = \frac{\partial\rho_O}{\partial W_W} = \frac{W_A(\rho_W - \rho_A)}{(W_A - W_W)^2} \quad (4).$$

$$c_{\rho_A} = \frac{\partial\rho_O}{\partial\rho_A} = -\frac{W_W}{W_A - W_W}$$

Eq. 3 assumes that there is no correlation between influence quantities. This can be reasoned in that each of the influence quantities is determined using *different* analysis (i.e., analytical modeling and repeated measurands).

The use of a measurement model shows the relationship of indirect measurements, which converts potentially multiple, individual values into the corresponding value of the measurand of interest, therefore the ability to estimate a near-complete solution of the measurement uncertainty. However, this method does not take into account the uncertainty contribution from the measurement process itself. Errors from the measurement process can be the result of intrinsic and extrinsic factors which affect the measurement result systematically and randomly. Accounting for these measurement process errors into an uncertainty contribution is done through experimental data, specifically repeated measurements [6]. With that in mind, the *total, expanded uncertainty* is estimated by adding in quadrature the combined standard uncertainty, determined by sensitivity analysis, and the sample standard deviation of the repeated measurements (measurement process), $s(MP)$ as shown in Eq. 5,

$$U_T = 2\times\left[u_{\rho_O}^2 + s^2(MP)\right]^{1/2} \quad (5).$$

Density of Water

The mathematical model for the density of water is a function of the effects of dissolved air and pressure. Dissolved air takes into account the temperature of the water, T_W, and the interval of deaeration (removal of air molecules), t, while the pressure accounts for the compressibility of the water, C, the barometric pressure, B, and the immersion depth, I. The term which represents the deaeration of air contributes to the water density in parts per million (ppm) so has an influence of approximately multiplying the model by 1, so is not accounted for in the model. The measurement model is shown below in Eq. 6,

$$\rho_W = \left[1 - \left(\frac{(T_W - 3.9863)^2}{508929.2}\right)\left(\frac{T_W + 288.9414}{T_W + 68.12963}\right)\right]\times [0.999973]\left[\frac{1}{1 - C\left(\frac{B}{760} + \frac{I}{1033} - 1\right)}\right] \quad (6).$$

Experimentally, the environmental parameters T_W and B contribute to the uncertainty most, where the other parameters can be incorporated into the model with conventionally known values. A compressibility value of $0.063\ ppm/mmHg$ is looked up [7] and an immersion depth of $15.88\ cm$ is calculated from the center of gravity of the immersion tank used in the measurement process [8]. Hence, substituting these values and simplifying Eq. 6 yields a simplified measurement model,

$$\rho_W = \left[1 - \left(\frac{(T_W - 3.9863)^2}{508929.2}\right)\left(\frac{T_W + 288.9414}{T_W + 68.12963}\right)\right] \times [0.999973]\left[\frac{1}{1 - 6.19 \times 10^{-8} B}\right] \quad (7).$$

Density of Air

The density of the part in air is mathematically modeled as a function of environmental factors, namely ambient temperature T_A; relative humidity RH; and barometric pressure B. All laboratory measurements should be taken at the industry-standard of 20°C but ambient temperature fluctuations are periodic so the range can vary within the laboratory specification of $20.0℃ \pm \Delta T$. The model is represented by Eq. 8,

$$\rho_A = \frac{0.464554B - RH(0.00252T_A - 0.020582)}{T_A + 273.16} \quad (8).$$

It should be noted that this model represents measurements performed within a temperature range of 20°C to 30°C and can be adjusted for the rare occasion of measurements performed outside this range [3]. This adjustment for a wider temperature range makes the model nonlinear; however, this will have a negligible effect somewhere in the range of $< 1\ \mu g/cm^3 = 1 \times 10^{-6}\ g/cm^3$ [5].

UNCERTAINTY CALCULATIONS

Weight

Error sources that contribute to the uncertainty in the weight of the parts are a combination of systematic biases and random fluctuations. Significant systematic biases are the calibration, resolution and linearity [9] of the apparatus. As for the random fluctuations, repeatability and reproducibility are contributors. Therefore, the uncertainty is modeled below,

$$u_W = \left[\left(\frac{x_{CAL}}{k}\right)^2 + \left(\frac{x_{RES}}{\sqrt{6}}\right)^2 + \left(\frac{x_{LIN}}{\sqrt{3}}\right)^2 + x_{SD}^2\right]^{\frac{1}{2}} \quad (9)$$

where the balance contributors are x_{CAL} (calibration); x_{RES} (resolution); x_{LIN} (linearity); and x_{SD} (sample standard deviation).

Density of Water

Computing the standard uncertainty for the water density is performed via the principles of the GUM. Per the GUM, the standard uncertainty is calculated below as

$$u_{\rho W} = \left[\left(c_{T_W} \cdot u_{T_W}\right)^2 + \left(c_B \cdot u_B\right)^2\right]^{\frac{1}{2}} \quad (10)$$

where the sensitivity coefficients are calculated in the Appendix. The associated uncertainties for the water temperature and barometric pressure are determined in Eq. 11,

$$u_{T_W} = \left[\left(\frac{\Delta T_W}{\sqrt{6}}\right)^2 + \left(\frac{U_{95}(T_{W_{Sensor}})}{2}\right)^2\right]^{\frac{1}{2}}$$
$$u_B = \left[\left(\frac{TOL_B}{\sqrt{3}}\right)^2 + \left(\frac{U_{95}(B_{Sensor})}{2}\right)^2\right]^{\frac{1}{2}} \quad (11).$$

Density of Air

Similarly, the standard uncertainty of air is calculated as follows,

$$u_{\rho_A} = \left[(c_B \cdot u_B)^2 + (c_{RH} \cdot u_{RH})^2 + \left(c_{T_A} \cdot u_{T_A}\right)^2\right]^{\frac{1}{2}} \quad (12)$$

where the sensitivity coefficients are calculated in the Appendix. The associated uncertainties for the water temperature and barometric pressure are determined in Eq. 13,

$$u_B = \left[\left(\frac{TOL_B}{\sqrt{3}}\right)^2 + \left(\frac{U_{95}(B_{Sensor})}{2}\right)^2\right]^{\frac{1}{2}}$$
$$u_{RH} = \left[\left(\frac{TOL_{RH}}{\sqrt{3}}\right)^2 + \left(\frac{U_{95}(RH_{Sensor})}{2}\right)^2\right]^{\frac{1}{2}} \quad (13).$$
$$u_{T_A} = \left[\left(\frac{\Delta T_A}{\sqrt{2}}\right)^2 + \left(\frac{U_{95}(T_{A_{Sensor}})}{2}\right)^2\right]^{\frac{1}{2}}$$

EXAMPLE: SURROGATE PART

The following example is an application of determining the measurement uncertainty associated with the density determination of a surrogate part. This example is taken from the original report [1] but revised with the new derived formulae. Suppose the part is repeatedly weighed three times, in water and in air, where the average values (and spreads) are $W_W = 1065.150 \pm 0.001\ g$ and $W_A = 1124.050 \pm 0.001\ g$. As for the systematic errors associated

with the mass-balance, it is assumed that the mass balance used provides very accurate and precise results. For this mass balance, the following values are taken from the calibration certificate: $x_{cal} = 5 \times 10^{-5} g$ (at 95%, so $k = 2$), $x_{res} = 0.0001\ g$ and $x_{linear} = 0.0005\ g$. Substituting the values into Eq. 9 and calculating the uncertainties yields,

$$u_{W_W} = 0.001\ g$$
$$u_{W_A} = 0.001\ g \quad (14).$$

Next, the density of the part in both water and air are calculated. For these calculations, the environmental parameters used are $T_A = 20$℃, $T_W = 19.88$℃, $B = 586.74\ mmHg$, and $RH = 20\%$. For the sensitivity coefficients associated with the density of water, substituting in the values in Eq. A-1, one gets

$$c_{T_W} = -2.0503 \times 10^{-4}\ g/(cm^3 \cdot ℃)$$
$$c_B = -1.0782 \times 10^{-10}\ g/(cm^3 \cdot mmHg) \quad (15).$$

Assuming that $\Delta T_W = 0.5$℃, $U_{95}(T_{W_{Sensor}}) = 0.10$℃, $TOL_B = 72.6\ mmHg$, $U_{95}(B_{Sensor}) = 0.15\ mmHg$, the results from Eq. 15 and computing the value for Eq. 7, the density of water and it's uncertainty is determined to be

$$\rho_W = (0.9983 + 4.309 \times 10^{-5})\ g/cm^3 \quad (16).$$

Similarly, the sensitivity coefficients for the density of air, substituting the given parameters in Eq. B-1, one gets

$$c_B = 0.0016\ g/(cm^3 \cdot mmHg)$$
$$c_{RH} = -0.0001\ g/cm^3$$
$$c_{T_A} = -0.0032\ g/(cm^3 \cdot ℃) \quad (17).$$

Assuming that $TOL_{RH} = 0.05$, $U_{95}(RH_{Sensor}) = 0.01$, $\Delta T_A = 1$℃ , $U_{95}(T_{A_{Sensor}}) = 0.25$℃, the results from Eq. 17 and computing the value for Eq. 8, the density of air and it's uncertainty

$$\rho_A = (9.3 \times 10^{-4} + 6.7 \times 10^{-5})\ g/cm^3 \quad (18).$$

With the necessary values determined for the surrogate part density, first the sensitivity coefficients associated with the standard uncertainty of the surrogate part are determined using Eq. 4 where

$$c_{W_A} = -0.3062\ cm^{-3}$$
$$c_{\rho_W} = 19.0844\ (unitless)$$
$$c_{W_W} = 0.3231\ cm^{-3}$$
$$c_{\rho_A} = -18.0844\ (unitless) \quad (19).$$

Substitution of these values into Eq. 3 yield a standard uncertainty of $\pm 0.0015\ g/cm^3$, however, the *total expanded uncertainty* (measurement process uncertainty was $\pm 0.0020\ g/cm^3$) was caluated using Eq. 5

$$U_T = 0.005\ g/cm^2 \quad (20).$$

Finally, calculation of the surrogate part density (Eq. 2) and it's uncertainty yields

$$\rho_O = (19.034 \pm 0.005)\ g/cm^2 \quad (21).$$

The original example uncertainty was determined to be $\pm 0.445\ g/cm^3$, which is abnormaly larger than the new result. Two major reasons for this are, first the sensitivity coefficients in the original report were calculated using *total* derivatives instead of *partial*. This in turn allows the various influence quantities to vary *simultaneously* and not *individually*, thus the potential for double counting. Secondly, all the standard uncertainties calculated in the original report were assumed to vary normally at 1σ.

CONCLUSION AND FUTURE WORK

Application of the principles recommended by the GUM was performed on the governing measurement models used for the density determination via hydrostatic weighing. An original example was re-evaluated to determine the measurement uncertainty and compared to the original result where there was a significant difference in the results.

ACKNOWLEDGEMENTS

The authors would like to thank Los Alamos National Laboratory (LANL) for funding this research as well as the National Nuclear Security Administration (NNSA).

REFERENCES

[1] M. G. Martinez, "Uncertainty for Part Density Determination," LANL, Los Alamos, 2001.

[2] BIPM, "JCGM 100:2008 - Evaluation of Measurement Data - Guide to the Expression of Uncertainty in Measurement," BIPM, Paris, 2008.

[3] H. A. Bowman, R. M. Schoover and M. W. Jones, "Procedure for High Precision Density Determination by Hydrostatic Weighing," *Journal of Research of the National Bureau of Standards - C. Engineering and Instrumentation,* vol. 71C, no. 3, pp. 179-198, 1967.

[4] F. E. Jones, "The Air Density Equation and the Transfer of the Mass Unit," Journal of Research of the National Bureau of Standards, vol. 83, no. 5, pp. 419-428, 1978.

[5] F. E. Jones and R. M. Schoonover, Handbook of Mass Measurement, 1st ed., Boca Raton: CRC Press, 2002.

[6] T. M. Adams, "G104 - A2LA Guide for Estimation of Measurement Uncertainty in Testing," American Association for Laboratory Accreditation, Frederick, 2002.

[7] A. C. Y. and M. C. J., Fluid Mechanics: Fundamentals and Applications, 2nd ed., McGraw-Hill Higher Education, 2006.

[8] L. M. Valdez, M. O. Valdez and N. T. Ortiz, "Denisty Analysis Cart," LANL, Los Alamos, 2006.

[9] "Basic Mass Metrology Reference Notebook," NIST, Gaithersburg, 2003.

APPENDICES: SENSITIVY COEFFICIENTS

A. Density of Water

$$\frac{\partial \rho_W}{\partial T_W} = \frac{63.4849T_W^3 + 15406.4T_W^2 + 1.2153 \times 10^6 T_W - 5.0932 \times 10^6}{(B - 1.6155 \times 10^7)(T_W + 68.1296)^2}$$

$$\frac{\partial \rho_W}{\partial B} = -\frac{1.2163 \times 10^{-13}[(T_W - 3.9863)^2(T_W + 288.941)]}{(1 - 6.19 \times 10^{-8}B)^2(T_W + 68.1296)} \quad \text{(A-1)}$$

B. Density of Air

$$\frac{\partial \rho_A}{\partial B} = \frac{0.4646}{T_A + 273.16}$$

$$\frac{\partial \rho_A}{\partial RH} = \frac{0.0206 - 0.0025T_A}{T_A + 273.16} \quad \text{(B-1)}$$

$$\frac{\partial \rho_A}{\partial T_A} = -\frac{(0.4646B + 0.7089RH)}{(T_A + 273.16)^2}$$

THE NEXT GENERATION HETERODYNE INTERFEROMETRIC GRATING ENCODER SYSTEM FOR MULTI-DIMENSIONAL DISPLACEMENT MEASUREMENT OF A WAFER STAGE

Lei J. Wang[1], Ming Zhang[1*], Yu Zhu[1], Wei N. Ye[1], Si Q. Ding[2], Z. Jia[2], Y. Xia[3]

1. State Key Laboratory of Tribology & Beijing Key Lab of Precision/Ultra-precision Manufacturing Equipments and Control, Department of Mechanical Engineering, Tsinghua University, Beijing, 100084, China

2. Beijing U-precision Tech Co., Ltd, Beijing, 100084, China

3. School of Mechatronics Engineering, University of Electronic Science and Technology, Chengdu 611731, China

INTRODUCTION

A wafer stage is an essential part for a lithography tool to ultra-precisely pattern integrated circuit on a wafer with high efficiency. In the past, multi-axis heterodyne plane-mirror interferometer system was used for the ultra-precision displacement measurement of the wafer stage. However, as the semiconductor process is scaling down continuously, the accuracy enhancement of this system is becoming more and more difficult to satisfy the requirement of the wafer stage due to its high environmental sensitivity. Hence, an interferometric grating encoder with high environmental robustness is more favorable to meet the ever-increasing measurement requirement of a wafer stage in non-vacuum environment [1].

A grating encoder should satisfy several basic requirements to be applied to a wafer stage. Firstly, in order to feedback the position of stepping/scanning and focus adjusting movement of a wafer stage, a grating encoder should at least simultaneously measure a long stroke with hundreds of millimeters along the in-plane direction (X or Y) and a short stroke with several millimeters along the out-of-plane direction (Z). Moreover, the measuring repeatability along the in-plane and out-of-plane should reach to sub-nanometer level and nanometer level, respectively. Secondly, the rotated/tipped/tilted tolerances (△Rx/△Ry/△Rz) of grating encoder should reach to several micro-radians to satisfy the requirement of level adjustment of the wafer stage. Thirdly, the measurement velocity should be achieved to several meters per second. Finally, the read-head of grating encoder should be as small and light as possible to be mounted on the wafer stage.

Former work of interferometry based grating encoders which could simultaneously measure multi-dimensional displacements have been demonstrated [2-5]. Nevertheless, partial proposed encoders couldn't satisfy all the basic requirements, which limit the application in the wafer stage [2-4].In this abstract, the next generation heterodyne interferometric grating encoder system which is very suitable for the wafer stage is introduced.

PRINCIPLE

Figure 1 shows the schematic diagram of the proposed heterodyne interferometric grating encoder system. The system is mainly made up of single-frequency laser module, acoustic-optical modulator module, fiber module, read head module, scale grating and phase meter module. Next, we will describe the design considerations of the system for the application in the wafer stage.

The basic way to simultaneously obtain the in-plane and out-of-plane motion for a grating encoder is to persist the Doppler shifting frequencies both along X and Z direction. As the Figure 1 illustrated, two double pass measurement beams with two different frequencies (f1 and f2) in Littrow condition separately interfere with two internal reference beams (f2 and f1) to form two heterodyne interference measurement signals. If there are relative displacements Δx in in-plane direction and Δz in out-plane direction between read head and grating, the phase changes of the two measurement beams casued by droppler frequency shifting can be written as:

$$\begin{cases} \Phi_{d1} = \dfrac{4\pi}{p}\Delta x + \dfrac{8\pi\cos\theta}{\lambda}\Delta z \\ \Phi_{d2} = -\dfrac{4\pi}{p}\Delta x + \dfrac{8\pi\cos\theta}{\lambda}\Delta z \end{cases}$$

As the two heterodyne singals are AC singals, the performance of anti-disturbance of the encoder is more stronger than that of homodyne signals.

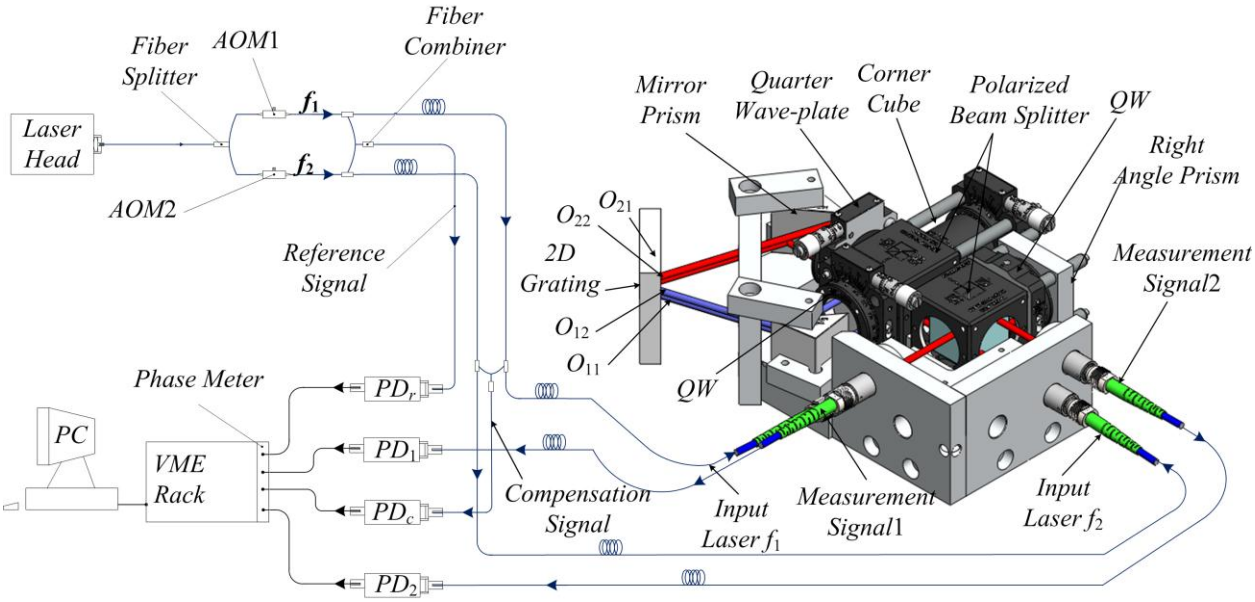

FIGURE 1. The Scheme diagram of principle system.

The two heterodyne singals containing two phase shifts subsenquently detected by a multi-axis heterodyne phase meter, and the signals can be expressed as below:

$$\begin{cases} I_{M1} \propto \cos\left(2\pi\left(f_2 - f_1\right)t - \left(\underbrace{\frac{4\pi}{p}\Delta x + \frac{8\pi\cos\theta}{\lambda}\Delta z}_{\Phi_1}\right)\right) \\ I_{M2} \propto \cos\left(2\pi\left(f_2 - f_1\right)t - \left(\underbrace{\frac{4\pi}{p}\Delta x - \frac{8\pi\cos\theta}{\lambda}\Delta z}_{\Phi_2}\right)\right) \end{cases}$$

Here, θ=arcsin(λ/2p) is the Littrow angle, p is the pitch of grating, and λ is the wavelength of dual-frequency laser beams.

A heterodyne phase meter is used to read out the phase shifts contained in a heterodyne measurement signals. A reference heterodyne singal is necessary for the work of the phase meter. In our system, a reference heterodyne signal is formed by spilting beams from two separated dual-frequency beams (f1 and f2) and combining them together to form co-axis interference in fibers, as illustrated in Figure 1.

As Φ1 and Φ2 could be read out by the phase meter, the displacement values of Δx and Δz can be simultaneously calculated as:

$$\begin{cases} \Delta x = \dfrac{p}{8\pi}\left(\Phi_1 + \Phi_2\right) \\ \Delta z = \dfrac{\lambda}{16\pi\cos\theta}\left(\Phi_1 - \Phi_2\right) \end{cases}.$$

The dual-frqency beams (f1 and f2) is the key point to obtain heterodyne signals. As the measurement velocity is restricted by the frequency difference between f1 and f2, the dual-frequency laser beams of our system are generated by two acoustic-optical modulators to satisfy the requirement of maximum velocity.

Due to the adoption of Littrow incidence, the proposed grating encoder is immune to the off-axis (Δz) deviation or the out-plane displacement. Moreover, a high grating diffractive efficiency in Littrow condition can also be gotten for our grating encoder.

A way to solve the problem of rotated/tipped/tilted sensitivity is to redirect a measurement beam twice by a corner cube between the read-head and the grating. As the input light is parallel to the output light for the conner cube, only beam walk-off produces between measurement and reference beam when the grating rotates/tips/tilts. The contribution to the signal strength of beam walk-off is much less than a beam angle between measurement and reference beam for a co-axis interference. In addition, a four times optical divisions can also be obtained with a twice redirection.

Periodic nonlinearity (PNL) is one of the main errors of a heterodyne type interferometer with a free space coaxis light. This error is caused by the polarization and frequency leakage of imperfect polarized optics. A solution to depress the periodic nonlinearity is to transmit the dual-frequency laser beams (f1 and f2) separately to

greatly reduce the nonideal leakage input to the photodetector [6]. In our system, the optical path is designed in this way to depress the PNL down to picometer level.

In our system, as only the readhead of our system is mounted on the wafer stage, both of the dual-frequency laser beams and optical heterodyne signals are transmited by fibers. The laser head radiates a single-frequency linear-polarized laser with high stability by a single-mode polarization maintaining fiber. As the diffractive efficiency of the 2D grating is very low, a high power laser head is needed, and the laser power is about fifty milliwatts. The dual-frequency laser beams are generated by two fiber-coupled acoustic-optical modulators and transmitted to the read-head by two single-mode polarization maintaining fibers, respectively. As a result, two spatial sperated linear-polarized beams with the frequency of f1 and f2 are transmitted to the readhead. In addition, the heterodyne signals are transmitted to the multi-axis phase-meter by multi-mode fibers. In this way, a flexible encoder system is formed. The main advantage of the flexible system is easy for fast module replacement. Another advantage is that the wavefront of the beam is smoothed compared with a free-space transmission beam, which helps depress the measurement error caused by wavefront distortion.

As all the fibers are fixed on a cable stage which synchronously moves with the wafer stage, the grating encoder system should be immune to the disturbance caused by high speed fiber motion. In our system, a compensation signal is also inserted to compensate the measurement error caused by high speed fiber motion. The compensation heterodyne signal is also formed by spilting beams from two separated dual-frequency beams (f1 and f2) and combining them together to form co-axis interference in fibers. In order to greatly depress the fiber disturbance, the fibers to form compensation signals is very near to the readhead. The phase compensation value is also read out by the heterodyne phase meter as the measurement signal, and then used in the dipalcement calculation equation to compensate the additional measurement error.

EXPERIMENT SETUP

Figure 2 shows the photograph of preliminary experiment setup. The setup consists of a PI six-DOF fine stage and the principle system. The wavelength of the laser is 785 nm and the diameter is 3mm. At present, a one-dimensional grating with a pitch of 833.3nm is used. Subsequently, a custom-built two-dimensional grating will be applied to the principle system. In the experiment setup, the grating is mounted on the motion part of the fine stage. The left part of the system together with stator of the fine stage are fixed on a optical bench. We operate seveal experiment to verify our grating encoder system based on this experiment setup in a conventional laboratory environment and vibration isolator.

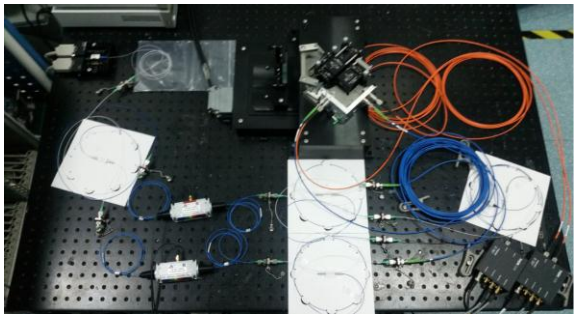

FIGURE 2. The Photograph of experiment setup.

RESULT

MEASUREMENT RESULT

We perform a measurement experiment based on the experiment setup to verify the measurement principle of the system. Figure 3 shows the measurement curve when the fine stage moves as a sine wave (50μm, 0.5Hz) along the X direction, a triangle wave (50μm, 0.5Hz) along the Z direction and an ellipse in in-plane (sine wave (50μm, 0.5Hz)) and out-of-plane (cosine wave (30μm, 0.5Hz)) displacement simultaneously. The measurement curve indicate that the measurement curve is nearly consistent with the motion of the Fine stage, which verifies the principle of grating encoder system.

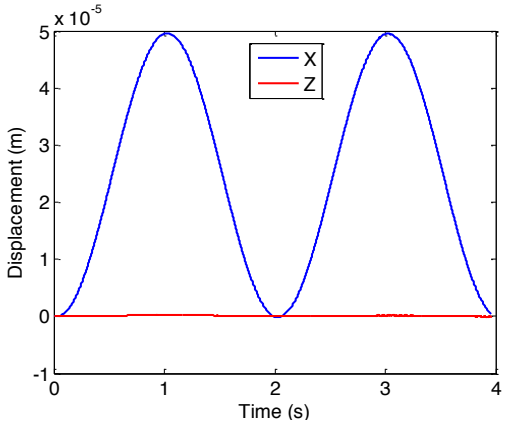

(a) Fine stage moves as a sine wave (50μm, 0.5Hz) along the X direction

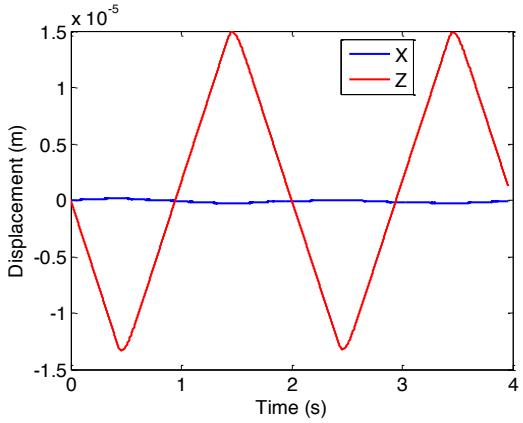

(b) Fine stage moves as a triangle wave (50μm, 0.5Hz) along the Z direction

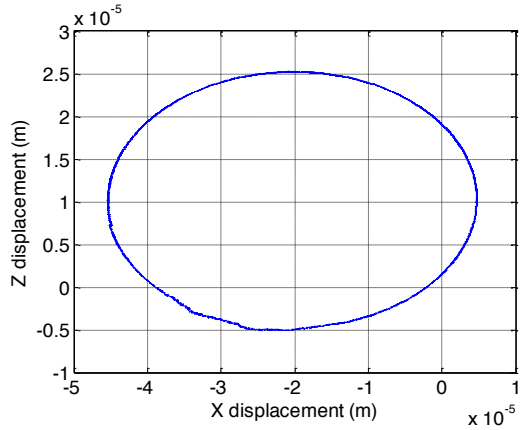

(c) Fine stage moves as an ellipse in in-plane (sine wave (50μm, 0.5Hz)) and out-of-plane (cosine wave (30μm, 0.5Hz)) displacement simultaneously

FGURE 3. The measurement curve of the proposed system.

INITIAL TOLERANCES DEMONSTRATION

We perform a tolerance demonstration experiment based on the experiment setup. In this experiment, the fine stage is operated to rotate along X/Y/Z direction and move along Z in a square wave. The rotation and motion amplitude of the square wave are 500μrad and 800μm. The two value are the largest rotation and motion stroke of the fine stage. Figure 5 shows the initial experimental result of the tolerances of principle system. The experiment results indicate that all the amplitudes of the AC signals change little, which demonstrates our system has large tolerance and large Z motion stroke. Next, we will upgrade the experiment setup to perform the experiment for demonstation of angle tolerances with several milliradians and Z motion stroke with several millimeters.

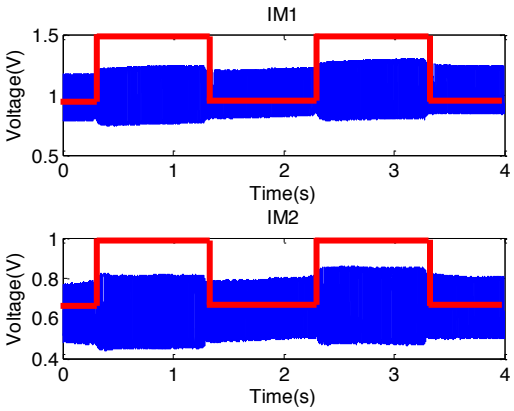

(a) *The signal intensity of the system when the grating rotates along* X direction in a square wave (500μrad)

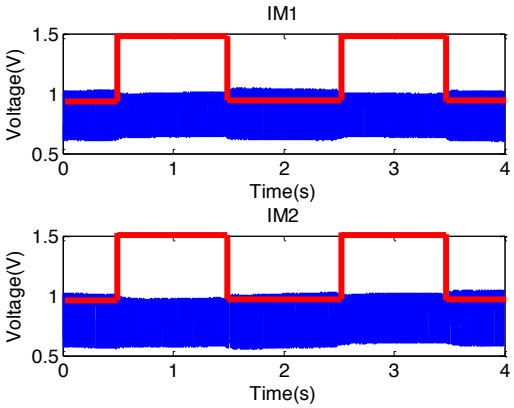

(b) *The signal intensity of the system when the grating rotates along* Y direction in a square wave (500μrad)

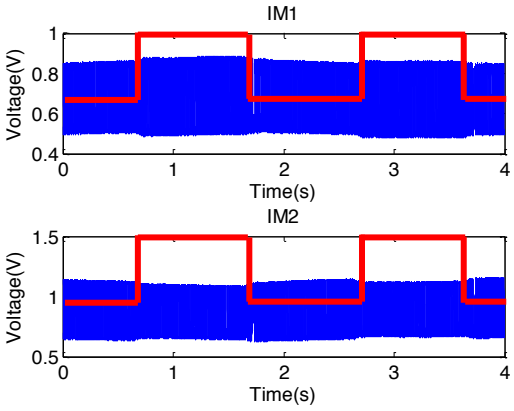

(c) *The signal intensity of the system when the grating rotates along* Z direction in a square wave (500μrad)

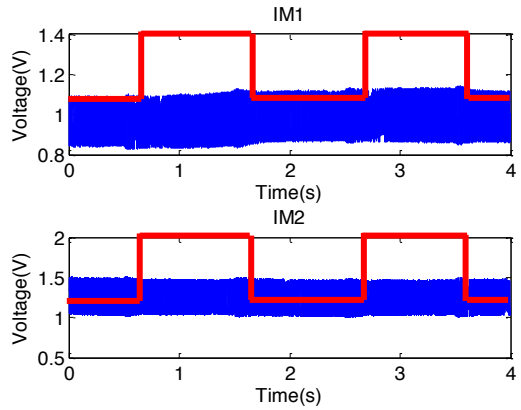

(d) *The signal intensity of the system when the grating moves along* Z direction in a square wave (800μm)

FGURE 4. The intial experimental signal intensity of the system when the grating rotates/tilts/tips with large tolerances and moves along Z direction with large stroke.

RESULT OF DYNAMIC FIBER DISTURBANCE COMPENSATION

We insert a high speed linear motion stage to the experiment setup to verify the compensation effect of the dynamic fiber disturbance. Figure 5 shows the photograph of fiber disturbance experiment setup. In this experiment, the fine stage is static, the fibers of the system is fixed on a high speed linear motion stage, and the linear motion stage moves back and forth at a maximum speed of 250mm/s. The measurement values and compensation value are acquired simultaneously with a 5KHz frequency. The acquired compensation value is used to correct the measurement values.

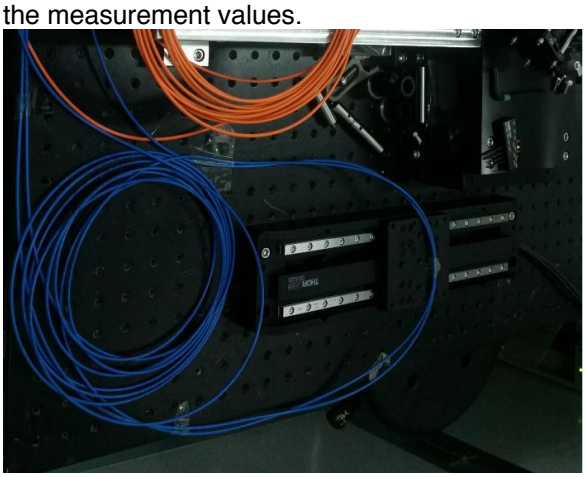

FIGURE 5. The Photograph of fiber disturbance experiment setup.

Figure 7(a) shows the experimental result of the measurement stability under compensation and uncompensation in time domain. As shown in the Figure 6 (a), the X Stability is greatly improved after compensation, which demonstrates the effectiveness of compensation. In addition, as the red line shown in the figure, due to the destructive effect of the displacement calculation, the Z stability is insensitivity to fiber disturbance.

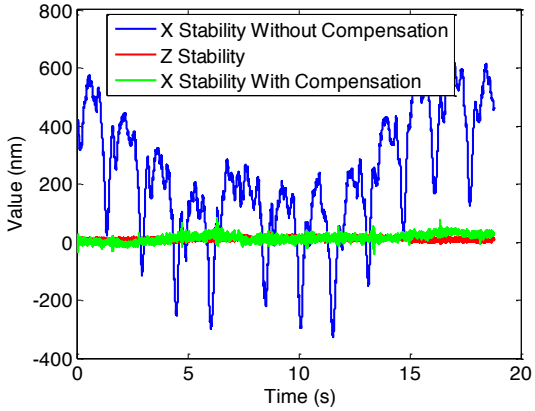

(a) Time Domain

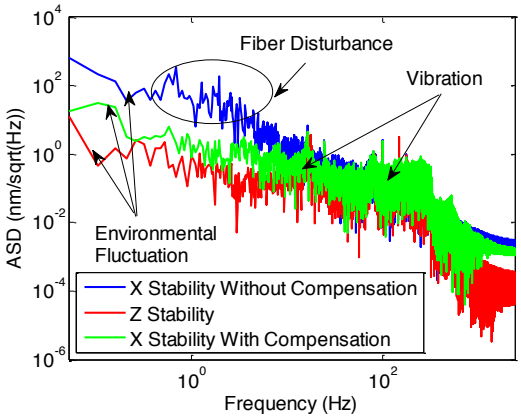

(b) Frequency Domain

FIGURE 6. Experimental result of measurement stability under compensation and uncompensation.

As vibration and environmental fluctuation also lead to measurement unstabiltiy, we aslo give the result in frequency domain to identify the residual compensation error. Figure 6 (b) shows the ASD (Amplitude Spectral Density) of Figure 6 (a). According the figure, the measurement unstability casued by fiber disturbance is basically eliminated, the left measurement unstability is mainly caused by vibration and environmental fluctuation. Next, we will upgrade the vibration isolator and environmental to improve the measurement stability.

INTEGRATED READ HEAD

In order to mount the small enough read head on the wafer stage, based on the principle system, we are now fabricating an integerated read head. In the integrated read head, all the optical parts are bonded together as a monolith by optical bonding technology to greatly reduce the size and mass of the read-head.

We will give more results of the grating encoder system in the following research, and we will keep on report the progress of the next generation heterodyne grating encoder and its application for a wafer stage in China.

ACKNOWLEDGE
This work was supported by the China Postdoctoral Science Foundation (No. 2017M610885)

REFERENCES

[1] Jong F, Pasch B, Castenmiller T, et al. Enabling the lithography roadmap: an immersion tool based on a Novel Stage Positioning System. Proc. SPIE. 2009; 7274: 72741S-1-72741S-10.
[2] Kimura A, Gao W, Arai Y, et al. Design and construction of a two-degree-of-freedom linear encoder for nanometric measurement of stage position and straightness. Precision Engineering. 2010; 34: 145-155.
[3] Guan J, Köchert P, Weichert C, et al. A high performance one-dimensional homodyne encoder and the proof of principle of a novel two-dimensional homodyne encoder. Precision Engineering. 2013; 37: 865-871.
[4] Wang L., Zhang M, Zhu Y. et al., A novel heterodyne grating interferometer system for in-plane and out-of-plane displacement measurement with nanometer resolution. In 29th Annual Meeting of the American Society for Precision Engineering, Proc. ASPE Annual Meeting ASPE. 2014.
[5] de Groot P, Badami V and Liesener J. Concepts and geometries for the next generation of precision heterodyne optical encoders. In 31th Annual Meeting of the American Society for Precision Engineering, Proc. ASPE Annual Meeting ASPE. 2016.
[6] Meskers A, Ellis J, Spronck J, et al. Fiber coupled sub nanometer displacement interferometry without periodic nonlinearity. In 10th International Symposium of Measurement Technology and Intelligent Instruments, 2011.

GEOMETRIC ERROR MEASUREMENT AND COMPENSATION OF A ROTARY TABLE USING A CIRCULAR BALL PLATE ARTIFACT

Qichang Wang, Gert Goch
Center for Precision Metrology
University of North Carolina at Charlotte
Charlotte, NC, United States

1. INTRODUCTION

In industrial scale inspection processes of gears and bearings, rotary tables in coordinate measuring machines (CMM) and gear measuring instruments (GMI) play a critical role in saving measuring time. They also improve the accessibility to the measuring object like involute gear flanks, while simplifying the probing styli geometry.

Although the benefits are undoubtable, a rotary table has six error motions [Fig. 1]. Each one consists of synchronous and asynchronous error motions. The synchronous error motion represents the portion of total error motion that occurs at integer multiples of the rotation frequency. The asynchronous error motion consists of the periodic portion of total error motion that occurs at frequencies other than integer multiples of the rotation frequency, as well as the non-periodic portion [1].

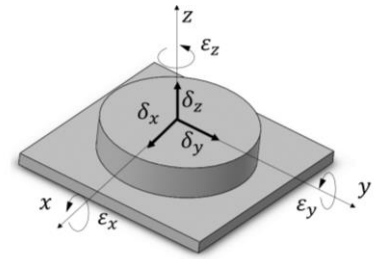

δ_x radial error motion along x-axis
δ_y radial error motion along y-axis
δ_z axial error motion along z-axis
ε_x tilt error motion about x-axis
ε_y tilt error motion about y-axis
ε_z angular positioning error about z-axis

FIGURE 1. Rotary table error motions

The performance of a GMI or a 4−axis CMM is limited by the uncalibrated and uncompensated axial, radial and tilt error motions of a rotary table. Several methods were proposed to calibrate rotary axes in five axis machining tools. Suh [2] used two autocollimators, a master ball and 3 LVDTs to measure six error motions. Lei [3] inspected the radial error motion with a double ballbar (DBB). Zhang [4] applied a DBB to calibrate the radial, axial and tilt error motions. However, these methods are either inconvenient or not suitable for the calibration of high precision rotary tables. An alternative is using a circular ball plate artifact as the measuring object [5].

This paper provides a complete deviation mapping solution to reduce the measurement uncertainty of GMI and 4-axis CMM. Numerical simulations were conducted to verify the introduced solution based on a developed mathematical model.

The measurement procedure and data processing method are presented in Sections 2 and 3. The mathematical model and numerical simulation are discussed in Sections 4 and 5.

2. MEASUREMENT PROCEDURE

While this paper focuses on numerical simulation, the measurement procedure is briefly discussed for illustration purpose.

A circular ball plate artifact was selected as the measuring object. On the base plate, $N = 12$ high precision spheres were evenly distributed in a circular pattern [Fig. 2]. The ball plate was centered on the rotary table. Then, the rotary table was calibrated at M rotary positions in each cycle, where M was a multiple of N. At every angular step ($360°/M$), multiple points were probed on the upper hemisphere of each sphere.

FIGURE 2. Circulate ball plate artifact made by Hexagon Manufacturing Intelligence with 6 ceramic spheres and 6 tungsten carbide spheres.

3. DATA PROCESSING

The proposed solution adopted the multiple measuring technique and least squares approximation technique to achieve low measurement uncertainty. The principle of deviation separation is explained in Sections 3.2 − 3.4. Approximation technique is introduced in Section 3.5 to determine the error motions.

3.1 Workpiece coordinate system

A workpiece coordinate system (WCS) was built at the initial rotary position. Firstly, each sphere center point was determined with multiple probing points. Then, a circle and a plane were approximated to the sphere center points. The circle center was defined as the origin O_w of WCS. The $+x$ direction was set from the origin to the 1^{st} sphere center point. The $+z$ direction was defined along the normal direction of the plane (away from the artifact).

3.2 Angular positioning deviation

The angular positioning deviation ε_z was determined by applying the three-rosette method invented by Physikalisch-Technische Bundesanstalt (PTB) [7]. ε_z was separated from the angular deviations of the CMM and spheres on the artifact in the Cylindrical CS. Günther [6] tested and verified this method by calibrating a ball plate. The angular deviations of the CMM $\Delta\tau_{m(k)}$ were firstly calculated and compensated, as shown on the left side of Eqn. 1. The subscript k was determined by i and j, which referred to the j^{th} sphere and i^{th} rotary position respectively. Then, at the i^{th} rotary position, the mean value of the residual angular deviations was taken as $\varepsilon_{z(i)}$, because the angular deviations of *N* spheres sum up to zero according to the closure theory (Eqn. 2).

$$\frac{1}{N}\sum_{j=1}^{N}\Delta\tau_{(i,j)} - \frac{1}{N}\sum_{k=1}^{N}\Delta\tau_{m(k)} = \frac{1}{N}\sum_{j=1}^{N}\Delta\varphi_{(j)} + \varepsilon_{z(i)} + residual \quad (1)$$

where

$$\sum_{j=1}^{N}\Delta\varphi_{(j)} = 0 \quad (2)$$

3.3 Translational error motions

A rotary table performs two translational error motions δ_x and δ_y in the XY plane. Therefore, it is impossible to determine both error motions by applying the three-rosette method in the radial direction in the Cylindrical CS.

An alternative is tracking the 3-D path of artifact center, which records the translational error motions. The 3-D paths were investigated in the x, y and z directions independently (Eqn. 3, 4 and 7). The right sides of Eqn. 3 and 4 consist of three parts. The first parts contain eccentricity information. Eccentricity is defined by the distance between the artifact center and z reference axis (axis average line) along x- and y-axes, represented by H_x and H_y. θ refers to the angular position of rotary table. The second parts consist of the synchronous and periodic asynchronous error motions at the i^{th} rotary position. The third parts are residuals, which include the non-periodic asynchronous error motion and deviations from the measuring system.

$$\Delta x_{(i)} = R_q cos(\eta + \theta) + \delta_{x(i)} + residual \quad (3)$$

$$\Delta y_{(i)} = R_q sin(\eta + \theta) + \delta_{y(i)} + residual \quad (4)$$

where

$$R_q = \sqrt{H_x^2 + H_y^2} \quad (5)$$

$$\eta = tan^{-1}\left(\frac{H_y}{H_x}\right) \quad (6)$$

The vertical path of the artifact center reflects the axial error motion δ_z.

$$\Delta z_{(i)} = \delta_z + residual \quad (7)$$

3.4 Tilt error motions

To determine the tilt error motions $\varepsilon_{x(i)}$ and $\varepsilon_{y(i)}$ at the i^{th} rotary position, a plane was approximated to all the sphere center points. It should be noted that the artifact also has constant tilt deviations ε_{Ax} and ε_{Ay} with respect to the z reference line. In one cycle, the vector $[\varepsilon_{Ay}; -\varepsilon_{Ax}; 1]$ describes a cone. Therefore, the determined surface normals consisted of three parts: tilt deviations of the artifact, tilt error motions and residuals (Eqn. 8).

$$\overrightarrow{n_{(i)}} = \begin{bmatrix} cos\theta_{(i)} & -sin\theta_{(i)} & 0 \\ sin\theta_{(i)} & cos\theta_{(i)} & 0 \\ 0 & 0 & 1 \end{bmatrix}\begin{bmatrix} \varepsilon_{Ay} \\ -\varepsilon_{Ax} \\ 1 \end{bmatrix} + \begin{bmatrix} \varepsilon_{y(i)} \\ -\varepsilon_{x(i)} \\ 1 \end{bmatrix} + \begin{bmatrix} residual \\ residual \\ 1 \end{bmatrix} \quad (8)$$

3.5 Approximation technique

Approximation technique was introduced to solve 3 problems at once: determining the nontrivial unknown constants in Eqn. 3, 4 and 8; generating a deviation map; minimizing the residuals resulting from the probing system, CMM guideways, etc.

Trigonometric polynomials (Eqn. 9) [10] were

approximated to the data on the left sides of Eqn. 1, 3, 4, 7 and 8.

$$poly = \sum_{m=1}^{N}[a_{m.c}cos(m\theta) + a_{m.s}sin(m\theta)] \quad (9)$$

For Eqn. 3, 4 and 8, the $m = 1$ terms offered the H_x, H_y, ε_{Ax} and ε_{Ay}, while $m = 2, \dots, N$ terms represented δ_x, δ_y. ε_x and ε_y respectively. For Eqn. 1 and 7, $m = 1, \dots, N$ terms represented δ_z and ε_z.

4. MATHMATICAL MODEL

To verify the introduced data processing method in numerical simulations, a simplified mathematical model (Fig. 3 and Eqn. 10) was developed based on the rigid body assumption. The parameters are explained in Table 1.

$$R_{CF}\left([H_W]_C + R_{WC}[S_{(j)}]_W\right) + [\Delta C_{(i)}]_F + [T_C]_F + [\Delta P_{m(k)}]_F + [\Delta P_{n(i,j)}]_F + [\Delta P_{p(i,j)}]_F = [P_{m(i,j)}]_F \quad (10)$$

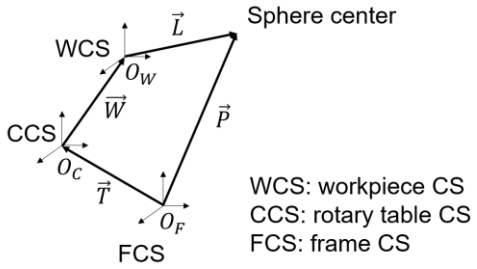

FIGURE 3. Mathematical vector model

TABLE 1. Parameter description

$[S_j]_W$	Position of the j^{th} sphere in the WCS
R_{WC}	Rotation matrix form the WCS to the FCS
$[H_W]_C$	Position of O_W in the CCS
$[\Delta C_i]_F$	Translational error motions at the i^{th} rotary position in the FCS
$[T_C]_F$	Position of O_C in the FCS
R_{CF}	Rotation matrix from the CCS to the FCS
$\Delta P_{p(i,j)}$	Non-repeatable deviation between the actual and approximated center point of the j^{th} sphere at the i^{th} rotary position
$\Delta P_{n(i,j)}$	Non-repeatable deviation of length measurement from the artifact center to the j^{th} sphere at the i^{th} rotary position
$\Delta P_{m(k)}$	Systematic deviation of probing system and CMM guideways at the k^{th} measuring position

The deviations of the probing system and CMM guideways were simplified into three terms – $\Delta P_{p(i,j)}$, $\Delta P_{n(i,j)}$ and $\Delta P_{m(k)}$.

$\Delta P_{p(i,j)}$ represents the non-repeatable deviation between the actual and the approximated center point of the j^{th} sphere at the i^{th} rotary position. This deviation originates from the non-repeatable probing deviations in the radial direction of a sphere, following Gaussian distribution within $[\ -P_{FTU,MPE}/2\ ,\ P_{FTU,MPE}/2\ ]$. $P_{FTU,MPE}$ is the maximum permissible single-stylus form deviation of the measuring system [8].

$\Delta P_{n(i,j)}$ represents the non-repeatable deviation of length measurement from the artifact center to sphere center point, following Gaussian distribution within $[-R_{0,MPL}/2,\ R_{0,MPL}/2]$. $R_{0,MPL}$ is the maximum permissible limit of the repeatability range [9].

$\Delta P_{m(k)}$ represents the total systematic deviation of probing system and CMM guideways at the k^{th} measuring position. In the calibration, $M \times N$ sphere center points locate near *M* ideal measuring positions. If the CMM has been deviation mapped, $\Delta P_{m(k)}$ represents the residuals of systematic deviations after deviation mapping. In either case, it is reasonable to regard $\Delta P_{m(k)}$ as a constant, because the deviations of *N* sphere center points at one measuring position is below 1.0 mm. $\Delta P_{m(k)}$ is a random value within $0.5 \times \left[-E_{L,MPE} + R_{0,MPL}, E_{L,MPE} - R_{0,MPL}\right]$. $E_{L,MPE}$ represents the maximum permissible deviation of length measurement [9] from the artifact center to the sphere center point.

5. NUMERICAL SIMULATION

Numerical simulations were performed based on the introduced mathematical model. Most parameters were picked to monitor the real measurement setup.

TABLE 2. Input values of some parameters

CMM	$P_{FTU,MPE}$	$0.80\mu m$
	$R_{0,MPL}$	$0.60\mu m$
	$E_{L,MPE}$	$(1.2 + L/500)\mu m$
Artifact	N	12
	R_{s0}	$200.0mm$
	H_x	$24.000\mu m$
	H_y	$-18.000\mu m$
	ε_{Ax}	$-0.54''$
	ε_{Ay}	$3.83''$
Rotary table	M	$4 \times 12 = 48$

5.1 Simulation input

Some parameters are listed in Table 2. The artifact had 12 spheres and the rotary table was calibrated in 48 angular positions at each cycle. R_{s0} was the nominal distance from the artifact center to sphere center. The radial, axial and tangential deviations of spheres were within $[-20\mu m, +20\mu m]$. Systematic error motions can be found in Figures 5 to 7. The magnitude of non-periodic deviations were around 10% of the corresponding maximum systematic deviations.

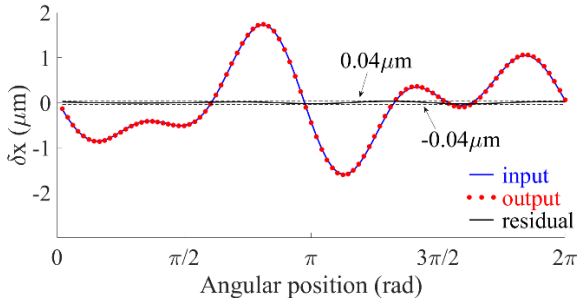

(a) δ_x

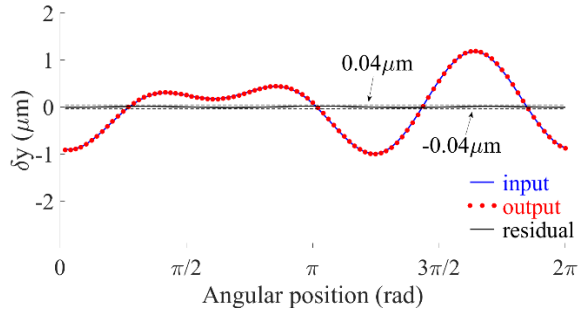

(b) δ_y

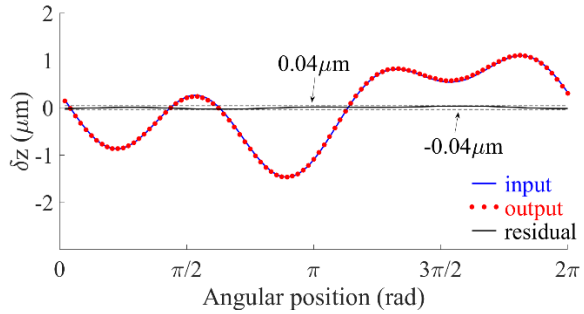

(c) δ_z

FIGURE 5. Simulation results for translational error motions δ_x , δ_y and δ_z with maximum deviations less than $0.04\mu m$.

5.2 Simulation results

Figures 5 to 7 demonstrate that the simulation outputs matched the corresponding inputs. The maximum residuals were not larger than $0.04\mu m$ for the translational error motions and 0.03" for the tilt and angular positioning error motions. These results indicate that the proposed method can not only perform ultra-high accurate calibration at sampled rotary positions, but also enables a precise prediction for the remaining rotary positions.

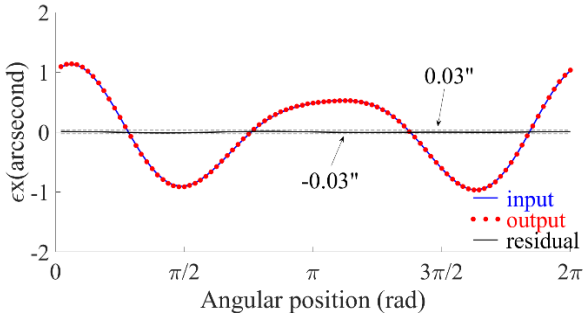

(a) ε_x

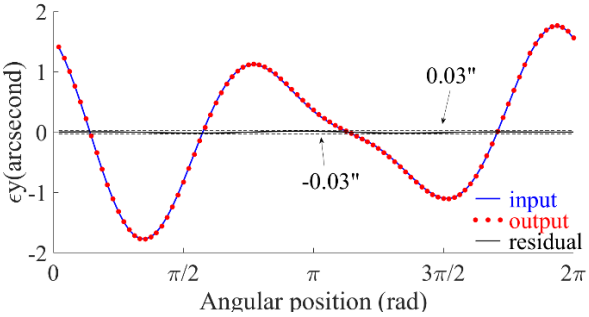

(b) ε_y

FIGURE 6. Simulation results for tilt error motions ε_x and ε_y with maximum deviations less than 0.03".

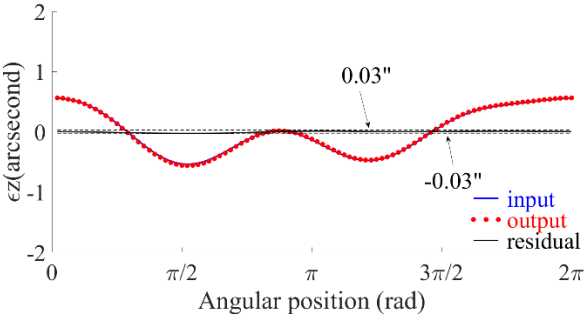

FIGURE 7. Simulation results for angular positioning deviation ε_z with maximum deviation less than 0.03".

5.3 Discussion

The proposed method solved one critical challenge, which was minimizing the residual deviations resulting from deviation sources like probing system and CMM carriages. This goal was achieved by applying three levels of least squares approximation to calculate the sphere

center points, artifact center and the error motions of an entire rotation.

The second challenge was handling the uncalibrated non-ideal artifact properly. While providing multiple highly repeatable reference points, the spheres typically still have radial, axial and tangential deviations in the low two-digit micrometers range, even for a well-made artifact. Moreover, because of imperfect fabrication, assembly and clamping, the artifact typically has tilt deviations ε_{Ax} and ε_{Ay} in the one-digit arcseconds range. In addition, since the artifact center is invisible, two-digit micrometers range eccentricities H_x and H_y typically exist even with careful alignment.

Because this measurement setup contains a considerable number of deviations, the traditional reversal techniques cannot separate the H_x, H_y ε_{Ax} and ε_{Ay} with sufficiently low uncertainty, which is critical when the magnitudes of error motions are in a low micrometer and arcsecond range. The applied least squares approximations successfully separated the tilt and eccentricity of artifact, as shown in Tables 3 and 4. It also further improves the accuracy of ε_z, since the three-rosette method only takes the mean value of multiple measurement at one angular position.

TABLE 3. Eccentricity of the artifact

	input	output	residual
H_x	$24.000\,\mu m$	$23.996\,\mu m$	$-0.004\,\mu m$
H_y	$-18.000\,\mu m$	$-17.992\,\mu m$	$0.008\,\mu m$

TABLE 4. Tilt deviations of the artifact

	input	output	residual
ε_{Ax}	1.023"	1.017"	−0.006"
ε_{Ay}	6.460"	6.461"	0.001"

6. SUMMARY

This paper presents a complete deviation mapping solution to measure and compensate the error motions of a rotary table. It can help GMI and 4-axis CMM manufacturers and users to improve the measurement accuracy of the entire system. Numerical simulations successfully verified the proposed solution, based on a mathematical model.

7. ACKNOWLEDGEMENT

The authors gratefully acknowledge the financial support by the Center for Precision Metrology and its affiliated companies. A special thank goes to Dr. Jimmie Miller for his insightful discussions on the mathematical model.

8. REFERENCES

[1] ISO 230-7:2006(E). Test code for machine tools: Geometric accuracy of axes of rotation.

[2] Suh SH, Lee ES, Jung SY. Error modelling and measurement for the rotary table of five-axis machine tools. The International Journal of Advanced Manufacturing Technology. 1998 Sep 1;14(9):656-663.

[3] Lei WT, Sung MP, Liu WL, Chuang YC. Double ballbar test for the rotary axes of five-axis CNC machine tools. International Journal of Machine Tools and Manufacture. 2007 Feb 28;47(2):273-285.

[4] Zhang Y, Yang J, Zhang K. Geometric error measurement and compensation for the rotary table of five-axis machine tool with double ballbar. The International Journal of Advanced Manufacturing Technology. 2013 Mar 1:1-7.

[5] Kunzmann H, Schepperle K, Trieb G, Waldele F, (inventors); Carl-Zeiss-Stiftung, (assignee). Method of measuring rotary-table deviations. United States patent US 4,819,339. 1989 Apr 11.

[6] Guenther A, Stöbener D, Goch G. Self-calibration method for a ball plate artefact on a CMM. CIRP Annals-Manufacturing Technology. 2016; 65(1):503-506.

[7] Kniel K, Härtig F, Osawa S, Sato O. Two highly accurate methods for pitch calibration. Measurement Science and Technology. 2009; 20(11):115110.

[8] ISO 10360-5:2010(E). Acceptance and reverification tests for coordinate measuring machines: CMMs using single and multiple stylus contacting probing systems.

[9] ISO 10360-2:2009(E). Acceptance and reverification tests for coordinate measuring machines: CMMs used for measuring linear dimension

[10] Miller J. Two-dimensional matrix-based non-complex axis-of-rotation error modeling. Precision Engineering. 2016; 44:93-108.

Reference Metrology System for Compensation of Level Control in Precision Stage System

Siwoong Woo, Sang-Hyun Park
Mechatronics R&D Center
Samsung Electronics Co. Ltd.
Republic of Korea

INSTRUCTIONS

In the precision stage system, passive isolators are commonly used to attenuate high frequency vibration from floor to the stage and keep the stage's level [1]. For the level control, height of the passive isolators is measured and used as feedback signal. Assumption here is that the floor is infinitely rigid, and experiences no deformation. In reality, however, mass center of the stage keeps moving around, and causes the floor to get deformed more or less depending on its structural stiffness. In this practical condition, the stage system gets inclined even though its level is relatively controlled based on the control mentioned above. Unbalanced stage motion leads to pitching or rolling of its tool position resulting in unsatisfactory repeatability.

To address this problem, the floor deformation has to be measured and compensated to maintain the level of a stage system. Reference Metrology System (RMS) consists of sensor(s), a controller and a set of passive isolators. The sensor measures rotational errors (θx and θy) of the stage caused by the floor deformation, and the controller calculates input signals for each passive isolator to compensate the measured rotational errors. Passive isolators then generate the calculated force and attempt to maintain the level of the stage system.

In this paper, we will propose RMS as a solution for absolute level control of precision stage systems, carry out its design, and simulate its performance.

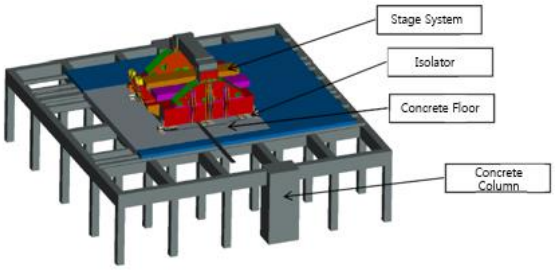

FIGURE 1. System Overview

SYSTEM OVERVIEW

The stage system is installed on a concrete floor in the n^{th} floor, which is resting on vertical columns coming from the $n\text{-}1^{th}$ floor. This concrete structure is loaded with an 80 ton stage system including a 6 ton moving mass. There are 6 pneumatic passive isolators being mounted between the stage system and the concrete floor for support of the total mass. Figure 1 shows a solid modeling of the stage system and the floor structure.

FEA SIMULATION

Boundary Conditions

The floor itself and its columns were defined as concrete material, while the isolators and H-beams integrated underneath the floor were defined as structural steel. Table 1 shows properties of the material.

After material definition, conditions for load and support were defined. To obtain a value of a deflection, load was placed on top of the passive isolators. The load on the passive isolators is composed of two components. First component is associated with the fixed mass of the stage system, 74 tons, which can be evenly distributed over the 6 isolators.

Second component of the load corresponds to the moving mass of the stage, 6 tons, which then can be redistributed over the isolators depending on the position of the moving mass. Separating the load into two parts allows calculations in two steps which fully incorporate the dynamics of the stage.

TABLE 1. Material Specification

	Concrete	Structural Steel
Density[kg/m^3]	2300	7850
E-modulus[MPa]	30000	200000

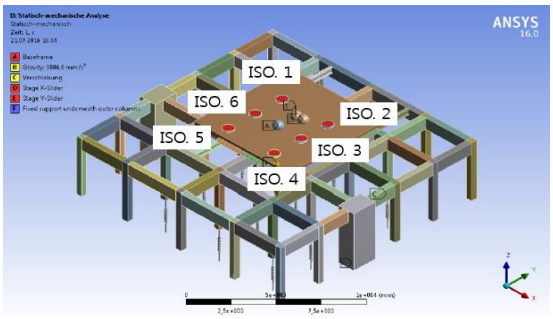

FIGURE 2. Boundary Conditions of FEA Model

To evaluate the stiffness of the floor, it was necessary to define a compensation-stiffness underneath the columns in terms of a spring support. This spring stiffness was calculated using the following equation.

$$\frac{1}{k_{real}} = \frac{1}{k_{fixed}} + \frac{1}{k_{spring}}$$

$$k_{spring} = \frac{k_{fixed} \times k_{real}}{k_{fixed} - k_{real}}$$

$$= \frac{(2.29 \times 10^9) \times (1.85 \times 10^8)}{(2.29 \times 10^9) - (1.85 \times 10^8)}$$

$$= 2.01 \times 10^8 \; N/m$$

where k_{real} is measured value while k_{fixed} is FEA result from the fixed conditions.

The inner columns of the floor model are modeled as spring supports, of which load is equally distributed (parallel connection). The outer columns are modeled as fixed supports.

Three different load cases were simulated with respect to the boundary conditions mentioned above. These cases are identified in Table 2.

Simulation Results

Table 3 summarizes simulation results for the deflection of the 6 passive isolators, with respect to the deformation of the floor, for 3 different stage positions (center, near Iso. 1, and near Iso. 4) where 3 representative load cases (Table 2) occur.

TABLE 2. Load Cases

	X-position	Y-position
Center	0 mm	0 mm
Near Iso. 1	-560 mm	1400 mm
Near iso. 4	560 mm	-1400 mm

TABLE 3. Simulation Results

	Center	Near Iso. 1	Near Iso. 4
Iso. 1	-3.554 mm	-3.594 mm	-3.535 mm
Iso. 2	-3.810 mm	-3.821 mm	-3.799 mm
Iso. 3	-4.363 mm	-4.354 mm	-4.372 mm
Iso. 4	-4.474 mm	-4.442 mm	-4.507 mm
Iso. 5	-3.979 mm	-3.957 mm	-4.001 mm
Iso. 6	-4.016 mm	-4.017 mm	-4.015 mm

Based on these deflection values, it is possible to calculate the maximum level change during the stage motion by referring to the values at the two farthest stage positions (two utmost load cases). Changes in deflection at each of these isolators are observed for the two changing load cases (both between Iso.1 and Center, and between Iso.4 and Center). They are shown in Table 4.

TABLE 4. Calculation of Max. Deflection

	ΔIso. 1 (Iso.1 - Center)	ΔIso. 4 (Iso.4 - Center)
Iso. 1	-0.020 mm	0.020 mm
Iso. 2	-0.011 mm	0.011 mm
Iso. 3	0.009 mm	-0.009 mm
Iso. 4	0.033 mm	-0.032 mm
Iso. 5	0.022 mm	-0.022 mm
Iso. 6	-0.001 mm	-0.001 mm

The maximum level change is finally obtained by the following calculation.

$$\max.\ \Delta\text{Iso.}1 \text{ to } \Delta\text{Iso.}4 = 0.053 \text{ mm}$$

The linear change of 53 μm corresponds to tilt of stage about 9.6 μrad considering the distance between the two isolator (Iso. 1 and Iso. 4) positions.

CONCEPT DESIGN

Previous Level Control System

The level control in the passive isolation system keeps the height of the isolators constantly. The height is measured between the top and bottom of the isolator, and is the value that the position control loops attempt to keep constant.

The position sensor is not able to recognize absolute movement of the bottom and top of the isolator, but relative movement between the two. This relative movement is the error that previous control system attempts to minimize.

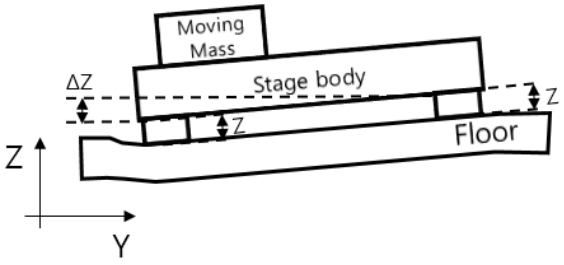

FIGURE 3. Schematic of Previous Level Control System with Floor Deformation.

However, from FEA simulation results it is known that the floor stiffness is not infinite. This means when a 6 ton of the moving mass moves on the stage, the floor is deformed by 53 μm, which cannot be compensated by the current leveling system. So, additional mean is needed to keep the stage's height and level. Figure 3 shows this more schematically.

Novel Concept

To measure the stage's inclination, the RMS was designed to be installed on the stage system as shown in Figure 4. The mechanical integration of the RMS was done with two inclinometers for measurement of X-rotation and Y-rotation errors of the stage system.

Sensor Requirements

Based on the calculations from the simulated deformation of the floor, sensor resolution and bandwidth should be higher than 0.5 μrad and 2 Hz, respectively. As long as the sensor meets the specifications given above and can be used in a cleanroom condition, off-the-shelf sensors can be used.

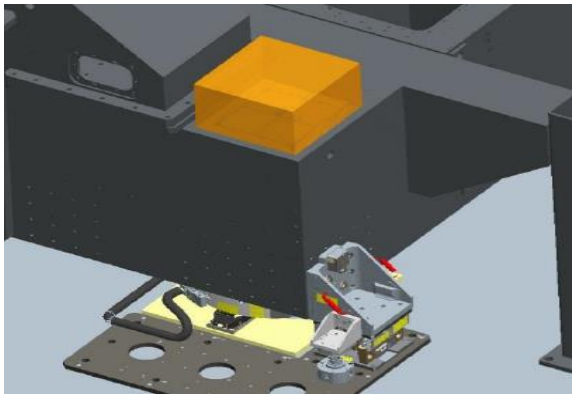

FIGURE 4. Concept of Proposed System

Control Concept

The general concept is to use the inclinometer to keep the system level in a similar way as the positon control loops are used to level the system. This means a PI controller with a low pass filter.

To make this possible it is necessary to have a sufficient bandwidth in the control loop and a right amount of disturbance rejection. Figure 5 shows the control loop bandwidth identified in the simulations.

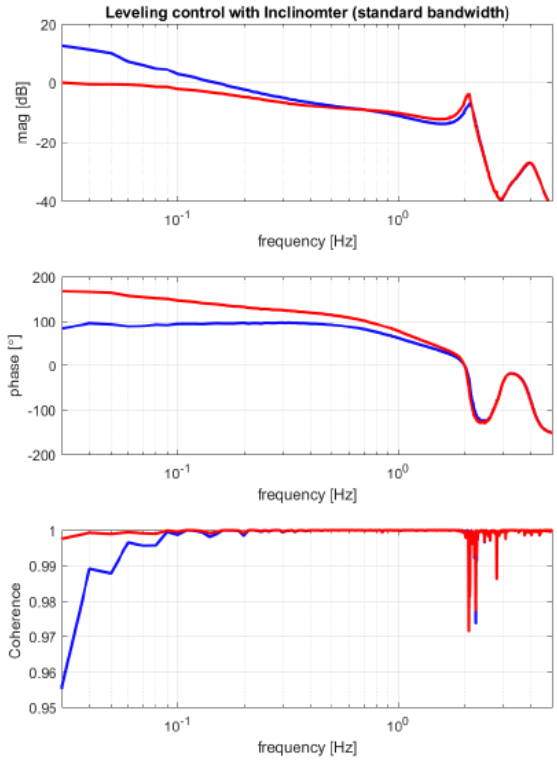

FIGURE 5. Position Control Loop Performance

In the case above, the control bandwidth of the position loop is about 0.22 Hz, which is considered as a safe tradeoff between disturbance rejection and influence on the transmissibility. To reach control bandwidth of 0.22Hz, it is recommend to have sensor bandwidth of 2 Hz for sufficient phase margin.

Figure 6 shows improvement of the leveling control after applying the RMS. Leveling error was reduced to ±10 μm (with RMS) from ±250 μm (without RMS).

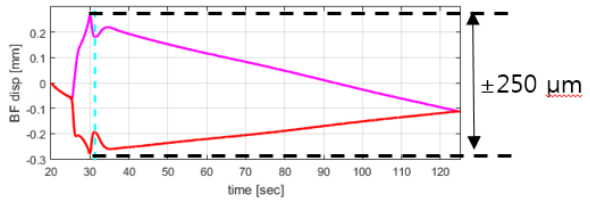

(a) Without RMS

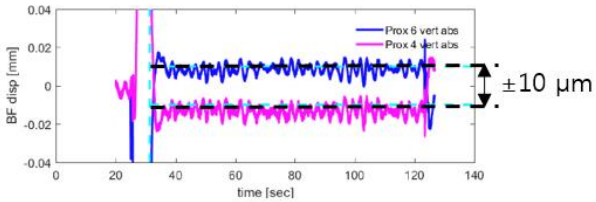

(b) With RMS

FIGURE 6. Levelling Performance without and with RMS

CONCLUSION AND FUTURE WORK

With the realistic floor (based on actual construction design of the factory) and stage modeling, FEA simulation has been performed, and the results show that the floor deformation can reach up to 53 µm. Because of this floor deformation, the stage system is subject to incline while deteriorating its precision setup although the passive isolators try to control the leveling of the stage system.

To solve this problem, an additional control loop including an inclinometer, so called RMS, has been carefully designed and simulated. This sensor feedback system had more than 2 Hz bandwidth and reached the required leveling performance of ±10 µm for the 6 ton mass of the moving part of the stage system with sufficient phase margin.

Actual RMS system has been built, will be installed, and verified in the real stage system as a future work.

REFERENCES

[1] A. Schellekens, el al, Design for precision: Current status and trends, Annuals of the CIRP, 1998; 47: 557-586.

Large Area Inspection using a Multi-point, Tip-Based Nanometrology System

Tsung-Fu Yao, and Michael Cullinan
Department of Mechanical Engineering,
The University of Texas at Austin
Austin, Texas, United States of America

Abstract

In order to overcome the critical drawback of limited field of view, this project develops a multi-point tip-based nanometrology system which uses multiple AFM probes within a system to measure a sample area. Even though a single image drawn by one AFM tip is extremely narrow compared with the bulk sample, this system can still be used to get the distribution of feature characteristics on the sample through the use of multiple independent AFMs simultaneously. Previous work has demonstrated an approach method to bring the single-chip AFM tip proximate to the inspected surface. This approach method combined with double layered multi-point inspection stage allows the system presented in this paper to be able to execute a quick wafer-scale inspection of nanoscale features, which has a great potential to help the development of process control in nanomanufacturing systems.

Introduction

Tip-based nanometrology techniques, such as Atomic Force Microscopes (AFMs), are good at capturing topography of a sample with very high resolution over micron-scale areas. However, for a wafer-level inspection, micron-scale imaging extent only provide a local inspection and is not representative of the overall topography. Therefore, multiple inspections at different locations are necessary. Unfortunately, imaging at multiple locations is also time-consuming and slows down the throughput of in-line inspection. In order to get over the critical drawback, this paper presents an inspection system that uses multiple MEMS-based AFMs to make multi-point inspections on a single wafer simultaneously.

This in-line inspection system, as shown in Figure 1, uses single-chip AFM system [1] which embeds every necessary component in the atomic force scanning by MEMS method. Multi-point metrology system takes advantage of small size of the single-chip AFM system. The difficulties are located on designing a stage that contains (co-grounds) multiple motion stages together and make all AFMs working separately. Not only the scanning function but also the positioning capability should be individually controlled in each AFM unit.

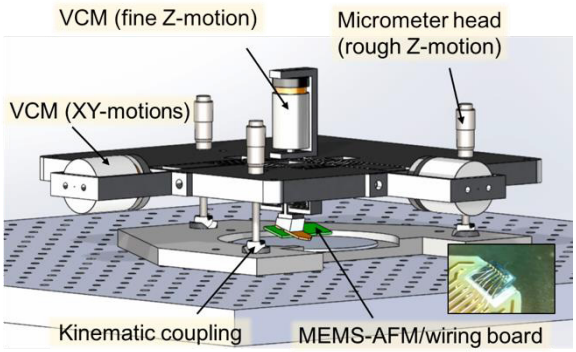

Figure 1. Schematic of the single-point in-line inspection system

In this study, the multi-point inspection system sets a peripheral layout putting 4 single-chip AFMs around the center, and a fifth AFM chip is put right on the center. Figure 2 shows the schematic of multi-point AFMs layout on the 4-inch wafer sample. In overall, 4 peripheral AFMs are put around with a constant distance from the center, and a fifth AFM is put right in the center. This layout let the inspection system be able to compare the fabrication results from center to edge parts and also the inspector could analyze the pattern uniformity over the sample. All the motion stages use flexure mechanisms to get mm-scale displacements. Thanks to the advantage of highly precision and simple mechanical structure, double parallelogram flexure modules (DPFMs) is a good candidate to be utilized in the motion stage for XY positioning. Even though there is still some parasitic motion error on unwanted direction due to the asymmetry in flexure layout, the formed skewed coordinate system can be compensated by closed-loop control with feedback from strain gauges on flexures. The z-motion (AFM approach) of each AFM is divided into two parts, one is rough motion, made by three micrometer heads built on the kinematic coupling, the other is fine motion, generated by a closed-loop controlled voice coil motor, which has a minimum step of 20 nm. In fine approach, the system uses feedback from the AFM system detecting tip-sample separation. A

proportional control (P-control) is performed during the fine approach to hold the AFM on a set point. In the multi-point metrology positioning, only the rough approach is not separately done for each AFM system since it connects to the kinematic couplings between AFM motion stage and wafer holder stage.

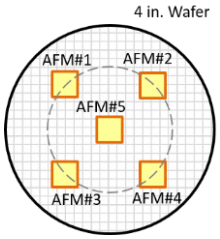

Figure 2. Multi-point AFMs layout

Positioning Stage Design

The multi-point metrology system in this study is designed for a 4-inch wafer sample. The 4 peripheral AFMs are located at 60% of wafer radius from the center, and arranged in circular pattern in order to make a symmetrical multi-inspection. By this the developed in-line inspection system could be capable of checking the patterning results both in the periphery and center regions in one measurement. However, this concept needs multiple individual motion stages, each is in charge of a single AFM's XY motion, but all grounded to the same stage.

In motion design, flexural concept has benefits of simple mechanism and repeatable motion. It is easy to make independence between two axes within one plane. Awtar has shown a constraint map [2] of double parallelogram flexure stage designed for large–range displacement. The symmetric arrangement of flexure module gives highly stiff and constrained motion along both axes. However, to fit multiple motion stages into a limited room, the symmetry would interfere with each other. In this study, the multi-point metrology system breaks the symmetry and leaves one flexure for each axis. Although this would induce parasitic error in axes, but the motion can be compensated from another actuation by after-calibration since high repeatability of flexure mechanism.

Moreover, the motion stage for center AFM site is still difficult to fit. Considering the motion range need to be millimeter scaled so that the system can finely adjust the interesting point on the wafer, which makes a relatively big occupancy of flexure. Therefore, the system uses a second layer which put the center motion stage and coupled to the 4 AFMs layer, as shown in Figure 3. Because the second layer is assembled out-of-plane, it uses an extension rod to make it leveling to others. By this, there will be a height difference between the center AFM and peripheral ones and which is determined by machining tolerance. The difference can be compensated by the fine Z motion afterwards.

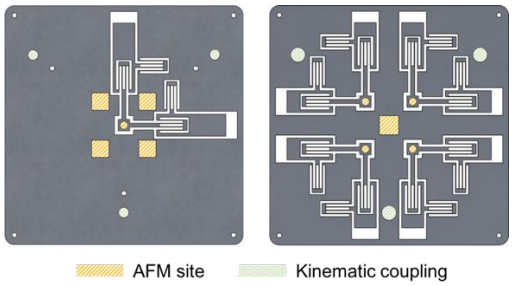

Figure 3. Double layered AFM stage

Multi-Z Motion

The Z motion is responsible for the AFM approach, which is the most critical function during the inspection since the cantilever at the front end is easy to damage even under small force. The system does not want to run the AFM at too high speed, that takes risk of the probe tip running into the sample surface, but slows approach also lowers the inspection throughput. Therefore, a proper way to balance these considerations is to make an adjusting strategy during approach. The strategy adjusts the VCM's exerting force and step size according to the instantaneous position of AFM cantilever. A proportional feedback control (Figure 4) is used in approach mechanism. There is a tradeoff between control error and approach time. In order to avoid the overshoot as possible, the proportional gain has to be decreased but doing so increases the approach time as well.

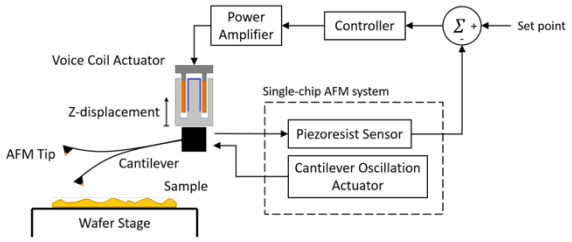

Figure 4. Fine-Z feedback control schematic

As mentioned before, double layered design introduces a height difference between the center and peripheral AFMs. A customized spacer is used to compensate the height difference but the machining tolerance may still be introduced in. Therefore, the stiffness of Z flexure should be softer than the design for single-point inspection system. The yielded translating capability can be used to compensate the machining tolerance and

make all the AFM cantilevers engaged with the operation range simultaneously. In the single-point inspection system performed before, the flexure module for fine-Z motion has a stiffness about 19.4 N/mm[3] which corresponds to 0.4-mm flexure thickness. The new version flexure has thickness of 0.3 mm, which shows a maximum displacement about 1.43mm in operation (11N driving force from VCM), and safety factor is about 3.76.

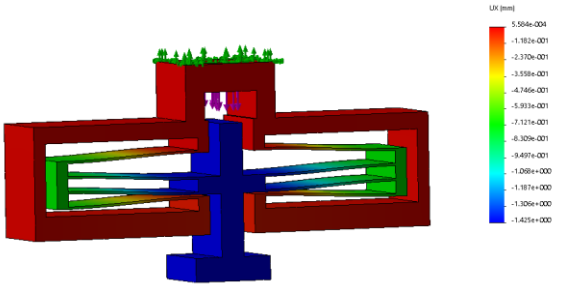

Figure 5. Displacement FEA analysis on 0.3-mm thickness flexure module

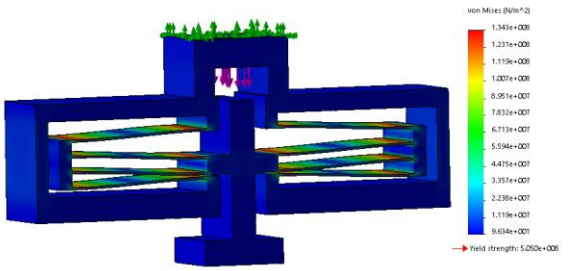

Figure 6. Stress FEA analysis on 0.3-mm thickness flexure module

Multi-AFM Driving

The AFM unit is made from ICSPI, Corp, as shown in Figure 7. This AFM system compress all the essential components such as electrothermal microactuator, force and resistive/thermal sensor, and microcantilever into a 0.25-mm^3 chip. What an operator needs to do is just to wire the signal out to a driving board dealing with all the input/output processes from a distance away. In the multi-point metrology system, it distributes 5 single AFM chips over the sample wafer area, and individually drives each AFM by 5 driving boards, respectively. The schematic is shown in Figure 8. The AFM from ICSPI uses piezoresistive sensor to detect cantilever strain during imaging, therefore, the collected signal has to pass an instrumentation amplifier then output into the driving board. The interface between the PC and devices is programmed and compiled from NI Labview software.

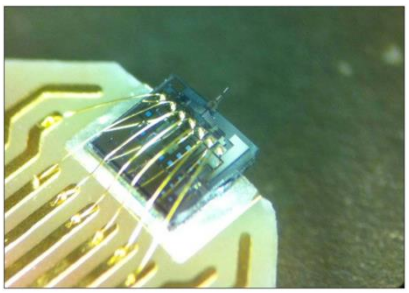

Figure 7. sc-AFM die-bonded and wirebonded onto a carrier PCB for facile, rapid exchange[1]

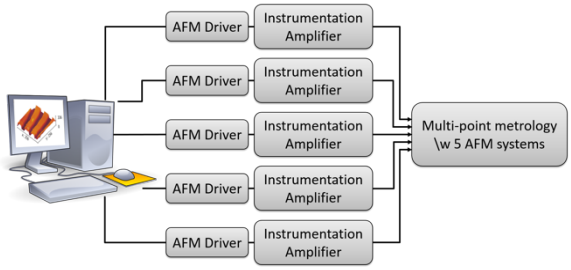

Figure 8. Multi-AFM system control schematic

Results

Figure 9 shows photos of the developed system, which includes a double-layered AFM positioning stage and a wafer stage, coupled together by kinematic coupling. The single-chip AFMs arranged according to the layout shown in Figure 2. In close-loop control, the system uses feedback from AFM system, and in average it takes about 4 seconds (Figure 10) to get all the AFM system to move into position for imaging, even faster than the time cost in single-point inspection system, which has been shown about 5.34 seconds [3] .

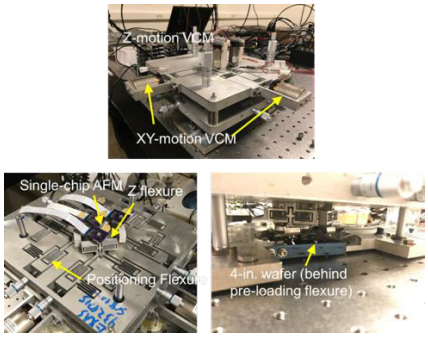

Figure 9. Photo of 5-chip AFM inspection stage

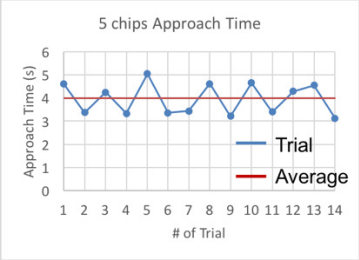

Figure 10. Approach time with 5 AFMs driving in parallel

The connection between AFM driver board and PC is via USB interface. In the proposed multi-point metrology system, basically it just copies the single-point inspection system several times and connect all the USB cables to the PC host ports. Currently, the program reopens the interface to contact each USB port and control all of them in parallel, but this way will greatly waste redundant hardware resource then lower the computation speed. In this study, the program is performed on a laptop with an i7-4610M @ 3.00GHz CPU with 16.0 GB RAM. The test driving shows 4 is the most number of AFM chips that this hardware configuration can deal without speed deterioration. The time counting result is shown in Figure 11, the system could finish scanning within 90 seconds or 25 seconds, with a 256x256 or 128x128 pixel resolution imaging, respectively. The number of AFM does not harm the imaging speed before 4 chips running. However, when the 5th chip joins the system, the hardware usage gets to the computational limit and starts to lower down.

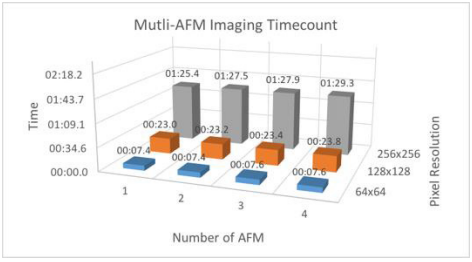

Figure 11. Time counting to multi-AFM system imaging

The multi-AFM scanning result is shown in Figure 12. The AFM #2 is determined the fifth device by the windows operation system, so in this measurement it discards this location and only does the other four for testing. The specimen used in the measurement is a stepped grating sample (Ted Pella, Inc.) with 100-nm step height and 3 μm period SiO_2 structures on Si wafer. Since we did not get any result from the AFM #2 so it shows blackout at its location. There is an obvious stripe noise happened at AFM #1 and #4 but stripe is not shown in AFM #3 and #5. Also, from the open-loop noise test, shown in Figure 13, both of them have relatively larger noise than the other two, which means a disturbance is entering to the system making some noise and affecting the stability of AFM itself. This noise causes by a horizontal vibration in individual AFM kinetics. Since the noise only happens on some specific AFM locations, it is highly possible that coming from the mechanical assembly tolerance and interference. The spots shown from the AFM #3 is due to the sample damages and scratches in place. Beyond these issues, the AFM #5 demonstrates a sub-nm vertical imaging resolution can be achieved by this multi-AFM measurement.

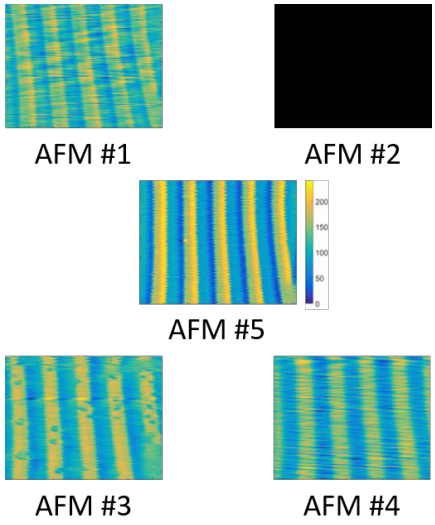

Figure 12.Multi-AFM measurement result, 5 single-chip AFMs running in parallel (128x128 pixel resolution)

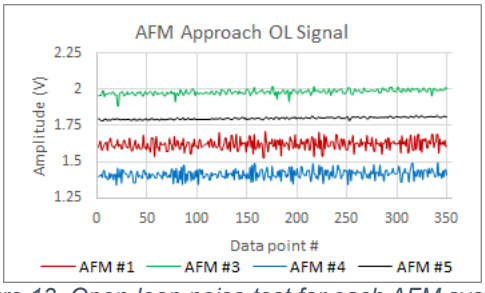

Figure 13. Open-loop noise test for each AFM system used in the multi-AFM measurement, the noise levels are: 33.8 mV(AFM #1), 17.2 mV(AFM #3), 31.0 mV(AFM #4) and 6.84 mV(AFM #5)

Conclusion and Future Works

By a double layered design, a multi-point

tip-based nanometrology system has been built. The system is capable of finishing the multi-probe AFM approach in a similar amount of time to the previous single-point inspection system. In order to compensate the height difference between center and peripheral AFMs introduced by the double layer, a softer Z flexure is utilized. Overall, the throughput of multi-point nanometrology system in this study is approximately four times that of the single-point inspection previously reported. And also, the increased throughput doesn't sacrifice the imaging resolution of metrology, the current multi-AFM metrology is able to finish 4-site sub-nm scanning within 24 second.

The multi-point inspection system, which is potentially capable of generating five images in a single measurement. However, due to the computation hardware limitation, the current multi-point metrology system can only afford 4 chips running. Fortunately, it is just a speed bottleneck in the control part, not in the AFM device. An optimization to the control schematic is necessary in the future. A modification in driving board should be done, for example, to integrate 5 driving boards into one single PCB and use a Field-programmable gate arrays (FPGA) chip in this board to do all the driving/data-collecting jobs. By doing so, the PC is only responsible of giving commands to the driving board and grab the result once data collecting is finished. Since most of all the computational operations are dealt in that FPGA chips, which does not need to worry about the hardware resource usage in PC, technically the maximum number of AFM chips that can be simultaneously driven will be greatly enlarged.

Another idea to extend the field of view of an AFM inspection is to make the metrology scan extra sites nearby and overlapped to the first one scanning. After collecting all the images, an image-stitching algorithm is deployed to connect all the images together. This idea does not save time for inspection but it provides another choice to do a wafer-review when the operator suspects a defect

References

[1] Sarkar, N., Strathearn, D., Lee, G., Olfat, M., & Mansour, R. R. (2015, January). A 0.25 mm 3 atomic force microscope on-a-chip. In *Micro Electro Mechanical Systems (MEMS), 2015 28th IEEE International Conference on* (pp. 732-735). IEEE.

[2] Awtar, S., & Parmar, G. (2013). Design of a large range XY nanopositioning system. *Journal of Mechanisms and Robotics*, *5*(2), 021008.

[3] Yao, T. F., Duenner, A., & Cullinan, M. (2016). Quick approach mechanism for tip-based in-line nanometrology systems. In *Proceedings - ASPE 2016 Annual Meeting* (pp. 121-125). American Society for Precision Engineering, ASPE.

DEVELOPMENT OF AN INNOVATIVE SENSOR FOR MEASURING TWO DEGREE-OF-FREEDOM MOTIONS OF SINGLE-AXIS LINEAR NANOPOSITIONOING STAGE

Abolfazle Zolfaghari[1], Seongkyul Jeon[1], Gyu Ha Kim[2], ChaBum Lee[1]
[1]Department of Mechanical Engineering
Tennessee Technological University
Cookeville, TN, USA
[2]Division of Research & Development
TRI-N Co. Ltd.
Gumi, South Korea

INSTRUCTIONS

High precision multi degree-of-freedom (DOF) measurement is a key technology in industrial equipment (machine tools, lithography machines, or surface profilers) used in manufacturing or inspection systems [1-3]. Multi-DOF motion errors of the precision stages negatively affect the equipment's overall performance, which makes quality control of products difficult. Such motion errors, which are called parasitic or out-of-plane motions, include three linear errors (*x*, *y* and *z* axes) and three angular errors (pitch, roll and yaw axes). The three angular errors of linear stages are highly associated with Abbé errors and cosine errors and manufacturers or users must assess the performance boundaries of precision stages from design to production.

The metrology capability required to measure micrometer-to-nanometer scale parasitic motion of flexure mechanisms has been reported a few tens of years ago. It is considered as one of the most challenging topics in the areas of precision measurement and manufacturing because parasitic motions are inevitable in all linear or angular motion systems. Non-contact sensors such as capacitive sensors (CS), laser interferometers, or grating interferometers are typically used for motion measurement of such precision systems [3-7]. Among three conventional sensors, the CS is primarily used because of its high resolution and compact size. However, measuring the angular motion with CS causes a few complications. When it comes to angular displacement of the flexures, the CS measures the change in capacitance of the projected area in principle and shows different sensing behaviors (gain and offset) than those from measuring single-axis linear displacement. The CS are usually calibrated with the probe perpendicular to the target surface. As the angle of the target changes, the output will show an offset shift from the actual gap between the probe's center axis and the target.

Here, a novel sensing method based on optical knife-edge sensors (OKES) is presented and applied to the measurement of motion error of the flexure-based nanopositioning system. The OKES has been recently introduced by Lee for linear displacement motion measurement in nanopositioning systems [8-10]. From the Lee's previous research, the OKES shows high resolution, linearity, sensitivity, a millimeter measuring range, and positioning control effectiveness. In addition, the OKES is compact and low-cost such that it can be easily fit into a compact system such as the aforementioned nanopositioning stage. In this study, the two DOF OKES is proposed and discussed in terms of linear and angular displacement measurement results, configuration, and control effectiveness of the nanopositioning stage. Two CS are used as a baseline comparison to the OKES. The measurement results of the two sensors are compared and discussed in detail.

MEASUREMENT PRINCIPLE

An incident wavefront of light diffracts or bends when it is incident on the sharp edge of an object transverse to the propagation direction. This phenomenon creates a secondary wave emanating from the edge of the obstacle. Due to interference between the two superimposed waves, a geometrical wave from the primary source of light and the boundary diffraction wave from the secondary source, a diffraction pattern can be observed the measurement plane. This effect is explained by the Huygens-Fresnel Principle [11]. From the previous study [8-10], the diffraction fringe pattern moves according to the distance between the light source and the knife-edge and the knife-edge to the detector.

The optical properties of the laser, knife-edge surface conditions, and detector size are related with the creation of the interferometric fringes. Although knife-edge diffraction theoretically well-developed [8], the experimental approaches to knife-edge diffraction for displacement sensing and positioning control of precision stages have been recently introduced by Lee [8-10]. Lee created a design principle for the OKES by deriving a mathematical model and characterizing its sensing performance in terms of the operation range, positioning accuracy, resolution, linearity, bandwidth, and control effectiveness with the nanopositioning system.

MEASUREMENT SYSTEM

The OKES-based measurement system consists of a double-sided knife-edge mounted on the additive manufactured-flexure stage along the traveling axis as illustrated in Figure 1a. The stage moves along the *X* direction, and □, □, and □ represent roll, pitch, and yaw, respectively. An array of prisms and beam splitters (BS) is arranged such that four separated laser beams with equal intensity are incident to the knife-edge, as shown in Figure 1b. The interference signal between the resulting superimposed waves is measured by four photodetectors (PD) aligned with the laser sources, respectively. The intensity changes of the interference represent the motion of the nanopositioning stage. The double compound-type flexure mechanism used was fabricated by a stereolithography process to demonstrate the proposed measurement concept and is driven by a voice coil motor (VCM) aligned with the travelling axis of the stage. The flexure mechanism (100 × 110 × 25 mm^2) was designed by estimating the compliance, stress, and force applied from the VCM to the flexure. From the experiment, the stiffness of the stage was measured to be 43.5 μm/N. The VCM is limited to 10N max, so the total travel range is determined to be approximately 500 μm (±250 μm).

The measurement principle used to measure both the linear and pitch motion of the stage is schematically described in Figure 2. Each OKES is aligned along the upper and lower parallel lines (UL, LL). In Figure 2a, the black box indicates the knife-edge, and the blue-dot box represents the linear motion of the knife edge. The red-circle A, B, C and D represent beam spots where the beams are incident, and A', B', C' and D' spots indicate the current beam spots in the knife-edge, respectively. Figure 2b similarly shows the pitch motions of the stage. The *X* and *β* are the linear and angular displacement, and *H* and *W* are the horizontal and vertical distances between beam centers. While the stage is moving, the intensity of interference of the superimposed waves is measured by four PD's (PD_a, PD_b, PD_c and PD_d) as photo voltaic signals. Based on the responses of each PD, the linear and angular displacement of the stage can be expressed as

$$\Delta UL_X = K_U \frac{V_A - V_B}{V_A + V_B}, \tag{1a}$$

$$\Delta LL_X = K_L \frac{V_C - V_D}{V_C + V_D}. \tag{1b}$$

where ΔUL_X and ΔLL_X are the measured displacement from each OKES located at *UL* and *LL*, V_i is the voltage output to be measured at PD_i, and K_U and K_L are the sensitivity that can be obtained from the calibration process. Based on the geometric relationship as shown in Figure 2, the linear and angular displacement of the stage can be expressed as

$$\Delta X = \frac{\Delta UL_X + \Delta LL_X}{2}, \tag{2a}$$

$$\Delta \beta = \frac{\Delta UL_X - \Delta LL_X}{2}. \tag{2b}$$

EXPERIMENTS

The two-DOF OKES was integrated with the flexure mechanism as shown in Figure 3. Each PD output was amplified using a current-to-voltage converter and operation amplifiers. A low pass filter with a cutoff frequency of 2 kHz was added at the end of the amplifier. The electronics bandwidth was determined to be 2 kHz and able to collect 1st order and high order natural frequencies due to lack of torsional stiffness of the flexure stage. The experiment was performed on a vibration-isolated table. Two CS were used for a baseline comparison with the two-DOF OKES. Each OKES along the LL and UL lines were calibrated while moving the stage along the *X*- axis. In Figure 4, the OKES sensitivities were found to be 39.6 mV/μm (nonlinearity 0.091% in full scale, 95% confidence level) and 42.4 mV/μm (nonlinearity 0.095% in full scale, 95% confidence level), respectively. Nonlinearity was calculated from linear-fitting error (standard deviation) of the calibration results. Here the OKES at the LL and UL lines were denoted as OKESL and OKESU, respectively. The sensor nonlinearity was calculated as a residual sum of linearity error over the full scale of 500 μm. The effective linear

displacement was calculated from Eq. (2a), and the sensitivity was found to be 41 mV/μm (nonlinearity 0.093% in full scale, 95% confidence level).

Based on the calibration results of the OKES, the pitch motion of the flexure stage was measured (calculated from Eq. (2b)) while moving the flexure stage over a 300 μm range in open-loop. Similarly to the previous calibration process, two CS (10 nm resolution, 200 Hz bandwidth, □5 mm effective sensing electrode) were used for comparison. The pitch motion was calculated by dividing the difference of two CS outputs by the distance between the two CS. Figure 5 shows the pitch motion measured by the OKES. The OKES sensitivity was found to be approximately three times larger than the CS. It shows the pitch error measured by OKES increases as the linear displacement increases and reaches a maximum of approximately 600 arcsecond at the full 300 μm linear motion.

The discrepancy between the OKES and CS can be explained based on the measuring principal of each sensor. As discussed in Section 1, there are a few issues regarding the measurement of an angular motion with CS because it measures the change in capacitance over the projected area (diameter of sensing electrode). Since the CS are calibrated with the sensing electrode perpendicular to the target surface, the measurement of angular motions becomes nonlinear. This nonlinearity becomes worse as the effective sensing diameter of CS approaches the dimension of the sensing target, making the CS less sensitive to the angular motion. Because flexure stages produce linear and angular displacement simultaneously, measuring two motions at the same time with CS may not be effective. In fact, the CS with an effectively small sensing electrode diameter is preferred. Angular-sensitive CS, autocollimators [1], or triple beam interferometers [13] can be used to measure the pitch motion of the flexure stage more accurately. This study focuses on developing a modified two-DOF OKES to provide measurement capabilities for motion error characterization of the flexure stage in a compact, convenient, and low-cost manner. The systematic error (difference between true value and measured value) of the two sensors will also be characterized in the future work.

Figure 6 shows the step response in closed-loop. It can be seen that the OKES shows a good agreement with CS results in terms of rising time (5 ms), overshoot and settling time (150 ms) for the forward direction, and falling time (5 ms) and settling time (200 ms) for the backward direction. The positioning resolution of CS and OKES was estimated by calculating standard deviation of the steady-state responses in Figure 6(b) and (e). The positioning resolutions for linear and angular displacement curves were 12.4 nm and 1.5 arcsec for OKES and 12.2 nm and 0.6 arcsec for CS, respectively.

CONCLUSION

A high-precision, compact, and low-cost sensing system based on two DOF OKES was introduced. It could simultaneously measure linear and angular displacement of the flexure stage. The linearity, resolution, bandwidth, and control effectiveness of the proposed sensing system were verified by comparison with measurement results obtained by CS. For linear motion, the two sensors showed good agreement. However, a large discrepancy between the two sensors was found during angular motion measurement. This is because the CS shows different sensor sensitivity when it measures the angular motion and is less sensitive to the angular motion when the diameter of the CS sensing electrode is relatively large when compared to the measuring range and target size. The absolute comparison between the two sensors was not included in this work, and autocollimators or triple-beam interferometers should be used to obtain the true angular motion of the flexure stage and to quantitatively compare the two sensor outputs in the future work. As a result, the two-DOF OKES can be considered a promising alternative to CS for controlling the position and monitoring motion error of precision motion devices.

ACKNOWLEDGEMENT

The research was supported by NSF (Award Number: CMMI 1463502) through Tennessee Technological University. Similarly, this work was supported by the Technology Innovation Program (or Industrial Strategic Technology Development Program (10067396, Development of low-cost industrial robot system with low-cost actuator and sensing modules) funded by the Ministry of Trade, Industry & Energy (MOTIE, Korea).

REFERENCES

[1] W. Gao, Precision nanometrology: Sensors and measuring systems for nanomanufacturing, Springer (2010).

[2] S.T. Smith, Flexures: Elements of Elastic Mechanisms, Taylor & Francis, London, England (2002).
[3] C.B. Lee, C.K. Stepanick, S.K. Lee, and J.A. Tarbutton. Cross-coupling effect of large range XY nanopositioning stage fabricated by stereolithography process. Precision Engineering. 46, 81-87 (2016).
[4] Y.K. Yong, S.O.R. Moheimani, B.J. Kenton, and K.K. Leang. Invited review article: high-speed flexure-guided nanopositioning: mechanical design and control issues. Review of Scientific Instruments. 83, 121101 (2012).
[5] C.B. Lee, S. Jeon, C.K. Stepanick, A. Zolfaghari, and J.A. Tarbutton. Investigation of optical knife edge sensor for low cost, large-range and dual-axis nanopositioning stages. Measurement. 103, pp. 157-164 (2017).
[6] A.J. Fleming. A review of nanometer resolution position sensors: Operation and Performance. Sensors and Actuators A: Physical.190, 106-126 (2013).
[7] G. Parmar, K. Barton and S. Awtar. Large dynamic range nanopositioning using iterative learning control. Precision Engineering. 38(1), 48-56 (2014).
[8] C.B. Lee, S-K. Lee, and J.A. Tarbutton. Novel design and sensitivity analysis of displacement measurement system utilizing knife edge diffraction for nanopositioning stages. Review of Scientific Instruments. 85 (2014) 095113.
[9] C. Lee, S-K. Lee, and J.A. Tarbutton, Positioning control effectiveness of optical knife edge displacement sensor-embedded monolithic precision stage. Sensors and Actuators A. 233, 390-296, (2015).
[10] C.B. Lee, S. Jeon, C.K. Stepanick, A. Zolfaghari, and J.A. Tarbutton. Investigation of optical knife edge sensor for low cost, large-range and dual-axis nanopositioning stages. Measurement. 103, pp. 157-164 (2017).
[11] E. Hecht, Optics, 4th ed. Addison-Wesley Longman Inc., 1987.
[12] C.B. Lee and J.A. Tarbutton, Compliance and control characteristics of an additive manufactured-flexure stage. Review of Scientific Instruments 86, 045107 (2015).
[13] G. Jaeger. Limitations of precision length measurement based on interferometers. XIX IMEKO World Congress, Sep. 6-11, 2019, Lisbon, Portugal.

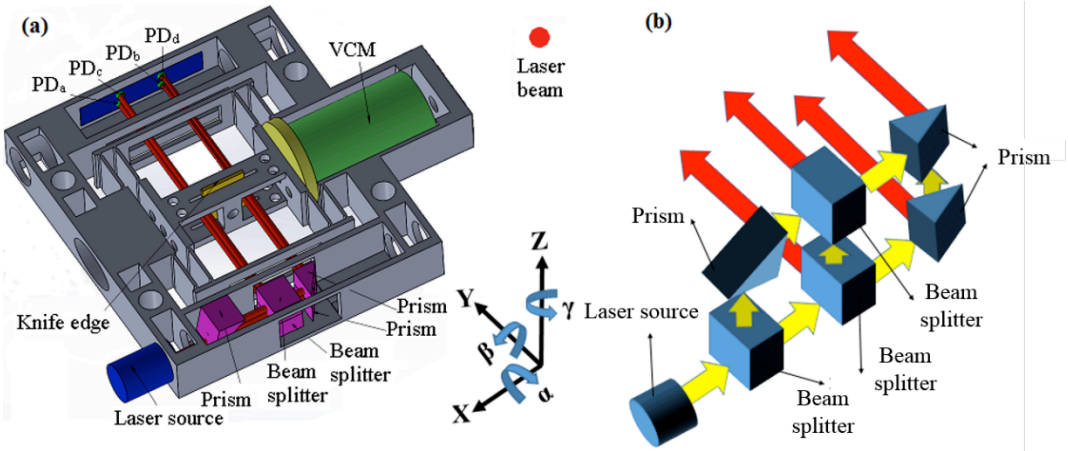

FIGURE 1. System configuration: (a) schematic of flexure stage with OKES and (b) configuration of laser beam splitting.

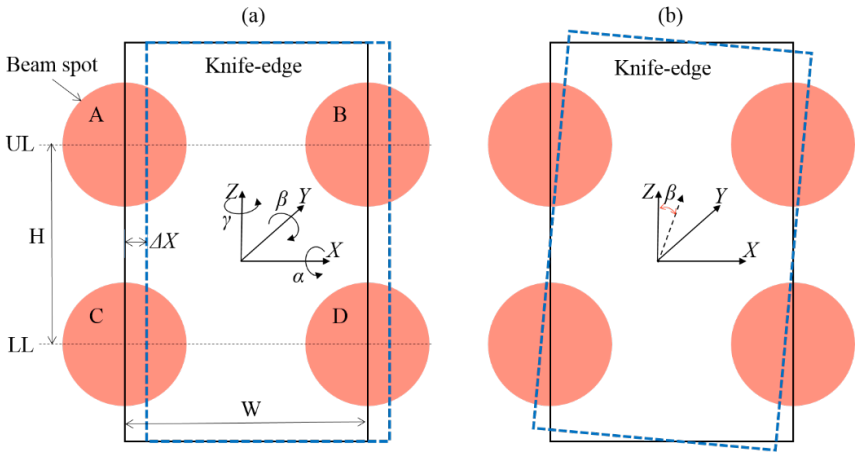

FIGURE 2. Motion error separation method: (a) linear *X* motion and (b) pitch □ error.

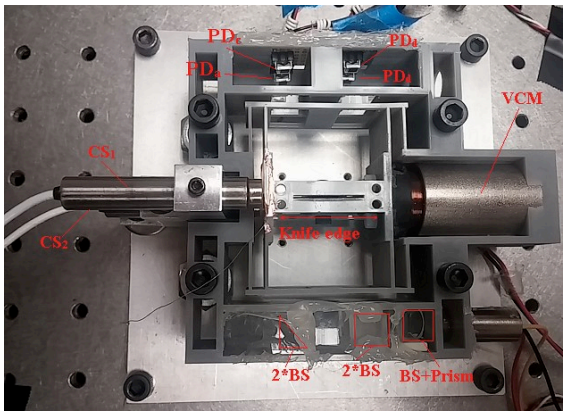

FIGURE 3. Experimental setup.

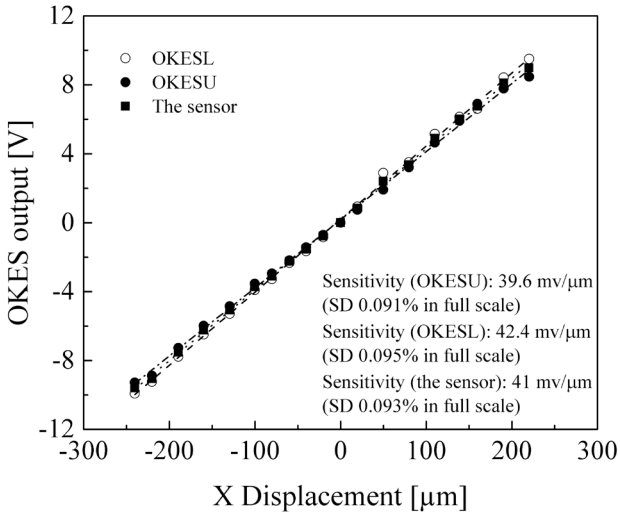

FIGURE 4. Calibration results of OKES: OKESU (upper OKES), OKESL (lower OKES) and standard deviation (SD).

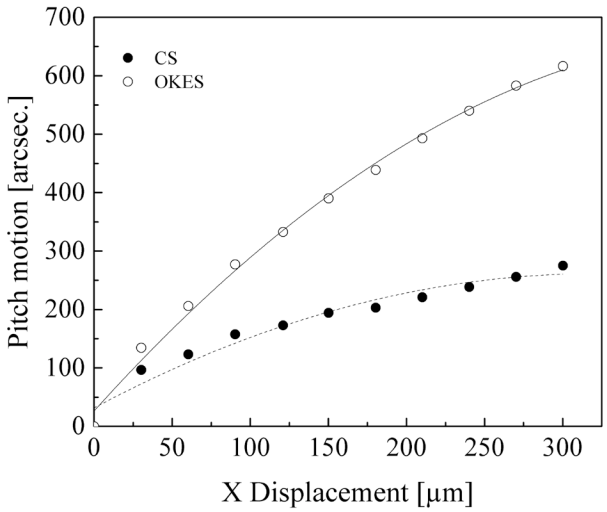

FIGURE 5. Pitch motion measurement of the stage with respect to the linear displacement.

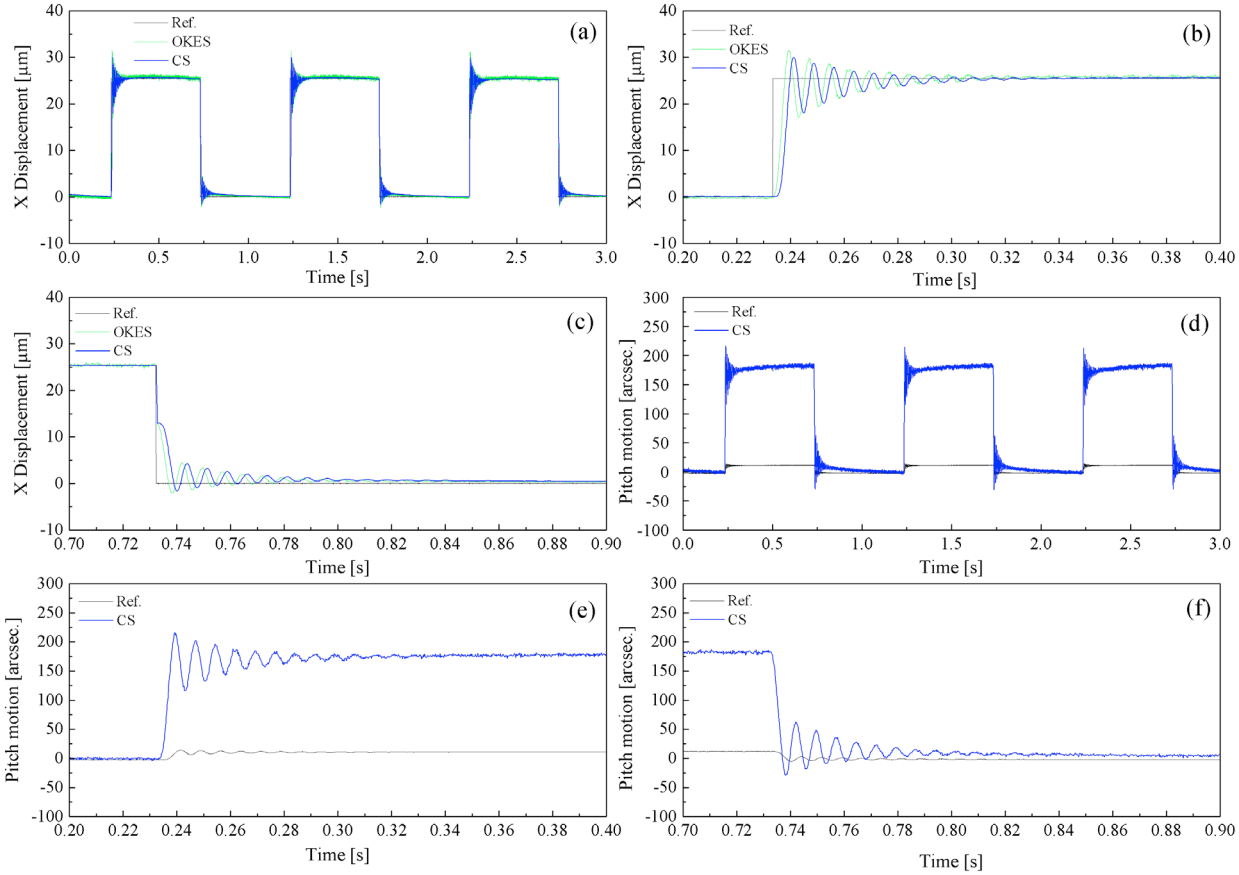

FIGURE 6. Results of closed-loop 25 μm step response: (a) linear motion step response, (b) rising step in detail, (c) falling step in detail, (d) pitch motion step response, (e) pitch motion step response in rising step, and (f) pitch motion step response in falling step.

AXIAL AND RADIAL STATIC STIFFNESS TESTING FOR ULTRA-PRECISION AIR BEARING SPINDLE

Sam Arneson, David A. Arneson, Byron R. Knapp, and Daniel Oss
Professional Instruments Company
Hopkins, Minnesota, USA

INTRODUCTION

Diamond machining and ultra-precision grinding can be used to manufacture optical surfaces with sub-nanometer surface finish and sub-micrometer form accuracies. Increasing demand for advanced optics requires continuous improvement of ultra-precision machines. In particular, spindles with high stiffness and low error motions are critical to machine performance. While sub-micrometer error motions were sufficient early in the development diamond turning, current processes require spindles with nanometer-level error motions for direct machining of optical surfaces.

This paper describes the testing used for the axial and radial static stiffness of the Professional Instruments ISO 5.5 PG air bearing spindle.

FIGURE 1 *Professional Instruments ISO 5.5 PG air bearing spindle*

BACKGROUND

The 10,000 RPM ultra-precision air bearing spindle shown in Figure 1 is produced for diamond-turning and grinding applications [1]. The cross section in Figure 2 shows the combination of porous graphite journals and compound compensated captured thrusts (grooved face fed by annular restrictor). A brushless permanent magnet motor and two encoders are mounted directly to the rotor. A 1,024 line-count encoder is used for motor commutation and high speed operation, while a 9,000 line-count encoder is used for positioning and low speed operation. Front and rear radial bearings, as well as the motor, are water-cooled. Vacuum is supplied to the chuck via a non-contact rotary union.

STIFFNESS TESTING

Static stiffness is a crucial indicator for spindles to be used in precision machining applications —particularly central stiffness under light cutting loads. “Central stiffness” in this context is defined as the ability to respond to small increases in force applied to the spindle, such as those from drive influence, unbalance, or interrupted cutting forces, especially when the rotor is centered [2].

The tests are done using indicators mounted in short, stiff structural loops for accurate stator-to-rotor displacement measurement. It is important to test from low displacement to high displacement to verify spindle stiffness linearity. The linearity of a spindle is a better measure for the quality of the spindle than the total deflection of the spindle [3].

Displacements are measured with diamond-tipped Mikrokators. They are taut-band, frictionless instruments capable of responding to nanometer level displacements, but only if robustly mounted on heavy arms and posts [4].

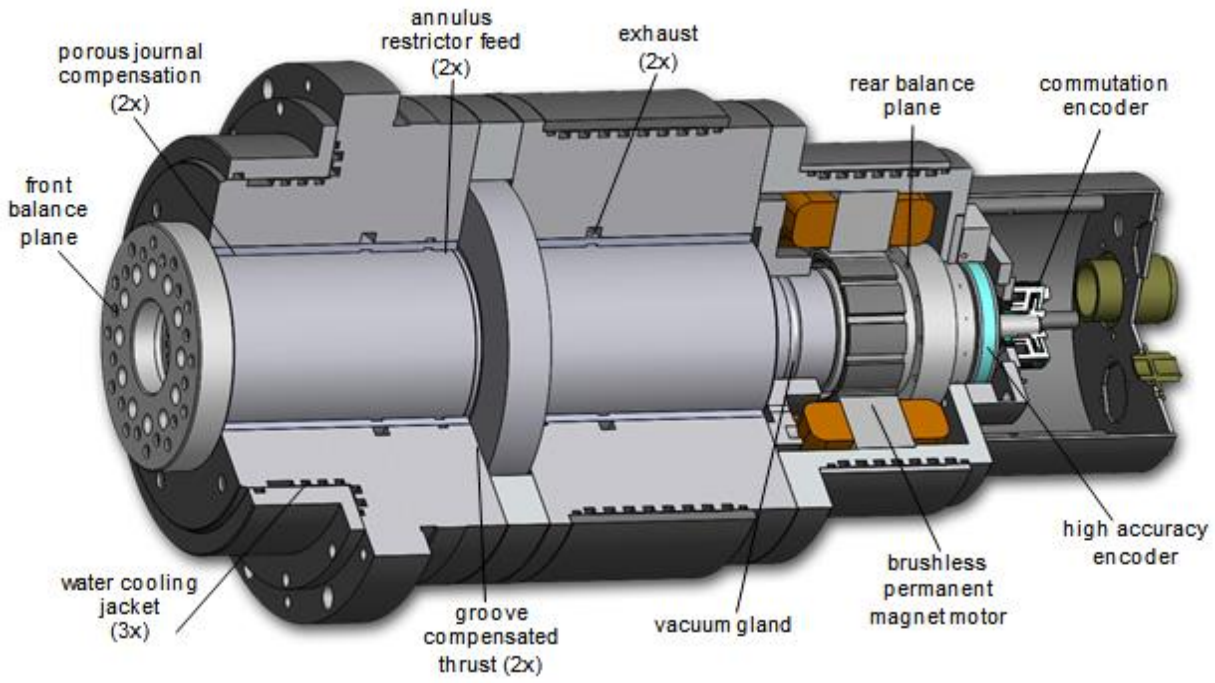

FIGURE 2 *Cross section of porous graphite spindle showing important features*

Air bearing pistons are used to apply the force rather than conventional load cells due to their low friction and low hysteresis, making setup easier and enabling testing over the full range of displacement

RADIAL TEST

For this test, the spindle is positioned horizontally and an air bearing piston is used to apply force to the spindle rotor (Figure 3). The results of the radial test (Figure 4, sampled at more than 10 increments of applied load) show that the stiffness at the nose is linear from no load through the ultimate capacity at 150 N/µm.

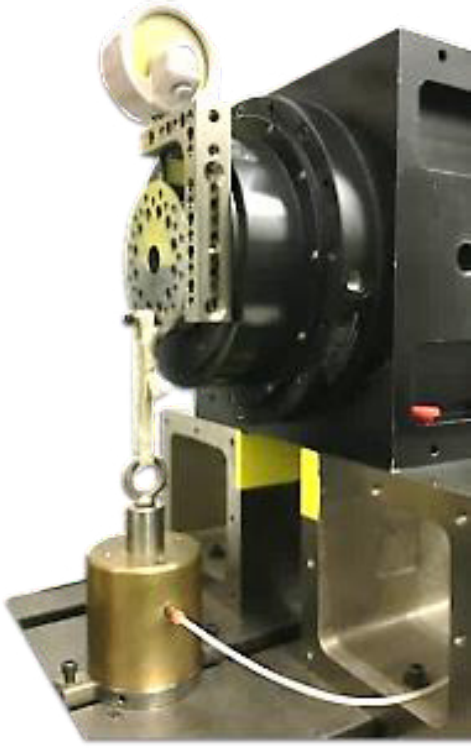

FIGURE 3 *Setup for radial static stiffness test*

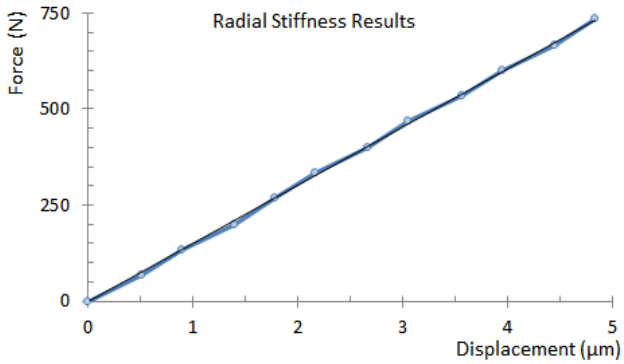

FIGURE 4 *Radial stiffness results are linear at 150 N/µm*

AXIAL TEST

In this test, the spindle is positioned vertically with the air bearing piston applying a downward force while the indicator is mounted on the bottom of the spindle (Figure 5). The resulting axial stiffness is linear from no load to ultimate capacity at 700 N/µm (Figure 6, tested at 6 increments of applied load).

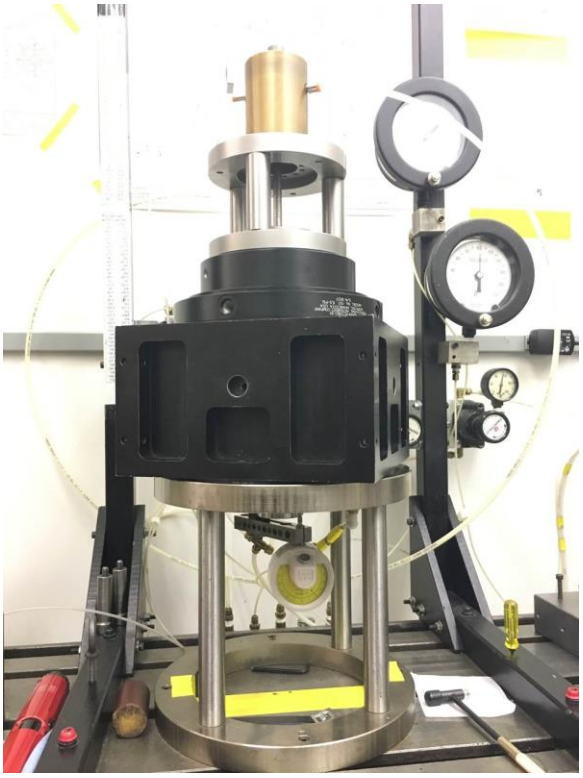

FIGURE 5 *Setup for Axial Static Stiffness test*

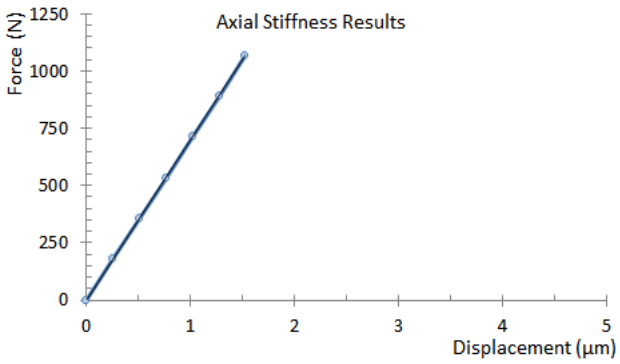

FIGURE 6 *Axial stiffness results are linear at 700 N/µm*

CONCLUSION

The methods and results of ultra-precision spindle stiffness testing are described. The test results demonstrated static stiffness for axial and radial of the ISO 5.5 Porous Graphite spindle was linear at 150 N/µm and 700 N/µm respectively.

REFERENCES

[1] B. Knapp et al. Design And Characterization Of A New Porous Graphite Diamond Turning Spindle. Professional Instruments. ASPE 2017 Spring Topical Meeting.

[2] M. Liebers et al. Measuring central stiffness of an air bearing spindle. Professional Instruments. EUSPEN 15 (2015).

[3] C.A. Luttervelt et al. Stiffness Measurements as a Check of Machine-Tool Spindles. Annals of the CIRP Vol. 31/1/1982.

[4] M. Liebers et al. Description of an apparatus for testing air bearing pad performance. Professional Instruments, EUSPEN 16 (2016).

IN-LINE, TIP BASED NANOMETROLOGY FOR ROLL-TO-ROLL MANUFACTURED MATERIALS AND ELECTRONIC DEVICES

Liam G. Connolly and Michael Cullinan
Department of Mechanical Engineering
The University of Texas at Austin
Austin, Texas

INTRODUCTION

Flexible electronic devices have shown extreme promise due to their low weight, mechanical flexibility and durability, with a low projected cost and large area processing compared to silicon wafer based electronics [1]. Devices with applications ranging from water purification, wearable sensor arrays, displays, batteries, solar cells and super-capacitors in a multitude of industries including healthcare, transportation, energy, mobile devices, and embedded systems are found to have improved performance at lower cost when compared to traditional, wafer-based electronics [1]. The proliferation of these promising devices will bring truly enormous benefit to society.

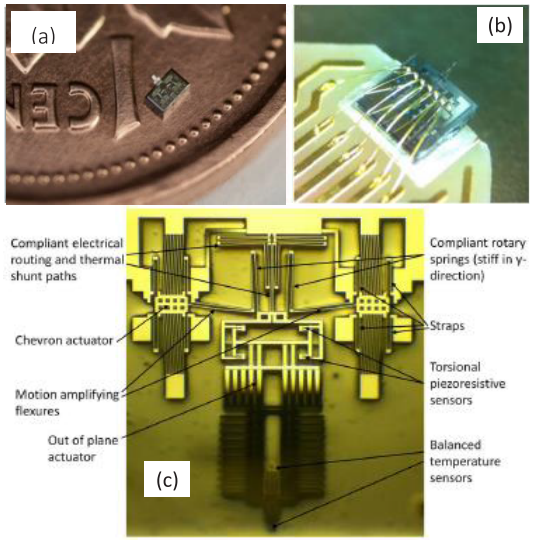

FIGURE 1. *(a) A single chip AFM, (b) packaged instrument, and (c) layout of MEMS chip* [2]

However, one of the most significant barriers to the widespread adoption of these devices is the challenge in transitioning from small-scale to large volume production. This issue is rooted in two conditions necessary for the viability of a new technology. First, the yield of the production must be high enough to justify mass manufacturing and second, the capital development costs to transition from prototype to volume-scale manufacturing must not exceed potential gains. These factors are both highly dependent on the ability to conduct fast and accurate metrology.

Novel atomic force microscope (AFM) technology has enabled a new class of compact measurement devices. These microelectromechanical systems (MEMS) based AFM devices (ICSPI Corp.), as seen in Fig. 1, work by utilizing electrothermal actuators coupled to flexure mechanisms to control lateral movement of the cantilevered AFM tip and a vertical bimorph actuator for moving the tip relative to the surface of the sample. The device also contains strain gauges to measure the interaction force between the sample and AFM tip. A closed loop feedback control system is used to maintain a constant height above the sample. The magnitude of the voltage outputted to the chip to maintain this height is measured and, in conjunction with a calibration, is utilized to record the surface topology of the sample. By implementing double parallelogram flexure mechanisms (DPFM) spanning the micro and macro scales in a coupled design, a low-cost system can accurately and precisely measure surface topology of nanopatterened electronic devices [2], [3].

SYSTEM OVERVIEW

Unwind-Rewind Subsystem

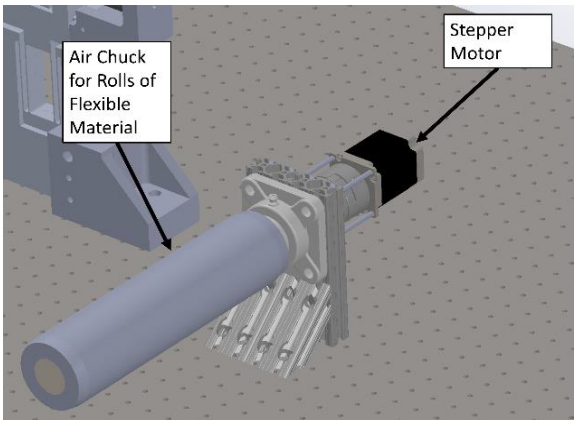

FIGURE 2. Cantilevered Unwind/Rewind Device

The material which flows through the system is regulated by the Unwind-Rewind subsystem, as shown in Fig. 2. The flexible substrate to be evaluated is loaded onto spools at either end of the system. These spools are mounted on cantilevered aluminum core chucks supported by alloy steel journals and driven by stepper motors to precisely control the unwind-rewind velocity (NEMA23, TinyG CNC Controller, TI DRV8818).

By regulating the speed of these motors another function is accomplished in-lieu of a traditional clutch-and-break device: tension control. Through a managed difference in the angular velocities of the independent unwind and rewind spools, the ideal level of web tension for measurement is achieved in addition to the primary role of this subsystem, regulating the overall speed of the web line. This tension level is very small in comparison to typical industrial systems (~10 N). In essence, it serves to ensure that the web is fully taught when moving through the system and flush when passing over the polished, stainless steel metrology roller, discussed in its' respective subsystem.

Metrology Subsystem

The web will then pass over a large, smooth, stainless steel idler roller supported at each end with air bushings (OAV Air Bearings), and the surface topology will be measured by the AFM directly over the precipice of this roller. To enable approach during system startup along with the ability to easily perform system maintenance or swap web samples, the positioning of the AFM chips is split into two paradigms: coarse and fine approach positioning, as shown in Fig. 3.

First, two vertical DPFM monoliths, each consisting of two water-jet manufactured half inch 6061-T6 Aluminum flexure plates, are rigidly bolted together and fixtured. Each side of the positioning system is rigidly connected to one

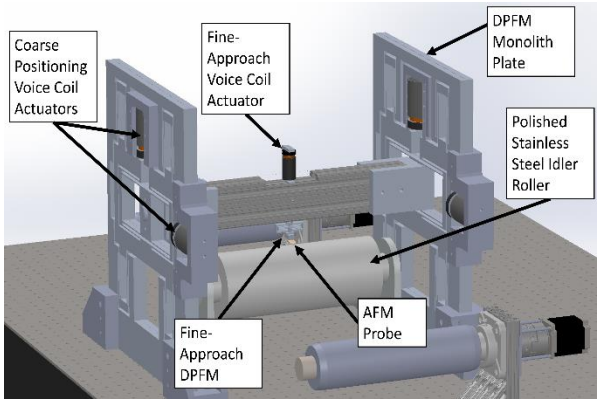

FIGURE 4. Metrology Subsystem

another by an extruded aluminum bar as can be seen in Fig. 4. This will provide coarse positioning of the AFM array which is held in the same bar. This system will move the AFM chips in the X and Z directions to within 200 µm of the web line and hold them with a high degree of stability, providing isolation from external disturbances by means of the proposed DPFM monolithic and a voice coil actuator (MotiCont, LVCM-051-064-02) with position feedback provided by high accuracy capacitance probes (CPL290, LION Precision). The fine approach of the AFM will be provided by the actuation of a Fine-Z DPFMs as shown in Fig. 4. This will be separately controlled by an independent voice coil actuator (MotiCont, LVCM-025-038-01). Feedback will be provided by strain gauges mounted on each individual Fine-Z flexure beam and calibrated to the same accuracy as the capacitance probes. This will allow for real-time, individual adjustment of each AFM such that the ideal separation distance between the AFM and web is maintained; that the chip remains within the MEMS vertical thermoelectric actuation systems' range of 10 µm.

Finally, the vertical and horizontal actuation system in the AFM devices will scan each

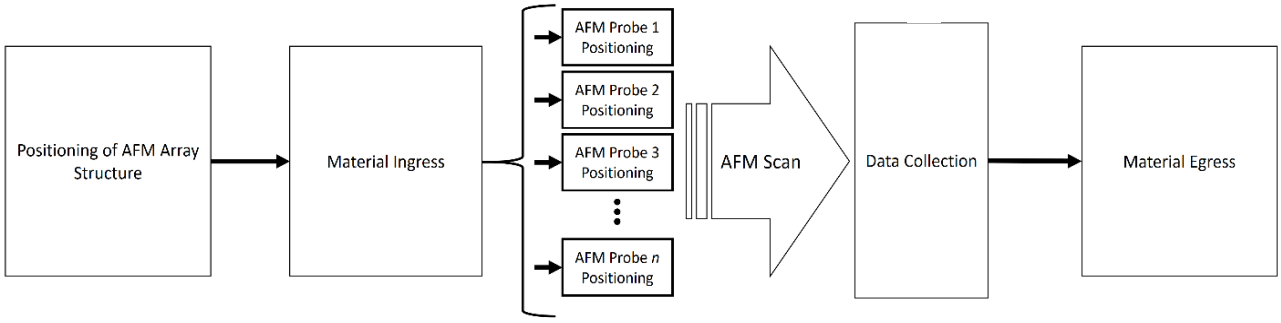

FIGURE 3. System Flow Schematic of Probe Positioning Division of Labor

cantilever tip in a non-contact “tapping” mode to determine surface topology data. This allows for three separate, compound levels of isolation from any outside disturbances insuring optimal data collection.

DESIGN OF COARSE XZ POSITIONING

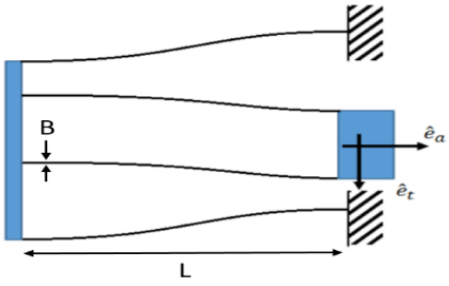

FIGURE 5. *DPFM Geometry*

MECHANISM

The double-monolith, coarse XZ positioning system is parametrically designed using a lumped-spring modeling approach, shown in equations (1) through (4) depicting the calculation for both stiffness and maximum range [4]–[6]. Here *E* represents the material’s Young’s Modulus, *I* the moment of inertia, and *k* as the equivalent stiffness in the spring model. The flexure parameters *L, B*, *H* and *FOS* represent the flexure beam length, width, depth and factor of safety respectively, as shown partially in Fig. 5.

$$EI\,Y'' = M + FL \tag{1}$$

$$k_y = \frac{24EI_x}{L_x^3} \tag{2}$$

$$k_x = \frac{48EI_y}{L_y^3} \tag{3}$$

$$\mathrm{Disp_{Max}} = \sigma_y * \frac{L^2}{3E*h*FOS} \tag{4}$$

Based on this parametric analysis the following parameters are chosen for the proposed design.

Parameter	Value	Parameter	Value
L_X	80 mm	K_X	46,144 N/m
L_Z	95 mm		
H_X	25.4 mm	K_Z	32,659 N/m
H_Z	25.4 mm		
B_X	1.5 mm	Maximum Range (X)	2.8 mm
B_Z	2 mm		
FOS	3	Maximum Range (Z)	4.18 mm

TABLE 1. *Design Parameters for Coarse Flexure Monolith*

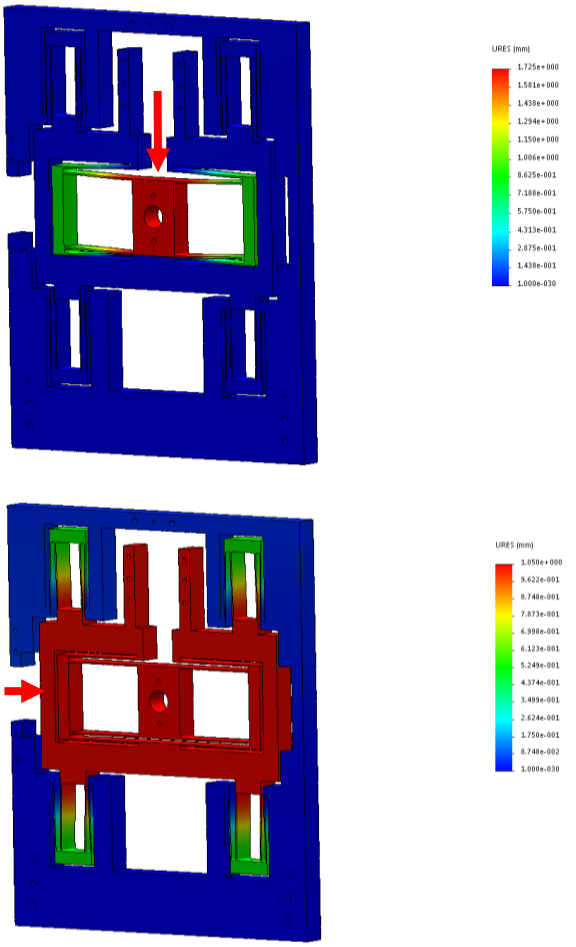

FIGURE 6. *Static FEA Results of Coarse Z Flexure Actuation*

This design will enable both accurate positioning of the mounting-bar holding the array of AFM chips while also providing a large enough range of motion to ensure that the AFM tips never passively contact the web line in a destructive manner.

Further, the resonant modes of this design are evaluated by FEA to ensure that the system could operate at a frequency high enough to accurately position the AFM array. Simulation results show that the lowest resonant modes for the X and Z flexures are 23.10 (Mode 1) and 48.83 Hz (Mode 3) respectively, indicating low levels of mechanical vibration when compared to typical long-range DPFM stages with resonance below 10 Hz.

An additional FEA study is conducted to measure and confirm the static displacement of the stage

in response to the maximum force provided by the voice coil actuator and evaluate the maximum stress found in the flexure beams by means of the Von Mises' criteria. The results of this study is shown in Fig. 6. This gives a maximum range in the Z direction of 1.435 mm and a maximum range in the X direction of 0.75 mm given the chosen actuators which is within the design requirements. The study found that the maximum stress which occurs in both the X and Z flexure beams is within the FOS of three with respect to the materials Yield strength [7].

By taking the simulated displacement and the given actuation force the values for flexure hinge spring constant, *k,* can be calculated from the FEA studies with Eq. 5.

$$k = \frac{\text{Force}}{\text{Displacement}} \tag{5}$$

In comparision to the parametrically calculated values, k_Z is found to be within 7%, an aceptable amount of varience. k_X is found to be off by roughly 24%. It is thought this is most likely due to non-linearites in the DPFMs not captured within the lumped-spring modeling approach. Moreover it is believed that this error is more significant in the X-direction than the Z-direction because there are four complete DPFM geometries as opposed to just two, and thinner flexure beams by 0.5 mm amplify the effect of constant radius fillets added between the flexure beams and lands to enable accurate waterjet manufacturing. However, these suspcions have not been accurately modeled or confirmed.

DESIGN OF FINE Z POSITIONING MECHANISM

An additional design incorporating a symmetric DPFM controls the fine adjustment of AFM position in the Z-axis. This flexure provides nanometer scale positioning of the AFM once it is moved to within 200 µm of the web line. The beam depth is limited to 10 mm to conform to space constraints, and beam thickness is limited to the 0.5 mm minimum achievable resolution of the waterjet machine used to fabricate the flexures. The design of this DPFM is optimized to provide better than 10 nm of accuracy in Z position, constrained primarily by the amount of noise present in the voice coil amplifier (Apex Microtechnology, PA02A) [6].

An additional static displacement FEA study in response to an 8 N actuation force is conducted

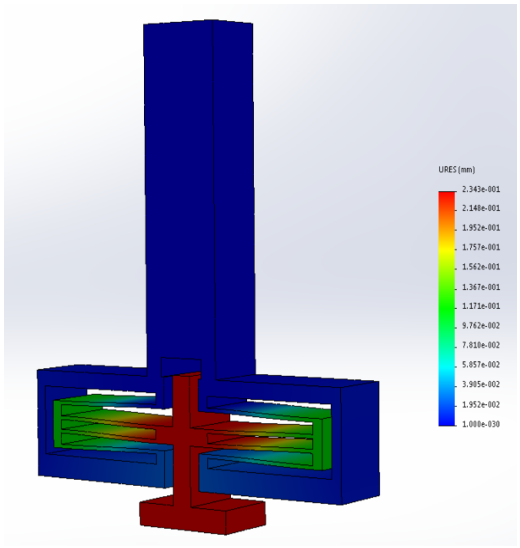

FIGURE 7. *Static Disp. of Fine-Z Flexure*

to confirm the stiffness and range of the flexure mechanism as shown in Fig. 7. The maximum stress present in the flexure beams (Von Mises criteria) is also measured and found to be within a safety factor of three when made of the proposed 7075-T6 aluminum [7]. The actuation force generates a maximum displacement of 0.234 mm, which is acceptable for the proposed design.

PRELIMNARY RESULTS

Initial evaluation of the metrology subsystem brought split results. Fig. 8 shows the error in individual motion axis of each DPFM monolith as the system moves in a 100 µm diameter circle.

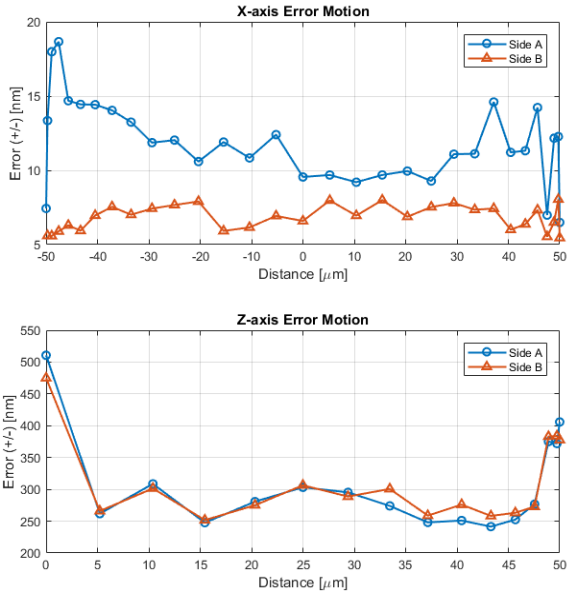

FIGURE 8. *DPFM Monolith Error Motion during 100 µm diameter circular movement*

Firstly, the X-axis motion of each DPFM monolith performs at a high repeatability and low noise with the mean error in the X-axis recorded at ± 9.4 nm. The motion in the Z-axis of the DPFM monoliths is less than favorable during initial testing with an average error level of ±307.6 nm.

After evaluating potential electrical and building sources of noise, it was discovered that a misalignment in fixturing brackets led to an undesirable pre-load in the Z-axis DPFMs. This out-of-plane preloading will significantly lower the level of damping, and thus raise levels of mechanical noise in DPFMs. Through a careful alignment of DPFM monolith mounting hardware, the Z-axis mechanisms perform at a level commiserate with the X-axis.

ACKNOWLEDGMENTS
The authors would also like to thank Tsung-Fu Yao, Nilabh Roy, and Ian Lander for the many informative discussions that helped to shape this work. This material is based upon work supported by the National Science Foundation Graduate Research Fellowship program under Grant No. 2017251210. Any opinions, findings, and conclusions or recommendations expressed in this material are those of the authors and do not necessarily reflect the views of the National Science Foundation.

REFERENCES
[1] A. Nathan *et al.*, “Flexible electronics: The next ubiquitous platform,” *Proc. IEEE*, vol. 100, no. SPL CONTENT, pp. 1486–1517, 2012.
[2] N. Sarkar, G. Lee, and R. R. Mansour, “CMOS-MEMS dynamic FM atomic force microscope,” in *Transducers 2013*, 2013, no. June, pp. 916–919.
[3] T.-F. Yao, A. Duenner, and M. Cullinan, “In-line metrology of nanoscale features in semiconductor manufacturing systems,” *Precis. Eng.*, 2016.
[4] N. Roy and M. Cullinan, “Design of a Flexure Based XY Precision Nanopositioner with a Two Inch Travel Range for Micro-Scale Selective Laser Sintering,” *Proc. Annu. Meet. Am. Soc. Precis. Eng. 31st Annu. Meet.*, pp. 1–2, 2016.
[5] X. Zhou, D. Wang, J. Wang, and S. C. Chen, “Precision design and control of a flexure-based roll-to-roll printing system,” *Precis. Eng.*, vol. 45, pp. 332–341, 2015.
[6] S. Awtar and G. Parmar, “Design of a Large Range XY Nanopositioning System,” *Vol. 2 34th Annu. Mech. Robot. Conf. Parts A B*, vol. 5, no. May 2013, pp. 387–399, 2010.
[7] MIL-HDBK-5H, “METALLIC MATERIALS AND ELEMENTS FOR AEROSPACE VEHICLE STRUCTURES,” December, 1998.

DESIGN OF A PRECISION, ACTIVE, HIGH-STRAIN COMPOSITE (HSC) HINGE

Michael A. Echter[1,2], Mark J. Silver[3], and Michael E. Peterson[4]
[1]**Structural & Thermal-Fluids Engineering**
Massachusetts Institute of Technology Lincoln Laboratory
Lexington, MA, USA
[2]**Department of Mechanical Engineering**
University of Rochester
Rochester, NY, USA
[3]**Advanced Capabilities and Technologies**
Massachusetts Institute of Technology Lincoln Laboratory
Lexington, MA, USA
[4]**Space Vehicles Directorate**
Air Force Research Laboratory
Kirtland AFB, NM, USA

INTRODUCTION

The Deployable In-Space Coherent Imaging Telescope (DISCIT) research effort at MIT Lincoln Laboratory seeks to develop scalable technologies for enabling deployable large aperture imaging telescopes in a small-sat or CubeSat form factor. The initial demonstration is aimed at the CubeSat form factor, with a 0.7 m deployable sparsely filled primary mirror array. A schematic of the baseline sparse-aperture design for DISCIT is shown in Figure 1. The primary mirror segments will be deployed and initially positioned using high-strain composite (HSC) hinges, with piezoelectric actuation methods being researched to facilitate phasing the individual mirror segments for optical alignment. This capability, in concert with the HSC hinges, creates a novel optomechanical design that permits precise positioning within a deployable, active structure.

A system such as DISCIT could provide affordable, high-resolution, persistent space-based imaging in a low-SWaP (size, weight, and power) design over existing technologies. A key challenge with deploying a sparsely filled primary in an imaging telescope is the precision required to collocate the mirror segments relative to the other optical components. DISCIT addresses this in two steps: (1) the primary mirror segments are deployed and coarsely positioned using flexible composite hinges to achieve better than ± 5 μm piston and axial positional repeatability and ± 50 μrad pitch and roll angular repeatability, and (2) the mirror segments are then phased using piezoelectric actuators that accomplish the final precision alignment of the optical system. With this second fine correction step the composite hinges only need positional and angular repeatability within the capture range of the piezoelectric actuators.

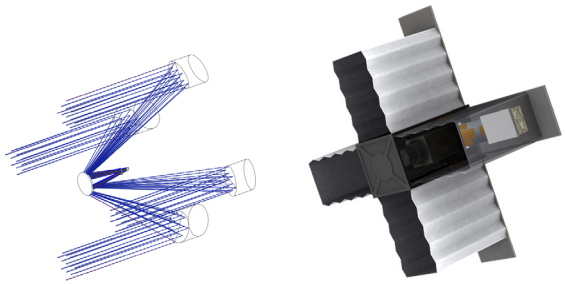

FIGURE 1. Cartoon of sparsely filled primary optical design (a) and CubeSat concept (b). One baffle is transparent to show the sparse aperture.

The HSC hinge under development at MIT Lincoln Laboratory is shown in Figure 2 in the deployed and stowed states. The hinge consists of two thin-shell composite laminates fixed at either end, creating a stiff structural member approximately 85 mm wide with a free-edge length of 300 mm. When the hinge is buckled in the center by squeezing the two laminate tapes together, the tip of the hinge where a mirror would be mounted can be folded back toward the fixed root. A cus-

DISTRIBUTION STATEMENT A. Approved for public release: distribution unlimited.

tom laminate is needed to withstand the large, localized strains when folded but still achieve the required positional and angular repeatability following a stow cycle.

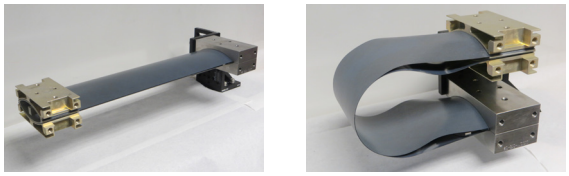

(a) (b)

FIGURE 2. Photographs of a HSC test hinge in the deployed (a) and stowed (b) states.

This paper presents a developmental overview of the flexible composite hinges used to deploy the primary mirror segments, examining materials testing for determining the elastic properties of the laminate. For performing the final precision alignment of the deployed hinge tip, placement of Macro Fiber Composite patch actuators bonded to the hinge laminates in a specific arrangement will be discussed. These bonded actuators induce in-plane strains and enable a low-SWaP design for multi-DOF active alignment of the primary mirror segments. For developing the actuator layout a finite element model is used, incorporating the elastic properties determined through the materials testing, to optimize the placement of the Macro Fiber Composite patch actuators for achieving the necessary levels of isolated piston, pitch, and roll actuation for optical alignment.

MATERIALS TESTING

In order to create a finite element shell model to develop the multifunctional HSC hinge, the elastic properties are needed for defining the laminate. The orthogonal elastic moduli, Poisson's ratio, and shear modulus define the bulk laminate properties for a balanced and symmetric laminate [1]. The elastic moduli and Poisson's ratio were acquired from traditional tensile tests of laminate specimens in orthogonal directions, while the shear modulus was acquired from a 45° off-axis tensile test. The laminate characterization incorporated a digital image correlation technique for measuring strain, and micrographing of laminate cross sections for qualitative inspection of the test specimens.

Testing Parameters

The laminate being used in this research is a four-ply balanced and symmetric $[\pm 45^\circ/0^\circ]_s$ layup of JPS AstroQuartz II 525 plain weave (AQ-PW) exterior plies oriented at $\pm 45^\circ$ and two unidirectional carbon fiber IM10 (IM10-UD) interior plies at 0° impregnated with Patz PMT-F7 epoxy resin, a cartoon of which is shown in Figure 3. This laminate layup sequence has been shown with similar materials by Peterson and Murphey [2] and was chosen to balance several requirements for high-strain composite hinges, tailoring the laminate to take advantage of the properties associated with the two lamina types. The central unidirectional plies provide high axial and bending stiffness, and resist creep when the laminate is held in a flexured state. Since unidirectional plies alone have a low transverse strength, the exterior plain weave plies at $\pm 45^\circ$ help prevent the unidirectional plies from failing during bending by adding shear and bending stiffness. The plain weave plies also add torsional stiffness to the laminate versus a purely unidirectional laminate, which is important for open cross section structures such as HSC hinges.

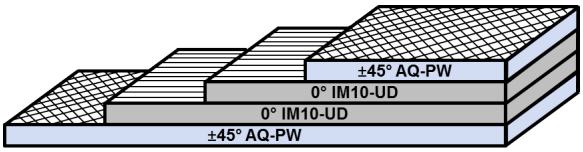

FIGURE 3. $[\pm 45^\circ(a)/0^\circ(b)]_s$ – Four-ply balanced and symmetric layup of AstroQuartz (a) plain weave fabric and IM10 (b) unidirectional carbon fiber laminae.

The ASTM D3039/D3039M standard was used to define the tensile testing parameters and laminate coupon specifications [3]. The laminate under evaluation in this research is best suited by this standard, which addresses the determination of tensile properties of polymer matrix composite materials reinforced by high-modulus fibers for balanced and symmetric laminates. Based on the tensile specimen testing and geometry requirements outlined in the standard, five coupons 85 mm long by 13 mm wide were prepared at 0° (axial) and 90° (transverse) each and five coupons 108 mm long by 12.5 mm wide at 45° (shear) to determine the effective elastic properties of the bulk laminate. End tabs are not required by the standard and were not incorporated in this testing since the pneumatic grippers used to hold the coupons during testing had a serrated interface. The length of the coupons was selected to minimize effects from the grippers, providing a uniform gauge region for measuring strain over

an approximately 10 mm square in the center of the coupons. The grippers for all testing held the coupons 20 mm at the ends at 40 psi and pulled at 1 mm/min.

An Instron 5944 tabletop testing system and 2 kN load cell were used with an Instron AVE (Advanced Video Extensometer) to perform strain measurements by capturing high frame rate images of the samples under test for post-processing. Instead of using a clip-on extensometer that can only measure strain in one orientation, or a traditional strain gauge rosette, the AVE allows a non-contact measurement to be performed by analyzing the captured images and comparing reference features frame-by-frame to calculate strain. Figure 4 shows an example of the speckle pattern that was used on the test specimens for performing the digital image correlation technique; black and white spray paints were used to create the speckle pattern by lightly misting the paints over the sample and produce the stochastic, non-repeating structure.

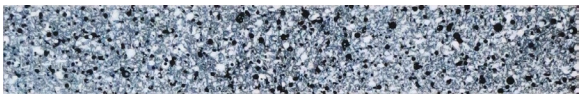

FIGURE 4. Example of the speckle pattern on the test specimens used for the digital image correlation strain measurements.

Following a tensile test the load cell data and images captured by the AVE were post-processed using Instron's DIC-Replay software. A virtual strain gauge was used to bound the measurements to a square region in the center of the specimen in order to minimize edge effects from the sample holder grips [4]. The strains measured within this region were then used in conjunction with the load cell data to produce the stress-strain data for each test specimen, and were exported for further post-processing and analysis in MATLAB to calculate the effective elastic properties of the bulk laminate.

Determination of Elastic Properties

As previously described, five coupons 85 mm long by 13 mm wide were prepared at 0° (axial) and 90° (transverse) each to determine the longitudinal modulus E_1, transverse modulus E_2, and Poisson's ratio ν_{12} of the bulk laminate. For determining the shear modulus G_{12}, five coupons 108 mm long by 12.5 mm wide were prepared at 45° for an off-axis tensile test. Each coupon was cut from a larger parent laminate using a guillotine cutter, ensuring all free-edges were clean cuts and consistent coupon-to-coupon. The width and thickness of each coupon were measured using a Mitutoyo MDC-1 SB digital flat anvil interface micrometer with a resolution of 0.001 mm and instrument accuracy of $\pm$0.002 mm, both within the tolerance outlined in the ASTM D3039/D3039M standard. The coupons were measured in five locations along the length and averaged for determining the widths and thicknesses used as inputs to Instron's Bluehill testing software for calculating laminate stresses throughout the tests.

The stress and strain data were output from Instron's DIC-Replay software for post-processing in MATLAB. Figure 5 shows an example of typical stress-strain curves, in this case for the axial laminate coupons for determining the longitudinal modulus. The raw data are plotted for each coupon with a linear best fit over the initial strain range. The slopes of the stress-strain fits were used for determining the elastic modulus for each coupon, which were then averaged for a final value. The longitudinal elastic modulus was determined to be $E_1 = 110.6$ GPa, and the transverse elastic modulus $E_2 = 9.6$ GPa. Poisson's ratio was determined in a similar manner by plotting the longitudinal and transverse strains from the axial strain data. A linear fit was again used over the same initial strain range for each coupon and the slopes averaged to determine a Poisson's ratio of $\nu_{12} = 0.489$.

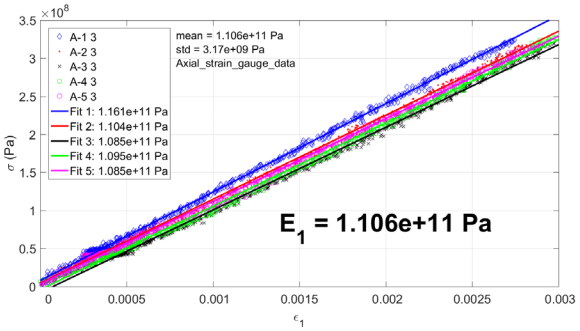

FIGURE 5. MATLAB post-processing of axial stress-strain data for determining E_1.

Fowser et al. showed that for balanced and symmetric laminates the effective laminate shear modulus G_{12} could be determined by performing a 45° off-axis tensile test and using the equation

$$G_{12} = \frac{E_x}{2(1+\nu_{xy})}$$

where E_x is the elastic modulus and ν_{xy} the Pois-

son's ratio in the off-axis testing orientation of 45° [5]. The same method of applying a linear fit over the initial strain range and averaging the slopes was used to determine the off-axis longitudinal modulus to be $E_x = 15.2$ GPa and the off-axis Poisson's ratio to be $\nu_{xy} = 0.307$. Using the aforementioned equation, the effective laminate shear modulus was calculated to be $G_{12} = 5.81$ GPa.

Cross-sectional Micrographing

In addition to quantitative material testing, a qualitative inspection method of the laminate coupons has been developed. Cross-sectional micrographing samples of the coupons were prepared after tensile testing by potting small specimens of the laminates in 30 mm Struers FixiForms using Struers EpoFix epoxy resin; three micrographing samples of five specimens were potted corresponding to the axial, transverse, and shear coupons. The coupons were held vertical in the forms with Struers MultiClips to properly orient the laminates for sectioning, grinding, polishing, and inspection.

After the samples were cured and removed from the FixiForms, a Struers Minitom low-speed precision cut-off machine was used with a Struers 330CA high concentration diamond cut-off wheel to section the samples. The work pieces were planarized using a Lapmaster 12 with 600 grit silicon carbide abrasive and oil-based Lapmaster Lapping Vehicle #6 in a 1:20 ratio. Following planarization Hyprez 6 μm and 2 μm diamond slurries were used to gradually polish the surfaces on soft tin-lead metal laps. Transition from the 6 μm slurry to the 2 μm slurry would occur only after visual inspection of each work piece under a microscope, observing qualitatively for homogeneity of the finish before proceeding. For the final polishing step the samples were held to a Politex Reg II 08 black felt pad adhered to an Ultra Tec polishing machine and saturated with Syton HT 50 colloidal silica and filtered water. The final polished micrographing samples are shown in Figure 6 for the axial, transverse, and shear laminate specimens.

The primary motivation for developing micrographing capabilities was to examine the consistency of the specimens, verifying proper consolidation of the laminae. To examine the laminate cross-sections, a Nikon Epiphot 200 inverted metallurgical microscope was retrofitted with a Thorlabs DCU224M CCD camera for capturing micro-

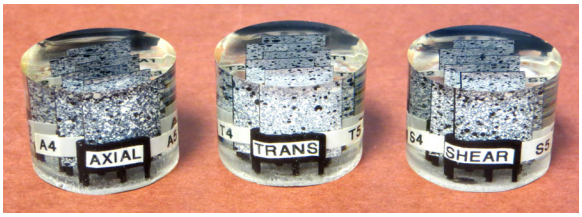

FIGURE 6. Potted and polished micrographing samples of the laminate coupons from the axial, transverse, and shear tensile testing.

graphs using the open source microscopy software μManager. The camera was calibrated using a micrometer calibration slide to permit measurements to be made in μManager for comparing laminate thickness measurements with the micrometer measurements previously described. Figure 7 shows 20X micrographs of the axial, transverse, and shear specimens from the tensile testing coupons. The axial specimen clearly shows the ends of the IM10-UD fibers in the center of the laminate, while the transverse specimen shows these fibers along their length. In the shear specimen micrograph the AQ-PW exterior plies show both longitudinal fibers and fiber ends due to the 45° orientation of these plain weave laminae. The epoxy matrix of the laminates is visible in all three micrographs, bounding the fibers closely at the exterior plies inside the darker potting resin visible at the edges.

ACTIVE HSC HINGE DESIGN

The hinge design for this research was developed on a similar scale to a cube-sat architecture for demonstrating the technology until the size and packaging requirements for a final system are established. The flat width of the laminate tapes in the hinge design was set at 85.0 mm, which corresponds to the separation distance of the side rails on a standard cube-sat with clearance, allowing the hinge to be folded and stow within a cube-sat volume; the free-edge length of the tapes was set at 300 mm, or the length of a 3U cube-sat. An oversized layup was consolidated on a 15.2 cm diameter cylindrical mandrel with the 0° direction of the laminate oriented along the length of the mandrel, which is also along the length of the hinge. The tapes for the test hinge were cut to the final 85.0 mm flat width and full length of 400.8 mm using a guillotine cutter, after which the sharp edges were lightly sanded for safer handling. Two holes were punched at each end for locating the midline of the tapes and aligning with the end brackets during hinge assembly.

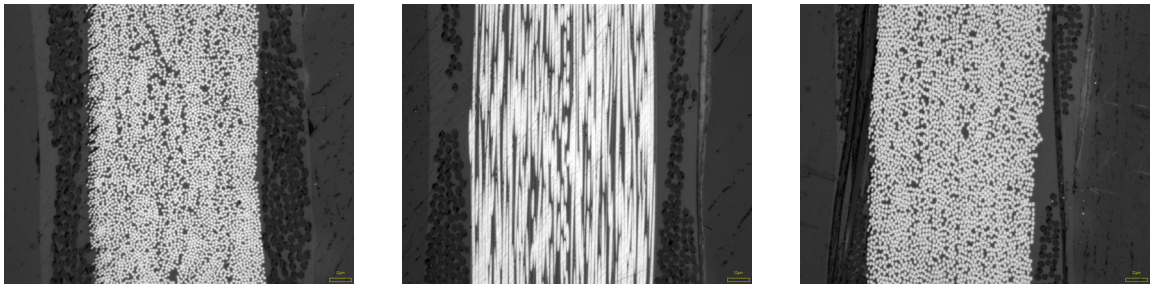

(a) (b) (c)

FIGURE 7. Micrographs of axial (a), transverse (b), and shear (c) cross-sections at 20X magnification.

The tip brackets were fabricated from aluminum and light weighted to minimize gravity loading effects on the creep recovery after deployment, while the root brackets were fabricated out of Invar to minimize thermal effects on the deployment positional repeatability. To set the spacing and alignment of the components for the 300 mm free-edge length, a dedicated assembly fixture with pins was used to interface with the clearance holes in the end brackets and tapes. A single bonding operation was implemented for assembling the end brackets and laminate tapes using Hysol EA 9394 epoxy with 178 μm glass beads to enforce a uniform bondline thickness.

Actuator Placement

In order to determine where best to place patch actuators on the laminate tapes, a finite element model was created to examine high strain regions corresponding to discrete degrees of freedom for alignment. An ABAQUS shell model using the elastic properties determined through the materials testing was developed of the hinge tape geometry previously described. Constraints were used at the root and tip with reference points for applying boundary conditions and loads to, with the root fixed in all six degrees of freedom. Three load cases were examined – piston, pitch, and roll to represent the three degrees of freedom to be controlled by the actuators. Displacements and rotations for each load case were applied at the tip reference point to induce strains in the model. Plots of the resulting strain energies are shown in Figure 8 for each degree of freedom motion.

The results from the finite element analysis were imported into a custom MATLAB actuator placement algorithm to perform a search of the strain components to determine the most efficient placements for the patch actuators by locating the actuators in the regions of highest strain, tak-

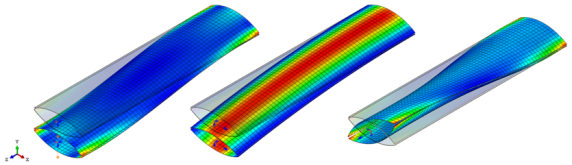

FIGURE 8. (left to right) FE model strain energy results for induced piston, pitch, and roll motions.

ing into consideration the sizes and number of patches desired [6, 7]. Macro Fiber Composite actuators from Smart-Material Corp. were selected for their anisotropic actuation and conformal properties, with two sizes identified for placement optimization through the algorithm. Figure 9 shows the actuator placements determined by the algorithm corresponding to the piston, pitch, and roll finite element analyses. Using these results and qualitative knowledge of how the hinge folds – that it gets bucked in the middle and experiences a large curvature change – the final layout selected for experimental testing was established.

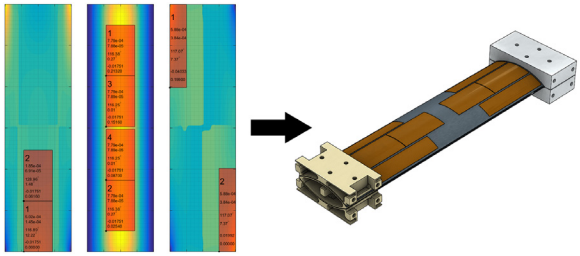

FIGURE 9. (left to right) MATLAB actuator placement algorithm results for piston, pitch, and roll motions; CAD model of selected actuator layout.

The actuators were bonded in four groups to a HSC hinge using a vacuum bagging technique. The regions where the actuators were to be bonded were first masked off and a layer of 3M DP460 high-shear high-peel strength epoxy was

spread over the laminate. The Macro Fiber Composite actuators were then positioned and silicone pads were placed on top to aid in compression while under vacuum. Lenticular spacers were inserted between the laminates in the hinge to prevent the tapes from buckling under the vacuum during the room temperature cure. Once all of the actuators had been bonded, electrical leads were soldered to the actuators and wired to breakout boxes located at the root to complete the active HSC hinge assembly shown in Figure 10.

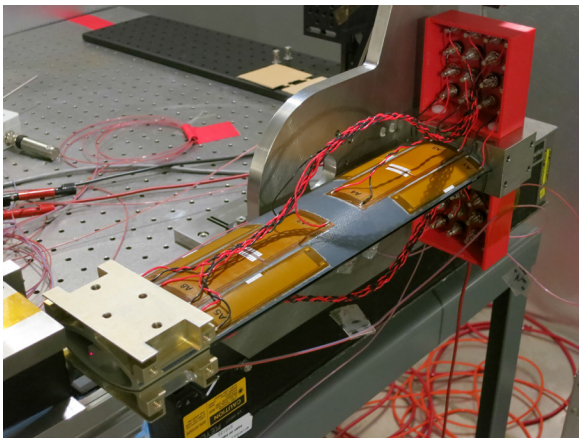

FIGURE 10. Completed active HSC hinge.

PRELIMINARY RESULTS

Using the testing apparatus from previous work by the authors [8], the active HSC hinge performance will be characterized. Preliminary measurements of the deployment repeatability have demonstrated better than ± 5 µm piston and axial positional repeatability and ± 50 µrad pitch and roll angular repeatability, showing similar deployment performance to HSC hinges without Macro Fiber Composite actuators bonded to the tapes. Testing of individual actuators have shown actuation ranges that greatly exceed the deployment repetabilities, which will allow for post-deployment correction for optical alignment. Further measurements are required to fully characterize the accuracy, resolution, repeatability, and ranges for both open- and closed-loop positioning of each degree of freedom.

ACKNOWLEDGMENTS

The authors would like to thank Todd Mower, Ethan Parsons, and Jon Schoenenberger for their discussions on materials testing methodologies, and Jack Brinkerhoff for his contributions developing the micrographing polishing technique.

DISTRIBUTION STATEMENT A. Approved for public release: distribution unlimited. This material is based upon work supported by the Assistant Secretary of Defense for Research and Engineering under Air Force Contract No. FA8721-05-C-0002 and/or FA8702-15-D-0001. Any opinions, findings, conclusions or recommendations expressed in this material are those of the author(s) and do not necessarily reflect the views of the Assistant Secretary of Defense for Research and Engineering.

REFERENCES

[1] Barbero EJ. Finite element analysis of composite materials using AbaqusTM. CRC press; 2013.

[2] Peterson ME, Murphey TW. Large deformation bending of thin composite tape spring laminates. In: 54th AIAA/ASME/ASCE/AHS/ASC Structures, Structural Dynamics, and Materials Conference; 2013. p. 1667.

[3] ASTM. Standard test method for tensile properties of polymer matrix composite materials. ASTM D3039/D3039M. 1995;.

[4] Pagano N, Halpin J. Influence of end constraint in the testing of anisotropic bodies. In: Mechanics of Composite Materials. Springer; 1994. p. 2–16.

[5] Fowser SW, Pipes RB, Wilson DW. On the determination of laminate and lamina shear response by tension tests. Composites Science and Technology. 1986;26(1):31–36.

[6] Gupta V, Sharma M, Thakur N. Optimization criteria for optimal placement of piezoelectric sensors and actuators on a smart structure: a technical review. Journal of Intelligent Material Systems and Structures. 2010;21(12):1227–1243.

[7] Bachmann F, Bergamini AE, Ermanni P. Optimum piezoelectric patch positioning: A strain energy–based finite element approach. Journal of intelligent material systems and structures. 2012;23(14):1575–1591.

[8] Silver MJ, Echter MA, Reid BM, Banik J. Precision High Strain Composite Hinges for the Deployable In-Space Coherent Imaging Telescope. In: AIAA SciTech Forum. American Institute of Aeronautics and Astronautics; 2016. p. 0969.

AN INSTRUMENT TO MEASURE TEMPORAL STABILITY OF SPRING COMPRESSION FORCE

Adam W. Jaycox [1],Kevin M. Lawton[2], Steven R. Patterson[2]
[1]Lawrence Livermore National Laboratory
Livermore, CA
[2]Mechanical Engineering and Engineering Science Department
University of North Carolina at Charlotte
Charlotte, NC

INTRODUCTION

Mechanisms incorporating loaded springs to provide a known force over long periods of time must account for the potential of stress relaxation leading to a change in spring force and concomitant change in mechanism performance. If the intended period of operation is many years, it is impractical to test springs for a period equal to the lifetime of the mechanism in order to determine the adequacy of the design. Instead, the force of the spring at a precisely known deflection must be measured over a shorter period of time but to a much higher degree of precision than that required by the mechanism, and the results combined with an appropriate constitutive model to predict performance of the spring over the mechanism lifetime.

Methods for making such measurements [1, 2] have typically required the long-term dedication of an instrument for each measurement made. This makes it difficult to gather statistical data regarding constitutive model parameters or create experimental designs with parameter variation. To address this limitation, an instrument for measuring the force relaxation of springs has been developed which does not require the continuous presence of the spring in the instrument. Instead, springs are mounted in a removable carrier that maintains loading when removed from the instrument.

The instrument is intended to measure multiple test samples and provide sufficient precision of force and deflection measurement that spring force variations in service can be forecast over periods that exceed the measurement window by at least an order of magnitude. This requires sub-micrometre deflection control and force measurement with a resolution of several parts in 10^5.While the instrument is designed to accommodate a range of potential spring loads, the initial testing has been carried out with a nominal load of $100\,\mathrm{N}$.

INSTRUMENT DESIGN

The measurement system comprises a simple carrier for the spring which maintains load when the carrier is not undergoing measurement, and a high precision compression dilatometer that measures the current spring force with minimum perturbation of its loading. In the ideal case, the spring dimension would be maintained by an adjustable load while the carrier constraint was removed and the load transferred to the dilatometer. However, this would require a considerably more complex carrier, raising the cost and difficulty of measurements. Instead, a fixed passive carrier is used and a high sensitivity measurement assures that a very small dimensional change is required to transfer the load.

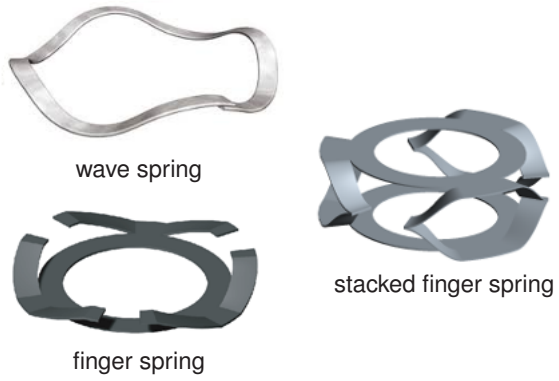

FIGURE 1. Springs used for initial testing

The initial spring carrier was designed to accommodate a class of circular leaf springs illustrated in figure 1. The stacked finger springs are an attempt to minimize the potential effect of friction due to lateral motion at the feet of the spring by stacking two springs symmetrically. Springs were chosen which compress to a nominal height of 1 mm to 2.5 mm when subjected to loads in the

range of 50 N to 100 N. The nominal elastic axis of these springs lies on their center of symmetry. However, as will be discussed later, variations in geometry may result in a small decentration of the elastic axis. Springs used for initial testing were fabricated from carbon steel.

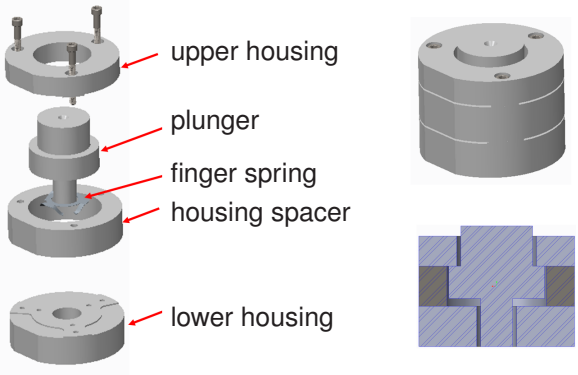

FIGURE 2. Carrier used to constrain the spring during storage and measurement.

The design of the spring carrier is shown in figure 2. The components of carrier are machined from 17-4PH stainless steel (UNS S17400) which is subsequently age hardened before grinding. The housing spacer is ground flat and parallel The corresponding surfaces on the upper and lower housing have machined reliefs leaving three pads to provide a semi-kinematic mounting surface which is then ground flat. The carrier is then assembled with a strong preload in place of the spring and the lower surface of the assembly is ground so that the lower housing and end of the plunger lie in the same plane. The carrier is then reassembled with the spring. The degree of compression used for the test is determined by the dimension of the spacer. Because the cross section of the load path through the spacer is much larger than that of the attaching screws, strain relief of the screws has a negligible influence on the spring compression. Diametrical clearance between the plunger and the housing assures that when the plunger is not resting on the upper housing, the entire load is carried by the spring with no friction effects.

During operation, an increasing load is applied to the top of the plunger until the top of the plunger flange disengages from the upper housing. This load value then represents the current force exerted by the spring. Disengagement is determined by observing the relationship between applied load and the displacement of the bottom of the plunger relative to the bottom of the lower housing. During this measurement process, the dimensional change in spring compression is limited to the value required to overcome the elastic deformation of the carrier and the solid interface at the flange.

The compression dilatometer, then, comprises two major subsystems: a measurement system located below the carrier, and a precision loading system above it. The loading system in turn comprises a set of passive weights that provide the majority of the load and a computer-controlled adjustable loading mechanism to provide controlled small changes in load about the nominal spring force. By using such a hybrid loading approach, the force uncertainty of the adjustable mechanism is a much smaller fraction of the total load than would be the case with a single adjustable load.

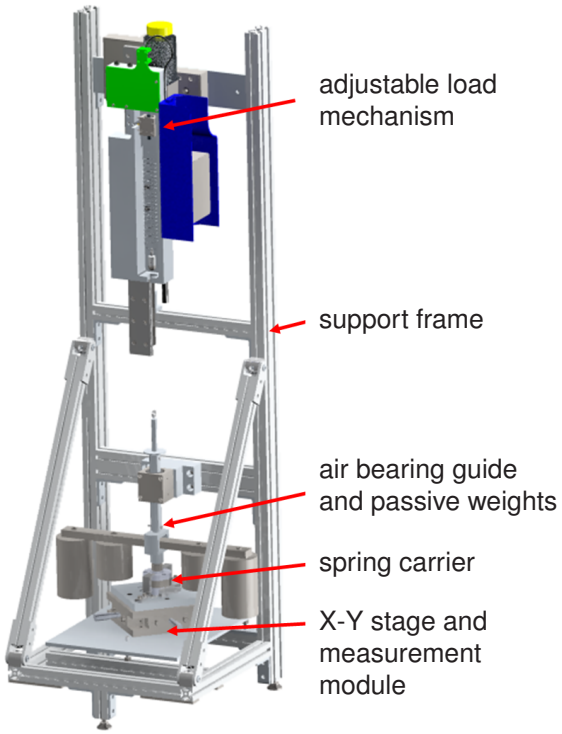

FIGURE 3. Overall design of the compression dilatometer. The measurement system is not shown, as it is completely enclosed by the X-Y stage.

The overall arrangement of the instrument is shown in figure 3. The line of action of the loading mechanism and measurement unit are collinear. The spring carrier is mounted to an X-Y stage which allows the elastic axis of the spring (which

may not exactly coincide with the mechanical center line of the carrier) to be positioned on the instrument axis. The passive weights are arranged symmetrically around a linear air bearing which defines the line of action of the loading mechanism. The weight assembly is connected to the adjustable loading mechanism by a wire.

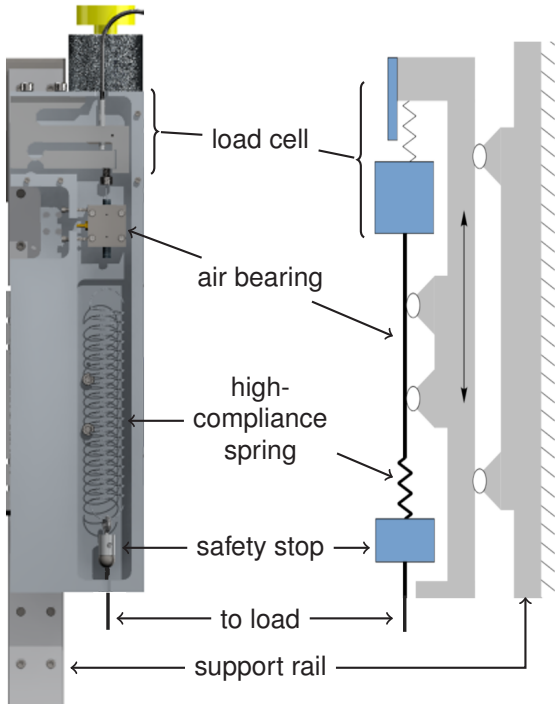

FIGURE 4. Adjustable load mechanism.

The adjustable load mechanism rides on a linear slide and is positioned by a stepper-motor-driven leadscrew with a 5 µm resolution. A high compliance (25 mN/mm) spring connects the load cell to the weight assembly, providing a variable loading resolution of 125 µN. Given a nominal load of 100 N, this provides the capability to resolve relative stress relaxation of 1.25×10^{-6}. When the mechanism is in the fully up position, the safety stop engages the bottom of the housing and the weight assembly is fully supported from the load mechanism. Driving the stepper motor allows the weight assembly to be controllably lowered until it rests on the spring carrier plunger. As long as the weight of the weight assembly less the tension from the fully extended high compliance spring is smaller than the force required to further compress the spring, there will be no motion of the plunger. As the load mechanism is further lowered, the high compliance spring extension is reduced and the net force on the spring carrier smoothly increases. The stepper motor is computer-controlled to increase the load until a predetermined extension of the plunger with respect to the lower spring carrier housing is achieved. The value of the variable load is measured by a single-beam flexure load cell fabricated from hardened A2 tool steel. The beam deflection is measured with a Philtec model μDMS-RC25 non-contact fiber-optic transducer. The calculated maximum stress in the supporting flexure is 81 MPa, a small fraction of the yield strength of the material.

The measurement system, shown in figure 5, comprises a high-resolution capacitance gauge mounted in a reference assembly which is spring-loaded upwards and supported by flexures that fix the lateral position of the reference assembly but allow angular motion of its front face. That front face is fitted with three balls that rest against the flat bottom surface of the lower spring carrier housing so that the capacitance gauge returns a measurement of the plunger extension with respect to the bottom surface which is minimally influenced by any strain that may occur in the load path.

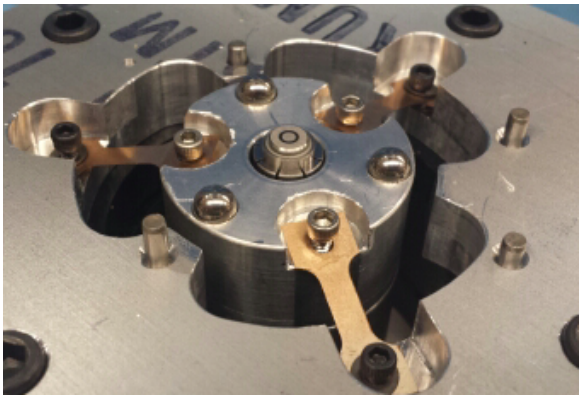

FIGURE 5. Measurement probe assembly showing capacitance gauge, flexure support and ball feet for kinematic reference to the lower spring carrier housing. The pins extending upwards from the mounting plate are aids for repeatably repositioning the spring carrier.

EXPERIMENTAL RESULTS

Load Cell

The load cell was calibrated using a series of weights in the range of 0.2 N to 2.0 N which were calibrated using a laboratory balance. The uncertainty of of the calibration weights was 0.1 mN for weights less than 1 N and 0.2 mN for weights

greater than 1 N. A third-order polynomial calibration curve was developed for the load cell. Deviation from this curve is less than 1 mN. However, it was observed that the load cell exhibited approximately 10 mN of hysteresis depending on whether load was increasing or decreasing towards the calibration value. This hysteresis represents a serious limitation to the instrument for general use. However, the intended operation consistently presents a decreasing load to the cell during spring measurement, so the larger influence of hysteresis can be avoided.

Repeatability of the load cell was assessed by repeatedly loading and unloading the cell with a 0.9 N weight. This procedure assesses the mid-range repeatability of the cell under conditions of unidirectional loading. The observed maximum variation of the measurement over ten cycles was 0.8 mN. The sensitivity of the load cell to temperature and humidity variation was measured, and associated calibration curves were developed. Peak-to-peak variation of the corrected data was less than 1.3 mN over a period of 5 days of typical laboratory environmental variation(0.2 °C, 10% RH).

Overall stability of the load cell at fixed loading was assessed over a period of 60 hours. The result of that stability test is shown in figure 6. At least part of the apparent drift in reading may show the effect of anelastic settling in the steel of the flexure. This effect would appear to contribute as much as 4 mN error to readings that are not taken with careful time controls. If the instrument is used for continuous measurement of slowly varying loads, then the standard deviation of the portion of the curve between 30 h to 60 h (0.25 mN) is likely to be more representative of the load measurement uncertainty.

Measurement Assembly

The repeatability of the measurement assembly was determined using a solid “null carrier” with dimensions identical to those of the spring carrier. The null carrier was repeatedly clamped in place using the same procedures employed for the spring carrier and then removed. The standard uncertainty of the capacitance gauge reading across thirty cycles was 766 nm. The stability of the capacitance gauge was measured over the same 60 hour period of the the load stability shown in figure 6. The results of that test are shown in figure 7. The standard uncertainty

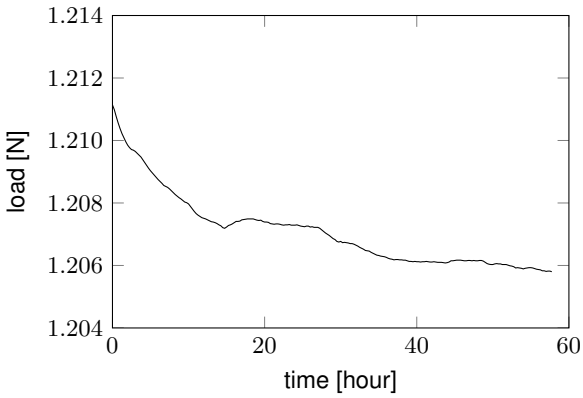

FIGURE 6. Stability of load cell reading with a rigid dummy carrier assembly.

across the 60 hours is 16 nm. Given that the largest value of stiffness of springs studied with this instrument are of order 100 N mm^{-1}, this corresponds to a contribution to load uncertainty less than 1.6 mN.

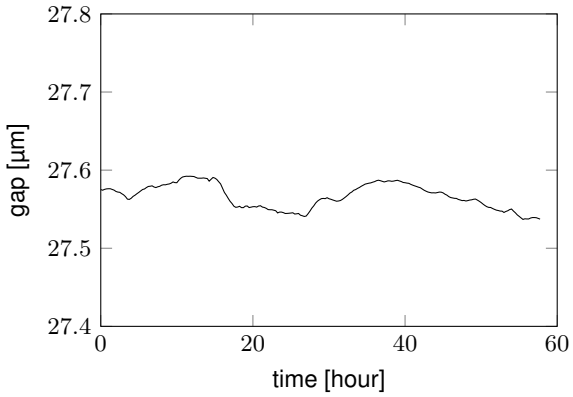

FIGURE 7. Stability of measurement assembly reading for fixed load over a 60 hour test interval.

Spring Testing

A relatively slow transition of load from the housing to loading mechanism as the load is increased can be observed when the geometric axis of the spring is aligned with the load axis. An example of this “soft lift-off” is shown in figure 8. This is the result of angular motion of the plunger as it begins to break contact with the housing. During that transition, the loading mechanism and the housing share the load until all contact between the plunger and the housing is lost. This reflects a difference between the elastic center of the spring and its geometric center due to small variations in the geometry or material condition of each spring leg. One result of such a soft

lift-off is that a relatively large perturbation of the spring is required to get an accurate measure of the spring force. To address this limitation, the plunger angle was measured during load application and the position of the carrier adjusted with a manual X-Y stage to eliminate angular motion. A resulting lift-off curve when angular motion is controlled is shown in figure 9. Here the transition from the stiffness of the plunger-housing assembly to the much lower stiffness of the spring is accomplished in the first micrometre of travel.

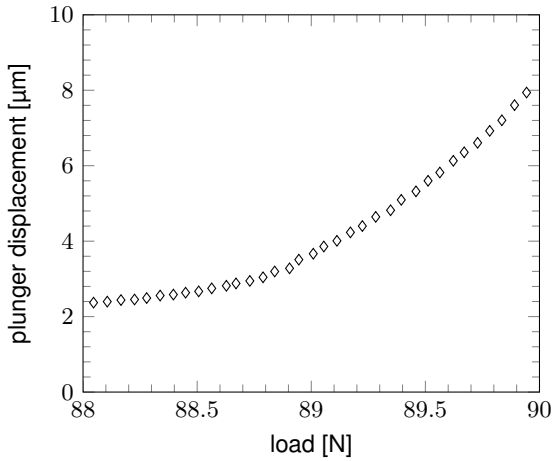

FIGURE 8. Plunger displacement as a function of applied load when the spring is geometrically centered on the loading mechanism line of action.

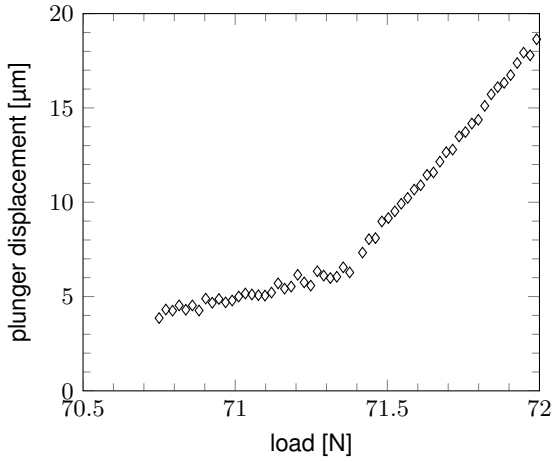

FIGURE 9. Plunger displacement as a function of applied load when the spring is elastically centered on the loading mechanism line of action.

A measurement of the force relaxation of a loaded wave spring over a ninety hour period was carried out at a nominal load of 46 N by adjusting the loading mechanism to maintain a constant plunger displacement. The results of this measurement are shown in figure 10.

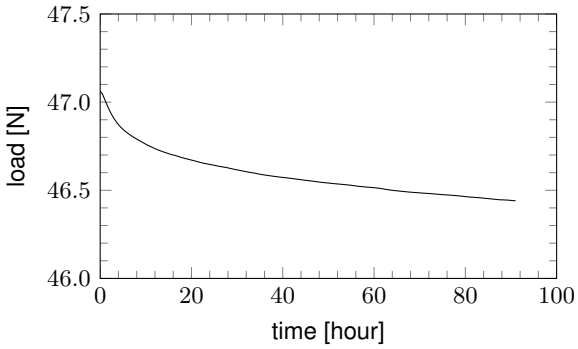

FIGURE 10. Force relaxation of a wave spring

Figure 11 shows the result of a measurement of the relaxation of a stacked finger spring assembly over a period of four months. The data gap between days 55 and 64 represent a period of instrument maintenance. The data after day 64 has been adjusted by 0.265 N as a result in the change in operating point. This corresponds to a change in plunger displacement of 5 µm.

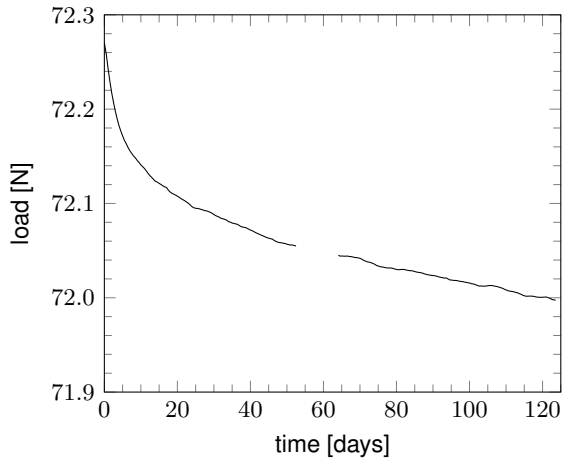

FIGURE 11. Force relaxation of a stacked finger spring assembly

ACKNOWLEDGMENTS

The authors gratefully acknowledge the continuing support of Lawrence Livermore Laboratory. Lawrence Livermore National Laboratory is operated by Lawrence Livermore National Security, LLC, for the U.S. Department of Energy, National Nuclear Security Administration under Contract DE-AC52-07NA27344.

REFERENCES

[1] Patterson SR, Badami VG, Lawton KM, Tajbakhsh H. The dimensional stability of lightly-loaded epoxy joints. American Society for Precision Engineering; 1998. p. 376–379.

[2] Lawton KM, Lynn KC, Ren D. The measurement of creep of elgiloy springs with a balanced interferometer. Precision Engineering. 2007;(31):325–329.

ERROR ANALYSIS FOR A HIGH-PRECISION FIVE DEGREE OF FREEDOM HYBRID MECHANISM FOR HIGH-POWER HIGH-REPETITION RATE LASER OPERATIONS

Shah Karim[1*], Samanta Piano[1], Richard Leach[1], Martin Tolley[2]
[1]Manufacturing Metrology Team, Faculty of Engineering, University of Nottingham, Nottingham, NG7 2RD, UK
[2]Central Laser Facility, Science and Technologies Facilities Council, Oxfordshire, UK

INTRODUCTION

To take advantage of high-power lasers for fusion energy applications, large-scale facilities need to operate at high repetition rates. The challenge of positioning and aligning a target at the laser focus with an accuracy of few micrometres (typically $\pm 4\ \mu m$) is significant, but it is a fundamental requirement for a high-power laser interaction to ensure that targets are reproducibly accessible to the highest intensities available [1]. This represents a serious problem for a high-repetition rate laser system in which a fresh target has to be positioned and aligned at the laser focus at a rate of at least 0.1 Hz (with plans for 10 Hz or higher in future). To meet the specifications for target positioning accuracy and target surface quality, the Central Laser Facility (CLF) has designed and developed a new high-accuracy microtargetry system (HAMS) for accurate mounting and motion control of targets for the Astra-Gemini laser [2].

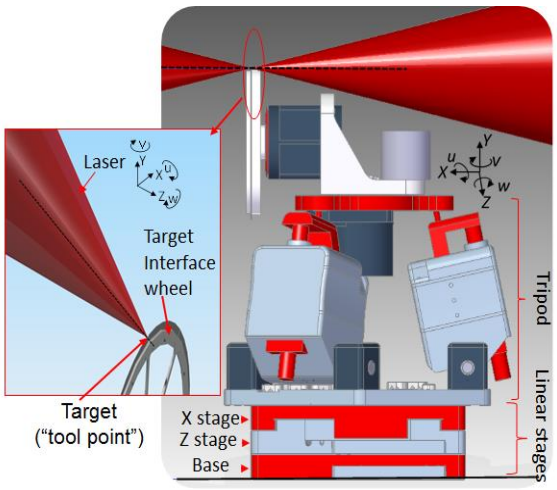

FIGURE 1. Laser-target interaction (L); HAMS with target interface wheel (M) (adapted from [2] and [3]).

HAMS is based on a tripod design architecture mounted on a two-axis linear stage to control all five degrees-of-freedom for positioning and aligning a target at the laser focus (Figure 1). Essentially, HAMS carries an interface wheel to which target sections, made from a silicon wafer, are attached and a number of different target sizes are patterned around the circumference of the section. Positioning and alignment accuracy of the target using HAMS will be dependent upon a number of factors, such as the target geometry, accumulation of errors on the motion stages and the tripod of HAMS (rotational and translational motion errors, orthogonality errors, errors due to wobble/eccentricity, etc.).

Research is currently being carried out to reduce the errors propagated through the individual elements of HAMS, such that the accumulated accuracy is within the defined specification ($\pm 4\ \mu m$, for instance), which is dependent on the positioning and alignment requirements of the laser system [3].

HAMS has a hybrid kinematic structure, which consists of parallel and serial mechanisms. In serial mechanisms, individual axes are built one on top of the other, with the lower axis carrying the one above it [4]. Conversely, parallel mechanisms have closed-loop architectures, in which the positioning actuators are arranged in parallel rather than being stacked one on top of the other, requiring all the actuators to move simultaneously to effect any change in end-effector position or orientation [5]. Hybrid structures are designed to exploit the advantageous characteristics of both types of kinematic structure [6]. For example, a hybrid structure can provide an effective solution for an application that requires high-precision motion over a relatively large workspace. The hybrid

structure has recently received much attention and considerable research is going on to utilise hybrid structures in industrial applications, for example, Tricept and Exechon are two commercially successful hybrid machine tools [7,8]. Nevertheless, despite the promising prospect of hybrid kinematic structures, comprehensive studies of their design, kinematics, dynamics and error sources are lacking in the literature [8].

In this work, an analysis of the error sources of HAMS is presented by developing a kinematic model to demonstrate how the errors affect the positioning accuracy of microtargets during the target alignment process of laser operations.

DEVELOPING ERROR MODEL FOR HAMS

As with any other precision machine, a hybrid structure's performance can be affected by a wide range of errors, particularly geometric errors that arise from manufacturing and assembly [9,10]. Identifying these sources of error to develop effective error compensation strategies is particularly important for high-precision applications [11]. The process of an effective error compensation typically starts with the identification of the machine's linkage structure, leading to the development of a kinematic model that eventually derives an expression for the positional errors along the *x*, *y* and *z* axes at the target (tool point). Error compensation using this kinematic model is a dynamic approach of error elimination: it considers the interaction between the various error sources rather than considering each error independently [11]. An error compensation process essentially follows the procedure of developing a kinematic model to include the most significant errors, measuring them, synthesising those errors into the model and installing error compensation [11].

Developing an error model for a hybrid structure can be challenging for a number of reasons, in particular:

- The error sources of serial kinematic structures are well known [10-13], while the error sources of parallel mechanisms are less well understood.
- Kinematic analysis of a parallel structure may be difficult, since determining a set of input joint variables to achieve a known pose (position and orientation) of the moving platform (called "direct kinematic analysis") can be complex. Error analyses of serial structures are mostly carried out following direct kinematic analysis [6].
- Many types of errors can be related to the machining and assembly of parallel mechanisms, such as platform frame errors, pin joint errors and spherical joint assembly errors. Theoretical analysis to understand the effects of all these can be difficult. As such, some researchers have tried to study the effects of the significant manufacturing and assembly errors concerning parallel kinematic mechanisms [9,14]. In most cases, it is unclear what the actual effect of the errors will be on the final position of the target, since some error averaging effects are believed to take place for parallel structures.

Following the above discussion, a more practical strategy to develop an error model of a hybrid structure is to focus on the application to which the parallel structure will provide its motions (translational and/or rotational). This could mean that while developing a model, one should consider (a) errors that may have significant effects on particular motion/s of the parallel structure, (b) errors that come from generalised sources, i.e. manufacturing and assembly errors will have general effects on the error sources, rather than individual effects, (c) errors, when angular in nature, that can potentially interact with each other or can get amplified by the structural offsets to produce significant translational errors at the target.

KINEMATIC STRUCTURE OF HAMS

The two degree-of-freedom (DOF) serial type linear *xz* system provides two translation motions (along the *x* and *z* axes) to this mechanism. Three other motions, of which one rotational motion about *x* axis (called tip, *u*) and one translational motion along *y* axis, and one further rotational motion about *y* axis (called tilt, *v*) come from parallel link tripod and from the rotary motor attached to the moving stage of tripod, respectively (Figure 1). An additional rotary motion (around the *z* axis) is required to rotate the wafer target wheel; but this motion is not related to the tripod or linear *xz* system. Moreover, as the linear *xz* system is widely used in industry and the technology is well developed, this research will focus on the error model analysis of the 3 DOF parallel mechanism.

The tripod can be described as a *RPS* system, where *R*, *P* and *S* denote revolute, prismatic and spherical joints respectively. One end of each of

the three actuated prismatic joints (legs) is attached to a non-actuated revolute joint, while the other end of the leg is fixed to the moving platform with a non-actuated spherical joint [15]. *RPS* parallel mechanisms have been widely applied to electronic game mechanisms, virtual reality movies, simulation of aircraft and vehicles, and simulation of earthquakes and vibration [16].

Figure 2 schematically represents the kinematic structure of HAMS, describing the geometrical relationship between the coordinate systems that are placed at the points of interest, such as point *T*, which is the target. The machine's origin with respect to the reference frame $X_0Y_0Z_0$ is placed at point *O* on the top surface of machine base. The tripod platform is considered as parallel to the base, i.e. parallel to X_0Z_0.

MODELLING TECHNIQUE

The position and orientation of the end-effector frame *T* (with coordinate $X_TY_TZ_T$ as shown in Figure 2) with respect to the inertial reference frame *O* is represented by the homogeneous transformation matrix (HTM), M_T [17]. The elements of M_T depend on the three position and three orientation parameters of frame *T* with respect to frame *O*, for example:

$$\boldsymbol{M_T^o} = \begin{bmatrix} O_{ix} & O_{iy} & O_{iz} & P_x \\ O_{jx} & O_{jy} & O_{jz} & P_y \\ O_{kx} & O_{ky} & O_{kz} & P_z \\ 0 & 0 & 0 & P_s \end{bmatrix} \quad (1)$$

where, O_{lm} $(l = i, j, k \text{ and } m = x, y, z)$ are the direction cosines (unit vectors *i*, *j*, *k*), representing the orientation of frame *T*'s coordinate axes with respect to the reference coordinate frame, and they have scale factors of zero. P_m $(m = x, y, z)$ represents the position of *T*'s coordinate system's origin with respect to the reference coordinate frame .

The matrix M_T is formed by multiplying the M_i matrices, where M_i represents the interconnected coordinates between point *O* and point *T*:

$$\boldsymbol{M_T = M_1 M_2 M_3 \ldots} \quad (2)$$

From equation (2), known as the "loop closure equation", six scalar equations can be extracted, which give the end effector coordinates X_T^{ideal} (no error) when the mechanism's structural parameter, ***S*** (for example, offsets between two links), and configuration parameter, ***C*** (for example, joint angle), are known, as shown in the following equation [18]:

$$\boldsymbol{X_T^{ideal} = f^{ideal}(S, C)}. \quad (3)$$

However, when the errors are considered in the model, the loop closure equation becomes $\boldsymbol{M_{T_{err}}}$,

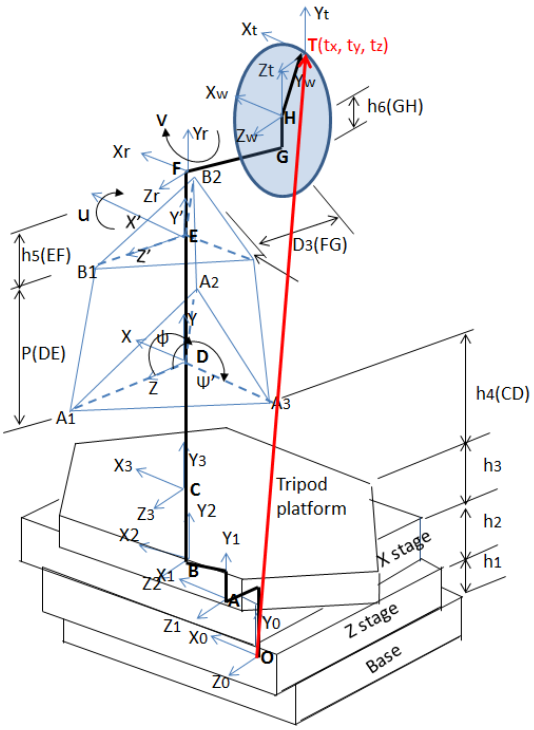

FIGURE 2. Kinematic model of HAMS.

where $\boldsymbol{E_i}$ represents the HTMs defining the errors related to the relevant coordinates between the points *O* and *T* [18]:

$$\boldsymbol{M_{T_{err}} = M_1 E_1 M_2 E_2 M_3 E_3 \ldots} \quad (4)$$

The end-effector's coordinates can be calculated from the equation (5), where ***E*** denotes the HTM that describes the errors' position and orientation with respect to the reference coordinate frame:

$$\boldsymbol{X_T^{real} = f^{real}(S, C, E)}. \quad (5)$$

Thus, the end effector's position and orientation error $\Delta \boldsymbol{X}$ can be defined as the 6×1 matrix which represents the difference between the real position and orientation of the end-effector and the ideal one:

$$\boldsymbol{\Delta X = X_T^{real} - X_T^{ideal}}. \quad (6)$$

The matrix $\Delta \boldsymbol{X}$ needs to be calculated for a given set of errors [18]. The first step of the error analysis is to determine which errors significantly affect the end effector's position and orientation and then measure them.

ERROR DEFINITIONS FOR HAMS

As mentioned above, the parallel part of HAMS and the rotary motor attached to the moving stage provide tip and tilt rotational motions. Two orientation errors related to tip and tilt are reported in this paper. These errors are considered as "generalised errors" as indicated before. Assuming that parallelism and vertical errors of this structure are negligible, tip and tilt errors have been found to have significant influence on the position and orientation of the target.

The first error is related to the *RPS* structure. The tip motion, *u*, of this structure induces a small amount of translation motion, $\delta_{x_{err}}$ and $\delta_{z_{err}}$, perpendicular to the respective axis of rotation and a rotation around the vertical direction, u_{err}, (Figure 3, top). These parasitic motions take place in the constrained direction of the motion and may have an unwanted "decentering" effect on the moving platform, causing the positional deviations at the tool point [15,16]. A typical HTM to represent these parasitic errors of HAMS can be written:

$$T_{tip_{err}} = \begin{bmatrix} \cos u_{err} & 0 & -\sin u_{err} & \delta_{x_{err}} \\ \sin u \sin u_{err} & \cos u & \cos u_{err} \sin u & 0 \\ \cos u \sin u_{err} & -\sin u & \cos u \cos u_{err} & \delta_{z_{err}} \\ 0 & 0 & 0 & 1 \end{bmatrix} \quad (7)$$

The second type of error is generated from the tilt motion, which is the rotation about the vertical axis *y*. Ideally, a rotating body should rotate about its axis of rotation without any error; however, in reality the axis of rotation of the upper part of HAMS, mounted on the moving stage, revolves around the *y* axis of the reference coordinate with two radial errors $\delta_{x_{rad}}$ and $\delta_{z_{rad}}$ along *x* and *z* axes, one axial error $\delta_{y_{axial}}$ along *y* axis and two tilt errors ε_x and ε_z about *x* and *z* axes (Figure 3, bottom) [17]. These error motions can be described by the following HTM (a first order approximation is applied since the error terms are considered small as compared to tip and tilt magnitudes):

$$T_{tilt_{err}} = \begin{bmatrix} \cos v & A & -\sin v & \delta_{x_{rad}} \\ \varepsilon_z & 1 & \varepsilon_x & \delta_{y_{axial}} \\ \sin v & B & \cos v & \delta_{z_{rad}} \\ 0 & 0 & 0 & 1 \end{bmatrix}$$

where $A = (\sin v\ \varepsilon_x - \cos v\ \varepsilon_z)$ and $B = (-\sin v\ \varepsilon_z - \cos v\ \varepsilon_x)$.

(8)

ERROR MEASUREMENTS

The positional deviations in the *z* and *x* directions (*z* is the sensitive direction as it is along the laser axis) as a result of error motions of tip and tilt were measured using a linear and angular interferometer (Renishaw model XL-80). These measurements of the positional deviations are achieved by determining the linear displacements of the moving part (moving stage or target wheel) when HAMS moves in an angular manner (*u* or *v*).

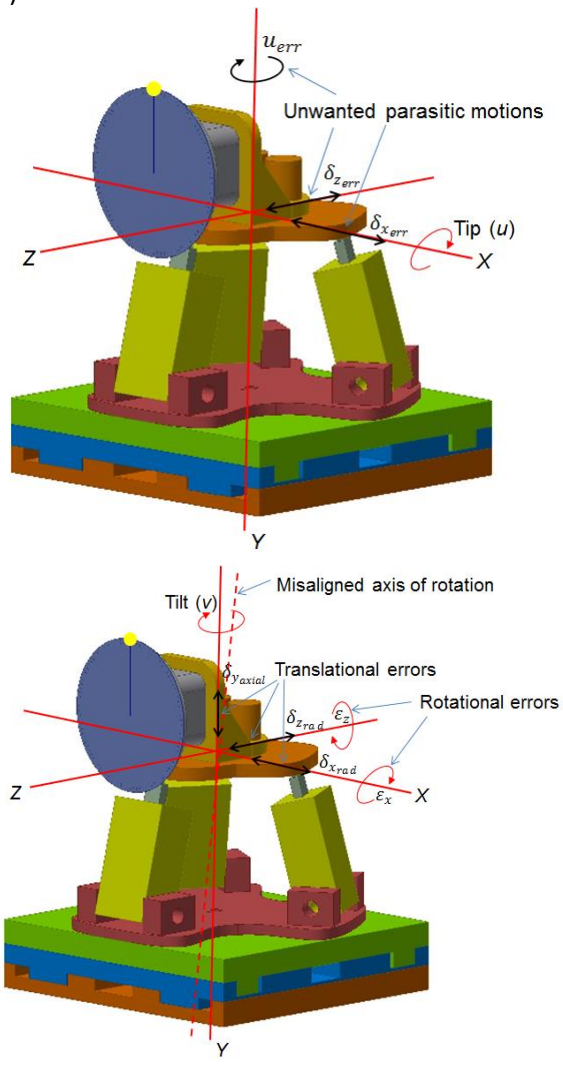

FIGURE 3. Rotational error motions of HAMS: for tip (top) and for tilt (bottom).

The error measurements were carried out following two steps:

- linear displacements were measured for the moving stage (or for the vertical axis of rotation of the moving stage). These

measurements provide the error components related to tip and tilt: u_{err}, ε_x and ε_z.

- linear displacements were measured at the target (*T* as shown in Figure 2) of the target wheel to calculate the positional deviations of the target.

During the interferometer measurements, an environmental compensator unit (Renishaw model XC-80) was used to reduce the measurement errors resulting from the variations in air temperature, air pressure and relative humidity, all of which affect the refractive index of the ambient air. However, a small number of other influence factors contributed towards the measurement uncertainty, for example, (a) ideally, linear displacements for the moving stage would be measured at the centre of reaction of the stage, but it was not possible due to the inaccessible central area of HAMS. Instead, displacements were measured as close to the centre of the stage as practical. (b) accurate measurements of the structural offsets were difficult to achieve. The overall measurement uncertainty arising from the repeatability of the measured distances and from the laser interferometer was found not to exceed 200 nm (at a coverage factor *k* = 2, giving a confidence level of approximately 95 %).

RESULTS AND DISCUSSION

The results shown here are the experimental results of tip motion errors, compared with the predicted positional deviations of error model. It is found that tip causes a very large positional deviation at the target, especially in the *z* direction (Figure 4 and Figure 5). As seen from equation (7), the linear displacements measured at the centre position of the moving platform of the tripod represent the two translational parasitic motions of the *RPS* structure ($\delta_{x_{err}}$ and $\delta_{z_{err}}$), which can cause some positional deviations at the target. However, it is the parasitic rotational error motion (u_{err}) that can have a significant effect on the positional deviations of the target (u_{err} can be calculated from an expression of the model by using the measured values of $\delta_{x_{err}}$ and $\delta_{z_{err}}$). These deviations are due to the rotational error being amplified by the Abbe offsets. The structure of HAMS that is mounted on the moving platform is such that the target on the target wheel is at offsets of 118 mm and 96 mm along *y* and *z* direction respectively from the centre of the moving platform (responsible for the tip motion). If there were no offsets in the horizontal and vertical directions from this centre, theoretically, there would only be the positional deviations at the target due to two parasitic translational motion errors $\delta_{x_{err}}$ and $\delta_{z_{err}}$.

However, it is not only this rotational error (u_{err}) that gets amplified and causes deviations at the target. The model predicts that the tip motion itself, even in the absence of all the parasitic motion errors, is responsible for a considerable positional deviation at the target due to the Abbe offsets.

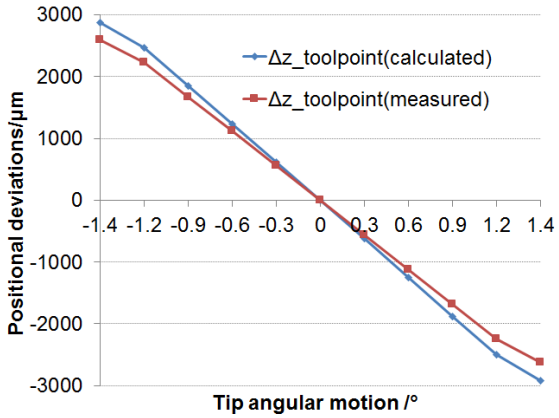

FIGURE 4. Comparison of the calculated and measured positional deviations of target in the z direction due to tip and its associated parasitic error motions.

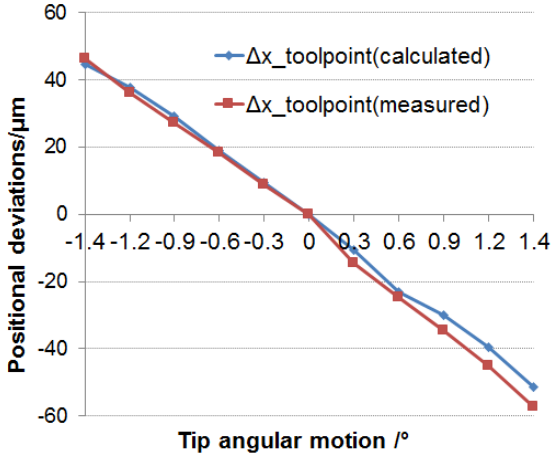

FIGURE 5. Comparison of the calculated and measured positional deviations of target in the x direction due to tip and its associated parasitic error motions.

CONCLUSION

An effective kinematic model to compensate the errors of parallel kinematic structures can be developed by considering the most significant errors associated with the motion/s produced, by measuring the errors and by validating the model results against experimentally determined values.

Among the two types of motion errors (tip motion error and tilt motion error) that may have significant effects on the positional deviations of the target or tool point, the effects of parasitic motion errors (tip motion error) is reported here for the parallel kinematic structure of HAMS. The result suggests that some errors are generated because of the kinematic nature of the structure (*RPS* structure), while some errors are a result of the amplifications of the errors by structural offsets.

The authors gratefully acknowledge the help and support of Mr Sam Astbury and Mr Chris Spindloe of CLF (STFC) and Dr Wahyudin Syam (University of Nottingham).This research project is jointly funded by STFC (Oxfordshire, UK) and EPSRC (grants EP/M008993/1 and EP/L016567/1).

REFERENCES

[1] Symes D R, Booth N, Baraclough M, Indorf G, Oliver P, Scott G G, Neely D, Spindloe C, Heathcote R I, Clarke R J P, Foster S, Gregory C D, Rajeev P P. Progress on Positioning of Solid Targets for Gemini. Central Laser Facility Annual Report 2014; 15.

[2] Spindloe C, Arthur G, Hall F, Tomlinson S, Potter R, Kar S, Green J, Higgingbotham A, Booth N, Tolley M. K. High Volume Fabrication of Laser Targets using MEMS Techniques. J Physi: Conf Ser 2016; 713: 012002.

[3] Booth N. Clarke R. Heathcote R. Neely D. Pattathil R. Rusby D. Spindloe C. Symes D. Tolley M K, Tomlinson S. High-rep Rate Target Development for Ultra-intense Interaction Science at the Central Laser Facility. Proc SPIE 2014; 9211: 9211071-8.

[4] Niku S B. Introduction to Robotics: Analysis, Control, Applications. John Willey and Sons. USA: 2011.

[5] Allen J M, Axinte D A, Pringle T. Theoretical Analysis of a Special Purpose Miniature Machine Tool With Parallel Kinematic Architecture: Free Leg Hexapod. ProcIMechE Part B: J. Eng Manufac 2011.

[6] Liu X J, Wang J. Parallel Kinematics: Type, Kinematics and Optimal Design. Springer. New York: 2014.

[7] Milutinovic M, Slavkovic N, Milutinovic D. Kinematic Modelling of Hybrid Parallel Serial Five Axis Machine Tool. FME Transactions 2013; 41: 1-10.

[8] Harib K H, Sharifullah A M M, Moustafa K A F. Optimal Design for Improved Hybrid Kinematic Machine Tools. Ann CIRP 2013; 12: 109-14.

[9] Hu P H, Yu C W, Fan K C, Dang X M, Li R J. Error Averaging Effect in Parallel Mechanism Coordinate Measuring Machine. Appl Sci 2016; 6: 383-395.

[10] Wang F S, Chen S L. Geometric Error Measurement and Compensation of a Six-degree-of-freedom Hybrid Positioning Stage. ProcIMechE Part B: J Eng Man 2008; 222**:** 185-200.

[11] Ramesh R, Mannan M, Poo A N. Error Compensation in Machine Tools — a Review, International J Mach Tool Manufac 2000; 40: 1257-1284.

[12] Sartori S, Zhang G X. Geometric Error Measurement and Compensation of Machines. Ann CIRP 1995; 44: 599–609.

[13] Schwenke H, Knapp W, Haitjema H, Weckenmann A, Schmitt R, Delbressine F. Geometric Error Measurement and Compensation of Machines—An update. Ann CIRP 2008; 57(2): 660-675.

[14] Chen S L, Chang T H, Hsei M H. Analytical Modelling of the Effects of Manufacturing Errors on the Accuracy for a TRR-XY Hybrid Parallel Link Machine Tool. Proc Mech Eng 2001; 215: 1203-1216.

[15] Carretero J A, Phdhorodeski R P, Nahon M A, Gosselin C M. Kinematic Analysis and Optimisation of a New Three Degree of Freedom Spatial Parallel Manipulator. J Mech Design 2000; 122: 17-24.

[16] Li Q, Herve J M. 1T2R Parallel Mechanisms Without Parasitic Motion. IEEE. 2010; 26: 401-410

[17] Slocum A H. Precision Machine Design. Prentice-Hall. New Jersey: 1992.

[18] Mavroidis C, Dubowsky S. Drouet P, Hntersteiner J, Flax J. A Systematic Error Analysis of Robotic Manipulators: Application to a High Performance Medical Robot. Proc IEEE1997; 980-985.

DESIGN AND TESTING OF AN AIR BEARING SPINDLE AT LOW SPEED FOR NANOMETER-LEVEL ASYNCHRONOUS ERROR

Byron Knapp, Dave Arneson, and Dan Oss
Professional Instruments Company
Hopkins, Minnesota, USA

INTRODUCTION

Aerostatic bearing (air bearing) spindles are used in precision metrology and manufacturing because of their low error motions. The most demanding form metrology applications require spindles with nanometer-level asynchronous error motion and smooth rotary motion at low speed. Achieving this level of accuracy requires refinement of the bearing compensation using metrology feedback to guide the design process. Efforts to achieve reduced asynchronous error motion at low speed (0.3 RPM) led to a modified bearing design that resulted in improved asynchronous (1 nm) for a form measuring application.

BACKGROUND

The spindle shown in Figure 2 features a brushless permanent magnet motor and two encoders. A 1,024 line-count encoder is used for motor commutation and high speed operation, while a 9,000 line-count encoder is used for positioning and low speed operation. Front and rear radial bearings, as well as the motor, are water-cooled. Vacuum is supplied to the chuck via a non-contact rotary union.

The standard design features an axial bearing with groove compensation using an annular slit restrictor feed from the porous journal sleeves. This compound compensation scheme results in excellent load and stiffness properties but it was found that error motion at 0.3 RPM showed 1 nanometer print through of the 90 face grooves. At speeds above 10 RPM, this groove print through is not observed. Although the print through did not affect asynchronous error, a bespoke spindle was designed without the grooves to improve synchronous error motion at 0.3 RPM. Removing the groove compensation did not affect the dynamic stiffness and error motion was improved. However, without compound compensation, the axial load capacity and static stiffness were reduced.

NON-ROTATING NOISE

One important consideration in air bearing spindle design is the stability of the pressurized air film. Large amplitude instability (pneumatic hammer) has been addressed in the literature [1] and is largely solved in practice. However, nanometer-level vibration remains a concern in the most demanding applications. Previous work demonstrated the measurement of these vibrations [2]. These tests have been a useful tool in developing a new air bearing spindle for a form metrology instrument with 1 nanometer asynchronous error.

The measurement setup to quantify noise is shown in Figure 1. A special low-noise capacitive sensor (Lion Precision 2G-C8-1.2 Superprobe C23-C, 0.5 μm/V) targets a 25 mm diameter lapped sphere. A sphere of 25 mm diameter is used for calibration to determine the target correction factor (0.909). The sensor amplifier (Lion Precision CPL490) incorporates a 15 kHz first-order, low-pass analog filter with linear phase response.

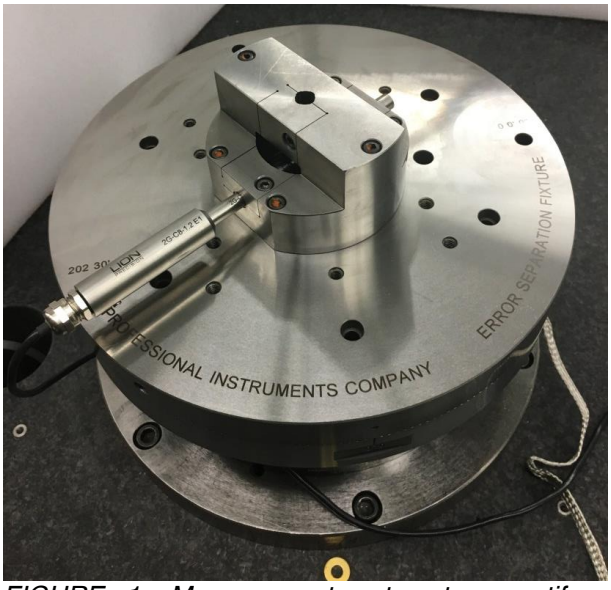

FIGURE 1. Measurement setup to quantify nanometer-level bearing vibration.

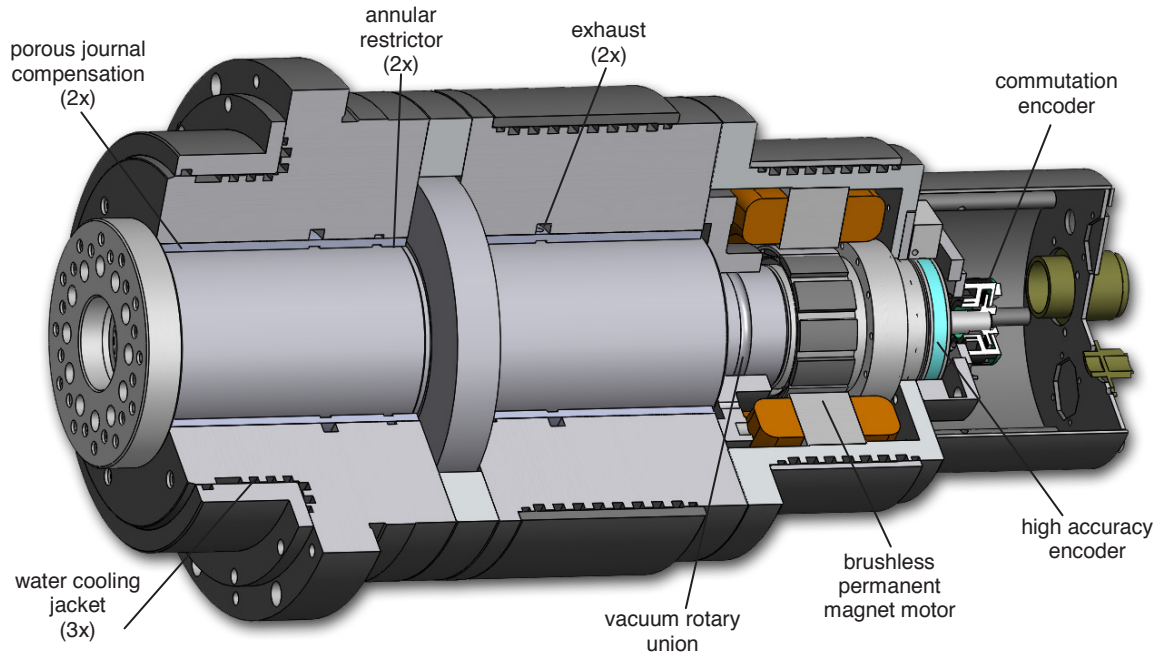

FIGURE 2. *Cross section of porous graphite spindle showing important features.*

The 24-bit data acquisition system (Data Physics Quattro) records sensor displacement over 16 seconds with a 200 Hz bandwidth while the spindle is not rotating. Resolution of the sensor at full bandwidth (15 kHz) is 420 picometers, but at 200 Hz bandwidth, the sensor noise is less than 250 picometers. The noise of the spindle and measurement loop at 0.7 MPa air pressure is 380 picometers peak-to-peak as shown in Figure 3.

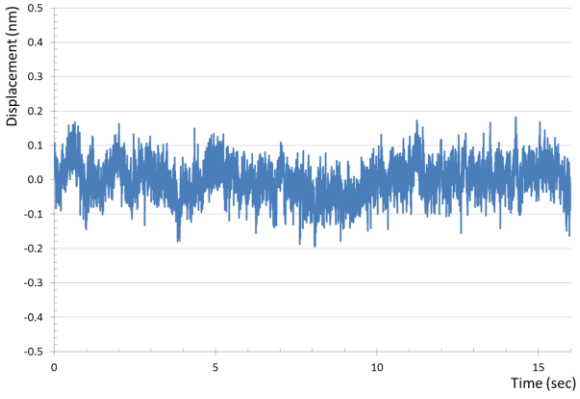

FIGURE 3. Bearing and setup vibration with thermal drift removed showing 380 picometers peak-to-peak noise at 0.7 MPa air pressure.

A linear model is used in post processing to remove thermal drift. The noise is unchanged over a range of inlet air pressures from 0.4 MPa through 1.0 MPa demonstrating the robustness of the design.

ERROR MOTION TESTS

An expansive amount of research has been published regarding metrology of axes of rotation leading to the development of a definitive resource by Marsh describing the experimental procedures needed to accurately capture error motion of a spindle [3]. The spindle error motion measurement task is complicated by the nanometer-level magnitude of the errors. Testing of the air bearing spindle for this form metrology application must reliably characterize radial asynchronous errors smaller than 1 nm.

The test setup for error motion measurement is shown in Figure 4. The low noise capacitive sensor (Lion Precision 2G-C8-1.2 with CPL 490) targets the 25 mm diameter sphere (0.909 target correction). The data acquisition system (Lion Precision SEA 9.0) is triggered by the 1,024-line count encoder, providing immunity to synchronization errors caused by speed variation.

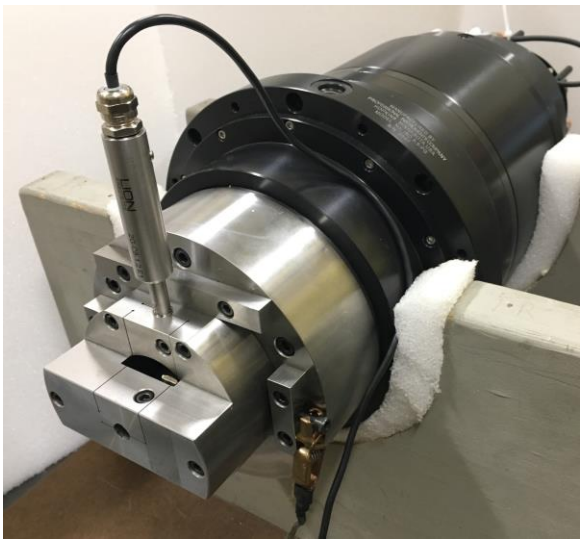

FIGURE 4. Setup for slow speed radial error motion test.

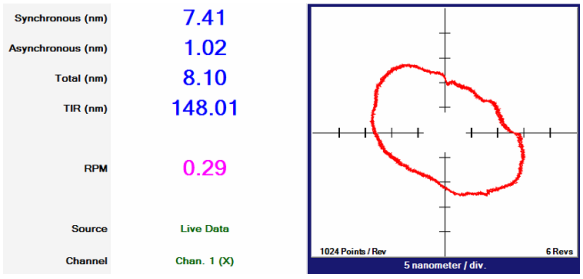

FIGURE 5. Slow speed asynchronous error motion is 1.0 nm. Artifact error and thermal drift are not removed.

The results of the 0.3 RPM asynchronous error motion tests are shown in Figure 5. The new spindle design achieves 1 nm asynchronous without removal of thermal drift and despite using the capacitive sensor at full bandwidth (15 kHz). The form metrology instrument will incorporate thermal drift removal and use a lower bandwidth (200 Hz) which further reduces the asynchronous.

DYNAMIC TESTING

A modal impact test is used to evaluate the new air bearing compensation and determine the effect on the first axial resonance (Figure 6). An impact hammer (Kistler 500 N) excites the structure in the axial direction and an accelerometer (Kister K-Shear 25g) measures the response. The spindle is supported on compliant foam to minimize boundary condition influences.

FIGURE 6. Setup for axial modal impact test.

With an inlet pressure of 0.7 MPa, the first mode is highly damped and above 1,700 Hz (see Figure 6). This result is unchanged from the compound compensation design despite the decrease in static stiffness. This result verifies that the dynamic response of the design without grooves is unchanged.

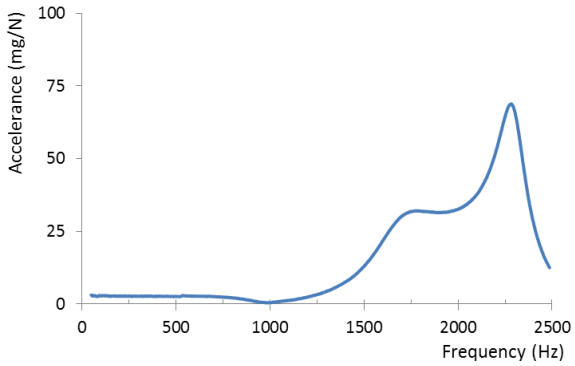

FIGURE 7. Axial frequency response function shows the first resonance above 1,700 Hz.

CONCLUSION

Design and testing of a bespoke spindle for ultra-precision form metrology is described. The air bearing compensation is designed to minimize errors at very low speed (0.3 RPM). Baseline noise measurements of the air bearing spindle, capacitive sensor, and measurement loop are shown with 380 picometer peak-to-peak with thermal drift removed. The error motion measurements with the spindle rotating at 0.3 RPM demonstrate 1 nm asynchronous as required for the form metrology application. The dynamic response shows the first natural frequency is highly damped and above 1,700 Hz.

REFERENCES

[1] Stout K et al. 2000 The design of aerostatic bearings for application to nanometer resolution manufacturing machine systems Tribology International vol 33 issue 12 (Elsevier) pp 803-9.

[2] Marsh E et al. 2008 Effects of gas composition on asynchronous error motion in externally pressurized spindles Precision Engineering vol 32 issue 2 (Elsevier) pp 143-7.

[3] E Marsh. Precision Spindle Metrology, Second Edition. Destech Publications, Inc. Lancaster, PA: 2010.

LONG-TERM CREEP MEASUREMENTS OF 302 STAINLESS STEEL AND ELGILOY®

Kevin M. Lawton, Steven R. Patterson
Mechanical Engineering and Engineering Science Department
University of North Carolina at Charlotte
Charlotte, NC

INTRODUCTION

Mechanisms incorporating loaded elastic elements to provide a known force over long periods of time must account for the potential of stress relaxation leading to a change in force and concomitant change in mechanism performance. If the intended period of operation is many years, it is impractical to test elastic components for a period equal to the lifetime of the mechanism in order to determine the adequacy of the material choice and design. Instead, designers must rely on an assumed constitutive relationship and data collected at shorter periods of time. When the elastic load is small compared the yield stress of the material, the long-term stability may be dominated by internal stress relief or thermally activated phase transitions. At loads of a significant fraction of the yield strength, however, the behavior will be dominated by the external load and response of the material to that load, typically by dislocation motion.

Creep at temperatures in excess of half the melting temperature of the material or at stresses very close to the yield stress have been extensively studied[1, p983]. The restriction to these temperature and stress regions is the result of both the common range of application of the data and the limitations of instrumentation used in studies. For some applications of very high precision or very long service, an understanding of very low levels of creep at lower temperatures and stress is desired. At these lower loads and room temperature, however, there is much less data since applicable experiments require the stable measurement of very small strains over long periods of time. Here the term creep is used to refer to the irrecoverable time-dependent plastic deformation while the recoverable time-dependent strain is referred to as anelasticity.

Models adapted from other temperature and load regions include logarithmic strain followed by linear strain, and strain-induced hardening (Bailey-Norton) models. At moderate time scales, there is considerable similarity between these models. But at long times they provide very different estimates of dimensional change.

To help establish a constitutive relation applicable to precision instrument design, we have carried out a series of measurements at time scales ranging from tens of days to periods exceeding six years. Measurements have been using both UNS30200 stainless steel and the proprietary Elgiloy®spring steel (40 Co - 20 Cr - 15 Ni -7 Mo - 2 Mn)[2].

EXPERIMENTAL METHOD

A gravity-loaded dilatometer was constructed as shown in figure 1. The wire segment of nominal 150 mm length is held between two clamps. The lower clamp is connected to a beam which is constrained by an air bearing and contains a weight pan which is used to provide an axial load to the wire. The position of the beam is measured relative to the upper clamp by a transducer. In early tests the transducer was an LVDT. This was later changed to a capacitance gauge in order to avoid potential friction should the core of the LVDT contact its bore. The entire experimental apparatus, including capacitance gauge measurement electronics, is placed on an air-isolated table in a temperature controlled chamber [3] which maintains the apparatus environment at a nominal 20 ℃ with a stability of order 0.01 ℃. After the load is initially applied to the wire, the capacitance gauge is adjusted so that the subsequent creep will be within the range of the gauge. For this reason, there is no direct measurement of the elastic dilatation of the wire, which is large compared to the creep and outside the measurement range of the capacitance gauge. The initial measurement data is also affected by the small changes in temperature that accompany these manual adjustments. Thermal equilibrium of the instrument is obtained within 24-36 hours of the initial loading and adjustment. As a consequence, very rapid anelastic effects cannot be accurately measured.

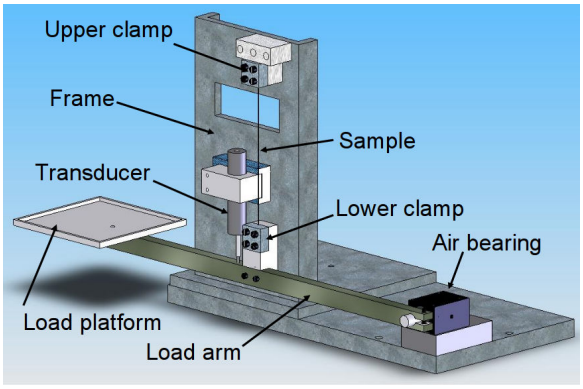

FIGURE 1. Apparatus used to measure long-term creep of wires under axial load.

The value of the output of the LVDT or capacitance gauge is recorded periodically. Because of the long period of measurement, it has been necessary to exclude from the fit some data that reflects transient failure of the laboratory air conditioning and compressed air supply. Some data has also been excluded during periods of large humidity swings in the building, since the capacitance gauge has some sensitivity to humidity and the chamber does not provide great attenuation of laboratory humidity variations.

EXPERIMENTAL RESULTS

Elgiloy®

A wire sample with rectangular cross section 0.1 mm by 1.0 mm and 149 mm length was loaded at 993 MPa. This is 90 percent of the published yield strength of the material [2], though specific properties are known to vary with the cold work and temper of the material. To determine the strength of the material used in these experiments, the transducer was replaced with a longer range LVDT and weight successively added to the weight pan to produce a stress-strain curve for the material up to tensile failure. Figure 2 displays the observed deviation of the measured strain from the linear response at loads below 0.5 GPa. From this curve, the 0.2% yield strength is near the tensile strength of 1.7 GPa and considerably above the load for the experiment. However, the material begins 0.01% microyielding below 700 MPa, well below the experiment load. It is clear, then, that at 993 MPa load there is sufficient stress to induce measurable dislocation motion.

The dilatation of the sample was measured for a period of 2333 days (6.4 years). A Bailey-Norton

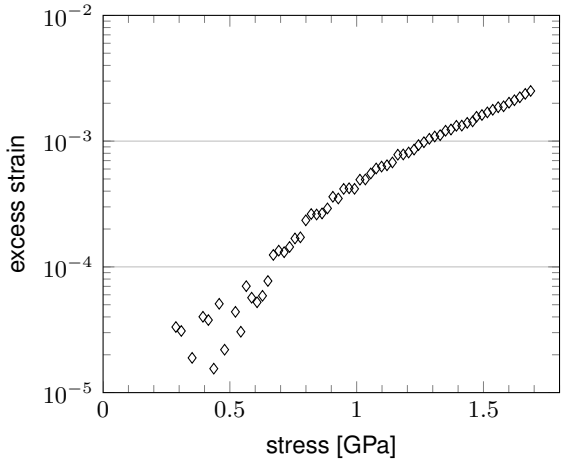

FIGURE 2. Excess strain of an Elgiloy® wire as a function of applied stress. Values below 5×10^{-5} *reflect measurement noise.*

(B-N) creep curve

$$\epsilon = Ct^n \tag{1}$$

with constant, C, was fit to the first 181 days of data (figure 3). The fit is a good one across most of the domain, with a RMS deviation of the data from the B-N fit across this interval of 1.2×10^{-6}. This value is small compared to the total creep strain and comparable to the instrument uncertainty. However, there is a significant deviation of the data from the B-N curve observed during the first five days of the test (figure 4). This is attributed to anelastic settling during which the response of the wire appears to be largely viscoelastic. Anelasticity is related to internal material damping and follows the expected exponential time dependence[1, p. 986].

The observed creep strain across the full period of the test is shown in figure 5. The periodic excursions of the experimental data above the plotted B-N curve represent periods during which the lack of environmental humidity control caused measurement errors in the capacitance gauge. To avoid compromising the integrity of the long term data, no major modifications of the experimental setup were made during the period of the experiment. Instead, data is considered valid only during the periodic intervals of stable humidity.

In addition to the B-N curve based on the first 181 days of data, two other extrapolations of the early data are shown. The linear extrapolation is based on an assumption that the sample is undergoing

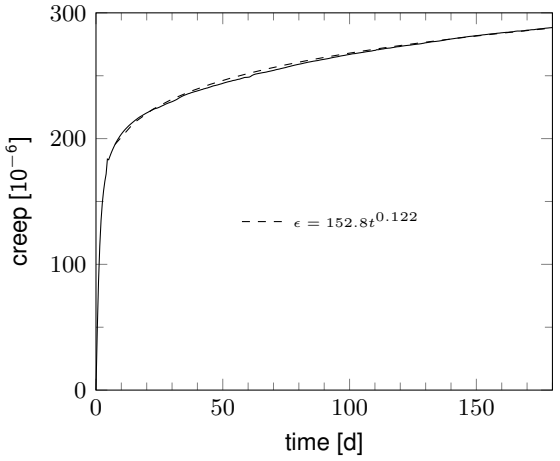

FIGURE 3. Initial creep of an Elgiloy® wire under 993 MPa *axial stress with best-fit Bailey-Norton creep curve.*

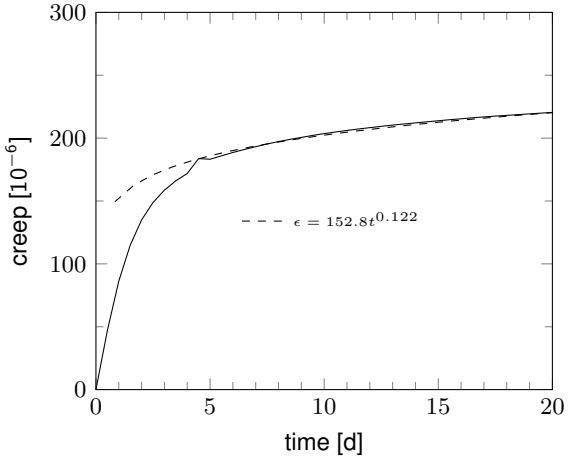

FIGURE 4. Early creep of an Elgiloy® wire under 993 MPa *axial stress with best-fit Bailey-Norton creep curve, showing anelastic settling during the first five days.*

classic secondary (steady state) creep , and uses the last 30 days of the early data to estimate the slope. It is clear that the assumption of secondary creep considerably overestimates the subsequent creep strain.

The logarithmic extrapolation follows the commonly accepted model of creep at temperatures well below the melting temperature:[1]

$$\epsilon = \epsilon_0 \log(1 + \nu t) \tag{2}$$

This model provides a much more reasonable estimate of the creep strain. It is, however,

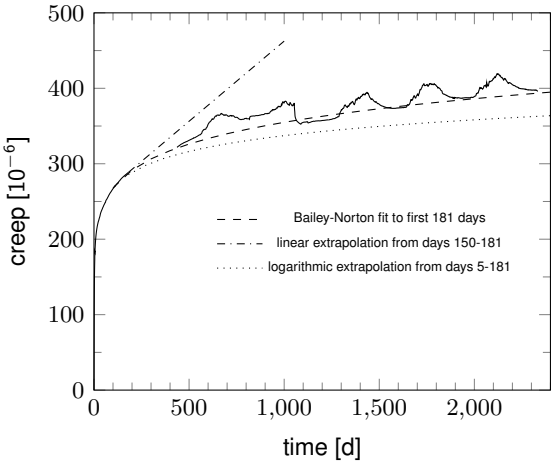

FIGURE 5. Long-term creep of an Elgiloy® wire under 993 MPa *axial stress with Bailey-Norton, linear, and logarithmic creep extrapolations based on the first 181 days of data.*

not as good a fit to the early data as the B-N (RMS 2.2×10^{-6} versus 1.2×10^{-6}) and underestimates the creep strain at 6.4 years by approximately 8%.

UNS30200

A sample of 0.1 mm diameter cold-drawn UNS30200 stainless steel wire with a nominal tensile strength of 2 GPa was tested under successive loads of 0.97 GPa, 1.17 GPa, 1.30 GPa, and 1.45 GPa. Table 1 summarizes the load, period of test and total accumulated creep strain. The intent of this set of measurements was to provide a basis for extending the simple form of the Bailey-Norton relation in equation (1) to the case of time-varying load.

TABLE 1. Loading Schedule and Accumulated Creep Strain of UNS30200 wire

Sequence	Load [GPa]	Duration [day]	Total Strain [10^{-6}]
1	0.97	138	27
2	1.17	238	87
3	1.30	91	104
4	1.45	64	150

In its conventional form, the Bailey-Norton equation takes the constant multiplier to be a power function of the applied stress, and the time exponent to be temperature-dependent but independent of the stress:

$$\epsilon(t) = A\,\sigma^n\,t^m \tag{3}$$

It is straightforward to show that this can be placed in the form of a differential equation relating creep strain rate to creep strain.

$$\dot{\epsilon} = A\, m\, \sigma^n\, t^{m-1} = m\, A^{\frac{1}{m}}\, \sigma^{\frac{n}{m}}\, \epsilon^{\frac{m-1}{m}} \qquad (4)$$

This formulation provides an extension to varying stress which is plausibly connected to a physical mechanism of strain-hardening. This expression also allows the underlying Bailey-Norton form to be extended to the case of time varying stress. In the case of time-varying stress, it is straightforward to show the solution of differential equation 4 is

$$\epsilon(t) = A \left[\int_0^t \sigma^{\frac{m}{n}} \right]^n \qquad (5)$$

For any subsequent loading, then, the observed relative creep from the beginning of the test should have the form

$$\epsilon + \epsilon_a = \left[\epsilon_a^{\frac{1}{n}} + [A\sigma^m t^n]^{\frac{1}{n}} \right]^n = \left[\epsilon_a^{\frac{1}{n}} + \epsilon_{BN}{}^{\frac{1}{n}} \right]^n \qquad (6)$$

where t is the time from the beginning of the test, ϵ_a is the accumulated strain from previous tests, and ϵ_{BN} is the simple , time-dependent, Bailey-Norton expression for the current test.

The observed relative creep during the first 60 days of each test is shown in figure 6. Data at loadings of 0.97 GPa and 1.30 GPa have been corrected for variations in laboratory humidity, a correction which has introduced additional uncertainty into the data which can be seen in the apparent noise of the curve. The data taken with loads of 1.17 GPa and 1.45 GPa were taken during periods of better humidity control, with the later benefiting from an active humidity control that was installed on the test chamber.

The test data shows qualitative agreement with the strain hardening model. Both the 1.17 GPa and the 1.30 GPa tests show lower strain rates than the original test even though they are conducted at a larger load. This could not be case unless the previous creep had modified the material creep properties. It is not required, however, for the creep rate at higher stress to be smaller than the initial stress, only that it be smaller than would have been the case had it been applied to virgin material. Hence the larger creep rate observed at 1.45 GPa is not necessarily an anomaly in the context of Bailey-Norton-like creep. Indeed, Kassner suggests that the stress exponent, m,

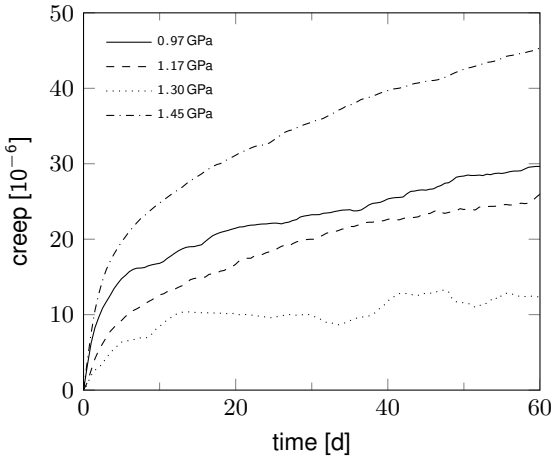

FIGURE 6. Creep of UNS30200 wire.

will likely be in excess of 5 at temperatures in the so-called “power law breakdown” region below half the melting point[4, p. 11]. If this is the case, then the contribution of stress to the creep rate will be more than seven-fold greater in the case of the last test than the initial loading. The creep at the higher loading is by contrast less than half that of the initial case.

While the observed creep rates are qualitatively consistent with the strain hardening model, they are not quantitatively consistent with a model based on equation (6) in which A, m, and n are simple constants independent of stress. To develop a more complete phenomenological constitutive model will require additional measurements, most likely at different stress applied to starting material which is in the same state.

ACKNOWLEDGMENTS

The authors gratefully acknowledge the Lawrence Livermore National Laboratory, whose continuing support has made these measurements possible. Lawrence Livermore National Laboratory is operated by Lawrence Livermore National Security, LLC, for the U.S. Department of Energy, National Nuclear Security Administration under Contract DE-AC52-07NA27344.

REFERENCES

[1] Weertman J, Weertman JR. Mechanical Properties, Strongly Temperature Dependent. In: Cahn RW, editor. Physical Metallurgy. 2nd ed. North-Holland Publishing Company; 1970. p. 983–1010.

[2] Elgiloy® [Specification sheet]. 356 N. Cross Street; Sycamore, IL: Elgiloy Specialty Metals, Inc.; undated.

[3] Lawton KM, Patterson SR. A High Stability Air Temperature Control System. Precision Engineering. 2000;24(2):174–182.

[4] Kassner ME. Fundamentals of Creep in Metals and Alloys. 2nd ed. Radarweg 29: Elsevier; 2009.

DEVELOPMENT OF NOVEL TWO-DOF NANO-POSITIONING STAGE WITH HIGH THERMAL STIFFNESS

Jae-Chang LEE, Hoon-Hee LEE and Seung-Han YANG
School of Mechanical Engineering
Kyungpook National University
Daegu, Republic of Korea

INSTRUCTIONS

This Micro/nano-positioning stages play a significant role in meeting the stringent requirements of micro-manufacturing, micro/nano-positioning and ultra-precision instruments, such as atomic force microscopes (AFMs) and scanning probe microscopes (SPMs). These nano-positioning stages are usually required to attain high positional accuracy and high traveling speeds of several hundred hertz. Therefore, these stages are typically constructed using piezoelectric actuators (PEA) and flexible hinges as the actuator can provide the extremely fine resolution, high response and large force generation required. Moreover, stages based on flexible hinges exploit the advantage of compliant mechanisms, whereby a flexible monolithic joint can deform elastically to offer accurate and repeatable fine movement.[1] It is possible to achieve ultra-precise positioning due to characteristics such as zero backlash, no wear, no required lubrication and low friction. Therefore, these stages provide repeatable and smooth motion to fulfill the requirement of accurate nano-positioning.

To achieve 2-degree-of-freedom (DOF) nano-positioning, the aforementioned mechanisms can be utilized simply by adding two separate 1-DOF stages(with one mounted on the other). Serial mechanisms have many shortcomings, such as accumulation of motion errors along the chain, parasitic motions and decreased dynamic characteristics.[2] However, parallel mechanisms are widely used to obtain high motion accuracy and high mechanical stiffness, leading to high resonant frequencies. Also, these mechanisms typically have a symmetrical configuration and therefore are less sensitive to temperature variation.[1]

Recent research has focused on the design of multi-DOF precision positioning stages. Li et al. proposed a parallel kinematic high bandwidth XY nano-positioning stage.[3] Cai et al. focused on the design of a planar 3-DOF stage with a T-shape flexible hinge mechanism to provide in-plane motion with relatively large out-of-plane stiffness.[4] Zhu et al. proposes a novel 2-DOF piezo-actuated parallel kinematic positioning stage with multi-level amplification based on a Scott-Russell and Z-shaped flexure hinge mechanism.[5] Yong et al. proposed an XY nano-positioning stage with a relatively high resonance frequency, scan range and decoupling between its two axes.[6] Zhu et al. developed a hybrid displacement amplification mechanism for a flexure-based vertical nano-positioning stage with a large travel range.[7] Xu et al. presented a design procedure for a new decoupled flexure-based XYZ-compliant parallel-kinematics micro-positioning stage, and designed a compact 3-DOF stage consisting of three monolithic limbs having both input and output decoupling properties.[8]

Previous research suggests that significant stage deformation is due to various thermal conditions weakening the stage structures. Thermal expansion can severely limit the precision, repeatability and overall performance of a nano-positioning stage. More precisely, the results show a temperature-dependent drift in motion and high thermal stresses, which ultimately lead to cracking, warping or loosening of components. Unfortunately, to achieve the precision required in nano-positioning, these thermal effects cannot be ignored.[9] Therefore, additional systems, such as precise environmental control systems, are required to minimize the effects of thermal deformation. However, since this requires expensive installation and maintenance costs, alternatives such as structural compensation through optimal design are desirable. Additionally, maintenance of the stage is difficult because it is composed of a single monolithic structure, and any damage to the flexible hinges requires the whole stage to be replaced. Also, the complexity of the stage requires high fabrication costs, so that the assembly-based design technique is desirable for a more effective maintenance.

In this study, a novel 2-DOF nano-positioning stage with an amplification mechanism is proposed. An optimal structure was designed, based on a mechanism that structurally offsets any thermal deformation. In addition, a flexible joint was developed, based on a monolithic limb assembly, for effective maintenance and reduction of machining costs. This paper is organized as follows: the mechanical design of the proposed stage is presented in Section II and Finite Element Analysis (FEA) is conducted to evaluate the thermal behavior and dynamic performance. In Section III, the experimental setup and identification of the stage performance are presented. To verify the effectiveness of the proposed stage, a prototype was fabricated for performance tests. Finally, conclusions are drawn in Section IV.

MECHANICAL DESIGN

For a 2-DOF nano-positioning stage, in addition to realizing a large travel range, it is crucial to ensure positional accuracy for both axes. FIGURE 1 shows a nano-positioning stage based on an amplification mechanism. As far as the designed XY stage with PEA is concerned, when a large stage workspace is required, the stroke of the PEA can be amplified by adopting a simple lever mechanism connected to a decoupler. To improve the limited displacement of micro/nano-positioning stages based on flexible hinges, a highly efficient leverage mechanism can be used for motion amplification, as illustrated in FIGURE 1 (a)–(b). The amplified motions are transferred to the moving part to drive the end-effector. The motion range of the PEA is amplified by the lever, which can be described as follows:

$$r = \frac{d_{lev}}{d_{pzt}} \tag{1}$$

Where r denotes the displacement amplification ratio of the lever, and d_{lev} and d_{pzt} denote the output displacement of the lever tip and output displacement of the PEA, respectively. In general, conventional 2-DOF nano-positioning stages (including stages with amplification mechanisms) are structurally deformed by thermal errors and can affect the posture of platform. Depending on the structure, the platform exhibits translational or rotational motion in a certain direction due to thermal deformation. FIGURE 1 (c) shows these deformations by thermal variations.

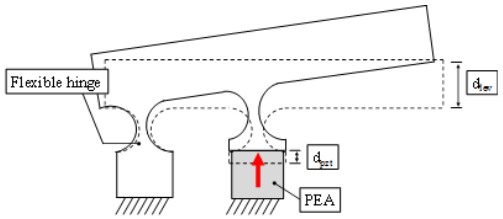

(a) Amplification mechanism

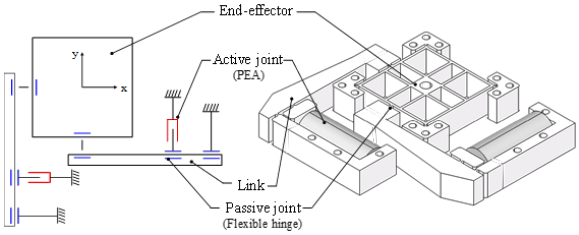

(b) 2-DOF nano-positioning stage

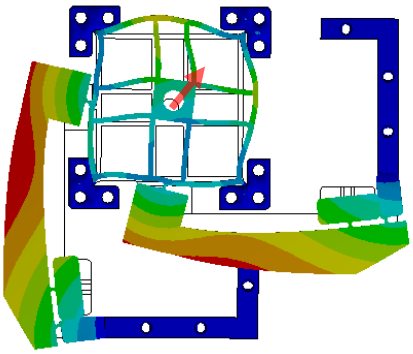

(c) Simulation for thermal deformation evaluation
FIGURE 1. The figure identification

In this paper, the optimal design of the nano-positioning stage is focused on minimization of structural thermal deformation. The basic concept of the proposed nano-positioning stage structure, including the amplification mechanism, is shown in FIGURE 2 (a). In each stage, there are two PEAs that each provide the required input displacement to the X- and Y-axes, respectively. An amplification lever is integrated into each axis of the stage to amplify displacement of the piezoelectric actuators. A minimum variation of the center deflection is needed to obtain optimal amplification from the lever. The amplified motions are transferred to the inner section to move the platform. Circular flexures are used in the design of the amplification levers, since they provide a more accurate rotational motion and avoid the twisting resonant modes that often occur at low frequencies.[6] The two stages represent the rotational motion of the end-effector due to thermal error, and each stage causes rotation in the opposing direction, according to the

structure. Therefore, a structure capable of canceling this thermal deformation was designed based on the thermal deformation tendencies of the structure.

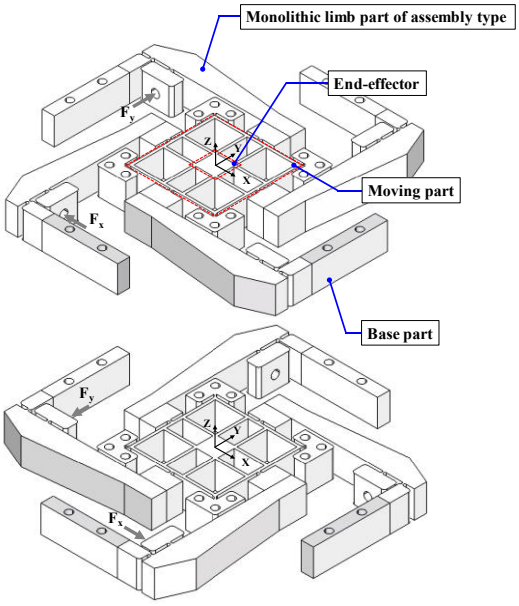

(a) 2-DOF stage based on the amplification mechanism

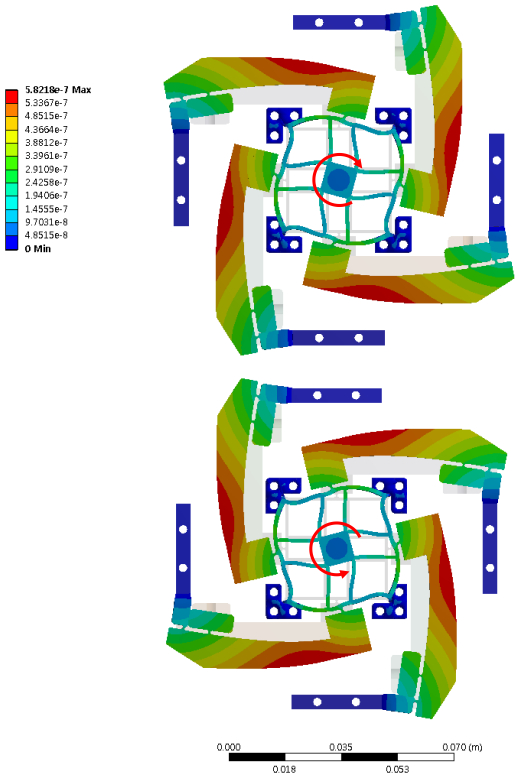

(b) Simulation investigation of deformation through an increase in temperature

FIGURE 2. Basic design concept of proposed stage

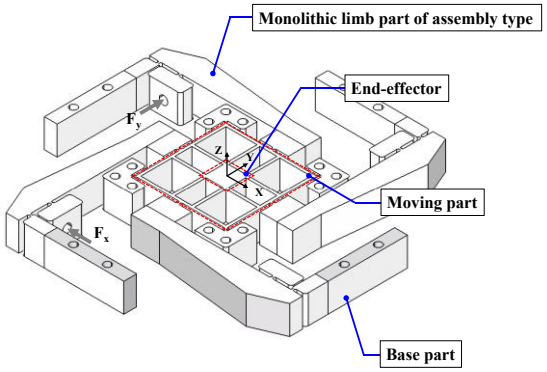

(c) Simulation for thermal deformation evaluation

FIGURE 3. Configuration of the proposed 2-DOF nano-positioning stage

The proposed nano-positioning stage is designed as a multi-stage structure, as shown in FIGURE 3. The top and bottom structures cause rotational motion in the same direction due to the thermal effect, and the middle structure generates an opposing rotational motion. Since the design has structural symmetry, it will naturally compensate for the positioning errors of each end-effector using structural deformation. Therefore, the flexure hinges of the stage will exhibit deformations according to the thermal conditions, but the platform will maintain the same position regardless. However, since the proposed stage structure cannot be processed by conventional machining methods, such as Wire-Electrical-Discharge-Machining (WEDM), a flexible hinge-based assembly concept is proposed. The two piezoelectric actuators are located at the center of the stage to minimize the influence of Abe's offset. Also, it is possible to reduce the processing cost of this stage and to perform efficient maintenance by offering a constructible monolithic limb. This is a new hinge mechanism design that can be applied to multi-DOF stages with complex structures, since it can be assembled separately. In addition, because it is possible to assemble a hinge from different material, it is easy to improve and maintain the structural rigidity of the stage. The proposed structure was evaluated using ANSYS FEA software. The simulation results show structural deformation due to thermal variations, as shown in FIGURE 4. The flexure hinges show a contracted or expanded stage; however, the end-effector maintains its position. Therefore, the validity of the proposed structure design has been verified by simulation results. FEA simulations are conducted to investigate the X and Y motions of the stage, as shown in FIGURE 5. The first two natural frequencies

from the FEA are 1,032 Hz and 1,036 Hz, respectively. The first natural mode shape indicates a translational motion of the stage in the X-direction, while the second mode shape shows the motion in the Y-direction.

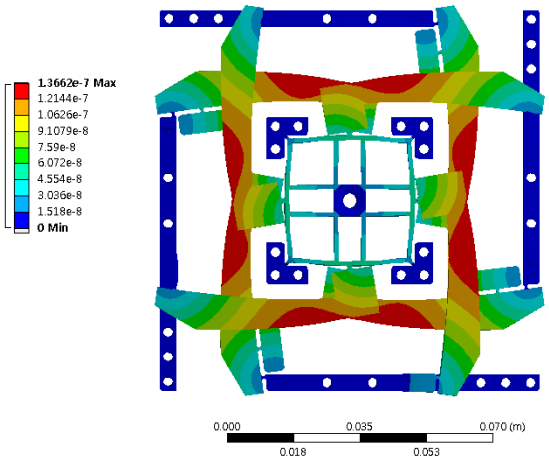

(a) Under decreasing temperature conditions

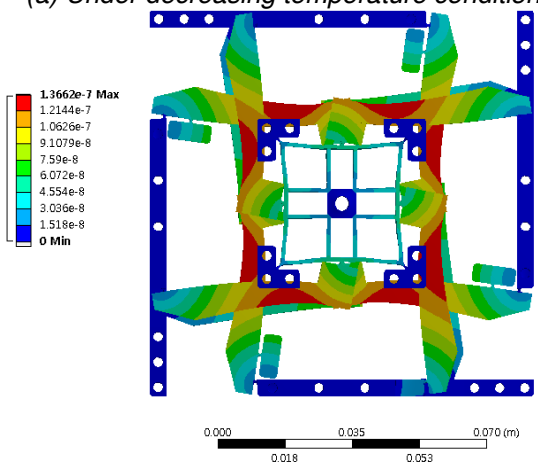

(b) Under increasing temperature conditions

FIGURE 4. Analysis of structural deformations due to variations in temperature

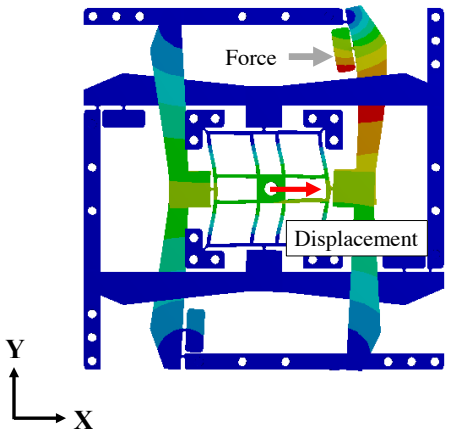

(a) Displacement results in the X-direction

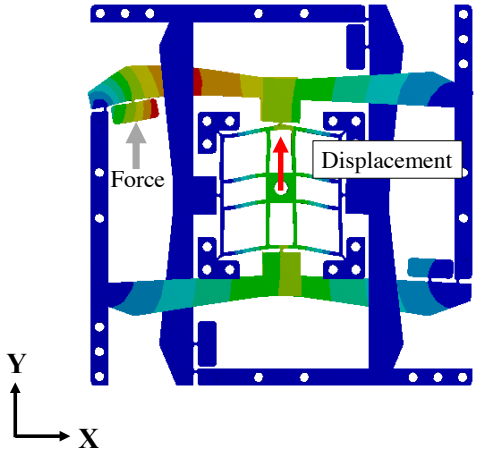

(b) Displacement results in the Y-direction

FIGURE 5. Analysis simulation of desired 2-DOF motions of the nano-positioning stage

EXPERIMENTS

In this section, the experimental setup is described, along with the characterization of the 2-DOF nano-positioning stage. Using the results predicted by the ANSYS software, a prototype of the proposed stage was fabricated using the WEDM technique due to its high accuracy. The constructible monolithic limb design and moving parts are shown in FIGURE 6. The limb and moving part were combined using a bolt fastening, and the final stage assembly is shown in FIGURE 6 (b). A PEA with a nominal stroke of 15 μm was used to drive the developed stage, and the input displacement of the end-effector was measured using capacitive sensors.

The fabricated stage has a compact size of 100 × 100 × 50 mm, as shown in FIGURE 6. The dimensions for the designed component parts (the link and moving part) are as follows: the moving part is a square, and the total length (L1) and inter length (L2) are 44 mm and 32 mm, respectively, with thickness (L3) of 1 mm; the height of moving part L5 is 5 mm, L6 is 10 mm, and L7 is 5 mm; the length of the monolithic limb and flexures, L9, is 8 mm, and L10 is 10 mm; the dimensions D1 and D2 of the flexible hinge are both 1 mm.

To minimize the uncertainties of the measurement results, the manufactured stage was fixed to an anti-vibration table. To accurately investigate the deformation due to thermal errors, a sensor was fixed to the platform to measure 2-DOF motion of the end effecter. A small steel block with a fine surface finish was attached to the end effector to measure the 2-DOF motions. Two capacitive sensors were place in close proximity to the

adjacent surfaces of the steel block to the displacement along the X- and Y-direction.

In the initial experiment, the performance of the stage was evaluated under a no-load condition. The experiments were conducted to investigate the performance of the developed stage. The feasibility of the 2-DOF motion was verified using a step response and the resolutions for two translational motions were investigated. The performance of the compensation procedure was assessed, based on a recursive algorithm, to achieve ultra-precision positioning. The results of this experiment are shown in FIGURE 7. Clear step-like motion was observed, with a resolution of 20 nm for the translational motion. The motion performances were evaluated in real-time using LabVIEW software.

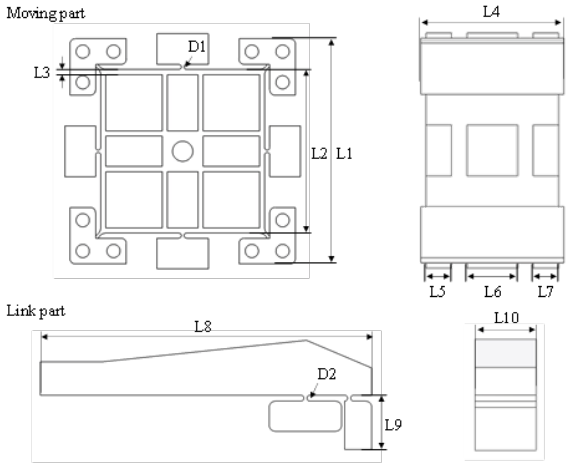

(a) Schematic drawing of the link and moving part

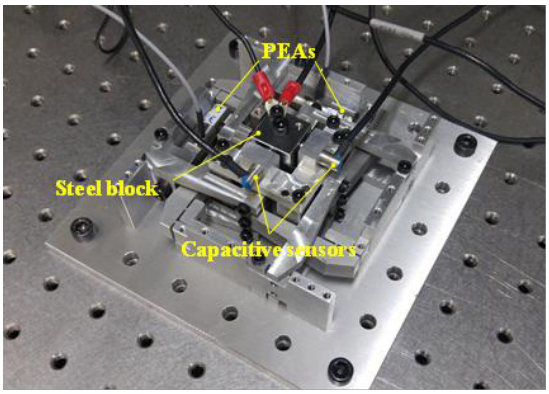

(b) Assembly

FIGURE 6. Fabrication of the designed 2-DOF nano-positioning stage

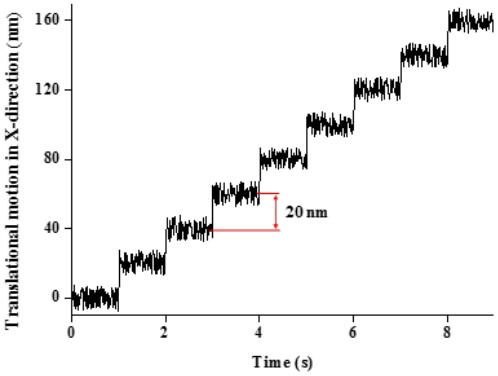

(a) Translational motion of X-axis

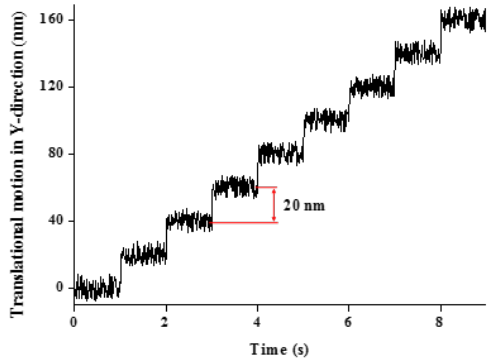

(b) Translational motion of Y-axis

FIGURE 7. Step response of the 2-DOF nano-positioning stage

The high-speed transfer performance of the nano-positioning stage was investigated using a triangular signal with frequencies of 250 Hz and 500 Hz. The experimental results show a similar triangular signal, as shown in FIGURE 8. Finally, a laser interferometer (XL80; Renishaw Plc., U.K.) was used to verify the transfer performance of the proposed 2-DOF stage. These were then compared to two previous measured results and repeated five times for repeatability. Under these specific experimental conditions, each axis was linearly transferred, and the 2-DOF motion was measured and investigated in a static stage. As shown in the experimental results, the maximum deviations of the translational motions were approximately 100 nm and 170 nm, respectively. The difference between the results obtained using the capacitive sensor and the laser interferometer were within the accuracy of the stage itself, proving the performance validity of the nano-positioning stage.

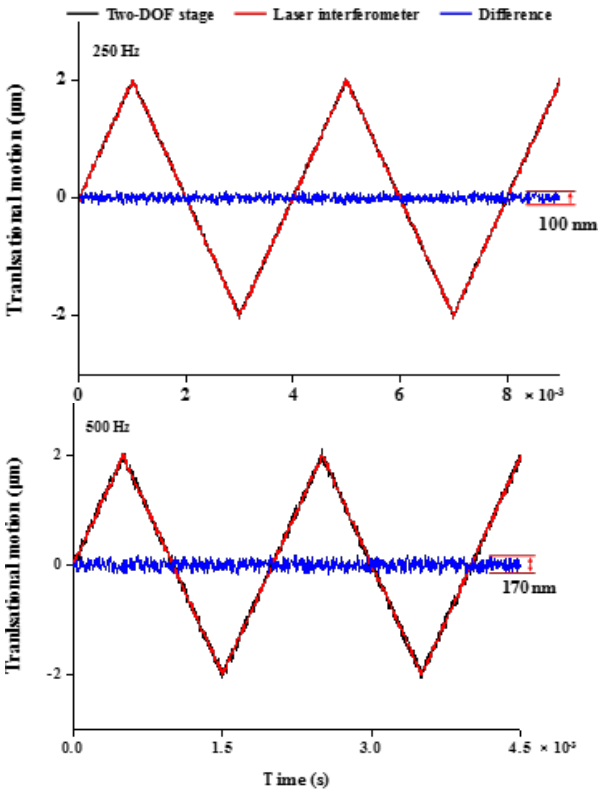

FIGURE 8. Tracing performance and verification of the stage

CONCLUSIONS

In this study, a new 2-DOF nano-positioning stage was developed to minimize distortion due to thermal variation. A three-stage laminated structure stage was proposed to cancel out any structural thermal deformation. In addition, a constructible monolithic limb based on a flexible hinge was designed for efficient maintenance and cost reduction. This will contribute greatly to the design of stages with complicated structures that cannot be manufactured by conventional methods. To verify the validity of the proposed stage structure, the structural thermal deformation was examined using FEA software. The stage was designed and fabricated to evaluate its own ultra-precise 2-DOF translational motion. Also, it can quantitatively evaluate and verify the transfer performance in comparison with the results of the laser interferometer. This new assembly based ultra-precision stage can improve the performance of a multi-DOF stage by allowing for flexible design. Additionally, this work may contribute to high-precision measurements and compensation, thereby enhancing positional accuracy.

ACKNOWLEGE

This work was supported by a National Research Foundation of Korea (NRF) grant funded by the Ministry of Education (2010-0020089) and the Korea Government (2017R1A2B2009475).

REFERENCES

[1] Gao P, Swei S, Yuan Z. New Piezoelectric Precision Micropositioning Stage Utilizing Flexure Hinge. Nanotechnology. 1999; 10: 394-398.

[2] Zhu Z, Zhou X, Liu Z, Wang R, Zhu L. Development of a Piezoelectrically Actuated Two-DOF Fast Tool Servo with Decoupled Motions for Micro-/Nanomachining. Precision Engineering. 2014; 38: 809-820.

[3] Li C, Gu G, Yang M, Zhu L. Design, Analysis and Testing of a Parallel Kinematic High Bandwidth XY Nano-positioning Stage. Review of Scientific Instruments. 2013; 84: 1-12.

[4] Cai K, Tian Y, Wang F, Zhang D, Shirinzadeh B. Development of a Piezo-driven 3-DOF Stage with T-shape Flexible Hinge Mechanism. Robotics and Computer-Integrated Manufacturing. 2016; 37: 125-138

[5] Zhu W L, Zhu Z, Shi Y, Chen X, He Y, Ehmann K F. A Novel Piezoelectrically Actuated 2-DOF Compliant Micro/Nano-positioning Stage with Multi-level Amplification. Review of Scientific Instruments. 2016; 87: 105006-1~13.

[6] Yong Y K, Aphale S S, Moheimani S O R. Design, Identification and Control of a Flexure-based XY Stage for Fast Nanoscale Positioning. IEEE Transactions on Nanotechnology. 2009; 8: 46~54.

[7] Zhu X, Xu X, Wen Z, Ren J, Liu P. A Novel Flexure-based Vertical Nano-positioning Stage with Large Travel Range. Review of Scientific Instruments. 2015; 86: 105112-1~10.

[8] Xu Q S, Li Y M. Design of a New Decoupled XYZ Compliant Parallel Micropositioning Stage with Compact Structure. Proceedings of the 2009 IEEE International Conference on Robotics and Biomimetics. 2009; 901~906.

[9] Yong Y K, Moheimani S O R, Kenton B J, Leang K K. Invited Review Article: High-speed Flexure Guided Nano-positioning: Mechanical Design and Control Issues. Review of Scientific Instruments. 2012; 83: 121101-1~18.

A FLEXURE-BASED MULTI-LAYER ROLL-TO-ROLL PRINTING SYSTEM

Chenglin Li and Shih-Chi Chen*
Department of Mechanical and Automation Engineering
The Chinese University of Hong Kong
Shatin, N.T., Hong Kong SAR, China
*Email: scchen@mae.cuhk.edu.hk

In this paper, we present the design and characterization of a fully automated flexure-based multi-layer roll-to-roll (R2R) printing system for continuous fabrication of multi-layer devices. The new R2R system achieves nanometer level multi-axis positioning precision and submicron level cross-layer registration precision via the development of a five-axis roller positioner and a new vision-based alignment method that enables the use of two low resolution cameras to achieve nanometer level precision.

PRECISION MULTI-LAYER R2R PRINTING

R2R printing technologies, e.g., gravure and flexography, have been widely utilized in many emerging applications such as organic photovoltaic (OPV) devices and flexible electronics. They present tremendous advantages in terms of cost and throughput. Recently, contact printing techniques, e.g., MCP and nanoimprint lithography (NIL), have been successfully implemented on R2R platforms, driving the print resolution of R2R platforms to submicron level [1, 2]. However, one critical issue to be addressed in the aforementioned R2R systems is that they lack the capability to register the patterns precisely across layers, which fundamentally limits the system to produce complex and functional devices. Although new multi-axis precision alignment methods, e.g., vision-based method (~200 nm/ sub-microradian for linear/angular alignment) [3], have been proposed and demonstrated, they have never been applied to state-of-the-art R2R systems to realize multi-layer printing.

To realize multi-layer precision R2R printing, one must have a (1) multi-axis positioner for controlling the rollers with nanometer level repeatability and precision, and (2) practical metrology solution that provides nanometer level accuracy for in-plane measurements. Current R2R systems use conventional bearings to guide the printing motion, resulting in low repeatability and precision; these R2R systems also lack the required degrees of freedom (DOF) to correct the "roll" and "yaw" errors of the roller, i.e., rotational errors in the θ_X and θ_Y directions respectively as illustrated in Fig. 1, resulting in non-uniform distribution of the print pressure (Fig. 1A) and angular misalignment between the patterned layers (Fig. 1B). To address these issues, we will use flexures [4-7] to design precise and highly repeatable mechanisms to guide the motion of rollers in a R2R system.

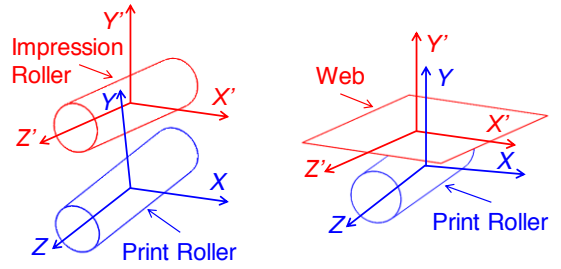

A B

FIGURE 1. Illustration of different types of misalignments in a R2R system. A: "roll" error; B: "yaw" error.

FIVE-AXIS ROLLER POSITIONER

Previously, we have developed a flexure-based R2R system for single-layer large-area continuous printing [1, 8-9], achieving a 100 nm print resolution on a 4" web. Based on this work, we have developed a five-axis roller positioner to realize precision multi-layer R2R printing for fabricating complex devices of 100s nm resolution. The challenge lies in the precise position control between the web and the print roller, to which the stamp is attached.

Figure 2 presents the CAD model of the five-axis roller positioner, where two monolithic compliant *X*-*Y* stages are installed to support and guide the compliant *Z* stage. The print roller is mounted on the *Z*-stage so that it has five DOF error correction capability, i.e., *x*, *y*, *z*, θ_X, and θ_Y. Each *X*-*Y* stage is driven by two voice coil actuators (VCA) (X_I, X_O, Y_I, and Y_O, NCC03-15-

050-2X, H2W) and provides decoupled motion guidance capability in the *X* and *Y* axes. The compliant *Z* stage is also driven by a VCA (*Z*, NCC05-18-060-2PBS, H2W). VCAs are used due to their high bandwidth (400 Hz) and high force output (~28 N/Amp). A stepper motor (NEMA 23, NI) is connected to the shaft, i.e., print roller, with an elastomeric coupler and controls the printing process (motion in θ_Z).

Figure 3 presents simulated results of the five-axis positioner, which yields decoupled motions in five axes, i.e., *x*, *y*, *z*, θ_X, and θ_Y.

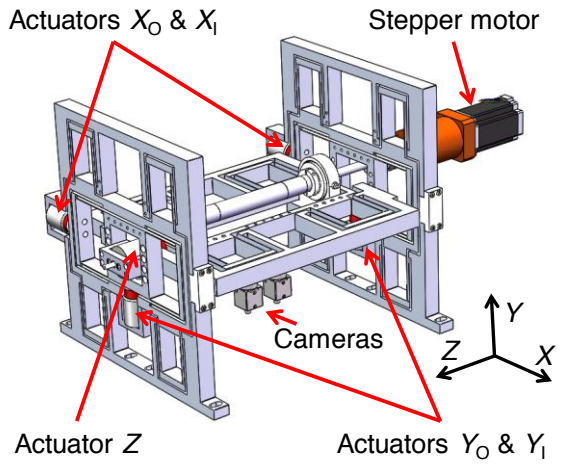

FIGURE 2. CAD model of the flexure-based five-axis roller positioner

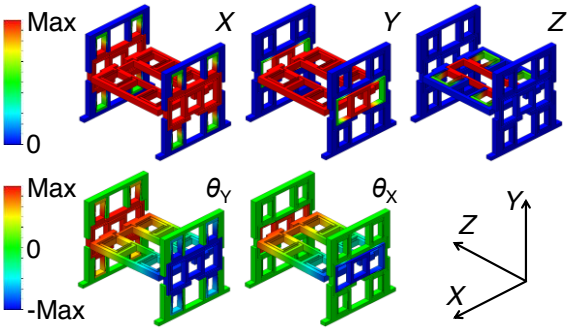

FIGURE 3. Simulated results of the five-axis positioner, demonstrating decoupled motion control in the X, Y, Z, θ_X, and θ_Y axes.

ASSEMBLY AND CHARACTERIZATION

To characterize the dynamic properties of the five-axis roller positioner, an impulse response experiment is conducted. Based on the measured displacement data from the capacitance probes, resonant frequencies in different axes are calculated by fast Fourier transform (FFT). Table 1 summarizes the performance specifications of the positioner, including the resonant frequencies, strokes, and minimum increments in all six axes.

TABLE 1. Specifications of the five-axis roller positioner.

	Frequencies	Strokes	Min. increments
X	10.0 Hz	±1 mm	50 nm
Y	9.5 Hz	±1 mm	75 nm
Z	19.0 Hz	±1 mm	200 nm
θ_X	32.5 Hz	±1 mrad	2 μrad
θ_Y	28.0 Hz	±1 mrad	2 μrad
θ_Z	83.5 Hz	-	-

To characterize the cross-axis motion coupling effect, static displacement experiments are performed to identify the matrix, S_X, that maps actuator input voltages, X_A, to mechanism displacements, X_C. Six capacitance probes are fixed on a vibration isolation table to monitor the motions of the roller positioner. Assuming small displacements, Eqs. (1) and (2) can be used to obtain the matrix S_X [10]. The analytical solution of S_X is shown in Eq. (3), where a, b, c, d, and e are constant parameters related to the characteristics of the VCAs and flexural stages. The analytical S_X indicates that the motions in the *X*, *Y*, and *Z* axes are decoupled. Nevertheless, due to manufacturing errors and misaligned actuators and sensors, the measured S_X has deviations, and the motions in different axes are coupled to a certain degree. The measured results are shown in Eq. (4). The units used in Eqs. (1)–(4) are microns, microradians and millivolts.

$$X_C = S_X X_A \rightarrow \left[\Delta x \quad \Delta\theta_y \quad \Delta y \quad \Delta\theta_x \quad \Delta z\right]^{\mathrm{T}} = S_X \left[x_{\mathrm{I}} \quad x_{\mathrm{O}} \quad y_{\mathrm{I}} \quad y_{\mathrm{O}} \quad z\right]^{\mathrm{T}} \tag{1}$$

$$X_A = S_X^{-1} X_C \tag{2}$$

$$S_X = \begin{bmatrix} a & a & 0 & 0 & 0 \\ b & -b & 0 & 0 & 0 \\ 0 & 0 & c & c & 0 \\ 0 & 0 & -d & d & 0 \\ 0 & 0 & 0 & 0 & -e \end{bmatrix} \tag{3}$$

$$S_X = \begin{bmatrix} 2.35 & 2.45 & 0.15 & -0.13 & -0.07 \\ 2.93 & -2.86 & -0.07 & 0.05 & 0.07 \\ -0.07 & 0.23 & 2.12 & 1.04 & -0.04 \\ 0.02 & -0.04 & -2.57 & 3.43 & -0.09 \\ -0.55 & 0.58 & 0.04 & 0.02 & -1.46 \end{bmatrix} \tag{4}$$

POSITIONING EXPERIMENTS

Static positioning experiments in selected axes (*X*, *Z*, and θ_Y) are performed to demonstrate the precision of the roller positioner. In these experiments, the matrix, S_X^{-1} , is used in a closed-loop PID controller for correction, and the position feedback signals are obtained from the six capacitance probes. Figure 4 plots the measured displacements (left column) and off-axis errors (right column) versus closed-loop displacement commands. The results show that the off-axis translational and rotational errors are controlled within ±50 nm in *X*/*Y*/*Z* axes, and ±100 nrad in θ_X/θ_Y axes; the errors are comparable to the resolution of the capacitance probes (C8/CPL190, Lion Precision, resolution: 20 nm).

Figure 5 presents the positioning results in all five axes under the PID control. In this experiment, the positioner is commanded to perform 10-*μ*m and 30-*μ*rad steps in the *X*, *Y*, *Z*, θ_X and θ_Y axis in a sequential fashion, with each step held for 20 seconds. As Fig. 5 shows, the motion in one axis does not affect motions in other five axes. It is found that, under closed-loop control, the *X*, *Y*, *Z*, θ_X and θ_Y axes have a resolution of ±100 nm, ±200 nm, ±200 nm, ±2 *μ*rad and ±2 *μ*rad respectively. Note that error motions in θ_Z axis are mainly caused by manufacturing errors, which are relatively small, i.e., within ±3 *μ*rad in this experiment.

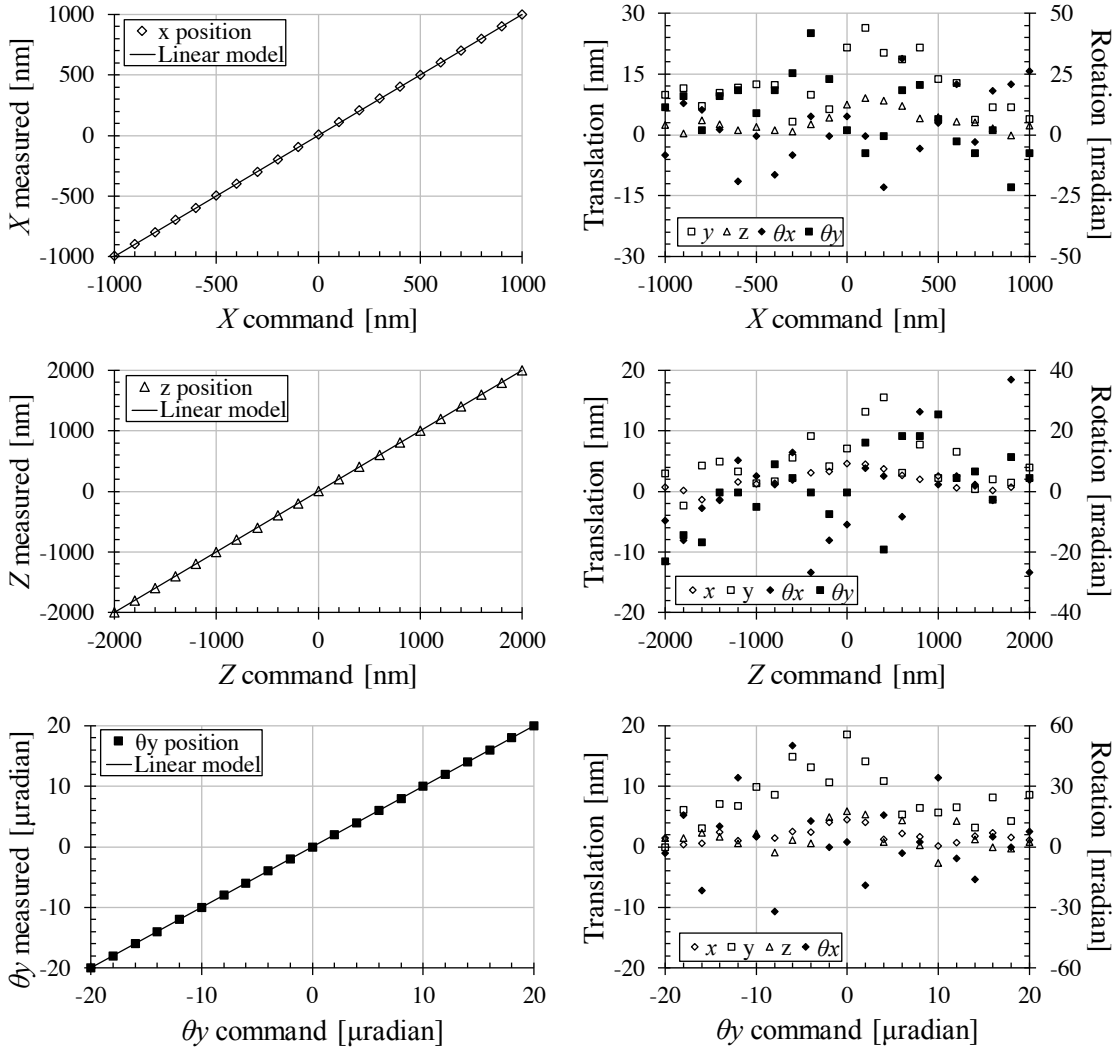

FIGURE 4. X, Z, and θ_Y positioning results under closed-loop control.

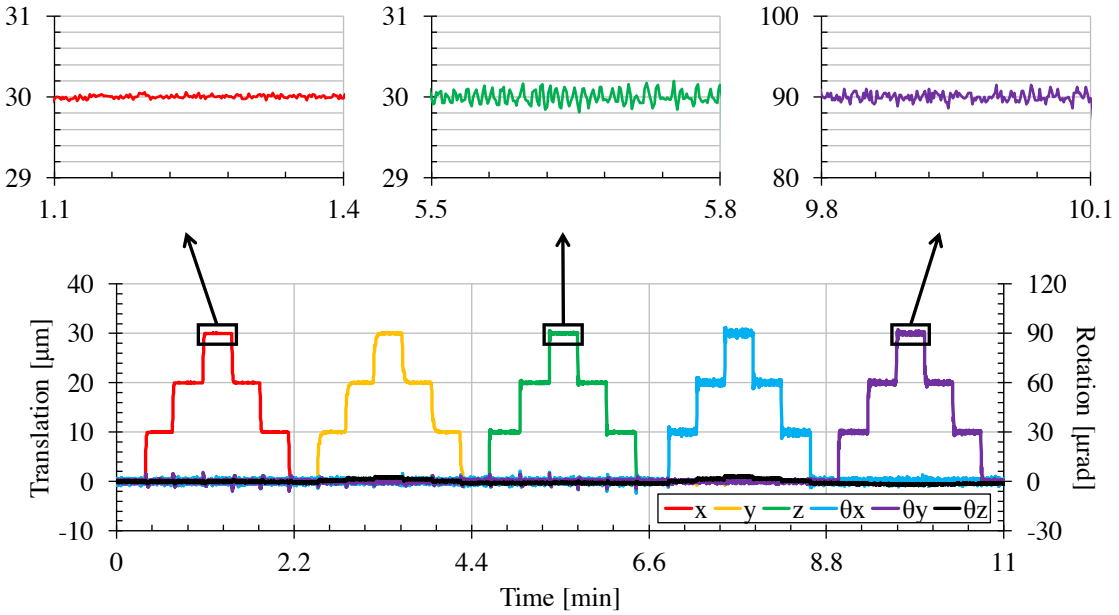

FIGURE 5. Positioning results in all five axes, i.e., X, Y, Z, θ_X, and θ_Y axes, with PID control

MULTI-LAYER ALIGNMENT – SIMULATION AND VERIFICATION

In this section, we present a vision-based method that employs two low resolution cameras to achieve nanometer level precision. Inspired by the vision-based absolute planar encoder design [3, 11], we have designed a new hybrid alignment mark, as shown in Fig. 6A, to be printed on the edges of the web along with the first layer patterns. The alignment mark consists of periodic grid patterns and cross marks. First, by comparing the position of the cross mark with the center of the camera, position measurement can be achieved with a resolution equal to the pitch of the grid pattern, i.e., 10s μm. Following that, a discrete Fourier transform (DFT)-based phase estimation method is used to determine the position within each period of the grid pattern, achieving nanometer level linear position measurement as well as sub-microradian level angular position measurement.

Simulated experiments are performed in MATLAB to verify the capability and feasibility of the alignment algorithm, where translational and rotational displacements are introduced to the image. In the experiment, the test alignment mark (Fig. 6C) has a resolution of 512 × 512 pixels, and the pitch of the 2D grid pattern is 4 pixels in both *X* and *Z* directions. Through pattern recognition of the cross mark, we can estimate the absolute position in the *X* and *Z* axes with a resolution of one pixel (~5 microns).

Next, the amplitude and phase spectrum of the image is obtained by 2D DFT (Fig. 6D and 6E). Based on the four fundamental frequency components (maximum amplitudes, red and green points in Fig. 6D), the absolute angular resolution is found to be ±4 milliradians. By analyzing the phase spectrum with the four fundamental frequency components, high resolution positioning sensing can be achieved, i.e., 0.3% error (~10s nm for practical application) in *X*/*Z* axes and ±0.5 microradians in θ_Y axis. Note that the angular position variation between successive images need to be less than 1 mrad in order to obtain the precision stated above.

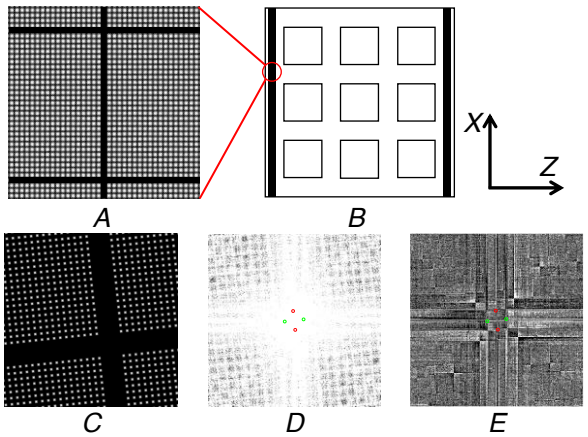

FIGURE 6. Design of the hybrid alignment mark (A) to be printed on the two edges of the web (B); MATLAB simulation results: hybrid alignment mark with displacements in X/Z/θ_Y

axes (C), and its spectrum in amplitude (D) and phase (E). The red and green points show the fundamental frequency components.

SYSTEM INTEGRATION

Figure 7 presents the prototype multi-layer R2R printing system, integrated with the five-axis roller positioner. The system includes a rewinding module, unwinding module, tension control module, web guide module, and two printing modules, where the right one prints the first layer, and the left one registers and prints the subsequent layers.

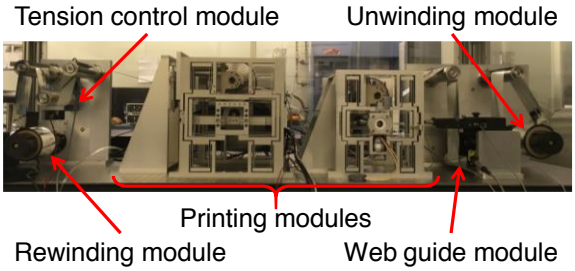

FIGURE 7. Prototype flexure-based R2R system with integrated five-axis roller positioner for precision multi-layer printing

CONCLUSION

We have presented the design and characterization of a flexure-guided five-axis roller positioner and a new vision-based alignment method for multi-layer R2R printing, achieving 100s nanometer positioning and registration precision. The roller positioner is driven by five high performance VCAs, where capacitance probes are used to monitor the displacement in different axes in real time. Closed-loop control is implemented to the system, achieving a resolution ±50 nm in *X*/*Y*/*Z* axes, and ±100 nrad in θ_X/θ_Y axes. These promising results show that R2R fabrication may achieve comparable resolution with photo-lithography at a much lower cost.

ACKNOWLEDGMENT

This work is supported by the HKSAR Research Grants Council (RGC), Theme Based Research Scheme (TRS), T23- 407- 13N.

REFERENCES

[1] Zhou X, Wang D, Wang J, and Chen S. Precision Design and Control of a Flexure-based Roll-to-roll Printing System. Precision Engineering. 2016, 45, 332-341.

[2] Ahn SH, Guo LJ. Large-area Roll-to-roll and Roll-to-plate Nanoimprint Lithography: A Step toward High-throughput Application of Continuous Nanoimprinting. ACS Nano. 2009, 3(8), 2304-2310.

[3] Cao Z, Chen Z, and Huang PS. A Vision-based Absolute Planar Encoder for High Precision In-plane Position Measurement. Proc. of the Annual Meeting of the ASPE, Portland, OR, USA, Oct. 2016, pp.161-66.

[4] Howell L. Compliant Mechanisms. John Wiley and Sons Inc. New York: 2001.

[5] Li C, Wang J, and Chen S. "Flexure-based Dynamic-tunable Five-axis Nanopositioner for Parallel Nanomanufacturing. Precision Engineering. 2016, 45, 423-434.

[6] Chen W, Yang S, Liu J, Chen W, and Jin Y. Design of a Novel 5-DOF Flexure-based Compound Alignment Stage for Roll-to-roll Printed Electronics. Review of Scientific Instruments. 2017, 88(2), 025002.

[7] Paolo B. Design and Development of High Precision Five-axis Positioning System for Roll-to-roll Multi-layer Microcontact Printing. Master Thesis. Massachusetts Institute of Technology. 2009.

[8] Zhou X, Xu H, Cheng J, Zhao N, and Chen S. Flexure-based Roll-to-roll Platform: A Practical Solution for Realizing Large-area Microcontact Printing. Scientific Reports. 2015, 5, 10402.

[9] Wang D, Zhou X, and Chen S. Control Strategy for Flexure-based Precision Roll-to-roll Machine. Proc. of the Annual Meeting of the ASPE, Austin, TX, USA, Nov. 2015, pp.27-31.

[10] Culpepper ML, Anderson G. Design of a Low-cost Nano-manipulator which Utilizes a Monolithic, Spatial Compliant Mechanism. Precision Engineering. 2004, 28(4), 469–482.

[11] Chen ZH, and Huang PS. A Vision-based Method for Planar Position Measurement. Measurement Science and Technology. 2016, 27(12), 125018.

LARGE STROKE HIGH SUPPORT STIFFNESS FLEXURE BASED UNIVERSAL JOINT

M. Naves[1], R.G.K.M. Aarts[2], and D.M. Brouwer[1]
[1]**Precision Engineering**
University of Twente
Enschede, The Netherlands
[2]**Structural Dynamics, Acoustics and Control**
University of Twente
Enschede, The Netherlands

ABSTRACT
Universal two degree of freedom flexure joints are often used for parallel manipulators or applications which demand transmission of torque. However, contemporary flexure-based universal joints are limited to small deflection angles caused by their strong loss of stiffness in support directions when deflected or are initially already compliant in the intended support directions. In this paper, a new concept for a high performance large stroke universal flexure joint is presented which can maintain a high level of support stiffness in both translational and torsional directions over its total range of motion of $\pm$25 degrees.

INTRODUCTION

Universal joints are commonly used for applications which require transmission of rotation from one direction to another, or spatial motion stages such as parallel manipulators [1]. For high precision mechanisms flexure-based joints are used for their deterministic behavior. However, these joints are restricted to only small deflection angles, suffer from a lack of support stiffness in load carrying directions and support stiffness decreases strongly with deflection [2]. Furthermore, motion in the two independent rotational degrees of freedom is often obtained by serial stacking of compliant elements, resulting in under-constrained intermediate bodies and low support stiffness [3].

We have shown that the folded leafspring has proven to be a flexure element that properly maintains a high level of support stiffness over a large range of motion and can be used to construct high stiffness large stroke spherical flexure joints [4]. In this paper, we present a new concept for a two degree of freedom universal flexure joint comprising folded leafsprings, resulting in a high level of stiffness in all support directions over a large range of motion.

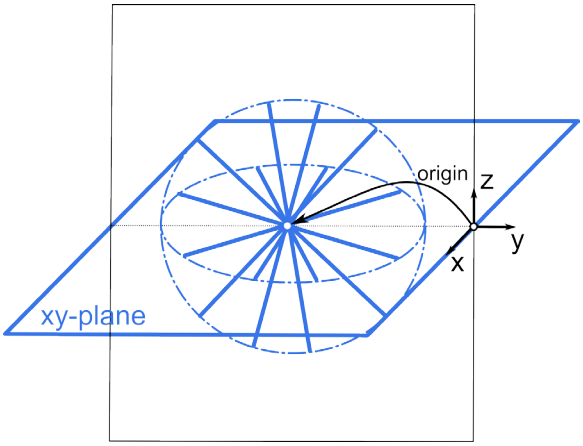

FIGURE 1. Representation of the constraint space for a universal joint, either intersecting the origin or positioned in the xy-plane [5]

CONCEPTUAL DESIGN

A folded leafspring has the property to only constrain the translational degree of freedom collinear to the intersection of the two leafsprings, provided by the folding line. Therefore, in order to obtain the required two degrees of freedom for the universal joint, at least four folded leafsprings are required each constraining a single degree of freedom. To allow for tip/tilt rotational motion only, the constraints have to either intersect the instant center of rotation, or have to lay in a plane which coincides the instant center of rotation [5], illustrated in figure 1. To ensure motion is constrained in all intended four support directions, the folding line of at least one folded leafspring has to intersect the instant center of rotation, and at least one

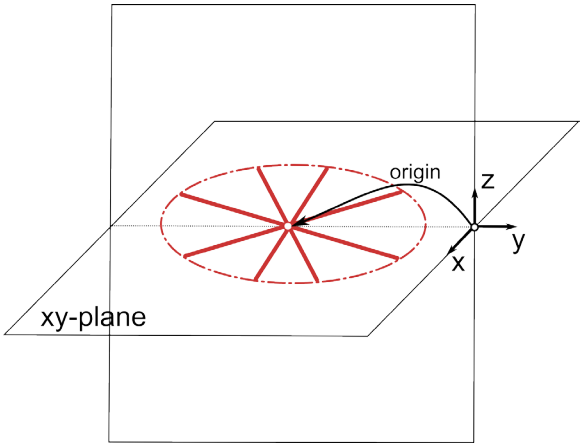

FIGURE 2. Representation of the freedom space for the universal joint, provided by all rotational degrees of freedom with the axis of rotation positioned in the xy-plane intersecting the origin [5]

has to lay in the plane coinciding with the instant center of rotation. We define the instant center of rotation as the origin and rotation around the x- and y-axis as the required tip/tilt motion. Therefore, all constraints have to either intersect the origin "O" or have to lay in the xy-plane "XY". The considered degrees of freedom are schematically illustrated in figure 2.

If we only take into account the exact constrained solutions, three distinctive topologies can be conceived. The first solution, shown in figure 3, is an exact constrained universal joint consisting of three folded leafsprings with the folding line in the xy-plane and one folded leafspring intersecting the instant center of rotation (named O^1XY^3). The second solution consists of two folded leafsprings both intersecting the xy-plane and the instant center of rotation, O^2XY^2, illustrated in figure 4. The last remaining solution contains a single folded leafspring in the xy-plane and three intersecting the instant center of rotation, O^3XY^1, illustrated in figure 5.

To potentially improve support stiffness, over-constrained topologies can be considered by adding extra folded leafsprings. An example of an over-constrained rotational symmetric topology consisting of six folded leafsprings is provided in figure 6. This topology consists of both three folded leafsprings intersecting the xy-plane and the origin (O^3XY^3).

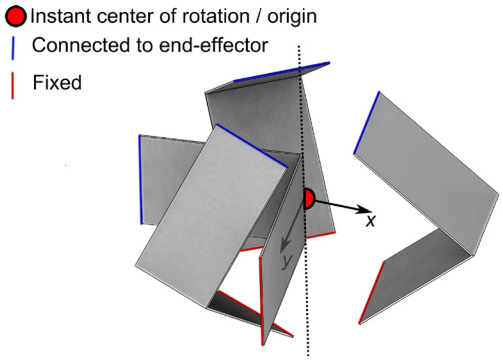

FIGURE 3. Topology with three folded leafsprings with the folding line in the xy-plane and a single folded leafspring intersecting the origin (O^1XY^3)

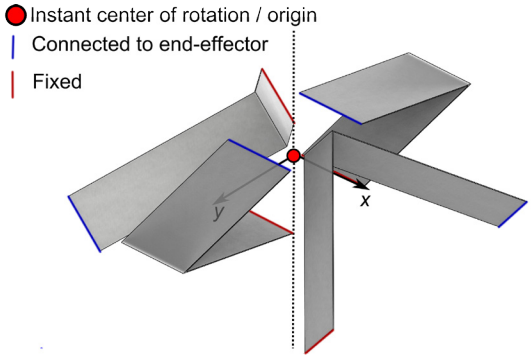

FIGURE 4. Topology with two folded leafsprings with the folding line in the xy-plane and two folded leafspring intersecting the origin (O^2XY^2)

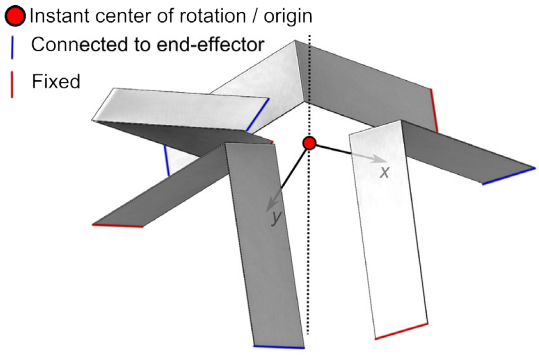

FIGURE 5. Topology with one folded leafspring with the folding line in the xy-plane and three folded leafspring intersecting the origin (O^3XY^1)

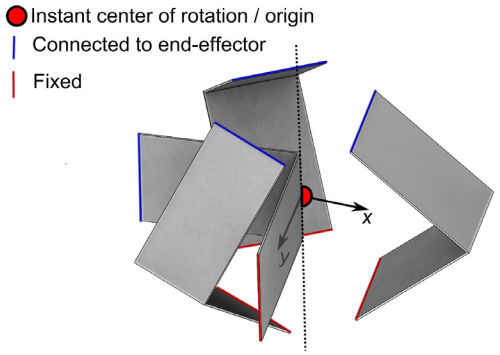

FIGURE 6. Over-constrained rotational symmetric topology with three folded leafsprings with the folding line in the xy-plane and three folded leafspring intersecting the origin (O^3XY^3)

PERFORMANCE COMPARISON

To compare the performance of the described joint topologies, a shape optimization algorithm is used to optimize the designs and to compare the support stiffness [6]. For this comparison the topologies which are not under-constrained, with a maximum of 3 folded leafsprings with the folding line in either the xy-plane or intersecting the origin, are optimized. To restrain the number of design parameters, both the folded leafsprings with the folding line in the xy-plane and the folded leafsprings with the folding line intersecting the origin are positioned in a rotational symmetric matter around the z-axis. As an example, the joint topologies shown in figure 3-6 are constructed in this rotational-symmetric matter.

For the optimization, the performance is evaluated over the entire range of motion with the flexible multi-body software SPACAR [7] to efficiently calculate the strong non-linear stiffness behavior. Due to the intertwined nature of the flexures and to ensure maximum usage of the design space, designs are optimized to only just avoid collision between flexures over its full range of motion. For this optimization case, we consider an universal joint with steel flexures (E-modulus: 210GPa, G-modulus: 80GPa) which allows for a tip/tilt bidirectional motion of 25 degrees. Furthermore, maximum actuation moment is restricted to 5Nm and the stress due to deformation is limited to 300MPa. As optimization criterion, the torsional stiffness around the z-axis is considered which is evaluated at maximum tip/tilt angle. Additionally, a constraint is set on the minimum translational support stiffness in x-, y- and z-direction of 1000 N/m. The results of the optimized topologies is given in table 1. It has to be noted that the optimization results are strongly affected by the considered optimization case and results can differ for other cases. However, from the obtained results for this specific case, an indication can be given for the level of support stiffness which can be obtained for an universal joint which allows for 25 degrees tip/tilt motion and some distinct properties for some of the joint topologies can be identified.

Table 1 shows for the first exact constrained joint topology O^1XY^3 a high level of translational support in x- and y-direction combined with a good level of torsional stiffness (K_{rz}). This high level of stiffness is provided by the three folded leafsprings with the folding-line in the xy-plane. Translational stiffness in z-direction is limited as it depends on a single flexure intersecting the origin. Joint topology O^2XY^2 attains similar stiffness values where torsional and translation support in x-direction is provided by the flexures in the xy-plane and support in y- and z-direction is obtained from the flexures intersecting the origin. At last, joint topology O^3XY^1 only provides limited torsional support as only a single flexure is contributing to the torsional stiffness.

Furthermore, it can be observed that the over-constrained asymmetric joint topologies (O^2XY^3 and O^3XY^2) provide no improvement in performance, despite the increased number of flexures. This is caused by a reduction of the feasible design space which is free of collision for the increased number of flexures. Especially for asymmetrical topologies, collision is hard to avoid which effectively results in a reduction of performance. For the symmetric over-constrained topology O^3XY^3 collision can be avoided more effectively and therefore, an increase of performance is obtained.

EXPERIMENTAL VALIDATION

The results obtained from the optimization have been used to design and manufacture the O^3XY^3 joint topology. A prototype of this joint is pictured in figure 7. Due to the spatial layout of the flexures, two 3D-printed frame parts (in orange) are used to connect to both ends of the folded leafsprings. To allow for proper clamping force on the leafsprings, the frame parts are reinforced by two

TABLE 1. Support stiffness of optimized universal joint topologies at 25 degrees tilt

Topology	K_x [N/mm]	K_y [N/mm]	K_z [N/mm]	K_{rz} [Nm/rad]
O^1XY^3	13.0	14.3	1.0	28.9
O^2XY^2	17.7	13.4	15.9	27.6
O^3XY^1	6.9	4.9	3.1	3.9
O^2XY^3	1.1	2.4	3.2	21.9
O^3XY^2	6.4	9.1	1.7	15.7
O^3XY^3	3.0	2.6	3.2	44.7

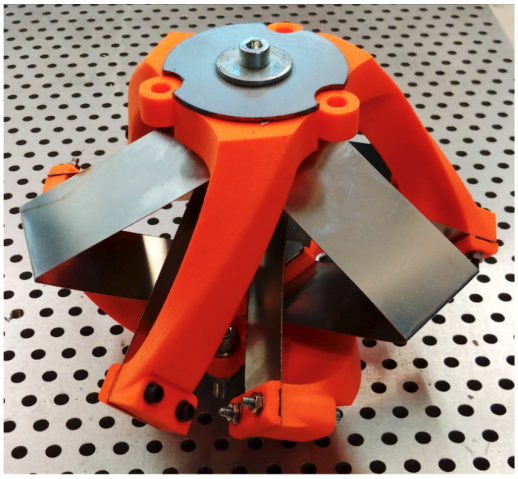

FIGURE 7. Prototype of the O^3XY^3-joint consisting of 3d-printed frame parts and spring-steel folded leafsprings

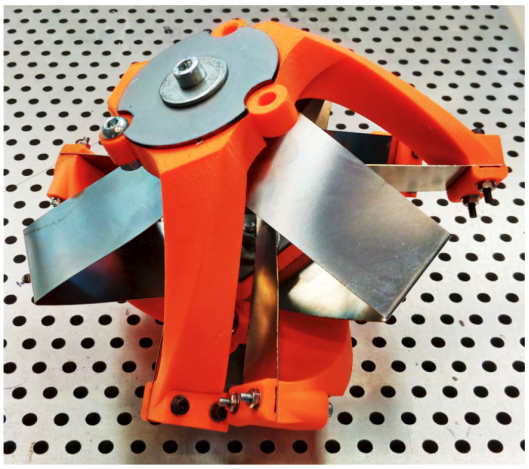

FIGURE 8. Prototype of the O^3XY^3-joint at 22.5 degrees tilt angle

steel plates. Furthermore, the two sets of three folded leafsprings are manufactured from 0.3mm thick spring steel and folded to the required folding angle (not necessary 90 degrees). First observations confirm the high level of translational and torsional support stiffness over its full range of motion and the allowed deflection angle of $\pm$25 degrees tip/tilt (figure 8).

DISCUSSION

In order to provide a higher level of support stiffness for the universal joint, over-constrained designs are considered. Although over-constrained designs can results in an increased level of support stiffness, care has to be taken when designing over-constrained. In order to prevent high levels of internal stress, buckling, or reduction of support stiffness caused by misalignment in over-constrained designs, misalignments have to be reduced to a minimum. For typical flexure mechanisms, misalignments below 50% of the misalignment at which bifurcation occurs does not significantly influence the systems natural frequencies and stiffness and gives a good indication of the alignment accuracy which has to be obtained [8]. However, over-constrained issues primarily arise when considering undeflected or small stroke compliant mechanisms, at which the flexures provide a high level of support stiffness in the directions in which motion is constrained. When larger deflections are considered, support stiffness in the constrained directions typically drops caused by the deformation of the flexures, resulting in a mitigation of internal stress caused by miss-alignments and therefore reducing over-constraint related problems.

CONCLUSION

To obtain a flexure based universal joint allowing for large tip/tilt angles while simultaneously maintaining a high level of support stiffness,

a series of folded leafsprings are combined and positioned such to allow for tip/tilt motion only. By only considering exact constrained solutions, a good level of support stiffness can be obtained. An increase in performance can be achieved by using over-constrained topologies. However, care has to be taken to maintain a proper level of symmetry in order to efficiently allow for the avoidance of collision. Based on the obtained optimization results considering a two-DOF universal joint allowing for $\pm$25 degrees of tip/tilt-motion, a prototype has been manufactured. Preliminary results confirm the high level of support stiffness in all support directions and the available range of motion.

REFERENCES

[1] Moon YM, Kota S. Design of compliant parallel kinematic machines. ASME Design Engineering Technical Conferences and Computer and Information in Engineering Conference. 2002;(1):34204.

[2] Trease BP, Moon YM, Kota S. Design of Large-Displacement Compliant Joints. Journal of Mechanical Design. 2005;127(4):788.

[3] Farhadi Machekposhti D, Tolou N, Herder JL. A Review on Compliant Joints and Rigid-Body Constant Velocity Universal Joints Toward the Design of Compliant Homokinetic Couplings. Journal of Mechanical Design. 2015;137(3):032301.

[4] Naves M, Aarts RGK, Brouwer DM. Large stroke three degree-of-freedom spherical flexure joint. In: EUSPEN 2017 17th International Design Engineering Technical Conference. Hannover; 2017. .

[5] Hopkins JB, Culpepper ML. Synthesis of multi-degree of freedom, parallel flexure system concepts via Freedom and Constraint Topology (FACT) - Part I: Principles. Precision Engineering. 2010;34(2):259–270.

[6] Naves M, Brouwer DM, Aarts R. Building block based spatial topology synthesis method for large stroke flexure hinges. Journal of mechanisms and robotics. 2017;.

[7] Jonker JB, Meijaard JP. In: SPACAR — Computer Program for Dynamic Analysis of Flexible Spatial Mechanisms and Manipulators. Berlin, Heidelberg: Springer Berlin Heidelberg; 1990. p. 123–143.

[8] Meijaard JP, Brouwer DM, Jonker JB. Analytical and experimental investigation of a parallel leaf spring guidance. Multibody System Dynamics. 2010;23(1):77–79.

PRECISION MECHANICAL DESIGN AND TEST OF MINIATURE DYNAMIC MIRROR BENDERS WITH LAMINAR FLEXURE BENDING MECHANISM FOR X-RAY MICROFOCUSING

Deming Shu[1], Aiguo Li[2], Steven P. Kearney[1], Chengwen Mao[2], Jayson Anton[1,3], Shuai Yan[2], Dongxu Liang[2], and Yaolin Pan[2]

[1]Advanced Photon Source, Argonne National Laboratory, Argonne, IL 60439, U.S.A.
[2]Shanghai Synchrotron Radiation Facility, Shanghai Institute of Applied Physics, Shanghai 201204, China
[3]University of Illinois at Chicago, Chicago, IL 60607, U.S.A

INTRODUCTION

The 7 GeV Advanced Photon Source (APS) at Argonne National Laboratory (ANL) is a national user facility for synchrotron radiation research. The Shanghai Synchrotron Radiation Facility (SSRF) at the Shanghai Institute of Applied Physics (SINAP) is a 3.5 GeV third generation synchrotron radiation source. Both SSRF and APS have a keen interest in the development of novel Kirkpatrick-Baez (K-B) mirror [1] mount stages for synchrotron radiation applications. Recently, collaboration between ANL and SINAP, as a part of the Argonne Strategic Partnership Project (SPP), has produced several designs for novel miniature dynamic mirror benders using laminar nanopositioning flexures, a technique developed at the ANL [2-5].

The motivations of the novel designs are to develop compact, cost-effective flexure mirror benders with high stability, especially in cases for x-ray focusing optics coated with multilayers in a K-B configuration. As the final focusing elements immediately upstream of the sample, the dynamic mirror benders provide high precision figuring to allow the mirror figure to be tuned to optimize the focusing at different incidence angles to cover a wide energy range [6,7]. Additionally, the cost-effective flexure mirror benders with high stability are also suitable for regular x-ray mirrors with various metal coatings.

PROTOTYPE DESIGN OF MINIATURE DYNAMIC MIRROR BENDERS WITH 90-mm LONG X-RAY MIRROR

A prototype of the miniature dynamic mirror bender with closed-loop control configuration for 90-mm-long x-ray mirror has been designed and constructed for preliminary mechanical and optical tests. Figure 1 shows the design of the Z7-5006 miniature dynamic mirror bender. The mirror bender consists of a base, a pair of laminar flexure mechanism modules, a pair of bending arms, a Newport™ NPM-140 piezo micrometer adapter with 90 micron travel range [8] for the short bending arm, and two manual adjusters for both long and short bending arms. Figure 2 is a Photograph of the Z7-5006 prototype dynamic mirror bender with closed-loop control configuration.

The flexure bending mechanism module is a solid laminar bonded complex structure. It is designed as a tip-tilting mechanism with ultrahigh positioning sensitivity and stability. The module is constructed with stacks of thin metal weak-link sheets which are manufactured using photochemical machining processes with lithography techniques [2].

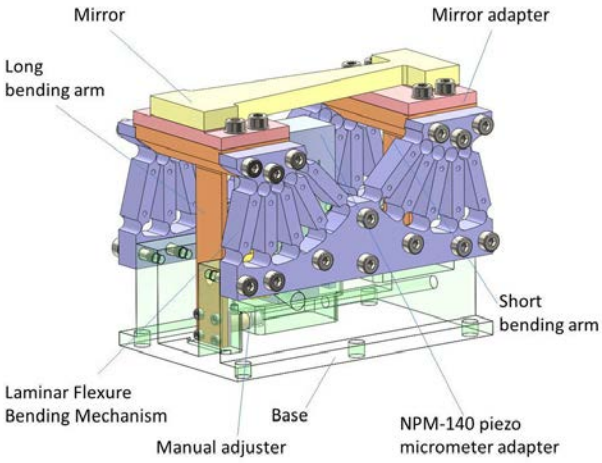

Figure 1. 3-D model of the Z7-5006 miniature dynamic mirror bender with Newport™ NPM-140 piezo micrometer adapter for closed-loop control configuration.

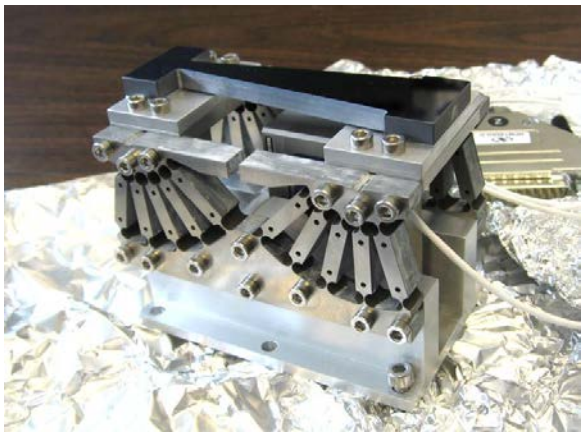

Figure 2. Photograph of the Z7-5006 prototype dynamic mirror bender with closed-loop control configuration.

With the same flexure bending mechanism module, and using two Newport™ Picomotor™ 8301 actuators, the Z7-5006 miniature dynamic mirror bender can also be configured for open-loop control with more cost-effectiveness as shown in Figure 3.

Finite element analysis (FEA) study for the Z7-5006 bending mechanism showed that, with a 15.1 N load applied to the short bending arm and an 11.4 N load applied to the long bending arm (to simulate a bending moment of ~1 N·m), the maximum displacement of the long bending arm is ~0.97 mm, the maximum displacement of the short bending arm is ~0.57 mm. With the same load condition, the maximum Von-Mises stress on the 8-mm-thick weak-link modules reaches ~109 MPa, which is only less than 10% of the material yield stress for 17-7-PH stainless steel.

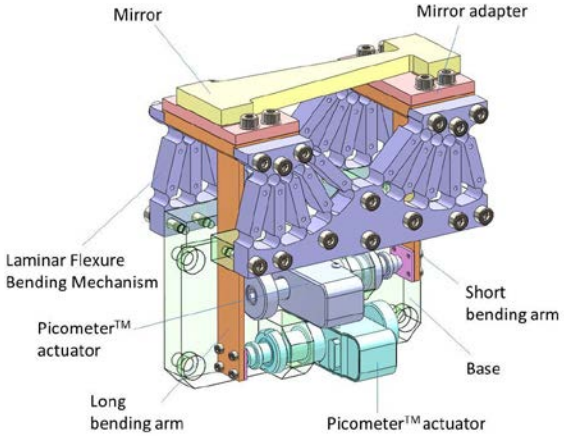

Figure 3. 3-D model of the Z7-5006 miniature dynamic mirror bender with open-loop control configuration.

PROTOTYPE DESIGN OF MINIATURE DYNAMIC MIRROR BENDERS WITH 160-mm LONG X-RAY MIRROR

A prototype of the miniature dynamic mirror bender Z7-5005 with closed-loop control configuration for 160-mm-long x-ray mirror has been designed as shown in Figure 4. The mirror bender consists of a base, two pair of laminar flexure mechanism modules, a pair of bending arms, two Newport™ NPM-140 piezo micrometer adapters with 90 micron travel range [8], and two manual adjusters for both bending arms. Two sets of capacitive sensors (probe model C3R with CPL350 readout electronics from Lion Precision™) are applied in the mirror bender design to ensure the bender's positioning reproducibility.

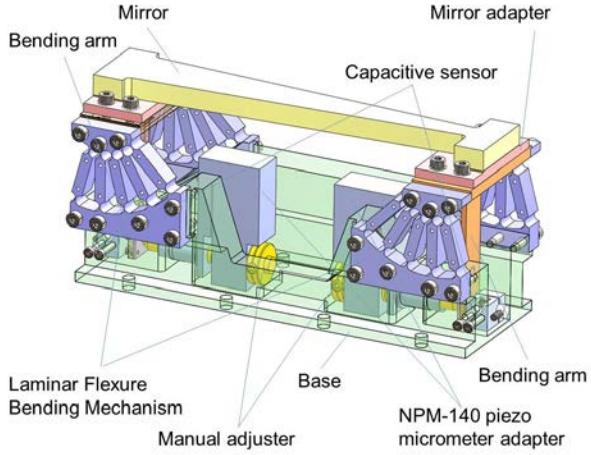

Figure 4. 3-D model of the Z7-5005 miniature dynamic mirror bender with open-loop control configuration.

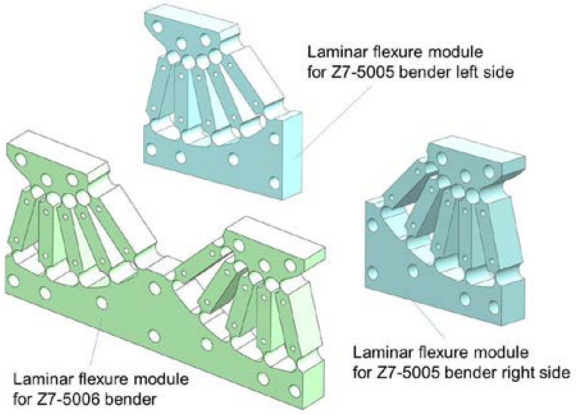

Figure 5. 3-D models of the monolithic laminar flexure module for Z7-5006 bending mechanism, and two separate laminar flexure modules for Z7-5005 bending mechanism.

Same as the Z7-5006 bending mechanism, the Z7-5005 flexure bending mechanism module is a solid laminar bonded complex structure. It uses the same tip-tilting mechanism with ultrahigh positioning sensitivity and stability. However, to gain the design flexibility for longer mirror, unlike the monolithic design for Z7-5006 bending mechanism, the Z7-5005 bending mechanism module is constructed with two separate stacks for left and right sides bending arms as shown in Figure 5.

PRELIMINARY TEST WITH LONG TRACE PROFILER AND X-RAYS AT SSRF

A prototype of the miniature dynamic mirror bender Z7-5006 with closed-loop control configuration has been tested at the SSRF optics lab with long trace profiler (LTP) as shown in Figure 6. Figure 7 shows a schematic diagram of the silicon test mirror for the Z7-5006 miniature dynamic bender prototype. The 90 mm long silicon mirror has an effective optical length of 66 mm and thickness of 5.5 mm. The width of the mirror is designed to perform the optical figuring of the mirror under bending [7]. With a tunable bending moment between 0.35 N·m to 0.71 N·m, the elliptical mirror figure radiuses are tunable between curvatures of 24 m–88 m to 12 m-44 m.

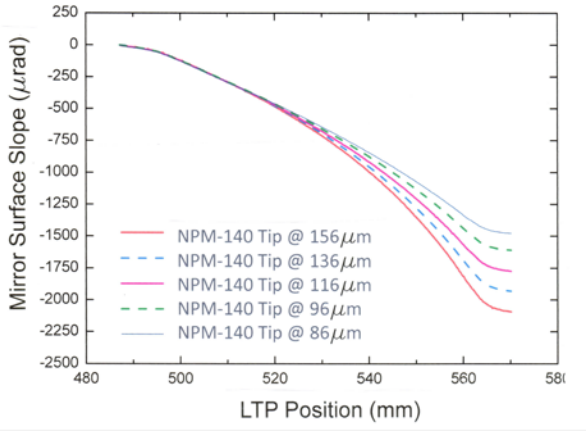

Figure 6. Preliminary test results of the Z7-5006 miniature dynamic mirror bender at the SSRF optics lab with LTP.

A ~350 nm FWHM 1-D focusing has been observed at the SSRF undulator beamline BL15U in February 2017. Figure 8 shows a photograph of the Z7-5006 miniature dynamic mirror bender testing at the SSRF beamline BL-15U. Figure 9 shows a photograph of the Z7-5006 miniature dynamic mirror bender testing at the APS nanopositioning support laboratory with laser interferometers on an invar frame.

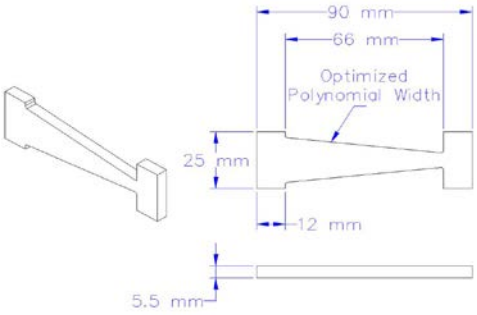

Figure 7. Schematic diagram of a silicon test mirror for the Z7-5006 miniature dynamic bender.

SUMMARY

The mechanical design of prototypes for the miniature dynamic mirror benders with 90-mm-long and 160-mm-long x-ray mirrors are presented in this paper. Both Z7-5005 and Z7-5006 mirror benders are designed with configurations for open-loop or closed-loop controls. Capacitive sensors can be applied to the Z7-5005 and Z7-5006 mirror benders to ensure bender's positioning reproducibility. Table 1 summarizes the design specifications of the Z7-5005 and Z7-5006 prototype miniature dynamic mirror benders with closed-loop control configuration for 90-mm-long and 160-mm-long x-ray mirrors.

A ~350 nm FWHM 1-D focusing using Z7-5006 miniature dynamic mirror bender with 90-mm-long mirror has been observed at the SSRF undulator beamline BL15U. Further test of the Z7-5005 and Z7-5006 mirror benders with LTP and x-rays are in progress.

Table 1. Design specifications of the prototype Z7-5005 and Z7-5006 miniature dynamic mirror bender with closed-loop control configuration and capacitive sensor

Overall dimensions (mm) for 160-mm-long mirror (Z7-5005)	166 (L) x 62 (W) x 75 (H)
Overall dimensions (mm) for 90-mm-long mirror (Z7-5006)	96 (L) x 62 (W) x 75 (H)
Normal load capacity (kg)	0.2
Driver type	Newport™ NPM-140 Piezo micrometer adapter with closed-loop control option
Driver encoder type	strain-gauge
Driver axial load capacity (N)	100
Driver closed-loop travel range (micron)	90
Driver min. incremental (nm)	1
Manual adjustment option	Yes
Tunable bending moment (N.m)	0.1 - 1
Capacitive sensor type	Lion Precision™ C3R with CPL350

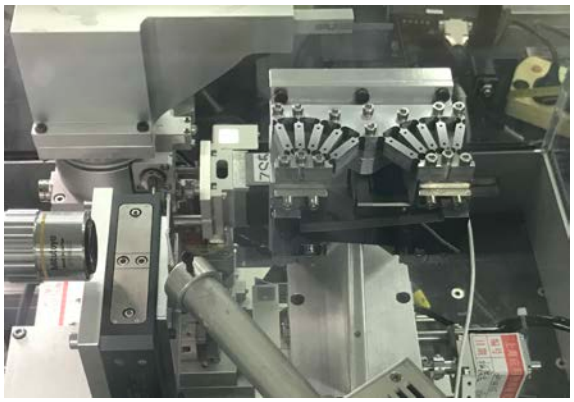

Figure 8. Photograph of the Z7-5006 miniature dynamic mirror bender testing at the SSRF beamline BL-15U.

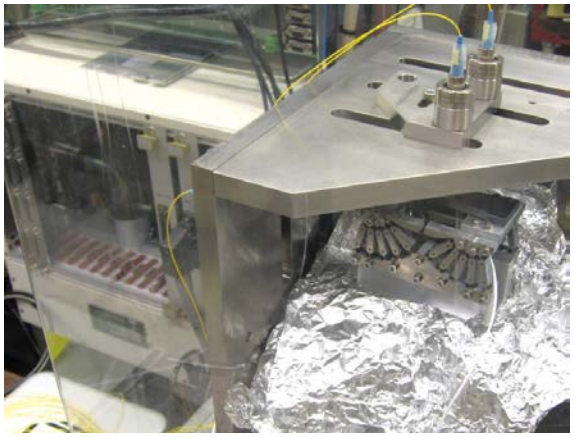

Figure 9. Photograph of the Z7-5006 miniature dynamic mirror bender testing at the APS nanopositioning support laboratory with laser interferometers on an invar frame.

ACKNOWLEDGEMENTS

Work supported by the U.S. Department of Energy, Office of Science, under Contract No. DE-AC02-06CH11357 and Argonne SPP project 85E77. Work at SINAP supported by National Natural Science Foundation of China (U1332120).

REFERENCES

[1] Kirkpartrick, P. and Baez, A. V. Formation of Optical Images by X-Rays. JOSA. 1948; 38(9): 766-773.

[2] U.S. Patent granted No. 6,607,840, D. Shu, T. S. Toellner, and E. E. Alp, 2003.

[3] U.S. Patent granted No. 6,984,335, D. Shu, T. S. Toellner, and E. E. Alp, 2006.

[4] D. Shu, T. S. Toellner, E. E. Alp, J. Maser, J. Ilavsky, S. D. Shastri, P. L. Lee, S. Narayanan, and G. G. Long, AIP CP879, 1073-1076 (2007)U. Osaka and C.R. Ultra, Jpn. J. Appl. Phys. 50 (2006) 1.

[5] D. Shu, A. Li, S. P. Kearney, C. Mao, J. Anton, and Y. Pan, Proceedings of MEDSI 2016, Barcelona, Spain.

[6] R. Barrett, J. Härtwig, C. Morawe et al, Synchrotron Radia-tion News, 23, No.1, 36-42 (2010)

[7] A. Li and C. Mao, Private Communications (2016)

[8] http://www.newport.com/Picomotor-Piezo-Linear-Actuators/

The submitted manuscript has been created by UChicago Argonne, LLC, Operator of Argonne National Laboratory ("Argonne"). Argonne, a U.S. Department of Energy Office of Science laboratory, is operated under Contract No. DE-AC02-06CH11357. The U.S. Government retains for itself, and others acting on its behalf, a paid-up nonexclusive, irrevocable worldwide license in said article to reproduce, prepare derivative works, distribute copies to the public, and perform publicly and display publicly, by or on behalf of the Government.

Design, Development and Testing of Large-caliber Precision CNC Double-sided Polishing Machine

Xinyao Sun[1], Zhanyu Zhang[1], Junyin Chen[2], Jun Zha[1], YaolongChen[1]
1Xi'an Jiaotong University State Key Laboratory for Manufacturing System Engineering
Xi'an, Shaanxi, China
2Jiangsu Yichuang Institute of Intelligent Equipment Co.Ltd
Xuzhou, Jiangsu, China

STRUCTURAL DESIGN OF DOUBLE COLUMN HYDROSTATIC GUIDEWAY SYSTEM WITH MOVING BEAM

Precision double-sided polishing machine is the principal equipment for processing large diameter and high-precision flat optics. Structure design should be simple as far as possible, to reduce the error caused by the accumulation of intermediate transmission links, transmission links on one hand will increase the whole equipment total error, reduce the precision of the machine tool, just. On the other hand will reduce the stiffness of machine tool. It will also affect the mechanical working precision.

The processing requirements of the workpiece thickness error is less than 3 μm, so the whole equipment should have enough stiffness, parallelism error, at the same time it should have sufficient heat resistance, resulting in the polishing process will not produce heat deformation. The polishing fluid used in the polishing process is corrosive, so the polishing disk is made by marble material, which is corrosion resistant and difficult to deform. The hydrostatic support has the advantages of high rigidity, high precision, good damping performance, small frictional resistance, long service life, so the hydrostatic slide as the key functional components are widely used in ultra-precision machine tool[1-4], in order to improve the precision of the machine, so as to achieve the purpose of improving the mechanical working precision.

In this paper, the double column hydrostatic guideway is used to realize the combination of the guideway and the column. The structure of the machine tool is simplified. At the same time, the influence of the geometrical error of the guideway on the kinematic error is studied.

Design of double column guideway system

In view of the large stiffness and better anti overturning ability of the machine tools, closed hydrostatic guideway is used.

At the joint of the column and the crossbeam, each of the two bearings is used to fix the bushing and the moving cross beam, so as to drive the moving beam to move in a straight line along the column guideway, as shown in figure 1. To reduce the weight of moving beam adopt casting structure with V type rib, the structure has good rigidity.

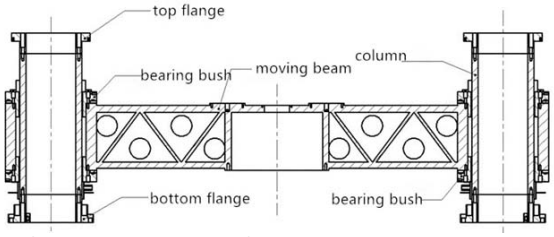

FIGURE 1. Design of hydrostatic guideway with double column and moving beam

An opposed equal area four oil cavity structure with an axial oil return groove is designed on the hydrostatic slideway, and each oil cavity has an oil inlet and a pressure hole. Between the guideway and the bush, the oil film clearance is 20 μm. The design tolerance of the guideway and the bush is defined as the 1/10 of the oil film clearance, that is, 2 μm.

INFLUENCE OF ANGLE ERROR OF MOVING BEAM ON PARALLELISM OF WORKPIECE UNDER ECCENTRIC FORCE

The center of the workpiece should be deviated from the center of the polishing disk, so that the center point of the workpiece can be polished. The workpiece and the center axis of the polishing disk will have a certain inclination angle, which will produce eccentric force. The movable beam system is subjected to eccentric force in the upper polishing disk tilt will produce angle error, parallelism effect of workpiece. Due to the high requirement of parallelism and

precision in the design of machine tools, the angle error of machine tools should be guaranteed within the specified range.

The error of moving beam under eccentric force

In the process of polishing, the straight axis feed speed is very low (less than 10 μm/h), so it is necessary to carry out static analysis moving beam system, the static deformation analysis to study the impact mechanism.

The eccentric force acting on the disk can be decomposed into forces in the o-yz plane and in the o-xz plane. The force principle of the two planes is basically the same. When the geometric center of the workpiece coincides with the geometric center of the polishing disk, the machine is in the state of 1 without any tilting, When the workpiece moves to deviate from the geometric center of the polishing disc, the flip disc produces an overturning moment under the action of the eccentric force F, so that the moving beam is tilted, and the machine tool is in state 2. Let e be the eccentricity of the geometric center of the workpiece, u is the stiffness of the individual oil pad, d is the oil cavity distance of the two bearing shells on the same side, and l_1 is the distance between the center line of the moving beam and the force center. The force is shown in the fig2.

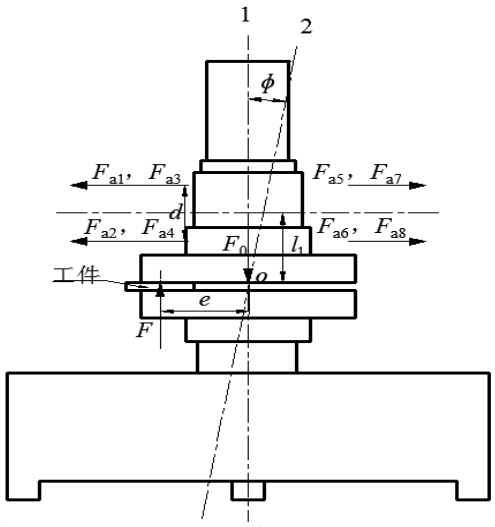

FIGURE 2. Machine tool force diagram

It can compute that:

$$-4u\left(l_1+\frac{d}{2}\right)^2\cdot\sin\theta\cos\theta$$
$$+4u\left(l_1-\frac{d}{2}\right)^2\cdot\sin\theta\cos\theta$$
$$+F\cdot e=0$$

If the inclination angle on another plane is φ, then it can be obtained:

$$-4u\left(l_1+\frac{d}{2}\right)^2\cdot\sin\phi\cos\phi$$
$$+4u\left(l_1-\frac{d}{2}\right)^2\cdot\sin\phi\cos\phi$$
$$+F\cdot e=0$$

Stiffness analysis of hydrostatic supporting

When analyzing the error model of the moving beam, it is found that the stiffness of the hydrostatic support has an important influence on the angle error. Therefore, the stiffness of the oil cushion is required to calculate the inclination error.

The main size of the annulus restrictor selected:

$d_c=8mm$, $l_c=6mm$, $h_c=35\mu m$

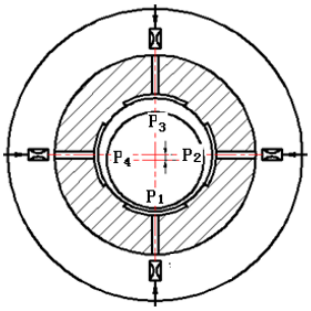

FIGURE 3. Bearing bush

J_0 is the stiffness value of the opposed oil pad, while the stiffness of the individual oil pad is:

$$u=\frac{J_0}{2}$$

When the bearing radius clearance is =20μm, it can be calculated:

$$J_0=2512.45\ \text{N/μm}$$

The stiffness values are substituted into the error model, and the angle error can be obtained:

$$\sin\theta=\sin\phi=1.33\times10^{-6}$$

The size of the workpiece is 430 * 430mm and the diagonal distance is 608mm. The maximum parallelism error of the workpiece is:

$$\delta=608\times\sin\theta=0.8\ \mu\text{m}\ <\ 3\ \mu\text{m}$$

Therefore, the design of the structure meets the requirements of the project.

INFLUENCE OF CONTOUR ERROR OF GUIDEWAY ON PARALLELISM OF WORKPIECE

When the moving beam moves along the rail, the straightness of the guideway will produce linear deviation and angular deviation, which will affect the parallelism precision of the workpiece. The contour error of the guide rail has a great influence on the straightness of the hydrostatic guideway, and will directly affect the angle deviation of the moving beam and affect the working accuracy.

Contour error model of closed hydrostatic guideway

Bearing in motion, contour error of guide will lead to oil pad oil film thickness changes, so that the oil film bearing capacity fluctuate to maintain balance, to deviate from the ideal trajectory, the moving beam forming linear deviation and angle deviation. As shown in fig4, δ(x) for linear deviation, and ε (x) is the angle deviation. λ is the profile errors of wavelength. Therefore, it is necessary to establish the balance equation of bearing bush to solve the linear deviation and angle deviation of the slider. During the analysis process, need to assume that the lubricating oil for viscous incompressible fluid; oil pressure and oil viscosity constant; machine tool linear shaft has small feed speed (10μm/h), not to consider the dynamic effect in the process of movement.

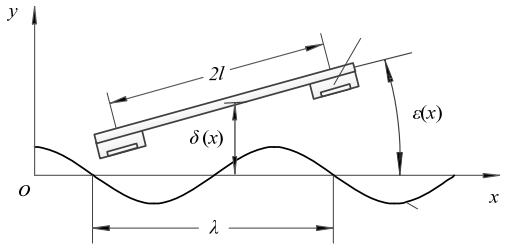

FIGURE 4. Bearing bush movement form

Establishment of equilibrium equation and solution of geometric error

The column rail form is four oil cavity closed hydrostatic guideway, which can be equivalent to the mechanical model shown in figure 5. Among them, eyj (x) for linear displacement along the y direction of the oil pad center, kfj (x) for oil pad oil film stiffness of fbj (x) generated in the process of movement to keep in balance the bearing oil film force balance, fej (x) bearing capacity variation for oil cushion oil film, j said the number j oil pad, l as the center of the slider to the bearing center distance.

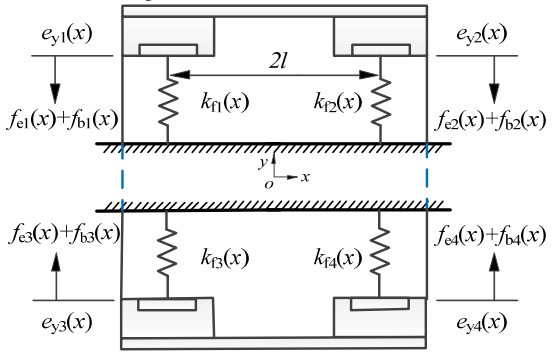

FIGURE 5. Mechanical equivalent model of column hydrostatic guideway

The linear deviation eyj (x) of each oil cushion center is :

$$e_{yj}(x) = me_{yx}(x) + n\varepsilon_{zx}(x)l \qquad (j = 1,2,3,4)$$

m - direction coefficient (from 1 to 4 oil pad, followed by -1, -1,1,1); e_{yx}(x) - block linear deviation /m along the direction perpendicular to the direction of movement; n - direction coefficient (from 1 to 4 oil pad, followed by 1, -1, -1,1; ε_{ZX}(x) - slider pitch angle /rad.

After solving, the change curve of inclination error and straightness between center distance and geometric error wavelength ratio is obtained as shown in Fig. 6,7. The straightness of the worktable (moving beam) in the drawing is based on the trajectory of the center of the worktable, and is obtained by the least square method. The angle error is the maximum inclination of the table in all its strokes.

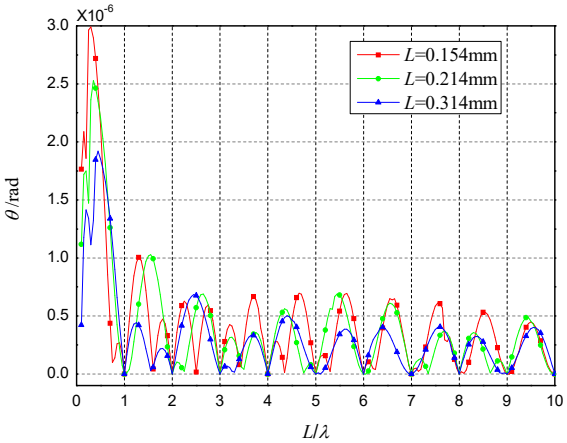

FIGURE 6. The change curve of angle error versus center distance and geometric error wavelength ratio (Ps=4MPa, h0=20μm)

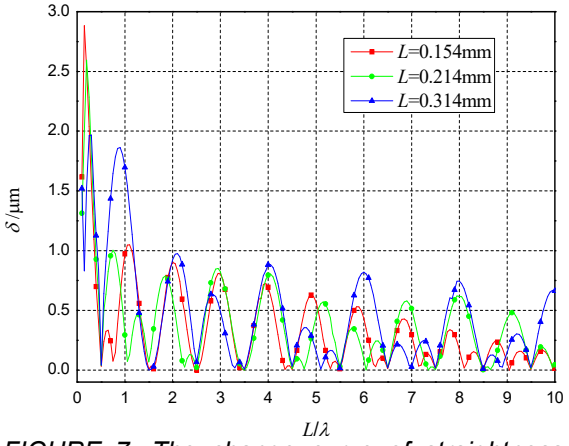

FIGURE 7. The change curve of straightness versus center distance and geometric error wavelength ratio (Ps=4MPa, h0=20μm)

TESTING OF GUIDEWAY CONTOUR ERROR MODEL

Because the average oil pad thickness is used instead of theoretical oil pad thickness, the fluid characteristics of the oil pad on the oil sealing surface are analyzed, but the pressure of the actual oil pad surface is not linearly distributed, and there is bound to be an error. Therefore, the method of simulation and experiment is used to verify the contour error of the guideway. Comparing the experimental data with the simulation data, the calculation accuracy is analyzed.

Simulation test of contour error of guideway

Using COMSOL Multiphysics to find simulation results. The pressure distribution diagram of the sealing surface of the oil pad is obtained, as shown in figure 8.

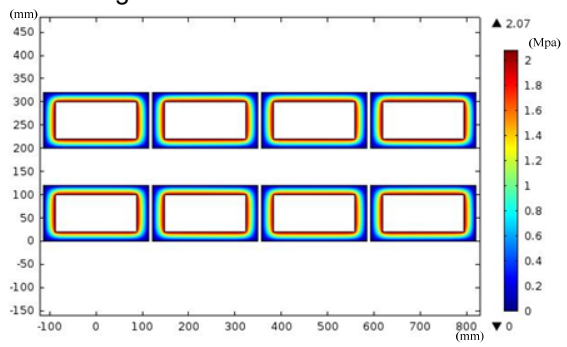

FIGURE 8. Oil film pressure distribution of sealing surface

Different λ values are taken, and the ratio of the center distance to the rail profile is defined as the ratio of the error wavelength to the coefficient n:

$$n=L/\lambda$$

Different λ values are brought into the simulation calculation, and the relationship between the different n values and the tilt error θ can be obtained, the results are compared with those computed by the contour error model of the rail, as shown in figure 9. According to the simulation results, the trend of the curve is the same as that of the previous results. The error size of the two methods is analyzed. After comparison, the error rate is 7.6%, which is the difference between the actual oil film and the average oil film. The analysis shows that the calculation accuracy meets the needs of engineering applications.

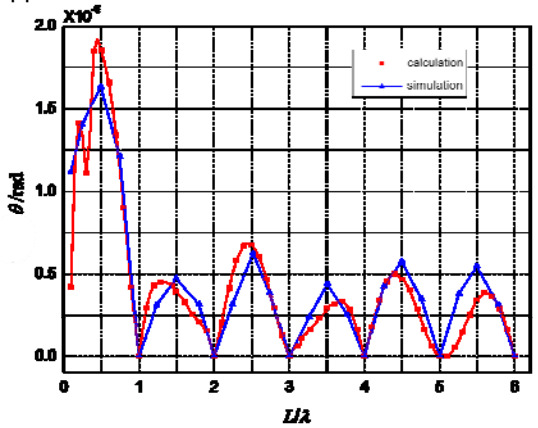

FIGURE 9. Comparison of calculation results and simulation results

Model error test of rail contour

Using the indirect method for measuring, which is below the polishing disk as the base, the upper polishing disk axis and verticality measurement of polishing disk, resulting in two discs of parallelism. When measuring, the micrometer (accuracy: 1μm) absorption in the upper polishing disk, and then put in the hand lever indicator of polishing disk, rotating throwing disk, reading change lever indicator value is two behind the parallelism error of disks. Measuring the parallelism of the upper and lower projection disks at different positions of the z axis, we can know the tilt changes of the polishing disk in motion. In order to eliminate the flatness error under the influence of polishing disk, need flatness error record of polishing disk around the value, later in the process of measurement minus the change in value of each position value can be obtained by the parallel measurement more accurate value.

By comparison, it is found that the error rate of rail contour error model is 2.4% compared with that obtained by COMSOL simulation, and the maximum error rate is 9.2%. The fitting for the rail curve profile errors model is fitted according to the sine curve, and the actual contour error curve is a superposition of sine curve by a series of different wavelengths and obey the amplitude of the composition, the calculation error has great impact on the profile error model, while the actual situation in the two column are affected factors of parallelism error, the actual profile errors, so that the contour error model accords with practical engineering requirements.

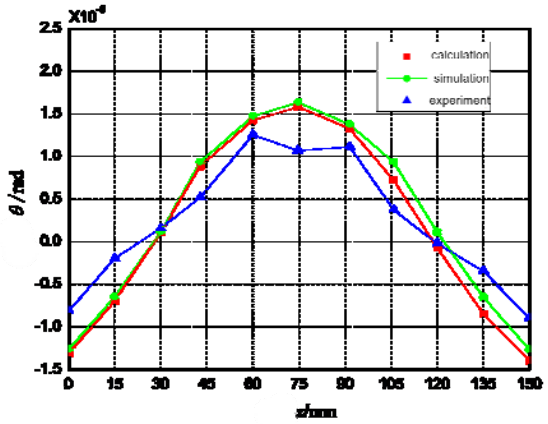

FIGURE 10. The comparison of experimental value, calculation value and simulation value (L/λ=2.6)

REFERENCES

[1] Liu T, Gao WG, Tian YL, Mao K, Pan GX,Zhang DW. Thermal simulation modeling of a hydrostatic machine feed platform[J]. Adv Manuf Technol, 2015, doi:10.1007/s00170-015-6881-0.

[2] Liang YC, Chen WQ, Sun YZ, Luo XC, Lu LH, Liu HT. Amechanical structural-based design method and its implementationon a fly-cutting machine tool design[J]. Adv Manuf Technol, 2014,70(9-12):1915–1921.

[3] Schellekens P, Rosielle N, Vermeulen H,Vermeulen M,Wetzels S,Pril W. Design for precision: current status and trends[J]. Manuf Technol, 1998, 47(2):557–586.

[4] Hwang J, Park CH, Gao W, Kim S-W. A three-probe system for measuring the parallelism and straightness of a pair of railsforultra-precision guideways[J]. Mach Tools Manuf , 2007, 47(7–8):1053–1058.

[5] Zha, J., Lv, D., Jia, Q. et al. Motion straightness of hydrostatic guideways considering the ratio of pad center spacing to guide rail profile error wavelength[J]. Int J Adv Manuf Technol (2016) 82: 2065. doi:10.1007/s00170-015-7515-2

DESIGN OF A HIGH-SPEED OSCILLATING BLADE MICROTOME

Ji Wang, Chenglin Li, and Shih-Chi Chen*
Department of Mechanical and Automation Engineering
The Chinese University of Hong Kong
Shatin, N.T., Hong Kong SAR, China
*Email: scchen@mae.cuhk.edu.hk

In this paper, we present the design and characterization of a new high-speed oscillating blade microtome that achieves a substantially higher cutting speed (0 - 300 Hz) and amplitude (0 – 500 μm) than conventional oscillatory tissue cutters; and analytic models that can predict and cutting force, resulting in improved sectioning quality and minimum section thickness. The high cutting amplitude and speed are achieved by driving the cutting mechanism in resonance. Based on the new microtome, we study soft tissue sectioning processes both theoretically and experimentally. The results indicate that a high oscillatory frequency and cutting amplitude will generate higher shear cutting forces, thereby achieving better sectioning results.

DESIGN PRINCIPLE

Previously, we reported a flexure-based vibrating blade microtome [1], integrated with a multiphoton microscope for 3D whole brain imaging. (commercialized by TissueVision Inc.), and an improved design that further minimizes of out-of-plane error motions of the oscillating blade, achieving better performance [2]. In these systems, the operating frequency is designed to be 0 - 100 Hz. The reasons include (1) most commercial systems section soft tissues below 80 Hz; and (2) it is difficult to reduce the out-of-plane motion errors to be < 1μm at high cutting frequency. As our theoretical study has confirmed that a higher cutting frequency yields superior sectioning result [2], in this paper we report the development of a microtome that operates fast enough to exploit the predicted benefit. The design goals include a higher cutting speed (0 - 300 Hz), amplitude (0 – 500 μm), and minimized out-of-plane error motion (< 500 nm).

Figure 1 presents the CAD model of the high-speed oscillating blade microtome. In the design, the oscillatory motion of the blade holder is guided by four parallel beams. The symmetric flexure design ensures a repeatable and linear cutting path as well as high mechanical resonant frequency. A voice coil motor (VCM) directly drives the blade holder, where the load is applied to the blade holder assembly's center of mass to minimize out-of-plane error motions. During operations, the VCM drives the blade to generate reciprocating linear motions and forces.

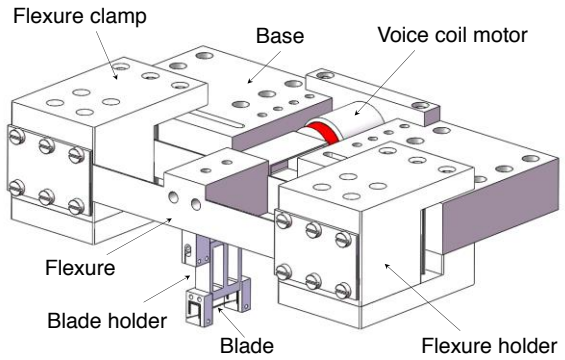

FIGURE 1. CAD model of the high-speed oscillating blade microtome, where a VCM drives the blade holder assembly generating linear cutting paths

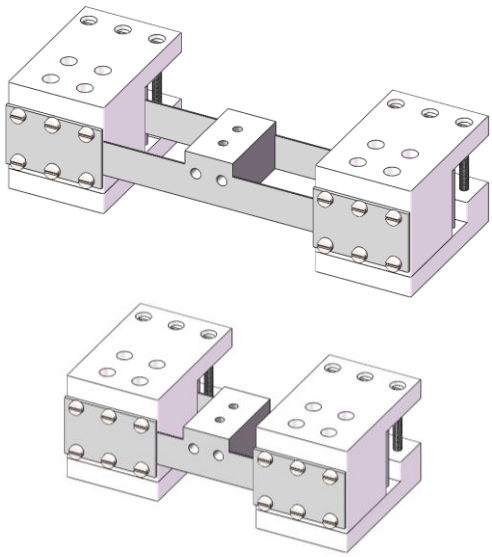

FIGURE 2. Illustration of frequency tuning by adjusting the lengths of clamped beams

As shown in Figure 2, by adjusting the effective lengths of the four parallel beams, the resonant

frequency of the system can be controlled. It is worthwhile to note that the system is purposely operated at a speed close to the resonant frequency to amplify the blade oscillating amplitude. This is required as the VCM has limited force output to generate enough amplitude at high frequency.

Next, we model and study how tuning the resonant frequency can amplify the oscillating amplitude. The driving force generated by the VCM is proportional to the current input before the force reaches the output limit. Assuming the driving force generated by the VCM is $F = F_0\cos\omega t$, the blade displacement (y) in the oscillating direction can be obtained based on the theory of mechanical vibration [3] as presented in Eq. (1) and (2):

$$y = A\cos(\omega t - \theta) \tag{1}$$

$$A = \frac{1}{\sqrt{\left(1-s^2\right)^2 + \left(2\zeta s\right)^2}} y_0 \tag{2}$$

where A is the blade vibrating amplitude; $s = \omega/\omega_0$ is the ratio of the driving frequency to the system natural frequency; and y_0 is the blade displacement corresponding to a static loading with the same force amplitude. Assuming the four parallel beams in Fig. 1 have identical dimensions and the length, width and thickness of each beam are l, b, and t respectively, the stiffness of the structure can be found as:

$$k = \frac{4Ebt^3}{l^3} \tag{3}$$

Accordingly, y_0 and the resonant frequency of the structure can be expressed as:

$$y_0 = \frac{F_0 l^3}{4Ebt^3} \tag{4}$$

$$\omega_0 = \sqrt{\frac{4Ebt^3}{ml^3}} \tag{5}$$

where m is the mass of the blade holder structure. Figure 3 presents simulated dynamic responses of the microtome, where the damping ratio is set to 0.1. In the simulation, we study and observe the system response by (1) doubling the input current; and (2) doubling the input current and shortening the beam length from l to $0.8l$. According to Eq. (5) the new resonant frequency becomes $1.25\omega_0$ when the beam length is shortened, which is confirmed in Fig. 3. One can observe from Fig. 3 that a very high or low driving frequency ω will result in small blade displacements (A). As at high operating frequency, the VCM has small force output, adjusting the beam length, i.e., adjusting the system resonant frequency, can be an effective way to increase blade displacements, as indicated by the blue curve in Fig. 3.

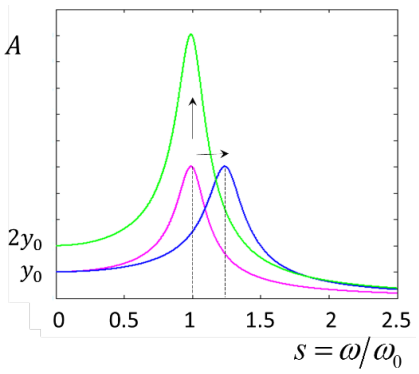

FIGURE 3. Simulated dynamic responses of the frequency tunable oscillating blade microtome

THEORY OF SOFT MATERIAL CUTTING

The general goal of tissue sectioning is to achieve high flatness and thin sections with minimal tissue deformation. In this paper, we model and calculate maximum tissue deformation during the cutting process and use it as an indicator of cutting quality. As reported in our earlier work [2], small cutting forces or small tissue deformation leads to the better the cutting quality.

Previous studies on soft tissue cutting have been focused on understanding how pressing and slicing forces applied to a cutting tool can influence the incision outcome [4-7]. However, these studies and models are limited to static loading conditions and cannot describe dynamic cutting conditions, i.e., cutting tissues with an oscillating blade. In a typical oscillatory tissue cutting process, a blade oscillates transversely at a constant frequency and moves towards a sample at a constant speed (i.e., feed rate), where the entire operation is performed in a water bath to reduce friction and vibration. The operation parameters include (1) blade oscillation frequency (ω), (2) oscillation amplitude (A), and (3) sample feed rate (v). As shown in Fig. 4, we model the oscillatory cutting process by considering a soft sample fixed on a linear stage and moves towards a blade that oscillates transversely. The vibration amplitude

and velocity can be mathematically described as $y = A\cos(\omega t - \theta)$ and $y' = -A\omega\sin(\omega t - \theta)$ respectively. The cutting force applied to the sample from the blade consists of the normal force (F_x) and reciprocating shear force (F_y), where F_y consists of the friction force and adhesion force; note the adhesive force is not considered in the following analysis as it becomes negligible when cutting is performed in the water bath. The sliding motion between the blade and the soft material along the y-direction produces shear forces and can be described as $F_y = \mu F_x$. Previous studies show that the friction coefficient (μ) between a viscoelastic material and a rigid surface is a function of the physical properties of the contact interface as well as the sliding velocity, and the friction coefficient can be modeled as [8]:

$$\mu = \nabla z \frac{G_2(\omega')}{G^*(\omega')} \tag{6}$$

where ∇z is the root mean square (RMS) of the gradient of the blade surface, which is a constant in the model; $G_2(\omega')$ and $G^*(\omega')$ are the loss shear modulus and the absolute shear modulus of the material respectively; ω' is the characteristic frequency, defined as $\omega' = 2A\omega/\pi d$, where d is the characteristic diameter of a local contact region between the blade and the material. Note that d is a constant for the same cutting blade [8]. Accordingly, we can express F_y as Eq. (7):

$$F_y = F_y^* \sin(\omega t - \theta) \tag{7}$$

$$F_y^* = \nabla z \frac{G_2(\omega')}{G^*(\omega')} F_x \tag{8}$$

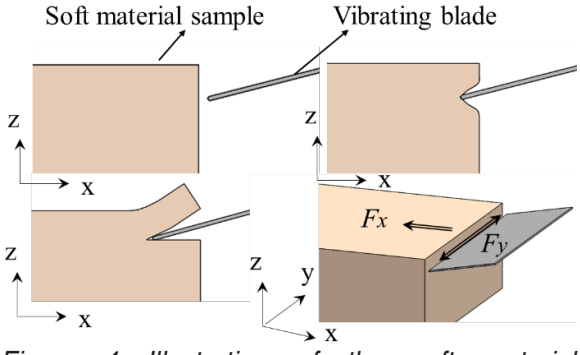

Figure 4 Illustration of the soft material sectioning process and model

The material sectioning process can be divided into two stages: (1) crack initiation; and (2) crack propagation (Fig. 4). At the first stage, the material in the vicinity of the blade tip deforms under F_x and F_y, where F_x continues to rise as the material is fed to the oscillating blade; and F_y increases with F_x according to Eq. (8). At the second stage, the critical stress condition is reached and a crack is generated and starts to propagate. Note that F_x reaches the maximum value at the critical point and decreases to a stable value as the crack propagates.

At the crack initiation stage, it is assumed that the material around the blade tip is under a line loading of a half space. This assumption is valid because the radius of the blade tip is much smaller than the thickness of the sectioned slice. Based on elastic contact mechanics [9] and assuming Poisson's ratio of the soft material is 0.5, i.e., the material is incompressible, the stress and strain tensor can be obtained in cylindrical coordinates as:

$$\boldsymbol{\sigma} = \begin{bmatrix} -\frac{2F_x\cos\theta}{\pi rL} & 0 & \frac{F_y}{\pi rL} \\ 0 & 0 & 0 \\ \frac{F_y}{\pi rL} & 0 & -\frac{F_x\cos\theta}{\pi rL} \end{bmatrix} \tag{9}$$

$$\boldsymbol{\varepsilon} = \begin{bmatrix} -\frac{F_x\cos\theta}{2G^*\pi rL} & 0 & \frac{F_y}{G^*\pi rL} \\ 0 & \frac{F_x\cos\theta}{2G^*\pi rL} & 0 \\ \frac{F_y}{G^*\pi rL} & 0 & 0 \end{bmatrix} \tag{10}$$

As the cutting frequency increases, soft or viscoelastic materials become stiffer and intuitively one may expect superior cutting results. Experiments show critical fracture stress of soft material varies significantly with loading frequency, but the critical maximum principle strain does not change as much. Accordingly, we use the maximum principle strain to determine the onset of crack [10]. Given the radius of the blade tip as r_0, the maximum principle tensile stress ε_t can be obtained from Eq. (9) as $\varepsilon_t = F_y^* / 2\, G^*\pi r_0 L$, at the material surface when $\theta = \pi/2$. Notice that ε_t is not directly related to the compressive force F_x. As F_y^* is determined by F_x, the crack onset state can be written as:

$$F_{x\max} = \frac{2\pi r_0 L \varepsilon_t G^*(\omega)}{\nabla z \, G_2(\omega') / G^*(\omega')} \quad (11)$$

As mentioned before, the maximum tissue deformation indirectly indicates the cutting quality. From Eq. (10), one may find that the level of material deformation is determined by a coefficient $F_x/2G^*(\omega)\pi L$. Therefore, we define the reciprocal of the deformation coefficient as the factor of sectioning quality, i.e., $K= 2G^*(\omega)\pi L/F_{xmax}$. It can be expressed as Eq. (12). Note that the higher K, the better the sectioning quality.

$$K = \frac{\nabla z \, G_2(\omega') / G^*(\omega')}{r_0 \varepsilon_0} \quad (12)$$

Since ∇z ,r_0 and ε_0 are all constants, K is determined by $G_2(\omega')/G^*(\omega')$ which is determined by the material property and blade speed. Generally, for soft materials, G_2/G^* increases with frequency until it converges to 1. Therefore, we can conclude that a microtome will produce better cutting results at high blade oscillation frequency. The high cutting frequency advantage becomes negligible when G_2 is close to G^*.

CUTTING EXPERIMENTS

To demonstrate and study the advantage of high-speed sectioning, we perform experiments on agarose gel samples (2% and 2.5% concentration) and slice them into sections of 500 μm thick. The entire cutting process is performed in water; and thus the sectioned gel floats on the water surface instead of adhering to the blade. During the experiments, the forces in different directions are measured, i.e., F_x (i.e., sample feeding force) and F_y (blade cutting force); blade vibration frequency (ω) is set to 40 Hz, 100 Hz and 200 Hz; the vibration amplitude is set to 100 μm, 200 μm, and 400 μm; and the sample feed rate (u) is set to 0.1 mm/s.

Figure 5 presents the experimental results plotted with the theory prediction from Eq. (11), where each data point represents a successful experiment of different sectioning parameters. We find that at low sectioning frequency (40 Hz), the microtome fails to section the agarose gel when A = 100 μm. At 200 Hz the microtome successfully sections all gels under all experimental conditions. Note that at 200 Hz the cutting force (F_{xmax}) is lower which means tissue deformation is smaller. The mathematical expression of complex shear modulus of agarose gel is reported in [11].

The experimental and theoretical results proves the advantage of high frequency sectioning that when ω = 200 Hz the lowest cutting force F_{xmax} is produced for each blade vibration amplitude. Notably, Figure 6 also shows that at the same frequency and feed rate, high cutting amplitudes contribute to low cutting force. For example, when A = 400 μm, smooth sections can be obtained under all cutting frequencies and feed rates. Although the results suggest that a combination of high cutting frequency and amplitude is preferred, the curves of F_{xmax} tend to converge, which means increasing the parameters only have limited effect. Moreover, driving the blade to operate at high amplitude and frequency simultaneously is mechanically difficult to achieve and can magnify the out-of-plane error motions, leading to inferior cutting results.

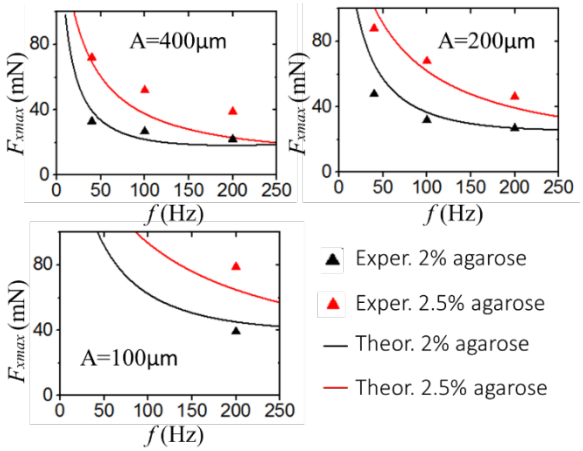

FIGURE 5. The measured and theoretical F_{xmax} for each experiment group

Figure 6 presents our recent results of successive tumor sectioning based on the new microtome, where the tumor is prepared to have a size of 10 × 10 × 10 mm^3. Each resulting section is 200 μm in thickness. The sectioning is performed at 200 Hz with a blade amplitude of 200 μm and a sample feed rate of 0.1 mm/s.

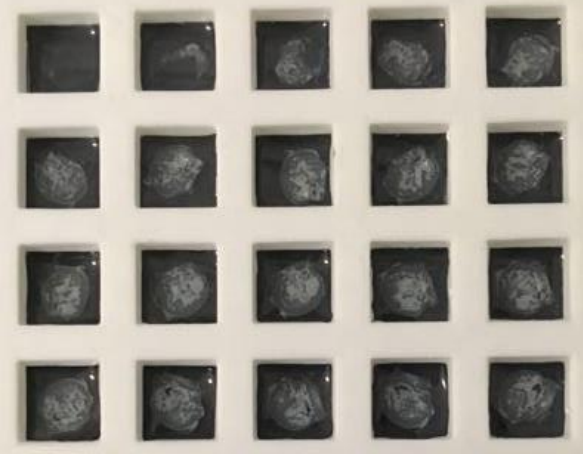

FIGURE 6. Successive tumor sectioning with a section thickness of 200 µm

CONCLUSION

In conclusion, we have developed (1) a high-speed oscillating blade microtome that operates in resonance, achieving a tunable operating frequency (0 – 300 Hz) and amplitude (0 – 500 µm); and (2) parametric models that can predict the cutting force and the sectioning quality of any soft samples. Experiments have been performed on agarose gel and tumor samples to verify the model accuracy as well as the capability of the new microtome with a range of different cutting parameters.

ACKNOWLEDGMENT

This work is supported by the HKSAR Research Grants Council (RGC), General Research Fund (GRF), CUHK 14201214.

REFERENCES

[1] Chen S, Panas R, Culpepper ML, Ragan T. Design of a Precision Flexure-based Vibration Microtome for Whole Organ Imaging. Proc. of the Annual Meeting of the ASPE, San Diego, CA, Oct. 2012, pp.186-89.

[2] Wang J, Chen S. Study of Soft Tissue Cutting based on a Precision Vibrating Blade Microtome. Proc. of the Annual Meeting of the ASPE, Austin, TX, USA, Nov. 2015, pp. 100-104.

[3] Bishop RED, Johnson DC. The Mechanics of Vibration. Cambridge University Press. Cambridge. 2011.

[4] Atkins AG, Xu X, Jeronimidis G. Cutting, by 'Pressing and Slicing,' of Thin Floppy Slices of Materials Illustrated by Experiments on Cheddar Cheese and Salami. Journal of Materials Science. 2004; 39: 2761-2766.

[5] Reyssat E, Tallinen T, Le Merrer M, Mahadevan L. Slicing Softly with Shear. Phys. Rev. Lett. 2012; 109(24): 244301.

[6] Han P, Ehmann K. Study of the Effect of Cannula Rotation on Tissue Cutting for Needle Biopsy. Med. Eng. Phys. 2013; 35: 1584.

[7] Mahvash M, Dupont PE. Mechanics of Dynamic Needle Insertion into a Biological Material. IEEE Transactions on Biomedical Engineering. 2010; 57(4): 934-943.

[8] Popov VL. Contact Mechanics and Friction. Springer. Berlin. 2010.

[9] Johnson KL, Contact Mechanics, Cambridge University Press, Cambridge, England, 1987.

[10] Perez N, Fracture Mechanics, Kluwer Academic Publishers, Boston, USA, 2004.

[11] Chen Q, Suki B, An K. N. Dynamic Mechanical Properties of Agarose Gels Modeled by a Fractional Derivative Model. Journal of Biomechanical Engineering. 2004, 126, 666-671.

DESIGN STRATEGY FOR CRYOGENIC OPTICAL HOUSING USING STEWART TRUSS WITH DISSIMILAR MATERIALS

Brian E. Yoxall, Richard C. Montesanti, Jay V. Bixler, William E. Hunt, Paul J. Kuzmenko, Robert E. Priest
Lawrence Livermore National Laboratory
Livermore, CA, USA

INTRODUCTION

This paper presents methodologies for using a static hexapod to integrate a set of cryogenic optics and a focal plane detector via an exact kinematic constraint. Design, analysis, fabrication and assembly considerations are examined to ensure the hexapod is sufficiently robust for load cases including acceleration extremes, temperature changes coupled with dissimilar material CTE (coefficients of thermal expansion), and fabrication/assembly tolerances. Key risks and their mitigations are discussed, as well as trade-offs considered during the design phase.

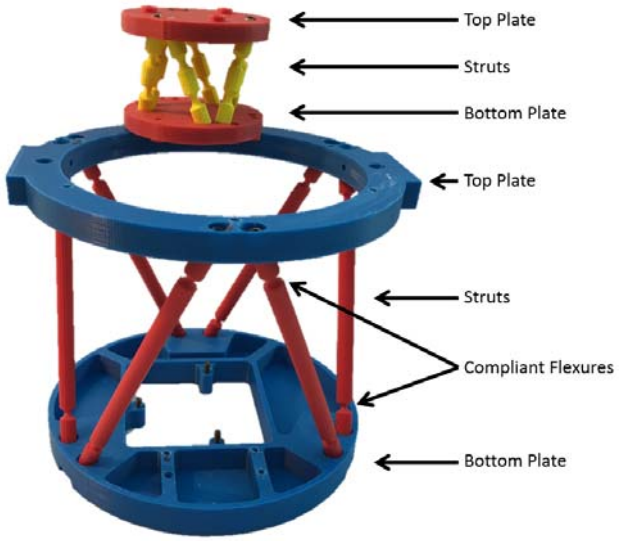

Figure 1: Two 3D printed models of static hexapods (Stewart trusses) designed, analyzed, and built using the process described in this paper. Each hexapod consists of a top plate, bottom plate, and six struts linking the two. The struts have compliant flexural sections at each end to accommodate misalignment, fabrication tolerance, and temperature load cases (when used with dissimilar materials).

BACKGROUND

The Stewart Truss [1] provides a six degree of freedom mechanism controlled by manipulating six adjustable-length links between a base and platform. Commercially available Stewart truss mechanisms, referred to as hexapods, provide precise control using nanometer-scale resolution piezoelectric positioners, and similar platforms have been made into six DOF force/torque sensors [2]. The hexapod concept works equally well on passive systems lacking the active control requirement, and they can provide a simple, stiff mechanical coupling between two separate system components that can be static or manually adjustable [3]. Figure 1 shows two 3D printed models of Stewart trusses designed and built for cryogenic optical housings using the process described in this paper.

DESIGN STRATEGY

The objectives of a design task are to create a system that meets requirements and functions as needed, with goals to exceed expectations within schedule and budget. Many paths can satisfy these objectives and goals, but the following strategy was successful in two optical designs fielded at LLNL in 2016 and 2017:

- Clear requirements definition to bound problem
- Selecting design parameters to vary in meeting requirements
- Analysis and/or tests for grading performance of design in satisfying requirements
- Iteration and feedback

SYSTEM REQUIREMENTS

The optical system requirements drive the analyses and shape the hexapod design. For the optical systems designed and described in this work, requirements derive from mechanical tolerances for subsystem positions based on

LLNL-PROC-737516

optical system sensitivity analysis, operating environment, different assembly/operating temperatures, and challenging acceleration conditions.

The optical system performance drives tight alignment and stability requirements between the lenses and focal plane in six degrees of freedom. The system is operated in an ambient temperature range spanning +/-20°C and for a variety of orientations to the gravity vector. Additionally, the use case for the optical system requires robustness to high acceleration loads. The size of the hexapod system is driven by mechanical interfaces to the lenses, focal plane, and housing subassemblies.

The optical system requires the focal plane to be held at a steady temperature in the range of 110-150K. The hexapod bottom plate material matches the focal plane baseplate to avoid deformation during cooldown. The optics are to be held at a steady temperature in the range of 165-200K; the lens cell and hexapod upper plate are made from aluminum due to weight requirements.

DESIGN PARAMETERS

The passive hexapod structure is a relatively simple system, but there are still several design parameters available to use in satisfying system requirements and functionality.

The specification of mechanical tolerances involves understanding their derivation from the optical system requirements, the cost and complexity of fabrication for a given design, and the design effort in labor hours. Very often, optical specifications reflect an optical engineer's ideal system and are derived from a requirement like "diffraction limited spot size on the detector pixels". A machine shop will approach mechanical tolerance from a different perspective, i.e. the tighter tolerances and exquisite machining drive longer schedules and higher costs. The tolerance specification knob is critical to attend to early on. In our optical designs, the diffraction limited spot size is smaller than focal plane pixels, the mechanical tolerances can be relaxed somewhat from "diffraction limited" to "pixel filling" performance.

The mechanical design parameters of the hexapod system are the dimensions for the top and bottom plates of the hexapod, the size and location of the hexapod struts, design of the flexure dimensions, and material choices for each of the three components (top plate, bottom plate, and struts).

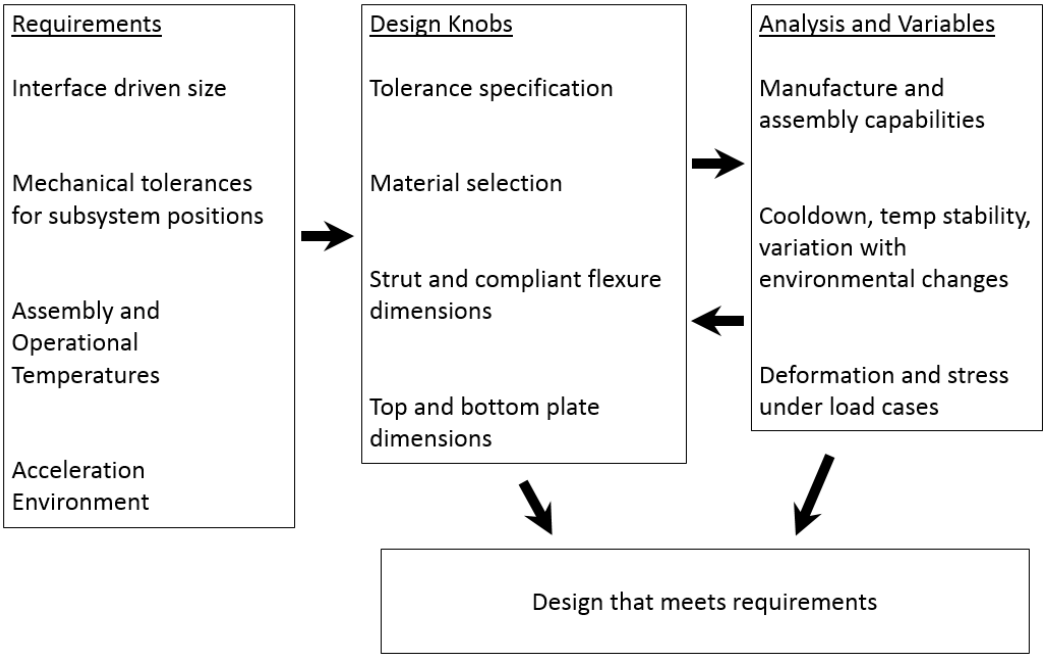

Figure 2: shows the interplay between requirements, design variables, and analyses required to meet the intended performance of the system.

The hexapods top and bottom plate materials are pre-determined to match the housing materials for the lens assembly (top plate) and focal plane (bottom plate). A commercially available cryocooler provides temperature control of the optical system and careful modelling of thermo-mechanical links between components is required to meet the temperature goals. Materials considered for the hexapod struts include grade 5 titanium, 17-4 PH SST, and carefully designed composites including low thermal conductivity materials. Aluminum was not considered due to the required flexing during cooldown at the strut flexural regions. The diameter and length of the struts were also tunable design parameters

ANALYSIS

Several analyses were used to tune the design parameters leading to a final hexapod design.

The thermal analysis on the system was performed in two steps. Figure 3 shows a thermal block diagram of the system with the major system components (110-150K parts at focal plane, 165-200K parts at the lenses, and the cryocooler cold tip). Simple thermal approximations are made for all of the load cases and thermal transfer along cold-straps and through the hexapod, then a step-wise numerical solution for the thermal blocks is used to simulate the cooldown performance and final temperatures. Figure 4 shows the cooldown curves provided by this analysis for the final hexapod configuration.

A finite element analysis (FEA) of thermal contraction for the hexapod with correct material properties for the top/bottom plates and struts was constructed. The materials in the hexapod contract by different amounts when cooled from room temperature to the operating condition, and the FEA stress calculation feeds into the design of the compliant flexure dimensions and location.

A FEA is also used to assess performance of the system against expected operational and transient load cases. Calculated stresses and deflections are fed back into the design, strut and top/bottom plate dimensions are tuned until the hexapod stiffness and stability meet the optical requirements. Figure 5 shows an example of the FEA results for one of the expected load cases, a 45 lbf sideways load applied to the bottom plate with the top plate constrained.

Finally, the system is analyzed for stress as a function of fabrication errors to determine how tightly controlled the machining process must be. Typical manufacturing tolerances (e.g. +/- 0.002" on the strut lengths) are considered by using FEA on intentionally mismatched strut lengths and/or end plate features. The FEA is iterated and results for displacement and stress in the hexapod are used to determine how precisely the components must be fabricated and inform the production of part drawings.

SUMMARY

Each step in the design process feeds back into the elements of the hexapod, largely the dimensions and features on the hexapod struts, and each analysis is useful in delivering a system that meets requirements. The simple static hexapod is a compact, efficient mechanism for supporting a precision optical system, but ensuring the performance during use at cryogenic temperatures requires a rigorous and iterative design process.

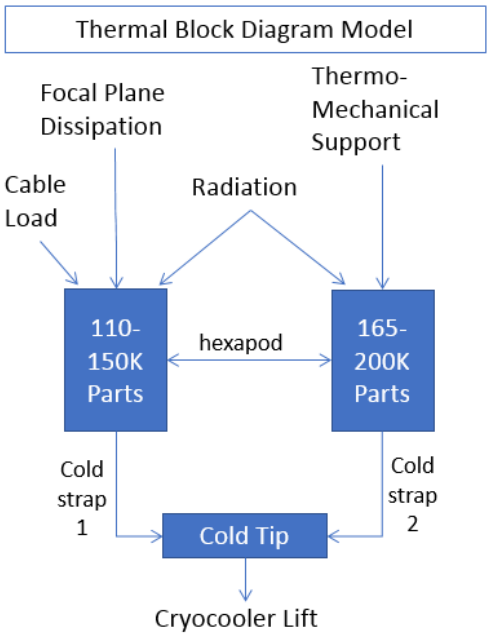

Figure 3: Thermal block diagram of the hexapod in the optical system. Heat transfer (blue lines) is modelled with simple thermal calculations. Temperatures of the major mechanical elements numerically calculated to simulate the cooldown performance of the system.

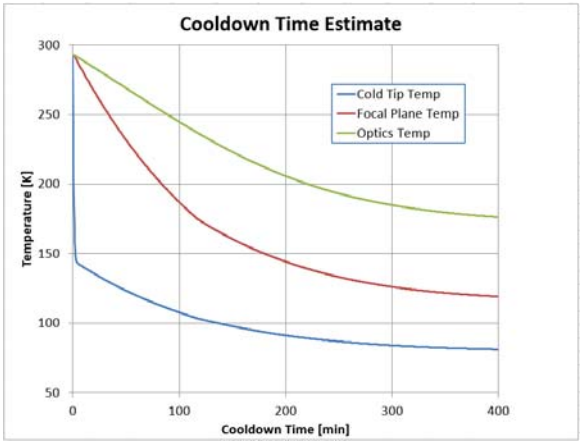

Figure 4: Cooldown time calculations from Thermal Block Diagram Model analysis.

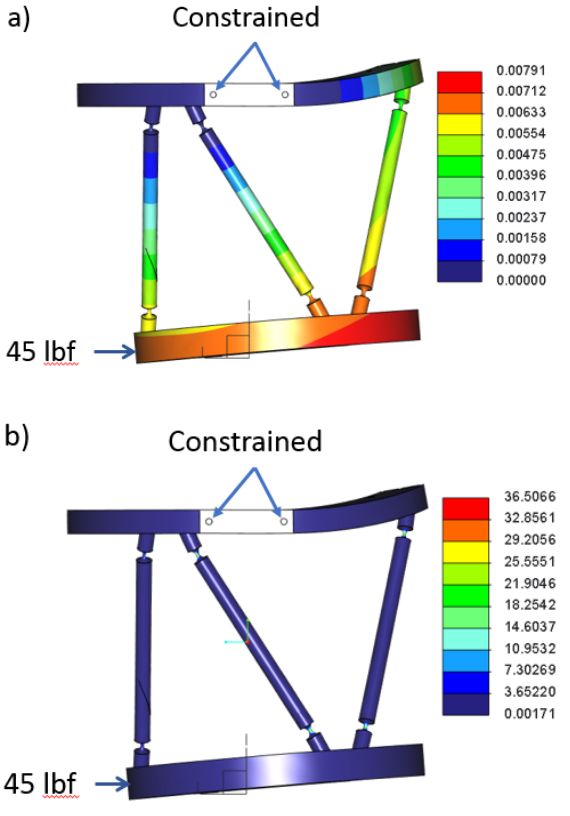

Figure 5: a) FEA results showing displacement (in inches) for the hexapod constrained at the top-plate with a 45 lbf static load applied to the bottom plate, and b) stress (in ksi) in the hexapod for the same loading condition.

Figure 6: Photo of the one completed hexapod, featuring dissimilar top plate, bottom plate, and strut materials. This design was the thermo-mechanical connection between a lens assembly and focal plane. Scale ruler is inches.

Figure 7: Photo of 2nd completed hexapod design with dissimilar top, bottom, and strut materials. This design was the thermo-mechanical link between a focal plane and external environment. Scale ruler is inches.

EXTENSION TO ATHERMALIZED STRUCTURES

The static hexapod topology provides a basis for creating a mass and volume efficient athermalization structure between optical components. Yoder [4] describes various athermalization structures for this purpose: metering rods, trusses, and tubes utilizing materials with differing coefficients of thermal

expansion are used to compensate for temperature- induced focus changes caused by the temperature dependence of index of refraction (for refractive systems) and length changes in the support structure (for refractive and reflective systems). Figure 8 shows a nested hexapod that was designed and built to provide passive athermalization between two sets of optical components in a related project to the subject of this paper.

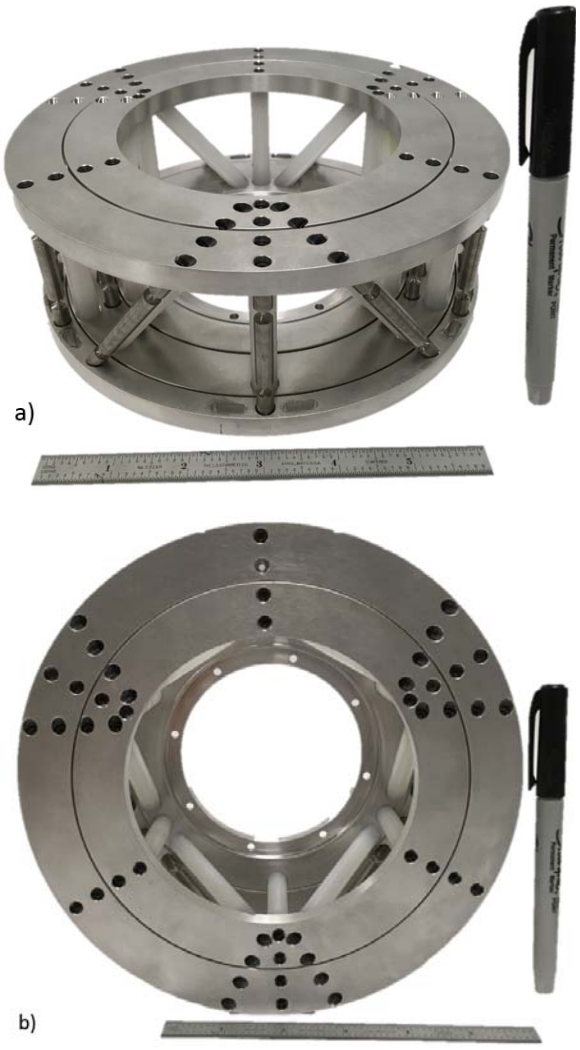

Figure 8a) Iso and b) top views of a nested hexapod structure used for passive athermalization between optical components. Four sets of hexapod struts, alternating between high and low CTE, are arranged in a fold-back configuration for an axially-compact arrangement. Axially-aligned struts are added to the low-stiffness high-CTE struts to preserve axial stiffness of the entire structure. Scale rulers are inches.

ACKNOWLEDGEMENTS

This work was performed under the auspices of the U.S. Department of Energy by Lawrence Livermore National Laboratory under Contract DE-AC52-07NA27344.

REFERENCES

[1] D. Stewart, "A Platform with Six Degrees of Freedom," Proceedings of the Institution of Mechanical Engineers, vol. 180, no. 1, pp. 371-386, 1965.

[2] T. Dwarakanath, "Beam type hexapod structure based six component force-torque sensor," Mechatronics, vol. 21, no. 8, pp. 1279-1287, December 2011.

[3] N. Shingleton, D. Kalantar, R. Wood, T. McCarville, J. Klingmann and A. Manuel, "Alignment of an x-ray imager line of sight in the National Ignition Facility (NIF) target chamber using a Diagnostic Instrument Manipulator (DIM) and Opposed Port Alignment System (OPAS)," Proc. SPIE 8505, Target Diagnostics Physics and Engineering for Inertial Confinement Fusion, 85050A, 15 October 2012.

[4] P. Yoder, Mounting Optics in Optical Instruments, Second Edition, Bellingham, WA: SPIE Press, 2008.

LLNL-PROC-737516

GANTRY-TYPE MACHINE TOOL ACCURACY ENHANCEMENT THROUGH GEOMETRIC ERROR REAL-TIME COMPENSATION BASED ON OPEN-ARCHITECTURE PA CNC

Chengyong Zhang, Hongdong Cong, and Yaolong Chen
State Key Lab for Manufacturing Systems Engineering
Xi'an Jiaotong University
Xi'an, Shaanxi, China

INSTRUCTIONS

With the rapid development of modern manufacture industry, the demand for high machining accuracy of machine tools is increasing. The geometric error is one of the main factors affect the machining accuracy [1]. So, reducing or eliminating the geometric error is an important way to enhance the machine tool accuracy.The traditional way to reduce the geometric error is by improving the machining and assembling accuracy of each component, which is called error preventive technology. However, it may be impossible for achieving the high machine tool accuracy through the error preventive technology due to the limitation of component machining accuracy, and the cost is quite expensive.

In addition, error compensation technology has been proved as an economical and effective way to improve the machine tool accuracy, because the geometric errors with the systematic and repeatable features can be accurately compensated [2]. However, error compensation cannot replace the effort of mechanical design, but rather an essential addition to it [3]. According to the different compensation methods, the geometric error compensation can be divided into off-line compensation and on-line compensation. The new compensated NC code is obtained in off-line compensation through the design of post-processor or NC program editor [4]. But the off-line method can only compensate for the error at the control points (such as the start and end points of the lines/circles, or the control points of splines)[5], and the tool tips in the tool path are still affected by the geometric errors. In addition, it is possible to improve the accuracy of the tool path by increasing the compensated points while modifying the NC program, but this will increase the NC program quantity.

Geometric error real-time compensation can generate more accurate features and surfaces of parts compared with the off-line compensation method. Zhang et al.[6] realized the real-time compensation of geometric and thermal errors for the five-axis machine tool with Fanuc CNC system by using the external machine zero point shift method. Based on the handwheel offset method, Cui et al.[7] proposed an error compensation implementing strategy for the machine tool with Siemens 840D CNC system, and realized the accuracy improvement of a heavy-duty CNC floor-typed boring and milling machine tool. Although the above real-time compensation methods can greatly improve the machine tool accuracy, the implementation of these methods requires the design and addition of external compensation controllers, which increases the cost of error compensation.

In this paper, the gantry-type machine tool accuracy is enhanced through the geometric error compensation to meet the design accuracy requirements, that is, the maximum volumetric error in the machine space under consideration is less than 30 μm. But the CNC system of Gantry-type machine tool is PA 8000 CNC system of POWER AUTOMATION GmbH and it does not have the volumetric error compensation functionality. Besides, this system is an open-architecture CNC system, which allows users to embed their own algorithms in the interpreter and interpolator of the system through the concept of compile cycle. So, in order to improve the accuracy of machine tools without increasing costs, a geometric error real-time compensation algorithm based open-architecture PA CNC is proposed.

VOLUMETRIC ERROR MODEL OF GANTRY-TYPE MACHINE TOOL

The volumetric error model of the machine tool is a prerequisite for the accurate compensation of geometric errors. The widely used and effective error modeling method is the homogeneous transfer matrix (HTM). In this method, the machine tool components are assumed to be rigid

bodies, the HTM is used to describe the transfer relation of volumetric error, and then the volumetric error model is established.

Before establishing the volumetric error model, some specifications are set as follows: all coordinate systems are the right-hand Cartesian coordinate system, the displacement errors are positive when they are in the same direction with the coordinate axes, and the angular deviations are positive when they meet the right-hand rule [8]. Therefore, considering the position $(t_x, t_y, t_z)$of tool tip in the tool coordinate system (TCS), the volumetric error model of Gantry-type machine tool is obtained according to the modeling process in [8] as

$$\begin{cases} \Delta x = \delta_{xx} + \delta_{xy} + \delta_{xz} + zS_{xz} + z\varepsilon_{yx} + z\varepsilon_{yy} \\ -t_y\left(\varepsilon_{zx} + \varepsilon_{zy} + \varepsilon_{zz}\right) + t_z\left(\varepsilon_{yx} + \varepsilon_{yy} + \varepsilon_{yz}\right) \\ \Delta y = \delta_{yx} + \delta_{yy} + \delta_{yz} + xS_{yx} - zS_{yz} + x\varepsilon_{zy} - z\varepsilon_{xx} \\ -z\varepsilon_{xy} + t_x\left(\varepsilon_{zx} + \varepsilon_{zy} + \varepsilon_{zz}\right) - t_z\left(\varepsilon_{xx} + \varepsilon_{xy} + \varepsilon_{xz}\right) \\ \Delta z = \delta_{zx} + \delta_{zy} + \delta_{zz} - x\varepsilon_{yy} - t_x\left(\varepsilon_{yx} + \varepsilon_{yy} + \varepsilon_{yz}\right) \\ +t_y\left(\varepsilon_{xx} + \varepsilon_{xy} + \varepsilon_{xz}\right) \end{cases} \tag{1}$$

where *x*, *y* and *z* are nominal displacements of feed axes, $\delta_{xx}, \delta_{yy}, \delta_{zz}$ represent the positioning errors of X-, Y- and Z-axis, respectively, δ_{yx}, δ_{zx} represent the Y and Z straightness errors of X-axis, respectively, δ_{xy}, δ_{zy} represent the X and Z straightness errors of Y-axis, respectively, δ_{xz}, δ_{yz} represent the X and Y straightness errors of Z-axis, respectively, $\varepsilon_{xx}, \varepsilon_{yx}, \varepsilon_{zx}$ represent the pitch, yaw and roll of X-axis, respectively, $\varepsilon_{xy}, \varepsilon_{yy}, \varepsilon_{zy}$ represent the pitch, yaw and roll of Y-axis, respectively, $\varepsilon_{xz}, \varepsilon_{yz}, \varepsilon_{zz}$ represent the pitch, yaw and roll of Z-axis, respectively, S_{yx}, S_{xz}, S_{yz} are the squareness errors between X- and Y-axis, X- and Z-axis, Y- and Z-axis.

REAL-TIME COMPENSATION OF GEOMETRIC ERROR

The flowchart for the proposed geometric error compensation strategy is shown in Fig.1, which includes off-line and on-line two modules. The off-line module mainly models the geometric errors, and obtains the fine (small axis position interval) geometric error tables. For each interpolation cycle in the on-line module, the system uses the X/Y/Z instantaneous reference position command and the fine geometric error tables to obtain the volumetric error value at this reference command point, then gets the modified X/Y/Z position command which will be output to the position loop controller of the machine tool.

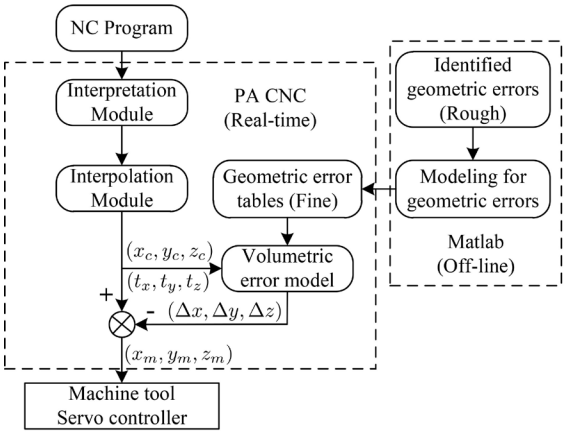

FIGURE 1. Flowchart for geometric error compensation

1) off-line module of geometric error compensation strategy

Firstly, the method of indirect measurement based on the volumetric error model(Eq.(1)) is used to identify 21 geometric errors of the gantry-type machine tool. But, the identified 18 position-dependent geometric errors (excluding the 3 squareness errors) are discrete and cannot be used directly for error compensation due to the large measurement interval. So, 18 geometric errors should be modeled so that each geometric error is expressed as a continuous function of the corresponding axis position, and the cubic spline interpolation method is used to model these geometric errors in this paper.

When the cubic spline interpolation method is used to model the errors, each obtained geometric error model has a lot of multiplication, resulting in a high computational cost. In the 2 ms interpolation period, using the geometric error models to calculate the volumetric error at the reference command point will take up too much system time, which will affect the stability of the system. Therefore, the method used in this paper is as follows: the identified geometric errors are modeled in off-line situation by using the caspa function (cubic spline interpolation function) in MATLB so that the geometric errors are expressed the continuous function of the corresponding axis position, and then the fine (small axis position interval) geometric error tables are obtained. These geometric error tables are the basis for effective compensation of the geometric errors and can be written to the CNC system either by PLC reading

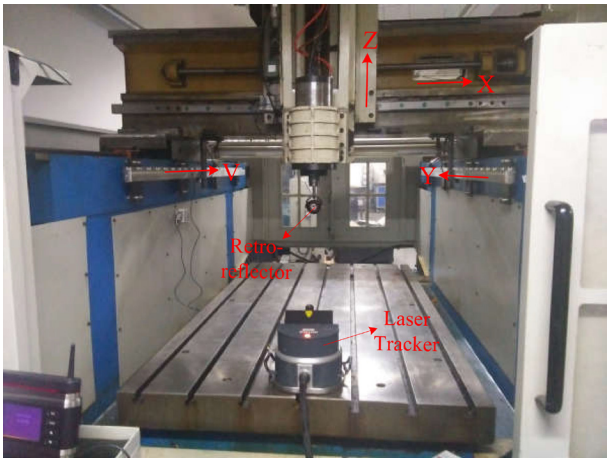

FIGURE 2. Gantry-type machine tool experimental setup

or by manual input.

2) real-time module of geometric error compensation strategy

For the geometric error real-time compensation, the X/Y/Z instantaneous reference position command (x_c, y_c, z_c) in MCS and the position (t_x, t_y, t_z) of tool tip in TCS are first acquired, and each geometric error at this position command point is obtained by means of look-up table and linear interpolation method. Taking the positioning accuracy of X-axis as an example, x_c is determined in the subspace $[x_i, x_{i+1}]$ of the X-axis positioning error table through the method of look-up table and the corresponding error interval is $[e_i, e_{i+1}]$, and then the method of linear interpolation is used to obtain the positioning error at x_c

$$\delta_{xx} = e_i + \frac{x_c - x_i}{\Delta x}(e_{i+1} - e_i) \tag{2}$$

where Δx is the interval of the subspace, $\Delta x = x_{i+1} - x_i$. The other geometric errors can be obtained in a similar way, and then the volumetric error vector $(\Delta x, \Delta y, \Delta z)$ at (x_c, y_c, z_c) can be obtained using the volumetric error model(Eq.(1)). The volumetric errors can be compensated by adding reversal motions to the corresponding axis. Finally, the position command output to the position loop controller of the machine tool is:

$$\begin{cases} x_m = x_c - \Delta x \\ y_m = y_c - \Delta y \\ z_m = z_c - \Delta z \end{cases} \tag{3}$$

GEOMETRIC ERROR IDENTIFICATION EXPERIMENT

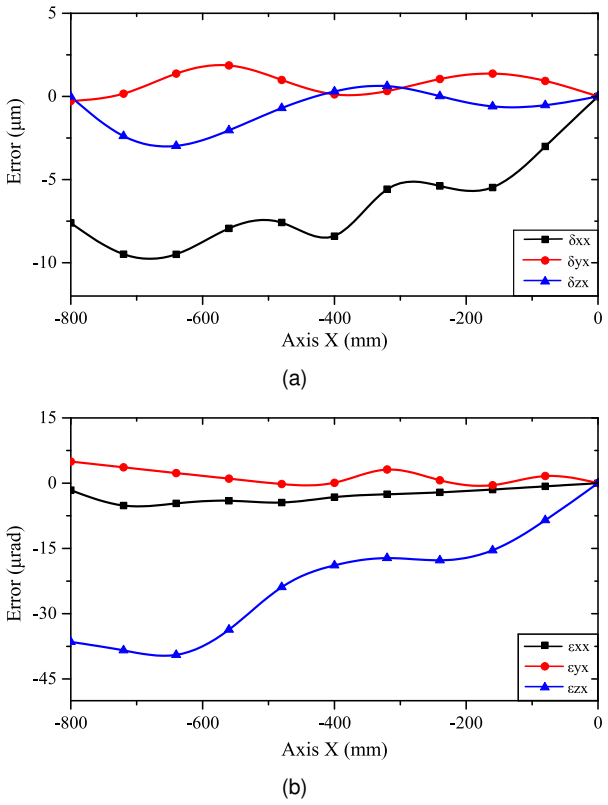

FIGURE 3. Identified geometric errors of X-axis, (a) displacement errors (b) angular errors

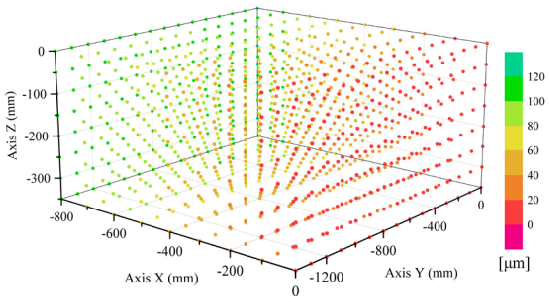

FIGURE 4. Volumetric error distribution of gantry-type machine tool

The 21 geometric errors of the gantry-type machine tool were identified using an Etalon laser tracker, and the experimental setup is shown in Fig.2. In this experiment, the measurement ranges of the X-,Y- and Z-axis were set to (-800 mm, 0 mm), (-1400 mm, 0 mm) and (-350 mm, 0 mm), respectively, and the measurement intervals of the three axes were set as 80 mm, 140

mm and 35 mm, respectively. A total of 6 laser tracker positions, three retro-reflector positions (in TCS) and 1362 measured points were set in the measurement planning. The measurement was carried out after the two and a half hours warm-up process of the machine tool, and the moving speeds of the X-, Y- and Z-axis were set to 3m/min. The entire measurement process took two and a half hours, during which the temperatures measured by three temperature sensors changed between [21.5°C-22.0°C].

The identified geometric errors of X- axis are shown in Fig.3, and the geometric errors of Y- and Z- axis are not shown due to the limitation of this article. The identified squareness errors are $S_{yx} = -151.1\mu\text{rad}$, $S_{xz} = 2.8\mu\text{rad}$ and $S_{yz} = 5.2\mu\text{rad}$. In addition, the volumetric error distribution of the whole measurement space is also obtained using the identified 21 geometric errors, as shown in Fig.4, where the maximum volumetric error is 121.8 μm, and the minimum volumetric error is 0 μm, which does not meet the design accuracy requirements.

GEOMETRIC ERROR REAL-TIME COMPENSATION EXPERIMENT

The identified geometric errors are used to compensate the gantry-type machine tool according to the provided real-time compensation method , and then the geometric errors are identified again using a laser tracker. In order to verify the compensation effect, the measurement intervals of the three axes were changed to 100 mm, 175 mm and 50 mm. The identified geometric errors after compensation are shown in Fig.5. Compared with the geometric errors before compensation, in addition to $\delta_{\text{xx}}, \delta_{\text{yx}}, \varepsilon_{xx}, \varepsilon_{zx}, S_{yz}$, the other 16 errors are reduced after compensation. In addition, the volumetric error distribution of the whole measurement space is also obtained using the identified 21 geometric errors, as shown in Fig.6, where the maximum volumetric error is 14.5 μm, and the minimum volumetric error is 0 μm. The comparison between Fig.6 and Fig.4 shows that the accuracy of the machine tool is improved by more than 88%.

According to ISO stander 230-6 [9], the diagonal measurement was conducted to further verify the effect of geometric error real-time compensation. The measurement paths were four diagonals shown as follows (Unit: mm): NPP[from (-187.374, -1100, -299.301) to (-800,0,0)], PPP[from (-598.73, -1100, -305.241) to (0,0,0)], PN-

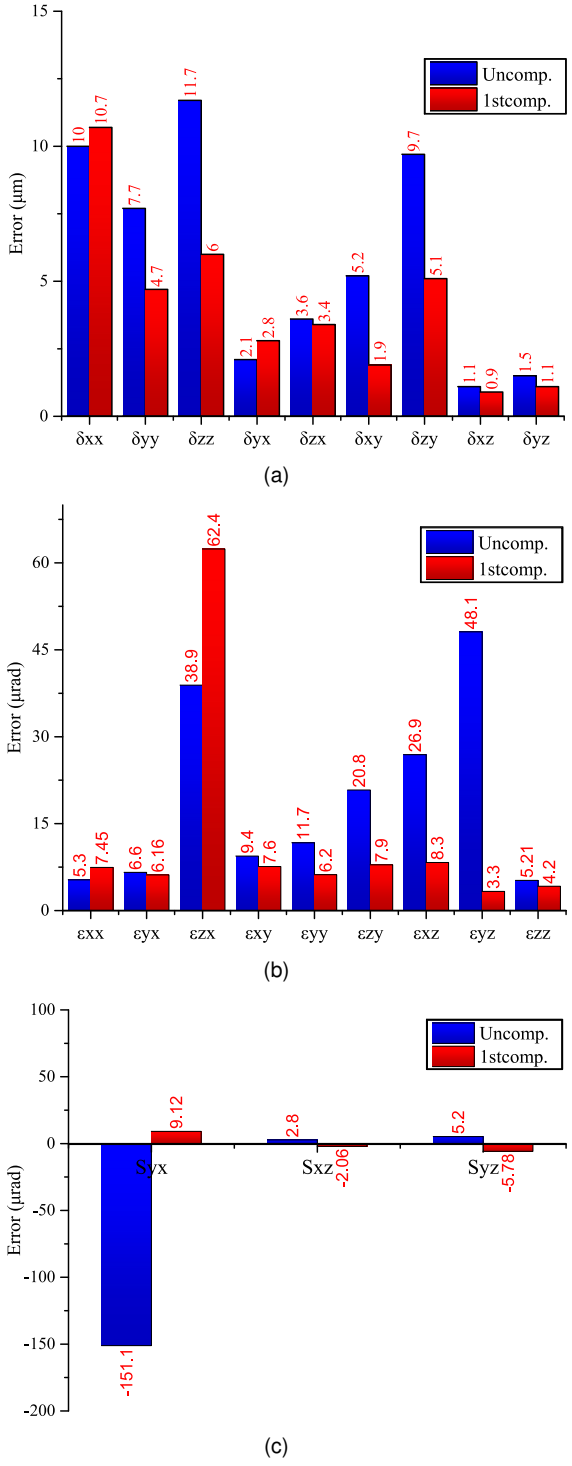

FIGURE 5. Comparisons between geometric errors after compensation and geometric errors before compensation (a) displacement errors of X-, Y- and Z-axis (b) angular errors of X-, Y- and Z-axis (c) squareness errors (comp. means compensation)

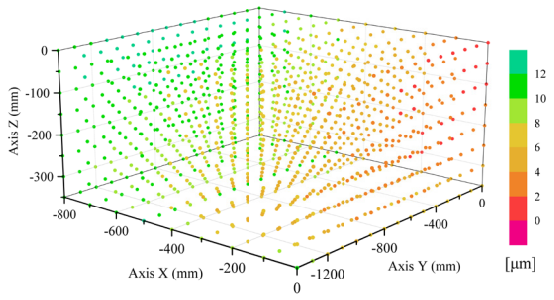

FIGURE 6. Volumetric error distribution of gantry-type machine tool after compensation

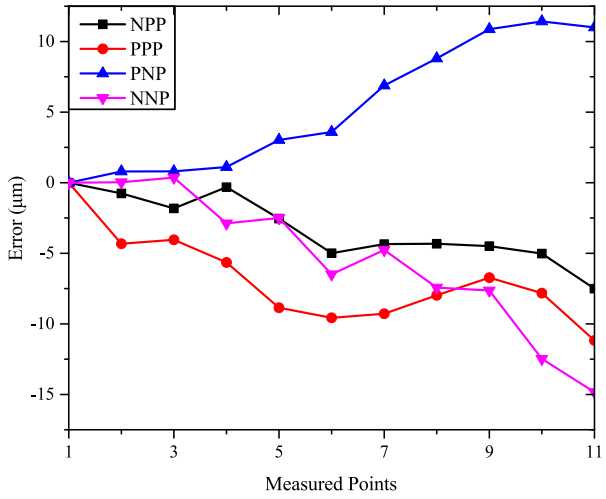

FIGURE 7. Diagonal positioning errors after compensation

P[from (-615.905, -200, -306.124) to (0,-1400,0)], and NNP[from (-166.477, -200, -296.623) to (-800,-1400,0)]. Here, P means the positive direction of the feed axis, and N means the negative direction of the feed axis. A total of 11 points were measured for each diagonal. The diagonal measurement results after compensation are shown in Fig.7. The maximum diagonal positioning error after compensation is 14.83 μm.

ACKNOWLEDGMENTS

This work was funded by the following funds:(1) National Science and Technology Major Project of China (2015ZX04005001); (2) National Science and Technology Major Project of China (2015ZX04001002)

REFERENCES

[1] H. Schwenke, W. Knapp, H. Haitjema, et al., Geometric error measurement and compensation of machinesan update, CIRP Ann.-Manuf.Technol. 57 (2) (2008) 660-675.

[2] G. Cui, Y. Lu, J. Li, D. Gao, Y. Yao, Geometric error compensation software system for CNC machine tools based on NC program reconstructing, Int. J. Adv. Manuf. Technol. 63 (1) (2012) 169-180.

[3] N. Barakat, M. Elbestawi, A. Spence, Kinematic and geometric error compensation of a coordinate measuring machine, Int. J. Mach. Tools Manuf. 40 (6) (2000) 8333-850.

[4] A. Khan, W. Chen, A methodology for systematic geometric error compensation in five-axis machine tools, Int. J. Adv. Manuf. Technol. 53 (5) (2011) 615-628.

[5] H. Shen, J. Fu, Y. He, X. Yao, On-line asynchronous compensation methods for static/quasi-static error implement ed on CNC machine tools, Int. J. Mach. Tools Manuf. 60 (2012) 14-26.

[6] Y. Zhang, J. Yang, S. Xiang, H. Xiao, Volumetric error modeling and compensation considering thermal effect on five-axis machine tools, Proc. Inst. Mech. Eng. Part C: J. Mech. Eng. Sci. 227 (5) (2013) 1102-1115.

[7] G. Cui, Y. Lu, D. Gao, Y. Yao, A novel error compensation implementing strategy and realizing on siemens 840D CNC systems, Int. J. Adv. Manuf. Technol. 61 (5) (2012) 595-608.

[8] Z. Li, J. Yang, K. Fan, Y. Zhang, Integrated geometric and thermal error modeling and compensation for vertical machining centers, Int. J. Adv. Manuf. Technol. 76 (5)(2015) 1139-1150.

[9] ISO 230-6:2002, Test code for machine tools-part 6: determination of linear displacement accuracy on body and face diagonals, International Organization for Standardization.

ANALYSIS OF ERROR MOTIONS OF HYDROSTATIC ROTARY TABLE

Penghai Zhang[1], Yaolong Chen[1], and Hongdong Cong[1]
[1]School of Mechanical Engineering
Xi'an Jiaotong University
Xi'an, Shaanxi, P.R. China

INTRODUCTIONS

Hydrostatic rotary tables are widely used in precision, ultra-precision processing technology. Hydrostatic bearings are more suitable for precision machining applications since they have much lower error motions, higher damping, and longer life than rolling element bearings. Their high precision comes from the error averaging effect of the pressured oil film which is closely related to not only the geometric errors of bearings but also the structural parameters such as the width of land, the width of exhausted groove, the film thickness and the number of recesses. When the hydrostatic journal and thrust bearings are designed, the number of recesses is usually set to four or six compared to three or five which is selected from the standpoint of higher rigidity, lower heat and easier manufacturing. But it's difficult to know which bearings have higher precision. Generally, the calculation of error motions of hydrostatic bearings is complicated using the methods such as CFD or FEM. In this article, approximate formulas are established to theoretically prove that the journal and thrust bearings with six recesses have higher precision compared to the bearings with three, four and five recesses under quasi-static condition. In the model, the geometric errors of shaft of journal bearing and thrust plates of thrust bearings are decomposed into harmonic waves based on the Fourier transform. The order of harmonic wave is defined as wave number. For journal bearing, wave number represents the number of harmonic waves on the shaft. For thrust bearings, wave number represents the number of harmonic waves on the thrust plates. **The formulas illustrate the direct relationship among structural parameters, geometric errors (represented by wave number and amplitude), and error motions of hydrostatic rotary tables with any number of recesses,** reducing the difficulty of calculation. Furthermore, definitions of error averaging ratio are made for the relationship between the geometric errors of rotary part and error motions of bearings based on the approximate formulas. Based on the theory, it is obvious that the bearings with six recesses have priority over the bearings with three, four and five recesses in the view of rotation accuracy. This article provides a theoretical basis for analysis of error motions of hydrostatic rotary table and determining the number of recesses in the design.

MODEL AND THEORY

Model of Hydrostatic Rotary Table

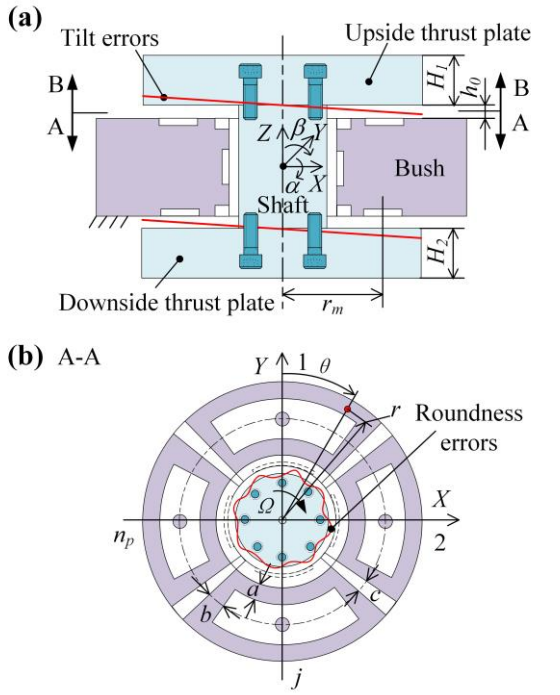

FIGURE 1. Structure of hydrostatic rotary table, (a) cutaway view and tilt errors of thrust plates, (b) structure of thrust bearing and roundness errors of shaft.

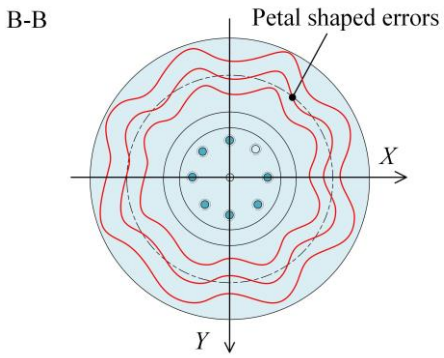

FIGURE 2. Petal shaped errors of thrust plates.

As shown in Fig. 1(a), the hydrostatic rotary table consists of two thrust bearings and one journal bearing. The two thrust bearings are made up of one bush and two thrust plates. The journal bearing is made up of one shaft and the bush. Both the thrust bearings and journal bearing have four pads separated by exhausted grooves. The two thrust plates are connected to the shaft by several screws, forming the H-type gap. The static part of bearing is mad up with the bush, while the rotary part of bearing is made up of the two thrust plates and the shaft. When the bearing is rotating at angular velocity Ω, the rotary part is deviated from the symmetrical position causing the horizontal, angular and vertical displacements of the shaft center. A Cartesian coordinate system XOY is established at the center of bush. Then, the error motions of shaft center can be expressed by the radial error motions X, Y, the tilt error motions α, β, and the axial error motion Z. The positive directions of tilt error motions α, β is around X, Y, respectively.

Constant Parts of Tilt Errors of Thrust Plates Caused by Manufacture and Assembly

In order to get a uniform expression and simplify the analysis process, the tilt errors of thrust plates can be treated as the initial angles and displacements with respect to the coordinate system XOY shown in Fig. 1(a). In this situation, the tilt angles have constant parts and time-varying parts. The constant parts are mainly caused by manufacture and assembly. For the upside thrust plate, the constant parts are α_{10}, β_{10}. For the downside thrust plate, the constant parts are α_{20}, β_{20}. The film thickness changes of upside and downside thrust plates Δh_1, Δh_2 caused by the constant parts of thrust plates, can be expressed as follows:

$$\begin{cases}\Delta h_1 = r\cos(\theta-\Omega t)\tan\alpha_{10} - r\sin(\theta-\Omega t)\tan\beta_{10} \\ \Delta h_2 = -r\cos(\theta-\Omega t)\tan\alpha_{20} + r\sin(\theta-\Omega t)\tan\beta_{20}\end{cases} \quad (1)$$

Time-Varying Parts of Tilt Errors of Thrust Plates Caused by Deformation

The time-varying parts of tilt errors are caused by structure deformation. For the upside thrust plate, the time-varying parts are α_{11}, β_{11}. For the downside thrust plate, the time-varying parts are α_{21}, β_{21}. Then, the film thickness changes of upside and downside thrust plates Δh_1, Δh_2 caused by deformation, can be expressed as follows:

$$\begin{cases}\Delta h_1 = r\cos(\theta)\tan\alpha_{11} - r\sin(\theta)\tan\beta_{11} \\ \Delta h_2 = -r\cos(\theta)\tan\alpha_{21} + r\sin(\theta)\tan\beta_{21}\end{cases} \quad (2)$$

Petal Shaped Errors of Thrust Plates

As shown in Fig. 2, the petal shaped errors of thrust plates include the sinusoidal errors in the circumferential direction and the bowl shaped errors in the radial direction. It is worth noting that the sinusoidal errors have two sources. The first source is the harmonic component of flatness of thrust plates in the circumferential direction based on the Fourier transform. The second source is the harmonic component of deformation of thrust plates caused by the locked screws. The bowl shaped errors represent the constant parts of deformations of thrust plates under the constant recess pressures. Then the film thickness changes of upside and downside plates Δh_1, Δh_2 can be expressed as follows:

$$\begin{cases}\Delta h_1 = \sum_{i=0}^{m_{11}} C_{1i} r^i \sin\left(n_1(\theta-\Omega t)+\phi_{1C0}\right) + \sum_{i=0}^{m_{12}} D_{1i} r^i \\ \Delta h_2 = -\sum_{i=0}^{m_{21}} C_{2i} r^i \sin\left(n_2(\theta-\Omega t)+\phi_{2C0}\right) - \sum_{i=0}^{m_{22}} D_{2i} r^i\end{cases} \quad (3)$$

where, for the sinusoidal errors of upside thrust plate, n_1 is the wave number, C_{1i} is the changing coefficient, ϕ_{1C0} is the initial phase angle, and m_{11} is the order of polynomial fitting. For the bowl shape errors of upside thrust plate, D_{1i} is the changing coefficient, and m_{12} is the order of polynomial fitting. Similarly, the downside thrust plate also has the similar parameters, n_2, C_{2i}, ϕ_{2C0}, m_{21}, D_{2i}, m_{22}.

Roundness Errors of Shaft

As shown in Fig. 1(b), based on the Fourier transform, the roundness errors of shaft can be decomposed into harmonic waves with different frequencies. The film thickness change Δh_3 caused by one kind of harmonic wave with a certain frequency can be expressed as follows:

$$\Delta h_3 = -E_3 \sin\left[n_3 \left(\theta - \Omega t \right) + \phi_{3E0} \right] \tag{4}$$

where E_3 is the amplitude of harmonic wave, n_3 is the wave number, and ϕ_{3E0} is the initial phase angle.

Film Thickness

The film thicknesses of journal bearing h_3, upside thrust bearing h_1 and downside thrust bearing h_2 can be written as follows:

$$\begin{cases} h_1 = h_0 + Z - r\sin\theta\tan\beta + r\cos\theta\tan\alpha + \Delta h_1 \\ h_2 = h_0 - Z + r\sin\theta\tan\beta - r\cos\theta\tan\alpha + \Delta h_2 \\ h_3 = h_{30} - \left[X - \beta(Z-y) \right]\sin\theta - \left[Y + \alpha(Z-y) \right]\cos\theta + \Delta h_3 \end{cases} \tag{5}$$

Quasi-static equilibrium equations

The rotary part is under quasi-static condition when the angular velocity Ω is very slow. For hydrostatic bearing with n_p recesses, the quasi-static equilibrium equations can be written as follows:

$$\begin{cases} \sum_{j=1}^{n_p} F_{Xj} = \sum_{j=1}^{n_p} -p_{r3j} A_{e3} \sin\left(\frac{2\pi}{n_p}(j-1) \right) = 0 \\ \sum_{j=1}^{n_p} F_{Yj} = \sum_{j=1}^{n_p} -p_{r3j} A_{e3} \cos\left(\frac{2\pi}{n_p}(j-1) \right) = 0 \\ \sum_{j=1}^{n_p} M_{\alpha j} = \sum_{j=1}^{n_p} \left(p_{r1j} - p_{r2j} \right) A_e \cos\left(\frac{2\pi}{n_p}(j-1) \right) = 0 \\ \sum_{j=1}^{n_p} M_{\beta j} = -\sum_{j=1}^{n_p} \left(p_{r1j} - p_{r2j} \right) A_e \sin\left(\frac{2\pi}{n_p}(j-1) \right) = 0 \\ \sum_{j=1}^{n_p} F_{Zj} = \sum_{j=1}^{n_p} \left(p_{r1j} - p_{r2j} \right) A_e = 0 \end{cases} \tag{6}$$

It can be equivalent to the following equation.

$$\begin{cases} \sum_{j=1}^{n_p} {\Delta h_{e3j}}^3 \sin\left(\frac{2\pi}{n_p}(j-1) \right) = 0 \\ \sum_{j=1}^{n_p} {\Delta h_{e3j}}^3 \cos\left(\frac{2\pi}{n_p}(j-1) \right) = 0 \\ \sum_{j=1}^{n_p} \left({\Delta h_{e1j}}^3 - {\Delta h_{e2j}}^3 \right) \cos\left(\frac{2\pi}{n_p}(j-1) \right) = 0 \\ \sum_{j=1}^{n_p} \left({\Delta h_{e1j}}^3 - {\Delta h_{e2j}}^3 \right) \sin\left(\frac{2\pi}{n_p}(j-1) \right) = 0 \\ \sum_{j=1}^{n_p} \left({\Delta h_{e1j}}^3 - {\Delta h_{e2j}}^3 \right) = 0 \end{cases} \tag{7}$$

Refer to the references [1] and [2] for the equivalent change of third power of film thickness.

Error Motions under Quasi-static Condition

Then, for hydrostatic bearing with n_p recesses, the radial, tilt and axial error motions, X, Y, α, β, Z, can be derived as follows:

$$\begin{cases} X = -\frac{2K_{32}E_3}{n_p K_{31} n_3} \sum_{j=1}^{n_p} \sin\left(\frac{2\pi}{n_p}(j-1) \right) \sin\left(n_3 \left(\frac{2\pi}{n_p}(j-1) - \Omega t \right) + \phi_{3E0} \right) \\ Y = -\frac{2K_{32}E_3}{n_p K_{31} n_3} \sum_{j=1}^{n_p} \cos\left(\frac{2\pi}{n_p}(j-1) \right) \sin\left(n_3 \left(\frac{2\pi}{n_p}(j-1) - \Omega t \right) + \phi_{3E0} \right) \\ \alpha = -\frac{\beta_{10}+\beta_{20}}{2}\sin(\Omega t) - \frac{\alpha_{10}+\alpha_{20}}{2}\cos(\Omega t) - \frac{\alpha_1+\alpha_2}{2} \\ \quad - \frac{K_{1\theta}C_{10}}{n_1 K_2 n_p} \sum_{j=1}^{n_p} \sin\left(n_1 \left(\frac{2\pi}{n_p}(j-1) - \Omega t \right) + \phi_{1C0} \right) \cos\left(\frac{2\pi}{n_p}(j-1) \right) \\ \quad - \frac{K_{2\theta}C_{20}}{n_2 K_2 n_p} \sum_{j=1}^{n_p} \sin\left(n_2 \left(\frac{2\pi}{n_p}(j-1) - \Omega t \right) + \phi_{2C0} \right) \cos\left(\frac{2\pi}{n_p}(j-1) \right) \\ \beta = -\frac{\beta_{10}+\beta_{20}}{2}\cos(\Omega t) + \frac{\alpha_{10}+\alpha_{20}}{2}\sin(\Omega t) - \frac{\beta_1+\beta_2}{2} \\ \quad + \frac{K_{1\theta}C_{10}}{n_1 K_2 n_p} \sum_{j=1}^{n_p} \sin\left(n_1 \left(\frac{2\pi}{n_p}(j-1) - \Omega t \right) + \phi_{1C0} \right) \sin\left(\frac{2\pi}{n_p}(j-1) \right) \\ \quad + \frac{K_{2\theta}C_{20}}{n_2 K_2 n_p} \sum_{j=1}^{n_p} \sin\left(n_2 \left(\frac{2\pi}{n_p}(j-1) - \Omega t \right) + \phi_{2C0} \right) \sin\left(\frac{2\pi}{n_p}(j-1) \right) \\ Z = -\frac{K_{1\theta}C_{10}}{2n_1 K_3 n_p} \sum_{j=1}^{n_p} \sin\left(n_1 \left(\frac{2\pi}{n_p}(j-1) - \Omega t \right) + \phi_{1C0} \right) - \frac{K_{1r}D_{10}}{2} \\ \quad - \frac{K_{2\theta}C_{20}}{2n_2 K_3 n_p} \sum_{j=1}^{n_p} \sin\left(n_2 \left(\frac{2\pi}{n_p}(j-1) - \Omega t \right) + \phi_{2C0} \right) - \frac{K_{2r}D_{20}}{2} \end{cases} \tag{8}$$

where

$$\begin{cases} K_{33} = 2b_3 L_3 + 2a_3 \left(\frac{\pi D}{n_p} - c_3 - 2b_3 \right) \\ K_{31} = DL_3 \sin\left(\frac{\pi}{n_p} - \frac{c_3}{D} \right) - D\left(L_3 - 2a_3 \right) \sin\left(\frac{\pi}{n_p} - \frac{c_3}{D} - \frac{2b_3}{D} \right) \\ K_{32} = DL_3 \sin\left(n_3 \left(\frac{\pi}{n_p} - \frac{c_3}{D} \right) \right) - D\left(L_3 - 2a_3 \right) \sin\left(n_3 \left(\frac{\pi}{n_p} - \frac{c_3}{D} - \frac{2b_3}{D} \right) \right) \end{cases} \tag{9}$$

$$\begin{cases} K_3 = \left(\frac{\pi}{n_p} - \frac{c}{d_m} \right) K_4 - \left(\frac{\pi}{n_p} - \frac{c}{d_m} - \frac{2b}{d_m} \right) K_6 \\ K_2 = \frac{2}{3}\sin\left(\frac{\pi}{n_p} - \frac{c}{d_m} \right) K_5 - \frac{2}{3}\sin\left(\frac{\pi}{n_p} - \frac{c}{d_m} - \frac{2b}{d_m} \right) K_7 \end{cases} \tag{10}$$

$$\begin{cases} K_4 = \left(r_m + \frac{L}{2} \right)^2 - \left(r_m - \frac{L}{2} \right)^2 \\ K_5 = \left(r_m + \frac{L}{2} \right)^3 - \left(r_m - \frac{L}{2} \right)^3 \\ K_6 = \left(r_m + \frac{L}{2} - a \right)^2 - \left(r_m - \frac{L}{2} + a \right)^2 \\ K_7 = \left(r_m + \frac{L}{2} - a \right)^3 - \left(r_m - \frac{L}{2} + a \right)^3 \end{cases} \tag{11}$$

$$\begin{cases} K_{1\theta} = \sin\left(n_1 \left(\frac{\pi}{n_p} - \frac{c}{d_m} \right) \right) K_{1\theta 1} - \sin\left(n_1 \left(\frac{\pi}{n_p} - \frac{c}{d_m} - \frac{2b}{d_m} \right) \right) K_{1\theta 2} \\ K_{1r} = \left(\frac{\pi}{n_p} - \frac{c}{d_m} \right) K_{1r1} - \left(\frac{\pi}{n_p} - \frac{c}{d_m} - \frac{2b}{d_m} \right) K_{1r2} \\ K_{2\theta} = \sin\left(n_2 \left(\frac{\pi}{n_p} - \frac{c}{d_m} \right) \right) K_{2\theta 1} - \sin\left(n_2 \left(\frac{\pi}{n_p} - \frac{c}{d_m} - \frac{2b}{d_m} \right) \right) K_{2\theta 2} \\ K_{2r} = \left(\frac{\pi}{n_p} - \frac{c}{d_m} \right) K_{2r1} - \left(\frac{\pi}{n_p} - \frac{c}{d_m} - \frac{2b}{d_m} \right) K_{2r2} \end{cases} \tag{12}$$

$$\begin{cases} K_{1\theta 1}=\sum_{i=0}^{m_{11}}\frac{2}{i+2}\frac{C_{1i}}{C_{10}}\left(r_m+\frac{L}{2}\right)^{i+2}-\sum_{i=0}^{m_{11}}\frac{2}{i+2}\frac{C_{1i}}{C_{10}}\left(r_m-\frac{L}{2}\right)^{i+2} \\ K_{1\theta 2}=\sum_{i=0}^{m_{11}}\frac{2}{i+2}\frac{C_{1i}}{C_{10}}\left(r_m+\frac{L}{2}-a\right)^{i+2}-\sum_{i=0}^{m_{11}}\frac{2}{i+2}\frac{C_{1i}}{C_{10}}\left(r_m-\frac{L}{2}+a\right)^{i+2} \\ K_{1r1}=\sum_{i=0}^{m_{12}}\frac{2}{i+2}\frac{D_{1i}}{D_{10}}\left(r_m+\frac{L}{2}\right)^{i+2}-\sum_{i=0}^{m_{12}}\frac{2}{i+2}\frac{D_{1i}}{D_{10}}\left(r_m-\frac{L}{2}\right)^{i+2} \\ K_{1r2}=\sum_{i=0}^{m_{12}}\frac{2}{i+2}\frac{D_{1i}}{D_{10}}\left(r_m+\frac{L}{2}-a\right)^{i+2}-\sum_{i=0}^{m_{12}}\frac{2}{i+2}\frac{D_{1i}}{D_{10}}\left(r_m-\frac{L}{2}+a\right)^{i+2} \\ K_{2\theta 1}=\sum_{i=0}^{m_{21}}\frac{2}{i+2}\frac{C_{2i}}{C_{20}}\left(r_m+\frac{L}{2}\right)^{i+2}-\sum_{i=0}^{m_{21}}\frac{2}{i+2}\frac{C_{2i}}{C_{20}}\left(r_m-\frac{L}{2}\right)^{i+2} \\ K_{2\theta 2}=\sum_{i=0}^{m_{21}}\frac{2}{i+2}\frac{C_{2i}}{C_{20}}\left(r_m+\frac{L}{2}-a\right)^{i+2}-\sum_{i=0}^{m_{21}}\frac{2}{i+2}\frac{C_{2i}}{C_{20}}\left(r_m-\frac{L}{2}+a\right)^{i+2} \\ K_{2r1}=\sum_{i=0}^{m_{22}}\frac{2}{i+2}\frac{D_{2i}}{D_{20}}\left(r_m+\frac{L}{2}\right)^{i+2}-\sum_{i=0}^{m_{22}}\frac{2}{i+2}\frac{D_{2i}}{D_{20}}\left(r_m-\frac{L}{2}\right)^{i+2} \\ K_{2r2}=\sum_{i=0}^{m_{22}}\frac{2}{i+2}\frac{D_{2i}}{D_{20}}\left(r_m+\frac{L}{2}-a\right)^{i+2}-\sum_{i=0}^{m_{22}}\frac{2}{i+2}\frac{D_{2i}}{D_{20}}\left(r_m-\frac{L}{2}+a\right)^{i+2} \end{cases} \quad (13)$$

Definitions of Averaging Coefficients

The error motions are smaller than the geometric errors of rotary part and this phenomenon is called the error averaging effect. The averaging coefficients can be defined as the ratios between the amplitudes of error motions and the amplitudes of geometric errors of rotary part. They can be used as quantitative indicators of error averaging effect. For hydrostatic rotary table with n_p recesses, the radial averaging coefficients δ_X , δ_Y , the tilt averaging coefficients γ_α , γ_β and the axial averaging coefficient ε can be defined as follows:

$$\begin{cases} \delta_X=\frac{\max(|X|)}{E_3} \\ \delta_Y=\frac{\max(|Y|)}{E_3} \\ \gamma_\alpha=\frac{\max(|\alpha|)}{|\alpha_{10}+\alpha_{20}|+|\beta_{10}+\beta_{20}|+|\alpha_{11}+\alpha_{21}|+|\beta_{11}+\beta_{21}|+|C_{10}+C_{20}|/r_m+|D_{10}+D_{20}|/r_m} \\ \gamma_\beta=\frac{\max(|\beta|)}{|\alpha_{10}+\alpha_{20}|+|\beta_{10}+\beta_{20}|+|\alpha_{11}+\alpha_{21}|+|\beta_{11}+\beta_{21}|+|C_{10}+C_{20}|/r_m+|D_{10}+D_{20}|/r_m} \\ \varepsilon=\frac{\max(|Z|)}{|C_{10}+C_{20}|+|D_{10}+D_{20}|} \end{cases} \quad (14)$$

RESULT AND DISCUSSION

All the averaging coefficients are based on the parameters of hydrostatic rotary table listed in Table 1.

Parameters of Hydrostatic Rotary Table in Calculation

TABLE 1. Parameters of hydrostatic rotary table.

Parameters of thrust bearings	**Value**
Bearing middle radius r_m /mm	148.5
Pad length L /mm	47
Land width a /mm	16
Land width b /mm	17
Exhausted groove width c /mm	6
Film thickness h_0 /μm	20
Recess number n_p	3, 4, 5, 6, …
Pressure ratio λ	0.5
Thickness of upside thrust plate H_1 /mm	45
Thickness of downside thrust plate H_2 /mm	45
Parameters of journal bearing	**Value**
Journal diameter D /mm	250
Pad length L_3 /mm	56
Land width a_3 /mm	14
Land width b_3 /mm	19
Exhausted groove width c_3 /mm	6
Film thickness h_{30} /μm	20
Recess number n_p	3, 4, 5, 6, …
Pressure ratio λ	0.5
Parameters of hydrostatic rotary table	**Value**
Inlet pressure p_s /MPa	2
Oil grade	#32
Temperature /℃	20

For tilt errors and bowl shaped errors of thrust plates.

Based on Eq. (8), the constant part of tilt errors of thrust plates will result in synchronous tilt displacements which are not tilt error motions. The averaging coefficients for time very part of tilt errors of thrust plates are 0.5. The bowl shaped errors of thrust plates just result in constant linear displacements which are also not axial error motion.

For the Hydrostatic Rotary Table with Three Recesses

As shown in Fig. 3, for the hydrostatic rotary table with three recesses, the harmonic waves of shaft and thrust plates with wave numbers n =2, 4, 5, 7, … , (expressed as $3i+1$, $3i+2$), have a major impact on the radial and tilt error motions, while the harmonic waves of shaft and thrust plates with wave numbers n =3, 6, 9, 12, … , (expressed as $3i$), have no influence on the radial and tilt error motions. The harmonic waves of thrust plates with wave numbers n =3, 6, 9, 12, … , (expressed as $3i$), have a major impact on the axial error motion, while the

harmonic waves of thrust plates with wave numbers n=1, 2, 4, 5, … , (expressed as $3i+1$, $3i+2$), have no influence on the axial error motion.

For the Hydrostatic Rotary Table with Four Recesses

As shown in Fig. 4, for the hydrostatic rotary table with four recesses, the harmonic waves of shaft and thrust plates with wave numbers n=3, 5, 7, 9, … , (expressed as $4i+1$, $4i+3$), have a major impact on the radial and tilt error motions, while the harmonic waves of shaft and thrust plates with wave numbers n=2, 4, 6, 8, … , (expressed as $4i$, $4i+2$), have no influence on the radial and tilt error motions. The harmonic waves of thrust plates with wave numbers n=4, 8, 12, … , (expressed as $4i$), have a major impact on the axial error motion, while the harmonic waves of thrust plates with wave numbers n=1, 2, 3, 5, … , (expressed as $4i+1$, $4i+2$, $4i+3$), have no influence on the axial error motion.

For the Hydrostatic Rotary Table with Five Recesses

As shown in Fig. 5, for the hydrostatic rotary table with five recesses, the harmonic waves of shaft and thrust plates with wave numbers n=4, 6, 9, 11, … , (expressed as $5i+1$, $5i+4$), have a major impact on the radial and tilt error motions, while the harmonic waves of shaft and thrust plates with wave numbers n=2, 3, 5, 7, … , (expressed as $5i$, $5i+2$, $5i+3$), have no influence on the radial and tilt error motions. The harmonic waves of thrust plates with wave numbers n=5, 10, 15, … , (expressed as $5i$), have a major impact on the axial error motion, while the harmonic waves of thrust plates with wave numbers n=1, 2, 3, 4, … , (expressed as $5i+1$, $5i+2$, $5i+3$, $5i+4$), have no influence on the axial error motion.

For the Hydrostatic Rotary Table with Six Recesses

As shown in Fig. 6, for the hydrostatic rotary table with six recesses, the harmonic waves of shaft and thrust plates with wave numbers n=5, 7, 11, 13, … , (expressed as $6i+1$, $6i+5$), have a major impact on the radial and tilt error motions, while the harmonic waves of shaft and thrust plates with wave numbers n=2, 3, 4, 6, … , (expressed as $6i$, $6i+2$, $6i+3$, $6i+4$), have no influence on the radial and tilt error motions. The harmonic waves of thrust plates with wave numbers n=6, 12, … , (expressed as $6i$), have a major impact on the axial error motion, while the harmonic waves of thrust plates with wave numbers n=1, 2, 3, 4, 5, … , (expressed as $6i+1$, $6i+2$, $6i+3$, $6i+4$, $6i+5$), have no influence on the axial error motion.

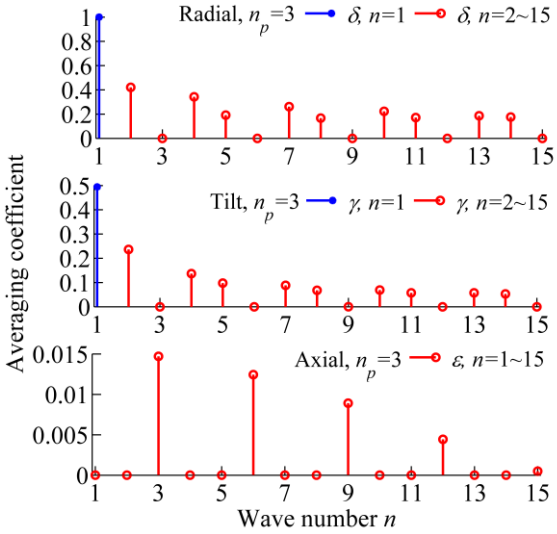
Radial, n_p=3 δ, n=1 δ, n=2~15
Tilt, n_p=3 γ, n=1 γ, n=2~15
Axial, n_p=3 ε, n=1~15
Averaging coefficient
Wave number n

FIGURE 3. Averaging coefficients for hydrostatic rotary table with three recesses.

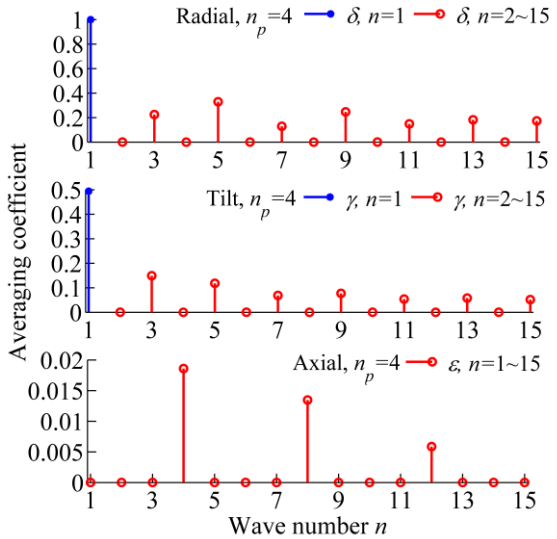
Radial, n_p=4 δ, n=1 δ, n=2~15
Tilt, n_p=4 γ, n=1 γ, n=2~15
Axial, n_p=4 ε, n=1~15
Averaging coefficient
Wave number n

FIGURE 4. Averaging coefficients for hydrostatic rotary table with four recesses.

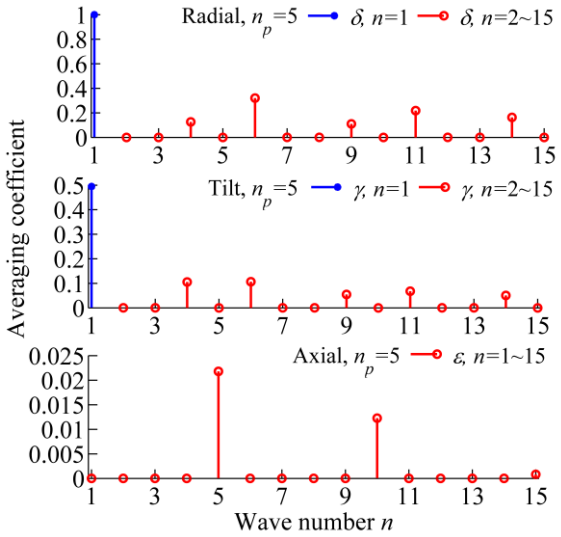
Radial, n_p=5 δ, n=1 δ, n=2~15
Tilt, n_p=5 γ, n=1 γ, n=2~15
Axial, n_p=5 ε, n=1~15
Averaging coefficient
Wave number n

FIGURE 5. Averaging coefficients for hydrostatic rotary table with five recesses.

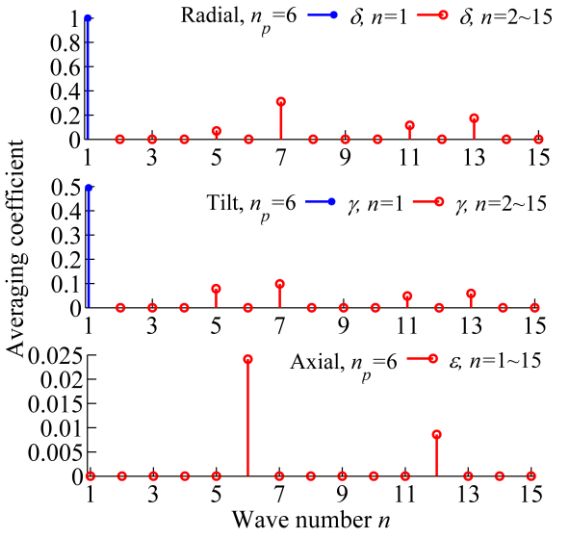
Radial, n_p=6 δ, n=1 δ, n=2~15
Tilt, n_p=6 γ, n=1 γ, n=2~15
Axial, n_p=6 ε, n=1~15
Averaging coefficient
Wave number n

FIGURE 6. Averaging coefficients for hydrostatic rotary table with six recesses.

For the Hydrostatic Rotary Table with n_p Recesses

Compared with Figs. 3~6, it can be concluded that, the for the hydrostatic rotary table with n_p recesses, the harmonic waves of shaft and thrust plates with wave numbers $n = n_p i + 1$, $n_p i + n_p - 1$, have a major impact on the radial and tilt error motions, while the harmonic waves of shaft and thrust plates with wave numbers $n = n_p i$, $n_p i + 2$, … , $n_p i + n_p - 2$, have no influence on the radial and tilt error motions. The harmonic waves of thrust plates with wave numbers $n = n_p i$, have a major impact on the axial error motion, while the harmonic waves of thrust plates with wave numbers $n = n_p i + 1$, $n_p i + 2$, … , $n_p i + n_p - 1$, have no influence on the axial error motion. Here, i is a non-negative integer.

Therefore, increment of recess number can improve rotation accuracy of hydrostatic rotary table since the number of harmonic waves of shaft and thrust plates having influence on error motions can be reduced. The hydrostatic rotary tables with six recesses have advantage compared with the rotary tables with three, four and five recesses in the view of motion accuracy. Since the increment of recess number will result in the structural complexity, it is better to choose a moderate number of oil chamber.

CONCLUSION

In the view of rotation accuracy, the hydrostatic rotary tables with six recesses have advantage compared with the rotary tables with three, four and five recesses. Increment of recess number can improve rotation accuracy of hydrostatic rotary table since the number of harmonic waves of shaft and thrust plates having influence on error motions can be reduced.

Acknowledgements

This work was financially supported by the National Natural Science Foundation of China (NSFC51275395); and the National Science and Technology Major Project of the Ministry of Science and Technology of China (2017ZX04013001).

REFERENCES

[1] Zhang P, Chen Y, Zha J. Relationship between geometric errors of thrust plates and error motions of hydrostatic thrust bearings under quasi-static condition. Precision Engineering. 2017, Vol.50, pp. 119-131.

[2] ZHANG P, CHEN Y, ZHA J, et al. Approximate formulas for the motion errors of hydrostatic guideways under quasi-static condition. ASPE 2016 annual meeting, 2016, pp. 467-472.

VACUUM COMPATIBLE CONTACTLESS ACTIVE MAGNETIC LINEAR BEARINGS FOR HIGH CLEANLINESS ROBOTIC APPLICATIONS

R. Baade[1], A.T.A. Peijnenburg[2] and M. Steinbuch[1]
[1]**Faculty of Mechanical Engineering**
Eindhoven University of Technology
Eindhoven, The Netherlands
[2]**VDL Enabling Technologies Group**
Eindhoven, The Netherlands

MOTIVATION

Requirements on both particulate and molecular contamination are becoming increasingly stringent in many industrial robotic applications, e.g. substrate handling in semiconductor, MEMS, flat panel and solar industry. This holds for both atmospheric and in-vacuum operating robots. Conventionally these robots are constructed as SCARA or double SCARA structures where rigid links are connected by rotational joints. The joints typically contain ball bearings and contamination seals to prevent contamination from reaching the clean process environment. Examples of such contamination seals are ferrofluid-, labyrinth- and differentially pumped gas purged seals. These seals are dominant in the cleanliness performance of the robot. Generally it holds that high performance seals significantly contribute to the mass, cost and complexity of the robots. Considering the workspace and required degrees of freedom, kinematic structures containing prismatic joints can potentially improve performance. Difficulty lies in lubricating and sealing of conventional rolling element linear bearings, especially for in-vacuum applications. This applies not only to prismatic bearings of industrial robotics, yet also to long stroke linear motion systems in general.

INTRODUCTION

Magnetic bearings could provide an advantageous alternative to conventional rolling element bearings [1]. Given that magnetic bearings are contactless, there is no mechanical friction and thus very little particle generation. Moreover, there is no need for lubrication which enables in-vacuum operation without significant outgassing or molecular contamination. These aspects make that contamination seals can be omitted.

The main challenges of applying magnetic bearings in high-tech in-vacuum systems lie in minimization of heat dissipation in the coils, minimizing eddy-current effects, implementation of a stable position control loop and linearization of the typically non-linear characteristics.

STATE OF THE ART

Magnetic bearing technology is already utilized in industrial applications. Rotary magnetic bearings are commercially available and applied in for example medical systems, turbo molecular vacuum pumps, cryogenic systems and machine tools [2, 3, 4]. Another category are bearingless motors where the rotor is magnetically suspended [5]. Magnetic levitation is widely used in the actuation of planar stages, typically based on Lorentz forces [6, 7]. A separate type of magnetic bearings is based on reluctance forces, for example as applied by Philips Applied Technologies [8]. A similar concept can also be used as actuator [9]. Although utilized in other fields, a thorough literature scan has found no evidence of magnetic bearing technology being applied on a commercial scale in high cleanliness substrate handling robotics. This is mainly due to the fact that typical magnetic bearings are relatively heavy, large in size and high in cost when compared to conventional rolling element bearings. Other potential issues are control stability, stiffness and energy dissipation in thermally critical systems and vacuum environments.

BEARING CONCEPT

The proposed bearing concept consists of small bearing elements which constrain a single translational degree of freedom of one rigid body w.r.t. another rigid body. Multiple bearing elements can be combined to constrain multiple degrees of freedom.

Single bearing module

The variable reluctance bearing modules are based on the bearings proposed in [8], and depicted schematically in figure 1. Each bearing module consists of a laminated e-core (1), where

a permanent magnet (2) is mounted on the central tooth. A static back iron (3) is placed at a distance g_1 from the e-core assembly. This system defines a low reluctance path where the resulting magnetic flux density in the air gap will yield a gap dependent attraction force between the e-core and the back iron. A coil (4) wound around the central tooth of the e-core is used to either magnify or reduce the magnetic flux density in the air gap, based on the direction and magnitude of the current running through the coil. Note that this system can only generate an attraction force and no repelling force between the e-core and back iron.

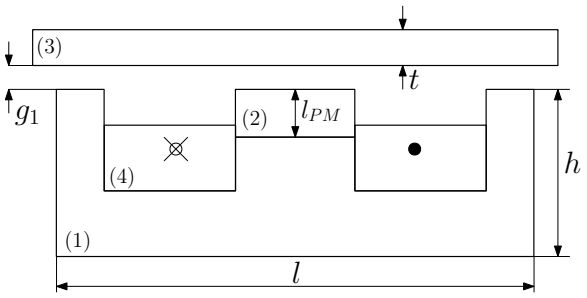

FIGURE 1. Schematic model of a single bearing module.

Pre-load mechanism

By applying a constant pre-load in the direction opposite to that of the attraction force, the net force on the bearing modules can be controlled, and thereby also the position of the bearing modules. Depending on the orientation of the bearing modules, gravity could provide at least part of this pre-load. The pre-load is enhanced by applying a second permanent magnet (5) on the opposed side of the e-core, as shown in figure 2. This second permanent magnet will create a pre-load force in the air gap g_2. Energy dissipation of the bearing modules can be minimized by tuning the magnetic pre-load force such that all static forces are balanced. In this case, the electromagnet is only required to counteract dynamic disturbances. Manufacturing tolerances and the relatively large variations on the dimensions and magnetic moment of permanent magnets introduce deviations from this static force balance. An adjustment mechanism (6) is introduced in between the e-core and the second permanent magnet to tune the pre-load force such that the static forces are balanced and dissipation is minimized.

Combining this system with a position sensor (or

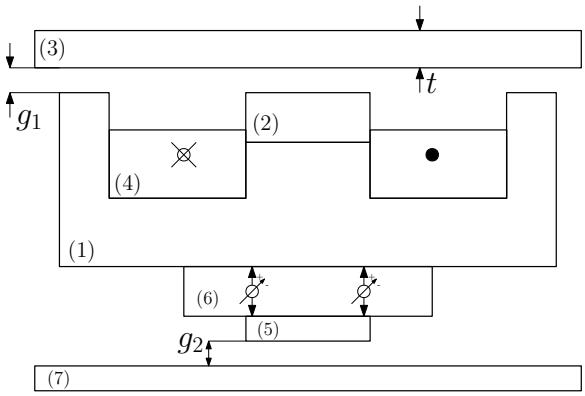

FIGURE 2. Schematic model of a single bearing module including adjustable pre-load mechanism.

flux sensor) and motion control software, consisting of a current control loop and a position control loop, the air gap (g_1) can be actively controlled to compensate for dynamic disturbance forces by regulating the current through the electromagnet (4). For the sake of cleanliness, this entire device can be enclosed in a non-magnetic material, for example stainless steel.

STRAIGHT GUIDE

The bearing modules described in the section above are able to constrain or control a single degree of freedom. Figure 3 shows a schematic concept of a single bearing module. Multiple of these bearing modules can be combined to constrain multiple degrees of freedom.

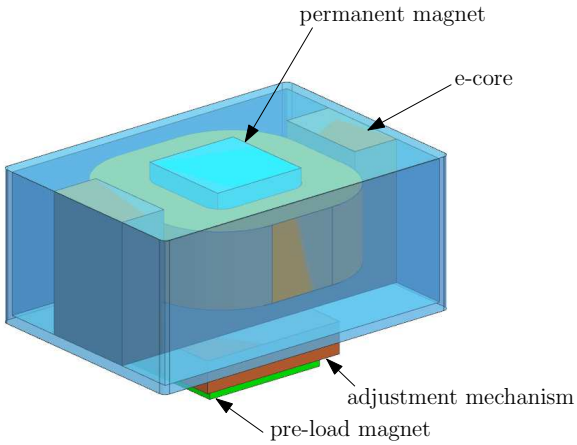

FIGURE 3. Illustrative representation of a single bearing module.

This section gives an example where the bearing modules are implemented in a straight guide with a stroke of approximately 600 mm, as part

of a substrate handling robot. The straight guide must constrain five degrees of freedom of a carriage with respect to a beam, the proceeding link of the robot. This concept is depicted in figure 4. In this example five magnetic bearing modules are applied, as an alternative to a concept containing one or two conventional profiled railways. Three bearing modules constrain the out of plane degrees of freedom of the carriage w.r.t. the beam, namely z, ϕ and ψ. Two additional bearing modules impose the remaining in-plane degrees of freedom y and θ.

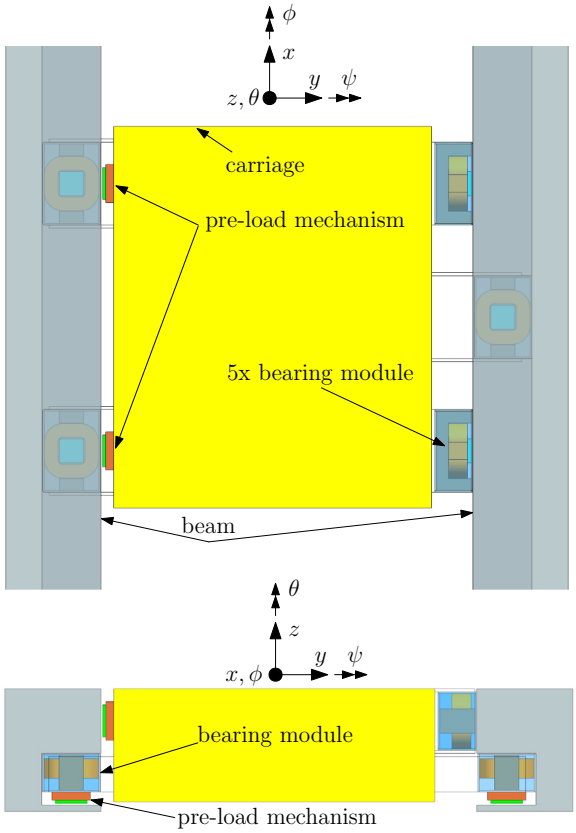

FIGURE 4. Upper figure: Top view of a straight guide concept containing five single DOF bearing modules. Lower figure: Front view of the straight guide concept.

Pre-loading for the three out of plane bearings is located at the bottom side of the e-core. The pre-loading consists of a permanent magnet which is mounted to an adjustment mechanism. The in-plane degree of freedom are pre-loaded by a permanent magnet on the opposed side of the carriage. In contrast to conventional rolling element linear bearings where five degrees of freedom (DOF) are constrained, the five constrained DOFs can be controlled actively using AMBs and thereby correct for undesired dynamic behavior of the robot.

MAGNETIC CIRCUIT MODELING

The reluctance force generated by the bearing modules is nonlinear in both the gap length and current. Considering the gap requires to remain constant at a specific value, given the bearing function, the system can be linearized around the gap-and current setpoint [10]. First order linearization of the actuator force yields:

$$F_{lin}(i,g) = F(i_0,g_0) + \frac{\delta F}{\delta i}|_{i_0,g_0}(i-i_0) + \frac{\delta F}{\delta g}|_{i_0,g_0}(g-g_0)$$

Separating the constant terms from the linear terms yields:

$$\begin{aligned} F_{lin}(i,g) &= \frac{\delta F}{\delta i}|_{i_0,g_0} i + \frac{\delta F}{\delta g}|_{i_0,g_0} g + F(i_0,g_0) \\ &\quad - \frac{\delta F}{\delta i}|_{i_0,g_0} i_0 - \frac{\delta F}{\delta g}|_{i_0,g_0} g_0 \\ &= Ki + c_a g + C \end{aligned}$$

Here, $\bar{K}$ and $\bar{c_a}$ are the motor constant and actuator stiffness, evaluated at the linearization point respectively. The resulting linearized reluctance force consists of a current contribution, a stiffness component and a constant force term. Table 1 shows a sensitivity analysis on the linearization error due deviations in gap and current setting from the linearization point. It is observed that the linearization errors in gap variations are relatively small. The error in current variations is more significant, the feedback controller has to compensate for these linearization errors.

TABLE 1. Sensitivity analysis linearization of inductance and motor constant.

L/g [%/μ]	K/g [%/μ]	K/i [%/A]
-0.1	-0.2	-12.5

Finite element modeling (FEM) simulations of the magnetic circuit have been performed to validate the analytical model. Two different finite element package have been used and compared, namely Finite Element Method Magnetics (FEMM) and Ansoft Maxwell v3. Both packages show similar results. The FEM simulation force to current

results show a significant difference with the analytical results of approximately 30 percent (see figure 5). Analysis has shown that this is mainly due to flux leakage effects near the permanent magnet, depicted by the FEM simulation result in figure 6.

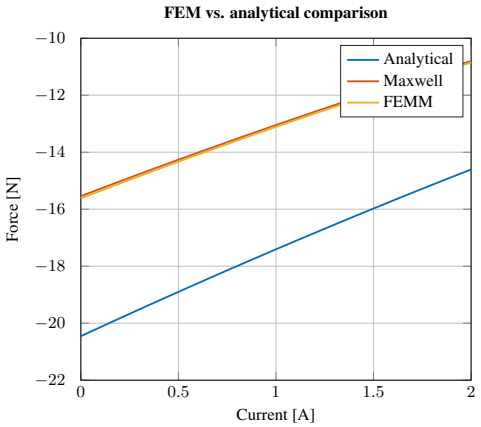

FIGURE 5. Plot showing reluctance force vs. current through the coil for two different finite element model packages and analytical results.

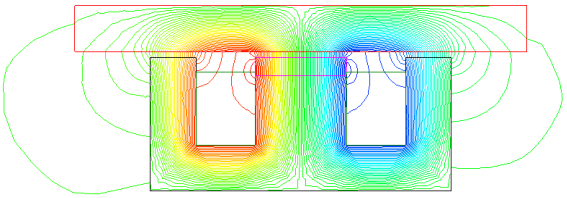

FIGURE 6. FEM simulation results showing flux leakage near the permanent magnet using Finite Element Method Magnetics software [11].

CONTROL

The non-linear characteristics of the reluctance based actuator complicate the motion control [12, 13]. The fact that the actuators are applied as bearings, makes that the force relation can be linearized around the steady-state gap and current setpoint. Moreover, the addition of the permeant magnet on the central tooth of the actuator increases the effective air gap and reduces the non-linearities.

A control system for a single bearing module is created. The control system contains two feedback loops, an internal current control loop and a position control loop, as shown in figure 7. Controller design is based on the linearized bearing model. The controllers are implemented in a Matlab Simulink model where the bearings are modelled by the actual non-linear characteristics. The feed-back controllers must compensate for the linearization errors. Effects such as magnetic hysteresis and saturation are not included in these simulations, due to the relatively low flux density in the system it is expected that these effects are negligible.

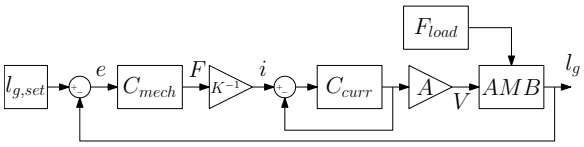

FIGURE 7. Control loop implemented in Mathworks Simulink model.

Position control loop

The mechanics of the bearing system in actuation direction can be modelled by an inertia, no additional damping is included in this model. The linearized force relation, as described before, consists of a current dependent term (Ki), a position dependent term (stiffness c_a) and a constant term. The transfer function describing the mechanical system is given by:

$$G_m(s) = \frac{1}{(ms^2 - c_a)}$$

The external disturbance force acting on the system, due to robot motion, is not included in this transfer function and is modeled by an external disturbance input d. A feedback controller is designed and is composed of a lead filter to create sufficient phase margin. Secondly a controller gain is added to achieve the desired cross-over frequency, which is set at 100 Hz.

The transfer function describing the effect of disturbance d on the position error e is given by the negative process sensitivity.

$$-PS(s) = \frac{-G_m(s)}{1 + G_m(s)C_m(s)}$$

For low frequencies up to the bandwidth, the amplitude of the process sensitivity is equal to the inverse of the magnitude of the mechanical controller. For frequencies above the bandwidth, the process sensitivity follows the mass line (-2 slope) of the plant. In order to minimize the effect of the external disturbances on the position error, the magnitude of the process sensitivity should be small. For frequencies below the bandwidth this corresponds to a high controller gain. The controller gain is increased, and the process sensitivity is decreased, by adding an integrator. This

integrator will also reduce the residual static error due to the increased magnitude at low frequencies.

Simulation results

The position controller as described above, and a simple current controller are implemented in a Mathworks Simulink model combined with the actual non-linear behavior of the bearing module. An external load is included to represent dynamical disturbances due to robot motion. This disturbance force profile is obtained through a multibody dynamics model of substrate handling robot. The gap setpoint is set to $0.5\,\mathrm{mm}$. Figure 8 shows the actual position (air gap), and the position error of a single bearing module over time. The variation of the position error over time is caused by the external load profile. It can be noticed that the position error is remains well within plus or minus $0.1\,\mu\mathrm{m}$, under dynamical loading. For the application of a linear guide in a substrate handling robot, this is sufficient and comparable to the accuracy of a conventional rolling element bearing.

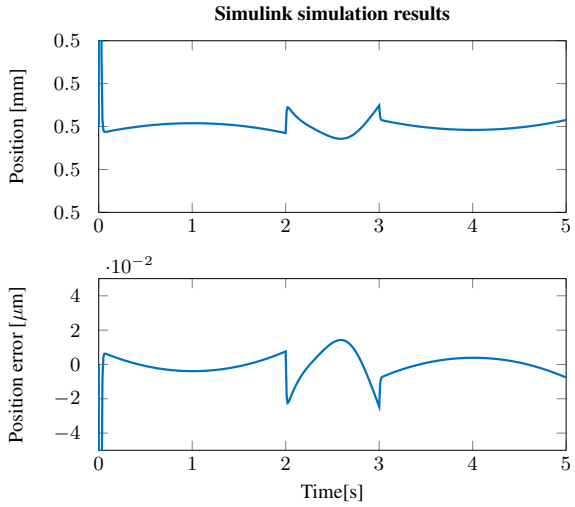

FIGURE 8. Simulink results showing air gap and position error over time during during dynamical loading of a single bearing element.

CONCLUSIONS AND FUTURE WORK

This work is part of a larger project on the design and realization of a high cleanliness substrate handling mechanism. Considering the high cleanliness requirements on the substrate handling mechanism, the magnetic bearing modules as presented in this paper appear to be a promising solution. Given the results of the theoretical simulations, application of these bearings seems feasible. Currently a test-setup is being developed where a single bearing module can be analyzed. The stability of the system under closed loop control will be evaluated for various operation points. Secondly a characterization of the reluctance force for various current and gap setpoints will be conducted and compared to the simulation results. Additionally, the maximal achievable stiffness will be assessed.

REFERENCES

[1] Peijnenburg ATA, Vermeulen JPM, van Eijk J. Magnetic levitation systems compared to conventional bearing systems. Microelectronic Engineering. 2006;83:1372–1375.

[2] Qian KZ, Yuan HY, Zeng P, Ru WM. A novel permanent maglev rotary LVAD with passive magnetic bearings. Journal of Medical Engineering & Technology. 2005;29:235–237.

[3] Schweitzer G, Bleuler H, Traxler A. Active Magnetic Bearings; Basics, Properties and Applications of Active Magnetic Bearings. Hochschulverlag AG an der ETH Zrch; 1994.

[4] Bleuler H, Cole M, Keogh P, Larsonneur R, Maslen E, Nordmann R, et al. Magnetic Bearings; Theory, Design and Application to rotating machinery. Schweitzer G, Maslen EH, editors. Springer; 2009.

[5] Zhou L, Trumper DL. Reluctance Force Magnetic Suspension Characteristics and Control for Cylindrical Rotor Bearingless Motors. Transactions of the ASME. 2017 March;139.

[6] Lu X. A Novel Long-Stroke Planar Motor. In: Proceedings of ASPE 2011 Annual Meeting; 2011. .

[7] Choi YM, Lee MG, Jeong J. A new magnetic bearing using Halbach magnet arrays for a magnetic levitation stage. Review of Scientific Instruments. 2017 August;88.

[8] de Klerk ACP, Angelis GZ, van Eijk J. Design of a next generation 6 DoF stage for scanning application in vacuum with nanometer accuracy and mGauss magnetic stray field. Proceedings of the 19th annual ASPE meeting. 2004;.

[9] Hamelinck R. Adaptive deformable mirror, based on electromagnetic actuators. Eindhoven University of Technology; 2010.

[10] A E Fitzgerald SDU C J Kingsley. Electric machinery. 6th ed. McGraw-Hill; 2003.

[11] Meeker D. Finite Element Method Magnetics, reference manual; 2015.

[12] Katalenic A. Control of reluctance actuators for high-precision positioning. Eindhoven University of Technology; 2013.

[13] Trumper DL, Olson SM, Subrahmanyan PK. Linearizing Control of Magnetic Suspension Systems. IEEE Transactions on Control Systems Technology. 1997 July;5(4).

A HIGH PERFORMANCE FEEDFORWARD TUNING APPROACH FOR ULTRA-PRECISION MOTION CONTROL

Luyao Dai[1], Xin Li[1], Yu Zhu[1], and Ming Zhang[1]
[1]State Key Laboratory of Tribology, Department of Mechanical Engineering
Tsinghua University
Beijing, China

INTRODUCTIONS

For ultra-precision motion systems like the wafer stage of lithography machine, large tracking error during acceleration or deceleration phase will lead to a long settling time, attenuating the throughput of the entire system. To handle this problem, feedforward control is exploited to achieve high tracking accuracy and small settling time. A widely used feedforward strategy is model-based feedforward control, which utilizes feedforward controller to approximate the inversion of the plant model. Since the exact plant model is usually unknown, therefore, a variety of control techniques are developed to improve the performance of feedforward controller.

In [1], a model-based feedforward controller, which includes acceleration and snap feedforward, is combined with a finite impulse response filter (FIR). The FIR coefficients are tuned by off-line data-based algorithm. In [2], an adaptive feedforward method is proposed, in which RLS algorithm is used to tune acceleration feedforward coefficient on-line. Other methods can be found in [3-7]. Although these methods prove to be effective to reduce tracking error during acceleration or deceleration phase and then reduce settling time, the mechanism of generation of tracking error during acceleration or deceleration phase remains unknown.

In this paper, the relationship between tracking error and reference trajectory to be tracked is quantitatively analyzed. Research shows that the shape of tracking error is decided by the derivatives of reference trajectory, DC gain of feedback controller and structure of feedforward controller. Based on theoretical analysis, a simple but effective feedforward tuning method is proposed. Experiment validates the relationship between tracking error and trajectory presented in this paper. Experiment also shows that tracking error during acceleration or deceleration phase can be largely reduced and zero settling time can be attained with the feedforward tuning method proposed in this paper.

PLANT DYNAMICS

The plant model of many precision motion systems like the wafer stage of lithography machine can be modeled as multi-mass system, see Figure 1. The transfer function of the plant is

$$G_p(s) = \frac{1}{m_t s^2}\prod_{i=1}^{N}\frac{\omega_i^2}{\left(s^2+2\zeta_i\omega_i s+\omega_i^2\right)} = \frac{1}{m_t s^2}+\frac{1}{m_t}\sum_{i=1}^{N}\frac{d_i}{\left(s^2+2\zeta_i\omega_i s+\omega_i^2\right)} \quad (1)$$

with m_t the total mass of the system, ω_i the resonant frequency, ζ_i the damping ratio and d_i the constant decided by model. Note that the multi-mass system showed in Figure 1 is the so-called non-colocated system [8], where system input and output are at the ends of the system. Deduction in the subsequent sections are based on non-colocated system, though it also applies for co-located system.

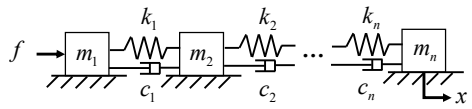

FIGURE 1. The model of multi-mass system.

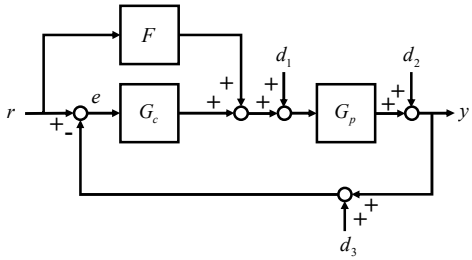

FIGURE 2. The two-degree-of-freedom control architecture.

QUANTITATIVE ANALYSIS OF TRACKING ERROR

The control strategy used here is the famous two-degree-of-freedom control architecture, see figure 2, where F is the feedforward controller, G_c the feedback controller, G_p the plant model, r the reference input, e the tracking error, y the system output, d_1 the force disturbance, d_2 the position disturbance and d_3 the sensor noise, respectively. Neglecting disturbances and sensor noise, the tracking error can be expressed as

$$e = S_r(s)\left(1 - G_p F\right) r \tag{2}$$

$S_r(s)$ is the sensitivity function

$$S_r(s) = \frac{1}{1 + G_p G_c} \tag{3}$$

A lead controller is first used as feedback controller, which is well enough to stabilize the multi-mass system showed in Figure 1 and of which the DC gain is finite.

$$G_c(s) = K\left(\frac{s+z}{s+p}\right) \tag{4}$$

z and p are the zero and pole of the lead controller, respectively. K is the controller constant. Assume that reference trajectory mainly contains low-frequency components which means $s \to 0$, the sensitivity function can be approximated by

$$\begin{aligned} S_r(s) &= \frac{m_t s^2}{m_t s^2 + G_c(s)\left(1 + \sum_{i=1}^{N} \frac{s^2 d_i}{\left(s^2 + 2\zeta_i \omega_i s + \omega_i^2\right)}\right)} \\ &\cong \frac{m_t s^2}{G_c(0)} \end{aligned} \tag{5}$$

If acceleration feedforward is used

$$F = m_a s^2 \tag{6}$$

then substitute (5) and (6) into (2), we can get

$$\begin{aligned} e &= \frac{m_t s^2}{G_c(0)}\left(1 - \frac{m_a}{m_t}\left(1 + \sum_{i=1}^{N} \frac{d_i s^2}{\left(s^2 + 2\zeta_i \omega_i s + \omega_i^2\right)}\right)\right) r \\ &\cong \frac{\left(m_t - m_a\right) s^2 r}{G_c(0)} = \frac{\left(m_t - m_a\right) \ddot{r}}{G_c(0)} \end{aligned} \tag{7}$$

It means that when acceleration feedforward coefficient is not close enough to the ideal value (the total mass of the system), tracking error is approximately proportional to the acceleration of reference trajectory. Since e, $\ddot{r}$, $G_c(0)$ are known, through equation (7), we can get the appropriate acceleration feedforward coefficient by

$$m_a = \frac{e G_c(0)}{\ddot{r}} \tag{8}$$

Another practical method is to use two different tracking error e_1 and e_2 attained by two different feedforward coefficient m_{a_1} and m_{a_2} under the same trajectory to tune the feedforward coefficient

$$m_a = \frac{e_1}{e_1 - e_2}\left(m_{a_2} - m_{a_1}\right) + m_{a_1} \tag{9}$$

Note that no extra information, like the DC gain of feedback controller, is required except tracking errors and corresponding feedforward coefficients. It is crucial to choose tracking error at which time instant should be used in equation (8) or (9). The mean value of tracking error during constant acceleration phase (if the trajectory has) is a good choice, during which the trajectory mainly contains low frequency components and thus equation (7) can provide better approximation.

When m_a is well-tuned, $m_a \approx m_t$, then tracking error becomes

$$\begin{aligned} e &= \frac{m_t s^2}{G_c(0)}\left(\sum_{i=1}^{N} \frac{-d_i s^2}{\left(s^2 + 2\zeta_i \omega_i s + \omega_i^2\right)}\right) r \\ &\cong \left(\frac{-m_t}{G_c(0)} \sum_{i=1}^{N} \frac{d_i}{\omega_i^2}\right) r s^4 \\ &= \left(\frac{-m_t}{G_c(0)} \sum_{i=1}^{N} \frac{d_i}{\omega_i^2}\right) \ddddot{r} \end{aligned} \tag{10}$$

A fourth-order feedforward term is needed to compensate for the residual error in (10), then the feedforward controller becomes

$$F = m_a s^2 + m_s s^4 \tag{11}$$

And the tracking error becomes

$$\begin{aligned} e &\cong \frac{m_t s^2}{G_c(0)}\left(-\frac{m_s s^2}{m_t} - \sum_{i=1}^{N} \frac{d_i s^2}{\left(s^2 + 2\zeta_i \omega_i s + \omega_i^2\right)}\right) r - \\ &\left(\frac{m_a}{m_t} \sum_{i=1}^{N} \frac{s^4}{\left(s^2 + 2\zeta_i \omega_i s + \omega_i^2\right)}\right) r \\ &\cong \frac{1}{G_c(0)}\left(-m_s - m_t \sum_{i=1}^{N} \frac{d_i}{\omega_i^2}\right) s^4 r \\ &= \frac{1}{G_c(0)}\left(-m_s - m_t \sum_{i=1}^{N} \frac{d_i}{\omega_i^2}\right) \ddddot{r} \end{aligned} \tag{12}$$

The third derivative and fourth derivative of trajectory is called jerk and snap, respectively. It shows that when acceleration feedforward is well-tuned, tracking error is approximately proportional to snap of reference trajectory. There is no need to know the exact resonant frequency ω_i and corresponding constant d_i to

calculate the fourth-order feedforward coefficient. With a well-tuned acceleration feedforward coefficient, the snap feedforward coefficient can be tuned by two groups of tracking errors with two different snap feedforward coefficient under the same trajectory like equation (9). After compensation of this term, the residual tracking error is approximately proportional to the sixth order derivate of reference trajectory. Compensation for this term requires a sixth order derivable trajectory and is out of discussion in this paper.

Deduction abovementioned requires that the DC gain of feedback controller is finite. However, disturbance attenuation is non-negligible for a practical control system and steady-state error is sometimes unexpected. Therefore, integrator is usually included in the feedback controller, rendering the DC gain of feedback controller infinite. For multi-mass system, a PID controller is sometimes a preferable choice

$$G_c(s)=\left(k_p+k_d s+\frac{k_i}{s}\right)\left(\frac{\omega_{lp}^2}{s^2+2\zeta_{lp}\omega_{lp}s+\omega_{lp}^2}\right) \tag{13}$$

k_p , k_d and k_i are the proportional, differential and integral part of PID controller, respectively. ω_{lp} and ξ_{lp} are the low-pass filter frequency and damping ratio respectively. With a PID controller, the approximation of sensitivity function becomes

$$\begin{aligned} S_r(s) &\cong \frac{m_t s^3}{m_t s^3+\left(k_p s+k_d s^2+k_i\right)}\cdot \\ &\quad \frac{1}{\left(1+\sum_{i=1}^{N}\frac{s^2 d_i}{\left(s^2+2\zeta_i\omega_i s+\omega_i^2\right)}\right)} \\ &\cong \frac{m_t s^3}{\tilde{G}_c(0)} \end{aligned} \tag{14}$$

$$\tilde{G}_c(0)=\lim_{s\to 0} sG_c(s) \tag{15}$$

Then equation (7) becomes

$$e\cong\frac{\left(m_t-m_f\right)\dddot{r}}{G_c(0)} \tag{16}$$

It means when acceleration feedforward coefficient is not close enough to ideal value, tracking error is approximately proportional to the third order derivative of reference trajectory. Similar change applies to equation (11).

Up to now, discussion is restricted to continuous domain. However, most control system at the moment is digital control system. The main difference is that there will be a zero-order holder between controller and plant model when it comes to digital control system, see Figure 3.

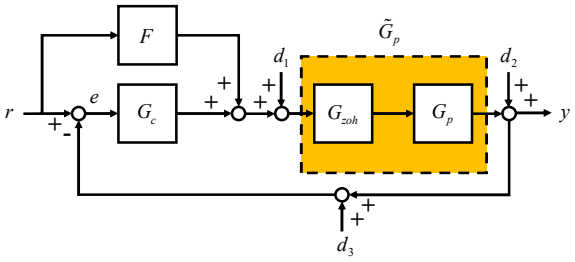

FIGURE 3. Control architecture of digital control system

The new equivalent plant model is

$$\begin{aligned} \tilde{G}_p(s) &= G_{zoh}(s)G_p(s) \\ &= \frac{1-e^{-Ts}}{Ts}G_p(s) \end{aligned} \tag{17}$$

T is the servo circle of the control system. The Taylor expansion of $G_{zoh}(s)$ is

$$G_{zoh}(s)=1-\frac{Ts}{2}+\frac{(Ts)^2}{6}-\frac{(Ts)^3}{24}+o\left((Ts)^3\right) \tag{18}$$

It can be proved that this series is convergent when $Ts\to 0$, which is usually satisfied. The change of plant model due to zero-order holder effect will not influence the approximation of sensitivity function but the shape of residual tracking error.

When a controller with finite DC gain is used as feedback controller and zero-order holder effect is considered, the residual tracking error with a well-tuned acceleration feedforward in equation (10) becomes

$$\begin{aligned} e &\cong \frac{m_t s^2}{G_c(0)}\left(\frac{Ts}{2}-\sum_{i=1}^{N}\frac{d_i s^2}{\left(s^2+2\zeta_i\omega_i s+\omega_i^2\right)}-\frac{T^2 s^2}{6}\right)r \\ &\cong \frac{m_t T}{2G_c(0)}\dddot{r}+\frac{m_t}{G_c(0)}\left(-\sum_{i=1}^{N}\frac{d_i}{\omega_i^2}-\frac{T^2}{6}\right)\ddddot{r} \end{aligned} \tag{19}$$

It shows that the residual tracking error is mainly composed of jerk and snap term, requiring a third order term in feedforward controller which is not needed in continuous domain. The relative magnitude between the two terms depends on plant model, servo circle, and frequency components of trajectory. If jerk term overpowers snap term, then the residual tracking error is approximately proportional to jerk of trajectory rather than snap, and if the feedback controller has an integrator, the residual tracking error is approximately

Table 1. The shape of residual tracking error under different DC gains of feedback controller and feedforward structures, acc means that the residual error has the shape of acceleration of reference trajectory, similar meaning goes for jerk, snap and so on.

	finite DC gain		infinite DC gain	
	continuous domain	discrete domain	continuous domain	discrete domain
untuned acceleration feedforward	acc	acc	jerk	jerk
tuned acceleration feedforward	snap	jerk	derivative of snap	snap
tuned jerk feedforward		snap		derivative of snap

proportional to snap rather than fifth order derivative. Tuning algorithm for jerk term in feedforward controller is similar with that of acceleration feedforward term.

The shapes of residual tracking error under different conditions are summarized in Table 1.

EXPERIMENT

Experiment is carried on the wafer stage showed in FIGURE 4. The stage consists of a long-stroke stage and a short-stroke stage. The long-stroke stage is used for long-stroke motion while the short-stroke stage on it is used for ultra-precision motion. Both stages are magnetic-levitated. The servo circle of this system is $200\mu s$.

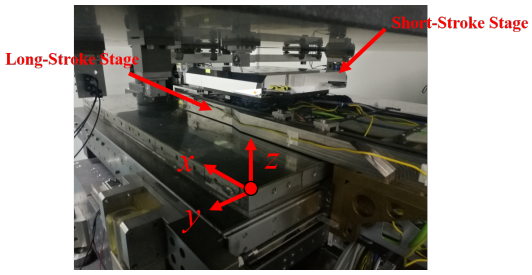

FIGURE 4. Wafer stage, the stage consists of a long-stroke stage and a short-stroke stage.

The long-stroke stage and short-stroke stage both have six degrees of freedom, all of which must be controlled. Experiment is carried on x axis. Data in this paper is from short-stroke stage which is measured by laser interferometer. Instead of lead controller and PID controller used in theoretical analysis, a double lead controller is used as feedback controller with finite DC gain

$$G_c(s) = K\left(\frac{s+z_1}{s+p_1}\right)^2 \qquad (20)$$

A PI plus double lead controller (a PI controller combined with a double lead controller) is used as feedback controller with infinite DC gain.

$$G_c(s) = K\frac{s+z_0}{s}\left(\frac{s+z_1}{s+p_1}\right)^2 \qquad (21)$$

The controller bandwidth (cross over frequency of open loop transfer function) of both controllers is 240Hz. The controllers are designed according to model from system identification, see Figure 5. Detailed controller parameters are listed in Table 2 and Table 3.

TABLE 2. The controller parameters of double lead controller.

K	z_1	p_1
8.0896	757.9	5889

TABLE 3. The controller parameters of PI plus double lead controller.

K	z_0	z_1	p_1
11.981	455.9	872	7659

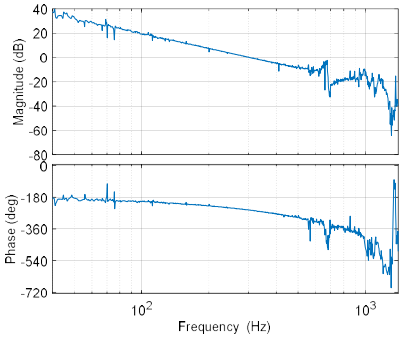

FIGURE 5. Closed-loop system identification of x axis.

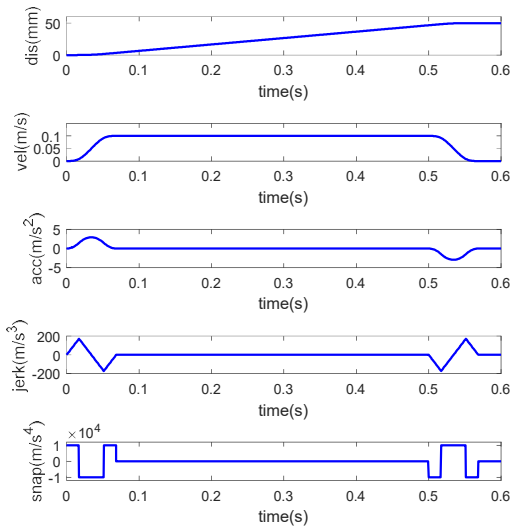

FIGURE 6. Trajectory used in experiment, dis stands for displacement, vel stands for velocity, and acc stands for acceleration.

Fourth order trajectory in Figure 6 is used in experiment. Figure 7 gives the tracking performance when acceleration feedforward coefficient is not tuned. As theoretical analysis predicted, the tracking error during acceleration or deceleration phase is approximately proportional to acceleration of reference trajectory when DC gain of feedback controller is finite (Figure 7(a)), to jerk of reference trajectory when DC gain of feedback controller is infinite (Figure 7(b)). Figure 7 also shows that settling time is still long if feedforward controller is not well tuned.

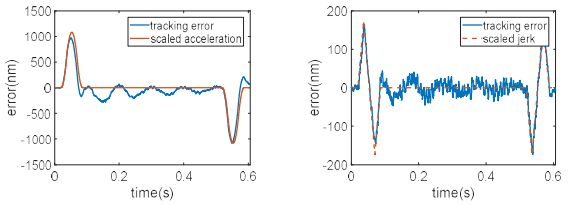

FIGURE 7. (a) tracking error with untuned acceleration feedforward when the DC gain of feedback controller is finite. (b) tracking error with untuned acceleration feedforward when the DC gain of feedback controller is infinite.

Feedforward coefficient can be easily tuned with equation (8) or (9). Figure 8 gives the tracking performance with well-tuned acceleration feedforward. As theoretical analysis predicted, with well-tuned acceleration feedforward in discrete domain, the residual error during acceleration or deceleration phase is approximately proportional to jerk rather than snap of reference trajectory when DC gain of feedback controller is finite (Figure 8(a)), to snap rather than derivative of snap of reference trajectory when DC gain of feedback controller is infinite (Figure 8(b)).

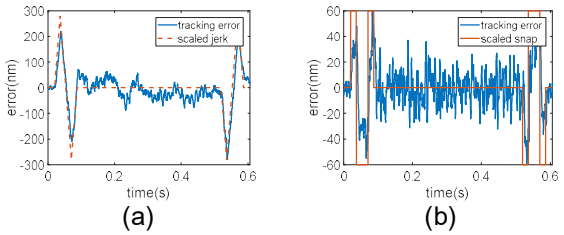

FIGURE 8. (a) tracking error with tuned acceleration feedforward when the DC gain of feedback controller is finite. (b) tracking error with tuned acceleration feedforward when the DC gain of feedback controller is infinite.

Figure 9 gives the tracking performance with tuned acceleration and jerk feedforward. Due to external disturbance, steady state error exists if feedback controller does not contain integral part (Figure 9(a)). Figure 9(a) and Figure 9(b) both show that tracking error during acceleration or deceleration phase has been greatly reduced and zero settling time has been attained. Snap feedforward may be required if more aggressive trajectory is taken.

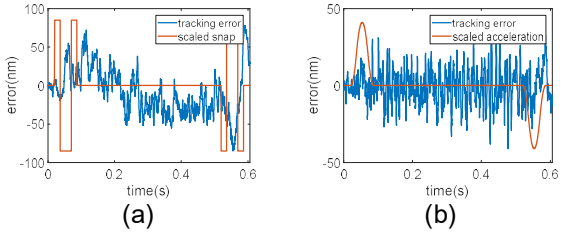

FIGURE 9. (a) tracking error with tuned acceleration and jerk feedforward when the DC gain of feedback controller is finite. (b) tracking error with tuned acceleration and jerk feedforward when the DC gain of feedback controller is infinite.

CONCLUSION

For multi-mass system, the shape of tracking error during acceleration or deceleration phase is influenced by feedback controller, feedforward

controller, reference trajectory and its derivatives. In continuous domain, if acceleration feedforward is not well-tuned, tracking error is approximately proportional to acceleration of trajectory for feedback controller with finite DC gain, to the jerk of trajectory for feedback controller with infinite DC gain. Once acceleration feedforward is well-tuned, the residual tracking error is approximately proportional to the snap of trajectory for feedback controller with finite DC gain, to the derivative of snap for feedback controller with infinite DC gain (if only one integrator is contained). For digital control systems, extra tracking error will occur due to zero-order holder effect, which makes the residual tracking error with well-tuned acceleration feedforward proportional to jerk of trajectory rather than snap when DC gain of feedback controller is finite, to snap rather than derivative of snap when DC gain of feedback controller is infinite. And this error term can be compensated by jerk feedforward. Based on these results, a simple but effective feedforward tuning method is proposed and validated by experiment.

REFERENCES

[1] Heertjes, M., Hennekens, D., & Steinbuch, M. (2010). MIMO feed-forward design in wafer scanners using a gradient approximation-based algorithm. Control Engineering Practice, 18(5), 495-506.

[2] Butler, H. (2013). Adaptive feedforward for a wafer stage in a lithographic tool. IEEE Transactions on Control Systems Technology, 21(3), 875-881.

[3] Lambrechts, P., Boerlage, M., & Steinbuch, M. (2005). Trajectory planning and feedforward design for electromechanical motion systems. Control Engineering Practice, 13(2), 145-157.

[4] Li, M., Zhu, Y., Yang, K., Hu, C., & Mu, H. (2017). An integrated model-data-based zero-phase error tracking feedforward control strategy with application to an ultraprecision wafer stage. IEEE Transactions on Industrial Electronics, 64(5), 4139-4149.

[5] Boeren, F., Oomen, T., & Steinbuch, M. (2015). Iterative motion feedforward tuning: A data-driven approach based on instrumental variable identification. Control Engineering Practice, 37, 11-19.

[6] Boeren, F., Bruijnen, D., van Dijk, N., & Oomen, T. (2014). Joint input shaping and feedforward for point-to-point motion: Automated tuning for an industrial nanopositioning system. Mechatronics, 24(6), 572-581.

[7] Heertjes, M., & Bruijnen, D. (2014, June). MIMO FIR feedforward design for zero error tracking control. In American Control Conference (ACC), 2014 (pp. 2166-2171). IEEE.

[8] Miu, D. K. (2012). Mechatronics: electromechanics and contromechanics. Springer Science & Business Media.

[9] Butler, H. (2011). Position control in lithographic equipment [applications of control]. IEEE Control Systems, 31(5), 28-47.

[10] Iwasaki, M., Seki, K., & Maeda, Y. (2012). High-precision motion control techniques: A promising approach to improving motion performance. IEEE Industrial Electronics Magazine, 6(1), 32-40.

MULTI-AXIS TRAJECTORY GENERATION WITH OPTIMAL FREQUENCY SPECTRUM FOR VIBRATION AVOIDANCE

Alper Dumanli, Burak Sencer
School of Mechanical, Industrial and Manufacturing Engineering
Oregon State University
Corvallis, Oregon, USA

INTRODUCTION

This paper presents a novel spline trajectory generation technique for precision machine tools and industrial manipulators. A major source of vibrations in production equipment is inertial vibrations that are induced due to the frequency content of reference motion commands, i.e. reference trajectory. Modern motion planners generate smooth reference commands based on jerk or snap limited acceleration profiles [1]. The time derivative of acceleration, e.g. jerk, is considered to be the key parameter that controls smoothness of acceleration profile and thereby influences level of excitation. Industrial robotic systems rely on minimum jerk [2] trajectories for vibration mitigation. In precision manufacturing, structural resonances of equipment are known, and hence the objective is to attenuate frequency content of motion commands at around resonances. This can be achieved through filtering in the form of input shaping [3]. However, post-filtering introduces phase delay and distorts reference trajectory, which in return causes large contouring errors in multi-axis contouring. This paper introduces a "direct spline trajectory generation" technique with a frequency optimized acceleration profile [4] to avoid exciting residual vibrations along 2D spline trajectories. Reference acceleration profile is generated by solving an optimization problem that minimizes motion command's frequency spectrum in a desired band. Effectiveness of the proposed trajectory generation scheme is evaluated by experimental comparison against minimum jerk trajectories.

FREQUENCY OPTIMAL 2D CONTOURING

Trajectories used in precision manufacturing applications consist of a sequence of reference points that are generated by linear, circular or parametric spine interpolation [1]. Fig. 1 shows a typical 2D toolpath generated by quintic spline interpolation [5] passing through *M+1* waypoints/knots. The displacement profiles of *x* and *y* axes for n^{th} segment are defined as 5^{th} order polynomials of s_n:

$$\left.\begin{aligned} x_n(s_n) &= x(s_n) = \sum_{i=0}^{5} \alpha_i s_n^i \\ y_n(s_n) &= y(s_n) = \sum_{i=0}^{5} \beta_i s_n^i \end{aligned}\right\} \quad (1)$$

where $s_n=s_n(kT_s)$ is the sampled displacement, i.e. arc length. Here the displacement profile is defined as 11^{th} order polynomial function of time $t=kT_s$:

$$s(kTs) = a_{11}s(kT_s)^{11} + a_{10}s(kT_s)^{10} + \cdots + a_0 \quad (2)$$

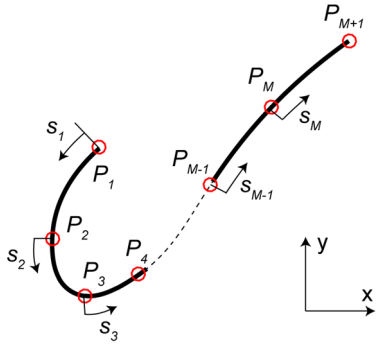

FIGURE 1. A Typical Spline Toolpath.

The axis acceleration profiles, i.e. d^2x/dt^2 and d^2y/dt^2, determine excitation forces delivered to the motion system and can derived through chain rule from equations (1) and (2) as:

$$\left.\begin{aligned} \ddot{x} &= \frac{d^2x}{dt^2} = \frac{d^2x}{ds^2}\left(\frac{ds}{dt}\right)^2 + \frac{dx}{ds}\frac{d^2s}{dt^2} = x''\dot{s}^2 + x'\ddot{s} \\ \ddot{y} &= \frac{d^2y}{dt^2} = \frac{d^2y}{ds^2}\left(\frac{ds}{dt}\right)^2 + \frac{dy}{ds}\frac{d^2s}{dt^2} = y''\dot{s}^2 + y'\ddot{s} \end{aligned}\right\} \quad (3)$$

The objective is to control the frequency spectrum of axis acceleration profiles by modulating the displacement and velocity profiles along the spline geometry. This can be achieved by finding parameters of the optimal displacement profile $\theta=[a_0, a_1, \ldots a_{11}]^T$, which minimizes the Discrete Fourier Transform (DFT) of axis accelerations within a predetermined $\omega\in[\omega_1,\omega_2]$ frequency band. The cost function for this problem can be postulated by taking DFT of axis acceleration profiles from Eq. (3) as follows:

$$J=\sum_{n=0}^{N}\left\{\left|\sum_{k=0}^{K}\ddot{x}(kT_s)e^{-j(\omega_1+n\Delta\omega)kT_s}\right|^2+\left|\sum_{k=0}^{K}\ddot{y}(kT_s)e^{-j(\omega_1+n\Delta\omega)kT_s}\right|^2\right\} \quad (4)$$

where $\omega_2=\omega_1+N\Delta\omega$, N determines the frequency discretization resolution and K is the number of total time samples in the trajectory.

LINEARIZATION OF THE OPTIMIZATION PROBLEM

Notice that the cost function given in Eq. (4) is non-linear due to the fact that x and y axis acceleration profiles are non-linear functions of tangential motion profile $\dot{s}$, $\ddot{s}$ and the geometric derivatives of the path x', x'', y' and y'' (see Eq. (3)). Although this problem can be solved using computationally expensive non-linear optimization techniques, the following presents an effective technique to determine the tangential motion profile.

We assume that an original tangential motion trajectory is already planned for this path. For instance, a minimum jerk path planning technique widely used in robotics literature, e.g. [6] and [7], may be used to plan a smooth trajectory for this path. This path is then used as a template to implement the following linearization techniques and hence final reference axis acceleration commands exhibit desired frequency characteristics.

Firstly, we start with the linearization of $\dot{s}^2$ which controls axis accelerations from Eq. (3). Using a simple 1st order Taylor series expansion around a point $\dot{s}(t=kT_s)=\dot{s}_T(kT_s)$,where $\dot{s}_T$ denotes the template feed profile, $\dot{s}^2$ can be expressed as

$$\dot{s}^2\cong(\dot{s}_T)^2+2(\dot{s}_T)(\dot{s}-(\dot{s}_T)) \quad (5)$$

Next, the geometric derivatives need to be evaluated at each time sample. Similarly, those geometric derivatives are also borrowed from template trajectory as:

$$\left.\begin{aligned}x'(kT_s)&\cong x'_T(kT_s)=x'(s_T(kT_s))\\x''(kT_s)&\cong x''_T(kT_s)=x''(s_T(kT_s))\\y'(kT_s)&\cong y'_T(kT_s)=y'(s_T(kT_s))\\y''(kT_s)&\cong y''_T(kT_s)=y''(s_T(kT_s))\end{aligned}\right\} \quad (6)$$

where x'_T, x_T'', y'_T and y_T'' denote geometric derivatives evaluated from the template trajectory. Illustration of the described approximation approach is given in Fig. 2.

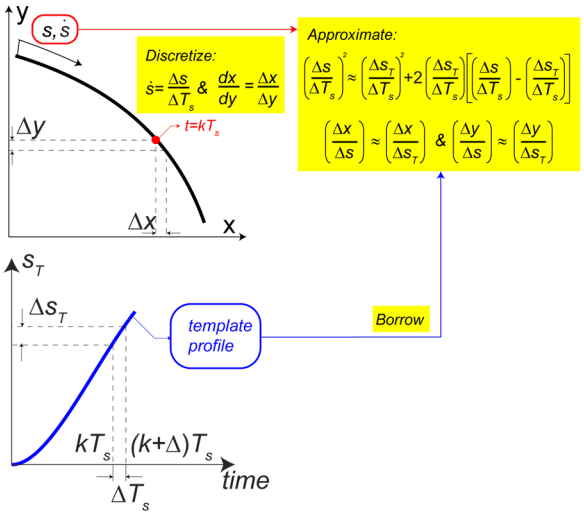

FIGURE 2: Approximation of nonlinear terms.

Substituting Eqs. (5) and (6) into Eq. (3), axis accelerations at k^{th} sample can be approximated;

$$\left.\begin{aligned}\ddot{x}(t=kT_s)&\cong x''_J\left(\dot{s}_J^2+2\dot{s}_J(\dot{s}-\dot{s}_J)\right)+x'_J\ddot{s}\big|_{t=kT_s}\\\ddot{y}(t=kT_s)&\cong y''_J\left(\dot{s}_J^2+2\dot{s}_J(\dot{s}-\dot{s}_J)\right)+y'_J\ddot{s}\big|_{t=kT_s}\end{aligned}\right\} \quad (7)$$

Finally, considering the entire trajectory consisting of M samples, Eq. (7) can be put in a vector form for mathematical convenience;

$$\left.\begin{aligned}\begin{bmatrix}\ddot{x}(0T_s)\\\ddot{x}(T_s)\\\vdots\\\ddot{x}(KT_s)\end{bmatrix}&=\left(2\boldsymbol{J_{X1}M_1}+\boldsymbol{J_{X2}M_2}\right)\underbrace{\begin{bmatrix}a_0\\a_1\\\vdots\\a_{11}\end{bmatrix}}_{\theta}-\boldsymbol{J_{X3}}\\\begin{bmatrix}\ddot{y}(0T_s)\\\ddot{y}(T_s)\\\vdots\\\ddot{y}(KT_s)\end{bmatrix}&=\left(2\boldsymbol{J_{Y1}M_1}+\boldsymbol{J_{Y2}M_2}\right)\underbrace{\begin{bmatrix}a_0\\a_1\\\vdots\\a_{11}\end{bmatrix}}_{\theta}-\boldsymbol{J_{Y3}}\end{aligned}\right\} \quad (8)$$

where

$$\boldsymbol{M_1}=\begin{bmatrix}0&1&2(0T_s)&\cdots&11(0T_s)^{10}\\0&1&2(T_s)&\cdots&11(T_s)^{10}\\\vdots&\vdots&\vdots&\ddots&\vdots\\0&1&2(KT_s)&\cdots&11(KT_s)^{10}\end{bmatrix}$$

$$\boldsymbol{M_2}=\begin{bmatrix}0&0&2&\cdots&110(0T_s)^{9}\\0&0&2&\cdots&110(T_s)^{9}\\\vdots&\vdots&\vdots&\ddots&\vdots\\0&0&2&\cdots&110(KT_s)^{9}\end{bmatrix}$$

$$\boldsymbol{J_{X1}}=diag\left\{x''_T(0T_s)\dot{s}_T(0T_s),\ldots,x''_T(KT_s)\dot{s}_T(KT_s)\right\}$$

$$\boldsymbol{J_{X2}}=diag\left\{x'_T(0T_s),\ldots,x'_T(KT_s)\right\}$$

$$\boldsymbol{J_{X3}}=diag\left\{x''_T(0T_s)\dot{s}_T^2(0T_s),\ldots,x''_T(KT_s)\dot{s}_T^2(KT_s)\right\}$$

$$\boldsymbol{J_{Y1}} = diag\left\{ y_T^{''}(0T_s)\dot{s}_T(0T_s), \ldots, y_T^{''}(KT_s)\dot{s}_T(KT_s) \right\}$$

$$\boldsymbol{J_{Y2}} = diag\left\{ y_T^{'}(0T_s), \ldots, y_T^{'}(KT_s) \right\}$$

$$\boldsymbol{J_{Y3}} = diag\left\{ y_T^{''}(0T_s)\dot{s}_T^2(0T_s), \ldots, y_T^{''}(KT_s)\dot{s}_T^2(KT_s) \right\}$$

are constant matrices. Using above linearized expressions for sampled accelerations $x(kT_s)$ and $y(kT_s)$, cost function J can be put in the following quadratic form

$$J = \underbrace{\left\| \begin{bmatrix} \boldsymbol{F}\left(2\boldsymbol{J_{X1}}\boldsymbol{M_1} + \boldsymbol{J_{X2}}\boldsymbol{M_2}\right) \\ \boldsymbol{F}\left(2\boldsymbol{J_{Y1}}\boldsymbol{M_1} + \boldsymbol{J_{Y2}}\boldsymbol{M_2}\right) \end{bmatrix}\theta - \begin{bmatrix} \boldsymbol{F}\boldsymbol{J_{X3}} \\ \boldsymbol{F}\boldsymbol{J_{Y3}} \end{bmatrix} \right\|^2}_{|\boldsymbol{A}\theta - \boldsymbol{b}|^2} \quad (9)$$

where

$$\boldsymbol{F} = \begin{bmatrix} e^{-j(\omega_1)0T_s} & e^{-j(\omega_1)T_s} & \cdots & e^{-j(\omega_1)KT_s} \\ e^{-j(\omega_1+\Delta\omega)0T_s} & e^{-j(\omega_1+\Delta\omega)T_s} & \cdots & e^{-j(\omega_1+\Delta\omega)KT_s} \\ \vdots & \vdots & \ddots & \vdots \\ e^{-j(\omega_1+N\Delta\omega)0T_s} & e^{-j(\omega_1+N\Delta\omega)T_s} & \cdots & e^{-j(\omega_1+N\Delta\omega)KT_s} \end{bmatrix}$$

Eq. (9) can be minimized in the sense of linear least squares to obtain the optimal trajectory parameters $\theta=[a_0, a_1, \ldots a_{11}]^T$.

Furthermore, kinematic boundary conditions such as initial and final position, velocity and acceleration constraints can also be imposed to further control the trajectory. They can be written in linear matrix form as:

$$\underbrace{\begin{bmatrix} 1 & (0T_s) & (0T_s)^2 & \cdots & (0T_s)^{11} \\ 0 & 1 & 2(0T_s) & \cdots & 11(0T_s)^{10} \\ 0 & 0 & 2 & \cdots & 110(0T_s)^9 \\ 1 & (KT_s) & (KT_s)^2 & \cdots & (KT_s)^{11} \\ 0 & 1 & 2(KT_s) & \cdots & 11(KT_s)^{10} \\ 0 & 0 & 2 & \cdots & 110(KT_s)^9 \end{bmatrix}}_{\boldsymbol{L}} \underbrace{\begin{bmatrix} a_0 \\ a_1 \\ \vdots \\ a_{11} \end{bmatrix}}_{\theta} = \underbrace{\begin{bmatrix} s_{init} \\ \dot{s}_{init} \\ \ddot{s}_{init} \\ s_{final} \\ \dot{s}_{final} \\ \ddot{s}_{final} \end{bmatrix}}_{\zeta} \quad (10)$$

and the final formal optimization problem is postulated as

$$\min_{\theta} J = \left|\boldsymbol{A}\theta - \boldsymbol{b}\right|^2, \; s.t.: \boldsymbol{L}\theta = \zeta \quad (11)$$

Converting (11) into an unconstrained optimization problem with the help of Lagrange Multipliers yields

$$\min_{\theta,\Lambda} J' = \left(\boldsymbol{A}\theta - \boldsymbol{b}\right)^{\dagger}\left(\boldsymbol{A}\theta - \boldsymbol{b}\right) + \Lambda\left(\boldsymbol{L}\theta - \zeta\right) \quad (12)$$

where Λ denotes the vector of Lagrange Multipliers and $(\boldsymbol{A}\theta-\boldsymbol{b})^{\dagger}$ indicates Hermitian Transpose of $(\boldsymbol{A}\theta-\boldsymbol{b})$. Analytical solution to the quadratic programming (QP) problem given in (12) is obtained as

$$\begin{bmatrix} \theta \\ \Lambda \end{bmatrix} = \begin{bmatrix} re\left(\boldsymbol{A}^{\dagger}\boldsymbol{A}\right) & \boldsymbol{L}^T \\ \boldsymbol{L} & \boldsymbol{0} \end{bmatrix}^{-1} \begin{bmatrix} \boldsymbol{A}^{\dagger}\boldsymbol{b} + \boldsymbol{A}^T\boldsymbol{b}^* \\ \zeta \end{bmatrix} \quad (13)$$

where $\boldsymbol{b}^*$ denotes the complex conjugate of $\boldsymbol{b}$.
Notice that the definition of the optimization problem so far has been for a single geometric spline segment. Since 2D toolpaths contain multiple spline segments, frequency spectrum of the total trajectory needs to be optimized through finding polynomial coefficients $[\theta_1, \theta_2, \ldots, \theta_M]$ of each displacement profile $[s_1, s_2, \ldots, s_M]$. In order to optimize the full/total trajectory, optimization problem depicted in (11) is expanded as

$$\min_{\theta} J_{full} = \left|\boldsymbol{A}_{full}\theta_{full} - \boldsymbol{b}_{full}\right|^2, \; s.t.: \boldsymbol{L}_{full}\theta_{full} = \zeta_{full} \quad (14)$$

where

$$\boldsymbol{A}_{full} = \begin{bmatrix} \boldsymbol{A}_1 & & & \boldsymbol{0} \\ & \boldsymbol{A}_2 & \ddots & \\ & & & \\ \boldsymbol{0} & & & \boldsymbol{A}_M \end{bmatrix}, \theta_{full} = \begin{bmatrix} \theta_1 \\ \theta_2 \\ \vdots \\ \theta_M \end{bmatrix}, \boldsymbol{b}_{full} = \begin{bmatrix} \boldsymbol{b}_1 \\ \boldsymbol{b}_2 \\ \vdots \\ \boldsymbol{b}_M \end{bmatrix}$$

$$\boldsymbol{L}_{full} = \begin{bmatrix} \boldsymbol{L}_{pos} \\ \boldsymbol{L}_{vel} \\ \boldsymbol{L}_{acc} \end{bmatrix}, \zeta_{full} = \begin{bmatrix} \begin{bmatrix} 0 & s_{1,final} & \cdots & 0 & \left(s_{M,final} - s_{M-1,final}\right) \end{bmatrix}^T \\ \begin{bmatrix} 0 & \cdots & 0 \end{bmatrix}^T \\ \begin{bmatrix} 0 & \cdots & 0 \end{bmatrix}^T \end{bmatrix}$$

and where $\boldsymbol{L}_{pos}$, $\boldsymbol{L}_{vel}$ and $\boldsymbol{L}_{acc}$ denote position, velocity and acceleration continuity constraint matrices respectively as

$$\boldsymbol{L}_{pos} = \begin{bmatrix} \begin{bmatrix} (0T_s)^0 & (K_1T_s)^0 \\ \vdots & \vdots \\ (0T_s)^{11} & (K_1T_s)^{11} \end{bmatrix}^T & & \boldsymbol{0} \\ & \ddots & \\ \boldsymbol{0} & & \begin{bmatrix} (0T_s)^0 & (K_MT_s)^0 \\ \vdots & \vdots \\ (0T_s)^{11} & (K_MT_s)^{11} \end{bmatrix}^T \end{bmatrix}$$

$$\boldsymbol{L}_{vel} = \begin{bmatrix} \begin{bmatrix} 0 & \cdots & 11(0T_s)^{10} \end{bmatrix}^T & & \boldsymbol{0} \\ & \boldsymbol{L}_{vel,cont} & \\ \boldsymbol{0} & & \begin{bmatrix} 0 & \cdots & 11(K_MT_s)^{10} \end{bmatrix}^T \end{bmatrix}$$

$$\boldsymbol{L}_{vel,cont} = \begin{bmatrix} \begin{bmatrix} \begin{bmatrix} 0 & \cdots & 11(K_1T_s)^{10} \end{bmatrix}^T \\ -\begin{bmatrix} 0 & \cdots & 11(0T_s)^{10} \end{bmatrix}^T \end{bmatrix}^T & & \boldsymbol{0} \\ & \ddots & \\ \boldsymbol{0} & & \begin{bmatrix} \begin{bmatrix} 0 & \cdots & 11(K_{M-1}T_s)^{10} \end{bmatrix}^T \\ -\begin{bmatrix} 0 & \cdots & 11(0T_s)^{10} \end{bmatrix}^T \end{bmatrix}^T \end{bmatrix}$$

$$\boldsymbol{L}_{acc} = \begin{bmatrix} \begin{bmatrix} 0 & \cdots & 110(0T_s)^9 \end{bmatrix}^T & & \boldsymbol{0} \\ & \boldsymbol{L}_{acc,cont} & \\ \boldsymbol{0} & & \begin{bmatrix} 0 & \cdots & 110(K_MT_s)^9 \end{bmatrix}^T \end{bmatrix}$$

$$\boldsymbol{L}_{acc,cont} = \begin{bmatrix} \begin{bmatrix} \begin{bmatrix} 0 & \cdots & 110(K_1T_s)^9 \end{bmatrix}^T \\ -\begin{bmatrix} 0 & \cdots & 110(0T_s)^9 \end{bmatrix}^T \end{bmatrix}^T & & \boldsymbol{0} \\ & \ddots & \\ \boldsymbol{0} & & \begin{bmatrix} \begin{bmatrix} 0 & \cdots & 110(K_{M-1}T_s)^9 \end{bmatrix}^T \\ -\begin{bmatrix} 0 & \cdots & 110(0T_s)^9 \end{bmatrix}^T \end{bmatrix}^T \end{bmatrix}$$

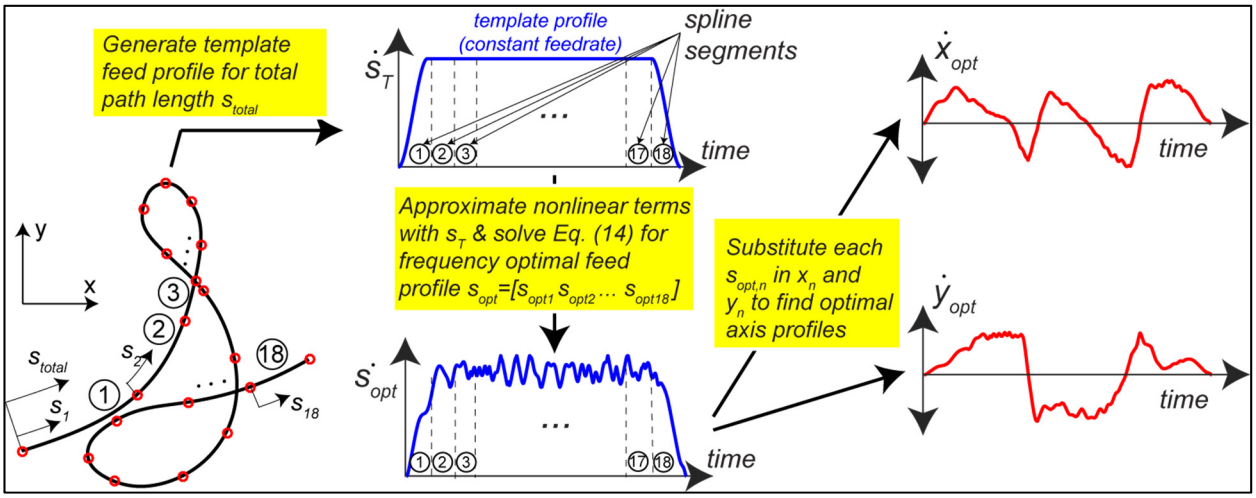

FIGURE 3: Trajectory Generation Strategy

Notice that the time required to travel along each spline segment is different where n^{th} spline segment has a duration of K_nT_s. Similar to the formulation given in (13), optimal displacement profile parameters for the full trajectory θ_{full} can be found analytically as

$$\begin{bmatrix}\theta_{full}\\ \Lambda_{full}\end{bmatrix}=\begin{bmatrix}re\left(\boldsymbol{A}_{full}^{H}\boldsymbol{A}_{full}\right) & \boldsymbol{L}_{full}^{T}\\ \boldsymbol{L}_{full} & \boldsymbol{0}\end{bmatrix}^{-1}\begin{bmatrix}\boldsymbol{A}_{full}^{H}\boldsymbol{b}_{full}+\boldsymbol{A}_{full}^{T}\boldsymbol{b}_{full}^{*}\\ \zeta_{full}\end{bmatrix} \quad (15)$$

Note that, acceleration and jerk limits along long moves can be incorporated as inequality constraints, which requires sequential quadratic programming (SQP) to be applied.

EXPERIMENTAL SETUP AND RESULTS

Proposed scheme allows direct generation of reference motion trajectories with frequency optimal acceleration profiles eliminating the need for post filtering. Solution procedure benefits from well-structured analytical expressions, which makes it suitable for real-time implementation on modern NC systems.

Fig. 3 presents the overall strategy to implement the proposed frequency optimal interpolation scheme on 2D spline tool-paths. In this experiment, the spline geometry shown in Fig. 4 is interpolated at constant speed and also based on the proposed technique. The path speed (feedrate) is set to 120 [mm/sec], and tangential acceleration is limited to 750 [mm/sec^2].

In order to demonstrate the effectiveness of the proposed technique, the planar motion platform shown in Fig. 5 is equipped with flexible beams with resonances in X and Y directions at *~8.4* and *~8* [Hz] respectively. In order to avoid exciting those resonances the attenuation band of the trajectory is set to $\omega\in[7.5,8.5]$ [Hz].

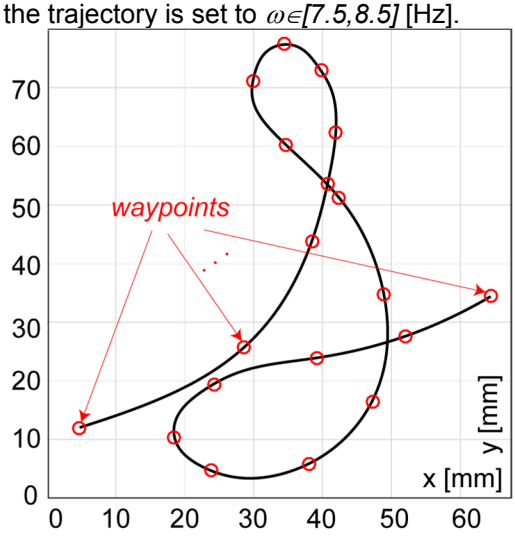

FIGURE 4: Geometric Path.

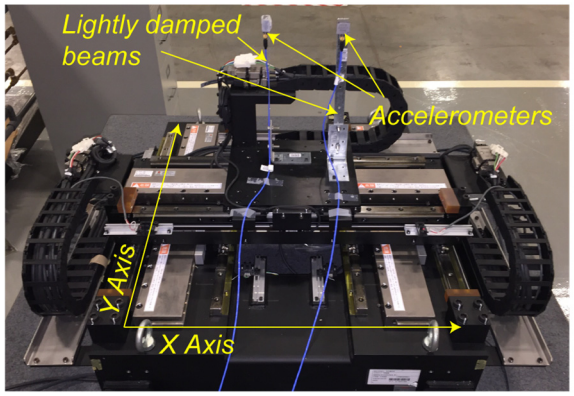

FIGURE 5: Experimental Setup.

Fig. 6 shows the original tangential motion profile and x and y axis motion commands. In comparison, Fig. 7 shows the trajectory

kinematics based on the proposed technique. As shown, the kinematic profiles fluctuate to attenuate the frequency spectrum in the desired band.

The frequency content of generated acceleration profiles is examined by taking DFTs of each acceleration profile shown in Fig. 8. As shown, proposed interpolation scheme can command reference motion with significantly attenuated frequency energy in a set band to effectively mitigate residual vibrations along 2D tool-paths. This eliminates the need for any post-filtering such as notch-ing or input shaping. The beams attached to the planar motion platform are equipped with PCB 3711B1130G accelerometers with a sensitivity of 6.8 [mV/(m/sec^2)]. Figures 9 and 10 show beam accelerations and their DFTs respectively for each axis. As seen, natural frequencies of the beams, which fall into attenuated frequency band, are significantly suppressed by the proposed trajectory generation method.

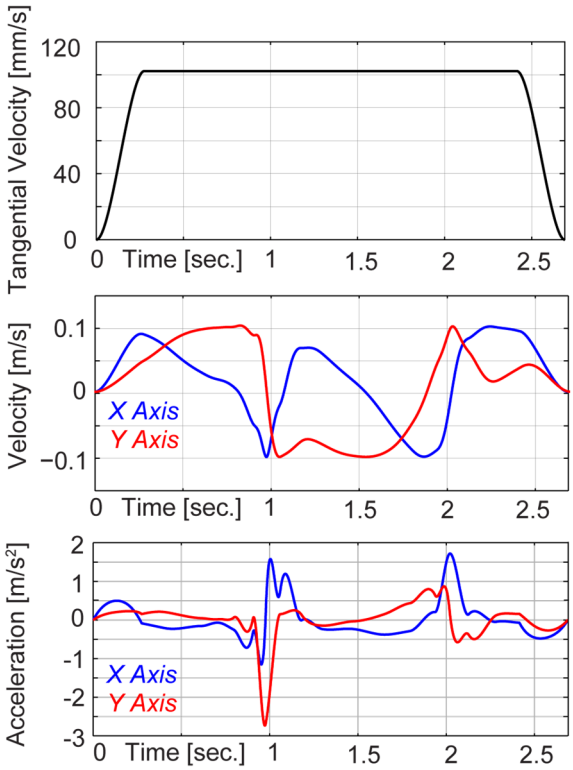

FIGURE 6: Kinematics of Template Trajectory.

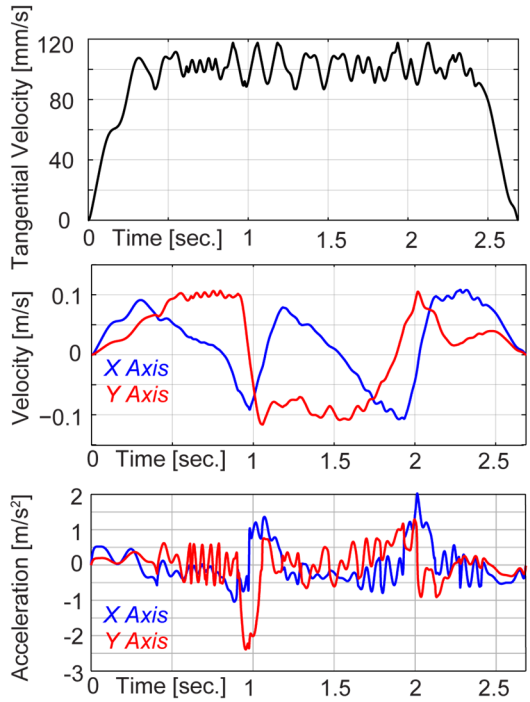

FIGURE 7: Kinematics of Proposed Trajectory.

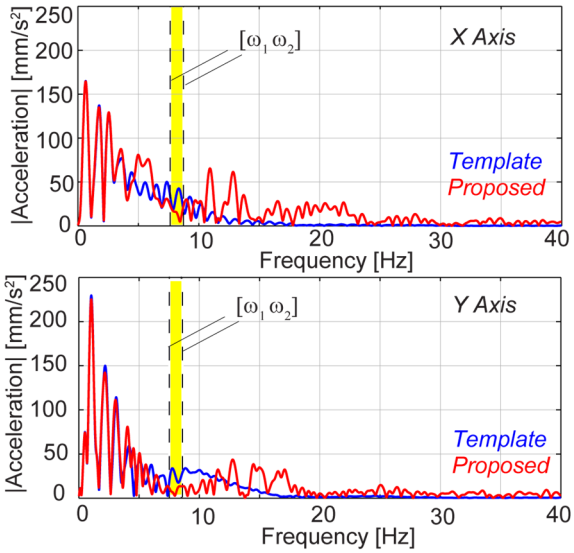

FIGURE 8: Frequency Spectrum of Acceleration Profiles.

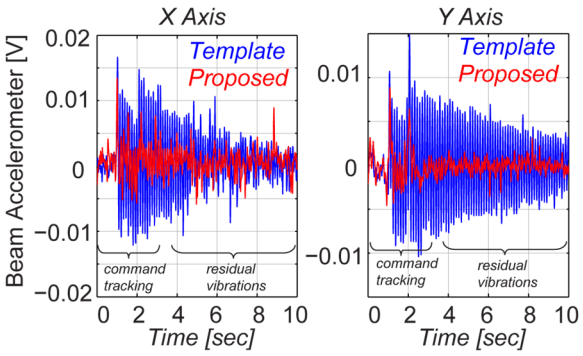

FIGURE 9: Beam Accelerations during Tracking Experiments.

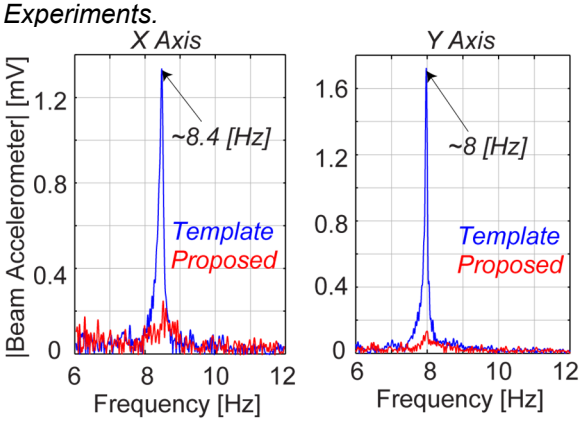

FIGURE 10: Frequency Spectrum of Beam Accelerations.

CONCLUSIONS

This paper presented a trajectory generation method for 2D to generate frequency optimal feed profiles along spline toolpaths. Proposed method generates a feed profile by solving an optimization problem where the frequency content of the resultant acceleration profiles of *x* and *y* axes is minimized. Experiments are carried out where the method is used to suppress natural frequencies of lightly damped beams attached to a planar motion platform and significant improvement compared to constant feedrate trajectories is observed.

REFERENCES

[1] Erkorkmaz, K. and Altintas, Y. High speed CNC system design. Part I: jerk limited trajectory generation and quintic spline interpolation. IMTM. 2001; 41(9): 1323-1345.

[2] Flash, T. and Hogan, N. The coordination of arm movements: an experimentally confirmed mathematical model. Journal of neuroscience. 1985; 5(7): 1688-1703.

[3] Singhose, W. and Singer, N.,. Initial investigations into the effects of input shaping on trajectory following. *ACC.* 1994; 3: 2526-2532.

[4] Sencer, B. and Tajima, S. Frequency Optimal Feed Motion Planning in Computer Numerical Controlled Machine Tools for Vibration Avoidance. Journal of Manufacturing Science and Engineering. 2017; 139(1): 011006.

[5] Wang F.-C., Wright P.K., Barsky B.A., Yang D.C.H. Approximately Arc-Length Parametrized C^3 Quintic Interpolatory Splines. Journal of Mechanical Design, Transactions of the ASME. 1999; 121(3): 430-439.

[6] Altintas Y., Erkorkmaz K.,. Feedrate optimization for spline interpolation in high speed machine tools. CIRP Annals-Manufacturing Technology. 2003; 52(1): 297-302.

[7] Chang B.-H., Hori Yoichi,. Trajectory Design Considering Derivative of Jerk for Head-Positioning of Disk Drive System With Mechanical Vibration. IEEE/ASME Transactions on Mechatronics. 2006 11(3): 273-279.

A LINEAR POSITIONING STAGE USING A THERMAL ACTUATOR

Chunjie Fan, Stuart T. Smith, Joshua Tarbutton
Center for Precision Metrology
The University of North Carolina at Charlotte
Charlotte, North Carolina, USA.

INTRODUCTION

A thermal actuator with 100 μm working range and 1000 N load has been designed and fabricated. The system uses a flexure based translation stage, steel frame, aluminum (or steel) tube, induction heater and optical displacement sensor. The thermal actuator uses induction heaters surrounding the aluminum tube with air flow through the tube center being used for heat removal. Addition of a spring loaded compression plate is used to apply loads to the stage of up to 1000 N. Figure 1 is a photograph of the prototype actuator, and Figure 2 shows the preload mechanism.

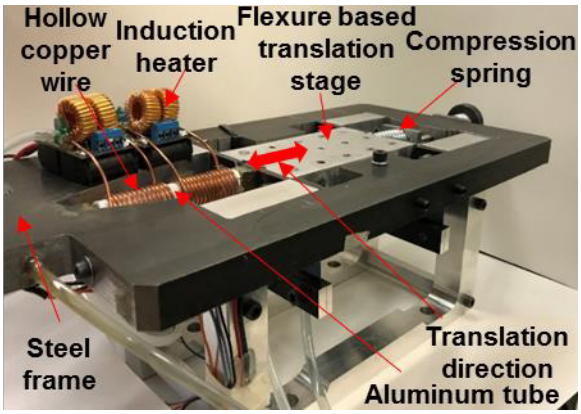

Figure 1: Prototype of thermally actuated flexure stage

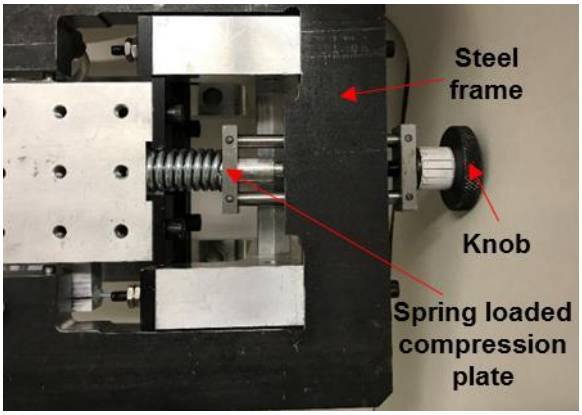

Figure 2: Preload compression spring

DETAIL EXPLANATION

A calibrated optical displacement sensor with the sensing element (mounted on the frame) and the knife (mounted on the stage) is used to measure the motion of the flexure based translation stage. The optical sensor gives a voltage output proportional to the displacement. Figure 3 shows the optical sensor and the knife that is attached to the underside of the moving platform.

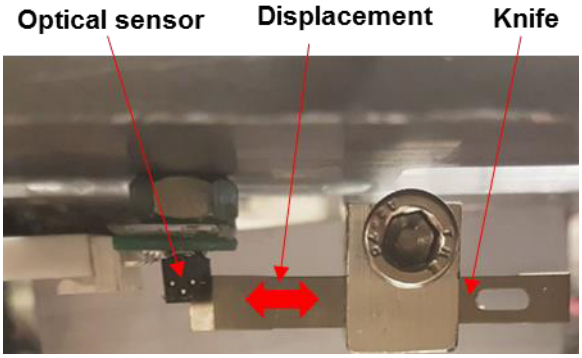

Figure 3: Calibrated optical knife-edge sensor and the knife

The induction heater generates an alternating current through the hollow copper wire. This current produces a rapid alternating magnetic field which penetrates into the aluminum tube and generates eddy currents that provide the heat to increase the temperature of the tube. Heat is removed using air flow through the center of the tube and controlled using a solenoid actuated pneumatic valve. The change in length of the tube with temperature generates the force to provide the linear motion of the stage that is, in turn, measured by the optical displacement sensor and used for feedback control. Hollow copper wire is used for the induction heater and a pump is used to drive cold water through the hollow wire. This can keep the temperature of the hollow copper windings below 20°C.

The actuation system of the thermal actuator is based on simultaneous heating and cooling to provide controlled motion. The heated actuator will transfer heat to the frame and the moving stage. To minimize thermal expansion of parts other than the actuator, the aluminum tube of the actuator is cooled at both ends using temperature controlled water. Figure 4 and Figure 5 show the details of the holes of the frame and moving platform through which the cooling water is pumped.

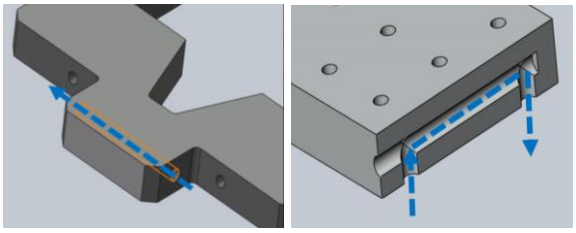

Figure 4 and 5: Channels for cooling water in the steel frame and the flexure stage

LabVIEW and an NI myRIO controller are used to control the source of electrical power to the induction heater and also measure the temperature and displacement. Figure 6 shows the locations of the two temperature sensors (located on the frame and the moving platform) that are in the proximity of the cooling channels in the frame and the platform. Temperature measurements are presented in the experiment section below.

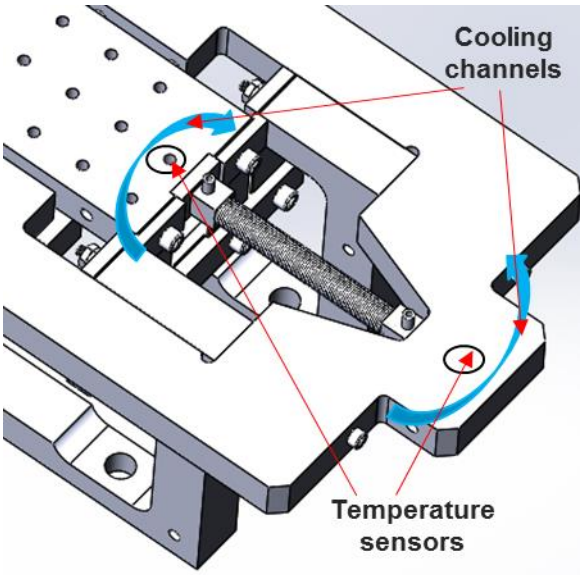

Figure 6: Temperature sensors location with the sensing elements beings mounted on the underside of the frame and the flexure stage

FEA SIMULATION

Since applied loads of up to 1000 N will be applied to the translation stage, it is necessary to know the stress and the deflection of the structural frame of the thermal actuator. SOLIDWORKS software is used for the finite element analysis and the results are shown in Figure 7 and Figure 8:

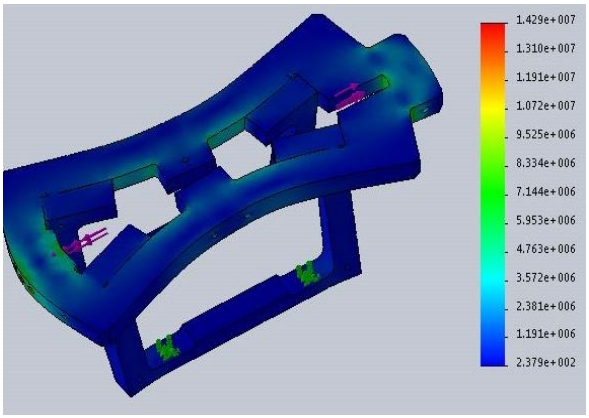

Figure 7: FEA Stress analysis of the structure of the thermal actuator frame

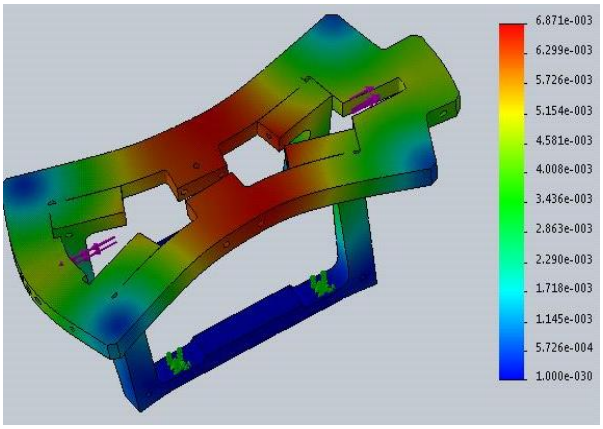

Figure 8: FEA Deflection analysis of the structure of the thermal actuator frame

Total deflection of the frame along the actuation axis is less than 3 μm which is small compared to maximum stroke of 100 μm.

CONTROL BLOCK DIAGRAM

To control motion of the stage, a myRIO sends PWM signals to the electrical power source of the induction heater. The measured voltage is fed to the myRIO through an external 16-bit analog to digital converter. The computer will transfer the voltage to displacement which will be compared with the desired value. Figure 9 shows the block diagram of the close loop control system.

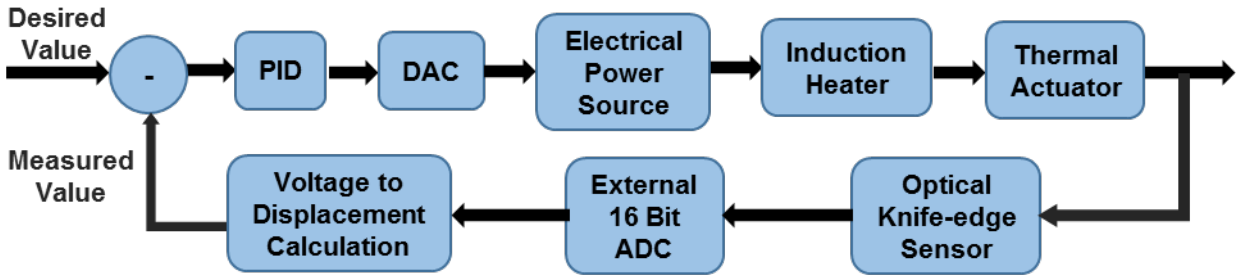

Figure 9: Control block diagram

EXPERIMENT

In the current study, the preload value is kept constant as the actuator is moved over a range of 100 μm. Preloads of 0 N, 500 N and 1000 N are tested and the measured responses are shown in Figure 11, through to Figure 19. The applied force is set by compressing the preload spring using the adjustment knob. Figure 10 shows how the preload force is applied to the flexure stage.

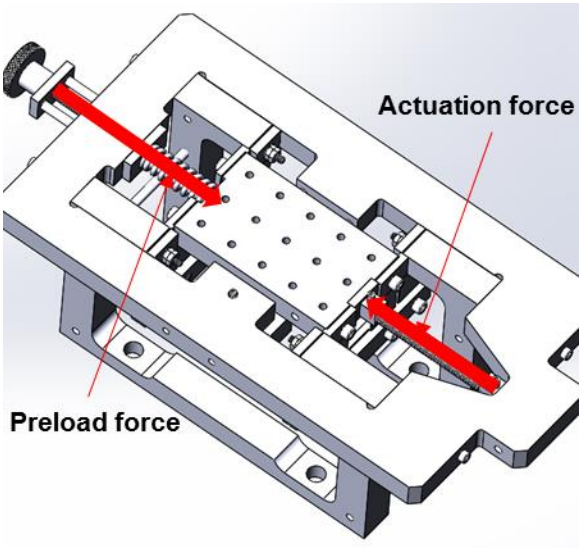

Figure 10: Applied force gives preload to the flexure stage

Initially the testing is carried out without any preload (0 N). Figure 11 shows a graph of the desired position and the measured position of the stage. Figure 12 and Figure 13 show the error and temperature variation during 20 μm positive and negative steps from 0-100-0 μm.

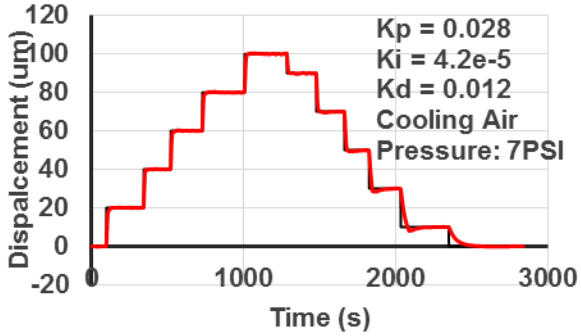

Figure 11: Displacement results under 0 N load. Desired value (black color), Measured value (red color)

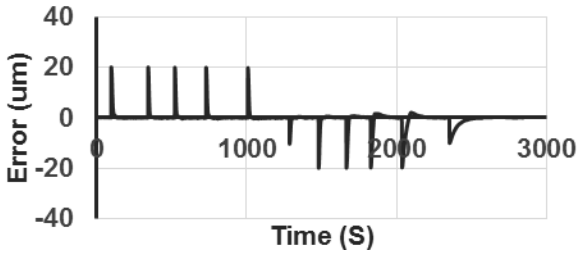

Figure 12: Error in the displacement under 0 N load

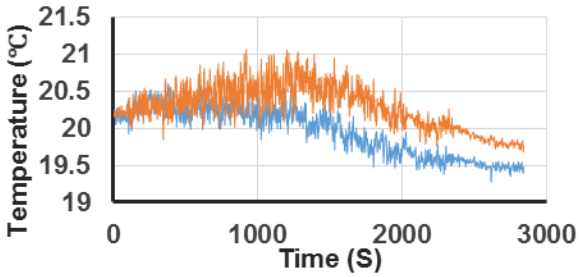

Figure 13: Variation in the moving platform and frame temperature under 0 N load during displacement. Frame temperature (orange color), Stage temperature (blue color)

The 20 µm step sequence is repeated for a preload of 500 N. Figures 14, 15 and 16 show the displacement, error and thermal variation results.

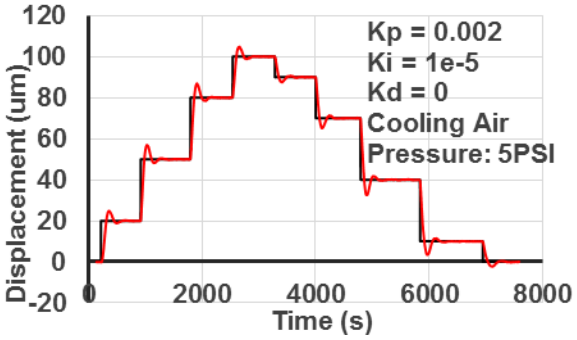

Figure 14: Displacement results under 500 N load. Desired value (black color), Measured value (red color)

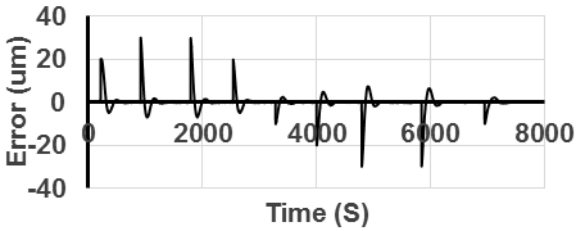

Figure 15: Error in the displacement under 500N load

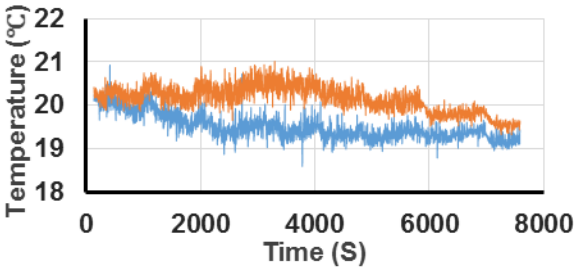

Figure 16: Variation in the moving platform and frame temperature under 500 N load during displacement. Frame temperature (orange color), Stage temperature (blue color)

For the 500 N preload, only PI control is used to control the motion. Air cooling is activated when the error is negative. The actuation response shows a small overshoot in Figure 14. After stepping, the steady state error settles to ±0.3 µm. The response time of the thermal actuator, measured as the time that the response is within this error band, is 180 s.

The same test was repeated by changing the preload value to 1000 N. Figures 17, 18 and 19 represents results of test under 1000 N load.

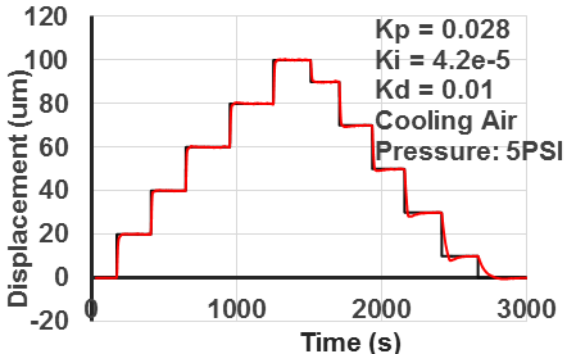

Figure 17: Displacement results under 1000 N load. Desired value (black color), Measured value (red color)

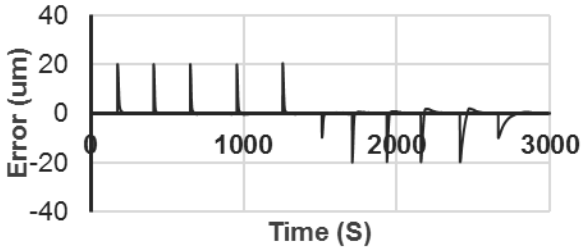

Figure 18: Error in the displacement under 1000 N load

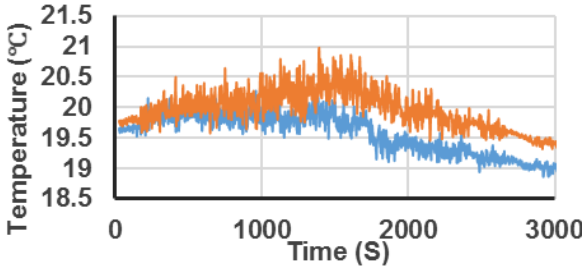

Figure 19: Variation in the moving platform and frame temperature under 1000 N load during displacement. Frame temperature (orange color), Stage temperature (blue color)

PID control is used for 1000 N load as well as the zero load test. Adjusting the Kp, Ki and Kd values results in a setting time of 30 s to stabilize at given desired position. Again the mean absolute error is less than 0.3 µm during steady state (see Figure 18). The frame and stage temperatures are maintained to within 20±1°C in these tests (see Figures 13, 16 and 19).

CONCLUSION

The inductively heat actuated stage is able to retain a constant position with variation of ±0.3 μm and with response times typically around 30 s to 100 s depending on controller settings. This thermal actuator is simple, rigid and relatively inexpensive. Additionally, the high work density of this actuation method enables the positioning of high loads using a relatively compact actuator.

FUTURE WORK

Many issues remain to achieve optimal performance. Using larger pumps to drive water through the frame and the stage, employing better methods for extracting the cooling capabilities of the air supply, and increasing the power of the induction heaters are currently being evaluated.

ACKNOWLEDGEMENTS

In completing this work, we acknowledge the helpful contributions of Michael Erickson, Ameya Parab, Jesse Groover, Christian Lomascolo.

REFERENCES

[1] Michael Erickson, Chunjie Fan, Gokul Mohandas, Ameya Parab, “Internet report”, Precision Machine Design, UNC Charlotte, 2017

[2] Stuart T. Smith, “Flexures: Elements of Elastic Mechanisms”, ISBN-10 9056992619, 2000

[3] Jean-Luc Dion, Remy Simard, “Electromagnetic inductor with ferrite core for heating electrically conducting material”, United States Patent, Patent Number (5101086), 1992

[4] Daniel Amariei, Yvan Meason, Ion Vela, “Analysis and Design of Thermal Actuators”, ANALELE Universitalii “EFTIMIE MURGU” Resila ANUL XIV, NR. 1, 2007, ISSN 1453 – 7397

BASIC CHARACTERISTICS OF NOVEL HYBRID ACTUATOR INTEGRATING A THERMAL BIAS ELEMENT AND AN ELECTROMAGNETIC DRIVING ELEMENT

Tadashi Hama[1], and Kaiji Sato[2]
[1]Interdisciplinary Graduate School of Science and Engineering
Tokyo Institute of Technology
Yokohama, Japan
[2]Department of Mechanical Engineering, Toyohashi University of Technology
Toyohashi, Japan

INTRODUCTION

Many industrial mechanisms are used in industry, and different applications demand different characteristics. Some applications require a high speed and high response motion. For example, semiconductor exposure apparatuses or coordinate measuring machines need to provide a high speed and high response motion [1]. On the other hand, motion mechanisms for other applications are required to generate a large thrust force rather than produce a high response motion. Injection molding machines or press machines are good examples.

In general, a high response motion and large thrust force generation are not compatible in one mechanism [2]. Electromagnetic linear motors can provide a high speed and high response motion, but they are not good at generating a large continuous force because the temperature of coils significantly rises and the continuous rating force is strongly limited. Additionally, the size of linear motors tends to increase with the increase of the continuous rating force. In contrast, electromagnetic motors with power transmissions can generate a large force easily, but it cannot provide a high speed and high response motion because of the large motor inertia. Indeed, variable transmissions or pneumatic/hydraulic actuators can realize both characteristics in one mechanism, which are often used for some variable speed motion mechanisms [2]. However, variable transmissions cannot realize both kinds of characteristics at the same time. Pneumatic/hydraulic actuators require a lot of additional equipment such as compressors or air tanks, which makes the total system large.

When actuators provide a high response motion with a large thrust force, they can provide a multifunctional vertical motion mechanism in a compact size. For example, they can give the attitude control mechanism with a vibration control function due to both of high response and large thrust characteristics for carrying precision machines (Fig. 1).

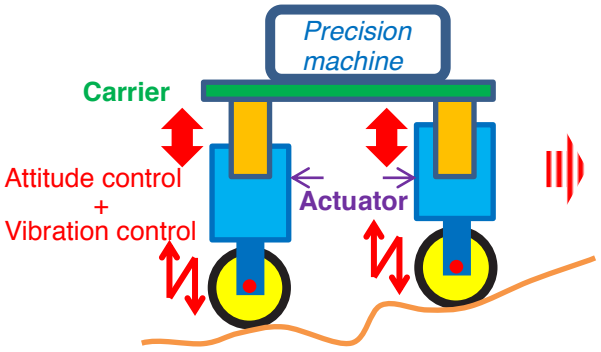

Fig. 1: One example of utilizing the vibration control function of the attitude control mechanism

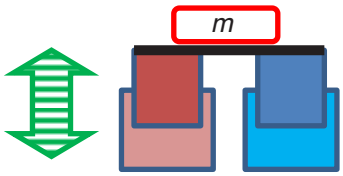

Fig. 2: Proposed combination of two elements

This study focuses on a novel hybrid actuator in which an element for generating a large variable bias force and an element for producing a high response motion are combined as shown in Fig. 2. In this study, the former one is called “the variable bias element” and balances with a weight load. The latter one is called “the high response element” and works as a direct drive electromagnetic actuator. This combination is expected to realize an efficient vertical motion mechanism with a large bias force per volume and high response.

This paper describes a compact hybrid actuator which can produce a high response motion with

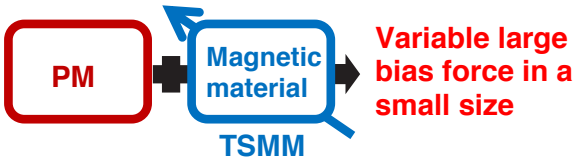

Fig. 3: Concept of the combination of PMs and TSMMs

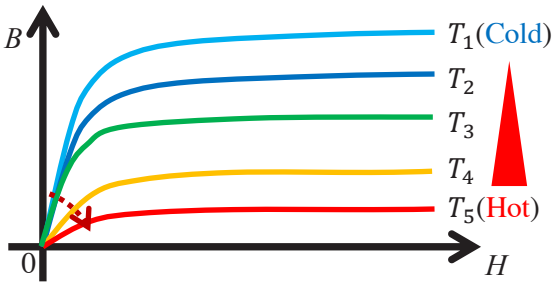

Fig. 4: Conceptual B-H curve of TSMMs

a large bias force for supporting a weight load. First, the concept of the hybrid actuator and the principle of the variable bias element are explained. Next, the structure of the hybrid actuator is proposed and the prototype actuator is introduced. After that, the basic characteristics of the prototype hybrid actuator are investigated experimentally.

CONCEPT OF THE HYBRID ACTUATOR

There are some methods for generating a variable continuous force as a bias force. The combination of a leverage and a spring whose direction of force can be changed works as a variable bias element [3]. The combination of a linear spring and a negative magnetic spring also acts as a variable bias element [4]. However, such passive mechanisms cannot adjust the bias force without a power source, and an additional actuator is necessary in order to balance with the weight load automatically. As a result, the total system becomes large. In this study, the fusion of these two elements is proposed to realize a compact actuator for a vertical motion mechanism which can provide a high response motion with a large bias force.

In order to make the combination of these elements compact and tractable, it is desirable that the variable bias element shares the same components with the high response element from the viewpoint of downsizing. As the high response element, an electromagnet is used with permanent magnets (PMs). Then, the combination of PMs and magnetic materials is

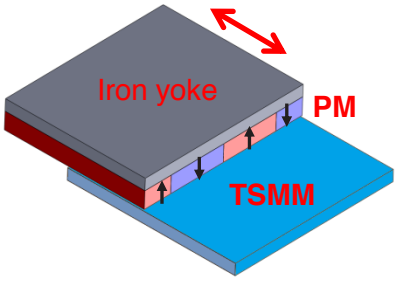

Fig. 5: Basic principle of the proposed variable bias element

adopted as the variable bias element to utilize a high energy density of PMs.

Generally speaking, PMs and magnetic materials have fixed magnetic characteristics, and the bias force generated from this combination cannot be changed. However, the variable force characteristic can be obtained by a special contrivance either in PMs or magnetic materials. In this study, the special magnetic materials which are called temperature sensitive magnetic materials (TSMMs) are used to generate a large bias force (Fig. 3). Fig. 4 shows the conceptual B-H curve of TSMMs. The saturation magnetic flux density decreases with the increase of the temperature, which means that the bias force can be controlled by the temperature adjustment.

In addition to the common use of magnetic components, there is a merit in the combination of the variable bias element using TSMMs and the high response element using an electromagnetic actuator. As mentioned above, electromagnetic actuators have a demerit of dissipating a lot of heat and consuming a large energy when they generate a large force. However, the heat from an electromagnetic coil of the high response element can be utilized for heating the TSMMs of the variable bias force with a special structure, which means one power supply and one coil can control both two functions.

PRINCIPLE OF THE VARIABLE BIAS ELEMENT

The basic principle of the proposed variable bias element is shown in Fig. 5. This principle has already been introduced in Ref. [5]. The mover consists of the iron yoke and PMs whose directions of poles are arranged alternately. A TSMM plate is fixed to the stator, and faces the PM array of the mover. The mover is attracted toward the position where the mover is aligned

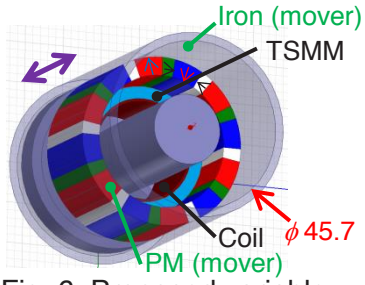

Fig. 6: Proposed variable bias element

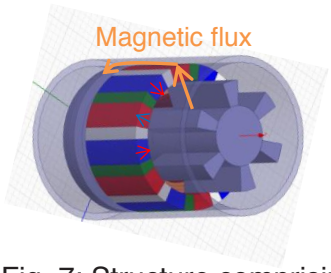

Fig. 7: Structure comprising the element for generating an electromagnetic force

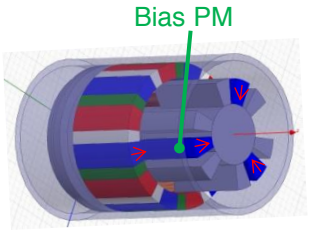

Fig. 8: Overall structure of the proposed hybrid actuator

with the TSMM plate, and the magnitude of the thrust force is reduced with the increase of the temperature. The thrust force is constant in almost all working range because the change of the magnetic resistance is constant with respect to the displacement of the mover. This constant force characteristic is desirable for the variable bias element. This is because the coil has to generate the thrust force only for making a motion of the weight load and it is not necessary to consume any power to change the TSMM temperature, when the displacement of the mover should be changed.

STRUCTURE OF THE PROPOSED ACTUATOR

Fig. 6 indicates the variable bias element of the hybrid actuator. Although the basic structure is the same as that mentioned in the previous chapter, the cylindrical shape and the Halbach PM array are adopted for the high thrust force per volume. The inner side of the TSMM cylinder is touched to an 83-turn coil, and the Joule heat caused by the applied current raises the TSMM temperature. Fig. 7 shows the structure which includes the part to generate an electromagnetic force for the high response motion. The protrusions made of iron are opposed only to PMs magnetized outward. When the current is applied to the coil, the magnetic flux goes through PMs magnetized outward, and the electromagnetic force is generated. The iron protrusions also affect the bias force. The bias force *Fb* is determined by the resultant force applied between the PMs and the TSMM cylinder (*Fpt*), and PMs and the iron protrusions (*Fpi*) as represented in Eq. (1).

$$F_b = F_{pi} - F_{pt} \qquad (1)$$

When the TSMM temperature is the minimum value, *Fb* should be zero. However, *Fpi* is not large enough to cancel *Fpt*. In order to increase the value of *Fpi*, additional bias PMs are located in three spaces between protrusions (Fig. 8).

In this actuator, the current applied to the coil changes the TSMM temperature and generates an electromagnetic force simultaneously. When the weight load is increased, the current is applied to heat the TSMM cylinder. At the same time, the applied current generates an electromagnetic force to the positive direction. After the sum of the bias force and the electromagnetic force becomes to be equal to the weight load, the current is controlled to be reduced so that the total force remains. Then, the motion control can be conducted with the total force equal to the weight load.

When the bias force should be increased, the TSMM cylinder can be easily heated to balance with it in the method mentioned above. However, when the bias force should be reduced, it is not easy to lower the TSMM temperature because the current applied to the coil cannot contribute to cooling the TSMM cylinder. In order to lower the TSMM temperature fast, the TSMM cylinder should be designed to spread out the heat over the basement. However, a lot of heat becomes necessary to keep the TSMM temperature for maintaining the bias force, which means the power consumption becomes large. Namely, there is a tradeoff between the cooling speed and the energy efficiency. In order to solve the problem, the thermal characteristic is desired to be variable. Fig. 9 shows the proposed structure of the heat switching element. The part A is a copper cylinder which is wound with a coil, and is thermally contacted with a TSMM cylinder. This part has twelve ridges inside it whose tops are inclined. The part B is a copper cylinder which is thermally contacted with a central iron core and a basement. This part also has twelve ridges outside it whose tops are inclined. The part A is supported rotatably and ridges of both parts can be touched to or separated from each other. Heat conductive sheet is stuck on each top of ridges for making sure the heat conduction. When they are touched to each other, the TSMM cylinder is thermally connected

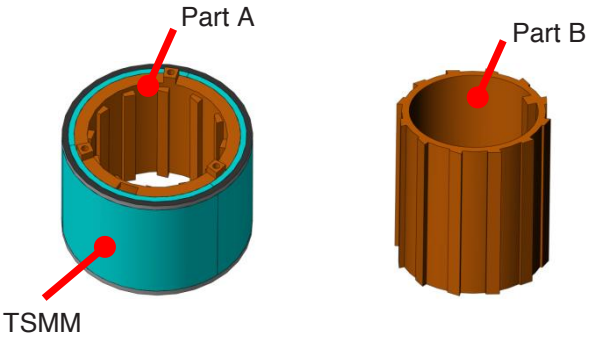

Fig. 9: Structure of the heat switching element

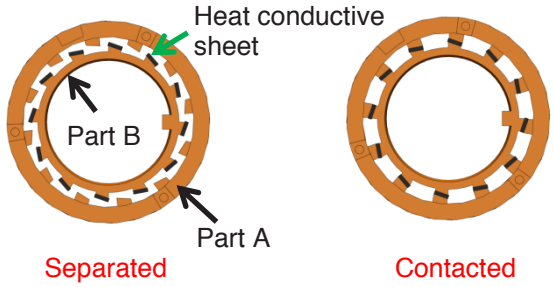

Fig. 10: Principle of the heat switching element

to the basement, and the TSMM temperature can be lowered (Fig. 10).

PROTOTYPE OF THE PROPOSED HYBRID ACTUATOR

Fig. 11 shows the structure of the stator and its exploded view. This actuator consists of a fixed part and a rotatable part. The fixed part comprises the iron bottom ring, the central iron core and the iron protrusions. The rotatable part comprises TSMM cylinder supported by the part A with an 83-turn coil between them, and the TSMM support for holding this combination. The thickness of the TSMM cylinder is 2.95 mm. The TSMM support is supported rotatably by two bearings fixed to the central iron core. The rotatable part is designed to rotate by 13 degrees. As shown in Fig. 12, the mover is guided by a pair of ball guides. The thickness of PMs is 4.5 mm. The gap between the TSMM cylinder and PMs is 500 μm.

BASIC CHARACTERISTICS OF THE PROTOTYPE ACTUATOR

The bias force is generated by the TSMM cylinder, and its value is determined from the temperature. When the weight load is changed, the TSMM temperature should be heated or cooled. Fig. 13 shows the temperature response when the TSMM cylinder is heated or cooled. At

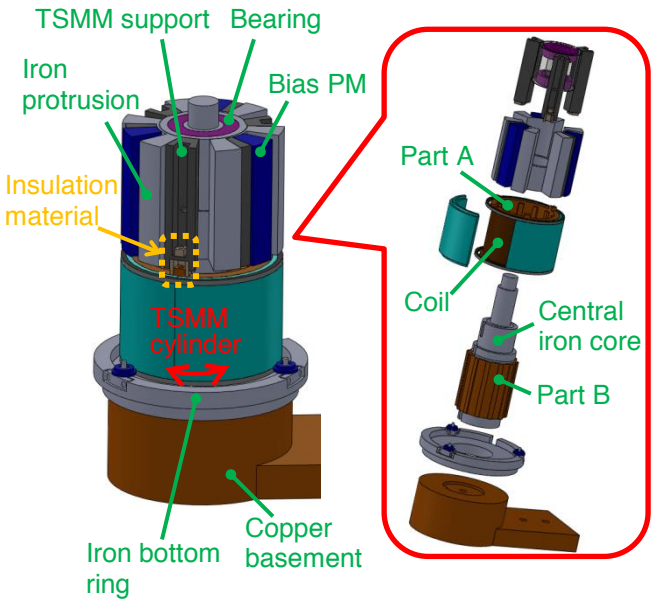

Fig. 11: Structure of the stator and its exploded view

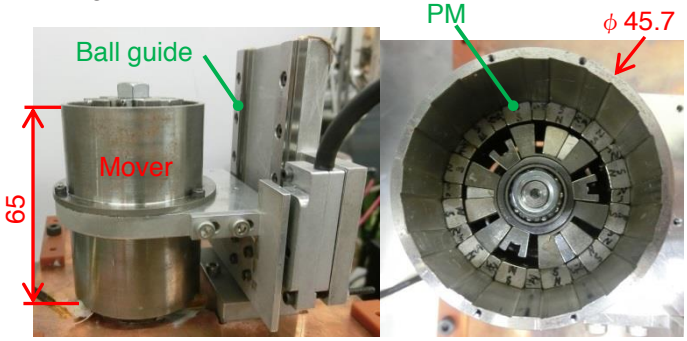

Fig. 12: External appearance of the prototype actuator

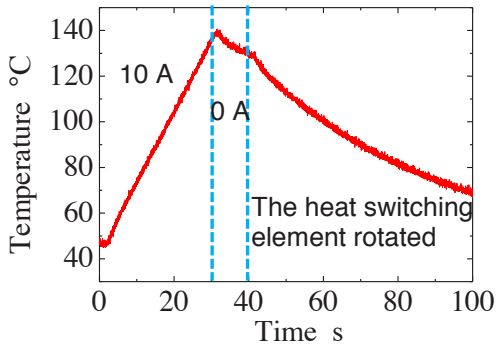

Fig. 13: Heating and cooling response of the TSMM temperature

first, the maximum current of 10 A is applied for 30 seconds, and the heat switching element is rotated with a torque of 40 mNm at 40 second. It

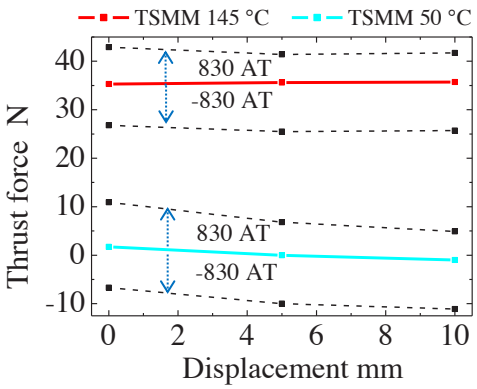

Fig. 14: Experimental thrust characteristics

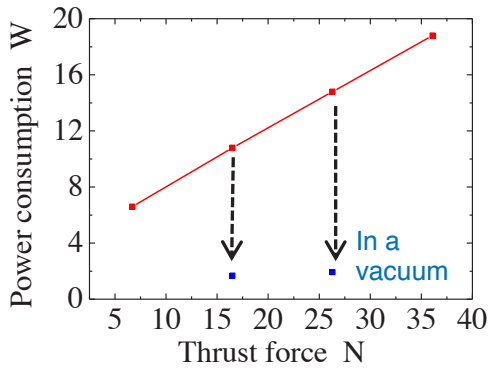

Fig. 15: Relationship between the steady state power consumption and the thrust force

can be seen that the TSMM cylinder is heated or cooled properly. In this experiment, the heat switching element is rotated manually, but this element is intended to work in conjunction with the electromagnetic force generated by the coil with one current controller going forward.

Fig. 14 shows the thrust characteristics with respect to the mover's displacement. The bias forces represented by the solid lines are almost constant regardless of the displacement. In other word, the constant thrust characteristic is realized. The maximum bias force is 35.6 N with the maximum temperature of 145 °C when the minimum bias force is set to 0 N with the minimum temperature of 50 °C. The dotted line represents the thrust force with a current applied for generating an electromagnetic force. The electromagnetic force is superimposed on the bias force, which means the motion control or the vibration control can be conducted with the bias force to support the weight load.

The relationship between the steady state power consumption and the thrust force is indicated in Fig. 15. The steady state power consumption in an air atmosphere shown by a red line is proportional to the thrust force. This result indicates that the power consumption is large and it is necessary to reduce it. In this actuator, the steady state power consumption is determined from the heat dissipation in the surface of the TSMM ring. Then, the actuator is put in a vacuum atmosphere of 0.2 Pa to improve the thermal isolation performance, and the steady state power consumption is measured. As indicated in Fig. 15, the steady state power consumption is largely reduced. If the TSMM cylinder can be in a vacuum atmosphere with a pressure-resistant shell in a gap between the TSMM cylinder and the mover's PMs, this actuator can support a weight load with small power consumption, which means the ideal combination of the efficient bias element and the high response motion is realized in one compact actuator.

CONCLUSION

In this paper, the compact hybrid actuator which can produce the high response motion with a large bias force has been proposed. The concept and the structure of the proposed actuator were explained. The basic characteristics were investigated experimentally, and the generation of the bias force and the electromagnetic force was confirmed. In the experiment to examine the steady state power consumption, its significant reduction was measured under vacuum. Thus, it is necessary to design the structure for setting the TSMM cylinder in a vacuum atmosphere with compactness and tractability in the future.

ACKNOWLEDGEMENT

This work was supported in part by Grants-in-Aids for Scientific Research under Grant 15J11845 and Grant 15K13853.

REFERENCES

[1] Z. Duan and Q. Wang, "Development of a novel high precision piezoelectric linear stepper actuator," Sens. Actuators A 118, 2005; 285-291.

[2] T. Takaki and T. Omata, "Load-Sensitive Continuously Variable Transmission for Robot Hands," in Proc. of 2004 IEEE Int. Conf. Robot. Autom., 2004; 3391-3396.

[3] B. M. Wisse, W. D. Dorsser, R. Barents and J. L. Herder, "Energy-Free Adjustment of Gravity Equilibrators Using the Vertual

Spring Concept," in Proc. of 2007 IEEE Int. Conf. Rehabil. Robot., 2007; 742-750.
[4] E. Fujita, N. Nakagawa, Y. Ogura and S. Kojima, "An Experimental Study for a Nonlinear Combination Spring using a Magnet-Spring," J. JSME, 2000; C66(645): 29-36. (in Japanese)
[5] T. Hama and K. Sato, "Basic Characteristics of a New Compact Actuator Using Temperature Sensitive Magnetic Materials," in Proc. of ICMT2015, 2015; C12-Paper89.

IDENTIFICATION OF FRICTION ENERGY DISSIPATION USING FREE VIBRATION VELOCITY: MEASUREMENT AND MODELING

Christoph A. Kossack, Tony L. Schmitz, and John C. Ziegert
Department of Mechanical Engineering and Engineering Science
University of North Carolina at Charlotte
Charlotte, NC

INTRODUCTION

Existing force-based methods for parametrizing friction models are limited by large uncertainties (approximately parts in 10^2 [1]). This paper provides experimental results for a new method that uses velocity measured during free vibration to quantify the energy dissipation in friction contacts. The final goal is a friction measurement method that provides reduced uncertainty, particularly for low friction and low velocity applications.

FRICTION MEASURING MACHINE

The friction measuring machine (FMM) was designed and constructed to provide relative (linear) motion between the pin and counterface in a friction contact using a parallelogram leaf-type flexure [2]. The FMM can therefore be represented by a single degree of freedom spring-mass-damper system.

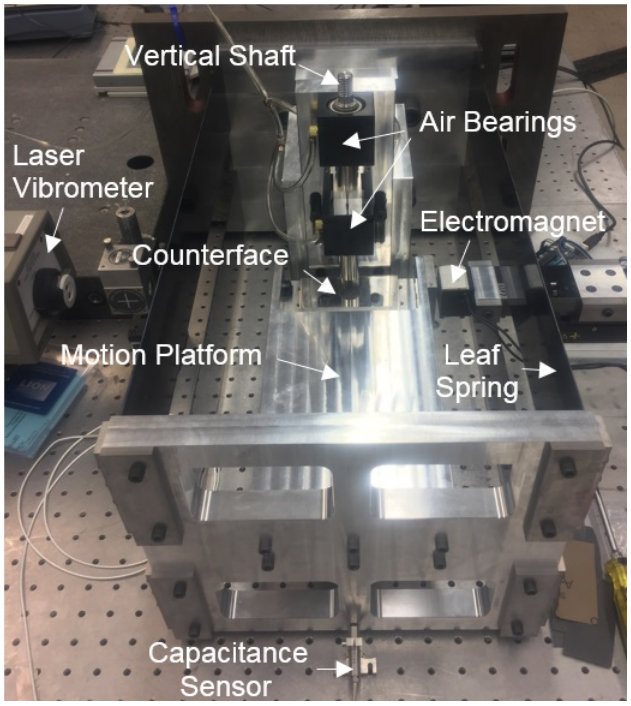

Figure 1. FMM photograph.

As shown in Fig. 1, the FMM uses four leaf springs to provide horizontal oscillating motion of the counterface. The FMM structure is based on a linear flexure mechanism. One end of each leaf spring is clamped to a rigid base, while the other is clamped to the faceplate that is attached to the motion platform. An electromagnet is used to capture the motion platform and displace it from its equilibrium position to provide the desired initial displacement. The force being applied by the electromagnet mechanism is located at the midpoint of the length of the flexures. This ensures that the faceplate will move parallel to the base plate, which, in turn, minimizes the rotation of the motion platform during friction testing.

A counterface is attached to the motion platform. The fixed pin is attached to the bottom of a vertical shaft which provides the dead weight normal force during friction tests. The shaft is held in place using two air bearings that are rigidly attached to the FMM base.

The gravitational load provides a constant normal force for the friction tests. The friction contact is completed when the pin is lowered onto the interchangeable translating counterface. The electromagnet is then used to move the motion platform to the desired initial displacement. Once the electromagnet is released, the system oscillates freely until it comes to rest.

The magnitude of the flexure's parasitic motion at the motion platform was estimated using Eq. 1 [2].

$$\Delta y = \frac{-3\Delta x^2}{5L} \tag{1}$$

Calculations show that the velocity measured with the laser vibrometer is two orders of magnitude larger than the parasitic motion for the range of tested displacements. To validate the calculations, a pair of capacitance sensors were used to measure the parasitic displacement of the motion platform and the results confirmed the analytical solution given by Eq. 1. Due to the small motion amplitude, the kinetic energy associated with the parasitic motion was neglected.

Free vibration velocity with no friction contact was measured to determine the instrument's dynamic characteristics, including the modal mass, *m*, stiffness, *k*, and viscous damping coefficient, *c*. A range of initial displacements was tested and a

nonlinear least-squares fitting algorithm was applied to Eq. 2 to determine the modal parameters [3].

$$m\ddot{x} + c\dot{x} + kx = 0 \quad (2)$$

CHARACTERIZATION OF SYSTEM DYNAMICS

The maximum allowable deflection for the FMM was calculated using Eq. 3:

$$\delta_{max} = \frac{\sigma_y L}{3Et}, \quad (3)$$

where *L* and *t* are the length and thickness of the leaf springs, respectively, and σ_y and *E* are the yield strength and elastic modulus for the spring material, respectively. The resulting maximum allowable deflection is 132 mm. A factor of safety of six was used to ensure that there would be no plastic deformation of the leaf springs. As a result the maximum testing displacement was 22 mm.

Free vibration, non-friction tests were performed with initial displacements ranging from {4 to 22} millimeters. For each test, the FMM was first moved to an initial displacement. The vibrometer was then initiated to begin collecting data. The motion platform was then released and allowed to oscillate freely for 45 s. The electromagnet was retracted upon release of the platform. For the flexure's natural frequency of 2.2 Hz, approximately 100 cycles were completed during the measurement interval.

Before the fitting algorithm was applied to the data set, the pre-slide velocity data was used to remove any initially velocity offset from zero and then a smoothing function was applied to the data. The first 10 cycles of the data set were also removed to ensure there were no residual effects from the electromagnet's release and charge dissipation. The fitting algorithm was then applied to the remaining data.

Equation 2 was the governing equation of motion for the system. Euler Integration was used in the fitting function to determine the modal parameters. The fitting algorithm was the Matlab® nonlinear least squares fitting algorithm *lsqnonlin*, which implements a trust region reflective fitting approach. Figure 2 displays a sample of the fitting results using this function and Fig. 3 shows a small section of Fig. 2 to better illustrate the fitting results.

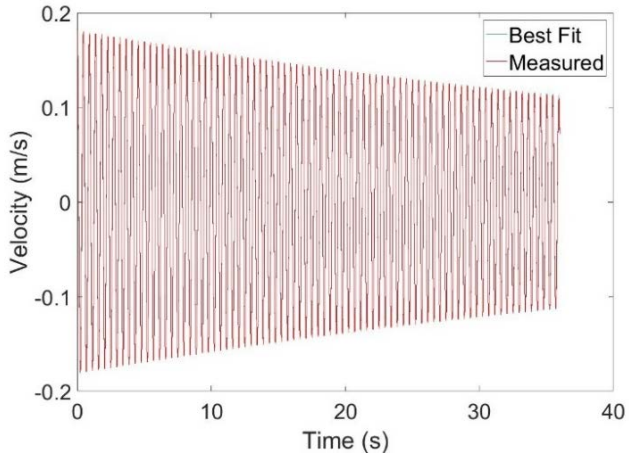

Figure 2. Velocity data fitting results.

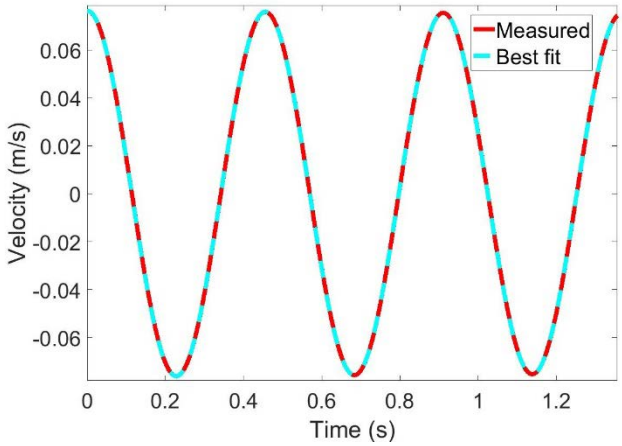

Figure 3. Section of velocity data fitting results.

The modal parameters identified using the fitting routine for various initial displacements are displayed in Table 1 and the mean values and standard deviations are presented in Table 2.

Table 1. Modal parameters from fitting results.

Initial Displacement (mm)	Peak Velocity (mm/s)	Mass (kg)	Stiffness (N/m)	Viscous Damping (Ns/m)
4	50	10.394	1981	0.222
6	76	10.395	1981	0.235
8	103	10.393	1981	0.245
10	129	10.397	1982	0.256
14	181	10.392	1982	0.278
16	207	10.389	1983	0.288
18	233	10.389	1984	0.299
20	258	10.385	1984	0.313
22	283	10.382	1984	0.327

Table 2. Mean and standard deviation of modal parameters.

Modal Parameters	m (kg)	k (N/m)	c (Ns/m)
Mean	10.391	1982	0.275
St. Deviation	0.0045	1.3	0.0341

The damping coefficient showed the highest variation. Upon further inspection it was discovered that there appears to be a direct relationship between the viscous damping coefficient and the initial displacement, and, therefore the peak velocity during the free vibration cycle. This relationship is presented in Fig. 4. The linear fit has an R^2 value of 0.997.

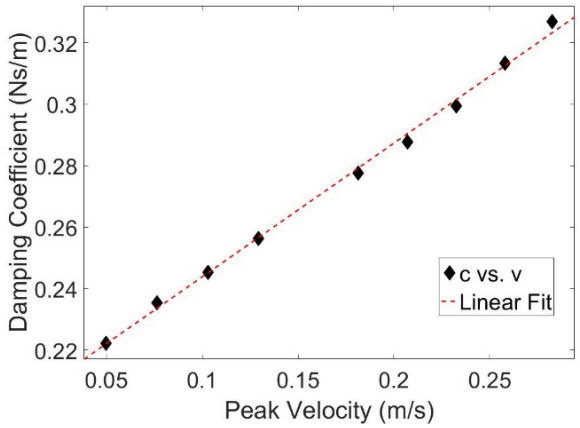

Figure 4. Linear fit of viscous damping coefficient versus peak velocity.

The clamps used to hold the leaf springs in place are the most likely source for this scaled energy dissipation. Losses can arise at the rubbing contact or through clamp elastic motion during vibration. Future tests will be completed to determine if the clamps are indeed the source for the variable viscous damping term. This will be done by designing and building two flexures with the same material and size: one monolithic and one with clamps.

FRICTION MODELS AND UNCERTAINTY

A single parameter Coulomb friction model was applied to determine the friction coefficient for the contact pair: a polytetrafluouroethylene (PTFE) pin on a polished steel counterface. To ensure a uniform interface between the polymer pin and steel counterface, a fine grit strip of sand paper was placed on the counterface and the polymer sample was run across it until its surface was parallel to the material plate. A normal force, *N*, of 14 N was applied for these tests.

Equation 2 was modified to include a friction force. The corresponding differential equation of motion is shown in Eq. 4, where the *m*, *k*, and *c* values were determined from free vibration tests with no friction contact. The friction force is $F_f = \mu N$, where μ is the friction coefficient and *N* is the normal force.

$$\begin{aligned} m\ddot{x} + c\dot{x} + kx + F_f &= 0, \dot{x} > 0 \\ m\ddot{x} + c\dot{x} + kx &= 0, \dot{x} = 0 \\ m\ddot{x} + c\dot{x} + kx - F_f &= 0, \dot{x} < 0 \end{aligned} \quad (4)$$

Due to the variations in the damping coefficient, two separate approaches were: 1) use the mean damping coefficient from the modal parameters; and 2) use the linear fit for the damping coefficient versus velocity.

For the former, a Monte Carlo simulation was completed to determine the propagation of uncertainties associated with each system parameter to the best fit on a single parameter friction model data set. This data set was artificially created to represent the perfect friction data set assuming a known Coulomb friction model. Each input variable was sampled 100,000 times from a normal distribution defined by the Table 2 standard deviations and its individual influence on the friction fitting equation of motion, Eq. 4, was determined. For the created data set the coefficient of friction, μ_d, was 0.15. Table 3 shows the results and Fig. 5 displays the probability density function for the case where all system parameter variables were randomly sampled in each iteration of the simulation. As expected, the highest uncertainty is associated with the damping coefficient. However, the highest sensitivity is presented by the modal mass.

Table 3. Monte Carlo simulation results.

μ_d			
Parameter	Mean	St. Dev.	dμ/dm (dk, dc)
m	0.150015	6.39×10^{-5}	1.31×10^{-2}
k	0.150018	2.09×10^{-5}	1.65×10^{-5}
c	0.150001	2.36×10^{-4}	6.93×10^{-3}
ALL	0.150021	2.48×10^{-4}	

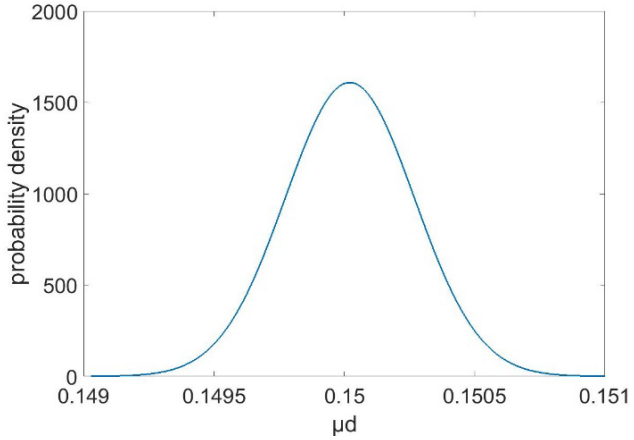

Figure 5. Probability density function for μ_d with m, k, and c variation.

In the second approach the linear relationship between viscous damping and velocity was applied. The fit is provided in Eq. 5.

$$c = 0.437\dot{x} + 0.2005 \quad (5)$$

Other potential damping models were tested as well, including Elliott and Tehrani's model [4] which implements a general nonlinear damping term for the analysis of a single degree of freedom system, Zaitsev's [5] model for nonlinear damping in doubly clamped beams, and a drag term to account for the flexure movement in air during oscillation. None provided a consistent result when applied to Eq. 2. Therefore, the simple viscous damping model was retained for friction fata fitting.

FRICTION FITTING RESULTS

The PTFE-polished steel contact pair was used to collect data sets at the same initial displacements as those that were used to establish the modal parameters. The repeatability of every initial displacement test was verified. Figure 6 shows five tests at the same initial displacement. It is observed that the measured velocity results are nearly identical.

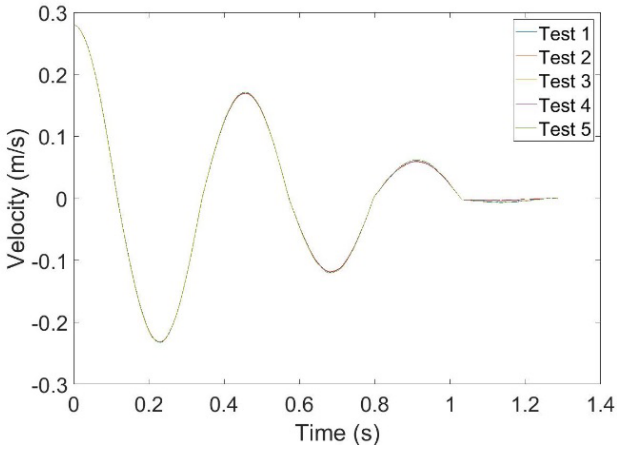

Figure 6. Vibrometer velocity data for five friction contact tests conducted at an initial displacement of 20 mm.

The friction fitting results for the mean and linear viscous damping approaches were similar. Table 4 shows the friction fitting results for initial displacements, x_0, ranging from {8 to 22} mm. Figure 7 displays a sample of the fitting for an initial displacement of 20 mm.

Table 4 Friction fitting results for various initial displacements, x_0.

	Linear c		Mean c	
x_0 (mm)	μ_d	v_{max} (m/s)	μ_d	v_{max} (m/s)
8	0.217	0.086	0.217	0.086
9	0.225	0.100	0.224	0.100
10	0.228	0.114	0.228	0.114
11	0.232	0.128	0.231	0.128
12	0.236	0.141	0.235	0.141
13	0.244	0.155	0.239	0.155
14	0.247	0.168	0.247	0.168
15	0.248	0.182	0.248	0.182
16	0.252	0.196	0.252	0.196
17	0.254	0.209	0.254	0.209
18	0.261	0.223	0.261	0.223
19	0.265	0.237	0.265	0.237
20	0.264	0.251	0.264	0.251
21	0.265	0.265	0.265	0.265
22	0.267	0.280	0.267	0.280

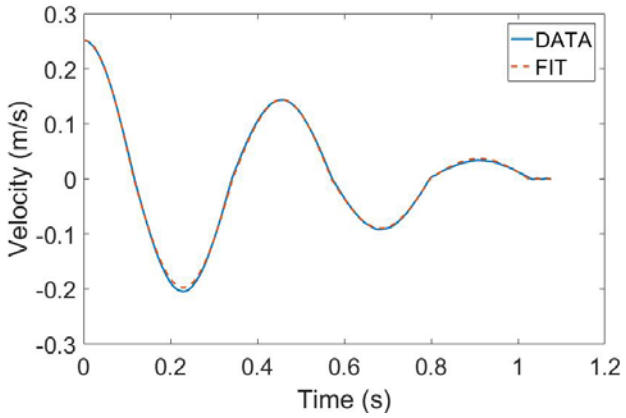

Figure 7. Friction fitting results using single parameter Coulomb friction model.

As with the viscous damping coefficient, the coefficient of friction displays a dependence on velocity as well. This is the case for both approaches, as can be seen in Fig. 8.

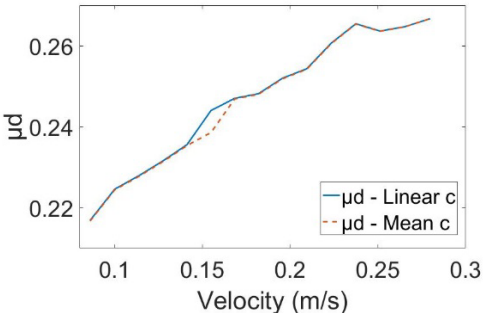

Figure 8. Friction coefficient versus velocity for both linear damping coefficient and mean damping coefficient approaches.

In this case, the relationship between μ_d and velocity can best be modeled through a power model; see Eq. 6. The Eq. 6 fit has an R^2 value of 0.99 and is visually presented in Fig. 9.

$$\mu_d = 0.311\dot{x}^{0.2116} + 0.03148 \qquad (6)$$

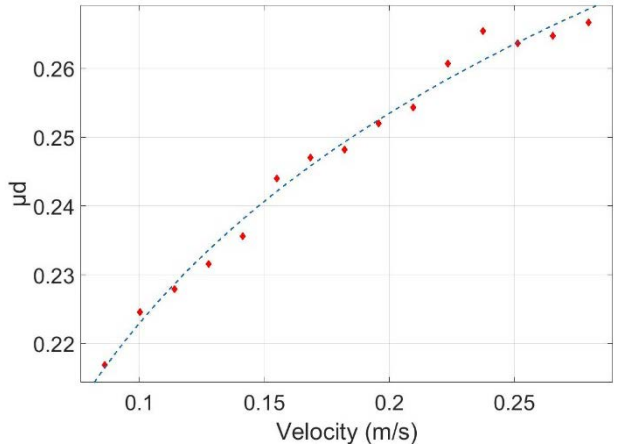

Figure 9. Power law fit for the μ_d versus velocity data.

The power law fit indicates that, at close to zero velocity, the friction coefficient is close to zero as well. As the velocity increases, so does energy dissipation. This behavior resembles the non-reversible friction model discussed by Wojewoda and Stefanski [6], where it is proposed that the sliding resistance due to friction is larger when an object accelerates from zero velocity than when is decelerates toward zero velocity. In both instances, the friction coefficient takes the same constant value once a specific velocity is reached.

The theory that the friction coefficient is larger or smaller depending on acceleration was tested in a separate simulation that considered the current acceleration at each time step of the Euler integration. This resulted in an improved fit to the data across the different initial displacement tests. The coefficient of friction was always found to be larger when the FMM was accelerating than when it was decelerating. Figure 10 displays these results and Eq. 7 displays the equation of motion.

$$\begin{aligned} m\ddot{x} + c\dot{x} + kx + \mu_{d1}N = 0 \quad ,\ddot{x} > 0 \\ m\ddot{x} + c\dot{x} + kx + \mu_{d2}N = 0 \quad ,\ddot{x} < 0 \end{aligned} \qquad (7)$$

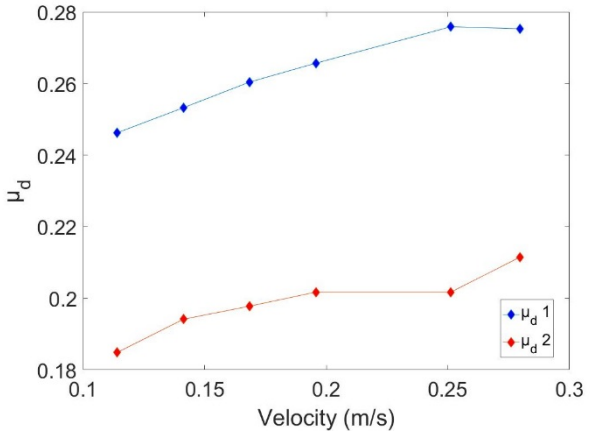

Figure 10. Dependence of the friction coefficient on acceleration (1 accelerating, 2 decelerating).

The final friction model for the data has yet to be determined. However, the ability to observe and measure the energy dissipation due to sliding friction velocity, rather than force, enables reduced uncertainty for this interrogation.

CONCLUSION

The goal of this research was to develop a new friction measuring method for low velocity, low friction applications. By using a laser vibrometer to measure velocity and using that data to determine energy dissipation due to friction, it is possible to achieve lower uncertainties when determining friction coefficients for sliding contact interfaces. The friction measuring machine (FMM) enables the relative contributions of structural and friction contact energy losses to be isolated and quantified. Once the system dynamics were established and the friction model was selected, it was possible to parameterize the sliding friction model.

REFERENCES

[1] Schmitz T, Action J, Ziegert J, and Sawyer WG (2005). On the Difficulty at Measuring Low Friction: Uncertainty Analysis for Friction Coefficient Measurements. Journal of Tribology 127: 673-678.

[2] Smith Stuart T (2000). Flexures: Elements of Elastic Mechanisms. CRC Press LLC, London UK.

[3] Schmitz T and Smith KS (2012). Mechanical Vibrations: Modeling and Measurement. Springer, New York, NY.

[4] Elliott, S.J. Tehrani, M.G. Langley, R.S (2015). Nonlinear damping and quasi-linear modelling. Royal Society Publishing.

[5] Zaitsev, S. Almog, R. Shtempluck, O. Buks, E. (2006) Nonlinear Damping in Nanomechanical Beam Oscillator. IEEE. 0-7695-2398-6.

[6] Wojewoda, J. Stefanski, A. Wiercigroch, M. Kapitaniak, T. (2008) Hysteretic effects of dry friction: modelling and experimental studies. Philosophical Transaction of the Royal Society, A.

THE VELOCIPROBE: PUSHING THE LIMITS WITH FAST AND ROBUST CONTROL

Sheikh T. Mashrafi[1], Curt Preissner[2], and Srinivasa M. Salapaka[1]
[1]Mechanical Science and Engineering
University of Illinois at Urbana-Champaign
Urbana, IL, USA
[2]Advanced Photon Source
Argonne National Laboratory
Argonne, IL, USA

INTRODUCTION

The Advanced Photon Source Upgrade (APS-U) at Argonne National Laboratory (ANL) will be capable of producing X-rays 100 times brighter than the present APS. X-ray microscopy with the high-flux X-rays of the APS-U requires fast and robust scanning capability of the X-ray zone plate optics. The control algorithm presented in this article enables the microscope to push the resolution and bandwidth limits by solving an optimization problem that incorporates the closed-loop objectives of large tracking bandwidth, good positioning resolution, robust stability to unmodeled dynamics, good disturbance rejection and adequate noise attenuation. Shorter scanning time and increased X-ray imaging resolution can be achieved with the proposed control algorithm. Up to 190% and 180% improvement in positioning resolution was achieved with H_∞ controllers for both scanning modes; in first mode the measured zone-plate stage displacement and in the second mode the measured relative displacement between the zone-plate and sample stage being the controller feedback, respectively, compared to the open loop.

THE VELOCIPROBE X-RAY MICROSCOPE

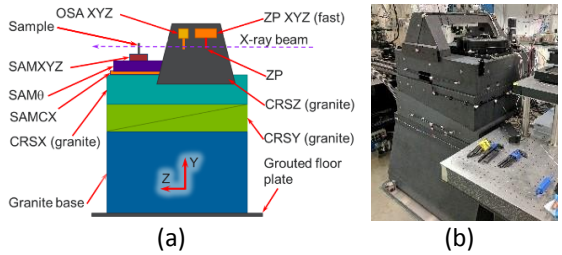

FIGURE 1. (a) Schematic of the Velociprobe X-ray microscope, and (b) the installed instrument at the APS beamline.

The Velociprobe is an X-ray microscope with novel in-house designed granite coarse positioning stages and state-of-the-art off-the-shelf Physik Instrumente (PI) nanopositioning stages. The stacked granite coarse positioning stages along with vented air bearings, provide motion along the Cartesian coordinates. The 3DOF PI flexure nanopositioning stage holding the zone plate focusing optics is attached to the top granite gantry in an inverted manner. This zone plate optics focuses the X-ray on to a spot on the sample which is attached to the sample holder positioned on the sample stages. The underlying idea is that during fine scanning of the nanopositioning stages the coarse positioning stage air bearings are vented, providing a very stable platform with minimal vibration (1.4 nm rms and 0.75 nm rms relative motion between the optics and the sample positions on a 5-100 Hz bandwidth, in the transverse and vertical directions respectively).

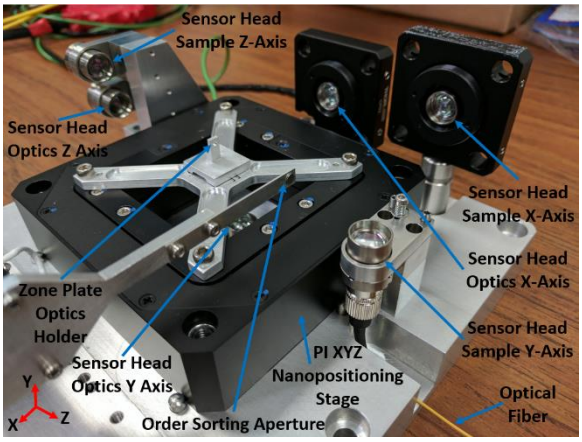

FIGURE 2. The Velociprobe nanopositioning stages.

The PI 3DOF nanopositioning stage is shown in Figure 2 during offline testing. Attocube fiber

interferometric sensors, with resolution ranging up to 1 pm, are used for measuring the stage displacements along the coordinate axes. The lasers exiting the sensor heads are reflected from the target surfaces on the optics stage and sample stages.

IDENTIFICATION

For the purpose of designing a control algorithm for the PI XYZ nanopositioning zone plate stages a mathematical model of the stages was generated by the frequency response based experimental identification technique. A bandlimited uniform white noise was given as an input to one of the zone plate stages at a time with no input to the remaining stages and the displacements from all three stages were measured. Experimental frequency response of the zone plate stages was then calculated from these time-domain input-output data. A parametric transfer function, which would act as the model for the respective stages, is then fit to the experimental frequency response.

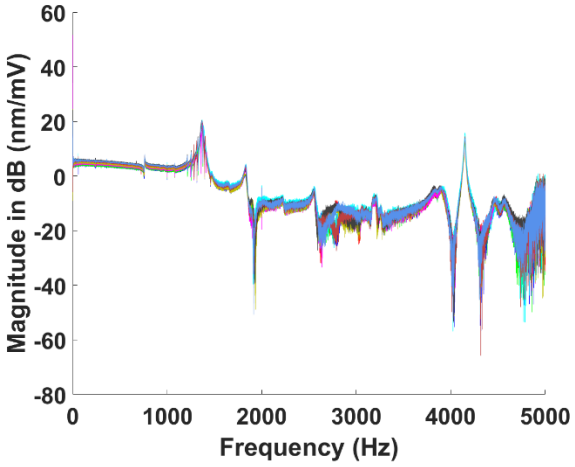

FIGURE 3. The transfer function estimates at 9 separate operating point for XX-stage (the physical plant that moves along X-axis due to X-stage input in mV and resulting in a displacement of X-stage in nm).

The PI stages are piezo-driven flexure-guided high-precision nanopositioning stages. The piezo actuators introduce non-linearity, while the flexure guidance results in complex dynamics. To account for the stage non-linearity, a range of experimental frequency response were obtained for each stage at different operating point spanning the volume of operation of PI XYZ stages. The frequency responses are then averaged and a parametric model is fit to this average frequency response. A small variation in these experimental frequency responses would mean that a linear model would be sufficient for controller algorithm to work effectively.

The variation of XX-stage dynamics with changing operating point is shown in Figure 3. The experimental frequency responses corresponding to different operating points are quiet close in all frequency range except close to 2800 Hz region. The average of this frequency responses are shown in the Figure 4.

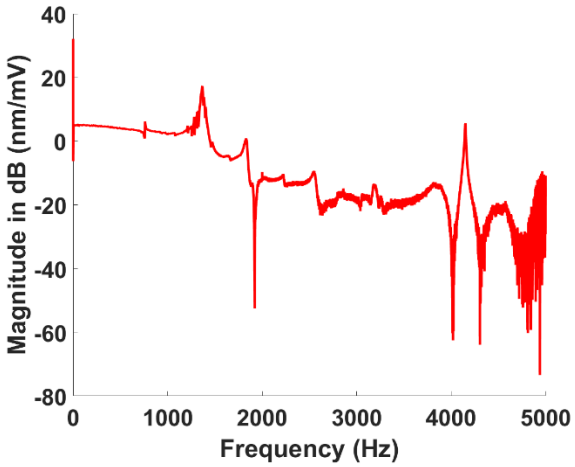

FIGURE 4. This figure shows the average transfer function estimate for XX-stage. The first resonance peak is at 1368 Hz.

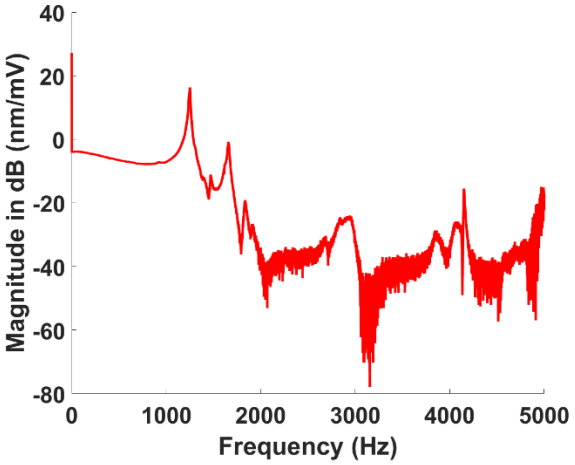

FIGURE 5. This figure shows the average transfer function estimate for the YY-stage. The first resonance peak is at 1251 Hz.

Similarly, the dynamics of the YY-stage was observed at different operating points, which only varied in high frequency range. The averaged

YY-stage frequency response is shown in Figure 5 with the first resonance peak at 1251 Hz.

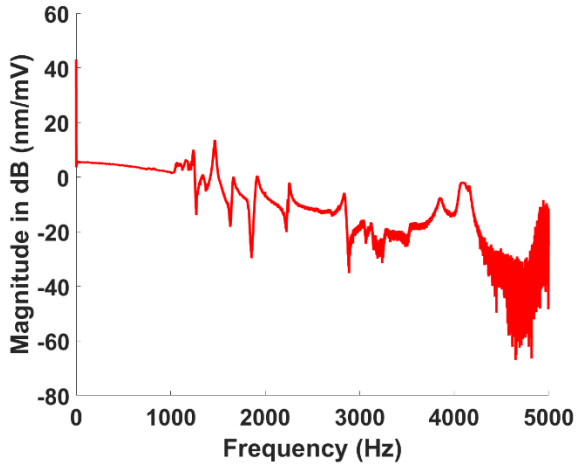

FIGURE 6. This figure shows the average transfer function estimate for ZZ-stage with the first resonance peak at 1241 Hz.

Figure 6 shows the averaged ZZ-stage dynamics with the first resonance peak being at 1241 Hz. The experimental frequency response did not vary significantly in low frequencies with varying operating point.

A parametric transfer function model is fitted to the averaged transfer function estimation calculation of each of the diagonal stages (XX YY, and ZZ). In case of YY-stage, the comparison between the experimental frequency response and the response of the model G_{yy} is shown in the Figure 7.

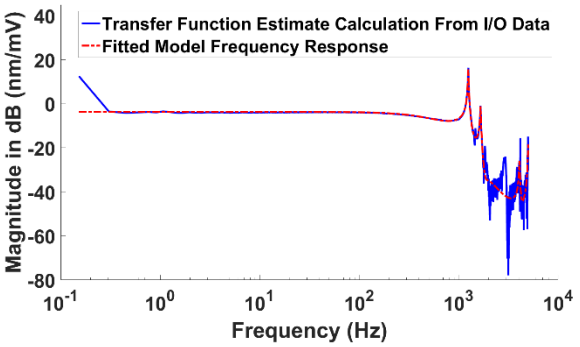

FIGURE 7. This figure shows the comparison between the transfer function estimate (blue solid line) of YY-stage calculated from YY-stage time-domain I/O data and the frequency response of the model G_{yy} (red dashed line).

CONTROL DESIGN

We used H_∞ feedback control architecture to obtain high-precision scanning of the PI XYZ zone plate optics stages required for X-ray imaging. The design objectives are to achieve small tracking error of the zone plate stages, small relative tracking error between the zone plate and the sample stages, rejection of environmental disturbances present in the APS beam line, attenuation of measurement noise and robust stability of the closed loop. The identified zone plate stage models are used to design the control algorithms.

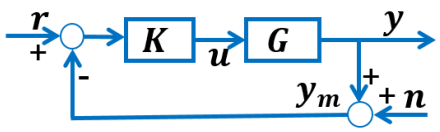

FIGURE 8. A transfer function block diagram of closed-loop system in negative feedback format is shown here. G is the identified plant model, K is the controller transfer function, r is the reference trajectory, u is the stage input, y is the stage displacement and n is the measurement noise.

As evident from Figure 8, the closed-loop stage dynamics and tracking error are given by $y = Tr - Tn$ and $e = Sr + Tn$, respectively. Here, $S = 1/(1 + GK)$ is the sensitivity transfer function and $T = GK/(1 + GK)$ is the complementary sensitivity transfer function. To make the tracking error small we need to make S small in a designed frequency band of interest to make the Sr term small, and T small in the high frequencies where measurement noise n is predominant. And for high precision tracking we need to achieve $y \approx r$ by making $T \approx 1$ over the designed bandwidth and T be small in the frequencies of n. The bound on control effort is achieved by keeping the closed-loop transfer function KS small in bandwidth frequencies, which assures that the controller does not saturate or generate voltage that is beyond the stage operating voltage.

In the H_∞ control approach all the design objectives are simultaneously incorporated in an optimization problem. The closed-loop transfer function block diagram of this architecture is given in Figure 9. The weighted tracking error $z_s = W_s(r - y)$, weighted stage displacement $z_t = W_t y$, and weighted control output $z_u = W_u u$ are the signals corresponding to the tracking bandwidth, noise attenuation and control effort

objectives. The transfer function matrix T_{wz} from exogenous inputs $w = [r \quad n]$ to the regulated outputs $z = [z_s \quad z_t \quad z_u]$ is minimized to achieve the mentioned objectives. The optimal control algorithm K is obtained by solving the minimization problem $\inf_K \|T_{wz}\|_\infty$.

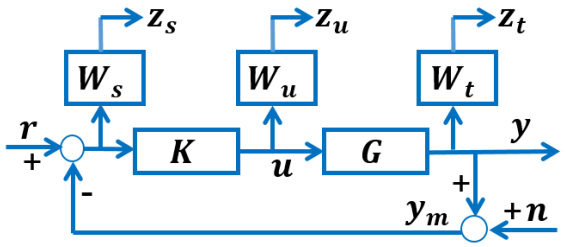

FIGURE 9. The closed-loop transfer function block diagram for H_∞ control architecture is shown. Here, G is the parametric model of the optics stage, r is reference signal, u is stage input, n is measurement noise, $W_{(.)}$ are design weights and $z_{(.)}$ are regulated outputs.

The design transfer functions W_s, W_t, and W_u are used to shape the closed-loop transfer functions S, T, and KS, respectively, by weighting them at appropriate frequencies. The corresponding multi-objective cost transfer function is given by $T_{wz} = [W_sS \quad W_tT \quad W_uKS]$. A performance weight W_s is designed as a low-pass filter that makes S small within the desired bandwidth, which results in small tracking error and good disturbance rejection. Designing complementary performance weight W_t as a high-pass filter shape results in T to be approximately equal to one at low frequencies and small in high frequencies, which gives good tracking and adequate measurement noise attenuation, respectively. Good positioning resolution of the scanning stages can be achieved with proper attenuation of measurement noise. The control effort weight W_u shapes the closed-loop transfer function KS to be small enough within bandwidth frequency so as to bound the control algorithm output that goes to the stages as voltage input. This prevents controller saturation, eases controller implementation and assures the controller output voltage is comfortably within the input voltage limit of the piezo stages.

RESULTS

Controllers designed for the Velociprobe X, Y, and Z zone-plate stages are implemented in diagonal manner during X-ray imaging experiments. The results shown in this article, covers the large -3 dB bandwidth controllers designed particularly to achieve good step scans of the focused X-ray beam spot. This was done by designing for a -3 dB bandwidth that is greater than the fourth or fifth harmonic frequencies of the reference steps. For one such controller combination, the -3 dB bandwidth for X, Y, and Z stage H_∞ controller are 166, 200, and 200 Hz, respectively. Figure 10 shows the tracking of zone plate Y-stage in both open loop and closed-loop with 1DOF H_∞ controller having a -3 dB bandwidth of 200 Hz.

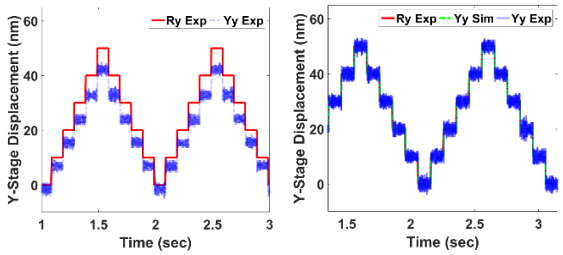

FIGURE 10. -3 dB staircase step tracking by the zone plate Y-stage, (a) open loop, (b) 1DOF H_∞ controller. Here, the reference signal, r (red) is a staircase steps with 10 nm steps at 10 Hz with 5 steps and the zone-plate stage displacement, y_1 is in blue.

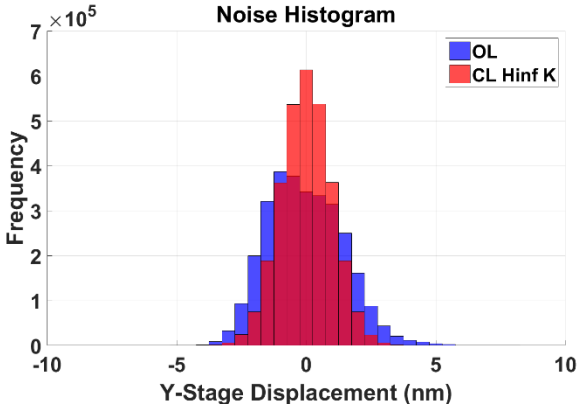

FIGURE 11. Noise histogram of Y-stage displacement for open loop and the diagonal controller implementation, resulting in a 3σ-resolution of 4.3 nm and 2.9 nm, respectively.

The noise histogram in Figure 11 is derived from the measured zone-plate Y-stage displacement with the previously mentioned diagonal controllers in operation. The 3σ-resolution calculated for zone-plate Y-stage displacement in

closed-loop is 2.9 nm, which is 132% improvement over the open loop. The 3σ-resolution for the X- and Z-stage with the H_∞ controller are 3.0 nm (186% improvement over open loop) and 1.5 nm (191% improvement over open loop), respectively. The open loop drift observed in case of X- and Z-stage is significantly larger compared to the Y-stage.

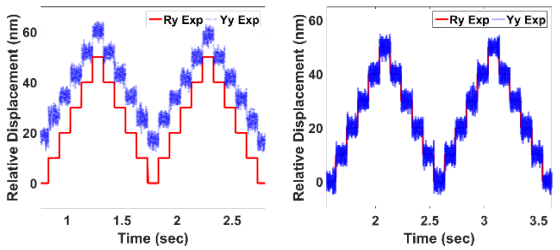

FIGURE 12. -3 dB relative tracking of a staircase step reference by the zone plate Y-stage and sample Y-stage, (a) open loop, (b) 1DOF H_∞ controller. The reference signal, r (red) is a staircase steps with 10 nm steps at 10 Hz with 5 steps. The relative displacement, $y_1 - y_2$ is in blue, where y_2 is the sample stage displacement.

The Figure 12 shows Y-stage tracking with the same controller implemented in diagonal form with the relative displacement between the zone plate stages and sample stages being used as the feedback signal. The benefit of the relative tracking is that, the optics stage is tracking two things, the first one being the reference signal to accomplish the step scan and the second one is the drifting sample stage. If the optics stage tracks the drifting sample stage, then relative position between the sample stage is very close to zero and limited by the resolution of the positioning system in closed-loop. According to the temperature data collected for over 24 hours the sample stage can drift thermally by over 600 nanometers or more in 12 hours due to heat generated from the sample stage driving mechanisms and encoders. Figure 12 shows the relative tracking of the zone plate and sample stage is much better in closed-loop compared to open loop.

In the case of relative tracking, the noise histogram of the relative displacement $y_1 - y_2$ is shown in the Figure 13. The 3σ-resolution achieved with the H_∞ controller for the Y-stage (relative displacement as feedback) is 5.0 nm, which is 179% improvement over the open loop. Even if the resolution of the controller implemented in relative displacement mode is comparatively worse than the zone-plate only case, the caveat is that the relative position of the zone plate and sample stage is only limited by this resolution value. Whereas with time (zone-plate only case) the sample stage can keep drifting away and result in significant X-ray imaging artifacts and image stitching errors.

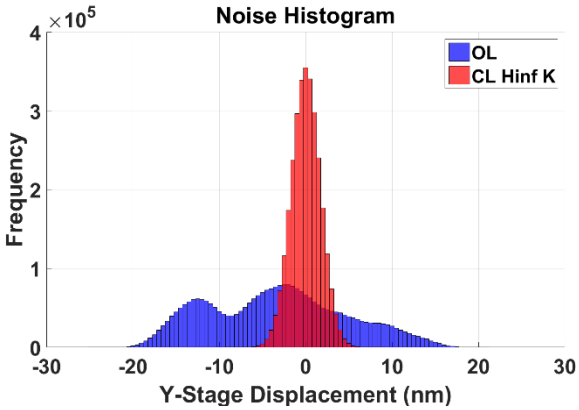

FIGURE 13. Noise histogram of Y-stage relative displacement for the open loop and H_∞ controllers diagonally implemented on all three stages, showcasing a 3σ-resolution of 24 nm and 5.0 nm, respectively.

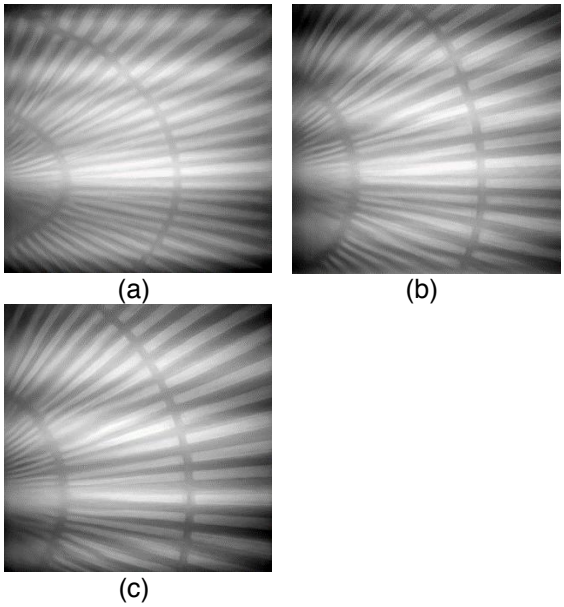

FIGURE 14. X-ray diffraction images of a Siemens Star test pattern reconstructed by Extended Ptychographic Iterative Engine (ePIE) technique *at APS beamline. (a) open Loop, (b) closed-loop zone plate stage only and (c) closed-loop differential displacement.*

The focused X-ray spot was scanned over a target region of the Siemens Star with the step scan technique. The X-ray images were reconstructed using the ePIE based on the intensity data collected by the detector. In the Figure 14 the periodic wavy pattern in horizontal direction is due to X-ray beam divergence. Figure 14a shows the reconstructed image of the Siemens Star in open loop, the case where we are not utilizing the measured stage displacement and correcting the position error. The open loop image reconstruction of the Siemens Star is radially deformed and has other imaging artifacts. The image reconstructed with the measured zone plate stage displacement signals being given to the controller as a feedback signal is shown in Figure 14b, which shows radial features with much less overlapping and imaging artifacts. In case of, Figure 14c the feedback signal to the controller was the relative displacement between the zone plate stages and the sample stages. The image with relative displacement has less number of imaging artifacts. Each of the images above took one hour of diffraction data collection while the focused X-ray spot is being scanned over a target region of the sample (Siemens Star). In longer imaging experiments that takes from 10-12 hours to 4-5 days the drift effect would be more significant and the implementation of the controller in the relative displacement mode would be beneficial. Also the overall time required to scan a target region on the sample is reduced eight folds. As for example, a scan that that took 2 hours before, takes about 15 minutes to step scan with the current H_∞ control architecture.

SUMMARY

This article shows the benefit of feedback control algorithm, specifically the H_∞ control architecture that we are showcasing, through the improvement of X-ray imaging capabilities in terms of speed of X-ray imaging resulting from large scanning bandwidth, better resolution of the optics scanning stages, better resolution of the X-ray diffraction images and reduced imaging artifacts. The open loop drift present in the zone-plate stages and the sample stages are being reduced by H_∞ controller for both operation modes; the zone-plate only and the relative displacement case. Better positioning resolution was achieved for the step scanning in closed-loop for both operation modes. At present, the designed controllers are not being utilized to the full potential because of the step scanning technique. The fly-scan technique implemented with the H_∞ controllers would reduce the time to scan a target region even more, giving the capability to scan large regions on a sample.

REFERENCES

[1] Mashrafi, S. T., Preissner, C., Salapaka, S. M. Fast scanning of X-ray Optics: An Optimal Control Approach. APSE 31st Annual Meeting, 2016.

[2] Borland, M. Ultra-Low-Emittance Light Sources. *Synchrotron Radiation News*, 27(6), 2-2. doi: 10.1080/08940886.2014.970927, 2014.

[3] Maser, J., Lai, B., Buonassisi, T., Cai, Z. H., Chen, S., Finney, L., . . . Vogt, S. A Next-Generation Hard X-Ray Nanoprobe Beamline for In Situ Studies of Energy Materials and Devices. [Article]. *Metallurgical and Materials Transactions a-Physical Metallurgy and Materials Science*, 45A(1), 85-97. doi: 10.1007/s11661-013-1901-x, 2014.

[4] Mashrafi S. T., Preissner, C., Salapaka, S. M., Zhao, H. Something for (almost) Nothing: X-ray Microscope Performance Enhancement through Control Architecture Change. ASPE 28th Annual Meeting, 2013.

[5] Lee C., Salapaka S. M. Robust Broadband Nanopositioning: Fundamental Trade-offs, Analysis, and Design in a Two-Degree-of-Freedom Control Framework. Nanotechnology, Volume 20, Number 3, 2009.

[6] Sebastian A., Salapaka S. M. Design Methodologies for Robust Nanopositioning. IEEE Transactions on Control Systems Technology, Volume 13, Number 6, 2005.

The submitted manuscript has been created by UChicago Argonne, LLC, Operator of Argonne National Laboratory ("Argonne"). Argonne, a U.S. Department of Energy Office of Science laboratory, is operated under Contract No. DE-AC02-06CH11357. The U.S. Government retains for itself, and others acting on its behalf, a paid-up nonexclusive, irrevocable worldwide license in said article to reproduce, prepare derivative works, distribute copies to the public, and perform publicly and display publicly, by or on behalf of the Government. The Department of Energy will provide public access to these results of federally sponsored research in accordance with the DOE Public Access Plan. http://energy.gov/downloads/doe-public-access-plan

Development of Dynamic Model to Estimate the Frequency Response of Four-Axis Machine Tools

Chang Kyu Song[1,2], Pham Van Dinh[1,2], and Chan Hong Lee[1]
[1]Department of Ultra Precision Machines & Systems
Korea Institute of Machinery and Materials
Daejeon, South Korea
[2]Department of Nano-Mechatronics
Korea University of Science and Technology
Daejeon, South Korea

INSTRUCTIONS

Machine tool manufacturing technology has been developed extensively in recent decades. The ultra- precision machining machines has been applied in high-tech fields such as semiconductor equipment, smartphone display, aerospace, etc. To ensure this accuracy, the machine tools have been designed and optimized through the virtual machine tools [1, 2]. Due to the machine tool is assembled from many components by fixed joints and kinematical joints. The machining accuracy and stability are depended on the kinematical joints. Hence, the dynamic of machine tool must be obtained through the simulation process by finite element method (FEM) to optimize the structure and materials [3]. The rigidity and stability of the spindle is analyzed through frequency response function (FRF) by receptance coupling substructure analysis (RCSA) [4]. The dynamic characteristics of bearings and guideway are invested to reduce the vibration and friction force, this role improves the accuracy and increases the performance of machine [5, 6]. Otherwise, dynamic model of machine tool for stage is developed to optimize the control systems [7], this method applies the SimMechanics software or ADAMS to analyze the dynamics. They have the advantages of allowing dynamic analysis of multi-axis machine tools that there is no need to formulate the motion equations, but these methods have some disadvantages such as complex modeling process, required massive computer, and slow computation time.

To overcome the disadvantages of the conventional methods, we proposed a novel solution that combines the energy method with Lagrange's Equation to establish the six degrees of freedom (DOF) motion equations for each axis of machine tool. The dynamic analysis results of the entire system were then established through the transformation matrix. This method transfers the complex multi-axis machine into the some multiple single axes to analyze the dynamic becoming easier. The dynamic analysis was applied for the control systems to optimize the control signals and the vibrations through the frequency response function. This research proposed novel method and applied it to analyse the frequency response of the four-axis machine tool with good agreement.

FORMALATION OF SIX DOF MOTION EQUATION FOR A SINGHLE AXIS

The six degrees of freedom (DOF) stage model is described in Fig.1, The stage is connected with base by eight couple spring-dampers that are arranged in horizontal and vertical directions. The six DOF of linear axis is presented with three linear motions along the X, Y, Z and three rotational motions around the axes, respectively.

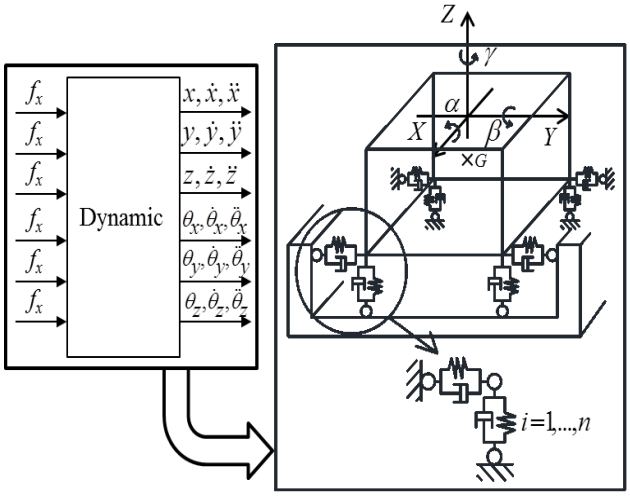

FIGURE 1. Six degrees of freedom (DOF) stage model.

The kinetic energy equation T, potential energy equation V, and energy dissipation equation D of linear axis are expressed as follows:

$$T = \frac{1}{2}v^T Mv + \frac{1}{2}\omega^T I\omega$$
$$V = \frac{1}{2}k_{yi}y_i^2 + \frac{1}{2}k_{zi}z_i^2 \quad (1)$$
$$D = \frac{1}{2}C_{yi}\dot{y}_i^2 + \frac{1}{2}C_{zi}\dot{z}_i^2$$

where v is the velocity of the stage in m/s, ω is the angular velocity in rad/s, I is the moment of inertia in kgm^2, M is the mass of stage in kg, k is the stiffness of the bearing in N/m, and C is the damping of the bearing in N/m.

The position and velocity of the spring-damper is presented as follows:

$$\begin{bmatrix} x_i \\ y_i \\ z_i \\ 1 \end{bmatrix} = \begin{bmatrix} x - P_{iy}\theta_z + P_{iz}\theta_y \\ y + P_{ix}\theta_z - P_{iz}\theta_x \\ z - P_{ix}\theta_y + P_{iy}\theta_x \\ 1 \end{bmatrix}$$
$$\begin{bmatrix} \dot{x}_i \\ \dot{y}_i \\ \dot{z}_i \\ 1 \end{bmatrix} = \begin{bmatrix} \dot{x} - P_{iy}\dot{\theta}_z + P_{iz}\dot{\theta}_y \\ \dot{y} + P_{ix}\dot{\theta}_z - P_{iz}\dot{\theta}_x \\ \dot{z} - P_{ix}\dot{\theta}_y + P_{iy}\dot{\theta}_x \\ 1 \end{bmatrix} \quad (2)$$

where x_i, y_i, and z_i represent the local bearing position in m, $\dot{x}_i, \dot{y}_i, \dot{z}_i$ is the velocity of local bearing position in m/s, x, y, and z represent the displacement in m, and θ_x, θ_y, and θ_z are the rotation angles in rad, P_{ix}, P_{iy}, and P_{iz} is the initial bearing position in m.

The Lagrangian equation can be written as follows:

$$\frac{d}{dt}\left(\frac{\partial T}{\partial \dot{q}_i}\right) + \frac{\partial V}{\partial q_i} + \frac{\partial D}{\partial \dot{q}_i} = \tau_i \quad (3)$$

Where $q = \begin{bmatrix} x & y & z & \theta_x & \theta_y & \theta_z \end{bmatrix}^T$

and $\tau = \begin{bmatrix} f_x & f_y & f_z & \tau_x & \tau_y & \tau_z \end{bmatrix}^T$

where f_x, f_y, and f_z, and τ_x, τ_y, and τ_z represent the axial force and torque about the X, Y, and Z axes, respectively.

Substituting Eq. (2) into Eq. (1), with the derivatives $\partial T/\partial \dot{q}$, $\partial V/\partial q$, and $\partial D/\partial \dot{q}$, and then substituting into Eq. (3). The motion equation of the linear axis can be presented as follows:.

$$[M]\ddot{q} + [C]\dot{q} + [K]q = [G]F \quad (4)$$

where [M] is the mass matrix, [C] is the damping matrix, and [K] is the stiffness matrix.

DEVELOPMET OF SIX DOF MOTION EQUATION FOR A FOUR-AXIS MACHINE TOOL

The four-axis machine tool in Figure 2 is separated into the two parts: the cutting tool XZ and workpiece YC. Thus, the forces acting on the X-axis include the driving force of the motor (F_{m1}) and the disturbance force from the Z-axis (F_{d1}). Seminally, the forces acting on the Y-axis also include the driving force of the motor (F_{m2}) and the disturbance force from the C-axis (F_{d2}). The motion equations of the four-axis machine can be obtained as follows:

FIGURE 2. Prototype of four-axis machine tool.

$$
\begin{aligned}
&[M_1]\ddot{q}_1 + [C_1]\dot{q}_1 + [K_1]q_1 = [G_{m1}]F_{m1} + [G_{d1}]F_{d1} \\
&[M_3]\ddot{q}_3 + [C_3]\dot{q}_3 + [K_3]q_3 = [G_3]F_3 \\
&[M_2]\ddot{q}_2 + [C_1]\dot{q}_2 + [K_2]q_2 = [G_{m2}]F_{m2} + [G_{d2}]F_{d2} \\
&[M_4]\ddot{q}_4 + [C_4]\dot{q}_4 + [K_4]q_4 = [G_4]F_4
\end{aligned} \tag{5}
$$

where M_1 , M_2, M_3 , M_4 are mass matrix of tables of X, Y, Z, C axis respectively, K_1 , K_2, K_3 , K_4 are stiffness matrix and C_1 , C_2, C_3 , C_4 are damping matrix of bearings.

$$q = [x \quad y \quad z \quad \theta_x \quad \theta_y \quad \theta_z]$$

and the disturbance forces can be separated as follows:

$$[M_1]\ddot{q}_{d1} + [C_1]\dot{q}_{d1} + [K_1]q_{d1} = [G_{d1}]F_{d1} \tag{6}$$

$$[M_2]\ddot{q}_{d2} + [C_2]\dot{q}_{d2} + [K_2]q_{d2} = [G_{d2}]F_{d2} \tag{7}$$

We first ignored the disturbance forces from Z. The C-axis was separated into the X and Y axes and we used a state-space method to obtain the position (x, y, and z) and angle (θ_x, θ_y, and θ_z) for each axis. Eq. (5) can be written as follows:

$$[M]\ddot{q} + [C]\dot{q} + [K]q = [G]F \tag{8}$$

In which

$$[M] = \begin{bmatrix} M_1 & 0 & 0 & 0 \\ 0 & M_3 & 0 & 0 \\ 0 & 0 & M_2 & 0 \\ 0 & 0 & 0 & M_4 \end{bmatrix}, [C] = \begin{bmatrix} C_1 & 0 & 0 & 0 \\ 0 & C_3 & 0 & 0 \\ 0 & 0 & C_2 & 0 \\ 0 & 0 & 0 & C_4 \end{bmatrix}$$

$$[K] = \begin{bmatrix} K_1 & 0 & 0 & 0 \\ 0 & K_3 & 0 & 0 \\ 0 & 0 & K_2 & 0 \\ 0 & 0 & 0 & K_4 \end{bmatrix}, [G] = \begin{bmatrix} G_{m1} & 0 & 0 & 0 \\ 0 & G_3 & 0 & 0 \\ 0 & 0 & G_{m2} & 0 \\ 0 & 0 & 0 & G_4 \end{bmatrix}$$

$$F = \begin{bmatrix} F_{m1} \\ F_3 \\ F_{m2} \\ F_4 \end{bmatrix}, q = \begin{bmatrix} q_{m1} \\ q_3 \\ q_{m2} \\ q_4 \end{bmatrix} \tag{9}$$

The mass, stiffness, damping, and position matrix for each axis can be obtained as described in [3].

Equation (8) is converted into Eq. (10), and the state-space model can be used to solve the dynamic problem in the Simulink environment.

$$\begin{cases} \dot{X} = AX + BU \\ Y = C'X \end{cases} \tag{10}$$

Similarly, Eq. (6) can be converted into Eq. (11), and the state-space model can be used to solve the dynamic problem in the Simulink environment to calculate the influences of the disturbance force from the Z-axis acting on the X-axis.

$$\begin{cases} \dot{X}_{d1} = A_{d1}X_{d1} + B_{d1}U \\ Y_{d1} = C_{d1}'X_{d1} \end{cases} \tag{11}$$

Similarly, Eq. (7) can be converted into Eq. (12), and the state-space model can be used to solve the dynamic problem in the Simulink environment to calculate the influences of the disturbance force from C-axis acting on the Y-axis.

$$\begin{cases} \dot{X}_{d2} = A_{d2}X_{d2} + B_{d2}U \\ Y_{d2} = C_{d2}'X_{d2} \end{cases} \tag{12}$$

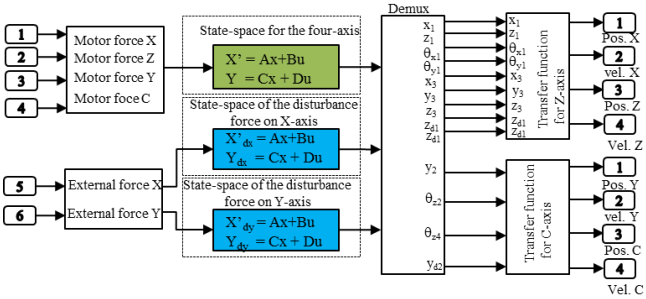

FIGURE 3. Dynamic modeling of the four-axis machine tool.

The state-space is applied to solve equations (10), (11), and (12), the dynamic modeling of the four-axis machine tool is established as figure 3. It includes three blocks: control system block, dynamic analysis block and transform matrix block.

RESULTS

The dynamic modeling of the four-axis machine is described as Fig.3. This dynamic model was combined with the control system of PMAC to simulate FRF of machine [7, 8]. The simulation

and experiment results were described in Figure 4.

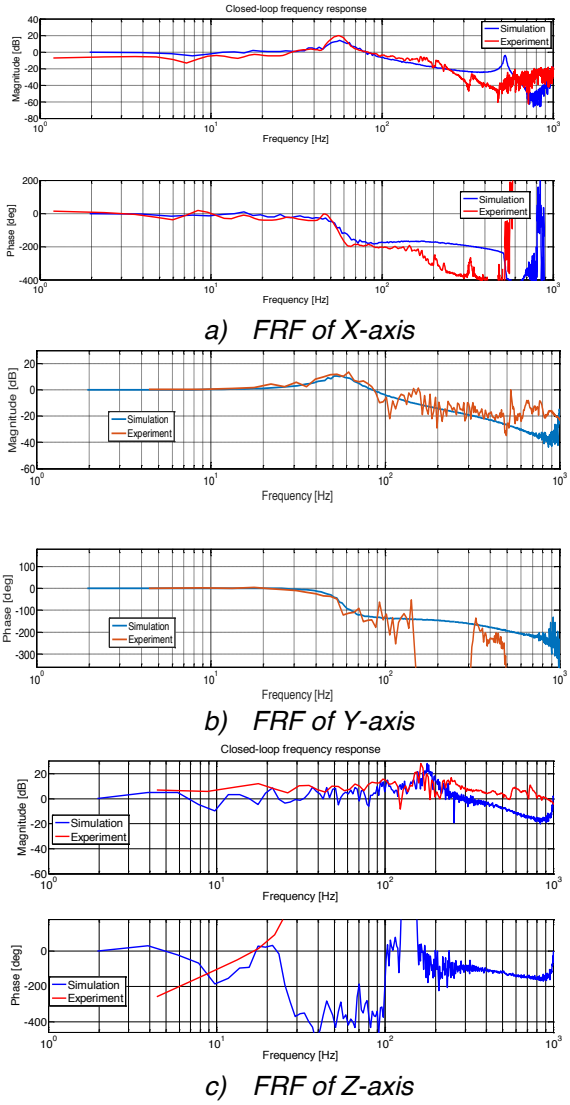

a) FRF of X-axis

b) FRF of Y-axis

c) FRF of Z-axis

FIGURE 4. Comparison FRF between Simulation and experiment results on Four-axis machine.

The differences between simulation results and experimental data were in good agreement on X and Y-axis. The experimental data on Z-axis was not good because the balance system had problem in experiment process. This problem will be solved in the future works.

CONCLUSIONS

This study proposed a novel mathematical method to analyse the dynamic of complex configurations and multi-axis machine tool. Its accuracy was demonstrated through experimental data and simulation results of a four-axis machine tool. The dynamic equations of the four-axis machine tool are generated and the dynamic model is established.

This method transfers the complex multi-axis machine into the some multiple one-axis machines to analyze the dynamic easier. The dynamic analysis was applied for the control systems to optimize the control signals and the vibrations through the frequency response function. The frequency response function estimated that no need to do the experiments.

REFERENCES

[1] Altintas Y, Brecher C, Weck M, Witt S. Virtual Machine Tool. CIRP- Manufacturing Technology. 2005; 54: 115-138.

[2] Altintas Y, Cao Y. Virtual Design and Optimization of Machine Tool Spindles. CIRP Annals - Manufacturing Technology. 2005; 54: 379-382.

[3] Zhang H, Zhao W, Du C, Liu H, Zhang J. Dynamic modeling and analysis for gantry-type machine tools considering the effect of axis coupling force on the slider–guide joints' stiffness. Journal of Mechanical Engineers. 2015; 230: 2036-2046.

[4] Kumar U, Schmitz T. Spindle dynamics identification for Receptance Coupling Substructure Analysis. Precision Engineering. 2012; 36: 435-443.

[5] Ohta H, Hanaoka G, Ueki Y. Sticking of a Linear-Guideway Type Recirculating Ball Bearing. Journal of Tribology. 2017; 139: 031103-1~031103-6.

[6] Jorgensen B, Shin Y. Dynamics of Machine Tool Spindle/Bearing Systems Under Thermal Growth. Journal of Tribology. 1997; 119: 875-882.

[7] Song C, Kwon S, Kim B, Ro S, Lee S. Dynamic Simulation of Multi-axis Machine Tools and Its Experimental verification. ASPE Annual Meeting, Boston, 2014.

[8] Kwon S, Song C, Kim B, Lee H. Physical Modeling and Experimental Verification for Multi-Axis Machinery Equipment. KSPE Conference, 2013. (in Korean)

SOFTWARE-BASED COMPENSATION OF VIBRATION-INDUCED ERRORS OF A COMMERCIAL DESKTOP 3D PRINTER

Deokkyun Yoon, Molong Duan, and Chinedum E. Okwudire
Department of Mechanical Engineering
University of Michigan
Ann Arbor, MI

OVERVIEW

Commercial desktop 3D printers are designed with light, but flexible, structures and driven with stepper motors to reduce their cost, size and weight. As a result, parts manufactured on such 3D printers suffer from surface waviness and registration errors (caused by stepper motors skipping counts) due to excessive vibration triggered by the motion of the print head or build platform. Such vibration-induced errors not only mar the aesthetics of 3D printed parts, but often lead to highly distorted and hence scrapped parts. The most common solution to this problem, not involving hardware modifications, is to reduce motion speed at the expense of productivity. This paper demonstrates the use of a software-based method called filtered B-splines (FBS) for mitigating vibration-induced errors of 3D printers without sacrificing productivity. In the FBS method, the motion command sent to the machine is parameterized using B-splines, whose basis functions are filtered using a model of the machine's dynamics. The control points associated with the filtered basis functions are then selected to minimize tracking errors. The effectiveness of the FBS method in mitigating surface waviness and registration errors is demonstrated on parts printed on a commercial desktop 3D printer.

INTRODUCTION

3D printing (aka additive manufacturing) is becoming a popular means for prototyping and manufacturing of complex part geometries. It is currently a $7.3 billion industry and, by 2020, the market for 3D printers and the accompanying services is expected to eclipse $21 billion [1]. Due to their relatively low cost, the commercial use of desktop 3D printers (i.e., printers priced below $5,000) is expanding in industries where customization and personalized products are important for consumers, e.g., prosthetics, jewelry, and accessories [2]. The cost of desktop 3D printers has been lowered, in large part, by constructing them using fewer and lighter structural members, and by controlling them using stepper motors driven by open-source micro-controllers. However, the resulting structural flexibilities cause the printers to vibrate excessively as the print head and/or build platform move rapidly during printing, thus causing errors that compromise printing performance. One common error caused by excessive vibration is surface waviness which mars the aesthetics of the 3D printed part, as shown in *FIGURE 1* (a). Moreover, as the machine vibrates, its stepper motors (which have no feedback sensors) are often unable to provide enough torque to hold position, hence they skip counts (i.e., lose track of their position) resulting in so-called registration errors. As shown in *FIGURE 1* (b), registration errors often distort the printed part severely, causing it to be scrapped.

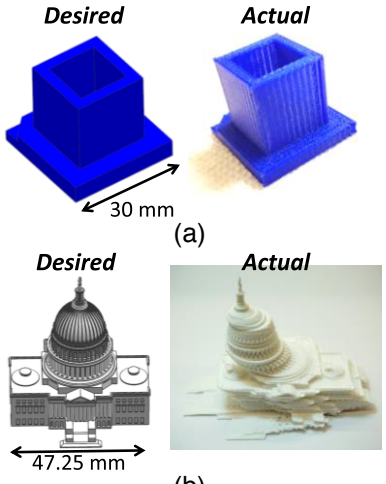

FIGURE 1. Excessive vibration of desktop 3D printers causes (a) aesthetically unpleasing surface waviness, and (b) scrapped part due to registration errors.

Vibration-induced errors in CNC manufacturing machines can be dealt with via hardware

modifications, e.g., by stiffening the machine or adding damping [3]. However, such solutions often involve additional material costs and weight, which are not desirable for desktop 3D printers. The errors could also be mitigated via active vibration control techniques [3]. However, such control techniques require feedback sensors and high-sample-rate real-time control hardware, which are not commercially viable for low-cost desktop 3D printers. An alternative approach, that does not require extra hardware or active control, is to generate the motion commands sent to the machine such that unwanted vibration is avoided or reduced (i.e., feedforward control) [3]. The most popular approach for achieving this goal, used on most desktop 3D printers, is to generate motion commands that are smooth (i.e., commands that have little or no high-frequency content). However, the attenuated high-frequency content of smooth motion commands often implies loss of motion speed (productivity), and results in suboptimal vibration reduction, because knowledge of the machine's dynamics is not exploited [3, 4]. Better vibration reduction can be achieved by using filters (e.g., FIR filters) or input shapers to generate motion commands with low frequency content around the resonance modes of the machine (assuming that its dynamics is known). However, filters and input shapers introduce time delays, which sacrifice productivity, and could severely degrade accuracy [4]. Okwudire et al. [4] presented a filtered B-spline (FBS) motion command optimization method for minimizing vibration-induced tracking errors subject to kinematic limits of a machine, without introducing time delays. The effectiveness of the FBS method was demonstrated in laboratory experiments by measuring the vibration of a metal block attached to a motion stage. However, its effectiveness in improving the quality of a manufactured part via online implementation was not studied. In this paper, the FBS method is briefly reviewed, and its online implementation on a commercial desktop 3D printer with structural flexibilities is presented. Parts are manufactured on the 3D printer, with and without the FBS method, and significant reductions in vibration-induced surface waviness and registration errors, without sacrificing productivity, are demonstrated.

OVERVIEW OF MOTION COMMAND OPTIMIZATION USING FILTERED B-SPLINES

FIGURE 2 (a) shows the servo dynamics, **G**, of a CNC machine to which motion command, **r**, is inputted and actual motion, **y**, is outputted. Due to the dynamics (e.g., structural flexibilities) present in **G**, tracking error, **e** = **r** – **y**, is created. In order to minimize **e**, a motion command optimizer, **C**, is introduced, as shown in *FIGURE 2* (b), to modify **r** to an optimal form, **r***, based on knowledge of the machine dynamics.

(a) *(b)*

FIGURE 2. Servo dynamics of CNC machine (a) without, and (b) with motion command optimization.

To achieve this goal, **r*** is assumed to be parameterized (temporally, not spatially) using a B-spline curve of degree m and $n + 1$ coefficients (control points), such that [4]

$$\underbrace{\begin{bmatrix} r^*(0) \\ r^*(1) \\ \vdots \\ r^*(E) \end{bmatrix}}_{\mathbf{r}^*} = \underbrace{\begin{bmatrix} N_{0,m}(\xi_0) & N_{1,m}(\xi_0) & \cdots & N_{n,m}(\xi_0) \\ N_{0,m}(\xi_1) & N_{1,m}(\xi_1) & \cdots & N_{n,m}(\xi_1) \\ \vdots & \vdots & \ddots & \vdots \\ N_{0,m}(\xi_E) & N_{1,m}(\xi_E) & \cdots & N_{n,m}(\xi_E) \end{bmatrix}}_{\mathbf{N}} \underbrace{\begin{bmatrix} p^*(0) \\ p^*(1) \\ \vdots \\ p^*(n) \end{bmatrix}}_{\mathbf{p}^*} \quad (n \le E) \tag{1}$$

where **N** and **p** are the basis function matrix and coefficient vector, respectively, while 0, 1, …, E are discrete time steps, and $\xi \in [0, 1]$ is the spline parameter, representing normalized time. A uniform knot vector $\mathbf{g} = \begin{bmatrix} g_0 & g_1 & \cdots & g_{m+n+1} \end{bmatrix}^T$ and matrix **N** are generated as

$$g_k = \begin{cases} 0 & 0 \le k \le m \\ \dfrac{k-m}{n-m+1} & m+1 \le k \le n \\ 1 & n+1 \le k \le m+n+1 \end{cases} \tag{2}$$

$$N_{j,m}(\xi) = \frac{\xi - g_j}{g_{j+m} - g_j} N_{j,m-1}(\xi) + \frac{g_{j+m+1} - \xi}{g_{j+m+1} - g_{j+1}} N_{j+1,m-1}(\xi)$$
$$\left(N_{j,0}(\xi) = \begin{cases} 1 & g_j \le \xi < g_{j+1} \\ 0 & \text{otherwise} \end{cases} \right) \tag{3}$$

Applying the modified (i.e., optimized) motion command, **r***, to the machine yields

$$\mathbf{y} = \mathbf{G}\mathbf{r}^* = \mathbf{G}\mathbf{N}\mathbf{p}^* = \tilde{\mathbf{N}}\mathbf{p}^* \tag{4}$$

where $\tilde{\mathbf{N}}$ is the filtered basis function matrix (i.e., **N** filtered by **G**). The optimal coefficients, $\mathbf{p}^*$, can be calculated by minimizing the 2-norm of **e**, resulting in the well-known least-squares solution:

$$\mathbf{p}^* = \left(\left(\tilde{\mathbf{N}}^T\tilde{\mathbf{N}}\right)^{-1}\tilde{\mathbf{N}}^T\right)\mathbf{r} \quad (5)$$

The motion command optimizer, **C**, therefore becomes

$$\mathbf{C} = \mathbf{N}\left(\left(\tilde{\mathbf{N}}^T\tilde{\mathbf{N}}\right)^{-1}\tilde{\mathbf{N}}^T\right) \quad (6)$$

B-splines exhibit a local property, meaning that a change in the lth coefficient, $p^*(l)$, influences only a small subset of $\mathbf{r}^*$. Using this local property, $\mathbf{p}^*$ (hence $\mathbf{r}^*$) can be calculated in small batches, as in look-ahead functionalities of modern CNCs, without requiring the controller to read the entire G-code in advance [5]. This feature drastically reduces the computational cost of the FBS method [5], thus facilitating recursive online implementation of the motion command optimizer, **C**, on low-cost desktop 3D printers, as demonstrated below.

APPLICATION OF FBS METHOD TO COMMERCIAL DESKTOP 3D PRINTER

Experimental set-up: Commercial desktop 3D printer

FIGURE 3 shows a commercially available desktop 3D printer (HICTOP Prusa i3) used in this paper to demonstrate the compensation of vibration-induced errors based on the FBS method. The motion of the printer's build platform is along the *x*-axis, while its print head moves along the *y*- and *z*-axes. All three axes of the printer are controlled by stepper motors, but the focus of this study is on controlling its *x*- and *y*-axis motions which generate significant vibration, due to the printer's flexible structure, as its print head and build platform move.

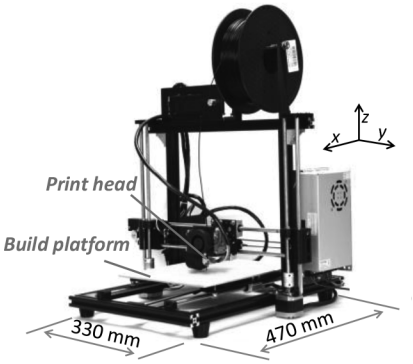

FIGURE 3. Commercial desktop 3D printer (HICTOP Prusa i3) used in this study.

FIGURE 4 shows the measured and curve fit *x*- and *y*-axis frequency response functions (FRFs) of the 3D printer. The FRFs are measured by applying swept sine acceleration signals to the printer's stepper motors (each having 12.5 μm stepping resolution) and measuring the relative acceleration of the build platform and print head using accelerometers (PCB Piezotronics 393B05 and Kistler 8704B100). The curve fit model is generated using MATLAB®'s *invfreqs* function. To identify the FRFs and implement the FBS method, the printer's proprietary motion controller is bypassed. Instead, axis-level motion (i.e., step and direction) commands are sent to the printer's stepper motors at 1 kHz sampling rate using a real-time controller (dSPACE DS1007 and DS5203) via stepper motor drives (Pololu DRV8825). A script written in MATLAB® reads a G-code file (generated using Cura™ software package) and parses the G-code information into axis-level motion commands, emulating motion command generators of 3D printers. The real-time controller optimizes the motion commands using the FBS method following the procedure outlined in the preceding section.

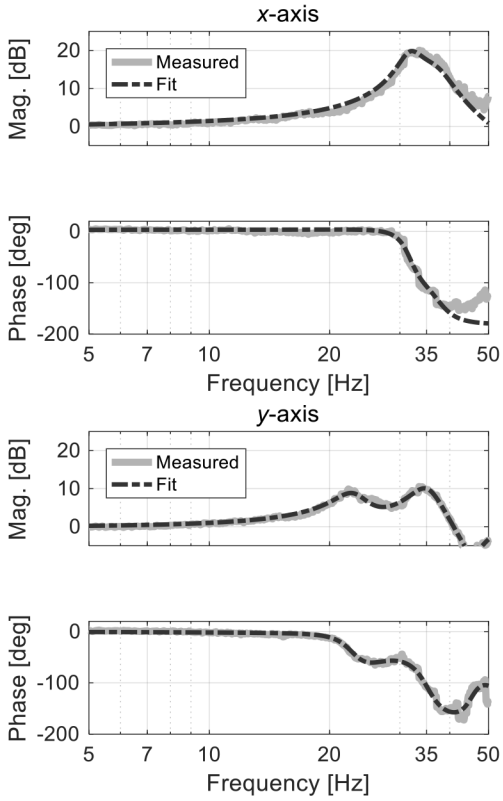

FIGURE 4. Frequency response functions of x- and y-axes of the 3D printer. Least-squares curve fitting is used to identify the axis level dynamics.

Case study I: Mitigation of surface waviness of 3D printed part

The square block model shown in *FIGURE 1* (a) is printed using the 3D printer of *FIGURE 3* with different acceleration limits imposed on the motion commands (while maintaining the feedrate at 60 mm/s for all cases). For each case, the part is printed using the unmodified motion commands (as the baseline approach), as well as the motion commands optimized via the FBS method. *FIGURE 5* (a) and (b) show the blocks printed using the two methods (both using acceleration limit of 7 m/s^2), and the 3D surface profile, *h*, of the highlighted surfaces, measured using a laser displacement sensor (Keyence LK G-10). Notice that the vibration-induced surface waviness of the baseline case is significantly reduced by the FBS method. *FIGURE 6* compares the surface roughness (RMS *h* values) of blocks printed using different acceleration limits. Observe that the surface quality of the baseline approach deteriorates significantly at higher acceleration limits compared to that of the FBS method, which stays relatively consistent for all acceleration limits investigated.

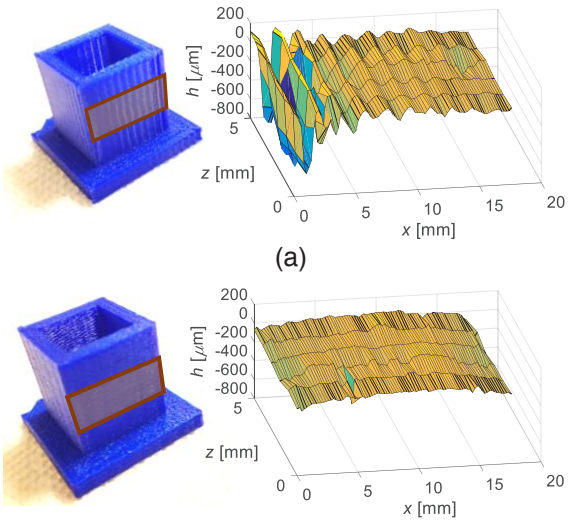

FIGURE 5. Comparison of photographs and measured surface profiles (h) of the highlighted surfaces of blocks printed using (a) baseline approach and (b) FBS method (both with acceleration limit of 7 m/s^2). Vibration-induced surface waviness of baseline case is greatly attenuated using FBS.

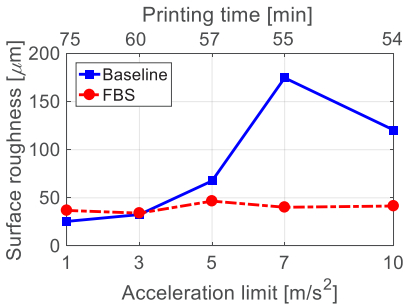

FIGURE 6. Surface roughness of 3D printed blocks comparing x- & y-axes commands generated using baseline (unmodified) and FBS (optimized) methods for different acceleration limits (total printing time).

Case study II: Mitigation of registration errors in 3D printed part

A scale model of the US Capitol, shown in *FIGURE 1* (b), is printed to demonstrate the common problem of vibration-induced registration errors in 3D printed parts, and the ability of the FBS method to mitigate them. The part is printed using the baseline approach and the FBS method, with different acceleration limits, while keeping the feedrate at 60 mm/s. As shown in *TABLE 1*, registration errors occur with the baseline case as the acceleration limit is increased above 3 m/s^2, causing severe distortion of the printed parts. However, the parts printed using the FBS method do not exhibit such registration errors. As a result, the FBS method enables quality prints at much shorter printing times compared to the baseline case.

To explain the reason for the registration errors, *FIGURE 7* compares the measured *x*-axis acceleration between print head and build platform for the baseline approach and FBS method (both with 7 m/s^2 acceleration limit). Notice that even though the acceleration of the motion command is limited to 7 m/s^2 (excepts for a few spikes here and there due to short distance travels), the actual acceleration of the baseline case turns out to be more than double this limit, because the build platform's motion heavily excites the resonance modes of the machine. The excessive vibration (i.e., acceleration) causes inertial loads that exceed the holding torque of the motors, hence they skip counts and lose track of their position. On the other hand, the FBS method maintains actual acceleration levels that are closer to the desired limit, hence avoiding the registration errors.

TABLE 1. 3D printed models of US Capitol using different acceleration limits (which influences total printing time). The FBS method eliminates the registration errors observed in the baseline case at higher acceleration limits; the feedrate is 60 mm/s for all cases.

Acc. limit	Printing time	Baseline	FBS
1 m/s^2	3:59 h		
3 m/s^2	2:42 h		
5 m/s^2	2:22 h		
7 m/s^2	2:12 h		
10 m/s^2	2:06 h		

CONCLUSION AND FUTURE WORK

The filtered B-spline (FBS) method [4] is implemented on a commercial desktop 3D printer to mitigate its vibration-induced errors. Two commonly observed classes of vibration-induced errors in 3D printed parts (i.e., surface waviness and registration errors) are investigated. Compared to the baseline approach, the FBS method is shown to significantly reduce surface waviness and eliminate registration errors for the cases studied, thus allowing the production of high quality printed parts at higher speed (i.e., shorter manufacturing time). Future work will implement the FBS method on low-cost open-source micro-controllers like Arduino and Raspberry Pi, rather than dSPACE, to further demonstrate its low computational cost and suitability for commercial desktop 3D printers.

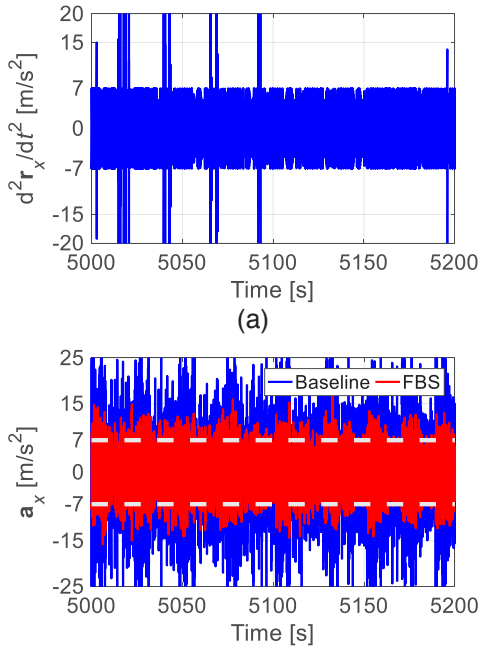

FIGURE 7. (a) Acceleration profile of x-axis reference command (unmodified). (b) On-machine measurement of x-axis acceleration. Dashed lines indicate the acceleration limit (7m/s^2) imposed.

REFERENCES

[1] Wohlers T, 3D Printing and additive manufacturing state of the industry annual worldwide progress report, Wohlers Report, 2015.

[2] Zaleski A, Here's why 2016 could be 3D printing's breakout Year, Fortune, http://fortune.com/2015/12/30/2016-consumer-3d-printing/, Accessed on Feb. 14th, 2017.

[3] Altintas Y, Verl A, Brecher C, Uriarte L, Pritschow G, Machine tool feed drives, CIRP Annals-Manufacturing Technology, 2011; 60(2): 779-796.

[4] Okwudire C, Ramani K, Duan M, A trajectory optimization method for improved tracking of motion commands using CNC machines that experience unwanted vibration, CIRP Annals-Manufacturing Technology, 2016; 65(1): 373-376.

[5] Duan M, Yoon D, Okwudire C, A limited-preview filtered B-spline approach to tracking control – with application to vibration-induced error compensation of a commercial 3D printer, Under preparation

DECOUPLABLE COARSE-FINE STAGE FOR IMPROVED PRECISION AND EFFICIENCY IN POINT-TO-POINT POSITIONING

Deokkyun Yoon, Bowen Zeng, and Chinedum E. Okwudire
Department of Mechanical Engineering
University of Michigan
Ann Arbor, MI

OVERVIEW

A decouplable coarse-fine linear stage design approach that enables improved precision and energy efficiency during rapid point-to-point positioning (i.e., stepping motion) is presented. The coarse stage is driven by an efficient rotary motor (via rack and pinion), mounted directly to the ground (i.e., no vibration isolation). On the other hand, the fine stage is driven by a less-efficient but more precise linear motor, which is mounted on the vibration-isolated machine base. The coarse stage drives the moving table with high efficiency and lowers residual vibration during the initial phases of the stepping motion, where actuation force requirements are high and vibration isolation is not needed. It is decoupled from the table, and the fine stage completes the final portion of the motion, where force requirements are low and precision/vibration isolation requirements are high. Experiments conducted with a prototype decouplable coarse-fine stage (at 0.5 m/s and 10 m/s^2 maximum speed and acceleration) demonstrate up to 92% improvement in linear motor heating and 82% reduction in residual vibration, respectively, compared to driving the table entirely by the fine stage.

INTRODUCTION

Linear motion stages are widely used in advanced manufacturing applications that require rapid and precise point-to-point positioning (stepping motion) such as substrate (e.g., Si wafer and glass) patterning and inspection [1, 2]. To reduce the effect of ground vibration being transmitted into the precise positioning, motion stages typically employ soft springs for isolation [3]. However, the presence of soft springs induces residual vibration during rapid motions, which degrade the precision of the stage [4]. To solve the residual vibration problem, passive and active approaches such as reaction force filtering [5], counter mass [6], and active vibration cancellation [7] are used. Moreover, to provide rapid motions (i.e., motions with large acceleration and speed magnitudes), linear motors (LM) must produce large actuation forces, requiring large electric currents, because they lack mechanical advantage [8]. The resulting copper losses lead to overheating of the motor coils and loss of efficiency. The most common solutions to the heat problem (and subsequent thermal errors) are forced cooling [9] and thermal compensation [10].

Most of the approaches discussed above focus on the residual vibration or overheating problem separately, without acknowledging the fact that the two are linked. Addressing the two problems simultaneously, the authors presented a permanent magnet (PM) based assist device approach that simultaneously reduces the LM actuation force requirements and residual vibration of isolated base for scanning (i.e., repeated back and forth) motions [11]. However, the PM assist device approach is not very effective for point-to-point stepping motions, which require the stage to stop at a given location for a period of time.

This paper presents a decouplable coarse-fine stage approach that achieves the simultaneous reductions of the LM actuation force and residual vibration of stage in point-to-point positioning scenarios.

DECOUPLABLE COARSE-FINE STAGE

Design concept

Figure 1 shows a schematic of the proposed decouplable coarse-fine stage design. Vibration isolators are used to isolate the machine base from the ground to ensure precise positioning during manufacturing. The fine stage (FS), mounted on the isolated base, is driven by LM force (u_{FS}), while the stage position (x_{FS}) is measured relative to the base. Due to the low-stiffness vibration isolators, the reaction force of

linear motor (u_{FS}) creates the residual vibration of base.

For point-to-point positioning, tracking errors while the stage is in motion (i.e., when the reference trajectory has non-zero velocity and acceleration) are not as important as the tracking errors at final positions. Therefore, to mitigate residual vibration during the high-acceleration portions of motion, a decouplable coarse stage (CS) is installed as shown in Figure 1. The CS is mounted on the machine ground and driven by another actuation force (u_{CS}), with higher efficiency than an LM. The bumpers mounted in-between the CS and FS ensure smooth (de)coupling of the stages (i.e., the bumpers absorb collision impact if there is relative velocity between the stages). As long as there is a finite distance between the FS and bumpers (i.e., $d > 0$ or $d < 2\delta$, where δ is the nominal gap between the FS and bumper), the two stages become decoupled and the vibration isolation performance of the original stage (i.e., the FS alone) is preserved. The kinematic limits of the two stages are chosen to be similar in magnitudes, such that the CS and FS can travel together in parallel. Note that the idea of a decouplable coarse-fine stage is not new (e.g., see [12]). However, the unique features of the proposed concept are: (1) when coupled, the CS and FS are driven in parallel not in series as in [12]; and (2) the CS is mounted on the ground while the FS is mounted to the isolated base, which is different from [12] where both stages are mounted on the isolated base.

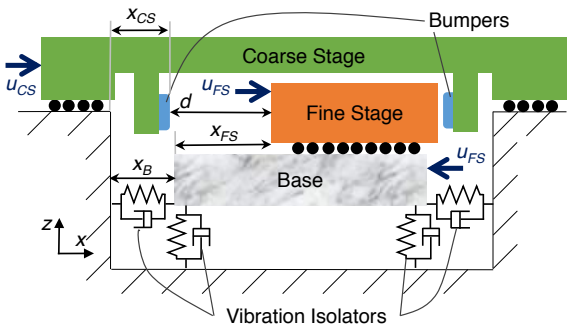

FIGURE 1. Schematic of proposed decouplable coarse-fine stage design.

Control strategy

The proposed decouplable coarse-fine stage is controlled to track two reference trajectories (r_{CS} and r_{FS}) using two 2-DOF controllers as shown in Figure 2. The controller and mechanical dynamics of the coarse-fine stage are respectively denoted with C and P, while the subscripts FB and FF are respectively used to indicate feedback and feedforward controllers. The main goal of these controllers is to have the FS track r_{FS} when reference velocity and acceleration ($r_{v,FS}$ and $r_{a,FS}$) are near zero.

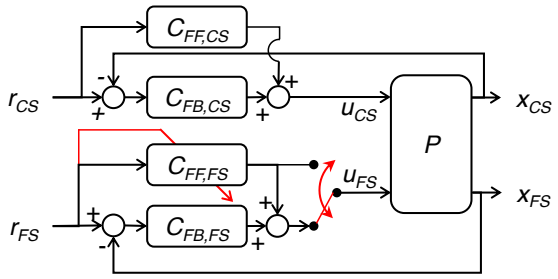

FIGURE 2. Controller block diagram of proposed decouplable coarse-fine stage.

A switching controller scheme is proposed for the FS control, so that the actuators driving FS and CS do not interfere each other when the bumpers are in contact. When the FS undergoes rapid positioning, $C_{FB,FS}$ (e.g., a PID-type controller with anti-windup) is deactivated, leaving the feedforward controller ($C_{FF,FS}$) alone for controlling the FS. The reference-specific feedforward controller is

$$C_{FF,FS}(s) = \begin{cases} u_{FS,acc} & r_{a,FS} > r_{a,thre} \\ m_{FS}s^2 & |r_{a,FS}| \le r_{a,thre} \\ u_{FS,dec} & r_{a,FS} < -r_{a,thre} \end{cases} \quad (1)$$

where the reference acceleration for FS ($r_{a,FS}$) is obtained by filtering r_{FS} through a double differentiator (e.g., s^2 in the Laplace domain). The reference acceleration threshold ($r_{a,thre}$) is used to determine the output of $C_{FF,FS}$ and the switching behavior of $C_{FB,FS}$ (i.e., if $|r_{a,FS}| > r_{a,thre}$, $C_{FB,FS} = 0$). During acceleration/deceleration, small magnitude forces ($u_{FS,acc}$ and $u_{FS,dec}$) are applied on the FS, so that it is pushed against the CS. This way, sensor-less control of d is achieved and the FS does not bounce between the bumpers excessively during the rapid positioning. The controllers for CS ($C_{FB,CS}$ and $C_{FF,CS}$) can be conventional (i.e., PID-type and acceleration feedforward, respectively).

As shown in Figure 1 and explained in the Design concept section, the bumpers make contact when d is 0 or 2δ. Consequently, if r_{CS} is generated according to r_{FS} such that correct d is maintained, very little control input force u_{FS} is

required. Therefore, the desired reference trajectory for CS ($r_{CS,des}$) is obtained by adding/subtracting δ to/from r_{FS}, based on assumption that $x_B \approx 0$;

$$r_{CS,des}(t) = \begin{cases} r_{FS}(t) + \delta & r_{a,FS}(t) > r_{a,thre} \\ r_{FS}(t) & |r_{a,FS}(t)| \le r_{a,thre} \\ r_{FS}(t) - \delta & r_{a,FS}(t) < -r_{a,thre} \end{cases} \quad (2)$$

However, $r_{CS,des}$ based on Eqn. (2) has trajectory discontinuities, thus the kinematic limits of the stage are violated. The optimal CS reference ($r_{CS,opt}$) satisfying the kinematic limits can be solved by minimizing the objective function (J);

$$\begin{aligned} &\text{minimize } J = \left(\mathbf{r}_{CS,opt} - \mathbf{r}_{CS,des}\right)^{\mathrm{T}} \left(\mathbf{r}_{CS,opt} - \mathbf{r}_{CS,des}\right) \\ &\textit{s.t.} \\ &\max\left(\mathbf{r}_{a,CS,opt}\right) \le a_{\max} \\ &\min\left(\mathbf{r}_{a,CS,opt}\right) \ge -a_{\max} \\ &\left|\mathbf{r}_{CS,opt}(i) - \mathbf{r}_{CS,des}(i)\right| \le \varepsilon \text{ for } \left|\mathbf{r}_{a,CS,des}(i)\right| \le r_{a,thre} \end{aligned} \quad (3)$$

where the bold face font is used to indicate discrete time sampled column vectors. Note that |·| is used to indicate absolute value of each vector element. The max(·) and min(·) operators respectively compute the maximum and minimum value element of the vector they operate on. The CS acceleration limit (a_{max}) ensures the solved $\mathbf{r}_{CS,opt}$ can be tracked by the CS. In addition, a fitting bound (ε) provides $\mathbf{r}_{CS,opt}$ very similar to $\mathbf{r}_{CS,des}$ for the acceleration/deceleration phases of motion (i.e., priority is given to fitting the acceleration/deceleration phases). Figure 3 shows the illustrative reference trajectory $r_{CS,opt}$ solved by the proposed optimization approach during the initial acceleration phase of a point-to-point motion. Notice that $r_{CS,des} \approx r_{CS,opt}$ during the acceleration portion of the trajectory.

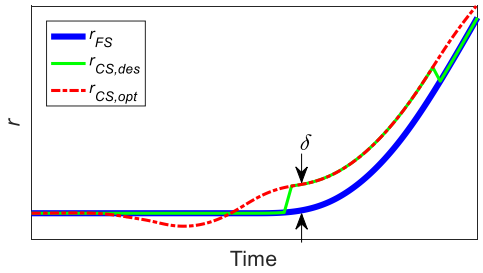

FIGURE 3. Illustration of the coarse-stage reference trajectory (r_{CS}) optimization process.

PROTOTYPE COARSE-FINE STAGE

A decouplable coarse-fine stage prototype is designed and manufactured according to the proposed design concept. Figure 4 shows the CAD model of the prototype.

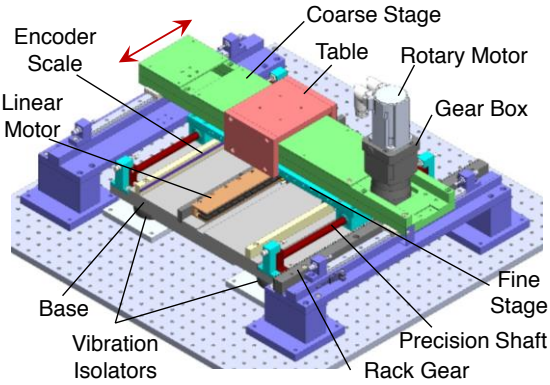

FIGURE 4. CAD model of decouplable coarse-fine stage prototype.

An air-core linear motor (Aerotech, BLMUC-95) drives the FS, guided by air bushings (New Way, S8013E02) riding on precision ground shafts. The FS position is measured by a linear encoder (Renishaw, T1000 readhead with 20 μm pitch scale) with 4.88 nm post-interpolation resolution (dSPACE, DS3002). A table for mounting substrates is attached to the FS. The FS is mounted on a 400 mm × 400 mm × 33 mm steel base, which is isolated from the ground via rubber vibration isolators (Vibra Systems, LF6045). A rotary servo motor (Kollmorgen, AKM21C) with a gear reducer with the 10:1 speed ratio (Stöber, PE series) drives the CS, which is riding on linear bearings (Misumi, SE2BLV16) attached to the machine ground. To convert from rotary motion to linear motion, rack and pinion gears (Atlanta Drive Systems, Module 2 Class 10) are installed for the CS. PWM amplifiers (Aerotech, Soloist CP10 and Kollmorgen, AKD P00606) power the motors with the 47 N and 1,059 N maximum (equivalent) force limits, respectively. The CS and FS become coupled (i.e., the bumpers make contact with the FS) when d = 0 mm & 0.8 mm (i.e., δ = 0.4 mm). The bumpers are made of Shore A70 hardness urethane.

Figure 5 shows the manufactured decouplable coarse-fine stage prototype and the stage's specifications are summarized in Table 1. For analysis of the stage performance and system identification, the isolated base vibration is measured by a laser displacement sensor

(Keyence, LK-G10) and accelerometers (Piezotronics, 393B05). Note that the measured base displacement and acceleration are not used for control. A real-time controller (dSPACE, DS1007 and DS5203 with sampling time T_s = 0.1 ms) is used to control the stage prototype.

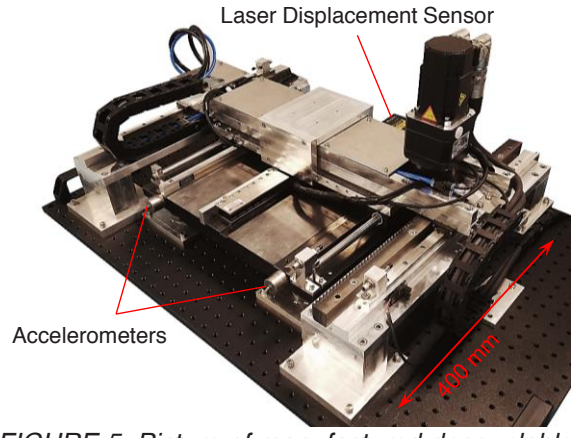

FIGURE 5. Picture of manufactured decouplable coarse-fine stage prototype.

TABLE 1. Specifications of manufactured coarse -fine stage prototype

FS Moving Mass (m_{FS})	3.4 kg
CS Moving Mass (m_{CS})	17.3 kg equivalent
Stage Travel	0.15 m
Natural Frequency of Isolated Base	7.9 Hz
FS Feedback Controller Bandwidth	240 Hz
CS Feedback Controller Bandwidth	70 Hz

EXPERIMENTAL RESULTS

Rapid point-to-point positioning experiments are conducted using the manufactured coarse-fine stage prototype. The tested step sizes range from 10 mm to 100 mm (i.e., 10, 20, 30, 50, 70, and 100 mm step sizes are used). The kinematic limits imposed on the r_{FS} generation are 0.5 m/s, 10 m/s^2, and 1,000 m/s^3, respectively. The same maximum acceleration limit as r_{FS} (i.e., a_{max} = 10 m/s^2) is used for $r_{CS,opt}$. The rest of optimization constraints and controller parameters are $r_{a,thre}$ = 5 m/s^2, ε = 1 μm, $u_{FS,acc}$ = −0.7 N, and $u_{FS,dec}$ = 0.7 N. To reduce the number of optimization variables, a 5th degree B-spline curve having the uniform knot spacing of 20 discrete time samples is adopted to represent $\mathbf{r}_{CS,opt}$ [11]. A representative reference trajectories for 50 mm point-to-point positioning are shown in Figure 6.

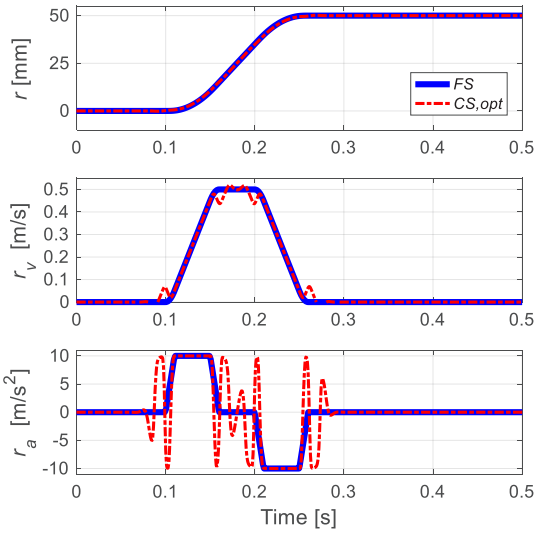

FIGURE 6. Rapid 50 mm point-to-point positioning reference trajectories (displacement, velocity, and acceleration) for the FS and CS. $r_{CS,opt}$ is optimized to provide the FS driving force when $|r_{a,FS}| > 5$ m/s^2.

The stage performance comparison between the baseline (i.e., $r_{CS} = r_{FS}$) and the proposed ($r_{CS} = r_{CS,opt}$) cases using the 50 mm step size reference trajectory are shown in Figure 7, highlighting the base vibration displacement (x_B), FS tracking error, and LM control input (u_{FS}) measurements. For the baseline case, the CS and FS travel together with a nominally fixed gap $d = \delta$, even though the actual d may deviate from the nominal value as $x_B \neq 0$ due to the residual vibration and backlash present in the rack and pinion gears. To illustrate the base vibration originated from the collision impact between the CS and FS, u_{FS} is set to 0 (i.e., the PWM drive for FS is disabled) and the CS is controlled to track r_{FS} (see CS only case). As shown in Figure 7 (a), significant residual vibration reduction is achieved with the decouplable coarse-fine stage (see Proposed and CS only cases and compare them to Baseline case). Because residual vibration is drastically reduced, the proposed approach achieves much better positioning performance as shown in Figure 7(b). Because the CS drives the FS during acceleration, the overall u_{FS} is consequently reduced as highlighted in Figure 7 (c), achieving a 31% RMS u_{FS} reduction (i.e., the RMS value is dropped from 8.55 N to 5.87 N).

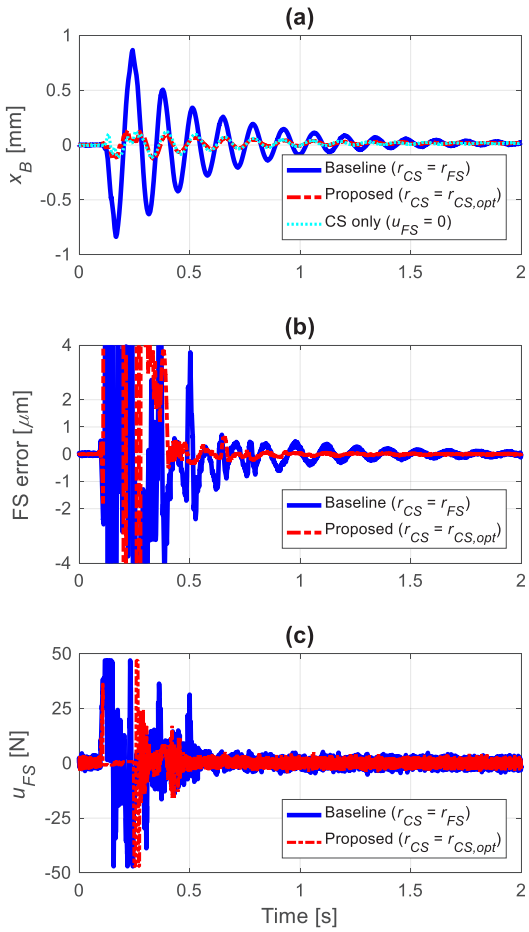

FIGURE 7. Comparison of (a) base vibration displacement, (b) FS tracking error, and (c) FS control input for rapid 50 mm point-to-point positioning.

The RMS base vibration displacement and FS control input over the range of step sizes tested are compared in Figure 8. Except the 10 mm step size case, significant improvement in residual vibration and control input is simultaneously achieved with the proposed decouplable coarse-fine approach.

The cost of reducing the residual vibration of base is u_{CS} in the decouplable coarse-fine approach. Therefore, the efficiency of both actuators (linear and rotary motors) must be compared across the cases tested. The copper loss (L_c) of motor is assessed by

$$L_c = \left(u_{RMS} / k_m\right)^2 \quad (4)$$

where u_{RMS} is the RMS force of motor over the motion duration and k_m is the motor constant. The motor constants of the prototype stage are

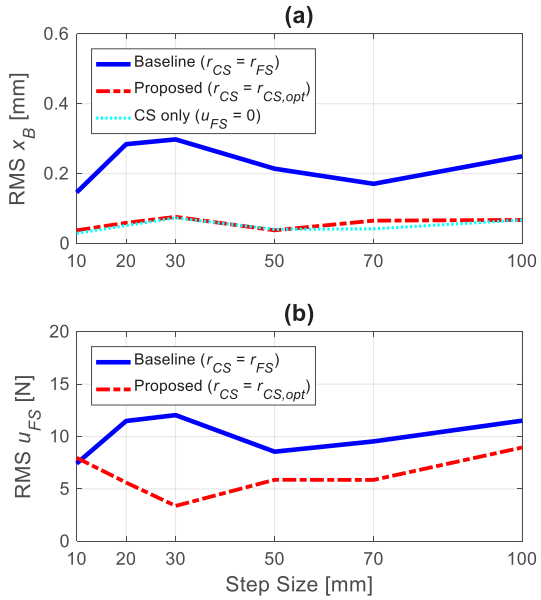

FIGURE 8. Comparison of (a) RMS base vibration displacement and (b) RMS FS control input over the stepping sizes tested (10 – 100 mm).

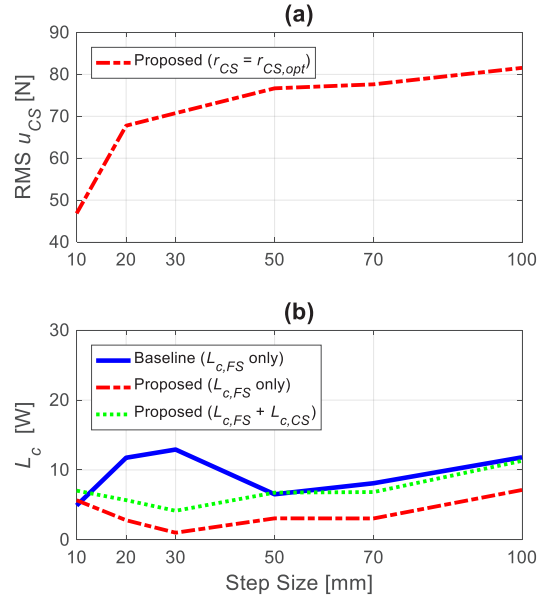

FIGURE 9. (a) CS control input and (b) comparison of measured copper loss over the stepping sizes tested (10 – 100 mm).

$k_{m,CS}$ = 39.95 N/W$^{0.5}$ and $k_{m,FS}$ = 3.35 N/W$^{0.5}$, respectively for the CS and FS. Notice the large efficiency gain for the CS from the mechanical advantage. The control input for CS is shown in Figure 10 (a) and the copper loss comparisons for the 2 s long point-to-point positioning are provided in Figure 10 (b). The proposed approach returns less copper loss from the LM

($L_{c,FS}$) when step sizes are larger than 10 mm. Even if the copper loss at the CS ($L_{c,CS}$) is accounted for, the proposed approach still performs better. Note that copper loss at the CS does not directly influence the thermal errors of FS, because the two stages are physically separated.

CONCLUSIONS

A decouplable coarse-fine stage with parallel driving approach that simultaneously reduces the linear motor (LM) control input and residual vibration of isolated base is proposed. By driving with more efficient actuator and mounting on the machine ground, the decouplable coarse stage simultaneously reduces the LM control input for the fine stage and residual vibration of isolated base. A switching controller with the optimized stage reference trajectories lowers the residual vibration by up to 82%, leading to more precise positioning, and the LM control input by up to 72% (i.e., 92% improvement in motor heating) in select point-to-point positioning experiments. Future works will investigate improved control strategy of the proposed decouplable coarse-fine stage design to robustly achieve LM control input reductions over a large range of point-to-point motions (e.g., step sizes less than or equal to 10 mm).

ACKNOWLEDGEMENT

This work is funded by the National Science Foundation's CAREER Award #1350202: Dynamically Adaptive Feed Drives for Smart and Sustainable Manufacturing. Manufacturing of the prototype stage is supported by Rackham Graduate Student Research Grant and Center for Entrepreneurship Engineering Prototyping Fund of the University of Michigan.

REFERENCES

[1] Lu C, Tsai D. Independent Component Analysis-Based Defect Detection in Patterned Liquid Crystal Display Surfaces. Image and Vision Computing. 2008; 26: 955-970.

[2] Butler H. Position Control in Lithographic Equipment. IEEE Control Systems. 2011; 31: 28-47.

[3] Rivin E. Vibration Isolation of Precision Equipment. Precision Engineering. 1995; 17: 41-56.

[4] Okwudire C, Lee J. Minimization of the Residual Vibrations of Ultra-Precision Manufacturing Machines via Optimal Placement of Vibration Isolators. Precision Engineering. 2013; 37: 425-432.

[5] You Y, Ahn H. A Passive Reaction Force Compensation (RFC) Mechanism for a Linear Motor Motion Stage. International Journal of Precision Engineering and Manufacturing. 2014; 15: 797-801.

[6] Wang Z, Cheng X, Nakamoto K, Kobayashi S, Yamazaki K. Design and Development of a Precision Machine Tool Using Counter Motion Mechanisms. International Journal of Machine Tools and Manufacture. 2010; 50: 357-365.

[7] Chen Y, Fuh C, Tung P. Application of Voice Coil Motors in Active Dynamic Vibration Absorbers. IEEE Transactions on Magnetics. 2005; 41: 1149-1154.

[8] Erkorkmaz K, Gorniak J, Gordon D. Precision Machine Tool X–Y Stage Utilizing a Planar Air Bearing Arrangement. CIRP Annals-Manufacturing Technology. 2010; 59: 425-428.

[9] Mize C, Ziegert J. Neural Network Thermal Error Compensation of a Machining Center. Precision Engineering. 2000; 24: 338-346.

[10] Altintas Y, Verl A, Brecher C, Uriarte L, Pritschow G. Machine Tool Feed Drives. CIRP Annals-Manufacturing Technology. 2011; 60: 779-796.

[11] Yoon D, Okwudire C. Active Assist Device for Simultaneous Reduction of Heat and Vibration in Precision Scanning Stages. Precision Engineering. 2016; 46: 193-205.

[12] Yazaki Y, Fujimoto H, Hori Y, Sakata K, Hara A, Saiki K. Method of Shortening Settling Time Using Final State Control for High-Precision Stage with Decouplable Structure of Fine and Coarse Parts. Electrical Engineering in Japan. 2016; 195: 39-49.

LLNL-CONF-728120

Microassembly Development for an Advanced Micromirror Array

Kenneth G. Enstrom, Timothy M. Uphaus, Robert M. Panas, and Christopher Harvey

Materials Engineering Division
Lawrence Livermore National Lab
Livermore, CA, USA

ABSTRACT

We have designed and initiated the operation of a custom microassembly system in order to fabricate a high fill-factor (99%) micro-mirror array design (10,000 1mm^2 mirrors). The micromirrors are driven with continuous closed-loop control and three degrees of freedom (DOFs)—tip, tilt, and piston—over large ranges (±10deg rotation and >±30μm translation) at high speeds (~40kHz small stepping rate), all [1]. The capabilities of this new mirror array will extend the performance of a variety of high-impact technologies including: (i) optical switches, (ii) high speed focusable LIDAR or other imaging, (iii) mobile laser communication systems.

The joining of the hexapod flexures, printed on the micro-mirror, to the actuator paddle is a non-trivial step in the assembly of the array design. Precise planarity, x,y,and theta z positioning must be kept in consideration when aligning the mirror legs to the actuator paddles for adhesion. Without proper consideration of these variables the mirror legs may be destroyed in the assembly process. This multifaceted alignment will be handled using a P.I. H-8116-axis miniature hexapod. The miniature hexapod will be used in tandem with a Nexiv VMR-3020 optical C.M.M during the assembly process to visually verify alignment as well as document the assembly process. A matlab scrip was utilized to facilitate the alignment process and output commands to the hexapod in order to bring the hexapod flexures in contact with the actuator paddles.

BACKGROUND

The fabrication process for the LLNL light-field directing array involves both the fabrication of a silicon MEMS chip and additively manufactured microflexures [2]. These components must be assembled carefully to complete the device. The difficulty in assembly lies in the varying properties of the two structures, as they have significant differences in stiffness, size, resolution and chemical compatibility [1]. This precludes many standard assembly techniques used in microfabrication, such as wafer bonding. Instead, a custom 6DOF assembly system is required to precisely bring the two structures into alignment to be cured together. This work bases the assembly process around a parallel kinematics hexapod, rather than the more conventional serial kinematics [3].

OVERALL HARDWARE LAYOUT

The Microassembly system is show above in FIGURE 1. The hexapod is mounted to a three cylinder-groove kinematic mount. The cylinder-groove is fabricated using a 6061-aluminum post with two ¼" sapphire cylinders cemented into a ½" wide slot at the top of the post. Three ¼" sapphire half spheres rest atop the cylinder v-grooves positioning the hexapod in its tray.

FIGURE 1: Micromirror assembly station.

MIRROR PLACEMENT

The assembly process begins with the measurement of the orientation of the respective components regarding the micromirror assembly station. Figure 2 highlights the center kinematic post used to attach the growth plate.

FIGURE 2: Mirror Kinematic Post

Comprehension of the assembly process begins with the orientation of the respective components in regards to our micromirror assembly station. FIGURE 2 highlights the center kinematic post used to attach the growth plate. Above the growth plate rests the inverted mirror-leg subassembly, FIGURE 3.

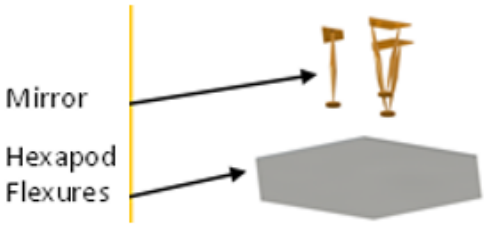

FIGURE 3: Micromirror-leg-subassembly.

This subassembly sits atop the stationary post in the center of the hexapod letting the hexapod move freely about it. The other half of the equation comes into play using a unique disk shown in FIGURE 4. This disk utilizes three sapphire spheres of known diameter and sphericity to establish a plane and arbitrary coordinate system. This coordinate system is established using a MATLAB script.

MEMS IN COORDINATE DISK

The MEMS half of the assembly comes into play using a unique coordinate disk shown in Figure 4. This disk utilizes three sapphire spheres of known diameter and sphericity to establish a plane and arbitrary coordinate system.

The next step to the process is to locate the Micromirror MEMS structures in the coordinate frame defined by the three sapphire spheres. This is important to know as later in the process, this coordinate disk will be flipped over so the MEMS structure is face down and kinematically anchored to the three grooves on the top of the hexapod, as shown in Figure 4. Thus, the chip location cannot be easily measured, but the sapphires can still be located by the optical measuring system. This allows for the location of the face of the MEMS chip to be inferred from the sapphire spheres. The coordinate disk can then be easily maneuvered in all 6DOF by the hexapod, to bring the face-down MEMS structure into contact with the face-down (legs-up) mirrors anchored to the center post. Such contact completes the assembly process.

As visualized Figure 4b, a three v-groove kinematic mount (face down) with 1/4" tool steel balls were used to locate the Chip Sapphire reference disk with the MEMS chip face up for measurement relative to the sapphires. This allows us to look at the face of the actuator paddle features that will be adhered to the hexapod flexure legs. The sapphires are located using the NexIV from a series of points on the surface (~650).

MEMS-MIRROR ALIGNMENT

Once the chip center position has been registered to the sapphire coordinate system, the disk is inverted and placed atop the hexapod. This process places the paddles facing in the negative z direction. The paddles on the 'MEMS chip' (glass plate at present) are now seated on the hexapod, held slightly above the mirror-leg sub-assembly, as shown in FIGURE 4.

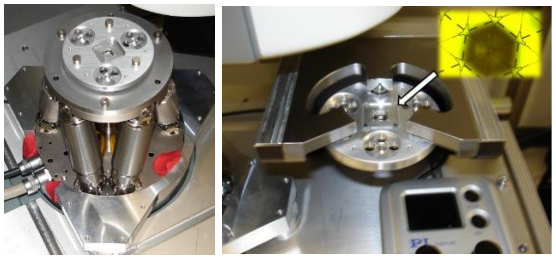

FIGURE 4: a) (left) Coordinate disk placed with MEMS chip face down onto hexapod, ready for assembly to mirrors below. b) (right) MEMS chip face up in sapphire coordinate disk, ready for location measurement.

The next step to the process is to establish a relation between the paddle geometry impeded into the sapphire disk and the coordinate system developed.

For ease of process checking, a translucent glass slide with an etching of the micro-paddle layout was used in place of a mems chip during trial runs. As visualized in FIGURE 4, a three v-groove kinematic mount with 1/4" tool steel balls were used to locate the Chip Sapphire reference disk. This allows us to look at the face of the actuator paddle features that will be adhered to the hexapod flexure legs. By looking at the disk upside down the sapphires are located using the Nexiv using a series of points on the surface (~650) then sphere fitting the data to find the diameter and origin of each sapphire. A coordinate system, later

detailed in the overview of the matlab processing section, is established at the averaged x-y-z location of the 3 spheres. The center location of the actuator paddle pattern is also registered at this point.

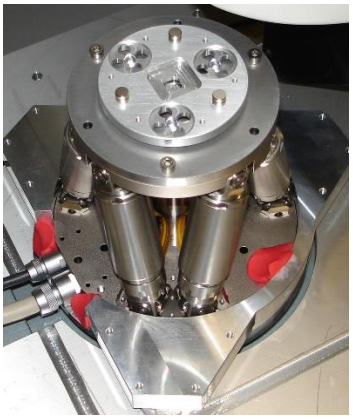

FIGURE 5: Chip-Sapphire reference frame disk inverted.

Once the chip center position has been registered to the sapphire coordinate system, the disk in inverted and placed atop the hexapod. This places the paddles facing in the negative z direction. The paddles now sit upside down slightly higher that the mirror-leg sub-assembly.

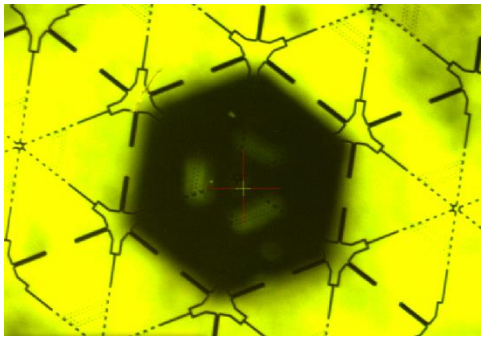

FIGURE 6: Nexiv view top down of the hexapod with both subassemblies.

At this point, the Nexiv is used to view the alignment of the glass paddle layout map resting above the mirror-leg subassembly. The main geometries of concern during this crucial step of assembly are composed two planes. The first plane is that of the glass plate with the paddle pattern. The second is the plane made up of the three average heights of the individual hexapod flexures. FIGURE 6 shows the Nexiv image pre-assembly of the first plane, the glass slide. FIGURE 7, below, shows the Nexiv image of the second plane of interest, the average flexure height plane.

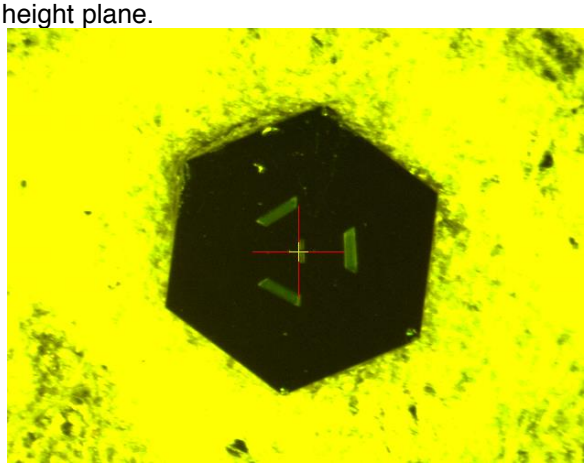

FIGURE 7: Nexiv view top down of the mirror and hexapod flexure subassembly.

The next step in the assembly process is to feature find using the Nexiv Auto-Measure software to locate the x-y-z center of each hexapod flexure. The flexure's have conveniently been created with a 5 micron gecko foot pattern for adhesion with a 10 micron center circle used to center find. These three center locations populate into the matlab code to generate the second plane as well as the center of symmetry of the three legs. FIGURE 8 below shows the center, 10 micron, gecko foot used for locating the individual leg.

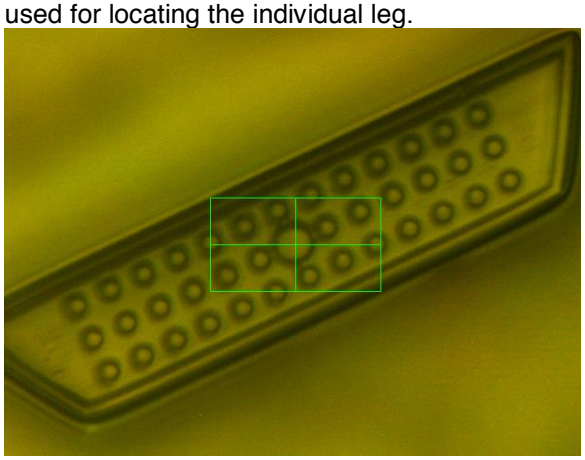

FIGURE 8: Nexiv view top down of the hexapod flexure gecko pattern.

The crosshair box in FIGURE 8 is an optical contrast comparator feature of the Nexiv software. This allows the program to scan differential z heights looking for sharpness of contrast in the allotted box area to find the z height of focus.

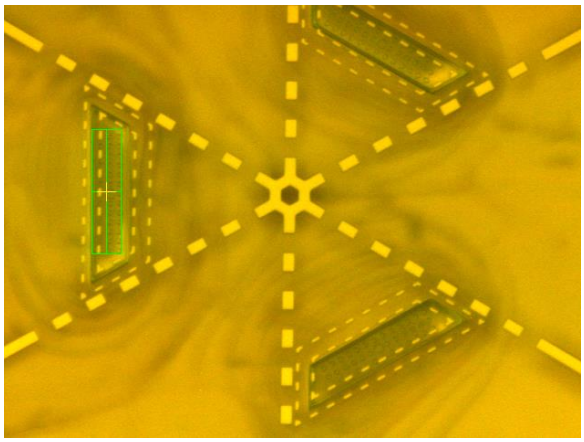

FIGURE 9: Nexiv view top down of the flexure-glass plate alignment.

After populating the two planes as well as symmetry centers into the matlab program, the two planes are centered and leveled to one another and brought to a predetermined z-offset from one another. Once alignment is visually confirmed on the Nexiv, shown in FIGURE 9, the z height of the hexapod is slowly lowered until contact is confirmed by the darkening of the flexure pads visualized in FIGURE 10.

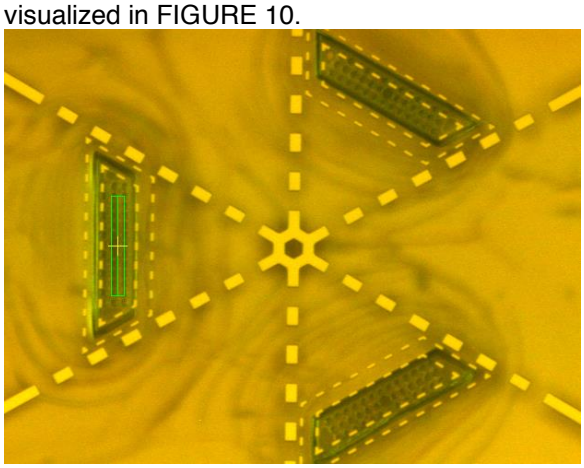

FIGURE 10: Visual confirmation of flexure contact with glass slide.

Once visual confirmation is established, FIGURE 10, the z is retracted upwards raising the glass slide off the mirror subassembly and the sapphire disk is lifted off the kinematic mount. This removal is necessary for the next assembly step. A ¼ inch lapped end steel pin is used to spread a small drop of epoxy in shear on the glass slide. This shearing has been tested to consistently create a glue layer of less than 10 micron.

Once the glue has set up, the sapphire disk is place on the hexapod and lowered to the specified z-offset to ensure alignment.

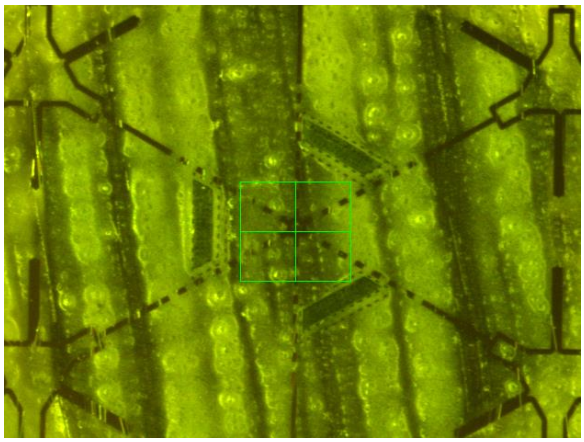

FIGURE 10: Visual confirmation of flexure alignment with glass slide post epoxy.

As before, once visual alignment is verified post kinematic mount cycling the z height is slowly lowered bringing the glass slide back into contact with hexapod flexures.

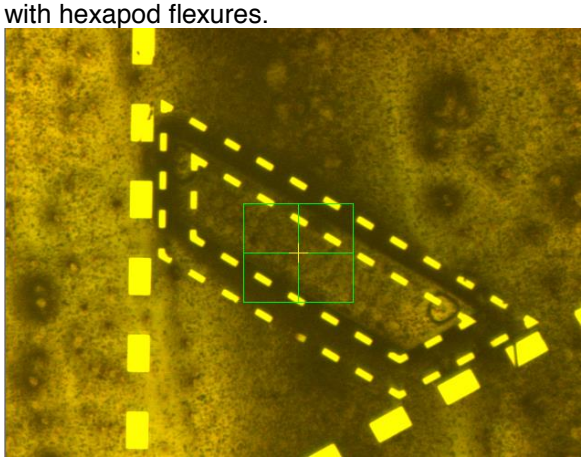

FIGURE 11: Visual confirmation of flexure contact with epoxy layer.

Once contact is confirmed, FIGURE 11, the epoxy cures overnight. Once the epoxy cures, the water soluble glue holding the mirror to the post kinematic clamp is saturated and the mirror-flexure-slide assembly is now merged and lifted away from the post using the hexapod.

CONCLUSION

We have designed and initiated operation of a custom microassembly system to fabricate a high performance micromirror design. The joining of the hexapod flexures, printed on the micro-mirror,

to the actuator paddle is one of the main hurdles in this fabrication effort.

REFERENCES

1. Hopkins, J.B., et. al., "A High-speed Large-range Tip-tilt-piston Micromirror Array," *JMEMS*, Vol 26, Issue: 1, pp 196-205, 2016.
2. Panas, R.M., et. al., "Hybrid Additive and Micro-Fabrication of an Micromirror Array," *ASPE 2015 Annual Mtg*, Austin TX, Nov 1-6, 2015.
3. Kunt, E. D., et. al., "Miniaturized Modular Manipulator Design for High Precision Assembly and Manipulation Tasks," *12th IEEE Workshop on Advanced Motion Control*, Sarajevo, Bosnia, March 25-27, 2012.

Fabrication of polycrystalline diamond molds by micro EDM

Shimpei Kasai[1], Tomoki Sodetai[2], Jiwang Yan[1*]
[1]Department of Mechanical Engineering, Keio University
Yokohama 223-8522, Japan
[2]Seiko Instruments Inc., Chiba 270-2222, Japan
[*]yan@mech.keio.ac.jp

1. INTRODUCTION

In recent years, there is a great demand for manufacturing micro-scale metal components with complex shapes. These components are currently manufactured by press molding, hence the fabrication of precise molds is a crucial issue. It is expected that the mold lifetime will be prolonged by using polycrystalline diamond (PCD) as the mold material. PCD is electrically conductive, and thus able to be machined by electrical discharge machining (EDM), which enables the transfer of complicated micro structures onto extremely hard materials.

However, EDM of PCD has a low machining speed due to the fact that electro discharges only occur on metal binders and not on diamond grains. Also, the processed surface quality is low due to the dislodgement of diamond grains. To solve these problems, EDM using carbon diffusion reaction between transition metal electrodes and diamond grains was proposed [1]. When diamond grains are heated by discharges and come into contacts with the transition metal, carbon diffusion occurs, enabling the gradual machining the diamond grains. This method is especially effective by using a high-speed rotary electrode made of transition metals [1]. However, rotary EDM cannot be used to fabricate complex 3D structures such as molds for micro gears.

In this research, we tried to apply the carbon diffusion reaction to die sinking EDM for PCD molds with a micro gear shape. In die sinking EDM, debris are easy to be trapped inside the discharge gap. To promote debris removal, we developed a device to vibrate the electrode and induce a flow in the dielectric fluid. The effect of carbon diffusion reaction in vibration-assisted die sinking EDM was investigated.

2. EXPERIMENT

Experiment was performed using a precision micro EDM machine, Panasonic MG-ED72 which enables control of voltage and electrostatic capacity. Experimental conditions were set to roughing and finishing steps, as shown in Table1. First, we manufactured a jig (Fig. 1) which can hold the electrode and suppress the vibration in X and Y directions. Copper and cupronickel (Cu:Ni = 7:3) electrodes with a diameter of 1.5 mm were used. As shown in Fig. 2, nickel in the cupronickel electrode is expected to cause carbon diffusion reaction. Two 0.5 mm-thick PCD plates were used as workpiece, which contain fine diamond grains having a mean size of 1 μm and 10 μm (referred to 1 μm PCD and 10 μm PCD, respectively). A piezoelectric element was used as the vibration generator, which resulted vibrations with an amplitude of 3-5 μm and a frequency of 500 Hz or 2 kHz.

Next, gear shapes were fabricated on PCD by using a cupronickel rod with a gear shape as the electrode (Fig. 3). This electrode was fabricated by wire-EDM and electrochemical machining (ECM), and has both roughing and finishing portions to enable one-step rapid fabrication. The EDMed surfaces were examined by a scanning electron microscope (SEM), a non-contact laser-probe profilometer, a laser micro-Raman spectrometer. The form errors of the fabricated gear molds were measured by a projector.

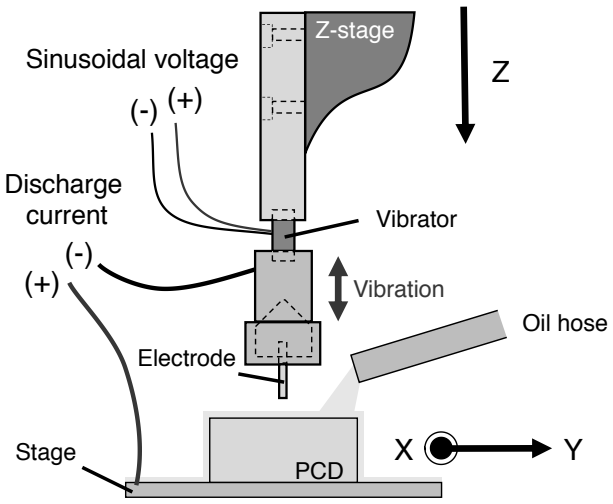

FIGURE 1. Manufactured jig and experiment setup.

TABLE 1. Experiment condition.

Machining steps	Roughing	Finishing
Voltage	90 V	70 V
Condenser capacity	1000 pF	220 pF
Feed speed	0.5 μm/s	0.3 μm/s
Dielectric fluid	EDM oil	

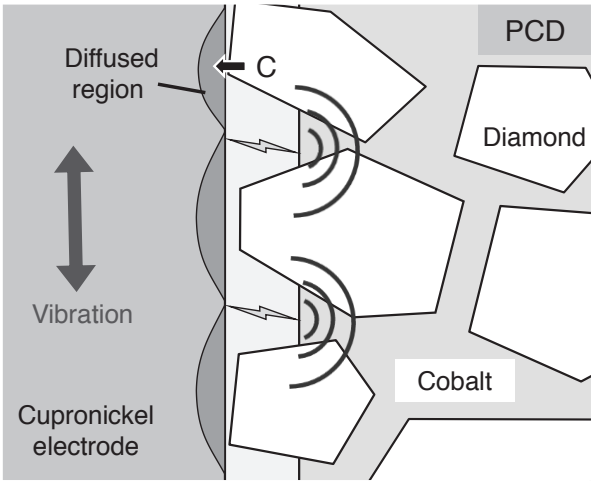

FIGURE 2. Schematic model for EDM of PCD using an electrode containing transition metals.

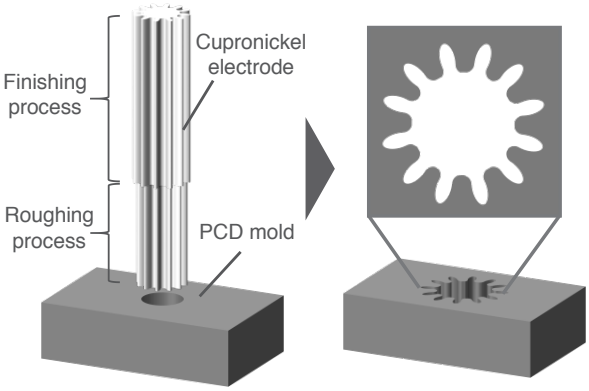

FIGURE 3. Two stepped cupronickel electrode and PCD mold having a micro gear shape.

3. RESULTS AND DISCUSSION

3.1 Comparison of machining depth

Three vibration conditions, normal vibration 1, vibration 2 with high amplitude and vibration 3 with high frequency were set as vibration-assisted die sinking EDM (Table 2). Copper electrode was used with/without vibration, to machine 10 μm PCD, and the machining depths were compared. As shown in Fig. 4, vibration assistance greatly improved machining depth at first phase. Compared with vibration 1, vibration 2 with higher amplitude can get high machining depth at first phase because of promotion debris removal. Therefore, vibration 3 with higher frequency improved machining depth compared with vibration 1 because of ultrasonic field forces and micro streaming in high frequency [2].

Next, copper and cupronickel electrodes were used with vibration (Amplitude 5 μm, Frequency 500 Hz), to machine 10 μm PCD for 3 hours. Fig. 5 indicates the machining depth, measured by a laser-probe profilometer, using two electrodes in rough and finishing process respectively. In the case of roughing process, there is not much difference between the two electrode materials. However, in the case of finishing process, the machining depth using the cupronickel electrode was deeper by 48% compared with the copper electrode. In this case, the carbon diffusion reaction was occurred, and the diamond grains were machined leading to efficient machining in finishing process because the low discharge energy which has short discharge gap will contact with cupronickel electrode more.

3.2 Comparison of surface roughness

1 μm and 10 μm PCD were machined and surface roughness on the wall of machined PCD was measured by a laser-probe profilometer. As

TABLE 2. Vibration conditions.

	Amplitude	Frequency
Vibration 1	3 μm	500 Hz
Vibration 2	5 μm	500 Hz
Vibration 3	3 μm	2 kHz

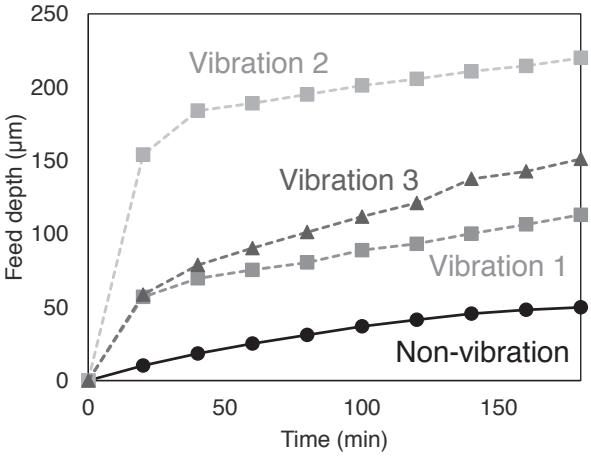

FIGURE 4. Result of machining depth with some vibration conditions.

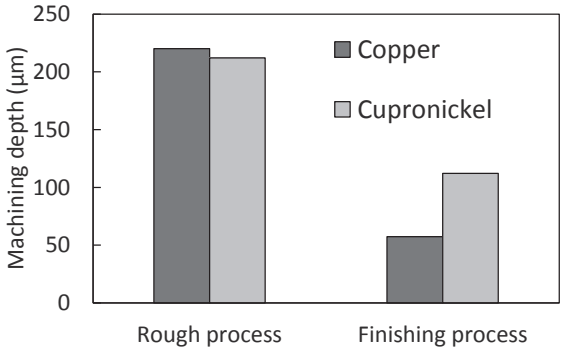

FIGURE 5. Result of machining depth with two electrodes

shown in Fig.6, in case of 1 μm PCD, there is not much difference between the two electrode materials about surface roughness Ra. On the other hand, surface roughness Rz using the cupronickel electrode was improved by 10% compared with the copper electrode. Fig. 7 shows the result of surface roughness on 10 μm PCD. As shown in Fig. 7, use of a cupronickel electrode reduces the surface roughness Ra by 34 % and Rz by 24% compared with copper electrode. In the case of coarse diamond grains, the carbon diffusion reaction was significant, and the diamond grains were quickly flattened, leading to a low surface roughness.

As shown in SEM micrographs of the 10 μm PCD surface (Fig.8), there are no noticeable diamond grains protrusion and dislodgements when using cupronickel electrode. In this case, the carbon diffusion reaction was effective, and the diamond grains were gradually removed leading to a low surface roughness. The effect of carbon diffusion reaction was more remarkable in 10 μm PCD because the bigger size of diamond grains will contact with cupronickel electrode more.

3.3 Raman spectroscopy analysis

Figs. 9 and 10 show the Raman spectra of the EDMed surfaces. Fig. 9 shows the Raman spectrum of the PCD surface machined using the copper electrode. There are two peaks at 1580 cm^{-1} and 1357 cm^{-1}, respectively. The peak at 1580 cm^{-1} (G band) indicates a crystalline graphite structure, and peak at 1350 cm^{-1} (D band) corresponds to microcrystalline graphite [3]. In general, there are same two peaks EDMed PCD surface [4]. Fig.10 shows the spectrum of the PCD surface using the cupronickel electrode. In this case, there is a sharp peak at 1332 cm^{-1} that corresponds to crystalline diamond. From these results, we may conclude that graphite on the EDMed PCD surface diffuses into the cupronickel and is removed by electrode because of carbon diffusion reaction.

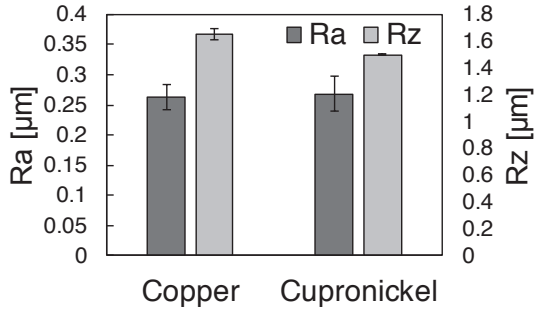

FIGURE 6. Surface roughness for 1 μm PCD.

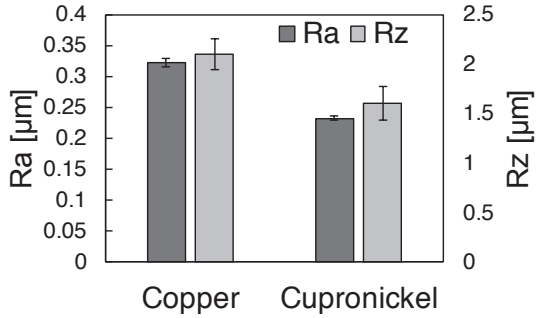

FIGURE 7. Surface roughness for 10 μm PCD.

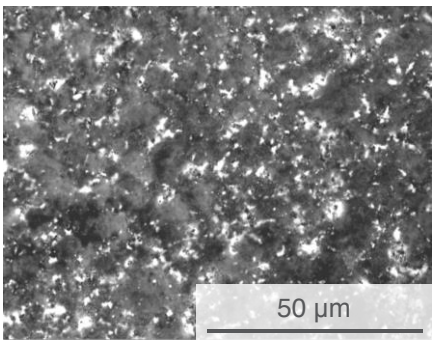

(a) By copper electrode

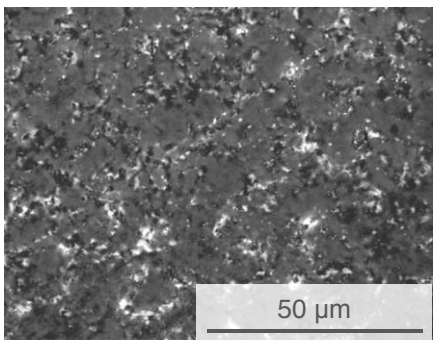

(b) By cupronickel electrode

FIGURE 8. Surface topography for 10 μm PCD.

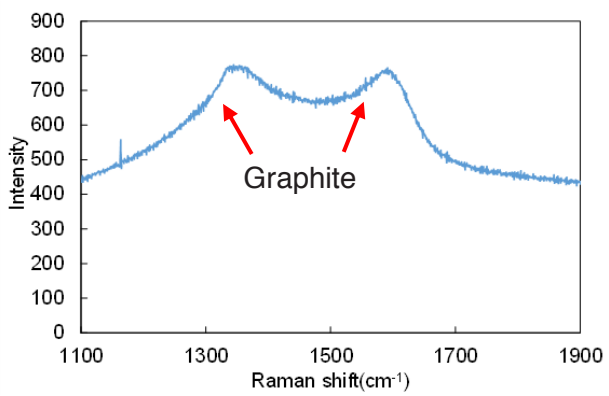

FIGURE 9 Result of Raman spectrum by copper electrode.

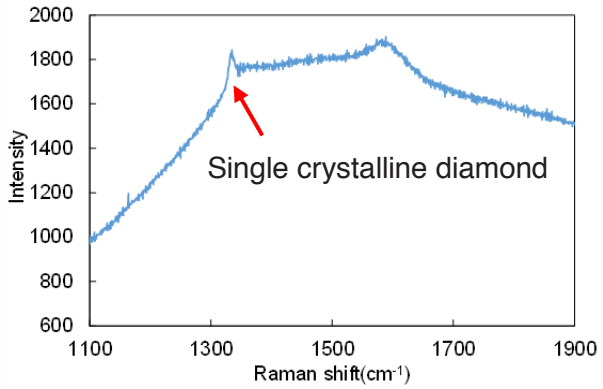

FIGURE 10 Result of Raman spectrum by cupronickel electrode.

3.4 Fabrication of gear-shape PCD molds

The gear shape was transferred to PCD using a vibration assisted cupronickel electrode. As shown in Fig.11, high precision fabrication of the gear shape was achieved. Fig.12 shows the SEM micrograph of gear wall. The PCD surface is smoothly machined. The surface roughness is 1.6 μmRz and the form error at the gear addendum was less than 2 μm, which is useable for the fabrication of precise metal gears by press molding.

4. CONCLUSIONS

1. Electrode vibration can improve machining speed.
2. Compared with copper electrode, use of a cupronickel electrode reduces the surface roughness Ra by 34 % and Rz by 24% for coarse grain (10 μm) PCD.
3. Graphite formation was reduced on the EDMed surface of using cupronickel electrode.
4. PCD molds with micro gear shapes were successfully fabricated at high precision.

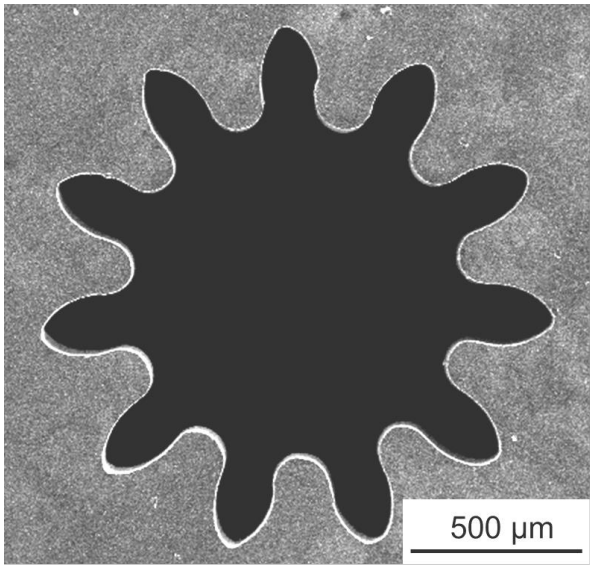

FIGURE 11 Gear shape on PCD.

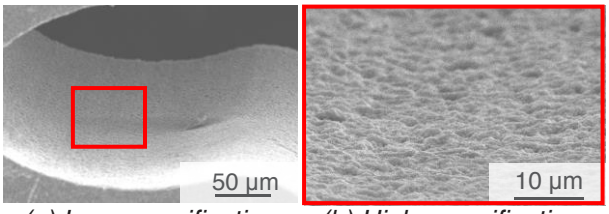

(a) Low magnification *(b) High magnification*

FIGURE 12 Gear wall.

REFERENCE

[1] J. Yan, K. Watanabe, T. Aoyama: Micro-electrical discharge machining of polycrystalline diamond using rotary cupronickel electrode, CIRP Annals-Manufacturing Technology, 63, 1, pp. 209-212 (2014)

[2] V.S.R. Murthi, P.K. Philip: A comparative analysis of machining characteristics in ultrasonic assisted EDM by the response surface methodology, Int J Prod Res, 25, 2 pp.259–272 (1987)

[3] D.S. Knight, W.B. White: Characterization of diamond films by Raman spectroscopy, J. Master. Res., 4, 2, pp. 385-393 (1988)

[4] Z. Zhang, H. Peng, J. Yan: Micro-cutting characteristics of EDM fabricated high-precision polycrystalline diamond tools, Int J Machine Tools & Manufacture, 65, pp. 99-106 (2013)

NUMERICAL AND EXPERIMENTAL INVESTIGATIONS INTO PRODUCTION OF HIERARCHICAL TEXTURES

Divyansh S. Patel[1], Mahesh Thalkar[1], V. K. Jain[1,2], and J. Ramkumar[1]
[1]Department of Mechanical Engineering
Indian Institute of Technology Kanpur,
Kanpur - 208016 (U.P.), India
[2]Department of Mechanical Engineering,
M. A. N. I. T. Bhopal,
Bhopal – 462003 (M.P.), India

INTRODUCTION

The role of hierarchical textured surfaces in the field of surface engineering has not been yet understood completely. However, super hydrophobicity of natural surfaces is a great example of hierarchical textures, and is being studied intensively with the aim of designing such engineered surfaces. The production of these hierarchical textures in a large scale is a big challenge for improving the performance of the functional surface in its working environment. This paper outlines a novel methodology for the production of hierarchical textures through sequential machining processes using Wire-electric discharge machining (EDM), laser surface texturing (LST) and electrochemical machining(ECM). Wire electric discharge machining (Wire-EDM) is one of the promising techniques, which can generate repetitive identical micro features in a single step. Micro wire of 180 μm is used for the production of arrays square micro-pillars of ≈140 μm machining in two normal directions. Produced micropillars are spaced ≈200 µm apart and, height of the micro-pillars is ≈100 µm. Second level of roughness on these micro-pillars array is imparted by machining micro-dimples using LST. The diameter and depth of the micro-dimples machined are ≈40 µm and ≈15 μm, respectively. For production of hierarchical textures in a large surface area of SS304, electrochemical sinking operation is employed. In addition, an attempt has been made to numerically simulate EC sinking process in COMSOL for predicting the textured surface and conducting the analysis of current density. Simulated and experimental hierarchical textures obtained through EC sinking operation are compared graphically, and both are found to closely fit. Geometrical parameters of the hierarchical textures are captured through optical microscopy and 3D optical profilomerty.

Background

Hydrophobicity, surface free energy, interfacial free energy and surface roughness are the key parameters which influence the interaction of an implant surface with the environment inside a human body. Cell attachment and human fibroblast spreading can be regulated by manipulating contact angle of surface of the implant [1,2]. In the field of tribology and machining, researchers are mimicking natural surfaces for reducing the friction, wear and enhancing tribological properties [3,4]. From last few decades, it has become a trend to follow the natural surfaces for example, lotus leave, shark-riblet structures etc. so as to achieve their vibrant multifunctional characteristics. It is found microscopically that super-hydrophobicity of a lotus surface exists for the reason that the microdroplet contacts at multiple locations of the hierarchical structure. There is no direct contact between the liquid and solid due to existence of air (gas), which results a composite mode of contact. Gecko feet and rose petals inspired surfaces are being produced for achieving high-adhesion super-hydrophobic surface [5]. A number of functions such as water repellency, self-cleaning, and defense against pathogens of these bioinspired surfaces are being replicated on metals and alloys to protect aero-foils and aircraft engines against the accumulation of ice during high altitude fly as well as, to make more weather proof infrastructures. The area of applications of hydrophobicity is quite wide, including power transmission lines, pipes of air conditioners and refrigerators drag reduction, radar or tele- communication antennas, weather proof infrastructures etc. There are recent studies for producing textures on metals using electrochemical machining because this machining process can machine any hard-to-machine metals at micro-/nanometer level without any heat affected zone [6–9]. There is

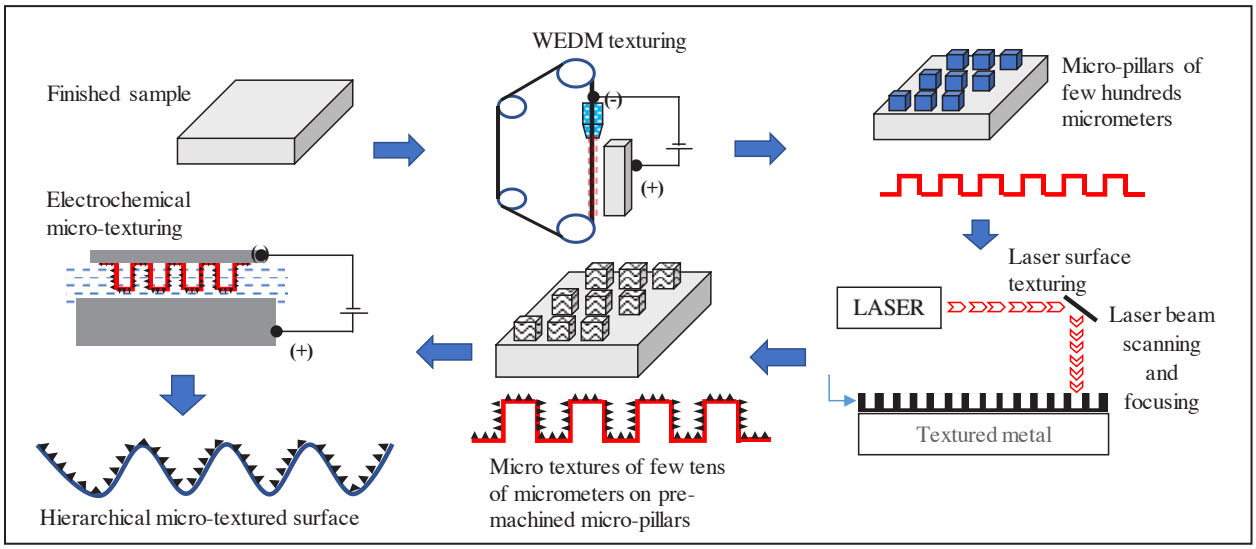

Figure 1: Schematic diagram representing sequential machining for producing hierarchical textures.

still significant research to be done to produce predefined hierarchical structures on a large metallic surface, since availability of literature is scares. Accordingly, this study proposes a novel sequential machining process to produce hierarchical structures on metal surface. A tool with combination of two-levels roughness is developed using Wire-EDM and LST. This pre-textured tool with hierarchical textures is incorporated in EC sinking process for texturing over large metallic surface area. In addition, texturing through electrochemical sinking has been numerically simulated to analyze the current density and shape of the anode deformation.

Hierarchical Texturing

Surface texturing is the process of generating a specific type of pattern on the surface in order to change its properties. Texturing with features on multiple scales can be produced, starting from the micro/ nanometer range extending up to millimetre range. The term "Hierarchical Texturing" defines the engineered surfaces that contain multiple engineered features (micro-holes, micro-asperities, micro-dimples, micro-/nano-hairs, micro-patterns at multiple levels etc.) of required geometrical parameters, which are purposely manufactured in order to enhance the functionality of the surface in the given environment. The Hierarchical textures can also be considered as combination of two or more geometrical features. This work reports a novel methodology of producing combination of two roughness patterns, first is square micro-pillars of ≈150 μm and second is of micro-dimples of ≈40 μm on the micro-pillars surface to address the hierarchically texturing on metal surface. Since, the sequential machining process is a cumbersome practise for generating hierarchical textures on a large surface, a pre-textured tool (through Wire-EDM and LST) can be employed in EC sinking to replicate the multiple roughness patterns over the surface. The methodology of the proposed sequential machining process can be understood from Figure 1.

EXPERIMENTAL INVESTIGATIONS

Wire-ED Texturing

Wire-EDM tool with 180 μm wire diameter is employed to produce micro-channels array in two perpendicular directions. Micro-pillars (Micro-electrodes array) of ≈ 140 μm are produced at the distance of 200 μm. Figure 2 shows the dimensioned microscopic view of micro-pillars array produced. Figure 2(a) shows micro-pillars of square cross section, having width of 140±10 μm. Figure 2(b) shows the focused bottom textured surface, the roughness produced due to melting and solidification during metal removal. Figure 2(c) shows the cross-sectional view of the textured surface with Wire-EDM, which reveals depth and pitch of the micro-pillars. The depth of micro-pillars is 100±5 μm and the distance between the two pillars is ≈ 200 μm.

Laser Surface Texturing

Pre-textured surface is exposed to pulsed Nd:YAG laser of 30 W power, wavelength 1064 nm, and 30 μm laser beam diameter. The parameters of the machine are regulated to

machine at least 4 micro-dimples of ≈40 μm diameter on the top of micro-pillar of ≈150x150 μm.

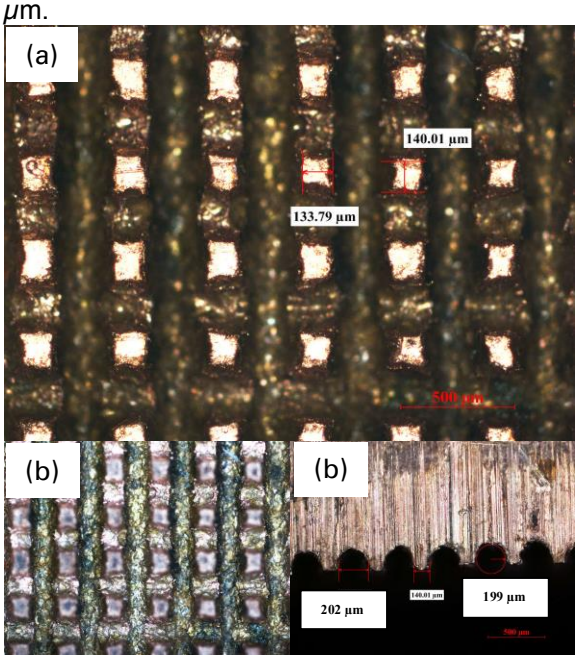

Figure 2: Micro-textures on copper sample produced through Wire EDM machining: (a) Square micro-pillars array, (b) Roughness at the bottom surface, and (c) Cross section showing the depth of the machined channels.

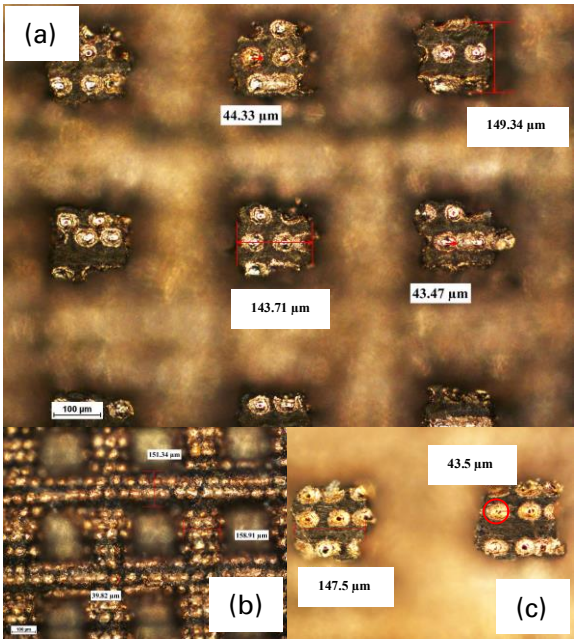

Figure 3: Micro-textures produced through LST: (a) Micro-pillars and micro-dimples at 20X magnification, (b) micro-dimples at the bottom surface, and (c) top view of micro-dimples at 50 X magnification.

Figure 3 (a) shows the image of top view of micro-pillars having micro-dimples of ≈ 40±5 μm. The depth of micro-dimples machined is 15±5 μm, measured through focusing optical microscope at the top and bottom of the dimple respectively. The bottom surface of the pre-textured surface is also machined with micro-dimples shown in Figure 3(b). Figure 3(c) shows image magnified at 50X and measured widths of micro-dimple and micro-pillars.

Electrochemical Texturing

Electrochemical sinking operation is experimented using the sequentially textured tool of copper. The electrolyte use is 1M $NaNO_3$, input voltage of 5 V, inter-electrode gap of 50 μm.

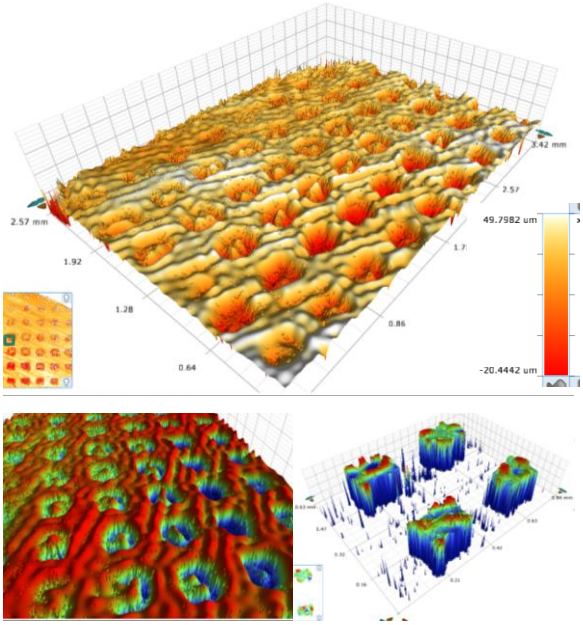

Figure 4: 3-D optical profilometry images: (a) EC textured surface, (b) Micro-bumps inside micro-dimples array, and (c) Profile of copper tool with roughness.

Figure 4(a) shows profile of hierarchical surface textures machined on SS304. The maximum depth of the micro-dimples is 20±5 μm, whereas width of the square micro-dimples obtained is 200±10 μm. Magnified view of the profile of hierarchical textures is shown in Figure 4(b), where, micro-bumps of ≈ 20 μm width generated due to micro-dimples on the copper tool. Figure 4(c) shows the 3-D image of pre-textured copper tool with micro-pillars and micro-dimples on the top surface produced through Wire-ED texturing and LST.

NEUMERICAL MODELLING

A	Area of electrode (m^2)
E	Electric field (V/m)
F	Faraday's constant (C/mol)
IEG	Inter electrode gap (μm)
J	Current density (A/m^2)
J_e	External current density (A/m^2)
J_n	Normal current density (A/m^2)
k	Dissolution constant for Anode ($m^3/A{\cdot}s$)
Q	Charge (C)
V_n	Velocity of mesh deformation (m/s)
V_x	Velocity in X direction (m/s)
V_y	Velocity in Y direction (m/s)
V_z	Velocity in Z direction (m/s)
v	Applied potential (V)
z	Valency, number of ions
ε_0	electrical field constant
εr	relative permittivity of electrolyte
ρ	Density of electrolyte (kg/m^3)
ρ_w	Density of anode (kg/m^3)
σ	Electrical conductivity (S/m)

Theoretical Analysis

1. Laplace equation is given by,

$$\nabla^2 v=0 \quad (1)$$

Where, ∇ is Laplace operator and v is potential field in electrolyte domain or nearby to electrode surface. In cartesian co-ordinate, Laplace equation defines conservation of potential field in electrolytic domain. Laplace equation is solved to give potential v at any point in electrolyte domain with necessary boundary conditions.

2. Ohm's law

$$J_n=-\sigma\cdot\nabla v \quad (2)$$

Where, J_n is the current density, it can be found by potential field solved by Laplace equation (1).

3. Faraday's Law

$$V_n=A\cdot J_n/(z\cdot F\cdot\rho_w) \quad (3)$$

$$V_n=-(k)\cdot J_n \quad (4)$$

Where, $k = (A/z\cdot F\cdot\rho_w)$ constant for anode material. All the parameters other than J_n for a particular material can be combined together into a constant denoted by k. Faraday's equation is used to find anode recession rate V_n is in the normal direction. '*A*' being the atomic weight, z is valency, F is Faraday's Constant equal to 96500 *C/mol*, ρ_w be the density of work piece material and J_n is current density in the normal direction obtained from Eq. *(2).* It is known that most commercial materials in use are alloys. Thus, the expression of V_n modified for alloy material is

$$V_n=-\frac{1}{F}\left(\sum_i \frac{(W_i/100)A_i}{\rho_{wi}\cdot z_i}\right)\cdot J_n \quad (5)$$

Where, i is the summation index denoting number of elements in the alloy and W_i is the weight percentage of a particular element in the alloy (or overall mixture).

Modelling and Simulation details

COMSOL Multiphysics 5.2 is used for the hierarchical textures on the work piece. Two-dimensional (2-D) model is studied by using the electric current sub-module under its AC/DC module, deformed mesh sub-module under the mathematics module and laminar sub-module under fluid flow module to analyze flow pattern around the tool electrode and in machining zone.

Geometry model and meshing

Geometric model being used with three electrodes having micro-dimples in 2-D model is shown in Figure 5.

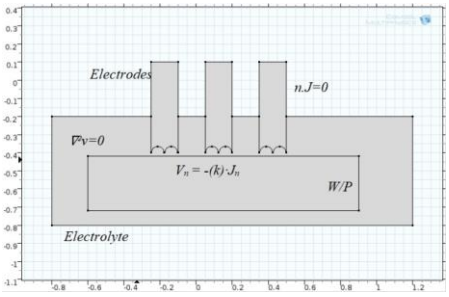

Figure 5: 2-D Geometry Showing tool, Workpiece and electrolyte with textures on tool electrode.

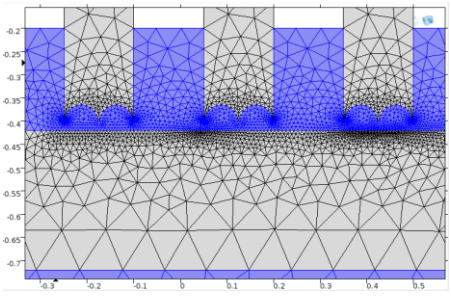

Figure 6: Fine triangular mesh distribution in the machining domain.

From the in-built material library of COMOSL, Copper is chosen as tool material with physical dimensions of 150 μm and 500 μm of width and height, respectively. Aqua solution of 1M $NaNO_3$ with conductivity of 10 S/m is used as

electrolyte. Steel is used as workpiece material of dimension 1500x300 μm from the in-built material library. Current density concentrates at sharp corners of cathode., To avoid this, sharp corners are rounded off with fillet of radius 2.5 μm. Inter electrode gap (IEG) is set to 50 µm. Simulation is executed with fine triangular mesh as shown in Figure 6.

Electric current, deformed geometry and turbulent flow, these three physical phenomena are solved simultaneously in the simulation process. Electric current physics is applied to all the three domains. Local charge density varies with divergence of current density,

$$\nabla \cdot J = QJ \quad (6)$$

With the specific electric conductance σ, the electric displacement field $\varepsilon_0\varepsilon_r E$ and the external vector of current density Je the vector of current density results to

$$J = (\sigma + \varepsilon_0\varepsilon_r \cdot \partial/\partial t)E + J_e \quad (7)$$

Equation (7) is outcome of Ohm's equation given by equation (2). E in the above equation is electrical field which is defined by the negative gradient of electric voltage,

$$E = -\nabla v \quad (8)$$

All outer boundaries and side boundaries of a tool electrode are electrically insulated with $n \cdot J = 0$ as shown in Figure 5. Ground potential is applied at textured face of tool electrode with v = 0. Electric potential with v = 10 V is applied at anode surface. All boundary conditions used in electric current domain are given in Table 2. Deformed Geometry physics is applied to analyze ablation of workpiece. Boundaries oriented in x y and z direction are prescribed with velocity $V_x=0$, $V_y=0$, $V_z=0$, respectively. Plane of workpiece where ablation takes place is prescribed with normal ablation velocity $V_n = -k \cdot (ec.nJ)$(Shown in Figure 5), Where V_n is ablation velocity of workpiece in normal direction. ec.nJ is normal current density obtained in the electric current module. The value of the constant k depends on the composition of the material of the workpiece. In the present case, Stainless steel is considered as a workpiece material. The value of k from the composition along with the density and electrochemical equivalence arises to 3.4×10^{-11} $m^3/A \cdot s$. All boundary conditions used in the deformed geometry are summarized in Table 3.

Table:1 TABLE OF CONSTANT

SN	Const.	Description	Value
1	σ	Electrical Conductivity	10 S/m
2	v	Applied potential	5 V
3	IEG	Inter Electrode Gap	25 µm
4	z	Valency number of ions	3
5	F	Faraday's constant	96500 C/mol
6	ρ	Density of electrolyte	1100 kg/m^3
7	k	Dissolution constant for Anode	3.4×10^{-11} $m^3/A \cdot s$
8	ε_0	electrical field constant	1
9	ε_r	relative permittivity of electrolyte	47
10	ρ_w	Density of anode	7800 kg/m^3

TABLE2: Boundary conditions for Electric Current

Boundary	BC	Value
Anode	Electric Potential	V=10 V
Cathode	Ground	V=0
Side walls of Cathode	Electric Insulation	$n \cdot J = 0$

Table:3 Boundary Condition for Deformed Geometry

Boundary	BC	Value
Surfaces facing in X direction	Prescribed Mesh velocity	$V_x=0$,
Surfaces facing in Y direction	Prescribed Mesh velocity	$V_y=0$,
Surfaces facing in Z direction	Prescribed Mesh velocity	$V_z=0$
Top surface of Anode	Normal Mesh velocity	$V_n = -k \cdot (ec.nJ)$

Table:4 Boundary condition (BC) for Turbulent Flow

Boundary	BC	Value
Inlet face	Inlet Velocity	$u = -U_0 \cdot n$
Exit Face	Pressure	P=0
All Internal walls	No slip	u=0

Analysis of Simulation Results

Experiment is simulated by keeping constant machining time of 5 s, conductivity of 10 S/m and applying input voltage of 5V. Maximum current density on anode surface found to be around 2.4×10^5 A/m^2 initially, at the end of 4 second current density decreased to 1.59×10^5 A/m^2. Figure ~~(7)~~ shows maximum current density at t = 0 to t = 4 seconds. Since MRR at the anode surface is proportional to the current density, dimple of *50 µm* depth and *280 µm* diameter is observed on the anode surface. Figure 8 shows a contour plot of anode surface

with micro-bumps inside the micro-dimples machined through pre-textured copper tool, i.e. combination of two roughness textures.

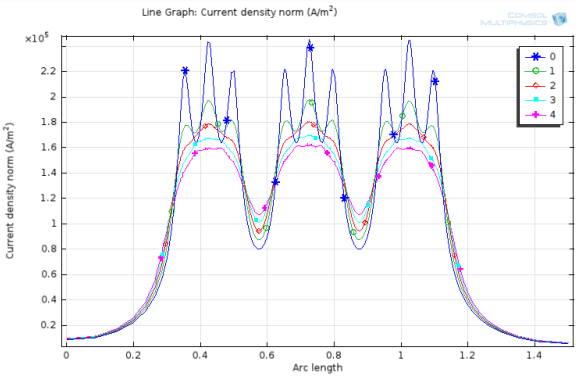

Figure 7: Current density at anode surface at different time intervals. Where 0 to 4 represents t= 0, t= 1 s, t= 2 s, t= 3s and t= 4s.

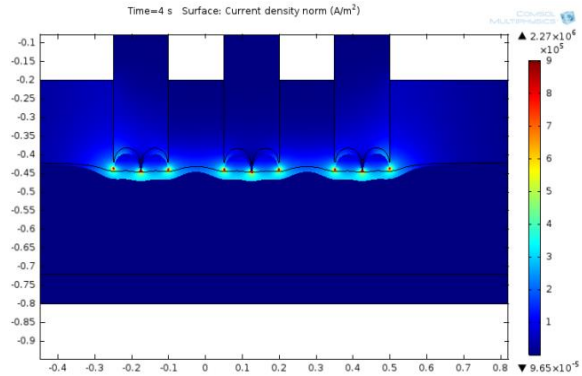

Figure 8: Predicted anode profile through EC sinking simulation.

CONCLUSIONS

This study aims to holistically address the issue of large-scale surface micro-texturing through ECMM but authors identify immense research scope in this domain still to be resolved such as lowering the dimensions of textures, addition of nanometer level textures, and development of theoretical model. A novel method of microelectrode array fabrication has been proposed using Wire-EDM. Micro-pillars are obtained on a flat surface of Cu with height ranging from 100±5 μm and width 140±10 μm. Through LST, micro-dimples array of 40 ±10 μm width and 15±5 μm depth is imparted as a second level of roughness on the micropillars. EC sinking with this multi-electrode tool array leads to the production of square micro-dimples of 200±10 μm spaced at 200±10 μm distance with impression of micro-bumps of ≈20 μm width. The study also reports 2-D numerical simulation of EC sinking process for producing micro-dimples using commercial software COMSOL 4.3a on flat stainless-steel surfaces. Comparison of theoretical and experimental results validates the study closely.

REFERENCES

[1] Ponsonnet L, Reybier K, Jaffrezic N, Comte V, Lagneau C, Lissac M, et al. Relationship between surface properties (roughness, wettability) of titanium and titanium alloys and cell behaviour. Mater Sci Eng C. 2003;23(4):551–60.

[2] Kubiak KJ, Wilson MCT, Mathia TG, Carval P. Wettability versus roughness of engineering surfaces. Wear. 2011;271(3–4):523–8.

[3] Niketh S, Samuel GL. Surface texturing for tribology enhancement and its application on drill tool for the sustainable machining of titanium alloy. J Clean Prod [Internet]. Elsevier Ltd; 2017; Available from: http://dx.doi.org/10.1016/j.jclepro.2017.08.178

[4] Walker JC, Kamps TJ, Lam JW, Mitchell-smith J, Clare AT. Tribological behaviour of an electrochemical jet machined textured Al-Si automotive cylinder liner material. Wear [Internet]. Elsevier B.V.; 2017;376–377:1611–21. Available from: http://dx.doi.org/10.1016/j.wear.2017.01.085

[5] Liu M, Zheng Y, Zhai JIN, Jiang LEI. Bioinspired Super-antiwetting Interfaces with Special Liquid-Solid Adhesion.pdf. 2010;43(3).

[6] Yang X, Liu X, Lu Y, Zhou S, Gao M, Song J, et al. Controlling the Adhesion of Superhydrophobic Surfaces Using Electrolyte Jet Machining Techniques. Sci Rep. Nature Publishing Group; 2016;6(1):23985.

[7] Patel DS, Jain VK, Shrivastava A, Ramkumar J. Electrochemical micro texturing on flat and curved surfaces: simulation and experiments. Int J AdvManuf Technol 2016; 10.1007/s00170-016-9700-3.

[8] Patel D, Jain VK, Ramkumar J. Micro texturing on metallic surfaces : State of the art. Proc IMechE Part B: J Engineering Manufacture.2016;10.1177/0954405416661583.

[9] Silva LRR, Costa HL. Tribological behavior of gray cast iron textured by maskless electrochemical texturing. Wear [Internet]. Elsevier B.V.; 2017;376–377:1601–10.

WAFER SCALE EXFOLIATION OF MONOCRYSTALLINE MICRO-SCALE SILICON FILMS

Martin J. Ward[1] and Michael A. Cullinan[1]
[1]Department of Mechanical Engineering
The University of Texas at Austin
Austin, Texas, United States of America

INTRODUCTION

This paper presents the development and simulation of a wafer scale exfoliation process and tool. The method uses an electroplated nickel tensile layer to propagate a crack across a wafer and produce exceptionally cost-effective single-crystal silicon thin films. The system produces silicon films with a thickness of between 5 μm and 35 μm across a 4 inch wafer.

The development of single crystal silicon thin-films creates opportunities for a variety of applications that take advantage of the resulting combination of flexibility and high performance. The process described here is particularly cost-effective compared to other methods of creating thin-film Si, such as etching or mechanical grinding, which further increases the envelope of applications, including flexible solar cells and wearable electronics [1,2]. Silicon exfoliation involves peeling the top layer off a wafer, including any device built into the surface. This approach has the advantage of leveraging existing semi-conductor fabrication techniques to produce flexible devices while other flexible device manufacturing methods require the development of completely new manufacturing procedures.

The exfoliation process is represented in Figure 1. In this process, an adhesion layer of titanium and a seed layer of nickel are evaporated onto a wafer and on top of any already fabricated devices. Then an approximately 30 μm layer of nickel is electroplated on top of the wafer. Electroplating is a cost-effective process, but it results in some thickness variation. Most of this variation is then removed by laser cutting the outer perimeter off; resulting in an approximately 3 inch wafer. The wafer is then heat treated to induce a residual tensile stress in the nickel. The process is designed such that this stress is just below the required amount to cause spontaneous exfoliation of the silicon wafer. After heat treating a specific external load is applied to exfoliate the film in a controlled manner in order to maintain uniformity and regulate thickness. A new tool is being designed to precisely apply this load.

PROTOTYPE TOOL DESIGN

Previous versions of this process used a wedge or blade-like tool to apply extra stress near the crack front [3]. This produced friction and vibrations that introduced roughness into the exfoliated surface. Other groups used a tape handle layer to apply a peeling force by hand [4]. When tested, this produced inconsistency in the load and exfoliation results, but reduced roughness. Therefore, to overcome these limitations, a tool that could replicate controlled peeling-like loads was proposed.

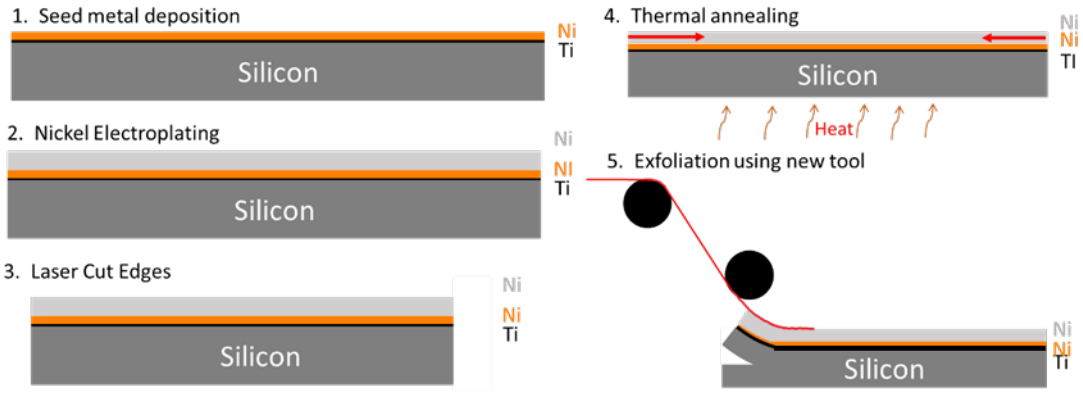

FIGURE 1. Exfoliation process flow

Design

To test this idea a prototype tool was built (shown in Figure 2) that could maintain a constant exfoliation angle, force, and speed. The tool was designed to be quickly manufactured and widely configurable to rapidly test different exfoliation concepts so that in the future a more advanced tool can be designed around the best one. The tool features a simple, adjustable roller design attached to a linear actuator. The roller heights and resulting angle are measured and clamped manually. The exfoliation force is set by clamping the handle film at a set preload, but a system for actively measuring the load during exfoliation is in the process of being added.

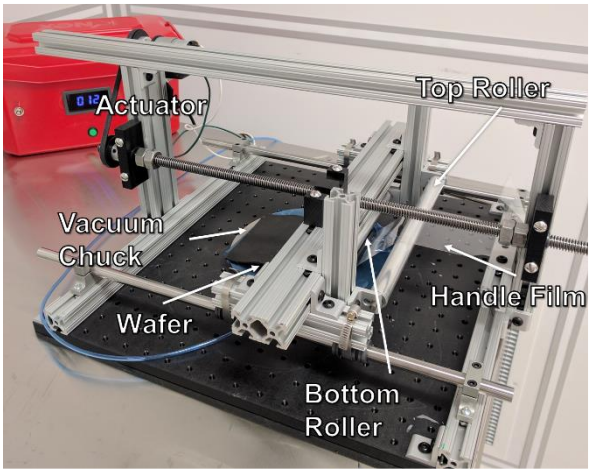

FIGURE 2. New exfoliation tool prototype

The wafer is flattened and adhered to a glass slide with double-sided adhesive polyimide tape and then secured with a vacuum chuck. The glass and tape are necessary because atmospheric air pressure is not enough to flatten the wafer that has been bowed by the tensile stress in the nickel. The flatten state creates a repeatable fixturing and helps define the stresses in the system. A handle film is then attached to the nickel surface with adhesive tape and the two-roller design moves the film across the wafer while maintaining a constant peeling angle and force to propagate the crack front. See Figure 1 for a side view of the roller configuration. Exfoliation speed can be adjusted via the PWM controller of the DC motor driving the leadscrew of the linear actuator. The test results shown here were done at a relatively slow speed of approximately 8 mm/min, but other speeds are being tested.

Results

Initial tests with 4 and 6 inch wafers using the prototype tool show good uniformity with thickness ranges from 5-35μm and a smooth surface. The samples also show improvement in usable area per wafer and reductions in roughness compared to earlier tests with the old blade-style tool. Test results are repeatable, but more testing and measurements need to be performed to develop a relationship between peeling angle, force, and crack depth.

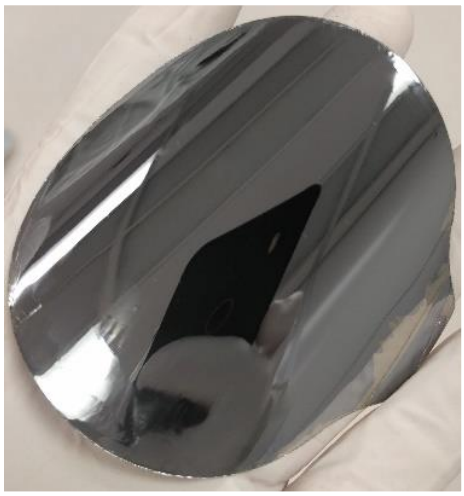

FIGURE 3. Exfoliated film sample. Silicon side up with nickel backing.

Figure 3 shows an example of film exfoliated using the prototype tool. The ceiling tiles are clearly visible reflected on the surface; there is no patterning on this sample.

METROLOGY

Critical to improving the exfoliation processes is being able to measure and quantify the produced films. Fully characterizing the process requires thickness profile measurements for both the exfoliated film and the electro-deposited nickel across as much of the wafer as possible. A curvature profile is also necessary to define the stress state. These measurements presented some significant challenges due to the necessary vertical resolution of a few microns and horizontal range spanning the entire wafer. The unsupported silicon film is also very brittle and can only be handled with a backing layer which eliminated all available direct measurement methods. The solution was to use a combination of dual KEYENCE LK-H207K laser displacement sensors (shown in Figure 4) for point thickness measurements and an Olympus OLS-4100 confocal microscope for long profile scans to

build a complete metrology map. Data processing and synthesis was performed in MATLAB.

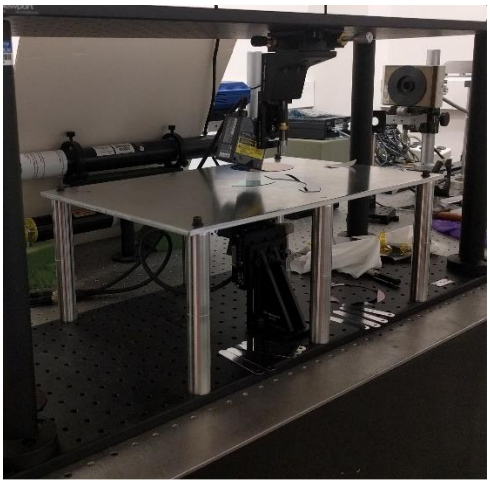

FIGURE 4. KEYENCE d*ifferential laser displacement thickness measurement system.*

Confocal line scans were taken between each stage of the process in a radial pattern and then leveled and subtracted from each other to find the film profiles. Point thickness measurements were also taken between stages in a defined grid pattern and combined with the lines scans to create a thickness profile. After the wafer has been through the thermal annealing process another set of lines scans are taken to define the curvature of wafer. The film thickness data, together with the post-anneal curvature profile can be used to estimate the stress state in the nickel using a modified Stoney's equation for (100) silicon wafers [5]. The results are shown in Figure 5.

The correlations between the nickel thickness and nickel stress and the resulting silicon film thickness can be inferred from the plots and the broad picture provided by the data will help build the relationship between the film thicknesses and stress state. This data helps inform and validate the FEA model being developed which is presented below.

MODELING

To better understand the ideal load that the tool would apply, a 2D FEA fracture mechanics model was created using ANSYS Mechanical's Fracture Tools. Previous work in the field of thin-film interfacial fracture mechanics indicates that a stable crack path in the substrate, parallel to the

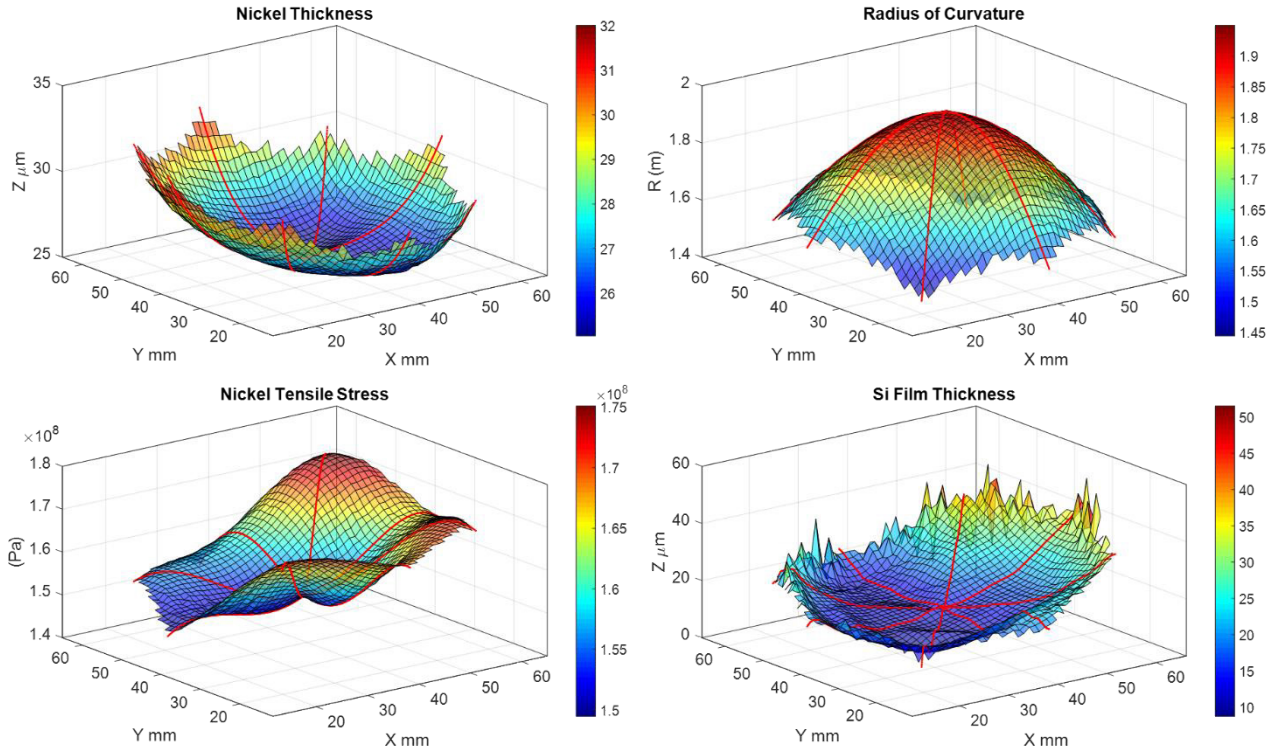

FIGURE 5. Metrology Surface Mapping. Red lines represent actual data, surface gird is a basic interpolation to aid visualization.

surface occurs when K_{II}=0 and that there is a characteristic crack depth for a given elastic system [6]. In this case the system is defined by the material properties, the film thickness, and the film stress for which the model can be run iteratively to solve for the characteristic crack depth. The purpose of the FEA model is to understand how to manipulate the characteristic crack depth when an external load is applied. Initial results from this FEA model and the analytical solutions from [4] indicate that changing the angle of the applied load will skew the mode mix ratio and therefore the characteristic crack depth. The final goal of the model is to form a complete design space that defines the produced film thickness for any given system and external load. The parameters could then be input into the new exfoliation tool which is presented below.

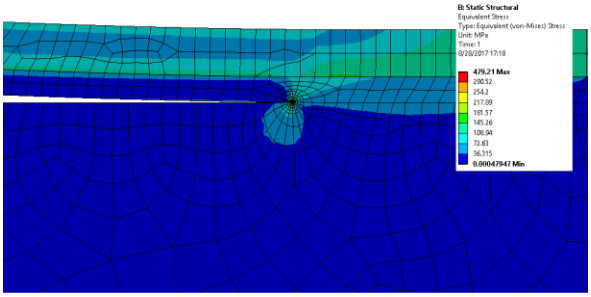

FIGURE 4. 2D FEA fracture model stress map

Figure 6 shows an example solution of the model with a layer of internally loaded nickel on top of the silicon substrate with a crack beneath the surface. The surface map shown is the equivalent stress of a typical crack system at its characteristic depth. K_I and K_{II} are calculated from the stress field.

Future Work

In the future, we will complete a design space exploration of the elastic system using the FEA model described above and validate test points using the current prototype. Information from those tests will be used to design and build an optimal tool with precision control over the external loads applied during exfoliation.

CONCLUSION

We have successfully demonstrated an exfoliation process to produce micron-scale single crystal silicon films over a wafer scale area. The construction of this tool and model provides the basis for scalable large area monocrystalline thin film devices.

ACKNOWLEDGEMENTS

The authors acknowledge and thank Miaomiao Yang for her experience, effort, insight, and support in accomplishing this work.

This work was supported in part by the National Science Foundation Nanosystems Engineering Research Center on Nanomanufacturing Systems for Mobile Computing and Mobile Energy Technologies (NASCENT), NSF EEC Grant No.1160494 and in part by the National Science Foundation Scalable Nanomanufacturing Program, NSF Contract No. ECCS-1120823. Any opinions, findings and conclusions or recommendations expressed in this material are those of the author(s) and do not necessarily reflect the views of the National Science Foundation. The author acknowledges the use of the NNCI facility at the Microelectronics Research Center, JJ Pickle Research Campus, UT-Austin, 10100 Burnet Rd, Austin, TX 78758.

REFERENCES

[1] Niepelt R, Hensen J, Knorr A, Stekenreiter V, Kajari-Schöder S, Brendel R. High-quality exfoliated crystalline silicon foils for solar cell applications. SiliconPV, Energy Procedia. 55 (2014) 570-577.

[2] Pang C, Lee C, Suh, K. Recent advances in flexible sensors for wearable and implantable devices. Journal of Applied Polymer Science. 2013; 10.1102: 1429-1441.

[3] Rao R, Mathew L, Saha S, Smith S, Sarkar D, Garcia R, et al. A Novel Low Cost 25 µm Thin Film Exfoliated Monocrystalline Si Solar Cell Technology. IEEE. 2001; 978-1-4244-9965-6/11.

[4] Bedell S, Shahrjerdi D, Fogel K, Lauro P, Bayram C, Hekmatshoar B, et al. Advanced flexible electronics: challenges and opportunities. Proc. of SPIE. Vol. 9083 90831G-1.

[5] Janssen G, Abdalla M, van Keulen F. Celebrating the 100th anniversary of the Stoney equation for film stress. Thin Solid Films. 2009; 517 1858-1867

[6] Drory M, Thouless M, Evans A. On the Decohesion of Residually Stressed Thin Films. Acta metall. 1988; Vol. 36, No.8, pp. 2019-2028

DEVELOPMENT OF MICRO BALL FORMING TO PROCESS MICRO STRUCTURE ON CURVED SURFACE

Yamaguchi K.[1], Nakano T.[1], Kakutani S.[1], Ota M.[1] and Egashira K.[1]
[1]Kyoto Institute of Technology
Matsugasaki, Sakyo-ku, Kyoto, Japan

INSTRUCTIONS

It is known that various surface function exceed the intrinsic properties of a material can be expressed by processing micro structure on a material surface, and it is possible to control optical properties, tribological characteristics, wettability and so on. It is expected the further development of product in various field by processing micro structure on the materials applying for various field such as energy saving field, environmental field and biotechnology field. Various processing methods such as micro cutting process, laser process and etching process have been developed for processing microstructure on a material surface [1-4]. However, these methods have many problems, such as low flexibility of process, low processing efficiency, use of chemicals in etching process that affect the environment. For this reason, a high efficiency microfabrication technique with small environmental burden is required. Thus, the authors developed Micro Ball Forming (MBF) method for processing microstructure onto the free-form surface [5]. Figure 1 shows the schematic diagram of MBF method [5]. In MBF process, a ball tool that has micro structure on the outer peripheral surface is pressed against a free form surface and move along the surface under a constant pressure for forming micro texture. It has no limits in rotational direction by using ball tool, whereas it can rotate only one direction in case of using roller tool. Therefore, high freedom movement of the tool is possible on the workpiece. Additionally by using constant pressure processing, it is not necessary to accurately measure the distance between the tool and the workpiece because the waviness of the workpiece and the positioning error can be absorbed. In author's previous studies, MBF device was developed, and evaluated its basic performance. Figure 2 shows the schematic diagram of MBF device. MBF device is consisted of hydrostatic fluid ball holding system and a constant pressure mechanism using a spring. In this study, a silicon nitride ball tool with micro structure on the whole surface was made by laser texturing method, and it is set in an

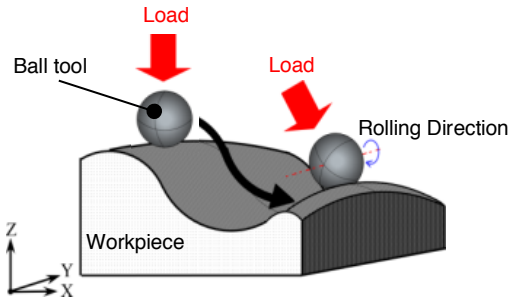

FIGURE 1. Principal of MBF method [5].

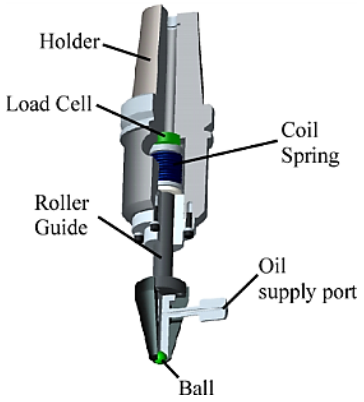

FIGURE 2. Schematic diagram of MBF device [5].

MBF device. The basic characteristics when using a ball tool having micro structure were evaluated by indentation experiments. As a result, it was clarified that an oil film is formed between the ball tool with micro structure and the holder. In addition, it was clarified that the depth of micro structure can be controlled by the hydraulic pressure and the processing load. Moreover, under the condition exceeding the certain load, it was found that the depth of micro structure is decreased by increasing processing load. Based on the above results, we tried to form the micro structure to a free form surface by MBF method, and it was clarified that texturing is possible across the whole area of free form surface.

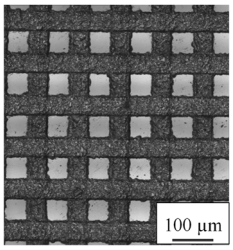

(a) Laser microscopic image.

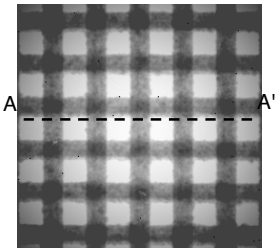

(b) Interferometric image.

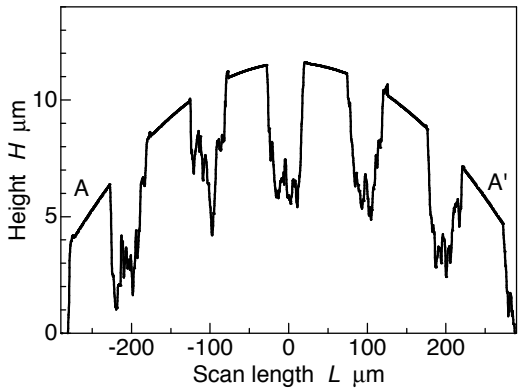

(c) Cross-sectional profile.

FIGURE 3. Shape of microstructure machined on ball tool.

TABLE 1. Experimental conditions of indentation using MBF device.

Spring constant	39.2 N/mm
Oil pressure	0.5, 1.0, 1.5, 2.0, 3.0 MPa
Ball tool	Si_3N_4 (Sφ10 mm)
Workpiece	Aluminum alloy (A5052) Pure titanium

BASIC CHARACTERISTICS OF MBF DEVICE

In this research, the basic characteristics of MBF device was evaluated by indenting Si_3N_4 ball to A5052 and pure titanium plates. The ball tool has grid-like groove on the surface and assembled into the MBF device. Fig.3 shows the surface of ball tool. The grid-like grooves were machined by using nanosecond green pulse laser. MBF device has a hydrostatic holding mechanism for rotating ball tool freely, and it is necessary to form oil film between the ball tool and the holder. Therefore, the relationship between oil pressure and the maximum load capable of forming oil film. Fig.4 shows the schematic diagram of the experimental method. Since it is extremely difficult to measure the actual oil film thickness, the floating height of the MBF device when operating the hydraulic pump was defined as the oil film thickness. Table 1 shows the experimental conditions. In this

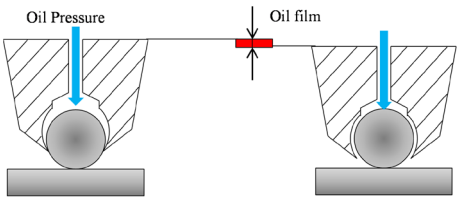

(a) Schematic diagram.

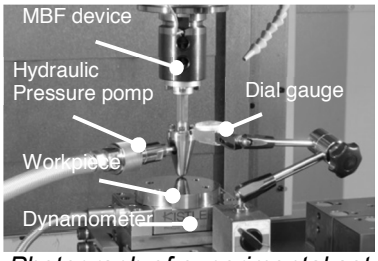

(b) Photograph of experimental setup

FIGURE 4. Experimental method of basic characteristics of MBF.

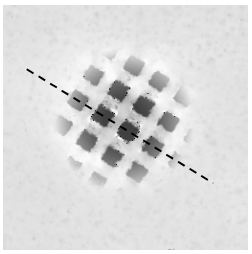

(a) A5052, 0.5 MPa

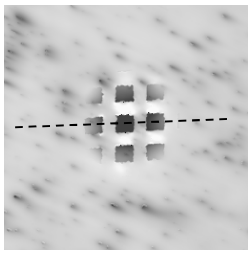

(b) Pure titanium, 0.5 MPa

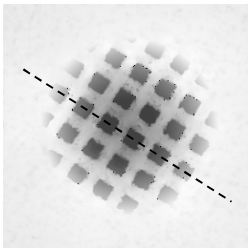

(a) A5052, 1.0 MPa

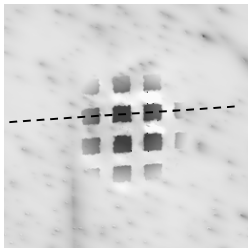

(b) Pure titanium, 1.0 MPa

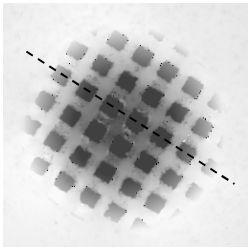

(d) A5052, 1.5 MPa

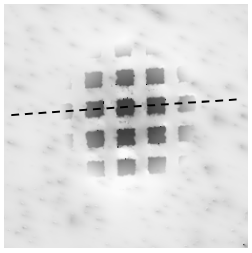

(f) Pure titanium,: 1.5 MPa

FIGURE 5. Indentation marks produced by Si_3N_4 ball tool.

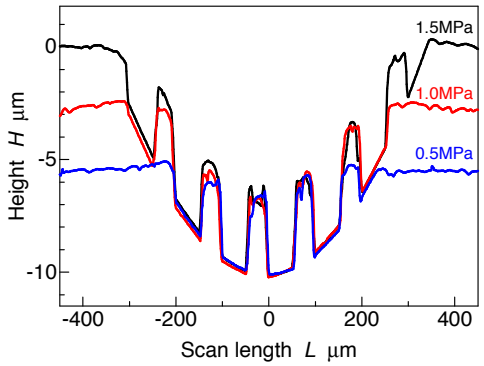

(a) A5052

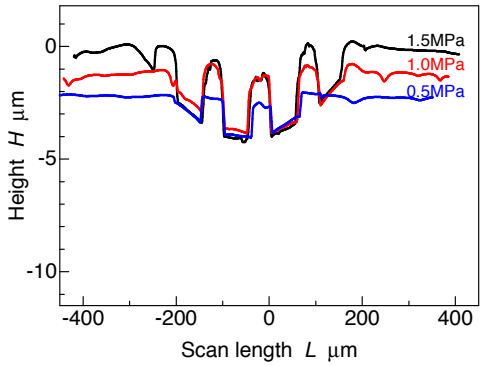

(b) Pure titanium

FIGURE 6. Cross-sectional profiles of indentation mark.

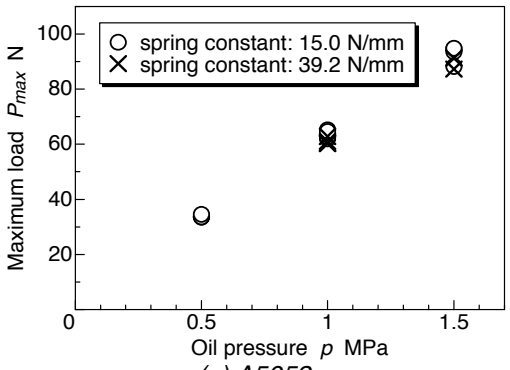

(a) A5052

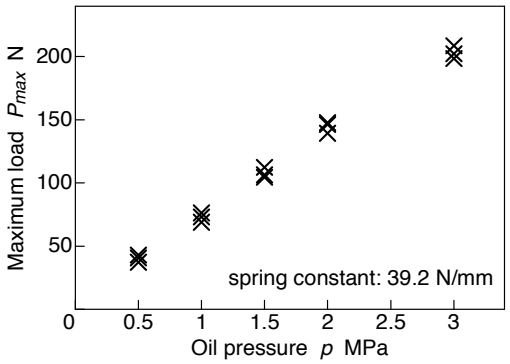

(b) Pure titanium

FIGURE 7. Relationship between oil pressure and maximum load.

experiment, an aluminum alloy (A5052) and a pure titanium plate were used for workpiece.

Figure 5 shows an example of indentation mark on the aluminum alloy surface when applying the maximum load at each oil pressure and Figure 6 shows the cross-sectional profiles of the dashed line in Figure 5. In both workpieces, it is found that the depth of indentation mark is increased by increasing oil pressure. From Figure 6, in the case of pure titanium, the protrusions at 0.5 MPa produced by indentation is lower than other conditions. This shows that the material is not filled in the groove of the ball tool surface. Moreover, the highest protrusion produced on aluminum alloy is higher than that of the case of pure titanium. This result indicates that the elastic recovery of pure titanium is larger than that of aluminum alloy.

Figure 7 shows the applied load just before the oil film breakage at each oil pressure, in other words, the maximum load that the oil film can be kept between the ball tool and the holder. In both workpieces, it is found that proportional relationship between oil pressure and maximum load. As a result, if the required depth of microstructure is determined, the oil pressure that is necessary for texturing by MBF method can be decided.

Texturing microstructure on flat surface by MBF

In the previous chapter, the basic indentation characteristics of MBF device were clarified. This chapter shows the texturing characteristics when horizontally feeding MBF device on a pure titanium plate. The ball tool was pressed on the workpiece surface at near the maximum load at each oil pressure, and then texturing was carried out by feeding the workpiece horizontally. The experimental conditions are shown in Table 2. The oil pressure was set to 1.0 and 3.0 MPa. The feed

TABLE 2. Experimental conditions of texturing on flat surface by MBF.

Spring constant		39.2 N/mm
Oil pressure		1.0, 3.0 MPa
Feed	speed	120 mm/min
	length	40 mm
Ball tool		Si_3N_4 (Sφ10 mm)
Workpiece		Pure titanium

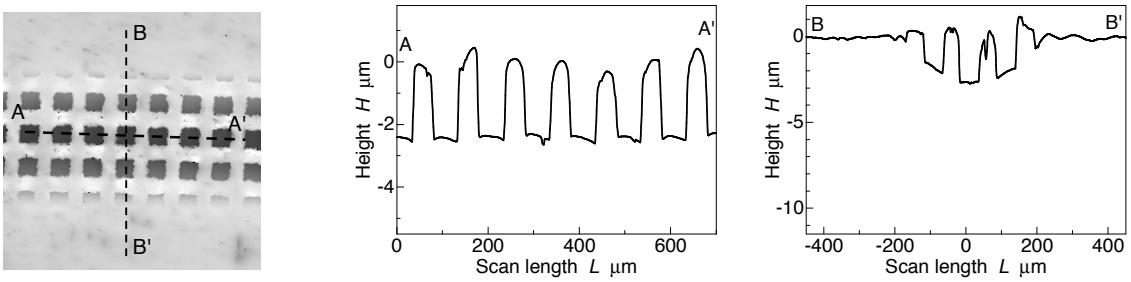

FIGURE 8. Textured surface at oil pressure was 1.0 MPa, feed speed was 120 mm/min.

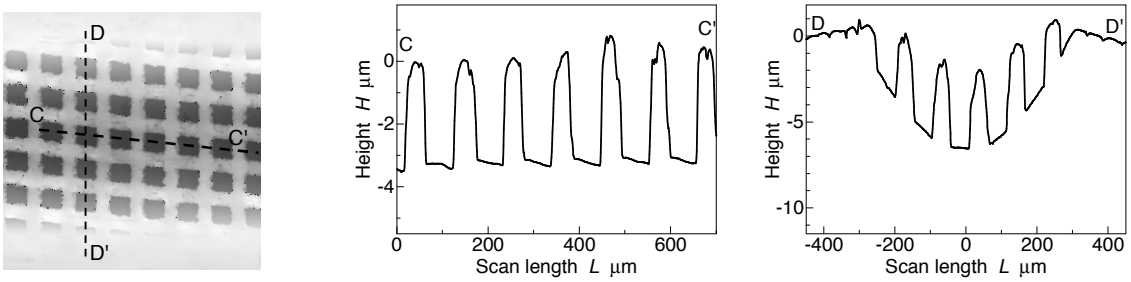

FIGURE 9. Textured surface at oil pressure was 3.0 MPa, feed speed was 120 mm/min.

speed was 120 mm/min and feeding length was 40 mm.

Figure 8 and Figure 9 show the textured surface. It is found that the microstructures can be formed on the workpiece surface at both oil pressure. The depth of the microstructures were almost same as that of indentation experiments and the shape of microstructures were not deviated. As a result, it was clarified that the ball tool can be rotated without slippage by feeding MBF device.

Texturing microstructure on curved surface by MBF

Texturing experiments were carried out on a titanium surface having the shape as shown in Figure 10 and Figure 11. The experimental conditions are shown in Table 3. The ball tool was pressed on the workpiece surface to approach the oil film thickness of 10 μm, and then MBF device was fed along the contour line of the workpiece by X, Y, Z axis of the machine tool. Figure 12 shows the feeding direction. The feeding direction was two types of reciprocating feed and spiral feed.

TABLE 3. Experimental conditions of texturing on curved surface by MBF.

Spring constant	39.2 N/mm
Oil pressure	3.0 MPa
Feed speed	240 mm/min
Ball tool	Si_3N_4 (Sφ10 mm)
Workpiece	Pure titanium

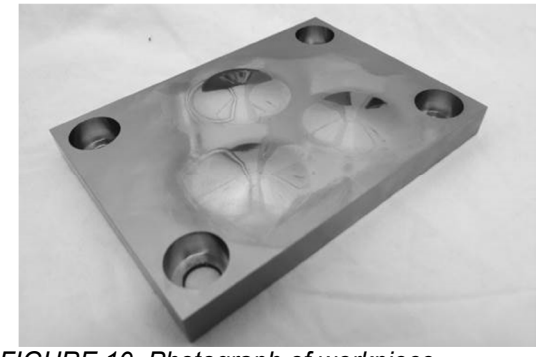

FIGURE 10. Photograph of workpiece.

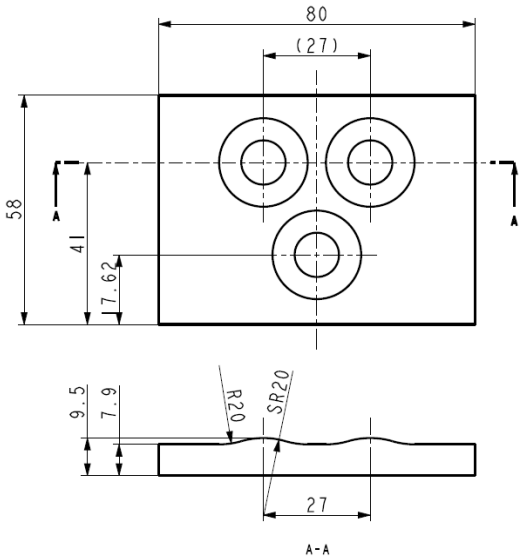

FIGURE 11. Schematic diagram of workpiece.

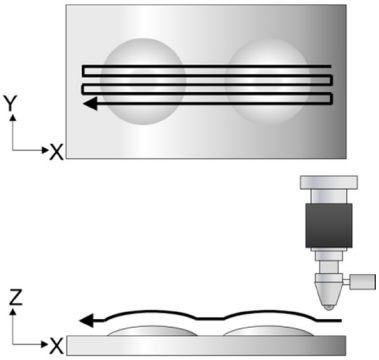

(a) Reciprocating feed.

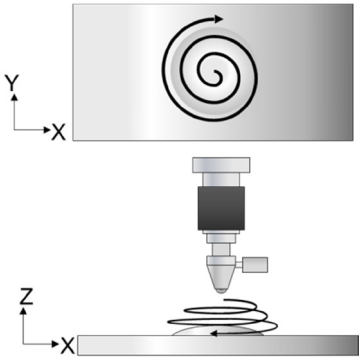

(b) Spiral feed.

FIGURE 12. Schematic diagrams of feeding direction.

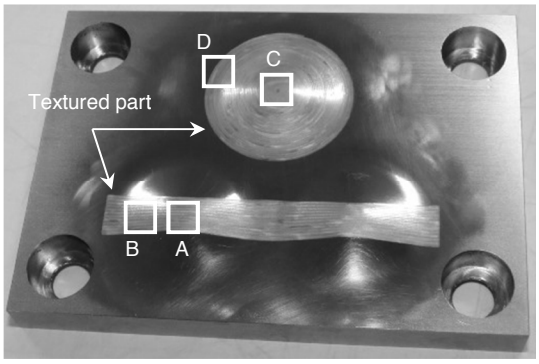

FIGURE 13. Photograph of curved workpiece after texturing by MBF.

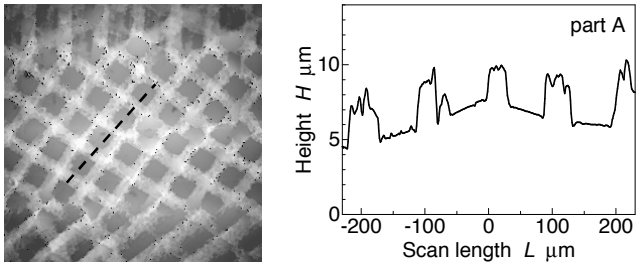

(a) Top of workpiece (part A in Figure 13).

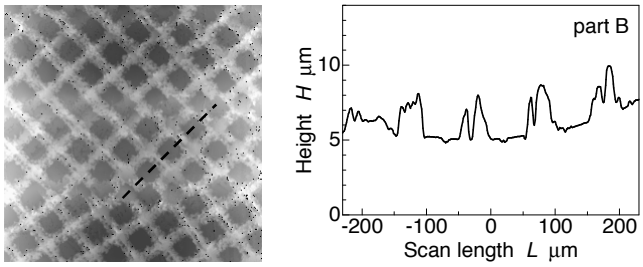

(b) Sloped surface of workpiece (part B in Figure 13).

FIGURE 14. Textured surface by MBF with reciprocating feed.

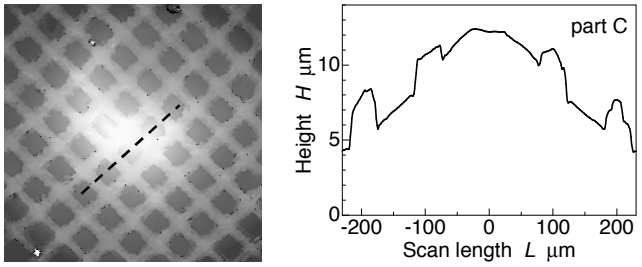

(a) Top of workpiece (part C in Figure 13).

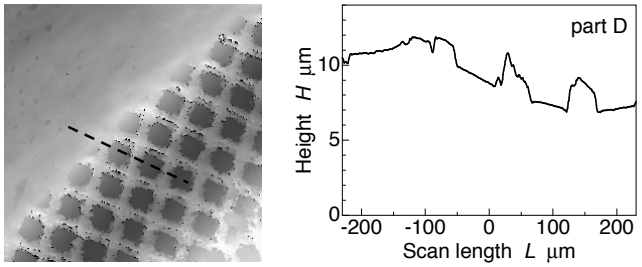

(b) Sloped surface of workpiece (part D in Figure 13).

FIGURE 15. Textured surface by MBF with spiral feed.

Figure 13 shows the photograph of the workpiece after the texturing by MBF. The microstructures were formed in the white dull part of the workpiece surface. Figure 14 and Figure 15 show the interferometric image and the cross-sectional profiles of the microstructures produced on the curved surface at each feeding direction. From these figure, it was found that the microstructures were transferred without slipping the ball tool even in the inflection point of the workpiece regardless of the feed direction. On the other hand, the boundary between tool passes clearly appeared in some areas. This boundary caused by transferring the spherical shape of the ball tool. It is thought that, the boundary between tool passes can be made as small as possible by controlling the applied load.

CONCLUSIONS

In this research, the basic characteristics of MBF device and the texturing characteristics when using a ball tool with microstructure were clarified. The following results were obtained:

(1) There is the proportional relationship between the oil pressure and the maximum load that the oil film can be kept between the ball tool and the holder.
(2) As a result of texturing experiment for the flat workpiece, it is clarified that the ball tool can be rotated without slippage by feeding MBF device.
(3) The microstructures were transferred without slipping the ball tool even in the inflection point of the workpiece regardless of the feed direction.
(4) It is thought that the boundary between tool passes can be made as small as possible by controlling the applied load although it appeared in some areas of the workpiece.

ACKNOWLEDGEMENT

This work was financially supported by THE AMADA FOUNDATION.

REFERENCES

[1] Shimizu J. Surface Texturing by Cutting. Journal of Japanese Society of Tribologists. 2015; 60; 3: 177-183 (in Japanese).
[2] Kawahara K., Ninomiya T., Sawada H. and Yokotani A. Femtosecond Laser Patterning and Anisotropic Wet Etching of Silicon Wafer for Fabrication of Periodic Structures. Journal of the Japan Society for Precision Engineering. 2009; 75; 10: 1211-1215 (in Japanese).
[3] Takada Y., Shinozaki M., Ota M., Egashira K., Yamaguchi K. and Hattori Y. Development of EDT equipment using wire tool electrode. Advanced Materials Research. 2015; 1136: 384-389.
[4] Lertphokanont V., Sato T., Oi M., Ota M., Yamaguchi K. and Egashira K. Friction Characteristics with Pin-on-Disc Friction Test on Microstructured Surface using Whirling Electrical Discharge Texturing. Advanced Materials Research. 2014; 1017: 417-422.
[5] Nakano T., Maeda K., Ota M., Egashira K., Yamaguchi K. and Uehara Y., Developed Micro Ball Forming device to produce microtexture on curved surface. Proceedings of the 16th International Conference on Precision Engineering. 2016: A201-8259.

DESIGN AND MODELLING OF A BIDIRECTIONAL THERMAL ACTUATOR

Cheng Zhao[1], Ian S. Ladner[1], Adam Song[2], Jonathan B. Hopkins[2] and Michael A. Cullinan[1]
[1]Department of Mechanical Engineering
The University of Texas at Austin
Austin, Texas, United States of America
[2]Department of Mechanical and Aerospace Engineering
The University of California, Los Angeles
Los Angeles, California, United States of America

INTRODUCTION

Thermomechanical actuators (TMAs) are considered to be an attractive choice for precision applications due to their high stiffness and force output in comparison to their electro-static counterparts as well as the capability to reach nanometer-level resolution with ranges of over several micrometers [1]. There have been prior attempts to achieve both expansion and contraction mechanisms for chevron-beam based TMA's [2]. However, they generally required separate designs where the location of constraint beams had to be altered for each mode.

The proposed actuator design allows for both push and pull actuation modes in a single device by joule heating separate portions of the device. Modelling of the actuator was done analytically through 1-D conduction bar element FEM and 3-D beam element FEM and results were compared with that from FEA software. Using the analytical model in conjunction with an optimization MATLAB program, four actuator designs were selected for initial fabrication that span across maximum force output and maximum stroke.

THERMAL ACTUATOR

Fabrication

The device is designed to be fabricated on an SOI wafer where the thermal actuator is made from the device layer and is electrically insulated from the handle layer by the buried oxide layer. By selectively etching the two layers and creating connections that go from the device layer to the handle layer and then back, it is possible to apply current to distinct portions of actuator while keeping them mechanically attached. Fig. 1. shows the actuator portion of a baseline device and Fig. 2. shows close-ups of the anchor portion.

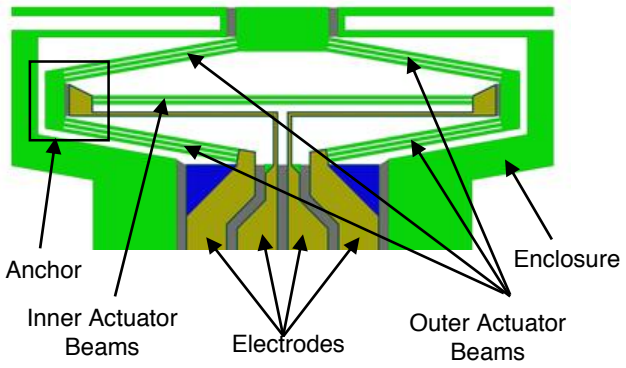

FIGURE 1. Frontal view of baseline bidirectional thermal actuator design. Green, gray, blue and gold indicate device-layer silicon, handle-layer silicon, silicon nitride and gold, respectively.

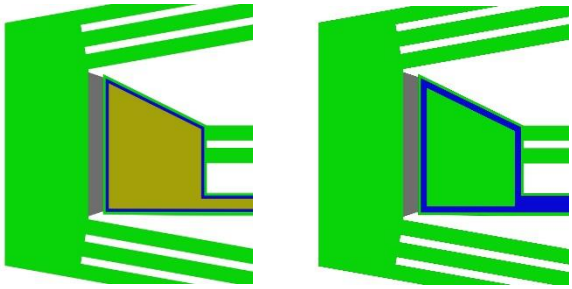

FIGURE 2. Close-up of anchor connecting outer and inner actuator beams, with (left) and without (right) gold layer shown.

Silicon nitride, followed by gold, is to be deposited, patterned and etched over portions of the actuator. The silicon nitride acts as electrical insulation that directs current to flow through the targeted joule heating components while also providing thermal resistance for the gold layer. Gold electrodes are patterned and used to direct current to flow through the actuation beams with

external electrical connections. As shown in Fig. 2 where the gold layer is hidden, it can be seen that there is an open pocket in the silicon nitride layer such that the gold layer is in contact with the device layer at the two ends of the inner actuator beams. Similar setup is located at the ends of the outer actuator beams.

Design

As shown in Fig. 1, the device contains two actuating components, the outer actuator and inner actuator, both contained within the outermost enclosure. The outer actuator consists of a pair of multi-chevron beam structures connected at the anchor and the inner actuator is a set of horizontal beams connecting the anchors through the handle layer.

When a voltage is applied across the two outer electrodes, current flows through the outer actuator and the chevron beams undergo joule heating and thermal expansion. The outward horizontal motion at the anchors is restricted by the inner actuator beams, resulting in an upwards displacement at the tip of the device. Conversely, when a voltage is applied across the two inner electrodes, current flows through the center beams. The thermally expanded beams push the anchors outwards which results in a downwards displacement at the tip of the device.

Modeling

For preliminary analysis and optimization, it was decided that conducting all thermal and mechanical studies with FEA software would require significant time investment due to the large number of design parameters that could be varied within the actuator, such as the number of beams, the beam lengths, the beam thicknesses and the angle of the beams. Thus, a 1-D conduction bar and 3-D beam FEM model of the actuator is constructed in MATLAB where the temperature profile based on the voltage applied, the stiffness and the tip displacement due to thermal expansion can be found. Only the actuating portion of the device, comprised of the outer and inner actuators as well as the connection between them, is studied in the analytical model as they are the components critical to the devices' performance and complimentary components such as the enclosure do not alter the results of optimization. This code allows for rapid estimation of relevant result and can be used for optimization in conjunction with a geometry generation tool.

Geometry Generation

The actuator designs are generated by varying a set of 11 governing geometrical parameters, namely the length, height and number of top, bottom and center beams, in addition to the angles of the top and bottom beams. The constraints on the parameters are then derived according to the geometric positions of the solid bodies such that there are no overlapping or interfering structures. Other geometric dimensions of the device are either fixed or adjusted accordingly to accommodate for the 11 changing variables. The geometries generated using this tool is then used as input to set up the analytical model bar/beam structures.

Thermal Model

First, it is necessary to obtain the temperature profile of the actuator in order to calculate the displacement of the tip due to the thermal expansion of the beams. Initial FEA studies with air convection set to all surfaces with heat transfer coefficient of $h \approx 40\ \mathrm{W/m^2K}$ [3] had an effect on the temperature profiles of the actuators of about 2% - 5% compared to the no convection simulations. Furthermore, heat loss through radiation in MEMS devices of this scale is expected to be minimal even at high temperatures (1000 ºC) [4], affecting less than 1% with rough calculations. Thus, conduction is considered to be the most prominent heat transfer mechanism by far and a 1-D conduction bar element FEM model was selected for the estimation of actuator temperature profiles.

The actuator is represented initially as a resistor-only electrical circuit where each resistor generates heat based on the joule heating equation, Eq. 1,

$$P = V^2 / R \qquad (1)$$

where the voltage, V, across the resistors can be found by solving the circuit through the MATLAB program and the resistances, R, can be found through Eq. 2,

$$R = \rho \frac{L}{A} \qquad (2)$$

where ρ is the resistivity of the resistor material, L is the length of the segment and A is the cross-sectional area of the segment. Images of the circuits corresponding to the baseline device for the two actuation modes can be seen in Fig. 3, where a set of actuator beams can be considered as the same number of resistors in parallel.

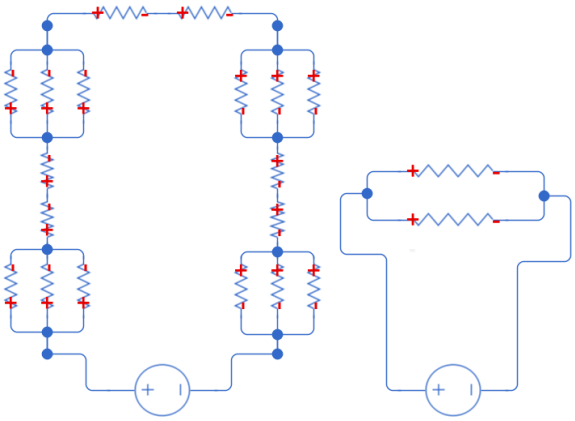

FIGURE 3. Baseline actuator resistor circuit in expansion mode (left) and compression mode (right).

A 1-D conduction FEM model representation of the whole actuator consisting of nodes and bar elements is then formed. To solve for temperatures at the nodes, the Fourier heat conduction equation, Eq. 3.

$$q = -Ak\frac{dT}{dx} \qquad (3)$$

is used where q is the rate of axial heat flow, k is the conductivity of the material, T is temperature and x is the distance along the element. This equation is then used to relate nodal temperatures to nodal heat flows in the matrix form, Eq. 4. [5],

$$\begin{bmatrix} Ak/L & -Ak/L \\ -Ak/L & Ak/L \end{bmatrix} \begin{Bmatrix} T_1 \\ T_2 \end{Bmatrix} = -\begin{Bmatrix} q_1 \\ q_2 \end{Bmatrix} \qquad (4)$$

where the subscript 1, 2 denote the two ends of a bar element. The square matrix is the element conductivity matrix, analogous to stiffness matrix of structural mechanics, which is generated for each element in the model and assembled into the global conductivity matrix. The boundary condition assumes that the bottom end of the devices will remain at room temperature. Five nodes, spaced evenly, are added to the middle of the bar elements, splitting each into six segments. With this procedure, the input heat flow derived from the resistor circuit is divided and applied among the five nodes to replicate the joule heating effect. Doing so also allows for a more detailed temperature profile result where the temperature at certain points along each element can be probed. Finally, the temperature at all the nodes in the model is solved using the known heat flow inputs as well as the set boundary conditions. The 1-D conduction visual representation of the baseline actuator without the added nodes is shown in Fig. 4.

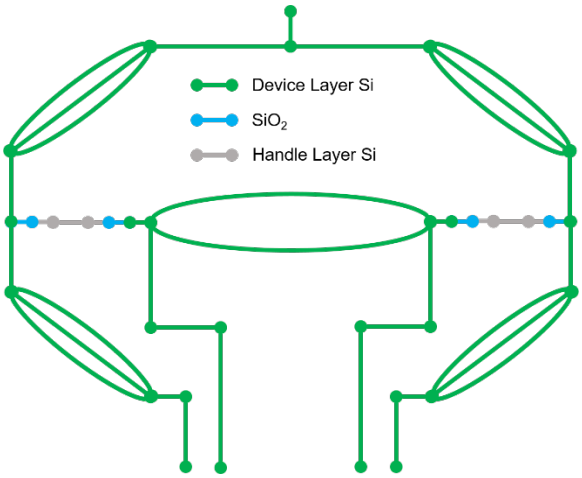

FIGURE 4. Visual representation of 1-D conduction model for baseline actuator, not drawn to scale.

Mechanical Model

Similar to the thermal model, the actuator is now represented as a 3-D beam element structure consisting of nodes and links. Due to symmetry, solving half of the actuator is sufficient. An image of the beam structure used to represent the actuator can be seen in Fig. 5.

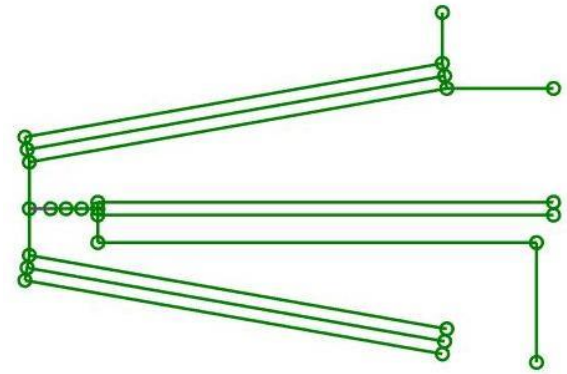

FIGURE 5. Frontal view of 3-D beam element structure for baseline actuator, generated with MATLAB program.

To solve for the beam structure's stiffness and displacements, the matrix equation, Eq. 5 is used,

$$[\mathrm{K}]\{\mathrm{D}\} = \{\mathrm{R}\} \qquad (5)$$

where $[\mathrm{K}]$ is the global stiffness matrix assembled using all of the element stiffness matrices of the members, which are modeled as Timoshenko beams, $\{\mathrm{D}\}$ is the nodal

displacement vector which can also be seen as boundary conditions and $\{R\}$ is the nodal forces vector which contains all external loads [5]. Transformation matrices for orienting 3-D beam elements and converting their element stiffness matrices to global coordinates are constructed using direction cosines. The necessity for the transformation matrices to be in 3-D occurs in the model at the anchor where two elements are normal to the plane of the actuator beams. Those elements are incorporated with the intention of mimicking the transition of device layer to handle layer and back.

The stiffness of the actuator is defined in this instance as the vertical force applied at the tip of the actuator divided by the resultant displacement of the tip. This value can be calculated using the MATLAB program by applying an arbitrary load at the tip. To estimate the tip displacement from thermal expansion, temperature profiles generated using the thermal model can be used as input. Based on the temperatures reached for each beam segment, external forces are applied at the end nodes such that the resulting axial strain matches the strain resulting from the thermal expansion. The equivalent loads applied at ends of beam elements is described by Eq. 6 [6]

$$R = \alpha \cdot \Delta T \cdot E \cdot A \qquad (6)$$

where α is the thermal expansion coefficient and E is the Young's Modulus of the material. The model is solved in the same method as the stiffness calculation, with the exception that the thermal loads are converted to equivalent external mechanical loads, which produces the displacement result from thermal expansion.

Stress and Buckling

Stress and buckling analysis for the actuator is done by applying the actuation force at the tip and finding the internal stresses as well as compressive forces for each beam member. The actuators are checked to ensure that no failure modes will occur based on a given voltage input. This capability assists in the estimation of appropriate operation parameters as well as resultant temperature ranges in the devices.

Optimization and Comparison with FEA

A BLOToptimization process [7] is configured using the 11 independent parameters as the optimization inputs, the total actuation force and stroke as the optimization objectives, and the geometric constraints as the constraint functions.

Stroke is calculated as the sum of the displacements of the tip in the expansion and in the compression mode. Actuation force is the product of the actuator stiffness and the tip displacement from thermal expansion in the two actuation modes, which can also be interpreted as the force required to restrict the tip from displacing given that the device is being joule heated. Fig. 6. shows the cloud plot of the performances of different actuator geometries calculated using the analytical model in conjunction with FEA, where each point corresponds to a distinct design.

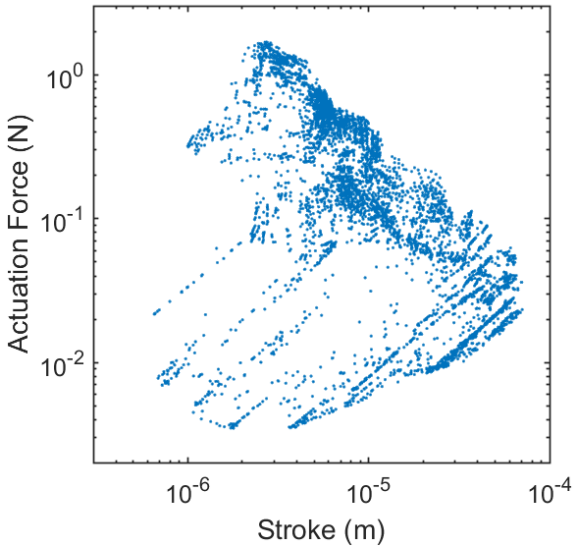

FIGURE 6. Cloud plot from optimization for performance of actuator designs.

Four actuator geometries are selected from the optimization for fabrication, ranging from one nearing highest force output to one nearing highest stroke while minimizing tradeoff. They are marked in Fig. 7.

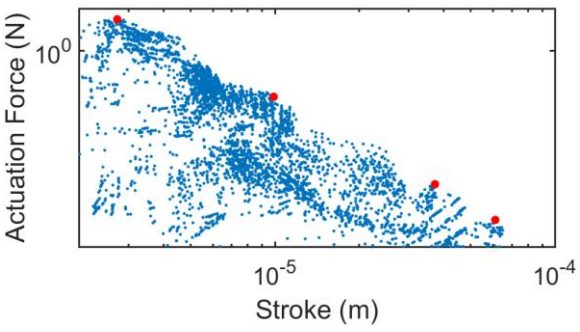

FIGURE 7. Zoom-in cloud plot with four selected designs from optimization marked in red.

As an example, the actuator geometry with the highest stroke out of the four (actuator #4) can be seen in Fig. 8 which differs quite drastically in appearance from the baseline.

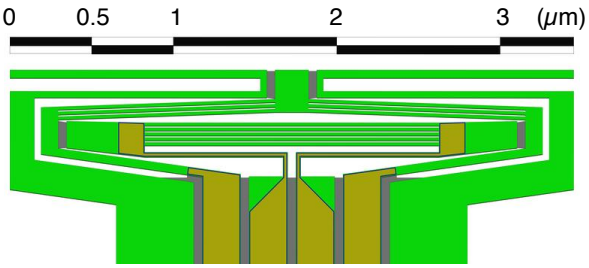

FIGURE 8. Optimized actuator configuration with highest stroke out of the selected four.

The four actuator geometries are further analyzed using COMSOL FEA software and results are compared with that from the analytical model.

Thermal Model

Table 1 shows the temperature comparisons for various probe points on actuator #4.

TABLE 1. Temperature comparisons between FEA and model results for expansion and compression modes of actuator #4.

Actuator #4 Temperatures	Expansion		
	FEA (ºC)	Model (ºC)	% Diff
TopBeamTipEnd	727.8	804.8	-10.6%
TopBeamAnchorEnd	505.2	536.9	-6.3%
TopBeamAvg	654.4	710.9	-8.6%
BottomBeamAnchorEnd	485.5	505.3	-4.1%
BottomBeamBaseEnd	139.8	131.9	5.7%
BottomBeamAvg	330.1	339.4	-2.8%
CenterBeamAvg	349.7	383.8	-9.7%
MiddleTopAvg	229.6	257.0	-11.9%
MiddleSideAvg	89.9	90.0	-0.1%
TipSideMin	727.9	805.6	-10.7%
TipBottomAvg	728.0	805.3	-10.6%
	Compression		
	FEA (ºC)	Model (ºC)	% Diff
TopBeamTipEnd	369.4	416.4	-12.7%
TopBeamAnchorEnd	393.9	416.4	-5.7%
TopBeamAvg	377.4	416.4	-10.4%
BottomBeamAnchorEnd	387.3	400.5	-3.4%
BottomBeamBaseEnd	87.8	90.4	-3.0%
BottomBeamAvg	225.8	245.4	-8.7%
CenterBeamAvg	768.8	783.8	-1.9%
MiddleTopAvg	437.6	447.3	-2.2%
MiddleSideAvg	157.8	145.1	8.0%
TipSideMin	377.3	416.4	-10.4%
TipBottomAvg	377.3	416.4	-10.4%

Comparisons indicate that the thermal model is generally accurate with an overall overestimation of temperature. Results from the other selected three actuator designs are also favorable with percentage differences generally below 20%.

Mechanical Model

Table 2 shows the stiffness comparisons for the four selected actuator designs.

TABLE 2. Stiffness comparisons between FEA and model results for the four selected actuators.

	FEA	Model	
Actuator #	Stiffness (N/m)	Stiffness (N/m)	% Diff
1	1.81×10^{6}	2.25×10^{6}	-23.8%
2	1.41×10^{5}	1.79×10^{5}	-26.8%
3	7.57×10^{3}	8.55×10^{3}	-12.9%
4	2.89×10^{3}	2.40×10^{3}	16.9%

The percent difference is somewhat larger than for the temperature study, however the same decreasing trend can be observed in both FEA and the model where the actuators with lower stiffness will have increasing tip displacements. Furthermore, this is in account of the fact that the stiffness covers a very large range, from as low as around 3000 N/m to as high as around 1.8×10^{6} N/m which is a factor of 600.

Table 3 shows the tip displacement comparisons due to thermal expansion of the four selected actuator designs.

TABLE 3. Tip displacement comparisons between FEA and model results for expansion and compression modes based on thermal expansion.

Actuator #	Expansion		
	FEA (μm)	Code (μm)	% Diff
1	3.03	2.65	12.6%
2	7.87	7.16	9.1%
3	18.97	18.15	4.3%
4	30.39	30.09	1.0%
	Compression		
	FEA (μm)	Code (μm)	% Diff
1	-1.04	-1.24	-19.4%
2	-7.27	-6.60	9.1%
3	-23.50	-31.11	-32.4%
4	-55.26	-48.90	11.5%

With the exception of two cases in compression mode, the results are generally comparable with the expected trend of increasing tip displacement with decreasing stiffness present in both.

Discussion

Numerous factors can be attributed to the difference in results between FEA and the analytical model. In the analytical model, approximations to geometrical dimensions must be made as to represent the device as a bar/beam structure. Furthermore, bar/beam FEM structures have idealized joints whereby elements are connected at a node, while meshes in FEA software are able to produce much more accurate representation of connections. Lastly, degrees of freedom and boundary conditions cannot be perfectly replicated in the analytical model due to the fact that they must also be applied at nodes. Specific to the thermal portion of the model, the theoretical calculation assumes that current passes through the entirety of the bar element cross-sectional areas while in FEA this assumption may not stand. Thus, it is likely that the general overestimation of the temperature in the analytical model is a result of this assumption of maximum joule heating, and with actuator designs that have beams with large cross-sectional areas, the difference of the results when compared to that of FEA would also be larger.

If time permits, optimization conducted purely through FEA software would likely produce more accurate results, however the analytical model appears to be consistent with general performance trends and is fairly accurate in its predictions, so it can suffice in terms of preliminary analysis and device selection.

CONCLUSION

This paper introduces a chevron beam based thermal actuator that is capable of bidirectional displacement. The modeling of the actuator is done analytically through a combination of 1-D conduction bar element FEM and 3-D beam element FEM with results comparable with that from FEA. Through optimization, four actuator designs ranging from high force output to high stroke are selected for fabrication.

ACKNOWLEDGEMENT

This work was supported in part by the Air Force Office of Science Research under award number FA9550-15-1-0321. Byung “Les” Lee is gratefully acknowledged.

REFERENCES

[1] Chen S-C, Culpepper M. Design of Contoured Microscale Thermomechanical Actuators. Journal of Microelectromechanical Systems. 2006; 15(5): 1226–34.

[2] Luo JK, Flewitt AJ, Spearing SM, Fleck NA, Milne WI. Three types of planar structure microspring electro-thermal actuators with insulating beam constraints. Journal of Micromechanics and Microengineering. 2005; 15(8): 1527–35.

[3] Hu XJ, Jain A, Goodson KE. Investigation of the natural convection boundary condition in microfabricated structures. International Journal of Thermal Sciences. 2008; 47: 820–824.

[4] Hickey R, Kujath M, Hubbard T. Heat transfer analysis and optimization of two-beam microelectromechanical thermal actuators. Journal of Vacuum Science & Technology A: Vacuum, Surfaces, and Films. 2002; 20(3): 971-974.

[5] Cook RD, Cook RD. Concepts and applications of finite element analysis. India: John Wiley & Sons (Asia); 2003.

[6] Zhu Y, Corigliano A, Espinosa HD. A thermal actuator for nanoscale in situ microscopy testing: design and characterization. Journal of Micromechanics and Microengineering. 2006; 16: 242-253.

[7] Hatamizadeh A, Song Y, Hopkins JB. Geometry Optimization of Flexure System Topologies Using the Boundary Learning Optimization Tool (BLOT). Proceedings of the American Society of Mechanical Engineers (ASME) International Design Engineering Technical Conferences and Computers and Information in Engineering Conference (IDETC/CIE); 2017 Aug 6-9; Cleveland, USA.

INVESTIGATION IN MICRO-EDM TECHNIQUES FOR LASER TARGET APPLICATION

Johan André, Nicolas Barnay, Alexis Gregoire, Cedric Chicanne, Marc Theobald
CEA / Valduc, FRANCE – 21120 Is-sur-Tille

INTRODUCTION

In order to produce laser targets for laser plasma experiments, CEA / Valduc operates different fields of mechanical machining techniques, including μ-EDM (electric discharge machining). In addition to conventional machining (ultra-precision milling and turning), this technique allows machining a wide range of geometries (revolution or prismatic shapes with narrow slices/pockets down to 5 μm) in a wide range of materials, from gold to some kinds of carbides.

The key point of this machining technique is the ability to shape hard materials (Boron carbide, Tungsten, stainless steel…) that could be hardly milled or turned. According to the laser target parts specifications (millimetric parts with micrometric wall thickness), the target department has developed several tools and methods to adapt μ-EDM process for target manufacturing (milling and turning-like methods with electrical discharges), to manufacture 3D shapes in hard materials.

MACHINE TOOL SETUP

The μ-EDM equipment used in the target department is a Sarix SX200 model that is between EDM wire cutting and EDM sinking. This device is commonly used as a 3 axis milling like process to realized 2D and 3D shape parts.

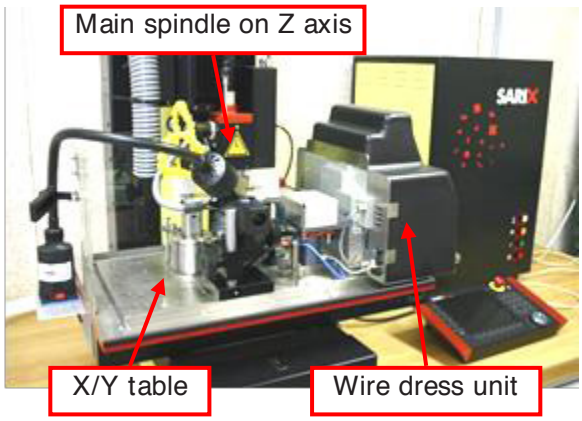

FIGURE 1. – μ-EDM, Sarix SX200 machine

By using a "built-in" wire dress device and switching the polarity of the erosion, electrodes can be shaped automatically as needed on the machine, allowing users to extend machine capabilities.

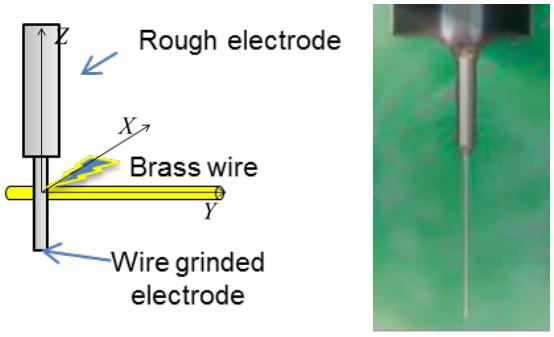

FIGURE 2. Electrode grinding setting and wire grinded electrode example.

Electrode grinding process consists in shaping the rough electrode (fixed in the main spindle and rotating along Z axis) by EDM method with brass wire. The brass wire circulation along Y axis ensures a constant fresh and abrasion free contact zone between electrode and brass wire.

The main purpose of this machine is to drill, carve or pocket different materials in order to produce target parts or micromechanics parts.

FIGURE 3. Example of a stainless steel mask with 35 µm matter bridges.

The typical specifications obtained with this technology are couple micrometer range tolerance associated with narrow slit capabilities (down to 10 µm width). As well, low mechanical stress induced by µ-EDM allows realizing narrow bridge; down to couple ten micrometers in common used materials (brass, aluminum, steel).

ADAPTATION TO TURNING EDM

The wire dress process can be considered as similar to a lathe, some revolution geometries could be obtained this way.

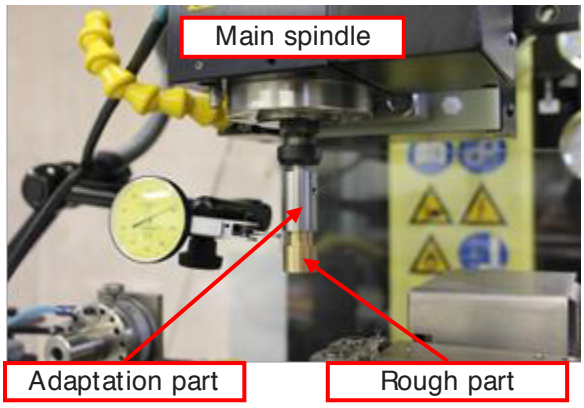

FIGURE 4. Adaptation for turning EDM setting.

It involves a specific adaptation to mount the rough piece into the Z/C axis. This adaptation consists in a specific part able to interface with the main spindle and hold part with a standard mandrel fixture. This part is back machind on the main spindle to limit runout effect.

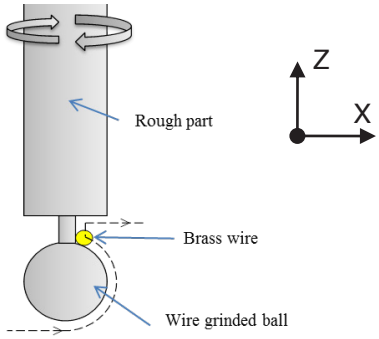

FIGURE 5. Cutting strategy.

First test has been performed to obtain spherical shape (ball machining). The main aim is to evaluate the process capability in terms of shape accuracy and surface finishing.
The cutting strategy consists in realizing the part in two steps: first rough cutting of a cylinder and the bottom face, and then, cutting the spherical shape from the bottom center axis to the top exterior (as described in FIGURE 5) in only one pass. The stalk diameter is 0.2 mm and the brass wire diameter is 0.3 mm.

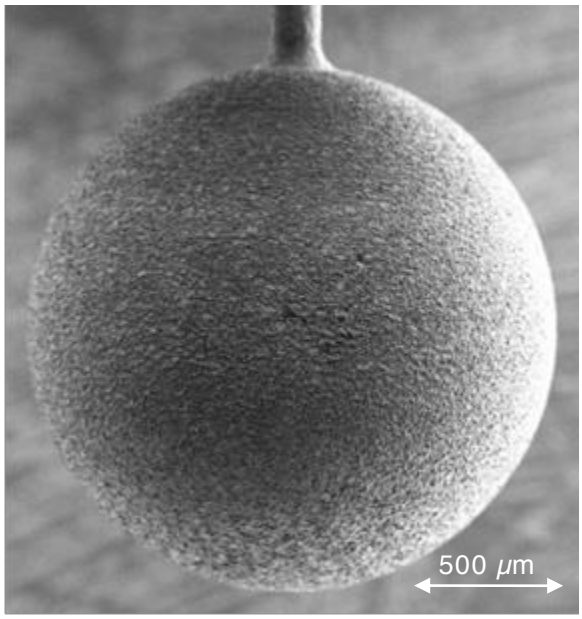

FIGURE 6. Tungsten carbide ball on stalk (SEM view).

The spherical shape accuracy is better than 5 µm (except in the stack zone). The arithmetic roughness is about 1,3 µm.

COMBINING MILLING AND TURNING PROCESS

The combination of the 2D milling and the turning EDM on the same machine allows reaching the complex geometries involved in laser targets elements.

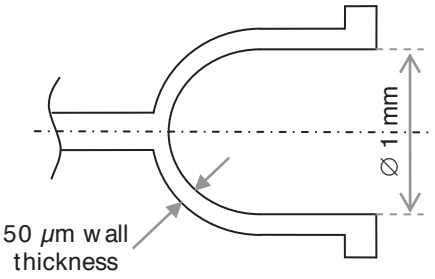

FIGURE 7. Cutting strategy of outer surface (rough and finishing)

The part realized for the test is a tungsten carbide tube with hemispheric bottom and 50 µm wall thickness. The strategy is to realize the outer surface then the inner surface. The outer surface is obtained by turning method and the inner surface by milling method with ball-end electrode; both operations are performed on the Sarix SX200.

Outer surface finishing

The cutting strategy is defined by computer assisted manufacturing software in two steps: rough cutting and finishing the shape (FIGURE 8) with tool radius (brass wire radius) and gap compensation.

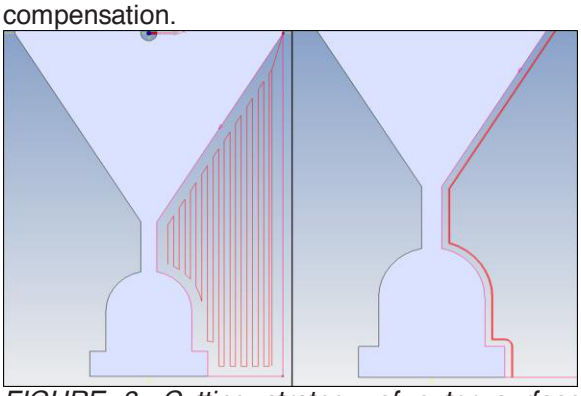

FIGURE 8. Cutting strategy of outer surface (rough and finishing).

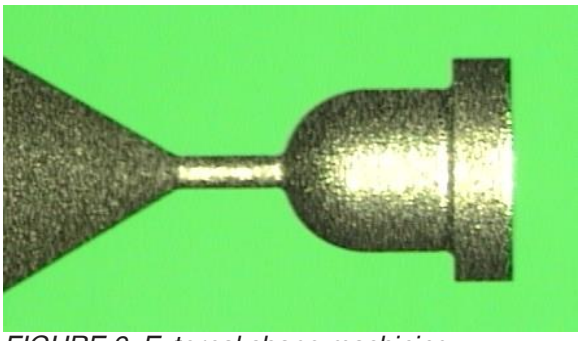

FIGURE 9. External shape machining

The outer surface is obtained with 10 µm shape accuracy and a similar surface finish as the ball cutting (arithmetic roughness between 1 and 2 µm).

Inner surface finishing

The inner surface is obtained EDM sinking method with a turning electrode. The tungsten carbide electrode is cutting, with the wire dress station, in the same shape as the inner surface of the part (cylinder with hemispheric bottom) with reduced dimensions for gap compensation. Several cycles (electrode and part cutting) have to be realized to compensate the electrode tool wear.

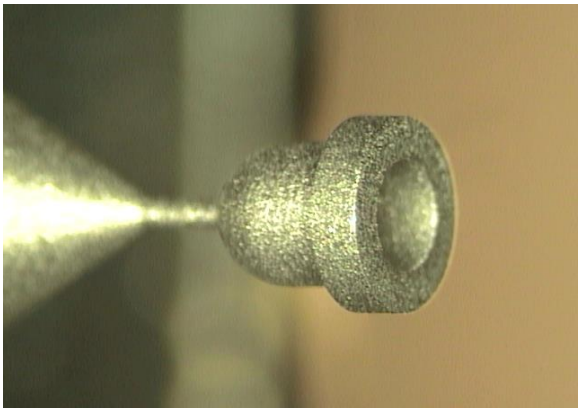

FIGURE 9. Internal shape machining

Optical observations reveal a similar surface finish as the outer shape. The inner diameter (∅ 1 mm) is obtained within 10 µm tolerance.
X-ray tomography has to be achieved to confirm the inner shape accuracy, especially in the spherical area.

CONCLUSION

These first tests have demonstrated that the combination of different methods of EDM on a same machine could be accurate enough for target elements machining at millimeter scale. These first investigations are mostly performed on steel and tungsten carbide and have to be carry on with hard to cut material. The next step is to improve the surface characteristics of the EDM by refining erosion parameters.

REFERENCES

[1] Hibbard R L., “An overview of the target fabrication operations at Lawrence Livermore National Laboratory”, ASPE Spring Topical Meeting (2005)

MECHANICAL MACHINING PROCESSES FOR LASER TARGET MANUFACTURING

Johan André, Julien Schunck, Alexis Gregoire, DeDemo Gregory, Cédric Chicanne, Marc Theobald
CEA / Valduc, FRANCE – 21120 Is-sur-Tille

INTRODUCTION

The target department of CEA produces laser targets in order to realize laser plasma experiments in different experimental facilities, especially on the Laser MegaJoule (LMJ, France). Laser experiments need a wide range of target geometries with common points: reduced dimensions (millimetric range) and thin wall thicknesses (micrometric range), as well as very strict dimensional and geometric specifications. According to these requirements, target specifications demand to machine different kinds of materials from metals (aluminum, copper, gold) to polymers and low density foams.
In most cases, a single target requires advanced material synthesis (low density foam, aerogel), complex shape machining and high accuracy in assembling and metrology process. In the same time, the rise of experimental configurations and the adaption for varied experimental facilities need a production process able to a quick and accurate response over a wide range of geometries and target scale. To match these aims, several adaptations have to be performed to develop specific processes, as well as recent technologies (additive manufacturing) have to be investigated to cross limitation of conventional technologies.

PROCESS DEVELOPMENT

Three main fields are investigated for machining operations: adaptations of machine tools, development of original process and parametric optimizations.

Machine tool adaptation

Several technologies are developed in order to meet different shapes on wide range of materials with the high required accuracy. As related [1] [3], [4]; the micro target application requires specific adaptation of these technics (customized machining setting, parameters) as well as combining them to obtain a final part, from the rough machining step to the finished part. Since a decade, diamond turning technology has become the heart of the machining process due to the very low tolerance (< 3 μm) and roughness (Ra < 10 nm) which can be obtained as well as the machining capability of low density material. Several developments have been done to adapt the machine setting to micro-machining and target application.

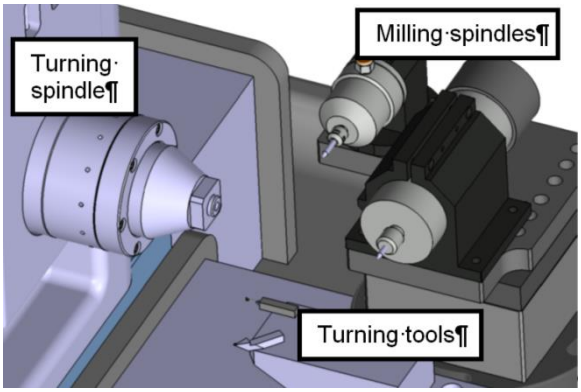

FIGURE 1. Example of combined turning/milling setting on 4 axis Moore Nanotech® 350FG

Figure 1 shows a combined turning/milling setting developed on 4 axis Moore Nanotech® 350FG. In this example, 2 radial milling spindles (60 000 RPM and 160 000 RPM) and 2 turning tools (for outer and bore machining) are disposed on the lathe. This kind of configuration offers several advantages. For one side, for complex parts, the number of process steps (turning and milling) can be reduced. Consequently, geometrical and dimensional variations between milled and turned surfaces can be optimized (and, hopefully, reduced) as well as the global process time can be reduced. For other side, this setting allows new machining optimization possibilities. Programming complex combined turning / milling operations using 4 axis motion (X, Y, Z, C), without dedicated software, is an issue. A specific post-processor

have been developed and, now, permits to use C.A.M. software for most applications.

In addition to the machine tool adaptations, specific process is developed to realize millimetric parts with micrometric (≈ 30 µm) wall thickness. The process is illustrated in Figure 2 and consists in realizing the part from a mandrel (with the inner shape of the part). Then, the mandrel is gold plated and machined again to the final outer shape of the part. Finally, the brass mandrel is removed by selective dissolution in an acid solution.

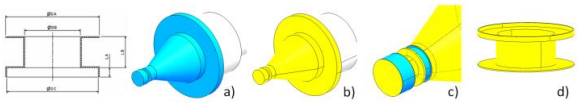

FIGURE 2. Machining of a gold "thin wall" part, a) Turning of brass mandrel, b) Gold plating, c) gold machining, d) selective dissolution of brass mandrel

From this process, several adaptations have been developed to meet target design requirements and to obtain polymer, gold/polymer and gold/aluminum part.

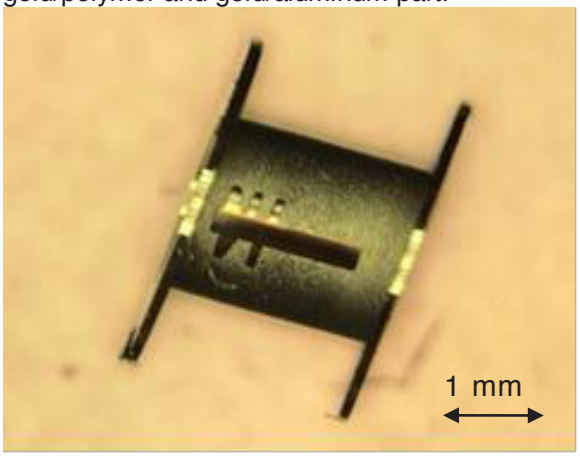

FIGURE 3. Example of 50 µm wall thickness gold tube.

For each kind of parts, the main problematic is the chemical compatibility between mandrel material, part material(s) and the type of selective dissolution used to remove the mandrel.

Low density foam machining optimization

Aerogel fabrication matter has to be considered for target application. This kind of material is brittle and sensitive to surface propagation of cracks introduced by machining stress. The main issue is the surface finish optimization to limit cracks and reduce the roughness.

As shows in FIGURE 4 – a, inappropriate machining parameters induce cracks issue. Several parametric tests were done, with ultraprecision lathe, by diamond turning mean (FIGURE 4 – b) and milling mean (FIGURE 4 – c). The main aim is to determine the optimal parameters for rough and half-finishing by turning method and for surface finishing by milling method.

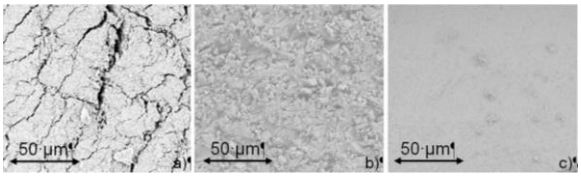

FIGURE 4. Comparison of surface finish (SEM), a) diamond turning – rough machining, b) diamond turning – finishing, c) milling

In terms of surface finish (TABLE 1.), the arithmetic roughness is significantly improved from more than 2 µm (rough diamond turning) down to 100 – 500 nm range (milling).

TABLE 1. Comparison of roughness (arithmetic roughness), a) diamond turning – rough machining, b) diamond turning – finishing, c) milling.

Process	Arithmetic roughness
Diamond turning rough machining	> 2 µm
Diamond turning finishing	700 – 1000 nm
Milling	100 – 500 nm

INTEGRATION OF ADDITIVE MANUFACTURING FOR TARGET PARTS FABRICATION

The development for 3D printing technologies allows realizing complex shapes impossible (or difficult) to obtain with other means, and in a short delivery time. Main difficulties for target application are the millimetric scale combined with the micrometric wall thickness, as well as the narrow tolerances required for the experiments.

In most cases, metallic target elements are obtained by electroplating method. As shows in Figure 2, this method consists in several steps

of machining and additions of material by electrodeposition.
From this standard process, several developments allow diversifying material and shape of the part produced. This process is composed of two ranges of technologies. In one hand, some processes add the selected material: Physical Vapor Deposition (PVD) or Glow Discharge Deposition (GDP) coating for thin layer of metal or polymer, electroplating process to obtained couple tens micrometers layer of metal (gold, copper) and polymer coating (epoxy resin or polystyrene) for larger thickness. In the other hand, several processes cut them in the right shape: mechanical machining (diamond turning and milling), micro-EDM and laser machining. In this situation, additive manufacturing can cross the limitations of each range of technologies mentioned previously by adding directly the selected material in the right shape.
In this context, additive manufacturing is a promising tool to obtain target parts as well as to develop process combining standard processes (coating and machining) with 3D printing.
The first approach consists in evaluating the potential of the SLA technology, with a Project 1200 (3D Systems) StereoLithography Apparatus (SLA) printer.

Application for protection cone

Most of the targets require protection cone (or disc).

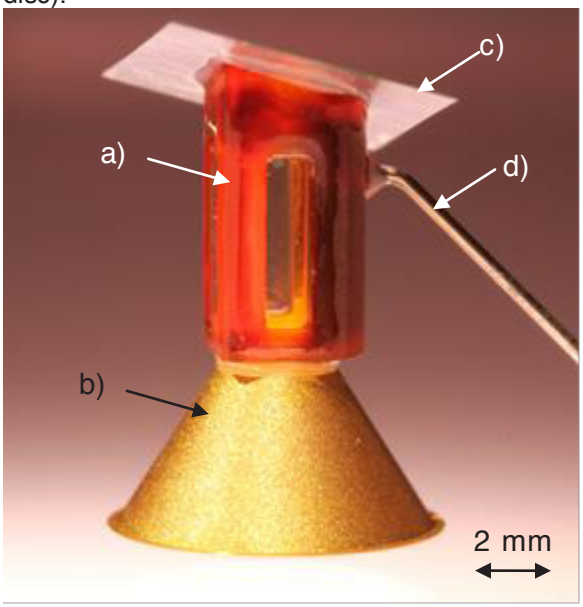

FIGURE 5. Example for laser target - a) gas filled gold/polymer hohlraum, b) protection cone, c) aluminum sample foil, d) gas filling tube.

These cones require a minimum thickness of metal (typically few micrometers of gold) to guarantee this protection. Due to quite large dimensions of these elements (about 10 mm length and / or diameter), a minimum thickness of about 40 μm is needed to guaranty mechanical stiffness required for handling this part without bend it.
The consequence of these technical limitations in term of wall thickness is the important weight of these protections: its can represent from 50% to 80% of the total weight of the target assembly. Experimentally, the mass of theses protections is the main contributor to the scrap generated by the target during experiment. Weight reduction of theses protections is an important purpose to limit diagnostic and optic damages in the experience chamber.

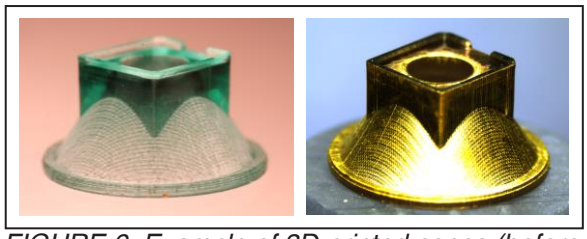

FIGURE 6. Example of 3D printed cones (before / after gold plating).

In the example shows in FIGURE 6, the cone's mass is reduced by a factor more than two by switching from a massive gold cone (40 μm thick) to 3D printed cone (180 μm thick with 5 μm gold thickness deposited by PVD).

Example of full target realization

FIGURE 7 shows a target, realized for the same purpose as the target in FIGURE 5, mostly obtained by additive manufacturing. This first prototype allows a reduction of 30% of weight as well as 50% off in term of process time (realization and assembly).

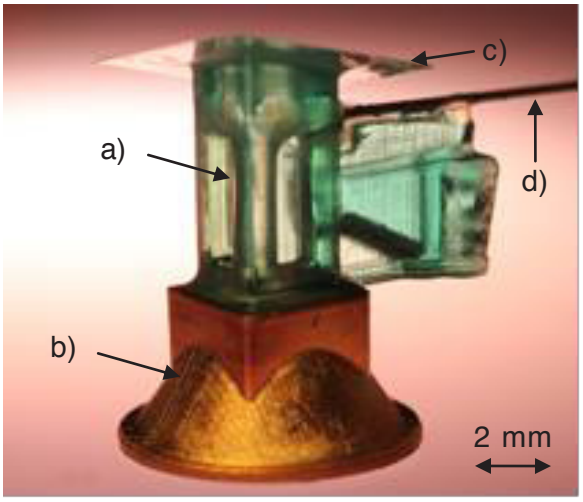

FIGURE 7. Example for laser target - a) gas filled polymer hohlraum, b) 3D printed cone, c) aluminum sample foil, d) gas filling tube.

This first test highlights that this technology allows realizing efficiently (in term of cost and delay) millimetric target parts, or sub-assembly parts, within 100 microns range accuracy.

CONCLUSION

In a context of constant growth of target complexity, these examples highlight the development problematic to meet physical requirement as well as to improve fabrication efficiency. Firstly, machine tool adaptations are required to cross limitations in terms of dimensional and geometrical accuracy and to be compatible with low dimensions of target parts. As well, the development of new process synoptic (mixing machining, assembling, chemistry process) is needed to open new possibilities in terms of geometries. Finally, most of the time, parametric optimization dedicated to a specific application (shape, material) is necessary to match dimensional, geometric or roughness specifications.
In any case, creativity and originality are the key to adapt standard process and machine tool to answer to specific requirement needed to build a laser target. As well, operator skill and knowledge of the target problematic are essential: handling and machining exotic material efficiently is an issue and require background in this field.
Metrology methods have also to be improved. The increase of process complexity needs accurate absolute measurement from common reference of the part to guarantee repositioning along the manufacturing process. For that, specific methods as well as in-situ measurement are under development. Foam and aerogel characterizations need to take up other challenges: transparent or diffusive surface combined with poor mechanical characteristics require to develop optical mean measurement able to detect the surface.
In addition to traditional technologies, others technics are explored (3D printing and MEMS technologies) for integration in the manufacturing process. With some developments and adaptations, these technics could cross technologic limitations and open onto new shape possibilities and material manufacturing.

REFERENCES

[1] Hibbard R L., “An overview of the target fabrication operations at Lawrence Livermore National Laboratory”, ASPE Spring Topical Meeting (2005)
[2] Obrey K.A.D., “Manufacturing complex silica aerogel target components”, Fusion Science & Technology, Vol 55 / N°4, pages 490-498 (2009)
[3] Day R.D., “Specialized machining techniques for target and diagnostic fabrication”, Fusion Science & Technology, Vol 55 / N°3, pages 301-307 (2009)
[4] Obrey K.A.D., “Utilizing conventional machining tools with customized machining techniques to manufacture multifaceted targets”, Fusion Science & Technology, Vol 63 / N°2, pages 247-251 (2013)
[5] Frederick C.A., “Fabrication of Ta_2O_5 aerogel target for radiation transport experiments using thin film fabrication and laser processes”, Fusion Science & Technology, Vol 55, pages 499-254 (2009)
[6] T. CARDENAS & al., “Additive Manufacturing Capabilities applied to inertial confinement fusion at Los Alamos National Laboratory”, Fusion Science & Technology, Vol 70, pages 288-294 (2016).

PRECISION HARD TURNING ON A LATHE RETROFITTED WITH AN OIL HYDROSTATIC SPINDLE

Dave A. Arneson, Byron R. Knapp
Professional Instruments Company
Hopkins, Minnesota, USA

INTRODUCTION

Hard turning has many advantages over grinding including: the ability to remove stock faster, simpler generation of complex shapes, and easier recycling of waste, but the spindles in commercial hard-turning machines tend to be large, expensive and fragile. For precision turning of hardened steels, air-bearing spindles may lack the ability to withstand sudden overloads. A high pressure oil hydrostatic spindle is a logical alternative due to its greater load capacity combined with microinch-level error motions. The squeeze film effect of the oil helps to prevent damage to the bearing surfaces during an overload. An oil hydrostatic spindle was retrofitted into a conventional CNC lathe to explore its effectiveness in precision turning of hardened steel. Spindle metrology tests demonstrate that this spindle has radial error motion less than 0.25 microinches. Cutting tests in hardened A-2 tool steel showed roundness errors better than 17 microinches and surface finishes better than 6 microinches Ra.

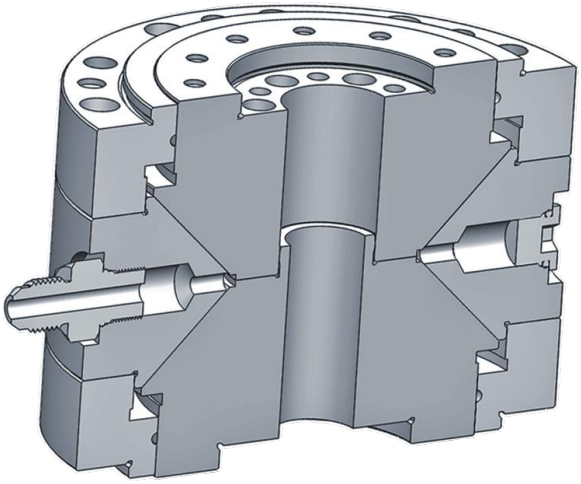

FIGURE 1. Biconic bearing surfaces of the 4RH oil hydrostatic spindle.

FIGURE 2. 4RH oil hydrostatic spindle.

DESIGN

The compact size and simple construction of the Professional Instruments Model 4RH biconic oil hydrostatic spindle shown in Figure 1 allows for this spindle to be used in a variety of situations.

The motivation for a step-compensated bi-conic spindle is derived from several potential advantages of the bi-conic design including:

- High bearing efficiency (load capacity for a given volume)
- High structural stiffness (enabling the use of higher bearing pressures)
- Higher oil film pressure than restrictor design
- Balance of radial, axial and tilt load capacities
- Design simplicity (reduced complexity)

This step-compensated design has several advantages over a pocketed design with restrictor-compensation:

- Increased bearing area
- No pocket “print-through” to error motion
- Higher-pressure bearing films
- Improved bearing stability
- No complicated up-stream restrictors

It is ideally suited to be retrofitted into existing machines. The squeeze film effects and lubricating properties of the oil help to prevent damage to the bearing surfaces during unexpected overloads. Spindle accuracy results shown in Figure 3 demonstrate that this spindle has radial error motion better than 6 nanometers. In this work, the oil hydrostatic spindle was retrofitted into an inexpensive Haas GT-20 CNC lathe.

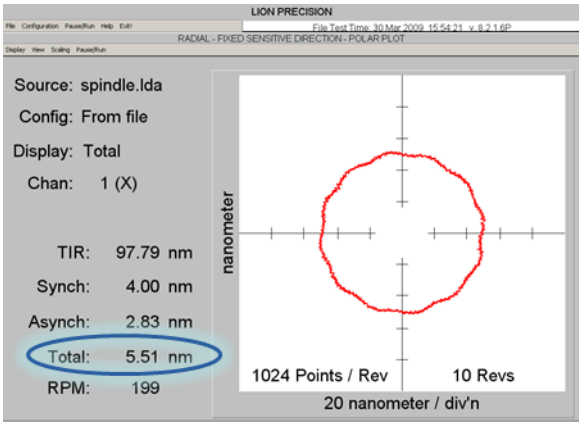

FIGURE 3. Radial error motion measurement of the oil hydrostatic spindle is 5.5 nm.

APPROACH

A cylinder of A2 tool steel hardened to 63 Rc was chosen as a representative material for test cuts. The cylinder is Ø2.5 inch by 3 inches long. A CBN insert (Sumitomo BNC 160 2NC-CCGW 09T304WG) with a 0.016 inch nose radius and positive wiper was used with flood coolant. The cone was cut at a constant spindle speed of 600 RPM. A depth of cut of 300 microinches was used with a feed rate of 600 microinches per revolution. This depth was chosen because such light cuts in hardened steel require the spindle to be extremely stiff.

FIGURE 4. Setup showing the hardened A2 tool steel cylinder testpiece.

RESULTS

Benefits of using the oil hydrostatic spindle are shown in surface finish and in form errors. A Mitutoyo SJ-400 surface profilometer was used to measure a surface roughness better than 6 microinches Ra perpendicular to the feed lines.

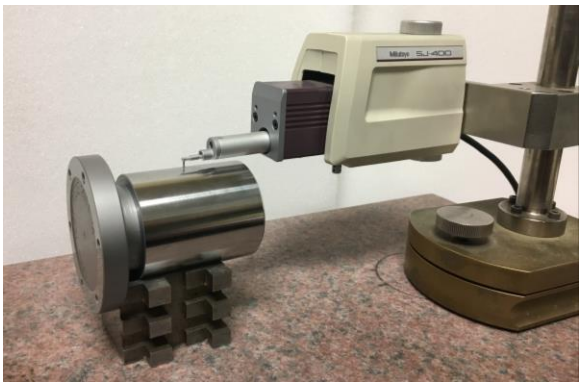

FIGURE 5. Surface profilometry setup.

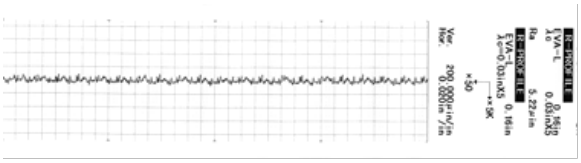

FIGURE 6. Surface profilometry demonstrates better than 6 microinches Ra.

Roundness of the cylinder is measured using a 4R Blockhead air bearing spindle with encoder for rotation. The analog signal from a high resolution lever-head LVDT probe with a ruby tip is processed by custom roundness software. The out-of-roundness measurement of the cylinder is shown in Figure 8.

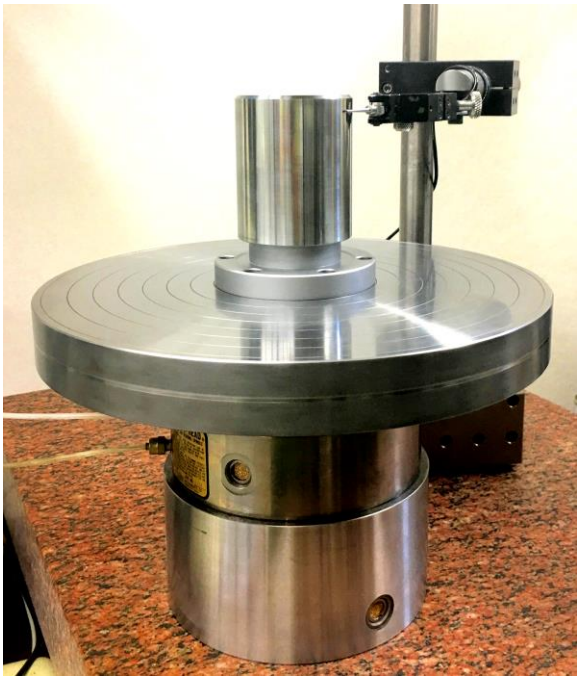

FIGURE 7. Roundness measurement setup.

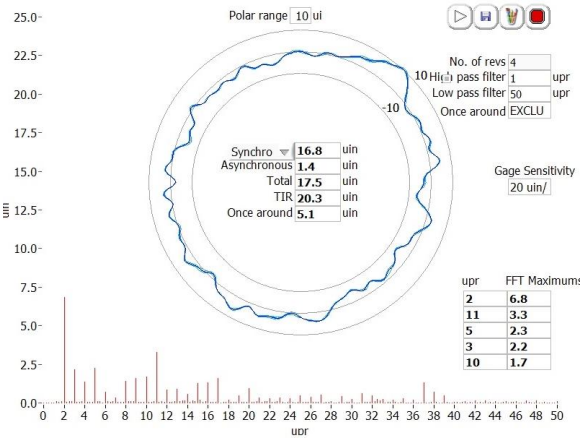

FIGURE 8. Roundness measurement result. Out-of-roundness of the hardened A2 tool steel cylinder, 3.8 inches from the flange is better than 17 microinches.

CONCLUSION

In precision industrial machining applications, an oil hydrostatic bearing can provide high load capacity and stiffness with extremely good error motions. The precision spindle enabled superior form and finish for hard turning despite using an inexpensive toolroom lathe as the testbed [1-3].

REFERENCES

[1] J. Kundrak et al. Accuracy of hard turning. Journal of Materials Processing Technology. 202 (2008):328–338.

[2] J.M. Zhou et al. Identification of cutting errors in precision hard turning process. Journal of Materials Processing Technology. 153–154 (2004):746–750.

[3] J. Lai, FE prediction of cutting error from thermal expansion of workpiece and tool in hard turning. SKF Engineering and Research Centre, The Netherlands, 2001.

[4] N.R. Kane, J. Sihler and A.H. Slocum. A hydrostatic rotary bearing with angled surface self-compensation. Precision Engineering, 27(2):125–139, 2003.

THERMAL ERRORS OF A LARGE 5-AXIS MACHINE TOOL DUE TO CUTTING FLUID INFLUENCES - EVALUATION WITH THERMAL TEST PIECE

Philip Blaser[1], Pablo Hernández-Becerro[2], Josef Mayr[2], Moritz Wiessner[1] and Konrad Wegener[1]
[1]Institute of Machine Tools and Manufacturing (IWF), ETH Zürich Leonhardstrasse 21, 8092 Zürich Switzerland
[2]inspire AG, Technoparkstrasse 1, 8005 Zürich, Switzerland

INTRODUCTION

Fluid media is essential for the operation of machine tools. Brinksmeier et al. [1] summarized the different tasks that the fluid elements perform in production machines, such as ensuring workpiece quality, reduction of tool wear, and the overall improvement of process productivity. Bryan [2] pointed out that the supply of the cutting fluid is one of the external influences causing thermally induced errors in machine tools.

Current research focuses on the characterization of the influence of the cutting fluid on the machine tool accuracy. Mayr et al. [3] compared the thermal response of a machine tool with and without cutting fluid during the rotation of the table-sided C-axis, showing experimentally the influence of the cutting fluid on the thermal behavior. The authors concluded that the cutting fluid does not avoid the warm up phases in precision machining and needs to be considered in the design of the numerical compensation strategies. Pavliček et al. [4] researched how the different cutting fluid media, oil and CO_2, affects the machine tool errors. For that purpose the authors designed a measurement device with retractable cover to protect the sensors against damage during the fluid supply. Hernández-Becerro et al. [5] concentrated on how the different modes to supply cutting fluid to the working space influence the thermally induced errors. By means of a precision level the variations of the tilt error motions of the Y- and Z-axis were evaluated for the different cutting fluid supply modes. It was concluded that the bed cutting fluid, which flushes out the chips from the back side of the bed to the chip conveyor, is the main thermal error source on the investigated machine tool.

Indirect measurement techniques captures the tool center point (TCP) errors as a superposition of the errors associated to the linear and rotary axes constituting the kinematic chain of the machine. Ibaraki and Knapp [6] reviewed the different indirect measurement schemes for three- and five-axis machine tools. Among the different reviewed indirect methods, machine tool manufacturers rely on machining tests in order to assess the machine accuracy during the manufacturing process. ISO 10791-7:2014 [7] shows different examples of test pieces for the evaluation of geometrical errors, by measuring different features of the workpiece. Other standards describing test pieces are available, such as VDI 3443 [8] for milling machines and VDI 5211 Part 2 [9] for 5-axis CNC machines. While these machining tests provide a demonstration of the overall accuracy, they do not allow to evaluate the position and orientation errors and error motions of the different axes.

The standardized test pieces are designed to evaluate the geometrical errors of machine tools. Current research concentrates on the creation of new designs of test pieces which are able to assess the thermal errors of 5-axis machine tools. Ibaraki and Ota [10] extended a previous design of a test piece for the measurement of thermally induced error motions of rotary axes. In order to measure the thermal effects, three different test pieces were manufactured every 25 minutes. The features characterizing the thermal deviations were measured directly on the machine, under the assumption that the linear axes have small volumetric errors in comparison with the rotary axes. Höfer and Wiemer [11] designed a compact test piece for the evaluation of the thermally induced translational displacements of the TCP. The test piece presented several reference surfaces manufactured at the beginning of the test cycle. The heat input of the system was the rotation of the spindle as well as several axes movements. Wiessner et al. [12, 13] proposed a new thermal test piece design for the thermal

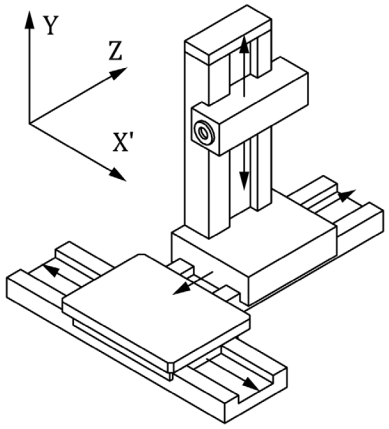

FIGURE 1. Schematic of linear axes of the machine tool under investigation adapted from ISO 10791-1:2015 [14]

characterization of machine tools with a rotary table. The test piece was conceived in order to provide X-, Y- and Z-displacements as well as one angular deviation of the rotary table. The results were compared to R-Test measurements showing a good correlation.

Figure 1 illustrates the schematic of the linear axes of the machine tool under investigation, used for aerospace and power engineering. In addition, the machine tool has a rotary axis on the workpiece side and a rotary head on the tool side. The kinematic chain according to ISO 10791-1:2015 [14] is: H [w B X b Z Y A (C) t] .

The thermal effect under investigation is the bed cutting fluid, which is shown in [5] to cause the most significant thermal errors among the different cutting fluid supply modes.

ENGINEERING OF THERMAL TEST PIECE

As a main design template the thermal test piece presented by Wiessner in [13] is chosen and adapted to the machine tool under investigation. The requirements of the test piece are to capture the thermal errors on a workpiece in X-, Y- and Z-Direction as well as the angular errors A, B and C by machining geometric features in set time intervals. Additionally the thermal radial growth of the test piece during manufacturing has to be separable from the thermal deviations of the geometric features. The machinability and the nomenclature of the deviations on the test piece strongly depends on the kinematic chain of the investigated machine tool. Figure 2 shows the thermal test piece with its geometrical features to identify

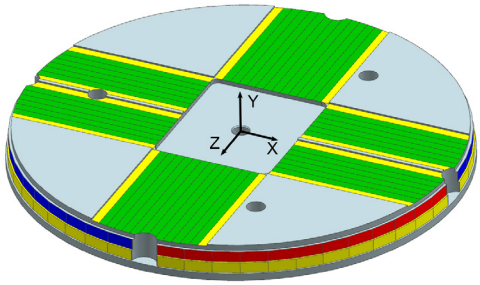

FIGURE 2. Thermal test piece

the thermal deviations of a large machine tool. For this specific test piece it is decided to generate 156 geometric features, the reference features are depicted in yellow in Figure 2. This way 12 thermal states of each error can be measured, listed in Table 1. A total of 60 Y-Tracks are designed to capture the deviations in Y-direction. The Y-Tracks milled parallel to the Z-axis reflect the angular deviations in A-direction while the Y-Tracks parallel to the X-axis allow to measure the angular deviations in C-direction. The 96 facets are engineered to capture X- and Z-deviation as well as radial growth. The measurement uncertainty of a coordinate measurement machine (CMM) consists, according to ISO 10360-1:2000 [15], of a fixed value and a term dependent on the measured length. Therefore, the reference facets are located close to the measurement facets in order to reduced the measurement uncertainty. This constitutes one of the major modifications from the previous design of the thermal test piece. The nominal diameter of the test piece measures 600 mm to cover a large part of the machine table. Due to its thermal expansion coefficient steel is chosen as material for the workpiece. To avoid an overdetermined fixture a 3-point fixture is chosen, the additional hole in the center of the test piece can be used for handling of the test piece.

MACHINING STRATEGY

At the beginning of the cutting procedure the test piece geometry is roughed, so that all the features have a finishing allowance of 0.2 mm to the programmed final shape. With this the cutting forces during the finishing operations are drastically reduced, and moreover the depth of cut at the features on the circumference is kept constant during the finishing cut leading to constant cutting forces. For the finishing a 12 mm diameter flat end mill is used. After roughing and before starting the test, the machine tool is kept in NC hold for 48 hours to reach an equilibrium with the environment. When

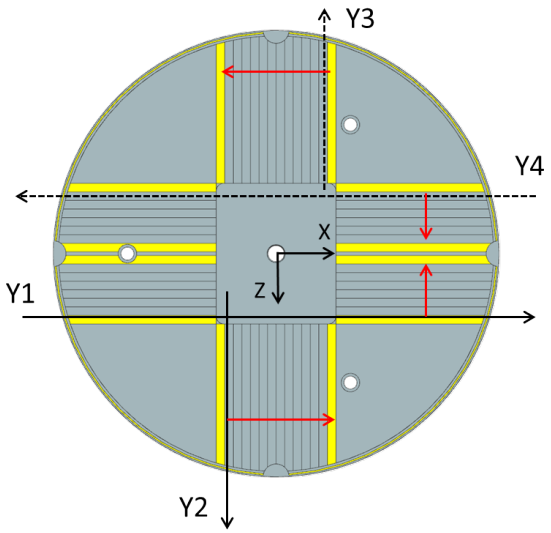

FIGURE 3. Milling sequence of the Y-Tracks

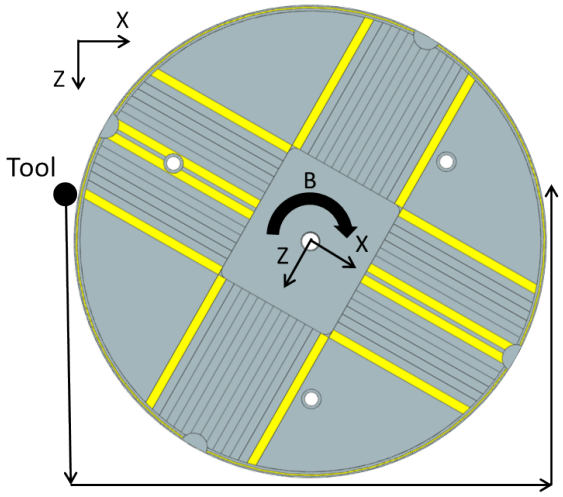

FIGURE 4. Milling sequence of the X- and Z-facets

the test is started the reference surfaces, yellow areas in Figure 2, are milled. For the manufacturing of each feature only one machine axis is moving at a time, to avoid interpolation errors. Figure 3 shows the milling sequence of the Y-Tracks. The Y1- and Y2-Tracks are milled, when the B table is at 0° position, for the Y3- and Y4-Tracks (dashed arrows) the table has to be indexed at 180°. This is due the fact that the working space does not cover the whole machine table. The Y2- and Y3-Tracks consist of 12 features, which are milled consecutively at each interval following the red arrow in Figure 3. However, there are only 6 Y1- and Y4-Tracks due to the limitations of the working space. Only after milling all the Y1-Tracks, the Y4-Tracks are milled in the following time intervals.

For the facets milled on the circumference of the test piece, the table has to be indexed in 6.923° steps for each interval. Then the tool moves in a straight path along the Z-axes to mill the X-facet followed by a movement in X-direction to mill the Z-facet and another movement in Z-direction for the second X-facet on the opposite side, these trajectories are illustrated in Figure 4. To mill the Z-facet on the opposite side, shown in the top side of Figure 4, the table is rotated by 180° and the same X-axis movement is performed, again due to reachability limitations of the machine tool. The benefit of milling the features on both sides of the circumference, is that the sensitivity of the thermal error increases and an averaging effect occurs and thus reducing the measurement uncertainty.

As mentioned in the Introduction, the objective of this test piece is to measure the thermal influences of the bed cutting fluid on the machine tool. Since the investigations are performed on a large machine tool, the thermal time constant are long. Therefore, a relatively long thermal load case is chosen. The bed cutting fluid is running for 12 hours followed by another 12 hours of no cutting fluid, in the same way as described by Hernández-Becerro in [5]. During the whole experiment, every 2h a set of features are milled. Besides these short milling operations, no axes or spindle movements are performed.

EVALUATION

Table 1 shows the identifiable errors of the test piece on the machine tool under investigation. The deviation of feature in X direction, E_{TPX}, is calculated according to Equation (1), where $F1$ and $F2$ are the distance between the reference and measured facets of two diametrically opposed facets. The nominal value of $F1$ and $F2$ is the nominal distance between reference and measurement facets, F_c, of 2 mm. The radial growth of the test piece, E_{TPR}, is also evaluated at the same facets, as explained in Equation (2).

$$\Delta E_{TPX} = \frac{F2 - F1}{2} \qquad (1)$$

TABLE 1. Nomenclature of deviations of the geometrical features on the test piece and measurement uncertainty

Error	Explanation	U(k=2)
E_{TPX}	Dev. of feature in X-direction	$2.5\ \mu m$
E_{TPY}	Dev. of feature in Y-direction	$1.8\ \mu m$
E_{TPZ}	Dev. of feature in Z-direction	$3.3\ \mu m$
E_{TPA}	Dev. of feature in A-direction	$18\ \mu m/m$
E_{TPB}	Dev. of feature in B-direction	-
E_{TPC}	Dev. of feature in C-direction	-
E_{TPR}	Radial growth of the test piece	$2.5\ \mu m$

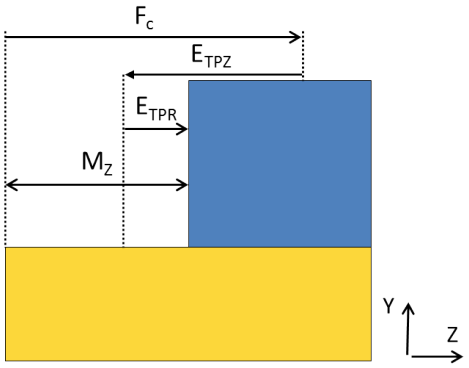

FIGURE 5. Evaluation of workpiece error E_{TPZ}

$$\Delta E_{TPR} = \frac{F1 + F2 - 2F_c}{2} \tag{2}$$

The evaluation of the deviation of feature in Z-direction, E_{TPZ}, is depicted in Figure 5. Due to the lack of accessibility of the tool to some part of the working space, the B-axis needs to be rotated. This implies that E_{TPZ} is to be measured differently as E_{TPX}, in order to avoid the affect of error motions of the B-axis in the evaluation. This requires that the measured distance, M_z between the facets is modified with the radial growth, E_{TPR}, and F_c according to Equation (3).

$$\Delta E_{TPZ} = F_c + E_{TPR} - M_Z \tag{3}$$

The deviation of feature in Y-direction, E_{TPY}, as well as the angular deviations of the features are measured on the tracks. As shown in Figure 6, E_{TPY} can be directly measured on each of the four tracks. The sign is consistent with the machine tool coordinates (see Figure 1). The design of the test piece allows the measurement of the

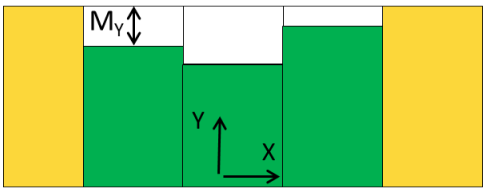

FIGURE 6. Evaluation of workpiece error E_{TPY}

deviation of feature in C-direction, E_{TPC}. However, due to the symmetry of the machine this deviation is below the measurement uncertainty with the used CMM for the evaluation. The magnitude of the B-deviations in combination with the designed facet length does not allow the measurement of the deviation of feature in B-direction, E_{TPB}. Nevertheless, the A-deviation, E_{TPA}, can be effectively measured with the current test piece design and are provided by postprocessing the CMM data, by comparing the angle of the Y-Tracks relative to the angle of the reference plane. The manufactured test piece is measured on a CMM, with an MPE of 1.8 + L/300 μm. The tracks are measured using a continuous zig-zag strategy generating 477 measurement points, while the distances between facets are measured at the geometric center of each surface evaluated with 5 measurement points. The measurement uncertainties for the linear deviation are estimated as combination of the uncertainty of the measured values. For the angular deviations a Monte Carlo simulation is performed with uniformly distributed measurement points on the track. A list of the measurement uncertainties is given in Table 1.

In Figure 7 the thermally induced linear deviations are depicted. The errors of the TCP in X-direction and the radial growth of the part is small in comparison with the errors in the other directions. This is caused by the thermo-symmetric machine tool design YZ-plane. During the production of the test piece, four different tracks are produced at each time step which can be used for the evaluation of the Y-deviations. These four tracks show similar tendencies and Figure 7 depicts the mean value. The Y- and Z-deviations react in the first 2 hours to the effect of the cutting fluid.

The test piece is designed in order to capture angular deviations in A-direction. Because of the limited stroke of the Z-axis, the B-axis needs to be rotated 180°. This provides two different values of the A-deviation with opposite signs. The ten-

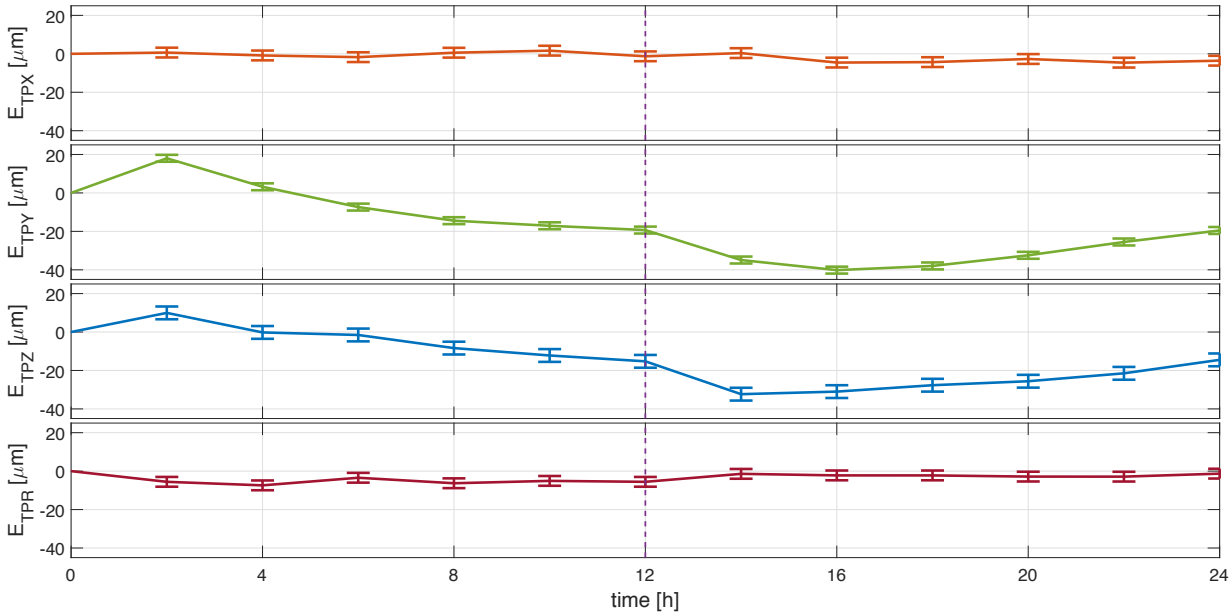

FIGURE 7. Measured linear deviations on the thermal test piece

dencies of both angular errors are the same, as depicted in Figure 8, which suggests that these errors are mainly caused by the tool-sided error motions or time-varying position and orientation errors of the tool sided axes. The difference between them can be attributed to a combination of the thermally induced error motions of the B-axis and measurement uncertainty.

CONCLUSIONS

This work has adapted a previously developed thermal test piece for the evaluation of the thermally induced errors to large machine tools. The proposed design allows the characterization of the linear errors and angular deviations in A-direction, which is one of the critical errors in the researched machine. The thermal piece evaluation shows that the measured angular deviations A-deviations reach values of 60 μm/m and the linear errors in Z-direction are in the order of 40 μm.

Indirect methods for thermal error characterization cannot fully estimate the different error sources, namely the time-varying position and orientation errors and error motions, of a 5-axis machine tool. The number of measurements points required for the thermal characterization is too large to be covered in a sufficiently short time without exciting the dynamics of the machine. The presented thermal test piece, in a similar manner as other indirect methods, provides an insight of the magnitude of the TCP deviations. Its easy implementation and its wide acceptance in industry makes the thermal test piece an interesting alternative for thermal machine tool characterization, providing a visualization of the manufacturing errors. In addition this work shows the effect of the cutting fluid in the accuracy of a 5-axis machine tool. One application of the presented machining test is the evaluation of design modifications and validation of compensation strategies.

ACKNOWLEDGMENTS

The authors would like to thank the Swiss Federal Office for Professional Education and Technology (CTI) and the Swiss National Science Foundation (SNSF) for their financial support.

REFERENCES

[1] Brinksmeier E, Meyer D, Huesmann-Cordes AG, Herrmann C. Metalworking fluidsMechanisms and performance. CIRP Annals - Manufacturing Technology. 2015;64(2):605 – 628.

[2] Bryan J. International Status of Thermal Error Research (1990). CIRP Annals - Manufacturing Technology. 1990;39(2):645 – 656.

[3] Mayr J, Gebhardt M, Massow BB, Weikert S, Wegener K. Cutting Fluid Influence on Ther-

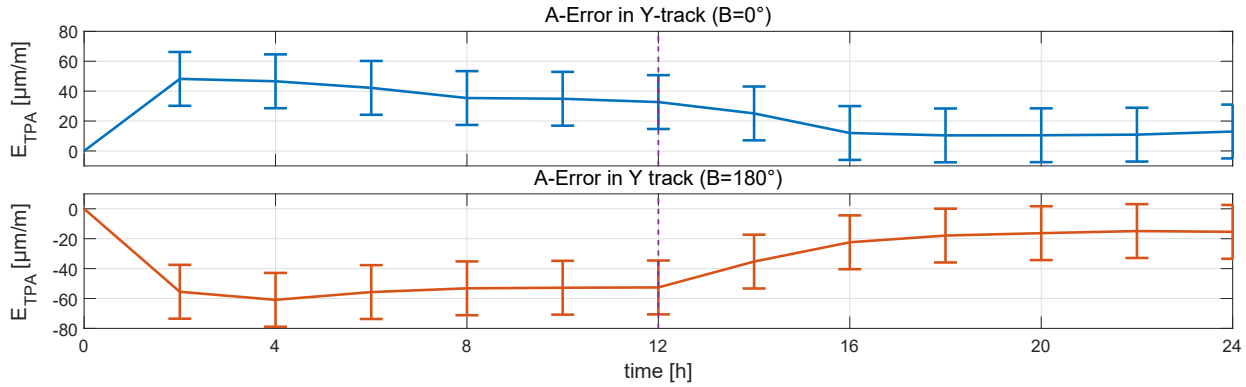

FIGURE 8. Measured angular deviations in A-direction on the thermal test piece

mal Behavior of 5-axis Machine Tools. Procedia CIRP. 2014;14:395 – 400.

[4] Pavliček F, Beer Y, Weikert S, Mayr J, Wegener K. Design of a Measurement Setup and First Experiments on the Influence of CO_2-cooling on the Thermal Displacements on a Machine Tool. Procedia CIRP. 2016;46:23 – 26.

[5] Hernández-Becerro P, Blaser P, Mayr J, Weikert S, Wegener K. Measurement of the effect of the cutting fluid on the thermal response of a five-axis machine tool. 2017;.

[6] Ibaraki S, Knapp W. Indirect measurement of volumetric accuracy for three-axis and five-axis machine tools: A review. 2012 03;6:110–124.

[7] ISO 10791-7:2014. Test conditions for machining centres –Part 7: Accuracy of finished test pieces. Geneva, Switzerland; 2014.

[8] VDI/DGQ 3443:1977-03. Statistische Prüfung der Arbeitsgenauigkeit von Fräsmaschinen. Düsseldorf, Germany; 1977.

[9] VDI/NGQ 5211 Part 2:2013-09. Testing guidelines and testing workpieces for high speed cutting (HSC) –Part 2: Milling machines and machining centres for the 5-axis simultaneous milling. Düsseldorf, Germany; 2013.

[10] Ibaraki S, Ota Y. A Machining Test to Evaluate Geometric Errors of Five-axis Machine Tools with its Application to Thermal Deformation Test. Procedia CIRP. 2014;14:323 – 328.

[11] Höfer H, Wiemer H. Generation of motion sequences for thermal load of machine tools. Production Engineering. 2017 Feb;11(1):75–83.

[12] Wiessner M, Blaser P, Mayr J, Böhl S, Knapp W, Wegener K. Thermal test piece for 5-axis machine tools, "under review". Precision Engineering;.

[13] Wiessner M, Gebhardt M, Knapp W, Wegener K. Test piece for visualization of thermally induced deviations on five-axis machine tools. 2014;.

[14] ISO 10791-1:2015. Test conditions for machining centres –Part 1: Geometric tests for machines with horizontal spindle (horizontal Z-axis). Geneva, Switzerland; 2015.

[15] ISO 10360-1:2000. Geometrical Product Specifications (GPS) –Acceptance and reverification tests for coordinate measuring machines (CMM) –Part 1: Vocabulary. Geneva, Switzerland; 2000.

STABILITY IN MODULATED TOOL PATH TURNING

Ryan W. Copenhaver, John C. Ziegert, and Tony L. Schmitz
Department of Mechanical Engineering and Engineering Science
University of North Carolina at Charlotte
Charlotte, NC

ABSTRACT

In this paper an experimental machining platform that provides in-process metrology during tube turning (orthogonal cutting) is used to determine cutting stability. The experimental machining platform provides in-process metrology for cutting force, tool vibration, feed motion, and chip formation for continuous feed and modulated tool path (MTP) turning. MTP is a tool path strategy that creates discontinuous chips by superimposing tool oscillations in the tool feed direction on the normal feed rate to repeatedly interrupt the cutting process. The tests were performed using AISI 1020 cold-drawn tube workpieces. The chip width was varied by conducting tests using different tube wall thicknesses to control machining stability. To determine cutting stability the system dynamics were measured using impact testing, the Fast Fourier Transform (FFT) was used to analyze the frequency content of machining signals, and once per revolution sampling (OPRS) of time domain signals was implemented.

INTRODUCTION

A major issue in conventional turning, boring, and threading operations is the generation of long continuous chips. In conventional turning techniques, the cutting edge engages the workpiece and it remains in contact at a user specified feed rate until the cut is completed. The result is continuous chips, which can wrap around the chuck and tool requiring manual removal. The buildup of continuous chips around the chuck and tool produces several unwanted results: increased machine downtime, degraded surface finish, tool damage, and increased risk to operator safety. Conventional methods to create discontinuous chips include: specialized rake face tool geometries (chip breakers) and high pressure coolant aimed at the rake face-chip interface. An alternative is modulated tool path (MTP), which was developed to repetitively break chips and manage chip length [1-6]. MTP breaks chips by intentionally creating an interrupted cut through a superposition of tool oscillations in the feed direction. Prior MTP efforts have demonstrated its effectiveness for controlling broken chip length in both turning [1-5] and threading [6].

In this paper, an experimental platform is described that provides machining stability control and metrology during tube turning (which approximates orthogonal cutting conditions) for cutting force, tool vibration motion, feed motion, spindle speed, and chip formation during constant feed and MTP turning. The experimental platform was devolved to explore unstable cutting (chatter) in MTP by measuring the relevant process signals. Unstable cutting, or chatter, is described as a self-excited vibration [8] that produces tool vibration near a natural frequency. The disadvantages of chatter include poor surface quality, scrapped parts, increased waste, increased tool wear, and, in severe cases, possible tool breakage.

To identify unstable cutting conditions, three steps were completed: 1) impact testing was conducted to identify the system dynamics; 2) the frequency content of the machining signals was analyzed to identify content near the dominant natural frequency; 3) once per revolution sampling (OPRS) was used to identify asynchronous vibrations.

MTP DESCRIPTION

MTP is a customized tool path strategy that produces discontinuous chips by superimposing tool oscillations in the tool feed direction to create an interrupted cutting operation. There are two user-defined MTP parameters: 1) the tool oscillations per spindle revolution, OPR; and 2) the oscillation amplitude relative to the global feed per revolution, RAF.

$$OPR = \frac{60 \cdot f}{\Omega} \tag{1}$$

$$RAF = \frac{A}{f_r} \tag{2}$$

In Eqs. 1 and 2, f denotes the tool oscillation frequency (Hz) in the feed direction, Ω is the spindle speed (rpm), A is the tool oscillation amplitude, and f_r is the global feed per revolution for a traditional, constant feed turning operation [7].

EXPERIMENTAL SETUP

The testbed for the experiments was a Haas TL-1 computer numerically-controlled (CNC) lathe (8.9 kW, 2000 rpm spindle). Tubular workpieces were machined from AISI 1020 cold-drawn steel. The outside diameter of the workpieces was 72 mm and the wall thickness was {1, 1.5, 2, and 2.5} mm. Concentricity and cylindricity of the outside and inside diameters with the rotational axis of the lathe spindle was assured by performing a finishing cut prior to conducting the experiments. Type C, 80° parallelogram carbide inserts with a zero rake angle, 7° relief angle, and a flat rake face were used (ANSI catalog number CCMW3252, Kennametal part number 3757916). Orthogonal tube turning was selected, so that the cutting speed, v_c, would not vary with a fixed spindle speed. Experiments were conducted at a cutting speed of 93.75 m/min with a nominal feed rate of 0.102 mm/rev. The commanded *OPR* and *RAF* values for all tests were 0.5 and 0.8, respectively. The tests were then repeated using a constant federate so that MTP could be compared to traditional turning. Stability of the cut was controlled by varying the tube wall thickness.

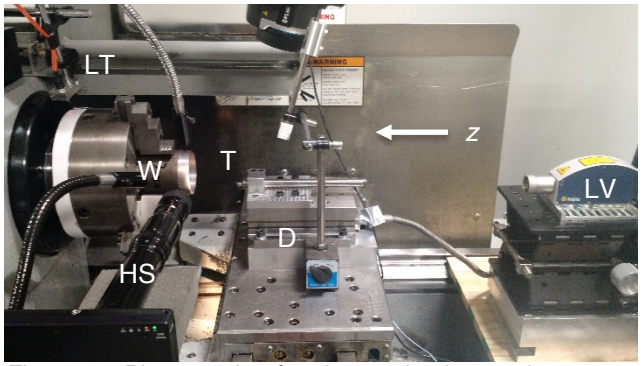

Figure 1. Photograph of orthogonal tube turning setup including: workpiece (W), tool (T), high speed camera, (HS), laser tachometer (LT), dynamometer (D), and laser vibrometer (LV).

Dynamic cutting forces were measured using a three-axis dynamometer (Kistler 9257B) mounted to the lathe's cross slide. A high speed camera (Fastec IL-3) with a maximum frame rate of 1250 frames/sec was mounted to a tripod which was fixed to the shop floor. A laser vibrometer (Polytec OFV-534/OFV-5000) was used to measure the feed direction motion (*z*). An accelerometer was fixed to the free end of the tool to measure the tool vibrations in the cutting direction. A laser tachometer was used to record a once per revolution trigger for OPRS signal analysis. A photograph of the setup is provided in Fig. 1 and additional views are provided in Fig. 2. The thrust direction is aligned with the spindle axis, while the cutting direction is tangent to the cut surface.

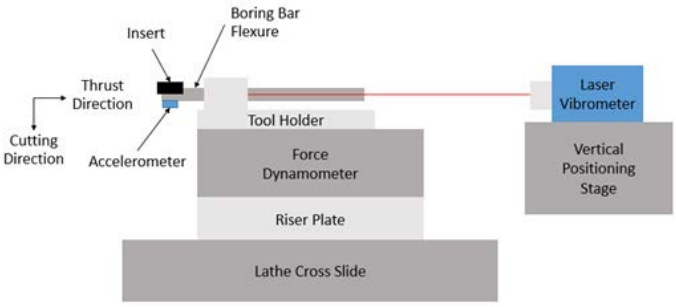

Figure 2. Side view of the experimental setup.

RESULTS

In this section, the experimental steps and results are described for: impact testing, frequency domain analysis, and time domain OPRS.

Impact Testing

The system dynamics must be identified to enable frequency domain analysis of the machining signals. To measure the system dynamics, impact testing was completed to identify the frequency response function (FRF). See Fig. 3, which shows the tool point FRF in the cutting direction (the thrust direction result was much stiffer and neglected).

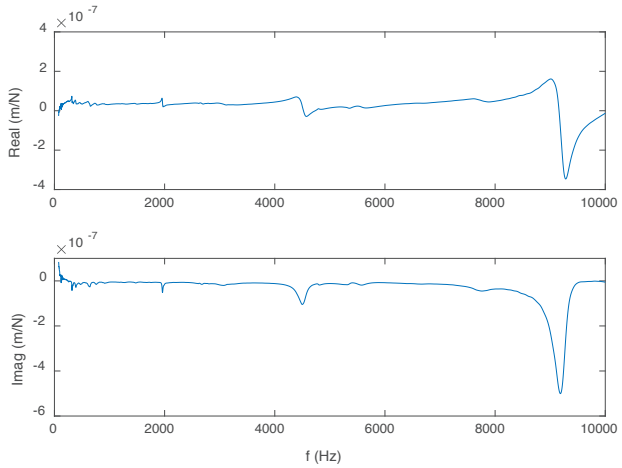

Figure 3. Tool point FRF.

In the tool point FRF there are multiple modes. The most flexible mode represents the bending mode of the boring bar. The bending mode has a natural frequency of 9191 Hz. This mode's natural frequency establishes the chatter frequency during unstable machining. Frequency content near the natural frequency indicates that chatter is occurring.

Fast Fourier Transform (FFT) Analysis

The FFT approach converts the time domain machining signals to the frequency domain so that the frequency content can be analyzed. Content in the frequency domain near the natural frequency indicates that the cut is unstable. This process was applied to the force and the acceleration signals in the cutting direction.

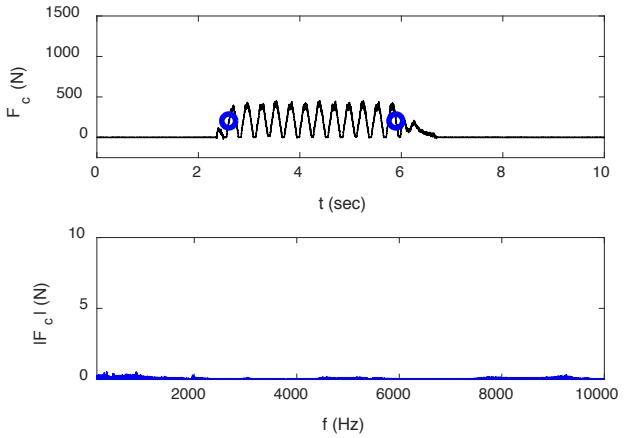

Figure 4. Time and frequency domain plots for the cutting direction force, F_c, with a chip width of 1 mm. (Top) Time domain cutting direction force component. (Bottom) Frequency content of the cutting force.

The time domain plot for the 1 mm chip width cutting direction force, F_c, is shown in Fig. 4 (top panel). The FFT is shown in the bottom panel. The circles on the time domain plot represent the range for the FFT calculation.

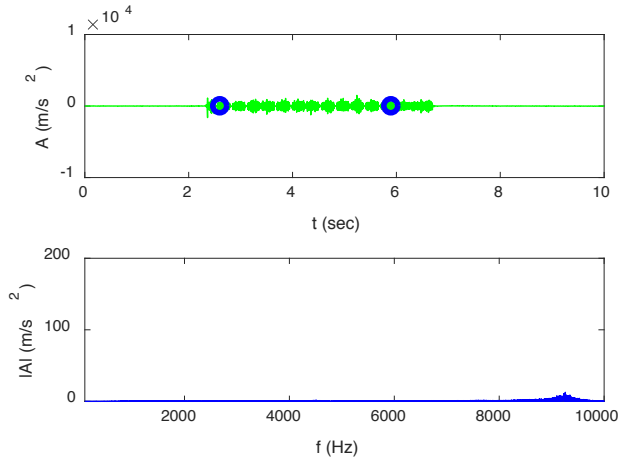

Figure 5. Time and frequency domain plots for accelerometer response, A, in the cutting direction with a chip width of 1 mm.

Figure 5 displays the accelerometer results for a 1 mm wall thickness. Similar to Fig. 4, there is no appreciable content near the natural frequency. This indicates that the cut was stable.

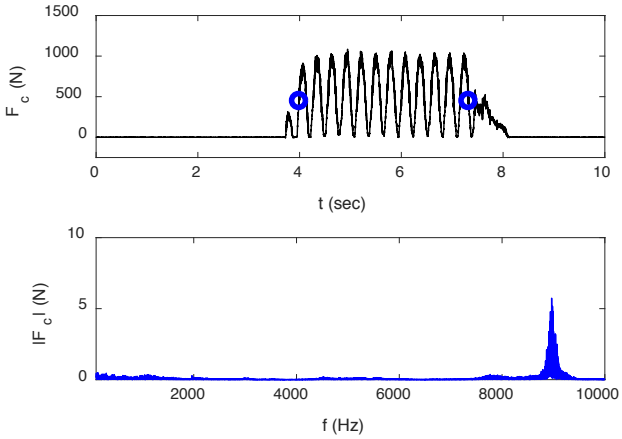

Figure 6. Time and frequency domain plots for the cutting direction force, F_c, with a chip width of 2.5 mm.

Figure 6 displays the time domain plot for the 2.5 mm chip width cutting direction force, F_c, in the top panel. The lower panel shows the frequency content. A peak is present near 9000 Hz, indicating unstable cutting conditions.

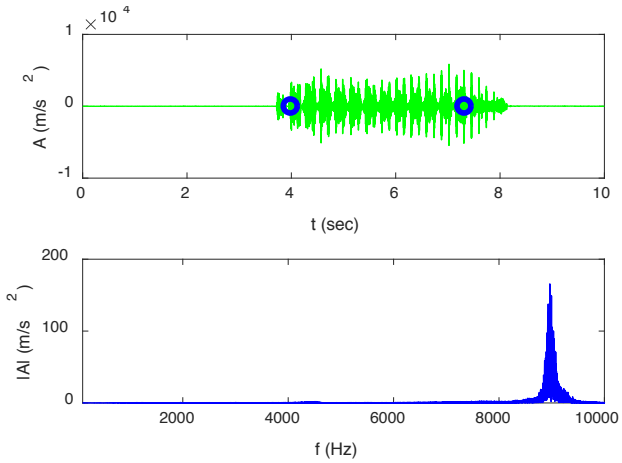

Figure 7. Time and frequency domain plots for accelerometer response, A, in the cutting direction with a chip width of 2.5 mm.

Figure 7 shows the time domain accelerometer results in the cutting direction in the top panel. The FFT of the signal is shown in the bottom panel. Both Figs. 6 and 7 show a peak in the force spectrum near 9000 Hz, which matches the bending mode of the cutting tool (Fig. 3). This indicates the presence of self-excited vibration.

OPRS Analysis

Using the laser tachometer to capture a once per revolution time stamp, the cutting force and acceleration signals were sampled to analyze stability. Sampled points that exhibit a low variance from a mean value are indicative of a stable cut. Conversely, if the variance of the sampled points is large, the cutting operation is unstable. The OPRS method was applied to complement the FFT method. OPRS was applied to the cutting direction force and acceleration signals, similar to the FFT method.

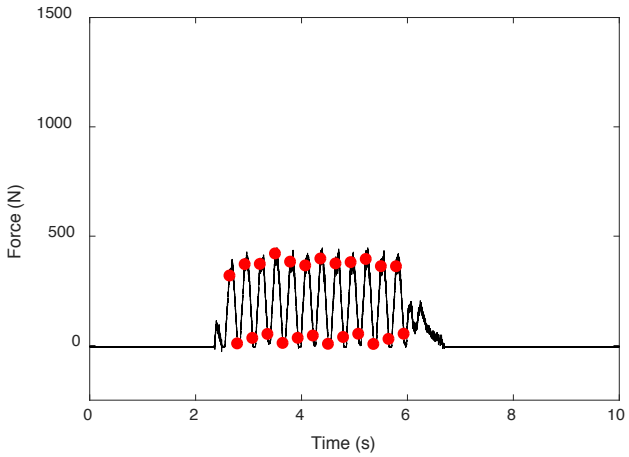

Figure 8. OPRS of the force signal in the cutting direction with a chip width of 1 mm.

Figure 8 contains the time domain force signal in the cutting direction. The once per revolution samples are shown by the dots. Two alternate repeating solutions are observed because the MTP OPR value of 0.5 indicates that one full tool oscillation occurs every two spindle revolutions.

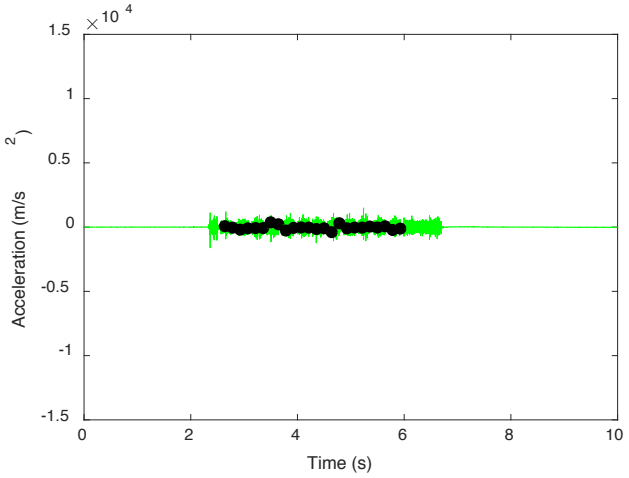

Figure 9. OPRS of the acceleration signal in the cutting direction with a chip width of 1 mm.

The acceleration signal in the cutting direction is shown in Fig. 9 with the once per revolution samples shown by the dots. Figures 8 and 9 both exhibit repeating behavior, indicating a stable cut. These results reinforce the stable cut conclusion obtained from Figs. 4 and 5.

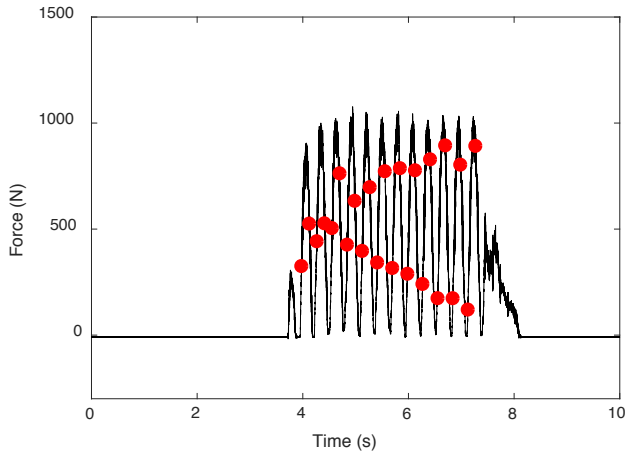

Figure 10. OPRS of the force signal in the cutting direction with a chip width of 2.5 mm.

The time domain force signal in the cutting direction, F_c, with overlaid once per revolution samples for a 2.5 mm chip width is displayed in Fig. 10.

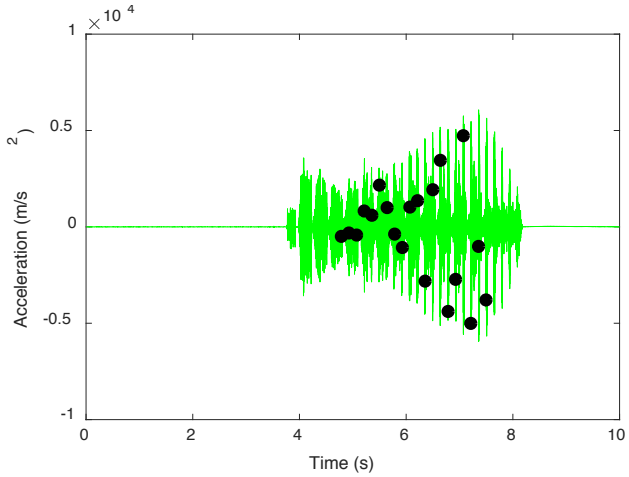

Figure 11. OPRS of the acceleration signal in the cutting direction with a chip width of 2.5 mm.

Figure 11 displays the acceleration signal with overlaid once per revolution samples. In both Figs. 10 and 11 the samples deviate substantially indicating that the motion is asynchronous with spindle rotation and that the cut is unstable. This agrees with the results shows in Figs. 6 and 7.

FFT and OPRS Comparison

For each test, the magnitude of the chatter frequency and the variance of the once per revolution samples were recorded. This was completed for both the MTP and constant feedrate tests. The FFT magnitudes and OPRS variances, σ^2, were then plotted against the associated chip width to give a global view of the change in stability as chip width was increased.

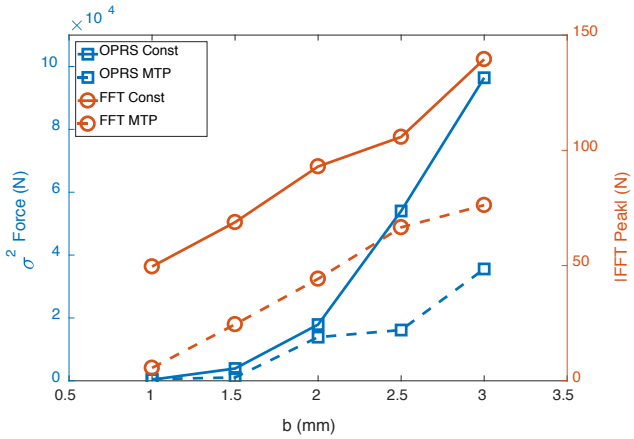

Figure 12. Force OPRS variance and FFT magnitude of both MTP and constant feedrate as chip width is varied.

The results for the force signal OPRS variance and FFT magnitude are presented in Fig. 12. The blue line with square markers denotes that the data set was obtained through the OPRS method, while the orange line with circular markers denotes the FFT method. A solid line indicates that the cut used a constant feedrate and a dotted line indicates that an MTP cut.

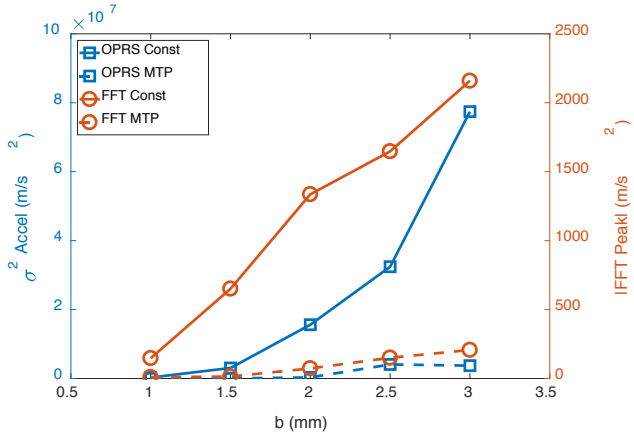

Figure 13. Acceleration OPRS variance and FFT magnitude of both MTP and constant feed rate as chip width is varied.

Figure 13 displays the OPRS variance and FFT magnitude for the acceleration signals. Both Figs. 12 and 13 show an upwards trend in both the FFT magnitude and OPRS variance indicating with the increase in chip width. This identifies the transition from stable to unstable cutting conditions.

CONCLUSIONS

This paper provided machining stability analysis for MTP and constant feed cutting conditions in tube turning. Stability was identified by analyzing the frequency content and synchronicity of the machining signals. The synchronicity was evaluated using a once per revolution sampling (OPRS) strategy. MTP provided a tool path strategy to create discontinuous chips by superimposing tool oscillations in the tool feed direction and repeatedly interrupting the cutting process. Results were presented for turning of AISI 1020 cold-drawn steel tubes. The system dynamics were obtained through impact testing and used to identify the chatter frequency as the bending mode of the flexible tool. The FFT was used to analyze the frequency content as a metric to determine machining stability. The OPRS technique was applied to provide an alternative stability identification metric. Both stability metrics were applied to a range of chip widths for both MTP and continuous feedrate cutting tests. Future work will including modeling and predicting cutting forces and tool vibration using time domain simulation of the MTP and continuous cutting tests.

ACKNOWLEDGMENTS

The authors gratefully acknowledge financial support from the UNC Charlotte Center for Precision Metrology Affiliates program and the donation of turning inserts from Kennametal.

REFERENCES

[1] Adams D. Chip Breaking in Turning Operations Using CNC Toolpaths. MS Thesis, UNC Charlotte, Charlotte, NC; 2008.

[2] Assaid TS. Generation, Measurement, and Assessment of Modulated Tool-Path Chip Breaking in CNC Turning Processes. MS Thesis, UNC Charlotte, Charlotte, NC; 2010.

[3] Smith KS, McFarland J, Tursky D, Assaid T, Barkman W, Babelay E, 2010, Simulating the Effect of Modulated Tool-Path Chip Breaking on Surface Texture and Chip Length. Y-12 Publication.

[4] Tursky D, 2010, Chip Breaking Through Oscillating CNC Toolpaths and its Effect on Chip Length, Tool Wear and Machine Dynamics. MS Thesis, UNC Charlotte, Charlotte, NC.

[5] Berglind L, Zeigert J. Chip Breaking Parameter Selection for Constant Surface Speed Machining. In: ASME 2013 International Mechanical Engineering Congress and Exposition Volume

2B: Advanced Manufacturing, San Diego, CA, 2013.
[6] Berglind L, Zeigert J, 2015, Modulated Tool Path (MTP) Machining for Threading Applications. Procedia Manufacturing, 1: 546-555.
[7] Copenhaver R, Rubeo M, Guzorek S, Landge S, Smith KS, Ziegert J, Schmitz T, 2017, A Fundamental Investigation of Modulated Tool Path Turning Mechanics. Transactions of the NAMRI/SME, 45.
[8] Schmitz T, Smith KS. Machining Dynamics: Frequency Response to Improved Productivity. New York: Springer, 2009.

FUNDAMENTAL EXPERIMENTS OF ADDITIVE MANUFACTURING METHOD BY SELECTIVE SOLIDIFICATION USING ELECTRICAL DISCHARGE

Katsushi FURUTANI, Takahiro TSUCHIYA, and Hiroki YAMAGISHI
Department of Advanced Science and Technology, Faculty of Engineering
Toyota Technological Institute
Tempaku-ku, Nagoya 468-8511 Japan

INTRODUCTION

Today, three-dimensional (3D) modeling machines by Fused Deposition Modeling (FDM) laminating ABS or PLA resin [1] become available at low cost and are widely used in various field: not only industries but also art or education. Ones by Powder Bed Fusion (PBF) can be used to fabricate prototypes and small-lot products by solidifying metal powder directly [2]. Because their heat sources such as laser or electron beam are still expensive, it is difficult to lower the cost of the machines.

Deposition or surface modification methods by electrical discharge with a green compact electrode [3] or in powder-suspended working oil [4] have been proposed. In these methods, the length of a current path changes with a progress of deposition so that it is difficult to keep machining performance and the maximum thickness was limited to submillimeter order. Although overlay welding by arc discharge can easily deposit a thick layer [5], it is difficult to fabricate an overhung shape or hollow structure because support structures cannot be used. Electrical discharge machining (EDM) with twin electrodes has been proposed to increase the removal rate by simultaneous discharge at two points in air or working oil [6].

This paper proposes an additive manufacturing (AM) method with metal power solidified by electrical discharge and describes a demonstration.

ADDITIVE MANUFACTURING BY ELECTRICAL DISCHARGE

The proposed method is basically a PBF. Figure 1 shows a principle of the AM. The unit consists of a discharge unit which works as a heat source to solidify powder, an XYZ feeding mechanism driven by sliced data of a 3D shape, a powder tank, a lift to move a powder bed and a roller to spread the powder. The feeding mechanism moves in the *x*- and *y*-directions to draw a sliced geometry. The feeding mechanism in the *z*-direction adjusts the discharge gap length. A discharge current flows from an electrode to another through the surface of the powder layer. The discharge heat and Joule heat melt and solidify the powder. By repeating the spread of the powder and solidification by discharge in air, a 3D shape is fabricated as well as an overhung one. The thickness of solidified layer does not affect the machining performance. Because unsolidified powder has the same density, it can be used as supports. Consequently, an overhung shape can be also fabricated.

Figure 2 illustrates a sequence of the AM method. (1) At the beginning of the sequence, the height of the powder bed is the same level as the top layer. (2) The bed is moved downward by 1-layer thickness. (3) The powder is spread across the build area. (4) Geometries

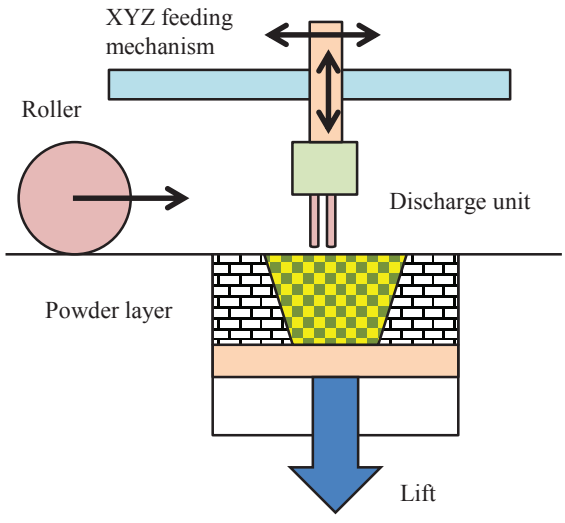

FIGURE 1. Principle of additive manufacturing by selective solidification of metal powder using electrical discharge.

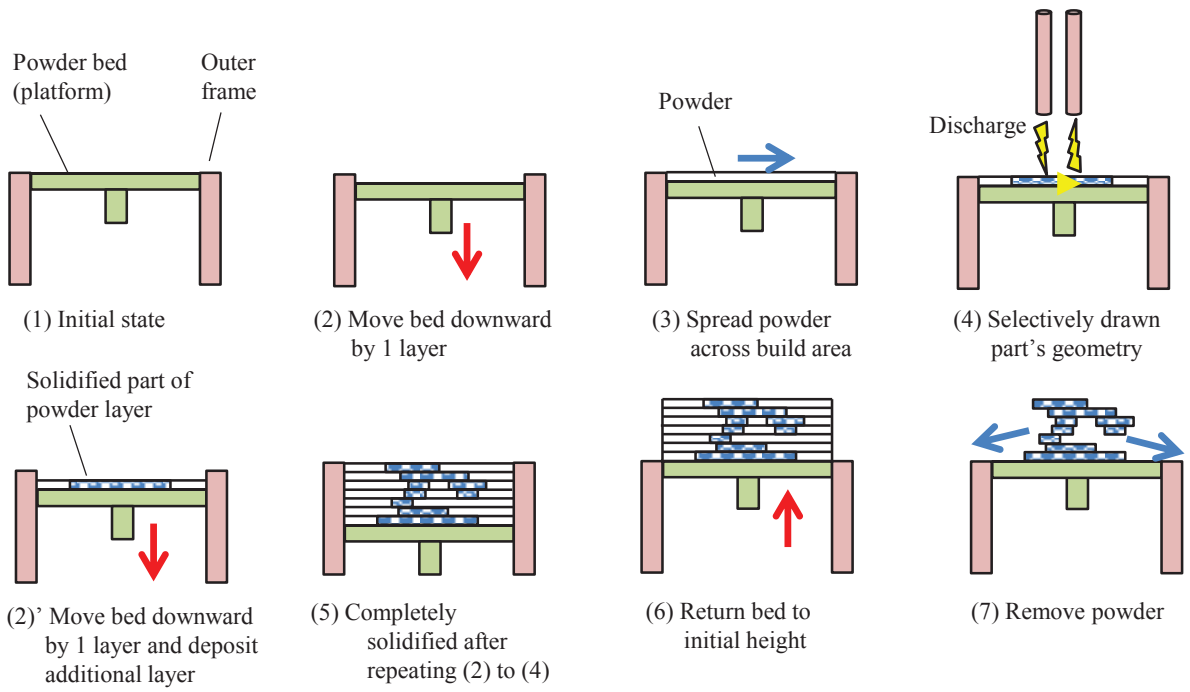

FIGURE 2. Sequence of additive manufacturing method by electrical discharge.

are selectively drawn by scanning discharge positions. (5) The process from (2) to (4) is repeated until the solid is completely formed. (6) The bed is returned to the initial height. (7) The unsolidified powder is removed.

It is expected to trim the surface by EDM in air [7] by alternating the machining conditions after the deposition process. The discharge circuit is generally more inexpensive than laser sources.

EXPERIMENTAL METHOD

Figure 3 shows a bipolar discharge circuit for the proposed method. The twin electrodes are connected to a capacitance discharge circuit with a bipolar DC power supply. The powder layer is connected to the ground through a high resistor to avoid the electrification. Then, the current does not flow the grounding resistor and the voltage of the powder is kept at the ground level.

Table 1 shows experimental conditions. The positive and negative voltages were set equal. The capacitance was experimentally determined. Figure 4 shows a pair of copper electrodes. The twin electrodes with a diameter of 0.5 mm were covered with fluororesin tubes for the insulation and were arranged in parallel with a center interval of 0.8 mm as shown in Fig. 5. Reduced

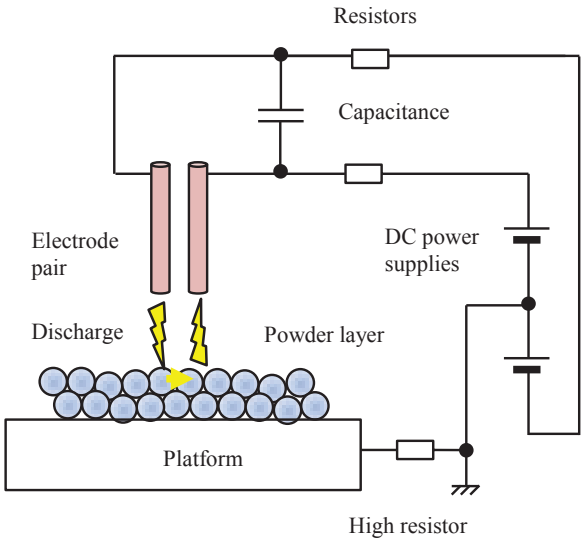

FIGURE 3. Bipolar RC-discharge circuit.

iron powder shown in Fig. 6 (a) was spread with a spatula with a thickness of 0.4 mm for the first layer and 0.2 mm for the rest. While a stage was manually driven in the *x*- and *y*-directions as illustrated in Fig. 5, a discharge occurred between the twin electrodes through the powder layer. Then, the power was selectively solidified layer-by-layer. At the end of the process, powder

TABLE 1. Machining conditions.

Applied voltage	±150 V
Capacitance	0.5 μF
Charging resistors	100 kΩ × 2
Grounding resistor	9.1 MΩ
Powder	Reduced iron powder, average diameter of 200 μm
Electrodes	Copper, diameter of 0.5 mm, interval of 0.8 mm
Feeding pitch	0.5 mm in X, Y directions

which was not solidified was removed with a brush.

EXPERIMENTS

Some powder scattered before and after the discharge. The work function of iron is larger than that of aluminum [8]. When they touch each other through their oxide layers, iron is negatively charged due to contact electricity. Consequently, the iron powder was negatively charged and was attracted toward the positive electrode. In addition, some parts of the iron powder melted or vaporized by the discharge heat. This also caused the scattering.

The fabrication process of 3D shapes was demonstrated. Figure 7 shows an example of a fabricated 3D shape. Four layers were fabricated by scanning for 4 mm horizontally. The thickness of the solid was approximately 1 mm. Figure 6 (b) shows an example of solidified powder. The solidified powder seemed to be sintered but not melted. Although the charge energy in the capacitor was 20 mW, the discharge power was over 2 kW because of a short pulse duration less than 10 μs. The powder around the discharge position sometimes scattered due to the discharge or adheres to the electrode. The solid did not collapse. The discharge energy is preferably kept lower than this case to bond the powder by melting.

Figure 8 shows another example with overhung shapes. After four layers were fabricated, two layers were fabricated in the orthogonal direction to the first layers. The total height was 1.4 mm. The unsolidified powder worked as a support material.

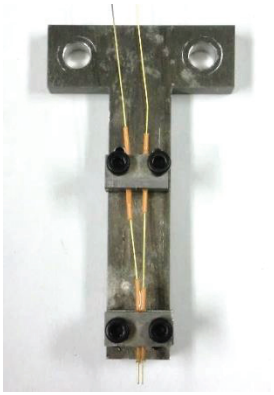

FIGURE 4. Pair of electrodes (30 mm × 55 mm).

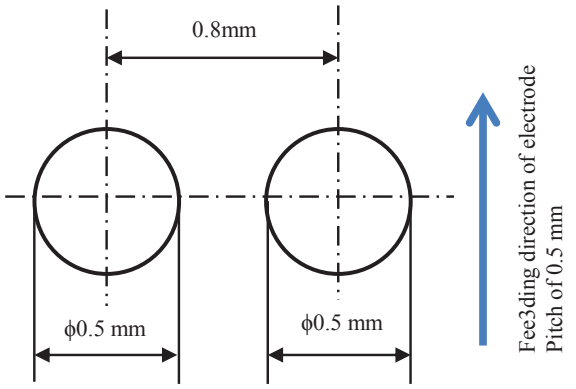

FIGURE 5. Arrangement of electrodes and feeding pitch.

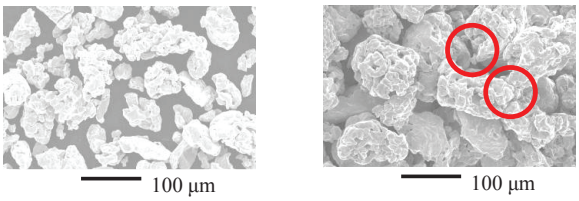

(a) Before solidification. (b) After solidification.
FIGURE 6. Ion powder.

CONCLUSIONS

The AM method with metal powder by electrical discharge is proposed. Conclusions can be drawn as follows.

(1) Three-dimensional shapes also with the overhangs were fabricated by the proposed AM method.
(2) The peak discharge energy generated with the capacitance circuit was too large to solidify by melting the powder.

(a) Before solidification.

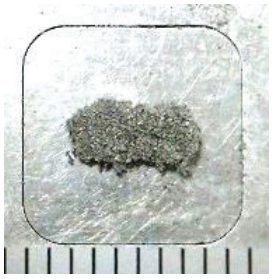

(b) After solidification.

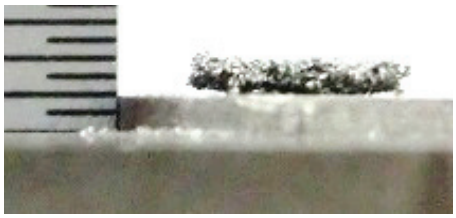

(c) Side view.
FIGURE 7. Laminated solid.

For the future works, appropriate machining conditions will be experimentally found by using a transistor discharge circuit which can be flexibly set the machining conditions.

ACKNOWLEDGEMENTS

This study was financially supported by JSPS KAKENHI Grant Number JP15K05735 and by Support Program “Research Center for Smart and Tough Machines” by MEXT, Japan.

REFERENCES

[1] Bourell D, Kruth JP, Ming L, Levy G, Rosen D, Beese AM, Clare A. Materials for additive manufacturing, CIRP Annals, 2017; 66: 659-681.

[2] Schmidt M, Merklein M, Bourell D, Dimitrov D, Hausotte T, Wegener K, Overmeyer L, Vollertsen F, Levy GN. Laser based additive manufacturing in industry and academia, CIRP Annals, 2017; 66: 561-583.

[3] Mohri N, Saito N, Tsunekawa Y. Metal surface modification by electrical discharge machining with composite electrode, Annals of CIRP, 1993; 42: 219-222.

[4] Furutani K, Saneto A, Takezawa H, Mohri N, Miyake H. Accretion of Titanium Carbide by Electrical Discharge Machining with Powder Suspended in Working Fluid, Precision Engineering, 2001; 25: 138-144.

[5] Abe T, Sasahara H. Dissimilar metal deposition with a stainless steel and nickel-based alloy using wire and arc-based additive manufacturing, Precision Engineering, 2016; 45: 387-395.

[6] Kunieda M, Muto H. Development of Multi-spark EDM, Annals of CIRP, 2000; 49: 119-122.

[7] Kunieda M, Yoshida M. Electrical Discharge Machining in Gas, CIRP Annals, 1997; 46: 143-146.

[8] Haynes WM, Ed. CRC Handbook of Chemistry and Physics (95th Ed.), CRC Press, Boca Raton, Florida, USA: 2014; 12-124.

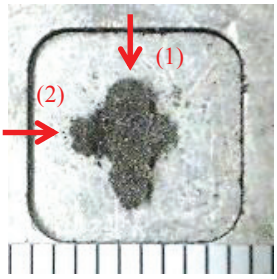

(a) Top view.

(b) Side view from (1).

(c) Side view from (2).

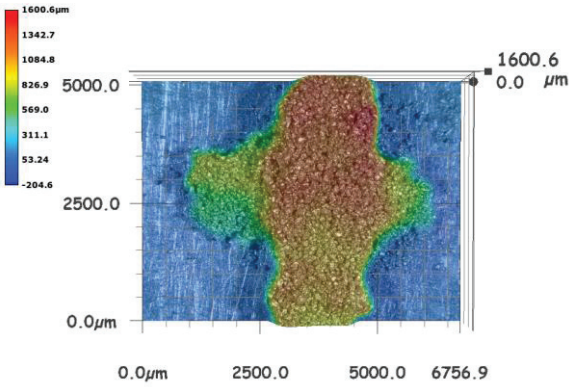

(d) Measured height.
FIGURE 8. Solid with overhang.

EFFECT OF THE ADDITIVE MANUFACTURING PROCESS ON CUTTING FORCES IN HYBRID MANUFACTURING

Michael Gomez[1], Andrew Honeycutt[1], Jarred Heigel[2], and Tony L. Schmitz[1]
[1]Department of Mechanical Engineering and Engineering Science
University of North Carolina at Charlotte, Charlotte, NC
[2]Production Systems Group
National Institute of Standards and Technology*, Gaithersburg, MD

INTRODUCTION

Powder bed fusion (PBF) enables metal components with complex geometries to be made via additive manufacturing (AM). Disadvantages of AM are rougher surface finish and lower achievable dimensional tolerances compared to computer numerically-controlled (CNC) machining [1]. Hybrid manufacturing combines additive and subtractive manufacturing strategies, which allows complex metal parts to be produced with the required surface finish and accuracy. An important consideration in hybrid manufacturing is the effect of the additive step on material removal in the subtractive step. Specifically, the cutting force is typically described using a force model that includes empirical coefficients that relate the required force to the commanded chip width and thickness. This paper explores the effects of the PBF process, as well as follow-on heat treating, on workpiece surface and material characteristics and, therefore, the corresponding cutting force coefficients.

CUTTING FORCE MODEL

The cutting force, which is often described using a mechanistic model with empirical coefficients, directly influences both the allowable, chatter-free material removal rate and surface location error (i.e., the geometric error caused by forced vibration during stable cutting). Surface location error is the difference between the locations for the actual and commanded surfaces. Therefore, an accurate cutting force model is needed to predict process parameters that will produce high quality parts.

The cutting force model applied in this study relates the uncut chip dimensions to the cutting force components using Eqs. 1-3:

$$F_t = k_t b h + k_{te} b \quad (1)$$

$$F_r = k_r b h + k_{re} b \quad (2)$$

$$F_a = k_a b h + k_{ae} b \quad (3)$$

where F_t, F_r, and F_a are the tangential, radial, and axial direction force components, respectively, which rotate with the cutter. The k_t, k_r, and k_a coefficients relate the force to chip area, where b is the axial depth of cut (chip width) and h is the instantaneous chip thickness. The edge coefficients, k_{te}, k_{re}, and k_{ae}, relate the force to the axial depth only and are associated with rubbing and non-cutting contact [2].

Experiments were completed to determine the cutting force coefficients at five different feed-per-tooth values. A new cutting insert was used for each cutting test in order to minimize the effects of tool wear on the force measurements. A single tooth cutter was used in order to eliminate the effects of tooth-to-tooth runout.

WORKPIECE DESCRIPTION

A pair of workpieces are shown in Figure 1A. Each workpiece consists of a wrought 17-4 stainless steel substrate (25 mm tall, 50 mm wide, 150 mm long) and a PBF deposited feature (25 mm tall, 15 mm wide, 140 mm long). A photograph of the PBF process during the creation of these figures is provided in Figure 1B. The process is repeated twice to create two pairs of workpieces, one that is heat treated at 650 °C for 1 hr to relieve the residual stress that is inherently created during the process, and the other pair that will be tested in the as-produced condition.

Within each workpiece, there are three material conditions of interest: the wrought substrate, the AM surface material, and the AM bulk material. The wrought substrate is a traditionally produced material that provides a baseline for which to compare the AM material. The AM surface material is the portion of PBF deposited material within 1 mm of the vertical faces of PBF feature. This material incorporates both the high residual stress and the rough surface generated by the PBF process. The AM bulk material is the remainder of the PBF feature and does not include the rough PBF surfaces.

Six different force models were established for the as-produced (not heat treated) substrate, AM surface, and AM bulk materials, as well as the heat-treated substrate, AM surface, and AM bulk materials. There were two goals for this approach. First, the impact of

* This publication was prepared by United States Government employees as part of their official duties and is, therefore, a work of the U.S. Government and not subject to copyright.

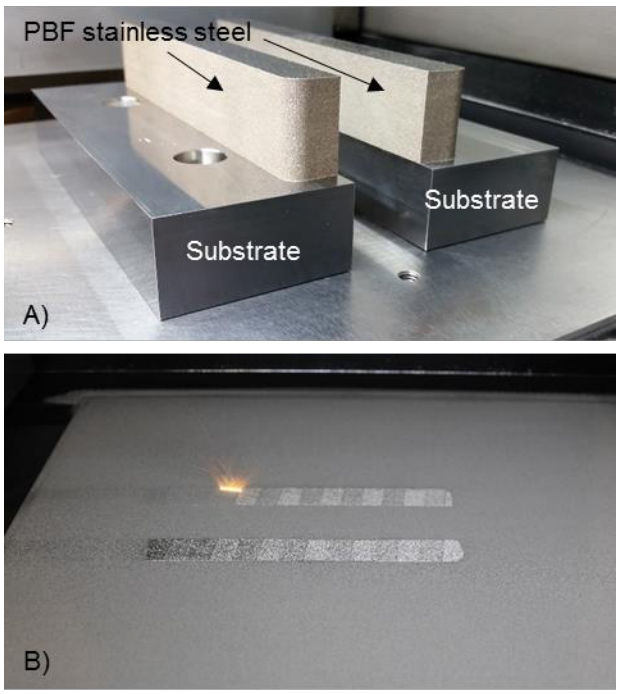

Figure 1. A) One pair of workpieces mounted on the PBF build platform. Each workpiece has a PBF stainless steel feature (top section) deposited on a wrought stainless steel substrate (bottom section with holes). B) Photograph of the PBF build process during the deposition of 1 pair of workpieces.

a variety of AM processing and post-processing effects can be compared to a baseline, as shown in Table 1. The as-produced AM surface of workpieces 1 and 3 has the greatest number of effects from the AM processing, including the residual stress and rough surface generated by the process, and any other possible differences between wrought and AM 17-4 stainless steel. The number of effects decreases by investigating the AM bulk, which removes the effect of the rough surface, and heat treating to remove residual stress. The second goal, is to demonstrate the difference between post-process machining that is required on many AM parts, which are likely heat treated prior to machining, and the intermittent machining that is implemented during hybrid processes, in which heat treatment is not performed before machining.

NON-LINEAR OPTIMIZATION MODEL

Tool wear can significantly affect cutting forces and machining stainless steel can lead to non-negligible wear rates. Therefore, a nonlinear optimization algorithm was used to determine the cutting force coefficients for each of the three materials within a single workpiece (wrought, AM surface, and AM bulk)

Table 1. Overview of the created workpieces and material regions of interest.

Workpiece	Material region	Heat treat	Effects
1 & 3	Substrate	no	- As-received baseline
1 & 3	AM surface	no	- Rough PBF surface - Residual stress - AM material difference from wrought
1 & 3	AM bulk	no	- Residual stress - AM material difference from wrought
2 & 4	Substrate	yes	- Heat-treat baseline
2 & 4	AM surface	yes	- Rough PBF surface - AM material difference from wrought
2 & 4	AM bulk	yes	- AM material difference from wrought

[3]. Using the experimental cutting force coefficients, a comparison can be made between the as-produced and annealed PBF cases. The nonlinear optimization method is advantageous because only a single cutting trial is required to determine the cutting force coefficients in a least-squares best fit sense.

The least-squares, nonlinear optimization method simulates the cutting forces over one cutter revolution using Equations 1-3. It then compares the simulated cutting forces to the measured cutting forces over a range of reasonable values for each of the six cutting force coefficients. The nonlinear optimization method seeks to minimize the difference between the simulated cutting forces and the measured cutting forces by Equation 4, where the fixed direction x, y, and z force components are determined from a projection of the rotating force components from Equations 1-3 using the cutter angle.

$$f(k_t, k_r, k_a, k_{te}, k_{re}, k_{ae}) = \sum \left\| \begin{Bmatrix} F_x \\ F_y \\ F_z \end{Bmatrix}_{simulated} - \begin{Bmatrix} F_x \\ F_y \\ F_z \end{Bmatrix}_{measured} \right\|^2 \quad (4)$$

CUTTING FORCE COEFFICIENTS

The machining setup for cutting force measurements is shown in Figure 2. The milling process was carried out using a new cutting insert (Sandvik Coromant

390R-070204E-MM S30T)† for each test to reduce the effects of tool wear on the force measurements.

A radial runout measurement was performed for the first set of cutting inserts. The purpose of these tests was to determine the change in cutting diameter as the insert is replaced. The normalized results are shown in Table *2*, where the measurements are performed using the machine spindle, a Mitutoyo dial indicator, and a Noga dial gage holder.

Figure 3 shows the results for the tangential and radial cutting force coefficients, k_t and k_r, at the commanded feed per tooth values as generated by the non-linear optimization model. Although there is some difference between the three materials at different feed per tooth values, there is generally no significant difference between the results for each material on the two as-produced workpieces. The results shown in Figure 3 demonstrate the repeatability in measurement results from the machining tests of as-produced workpieces.

Repeatability tests were conducted for the annealed workpieces 2 and 4. The results of the

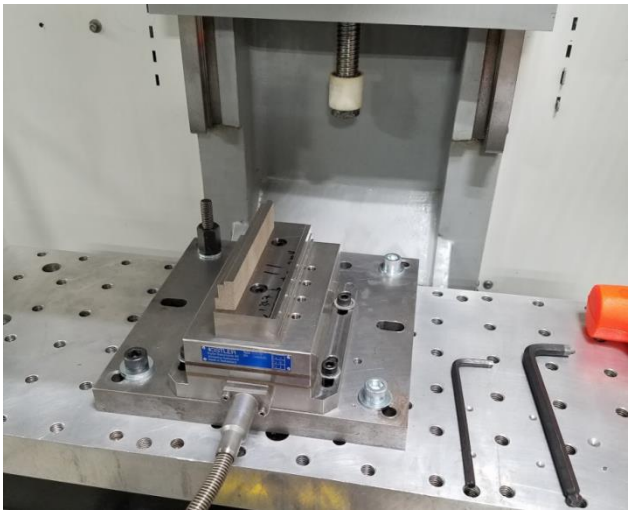

Figure 2. Machining experiment setup. The workpieces were mounted on a Kistler 9257B three-axis force dynamometer. All machining experiments were performed on a Haas TM-1 CNC milling machine.

Table 2. Radial measurement runout results.

Insert	Runout (μm)
1	0
2	152
3	50.8
4	25.4
5	76.2
6	127
7	0
8	25.4
9	-25.4
10	102

† Certain commercial equipment, instruments, or materials are identified in this paper in order to specify the experimental procedure adequately. Such identification is not intended to imply recommendation or endorsement by the National Institute of Standards and Technology, nor is it intended to imply that the materials or equipment identified are necessarily the best available for the purpose.

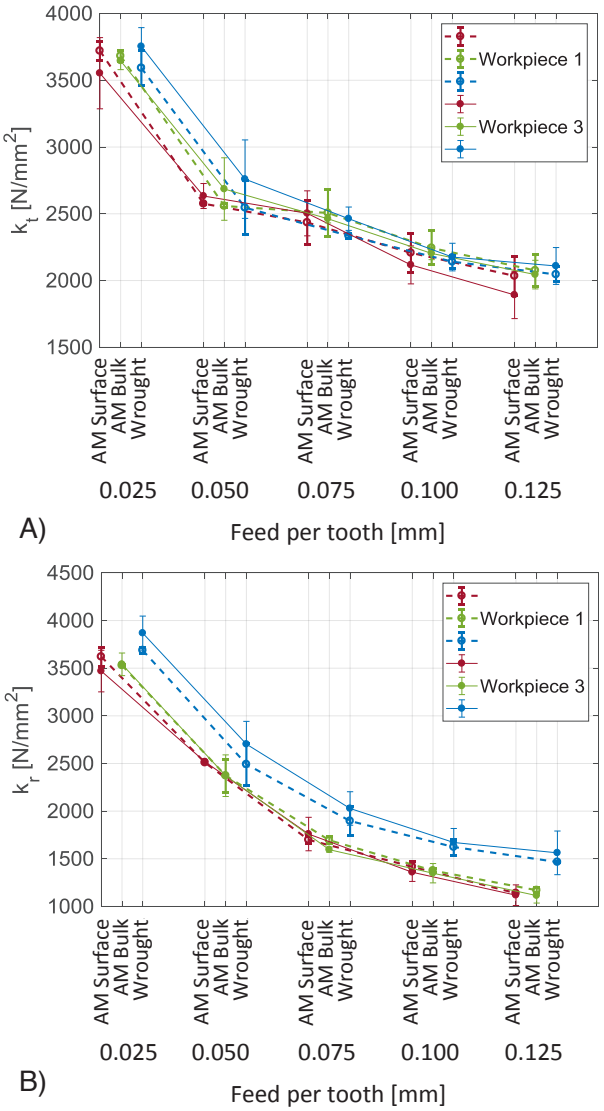

Figure 3. Mean values and 95% confidence intervals for A) tangential cutting force coefficients and B) radial cutting force coefficients for the as-produced workpieces. There were two sets of tests carried out on workpiece 1 and three sets of tests carried out on workpiece 3.

tangential cutting force coefficients and radial cutting force coefficients are provided in Figure 4. There is again no appreciable difference between the tangential cutting force coefficients for the two workpieces. Regarding the radial cutting force coefficients, while the error bars do not overlap between the two workpieces in each instance, it can be seen that there is limited variation in radial cutting force coefficients between the two.

The cutting force coefficient results for both the tangential and radial components can be grouped together to form a total of six cutting models for the as-produced and annealed workpiece categories. The results are shown in Figure 5. The annealing process increases both the tangential and radial cutting force coefficients (comparing solid line of the annealed cases to the dashed lines of the as-produced cases). A marked difference is apparent in the AM bulk material, where annealing increases both tangential and radial cutting force coefficients by a statistically significant amount.

From Figure 3 through Figure 5, it can be observed that the both the tangential and radial cutting force coefficients reduce with increasing feed

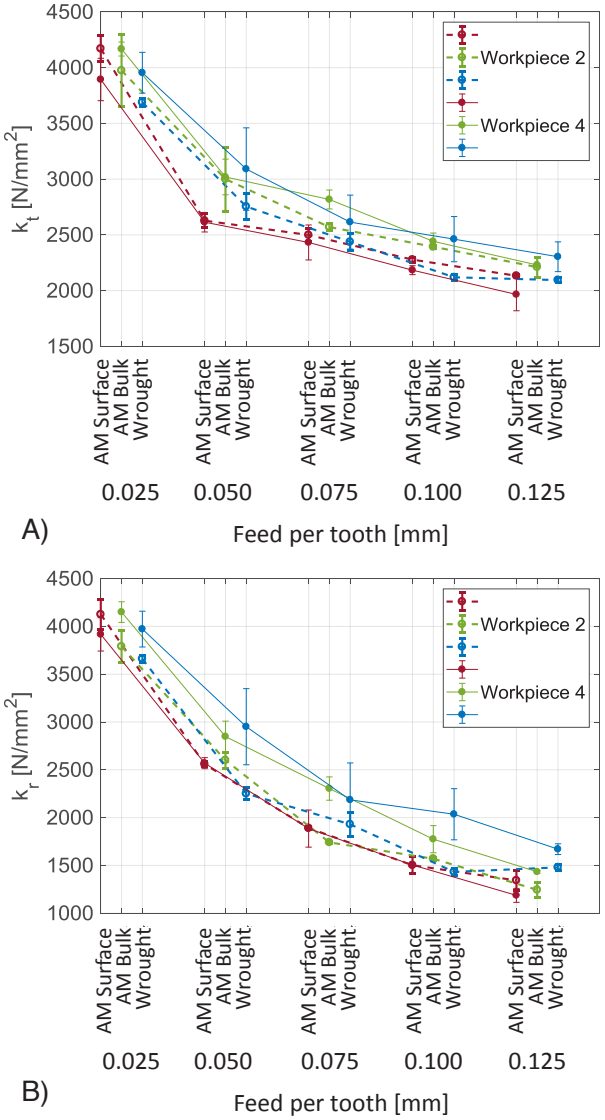

Figure 4. Mean values and 95% confidence intervals for A) tangential cutting force coefficients and B) radial cutting force coefficients for the annealed workpieces. There were two sets of tests carried out on workpiece 2 and three sets of tests carried out on workpiece 4.

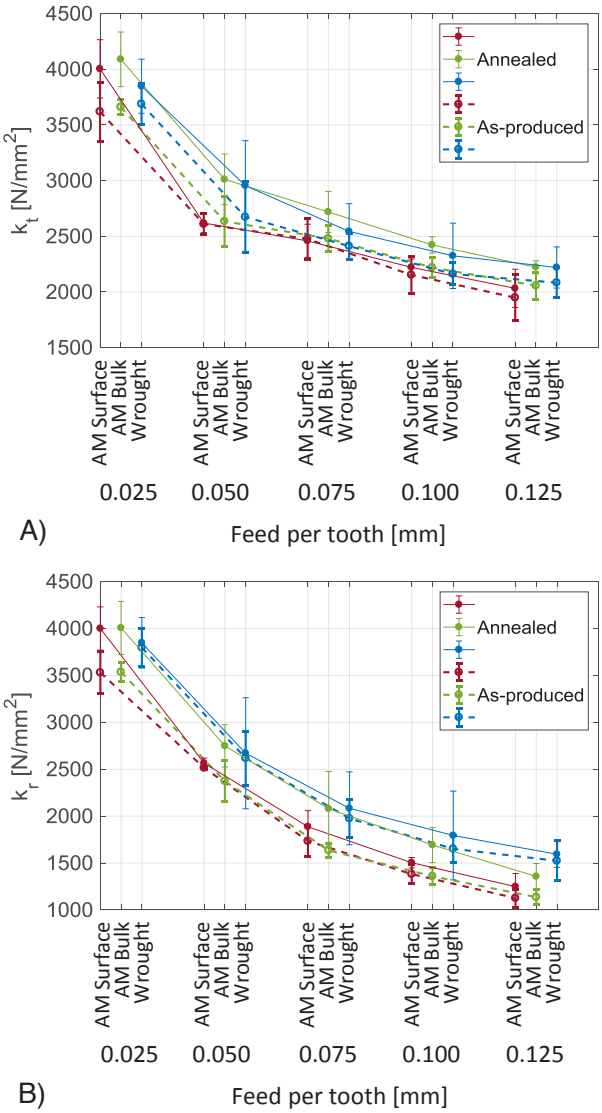

Figure 5. Comparison of the A) tangential cutting force coefficient and the B) radial cutting force coefficient for the as-produced and annealed workpieces materials.

per tooth. This phenomena occurs when the chip thickness approaches the cutting edge radius [4]. In this case, the rake angle appears to be negative which changes the chip formation [5]. To verify this behavior, a cutting insert was sectioned using wire electrical discharge machining (EDM) to expose the cutting edge radius. The cutting insert was placed in an scanning electron microscope (SEM) to obtain the approximate cutting radius. It was determined that the cutting edge radius is approximately 49 μm; see Figure 6. Therefore, a different cutting force model is needed to capture this effect. In follow-on analyses, the Kienzle force model will be applied [6]:

$$F_t = K_t b h^{1-m_t} \quad (5)$$

$$F_r = K_r b h^{1-m_r} \quad (6)$$

$$F_a = K_a b h^{1-m_a} \quad (7)$$

where there is a power law dependence on the chip thickness through the m coefficients and new cutting force coefficients, K, are defined.

ELASTIC MODULUS

A non-destructive means for identifying the elastic modulus was implemented. Specimens were machined from the initial workpiece and impulse excitation was used to determine the natural frequencies [4]. In these experiments, each specimen was subjected to a short duration impact from a dropped 9.5 mm diameter sphere; the response was measured using a digital microphone and the natural frequencies, f_n, were observed in the frequency domain. Free-free boundary conditions were approximated by placing the specimens on a soft foam base, as shown in Figure 7.

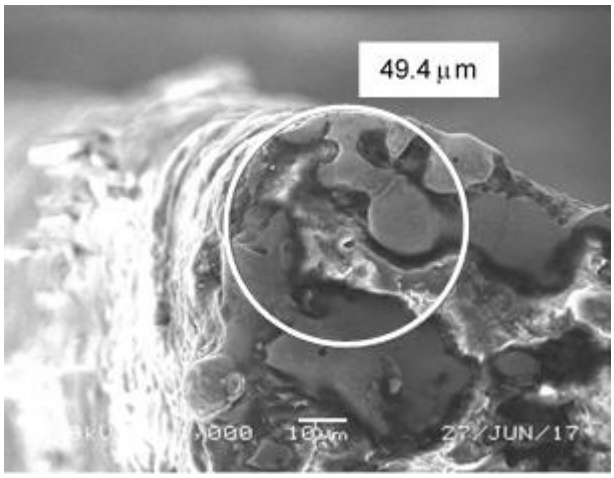

Figure 6. SEM image of the cutting edge radius.

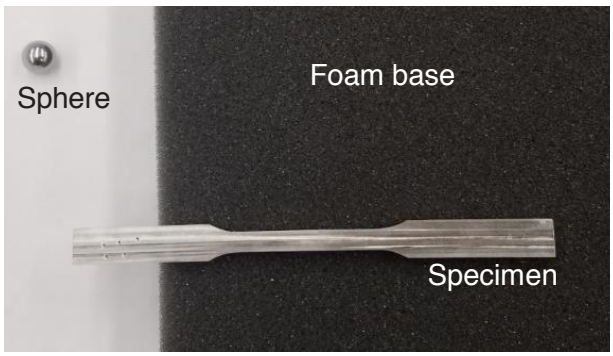

Figure 7. Experimental setup for the impulse excitation testing. The specimens were placed on a foam support and subjected to an impact from a dropped sphere. The sound was recorded using a microphone.

Once the natural frequencies were known, a finite element (FE) model was completed for the specimen and the elastic modulus was adjusted until the natural frequencies matched. There were two AM specimens used for the FE analysis: 1) as-produced; and 2) annealed. The specimens created using the wrought material will be measured in follow-on work. The measured dimensions were used to model the specimens in PTC Creo Parametric 3.0 and Creo Simulate was used to perform FE analysis. The measured density, ρ, and assumed Poisson's ratio, v, were assigned to the material which was subject to a free-free boundary condition. The simulation produced the first six vibrational modes. The elastic modulus was used as a fitting parameter for a best fit to the first three natural frequencies; see Figure 8.

Table 3 shows the first three measured natural frequencies for both AM specimens, as well as the measured Poisson's ratio and density and the assumed modulus of elasticity that brings the

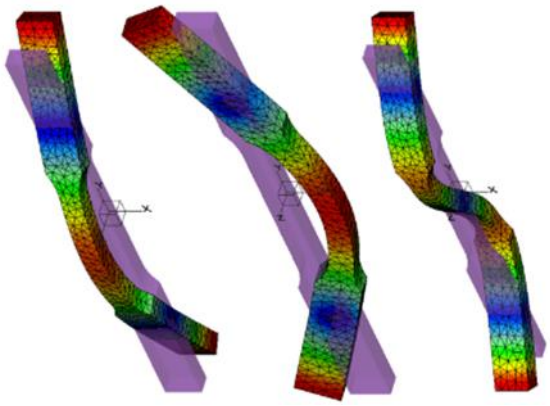

Figure 8. The first (left), second (middle), and third (right) bending modes produced by the FE simulation

Table 3. Material properties for the AM specimens.

Properties	As-produced	Annealed
f_{n1} (Hz)	1352	1378
f_{n2} (Hz)	1642	1667
f_{n3} (Hz)	3984	4058
υ	0.29	0.29
ρ (kg/m^3)	7873	7918
E (GPa)	188	195

simulation into agreement with the measurements. It is observed that both the density and elastic modulus were higher from the annealed specimens.

HARDNESS

Hardness tests were conducted on a Wilson Rockwell Series 2000 testing machine. A Rockwell C hardness scale, HRC, was selected. The results of the hardness tests are shown in Figure 9. The horizontal band represents the typical HRC values for 17-4 stainless steel. It can be seen that annealing reduced the hardness in the wrought material. However, it increased the hardness for the AM material. There is a characteristic increase in HRC values in both the in-plane (top) and out-of-plane (side) build direction.

CONCLUSIONS

The purpose of this study was to assess variations in the cutting force model for wrought and additively manufactured workpieces. Two conditions were considered: as-produced and annealed. The force model is critical because it is used in analyses used to predict machining stability and surface location errors. Therefore, an improved understanding of the effects of the additive manufacturing process on cutting force coefficients will give new insight into hybrid manufacturing strategies.

The results showed only minor differences in the coefficients between the various material states. The strongest effect was annealing, which increased the coefficients in all cases, particularly for the bulk additively manufactured material. A general trend of decreasing coefficients with increasing feed was observed. This is due to a change in the apparent rake angle and is well-known. To address this effect, the linear force model will be updated using the Kienzle model [6].

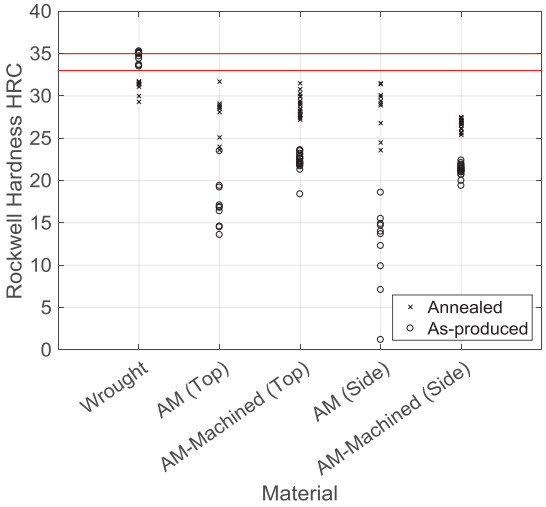

Figure 9. Rockwell hardness values for the wrought, as-produced, and annealed specimens. There were ten measurements completed for each case.

ACKNOWLEDGEMENTS

The authors gratefully acknowledge partial financial support from the UNC Charlotte Center for Precision Metrology Affiliates Program.

REFERENCES

[1] Cooke, A.L. and Soons, J.A., 2010, Variability in the geometric accuracy of additively manufactured test parts, 21st Annual International Solid Freeform Fabrication Symposium, Austin, TX

[2] Schmitz, T. and Smith, K.S., 2008, Machining Dynamics: Frequency Response to Improved Productivity, Springer, New York, NY.

[3] Rubeo, M. and Schmitz, T., 2016, Mechanistic force model coefficients: A comparison of linear regression and nonlinear optimization, Precision Engineering, 45: 311-321.

[4] Cossolino, L.C. and Pereira, A.H.A, 2010, Elastic moduli: Overview and characterization methods, ATCP Physical Engineering, Technical Review ITC-ME/ATCP, 10-11.

[5] Coelho, R.T., Braghini Jr., A., Valente, C.M.O. and Medalha, G.C., 2003, Experimental evaluation of cutting force parameters applying mechanistic model in orthogonal milling, Brazilian Society of Mechanical Science & Engineering, 247-248.

[6] Kienzle, O., 1952, Die Bestimmung von Kräften und Leistungen an spanenden Werkzeugen und Werkzeugmaschinen, In: Zeitschrift des Vereins deutscher Ingenieure, 657-662.

PRECISION MANUFACTURING OF INTERNAL INVOLUTE GEARS USING 5-AXIS MILLING CENTER

Jesse M. Groover, Gert Goch
Department of Mechanical Engineering and Engineering Science
University of North Carolina at Charlotte
Charlotte, NC, USA

INTRODUCTION

In the past, gears have largely been manufactured by means of complex tools and actuation systems [1]. The complexity, cost, and narrow applicability of the necessary systems, such as hobbing machines and tools, gear shapers, etc., has been inevitable due to limited computation power. With the rise of Computer Numerically Controlled (CNC) technology over the last few decades, new methods of gear manufacturing have been made possible, but have been largely neglected.

One limitation of CNC machines is the rudimentary coding language that controls the axes motions. To profile cut a contour, the software usually must segment the curve into a finite number of linear segments. This introduces form errors that are prohibitive for the flanks of gears. Most gear flanks, however, follow an involute profile [2] which has certain properties suggesting that it is possible to use the generation principle to mill high quality gears without the need for linear approximation. Simultaneous rotary and linear motions are used to achieve low form deviations. For example, external gears have been manufactured using a slot cutter on a five axis CNC machine [3], although this is not the preferred method in industry.

Internal gears have been widely used since planetary gear stages became standard in modern car transmissions, as well as other large components, such as gear boxes and pitch and yaw control mechanisms in wind energy systems [4]. But internal gears present geometrical limitations that inhibit certain production processes that are usual with other types of gears. With the aid of a standard five axis machining center and standard milling tools, high quality internal involute gears can be machined by means of the generation principle, without having to rely on the sophisticated machinery and tooling that was previously necessary.

This paper investigates the use of a Mori Seiki NMV5000DCG five axis milling center and standard 4 flute 3mm end mills in the production of internal involute gears.

Algorithms have been developed in MATLAB® to generate the G-code leading the machine to follow generation principle motion. Specifically, inverse time feed rates, as opposed to standard millimeters per minute feed rates, have been utilized to achieve simultaneous rotary and linear motion, complying with the generation principle. The tool paths have been constructed such that the tool does not leave the cut at all along the entire contour of the gear, including every tooth. Spur gears have been manufactured, and subsequently measured by means of a coordinate measuring machine (Leitz PMMF302016) and the Quindos7 software. Gear flanks with profile deviations of less than 5 µm have been produced. Future work will include improvements in profile deviations and surface finish, as well as investigations into the manufacture of helical gears.

DESCRIBING THE INVOLUTE

An involute curve can be visualized by imagining a string being unwrapped from around a cylinder. If the string is held taught while unwrapped, the end of the string will trace an involute curve relative to the fixed cylinder. Another way of visualizing the same scenario is to imagine the string being pulled off in a straight line as the cylinder rotates. Still, relative to the now rotating reference cylinder, the end of the string is tracing an involute. The cylinder is called the “base cylinder,” and its diameter is called the “base diameter.” In gears, the base diameter is rarely a physical, measurable quantity. Rather, it is a theoretical dimension used for the purposes of design. Mathematically, an involute is described parametrically as follows [5]:

$$\begin{aligned} x &= R_b * (\cos(\varsigma + \Lambda) + \varsigma * \sin(\varsigma + \Lambda)) \\ y &= R_b * (\sin(\varsigma + \Lambda) - \varsigma * \cos(\varsigma + \Lambda)) \end{aligned} \quad (1),$$

Where R_b is the radius of the base cylinder, ς is the "roll angle," or rotation of the base cylinder, and Λ is the initial offset angle, or the angular start position of the base cylinder.

It is easily seen that if the rotation of the cylinder is constant, the linear speed of the end of the string must also be constant. However, the fact that the speeds themselves are constant is not important. What matters is that the relationship is constant between the rotational speed of the cylinder and the linear speed of the end of the string. This relationship is as follows:

$$V = R_b * \omega, \quad (2)$$

Where V is the linear speed of the end of the string, R_b is the radius of the base cylinder, and ω is the rotational speed of the cylinder. This is called the "Generation Principle," and is the principle by which gears are often made.

For external spur and helical gears, "hobbing" is often used as a means of realizing generation principle motion [6]. For internal gears, however, hobbing is impossible due to simple geometrical limitations. Thus, other methods must be used, which do not take advantage of the generation principle. This paper attempts to address these limitations, and offer a solution.

APPLICATION TO MILLING

The basic approach used to apply generation principle motion to the manufacture of internal gears is as follows: In the example of the cylinder and the string, above, the gear blank is the cylinder. The tool travels in the straight line traversed by the endpoint of the string. This is shown in Figure 1.

In Figure 1, R_b is the base radius, R is the radius at point P, ζ is the "roll angle," or the angular distance traveled by the gear, and θ is the angular distance from the start point to point P.

So far, the involute is simply a curve in space. Theoretically, the only difference between an internal gear and an external gear is on which side of the curve the material lies. Functionally, there are some differences, such as "undercutting" in the tooth roots of external gears to avoid tooth interference [1], and other modifications. But these are unrelated to the mathematical properties of the involute, so for the purposes of this paper, they will be ignored.

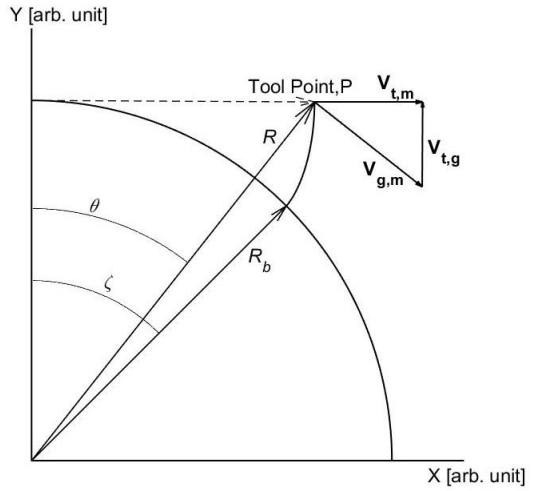

FIGURE 1. Generation principle applied to milling an involute curve.

To mill an involute curve, the contact point of a standard cylindrical end mill is placed at the "tool point" P, in Figure 1. The "contact point" is the line of contact between the edge of the tool and the nominal curve position. Thus, the center point of the tool, which is the programmed position, must be offset from the curve by the radius of the tool, in the direction normal to the involute curve. In generation principle motion, the tool point, or endpoint of the string, is always traveling in a path normal to the involute curve. Thus, the center point of the tool must simply lie along the path of tool motion, offset from the nominal curve by the radius of the tool. This is shown in Figure 2.

MACHINING CONSIDERATIONS

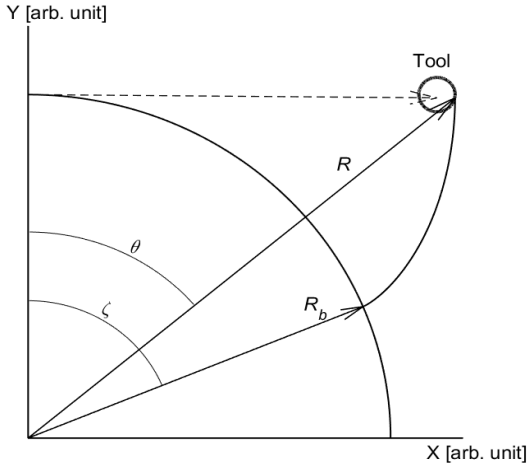

FIGURE 2. Tool placement through cut

Constant Cutting Speed

Originally, constant rotational and linear velocities were used. It was noted, however, that even though the machine may be traveling at a constant velocity, the tool is not traveling at a constant velocity through the part material. This causes significant variations in cutting conditions, primarily the chip load, or feed per tooth, throughout the cut. But, as pointed out before, constant machine speeds is not required. Instead, the relationship between the rotational speed of the gear and the linear speed of the tool must be constant. Thus, these were modified throughout the cut to try to get more constant cutting conditions.

Roughing the Gear Teeth

Another property of the involute provides a convenient method for roughing the tooth profile. By simply rotating the gear a certain amount at the beginning and continuing from there, an involute curve exactly parallel to the nominal can be created, as shown in Figure 3.

In Figure 3, Λ_1 and Λ_2 are the starting angles for involutes 1 and 2, respectively. ζ_1 and ζ_2 are the roll angles for involutes 1 and 2, respectively. As before, R_b is the base radius, and d represents the constant normal distance between the two curves.

Therefore, for roughing the gear teeth, to achieve constant radial immersion of the tool through the cut, the initial angle must simply be adjusted, and the path repeated. The start and end points must be modified to avoid running into the opposing involute, but the principle still applies.

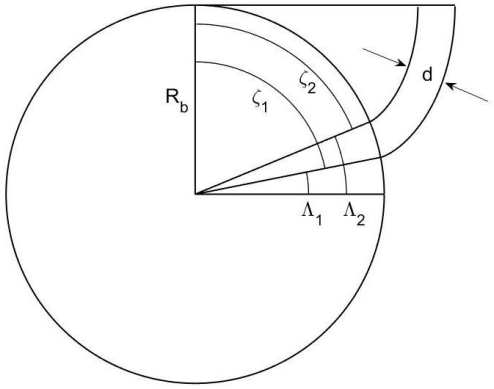

FIGURE 3. Parallel involutes used for roughing the gear teeth

IMPLEMENTATION

The tool must travel in a line tangent to the base circle. Between any point and circle on a plane in space, however, there exist two different tangent lines.

The tool was started on the base circle, at the top of the circle, traveling to the right, as shown in Figure 1. When the tool reached the desired end

TABLE 1. Sample measurement results of machined internal gear teeth by means of generation principle motion. All units are in μm.

Profile Deviations									
Name	Symbol	Left 9/1	Left 1/3	Left 1/2	Left 1/1	Right 1/1	Right 1/2	Right 1/3	Right 9/1
Profile Slope Deviation	$f_{H\alpha}$	9.7	-11.0	-8.5	-7.4	11.7	9.6	6.3	3.7
Profile Deviation, Total	F_α	16.2	19.9	16.8	13.9	13.1	11.6	9.7	7.0
Profile Form Deviation	$f_{f\alpha}$	11.0	17.5	14.5	14.4	6.1	7.1	7.8	6.5
Helix Deviations									
Name	Symbol	Left 9/1	Left 1/3	Left 1/2	Left 1/1	Right 1/1	Right 1/2	Right 1/3	Right 9/1
Helix Slope Deviation	$f_{H\beta}$	-6.5	-4.2	-4.5	-4.5	4.6	4.5	2.5	4.1
Helix Deviation, Total	F_β	9.1	6.3	6.2	7.1	7.9	8.5	6.4	7.4
Helix Form Deviation	$f_{f\beta}$	3.6	3.4	3.3	3.2	3.5	4.8	4.7	4.0

of the involute, however, it is possible for the tool to travel down the other tangent line, while the gear continues to rotate in the same direction, to cut the opposing flank.

In greater detail, the process used is as follows:

1. Beginning with the tool-gear contact point (point P, in Figure 1) on the base circle, the gear rotates clockwise as the tool travels along a straight line, according to the generation principle. This is the first involute.
2. When the end of the involute is reached, the tool remains stationary while the gear continues to rotate the angular width of the tooth root.
3. The tool now travels along the second line tangent to the base circle, towards the base circle, while the gear continues to rotate. Their speeds are coordinated to achieve generation principle motion. This is the second, opposing involute.
4. When the tool-gear contact point reaches the base circle, the gear stops and the tool profile mills the tooth tip, arriving at the start point of the next tooth.
5. This process is repeated for each tooth.

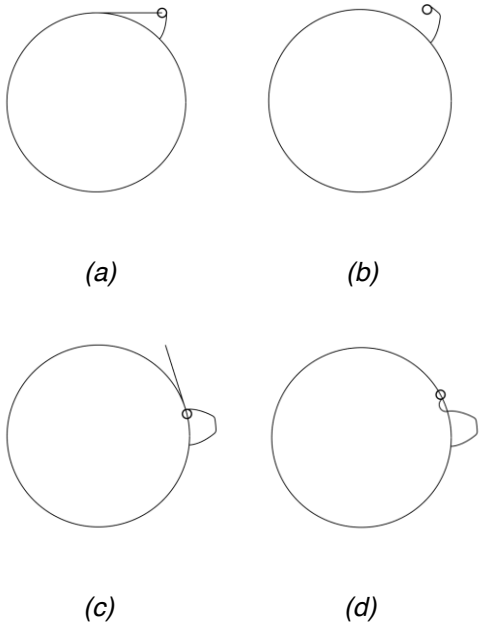

Figure 4. The process for each tooth: The first involute (a), the tooth root (b), the opposing involute (c), and the tooth tip (d).

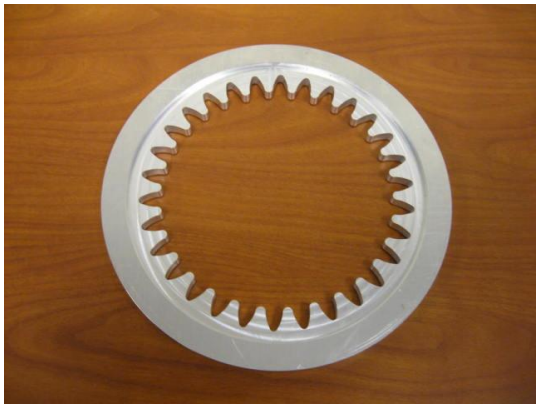

Figure 5. Machined Gear

The result is an efficient process wherein the tool must never leave the cut. This process is illustrated in Figure 4.

RESULTS

A 30-tooth internal spur gear with a 20° pressure angle was machined. The face width was 10 mm, and the pitch diameter was 150 mm. A 1/8" diameter, 4-flute carbide endmill with a 30° helix angle was used. The machined gear is shown in Figure 5. Sample measurement results are listed in Table 1, and shown in Figure 6.

LIMITATIONS

The process is limited by the size of the teeth desired to be cut. The diameter of the tool must be small enough to fully reach the tooth root. With small end mills, lower chip loads must be used, and the length of the tool is limited by stability considerations, effectively limiting the face width of the gear to be machined. With smaller tools, material removal rates are low, rendering the process slow.

CONCLUSIONS AND FUTURE WORK

Future work includes the further development of the process to improve accuracy and increase speed, and adaptation for the manufacture of internal helical gears. Work in the area of bevel gears is also planned.

AKNOWLEGEMENTS

The authors would like to offer their sincere thanks to Kang Ni and Yue Peng for their assistance in thinking through problems, and the measurement and evaluation of the manufactured gears. The Machine Tool Technologies Research Foundation (MTTRF) provided the Mori Seiki NMV5000DCG on which

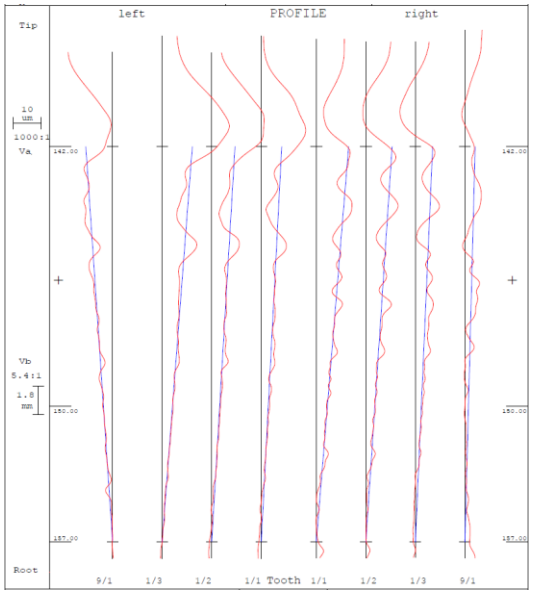

(a)

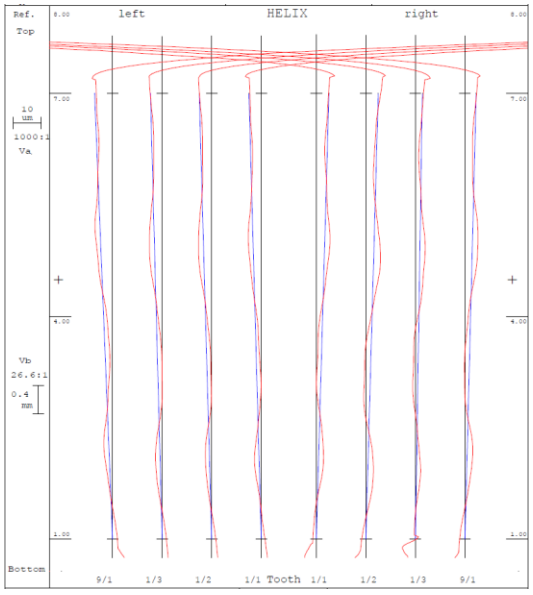

(b)

FIGURE 6. Results of gear measurement (a) in the profile direction, and (b) in the lead (helix) direction

the research was conducted, for which the authors are especially grateful. And lastly, the authors would like to express their gratitude to the ASPE for the opportunity to present this research.

REFERENCES

[1] Álvarez A., López de Lacalle L.N., Olaiz A., Rivero A. Large Spiral Bevel Gears on Universal 5-Axis Milling Machines: A Complete Process, Procedia Engineering, Volume 132, 2015, 397-404

[2] Grant G. B. A Treatise on Gear Wheels, University Press of the Pacific, Honolulu, Hawaii: 2000

[3] Stöbener D., Lübke K., Larsen P., Von Freyberg A., Ghebreyesus B., Goch G. An Approach for 5-Axes Gear Production with a Slot-Milling Cutter, The Proceedings of MTTRF 2012 Meeting, 2012, 115-120

[4] Goch G., Knapp W., Härtig F. Precision Engineering for Wind Energy Systems, CIRP Annals – Manufacturing Technology, Volume 61, Issue 2, 2012, 611-634

[5] Goch G. Gear Metrology, CIRP Annals – Manufacturing Technology, Volume 52, Issue 2, 2003, 659-695

[6] Bouzakis K.-D., Lili E., Michailidis N., Friderikos O. Manufacturing of Cylindrical Gears by Generating Cutting Processes: A Critical Synthesis of Analysis Methods, CIRP Annals – Manufacturing Technology, Volume 57, Issue 2, 208, 676-696

Force Measurement in Diamond Micro-Chiseling

**Dustin K. Gurganus, Nicholas E. Sizemore,
Joseph D. Owen, and Matthew A. Davies
Mechanical Engineering and Engineering Sciences,
University of North Carolina at Charlotte, Charlotte, NC USA**

BACKGROUND

For many years, optical design has been limited to rotationally symmetric refractive optics and planar diffractive optics. Ultra-precision diamond machining can expand the optical design space to encompass freeform optics including microstructured surfaces with the ability perform the tasks of multiple conventional optics. Diamond micro-chiseling (DMC) [1] further expands the design space by allowing the generation of hexagonal cube corners as shown in Figure 1 in a monolithic workpiece within one setup. Such structures cannot be machined by methods requiring a continuous tool path (e.g. turning, milling, flycutting). These reflective microstructures show superior efficiency to structured surfaces with pyramidal convex cavities or v-shaped [5] cavities, and cannot be generated by processes such as fly-cutting or milling.

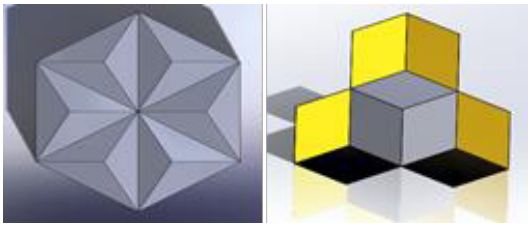

FIGURE 1: Fly-cut pyramidal retroreflector (LEFT) and a DMC single cube-corner high efficiency retroreflector (RIGHT).

The first retroreflectors were formed out of simple glass beads adhered to a surface. However, more modern approaches allow the manufacture of cube corners or micro-prisms for the efficient generation of high-performance retroreflectors. These micro-prisms are approximately 0.2 mm in size and are greater than 3 times more effective than their predecessor, returning up to 66% of the incident light (Figure 1). Hexagonal cube corner arrays were originally produced utilizing the “pin building method”. Each pin was ground to have three separately polished facets. The pins were then stacked to form a hexagonal cube corner structure. However, the stacking method has inherent errors and the smallest size achievable by this method was 500 μm. To overcome size limitations and assembly errors and enable mass-production of highly efficient cube corners, the process of DMC was introduced by Brinksmeier et al. [1]. The manufacture of these cube corners by micro-chiseling enables effective use of surface area, and since these are machined or imprinted, they are less sensitive to water and wear. Due to current technological constraints, these retroreflectors are expensive and difficult to manufacture. Also, at wider angles, the efficiency decreases. Until today, the DMC process stability and its limits are discussed based solely on properties of the generated surfaces. Furthermore, the loads occurring during DMC have not been measured. In this paper, we describe the measurement of cutting forces during DMC which can be used for process and tool condition monitoring.

FUNDAMENTALS OF THE PROCESS

DMC is a process which requires the chiseling of individual chips through a discontinuous tool path and rotations of the workpiece to create a desired pattern (Figure 2). This contrasts with fly-cutting or milling, which inherently produce continuous cutting paths.

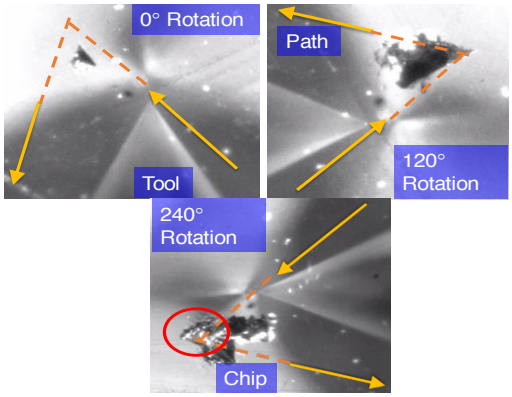

FIGURE 2: DMC process based on [1] performed within the here presented study.

The v-shaped dead sharp diamond tool used here for DMC is described in the next section. The process to produce one corner cube is as follows. First, the tool is aligned such that the clearance face produces the desired planar facet angle with respect to the working surface. Next, the tool is rotated about the shank of the tool and plunged into the surface until the desired depth is reached. The tool then retracts. Since the generation of the retroreflector requires overlapping cube corners, this process

is finally repeated two more times with a 120^0 rotation of the workpiece between each interval. This process can create arbitrary prismatic micro-cavities, hexagonal retroreflectors arrays ranging in size from 50 to 500 μm.

Following on research performed by Brinksmeier et al. [2], this paper focusses on the measurement of process loads by means of force-measurement for different chiseling-strategies. Knowledge of the mechanical loads during the complex process will allow for a better understanding of the process and thus enable optimization and process monitoring. It is expected that based on the assessment of the cutting forces, the chiseling parameters can be optimized for productivity and stability.

EXPERIMENTAL SETUP

This study involved two experiments in which cutting forces were measured. The first consisted of plunging with different depth-of-cut to find where the tip of the diamond tool experienced the highest forces. The second experiment consisted of machining of a full rough-cut cube corner array. Using force measurements, a more effective tool path was created to increase efficiency of this novel machining process.

All experiments were conducted on a Moore Nanotechnology 350FG as shown in Figure 3, The diamond tool had an included angle ε of 50°, a rake angle γ of 0°, and a side clearance angle, α, of approximately 22°. The tool was set to a 57.063° rotation in the positive B direction. The tool was mounted on a tool-post with a flexure based integrated dynamometer. The workpiece was a 25.4 mm diameter naval-brass disc mounted on a Kistler Type 9245C stationary dynamometer thus allowing equal/opposite force measurement on the tool and workpiece simultaneously.

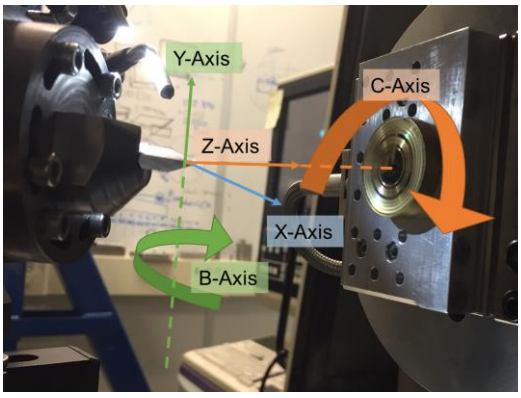

FIGURE 3: Axis of motion and rotation for the workpiece and the tool.

An tool post (Figure 4) with an integrated flexure-based dynamometer was designed and constructed for this study. The tool post consisted of multiple components to ensure a versatility of tool angle approaches and accurate force measurement. First, there are two angles of rotation for the tool post. One 360°-rotation about the shank of the tool, ϕ, and a ± 20°-rotation about the tip of the tool φ. These angles of rotation are achieved through two separate systems. A slotted tool holder face with screws allows rotation about the C-axis. The ± 20°-rotation about the tip of a tool is enabled by a goniometer with a foot clamp tightened by a hex head sleeve nut.

The combination of flexures and a capacitance probe enables the measurement of the axial component of the force at the tip of the diamond tool during DMC. An h-style leaf flexure mechanism is used for one-axis of force measurement while maintaining stiffness as shown in Figure 4, [4]. Analytical and FE calculations gave a flexure stiffness of 3.04 N/μm. Final calibrations and testing gave a measured stiffness of 2.91 N/μm. The difference between the calculated and actual values is approximately 5%.

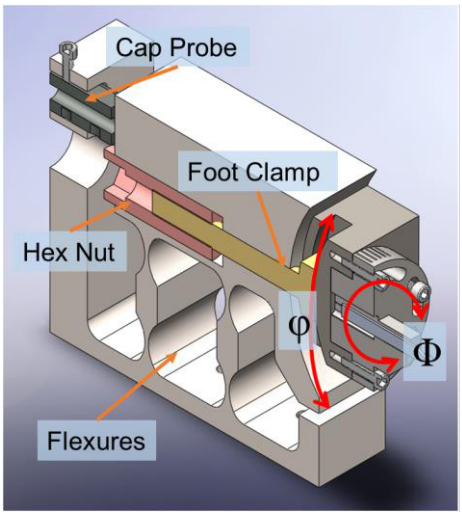

FIGURE 4: Tool post with two angles of rotation, flexure-based dynamitic system utilized for manufacturing of test retroreflectors and the axial directions of motion and force measurement.

The capacitance probe used to measure flexure displacement is a Lion Precision Model MFG3–0831 with a working distance of 2 mm and a resolution of 5 nm operating on a +/-10 V bandwidth. Also mounted on the tool post is a microscopy system enabling in-process monitoring of chiseling. The camera is an Edmond Optics EO-5012M MONO LE USB CAMERA with a telecentric lens. The lens has a working distance of 65 mm, primary magnification of 6x and a field of view of 1.1 mm. The camera detector has a 12.7 mm

sensor size and a pixel size of 2.2 μm^2. Direct mounting to the tool post allows for correlation of the process dynamics with forces. Multiple tests with varied cutting parameters were performed to evaluate the process forces. Seven initial cube corners were cut using various depths of chiseling. These cuts were performed with the workpiece in the same location, no rotation was performed. The second set of testing involved the cutting of a full cube corner also in the naval brass, which involves the rotation of the workpiece and dynamometer. A final test was performed where the flexure-based tool post machined a cube corner array in copper.

RESULTS AND DISCUSSION

There were two cutting strategies implemented. The first was a single direction cut with varying plunge depths (a_p). The second was the machining of an actual full cube corner complete with workpiece rotation.

Before any actual testing was completed, multiple experiments were performed to analyze the deflection of the flexures and the displacement read by the capacitance probe. A calibration relationship was established where average deflection was approximately 0.3 µm/N.

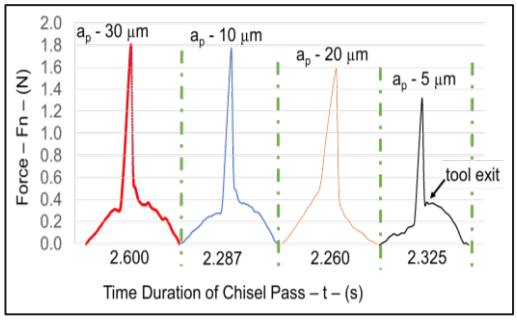

FIGURE 5: Characteristic force profile indicating the maximum values observed for the different cutting strategies

The initial cuts were taken in the same direction, but at various depths. The raw dynamometer data was digitally filtered (filtered F_z) with a 10 Hz low-pass filter. Figure 5 shows force profiles for each cutting depth. Forces recorded by the dynamometer increased as the depths of cut increased. However, when performing cuts at steps of 20 µm, the forces seemed to decrease when compared to a shallower cut of 10 μm. Further investigation is needed to understand this change.

The qualitative shape of the cutting forces is the same across all depths. The initial spike corresponds to the tool entering the material and reaching the full depth of cut. The drop occurs as the tool moves away. However, as the tool begins to exit the part there is a change in the force slope leading to a shoulder-like profile which correlated to chips building up on the tip of the tool. This observation has been taken into consideration and can be applied in later design paths to allow for a farther retraction distance from the workpiece to prevent chips from causing additional, and potentially damaging, forces on the diamond.

To analyze the force data, taken with the first cutting strategy, three data conditioning calculations were employed. First, component calculation was made to account for the angle of the tool as it entered the test piece (°):

$$F_{comp} = F_y \cos(57.063) + F_z \sin(57.063)$$

Second, the force magnitude was calculated.

$$F_{SRSS} = \sqrt{F_y^2 + F_z^2}$$

Lastly, the capacitance probe force deflection relationship was employed to calculate the forces.

$$F_{cap} = 2.91^{N/}_{\mu m} * Cap_{deflection}$$

Figure 6 contains a comparison of F_{cap} and F_{comp}.

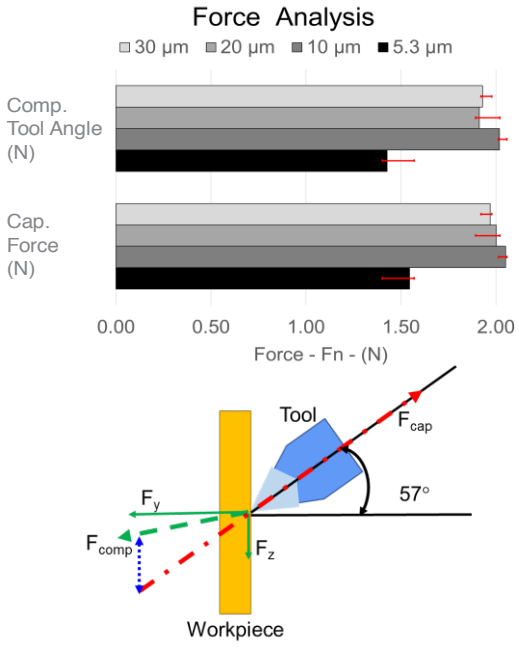

FIGURE 6: Maximum forces per cutting depth and a force diagram of the tool during the micro-chiseling process.

To complete a comparison, F_{comp} was projected

in the direction of F_{cap}. Figure 6 shows this comparison. There is strong agreement with a maximum error of approximately 7%.

The second cutting strategy considered the forces experienced through the entire process of micro-chiseling a cube corner. Figure 7 shows the component force measurements and the capacitance flexure-based measurements. Good qualitative agreement is again seen. This indicates that flexure based deflections can be used as an in-process monitor of the forces on the diamond tool.

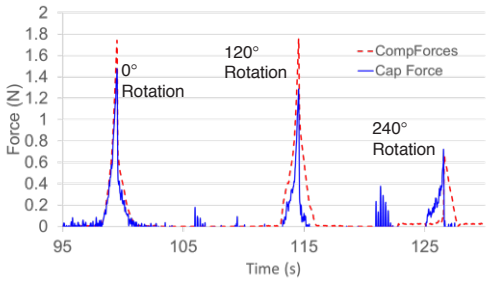

FIGURE 7: Example of a capacitance flexure-based readings and component forces comparison.

This plot shows a set of the chiseling within this the DMC process. This cut was the 3rd cut in the series of chisels and rotations. This section of data was chosen due to it being in the middle of the cutting process. Interestingly, the final cut, at 240° rotation seems to have lower forces associated with the cuts. This is thought to occur because the 0° and 120° rotation cuts have cleared out most of the material before the 240° cut begins.

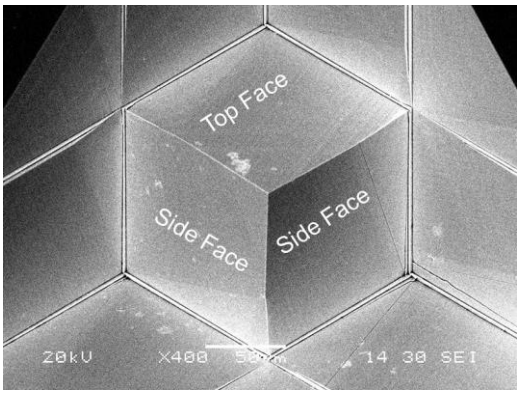

FIGURE 8: SEM of full cube corner cut by flexure based tool post in copper. The sides of the cube are labelled for clarity.

A scanning electron microscope (SEM) was used for qualitative assessment of the quality of the facets. Figure 8 shows the results including some edge degradation due to burr formation. Use of materials other than copper may reduce the burr formation and improve the cube corner quality further. There were concerns that the flexures would cause vibrational effects in the production of these cube corners, but the surface finish does not show any signs of tool vibration indicating that the flexure based dynamometer may be used for process monitoring during cutting.

CONCLUSIONS AND OUTLOOK

The study presents the first measurement of forces occurring during micro-chiseling. For micro-chiseling tests performed in the past, depths of cut were limited to 5 μm resulting in comparably long machining times. It is clear from the force data that those cuts were conservative. The force measurements by the presented approach were more sensitive than the dynamometer alone. The capacitance probe calculations displayed a similarity to the more complex calculation methods. This force measurement process can be adapted to compare various cutting methods and toolpaths as they are created. Using and building upon the data gathered from within this experiment can add to the path for DMC to become a production process. Furthermore, the force measurements will allow process monitoring for unexpected changes of the mechanical loads (e.g. by wear or tool breakage) during long term cutting of large corner cube arrays. Future research will be to test additional materials and tool paths.

REFERENCES

[1] E. Brinksmeier, R. Glabe and C. Fluke, "Manufacturing of molds for replication of micro cube corner retroreflectors," *German Academic Society for Production Engineering,* pp. 33-38, 2007.

[2] E. Brinksmeier and L. Scho¨nemann, "Generation of discontinuous microstructures by Diamond Micro Chiseling," *CIRP Annals - Manufacturing Technology,* pp. 49-52, 2014.

[3] E. Brinksmeierl, R. Gla¨be and L. Schönemann, "Review on diamond-machining processes for the generation of functional surface," *CIRP Journal of Manufacturing Science and Technology,* pp. 1-7, 2012.

[4] S. Smith, Flexures, Boca Raton, Florida: CRC Press LLC, 2000.

[5] T. Moriya, K. Nakamoto, T. Ishida and Y. Takeuchi:, "Creation of V-Shaped Microgrooves with Flat-ends by 6-Axis Control Ultraprecision Machining," *CIRP Annals - Manufacturing Technology, 59,* p. 61–66, 2010.

AN EXAMINATION OF SURFACE LOCATION ERROR AND SURFACE ROUGHNESS FOR PERIOD-2 INSTABILITY IN MILLING

Andrew Honeycutt and Tony L. Schmitz
Mechanical Engineering and Engineering Science
University of North Carolina at Charlotte, Charlotte, NC

INTRODUCTION

When stable machining conditions are selected, two additional considerations for high quality part manufacture are: 1) surface location error, or part geometric errors that occur due to forced vibrations; and 2) surface roughness. Surface location error, or SLE, is the difference between the machined surface location and the commanded location. SLE is measured and/or predicted to determine the influence of (stable) machining conditions on the error. Similarly, surface roughness is an important quality metric for machined parts since it influences fatigue, sealing performance, wear, and aesthetics, for example. However, prior studies of period-n bifurcations (instabilities) have evaluated neither SLE nor surface roughness. The purpose of this paper is to predict and measure both quantities for stable and period-2 bifurcation behaviors. Time domain milling simulation is used to predict SLE and surface roughness and these results are then compared to experimental results.

PERIOD-2 MILLING BIFURCATION

Period-2 milling bifurcations represent unstable dynamic behavior with a response time period that is double the forcing time period [1-7]. In order to determine if period-2 bifurcation behavior exists, the response of the physical system is measured and then synchronously sampled at the forcing frequency. For milling, the forcing frequency is the product of the cutting tool's rotating speed and the number of teeth (i.e., the tooth passing frequency). Poincaré maps may then be used as a visual aid to interrogate the process stability.

TIME DOMAIN SIMULATION

Time domain simulation enables the numerical solution of the coupled, time-delay equations of motion for milling in small time steps [8]. It is well-suited to incorporating the inherent complexities of milling dynamics, including the nonlinearity that occurs if the tooth leaves the cut due to large amplitude vibrations and complicated tool geometries (incorporating runout, or different radii, of the cutter teeth, non-proportional teeth spacing, and variable helix). The simulation is based on the Regenerative Force, Dynamic Deflection Model described by Smith and Tlusty [9]. As opposed to analytical stability maps that provide a global picture of the stability behavior, time domain simulation provides information regarding the local cutting force and vibration behavior, including SLE [10-24] and surface roughness, for the selected cutting conditions.

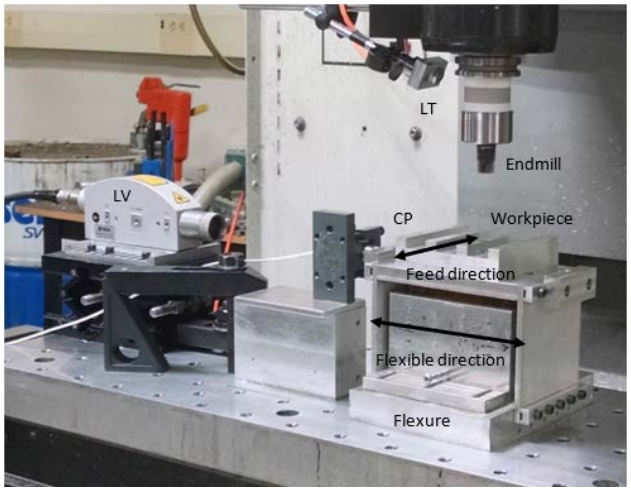

Figure 1. Flexure-based experimental setup with laser vibrometer (LV), laser tachometer (LT), and capacitance probe (CP). The feed direction and the flexible direction for the single degree of freedom flexure are also identified.

EXPERIMENTAL SETUP

The flexure-based setup displayed in Fig. 1 was used to define a physical system for simulation and testing [25-26]. The setup included a parallelogram leaf-type flexure with an aluminum workpiece mounted on top. The in-process vibration data was collected using a Polytec OFV-5000 laser vibrometer (velocity) and Lion Precision DMT20 capacitance probe (displacement). Both were aligned with the flexible direction for the single degree of freedom flexure. Note that the feed direction is perpendicular to this flexible direction. This orientation was selected to emphasize variations in surface location error and surface finish with machining conditions. Once per tooth sampling was accomplished using a laser tachometer and reflective target attached to the rotating tool holder. The flexure dynamics were

identified by modal testing: 125.8 Hz natural frequency, 0.0136 viscous damping ratio, and 1.75×10^6 N/m stiffness in the flexible (feed) direction. The dynamics for the 19.1 mm diameter, 0 deg helix angle tool (one insert) were symmetric: 1188 Hz natural frequency, 0.095 viscous damping ratio, and 4.24×10^7 N/m stiffness. The 6061-T6 aluminum alloy cutting force coefficients were: k_{tc} = 770×10^6 N/m^2, k_{nc} = 368×10^6 N/m^2, k_{te} = 22×10^3 N/m, and k_{ne} = 22×10^3 N/m. The up milling cutting conditions were: 5 mm axial depth, 2 mm radial depth, 0.35 mm/tooth, and variable spindle speed. Spindle speed values were selected to span from period-2 to stable cutting conditions while holding all other parameters constant. These spindle speeds and the corresponding behavior are listed in Table 1.

Table 1: Spindle speeds and bifurcation behavior for experiments.

Spindle speed (rpm)	Behavior	Spindle speed (rpm)	Behavior
3180	Period-2	3330	Stable
3190	Period-2	3360	Stable
3200	Period-2	3400	Stable
3210	Period-2	3500	Stable
3270	Stable	3600	Stable
3300	Stable		

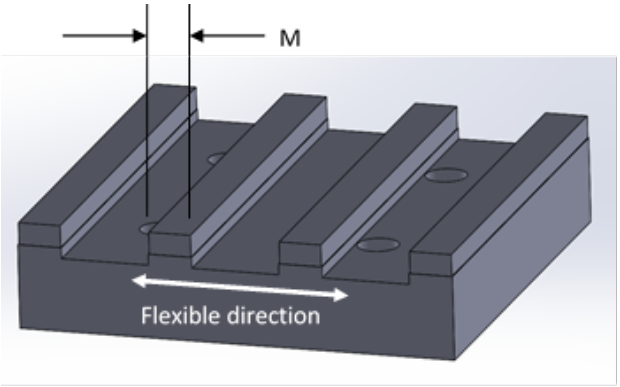

Figure 2. The workpiece included four ribs that were initially machined to the same dimensions. The {5 mm axial depth, 2 mm radial depth} cuts were then performed on one edge at a different spindle speed for each rib. The SLE was calculated as the difference between the commanded, C, and measured, M, rib widths. The flexible direction for the flexure is identified.

The workpiece geometry is presented in Fig. 2. The initial ribs were machined directly on the flexure so it could be ensured that the part was aligned with the machine axes. Low axial and radial depths were selected to minimize vibration levels and the same conditions were used to machine each rib. Prior to beginning the SLE/Ra experiments, a test workpiece was machined and the four ribs were measured on a coordinate measuring machine, or CMM, to evaluate the repeatability of the starting rib dimensions (Zeiss Prismo). The mean value was 9.82 mm with a standard deviation of 2.8 μm. Given the adequate repeatability of the initial ribs, the 11 spindle speeds in Table 1 were used to machine 11 ribs (three total workpieces). All machining conditions were identical other than spindle speed.

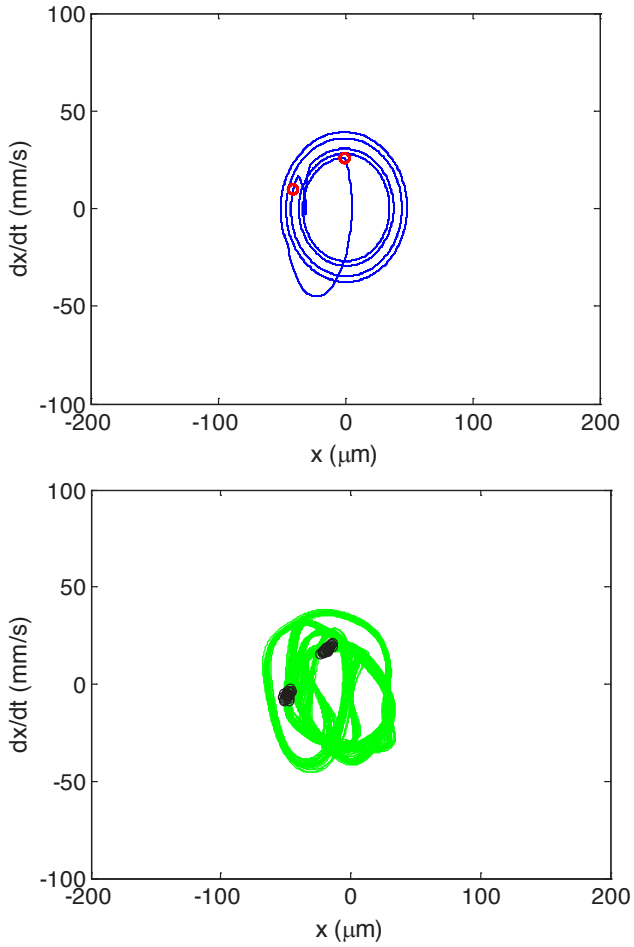

Figure 3. Predicted (Top) and measured (bottom) Poincaré maps for 3180 rpm. Period-2 behavior is seen. Note that x indicates the flexible direction for the flexure. The feed direction was y for these experiments.

The predicted and measured Poincaré maps for two of the 11 spindle speeds are presented in Figs. 3 and 4. Figure 3 displays the 3180 rpm results that exhibit

period-2 behavior. Figure 4 demonstrates stable behavior (3300 rpm).

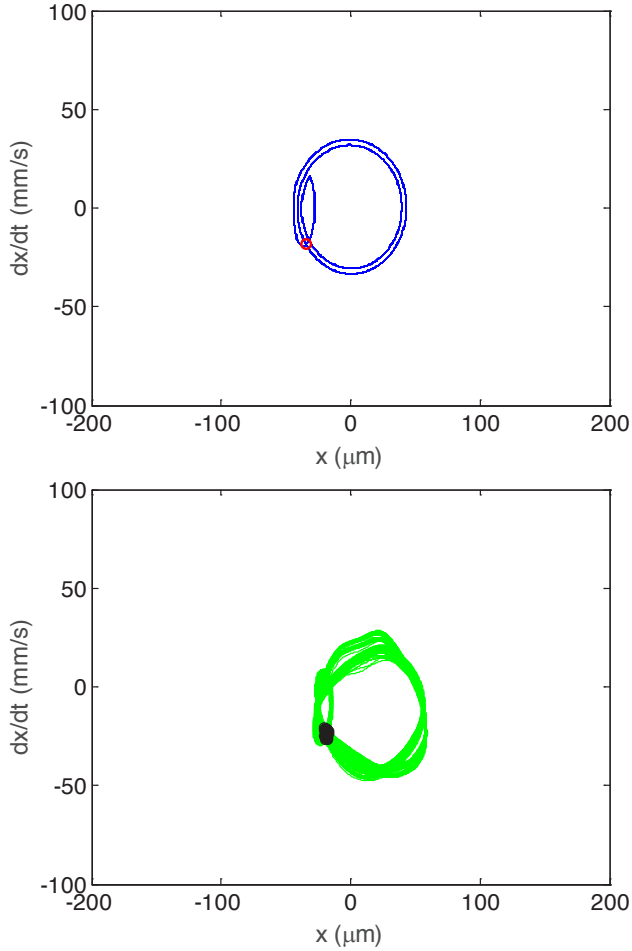

Figure 4. Predicted (left) and measured (right) Poincaré maps for 3300 rpm. Stable behavior is seen.

RESULTS

The SLE results are presented in Fig. 5. Four tests were completed under period-2 conditions (shown as the four experiment circles to the left of the dotted line) and seven were performed under stable conditions (shown as the seven experiment circles to the right of the dotted line). Good agreement is observed between the time-domain simulated prediction and the experimental behavior.

Figures 6 and 7 provide a direct comparison between the time domain simulation and the CMM surface points obtained by continuous scanning along the machined surface. In these figures the commanded surface is identified by the dashed line, the solid line is the CMM data, and the circles are the simulation results. The SLE is the difference between the commanded and actual surface and, again, good agreement is observed between simulation and measurement.

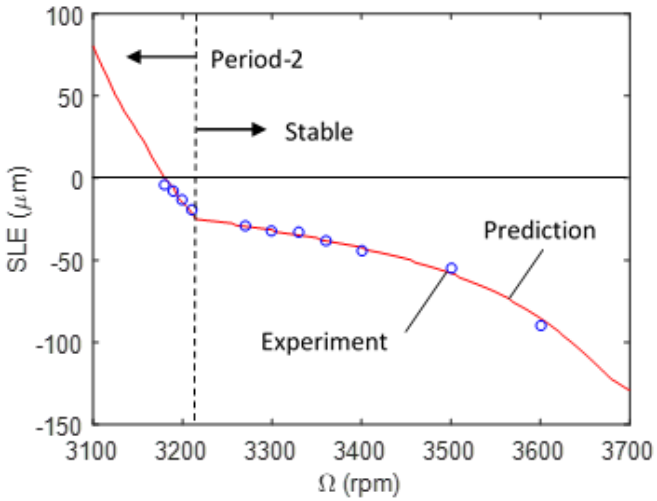

Figure 5. SLE prediction from time domain simulation (line) and experimental results from rib cutting tests (circles). The four period-2 bifurcation tests are identified.

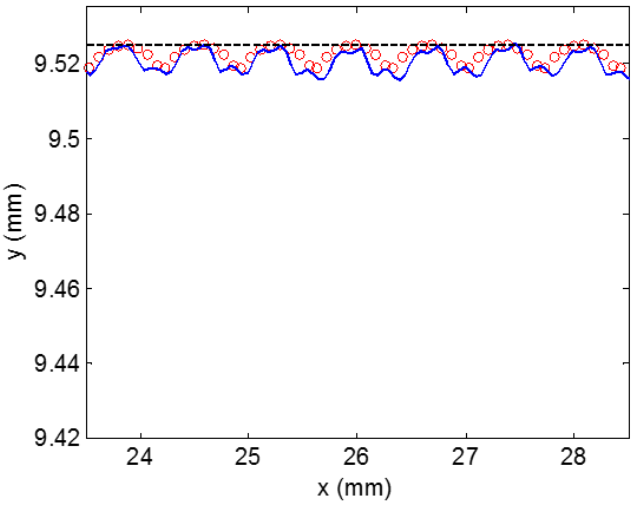

Figure 6. Commanded surface (dashed line), CMM scan (solid line), and simulation result (circles) for 3180 rpm (period-2). These results correspond to Fig. 3.

The surface roughness was also measured using a scanning white light interferometer (ZeGage, Zygo Corporation). These results are presented in Table 2, where the Ra values were calculated from a line scan at the midpoint of the axial depth of cut extracted from the surface topography. The Ra is clearly larger for

the period-2 conditions, where every other tool passage defines the surface roughness. The mean Ra for the period-2 conditions (four tests, 1.87 μm) is 5.2 times larger than the mean Ra for the stable conditions (seven tests, 0.36 μm).

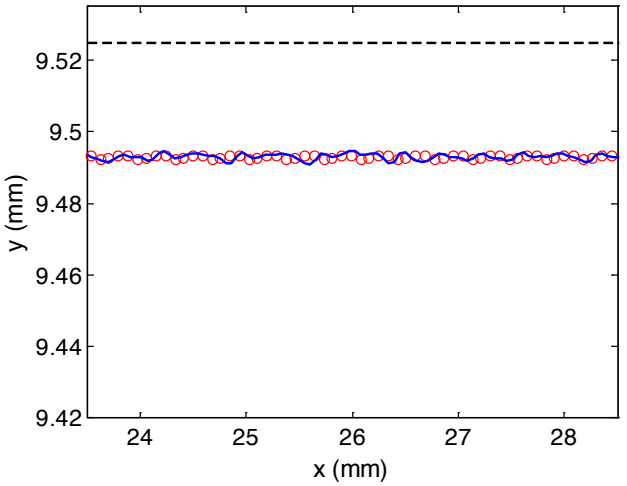

Figure 7: Commanded surface (dashed line), CMM scan (solid line), and simulation result (circles) for 3300 rpm (stable). These results correspond to Fig. 4.

Table 2. Surface roughness results for rib cutting tests.

Spindle speed (rpm)	Behavior	Ra (μm)
3180	Period-2	1.76
3190	Period-2	1.77
3200	Period-2	1.87
3210	Period-2	2.09
3270	Stable	0.28
3300	Stable	0.35
3330	Stable	0.44
3360	Stable	0.34
3400	Stable	0.39
3500	Stable	0.36
3600	Stable	0.35

The predicted and measured surface profiles are compared in Figs. 8 and 9. The change in cusp height and spacing between the period-2 (Fig. 8) and stable (Fig. 9) results is clearly seen.

The stability and SLE information is combined in Fig. 10. In this figure, the dark area represents secondary Hopf instability, the dotted area identifies the period-2 bifurcations, and the contour lines give the SLE as a function of spindle speed (horizontal axis) and axial depth of cut (vertical axis). Zero SLE is seen near the traditional best speed of 3774 rpm. However, a steep gradient for small changes in spindle speed is also seen near this speed (i.e., the zero SLE contour is vertical). A zero SLE contour is also observed within the period-2 zone. Interestingly, the SLE gradient is not as steep within the period-2 zone as it is near the best speed at 3774 rpm. This supports the possibility of producing acceptable parts under period-2 bifurcation machining conditions.

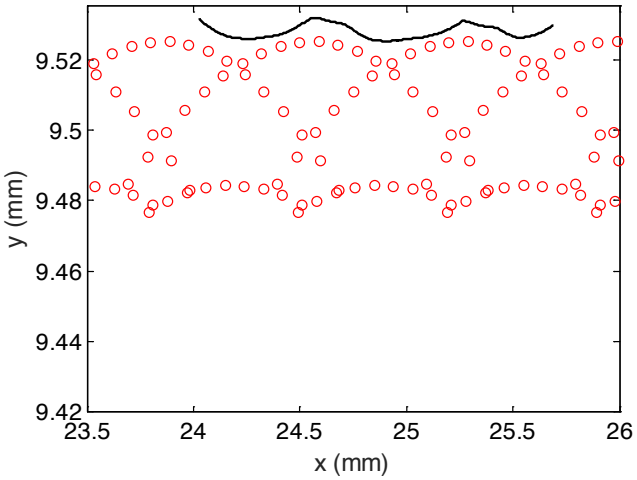

Figure 8. Scanning white light interferometer line scan (line) and simulation results (circles) for 3180 rpm (period-2).

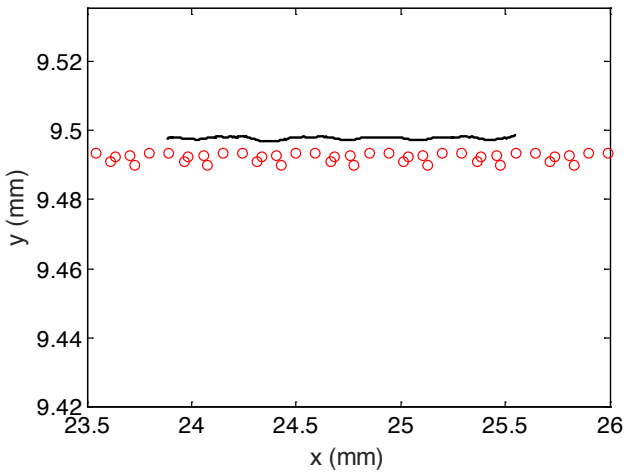

Figure 9. Scanning white light interferometer line scan (line) and simulation results (circles) for 3300 rpm (stable).

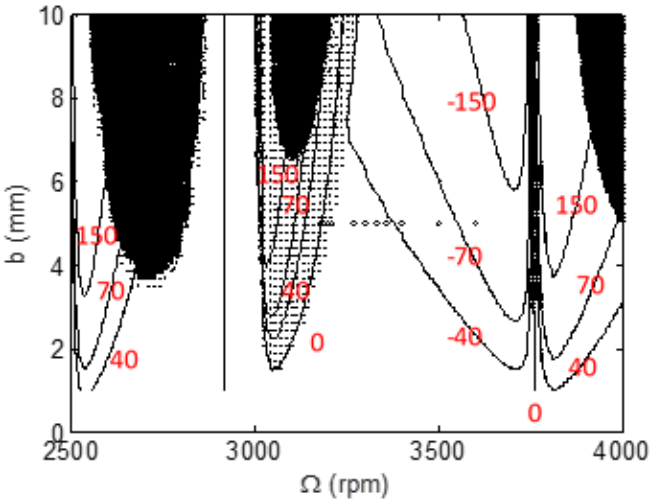

Figure 10. Combined stability and SLE map for rib cutting process dynamics. The secondary Hopf instability is represented by the dark zone, the period-2 behavior is identified by the dotted zone, and the SLE is given by the contours (i.e., lines of constant SLE).

CONCLUSIONS

Surface location error and surface roughness predictions were completed using time domain simulation for both stable and period-2 milling conditions. The predictions were compared to experiment using a flexure-based platform with displacement and velocity metrology. It was observed that the simulation accurately predicted the milling performance using: 1) Poincaré maps, which plot the displacement versus velocity and are used to identify period-2 behavior via periodic sampling; 2) surface location error measurements completed using a coordinate measuring machine; and 3) surface roughness measurements carried out using a scanning white light interferometer. It was shown that the surface location error for period-2 (unstable) behavior follows similar trends observed for (stable) forced vibration, so zero or low error conditions may be selected even for period-2 bifurcation behavior.

The surface roughness for the period-2 instability was seen to be larger than for stable conditions, although the final surface was still periodic. This increase in surface roughness occurs because the surface is defined by every other tooth passage and the apparent feed per tooth is increased.

ACKNOWLEDGEMENTS

This material is based on work supported by the National Science Foundation under Grant No. CMMI-1561221.

REFERENCES

[1] Davies, M.A., Pratt, J.R., Dutterer, B.S., and Burns, T.J., 2000, The stability of low radial immersion milling, Annals of the CIRP, 49(1): 37-40.

[2] Davies, M.A., Pratt, J.R., Dutterer, B., and Burns, T.J., 2002, Stability prediction for low radial immersion milling, Journal of Manufacturing Science and Engineering, 124: 217-225.

[3] Insperger, T. and Stépán, G., 2004, Vibration frequencies in high-speed milling processes or A positive answer to Davies, Pratt, Dutterer, and Burns, Journal of Manufacturing Science and Engineering, 126(3): 481-487.

[4] Mann, B.P., Bayly, P.V., Davies, M.A., and Halley, J.E., 2004, Limit cycles, bifurcations, and accuracy of the milling process, Journal of Sound and Vibration, 277: 31-48.

[5] Govekar, E., Gradišek, J., Kalveram, M., Insperger, T., Weinert, K., Stepan, G., and Grabec, I., 2005, On stability and dynamics of milling at small radial immersion, Annals of the CIRP, 54/1: 357-362.

[6] Honeycutt, A. and Schmitz, T., 2015, The extended milling bifurcation diagram, Procedia Manufacturing, 1: 466-476.

[7] Honeycutt, A. and Schmitz, T., 2016, A numerical and experimental investigation of period-n bifurcations in milling, Journal of Manufacturing Science and Engineering, 139(1): 011003.

[8] Schmitz, T. and Smith, K.S., 2009, Machining Dynamics: Frequency Response to Improved Productivity, Springer, New York, NY.

[9] Smith, K.S. and Tlusty, J., 1991, An overview of modeling and simulation of the milling process, Journal of Engineering for Industry, 113: 169-175.

[10] Kline, W., DeVor, R., and Shareef, I., 1982, The prediction of surface accuracy in end milling, Journal of Engineering for Industry 104: 272-278.

[11] Kline, W., DeVor, R., and Lindberg, J., 1982, The prediction of cutting forces in end milling with application to cornering cuts, International Journal of Machine Tool Design Research 22: 7-22.

[12] Tlusty, J., 1985, Effect of end milling deflections on accuracy, in: Handbook of High Speed Machining Technology (Ed. R.I. King), Chapman and Hall, New York, 140-153.

[13] Sutherland, J. and DeVor, R., 1986, An improved method for cutting force and surface error prediction in flexible end milling systems, Journal of Engineering for Industry, 108: 269-279.

[14] Montgomery, D. and Altintas, Y., 1991, Mechanism of cutting force and surface generation in dynamic milling, Journal of Engineering for Industry, 113(2): 160-168.

[15] Altintas, Y., Montgomery, D., and Budak, E., 1992, Dynamic peripheral milling of flexible structures, Journal of Engineering for Industry, 114(2): 137-145.
[16] Tarng, Y., Liao, C., and Li, H., 1994, A mechanistic model for prediction of the dynamics of cutting forces in helical end milling, International Journal of Modeling and Simulation, 14(2): 92-97.
[17] Schmitz, T. and Ziegert, J., 1999, Examination of surface location error due to phasing of cutter vibrations, Precision Engineering, 23(1): 51–62.
[18] Altintas, Y, 2000, Manufacturing Automation, Cambridge University Press, Cambridge, UK.
[19] Mann, B.P., Bayly, P.V., Davies, M.A., and Halley, J.E., 2004, Limit cycles, bifurcations, and accuracy of the milling process, Journal of Sound and Vibration, 277: 31-48.
[20] Schmitz, T., Couey, J., Marsh, E., Mauntler, N., and Hughes, D., 2007, Runout effects in milling: Surface finish, surface location error, and stability, International Journal of Machine Tools and Manufacture, 47(5): 841-851.
[21] Yun, W.-S., Ko, J., Cho, D.-W., and Ehmann, K., 2002, Development of a virtual machining system, Part 2: prediction and analysis of a machined surface error, International Journal of Machine Tools and Manufacture, 42: 1607-1615.
[22] Schmitz, T. and Mann, B., 2006, Closed-form solutions for surface location error in milling, International Journal of Machine Tools and Manufacture, 46(12-13): 1369-1377.
[23] Dombovari, Z. and Stépán, G., 2015, On the bistable zone of milling processes, Philosophical Transactions of the Royal Society A, 373: 20140409.
[24] Bachrathy, D., Munoa, J., and Stépán, G., 2016, Experimental validation of appropriate axial immersions for helical mills, The International Journal of Advanced Manufacturing Technology, 84: 1295-1302.
[25] Mann, B.P., Insperger, T., Bayly, P.V., and Stépán, G., 2003, Stability of up-milling and down-milling, Part 2: Experimental verification, International Journal of Machine Tools and Manufacture, 43(1): 35-40.
[26] Ransom, T., Honeycutt, A., and Schmitz, T., 2016, A new tunable dynamics platform for milling experiments, Precision Engineering, 44: 252-256.

FIXED-FREE BEAM DYNAMICS PREDICTION FOR THIN RIB MACHINING BY RCSA

Andrew Honeycutt, and Tony L. Schmitz
Department of Mechanical Engineering and Engineering Science
University of North Carolina at Charlotte, Charlotte, NC

INTRODUCTION

It is common practice to produce monolithic metallic components with thin ribs from solid billets by machining (subtractive manufacturing). This enables complex parts with high strength-to-weight ratio to be produced without significant assembly time and cost. Application domains range from aerospace structures to laptop cases. With the recent advances in metal additive manufacturing, it is also possible to produce near net shape parts that require only minimal machining to provide the desired surface finish and dimensional accuracy. This is particularly attractive for titanium alloys due to their high material cost and low machinability. The inherent challenge with this hybrid (i.e., combined additive and subtractive) approach is machining flexible parts. The low dynamic stiffness of the thin, near net shape ribs limits both machining stability (i.e., chatter can occur) and part accuracy (via the surface location errors that can arise from forced vibrations) [1].

In prior work, finite element analysis has been the primary tool to model and predict the thin rib dynamics and, in many cases, the change in the rib dynamics as material is removed [2-20]. In this paper, an analytical approaches is presented to describe the stiffness and natural frequency of fixed-free beams, as well as the change in stiffness and natural frequency as material is removed by milling. The specific challenge of near net shape machining, where an initially thin rib is machined to produce a thinner rib, is addressed. Fixed-free beams with stepped profiles are used to represent the thin ribs geometries and subsequent material removal.

ANALYTICAL MODEL

Receptance coupling substructure analysis (RCSA) is a frequency domain, analytical procedure used to couple component receptances in order to predict the assembly receptances [21-22]. In this work, the free-free receptances for the machined section of a beam were rigidly coupled to the remaining (unmachined) fixed-free section; see Fig. 1. Using rigid compatibility and equilibrium conditions, the assembly direct receptances, $H_{11} = \frac{Y_1}{F_1}$ and $H_{22} = \frac{Y_2}{F_2}$, at assembly coordinates Y_1 and Y_2 are written as a function of the component receptances at coordinates 1, $2a$, and $2b$; see [21] for the derivation. The required direct and cross receptances for the free-free (coordinates 1 and $2a$) and fixed-free (coordinate $2b$) components are:

- $h_{11} = \frac{y_1}{f_1}$, $h_{12a} = \frac{y_1}{f_{2a}}$, $h_{2a1} = \frac{y_{2a}}{f_1}$, $h_{2a2a} = \frac{y_{2a}}{f_{2a}}$, and $h_{2b2b} = \frac{y_{2b}}{f_{2b}}$, where y_i is the component displacement and f_j is the (internal) component force
- $l_{11} = \frac{y_1}{m_1}$, $l_{12a} = \frac{y_1}{m_{2a}}$, $l_{2a1} = \frac{y_{2a}}{m_1}$, $l_{2a2a} = \frac{y_{2a}}{m_{2a}}$, and $l_{2b2b} = \frac{y_{2b}}{m_{2b}}$, where m_j is the (internal) component moment
- $n_{11} = \frac{\theta_1}{f_1}$, $n_{12a} = \frac{\theta_1}{f_{2a}}$, $n_{2a1} = \frac{\theta_{2a}}{f_1}$, $n_{2a2a} = \frac{\theta_{2a}}{f_{2a}}$, and $n_{2b2b} = \frac{\theta_{2b}}{f_{2b}}$, where θ_i is the component rotation
- $p_{11} = \frac{\theta_1}{m_1}$, $p_{12a} = \frac{\theta_1}{m_{2a}}$, $p_{2a1} = \frac{\theta_{2a}}{m_1}$, $h_{2a2a} = \frac{\theta_{2a}}{m_{2a}}$, and $p_{2b2b} = \frac{\theta_{2b}}{m_{2b}}$.

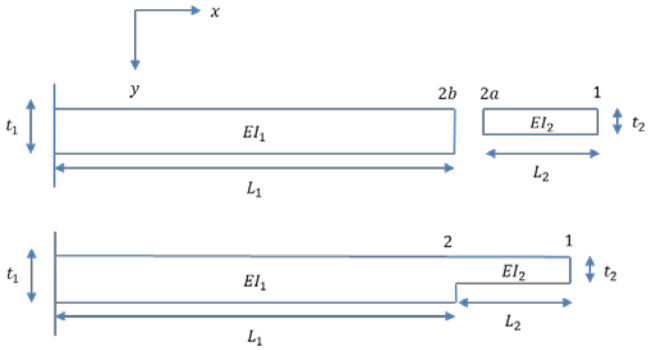

Figure 1. Beam model for RCSA. (Top) The two components and associated coordinates (1 and $2a$ for the free-free component and $2b$ for the fixed-free component) are identified. (Bottom) The assembly and associated coordinates (1 and 2) are shown.

The assembly receptances are provided in Eqs. 1 and 2 [21].

$$\begin{bmatrix} H_{11} & L_{11} \\ N_{11} & P_{11} \end{bmatrix} = \begin{bmatrix} h_{11} & l_{11} \\ n_{11} & p_{11} \end{bmatrix} - \begin{bmatrix} h_{12a} & l_{12a} \\ n_{12a} & p_{12a} \end{bmatrix} \left(\begin{bmatrix} h_{2a2a} & l_{2a2a} \\ n_{2a2a} & p_{2a2a} \end{bmatrix} + \begin{bmatrix} h_{2b2b} & l_{2b2b} \\ n_{2b2b} & p_{2b2b} \end{bmatrix} \right)^{-1} \begin{bmatrix} h_{2a1} & l_{2a1} \\ n_{2a1} & p_{2a1} \end{bmatrix} \quad (1)$$

$$\begin{bmatrix} H_{22} & L_{22} \\ N_{22} & P_{22} \end{bmatrix} = \begin{bmatrix} h_{2a2a} & l_{2a2a} \\ n_{2a2a} & p_{2a2a} \end{bmatrix} - \begin{bmatrix} h_{2a2a} & l_{2a2a} \\ n_{2a2a} & p_{2a2a} \end{bmatrix} \left(\begin{bmatrix} h_{2a2a} & l_{2a2a} \\ n_{2a2a} & p_{2a2a} \end{bmatrix} + \begin{bmatrix} h_{2b2b} & l_{2b2b} \\ n_{2b2b} & p_{2b2b} \end{bmatrix} \right)^{-1} \begin{bmatrix} h_{2a2a} & l_{2a2a} \\ n_{2a2a} & p_{2a2a} \end{bmatrix} \quad (2)$$

The component receptances can be obtained from measurements or models. Two modeling options are the Euler-Bernoulli and Timoshenko beams. In this work, the one-dimensional Timoshenko beam model was implemented to find the free-free receptances. This requires a numerical solution of the partial differential equation displayed in Eq. 3 [23-24], where $\hat{k}$ is a shape factor that depends on the beam's cross section [25]. To determine the required fixed-free receptances for the L_1 section component, the free-free receptances for this component (obtained from Eq. 19) were rigidly coupled to a rigid boundary (i.e., zero receptances). Equation 1 was also applied for this sub-step, where the $2b$ coordinate was assigned to the rigid boundary and the 1 and $2a$ coordinates to the L_1 section component.

$$\left(\frac{\partial^2 y}{\partial t^2} + \frac{EI}{\rho A} \frac{\partial^4 y}{\partial x^4} \right) + \left(\frac{\rho I}{\hat{k} AG} \frac{\partial^4 y}{\partial t^4} + \frac{EI}{\hat{k} AG} \frac{\partial^4 y}{\partial x^2 \partial t^2} \right) - \left(\frac{I}{A} \frac{\partial^4 y}{\partial x^2 \partial t^2} \right) = 0 \quad (3)$$

Table 1. Comparison of FE and RCSA natural frequency predictions.

L_1 (mm)	L_2 (mm)	FE f_n (Hz)	Analytical f_n (Hz)	% difference
150	0	217.96	217.87	0.04
146	4	221.79	221.70	0.04
142	8	225.51	225.42	0.04
132	18	234.28	234.19	0.04
122	28	242.03	241.96	0.03
100	50	253.20	253.37	-0.07
75	75	248.22	249.26	-0.42
50	100	219.84	221.82	-0.90
25	125	180.46	182.63	-1.20
10	140	157.53	159.54	-1.28
0	150	145.39	145.34	0.03

To provide a numerical validation of the analytical coupling approach, comparisons between the RCSA predictions and ANSYS finite element calculations were completed. Multiple beam geometries were tested where the beam thickness was reduced from 6 mm (t_1) to 4 mm (t_2) over a varying length, L_2. In each case, the natural frequency and modal stiffness were extracted by peak picking from the direct receptances. Natural frequency results are presented in Table 1 and Fig. 2, where the steel beam's elastic modulus was 200 GPa, its width was 20 mm, Poisson's ratio was 0.3, and the density was 7800 kg/m^3.

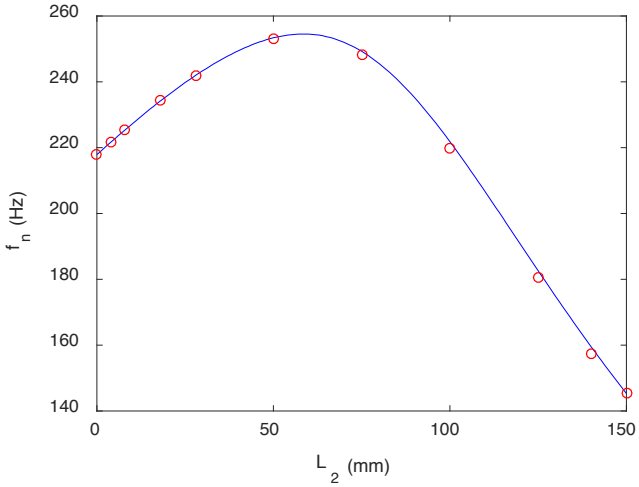

Figure 2. Graphical comparison of FE (circles) and RCSA (line) natural frequency predictions.

The k_1 stiffness results (from H_{11}) are presented in Table 2 and Fig. 3. The k_2 stiffness results (from H_{22}) are provided in Table 3 and Fig. 4.

Table 2. Comparison of FE and RCSA k_1 stiffness predictions.

L_1 (mm)	L_2 (mm)	FE k_1 (N/m)	Analytical k_1 (N/m)	% difference
150	0	6.59×10^4	6.58×10^4	0.24
146	4	6.61×10^4	6.59×10^4	0.24
142	8	6.62×10^4	6.60×10^4	0.24
132	18	6.63×10^4	6.62×10^4	0.22
122	28	6.61×10^4	6.60×10^4	0.13
100	50	6.24×10^4	6.26×10^4	-0.33
75	75	5.17×10^4	5.22×10^4	-1.12
50	100	3.84×10^4	3.91×10^4	-1.63
25	125	2.73×10^4	2.78×10^4	-1.84
10	140	2.21×10^4	2.25×10^4	-1.88
0	150	1.954×10^4	1.95×10^4	0.12

EXPERIMENTAL SETUP

Receptance measurements were completed using a modal hammer (PCB 086C04) to excite the beam and a laser vibrometer (Polytec OFV 5000 controller/OFV 534 laser head) to measure the velocity; see Fig. 5. The direct receptance measurements were performed at the aluminum beam's free end and at the change in thickness. The length of the reduced thickness section was changed by machining, where a 12.7 mm diameter three-flute solid carbide endmill

(approximately 100 mm stickout length) was used (0.1 mm/tooth, 3900 rpm). The beam thickness was removed in 10 mm axial steps with a final radial depth of 1 mm. The beam width was 44.96 mm. Measurements were performed after each machining pass.

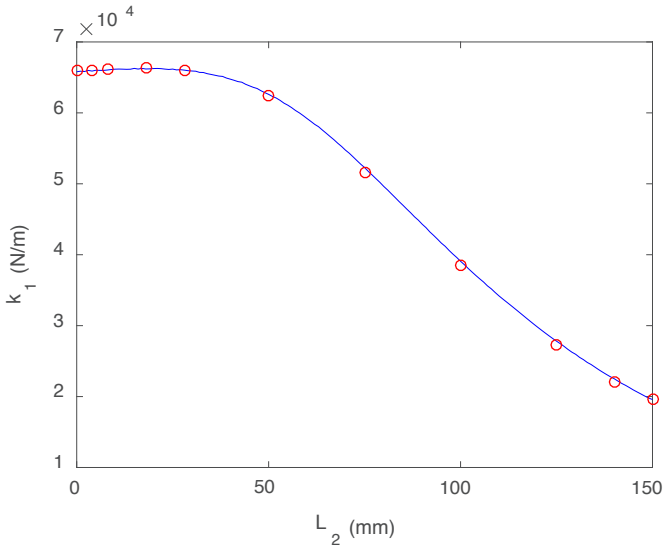

Figure 3. Graphical comparison of FE (circles) and RCSA (line) k_1 stiffness predictions.

Table 3. Comparison of FE and Raleigh method k_2 stiffness predictions.

L_1 (mm)	L_2 (mm)	FE k_2 (N/m)	Analytical k_2 (N/m)	% difference
150	0	-	-	-
146	4	7.12×10^4	7.10×10^4	0.24
142	8	7.70×10^4	7.68×10^4	0.25
132	18	9.49×10^4	9.46×10^4	0.26
122	28	1.19×10^5	1.19×10^5	0.28
100	50	2.23×10^5	2.22×10^5	0.50
75	75	6.45×10^5	6.37×10^5	1.27
50	100	3.60×10^6	3.52×10^6	2.21
25	125	7.19×10^7	6.99×10^7	2.78
10	140	3.25×10^9	3.15×10^9	3.12
0	150	-	-	-

RESULTS

A comparison between experiments and RCSA receptances was completed for the fundamental bending mode of the aluminum beam displayed in Fig. 5. For the RCSA beams models, the elastic modulus was 69 GPa, Poisson's ratio was 0.33, and the density was 2700 kg/m^3. The natural frequency results are displayed in Table 4 and Fig. 6. The k_1 stiffness results are presented in Table 5 and Fig. 7. The k_2 stiffness results are shown in Table 6 and Fig. 8. In all cases, the parameters were extracted by modal fitting.

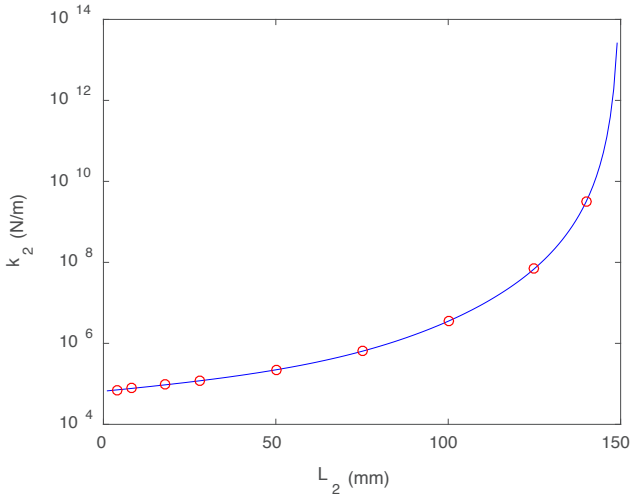

Figure 4. Graphical comparison of FE (circles) and RCSA (line) k_2 stiffness predictions (semilog scale).

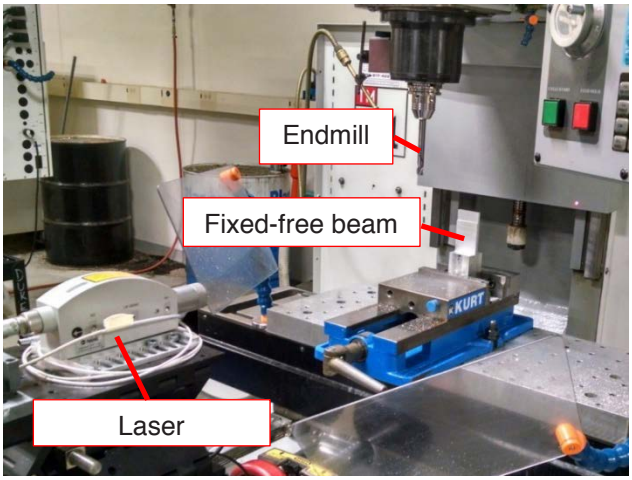

Figure 5. Experimental setup. The fixed-free aluminum beam was mounted in a vise which was clamped to the machine table. The laser vibrometer was used to measure the beam response due to a force impact (applied by a modal hammer).

Table 4. Comparison of experiments and RCSA predictions for natural frequency.

L_1 (mm)	L_2 (mm)	Experiment f_n (Hz)	RCSA f_n (Hz)	% difference
80	0	749	762.4	-1.78
70	10	776	790.39	-1.85
60	20	793	810.25	-2.18
50	30	804	820.04	-2.00
40	40	800	816.27	-2.03
30	50	781	795.15	-1.81

20	60	743	755.49	-1.68
10	70	691	700.45	-1.37
0	80	630	636.14	-0.97

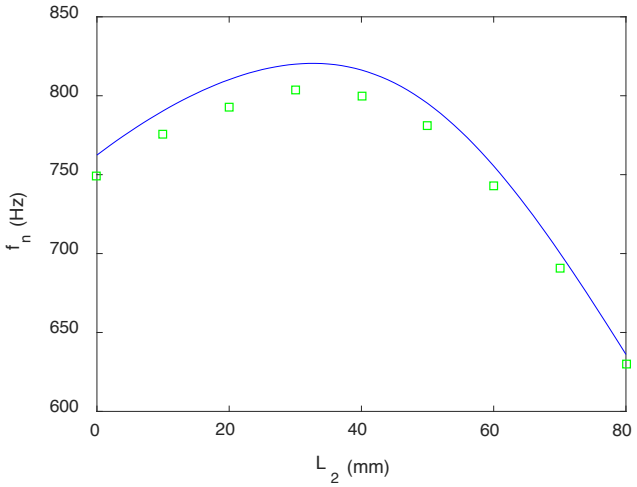

Figure 6. Graphical comparison of experiments (squares) and RCSA (line) natural frequency predictions.

Table 5. Comparison of experiments and RCSA predictions for stiffness k_1.

L_1 (mm)	L_2 (mm)	Exp. k_1 (N/m)	RCSA k_1 (N/m)	% difference
80	0	3.68×10^5	3.34×10^5	9.27
70	10	3.35×10^5	3.35×10^5	0.04
60	20	3.51×10^5	3.33×10^5	5.12
50	30	3.30×10^5	3.25×10^5	1.38
40	40	3.33×10^5	3.10×10^5	6.99
30	50	2.89×10^5	2.86×10^5	1.03
20	60	2.97×10^5	2.57×10^5	13.6
10	70	2.30×10^5	2.25×10^5	2.14
0	80	1.93×10^5	1.94×10^5	-0.40

Table 6. Comparison of experiments and RCSA predictions for stiffness k_2.

L_1 (mm)	L_2 (mm)	Exp. k_2 (N/m)	RCSA k_2 (N/m)	% difference
80	0	-	-	-
70	10	6.07×10^5	4.87×10^5	19.8
60	20	9.02×10^5	7.69×10^5	14.7
50	30	1.72×10^6	1.38×10^6	20.0
40	40	3.92×10^6	2.97×10^6	24.2
30	50	1.46×10^7	8.68×10^6	40.6
20	60	6.21×10^7	4.26×10^7	31.5
10	70	2.24×10^8	6.80×10^8	-203.5
0	80	-	-	-

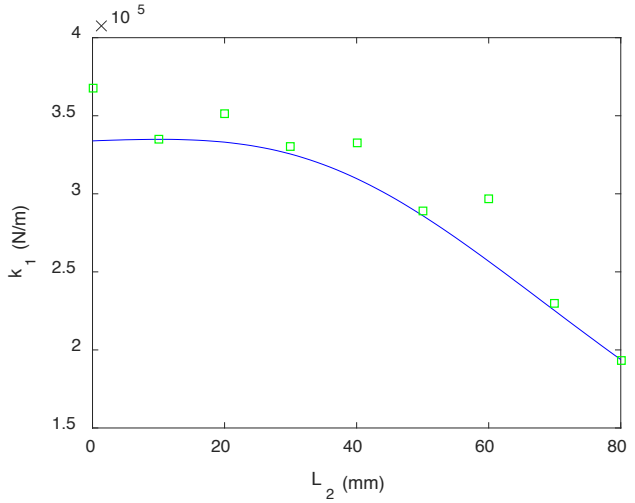

Figure 7. Graphical comparison of experiments (squares) and RCSA (line) k_1 stiffness predictions.

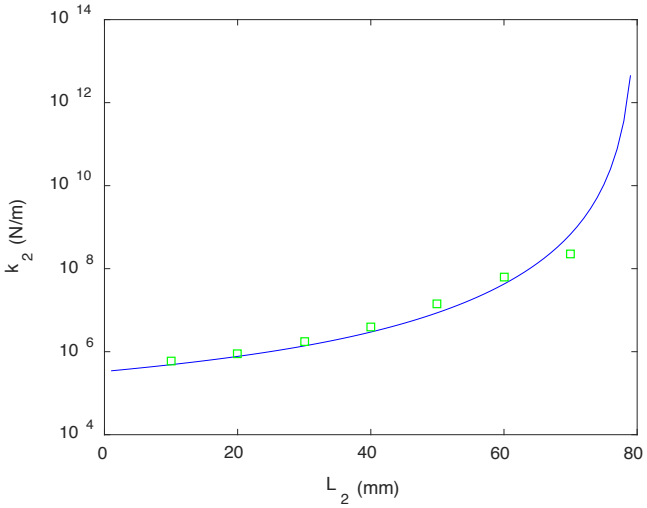

Figure 8. Graphical comparison of experiments (squares) and RCSA (line) k_2 stiffness predictions (semilog scale).

CONCLUSIONS

An analytical approach was presented for predicting thin rib, fixed-free beam dynamics with varying geometries. The method was based on receptance coupling substructure analysis (RCSA). Comparison with finite element calculations showed good agreement with the RCSA approach using the Timoshenko beam model to predict the component receptances.

Experiments were conducted to compare measured fixed-free beam receptances to RCSA predictions. An aluminum beam was machined between receptance measurements to change the thickness. The measured and predicted natural

frequencies agreed with an average percent difference of -1.74% for the nine beam profiles. The measured and predicted stiffness values for the fundamental bending mode at the beam's free end agreed with an average percent difference of 4.35% for the nine beam profiles. The measured and predicted stiffness values for the fundamental bending mode at the location of the beam's change in thickness agreed with an average percent difference of -7.53% for the seven beam profiles with a step change in thickness (i.e., the initial and final thin ribs are excluded from this analysis because they both have a uniform thickness).

In addition to the natural frequency and stiffness values, the dimensionless viscous damping ratios, ζ, were extracted from the measured direct receptances. These values are critical because first principle techniques for damping prediction are not available and the damping must, therefore, be included by the modeler based on experience or measurements. The results for the aluminum beam are displayed in Fig. 8 for all nine geometries; damping ratios were extracted from direct receptance measurements at both the free end and thickness change location. The average damping ratio is 0.28% with a standard deviation of 0.04%. The low damping for monolithic structures exacerbates the challenges associated with machining thin, near net shape ribs to produce the final thinner geometries.

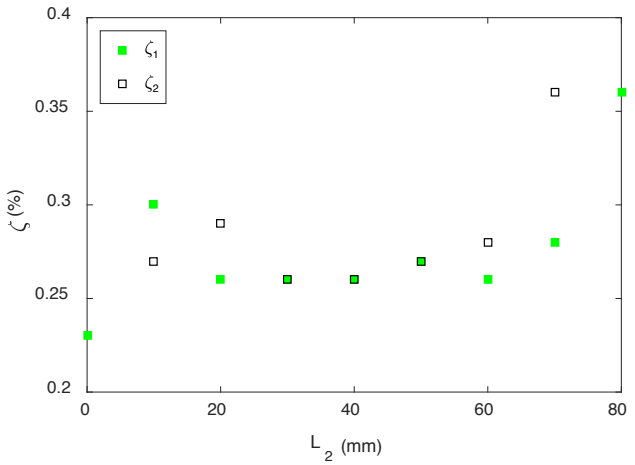

Figure 8. Experimental damping ratio values from direct receptances at the beam's free end, ζ_1, and at the location of the step change in thickness, ζ_2.

ACKNOWLEDGEMENTS

The authors thank Mr. Kadir Kiran for completing the ANSYS finite element computations and Dr. John Ziegert for helpful discussions. They also gratefully acknowledge partial financial support from Boeing and the National Science Foundation (Grant No. CMMI-1561221).

REFERENCES

[1] Schmitz, T. and Smith, K.S., 2009, Machining Dynamics: Frequency Response to Improved Productivity, Springer, New York, NY.

[2] Budak, E., Altintas, Y., 1995, Modeling and avoidance of static form errors in peripheral milling of plates, International Journal of Machine Tools & Manufacture, 35: 459-476.

[3] Tlusty, J., Smith, S., and Winfough, W., 1996, Techniques for the use of long slender end mills in high-speed milling, Annals of the CIRP, 45/1: 393-396.

[4] Smith, S. and Dvorak, D., 1998, Tool path strategies for high speed milling aluminum workpieces with thin webs, Mechatronics, 8: 291-300.

[5] Ning, H., Zhigang, W., Chengyu, J., and Bing, Z., 2003, Finite element method analysis and control stratagem for machining deformation of thin-walled components, Journal of Materials Processing Technology, 139: 332-336.

[6] Ratchev, S., Nikov, S., and Moualek, I., 2004, Material removal simulation of peripheral milling of thin wall low-rigidity structures using FEA, Advances in Engineering Software, 35: 481-491.

[7] Ratchev, S., Liu, S., Huang, W., and Becker, A.A., 2004, Milling error prediction and compensation in machining of low-rigidity parts, International Journal of Machine Tools & Manufacture, 44: 1629-1641.

[8] Bravo, U., Altuzarra, O., López de Lacalle, L.N., Sánchez, J.A., and Campa, F.J., 2005, Stability limits of milling considering the flexibility of the workpiece and the machine, International Journal of Machine Tools & Manufacture, 45: 1669-1680.

[9] Ratchev, S., Liu, S., and Becker, A.A., 2005, Error compensation strategy in milling flexible thin-wall parts, Journal of Materials Processing Technology, 162-163: 673-681.

[10] Thevenot, V., Arnaud, L., Dessein, G., and Cazenave-Larroche, G., 2006, Influence of material removal on the dynamic behavior of thin-walled structures in peripheral milling, Machining Science and Technology, 10/3: 275-287.

[11] Mañé, I., Gagnol, V., Bouzgarrou, B.C., and Ray, P., 2008, Stability-based spindle speed control during flexible workpiece high-speed milling, International Journal of Machine Tools & Manufacture, 48: 184-194.

[12] Rai, J.K. and Xirouchakis, P., 2008, Finite element method based machining simulation environment for analyzing part errors induced during milling of thin-walled components,

International Journal of Machine Tools & Manufacture, 48: 629-643.
[13] Seguy, S., Dessein, G., and Arnaud, L., 2008, Surface roughness variation of thin wall milling, related to modal interactions, International Journal of Machine Tools & Manufacture, 48: 261-274.
[14] Adetoro, O.B., Wen, P.H., Sim, W.M., and Vepa, R., 2009, Stability lobes prediction in thin wall machining, Proceedings of the World Congress on Engineering 2009 Vol I, WCE 2009, July 1-3, 2009, London, UK.
[15] Chen, W., Xue, J., Tang, D., Chen, H., and Qu, S., 2009, Deformation prediction and error compensation in multilayer milling processes for thin-walled parts, International Journal of Machine Tools & Manufacture, 49: 859-864.
[16] Gang, L., 2009, Journal of Materials Processing Technology, Study on deformation of titanium thin-walled part in milling process, 209: 2788-2793.
[17] Arnaud, L., Gonzalo, O., Seguy, S., Jauregi, H., and Peigné, G., 2011, Simulation of low rigidity part machining applied to thin-walled structures, International Journal of Advanced Manufacturing Technology, 54: 479-488.
[18] Izamshah, R., Mo, J.P.T , and Ding, S., 2011, Hybrid deflection prediction on machining thin-wall monolithic aerospace components, Proc. IMechE Part B: Journal of Engineering Manufacture, 226: 592-605.
[19] Smith, S., Wilhelm, R., Dutterer, B., Cherukuri, H., and Goel, G., 2012, Sacrificial structure preforms for thin part machining, CIRP Annals - Manufacturing Technology, 61: 379-382.
[20] Polishetty, A., Goldberg, M., Littlefair, G., Puttaraju, M., and Patil, P., 2014, A preliminary assessment of machinability of titanium allow Ti 6Al 4V during thin wall machining using trochoidal milling, Procedia Engineering, 97: 357-364.
[21] Schmitz, T. and Smith, K.S., 2012, Mechanical Vibrations: Modeling and Measurement, Springer, New York, NY.
[22] Bishop, R.E.D., and Johnson, D.C., 1960, The Mechanics of Vibration, Cambridge University Press, Cambridge, UK.
[23] Weaver, Jr., W., Timoshenko, P., and Young, D., 1990, Vibration Problems in Engineering, 5th Ed., John Wiley and Sons, New York, NY.
[24] Schmitz, T. and Duncan, G.S., 2005, Three-component receptance coupling substructure analysis for tool point dynamics prediction, Journal of Manufacturing Science and Engineering, 127/4: 781-790.
[25] Hutchinson, J., 2001, Shear coefficients for Timoshenko beam theory, Journal of Applied Mechanics, 68: 87-92.

THE CHALLENGES AND CONSEQUENCES OF MATERIAL UNCERTAINTIES IN METAL LASER POWDER BED FUSION

Bradley H. Jared, Brad Boyce, Jon D. Madison, Jakob Ostien, Jeff Rodelas, Brad Salzbrenner, Laura P. Swiler, Olivia D. Underwood, David J. Saiz
Sandia National Laboratories
Albuquerque, NM

Additive manufacturing (AM) offers unprecedented opportunities to design complex geometries and optimized topologies for performance gains inaccessible under conventional manufacturing constraints. AM also introduces the ability to generate engineered materials with microstructures and properties that are impossible via traditional synthesis techniques. However, to facilitate adoption in high consequence applications, fundamental questions regarding the intrinsic reliability and repeatable performance of additive metals must be answered. Distinct from traditional subtractive processes, component geometry and material are formed concurrently in additive processes and preclude an a priori knowledge of material performance from feedstock properties. Of particular interest are powder bed fusion processes where a laser scans across successive layers of metal powder to fuse material and generate a desired part geometry. Such layerwise processing enables access to volume elements, i.e. voxels, throughout every part with unprecedented opportunities for material control but also defect formation.

Predicting material performance is currently difficult for powder bed processes since it involves complex melting and solidification interactions, and is implemented on equipment with limited capabilities for process control and/or defect tracking. Consequently, material performance is commonly indeterminate and introduces unacceptable uncertainties. On-going research is working to reduce these uncertainties by exploring the process-structure-properties triad of stainless steel alloys. Material characterization and testing is identifying the nature of critical defects, quantifying their impact on material properties, and developing a basis for understanding defect formation mechanisms.

Work has focused on developing a fundamental understanding of laser powder bed fusion equipment, processes and stainless steel materials. As anticipated, bulk structural properties (strength, modulus, ductility, toughness) are dominated by material microstructure and are therefore influenced by feedstock powder, machine performance, process parameters and part geometry. Metallographic interrogation has identified defects associated with material phase transformations, feedstock porosity and/or contamination, and alloy segregation. Process induced porosity and inadequate material fusion, however, represent dominate defect forms which are influenced by laser parameters, feedstock quality, spatter from neighboring melt regions, and powder layer spreading interactions, Figure 1. Metal additive surfaces are also rougher, 5-25μm, than typical machined surfaces and thereby introduce additional failure modes associated with surface geometric stress concentrations, micro-cracks and un-melted powder.

The presented work has explored the performance of additively manufactured 17-4PH, a precipitation hardened stainless steel alloy. A monolithic part design was developed to facilitate high throughput testing, Figure 2, and produced by a vender external to Sandia. The tensile array incorporates six rows of 20 dogbone tensile specimens with a 1x1mm gage

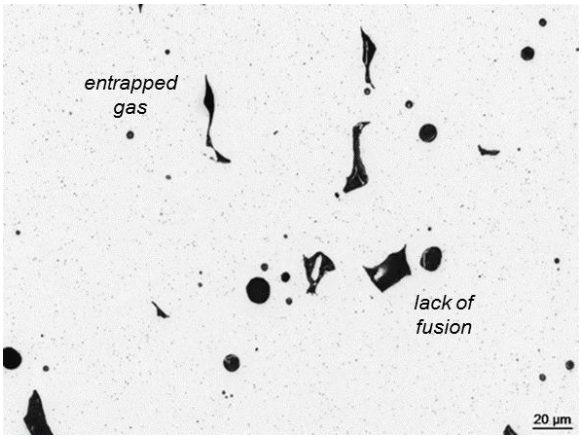

FIGURE 1. Representative material voids in 17-4PH stainless steel.

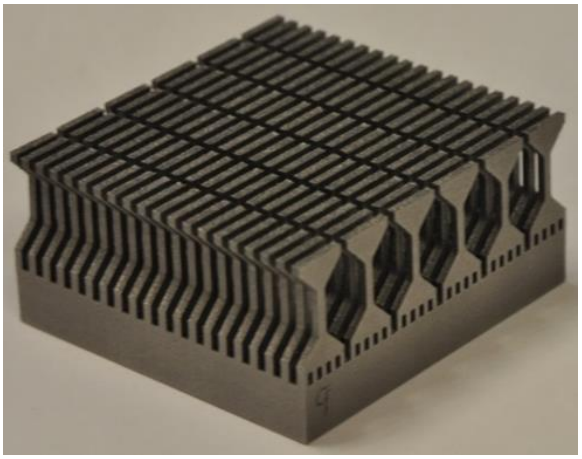

FIGURE 2. High throughput tensile sample with 120 1x1mm gage cross-section dogbones.

cross-section that are mounted onto a single base, roughly 40mm square. After printing, the entire part was solutionized and age heat treated using conventional industrial practices to achieve a H900 temper [1]. Dogbones were removed from the base by wire-EDM and then subjected to an extensive set of non-destructive evaluations. Dogbone density was measured via the Archimedes method, resonant response using resonant ultrasound spectroscopy, dogbone surface roughness using structured light scanning and internal material porosity content through X-ray computed tomography (CT).

One important challenge in characterizing additively manufacturing materials is the speed with which materials can be produced and modified via process changes. Another challenge for additive materials is the variability observed in their performance. To this end, a high throughput tensile test technique has been developed enabling the efficient quantification of material response distributions [1]. Figure 3 shows the grip ends of the tensile tester that have been designed for a conventional load frame. The grips are designed to provide

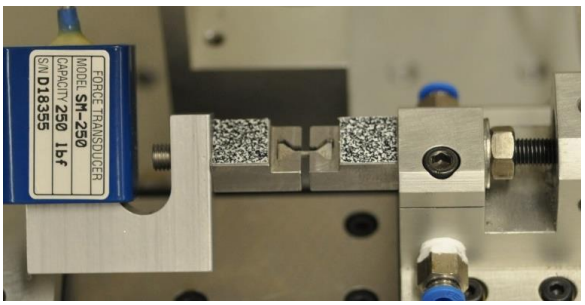

FIGURE 3. High throughput tensile tester.

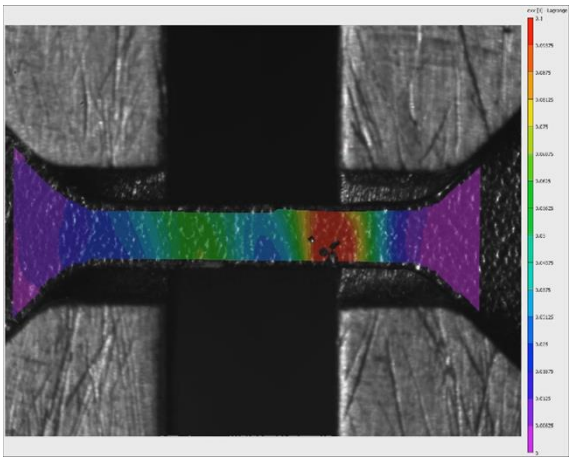

FIGURE 4. DIC strain field overlay onto an additive 17-4PH dogbone.

reference surface for dogbone placement, and are then precisely assembled and aligned into the load frame. As a result, dogbones can be dropped into place with minimal effort. Digital image correlation (DIC) is used to track material motion and strain, Figure 4. This eliminates the need for extensometer placement and alignment. The rough surface topology of additive metal parts provides an inherent speckle patter surface and is therefore advantageous for the technique.

"Drop-in" alignment coupled with DIC enables dogbone tensile test cycles on the order of 1-2 minutes. Such speed represents at an order of magnitude or more improvement in throughput compared to traditional techniques. Such a capability has enabled Sandia to better quantify the structural performance of additive materials and gain important insights into design margins and the mechanistic impacts of material defects onto performance.

Figure 5 provides the stress strain curves for 110 17-4PH dogbones removed from a single sample array similar to Figure 2. Significant scatter is observed in material behavior which has been linked to the presence of lack-of-fusion defects and excessive surface roughness. This scatter is similar to that observed in ceramics and metal castings, and as such the use of 3-parameter Weibull fits have proven valuable in determining design margins and thresholds [1]. Figure 6 provides representative Weibull plots for ultimate tensile strength and elongation to failure for the 17-4PH dogbones. It should be noted that the Weibull curves for wrought 17 4PH material that is commonly used in

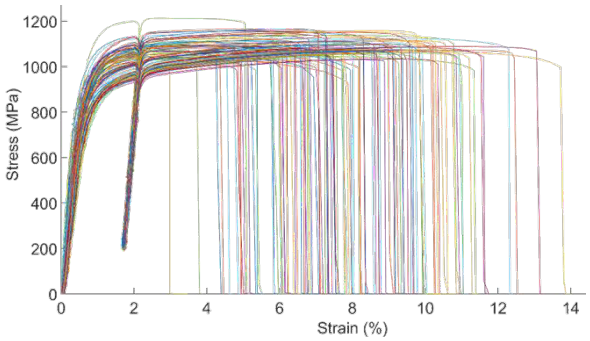

FIGURE 5. 110 stress-strain curves for 17-4PH dogbones.

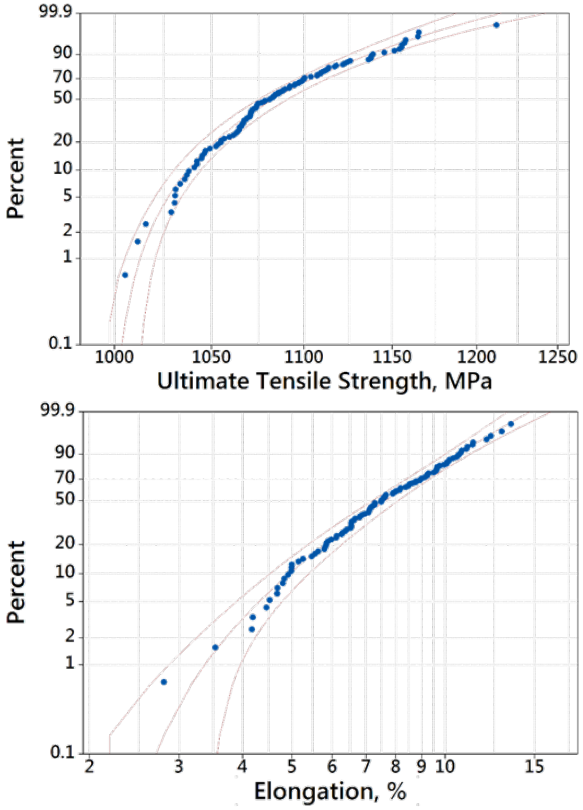

FIGURE 6. 110 17-4PH dogbone material performance for ultimate tensile strength (top) and elongation to failure (bottom) fit to 3-parameter Weibull distributions.

machined parts exhibits minimal scatter and has Weibull curves that are nearly vertical at the scales shown above.

The extensive inter-build performance variations observed prompted work to evaluate whether the non-destructive material evaluations of the dogbones could be utilized to predict material performance. Defect "signatures" are sought that are descriptive of and/or correlate to quantified material performance distributions. Figure 7 shows performance trends for material ultimate

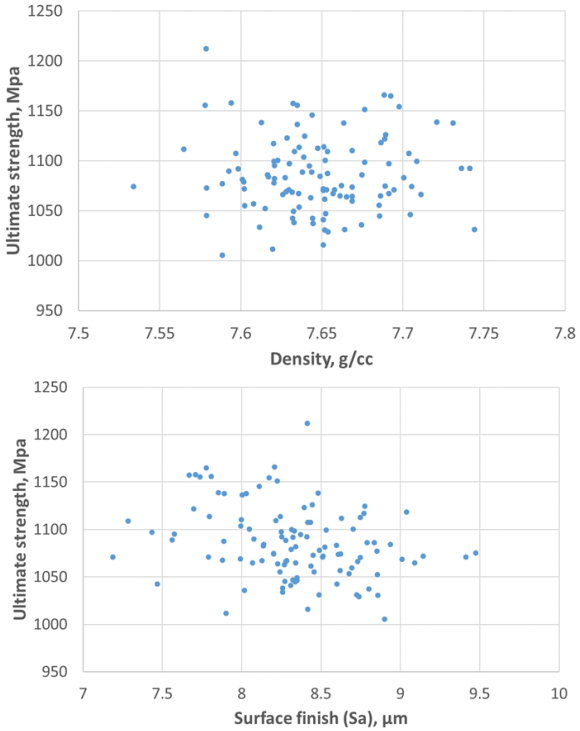

FIGURE 7. Trends of 17-4PH dogbone ultimate tensile strength with density (top) and surface finish (bottom).

tensile strength based on both Archimedes material density and optical surface finish measurements. Since these techniques are relatively quick and simple they would be ideal for rapid part qualification and acceptance. Unfortunately, no real trends or correlations emerged from these data sets. This prompted additional work to explore the correlations available by explicitly quantifying material structure (i.e. porosity) using X-ray computed tomography, Figure 8. The data set available

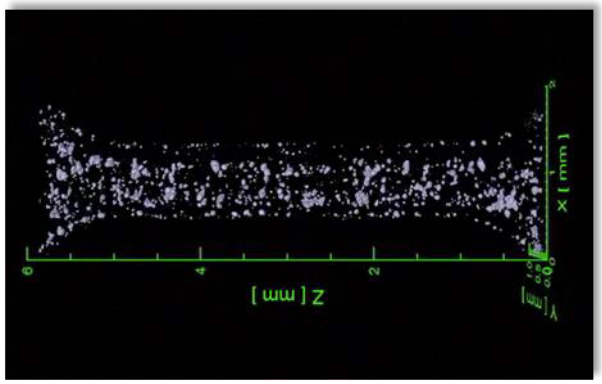

FIGURE 8. 17-4PH stainless steel tensile dogbone porosity map from computed tomography.

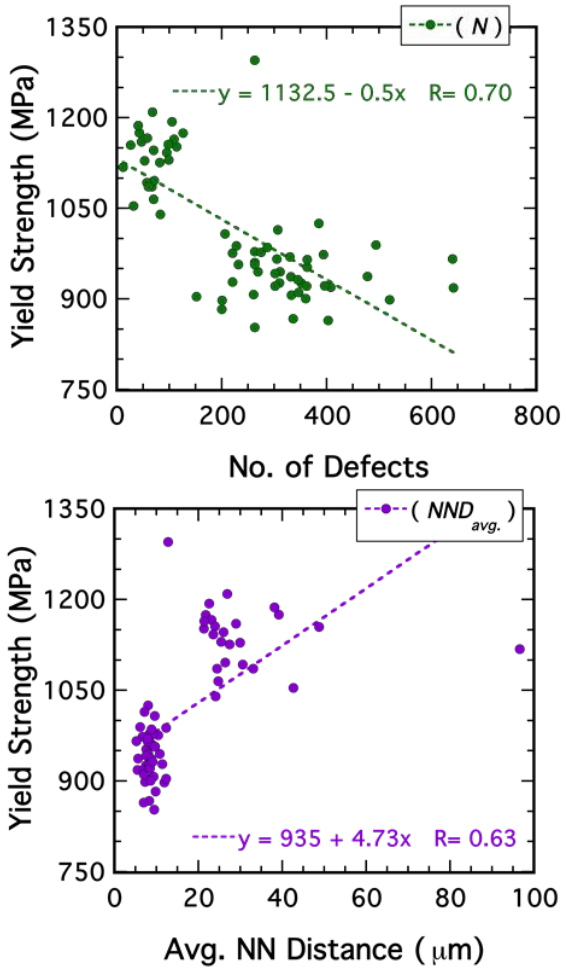

FIGURE 9. Trends of 17-4PH dogbone yield strength with number of porosity defects (top) and average distance between nearest neighbors (bottom).

through CT is extremely rich and provides potential correlation metrics ranging from total number of pores in the dogbone to the average distance between nearest neighbor pores. Figure 9 provides correlation plots for these two metrics for material yield strength. Correlations are weak, a trend observed across the data set for other porosity and material performance metrics. Grouping is observed in the data set which has been tied to measurement differences in the CT process. On-going work continues to explore correlations and methods to decouple material performance trends.

ACKNOWLEDGMENTS

Sandia National Laboratories is a multimission laboratory managed and operated by National Technology and Engineering Solutions of Sandia LLC, a wholly owned subsidiary of Honeywell International Inc. for the U.S. Department of Energy's National Nuclear Security Administration under contract DE-NA0003525. This document has been reviewed and approved for unclassified, unlimited release, SAND2017-9874A.

REFERENCES

[1] Salzbrenner B, Rodelas J, Madison J, Jared B, Swiler L, Shen Y, Boyce B. High-throughput stochastic tensile performance of additively manufactured stainless steel. Journal of Materials Processing Technology, vol. 241, pp. 1-12, 2017.

Analysis of hydrophobicity of micro-channel and micro-pillar patterns of polymer for orthodontic retainer fabricated by mechanical machining process

Tae-Jin Je[1,2], Ji-Young Jeong[1,2], Je-Ryung Lee[1], Eun-chae Jeon[1,2], Doo-Sun Choi[1]
[1]Dept. of Nano Manufacturing Technology
Korea Institute of Machinery and Materials
Daejeon 34103, Korea
[2]Dept. of Nano-Mechatronics
University of Science and Technology
Daejeon 34113, Korea

INSTRUCTIONS

Clear retainers for orthodontics are widely used by consumers due to their superior aesthetics and convenience. This device was fabricated by compressive forming using a specific polymer such as PETG(Polyethylene Terephthalate Glycol) at a high temperature. In this process, the demolding property of the material affects the quality of the device. Previous studies showed that materials with low surface energy provide a excellent demolding property. In general, materials that have low surface energy show the high hydrophobicity [1]. The hydrophobicity of a material can be evaluated by the contact angle of a droplet on the surface of the material. When the material had high hydrophobicity, the surface of the material had advantages such as high cleansing power. Therefore, if the surface energy of the clear retainer for the orthodontic was lower, the retainer had superior quality and a better demolding property. Methods that change the chemical composition and form micro/nano-structures on the surface have been applied to increase the hydrophobicity. Chemical processes have a limited capacity to increase the hydrophobicity. However, the formation of micro/nano-structures can be exploited to control the hydrophobicity according to their shape, size, and density.

In this study, micro-channel and micro-pillar patterns of PETG material for an orthodontic device were fabricated by a planing process using cutting tools. The patterns were fabricated with varying widths and distance between the patterns for analysis of the changing hydrophobicity in terms of the size and density of the patterns. The hydrophobicity of the machined patterns was analyzed by measuring the contact angle of a droplet. The measured data were then compared with Wenzel's and Cassie's theory.

CONTACT ANGLE THEORY

Two droplet shapes can form on the surface of a solid having micro structures. The first type is described by Wenzel's theory where the bottom of the structure is wetted by the droplet. The second type is given by Cassie's theory where the droplet is supported by the top surface of the structure. Fig. 1 shows the shapes of the droplet and the formula of the contact angle for each theory[2-3].

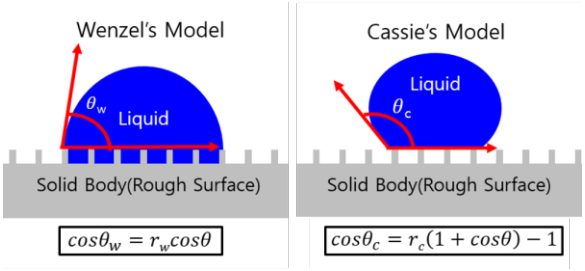

FIGURE 1. Droplet shape according to Wenzel's theory(left) and Cassie's theory(right)

θ is the contact angle of the droplet on the flat surface of the material. r_w and r_c are roughness factors. The roughness factor is the ratio of the actual contact area to its projection area on the flat surface. To calculate the roughness factor, the concept of the unit cell was applied. Fig. 2 shows the shapes of the unit cell of the micro patterns, and formulas for the roughness factor according to Wenzel's and Cassie's theories. Fig. 2 (a) shows the micro-channel pattern, and Fig. 2 (b) shows the micro-pillar pattern.

MACHINING OF THE MICRO-CHANNEL OF PETG MATERIAL AND ANAYSIS OF HYDROPHOBICITY

Machining of micro-channels with varying widths using planing method on PETG

We fabricated micro-channels to analyze the changing hydrophobicity according to the size and density of the pattern [4-5]. The widths of the channel were 20~100 μm. The machining method was a planing process a using diamond

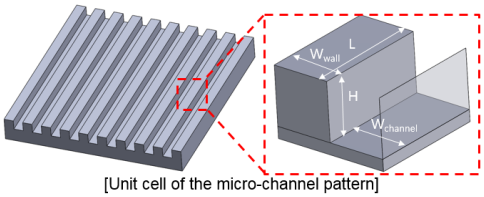

[Unit cell of the micro-channel pattern]

- Roughness Factor = $\frac{\text{Real contact area}}{\text{Projected are}}$

Wenzel's theory ➔ Rougnhess factor(r_w) = $1+\frac{2H}{(W_{wall}+W_{channel})}$

Cassie's theory ➔ Rougnhess factor (r_c) = $\frac{W_{wall}}{(W_{wall}+W_{channel})}$

(a) Unit cell and formula of the roughness factor of the micro- channel pattern

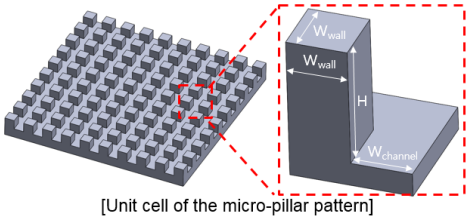

[Unit cell of the micro-pillar pattern]

- Roughness Factor = $\frac{\text{Real contact area}}{\text{Projected are}}$

Wenzel's theory ➔ Rougnhess factor(r_w) = $\frac{W_{wall}^2+W_{wall}\times 4H}{(W_{wall}+W_{channel})^2}$

Cassie's theory ➔ Rougnhess factor (r_c) = $\frac{W_{wall}^2}{(W_{wall}+W_{channel})^2}$

(b) Unit cell and formula of the roughness factor of the micro-pillar pattern

FIGURE 2. Unit cells and formulas of the roughness factor of the micro-patterns (a) channel pattern (b) pillar pattern

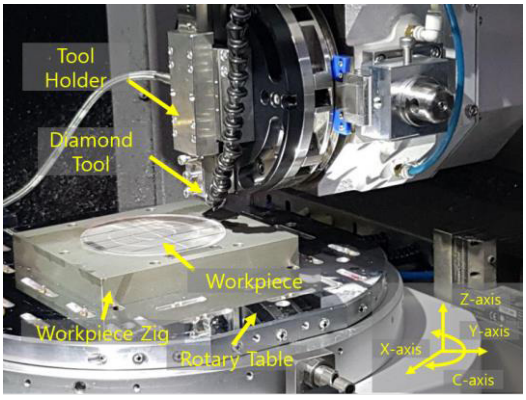

FIGURE 3. Mechanical machining system used in the planing process

TABLE 1. Conditions for machining the micro-channels on the PETG material

Variables	Conditions
Cutting tool	Widths 20 ~ 100 μm rectangular diamond tool
Cutting depth	5 um/pass
Cutting pitch	Tool width + channel wall width
Cutting speed	200 mm/sec
Mist oil	ISOPAR-H

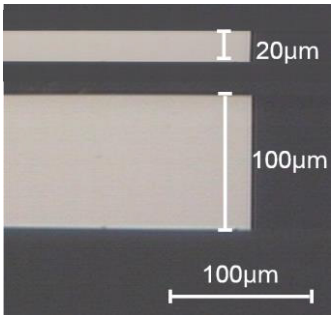

FIGURE 4. Rectangular diamond tools with widths of 20 μm and 100 μm

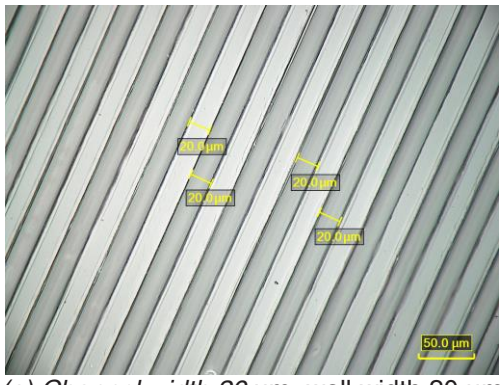

(a) Channel width 20 μm, wall width 20 μm

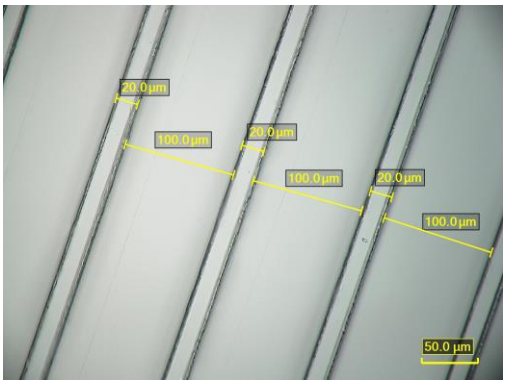

(b) Channel width 100 μm, wall width 20 μm

FIGURE 5. Optical microscope images of the machined micro-channel patterns (a) Channel and wall width were 20 μm and 20 μm (b) 100 μm and 20 μm

cutting tools. Fig. 3 shows the machining system used in this study. This machining system had X, Y, Z and C axes which have position control accuracy of 10 nm and 0.0001 °. The conditions for machining the micro-channel patterns are shown in Table 1. Rectangular diamond cutting tools having widths of 20 μm ~100 μm were used. Fig. 4 shows the images of the diamond cutting tool having widths of 20 μm and 100 μm. The machined patterns were measured by a 3D optical microscope and Fig. 5(a) shows the pattern having a channel width of 20 μm and a wall width of 20 μm. Fig. 5(b) shows the pattern with channel width of 100 μm and wall width of 20 μm. Because of the ductile property of PETG material, the top surface of the machined pattern had fine burrs. The shape of the unit cell of the pattern was changed by these burrs, and the hydrophobicity was expected to be affected.

Measurement of the contact angle of a droplet on the micro-channel patterns and analysis of changed hydrophobicity

A Phoenix300 was used to measure the contact angle of a droplet. The droplet was DI-water with a density of 0.998g/cm^3. The drop speed was 5mm/min. The contact angle on the flat surface was measured to calculate the contact angle using Wenzel's and Cassie's theories. Fig. 6 shows images of the droplet on the flat surface of the PETG where the contact angle was 78 °, and we confirmed the flat surface of the PETG have a hydrophilicity property. Fig. 7 shows images of the droplets on the micro-channel patterns in the parallel direction with the channel. The measured contact angles were greater than 130 °. The surface of the PETG material was changed from hydrophilic to hydrophobic by the machined channel pattern. On the other hand, the shape of the droplet in the vertical direction was different from that in the parallel direction. Fig. 8 shows the images of the droplet on the channel pattern in the vertical direction. The shape of the droplet was long along the channel. This is ascribed to the property of the fluid flowing along the channel. Fig. 9 provides a graph comparing the contact angles measured by experiments and calculated by Wenzel's and Cassie's theories. According to the increase of the channel width 20 μm to 100 μm, the contact angle of the droplet increased from about 128 ° to 142 °. This tendency of increasing contact angle was similar to the calculated contact angle by Cassie's theory. The contact angle measured at the channel width of 20 μm showed a large difference from the calculated contact angle. Because the number of the channel wall that contacted the droplet was increased when the c-

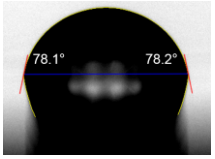

FIGURE 6. Contact angle of the droplet on the machined flat surface of PETG

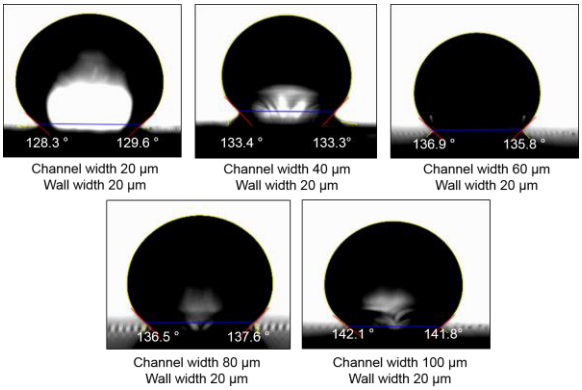

FIGURE 7. Images of the droplet on the micro-channel pattern in parallel direction (channel wall width 20 um, channel widths 20~100 μm)

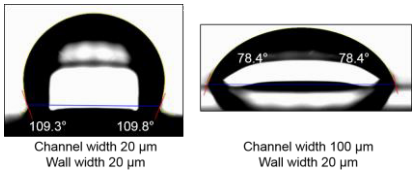

FIGURE 8. Images of the droplet on the micro-channel pattern in vertical direction (channel wall width 20 μm, channel widths 20 and 100 μm)

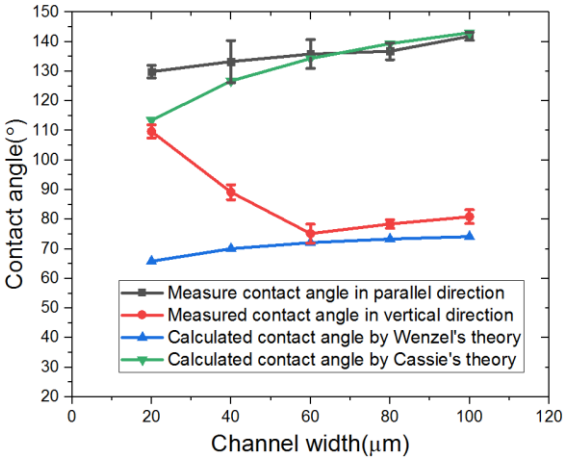
Contact angle(°)
Channel width(μm)
Measure contact angle in parallel direction
Measured contact angle in vertical direction
Calculated contact angle by Wenzel's theory
Calculated contact angle by Cassie's theory

FIGURE 9. Calculated and measured contact angles of the droplet on the channel patterns with varying channel widths 20~100 μm and channel wall width of 20 μm

-hannel width was narrow, the amount of fine burr contacting the droplet increased. These burrs decreased the contact angle by increasing the contact area with the droplet. Also, as the area of the channel increased (a smaller roughness factor), the hydrophobicity was accordingly greater.

MACHINING OF MICRO-PILLAR PATTERNS AND ANAYSIS OF HYDROPHOBICITY ACCORDING TO VARYING SHAPE DIMENSIONS

Machining of micro-pillar patterns with varying distance between patterns

In the above experiment, the hydrophobicity of the micro-channel patterns was increased as the roughness factor was decreased. Based on this, we tried to analyze the effect of the roughness factor on the hydrophobicity in the case of micro-pillar patterns. The shape of the micro-pillar pattern was a square with a width of 20 μm and a height of 20 μm. The distance between the pillars increased from 20 μm to 100 μm. The machining conditions were the same as the conditions for machining the micro-channel. Futhermore, cross machining of 90 ° was conducted at each cutting depth. Figs. 10 (a) and (b) show machined pillar patterns that had distances of 20 μm and 100 μm between the pillars. The top surface of the pillars had more burrs than the channel pattern by the interrupted cutting.

Measurement of the contact angle of the droplet on the micro-pillar patterns and analysis of changed hydrophobicity

Fig.11 presents images of droplets on the micro-pillar patterns. The left image shows a droplet on the pillar pattern where the distance between the pillars was 20 μm and the contact angle was about 124 °. The right image shows the droplet on the pillar patterns where distance between the pillars was 100 μm and the contact angle was 89 °. The property of the surface was changed from hydrophobic to hydrophilic with increasing the distance between the pillars. Fig. 12 presents a graph comparing the contact angles measured by experiments and calculated by Wenzel's and Cassie's theories. Where the distance was 20 μm, the measured contact angle was similar to the angle calculated by Cassie's theory. Where the distance was greater than 40 μm, the measured contact angles were similar to the angles calculated by Wenzel's theory. Finally, where the distance was 80 μm, the contact angle was smaller than 90 ° which mean the surface property changed from hydrophobic to hydrophilicity. This tendency was ascribed to the pattern not perfectly supporting the droplet. The contact width of the droplet and the pillar pattern in the case of distance of 20 μm was 2mm. In this case, the number of pillars was about 2500. In the same area, however, the number of pillars was 266 when the distance was 100 μm. Therefore, it was confirmed that maintaining a small roughness factor and increasing the number of the patterns that contacts the droplet were advantageous in terms of achieving greater hydrophobicity.

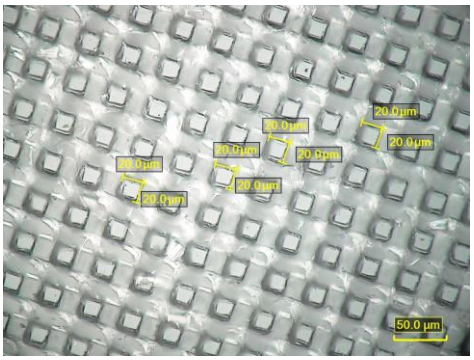

(a) Pillar width 20 μm, distance 20 μm

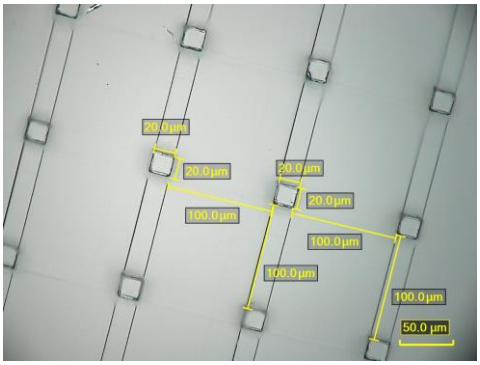

(b) Pillar width 20 μm, distance 100 μm

FIGURE 10. Optical microscope images of the machined square micro-pillar patterns (a) pillar patterns had width of 20 μm and distance of 20 um (b) pillar patterns had width of 20 μm and distance of 100 μm

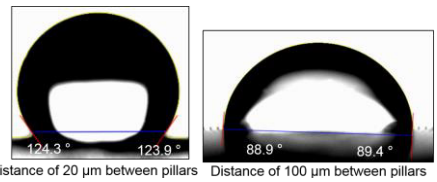

Distance of 20 μm between pillars Distance of 100 μm between pillars

FIGURE 11. Images of the droplet on the machined pillar patterns with distance of 20 μm(left image) and 100 μm(right image)

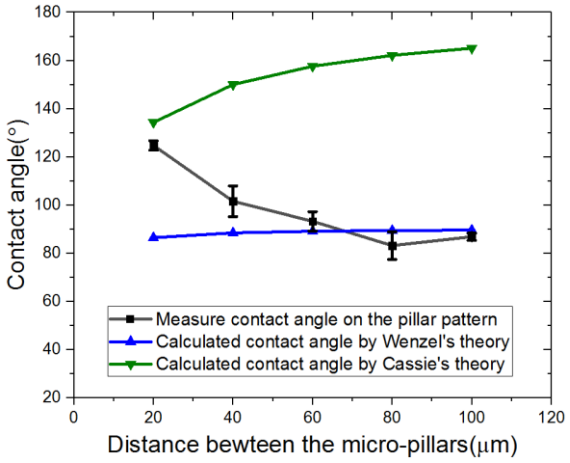
Contact angle(°)
Distance bewteen the micro-pillars(μm)
Measure contact angle on the pillar pattern
Calculated contact angle by Wenzel's theory
Calculated contact angle by Cassie's theory

FIGURE 12. Calculated and measured contact angles of the droplet on the micro-pillar patterns with varying distance of 20~100 um

CONCLUSION

In this study, micro-channel and micro–pillar patterns of PETG material with varying width and distance were fabricated by mechanical machining via a planing process. The hydrophobicity of the machined patterns was then analyzed by measuring contact angle of droplets. In the case of the micro-channel, the measured contact angle of a droplet in the parallel direction with the channel was similar to that given by Cassie's theory. However, the shape of the droplet in the vertical direction with the channel was long along the channel and the contact angle was smaller than that in the parallel direction. This is attributed to the property of the fluid flowing along the channel. In case of the micro-pillars, the measured contact angle was similar to that described by Wenzel's theory when the distance between pillars was greater than 40 μm. This phenomenon was caused by the number of pillars that contacted the droplet. Therefore, for high hydrophobicity, the roughness factor should be kept small and the number of pillars should be increased.

REFERENCES

[1] Kim B K, Jeong E J, Kwon K H, Yoo Y E, Choi D S and Kim J s. Controlling Mold Releasing Propensity-The Role of Surface Energy and a Multiple Chain Transfer Agent. Applied Materials and Interfaces. 2012; 4: 3465-3470

[2] Barthlott W, Neinhuis C. Purity of the Sacred Lotus, or Escape from Contamination in Biological Surfaces. Springer Transactions. Planta. 1997; 202: 1-8.

[3] Wenzel R N. Resistance of Solid Surfaces to Wetting by Water. Industrial and Engineering Chemistry Research. 1936; 988-994

[4] Cassie A B D, Baxter S. Wettability of porous surfaces. Trans Faraday Soc. 1944; 40: 546-551.

[5] Patankar N. On the Modeling of Hydrophobic Contact Angles on Rough Surfaces. Langmuir. 2003; 19: 1249-1253.

[6] Zhenyu S, Zhanqiang L, Hao S, Xianzhi Z. Prediction of Contact Angle for Hydrophobic Surface Fabricated with Micro-Machining Based on Minimum Gibbs Free Energy. Applied Surface Science. 2016; 364: 597-603

MULTI-PROBE ERROR SEPARATION

Eric E. Keller[1], Eric R. Marsh[1], Byron Knapp[2], Henry Arneson[1] and David Arneson[2]
[1]The Pennsylvania State University
University Park, PA, USA
[2]Professional Instruments
Hopkins MN, USA

INTRODUCTION

High precision hydrostatic bearing spindle or air bearing spindles are commonly characterized using an artifact with form error that dwarfs the error motion of the spindle[1]. Removing the form error from measurements is required for useful interpretation of test results. This paper demonstrates a technique called multi-probe error separation for removing this form error.

BACKGROUND

Spindles with very small error motion are used in many machines of importance in precision engineering, for example, diamond turning machines and precision grinding machines. For many of these processes, the final success of the machining operation is determined by the error motion of the spindle. Thus, characterization of the spindle error motion is of prime importance while designing a machining process. However, this means that a measurement system must be devised to measure these very small deviations from perfect motion. Typically, a precision spherical artifact will be attached to the spindle. However, these artifacts typically have form error significantly larger than the error motion of the spindle being measured. Thus an error separation technique must be used. It is common to use a reversal technique where the artifact is rotated 180 degrees between measurements. Multi-probe error separation uses 3 measurements that can be done either simultaneously or by rotating the spindle with respect to a single sensor and 3 readings are taken serially. Typically this rotaion is done by mounting the spindle on a precision rotary table with fine angular accuracy. A Moore rotary table with 2 vernier scales for degrees, minutes and seconds has been used successfully.

APPROACH

In order to separate spindle error motion from the eccentricity of the spindle, the multiprobe method is utilized. A schematic of the multiprobe technique is shown in 1.

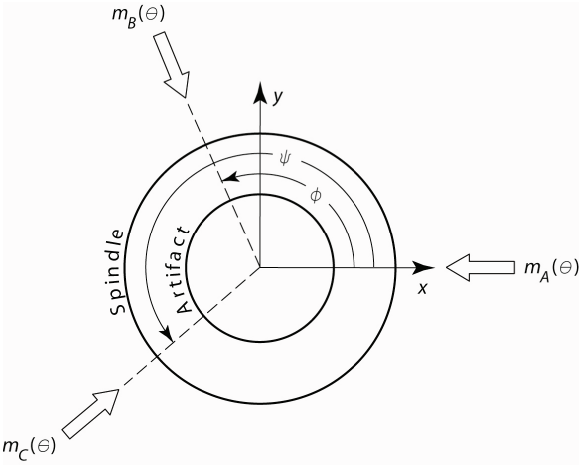

FIGURE 1. Multiprobe error separation measurements

This requires simultaneously sampling three sensors measuring the spindle circumference. The angle between the sensors is optimized to resolve the spindle shape to as high a frequency as desired within the angular resolution of the sensors [1]. The sensor mounting nest is shown in Figure 2 .

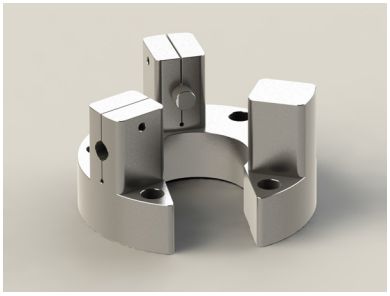

FIGURE 2. Capacitance probe holding fixture

A software program was written in the Matlab programming language to perform the required data acquisition and processing to perform multiprobe separation. To demonstrate the proper functioning of this software, it is expedient to perform a marker test. This test consists of marking a line

on the spindle with a permanent marker. The ink from the permanent marker affects the reading from the sensors in such a way that it appears to be a large outward excursion in the spindle circumference. If properly separated, the multiprobe separation will be limited to the spindle shape, and not the spindle error motion. Polar plots of the raw data from such a test are shown in Figure 3.

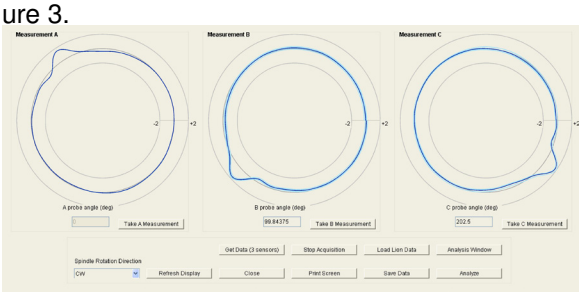

FIGURE 3. Raw data from 3 sensors for multiprobe error separation scheme

The results of the separation are shown in Figure 4. Inspection of this figure shows that the marker is only found on the artifact (workpiece) plot.

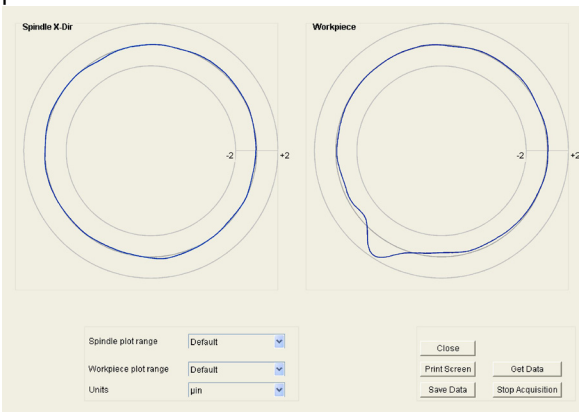

FIGURE 4. Results from multiprobe separation scheme showing error motion and spindle shape

The advantage to the multiprobe technique is that the error motion separation can be performed online. While the technique requires data in increments of a complete evolution of the spindle, there are a large number of manufacturing processes where this is an acceptable rate of analysis.

EXPERIMENT

A ball bearing spindle was instrumented for multiprobe analysis. Three capacitance probes were arranged at suitable angles around the spindle. The angular position of the spindle was measured using a 512 count optical encoder. The signal from the capacitance probes were acquired using a general-purpose data acquisition board hosted in a desktop PC. The capacitance probe signals were sampled at each negative-going transition of the optical encoder.

REFERENCES

[1] Marsh ER. Precision Spindle Metrology. 2nd ed. DEStech Publications; 2009.

Measurement of dynamic characteristics of hydrostatic spindle against radially applied external forces

Rei Kirigaya[1], Akio Hayashi[2], Dmytro Fedorynenko[3] and Yohichi Nakao[1]
[1]Department of Mechanical Engineering
Kanagawa University
Yokohama, Kanagawa, JAPAN
[2]Department of Mechanical Engineering
Kanazawa Institute of Technology
Kanazawa, Ishikawa, JAPAN
[3]Department of Mechanical Engineering and Woodworking
Chernihiv National University of Technology
Chernihiv, Ukraine

INTRODUCTION

Improvement of the machining accuracy of the precision parts such as the lens mold is highly demanded. In addition, the improvement of the surface quality of these precision parts is also needed. As well known, the machining accuracy and the surface quality are strongly depending on the performances of the machine tool spindle. Consequently, hydrostatic bearings are used for the spindle that is used for the ultra-precision machining with a single crystal diamond cutting tool. In general, aero pressure bearings are used for the spindle. However, the bearing stiffness of the aero pressure bearings is quite limited due to the compressibility of air, that is a typical disadvantage of the aero pressure bearings. Consequently, moderate depth of cut has to be used as the cutting condition. In order to overcome the limitation, a spindle supported by water hydrostatic bearings has been developed[(1)] in our previous study. As well known, water is an incompressible fluid, high bearing stiffness of the spindle can be designed if the water hydrostatic bearings are adopted with appropriate design procedure. In addition, it should be now mentioned that the machining accuracy and the generated surface quality are strongly depending on not only static characteristics but also dynamic characteristics of the spindle.

For example, during cutting process, various cutting forces are added to the spindle shaft. Even the constant depth of cut is used for the turning process, the spindle is subjected by the time-variant loads due to the influence of the spindle characteristics such as runout of the spindle. Accordingly, it is needed to investigate dynamic stiffness of the hydrostatic bearings of the machine tool spindle. In addition, it should be noted that the machining accuracy is not determined by not only dynamic stiffness of the hydrostatic bearings but also total dynamic characteristics of the spindle. Now, as well known, dynamic characteristics are determined by the dynamic stiffness, damping, vibration modes and frequency characteristics of oscillatory system. Measurements of the dynamic characteristics of spindle have been carried out by the measurement of the rotor displacement that due to impulse loads applied to the spindle rotor in various studies. These studies investigate that hydrostatic bearings have high damping coefficient against dynamic disturbances. Dynamic characteristic of a spindle against dynamic loads was also studied[(2)]. However, the dynamic characteristics of the water hydrostatic spindle have not been studied.

Accordingly, in this paper, the static characteristics and the dynamic characteristics of the developed water hydrostatic spindle are investigated. At first, the static stiffness of the thrust bearings and the radial bearings of the water hydrostatic spindle are investigated experimentally and the results are presented. Secondly, the dynamic characteristics of the spindle against time-variant radial forces with various frequencies are reported. As mentioned, the whole dynamic characteristics of the spindle are considered and investigated via experiments.

BASIC STRUCTURE AND SPECIFICATION OF WATER HYDROSTATIC SPINDLE

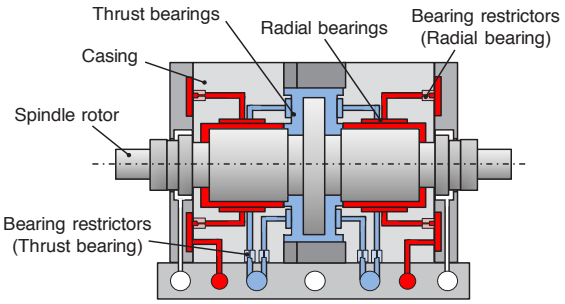

FIGURE 1. Schematic of water hydrostatic spindle

A basic structure of the water hydrostatic spindle considered in the present study is denoted in Figure 1. The water hydrostatic bearings of the spindle has two four-recessed radial bearings and two sided four-recessed thrust bearings. Specification of the spindle is summarized in Table 1. Bearing stiffness of the thrust and radial bearings significantly affect the machining accuracy of the precision machining. For example, the cutting force during precision cutting processes by a single crystal single point cutting tool is in general considered to be about 1 N at a maximum. However, resultant displacement due to the cutting force is very small as well. Thus, the bearing stiffness of the water hydrostatic spindle has been designed so that the resultant rotor displacement in the axial direction is about 1 nm, namely the static stiffness of the thrust bearing of 1000 N/μm.

TABLE 1. Spindle specification

Type of bearing	Thrust	Journal
Bearing stiffness [N/μm]	1000	500
Spindle speed [min^{-1}]	3000	
Bearing gap [μm]	10	12
Supply pressure [MPa]	2.1	2.5

The outer surface of the rotor and all bearing surfaces are coated by DLC in order to avoid undesirable corrosion and damage during spindle operation.

STATIC CHARACTERISTICS OF WATER HYDROSTATIC BEARINGS

Measurement of stiffness of thrust bearings

During face turning operation, the stiffness of the thrust bearings of the spindle has enormous influence on the machining accuracy. Thus, the stiffness of the thrust bearing of the water hydrostatic spindle was measured. In the experiments, measurements of the resultant rotor displacement and deformation of the spindle housing due to the axial external forces were carried out. The experimental rig is shown in Figure 2. In the experiments, the external axial forces were applied to the spindle rotor by the air cylinder and changed from 0 N to 1500 N. The axial forces are measured by the load cell which was placed between an end of the rotor and the air-cylinder. Additionally, measurement of the resultant displacement of the rotor and the deformation of the spindle including housing base were measured using capacitance sensors. The actual bearing displacement was obtained by compensating the influence of the deformation. Finally, the stiffness of the thrust bearing was obtained. The experimental results and compensated results are presented in Figure 3.

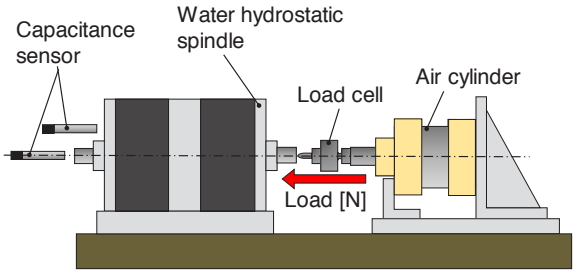

FIGURE 2. Measurement of thrust bearing stiffness

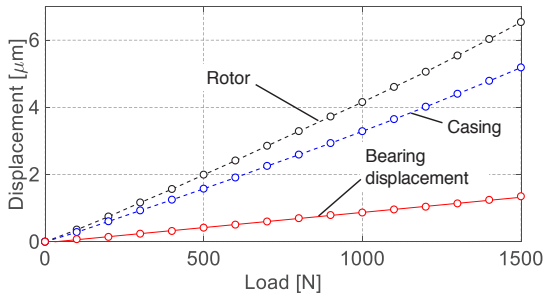

FIGURE 3. Experimental result of thrust bearing

From the experimental results, the stiffness of the thrust bearings is measured about 1100 N/μm. The result meets the design specification as presented in Table 1.

Measurement of stiffness of radial bearings

In the experiments, the resultant displacements and deformations of the rotor were also measured when static forces were applied to an end of rotor in the radial direction. The radial forces were applied by the piezo actuator and changed from 0 N to 1N. The applied external forces were measured by the load cell that was set between the rotor and the piezo actuator. The resultant displacement and deformation of the rotor were measured by the capacitance sensor which was placed at the opposite side of the rotor.

In the measurements, however, the measured displacement includes the influence of the deformation of the rotor due to the bending effects of the rotor that has to be removed from the original measured data. In order to compensate the influence of the bending, the deformation of the rotor due to the bending was calculated. Then the radial displacement of the bearing due to the radial deformation of the rotor was removed from the measured data. The results are shown in Figure 4.

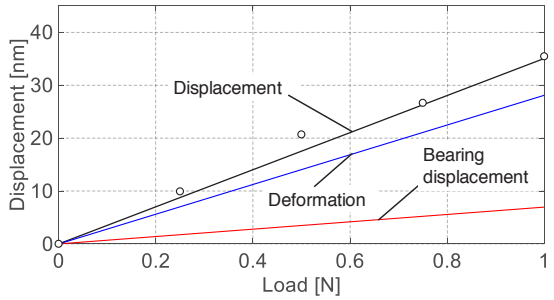

FIGURE 4. Experimental result of radial bearing

From Figure 4, it is verified that the total of the deformation and displacement of the rotor is 35 nm for the applied external force of 1N. Estimated resultant deformation is 28 nm. Accordingly, the actual bearing displacement can be estimated to be 7 nm if the external force is 1N.

DYNAMIC CHARACTERISTICS OF HYDROSTATIC SPINDLE

In the diamond turning process as shown in Figure 5, the cutting forces are applied to the spindle rotor via workpiece in the radial direction. Considering the influence of the runout of the spindle, it should be considered that the spindle is subjected to the time-variant forces.

Rated speed of the spindle that is considered in this paper is 3000 min^{-1}. Accordingly, the fundamental frequency of the time-variant force is 50 Hz if the spindle rotates at the rated speed. In this study, the frequent response of the spindle was thus measured. In the experiments, sinusoidal external forces were applied to the spindle in the radial direction at an end of the rotor.

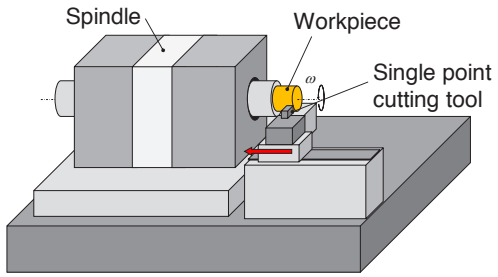

FIGURE 5. Turninng process

Experimental method and equipment

Figure 6 shows experimental rig for the measurement of the dynamic characteristics of the water hydrostatic spindle. In the experiments, sinusoidal forces with various frequencies were applied to an end of the rotor in the radial direction. The sinusoidal forces were generated by the driving force of the piezo actuator that was placed so that the actuator can push the rotor in the radial direction. Then the applied force was measured by the load cell that was placed between the rotor and the piezo actuator. In the experiments, the frequencies were changed from 0 Hz to 360 Hz. Furthermore, the amplitude of the sinusoidal forces was controlled to be 1 N. The resultant displacement of the rotor was measured using a laser displacement sensor which was located at the opposite side of the rotor.

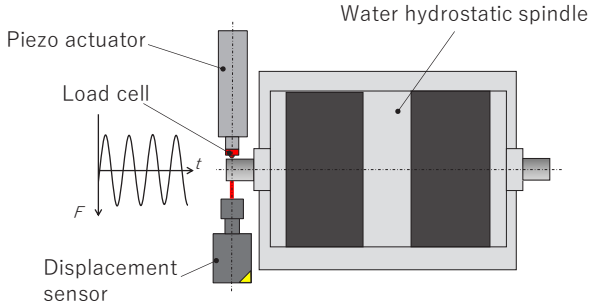

FIGURE 6. Experimental rig of measurement of dynamic characteristics of spindle

Experimental result

Typical measurement results are shown in Figure 7 (a) and (b). Comparing the results, it is observed that the amplitude of the displacement decreases as the frequency of the external force increases.

It is also verified that the phase between the external force and the displacement is significantly small if the frequency of the applied force is 80 Hz. In contrast, the phase lag is clearly observed if the frequency is 280 Hz.

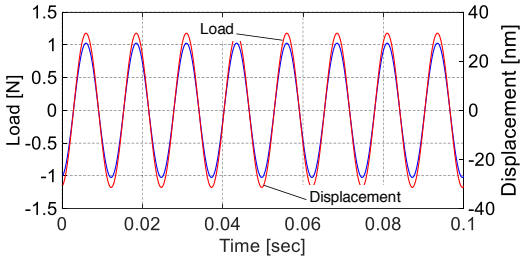

(a) 80 Hz

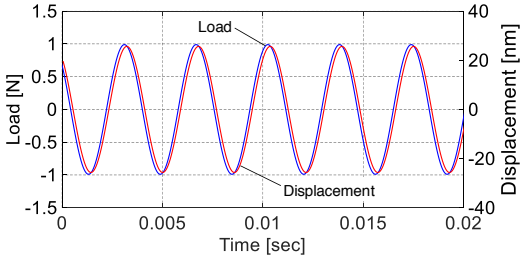

(b) 280 Hz

FIGURE 7. Applied sinusoidal force and displacement and deformation of spindle

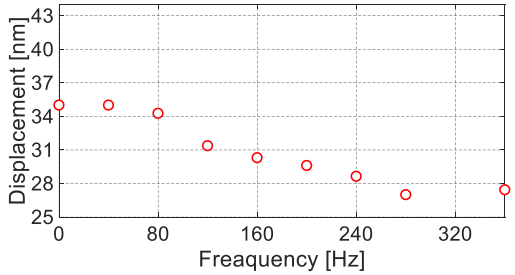

FIGURE 8. Frequency characteristics of spindle stiffness

In Figure 8, the amplitude of the resultant displacement of the spindle rotor is presented against variant frequencies of the external forces. The displacement including the deformation of the rotor due to the bending. Figure 8 represents that the amplitude decreases as the increase of the frequency.

Now, the dynamic stiffness of the hydrostatic radial bearings is considered. In the experiments, the amplitude of the applied forces was controlled to be 1N as described. Accordingly, it is verified that the dynamic stiffness of the spindle increases as the increase of the frequency in the range of the frequency up to 360 Hz. The characteristics of the spindle is significantly desirable to achieve the precise machining and to generate better surface quality of the parts. It is considered that the dynamic characteristics of the spindle are due to the damping characteristics of the water hydrostatic bearings though further investigation is still needed.

CONCLUSIONS

In this paper, the static and dynamic characteristics of the hydrostatic spindle were studied. Static bearing stiffness of the thrust and radial bearings were measured. The experimental results indicated that the static stiffness of the thrust bearings is about 1100 N/μm.

Dynamic stiffness of the spindle was also measured. In the experiments, the sum of the displacement and deformation of the rotor were measured for variant frequencies of the radial external forces of 1 N from 0 Hz to 360 Hz. From the experimental results, it is verified that the displacement of the spindle rotor gradually decreases with increase of the frequency of the sinusoidal external forces. For example, the displacement was 35 nm when the frequency is 0 Hz whereas it was 27.0 nm when the frequency is 360 Hz. The dynamic stiffness of the spindle increases in the frequency ranges. It is considered that the damping characteristics of the water hydrostatic bearings contribute desirable characteristics.

REFERENCES

[1] Kohei N, Akio H, Yohichi N. Design of Spindle Supported by Water Hydrostatic Bearings. Proc. of Annual Meeting of ASPE (2015)

[2] Adolfo D. Experimental Identification of Dynamic Force Coefficients for a 110 MM Compliantly Damped Hybrid Gas Bearing. Trans. of ASME, Journal of Engineering for Gas Turbines and Power, Vol. 137, Issue7(2015)

Laser Augmented Diamond Drilling Operation Using A Rotating Tool Design

Hossein Mohammadi and John A. Patten
Nano-manufacturing Laboratory
Manufacturing Research Center
Western Michigan University
Kalamazoo, MI, USA

ABSTRACT
Drilling is one of the basic and widely used machining operations in manufacturing. Even though it seems very simple, it gets complicated when it is encountering challenging and newly developed materials and precision engineering applications that need holes in high quality parts. Materials such as ceramics and composites have many applications in modern advanced technologies. Challenges of drilling these materials include extensive tool wear due to high hardness and damages to the workpiece because of high cutting forces. Locally decreasing the hardness and brittleness of these materials by thermally softening, for example by laser heating at the cutting zone, can enhance the cutting process and reduce the tool wear. In other machining processes such as turning and milling, since material removal is occurring at the surface and the cutting tool is exposed, it is easier to enhance or thermally assist the process. Examples include using laser either in ahead of the tool [1] or through the cutting tool [2]. In drilling operation though, except at the beginning of the hole, the drill bit is inside the workpiece and it is very difficult to access and assist with laser. To the best knowledge of authors, there is no any laser assisted drilling process reported in literature.
Laser Augmented Diamond Drilling (LADD) is a recently developed technology for drilling of hard and brittle materials [3-4]. It is a hybrid process that utilizes high compressive and shear stresses induced by a diamond tool/drill bit tip and laser heating to thermally soften, thus reducing the hardness and brittleness of the workpiece material. This process can increase the material removal rate (MRR), decrease the tool wear, improve the edges and surface finish, and minimize or eliminate sub-surface damages occurring during the drilling process.
There are many drilling techniques available to generate precise micro/macro holes in hard and brittle materials such as conventional and mechanical methods [5-6]. Nonconventional methods are such as electrical discharge machining, waterjet, micro-electrical chemical machining and ultrasonic machining [7-11]. However, some of these processes are limited in cost, machining efficiency, dependence on the material properties, and achievable aspect ratio. Laser ablation drilling is an alternative process for making holes in challenging materials as it is a non-contact process and able to drill almost any material. However, this process also suffers from size inaccuracy, tapered holes, redeposited material, micro cracks due to thermal stresses and heat affected zone [12].

ROTATING TOOL DESIGN

In regular drilling process typically it is the drill bit that rotates and the workpiece is stationary. Due to complexity of the LADD process the initial tests and studies have been carried out by a stationary tool and rotary specimen setup which is similar to drilling on lathe [13]. As the relative motion of the workpiece respect to the cutting tool is achieved, the obtained results are reliable enough. Results achieved by that configuration successfully showed that using laser can decrease the cutting force which helps to preserve the drill's cutting edge and therefore obtain a longer tool life. As an example, figure 1 shows the cutting forces achieved in drilling carbon fiber composite using different laser powers while other parameters were kept the same for all tests. The force reduction depends on parameters such as laser power, optical properties and laser absorption of the material.

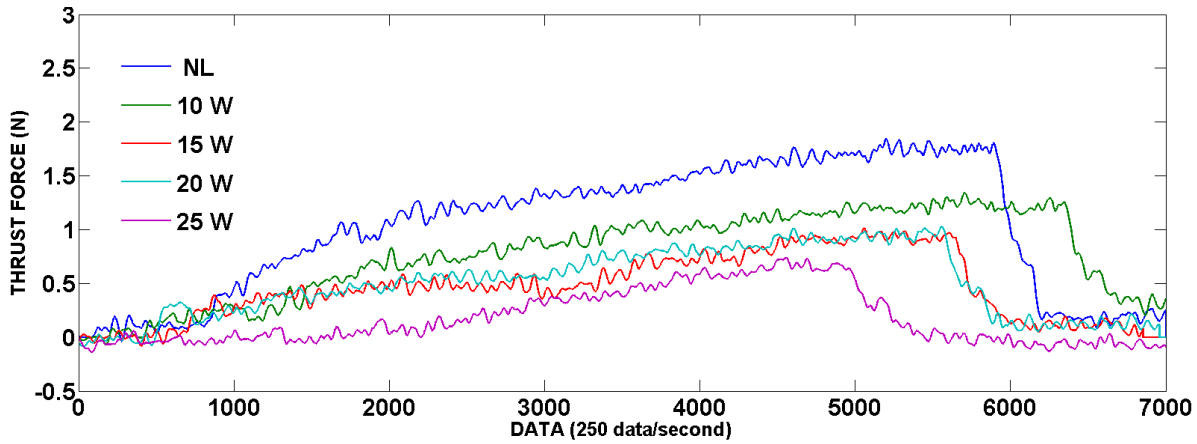

Figure 1: Cutting forces in LADD process of carbon fiber composite

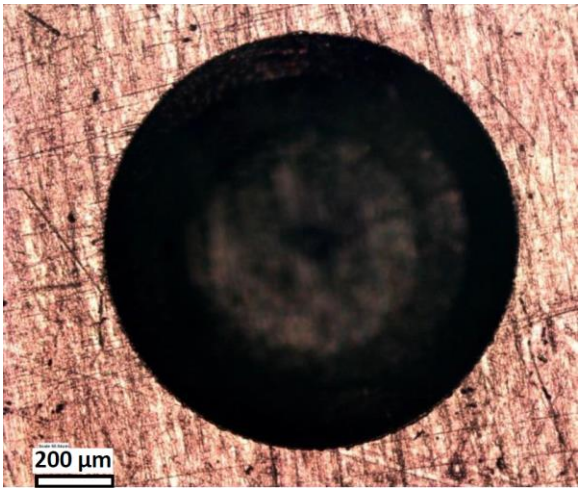

Figure 2: Carbon fiber composite drilled by LADD

Figure 2 also shows a drilled hole on a carbon fiber sample using the LADD technique. In the LADD process a cutting fluid can be used since laser will not be interrupted. This helps to achieve a better surface finish and also to control the heat dissipation and avoid any unwanted heat effect. In industry, a rotational tool setup has more applications and makes the process more versatile. For instance, large parts can be processed, multiple holes can be drilled and even a hand held (or robotic) tool is possible. In this configuration, shown in figure 3 schematically, a precise air bearing spindle, is coupled to an integral motor with a hollow shaft and the laser beam passes through the entire setup and then directly to a transparent drilling tool bit.

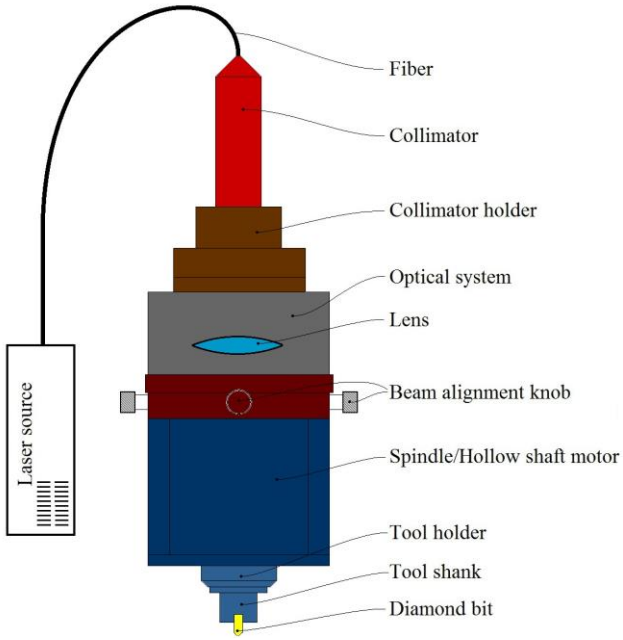

Figure 3: Schematic of the LADD rotating tool configuration

In this study for the first time a rotating tool configuration of the LADD system is presented. For this purpose, a custom made air bearing spindle attached to a motor on a common (hollow) shaft is mounted on a tribometer to perform the operation. A laser collimator attached to the system provides the laser beam and a lens inside the setup focuses it to the tip of a diamond drill bit. The whole setup is mounted on a tribometer with micrometer movement accuracy to be able to perform the drilling operation as shown in figure 4.

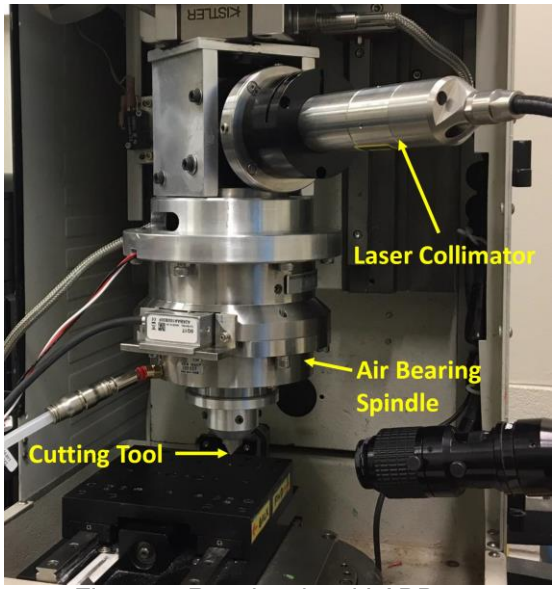

Figure 4: Rotational tool LADD system

The first challenge to overcome is the alignment of the tool respect to the optical axis of the system. The laser passes through a lens and focuses at the tip of the diamond tool. Since the laser beam is fixed with respect to the setup, the tip of the tool needs to be at the center of rotation. In the current version of the system, alignment achieved by using a fixture.

OPTICAL ANALYSIS

One important aspect of the LADD rotating tool configuration is its optical design. To evaluate how the designed system performs, the optical modeling software Zemax Optic Studio 16.5 is used to model the laser beam propagating through the focusing optics to the image plane. This is shown in figure 5, where the layout of the focusing optic and beam is shown as well as a 3D surface plot of the irradiance. The irradiance shows a Gaussian-like profile, as expected.

The diamond cutting tool (1.2 mm thickness) is then added into the model and the beam is focused at the cutting edge of the diamond. For this purpose, the diamond input surface was perpendicular to the beam propagation, in order to see how the material impacts the beam shape. Figure 6 shows the 2D cross sectional view of the irradiance at the output plane. The beam is symmetrical and circular and there is 30% reduction of the laser power due to absorption, reflection and scattering. Other optic components are neglected in this model as they can be eliminated while the cutting tool is essential.

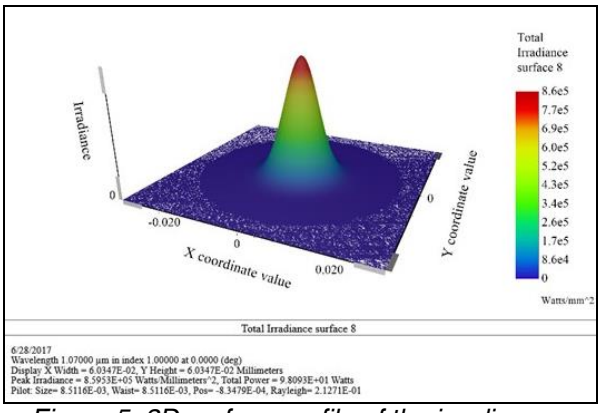

Figure 5: 3D surface profile of the irradiance

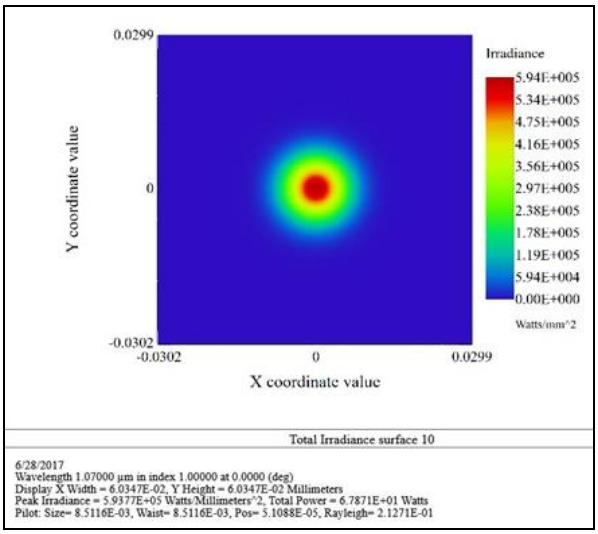

Figure 6: 2D beam profile of the focused spot

CONCLUSION

LADD is a recently developed technology for drilling of hard, brittle and challenging materials. It is hybrid process that combines the mechanical cutting and laser heating to thermally soften, thus reducing the hardness and brittleness of the workpiece material. For the first time a rotating tool configuration of the LADD system is presented. Optical analysis of the system shows that the laser power reduction is not significant, i.e., the optical transmission is adequate (but not yet optimized). The designed and manufactured system shown in figure 4 is currently under testing and results will be published in the near future.

ACKNOWLEDGEMENT

The authors would like to thank the National Science Foundation (PFI: AIR – TT, Award #: 1445017) for funding this study.

REFERENCES

[1] Anderson, M., Patwa, R., & Shin, Y. C. (2006). Laser-assisted machining of Inconel 718 with an economic analysis. International Journal of Machine Tools and Manufacture, 46(14), 1879-1891.

[2] Ravindra, D., Ghantasala, M. K., & Patten, J. (2012). Ductile mode material removal and high-pressure phase transformation in silicon during micro-laser assisted machining. Precision engineering, 36(2), 364-367.

[3] Mohammadi H., Bakir B., Patten J. (2016). Laser augmented Diamond Drilling of Hard and Brittle Materials. American Society of Precision Engineering, Proceedings of the 31st Annual Meeting, Portland, Or.

[4] Patten J., Mohammadi H., Laser Augmented Diamond Drilling Apparatus and Method, US Patent application #15/337,617 (10/28/2016)

[5] Egashira, K. and Mizutani, K., 2002. Micro-drilling of monocrystalline silicon using a cutting tool. Precision Engineering, 26(3), pp.263-268.

[6] Moon, J.S., Yoon, H.S., Lee, G.B. and Ahn, S.H., 2014. Effect of backstitch tool path on micro-drilling of printed circuit board. Precision Engineering, 38(3), pp.691-696.

[7] Jahan, M.P., Wong, Y.S. and Rahman, M., 2012. Evaluation of the effectiveness of low frequency workpiece vibration in deep-hole micro-EDM drilling of tungsten carbide. Journal of Manufacturing Processes, 14(3), pp.343-359.

[8] Ahn, S. H., Ryu, S. H., Choi, D. K., & Chu, C. N. (2004). Electro-chemical micro drilling using ultra short pulses. Precision Engineering, 28(2), 129-134.

[9] Rashed, C.A.A., Romoli, L., Tantussi, F., Fuso, F., Burgener, M., Cusanelli, G., Allegrini, M. and Dini, G., 2013. Water jet guided laser as an alternative to EDM for micro-drilling of fuel injector nozzles. Journal of Manufacturing Processes, 15(4), pp.524-532.

[10] Aziz, Muhammad, Osamu Ohnishi, and Hiromichi Onikura. "Novel micro deep drilling using micro long flat drill with ultrasonic vibration." Precision Engineering 36, no. 1 (2012): 168-174.

[11] Ziki, J.D.A. and Wüthrich, R., 2015. The machining gap during constant velocity-feed glass micro-drilling by Spark Assisted Chemical Engraving. Journal of Manufacturing Processes, 19, pp.87-94.

[12] Samant, Anoop N., and Narendra B. Dahotre. "Laser machining of structural ceramics—a review." Journal of the European Ceramic Society 29, no. 6 (2009): 969-993.

[13] Stephenson, D. A., & Agapiou, J. S. (2016). Metal cutting theory and practice. CRC press.

UPC 300 ULTRA PRECISE DIAMOND TURNING MACHINE OPTIMIZED FOR FREEFORM PRODUCTION

Dr.-Ing. Frank Niehaus[1], Dr.-Ing. Stephan Huttenhuis[1], and Daniel Gauch[2]
[1]Schneider GmbH & Co. KG
Fronhausen, Germany
[2]Schneider Optical Machines Inc.
Frisco, TX

INTRODUCTION

The need for increasingly complex optics and the demand for freeform optics with ultra-high precision specifications is growing quickly across numerous applications. Traditional precision optics fields such as telescopes, metrology and laser systems benefit from an overall reduction in size, simplified alignment and improved system performance. Rapidly evolving technologies such as LED illumination, augmented reality, or head-up displays (HUD) utilize freeform optics to create products that must conform to packaging limitations, regulatory requirements and consumer tastes [1], [2], [3].

The compact UPC 300 diamond turning system simplifies freeform manufacturing and increases efficiency by combining fully integrated non-contact surface measurements, an advanced GUI software package, corrective re-machining functions and a high accuracy long stroke fast tool into one compact system. Effectively combining multiple systems into one unit and eliminating time consuming multiple workpiece transportation, mounting and dismounting steps.

MACHINE DESIGN

The standard configuration of the UPC 300, as shown in Figure 1, includes two linear axes (X and Z) and the air bearing spindle with integrated encoder that acts as the C-axis. The linear axes use hydrostatic bearings and linear motors in combination with high frequency digital drive systems for optimal performance. The travel range of both linear axes is 350 mm.

In standard configuration workpieces, up to 300 mm in diameter can be machined. By applying an optional riser to elevate the spindle, the work piece capacity can be increased up to 700 mm. The design achieves a compact footprint with machine dimensions of only 1800 by 1200 mm².

The freestanding electrical cabinet can be positioned away from the machine to avoid thermal interference within the working space of the machine.

FIGURE 1. Ultra-Precision Machining Center UPC 300.

Figure 2 shows the unique axes configuration of the UPC 300 which has been specially designed to optimize fast tool machining. The fast tool is mounted on the X-slide while the workpiece spindle is mounted on the Z-slide. Therefore, the motion of the fast tool is perpendicular to the X-axis which leads to two benefits. First, any dynamic forces generated by the fast tool motion do not have to be compensated for by the linear motor of the underlying axis. Second, the dynamic forces of the fast tool are damped by the hydrostatic bearings which effectively direct the forces into the rigid granite base. The result is superior surface accuracy and finish quality.

The fast tool can be integrated onto the machine in two different ways. Either a manual height adjustment system using flexural bearings can be used, or a system that allows for an automatic alignment of the tool height. This feature enables for the first time in ultra-precision machining the tool height alignment on a fast tool without the need of additional axes. This prevents additional compliances in the setup and leads to more precise parts with better surface finish.

The automatic alignment feature is fully integrated into the software and eases the tool alignment process significantly, allowing a less experienced operator to perform this function. Additionally, the machine can select between two different tools mounted on the same fast tool slide without additional alignment or machine downtime.

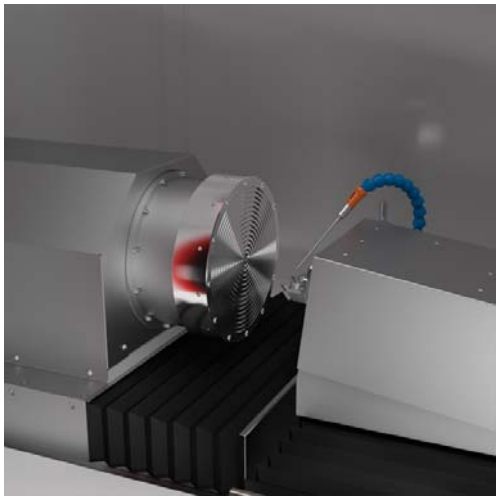

FIGURE 2. Axes layout of the UPC 300 with integrated Long Stroke Fast Tool.

LONG STROKE FAST TOOL

The integrated long stroke fast tool enhances the freeform machining significantly by allowing fast processing. The light weight design of the moving slide combined with powerful drives allows for high rates of acceleration, while still achieving surface roughness in the 10 Angstrom range. The ultra-precise fast tool with extended 30 mm stroke and robust dynamic properties enables the machining of freeform surfaces including designs with large departures from the best-fit sphere.

Therefore, the need for time consuming slow tool processing is minimized, which benefits productivity as well as the quality of the parts. As an example, the rotational speed for the HUD machining, shown in Figure 3, could be accelerated by 600% compared to the slow tool process.

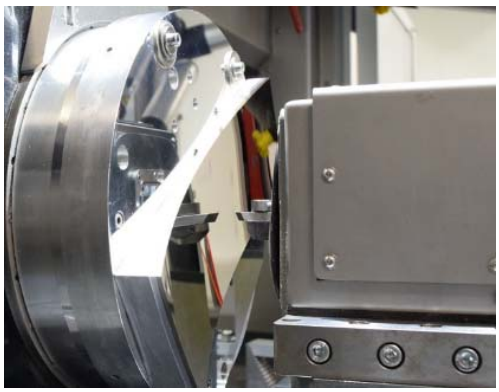

FIGURE 3. Machining of a HUD mirror using the Long Stroke Fast Tool.

OPTICAL METROLOGY

The integrated optical metrology system allows for the direct measurement of the machined part, including freeform surfaces while still mounted inside the machine. Figure 4 shows the sensor in front of a HUD mirror workpiece. Since it is a non-contact measurement system this technique can be used for the final quality control measurement leaving the delicate machined surface untouched. Further, the optical probe has no issues with non-circular shaped work piece geometries.

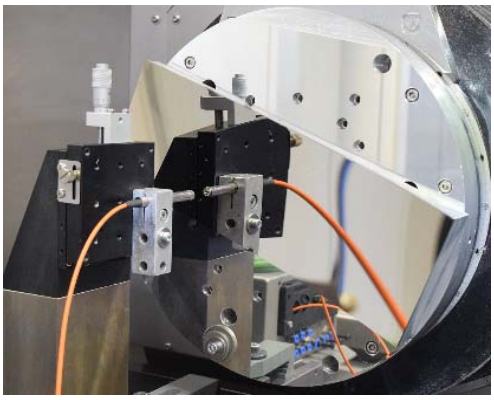

FIGURE 4. UPC 300 with integrated optical metrology.

The integrated metrology eliminates the need for time consuming dismounting, part transportation between machines, part remounting and the complex task of translating metrology and orientation data into a format the machine can use for corrective processing. Furthermore, to get accurate results with traditional methods, each step requires additional downtime to allow for temperature stabilization of the part, mounting fixture and associated equipment.

CORRECTIVE RE-MACHINING

The metrology result can be further used for a corrective re-machining step if higher accuracies are required. Using this functionality, accuracies of +/- 0.1 μm for complex freeform surfaces were achieved on aluminum mirrors.

The results of the corrective machining of a freeform telescope mirror with a diameter of about 120 mm are given in the following. Figure 5 shows the form error as a result of the full area measurement after the corrective machining.

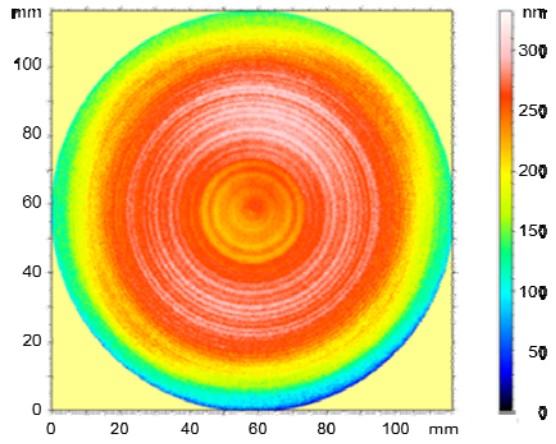

FIGURE 5. Measured form deviations over the full area of the freeform surface.

Figure 6 shows the cross section of this measurement. This highlights the important center portion of the workpiece, where over a diameter of 100 mm form accuracy deviation is below 100 nm.

The result of the corrective machining process is a 5-fold improvement in form accuracy over the original measurement. This significantly improved the optical functionality of the mirror.

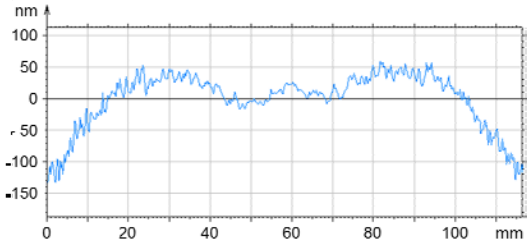

FIGURE 6. Cross section of the full area measurement

HUMAN MACHINE INTERFACE

All the aforementioned features are supported by the user-friendly human machine interface (HMI). In addition, the standard software can be utilized to load data files in various formats such as NURBS in STEP files, point clouds, etc. The operator quickly gets a visual representation of the part and the correct orientation of the part in the machine can be verified (see Figure 7).

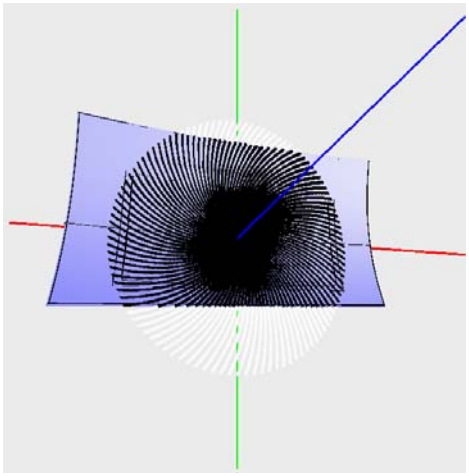

FIGURE 7. Visualization of freeform surface with spiral tool path for HUD machining

A process is built using the touchscreen interface to input critical parameters, tool specifications and mounting position. A tool path analysis can be performed virtually to determine if there are any interference or clearance issues which are highlighted in red on the displayed spiral path.

The integrated software automatically calculates the ideal tool path and extends it to fill in undefined areas, as shown in Figure 7, in order to minimize vibration and provide smooth

transitions along the edges of non-circular parts. Multiple parts can be machined at one time with the software calculating the tool path between parts to maintain smooth operation and reducing vibration.

CONCLUSION

The UPC 300 combines hardware, software and metrology systems into one fully integrated diamond turning solution. Its extraordinary fast tool stroke and dynamic properties allow for significantly reduced process times compared to slow tool machining while improving the level of accuracy. Combining machining and metrology into one system drastically reduces the footprint of the otherwise needed systems leading to improved cost of ownership over the life of the machine.

Added benefits are a reduction in the impact of external influences such as temperature fluctuations and potential damage during parts handling allowing for a more accurate, robust, and repeatable manufacturing process. The combination of powerful data handling capabilities, diamond turning, and metrology make the UPC 300 an ideal platform for fabricating freeform surfaces.

REFERENCES

[1] Scheiding S; et al. Ultra-precisely manufactured mirror assemblies with well-defined reference structures. Proceedings of SPIE 7739-08. 2010.

[2] Brecher C (Ed.). Mikrostrukturierte, local-funktionale Oberflächen für hocheffiziente Beleuchtungssysteme. Apprimus. Aachen. 2012.

[3] Dick L. High Precision Freeform Polymer Optics. Optik & Photonik. Wiley. Weinheim. 2012.

[4] Niehaus F, Huttenhuis S, Pisarski A. Corrective Machining of Freeform Surfaces Using the UPC 400. Proceeding of the ASPE Annual Conference. Boston. 2014.

Dry planarization method using transport of reactive species

Reiji Ryokume, Toshinobu Miyazaki,
Satoshi Matsuyama, Yasuhisa Sano, and Kazuto Yamauchi
Department of Precision Science and Technology,
Graduate School of Engineering, Osaka University,
Osaka, Japan

INTRODUCTION

A surface roughness has a significant influence on not only mechanical properties such as fatigue strength and wear resistance, but also electrical and optical properties. In recent years, the decreased surface roughness is demanded, particularly for aspheric lens molds. Aspheric glass lenses are generally formed using the grass pressing process. To withstand the high temperature and pressure conditions during the glass pressing process, molds are generally made from ceramic materials such as tungsten carbide (WC), silicon carbide (SiC), and diamond [1-3]. However, these materials are difficult to process. In the final process of mold formation, mechanical polishing with diamond abrasives is carried out. However, this conventional mechanical polishing has significant problems; the attainable surface roughness is limited owing to the crystalline anisotropy of the workpiece, and the introduction of damages such as scratches is practically unavoidable. Therefore, it is crucial to develop a less damaging polishing method that does not depend on crystalline anisotropy.

One ideal polishing method is known as catalyst-referred etching (CARE) [4-7]. A conceptual diagram of CARE is shown in Figure 1. CARE is an abrasive-free polishing method based on a chemical etching reaction. In this method, a pad with a catalytic property is utilized in etchants, by which reactive species are generated just on the pad surface. Therefore, the top-most sites on the work surface, which contacts the pad surface more frequently than the other sites, are preferentially removed by the catalytically induced etching reaction. The pad surface also acts as a reference plane. Till date, utilizing hydrofluoric acid solution and pure water as etchants, atomically highly ordered surfaces of SiO_2, single crystalline SiC, and GaN were obtained. However, it is difficult to incorporate CARE in a wet environment into a multiaxial numerical control processing machine to polish a free-form surface.

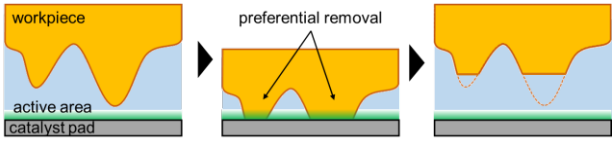

FIGURE 1. Conceptual image of CARE

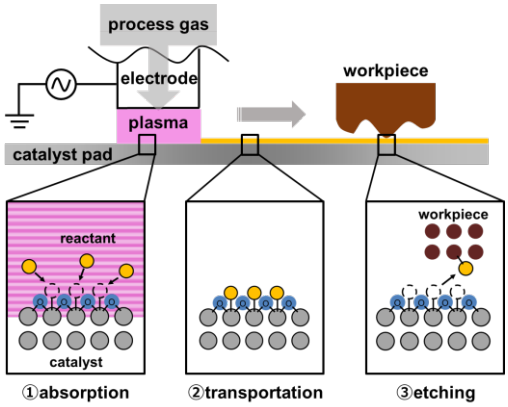

FIGURE 2. Schematic of CARE apparatus

To overcome this problem, Dry-CARE was developed as a new polishing method that employs the polishing mechanism of CARE in a dry environment. Figure 2 shows the schematic of the polishing mechanism of Dry-CARE. In this method, a pad with a catalytic property is utilized as a reference plane, as in CARE. Using an atmospheric pressure plasma, the reaction gas is effectively dissociated to produce a high density of reaction species. They are adsorbed onto the catalyst surface; therefore, the reaction is limited only to the area near the catalyst surface, which enables the reference plane to transfer onto the work surface. Currently, fluorine is utilized as the reactive species, in Dry-CARE, owing its high efficiency in the conventional CARE process. The indispensable properties of the catalyst used in Dry-CARE are a well adsorbent with fluorine and the very low vapor pressure of its fluoride. From this reason, Ni and Al_2O_3 were used as the catalysts.

This paper describes the results of polishing Si (100), diamond (100), and SiC ceramics.

EXPERIMENT

Si (001), diamond (100), and SiC ceramics were used as workpieces. The polishing conditions are given in Tables 1 and 2. The rotating pad is made from an Al alloy, on which sprayed coating Al_2O_3 or electroless-plated Ni with a thickness of 200 or 20 μm, respectively, is formed as the catalyst. The rotation speed of the pad is 10 rpm. Workpieces are fixed at a distance of 121 mm from the rotation axis of the pad. The distance between the workpiece and the position where the plasma was generated was fixed to 25 mm. Table 3 provides the conditions for plasma generation. The process gases were He and SF_6, the flow rates of which were 1485 and 15 sccm respectively. A capacitively coupled plasma was generated by supplying radio frequency (RF) power between an electrode and the pad. The distance between the electrode and the pad was 500 μm.

The experiments were conducted using Al_2O_3 and Ni as catalysts. The combination of the catalyst and workpiece is very important, because if their surface hardnesses are considerably different, the softer substance experiences considerable damage. In this study, Al_2O_3 was used with SiC ceramics and diamond, and Ni with Si and SiC ceramics.

First, the polishing of Si (001) was carried out with and without the plasma using Ni as the catalyst. This process was aimed at investigating the feasibility of Dry-CARE. Then, SiC ceramics and diamond (100) were polished in the same manner. The polished surfaces were observed using an optical interferometer and a scanning electron microscope (SEM). The removal rate (RR) was determined using the decrease in peak-to-valley (P-V) height.

Table 1. Polishing conditions with Ni catalyst

Workpiece	Si (001)	SiC ceramics
Catalyst	Ni (electroless plating 20 μm)	
Pressure	5 kPa	4.4 kPa
Rotating speed of pad	10 rpm	
Radius of gyration	121 mm	

Table 2. Polishing conditions with Al_2O_3 catalyst

Workpiece	diamond (100)	SiC ceramics
Catalyst	Al_2O_3 (sprayed coating 200 μm)	
Pressure	22 kPa	4.4 kPa
Rotating speed of pad	10 rpm	
Radius of gyration	121 mm	

Table 3. Conditions for plasma generation

Pressure	1 atm
Process gas	He & SF_6
Flow rate of He	1485 sccm
Flow rate of SF_6	15 sccm
Electric power	95 W (13.56 MHz)
Gap	500 μm

RESULTS AND DISCUSSIONS

Polishing of Si (001) with Ni catalyst

The polishing for Si (001) was carried out with and without plasma. The conditions are summarized in Tables 1 and 3. Interferometer images of the Si (001) surface before and after polishing without and with the plasma are shown in Figure 3. As can be seen in Figures 3(a) and 3(b), the morphology of the surface hardly changed, which means that mechanical phenomena such as friction have little influence on this polishing mechanism. In Figures 3(c) and 3(d), unlike Figures 3(a) and 3(b), a clear difference in the surface morphology can be seen with the removal of the top-most sites. Roughness values decreased from 437 to 6 nm root mean square (rms). Above all, Dry-CARE with Ni catalyst can realize polishing by the chemical etching reaction.

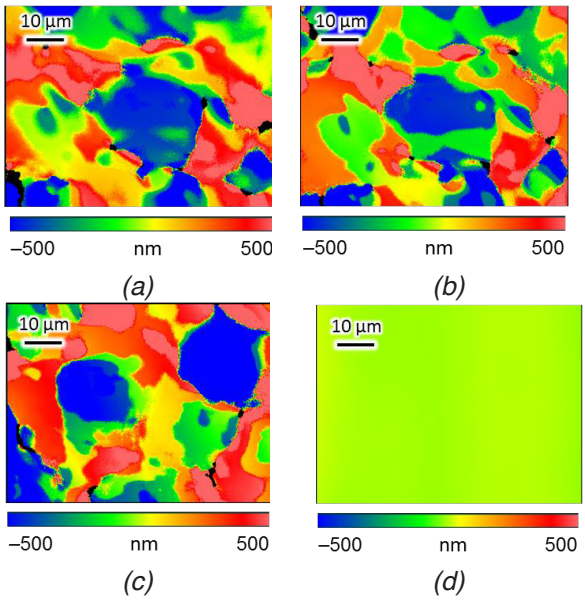

FIGURE 3. Optical interferometer images of Si (001). (a) before polishing; 341 nm rms [P-V: 2420 nm], (b) after 3 h polishing without plasma; 362 nm rms [P-V: 2544 nm], (c) before polishing; 437 nm rms [P-V: 2761 nm], (d) after 3 h polishing with plasma; 6 nm rms [P-V: 27 nm]

Polishing of SiC ceramics with Ni catalyst

The polishing for SiC ceramics was carried out for 8 h with plasma. The conditions are summarized in Tables 1 and 3. Figure 4 shows the time dependency of the surface roughness. After polishing for an hour, the value of the surface roughness was saturated at approximately 11 nm rms, which is higher than Si polished with Ni catalyst. This is because the Ni surface was deteriorated because of the damage introduced in the processing of SiC so far. Ni may be an inappropriate catalyst for SiC polishing, owing to its low hardness.

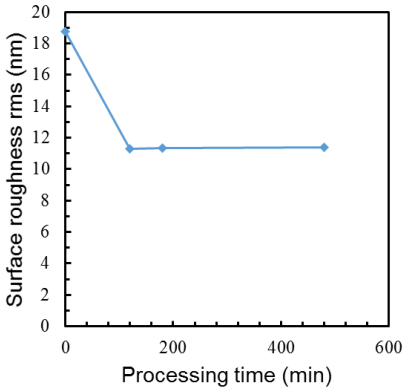

FIGURE 4. Dependence of surface roughness values on processing time. The workpiece was a SiC ceramic, and the catalyst was Ni.

Polishing of SiC ceramics with Al_2O_3 catalyst

The polishing of the SiC ceramic surface was carried out for approximately 10 h with plasma. The conditions are summarized in Tables 2 and 3. Figure 5 shows the time dependency of the surface roughness. After the initial 4 h of polishing, the value of the surface roughness decreased from 57 to 9 nm rms; however, in subsequent polishing, it was saturated at 4-5 nm rms. Optical interferometer images of the surface after 2 and 3 h polishing are shown in Figure 6. As can be seen in the figure, many pits are present on the polished surface. In comparison to Figure 6(a), the positions of some pits are different in Figure 6(b). This means that the formation and disappearance of pits happened at the same time. As the result, the attainable surface roughness was limited. Figure 7 shows the SEM image of a polished surface. The pits on the surface are due to intrinsic porosity; no fracture or deformation was observed around these pits, as is mentioned in [8]. It is also confirmed that no machining mark such as scratches are left.

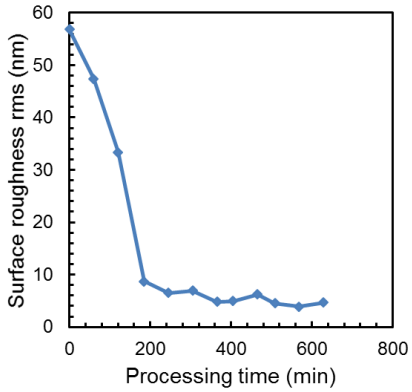

FIGURE 5. Dependence of surface roughness on processing time. The workpiece was a SiC ceramic, and the catalyst was Al_2O_3.

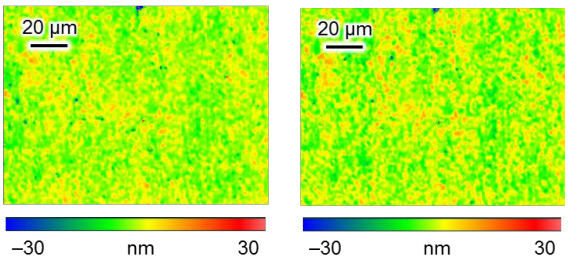

(a) *(b)*

FIGURE 6. Optical interferometer images of SiC ceramics after (a) 2 h polishing; 2.6 nm rms [P-V: 89 nm], and (b) 3 h polishing; 3.1 nm rms [P-V: 136 nm].

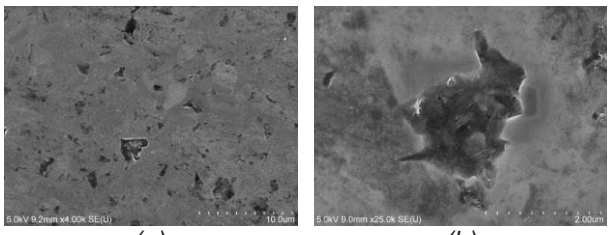

(a) *(b)*

FIGURE 7. SEM images of well-polished SiC ceramics.
(a)4000 and (b) 25000 magnification

Polishing of diamond (100) with Al_2O_3 catalyst

The polishing of diamond (100) was carried out for 3 h with and without plasma. The conditions are summarized in Tables 2 and 3. Interferometer images of the surface before and after polishing are shown in Figure 8. Without the plasma, the surface roughness hardly improved; in contrast, with the plasma, the value of the surface roughness decreased from 9.7 to 3.0 nm rms. Then, many grooves were prepared on a surface to determine the RR. Interferometer images of the surface before and after polishing are shown in Figure 9, while lines traces along the original polishing direction (A_1A_2 and $A_1'A_2'$) are plotted in Figure 10. As can be seen in Figure 9, the top-most sites on the surface were preferentially removed. The RR was 37 nm/h, which was measured by a decrease in the peak height. Furthermore, in the processed area along the perpendicular line trace (B_1B_2 and $B_1'B_2'$), roughness values decreased from 10.38 to 0.83 nm rms.

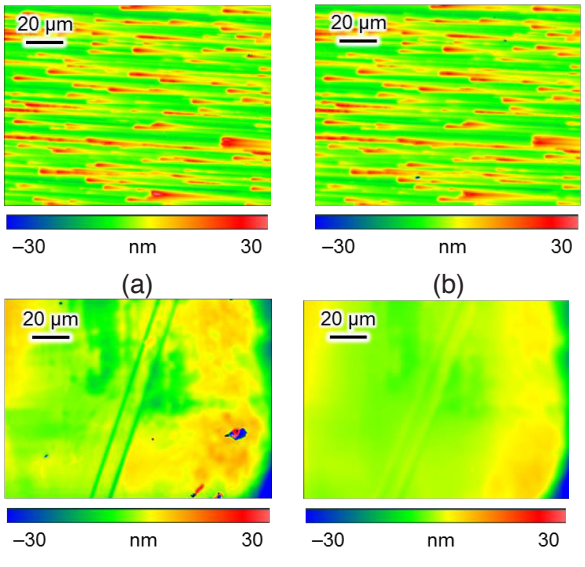

FIGURE 8. Optical interferometer images of diamond (100). (a) before polishing; 6.2 nm rms [P-V: 120 nm], (b) after 3 h polishing without plasma; 6.5 nm rms [P-V: 473], (c) before polishing; 9.7 nm rms [P-V: 394 nm], (d) after 3 h polishing with plasma; 3.0 nm rms [P-V: 19 nm]. The bottom-right part in (c) and (d) is the corner of the workpiece; therefore, surface roughness and P-V were measured avoiding this area.

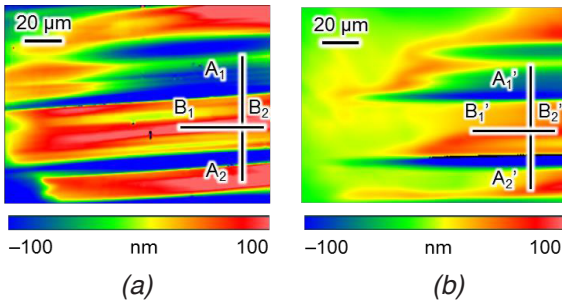

FIGURE 9. Optical interferometer images of diamond (100). The surface was damaged in advance. (a) before polishing; 73 nm rms [P-V: 831 nm], (b) after 3 h polishing with plasma; 36 nm rms [P-V: 245 nm]

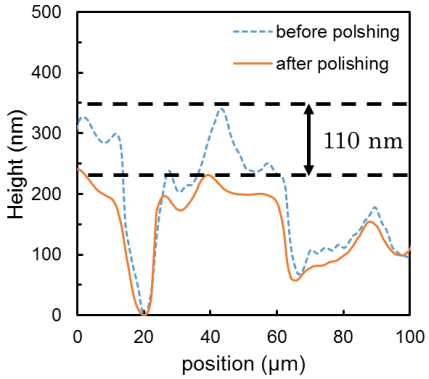

FIGURE 10. Cross-sectional shape of diamond (100) in Figure 9: before (A_1A_2), and after 3 h polishing ($A_1'A_2'$)

SUMMARY

Dry-CARE was developed for the polishing of mold materials. Ni and Al_2O_3 were utilized as catalysts. The polishing of Si (001) with Ni catalyst showed that this polishing method is based on a chemical etching reaction. This polishing method was also applied for SiC ceramics and diamond. The polishing of SiC ceramics with Al_2O_3 realized a 4-5 nm rms. This was a greater surface roughness than that obtained with Ni as the catalyst. Diamond (100) was polished with Al_2O_3 as the catalyst. In the polished area, the surface roughness decreased from 10.38 to 0.83 nm rms, and the RR was 37 nm/h. These results indicated that Dry-CARE can flatten Si, SiC ceramics, and diamond using Ni and Al_2O_3 as catalysts.

ACKNOWLEDGEMENT
The Japan Society for the Promotion of Science Core-to-Core Program on International Alliance for Material Science in Extreme States with High Power Laser and XFEL

REFERENCES
[1] J. Y. Choi, and H. D. Jeong. A study on polishing of molds using hydrophilic fixed abrasive pad. Int. J. Mach. Tool Manu. 2004; 44: 1163-1169.
[2] A. Beaucamp, Y. Namba, I. Inasaki, H. Combrinck, and R. Freeman. Finishing of optical moulds to λ/20 by automated corrective polishing. Manu. Technol. 2011; 60: 375-378.
[3] E. Brinksmeier, O. Riemer, and A. Gessenharter. Finishing of structured surfaces by abrasive polishing. Precis Eng. 2006; 30: 325-336.
[4] H. Hara, Y. Sano, H. Mimura, K. Arima, A. Kubota, K. Yagi, J. Murata, and K. Yamauchi. Novel abrasive-free planarization of 4H-SiC (0001) using catalyst. J. Electron. Mater. 2006; 35: L11.
[5] K. Arima, H. Hara, J. Murata, T. Ishida, R. Okamoto, K. Yagi, Y. Sano, H. Mimura, and K. Yamauchi. Document atomic-scale flattening of SiC surfaces by electroless chemical etching in HF solution with Pt catalyst. Appl. Phys. Lett. 2007; 90: 202106.
[6] T. Okamoto, Y. Sano, H. Hara, T, Hatayama, K. Arima, K. Yagi, J. Murata, S. Sadakuni, K. Tachibana, Y. Shirasawa, H. Mimura, T. Fuyuki, K. Yamauchi. Reduction of Surface Roughness of 4H-SiC by Catalyst-Referred Etching. Mater. Sci. Forum. 2010; 645–648: 775–778.
[7] T. Okamoto, Y. Sano, K. Tachibana, K. Arima, A. Hattori, K. Yagi, J. Murata, S. Sadakuni, K. Yamauchi. Dependence of process characteristics on atomic-step density in catalyst-referred etching of 4H-SiC (0001) surface. J. Nanosci. and Nanotechnol. 2011; 11: 2928.
[8] Z. Zhu, V. Muratov, and T. E. Fischer. Tribochemical polishing of silicon carbide in oxidant solution. Wear. 1999; 225-229: 848-856.

Manufacture and Assembly of Precision Planar Samples for Experiments at the National Ignition Facility

L. Savage, [1]C. Castro, [2]M. Lament, [1]R.J. Vargas, [1]R.M. Seugling, and [1]A. Nikroo

[1]Lawrence Livermore National Laboratory, Livermore, CA 94550

[2]Schafer Livermore Laboratory Inc., Livermore, CA 94551

Experiments at the National Ignition Facility (NIF) are comprised of multiple parts with tolerances ranging from nanometers to micrometers depending on the type of experiment. The Lawrence Livermore National Laboratory (LLNL) Target Fabrication group routinely uses single point diamond turning (SPDT) as the preferred method for manufacturing thin samples with engineered features such as steps that have nanometer level surface roughness and sub-micrometer form and parallelism. These stringent tolerances ultimately reduce the experimental uncertainty which corresponds to reduced number of experiments and allow for a more efficient use of the facility.

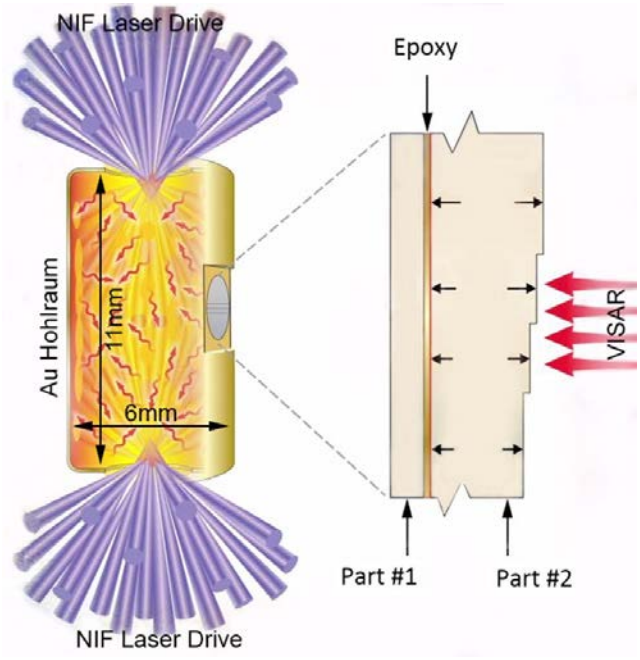

Figure 1: Left, the gold hohlraum is driven top and bottom using the NIF laser to create an x-ray drive on the sample shown on the right. Part #1 is ablated causing a pressure wave through the stepped sample, part #2. The velocity of the stepped profile is measured using a velocity interferometric diagnostic (VISAR[1]). Variation in thickness and form correlate to a velocity error.

Figure 1 shows a schematic of a planar assembly where the sample is a combination of two thin foils machined independently and assembled using adhesive. The individual components have a 2 μm tolerance on the absolute thickness with a 50 nm tolerance on the thickness variation over the area of interest. The parts are manufactured out of a range of materials including platinum, copper and tin as examples. Once the individual components are manufactured and metrology is complete the two parts are assembled together with a sub-micrometer glue bond. The final subassembly is measured and must meet a 100 nm tolerance on the thickness variation that the individual components. The combination of tight manufacturing and assembly tolerances, combined with the variety of materials of interest make the physics packages challenging to manufacture.

Individual components are machined using SPDT which requires multiple transfers on and off the machine to verify part quality throughout the machining process. Modern precision diamond turning machines can routinely create geometries meeting the tolerances discussed above if operating properly in a stable environment. However, due to the variability in material properties of the samples of interest and the multiple transfers between machining operations, maintaining and verifying the geometry meet the specification proves to be a sizeable challenge. Individual parts and final assembly is measured using a Double-Sided Scanning White Light Interferometry (D-S SWLI) configuration developed at LLNL[2]. The assembly of the components is done with diamond turned tooling and the final assembly is measured again with the DS SWLI setup. An example of the measurement including region of interest is shown in Figure 2.

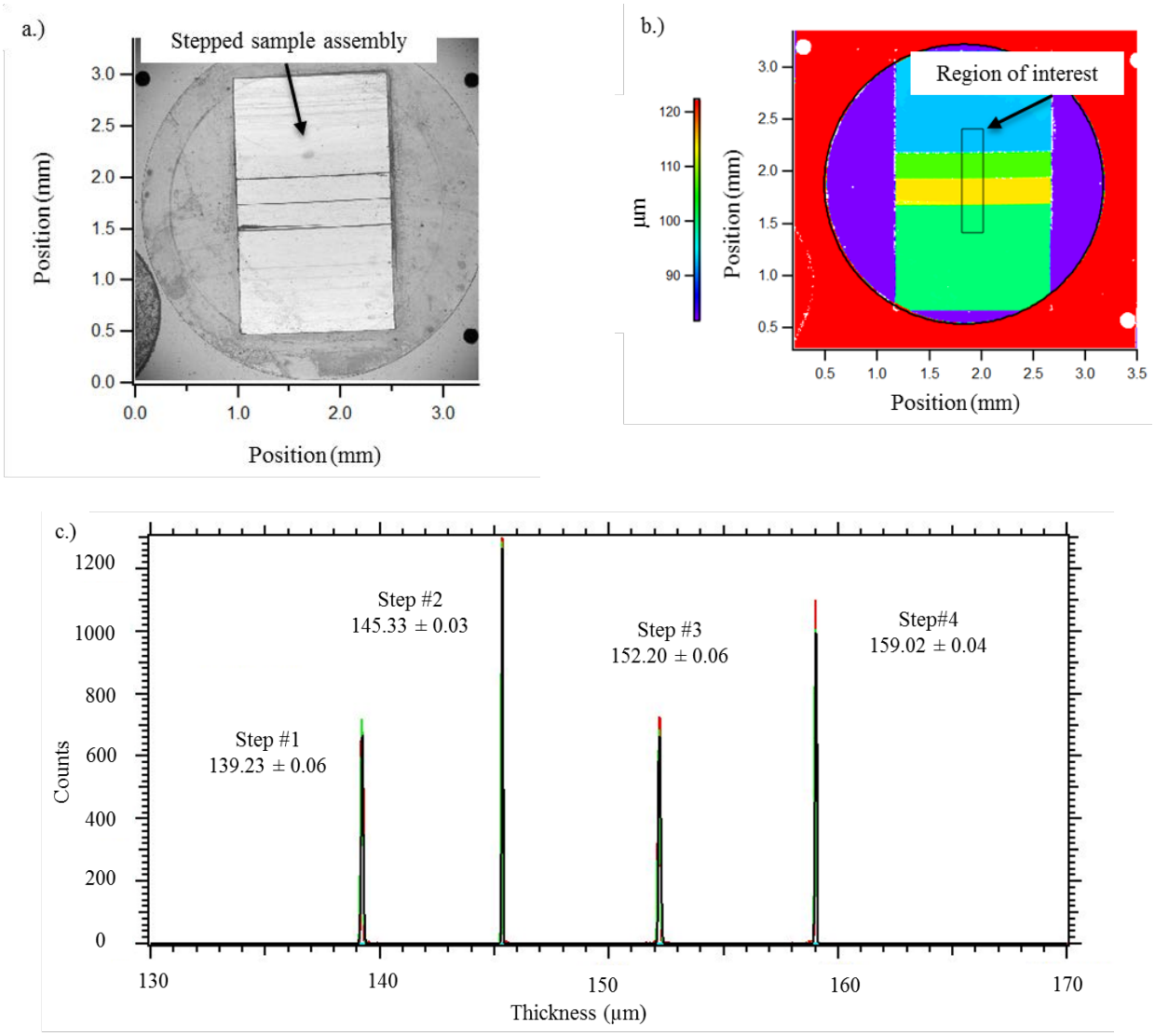

Figure 2: a.) Stepped sample assembly. b.) Step height measurement of single side of stepped assembly with region of interest highlighted. c.) FWHM of the thickness variation of each step over the region of interest.

The single- and double-sided measurements are done at multiple steps of the manufacturing process. Single sided measurements are done in process to confirm surface roughness and

flatness as the parts are machined. These measurements also confirm that the mounting and remounting of the parts do not distort the sample or introduce any damage to the part during handling. Double-sided measurements of the final parts and finished subassemblies are done as part of the acceptance process. The final subassembly requires the Full Width Half-Maximum (FWHM) of the thickness histogram over each individual step of the region of interest be 100 nm or less as shown in Figure 2c. The region of interest for these types of experiments is a rectangle nominally centered (±50 um) from the interface at the center step measuring 2 mm by 0.8 mm as shown in Figure 2b.

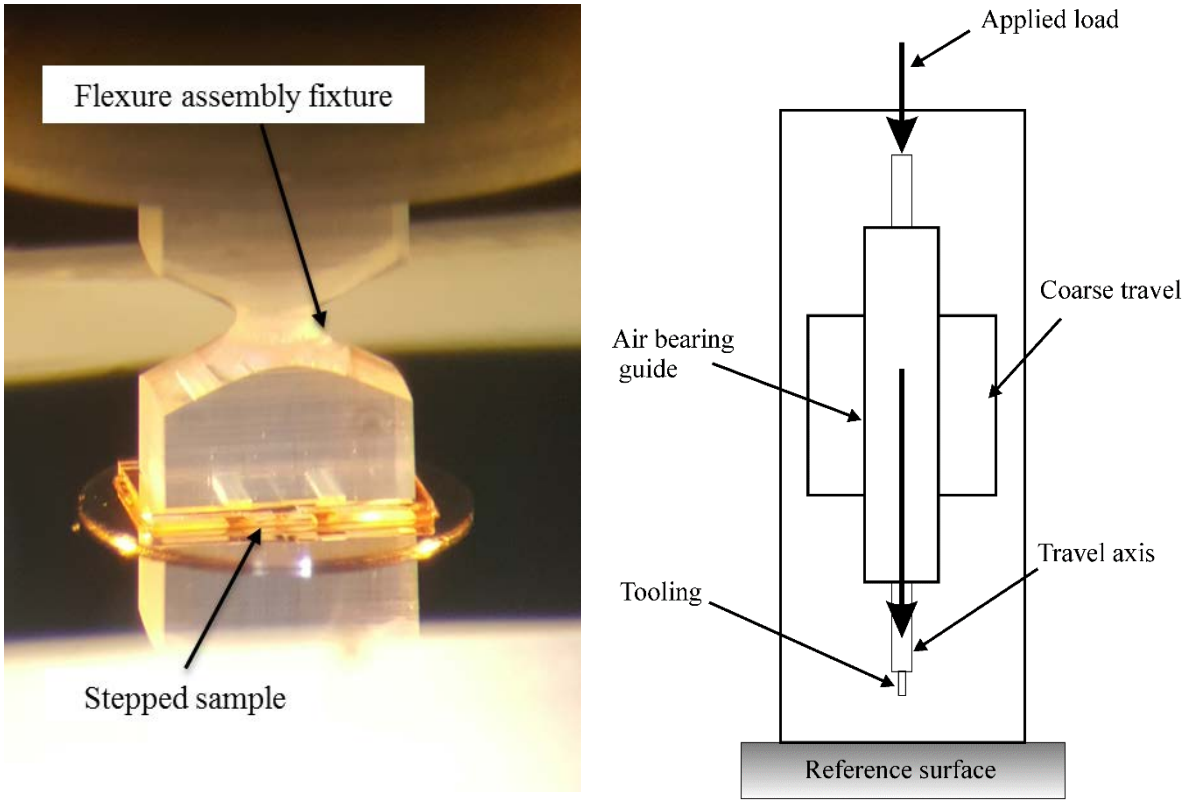

Figure3: Left, image of the flexure based assembly tooling during the assembly process. Right, schematic of the assembly set-up consisting of air-bearing linear guide allowing for friction free loading along the travel axis where a load can be applied and monitored by a force transducer (transducer not shown).

Once the individual components are manufactured to specification they are assembled using air bearing guided tooling that allows for friction free motion along the guided axis as illustrated in Figure 3. A load can be applied along the axis of travel and monitored with a force transducer (not shown). Precision machined tooling is manufactured to match the design of the parts being assembled as shown in the image in Figure 3. The system allows for guided linear motion relative to a reference surface and the fixture interface to the part has an integrated flexure to allow the assembly to conform to the reference surface without over constraining the sample causing distortion of the sample and/or assembly.

We have successfully manufactured over 100 individual components out of platinum, copper, aluminum, lithium fluoride, and tin. Many of these components been assembled into experiment packages with a current assembly yield of nearly 100%. To date we have fielded over 27 experiments that meet the specifications discussed in this paper. This poster will discuss the

precision engineering challenges of manufacturing and metrology of these samples and assemblies. In addition, future challenges involve adding more components to the assembly, assembling the components with glue-less bonds, and even softer materials like lead.

[1] Malone, R.M., *et. al*, 2003, *Design of an imaging VISAR diagnostic for the National Ignition Facility (NIF),* Proc. SPIE 5173, Current Developments in Lens Design and Optical Engineering IV, **23**.

[2] Seugling, R. M., Wilson, M.J. and Davis, P.J. 2010, *Double Sided Interferometer, Profiling Measurement Simultaneously Yields Thickness and Form*, 25th Annual Meeting of the American Society for Precision Engineering.

This work was performed under the auspices of the U.S. Department of Energy by Lawrence Livermore National Laboratory under Contract DE-AC52-07NA27344.

IM Number:

M-UBER: UBER-TYPE ASSIGNMENT FOR DISTRIBUTED OPERATOR MACHINING OPERATIONS

Tony L. Schmitz[1], Noel Greis[2], and John Ziegert[1]
[1]Mechanical Engineering and Engineering Science
University of North Carolina at Charlotte, Charlotte, NC
[2]Center for Digital Enterprise & Innovation
Kenan-Flagler Business School
University of North Carolina at Chapel Hill, Chapel Hill, NC

INTRODUCTION

Because computer numerically-controlled (CNC) machining is largely automated with only periodic tasks that require operator intervention, such as tool changes, part loading/unloading, etc., it is common practice to have an operator that oversees more than one machine simultaneously. The approach is to assign one operator to two (or perhaps three) machines in a cell. S/he is then responsible for serving only those machine interventions within his/her cell to ensure that the machines produce quality parts at the highest possible rate.

As an extension to this paradigm, a new approach, realized in a mobile software application, is proposed that enables Uber-type oversight of all machines in a production facility by a collection of operators, none of which are assigned to a particular machine or group of machines. It is referred to as Machining-Uber, or simply, M-Uber. In this scenario, each machine will send an alert when operator intervention is required. These alerts will be digitally distributed (e.g., by text message) to the assigned operator. This operator selection will depend on:

- geographic proximity to the machine in question (and, therefore, the travel time)
- other pending interventions
- the estimated time for the selected intervention
- the operator skill sets.

The objective function used to assign the operator to a selected intervention will be a global maximization of the cumulative time that all machines in the factory are engaged in part production (i.e., chip making in machining operations). To track operator location, radio frequency identification (RFID) tags can be embedded in a name tag, for example. The operator skill set will be archived in a database that is part of the software application. The operator availability will be set by monitoring his/her status through responses to other queries. Similar to Uber, the most feasible "driver" (operator) will be requested and the call will either be accepted or rejected. If rejected, the next best operator will be contacted. In this way, operator efficiency can also be tracked and reported.

ADVANTAGES

In the M-Uber approach, operators will not be limited to a single group of machines. This eliminates two scenarios that decrease factory efficiency:

- no machines in the cell require intervention
- more than one machine in the cell requires intervention.

In the first case, the operator is not needed at that time (operator idle). In the second, both machines will be idle and one will be idle longer than necessary because the operator can only service one at a time. With the conversion to a "floating" operator concept and the support of a "smart" assignment tool, we believe that M-Uber will offer the potential for improved responsiveness to machine stoppages, a corresponding increase in machine usage, and optimization of the number of required operators.

The economic impact of M-Uber, once matured, will be significant. It can be implemented in any manufacturing facility that uses CNC equipment; the domain includes aerospace, automotive, medical, heavy equipment, etc. It will minimize operator costs through its personnel optimization capability, while simultaneously enabling a quantitative method for assessing operator productivity. It will increase machine usage, which will result in higher part counts and, therefore, greater productivity and profit. Further, by continually monitoring machine status, it will serve as a "big data" resource that will contribute to preventative maintenance through trends in machine performance.

MOTIVATING EXAMPLE

The advantage of the M-Uber concept is demonstrated in Figs. 1-3. In Fig. 1, the traditional approach of one operator-to-two machines is depicted for six total machines (three operators). In Fig. 2, the M-Uber concept is implemented, again with three operators. In Fig. 3, after the distributions of machine usage have been studied, the optimized

result was found to be two, rather than three, operators. In the figures the machines are red and hatched if an intervention is required. They are green without hatching if operational (making chips). The operators' spatial location is identified by the position of the indicator (circle with operator number). The indicator is unfilled if the operator is idle and filled if engaged.

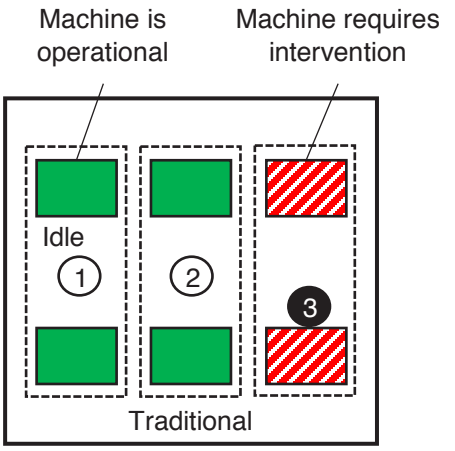

Figure 1: Traditional one operator-to-two machines setup. Operators 1 and 2 are idle and operator 3 is able to service only one of the two required interventions.

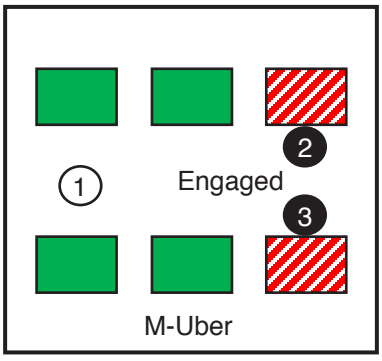

Figure 2: M-Uber setup. Operator 1 is idle, but operators 2 and 3 are able to service the two required interventions.

For the traditional approach (Fig. 1), it is observed that operators 1 and 2 are idle for the selected intervention state; operator 3 is only able to service one machine, while the other machine must wait until the first intervention is completed. For M-Uber (Fig. 2), operator 1 remains idle, but operators 2 and 3 are free to serve the two required interventions. After optimization (Fig. 3), M-Uber has matched the number of required operators to the intervention rate (on average) and productivity is increased. While this example is limited to six machines, the final solution will be implemented across the entire factory so the complexity is increased together with the potential for efficiency improvement.

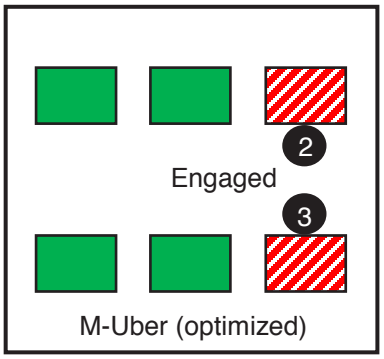

Figure 3: Optimized M-Uber setup. Based on machine usage data, the number of operators is optimized. Now two operators service the six machines.

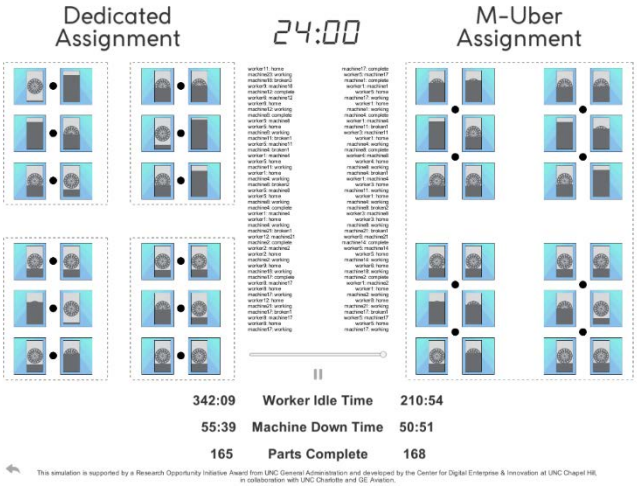

Figure 4: Simulation software that compares the traditional (dedicated) and M-Uber assignment techniques.

INITIAL RESULTS

An initial simulation has been programmed and demonstrated using data from a representative production facility; see the screen shot in Fig. 4. The interactive simulation shows the operators assignments graphically for four potential interventions:

1. tool change
2. anticipated maintenance
3. unscheduled maintenance
4. part complete, new setup.

The traditional (dedicated assignment) and M-Uber approaches are shown side-by-side. For the dedicated assignments, one person is assigned to two machines (12 operators, 24 machines). For M-Uber, eight operators are free to float between the 24 machines.

The simulation enables the cumulative worker idle time, machine down time, and number of parts produced to be compared over a fixed time period (24 hours is shown in Fig. 4). Based on initial simulations, it is shown that eight operators in the M-Uber approach are more productive than 12 operators using the traditional assignment strategy.

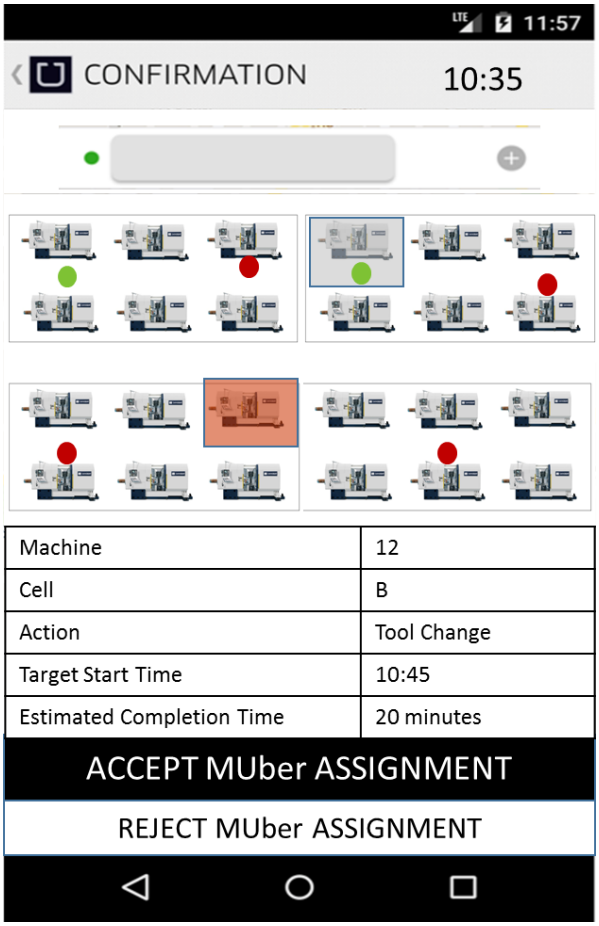

Figure 5: M-Uber assignment application. The assignment request will be delivered to the best operator via a handheld device.

As noted, the best operator is alerted when an intervention is required. This message will be sent via a modal device and include the following information:

- machine number
- cell number
- action required (intervention type)
- targeted start time
- estimated completion time.

Using the application, the operator will be able to accept or reject the assignment (similar to an Uber driver). The application concept is displayed in Fig. 5.

ACKNOWLEDGEMENT

This research was supported by a Research Opportunity Initiative (ROI) award from the University of North Carolina General Administration.

CONCLUSIONS

This paper provides a description of the new M-Uber approach to operator assignment in machining facilities. In this approach, an operator is not limited to servicing a single group of machines (e.g., a dedicated operator is assigned to two specific machines). A floating operator concept, where the operator is free to service any machine intervention in the facility, is combined with an Uber-type assignment tool to provide improved responsiveness to machine stoppages. The result is a corresponding increase in machine usage and an optimization of the number of required operators.

Milling of high-alloyed Steel Molds for Precision Injection-Molding of Microfluidical Parts

Joerg Schmuetz
Department VIII, Mechanical Engineering
Beuth University of Applied Sciences
Berlin, Germany

INTRODUCTION

Today, a large variety of microfluidical products is replicated efficiently by molding techniques. Microfluidical chips are increasingly used for blood analysis, cancer research, development of new pharmaceuticals and in-vivo drug delivery [1,2]. These microfluidical chips typically incorporate microscopic channels, reaction chambers or shallow holding-wells for cell growth. Well defined geometries and near-optical quality surface finishes are required to enable unobstructed fluid flow and inspection. Various techniques (e.g. Lithography, Microcontact Printing) have been proposed to manufacture molds or specific functional surfaces for Lab-on-a-Chip applications [3].

When small numbers of replications are needed, molds are industrially milled into ductile materials (e.g. Aluminum). With growing market demand, molding tools with a higher wear-resistance are needed. In this paper, the milling of high-alloyed steel molds for microfluidical parts is investigated.

Mold inserts with typical surface topographies (negative geometries for microscopic channels and larger wells) are designed and manufactured in a series of ball-end- and torus--milling operations in order to study chip- and burr-formation, surface roughness and geometrical accuracy of the generated microscopic structures.

The geometry of a typical tool insert is shown in figure 1. In this example, cylindrical holding wells with a diameter 3 mm and a height of 2 mm are connected with channels of various widths. The finest channel has a width of 150 μm at a uniform height of 1 mm.

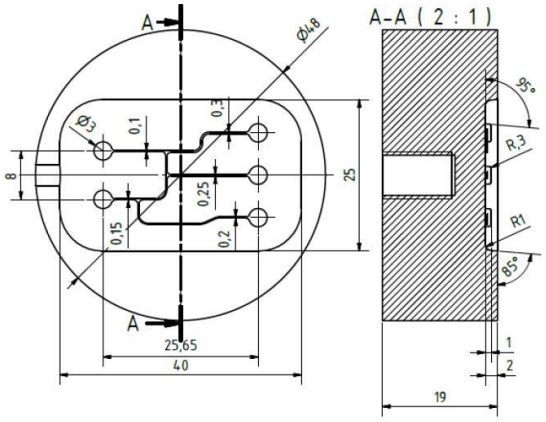

FIGURE 1. Geometry of a tool insert for the injection molding of a Lab-on-a-Chip [4]

In order to ascertain the minimal structure sizes in the milling of hardened high alloyed steel, a specimen with a separable machined surface is designed and manufactured prior to milling the actual molds.

WORKPIECE MATERIAL AND HEAT TREATMENT

The high-alloyed steel Boehler ISOPLAST M340 is chosen to manufacture various tool inserts with Lab-on-a-Chip molds. According to previous milling experiments with the same unhardened material, the generation of microstructures with lateral dimensions of 50 μm and maximum aspect ratios of 2:1 is feasible [5], but both burr formation and surface qualities need to be improved by hardening the workpiece material.

Therefore, the molds and the related specimen are tempered at 1.100 °C with a holding time of 30 minutes in a Nabertherm “LT-16” oven (9kW heating power) under atmospheric conditions before quenching in an oil-bath.. After quenching, the workpiece is annealed for 2.5 hours at 300° C in the same preheated oven.

The heat-treatment is performed after rough cutting the workpieces with all their microscopic features to a uniform machining allowance of 0.2 millimeters. This procedure is intended to achieve an evenly hardened surface and also ensures protection from oxidation.

Before heat-treatment, a hardness of 23.1 HRC is measured. Tempering, quenching and annealing yields a hardness of 43.3 HRC. Even though a considerable increase in surface hardness is achieved, the result is below the 58 HRC indicated in the material data sheet.

In future experiments, the size and temperature of the oil bath will be reconsidered to achieve faster cooling and a more homogeneous martensitic transformation. To rule out growth of secondary grains in tempering, the holding temperature will be reduced by 50°C.

MILLING SETUP

The milling experiments are carried out under dry cutting conditions (no cooling lubricant) on a Mikron HEM 500U milling machine with 3+2 numerically controlled axes and an 18.000 RPM spindle. In this standard U design, the table is mounted in a swing which allows for rotation and swivelling (B- and C-axes), while the three linear motions in x-, y- and z are performed by the spindle (cf. Fig 2).

The workpiece is fixed to a rectangular base plate, which enables quick changeovers from machining to metrology and back. The position of the workpiece is aligned to the machine by a tactile probe after chucking the base plate to the machine.

FIGURE 2. Geometry of a tool insert for the injection molding of Lab-on-a-Chip [4]

TOOLS

A set of tools is chosen for rough cutting and finishing of the molds and specimens. Rough cutting is performed in the unhardened material, using a 6 mm ball end mill and a torus mill with a diameter of 3 mm.

After hardening and annealing, the remaining machining allowance is milled out under dry cutting conditions with a set of hard metal torus mills, ranging from 3 to 1 mm in diameter. The two smaller torus mills are coated with TiAlN (cf. Fig. 3).

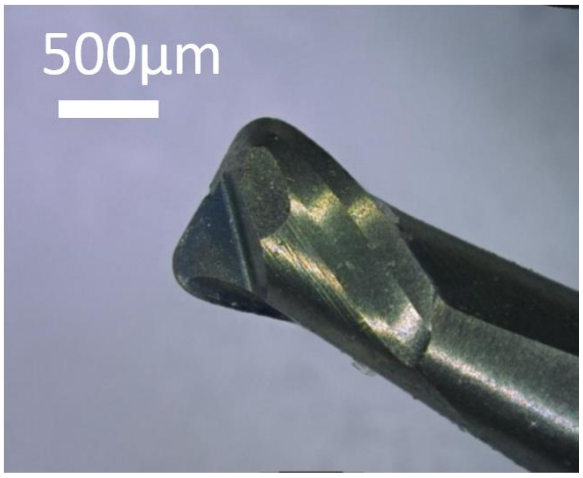

FIGURE 3. TiALN-coated torus mill with a diameter of 1 mm and a 0.2 mm nose radius. [4]

SPECIMEN WITH SEPARABLE LINEAR MICROSTRUCTURES

In order to investigate the minimal structure sizes in micro-milling of hardened M340 Isoplast steel, a specimen with linear microstructures is manufactured (cf. Fig 4).

The cubic specimen is assembled from two plane-ground halves, which are screwed and bolted together. After assembly, an array of linear lands with a height of 0.6 mm is rough-cut into the top of the assembled block so that the linear lands are perpendicular to the separation plane of the specimen. In rough-cutting, a machining allowance of 0.2 mm is left for heat treatment and finishing. Then, the specimen is hardened and annealed to 43.3 HRC as described previously.

After the heat treatment, the array of linear lands is finished by using the set of torus mills in Figure 3. In the final cut with the d = 1 mm torus mill, a lateral feed velocity of v_f = 200 mm/min is set while utilizing the maximum 18.000 RPM of the spindle. The uncut chip thickness is 0.1 mm.

Eventually, the two halves of the machined surface fall apart, after cutting through the specimen by wire EDM in a plane just above the screw and bolts.

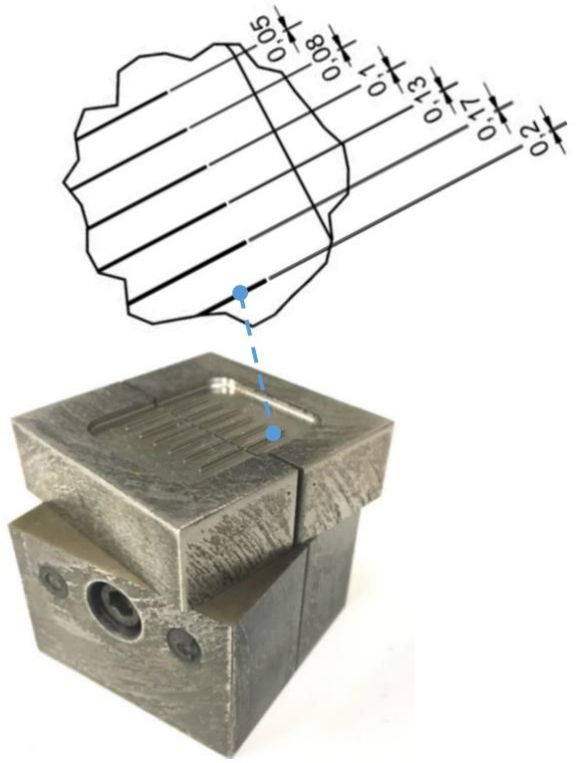

FIGURE 4. Specimen with vertically separable, linear microstructures. The height of the microscopic lands is 600 µm [4]

The cross sections of the milled microscopic lands are inspected in the separation plane by means of a KEYENCE VHX-S50 digital microscope (cf. Figure 5). The microstructures show no evidence of plastic deformation. Even the finest microscopic lands with a width of 50µm are produced well in the hardened steel. This leads to the assumption, that even smaller microstructures can be milled into the hardened M340 steel.

It is observed, that chip material is clinging to one flank of the microstructure, while the other flank does not show any sign of adherent chips and there is no visible burr formation or distortion.

Adherent chip material is only found, when down-milling out of the inspected plane (Fig 5 and 6). Presumably, the chip material is not separated from the part due to the brief interruption of cut that occurs, when the tool passes from one half of the specimen into the other.

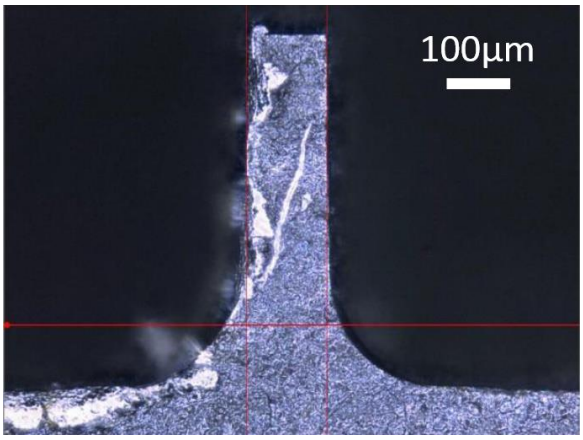

FIGURE 5. Face view of the separation plane with a milled microstructure. [4]

In die-making, well defined sidewalls are also needed. Inspection by digital microscope shows that both sidewalls and the adjoining radii are well defined [cf. Fig. 6].

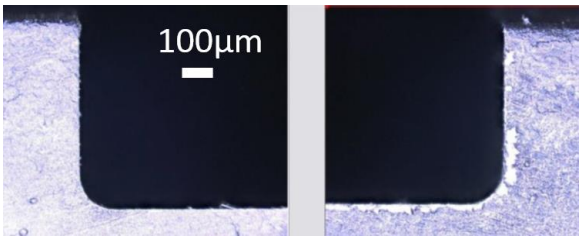

FIGURE 6. Face view of the separation plane with left and right shoulder of the machined surface. [4]

CHIP FORMATION

When cutting with ball-end- or torus-tools, the contact area of a single cutting edge with the workpiece material has the shape of a calotte [6].

Chips collected in finishing cuts with a d = 1 mm torus mill at an uncut chip thickness of 100 μm appear to be regularly shaped, compressed segments of a calotte, indicating that stable cutting conditions are reached (cf. Fig. 7).

One side of the chips clearly shows traces of shearing and segmentation, while the other side of the chips is smooth after contact with the rake face of the tool.

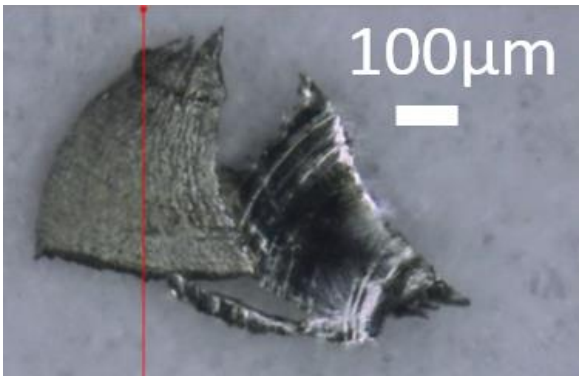

FIGURE 7. Chips formed in torus milling. [4]

TOOL PATH GENERATION AND SURFACE ROUGHNESS

The entire process chain is set up to enable quick design alterations and minimized machining times by applying CAD/CAM-techniques. Conventionally available CAM-operations, however, have to be optimized for the milling of microscopic structures and for the use of micro-milling tools in particular.

Special vertical infeed strategies and cutting paths are needed to protect both fragile tool edges and the integrity of the generated surfaces, respectively.

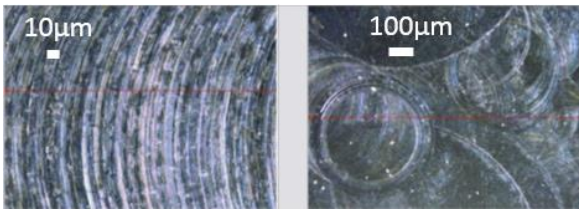

FIGURE 8. Evenly milled surface and uneven surface with tool rest- and reversal-marks. [4]

For vertical infeeds (z-direction), helicoidal tool paths are found to be most advantageous in order to protect tool edges. Where a helicoidal infeed motion is impracticable for geometric reasons, a downward ramp may also be applied.

When the torus mill is moving sideways in a uniform way, a regular surface pattern is found, that is commonly associated with face milling (cf. Fig. 8, left). Here, a surface roughness of R_a = 0.15 μm or R_z = 0.85 μm is measured, using a Perthen stylus probe [4].

For microfluidical applications, mechanical or electro-chemical polishing appears to be necessary to achieve a more uniform surface pattern without cutting marks. Previously known techniques for the mechanical polishing of tool inserts with microscopic features [7] need to be adapted to the polishing of hardened steel.

Moreover, conventional milling cycles often incorporate a reversal of direction while the tool is cutting. When the tool is moving laterally along the workpiece, the tool shaft is slightly flexed in one direction. A reversal of the movement and a very minute standstill releases the Flexure, thus leading to restmarks, which are found to be a few microns deep (cf. Fig. 8, right).

LAB-ON-A-CHIP MOLD INSERT

After establishing milling procedures to generate lateral structure sizes down to 50 μm, a tool die for the microfluidic chip is eventually milled into the hardened M340 steel [Fig. 9]. The exact geometries are described in Figure 1.

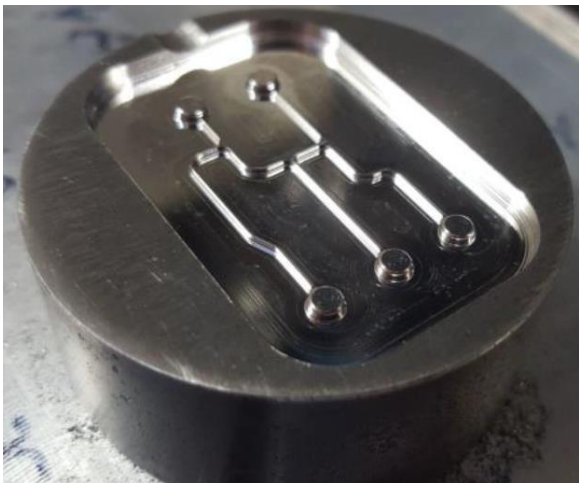

FIGURE 9. Mold Insert. [4]

The microscopic features are inspected by a Keyence digital microscope. Molds for holding wells as well as mold structures for meandering channels are well defined. With the tool feed motions derived from machining the separable specimen, the entire mold is milled with one set of tools and without breaking a tool edge. The coated hard metal mills are found to be well suitable for milling the hardened M340 Isoplast steel under dry cutting conditions.

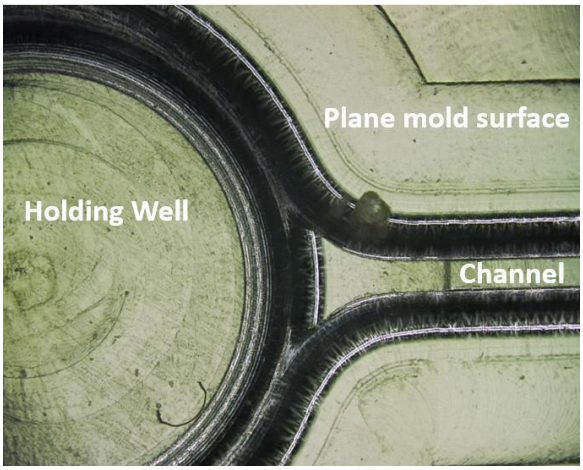

FIGURE 10. Section of the mold insert with mold for holding-well and adjoining microfluidic channel (top view). [4]

CHALLENGES IN MOLDING WITH CYCLIC OLEFIN COPOLYMER (COP)

Cyclic Olefin Copolymers (COP) appear to be particularly suitable for the mass production of Lab-on-a-Chip components, because they are translucent and less hygroscopic than other polymer materials.

On a macroscopic scale, the mold filling process, filling times and temperature distributions at different filling stages are predictable by the application of standard injection molding numeric simulations.

Fig 11 shows different filling stages as simulated for the injection molding of COP with a melt temperature of 270° C and a maximum injection pressure of 1.800 bar at the nozzle of the injection machine.

On a microscopic scale however, alternative simulation techniques are considered in order to fully understand melt flow, heat convection, heat conduction and solidification around microstructures [8]. In ongoing studies the Finite Volume Elements method is applied to simulate mold filling and solidification in molds with microscopic structures.

Since COP is comparably brittle, demolding and shrinkage around microscopic geometries are further issues that need closer investigation.

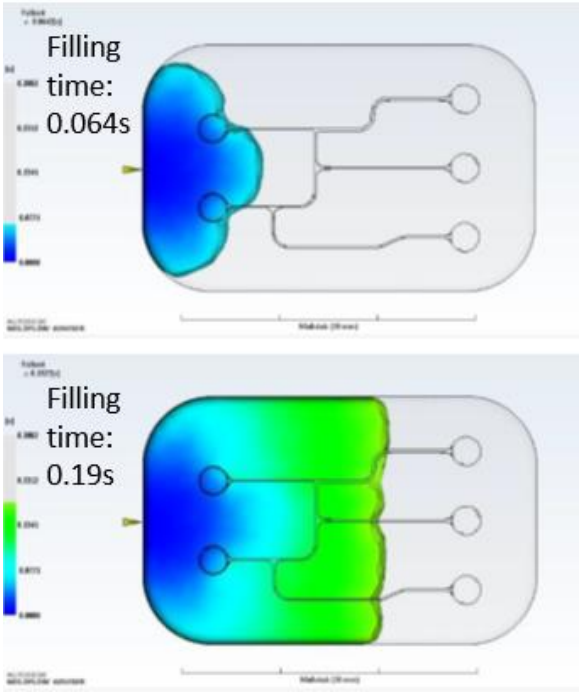

FIGURE 11. Simulation of Mold filling process, using Moldflow Software by Autodesk®. [4]

CONCLUSIONS

Molds for microfluidic applications with channel widths down to 50 μm are successfully milled in hardened M340 ISOPLAST steel, which is a highly wear resistant steel with a low susceptibility for corrosion.

In future investigations, the heat treatment procedure (i.e quenching and annealing) will be improved to yield a still higher hardness of up to 58 HRC.

Since the finishing cuts are performed in the hardened material, burr formation or plastic deformation are not observed by means of an optical microscope. Chips from finishing cuts clearly reveal traces of shearing and segmentation, indicating, that suitable cutting conditions are chosen.

Tool path generation and infeed strategies need particular consideration in torus- and ball-end-milling with small tool diameters in order to protect fragile tool edges and to avoid tool reversal marks on the milled surface.

Dry cutting conditions are well suited for the milling of the hardened tool inserts. In this case dry cutting conditions are preferred to prevent agglomerations of chips, which tend to clog microscopic structures in machining.

Even though a median roughness of R_a = 150 nm is reached, polishing is suggested to smooth the typical periodic roughness pattern produced in milling.

The melt flow and solidification in tool inserts with microscopic structures is hard to predict [8]. In ongoing investigations, the Finite Volume Elements method is applied to understand the replication of microstructures for optical- and microfluidic purposes.

REFERENCES

[1] Schimek, K. et al.: “Integrating biological vasculature into a multi-organ chip microsystem”. LabChip 13/2013, p. 3588-3598..

[2] Marx, U. et al.: “’Human-on-a-Chip” Developments: A Translational Cuttingedge Alternative to Systematic Safety Assessment and Efficiency Evaluation of Substances in Laboratory Animals and Man?”. ATLA Vol. 40, 2012, p. 235-257.

[3] Stoytcheva, M; Zlatev, R. (Editors): “Lab-on-a-Chip Fabrication and Application”, p. 90-93. Intech Open, 2016.

[4] Demir, A. et al. “Fräsen eines Formeinsatzes – Untersuchung des Hochgeschwindigkeitsfräsens”. Bachelor Project Report, Beuth University of Applied Sciences Berlin, 2016.

[5] Schmuetz, J.; Krueger, S.; Mallock, M.: „High-speed milling to produce high-alloy steel inserts”. ETMM European Tool & Mould Making, Vol. XVIII, 06/2016, Vogel Business Media, Wuerzburg.

[6] Schulz, H.; Hock, S.: “High-Speed Milling of Dies and Molds – Cutting Conditions and Technology”, Annals of the CIRP, Vol. 44/1/1995, p. 35-39.

[7] Gessenharter, A.: “Polieren strukturierter Formeinsätze für optische Bauteile“. Forschungsberichte aus der Stiftung Institut für Werkstofftechnik Bremen, Band 31. Shaker-Verlag, Herzogenrath, 2006.

[8] Schmuetz, J.; Heinrich, Th.: “Infuence of Polymer Melt Properties in Precision Injection-Molding of Microfluidical and Optical Parts”. Proceedings of the ASPE 2015 Annual Meeting in Austin, Texas, USA. pp. 591-594.

Fiber Based Tools for Precision Polishing Applications

Hossein Shahinian[1], Mohammed Hassan[1,2], Harish Cherukuri[1], Brigid Mullany[1]
[1]Department of Mechanical Engineering and Engineering Science
University of North Carolina at Charlotte
Charlotte, North Carolina, USA
[2] Mechanical Engineering Department, Faculty of Engineering
Helwan University, Cairo 11792, Egypt

INTRODUCTION

In this article, research on novel fiber based polishing tools is presented. The motivation for developing such tools, was to provide tooling capable of reducing mid-spatial frequency (MSF) errors on precision freeform and aspherical optics. MSF errors for most optical applications can be best described as periodic features with a spatial wavelength of 2 mm to 0.08 mm. The errors promote the scatter of light in a relatively small angle regime causing stray light and the appearance of flare on images produced by optics containing them [1-3]. MSF errors on precision optics are inevitable, given they are typically produced by sub aperture manufacturing technologies. Minimization of MSF errors to meet costumers specifications induces significant additional processing and cost for the fabricators, [4, 5]. Yet, solutions for MSF error reduction are very limited and incremental [6].

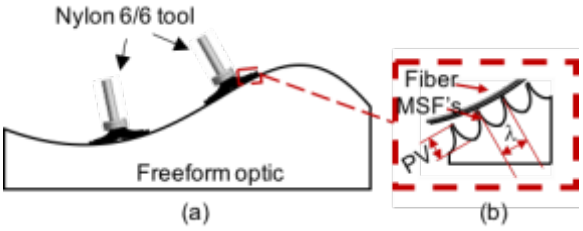

FIGURE 1. Fiber based tools original vision; (a) large scale conformity (b) small scale stiffness

The idea of using fibers to reduce these MSF errors originally stemmed from two inherent physical properties that fibers offer; 1) with a suitable combination of material and geometry, they can conform to any freeform shape on a large scale; and 2) they can maintain comparatively high stiffness on a local scale containing the MSF errors, see Fig.1. This local stiffness intuitively implies higher loads, and hence polishing rates, at the peaks of the MSFs, Fig. 1(b), thereby reducing the overall peak-to-valley (PV) magnitude of the features. The decrease in the PV has the implication of decrease in the slope of the errors, and as a consequence decrease in the amount of stray light.

The typical tooling configuration used in this article resembells a flat end paint brush, whereby the fibers are placed circumferentially, and aligned with the tool shank. In this case tweleve Nylon 6/6 fibers, each having a diameter of 1.6 mm, were used to create the tool. The tool is then lowered down towards the workpiece, causing the fibers to fan out, and establishing an anulus of contact with the workpiece, see Fig. 2.

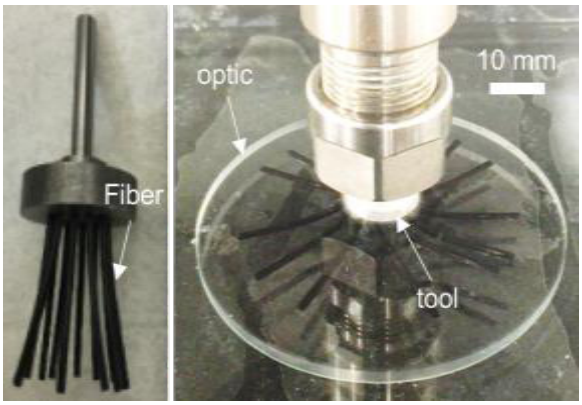

FIGURE 2. Flat-end tool design;(a) disengaged (b) engaged with workpiece

For any polishing tool to qualify for a precision polishing tool, three main requirements should be met; (1) the tool is capable of removing material in a 3-body abrasion configuration, (2) the surface finish of the part post the polishing operation should be in the order of < 5 nm rms to ensure low light scattering, and (3) a stable material removal function is requried to to achieve form errors less than $\lambda/4$, (λ the wavelength of the incident electromagnetic wave). In works published previosuly [7-10], it was shown that these requirements can be satisfied by fiber based tools. The ability of thses tools to reduce MSF features with sinosoiudal geometries and spatial wavlength of 1 mm was also demonstrated [9, 10].

In order to further investigate the ability of fibers based tooling to reduce MSF errors, a combined FE-analytical model, previously introducted in ref [4], is used to further evaluate the impact of fiber geometry on its ability to reduce MSF features. Additional testsing on a germaniun sample is described providing further evidendence of the tools ability to reduced unwanted MSF errors.

A COMBINED FE-ANALYTICAL MODEL

An analytical beam model that depends on FE results for beam loads (discussed in greater detail in [1] and [4] and summarized below) is used to study the suitability of various fiber geometries in reducing MSF features. The beam model consists of a simply supported beam with four supports and cross-sectional geometry identical to that of the fibers (Fig. 3). The supports represent the peaks of the MSF features in this idealized beam model. The beam is subjected to a shear force and moment at one end. The deflection of the beam due to these forces is used to evaluate the ability of a given fiber geometry to reducing MSF features. A negative deflection of the beam (deflection below the longitudinal direction of the beam) is considered undesirable since a fiber with a negative deflection between the peaks of the MSF features has the potential to increase MSF features. More specifically, it is desired to keep the deflection of the beam in the downward direction to less than 50 nm.

FIGURE 3. Beam model used for the MSF reduction studies.

The force and the moment loads acting on the beam are obtained from a three-dimensional finite element model [4] developed to study the interaction between a single fiber and the workpiece as the fiber is pushed down on the workpiece with a prescribed displacement based on experiments. The model was used to study the contact pressure and contact lengths that have a direct bearing on material removal rates. The deformed shapes of the fiber just before contact is established and right after complete contact is established are shown in Fig. 4. The length of the beam in the beam models is taken to be the length of the horizontal part of the fiber in Fig. 4 (right). The shear force and moment acting on one end of the fiber is the internal shear force and the moment at the corresponding location in the horizontal part of the fiber in Fig. 4 (right).

The beam is taken to be isotropic and linear elastic with Young's modulus and Poisson's ratio as 2.2 GPa and 0.4 respectively. For the workpiece, these quantities are 70 GPa and 0.3.

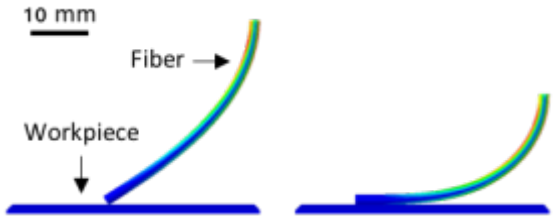

FIGURE 4. Finite element model of fiber-workpiece interaction: (left) fiber profile at initial contact (right) fiber profile post the completion of contact.

The beam model is used to study the effect of five different fiber geometeries on the maximum deflection in the downward direction and therefore, on the fibers' ability to reduce MSF features. The cross-sectional area and the beam length are the same for all the cases. The diameter of the fiber with the circular cross-section is 1.6 mm. The four additional cross-sections considered and their dimensions are shown in Fig. 5. The stiffness of each fiber (corresponding to the initial loading in the FE models to bend the fiber), calculated from $k = \frac{3EI}{L^3}$, is depicted in Fig. 6.

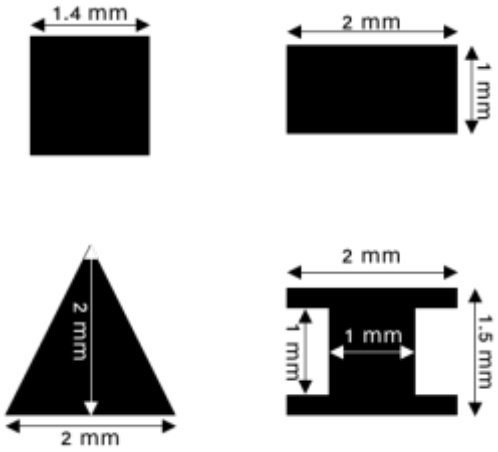

FIGURE 5. Various geometries considered in addition to the circular cross-section. The dimensions are based on constant cross-sectional area.

As mentioned above, the force and moment loads for the beam model are obtained from the FE model for each fiber geometry. The resulting deflection of the beam is calculated using the elementary beam theory. The results for maximum negative deflection are shown in Fig. 7. The maximum deflection below the neutral axis for the circular fiber occurs between supports 2 and 3 and is approximately 10 nm.

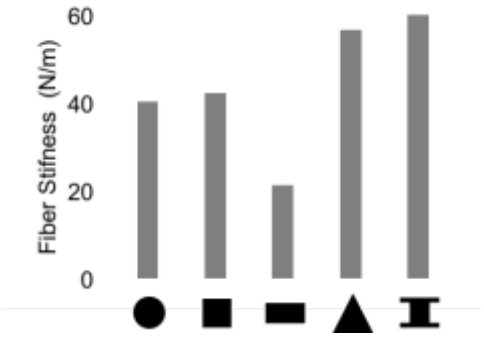

FIGURE 6. Fiber Stiffness vs cross section geometry

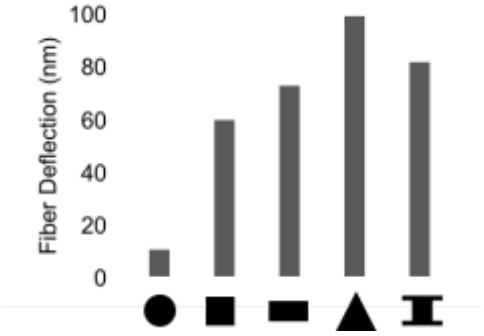

FIGURE 7. Maximum fiber deflection in the downward direction to 1 mm MSF spacing Vs cross section geometry.

For all the other geometries the maximum deflection below the neutral axis occurs between supports 3 and 4 and the magnitudes are much larger. Since the smaller the maximum downward displacement, the better the ability of the fiber to reduce MSFs, it can be concluded that for the geometries evaluated, the circular geometry is the best option for MSF error reduction. Upon comparing the stiffness values in Fig. 6 with the fiber deflections in Fig. 7, it is clear that correlation between the two is not immediately evident. A possible reason is that the fiber stiffness expression used is for point loads and not for the combined shear and moment loads. Furthermore, it doesn't take into account the possible inelastic deformations in the fibers. These issues are currently being investigated since any any correlation between fiber stiffness and the ability to reduce MSF features is of practical importance in the selection of fibers for polishing.

EXPERIMENTAL SETUP

MSF Sample

As discussed in the previous section, the circular Nylon 6/6 fiber tool, shows sufficient stiffness to MSF features of wavelength smaller than 1 mm. Previously [9, 10], success in removing MSF's from samples containing sinusoidal features was demonstrated. In this work, this ability is explored on MSF features with a cusped shaped geometry. The cusps are more reflective of the features found on surfaces generated by ultra-precision diamond turning operations; a process of high relevance to the precision optics community. In fact, the cusps imparted on the planar germanium workpiece used in testing were machined by a Nanotech 350 FG ultra-precision diamond turning machine. The sample has diameter of 65 mm, a thickness of 6 mm, while the generated cusps have a spatial wavelength of 1 mm and an approximate PV value of 200 nm.

Polishing Tool

The polishing tool has the same configuration as shown in Fig. 2. The fibers are made of Nylon 6/6 manufactured by Hahl Pedex®. The tool head is machined and 12 holes are drilled on the head that will serve as the fiber holders. The fibers are cut to 25 mm in length and glued to the aforementioned holes. The fiber has a diameter of 1.6 mm, and as it fans out over the workpiece it will have an approximate footprint size of 55 mm.

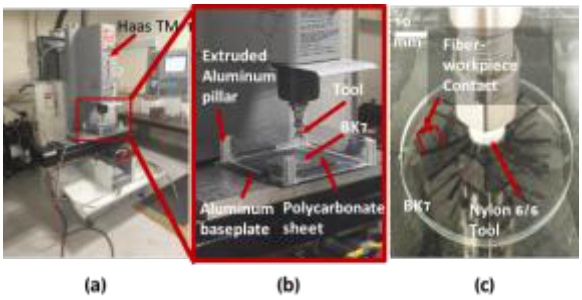

FIGURE 8. Polishing test bed (a) CNC machining center (b) Nylon 6/6 tool and surrounding slurry (c) Tool engaged with BK7 glass

Polishing Test Bed

The polishing test bed consist of a slurry bath attached to the table of the Haas-TM1 CNC milling machine. The part is fixed to the base of the slurry bath and is always submerged in polishing slurry, Fig. 8. To enable the tool run smoothly over the entire workpiece, the part is inserted into a 6 mm deep circular recess that was milled into 6.5 mm thick sheet of polycarbonate; this enables the sample to lie flush with the polycarbonate surface, providing a continuous surface for the tooling to transverse. The tool is attached to the machine tool's spindle. The silica based polishing slurry (UltraSol® 550) is mixed with H_2O_2 (weight ratio of 1:100). The H_2O_2 component of the slurry serves as the chemical reactor agent to promote germanium removal. The abrasive particles are nominally 65 nm in size [11].As outlined in ref [10] this is believed to enhance MSF reduction by discouraging material removal from the lower regions of the MSF features.

Supporting Metrology

The measurement of the sample is done with a Zygo Verifire AT1000 laser Fizeau interferometer. The 101.6 mm aperture size of the instrument enables the full aperture measurement of the Germanium sample. The instrument has a detector of 1000 × 1000 pixels. The implication is that the instrument is capable of measuring features with a 200 μm lateral scale (Nyquist limited). The reference flat used in the interferometer has a surface error less than λ/20 (λ = 633 nm).

MSF REDUCTION TEST AND RESULTS

The testing on the germanium sample is operated on two straight polishing paths, orthogonal to each other. On each path the tool is traveresed back and forth for 100 passes, with a spindle speed of 100 rpm and tool feed rate of 3 mm/s. The paths are selected as such to have a relatively uniform removal rate at the center of the workpiece.

Figure 9 shows the results of the testing. Comparing the Fizeau interferograms of the pre and post plishing state of the sample, Fig. 9(a) and Fig. 9(b), clear removal zones can be observed. While the removal seems to suffer from irreguralrities, this is not an concern as the polishing tool path, as well is the sample fixturing to the test bed were not optimized in this proof of concept test.

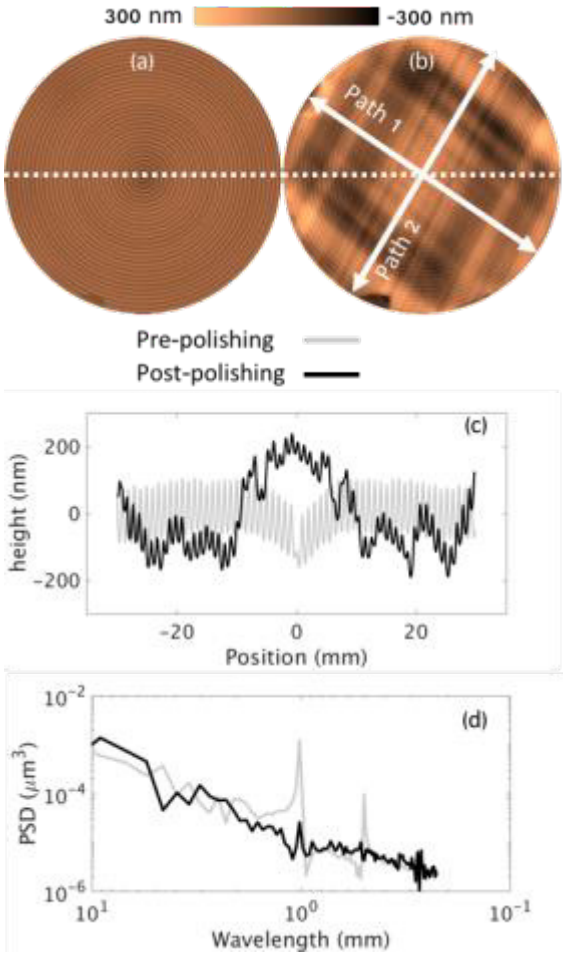

FIGURE 9. MSF sample polishing results; (a) pre, and (b) post polishing Fizeau interferograms, (c) pre and post polishing 2D profiles on the dashed lines, (d) average PSD of the pre and post polishing interferograms

In Fig. 9(c) linear profiles obtained from the interferograms, show obvious reduction of the PV of the cusp features. This indicates the success of the tool in reducing the MSF errors. Further verification of this success is provided in Fig. 9(d). The power spectral density (PSD) of the pre and post polishing interferograms in Fig. 9(d) clearly shows a considerable drop in their peak in the 1 mm wavelength regime. This promising result, clearly validates the modeling results, i.e. the Nylon 6/6 fiber, has the potential of reducing MSF errors.

CONCLUSIONS

The ability of fiber based tools to reduce pre-existing MSF errors on precision surfaces was demonstrated. Although proof of concept is provided, additional process development efforts

are needed to further optimize and fine tune the process for commercial applications. The potential of a combined FE-analytical model to assist in tool optimization is presented. Through this modelling approach, it should be possible to evaluate the impact of a fiber's cross sectional geometry on its resistance to local deformation between idealized MSF features. Initial testing confirmed the results for a fiber with a circular cross section. Additional modelling work is ongoing to better understand the fiber geometry-workpiece interactions, i.e. fiber-workpiece contact lengths, pressure distributions etc.

In summary, the presented tooling option offers a solution for critical MSF reduction on freeform surfaces, while the outlined modeling approach provides a design tool with the potential to expedite optimal tooling design. Future work is focusing on tooling design.

ACKNOWLEDGEMENTS

This research was partially supported by both the NSF I/UCRC Center for Freeform Optics (IIP-1338877 and IIP-1338898), and by NSF's IR/D program. Additional thanks to Dr. J. Owen for machining the germanium samples used in testing.

REFERENCES

1. Hull, T., et al. *Mid-spatial frequency matters: examples of the control of the power spectral density and what that means to the performance of imaging systems*. in *Proc. SPIE*. 2012.
2. Youngworth, R.N. and B.D. Stone, *Simple estimates for the effects of mid-spatial-frequency surface errors on image quality.* Applied Optics, 2000. **39**(13): p. 2198-2209.
3. Noll, R.J., *Effect of mid-and high-spatial frequencies on optical performance.* Optical Engineering, 1979. **18**(2): p. 182137-182137-.
4. Parks, R.E. *Specifications: Figure and Finish are not enough*. in *Proc. SPIE*. 2008.
5. Aikens, D., J.E. DeGroote, and R.N. Youngworth. *Specification and control of mid-spatial frequency wavefront errors in optical systems*. in *Optical Fabrication and Testing*. 2008. Optical Society of America.
6. Zhang, J., F. Wang, and G. Wang. *Multi-tool sub-aperture polishing high-slope asphere with low mid-spatial frequency errors*. in *7th International Symposium on Advanced Optical Manufacturing and Testing Technologies (AOMATT 2014)*. 2014. International Society for Optics and Photonics.
7. Shahinian, H., H. Cherukuri, and B. Mullany, *Evaluation of fiber-based tools for glass polishing using experimental and computational approaches.* Applied Optics, 2016. **55**(16): p. 4307-4316.
8. Shahinian, H. and B. Mullany, *Optical Polishing Using Fiber Based Tools.* Procedia CIRP, 2016. **45**: p. 183-186.
9. Shahinian, H. and B. Mullany. *Fiber Based Polishing Tools for Optical Applications*. in *Optical Fabrication and Testing*. 2017. Optical Society of America.
10. Shahinian, H., et al., *Fiber based tools; material removal and mid-spatial frequency error reduction.* Applied Optics, 2017. **Accepted for Publication**.
11. *Ultra-Sol 556.* Eminess Technologies Inc., Monroe, North Carolina, USA.

On Gyroscope Mechanism for Mobile Machining Machine

Jongyoup Shim, Segon Heo, Jooho Hwang and Seung-Kook Ro
Ultraprecision Machines and Systems Lab.
Korea Institute of Machinery & Materials
171 Jang-dong, Yuseong-gu, Daejeon, Korea

INTRODUCTION

For machining large parts in manufacturing generally a large machining machine is used with large supporting frame structure such as the gantry structure. If there are constraints on the space for the machine when a ship or an aircraft are to be repaired it is difficult to build the machine structure at the location of the part. The flexible manufacturing demands in the aerospace industry require more flexible, automated, mobile and intelligent machining machine. And the extreme environment such as nuclear power plant and space requires different strategy for manufacturing and machining parts. A mobile machining machine is proposed to perform those missions. It does not have supporting structures and guide mechanisms for movable parts. It is attached to the parts to be machined. It can crawl on the part's surface and machine it. In order to realize it the mobile mechanism, machining (manufacturing) head, dimensional metrology method and system integration (with CAM (Computer Aided Manufacturing) strategy) technology should be developed. Considering the mobile machine when the mechanical cutting method is used there is a need for decreasing cutting force transferred to the machine. The cutting force will affect the sticking stability and machining quality. Due to the limitation on the machine weight it is difficult to design stiff and rigid machine structure and this can increase the sensitivity to the external forces.

In this paper an external force absorbing method for the mobile machining machine is presented. The gyroscope which has spinning flywheel inside is used for the function. The CMR(Control Moment Gyroscope) is used for controlling the posture of a satellite and suppressing building vibration. The gyroscopic moment produced by the physical nature is implemented for those applications because the gyroscopic moment can be produced without interacting with external objects. For the first application of the gyroscope mechanism the drilling head is considered.

The theoretical equation formulation for simulating the torque absorbing principle and simulation results are presented. And also drill head design issues and related simulation results are also shown. For the first check of the operation principle a drill head with gyroscope has been manufactured and the preliminary experimental results are also presented.

MECHANISM DESIGN AND WORKING PRINCIPLE DESCRIPTION

The drilling head includes a drilling spindle, a gyroscope mechanism and the connecting part which can allow the head to rotate freely relative to the machine structure. With this configuration theoretically almost no cutting torque is transferred to the mobile machining machine. In order to explain the operation principle the first step is to imagine that there is no gyroscope in that drilling head. When the machine starts to drill into the part the reacting torque by the cutting process make the head rotate freely due to the connecting part. The connecting part can be designed by rotational ball bearing and connects the head to the machine. Therefore the free rotation makes it impossible for the machine to perform the drilling work.

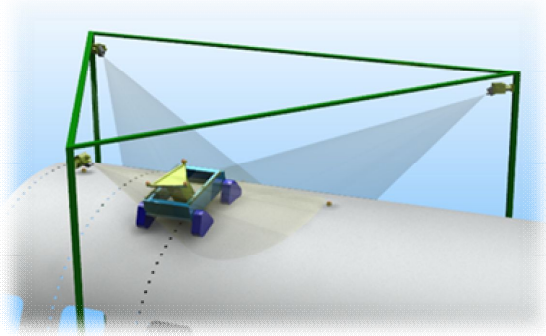

FIGURE 1. The mobile machining machine concept drawing showing the mobile machine and position/pose measurement system.

However, if the gyroscope mechanism is attached to the head body the drilling torque is absorbed and therefore the drilling work can be done. And considering the connecting part even though the drill process is being done no cutting torque is transferred to the machine structure.

According to the attaching configuration of the gyroscope mechanism it can be concluded that there are two kinds of mechanism configurations. The first one is that the position of the mechanism is the top of the drill head and the gyroscope spinning axis is perpendicular to the axis of the drill. The second one is that the mechanism is attached to the side of the head.

In order to study physically the operation of the mechanism proposed and design those parameters needed the physical modeling should be performed and the simulation should be done.

MECHANISM MODELING AND SIMULATION

For the first check of the mechanism the simpler configuration is selected and the modeling is done for the top-positioned gyroscope case. The physical modeling starts with the equation of the motion of the housing (spindle housing) including reaction forces by the motor and the gyroscope mechanism. The motor torque is due to the drilling torque and the inertia of the shaft. Neglecting the inertia effect of the shaft (and also the friction by the bearing) the motor torque is equivalent to the drilling torque during machining. And the more important reaction is from the gyroscope mechanism and this reaction force is the drill torque absorbing force. Modeling the housing by the moment of inertia, angular acceleration and torque the resulting equation can be formulated by the equation (1)

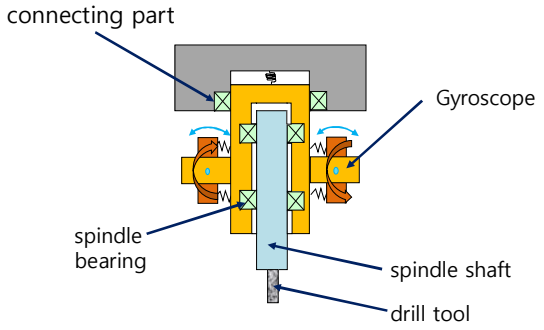

FIGURE 2. The drilling machining module with gyroscope mechanism which is attached to the side of the module.

$$M_{motor} - M_{gyro} = I_H \alpha \tag{1}$$

M_{motor} is the reaction torque by the motor and M_{gyro} is the reaction torque by the gyroscope mechanism. The I_H is the moment of inertia of the housing and the α is the acceleration.

The next modeling part is related with the gyroscope mechanism. Generally the gyroscope mechanism is composed of three parts which are the outer ring (gyroscope frame), inner ring (gimbal) and the spinning shaft with a rotor. The rotor is the main part which generates the gyroscopic moment for absorbing the drill torque. The rotor is rotating about the spinning shaft and the moment of inertia of the rotor and the rotation angular velocity are the important factors for the absorbing moment generation. The gyroscope frame is rigidly attached to the housing and the inner ring (gimbal) is attached to the frame with a rotation axis. The rotation axis can be realized by a rotational bearing and therefore the gimbal has one-degree-of-freedom motion.

$$M_{gyro} - M_{inner} = I_{frame}\ddot{\phi} \tag{2}$$

In equation (2) the equation of motion for the gyroscope frame is shown. The M_{gyro} is the reaction force by the housing and the M_{inner} is the reaction force by the gyroscope inner ring. And the Iframe is the moment of inertia of the gyroscope frame and the $\ddot{\phi}$ is the acceleration of the gyroscope frame. Therefore, M_{inner} includes the gyroscopic moment produced by the spinning rotor.

$$M_{inner}\vec{K} = -\sin\theta \cdot M_{inner}\vec{i} + \cos\theta \cdot M_{inner}\vec{k}$$
$$\vec{K} = -\sin\theta\,\vec{i} + \cos\theta\,\vec{k} \tag{3}$$

$$M_{inner}\vec{K} - \vec{r}\times\vec{F}_1 - \left(-\vec{r}\times\left(-\vec{F}_1\right)\right) = \dot{\vec{H}}_{oinner}$$
$$\vec{H}_{oinner} = [I]\vec{\omega}_{inner} \tag{4}$$

In equation (3) and (4) the angle θ is the rotation angle of the gimbal relative to the frame. The $\vec{i}, \vec{j}$ and $\vec{k}$ are the unit vectors which are attached to the gyroscope rotor and therefore they are defining the rotating coordinates. And the $\vec{K}$ vector is the unit vector which is in the initial state aligned with the $\vec{k}$ vector. The $\vec{F}_1$ is the reaction force by the spinning shaft which therefore includes the gyroscopic moment reaction. The $\vec{\omega}_{inner}$ is the angular velocity of the gimbal about the $\vec{j}$ axis and the $[I]$ is the inertia matrix of the gimbal.

$$\begin{aligned}
\sum M_x &= -I'\left(\ddot{\phi}\sin\theta + 2\dot{\theta}\dot{\phi}\cos\theta\right) + I\dot{\theta}\left(\dot{\Psi} + \dot{\phi}\cos\theta\right) \\
\sum M_y &= I'\left(\ddot{\theta} - \dot{\phi}^2\sin\theta\cos\theta\right) + I\dot{\phi}\sin\theta\left(\dot{\Psi} + \dot{\phi}\cos\theta\right) \\
\sum M_z &= I\frac{d}{dt}\left(\dot{\Psi} + \dot{\phi}\cos\theta\right)
\end{aligned} \tag{5}$$

And finally the equation of motion of the spinning rotor and shaft is formulated in equation (5). The $\dot{\Psi}$ is the angular speed of the spinning rotor. And by combining equation (1) to (5) the equation for performing the simulation can be obtained.

TABLE 1. The simulation parameters are shown for the gyroscope operation.

Simulation parameter	value
M_t(drill torque)	0.2 Nm (constant)
M_g(gyro mass)	1.6 kg
r(gyro radius)	40 mm
Ω(gyro rot. vel.)	20,000 rpm
Spindle size	100 mm dia., 150 mm length

TABLE 2. Drill torque calculation parameters are shown.

Drilling parameter	value
D(tool dia.)	5 mm
Material	Aluminum
F_z(feed per rev.)	0.1 mm/rev
K_c(material constant)	600 N/mm^2

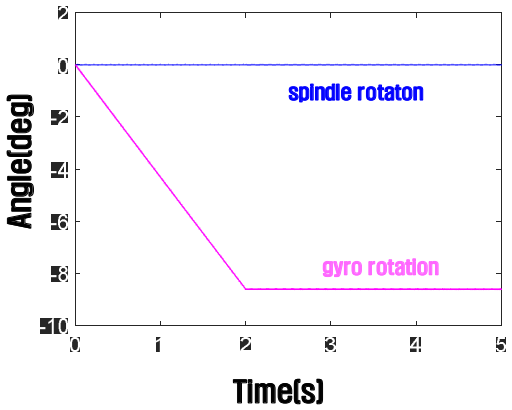

FIGURE 3. Simulation results with the physical parameters. The spindle (housing) does not rotate and the gyroscope gimbal rotates about 8 deg during two seconds.

In Figure 3 the simulation results are shown. At time of zero the 0.2 Nm drilling torque is applied to the tool and at the time of two seconds the torque disappears. As the drilling continues the housing does not rotate by the drill torque and the gyroscope gimbal rotates in the $\vec{j}$ direction. By the simulation results the proposed torque absorbing mechanism is verified.

EXPERIMENTAL DRILL HEAD AND THE MACHINING RESULTS

By the simulation process the gyroscope component parameters are determined. And the top-positioning gyroscope configuration is selected for the first experimental check and the mechanism is attached to the conventional machine tool by the BT-40 chuck as shown in Figure 5.

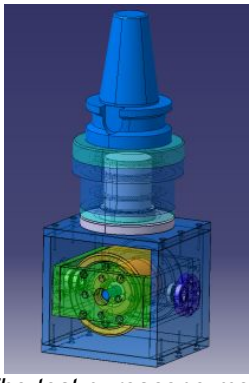

FIGURE 4. The test gyroscope mechanism draft is shown which includes a rotation bearing, a gimbal and a spinning rotor with a motor. The mechanism can be attached to the testing machine by the BT-40 chuck.

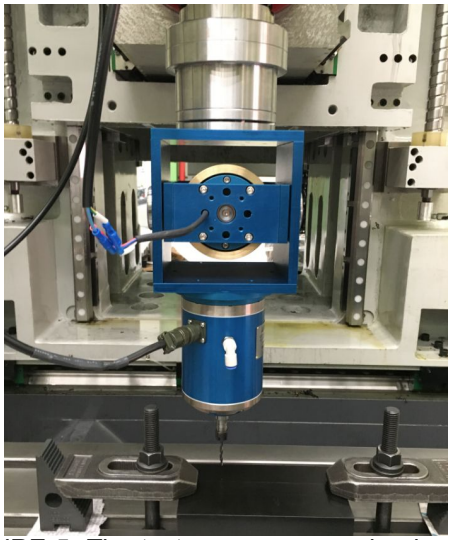

FIGURE 5. The test gyroscope mechanism with the drilling spindle is attached to the machine. The 4 mm diameter drill tool is attached to the spindle and two materials (poly-carbonate and aluminum) are drilled by the machining head successfully.

CONCLUSIONS AND DISCUSSIONS

The drill torque absorbing mechanism using a gyroscope mechanism for the mobile machining machine is proposed and verified experimentally. The next machining head prototype with the gyroscope mechanism is being designed with air turbine and active-type control which will result in more compact and efficient structure.

For further application the gyroscope moment can be used for tilting control of the mobile machine and this concept is being examined.

REFERENCES

[1] Uriarte L., Zatarain M., Axinte D., Yague-Fabra J., Ihlenfeldt S., Eguia J., Olarra A. Machine Tools for Large Parts. Annals of the CIRP. 2013 ; 62.

Material Behavior in Ultra-Precision Flycutting of Germanium

Nicholas E. Sizemore[1], Prithiviraj Shanmugam[1], Daniel Meyer[1,2], Joseph D. Owen[1] and Matthew A. Davies[1]
[1]Department of Mechanical Engineering and Engineering Sciences
University of North Carolina at Charlotte, Charlotte, North Carolina, USA
[2] Foundation Institute of Materials Science, Bremen, Germany

KEYWORDS: freeform optics, ultra-precision diamond machining, germanium, material behavior

BACKGROUND

In the past, optical designs were limited to rotationally symmetric optics. However today, due to additional design functionality, freeform optics are driving major changes in the manufacturing of optical components. Applications in the infrared (IR) are more prevalent because of less stringent surface and form tolerances. In fact, these tolerances generally are achievable with existing processes like ultra-precision diamond machining. The advantages of freeform optics are that they allow nearly arbitrary redirection of light in three dimensions. Because of this, traditional optical designs can be changed to reduce the number of components, reduce aberrations, and produce unobstructed optical systems with significantly reduced volume. To keep pace with these changes, the machinability of suitable materials for use in the IR, such as chalcogenide glass or germanium (Ge) must also be studied [1].

Due to its material properties and high index of refraction single-crystal Ge is ideal for infrared/thermal optical components including freeforms. The challenge is to machine it in complex configurations while avoiding brittle nature [2,3]. Single point diamond turning [1-2] is used to manufacture many Ge optics; however, freeform optics require more complex processes like coordinated axis turning, milling and flycutting where the dynamic and geometric machining parameters are more complex than in turning. Further, milling and flycutting are interrupted machining processes and there is little understanding of the cutting mechanics under these highly dynamic conditions. Owen et al. presented an approach to predict the forces in ball-milling and flycutting of Ge [4]. Here we extend that work by further investigating interrupted machining under well-controlled conditions.

This study isolates critical parameters and their effects in the surface and subsurface integrity through a simplified flycutting operation. The process enables analysis of the behavior of the material under highly controlled interrupted cutting conditions, and the data from this fundamental study can later be applied to more complex processes such as multi-axis diamond ball end milling. A preliminary investigation focused on isolated, single cuts [6], whereas the current study examines more complex cutting conditions and chip geometry.

EXPERIMENTAL ARRANGEMENT

Flycutting in a simplified configuration was chosen to generate single, isolated interrupted cuts. Key parameters such as the depth of cut a_p, the velocity (v_c), the feedrate (f) and the rake angle, γ, could be varied independently and their effects on the cutting mechanics can be isolated.

The experiments were conducted on the Moore Nanotechnology 350FG using a flycutting apparatus (125 mm diameter) and utilizing three axis mode (X-Y-Z or Y-Z-C). All experiments used monocrystalline Ge [1-2]. The workpiece was mounted to a Kistler 9245C mini-dynamometer. Figure 1 shows the experimental arrangement.

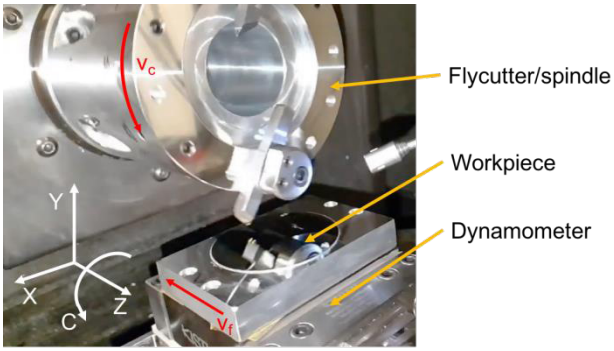

Figure 1: Flycutting apparatus, where v_f and v_c are the feed speed and cutting speed, respectively.

The tools used in these experiments were single-crystal diamonds with a nose radius of 0.5 mm and rake-angles, γ, of -45° (RNT 1), and -25° (RNT 2). The relief angle α was ≥7°. Each tool was in new condition from the manufacturer at the time the experiments began. No significant wear was observed.

The crystal orientation of the samples was such that the normal of the (100) was perpendicular to the cutting direction. The crystal orientation uncertainty was ±0.5°. Ge wafers that are diamond turned with this crystal orientation are known to have a characteristic surface feature that appears at the transition from ductile-dominated to brittle-dominated machining: a four-fold pattern due to the early emergence of surface fractures at less favorable crystal orientations, as described by Nakasuji et al. [5] and illustrated in Figure 2. All the samples were tested in the same configuration, which permitted material removal without adding additional brittle fracture due to the crystal orientation [5-6]. The Ge samples were supplied with chemo-mechanically polished (CMP) surfaces minimizing initial sub-surface damage. The CMP process introduced form error and thickness variations in the samples. This was compensated in the machine code. Previously, Sizemore et al. reported similar research in which the (111) face of the Ge was preliminary diamond turned [6].

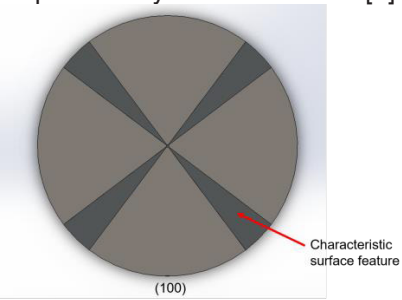

Figure 2: Characteristic surface fracture as described in Nakasuji et al [5].

A study on the effects of cuttings speeds was completed using orthogonal flycutting. The subsequent flycutting produced single, isolated cuts in the surface of the Ge wafer. The experiment was completed using six cutting speeds (0.5, 1.0, 1.5, 2.0, 4.0 and 8.0 m/s) and v_c-dependent feedrates ensured separation of the individual cuts. The tool was ramped into the workpiece with a step-down resolution of 10 nm to a maximum depth of cut of 600 nm. This allowed the identifications of $a_{p,max}$ at which a cut became fracture dominated. For the purpose of this paper, the effects of critical depth of cut $a_{p,crit}$ as a function of cutting speed was examined utilizing singular cuts that had approximately the same maximum depth of cut. Figure 3 illustrates a series of cuts imaged in a Zygo NexView scanning white light interferometer (SWLI).

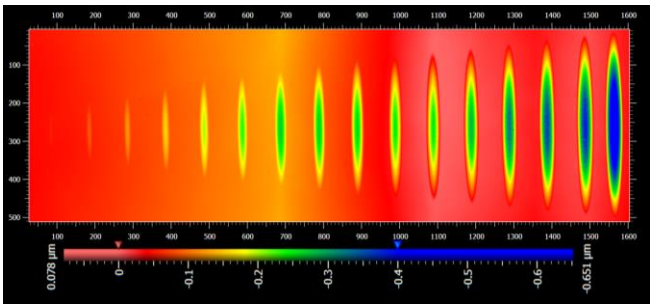

Figure 3: SWLI image of the isolated cuts produced.

A JEOL scanning electron microscope (SEM) was also used to examine the cuts. The results from the SWLI were processed using both Zygo's MetroPro® (Mx™) and a custom MATLAB® program.

ANALYSIS

Prior to any measurements of the surface finish in the cuts, the samples were cleaned, and the measurements took place in a class 10,000 cleanroom. The analysis process included the selection of similar isolated cuts at the various cutting velocities produced by the flycutting experiment. These cuts were selected by observing the depth of cut a_p corresponding to an obvious transition from ductile dominated to brittle dominated cutting. Because of the form errors in the maximum depth, $a_{p,max}$, had to be measured and cuts of nearly the same depth were compared.

Table 1: 50x Mirau objective specifications (Zygo).

Magnification	50x
Design	Mirau
NA	0.55
Working Distance (mm)	3.4
Optical Resolution (μm)	0.52
Slope limited (deg)	28.13
Field of View (mm²)	0.17

The SWLI was utilized to collect height-maps of the cuts produced in the experiments. A 50x Mirau objective was used with 1.0x digital zoom. Table 1 presents the specifications of the objective as provided by Zygo. The height-maps were masked and processed in Mx™ to remove and form with a 4th-order polynomial and filter long-wave fluctuations using an 80 μm high-pass FFT filter. Figure 4, image (a) depicts the process of isolating a cut and (b) shows the masking, form removal and filtering of the cut. Following this process, the edges along the width of the cut were removed. The purpose of masking and removal of form and edges from the cut was to more accurately map the change in surface roughness as a_p changed through the length of the cut.

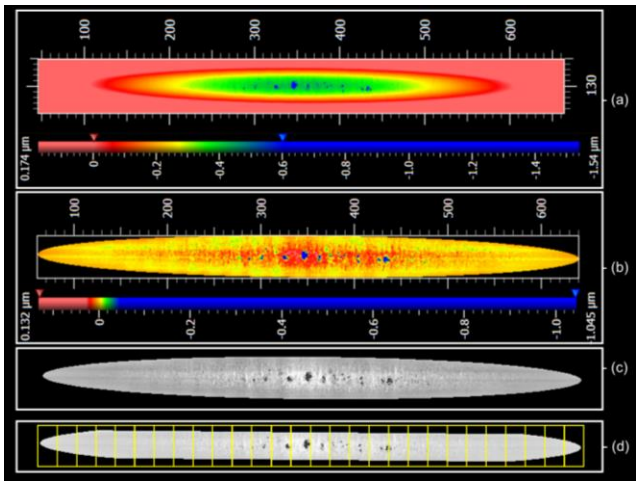

Figure 4: Process of analyzing the effect of cutting speed; (a) SWLI height-map of cut, (b) isolation and filtering of form, (c) SWLI intensity-map, (d) narrowing width of cut.

Each of the cuts, as represented by Figure 4, image (d), were processed using a MATLAB® program that segmented the surface along the length of the cut. These segments had equal lengths of 12.5 μm and no overlap. The analysis in MATLAB® recorded the S_a, S_q and S_z values of each of the segments. These values represent the surface arithmetical mean height, root mean squared height (RMS) and peak-to-valley (PV), respectively.

In analyzing the resulting plots, the S_z values were most sensitive to fracture dominated machining and were used to identify a transition point. S_a and S_q values are reported to describe the overall surface roughness.

RESULTS

The findings in the flycutting experiments produced qualitative results depicting transitions from ductile-to-brittle as the maximum depth of cut increased.

The surface roughness results from RNT 1 and RNT 2 are represented with a scatter plot of the S_a, S_q and S_z values as a function of length of cut. S_a and S_q utilize the left-hand y-axis, and S_z utilizes the right-hand y-axis. The subplots represent the variation in a_p and use the same x-axis as the roughness scatter plot. Figure 5 through Figure 10 show the results for each different cutting velocity and the tool used. They are plotted on the same scale for comparison.

Figure 5 shows the change in surface roughness as the depth of cut increases. Brittle fracture, at a v_c of 0.5 m/sec, occurred and ended at approximately the same $a_{p,crit}$ of 0.310 μm. Figure 6 shows, at a v_c of 2.0 m/sec, that the initiated brittle fracture at an $a_{p,crit}$ of 0.380 μm and brittle fracture ceases at shallower $a_{p,crit}$ of 0.210 μm. Finally, for a v_c of 8.0 m/sec, Figure 7 shows the surface roughness is seen to be improved at an approximate $a_{p,crit}$ of 0.400 μm, which is indicative of a more steady cutting process.

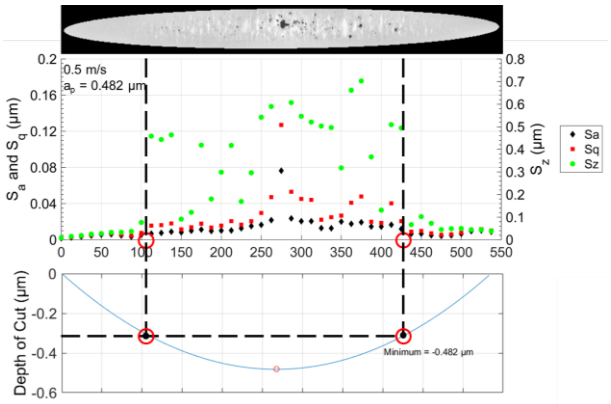

Figure 5: Single, isolated cut at a v_c of 0.5 m/sec with RNT 1.

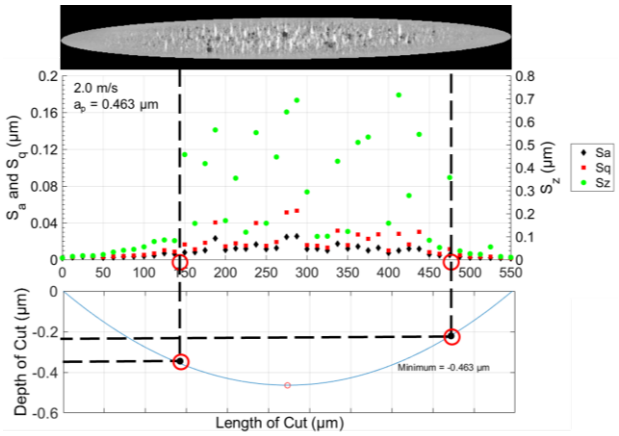

Figure 6: Single, isolated cut at a v_c of 2.0 m/sec with RNT 1.

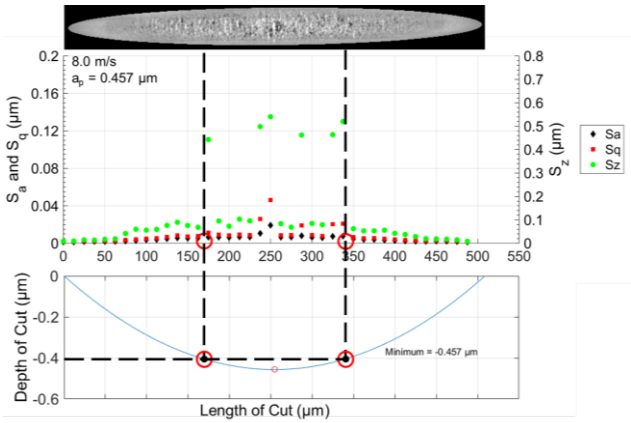

Figure 7: Single, isolated cut at a v_c of 8.0 m/sec with RNT 1.

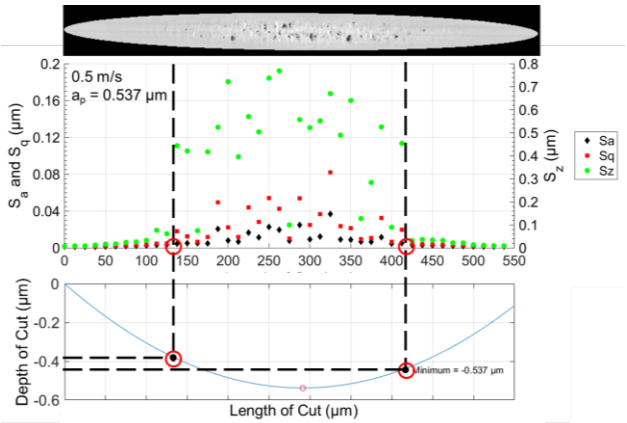

Figure 8: Single, isolated cut at a v_c of 0.5 m/sec with RNT 2.

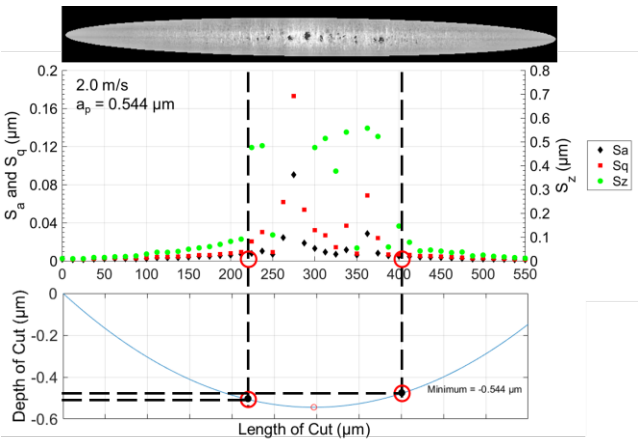

Figure 9: Single, isolated cut at a v_c of 2.0 m/sec with RNT 2.

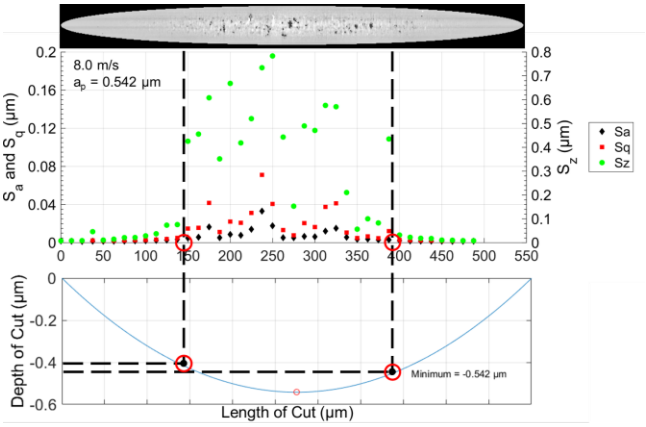

Figure 10: Single, isolated cut at a v_c of 8.0 m/sec with RNT 2.

The information in Figure 8 through Figure 10 illustrates the surface roughness results for RNT 2. Visually there is already an improvement in the material removal as compared with RNT 1. Figure 8, at a v_c of 0.5 m/sec, depicts a shallower brittle fracture than as the tool exits the Ge wafer. However, at a higher v_c of 2.0 m/sec, there is a shift in this pattern. Figure 9 expresses an increased limit in the $a_{p,crit}$ as compared to as when tool is exiting. Finally, the average surface roughness increases at a v_c of 8.0 m/sec, as seen in Figure 10.

Table 2 and 3 summarize the results from all six cutting speeds for RNT 1 and RNT 2. The tables include the measured lengths and depths of the individual cuts examined, as well as, the preserved "into fracture" and "out of fracture" critical maximum depths of cut.

Table 2: RNT1 critical depth of cut of "into" and "out of" brittle fracture.

v_c (m/sec)	Depth (µm)	Length (µm)	Into Fracture DoC (µm)	Out of Fracture DoC (µm)
0.5	0.482	565	0.310	0.310
1.0	0.442	544	0.330	0.290
1.5	0.438	518	0.383	0.180
2.0	0.463	550	0.380	0.210
4.0	0.508	569	0.230	0.250
8.0	0.457	532	0.390	0.400

Table 3: RNT2 critical depth of cut of "into" and "out of" brittle fracture region.

v_c (m/sec)	Depth (µm)	Length (µm)	Into Fracture DoC (µm)	Out of Fracture DoC (µm)
0.5	0.537	576	0.380	0.420
1.0	0.507	556	0.420	0.480
1.5	0.545	588	0.470	0.510
2.0	0.544	600	0.510	0.490
4.0	0.546	575	0.460	0.540
8.0	0.542	554	0.410	0.450

The critical depth of cut, $a_{p,crit}$ can be related to the cutting speed, v_c. Figure 11 shows $a_{p,crit}$ as a function of v_c. The squares depict the transition to brittle fracture dominated cutting occurring as the tool enters the workpiece, and the triangles depict the ceasing of brittle fracture dominated cutting as the tool exits the Ge wafer.

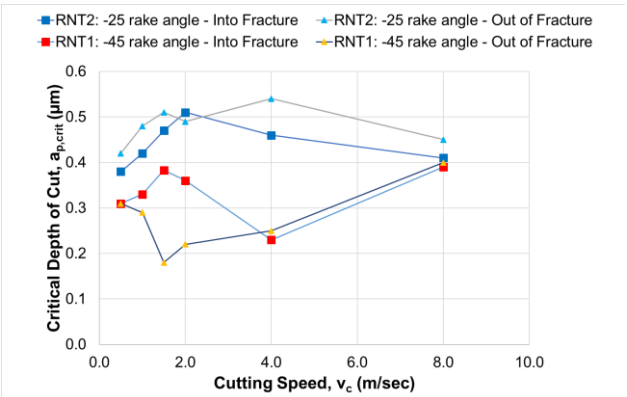
RNT2: -25 rake angle - Into Fracture
RNT2: -25 rake angle - Out of Fracture
RNT1: -45 rake angle - Into Fracture
RNT1: -45 rake angle - Out of Fracture
Critical Depth of Cut, $a_{p,crit}$ (µm)
Cutting Speed, v_c (m/sec)

Figure 11: Critical depth of cut as a function of cutting speed for RNT1 and RNT2.

The SEM was used to collect images of the cuts examined for a better visualization of the fracture dominated areas. The SEM was set in backscattering electron mode to image the topography of the cut surfaces. The resulting images depicted a much more fracture dominated area than was seen in the SELI images. Figure 12 shows the stages of fracture in various isolated cuts. Recall that the depth of cut increases from the left to the middle of the cut and begins to decrease in depth after passing the center point. The cutting speed for this set of cuts is 2.0 m/sec using RNT 2. Notice that as the maximum depth of cut increases from the bottom to the top and so does the occurrence of brittle fracture. Figure 13 shows a closer look at the center-most cut from Figure 12.

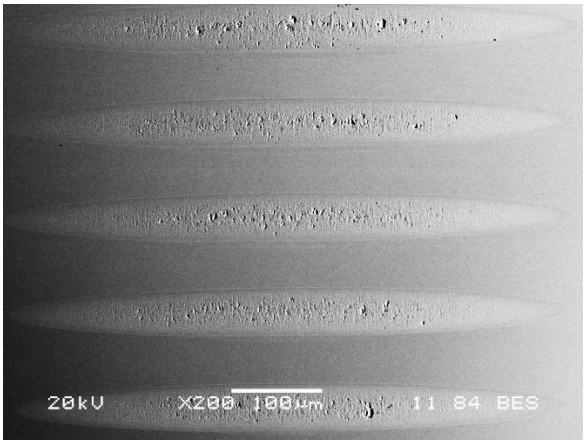

Figure 12: SEM image at x200 magnification of multiple isolated cuts.

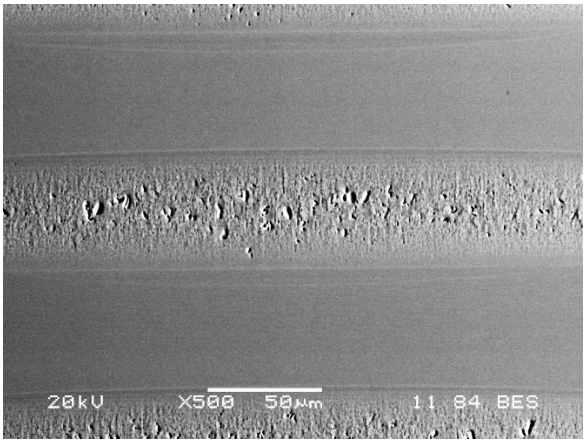

Figure 13: SEM image at x500 magnification of fracture-dominated area in an isolated cut.

CONCLUSION

The experiments conducted allowed for the identification of critical values and thresholds defining critical combinations of the cutting speed and depth of cut. The findings can be used to identify critical characteristics for interrupted cutting conditions that minimize surface and subsurface damage. Each study yielded linear micro-cuts in the surface that reveals the potential to machine brittle material using high material removal rates in a damage-free way. In particular, the results from this experiment exhibited that the - 25° rake angle tool (RNT 2) achieved much greater depths of cut before being dominated by fracture. The variation of the critical depth of cut going into fracture and leaving the fracture might be of high relevance for milling operations. Here, the observations might be helpful to choose the optimal parameters for up- and down-milling. Based on the presented results, these should vary. These results were examined using the Zygo NexView scanning white light interferometer (SWLI), JEOL Scanning Electron Microscope (SEM), and Kistler 9245C mini-dynamometer. The two single crystal diamond tools were examined in the SEM. It was found that both experienced no severe damage or perceivable dulling of the cutting edge.

In summary, critical depths of cut and suitable combinations of rake angles and cutting speeds are deduced from the study leading to clear recommendations regarding process windows for the manufacture of germanium freeform optics.

OUTLOOK

Future work includes examining a non-steady state, interrupted cutting operation that studies the effect of contact time between the tool and workpiece. This study will be broken into sections that review a simplified milling operation. The parameters that are most relevant to the topic include time-changing chip geometry, time-in-cut, etc. which can all be correlated to the characteristics of the surface and subsurface damage of machined samples.

Additionally, preliminary milling tests are planned in germanium (Ge), chalcogenide glass (IRG 26) and various grades of silicon carbide (SiC). These experiments will include: (1) FEA and time domain simulations of flycutting and milling of Ge, IRG 26 and SiC; (2) flycut and mill these materials while using a dynamometer to measure the cutting forces; (3) studying surface topography using SWLI and various modes of SEM; (4) studying subsurface damage using a spotting technique with a magnetorheological finishing fluid, which was similarly done by Shanmugam et al. [7]; (5) study of subsurface damage using confocal Raman spectroscopy by OSU; (6) study of the surface topography using the AFM.

ACKNOWLEDGEMENTS
This work was funded by the US National Science Foundation (NSF-Grant CMMI-1437225). The authors greatly acknowledge the financial support of the NSF.

REFERENCES
[1] Blackley, W.S., Scattergood, R.O., Ductile-regime machining model for diamond turning of brittle materials, Precision Engineering, 1991; 13(2):95-103.
[2] Lucca, D.A., Chou, P., Hocken, R.J., Effect of Tool Edge Geometry on the Nanometric Cutting of Ge, CIRP Annals - Manufacturing Technology, 47(1): 475-478.
[3] Yan, J., Maekawa, K., Tamaki, J., Kuriyagawa, T., Micro grooving on single-crystal germanium for infrared Fresnel lenses, Journal of Micromechanics and Microengineering, 2005, 15: 1925-1931.
[4] Owen, J.D., Troutman, J.R., Harriman, T.A., Zare, A., Wang, Y.Q., Lucca, D.A., Davies, M.A., The mechanics of milling of germanium for IR applications, CIRP Annals, 2016, 65(1): 109-112.
[5] Nakasuji, T., Kodera, S., Hara, S., Matsunaga, H., Ikawa, I., Shimada, S., Diamond Turning of Brittle Materials for Optical Components, CIRP Annals, 1990, 39(1): 89-92.
[6] Sizemore, N.E., Meyer, D., Owen, J.D., Davies, M.A.; Cutting Mechanics in Ultra-Precision Machining of Germanium; Conference: Proc. ASPEN/ASPE Spring Topical, 2017; 61-64.
[7] Shanmugam, P., Owen, J.D., Salzman, S., Troutman, J., Lambropoulos, J., Davies, M.A.; Fundamental of Material Removal in Silicon Carbide for Freeform Optics; Conference: Pro. ASPEN/ASPE Spring Topical, 2017; 35-38.

HOW TO REALIZE THE SELF-PROTECTIVE TOOL DURING CUTTING OF DIFFICULT-CUT MATERIAL?

SONG Xiaoqi[1] , Yukio TAKAHASHI[1] and Tohru IHARA[1]
[1]Department of Precision Mechanics
Chuo University
Tokyo, Japan

INTRODUCTION

Because tool wear is one of the parameters determining tool life, efforts have been put into controlling and reducing the tool wear during cutting. Over a range of cutting conditions, workpiece material accumulates around the tool cutting edge [1-4], which is always known as Built-up Edge (BUE). Studies by Song et al. confirmed that, from an experimental point of view, the thin and stable adhering layer, which called as Built-up Layer (BUL), produced by accumulating workpiece material on the tool rake face, has the tool protecting effects during cutting of difficult-cut materials [5]. However, the mechanisms governing the BUL formation process are still not fully understood. This is due to the following two facts: on one hand, with improved machine tools and cutting tools, the cutting speed can be increased up to above BUE formation range. On the other hand, few studies have been reported on the active use of BUE in the difficult-cut material cutting, because BUE can significantly change tool geometry and contact conditions at the tool and chip interface, which may results in overcutting, poor surface finish and so on.

Song et al. recently reported the nucleus formation mechanism of BUL and established a general relationship between adhesion phenomenon and friction by using the principle of minimum energy dissipation [6]. And the adhering time has also been discussed by treating the adhesion phenomenon as a non-equilibrium situation [7,8].

The main objective of this paper is to clarify the BUL formation mechanisms and propose a way to realize the self-protective tool (SPT) during cutting of difficult-cut material by actively and purposely making use of BUL. Firstly, thermodynamics of BUL formation is briefly reviewed. Then, the BUL formation process during cutting of hardened steel is examined. Thirdly, in order to predict the SPT function conditions, a simple BUL growth model is first proposed. And the qualitative comparisons are also provided to analyze capabilities of the growth model. Finally, the usefulness of SPT during cutting of difficult-cut material is discussed.

THERMODYNAMICS OF BUL FORMATION

What is BUL?

According to the previous studies [1-4], Built-up material formed on the tool face during cutting of metal material is still a major issue, especially in precision cutting. Researches conducted by Hoshi et al. [1], Tomac et al. [2], Trent et al. [3] and more recently Gomez-Parra et al. [4] clearly showed that Built-up material can be dissociated into three main regions: BUL on the tool rake face, BUE at the tool cutting edge, and Flank Built-up (FBU) on the flank face. Gomez-Parra et al. [4] also stated that BUL should be distinguished into two categories: the inner layer and the outer layer. However, among the studied literatures, all the authors highlighted that BUL is the predecessor of BUE.

In the author's opinion, in order to actively and purposely make use of Built-up material formed on the tool rake face during cutting, if Built-up material is thin, stable, and products the smaller depth of overcutting, it will be redefined as BUL which can work as a protecting layer [5]. Based on this definition, BUL is a thin and stable protecting layer, promoted by an accumulation of workpiece material on the tool rake face, and it does not grow to BUE or is difficult to form BUE.

Friction, Wear, BUL and Energy Dissipation

From the experimental observations, once BUL is formed, tool geometry and contact conditions are changed. Consequently, friction and wear phenomenon at the tool and chip interface become very complex. Here, we will give a model, to our knowledge, for the first time capturing the friction, wear and BUL formation mechanisms during cutting based on the fundamental principles of thermodynamics.

During the chip slides along the tool rake face, adhesion junctions commonly occur at the tool and chip interface in the presence of a high normal stress, high temperature. On the other hand, due to the large plastic deformation the real and apparent contact area are almost the same near the cutting edge, and this contact zone can be defined as the metal contact zone.

In the metal contact zone ($A_{(j)}$), if the potential energy between the tool clusters and workpiece clusters is strong enough, it may be favourable for the lattice to relax into commensurate area (clusters set), otherwise discommensurate (incommensurate and so on) is formed (Fig.1(a)). Chip clusters are locked in the minima of potential energy until the energy barrier is overcome. Then, the chip clusters rapidly drop into the next clusters set. In this slip action, the potential energy is dissipated and friction occurs. Namely, friction is determined by the atomic structures at the tool and chip interface. Since all the clusters sets can not slip at the same time, the movement of clusters can be described as a quasi-dislocation movement. This is the atomic scale cluster adhesion friction model [8].

By using this friction model, we proposed friction, wear and BUL formation mechanisms as shown in Fig.1 [6]. In region $A_{(j)}$, the total energy barriers prevent chip clusters from jumping to another energy minimum position. On a large time and space scale, if energy barriers are not overcome, the clusters sets become stable and there is no relative motion at the boundary. When the fracture (irreversible process) first happens in the tool (Fig.1(b)), the relative motion happens in the tool and tool wear forms. When the fracture first happens in the chip, the relative motion happens in the chip and adhesion is formed. Then, BUL forms through this repeated transfer and growth process. Using this model, we established the nucleus formation mechanism of BUL based on the principle of minimum energy dissipation [6]. On the other hand, wear can also be considered as resulting from the dissipation of frictional energy and it has been confirmed that wear loss could be correlated with the dissipated energy with a linear relationship [9].

EXAMPLE OF BUL

Analysis of BUL

As previously reported [5], the height of BUL has a decreasing trend as cutting speed increases above 40m/min during cutting of hardened steel S45C (H-S45C) and the minimum values are found at the low and high cutting speed (Fig.2). In order to study the influence of feed on the BUL formation, the height of BUL under different feed at cutting speed 40m/min are measured. As shown in Fig.3, the height of BUL decreases as the feed increases. The highest BUL is at feed 0.05mm. It indicates that not only the cutting speed but also the feed plays an important role in the BUL formation. Meanwhile, an excessive increase of average BUL area rate after cutting

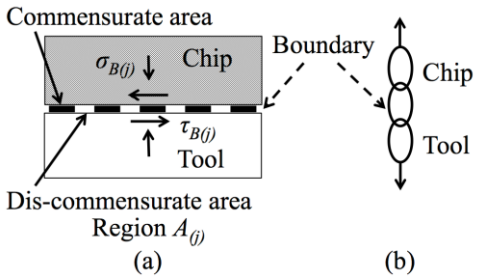

FIGURE 1. Contact model (a) and the weakest link model (b) in region $A_{(j)}$ at the tool and chip interface ($\sigma_{B(j)}$, $\tau_{B(j)}$: normal stress, shear stress).

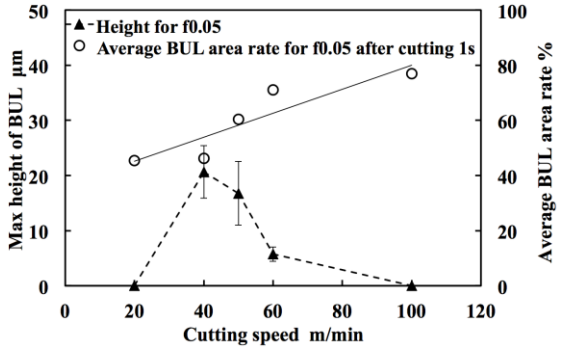

FIGURE 2. Variation of max height of BUL and average BUL area rate after cutting 1s with cutting speed for cutting H-S45C.

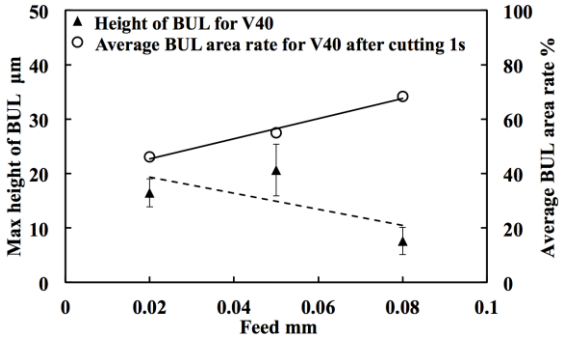

FIGURE 3. Variation of max height of BUL and average BUL area rate after cutting 1s with feed for cutting H-S45C.

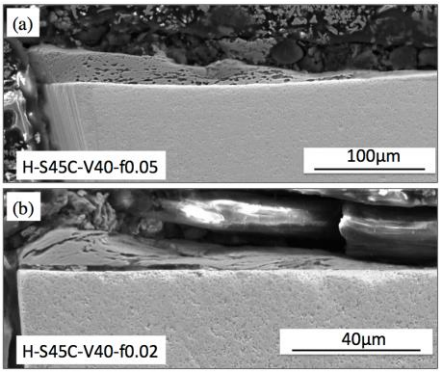

FIGURE 4. Metallographic cross section of BUL for cutting H-S45C at cutting speed 40m/min, feed rate 0.05mm/rev (a) and 0.02mm/rev (b).

1s is observed for the higher cutting speed or the larger feed (Fig.2, Fig.3). These phenomena can be related to the intensive energy dissipation at the tool and chip interface.
The typical microstructure of BUL is also displayed in Fig.4. It is confirmed that BUL has a typical lamellar microstructure and BUL can be considered as a thin and stable protecting layer on the tool rake face.

Observation of BUL Formation

Figure 5 shows the variation of BUL area rate distribution with cutting time at cutting speed 40m/min [6]. As shown, after cutting 10s the cutting process enters the steady state and the contact length is close to constant. The maximum BUL area rate is about at the middle of contact length. After cutting 60s, BUL continues to grow and the BUL area rate has a forward growing trend. An conclusion is that BUL formation has two different processes: the nucleus process and forward growing process [6].
Figure 6 shows the variation of BUL area rate distribution with cutting time at cutting speed 50m/min. It can be seen that the adhesion phenomenon become more intense. The forward growing trend can also be found, however, it becomes unapparent due to the fall-off of BUL (Fig.7). As shown in Fig.7, at the low cutting speed 20m/min, few adhesions only can be found near the cutting edge. When the cutting speed increases to 50m/min BUL falls off easily and the island-like distribution of BUL is formed. Figure 8 shows the variation of average BUL area rate with cutting time. It is can be seen that the average BUL area rate has a decreasing trend at the higher cutting speed. Therefore, it is believed that the thin and stable BUL formed at cutting speed 40m/min has a protecting effect and can be used to realize the SPT.

FORMATION MECHANISMS OF BUL

Proposed BUL Formation Mechanisms

According to the above analyses, BUL formation mechanisms can be understood in terms of the relation between the chip formation process and the adhesion phenomenon as illustrated in Fig.9. At the first step, adhesion junctions are generated at the tool and chip interface as the chip slides along the tool. Afterwards, the damage forms in the chip depending on the workpiece material properties, state of stress, deformation, sliding speed and so on. When step 2' occurs, the fracture generates in the chip, and material adheres to the tool. Then, adhesion accumulates and grows to form the nucleus of initial

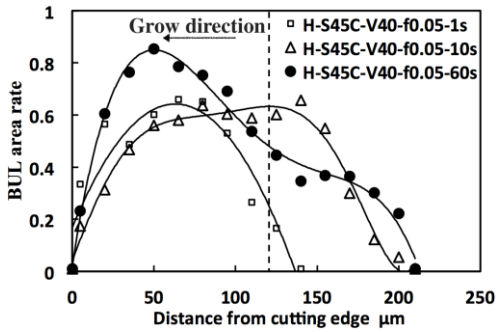

FIGURE 5. Variation of BUL area rate distribution with cutting time at cutting speed 40m/min, feed 0.05mm/rev for cutting H-S45C.

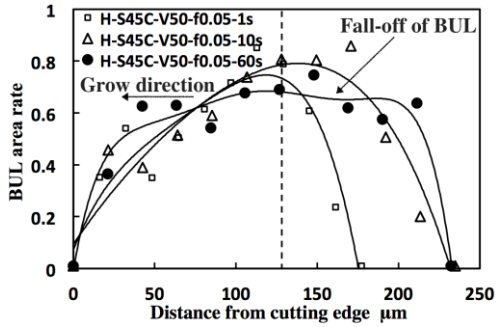

FIGURE 6. Variation of BUL area rate distribution with cutting time at cutting speed 50m/min, feed 0.05mm/rev for cutting H-S45C.

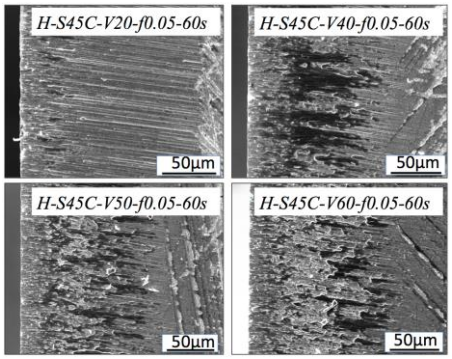

FIGURE 7. SEM images of tool rake face for cutting H-S45C under different cutting speed, feed 0.05mm/rev after cutting 60s.

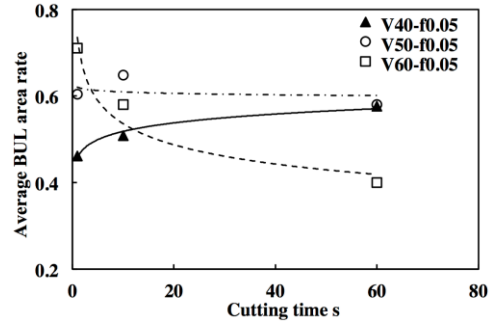

FIGURE 8. Variation of average BUL area rate with cutting time under different cutting speed, feed 0.05mm/rev for cutting H-S45C.

BUL at the middle of contact length through the repeated transfer and growth process at step 3'. Finally, the initial BUL grows from the middle of contact length to the cutting edge and BUL is formed at step 4'. If the fracture does not happen, step 2 takes place and BUL does not form at step 3. As mentioned above, BUL formation can be considered as a process of accumulating the workpiece material to form the layer structure on the tool face.

The macroscopic layer structure accumulation process of BUL mentioned above is similar to the Multi Built-up Layer model in [4]. However, this present study reveals that BUL is a thin and stable adhering layer, which does not grow to BUE. From the EPMA analyses on tool rake face under different cutting time, we confirmed that the cutting temperature favours the formation of BUL, but it is not the major factor [10]. In our opinion, BUL formation is a complex process, and the energy dissipation should be considered.

Modeling the Growth of BUL

Growth Model

Because the thin and stable BUL can be used to realize the SPT, it is necessary to predict the BUL formation conditions. Here, we present a simple BUL growth model as shown in Fig.10. In this model, it is assumed that the growth of BUL is a process of accumulating the workpiece material layer after layer, and the BUL height h_{ad} can be calculated by the overall number of adhering layer n and the thickness of each layer h_n. As previously underlined, BUL is depicted by the height of BUL, the cutting time and the BUL area rate. To establish the BUL growth model, the fundamental assumptions are as follows: 1) the growth direction of *n*-th layer is from the middle of contact length to the tool cutting edge, 2) the (*n*+1)-th layer is only formed on the top of *n*-th layer , 3) the (*n*+1)-th layer does not form until the formation of *n*-th layer finishes, and 4) BUL does not fall off until all layer forms.

Behavior of the First Layer

The first layer of BUL is very important for the determination of the BUL height. The thickness of first layer h_1 is given by:

$$h_1 = h_0 * A_1 * \omega_1 * t_{01} \quad (1)$$

where A_1, ω_1, t_{01} represent the contact area at the tool and chip interface, the adhesion area rate, the adhering time, respectively. Here, h_0 is defined as the average thickness grown per unit time of adhering layer during cutting process, which takes into account the influences of work hardening, softening, fall-off and so on. As the adhesion phenomenon is a non-equilibrium situation, t_{01} can be calculated by the reaction rate function proposed in [7,8].

Because adhesion changes the configuration of tool rake face, adopting a thermodynamic point of view, the adhered layer formation process can be seen as a process of configurational entropy variation. The variation of enthalpy ΔH on the tool rake face can be expressed as $\Delta H = N_1 \cdot \Delta E$, where N_1 is the number of adhered workpiece atoms unit area on the tool rake face, ΔE is the adhesion energy for one workpiece atom. The configurational entropy ΔS can be given by [11]:

$$\Delta S = k_b \, ln[N_0! \,/ (N_1! \, (N_0 - \, N_1)!)] \quad (2)$$

where k_b is Boltzmann's contestant, N_0 is tool atoms number unit area. At temperature T, the variation of the free energy ΔG in this process is given by $\Delta G = \Delta H - T\Delta S$. To find the equilibrium state, the change of free energy ΔG are uniquely characterized by the minimum energy as $\Delta G = min$. The equilibrium number of adhered workpiece atoms is calculated by $\Delta G / \Delta N_1 = 0$. Using Eqs. (2), the equilibrium configutational state can be given as:

$$\frac{N_0 - N_1}{N_0} \approx exp\left(\frac{-\Delta E}{k_b T}\right) = \sum_{m=1}^{\infty} \frac{\left(-\frac{\Delta E}{k_b T}\right)^m}{m!} \approx \left.\frac{-\Delta E}{k_b T}\right|_{m=1} \quad (3)$$

Further assuming that ω_1 equals to the ratio between workpiece atoms and tool atoms under

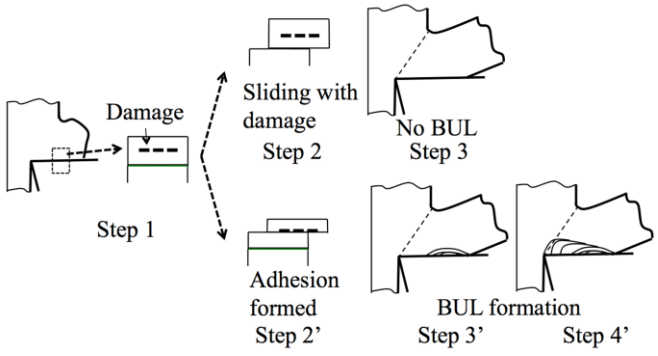

FIGURE 9. Proposed growth mechanisms of BUL.

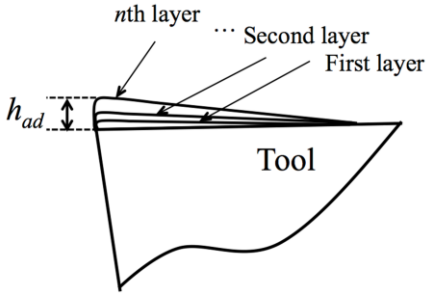

FIGURE 10. Model the growth of BUL.

equilibrium configutational state, Eq. (3) can be rewritten as:

$$\omega_1 = M/T + N \quad (4)$$

where M and N are constant.
Note that when ω_1 reaches the maximum value $\omega_1 = 1$, Eq. (4) is no longer relevant.

Growth of BUL

After the formation of first layer finished, the *n*-th layer can be formed. The thickness of *n*-th layer h_n can be defined by:

$$h_n = h_0 * A_n * \omega_n * t_{0n}\ , (n = 2,3, \dots n_{ad}) \quad (5)$$

where n_{ad} is the adhered layer number, A_n, ω_n, t_{0n} represent the contact area, the adhesion area rate, the adhering time of *n*-th adhered layer. However, it should be noted that the adhesion phenomenon for the *n*-th layer is generated between workpiece atoms and workpiece atoms.

Overall Model

Combining Eqs. (1) and (5), the BUL height can be estimated. To simplify the overall model, the values $\omega_n = \omega_1, t_{0n} = t_{01}, A_n = A_1$ are considered. Therefore, the height of BUL can be rewritten as:

$$h_{ad} = h_0 * n_{ad} * A_1 * \omega_1 * t_{01} \quad (6)$$

In Eq. (6), such as A_1, ω_1, t_{01} can be measured directly or estimated from experimental data. Because h_0 and n_{ad} are difficult to measure, here, we just give a semi-empirical estimation.

Modeling Results

Figure 11 presents the simulation results for the nucleus location of BUL, the contact length and height of BUL under different cutting speed for H-S45C by using the proposed nucleus formation mechanism in [6]. These results show good agreement with experimental results.
Predicted variations of height of BUL are ploted in Fig.12. In this study, $h_0 = 0.035\mu m$, $n_{ad} = 100$, $A_1 = 1$ are selected. To conduct the analysis, it is further assumed that the reduction of h_0 is 0% for the feed 0.02mm, 25% for 0.05mm, 50% for 0.08mm. As can be seen in Fig.12, the trends of simulation results show good agreement with the trends of experimental results (Fig.2 and Fig.3). The usefulness of BUL growth model is confirmed. And it reveals that parameter h_0 is also an important parameter for correctly predicting the thickness of BUL. As shown in Fig.12(a), it can also be seen that the predicted highest BUL is formed at cutting speed 40m/min. As result, we can forecast that the thin and stable BUL is formed at cutting speed 40 m/min, and it can be used to realize the SPT.

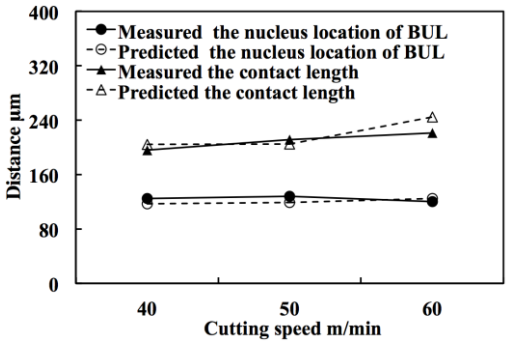
Measured the nucleus location of BUL
Predicted the nucleus location of BUL
Measured the contact length
Predicted the contact length
Distance μm
Cutting speed m/min

FIGURE 11. Predicted the nucleus location of BUL and the contact length for H-S45C.

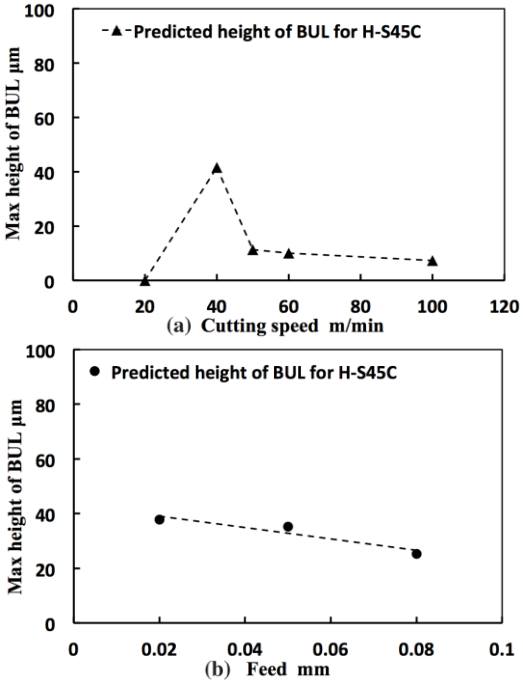
Predicted height of BUL for H-S45C
Max height of BUL μm
(a) Cutting speed m/min
Predicted height of BUL for H-S45C
Max height of BUL μm
(b) Feed mm

FIGURE 12. Predicted variation of height of BUL with cutting speed (a) and feed (b) for H-S45C.

USEFULNESS OF SPT

For Cutting H-S45C

In Fig.13, the variation of flank wear land width under different cutting speed and feed during cutting H-S45C are displayed. As shown, in general, flank wear land width has an increasing trend when the cutting time increases. It is also found that BUL formed at cutting speed 40m/min, feed 0.05mm/rev can protect the tool against flank wear, which is in agreement with the predicted results. For this reason, it is confirmed that the proposed growth model of BUL can be used not only to predict the height of BUL but also to forecast the best cutting conditions to realize the SPT. It should be noted that the height of BUL has a decreasing trend for the larger feed (Fig.3). As shown in Fig.13, it can be seen that the flank wear land width decreases

as the feed increases, this means that not only the BUL height but also the BUL area rate plays an important role in the protecting effect of BUL.

For Cutting Inconel 718

Influence of BUL on the flank wear land width during cutting of Inconel 718 is illustrated Fig.14. As shown in Fig.14, it can be seen that the flank wear land width has also an increasing trend as the cutting time increases. When cutting speed increases from 50m/min to 90m/min, the flank wear increases as the feed increases. However, at cutting speed 10 m/min, the thin and stable BUL is formed on the tool rake face, an insteresting conclusion is that, just like H-S45C, the flank wear land width decreases as the feed increases. This phenomenon is believed to be responsible for the protecting effects of BUL.

Considering experimental results for H-S45C and Inconel 718, it is confirmed that the SPT can be used to reduce the tool wear during cutting of difficult-cut material and we can predict the best conditions (the thin and stable BUL formation conditions) to realize the SPT by using the proposed growth model of BUL.

CONCLUSIONS

In order to study the BUL formation mechanisms and propose a way to realize the SPT during cutting of difficult-cut material by actively and purposely making use of BUL, the BUL formation mechanisms have been analysed through experimental studies and modeling. And the following conclusions can be drawn:

1) The relationship among the friction, wear and BUL formation can be establised by using the fundamental principle of thermodynamics.

2) BUL is a thin and stable protecting layer on the tool rake face and it does not grow to BUE or is difficult to form BUE.

3) It is confirmed that BUL formation has two different processes: the nucleus process and forward growing process. And the thin and stable BUL can be used to realize the SPT.

4) The growth model of BUL is proposed. The advantages of this simplified model rely on the capacity of simulating the BUL height and the prossibility to forecast the best cutting conditions (the thin and stable BUL formation conditions) to realize the SPT.

5) The usefulness of SPT is also examined. It is confirmed that the SPT can be use to reduce the tool wear during cutting of difficult-cut material.

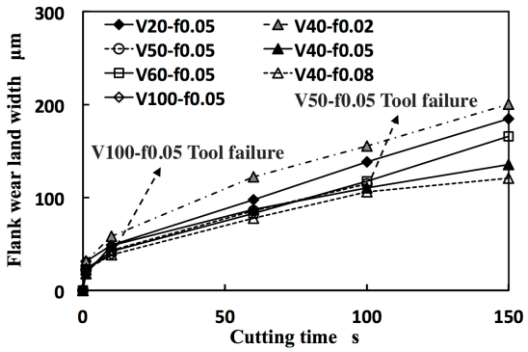

FIGURE 13. Variation of flank wear land width under different cutting speed and different feed for cutting H-S45C.

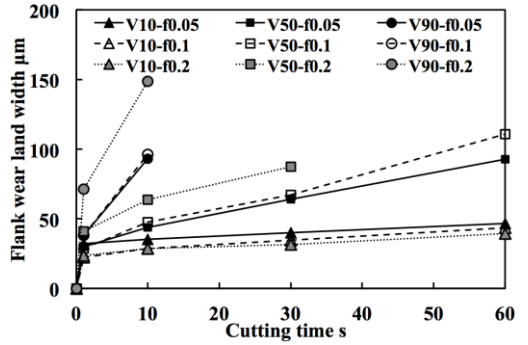

FIGURE 14. Variation of flank wear land width under different cutting speed and different feed for cutting Inconel 718.

REFERENCES

[1] Hoshi K. and Hoshi T., Memoirs of the Faculty of Engineering, Hokkaido University. 1969; 12(3): 241-271.

[2] Tomac N., Tonnessen K., Rasch F.O. and Mikac T., AMST'05 Adv. Manuf. Sys. and Tech.. 2005; 485: 183-192.

[3] E. Trent and P. Wright, Metal cutting 4th, Butteworth-Heinemann: 2000.

[4] Gomez-Parra A., Alvarez-Alcon M., Salguero J. and Marcos M., Wear. 2013; 302: 1209-1218.

[5] Song X.Q., Takahashi Y., He W.M., and Ihara T., JSPE. 2016; 82(9): 814-820 (In Japanese).

[6] Song X.Q., Takahashi Y., He W.M., and Ihara T., JSPE. 2017; 83(5): 445-452 (In Japanese).

[7] Song X.Q., He W.M., and Ihara T., Mech. Eng. Jour. of JSME. 2016; 3(6):15-00534.

[8] Ihara T., Science of machine. 2014; 66(10): 825-832 (In Japanese).

[9] Amiri M. and Khonsari M.M., Entropy. 2010; 12: 1021-1049.

[10] Song X.Q., Takahashi Y., He W.M., and Ihara T., Key Eng. Mat.. 2017; 749: 39-45.

[11] Roma F., Ramirez-Pastor A.J., Physica A. 2003; 328(3-4): 513-524.

PRECISION POLISHING TECHNOLOGY OF FERROELECTRIC PMN-PT SINGLE CRYSTALS FOR SMOOTHER SURFACES

Hideaki Takahashi, Hirofumi Suzuki and Yoshiharu Namba
Department of Mechanical Engineering
Chubu University
Kasugai, Aichi, Japan

INSTRUCTIONS

$Pb(Mg_{1/3}Nb_{2/3})O_3$-$PbTiO_3$ (PMN-PT) [1, 2] is a relatively recently invented single crystal composed of five elements. PMN-PT single crystals have higher dielectric and piezoelectric constants as well as higher electromechanical coupling than all other known ferroelectric materials. Transducers for medical ultrasonic use are one of its main applications. In this case, the distance resolution Δx can be expressed as

$$\Delta x = n \cdot C \cdot t/2N. \quad (1)$$

where n is the wavenumber, C is the acoustic wave velocity [m/s], t is the thickness of the vibrator [m] and, N is the frequency constant [Hz・m].

It is necessary to reduce the thickness t to obtain a high-resolution image. For higher-frequency operation, a thinner single-crystal plate is required. To fabricate thin plates, precision polishing [3-5] and ultraprecision grinding [6, 7] have been performed. However, the dielectric and electromechanical properties of PMN-PT single crystals markedly degrade with decreasing thickness caused by the polishing process [3, 4]. These properties may be recovered by heat treatment at 200 °C for 1 h [4]. Polished or etched surfaces on depolarized samples have micropatterns with the appearance of fingerprints owing to the domain structure [4, 8-10]. It has been clarified that the parts with positive polarity have a higher removal rate than those with negative polarity on a depolarized sample. In this paper, we describe the precision polishing of PMN-PT relaxor-based ferroelectric single crystals using various fine powders on different polishers to obtain smoother thin plates.

EXPERIMENTAL PROCEDURE

Polishing and Surface Observations

PMN-PT piezoelectric single crystals grown by the Bridgman method with pellet feeding [11] were cut into {001}-plane single crystals with dimensions of 8 mm × 7 mm × 0.4 mm thickness by a diamond saw blade, then lapped to a constant thickness. All six sides of each sample were {001} planes. Six samples were pasted on an alumina plate of 100 mm diameter and 7 mm thickness using electron wax, as shown in Figure1. Polishing was performed under the conditions shown in Table 1.

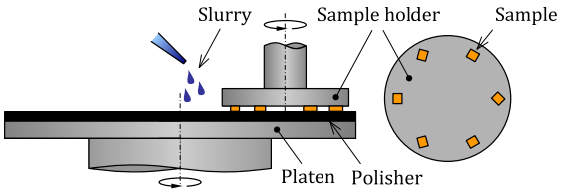

FIGURE 1. Schematic diagram of polishing.

TABLE 1. Experimental conditions of precision polishing.

Sample	Single crystal PMN-PT {001} 8 mm×7 mm×0.4 mm
Slurry	Abrasives; 7 nm SiO_2, 13 nm Al_2O_3, and 21 nm TiO_2 Solvent; Ultrapure water Grain concentration; 3 wt% pH; 4.6～12.0
Polisher	Foamed polyurethane and Polyester nonwoven cloth
Rotation of sample holder	50 min^{-1}
Rotation of polisher	50 min^{-1}
Applied pressure	15 kPa～24 kPa

Finished surfaces were observed using a laser confocal microscope, optical surface profiler and atomic force microscope (AFM). The very small depth of removal of 10 nm order was estimated from the change in the length of the Knoop indentation as a result of polishing [12]. On the other hand, the conventional removal rate was measured from the change in the sample thickness as a result of polishing using an electric micrometer. The surface and cross-sectional surface of the polishers were observed using a scanning electron microscope (SEM).

Poling Treatment and Measurement of Dielectric Constant

Polished samples with dimensions of 8 mm × 7 mm were coated on both sides with gold of 100 nm thickness as electrodes by a magnetron sputtering apparatus. Each sample was poled by applying an electrical field of 800 V/mm for 10 min in air at 25 °C. Figure 2 shows cross-sectional models of the depolarized and poled samples to be polished. The dielectric constant was measured at 1 kHz, 1.0 V rms and no DC bias using an LCZ meter in a temperature-controlled oven [4].

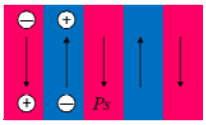

(a) Depolarized

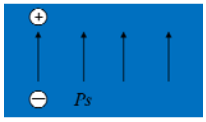

(b) Positively-poled

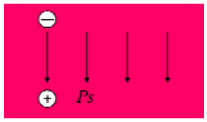

(c) Negatively-poled

FIGURE 2. Schematic cross-sectional models of depolarized and poled samples.

EXPERIMENTAL RESULTS AND DISCUSSIONS

Typical Features of Surfaces Polished Using Al_2O_3, TiO_2 and SiO_2

For the polishing of Si wafers, hard polyester nonwoven cloth, semi-hard polyester nonwoven cloth and soft foamed polyurethane are used as polishers for rough, medium and final polishing, respectively, in industry [13]. Figure 3 shows micrographs of the surfaces of depolarized samples on a foamed polyurethane polisher that were polished using Al_2O_3, TiO_2 and SiO_2 powders. The surfaces polished with Al_2O_3 and TiO_2 had the abrasives embedded on the finished surfaces as shown in Figures 3(a) and (b). On the other hand, there were no such embedded particles on the surface polished using SiO_2, although domain patterns were clearly observed [4]. The surface roughness values vary considerably among the surfaces owing to the embedded particles. It is clear that SiO_2 is the most suitable powder for polishing PMN-PT crystals.

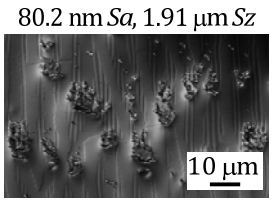

(a) Al_2O_3 (13 nm)

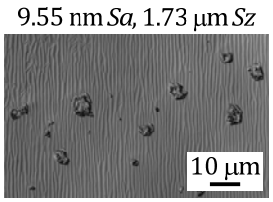

(b) TiO_2 (21 nm)

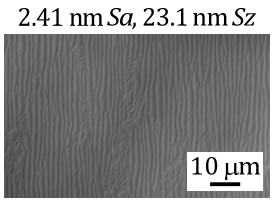

(c) SiO_2 (7 nm)

FIGURE 3. Differential interference micrographs of surfaces on depolarized samples polished using foamed polyurethane polisher.

Effect of Polishing Conditions on the Removal Rate and Surface Roughness in Different Polarizations when Using Foamed Polyurethane Polisher

Six samples were pasted as shown in Figure 1, and polished on a SiC #2000 abrasive paper to remove the coated gold then rinsed. The finished surface roughness was 0.2 μm *Sa*, measured using a 3D optical profiler. Figure 4 shows the relation between the removal rate of polishing using 7 nm SiO_2 with the foamed polyurethane polisher and the polishing time for different polarity. Figure 5 shows the change in surface roughness during the polishing process. Figure 4 and 5 show that the removal rate and surface roughness saturate with increasing polishing time.

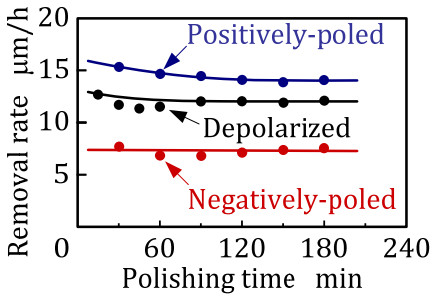

FIGURE 4. Effects of polishing time on removal rate for different polarities of the surfaces to be polished.

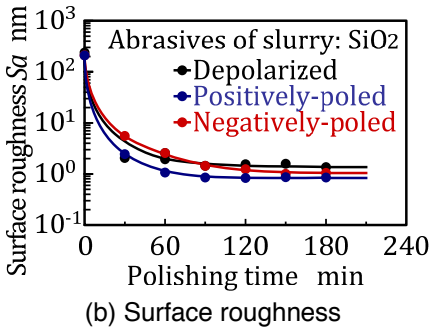

FIGURE 5. Effects of polishing time on surface roughness for different polarities of the surfaces to be polished.

Typical Features of Polished Surfaces in Different Polarization States when Using Foamed Polyurethane Polisher

We prepared three samples in different polarization states, as shown in Figure 2, and polished them using 7 nm SiO_2 powder and the foamed polyurethane polisher under a polishing pressure at 15 kPa. AFM images show considerably different features on the polished surfaces as shown in Figure 6. The depolarized sample shows a typical micropattern with the appearance of fingerprints [4] owing to the domain structure, as shown in Figure 6(a), and the surface roughness is 3 nm *Sa*. The positively poled sample has the smoothest surface of 0.3 nm *Sa* with microprotrusions of about 5 nm height, as shown in Figure 6(b). On the other hand, the negatively poled sample has a smooth surface of 0.5 nm *Sa* with micropits of about 5 nm depth, as shown in Figure 6(c). The area rates of the microprotrusions and micropits are 0.56% and 2.68%, respectively.

Figure 7 shows cross-sectional models of the polished surfaces with different polarities from Figure 6. In the poling process, B-site ions such as Mg, Nb and Ti may be displaced to the positively poled side [14, 15], resulting in the removal rate on the positively poled surface being higher than that on the negatively poled surface.

Such protrusions or pits may be generated or disappear during the polishing process. Thus, the pits were observed on a negatively poled sample surface during the polishing as an example, as shown in Figure 8. Figure 8(a) shows an AFM image of a negatively poled sample surface polished on the foamed polyurethane polisher using 7 nm SiO_2 powder.

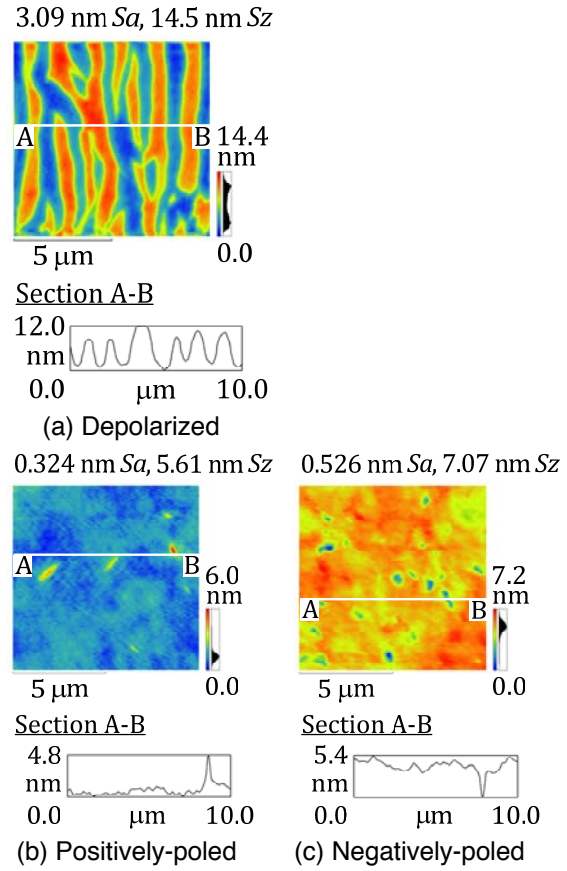

FIGURE 6. Surface structure of polished ferroelectric PMN-PT single crystals in different polarization states on foamed polyurethane polisher, measured using AFM.

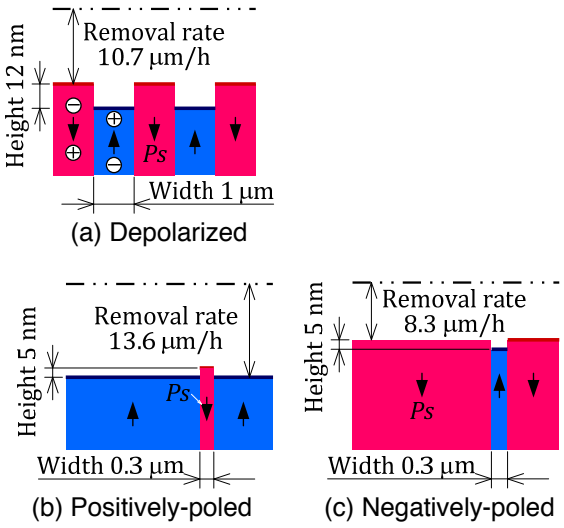

FIGURE 7. Cross-sectional models of polished surfaces with different polarities.

There are tiny pits in circles A and C. After polishing to removal depth of 47 nm and 89 nm, we took AFM images of the same area as shown in Figures 8(b) and (c), respectively. The pit in circle A appears in all the figures, but the pit in circle C is not present in Figure 8(c). There are no pits in the two circles B in Figure 8(a); however, new pits appear in Figures 10(b) and (c). From this figure, it was found that microprotrusions are formed on positively poled surface and micropits are formed on a negatively poled surface during polishing using the foamed polyurethane polisher.

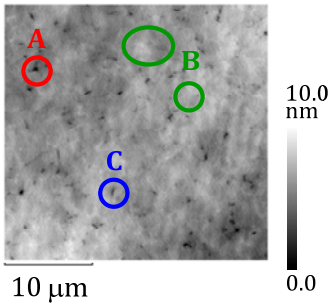

(a) As polished

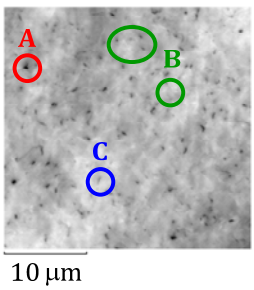

(b) After 47 nm polishing

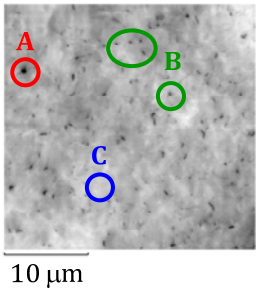

(c) After 89 nm polishing

FIGURE 8. AFM images of surfaces polished on a foamed polyurethane polisher for different depths of polishing.

Comparison of Foamed Polyurethane and Polyester Nonwoven Cloth

We tested the effectiveness of two different polishers for eliminating such protrusions or pits on polished surfaces. Figures 9 and 10 show AFM images of polished surfaces on positively poled and negatively poled samples, respectively. There are protrusions in Figure 9(a) and pits in Figure 10(a), although there are no such defects in Figures 9(b) and 10(b). Thus, we can remove such protrusions or pits by using a polyester nonwoven cloth as a polisher. The

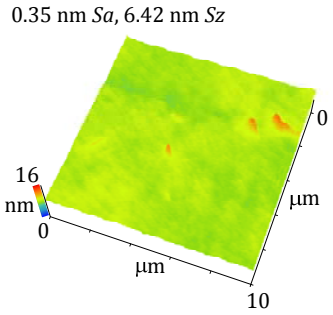

(a) On foamed polyurethane

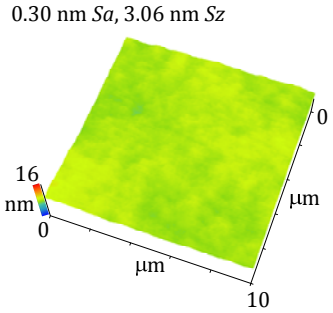

(b) On polyester nonwoven cloth

FIGURE 9. AFM images of polished positively-poled surfaces.

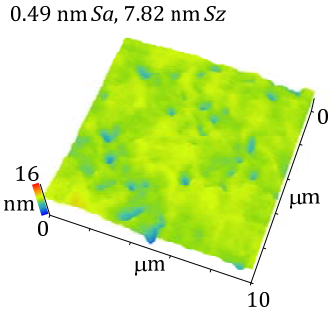

(a) On foamed polyurethane

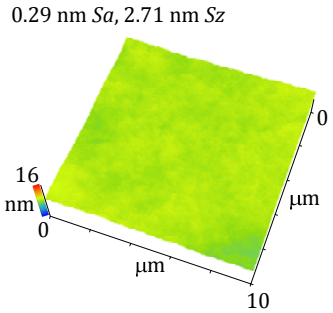

(b) On polyester nonwoven cloth

FIGURE 10. AFM images of polished negatively-poled surfaces.

required polishing depth is 2.5 μm for this purpose.

In the case of the foamed polyurethane polisher, the removal rates are 10.7 μm/h, 13.6 μm/h and 8.3 μm/h on depolarized, positively poled and negatively poled samples, respectively, as shown in Figure 7. On the other hand, the removal rates are 7.0 μm/h, 6.9 μm/h and 7.0 μm/h on depolarized, positively poled and negatively poled samples using the polyester nonwoven cloth, respectively. The removal rate using foamed polyurethane is higher than that using non-woven cloth.

Generation of Protrusions or Pits on Polished Surfaces Using Foamed Polyurethane Polisher

Here, we consider the cause of protrusions or pits during the polishing using the foamed polyurethane polisher. It is well known that spontaneous polarization is affected by stress, the temperature and the electric field [5]. Such spontaneous polarization may occur during the precision polishing of poled samples using a foamed polyurethane polisher as shown in Figures 6-8, 9(a) and 10(a). First we polished a positively poled sample using 7 nm SiO_2 and polyester nonwoven cloth, then we formed a Knoop indentation on the polished surface, as shown in Figures 11(a) and 12(a). These figures show a plastically deformed zone around the indentation. The red part around the indentation indicates a raised part. Then, we polished the sample using 7 nm SiO_2 and polyester nonwoven cloth. Distinctive patterns were observed around the indentation by laser confocal microphotography, as shown in Figure 11(b). Figure 12(b) shows an AFM image of the same area. This figure shows periodic irregularities outside the plastically deformed zone along the line joining A and B. The higher parts of the periodic irregularities may be considered as areas negatively poled by spontaneous polarization due to the indentation. The lower parts are the original positively poled surface. Since the periodic irregularities spread to the elastic deformation region outside the plastically deformed zone, the cause of the microprotrusions and pits by polishing using the foamed polyurethane polisher described in Figures 6-8 has been elucidated.

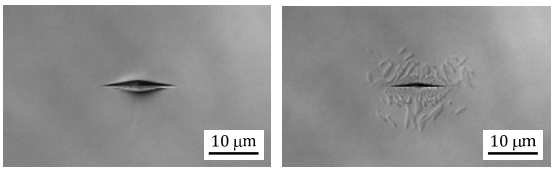

(a) After indentation (b) After polishing with polyester nonwoven cloth

FIGURE 11. Laser confocal micrographs of Knoop indentation on polished surface.

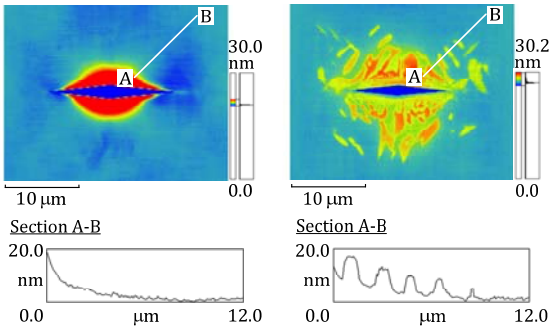

(a) After indentation (b) After polishing with polyester nonwoven cloth

FIGURE 12. AFM images of Knoop indentation on polished surface.

CONCLUSIONS

PMN-PT relaxor-based ferroelectric single-crystal {001} surfaces were poled and polished on foamed polyurethane and polyester nonwoven cloth polishers with SiO_2, Al_2O_3 and TiO_2 powders comprising particles of 7 nm, 13 nm and 21 nm diameter, respectively, and the removal rates and polished surfaces were evaluated. The following conclusions may be drawn from the results of this study.

1. The removal rate of precision polishing using the foamed polyurethane polisher and 7 nm SiO_2 powder depended on the polarity of the PMN-PT sample of positively poled sample had the highest removal rate and lowest surface roughness. On the other hand, a negatively poled sample has the lowest removal rate and a surface roughness value between those of the positively poled and depolarized samples. Neither poled samples exhibited a micropattern having the appearance of fingerprints owing to the domain structure after polishing.
2. The depolarized sample had an intermediate value of the removal rate and the highest surface roughness among the

samples, and also exhibited micropatterns on the domain structure after polishing.

3. Microprotrusions and pits appeared on the surfaces of the positively poled and negatively poled samples, respectively, polished using the foamed polyurethane polisher and 7 nm SiO_2 powder.
4. By using a polyester nonwoven cloth polisher with 7 nm SiO_2 powder, a very smooth surface of 0.3 nm *Sa* without any protrusions or pits was obtained on the poled sample.
5. When using 7 nm SiO_2 powder, there were no embedded particles on the polished surface and a higher removal rate and lower surface roughness than those when using Al_2O_3 powder were obtained.
6. The removal rate depended on the polarity and the abrasive material of the polishing fluid. The surface roughness depended on the polarity of PMN-PT sample.

ACKNOWLEDGEMENTS

The authors would like to express their sincere thanks to JFE Mineral Co., Ltd., Nippon Aerosil Co., Ltd., Toyoda Van Moppes Ltd., and Shimadzu Corp. for supplying the PMN-PT single crystals, ultrafine SiO_2 powder, polishing machine and new software for AFM, respectively. This work was partly supported by the Special Research Fund of Chubu University and the Osawa Scientific Studies Grants Foundation.

REFERENCES

[1] Shrout T R, Chang Z P, Kim N, Markgraf S. Dielectric behaviour of single crystals near the $(1-x)Pb(Mg_{1/3}Nb_{2/3})O_3$-$(x)PbTiO_3$ morphotropic phase boundary. Ferroelectrics Letters Section. 1990; 12: 63-69.

[2] Park S E, Shrout T R. Ultrahigh strain and piezoelectric behaviour in relaxor based ferroelectric single crystals. Journal of Applied Physics. 1997; 82:1804-1811.

[3] Lee H J, Zhang S, Luo J, Li F, Shrout T R. Thickness-Dependent Properties of Relaxor-$PbTiO_3$ Ferroelectrics for Ultrasonic Transducers. Advanced Functional Materials. 2010; 20:3154-3162.

[4] Takahashi H, Suzuki H, Namba Y. Surface topography and dielectric properties of polished PMN-PT single crystals, Annals of the CIRP. 2016; 65: 541-544.

[5] Zhang S, Li F, Jiang X, Kim J, Luo J, Geng X. Advantages and challenges of relaxor-$PbTiO_3$ ferroelectric crystals for electroacoustic transducers – A review, Progress in Materials Science. 2015; 68: 1-66.

[6] Namba Y, Takahashi H. Ultra-Precision Surface Grinding of PMN-PT Relaxor-Based $PbTiO_3$ Ferroelectric Single Crystals, Annals of the CIRP. 2010; 59: 589-592.

[7] Takahashi H, Namba Y, Suzuki H, Takahashi M. Effects of Ultra-Precision Surface Grinding on Dielectric Properties of PMN-PT Single Crystals. Journal of the Japanese Society for Precision Engineering. 2017; 83: 775-780. (In Japanese)

[8] Zhang S, Li F. High performance ferroelectric relaxor-$PbTiO_3$ single crystals: Status and perspective. Journal of Applied Physics. 2012; 111(031301): 1-50.

[9] Zhao K Y, Zhao W, Zeng H R, Yu H Z, Ruan W, Xu K Q, Li G R. Tip-bias-induced domain evolution in PMN-PT transparent ceramics via piezoresponse force microscopy. Applied Surface Science. 2015; 337:125-129.

[10] Wong M F, Zeng K. Mechanical Polishing Effects Toward Surface Domain Evolution in $Pb(Zn_{1/3}Nb_{2/3})O_3$-$PbTiO_3$ Single Crystals. Journal of the American Ceramic Society. 2011; 94: 1079-1086.

[11] Matsushita M. Piezoelectric single crystal ingot, producing method therefor and piezoelectric single crystal device, United States Patent 8119024 B1, August 20, 2012.

[12] Namba Y, Tsuwa H. Ultra-Fine Finishing of Sapphire Single Crystal, Annals of the CIRP. 1977; 25: 325-329.

[13] Doi T, Marinescu D, Uhlmann E ed. Handbook of Ceramics Grinding and Polishing (2nd Edition), Elsevier, Oxford: 2014.

[14] Reaney I M, Colla E L, Setter N. Dielectric and Structural Characteristics of Ba-and Sr-based Complex Perovskites as a Function of Tolerance Factor. Japanese Journal of Applied Physics. 1972; 33: 3984-3990.

[15] Bhalla A S, Guo R, Roy R. The perovskite structure - a review of its role in ceramic science and technology, Material Research Innovations. 2000; 4: 3-26.

TEMPERATURE MEASUREMENT OF BURNISHING PROCESS BY ELECTRO-CONDUCTIVE TOOL

Hayate Tanaka, Hidetake Tanaka, Haruhisa Sakamoto
Sophia University
Tokyo, Japan

INSTRUCTIONS

The surface finishing process has been evaluated by comprehensive performance. However, it's also evaluated by a productivity and an effect for environment. The burnishing is one of the surface finishing process for metal products after machining. This processing uses the plastic deformation of the workpiece surface and obtain a smooth surface. The burnishing has a lot of advantages as follows; It does not require additional finishing machine, but need to exchange a tool only. Therefore, it improves process time shorten. After burnishing, residual stress occurs in a processing surface of the workpiece. Therefore, fatigue strength and abrasion resistance of workpiece is improved. Because of using plastic deformation without any chips, it is regarded as a low emission process [1] [2]. Fig 1 shows the overview of burnishing process.

Appending electro-conductivity for burnishing tools is ideal for the practical burnishing process in order to simplify the set-up process utilizing the electro-conductivity between a workpiece and a burnishing tool. The authors had tried to study a relationship between tool temperature and tool wear and to measure tool temperature using the tool-workpiece thermocouple method. In order to measure tool temperature using this method, it is necessary that a tool have electro-conductivity. The authors developed and demonstrated an electro-conductive burnishing tool made of cemented carbide. However, it generated chips under the inappropriate burnishing conditions, which consisted of burnishing force, workpiece material, feed rate and rotation speed. On the other hand, conventional commercial burnishing tool made of single crystal diamond did not generate any chips under any burnishing conditions. The authors have tried to developed a new burnishing tools made of boron doped CVD diamond to satisfy electro-conductivity as well as enough hardness. The characteristics of the developed burnishing tool were verified and its usability was demonstrated by comparative experiments by use of a single crystal one.

If we tried measure tool temperature using above-mentioned method, it requires to calibrate the measured thermoelectromotive force as temperature. Furthermore, there is also a problem of whether the developed electro-conductive diamond tool and the workpiece form a thermocouple. The authors proposed a calibration experiment method, and demonstrated the relationship between the thermoelectromotive force and the temperature between the developed electro-conductive diamond tool and the workpiece.

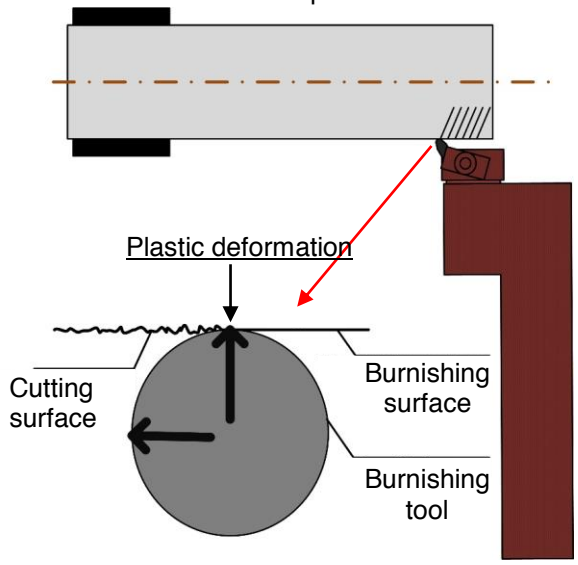

FIGURE 1. The burnishing process using plastic deformation.

TOOL-WORKPIECE THERMOCOULPLE METHOD AND BASICMEASUREMENT TEST

Fig.2 shows the principal of tool-workpiece thermocouple method [3]. A workpiece and a tool (they are different metal each other) are conjunct and it performs a thermocouple based on the seebeck effect. According to calibration of thermo-electromotive force against temperature by this method. The tool tip temperature during processing can be measured.

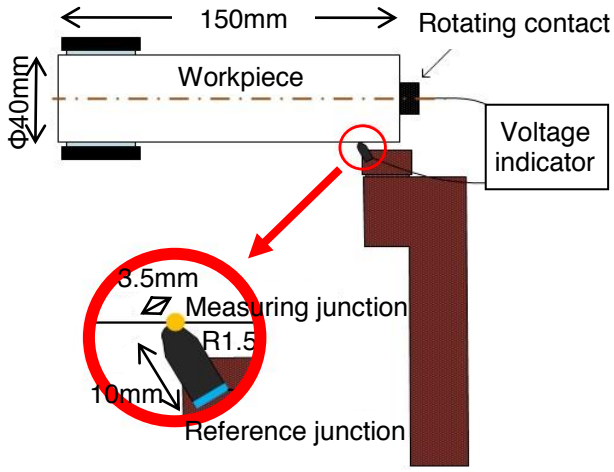

FIGURE 2. Overview of tool-workpiece thermocpouple method.

Table 1 shows the fundamental experimental results of measurement of tool temperature by tool-workpiece thermocouple method. Workpiece was aluminum alloy (ISO AlZn5-5MgCu) and burnishing tool was cemented carbide. According to Table 1, tool temperature while processing is 35 to 43 degree Celsius for each condition. It can be supposed that the principal factor of such lower tool temperature are high ductility, malleability and thermal conductivity of workpiece. Nevertheless, as this result, it is found that tool temperature can be measured by the proposed method.

TABLE 1. Cutting and burnishing conditions and experimental results (tool temperature)

		Cutting	Burnishing	
Feed rate	mm/rev	0.139	0.052	
Rotational speed	min^{-1}	710	395	510
Thermoelectromotive force	mV		0.6～0.7	0.6～0.9
Temperature	℃		35	43
Ra	μm	1.530	0.170	0.187
Rz	μm	6.805	1.187	1.274

EVALUATION OF ELECTRO-CONDUCTIVE DIAMOND TOOL FOR BURNISHING PROCESS

The left of Fig.3 shows the whole view of the developed electro-conductive diamond tool and the right one shows tool tip surface observed by a laser microscope (Olympus co. ; LEXT OLS4100). Tip of the tool consisted a boron doped CVD diamond, which has electro-conductivity.

Table 2-4 show experimental (cutting and burnishing) conditions. The authors selected two kinds of cylindrical shape workpieces made of stainless steel (ISO X10Cr Ni18-9) and aluminum alloy (ISO AlZn5-5MgCu) and processed by a lathe. In the case of some conditions that changed the rotational speed and feed rate were added and processed it on four conditions in total (Table 4).

Table 5 shows the arithmetic average surface roughness *Ra* and the maximum height roughness *Rz* of processing surface of the single-crystal diamond tool and electro-conductive diamond tool. The surface texture of electro-conductive diamond tool was almost equal to the single-crystal diamond tool.

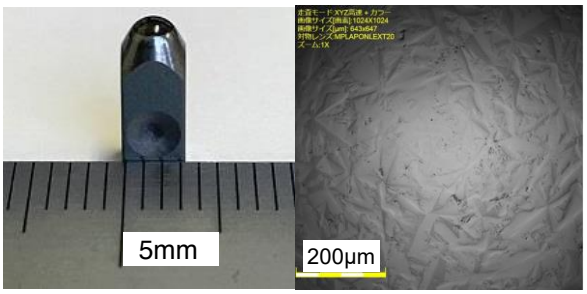

FIGURE 3. Electro-conductive diamond burnishing tool

TABLE 2. Experimental conditions (Cutting).

Rotational speed	min^{-1}	710
Feed rate	mm/rev	0.139
Cutting depth	mm	0.3

TABLE 3. Experimental conditions (Burnishing-aluminum alloy).

Rotational speed	min^{-1}	395
Feed rate	mm/rev	0.052
Burnishing force	N	32.5

TABLE 4. Experimental conditions (Burnishing-stainless steel).

		Conditions			
		1	2	3	4
Rotational speed	min^{-1}	395	710	395	710
Feed rate	mm/rev	0.05	0.05	0.14	0.14
Burnishing force	N	32.5			

TABLE 5. Tool surface roughness.

Tool material	*Ra*	*Rz*
Single crystal diamond	0.008μm	0.066μm
Electro-conductive diamond	0.013μm	0.097μm

Trial burnishing test was carried out under the conditions (Table 3, 4) after cutting under the condition (Table 2), using by a commercial single-crystal diamond tool and the electro-conductive diamond tool. For aluminum alloy, the arithmetic average roughness Ra and the maximum height roughness Rz of workpiece after cutting are as follows.

Ra=1.171μm, Rz=5.597μm

Fig.4 shows the arithmetic average roughness Ra and the maximum height roughness Rz of workpiece after burnishing. As it is found from the graph, the burnishing by the electro-conductive diamond tool has been done normally as well as the single-crystal diamond tool. From the results, it is found that electro-conductive diamond tool has tool performance as same as the single-crystal diamond tool.

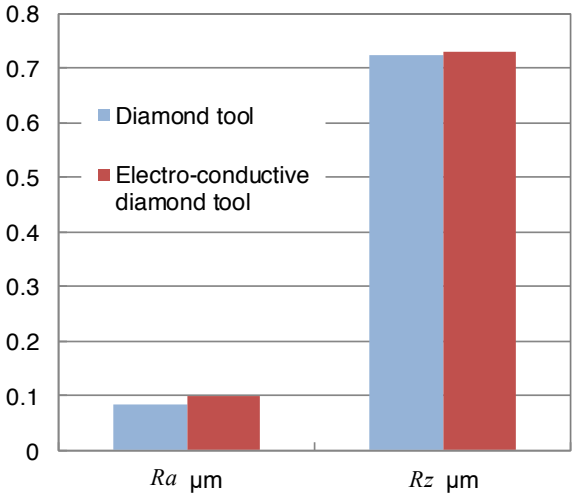

FIGURE 4. Surface roughness after burnishing (ISO AlZn5-5MgCu).

For stainless steel, the arithmetic average roughness Ra and the maximum height roughness Rz of workpiece after cutting are as follows.

Ra=1.550μm, Rz=6.967μm

And the authors experimented on four conditions for this workpiece by which it causes chips easily.

Fig.5 (a) –(d) shows the arithmetic average roughness Ra and the maximum height roughness Rz of workpiece after burnishing. As it is found from the graph, the burnishing by the electro-conductive diamond tool has been done normally as well as the single-crystal diamond tool. For stainless steel, although the electro-conductive diamond tool is slightly inferior to the single-crystal diamond tool in terms of tool performance.

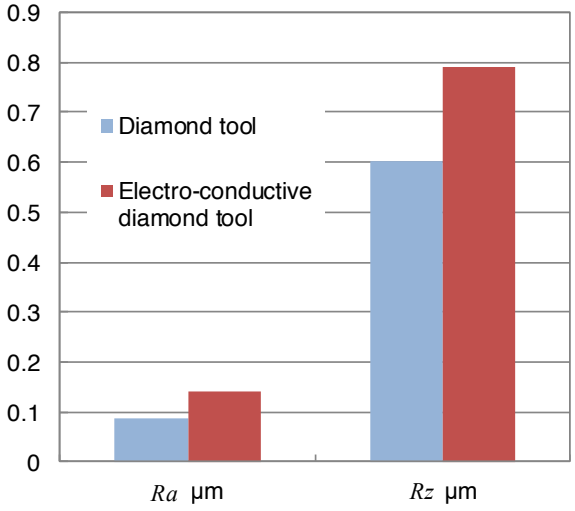

(a) Condition 1

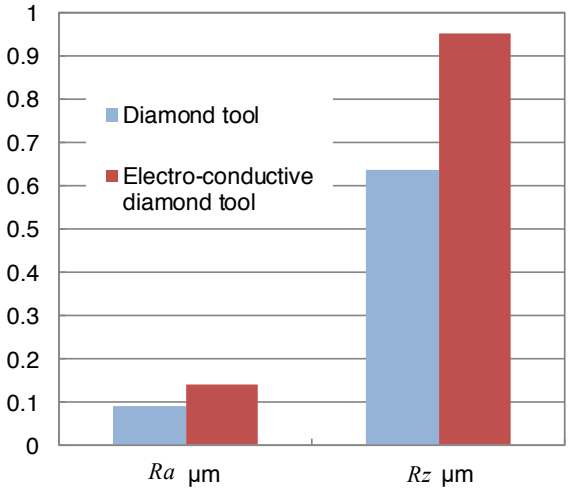

(b) Condition 2

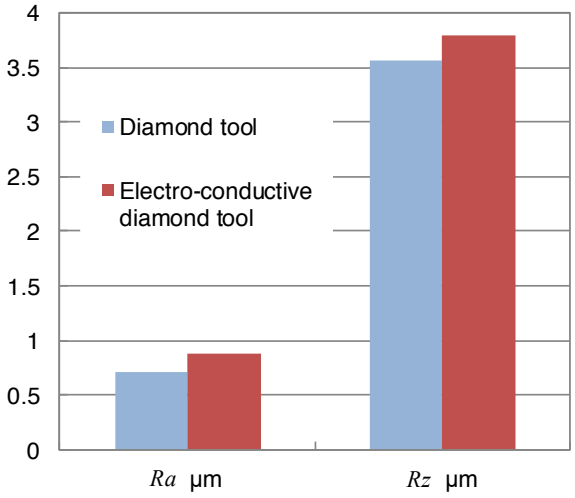

(C) Condition 3

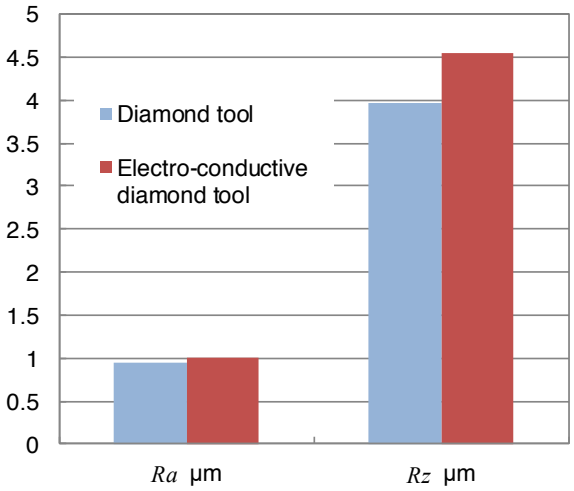

(d) Condition 4

FIGURE 5. Surface roughness after burnishing (ISO X10Cr Ni18-9).

Fig.6 shows roughness curve after cutting and burnishing. It can be seen that the burnishing process by the electro-conductive diamond tool is sufficiently processed. Consequently, the developed diamond tool has enough ability for burnishing.

CALIBRATION EXPERIMENT METHOD

Fig.7 shows a calibration experiment method, and Fig.8 shows the experimental setup. For a workpiece (solid round bar), drill a hole at the center of the bottom surface and insert a heater. The temperature was controlled by PID temperature controller. Then, the thermoelectromotive force which generated at that time with a voltage indicator was measured.

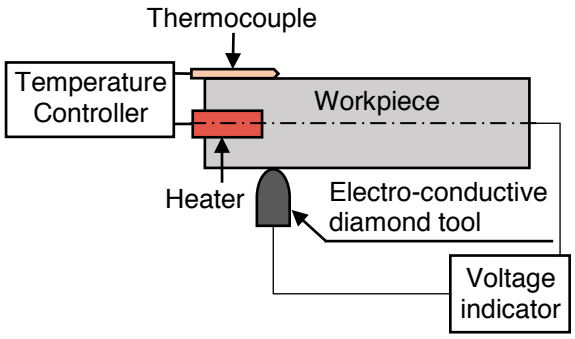

FIGURE 7. The calibration experiment method.

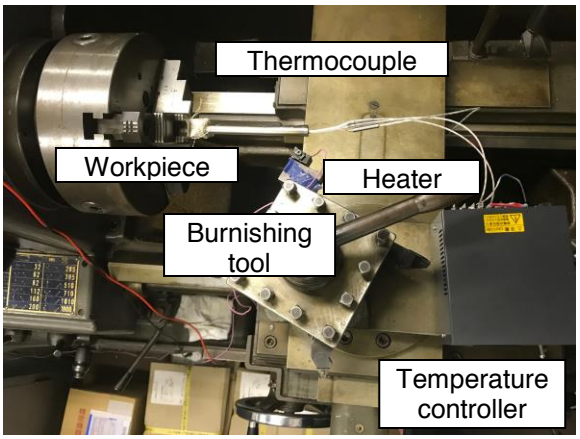

FIGURE 8. The overview of calibration experiment method.

EXPERIMENT OF THERMOELECTROMOTIVE FORCE MEASUREMENT

The authors measured the thermoelectromotive force at which the temperature of the tool and workpiece (ISO X10Cr Ni18-9) contact point was controlled by the above method. Where, the temperature was raised from 100℃ to 300℃ at 50℃ increments. The reference junction was set to room temperature (about 22℃).

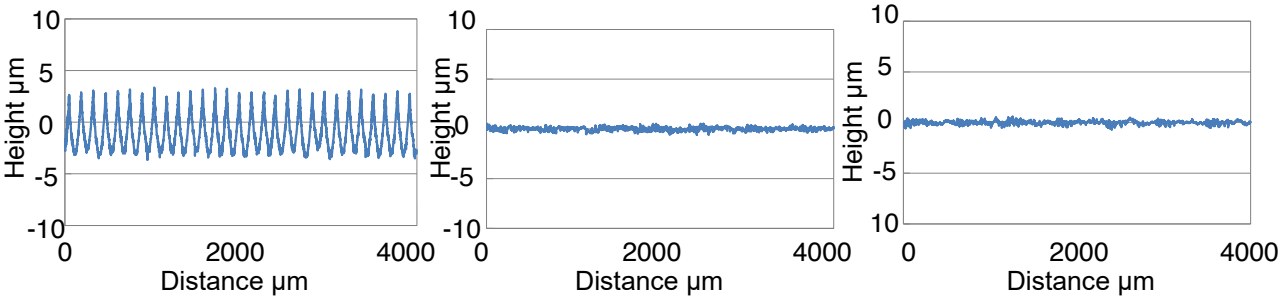

(a) Cutting

(b) Burnishing (Single crystal diamond)

(c) Burnishing (Electro-conductive diamond)

FIGURE 6. Roughness curves after cutting and burnishing.

Table 6 shows experimental results, and Fig.9 shows the results plotted on a graph. From this Table and Figure, it can be seen that the thermoelectromotive force is rising with the temperature rise. Also, as with the thermocouple characteristics, the thermoelectromotive force and the temperature have a linear relationship.
For thermocouple, it is used very small thermoelectromotive force to calibrate to temperature. Therefore, it is necessary to use one with higher resolution than the voltage indicator used in this experiment, or to use an amplifier that amplifies the measured thermoelectromotive force.

TABLE 6. Experimental results of thermoelectromotive force measurement.

Temperature	Thermoelectromotive force
℃	mV
100	0.2 - 0.3
150	0.3 - 0.4
200	0.4 - 0.5
250	0.6 - 0.7
300	0.8 - 0.9

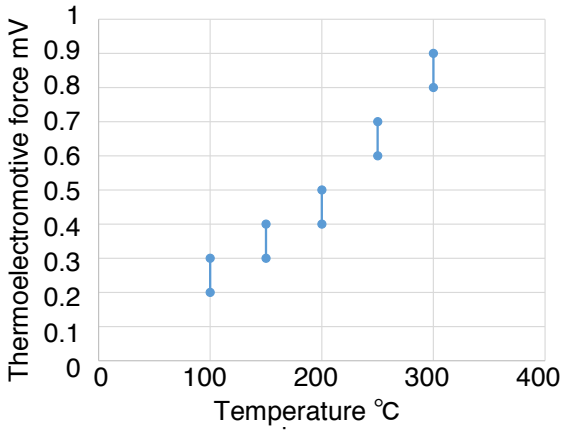

FIGURE 9. Relationship between thermoelectromotive force and temperature.

CONCLUSION

The tool temperature using tool-workpiece thermocouple method was demonstrated.
An electro-conductive diamond tool was developed and its tool performance was almost equal to the single-crystal diamond tool and verified the usability for the burnishing tool. The authors also verified whether thermocouple can be formed between (developed) electro conductive diamond tool and workpiece.

REFERENCES

[1] N.S.M. El-Tayeb., K.O. Low and P.V. Brevern, Influence of roller burnishing contact width and burnishing orientation on surface quality and tribological behavior of Aluminium 6061, Journal of Materials Processing Technology.

[2] Ishii, W., Tanaka, H. and Yanagi, K., 2009. An analytical study on surface modification effect in burnishing process. Proceedings of The Asian Symposium for Precision Engineering and Nanotechnology 2009.

[3] D.A. Stephenson. Tool-Work Thermocouple Temperature Measurements-Theory and Implementation Issues. Journal of Engineering for Industry. 1993;115 (4):432-437.

INVERTED DIAMOND CUTTING OF RIGHT TRIANGULAR RETROREFLECTORS: SURFACE QUALITY AND CUTTING FORCES

Tauhiduzzaman, M.[1]; Milliken, N.[2]; Tutunea-Fatan, O. R.[2]; Bordatchev, E.V.[1]
[1]National Research Council of Canada
London, Ontario, Canada
[2]Mechanical and Materials Engineering Department
Western University
London, Ontario, Canada

INTRODUCTION

Retroreflector (RR) is a passive optical element that returns the incoming light back to its original source by means of total internal reflection (TIR). Automotive industry relies on a particular type of RR called inverted corner cube (ICC) characterized by a superior retroreflectivity across a wide range of incident angles. However, the fabrication of automotive RRs is plagued by two main limitations: a) ICCs are produced through fairly expensive, largely manual and time-consuming pin-bundling technique developed in late 70's, and b) when ICCs are generated on curved surfaces, inherent manufacturing artifacts are formed in the final geometry degrading the optical performance of the RRs. Formation of such artifacts termed as "pockets" are shown in *FIGURE 1*.

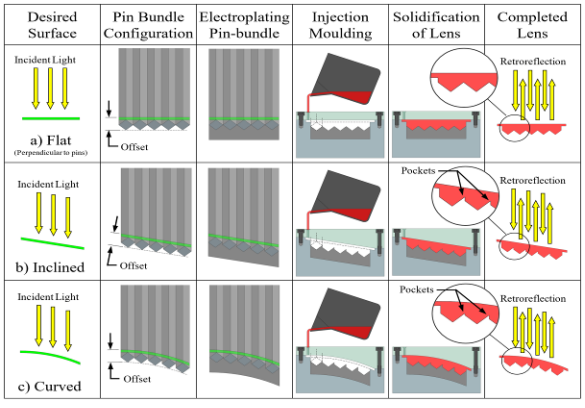

FIGURE 1: Pin-bundling technique and the formation of pockets

The ICC is comprised of three faces that are mutually orthogonal and that share a common vertex. The use of rotational tools and micromachining processes, e.g. micromills and micromilling, for fabrication of ICCs is desirable as requirements for optical surface quality of the facets below $S_a < 10$ nm and form shape in the inner corners cannot be achieved. These limitations significantly affect optical performance and functionality and make them unacceptable for tightly regulated safety applications including automotive. To provide alternative ways in advancing technologies for manufacturing light guide and retroreflective optical structures, new approaches have been developed for both design and fabrication of novel RRs that are no longer constrained to the conventional ICC shape. As such, right triangular prismatic (RTP) RRs and ultraprecise single point inverted cutting (USPIC) were proposed to represent viable alternatives to ICC RR design and pin-bundling fabrication technique, respectively [1, 2, 3]. Arrays of RTPs were successfully microfabricated in plastics and metals and their optical performance has demonstrated an enhanced RR functionality as shown in *FIGURE 2*.

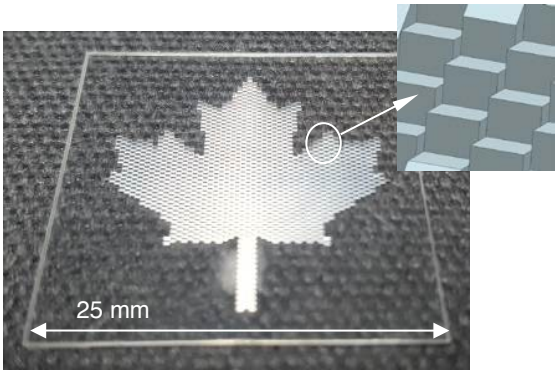

FIGURE 2: Canadian maple leaf fabricated on thin plastic using RTP structures

Along these lines, the primary objective of this work is to further investigate the USPIC process and preliminary assess correlations between surface roughness and cutting forces in the context of a time-efficient microcutting process that targets achieving optical surface quality. Geometric accuracy and surface quality play an important role in retroreflection. This is because

retroreflection is made up of a combination of reflections and TIRs and these behaviors are dependent on actual incident angles with respect to the surface. If optical form, geometry and surface quality are not satisfactory then the light will not be redirected in the desired way.

EXPERIMENTAL WORK

The goal of the cutting experiments was to find the sources of surface quality formation potentially attributed to the cutting tool condition, process parameters, cutting mechanics and dynamics, and non-uniformity of the cutting motions. Cutting experiments were conducted on a five-axis ultra-precision micromachining center Microgantry nano5X by Kugler GmbH characterized by a sub-micron positional accuracy. Vertical semi-orthogonal cuts in Al 6061 alloy were performed with a rectangular-wedged diamond tool of 1.0 mm width that mimics the bi-directional strategy [3]. The workpiece was fixtured to a 3-channel mini dynamometer attached to the rotary table of the machine tool in two different scenarios: A-C axis support and fixed Z-axis support. The micromachining system configuration and primary cutting motions used during cutting trials are depicted in *FIGURE 3* and the experimental conditions are listed in TABLE 1.

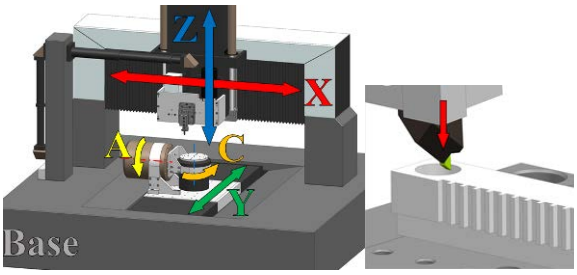

FIGURE 3: Micromachining system (left) and cutting experiment (right) configurations

TABLE 1: Cutting parameters

Speed, mm/min	Depth of cut, μm
10, 8, 6, 4, 2	5.0, 2.0, 1.0, 0.8, 0.6, 0.5, 0.4, 0.3, 0.2, 0.1

RESULTS AND DISCUSSIONS

Effect of cutting parameters on surface quality

The best areal surface roughness S_a of approximately 26 nm was achieved at 2 μm depth of cut (DOC) and 8 mm/min cutting speed at fixed support in Z-axis as shown in *FIGURE 4*a and 4b.

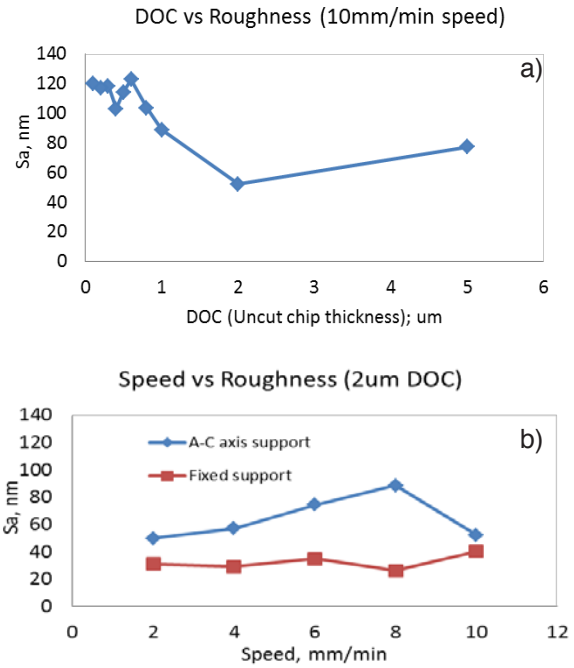

FIGURE 4: Effect of cutting parameters on surface quality

Effect of material anisotropy

The presence of weak material anisotropy (possibly grain boundaries) was revealed through white light interferometry (FIGURE 5a and 5b). The presence of material anisotropy leads to the additional variations of the cutting forces along tool path trajectory. As a result, specific areas with potentially higher hardness are pushed into surrounding material below the surface (~100-200 nm) creating clearly recognized concave areas with clearly defined boundaries. The use of other workpiece material (nano-structured aluminum [4], plated nickel-phosphorus [5]) might eliminate these surface defects.

Effects of cutting edge chipping and build-up formation

Signs of cutting tool edge chipping and dragging hard material particles were also observed on the RTP facet surface (FIGURE 5c). Two types of distinguishing trenches along tool path trajectory were found. Cutting edge chipping causes formation of protruded ribs with height above average surface level. In opposite, hard material particles form builds-up on the cutting edge and during cutting they are forming fairly deep extruded trenches.

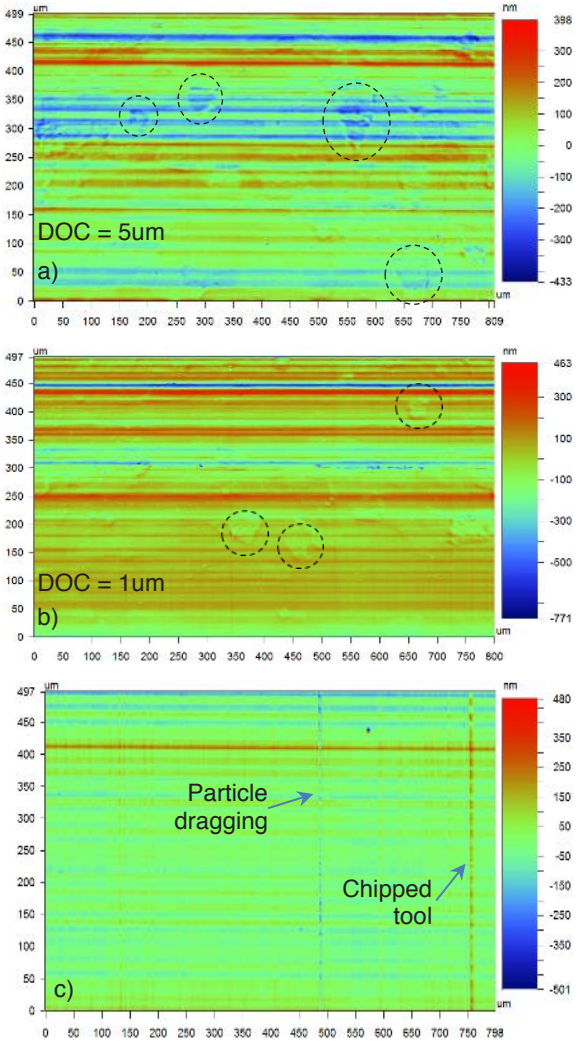

FIGURE 5: Effects of material anisotropy (a), tool edge chipping (b), and hard particle dragging (c)

More work is required to understand the onset of cutting edge chipping [3]. Particle dragging was investigated in the past [4] and might be possible to address through workpiece material changes as well as a superior chip management.

Normal-to-feed direction waviness/ripples

This likely represents the major contributor to the high surface roughness observed. Preliminary observations suggest that a vibration is present in the cutting direction shown by lines P1, P2 and P3 in *FIGURE 6*.

The vibration is more prominent when A-C axis is involved. Furthermore, a 7 Hz vibration (appx 42 mm^{-1}) is present in both fixturing modes (*FIGURE 7*). However, a higher spatial frequency is present in the A-C axis support scenario and this causes the deterioration of the surface quality. The cutting force signal has captured this occurrence and thereby the primary objective of this study is to understand the correlations between cutting forces and normal-to-feed ripples, in an attempt to propose cutting strategies capable to eliminate them.

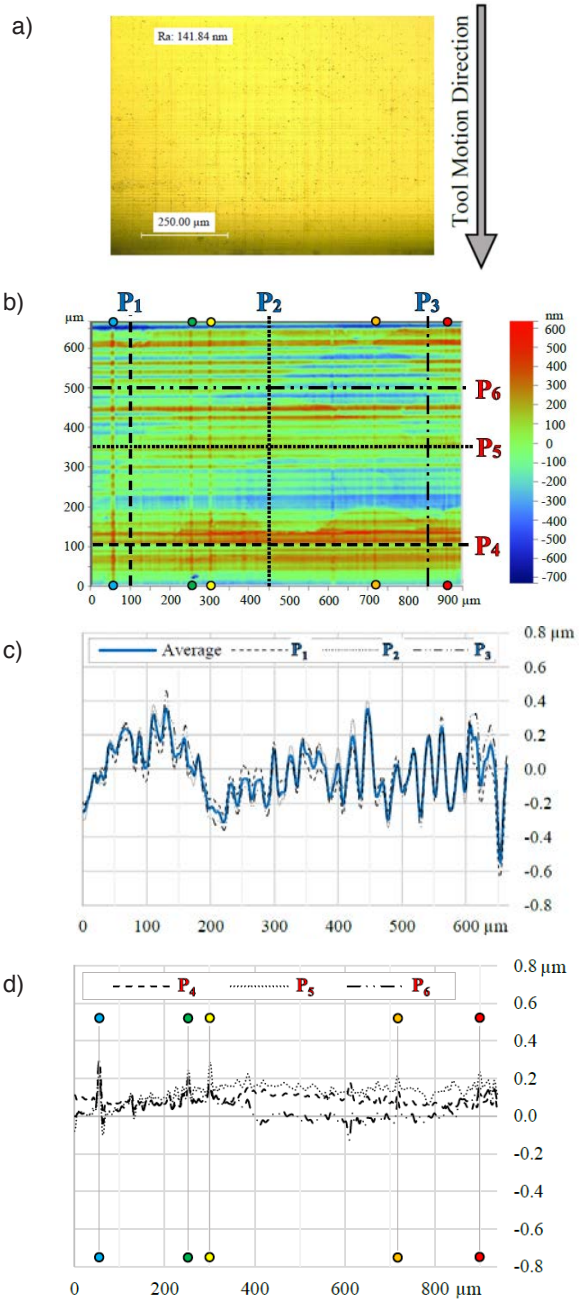

FIGURE 6: Surface quality and characteristics: a) optical image, b) surface topographical image, c) surface profiles along feed direction (P1, P2, P3), and d) surface profiles across feed direction (P4, P5, P6)

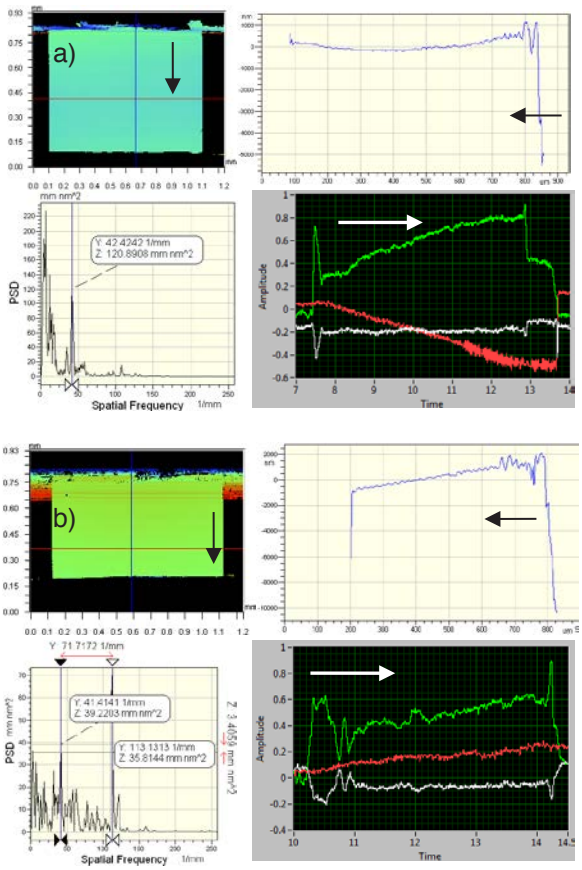

FIGURE 7: Surface white light interferometry and force measurements for workpiece mounted on fixed fixture (a) and A-C axis (b). Arrow represents the cutting direction.

The oscillations across the feed are not as clearly understood and their constant presence is suggestive of undesirable cutting mechanics. The periodicity of these surface characteristics is suspected to be system dynamics; however, as a prerequisite it is important to understand the cutting mechanics. This knowledge will help identify complications within the cutting kinematics and potentially allow modifications that will avoid tool damage and the introduction of undesirable system dynamics.

Cutting mechanics

Apart from the stiffness of the system which is causing a 7 Hz vibration, it is also obvious that there is an impact present during the entry of the tool from the force signals shown in *FIGURE 7*. There is also a sharp increase in cutting force near the exit. The entry impact can be minimized by using soft wax as a sacrificial layer for process damping. The reason for the increase in force near the exit is probably due to the direction change in shear angle that usually causes a burr formation. A detail chip analysis is required to conclude this observation. A similar approach of sacrificial layer can be taken to minimize this effect during exit as well.

FUTURE WORK

Further investigation of cutting mechanics and system dynamics monitoring is in progress with added data acquisition systems like capacitive sensors as shown in *FIGURE 8*.

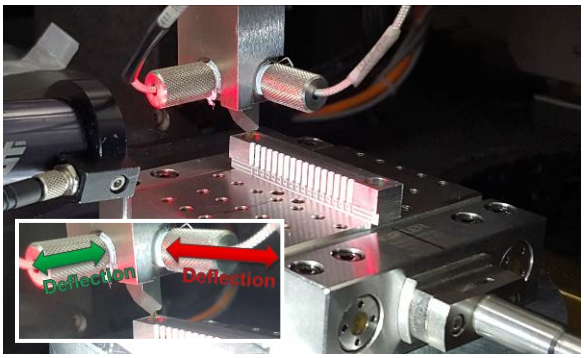

FIGURE 8: Setup with dynamometer and 2D capacitive sensor to detect deflection

REFERENCES

1. Hussein, S., Hamilton, B., Tutunea-Fatan, O.R., Bordatchev, E.V., Novel Retroreflective Micro-Optical Structure for Automotive Lighting Applications, SAE International Journal of Passenger Cars – Mechanical Systems. 2016; 9(2):497-506.
2. Hamilton, B., Milliken, N., Hussein, S., Tutunea-Fatan, O.R., Bordatchev E., Enhanced bidirectional fabrication of right triangular prismatic retroreflectors, Proceedings of the 31st ASPE Annual Conference, Portland, OR, USA. 65:36-41.
3. Hamilton, B.W., Hussein, S., Milliken, N., Tutunea-Fatan, O.R., Bordatchev, E.V., Fabrication of right triangular prism retroreflectors through 3½½-axis ultraprecise single point inverted cutting, Computer-Aided Design & Applications, 2017, published on-line on March 17, 2017, 11 p.
4. Tauhiduzzaman, M. and Veldhuis, S.C., Effect of material microstructure and tool geometry on surface generation in single point diamond turning, Precision Engineering, 2014, 38:481–491.
5. http://www.precitech.com/downloads/FactorsAffectingSurfFinish.pdf, last accessed on Mar. 22, 2017

Fundamental study on thermal stability of micro milling spindle supported by water hydrostatic bearings under spindle rotation

Tsubasa Yaguchi[1], Akio Hayashi[2] and Yohichi Nakao[3]
[1]Graduate School of Mechanical Engineering
Kanagawa University
Yokohama, Kanagawa, JAPAN
[2]Department of Mechanical Engineering
Kanazawa Institute of Technology
Kanazawa, Ishikawa, JAPAN
[3]Department of Mechanical Engineering
Kanagawa University
Yokohama, Kanagawa, JAPAN

INTRODUCTIONS

In recent years, various demands to machine precise micro parts and/or molds used in advanced industries such as automobile, aircraft, medial and electronics for instance. These parts are produced by ultra-precision machine tools. In order to machine the precise micro structures, high speed spindle must be a key component that determines the machining accuracy of the parts. Thus, the spindle of the ultra-precision machine tools for machining the precise micro structures needs high rotational accuracy, high bearing stiffness and high-speed spindle rotation. To meet the requirements, the spindles supported by hydrostatic bearings are in general used for the ultra-precision machine tools. The spindle supported by the hydrostatic bearings achieves better rotational motion with low friction by non-contact support of the rotor. However, even in the spindle supported by the hydrostatic bearings, heat generations due to the power loss cannot be avoided. The power loss is mainly due to the pressure drop of the lubricating fluid and the viscous friction of the lubricating fluid.

Heat generation causes thermal deformation of the spindle, and it influences the machining accuracy. Thus, in order to reduce thermal deformation, high precision liquid temperature control device for cooling the heat source has been developed [1]. However, the heat generation mechanism and temperature change of the spindle supported by hydrostatic bearings have not been understood sufficiently.

In general, oil or air is used as lubricating fluid for hydrostatic bearings. Oil hydrostatic bearings can achieve high bearing stiffness. However, since the viscosity of oil is high, heat generation under spindle rotation is significant. Thus, aero static pressure bearings are used for high-speed spindles because of the low viscosity of air. However, it is difficult to achieve high bearing stiffness of the aero static pressure bearings. This is attributed by the compressibility of air. In contrast, water is incompressible fluid with low viscosity. Additionally, water has the high specific heat and thermal conductivity. Thus, it is considered that high bearing stiffness with high thermal stability can be achieved by using water as lubricating fluid. For these reasons, a spindle supported by water hydrostatic bearings has been developed and investigated [2].

A goal of this research is to improve the thermal stability of the spindle supported by water hydrostatic bearings. Specifically, this study investigates the temperature change of the spindle supported by water hydrostatic bearings and the advantage of using water for the lubricating fluid.

The temperature change of the spindle supported by the water hydrostatic bearings has been investigated for the condition of the no-spindle rotation [3]. In this paper, the temperature change of the designed spindle is investigated with spindle rotation. The spindle and lubricating fluid are represented by a lumped parameter model. The temperature change of the spindle is then predicted based on the model. In addition, in order to clarify the thermal stability and the heat generation mechanism of the spindle, the temperature change of lubricating fluid and spindle body are measured. For example, the water used for lubricating fluid temperature at the upstream and

downstream of the spindle and the temperature of the spindle body are measured.

STRUCTURE OF WATER HYDROSTATIC SPINDLE

Figure 1 shows the basic structure of the designed spindle considered in this paper. The spindle is supported by water hydrostatic radial and axial bearings. In the spindle, the rotor has a cooling water channel. Supplying cooling water reduces the temperature increase in the spindle during high-speed spindle rotation. However, in the present paper, in order to investigate the fundamental heat generation mechanism of the spindle no cooling water was supplied into the cooling channel formed at the center of the rotor.

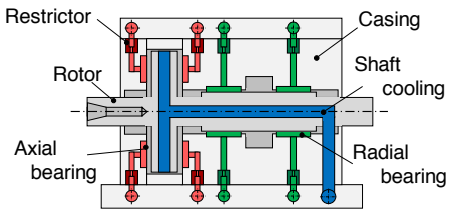

FIGURE 1. Structure of water hydrostatic spindle

NOMENCLATURE

c : specific heat of water and spindle
h : bearing gap
L_1 : length of radial bearing
m : mass of each part of spindle
P_f : power loss of lubricating fluid
P_g : power loss on bearing gap
p_r : recess pressure
P_{re} : power loss on bearing restrictor
p_s : supply pressure
q : flow rate of lubricating fluid
R_1 : radius of radial bearing
R_2 : radius of axial bearing
S : heat transfer area
T : temperature
α : coefficient of heat transfer
μ : viscosity of water
ρ : density of water
ω : angular speed of rotor

SUBSCRIPTION

ax : axial
b : casing
cw : cooling water
r : rotor
rd : radial
w : water

HEAT SOURCE OF HYDROSTATIC SPINDLE

The power loss due to the pressure loss of lubricating fluid at the bearing system is one of the heat sources. The bearing restrictor reduces the pressure of the lubricating fluid supplied to the recess through the bearing restrictor. Furthermore, the recess pressure of the lubricating fluid reduces to zero at the drain ports of the spindle. The fluid power is represented by the product of the pressure and the flowrate. Accordingly, the all power loss of the supplied lubricating fluid P is represented by Eq. (1).

$$P_f = p_s \times q \tag{1}$$

The power losses due to these pressure drops are represented by Eq. (2) and Eq. (3), respectively.

$$P_{re} = \left(p_s - p_r\right) \times q \tag{2}$$

$$P_g = p_r \times q \tag{3}$$

In addition, the power loss due to the viscous friction in the bearing small gaps is another heat source of the spindle supported by hydrostatic bearing. When the spindle speed increases, the influence of the viscous friction becomes significantly. Figure 2 shows the structure of hydrostatic beatings. The power loss in the radial bearings and the axial bearings due to the viscous friction P_{rd} and P_{ax} are then represented by Eq. (4) and Eq. (5).

$$P_{rd} = \frac{2\pi\mu R_1^3 L_1}{h_{rd}}\omega^2 \tag{4}$$

$$P_{ax} = \frac{\pi\mu\left(R_2^4 - R_1^4\right)}{h_{ax}}\omega^2 \tag{5}$$

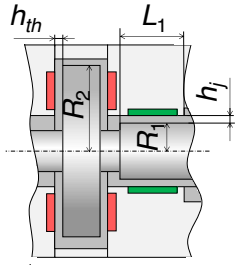

FIGURE 2. Structure of hydrostatic bearings

The power losses affecting the increase of the temperature of the lubricating fluid in the radial and axial bearings are calculated by Eq. (1), Eq. (4) and Eq. (5) as shown in Fig.3.

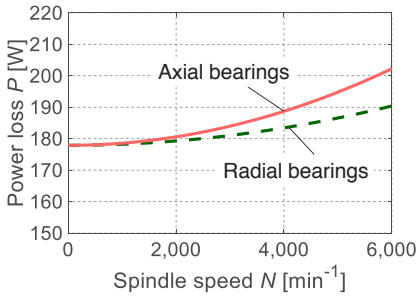

FIGURE 3. Power loss of hydrostatic bearings

CALCULATION OF SPINDLE TEMPERATURE

MATHEMATICAL MODEL

For simplicity, the temperature of the lubricating fluid, the temperature of the casing and rotor of the spindle are represented by a lumped parameter model. Thus, temperature distributions of the spindle are not considered in this study. Additionally, the thermal conductivity of air is significantly smaller than that of water, therefore it is assumed that there is no heat transfer between the spindle and the air around the spindle. In the calculation, it is considered that the temperature change of the lubricating fluid occurs due to the power losses in the bearing restrictors and the bearing gaps. The temperature change of the casing and the rotor is generated based on the heat transfer between lubricating fluid and each part of the spindle. Figure 4 shows the illustration of the simulation model of the introduced lumped parameter model. In Fig. 4, the surfaces in which the heat transfer is considered are emphasized. In addition, since the Nusselt number used for calculating the coefficients of heat transfer greatly varies depending on the flow velocity, it is calculated by in the model as well [4]. The temperatures of the lubricating fluid, the casing and the rotor can be calculated from the system of the differential equations given by Eq. (6) to Eq. (10).

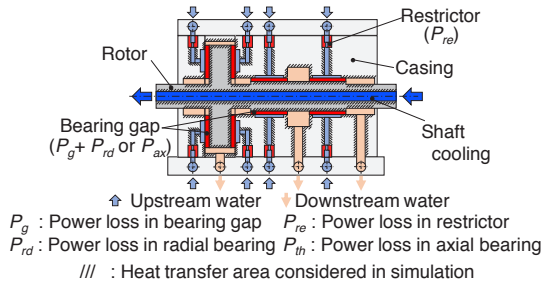

FIGURE 4. Basic illustration of simulation model

$$T_{w1} = T_{w0} + \frac{1}{c_w \rho_w q_w}\{P_{re} - \alpha_{b1} S_{b1}(T_{w1} - T_{b0})\} \tag{6}$$

$$c_b m_b \frac{dT_{b1}}{dt} = \alpha_{b1} S_{b1}(T_{w1} - T_{b1}) \tag{7}$$

$$T_{w2} = T_{w1} + \frac{1}{c_w \rho_w q_w}\{P_g + P_{rd} + P_{ax} - \alpha_r S_r(T_{w2} - T_r) - \alpha_{b2} S_{b2}(T_{w2} - T_{b2})\} \tag{8}$$

$$c_r m_r \frac{dT_r}{dt} = \alpha_r S_r(T_{w2} - T_r) - \alpha_{cw} S_{cw}(T_r - T_{cw}) \tag{9}$$

$$c_b m_b \frac{dT_{b2}}{dt} = \alpha_{b2} S_{b2}(T_{w2} - T_{b2}) \tag{10}$$

CALCULATION RESULTS

Calculation results of the temperatures of the lubricating fluid, the casing and the rotor are shown in Fig. 5 when spindle speed is 6,000 min^{-1}. In the calculation, the supply pressure of the lubricating fluid was set to 3 MPa, the initial temperatures of the lubricating fluid and each parts of the spindle was 20 ℃. In addition, the specific heat of each part of the spindle made by SUS304 was set to 0.59 kJ/(kgK).

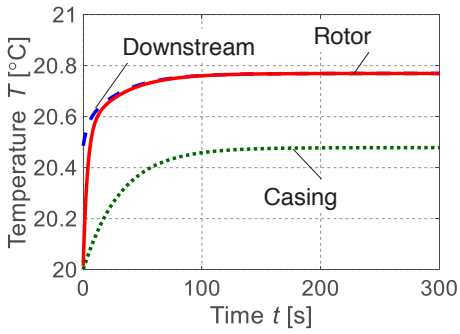

FIGURE 5. Temperature change of spindle

As shown in Fig.5, the temperature of the rotor increases to the same temperature as the lubricating fluid. In this case, the heat is transferred to the rotor from the lubricating fluid until the temperature differences between the rotor and the lubricating fluid is zero, namely until equilibrium state. In contrast, the temperature of the casing is lower than that of the lubricating fluid and casing about 0.3℃. The difference is due to the cooling effect of the

supply passages from the supply ports of the lubricating water to the bearing restrictors. Therefore, the simulation result indicates that the supply passages of the lubricating fluid can also be used for reducing the temperature increase of the spindle.

MEASUREMENT OF TEMPERATURE CHANGE OF SPINDLE

EXPERIMENTAL DEVICE

Figure 6 shows the experimental rig used in this study. In the tank A, the temperature of the lubricating fluid is controlled by the chiller equipment. The lubricating fluid was supplied from the tank A to the spindle by the water hydraulic piston pump. Water flowing out from the spindle flows into the tank B. The water in the tank B returns to the tank A, accordingly. The temperature of the water upstream and downstream of the spindle and the temperature of the outer surface of the casing of the spindle were measured using thermistor type of the temperature sensors. The temperature of the water downstream was measured at the radial and axial bearings, separately.

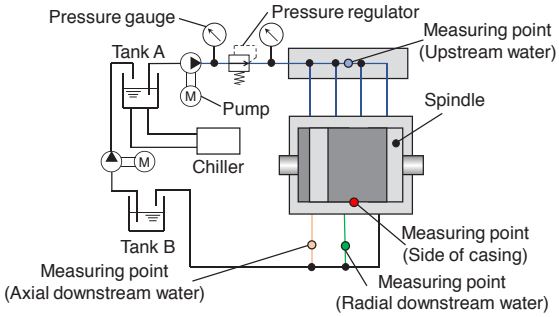

FIGURE 6. Experimental rig

EXPERIMENTAL RESULTS

In the experiments, supply pressure was set at 3 MPa, then the upstream and downstream temperatures of the lubricating fluid and the temperature of the casing were measured. During 10 minutes after starting the experiment, measurements were carried out without water supply. After then, the water flow was supplied to the hydrostatic bearings during from 10 to 40 minutes from the start of the experiments. Furthermore, from 40 to 70 minutes, the rotor of the spindle rotated at the spindle speed of 6,000 min^{-1}. Finally, temperatures were measured during 20 minutes with water flow and without spindle rotation. Figure 7 shows the experimental results. From the experimental result, it is observed that the temperature of water was not constant because of the influence of the performance of the chiller. Thus, the temperature differences dT_{rd} between the upstream water and radial downstream water, dT_{ax} between the upstream water and axial downstream water, dT_b between the upstream water and the casing were calculated, respectively.

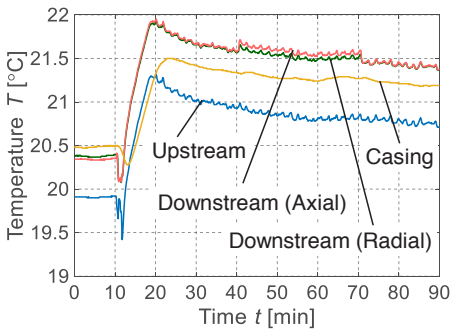

FIGURE 7. Measured temperature change

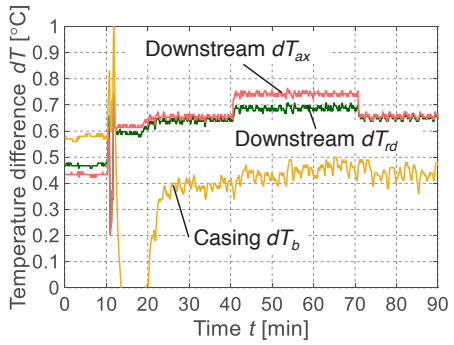

FIGURE 8. Temperature difference of downstream water and casing

Figure 8 shows the temperature differences dT_{rd} and dT_{ax} under the spindle rotation are 0.7 degrees Celsius and 0.75 degrees Celsius, respectively. The temperature increase shows the influences of the power loss of the water flow when the pressurized lubricating fluid released into atmosphere and the power loss of the viscous friction due to the spindle rotation. Additionally, under the spindle rotation, the temperature difference dT_{rd} is higher 0.05 degrees Celsius than that of no-spindle rotation. Similarly, the temperature difference dT_{ax} is 0.1 degrees Celsius. The difference of the temperature increases due to the influence of the viscous friction. Now, it is noted that the

temperature of the casing is lower than that of the downstream water. The reason is the cooling performance of the water flow through the supply channel designed in the casing.

COMPARISON BETWEEN NUMERICAL CALCULATION AND EXPERIMENTS

Comparing the experiment results with calculation results examines the validity of the introduced lumped parameter model. The experiments were made with the different rotational speeds of 2,000, 4,000 and 6,000 min^{-1}, respectively. Furthermore, the steady state temperature differences dT_{rd}, dT_{ax} and dT_b in the experimental results and the numerical calculation results were obtained. The results are compared as shown in Fig. 9 and Fig. 10, respectively.

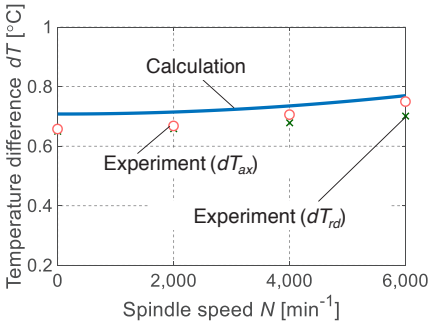

FIGURE 9. Temperature change of lubricating fluid

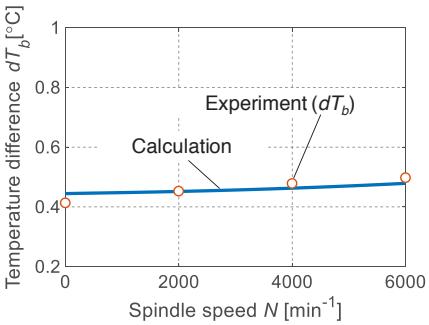

FIGURE 10. Temperature change of spindle

As shown in Fig. 9 and Fig. 10, the calculation results obtained by the lumped parameter model agree well with the experimental result. The difference between the calculations and the experiments is approximately only 0.1 ℃. The temperature change of the lubricating fluid and the casing due to the increase of the rotational speed is only 0.1 ℃ in the range from 0 min^{-1} to 6,000 min^{-1}. However, if the rotational speed of the spindle becomes much higher, the increase of the temperature of the lubricating fluid should be more significantly. For example, it can be predicted that the temperature increase of the lubricating fluid will be about 2.3 ℃ at spindle speed of 30,000 min^{-1} using numerical calculation by the introduced lumped parameter model.

Based on the temperature differences dT_{rd} and dT_{ax} of the lubricating fluid, the power loss P_1 consumed to increase the water temperature is obtained by Eq. (11), Eq. (12) and Eq. (13).

$$P_{rd1} = c_w \rho_w q_{rd} dT_{rd} \tag{11}$$

$$P_{ax1} = c_w \rho_w q_{ax} \times dT_{ax} \tag{12}$$

$$P_1 = P_{rd1} + P_{ax1} \tag{13}$$

The power losses P_{rd1} and P_{ax1} are performance index to indicate how much of the total power loss can be removed by the lubricating fluid.

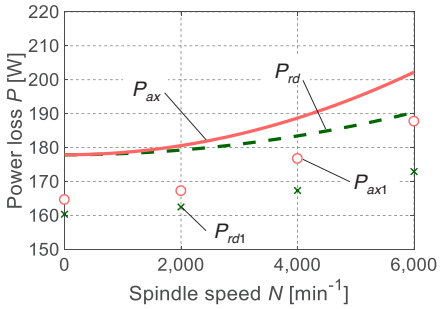

FIGURE 11. Power loss of lubricating fluid

Plots in Fig. 11 are the calculation results using Eq. (11) and Eq. (12). In addition, the solid line in Fig. 11 is the calculation results of the total power loss represented by P_f of the spindle that is determined by Eq. (1), Eq. (4) and Eq. (5). The power loss P_1 that was consumed to increase the temperature of water calculated by Eq. (13) must be lower than the total power loss P_f. As shown in Fig. 11, the difference between P_{ax} and P_{ax1} is only about 15 W, it is about 10 % of the total power loss. It is same as about the relationship between P_{rd} and P_{rd1}. This implies that most of the power loss generated inside the spindle is used for increasing the temperature of the lubricating fluid.

Now, in order to express more clearly the advantage of using water as the lubricating fluid, η is newly defined as Eq. (14). In Eq. (14), η represents the percentage of power loss

released to outside of the spindle by the lubricating fluid. Calculating η_{rd} and η_{ax} from the total power losses P_{rd} and P_{ax} caused by the radial and axial bearings and the power losses P_{rd1} and P_{ax1} used for the lubricating fluid are shown in Fig. 12, respectively.

$$\eta = \frac{P_l}{P_f} \times 100 \tag{14}$$

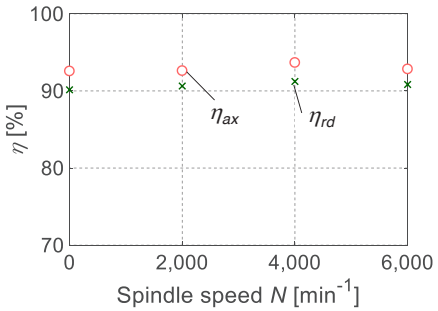

FIGURE 12. Cooling effect of water flow

As shown Fig. 12, the calculation results of η_{rd} and η_{ax} using Eq. (14), respectively. Both are approximately 90 %. Namely, 90 % of the power loss generated inside the spindle was released to the outside of the spindle by the lubricating flow. The result indicates a possibility to develop the spindle having higher thermal stability.

CONCLUSIONS

In this paper, thermal stability of a spindle under spindle rotation was studied by numerical calculations and experiments. The temperature change of the spindle can be predicted by the introduced lumped parameter model. In addition, the validity of the numerical calculation was verified by comparing numerical calculation and temperature measurement results.

Furthermore, the lubricating fluid removed 90 % of the power loss generated inside the spindle into the outside of the spindle. It was also clarified that using water as lubricating fluid is effective for the higher thermal stability of the spindle.

In the future works, prediction of the transient temperature changes by the introduced model will be investigated by comparing experimental result of the temperature change with numerical calculations. Temperature characteristics under higher spindle speeds over 10,000 min^{-1} will be investigated as well. Furthermore, effectiveness of the central shaft cooling for reducing the temperature increase of the spindle will be investigated as well.

REFERENCES

[1] Suzuki H., Urano K. and Kumehara H., Development of Highprecision Liquid-Temperature Regulator for Ultraprecision Machine Tool, Transactions of the Japan Society of Precision Engineering, Vol. 75, No. 5, 2009 (in Japanese)

[2] Nakao Y., Yamada K. and Suzuki K., Design of spindle supported by high stiffness water hydrostatic thrust bearing, Proc. of IMECE 2013 CD-ROM, 2013

[3] Yaguchi T., Hayashi A. and Nakao Y., Fundamental study on thermal stability of micro milling spindle supported by water hydrostatic bearing under non-spindle rotation, Proc. 9th International Conference on Leading Edge Manufacturing in 21st Century, CD-ROM, 2015

[4] JSME Data Book Heat Transfer 5th Edition Maruzen publishing Co., Ltd., pp. 23-78, 2009 (in Japanese)

Laser Cutting Out Process for Semiconductor Substrates Applying Laser Slicing Method

Yohei YAMADA[1], Tatsuki ABE[1], Junichi IKENO[1]
[1]Graduate School of Science and Engineering
Saitama University
Shimookubo 255, Sakura-ku, Saitama, Japan

INTRODUCTION

The demand for semiconductor continue to increase due to spreading smartphone or IoT concept. Semiconductor manufacturing technology continue to progress the advancement and the refinement. However, it is known that semiconductor substrates such as Si and SiC are difficult materials to machining. Therefore, the materials have problem regarding machining efficiency and cost. Here we proposed a laser slicing method as a new process for the semiconductor substrates [1]. The process creates micro cracks into material applying transmittivity of laser beam by focusing pulse laser beam on the inside. Each micro crack link by scanning the pulse laser as shown in Fig. 1. In our previous study, it was confirmed that Si wafers and sapphire glasses can be sliced thin with low kerf loss, small heat affect and small influence of crystal orientation. In addition, three-dimensional structures were fabricated on the sliced face.

In this study, a new laser cutting out method for a semiconductor substrate materials applying the laser slicing method was developed. This method can cut out the materials with high quality and high precision by scanning the laser beam to vertical direction from the bottom face to the top face as shown in Fig. 2. In this paper, we introduce the new cutting out method using correction collar and pulse energy control. As the result, high quality cutting out was realized.

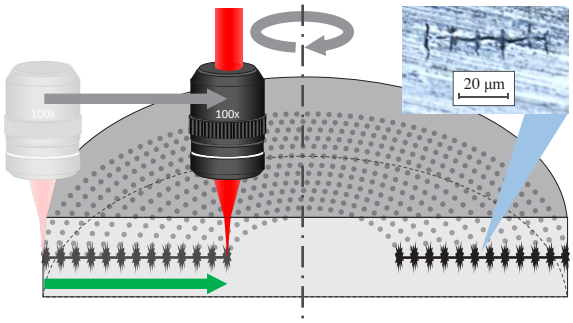

FIGURE 1. Laser Slicing Method.

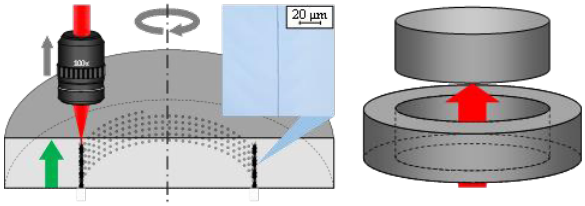

FIGURE 2. Laser cutting out method.

FEASIBILITY OF LASER CUTTING OUT METHOD

In order to confirm the feasibility of this method, a cutting out test was conducted by process conditions as shown in Table 1. The material was single crystal Si wafer with the thickness of 725 μm. A half-inch wafer was cut out. The test was conducted on a ultraprecision machine tool (TOSHIBA MACHINE : ULG-100). The machine tool have a nanosecond fiber laser (JENOPTIK : JenLas fiber ns 20). The Si wafer was set on a vacuum chuck. The run-out of chucked Si wafer surface was less than 500 nm.

The result is shown in Fig. 3. The half-inch wafer was cut out easily by making notches from four directions as shown in Fig. 3(a). However, the appearance of cross section was not constant along to thickness direction as shown in Fig. 3(b). On the bottom area, the micro cracks were not created. The surface had large waviness due to influence of crystal orientation. On the center area, cleavages were observed. On the top area, heat affect and chippings were observed. This nonconstant cross section has possible to occur product defect due to large cleavages or chippings. Therefore, the detail of creation of micro cracks in various conditions was investigated.

TABLE 1. Process conditions.

Wave length	nm	1064
Pulse width	ns	190
Pulse energy	μJ	5.0
Frequency	kHz	500
Crack clearance	μm	2.0
NA		0.85

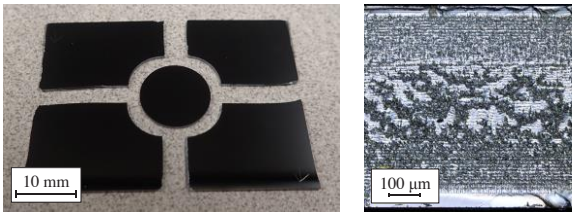

(a) Half inch wafer cutting out (b) Cross section
FIGURE 3. Cutting out test by previous method.

SHAPE OF MICRO CRACKS IN VARIOUS CONDITIONS

1. Pulse energy

The influence of pulse energy for the shape of micro cracks was investigated. Five lines were processed as shown in Fig. 4 and Table 2. The micro cracks were observed by microscope after blade dicing and etching.

Fig. 5 shows relationship between micro crack length and the position. Fig. 6 shows micro crack shapes on pulse energy of 8 µJ. It is found that the micro crack length becomes longer as the pulse energy becomes high. In addition, the crack length becomes shorter as the crack position becomes deep. It is thought that laser intensity was attenuated as the crack position becomes deep and the energy density was decreased by spherical aberration. The spherical aberration is detailed later.

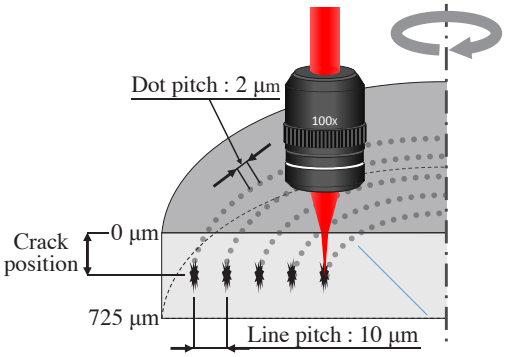

FIGURE 4. Experimental setup.

TABLE 2. Process conditions.

Wave length	nm	1064
Pulse width	ns	190
Pulse energy	µJ	2, 4, 6, 8
Frequency	kHz	500
Defocus DF	µm	-110, -90, -70, -50, -30, -10
Crack clearance	µm	2

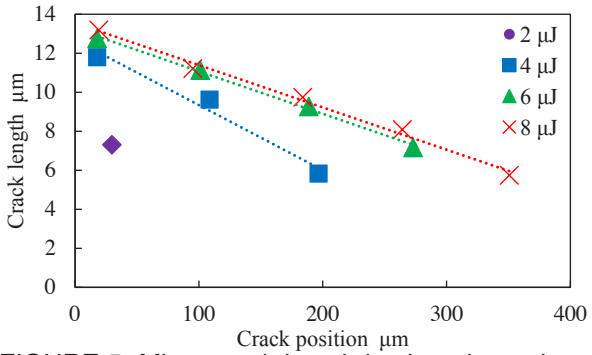

FIGURE 5. Micro crack length in changing pulse energy.

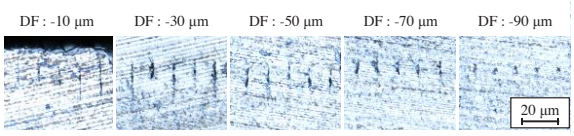

FIGURE 6. Shape of micro crack in changing crack position.

2. Crack clearance

The influence of crack clearance (dot pitch) was evaluated. The process conditions are shown in Table 3. Ten lines were processed on the same crack position. The results are shown in Fig. 7 and Fig. 8. It is found that the crack length becomes longer as the dot pitch becomes small. This result shows that an influence of next creation crack exists because of thermal shock wave or rising absorption coefficient [2].

Next, an observation of the crack with infrared microscope was conducted as shown in Fig. 9. On the dot pitch of 0.5 µm (Fig. 9(a)), each crack linked completely and the width of the line became wide. On the dot pitch of 2.0 µm (Fig. 9(b)), the width of the line became thin and the linkage of cracks were weak compared with 0.5 µm. On the over 2.0 µm as shown in Fig. 9(c), each crack became independent. In this method, the compatibility with small cracks and certain linkage of cracks is the most important factor. Therefore, it is thought that the optimum dot pitch is 2.0 µm.

TABLE 3. Process conditions.

Wave length	nm	1064
Pulse width	ns	190
Pulse energy	µJ	3.0
Frequency	kHz	500
Defocus DF	µm	-20
Crack clearance	µm	0.5, 1.0, 1.5, 2.0, 2.5, 3.0, 4.0, 5.0

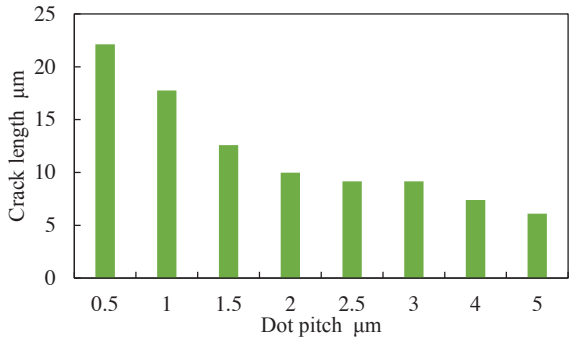

FIGURE 7. Micro crack length in changing crack clearance.

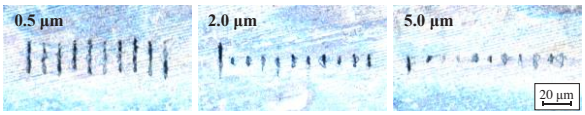

FIGURE 8. Shape of crack in changing crack clearance.

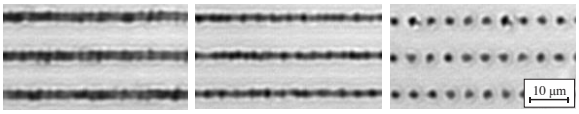

(a) 0.5 μm (b) 2.0 μm (c) 5.0 μm

FIGURE 9. Observation of crack line with infrared microscope.

3. Correction collar

Si has high refractive index material. Therefore, an influence of spherical aberration increases to use a high NA objective lens in this study use. When the laser beam is focused into material, the energy density decreased and micro cracks are not created in deep position because the laser beam is not focused by the spherical aberration as shown in Fig. 10(a). However, the spherical aberration can be compensated by a correction collar (CC). The correction collar can compensate the incident angle of laser beam. Consequently, the laser beam focused sharply into inside of material. Then, it is expected that the micro cracks can be created in deep area. Therefore, the crack shapes were evaluated in various correction collar as shown in Table 4.

The result shows in Fig. 11. The crack position becomes deeper as the compensation of collection collar becomes large. From this result, it was found that all cross section can be processed by using the collection collar. Moreover, as the same with the previous sections, the crack length becomes shorter as the crack position becomes deep. However, it shows the increasing area exists. This area shows maximum energy density area by compensating spherical aberration.

Next, in order to confirm the influence of crystal orientation, {100} face and {110} face were compared on the same process conditions as shown in Fig. 12. On the {100} face, the shape of micro cracks was linear. On the other hand, the shape on {110} face was slant. It is thought that the reason of this slant crack is the influence of crystal orientation. Si tends to cleave in the order of <111>, <110> and <100> direction [3]. Therefore, on the {110} face, the slant crack was created toward <111> direction. From this result, it is considered that this slant crack caused the cleavage area which was shown in Fig. 4(b). However, Fig. 12 also shows there are no slant cracks when the crack length becomes very short. Namely, the influence of crystal orientation can be ignored. In this investigation, it was found that the influence can be ignored in the case of the crack length is less than 7 μm.

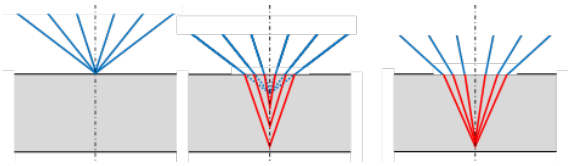

(a) Without correction collar (b) With correction collar

FIGURE 10. Effect of correction collar.

TABLE 4. Process conditions.

Wave length	nm	1064
Pulse width	ns	190
Pulse energy	μJ	3.0
Frequency	kHz	500
Correction collar	mm	0.0. 0.1, 0.2, 0.3, 0.4, 0.5, 0.6, 0.7, 0.8, 0.9, 1.0
Defocus DF	μm	-90, -80, -70, -60, -50, -40, -30, -20, -10
Crack clearance	μm	2.0

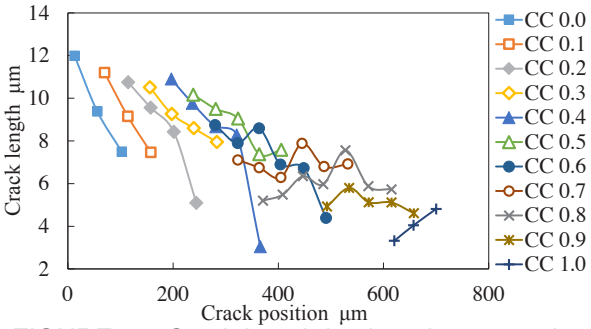

FIGURE 11. Crack length in changing correction collar.

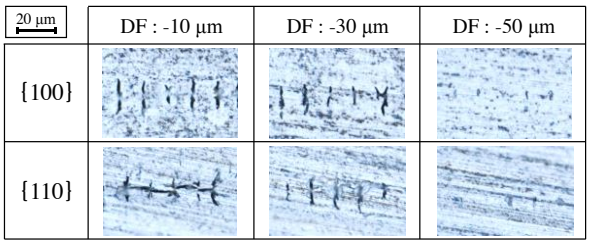

FIGURE 12. Crack shape difference in plane orientation

DEVELOPMENT A NEW LASER CUTTING OUT METHOD

From the results of previous chapter, high quality laser cutting out process without an influence of crystal orientation can be realized to control all crack length become less than 7 μm. Therefore, it is thought that it can be realized to change appropriate the correction collar for each target crack position. However, that method was not replicable due to artificial error of changing the correction collar by hand. Accordingly, a new laser cutting out method to control pulse energy and correction collar was developed.

1. Principle of a new developed method

An outline of the developed method is shown in Fig. 13. The correction collar which appropriate to material bottom face was fixed. Then, the laser beam scanned to vertical direction on the minimum pulse energy which can create a crack less than 7 μm length. Normally, as the crack position becomes deeper, micro cracks do not be created by the attenuation of laser intensity and the spherical aberration. Accordingly, micro cracks can be created by increasing pulse energy. In this case, there is a risk to create the cracks widely. However, when the laser intensity distribution is Gaussian, the laser density of a center point is the most highest. Therefore, the only a center point can be over threshold of cracks creation. Therefore, laser cutting out can be realized by increasing pulse energy as scanning to the surface.

To confirm the feasibility of the developed method, the creation of micro cracks on various pulse energy was investigated as shown in Table 5. The collection collar was fixed of CC1.0 mm which can be focused to the bottom face. The result shows in Fig. 14. It is found that the micro cracks can be created on the all positions by this method. In addition, by controlling pulse energy, micro cracks less than 7 μm can be created on the all positions.

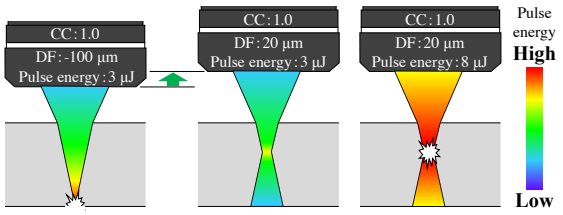

FIGURE 13. Principal of a new cutting out method.

Table 5. Process conditions.

Wave length	nm	1064
Pulse width	ns	190
Pulse energy	μJ	3.0, 3.5, 4.0, 4.5, 5.0, 5.5, 6.0, 6.5, 7.0, 7.5, 8.0, 9.0
Frequency	kHz	500
Correction collar	mm	1.0
Defocus DF	μm	-80, -60, -40, -20, 0, 20, 40, 60, 80, 100, 120
Crack clearance	μm	2.0

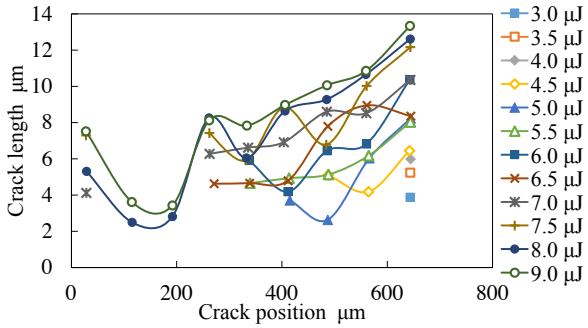

FIGURE 14. Crack length in changing pulse energy. (Correction collar is fixed 1.0 mm)

2 Observation of cross section

The cutting out test using the developed method was conducted. The process conditions are shown in Table 6. A target shape was half inch Si wafer of thickness 725 μm. The CC was fixed to 1.0 mm. Then, the distribution of pulse energy was set as shown in Fig. 15. These pulse energies can create the micro cracks which are less than 7 μm on each crack position. At the top surface, energy density becomes high because the effect of attenuation of laser intensity becomes low. It caused heat affect. Therefore, we stopped the process at 5 μm.

The cross sections of {100} and {110} face after the process are shown in Fig. 16. The cross sections became constant face compared with Fig. 3(b). The faces had no large cleavages. As the result, it was found that high quality cutting out can realized by the developed method.

However, there was difference in {100} and {110} face. The {110} face was roughed compared with {100} face. It shows the influence of crystal orientation exists. It had three different faces as shown in Fig. 17. Fig. 17(a) face occurred on conditions that the crack length becomes less than 2 μm. Each crack did not link. Then, it was cut out forcibly by external force. Therefore, the face has roughness as shown the surface roughness of 2.875 μmRz. Next, Fig. 17(b) face occurred on conditions that crack length becomes nearby 4 μm. Each crack linked finely. The smooth surface of 0.667 μmRz was obtained. On this laser cutting out method, this surface is the most suitable. Finally, Fig. 17(c) face occurred on conditions that crack length becomes nearby 6 μm. Large cleavages were observed. It is thought that this face occurred cleavage by the slant cracks as described in previous chapter. The surface roughness was 2.227 μmRz. In previous study, the influence of crystal orientation did not be observed in the case of crack length of less than 7 μm. It is shows that the shape of micro cracks is changed by interaction of crack lines to vertical direction (Line pitch). Fig. 18 shows micro cracks were laminated vertically 1 line, 2 lines and 3 lines. The 1 line cracks (Fig. 18(a)) were created straight cracks. On the other hand, the 2 lines and 3 lines (Fig. 18(b) and Fig. 18(c)) were created slant cracks. It is thought that the cracks were became longer over 7 μm because the next cracks were created on the top of the previous cracks. Therefore, the heat absorptivity at the overlapped area was increased. In order to resolve the problem, it is considered that it is effective to widen the clearance between previous cracks and next cracks (Line pitch). However, the detailed research has not been conducted yet. In the future, the optimum clearance will be researched.

TABLE 6. Process conditions.

Wave length	nm	1064
Pulse width	ns	190
Pulse energy	μJ	2.3, 2.6, 3.4, 4.2, 5.0, 5.7, 6.5, 9.3
Frequency	kHz	500
Correction collar	mm	1.0
Crack clearance (Dot)	μm	2.0
Crack clearance (Line)	μm	3.0

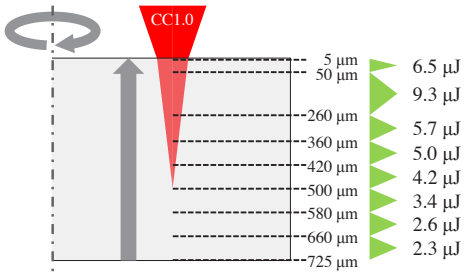

FIGURE 15. Distribution of pulse energy

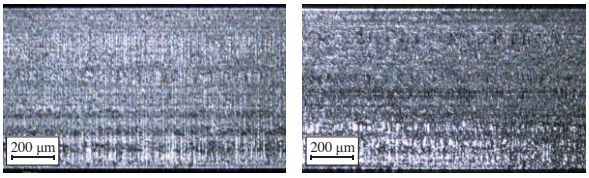

(a) {100} *(b) {110}*

FIGURE 16. Cross section of the developed method.

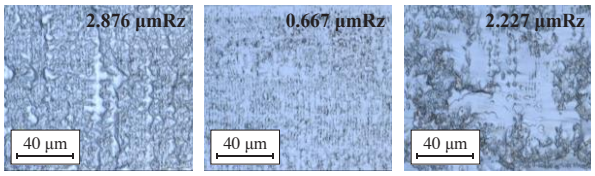

(a) *(b)* *(c)*

FIGURE 17. Different cross sections of the developed method.

(a) 1 line *(b) 2 lines* *(c) 3 lines*

FIGURE 18. Interaction of crack line in vertical direction.

3. Heat affect on top surface

In previous study, heat affect was observed to irradiate laser beam on top surface. It was thought that the heat affect caused chippings and large kerf loss. Therefore, in order to confirm the influence of heat affect, the cracks on top surface was observed.

Fig. 19(a) shows cracks on previous method which irradiate laser beam to the top surface. Si was melted and sputtered around. Deep grooves were formed in places due to laser ablation. The maximum width of crack lines was 6.9 μm. The edges after cutting out had a lot of chippings. It was thought that the heat affect on the top surface became initial crack and it causes product defeat. On the other hand, in the case of applying the developed method as

shown in Fig. 19(b), there was no heat affect. Only dot line was observed. The width of the line was less than 1 μm. The edges after cutting out were very sharp and it can be cut out by linking each dot. Fig. 20 shows comparison number of chippings at the circumference between the previous method and the developed method. It is clear that the number of chippings of the developed method was drastically reduced. From this result, it was found that this developed method can realize kerf loss of 1 μm and chipping less.

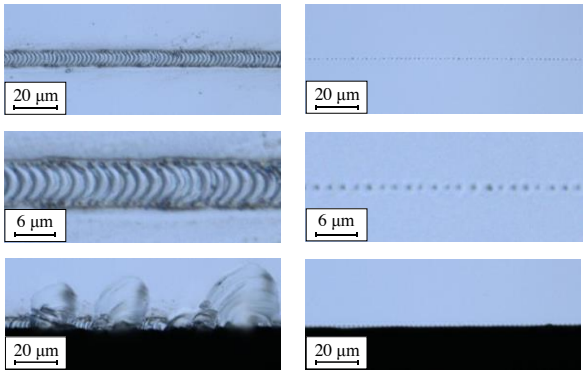

(a) Previous method (b) Developed method

FIGURE 19. Heat affect on top surface.

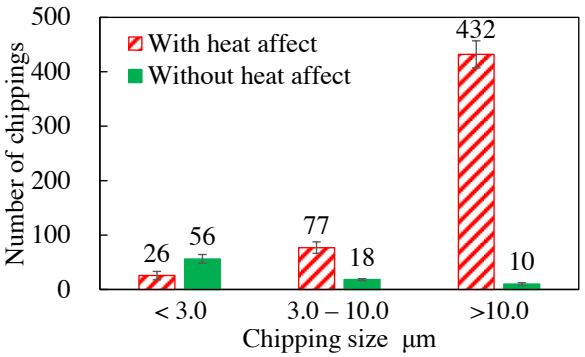

FIGURE 20. Comparison of number of chippings.

CONCLUSIONS

As new process of semiconductor substrates with high precision and high reliability, a laser cutting out method applying laser slicing method was developed. The results are summarized as shown below.

(1) Si can cut out easily by the micro cracks create into material inside by laser beam focused into the inside. Then the laser beam is scanned to vertical direction from material bottom face to top face. The micro cracks link each other.

(2) The micro cracks become larger as the laser pulse energy become high or the crack clearance become small.

(3) The micro cracks can not be created in deep position due to a spherical aberration. The spherical aberration can be compensated by correction collar of the objective lens. The micro cracks can be created in deep position by controlling the correction collar appropriately.

(4) In the case of the length of micro cracks becomes too long, slant micro cracks are created. The slant micro cracks cause large cleavage. However, when the length is less than 7 μm, there is no slant micro cracks. The influence of crystal orientation can be ignored.

(5) A new laser cutting out method using correction collar was developed. The length of micro cracks can be controlled less than 7 μm in all position by controlling pulse energy.

(6) A laser cutting out method with constant and smooth cross section can be realized. However, the influence of crystal orientation could not be ignored. It is considered that the micro cracks were became long due to the interaction of line pitch.

(7) The developed method can be cut out without heat affect on top surface. The chippings on the edges are reduced drastically and the kerf loss is less than 1 μm.

This work was supported by JSPS KAKENHI Grant Number 16K17991.

REFERENCES

[1] D. Sekine, J. Ikeno, N. Shinozuka, H. Suzuki: Study on three dimensional laser slicing technology, Proc. JSPE, 597-598, (2013) (in Japanese).

[2] E. Ohmura, M. Kumagai, M. Nakano, K. Kunom K. Fukumitsu, H. Morita: Analysis of Processing Mechanism in Stealth Dicing of Ultra Thin Silicon Wafer, Journal of Advanced Mechanical Design, Systems, and Manufacturing, 2, 4, 540-549, (2008)

[3] M. Nakamura, T. Goto, T. Sumomogi: The Effect of the Crystallographic Direction on Crack Generation in Ductile Mode Machining of Single-Crystal Silicon, Journal of the Japan Society for Precision Engineering, 69, 12, 1754-1758, (2003) (in Japanese).

IMPROVING SURFACE QUALITY OF THIN-WALLED DOUBLE SIDE ASPHERIC COMPONENT BY MACHINING PROCESS AND MEASUREMENT OPTIMIZATION

Jun Zha[1*], Jing Chu[1], Yaolong Chen[1] and Yipeng Li[1]
[1]School of Mechanical Engineering
Xi'an Jiaotong University
Xi'an, Shaanxi, China

ABSTRACT

For improve the surface quality of thin-walled double side aspheric component, two machining processes with different cutting tools and two precision measurement methods were conducted to evaluate the optimization method. Firstly, a cemented carbide ball end milling tools were used for semi-finish and finish machining the thin-walled double side aspheric component. And the surface quality were evaluated by the coordinate measuring machine measured data. Then, a diamond radius end milling tool was chosen for the semi-finish and finish machining processes in the second experiment. The CAD module was employed in coordinate measuring machine for research the surface quality. The results show that diamond radius end milling tool has an improved performance in obtaining high precision surface quality, and assisted CAD module makes the measurement results more precision.

INTRODUCTION

Due to the geometrical complexity and high-requirement accuracy of aspheric surface, the machining and measurement are still a common challenge in industry[1-3]. Successful machining of aspheric surface not only relies on the high precision of machine tools, but also largely depends measurement method[3]. Until now, the machining and measurement for single side aspheric surface have been investigated by many researchers[1-5], and lots of valuable approaches have been proposed. However, research on double side aspheric components are rarely reported in literatures. The thin-walled double side aspheric components have various applications in aerospace, illumination, and new energy fields. However, some obstacles exists nonetheless discourage efforts to improve surface quality of the thin-walled double side freeform components, such as the machining process optimization, clamping method, vibration caused deformation during the machining process and the accuracy measuring method. The aim of the present work is to obtain the thin-walled double side aspheric component with high surface quality. In this paper, two machining processes with different cutting tools and two measurement methods were used and the measured surface quality were compared.

THIN-WALLED DOUBLE SIDE ASPHERIC COMPONENT MODEL

To describe an aspheric component with a symmetrical optical axis of z, the curved surface of the component with respect to the position axis x, y, which is perpendicular to the optical path can be expressed as:

$$z = \frac{c_x x^2 + c_y y^2}{1 + \sqrt{1-(1+k_x)c_x^2 x^2 - (1+k_y)c_x^2 y^2}} \qquad (1)$$

In Eq.(1), the radius curvature at the vertex of the aspheric curve are defined as r_x, r_y and the eccentricity are given as e_x, e_y, then c_x=1/r_x, c_y=1/r_y, and $k_x = 1-e_x^2$, $k_y = 1-e_y^2$.

According to the described function, the model was given as Figure 1(a) shown. But it can't be applied for the machining processes because of poor rigidity and localizability. So, a new model contained two auxiliary supporters as shown in Figure 1(b) was established.

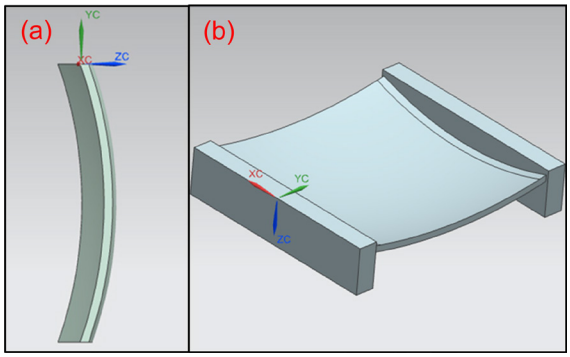

FIGURE 1. Thin-walled double side aspheric component model

EXPERIMENTS

Experiment Setup

The DMG HSC linear 75 precision machining center was adopted to conduct the experiments, as shown in Figure 2. Repositioning accuracy for three linear axes and two rotation axes were 3 μm and 5 sec, respectively. Two milling experiments with different tools in the semi-finish and finish machining processes were carried out respectively to determine the better one.

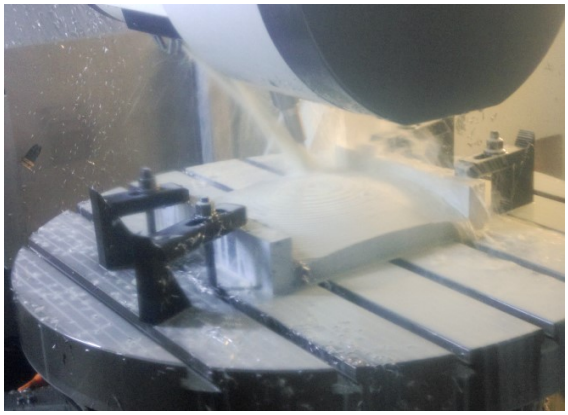

FIGURE 2. Experiment setup for machining

Experiment 1

The 6061-T651 aluminum alloys instead of K9 glass was used to machining the thin-walled double side aspheric surfaces. In the first milling experiment, a cemented carbide end milling tool with three cutting edge of diameter 22 mm and helix angle 50° was used for thin-walled double side aspheric component rough milling with the following machining parameters (spindle speed n=6000 rpm, feed rate f_z=0.3 mm/z, cutting width a_c=1.1 mm, machining allowance is 0.6 mm). The cutting tool adopted for semi-finish and finish milling was a cemented carbide ball end milling tool with four cutting edge of diameter 12 mm and helix angle 35°. Equal error step length and step distance approach were adopted to determined semi-finish machining parameters (spindle speed n=12000 rpm, feed rate f_z=0.3 mm/z, cutting width a_c=0.2 mm, cutting depth a_p=0.3 mm) and finish machining parameters (spindle speed n=12000 rpm, feed rate f_z=0.125 mm/z, cutting width a_c=0.05 mm, cutting depth a_p=0.05 mm). The Semi-finish machining was implemented by hierarchical processing method. The finished thin-walled workpiece was shown in Figure 3.

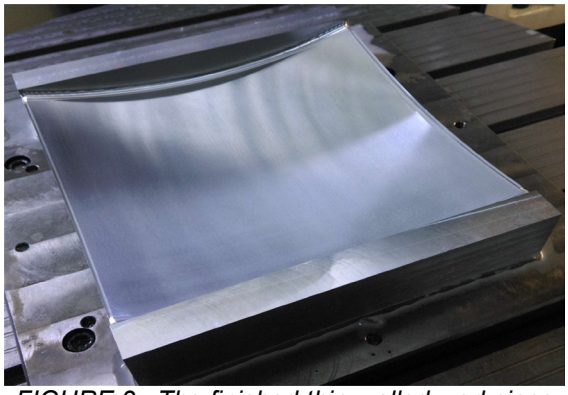

FIGURE 3. The finished thin-walled workpiece

Surface quality measurement 1

After the milling processes of thin-walled double side aspheric component, the surface quality was measured by a ultra-precision coordinate measuring machine which measurement error in any position was within 0.3+L/1000 μm using the contacted scanning method, as the Figure 4 shown. The measured data were analyzed by MATLAB. The peak-valley value for the concave and convex surface are 12.16 μm and 11.34 μm, respectively. And the corresponding RMS are 6.75 μm and 5.93 μm, the results were shown in Figure 5.

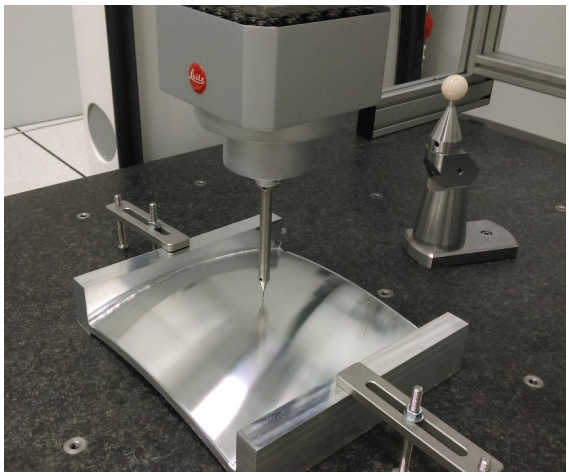

FIGURE 4. Surface quality measurement by coordinate measuring machine

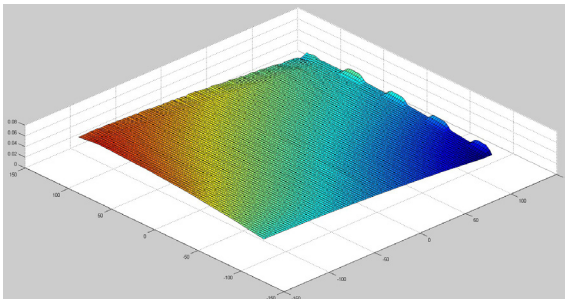

(a) Error distribution of concave surface

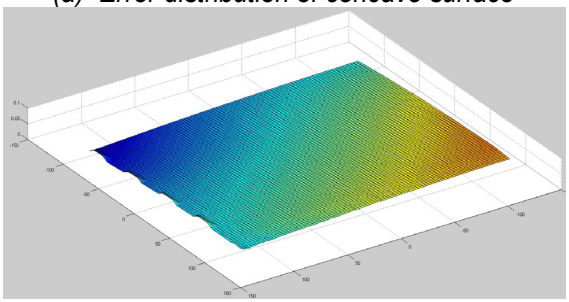

(b) Error distribution of convex surface

FIGURE 5. Error distribution by contacted scanning method

Experiment 2

The experiment results in above section shows that the PV form errors and the RMS form errors was bigger than 10 μm and 5 μm, respectively, that goes beyond the accuracy requirements. Which means the error distribution was uneven. In this section, the cutting tool was changed and the measurement method was optimized for the thin-walled double side aspheric component machining and surface quality evaluation.

In the second milling experiment, the rough machining process had the same cutting tool and machining parameters with the first experiment. The cutting tool adopted for both semi-finish and finish milling is a diamond radius end milling tool with four cutting edge of diameter 12 mm and helix angle 35°. Equal error step length and step distance were adopted to determined semi-finish machining parameters (spindle speed n=15000 rpm, feed rate f_z =0.5 mm/z, cutting width a_c=0.3 mm, cutting depth a_p=0.5 mm). Semi-finish machining process was implemented by hierarchical processing. The finish machining parameters are as follow(spindle speed n=15000 rpm, feed rate f_z =0.2 mm/z, cutting width a_c=0.035 mm, cutting depth a_p =0.1 mm).

Surface quality measurement 2

The measurement error of aspheric surface quality with ultra-precision three coordinate measuring machine, mainly consists of position deviation and angle deflection between the theoretical and actual coordinate system. In this section , the CAD surface measurement module was used to solve the issues. In the measurement system, the measurement coordinate system was establish based on the model of workpiece. The measured peak-valley value for the concave and convex surface are 8.53 μm and 7.12 μm, respectively. And the corresponding RMS are 2.45 μm and 3.04 μm, the results are shown in Figure 6.

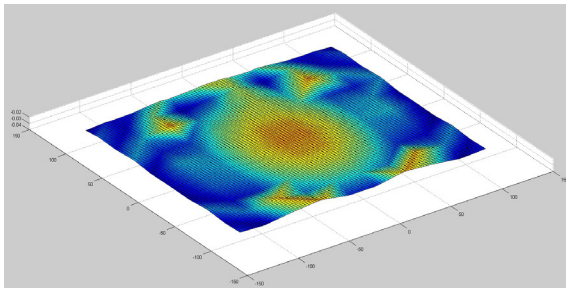

(a) Error distribution of concave surface

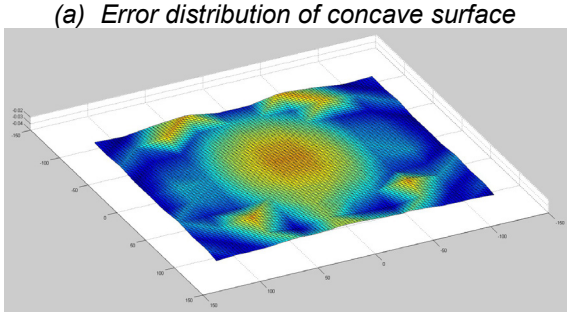

(b) Error distribution of convex surface

FIGURE 6. Error distribution by CAD module

CONCLUSIONS

In this paper, two machining experiments for thin-walled double side aspheric component using a five-axis precision machining center were described, and the measurement method were performed. The main results are as follows: The machining process with diamond radius end milling tool could obtain higher surface quality than cemented carbide ball end milling tool. The surface quality could be more accurate with assistance of the CAD surface measurement module. The PV values from 12.16 μm and 11.34 μm could be significantly improved to 8.53 μm and 7.12 μm, the RMS values from 6.75 μm and 5.93 μm could be significantly improved to 2.45 μm and 3.04 μm, with the optimized measurement method.

ACKNOWLEDGEMENT

This work was supported by the National Science and Technology Major Project of the Ministry of Science and Technology of China (2017ZX04013001).

REFERENCES

[1] El-Hayek N, Anwer N, Nouira H, et al. 3D Measurement and Characterization of Ultra-precision Aspheric Surfaces. Procedia CIRP. 2015; 27: 41-46.

[2] Cheung C F, Kong L B, Ren M J, et al. Generalized form characterization of ultra-precision freeform surfaces. CIRP Annals-Manufacturing Technology. 2012; 61(1): 527-530.

[3] Kong L B, Cheung C F, Lee W B, et al. An Integrated Manufacturing System for the Design, Fabrication, and Measurement of Ultra-Precision Freeform Optics. IEEE transactions on electronics packaging manufacturing. 2010; 33(4): 244-254.

[4] Henselmans R, Cacace L A, Rosielle P, et al. Design, realization and testing of the NANOMEFOS non-contact measurement machine for freeform optics. Proceedings of ASPE 2008 Annual Meeting, October 19 - October 24, 2008, Portland, Oregon, USA.

[5] Savio E, De Chiffre L, Schmitt R. Metrology of freeform shaped parts. CIRP Annals-Manufacturing Technology. 2007; 56(2): 810-835.

Arthors Index

Aarts, Ronald Godfried Karien Marie 398
Abe, Tatsuki 657
Abolbashari, Mehrdad 121, 272
Ahlen, Steven P. 208
Alagbe, Onaopemipo P.O. 147
Allgood, Kim 139
André, Johan 520, 524
Anton, Jayson 403
Arneson, David A. 352, 378, 528, 583
Arneson, Henry D. 583
Arneson, Samuel 352
Arumugam, Kumar 253
Austin, Sydney 109
Azari, Mohammad 121
Azimi, Farzad 204
Baade, Rick 433
Babaie, Jonathan 272
Badrawy, Sinan Joerg 158
Barada, Andrew H. 147
Barnay, Nicolas 520
Barron, Isaac 133
Bauer, Aaron M. 133
Bauza, Marcin B. 261
Biskach, Michael 139
Bixler, Jay V. 246, 417
Blaser, Philip 531
Bordatchev, Evgueni V. 647
Boyce, Brad 574
Brinksmeier, Ekkard 175
Brouwer, Dannis Michel 46, 398
Bruccoleri, Alexander R. 299
Brunelle, Matthew 198
Buice, Eric S. 208
Cao, Andrew. 103
Caskey, Gregory W. 90
Castro, Carlos 602
Chavez, Tom 36
Chen, Junyin 407
Chen, Shih-Chi. 99, 393, 412
Chen, Yaolong 257, 407, 422, 427, 663
Cheok, Gerry 281
Cherukuri, Harish P. 615
Cheung PhD, Chi-Fai 186, 219
Chicanne, Cedric 520, 524
Chizari, Samira. 109
Choi, Doo-Sun 578
Choi, Junoh 36
Chu, Jing 663
Claybaugh, Todd M. 208
Colonna de Lega, Xavier 20
Cong, Hongdong 257, 422, 427
Connolly, Liam G. 355
Cook, Adam W. 36
Copenhaver, Ryan 537
Cournoyer, Luc. 281
Crosby, Kyle 261
Cuadra, Jefferson A. 267
Cullinan, Michael Arthur 103, 170, 341
355, 504, 514
Dai, LuYao 439
Davies, Angela D. 241, 290
Davies, Matthew A. 133, 180, 558, 624
de Groot, Peter J. 20
DeDemo, Gregory 524
Delldonna, Kyle 20
Diantonio, Christopher B. 36
Ding, Si Q. 326
Dinh, Pham Van 474
Divin, C. 267
Doek, Cho-Eun. 214
Dong, Xin 52
Dow, Thomas A. 15
Dresel, Thomas 20
Duan, Molong. 478
Duan, Yutong 208
Duiven, Martijn 68
Dumanli, Ahment Alper. 57, 445
Dupont, Ralf 192
Dutterer, Brian S. 133
Eberle, Anna L. 261

Echter, Michael A. 360
Egashira, Kai 508
Elmadih, Waiel 164
Enstrom, Kenneth G. 489
Evans, Christopher J. 72, 90, 241, 315
Fan, Chunjie 451
Farahi, Faramarz 121, 272
Farahi, Navid 272
Fay, Martin F. 20
Fedorynenko, Dmytro. 585
Ferralli, Ian 198
Fess, Edward 180
Fujiyoshi, Kunitaka 305
Furutani, Katsushi 543
Garbowski, Tomasz 261
Garrard, Kenneth P. 15
Gauch, Daniel 593
Geng, Qiang 99
Gilfoy, Nathan. 20
Goch, Friedrich Gert. 151, 332, 553
Gomez, Michael 90, 547
Gregoire, Alexis 520, 524
Gregory, DeDemo 524
Greis, Noel 606
Groover, Jesse 117, 286, 553
Gu, Tian 95
Guenther, Anke 151
Gumerlock, Karl L. 147
Gurganus, Dustin K. 558
Habibi, Nasim. 121
Hains, Christopher 95
Hama, Tadashi 456
Hamel, Joshua 180
Han, Lin 257
Hansen, Hans Nørgaard 293
Harvey, Christopher 489
Hassan, Mohammed 615
Hayashi, Akio 585, 651
Heigel, Jarred. 547
Heilmann, Ralf K. 299
Henselmans MsC, Rens 68
Heo, Segon 620
Her, Tsing-Hua 253
Hernandez-Becerro, Pablo. 531
Hertz, Edward 299
Heysiattalab, Saeed 127
Ho, Lai-Ting 186
Honeycutt, Andrew 547, 562, 568
Hopkins, Jonathan B. 109, 514
Horvath, Nicholas. 133
Hovis, Clark D. 72
Hu, Jeujun 95
Hunt, William E. 417
Huttenhuis, Stephan. 593
Hwang, Jooho 620
Ihara, Tohru 630
Ikeno, Jun-ichi 657
Imura, Ryousuke 311
Jackson, John L. 246
Jain, Vijay Kumar 498
James, Justin H. 147
Jared, Bradley H. 36, 95, 574
Javidpour, Farid 78
Jaycox, Adam W. 366
Je, Tae-Jin 578
Jeon, Eun-Chae 578
Jeon, Seongkyul. 276, 346
Jeong, Ji-Young 578
Jia, Zhe 326
Johnson, Tyler 147
Kakutani, Shunsuke 508
Kang, Wenjun. 84
Karim, Shah 372
Kasai, Shimpei 494
Katsuki, Akio. 305
Kearney, John 139
Kearney, Steven. 403
Keeler, Gordon A. 95
Keller, Eric E. 583
Kim, Gyu Ha. 346
Kim, Gyung-Bum 214
Kirigaya, Rei. 585
Knapp, Byron R. 352, 378, 528, 583
Kossack, Christoph A. 462
Kuzmenko, Paul J. 246, 417
Ladner, Ian S. 103, 514

Lambropoulos, John C. 180
Lament, Mark 602
Lane, Brandon M. . . . . . No Abstract Available
Lawrence, Conner 90
Lawton, Kevin M. 366, 382
Leach, Richard K.. . . . . 164, 372
Lee, ChaBum 276, 346
Lee, Chan-Hong. 474
Lee, Hoon-Hee. 387
Lee, Jae-Chang 387
Lee, Je-Ryung 578
Lee, Lance 147
Lee, Vincent 281
Lee, Wing Bun 186
Li, Aiguo 403
Li, Chenglin 393, 412
Li, Duanhui. 95
Li, Lan 95
Li, Xin 439
Li, Yipeng 663
Liang, Dongxu 403
Liesener, Jan 20
Little, Steve 246
Liu, Samuel 219
Ludwick, Stephen J.. 46
Madison, Jon D.. 574
Maness, Chase 90
Mao, Chengwen. 403
Marsh, Eric R. 583
Mashrafi, Sheikh T.. 468
Maskery, Ian. 164
Masui, Shuzo 113
Matsumoto, Yuki. 113
Matsuyama, Satoshi. 143, 597
Mayr, Josef. 531
Mazzarella, James 139
Medicus, Kate M. 198
Meyer, Daniel 624
Michihata, Masaki. 113
Miller, Bill K. 95
Milliken, Nicolas 647
Mirkarimi, Paul 246
Miyazaki, Toshinobu. 597
Mohammadi, Hossein 589
Montaño, Joshua D.. . . . . 236, 321
Montesanti, Richard C.. . . . . 246, 417
Morse, Edward P.. . . . . 78, 84, 127
Mullany, Brigid A. 204, 615
Murakami, Hiroshi 305
Muralikrishnan, Bala. 223, 281
Murray, Carson. 90
Nagata, Ryosuke 305
Nakano, Takeshi. 508
Nakao, Yohichi 585, 651
Namba, Yoshiharu Y. 636
Natsume, Yudai 311
Naves, Mark. 398
Nayfeh, Samir Ali 24
Ni, Kang 151
Nicholas, Josep 147
Niehaus Dr.-Ing., Frank 593
Nikroo, Abbas. 602
Nuij, Pieter W. J. M. 68
Okwudire, Chinedum E. 46, 478, 483
Osier, Ted O. 147
Oss, Daniel D. 352, 378
Ostien, Jake 574
Ota, Minoru 508
Overschie, Peter Mark 40
Owen, Joseph D. 133, 180, 558, 624
Paap, Scott M. 95
Pan, Yaolin 403
Panas Ph.D., Robert Matthew 267, 489
Park, Sang-Hyun 337
Parks, Robert E.. . . . . 117, 286
Patel, Divyansh 498
Patten, John A.. 589
Patterson, Steven R. 366, 382
Peijnenburg, Antonius T. 46, 433
Peng, Yue. 151
Peterson, Michael E. 360
Piano, Samanta 372
Porter, Michael 109
Pouyafard, Ali. 290
Preissner, Curt 468
Priest, Robert E.. . . . . 246, 417
Quagliotti, Danilo 293
Rachakonda, Prem Kumar. 223, 281

Ramkumar, Janakrajan 498
*Ravindra Ph.D., Deepak . . No Abstract Available
Reese, Zachary 72
Reinholtz, William. 36
Riemer, Oltmann 175
Rijlaarsdam, David J. 68
Riveros, Raul Eduardo 139
Ro, Seung-Kook. 620
Robert, Aymeric 147
Rodelas, Jeff 574
Rolland, Jannick P.. 133
Ross, James 180
Roy, Nilabh Kumar 170
Ryokume, Reiji 597
Saavedra, Michael P. 36, 95
Saha, Sourabh K.. 103
Saiz, David J. 36, 574
Sajima, Takao. 305
Sakamoto, Haruhisa. 642
Salapaka, Srinivasa 468
Salzbrenner, Brad 574
Sano, Yasuhisa 143, 597
Sato, Kaiji 456
Satyanarayana, Harsha 230
Savage, Luke 602
Sawyer, Daniel S.. . . . . 223, 281
Schafer, Donald 147
Schattenburg, Mark Lee. 299
Schiesser, Eric 133
*Schlamminger, Stephan . . No Abstract Available
Schmitz, Tony L.. . . . . 90, 230, 462, 537
547, 562, 568, 606
Schmuetz, Joerg 609
Schönemann, Lars 175
Schunck, Julien 524
Sencer, Burak. 57, 445
Seugling, Richard M. 602
Shahinian, Hossein 72, 815
Shanmugam, Prithiviraj 180, 624
Shaw, Lucas. 109
Shi, Hongliang 147
Shilling, K. Meghan 281
Shim, Jongyoup 620
Shimada, Shoichi 311
Shu, Deming 403
Silver, Mark J.. 360
Sizemore, Nicholas E. 180, 558, 624
Smith, Brian E.. 147
Smith, Stuart T.. . . . . 30, 253, 451
Sodetai, Tomoki 494
Solly, Peter 139
Song, Adam 514
Song, Chang Kyu 474
Song, Jungki 299
Song, Xiaoqi. 630
Spaan-Burke, Theresa 40
Spaan, Henny A. M.. 40
Steinbuch, Maarten 433
*Stocker, Mark A. . . . . No Abstract Available
Suit, Brandon M. 15
Sun, Xinyao 407
Sun, Yanwen 147
Suzuki, Hirofumi Y.. 636
Suzuki, Yuki 113
Sweatt, William C. 95
Swiler, Laura P. 574
Syam, Wahyudin P. 164
Takahashi, Hideaki 636
Takahashi, Satoru. 113
Takahashi, Yukio 630
Takamasu, Kiyoshi 113
Tamagawa, Tomoyuki 311
Tanaka, Hayate 642
Tanaka, Hidetake 642
Tarbutton, Joshua. 451
Tauhiduzzaman, Mohammed 647
Tauke-Pedretti, Anna 95
Thalkar, Mahesh. 498
Thelin, Paul A. 246
Theobald, Marc 520, 524
Tolley, Martin 372
Tosello, Guido 293
Trumper, David L.. 63
Tsuchiya, Takahiro 543
Tutunea-Fatan, Remus R. 647
Uchiyama, Kosuke 305

Uda, Yutaka 311
Underwood, Olivia D. 574
Uphaus, Timothy M. 489
Uwakwe, Michael 315
Vaccaro, Colleen 90
Valdez, Lucas M. 236, 321
Valdez, Mario O. 236, 321
van Dam, Thomas 40
Vargas, Luis 90
Vargas, Richard J. 602
Verbaan, Kees 68
Verdirame, Justin M. 24
Villarraga-Gómez, Herminso 30
Wang, C. J. 186, 219
Wang, Dien 99
Wang, Ji 412
Wang, Jindong 127
Wang, Lei J. 326
Wang, Ling 223
Wang, Qichang 332
Ward, Martin 504
Watkins, Joel A. 246
Wegener, Konrad 531
Whitney, Randy A. 147
Whitsitt, Rebecca 198
Wiessner, Moritz. 531
Winrow, Edward G. 36
Woo, Siwoong 337
Wood, Michael 95
Xia, Ye 326
Yaguchi, Tsubasa 651
Yamada, Jumpei 143
Yamada, Yohei 657
Yamagishi, Hiroki 543
Yamaguchi, Keishi 508
Yamamoto, Takahiko 305
Yamauchi, Kazuto 143, 508, 597
Yan, Jiwang 494
Yan, Shuai 403
Yang, Seung-Han 387
Yao, Tsung-Fu 341
Yasuda, Shuhei 143
Ye, Wei N. 326
Yoon, Deokkyun 478, 483
Yoon, Jun Young 63
Young, Benjamin 204
Yoxall, Brian E. 246, 417
Zeng, Bowen 483
Zha, Jun 407, 663
Zhang, Bin 241
Zhang, Chengyong. 257, 422
Zhang, Lin 147
Zhang, Ming 326, 439
Zhang, Penghai 427
Zhang, William W. 139
Zhang, Zhanyu 407
Zhao, Cheng 514
Zhao, Rui 276
Zhu, Diling 147
Zhu, Yu 326, 439
Ziegert, John C. 117, 241, 272, 286
462, 537, 606
Zolfaghari, Abolfazl. 276, 346

Volume 67
ISBN 978-1-887706-74-2